Reinhart Poprawe
Constantin Häfner
Rolf Wester *Editors*

Tailored Light 2

Laser Applications

Second Edition

Springer

RWTHedition

The RWTH Aachen University, founded in 1870, today is one of Germany's leading universities of technology. In particular its engineering sciences enjoy a strong reputation in the scientific community and in industry on a national and an international level, and this is also true for the science faculty with its departments of biology, chemistry, physics, mathematics and computer science. The university profile is completed by the faculties of Arts and Humanities, Business and Economics and, last but not least, the Faculty of Medicine. The general focus of Aachen University is on interdisciplinarity, and its broad profile is ideal for tackling cross-cutting research issues addressing global challenges.

The RWTH Aachen University and the Springer-Verlag Publishing House have recently signed a cooperation agreement for the publication of selected works of authors from the RWTH Aachen University in a special English-language series named the "RWTHedition". The series evolved from the long-standing, fruitful cooperation between the two partners and its purpose is to foster the dissemination of cutting-edge research results to the international scientific community on a lasting basis, thus raising the international visibility of the university and facilitating scientific exchange worldwide.

Reinhart Poprawe · Constantin Häfner · Rolf Wester
Editors

Tailored Light 2

Laser Applications

Second Edition

Springer

Editors
Reinhart Poprawe
Chair for Laser Technology RWTH Aachen
University
Aachen, Germany

Rolf Wester
Fraunhofer Institute for Laser Technology
Aachen, Germany

Constantin Häfner
Fraunhofer Institute for Laser Technology
RWTH Aachen University Chair for Laser
Technology
Aachen, Germany

Preface

LASERS have exerted an incredible fascination since their invention. Everyone knows the word LASER associates it with directional light. What is less well known is that the abbreviation LASER actually stands for "Light Amplification by Stimulated Emission of Radiation." Laser light is the form of energy of the highest quality: directional, focusable in space and time, and transmitted at the highest velocity known to our universe: the speed of light. Laser light can be focused to physical limits in various dimensions: in space down to the laser light wavelength, in the time domain to the length of a single oscillation period equal to a few femtoseconds, and in frequency to bandwidths less than 1 kHz. Lasers are now ubiquitous in our daily lives and are key technology in a wide range of markets. The laser has not only enabled many fantastic and novel discoveries in science but also paved the way for numerous industrially and societal relevant innovations in our modern world.

We have paraphrased the credo of this book with the title "Tailored Light". The extraordinary breadth of parameter choices for individual laser sources and the associated precision allows these properties to be tailored to the requirements of the particular application process. As a result, lasers can now be found in almost all areas of social and economic life worldwide. With new applications emerging every year, the technology is a key driver of innovation, not only bringing economic benefits but also increasingly enabling the tackling of global challenges in alternative energy, mobility, and health.

The roots of this book can be found in a script of a laser course at RWTH Aachen University in the late 1990s. The book is divided into two parts, physical fundamentals of laser materials processing and engineering applications in a broad field of manufacturing and production engineering.

The book draws on more than 35 years of experience in the development of laser technology and laser processes developed by the staff of the RWTH Chair of Laser Technology and the associated Fraunhofer Institute for Laser Technology ILT. They are listed as authors in the individual chapters and great thanks are due to them for their efforts away from the daily challenge of developing innovative solutions for science, technology, and industry. This book provides an insight into the diversity and flexibility of laser applications and processes and thus contributes to the global

competitiveness of the application of laser technology and the development centers as competent partners of the innovators of this world.

Aachen, Germany   Reinhart Poprawe
                                                                        Constantin Häfner
                                                                              Rolf Wester

Contents

Part I
Physical Basics

Chapter 1
Physical Basics

Rolf Wester

1.1 Introduction

The first laser was presented by THEODORE MAIMAN in the year 1960 (Maiman 1960). Since 1963, the interaction of laser light with matter and its applications in the field of material processing are under ongoing investigation (Ready 1963; Linlor 1963). Today, a large array of laser material processing schemes are applied in industrial production. Although today material processing with laser light is used by engineers and technicians, there are still many physicists involved in the further development of lasers and laser material processing. This is due to historical reasons and the fact that laser material processing only recently found its way into the engineering sciences and that lasers are still opening up new fields of applications. Among other things, additive processes and fields of application for ultra short pulse lasers should be mentioned here. The physical processes that are involved in the interaction of laser light with matter are quite complicated and are still not fully understood. So laser technology remains being a challenge for physicists and also will be so in the future.

In Fig. 1.1, the processes during material processing with laser light are depicted schematically. The parameters listed comprise only a small part of all the influencing variables that are involved. Besides these parameters, dynamical processes in the workpieces like fluid dynamics and plasma formation have an important impact. With ultra short pulsed lasers, further physical processes like multiphoton absorption have to be considered. Processes with such a large number of influencing parameters cannot be optimized just by trial and error but make mandatory a fundamental inves-

R. Wester (✉)
Fraunhofer ILT, Aachen, Germany
e-mail: rolf.wester@ilt.fraunhofer.de

laser

plasma jet

melt

laser beam
wavelength
power
pulse duration
beam quality
polarization
mode order
spatio-temporal fluctuations

beam shapping
focus length
aperture
aberrations

material properties
absorption
heat conductivity
density
heat capacity
melt enthalpy
evaporation enthalpy
work piece geometry

dynamical processes
melt:
- surface tension
- viscosity
vapor:
- vapor density
- electron density
- temperature (and gradients)
- plasma absorption

Fig. 1.1 The minimum possible beam radius on the workpiece is determined by the laser wavelength, the laser beam quality and the focusing optics. The absorption of the laser radiation in the workpiece depends on the wavelength-dependent material properties and the characteristics and geometry of the workpiece surface. The absorbed radiation causes heating, melting and evaporation of the material. The melt is driven by shear stresses (gradient of surface tension or gas jet) and by pressure forces. The pressure forces can be caused by a gas jet or the off-flowing vapor. The vapor can absorb a substantial part of the laser energy and by this shield the workpiece against the laser beam

tigation of the underlying physical processes and their assured comprehension. The laser light hitting the workpiece is partly absorbed and partly reflected. The absorbed energy is given by

$$W_A = \int \int A(\lambda; I)\, I(\lambda, r, t)\, d^2r\, dt \qquad (1.1)$$

where $A(\lambda, I)$ is the intensity and wavelength-dependent absorption coefficient and $I(\lambda, r, t)$ the space- and time-dependent intensity at the wavelength λ. The absorption depends not only on the wavelength and polarization of the laser light but also on material properties and the characteristics and geometry of the workpiece surface. The beam cross section depends on the wavelength, the beam quality and the focusing optics. Because of heat conduction, a heat front moves into the material. The temperature in the workpiece depends on the absorbed intensity $I_{abs} = A_\lambda(I)\, I_\lambda$, the duration of the interaction t_p, the beam radius on the surface $2\, r_B$, the velocity v_p of the workpiece relative to the laser beam and the thermo-physical parameters of the material like heat conductivity K and heat capacity c:

$$T = T(I_{abs}, t_L, r_B, v_P, K, c) \tag{1.2}$$

After reaching the melting temperature, the melting enthalpy has to be supplied by the laser beam. During laser alloying, melt flow is forced by surface tension gradients. With processes like ablation or cutting with laser light, the melt is driven out by a gas jet supplied externally. With deep penetration welding, the melt flows around the pin hole and solidifies. Melt flow is thus an important physical process during many laser material treatment processes. With further increase, the material temperature evaporation sets in. The evaporation enthalpy has to be supplied by the laser beam too. The off-flowing vapor can reach pressures of up to 10^8 Pa. At these pressures, the melt can be driven out partly or totally. Material removal is in that case not only accomplished by evaporation but also by self-induced driving out of the molten material. This can save part of the evaporation enthalpy in the case of some material removal processes such as laser drilling.

The hot plasma can absorb a substantial part of the incident laser beam. The free electrons absorb energy from the laser field by the process of inverse bremsstrahlung and transfer part of this energy to the heavy particles like atoms and ions. By this, the atoms and ions are excited and ionized and their kinetic energy increases. The initially small number of free electrons grows exponentially. This further increases the absorption of the laser light. A part of the absorbed energy is transferred to the workpiece surface by radiation or by transport of kinetic, excitation or ionization energy. Plasma absorption can be so strong that no laser radiation reaches the surface any more. The plasma is further heated and expands rapidly. A laser driven shock-front is created that moves toward the laser beam. This case of total plasma shielding has to be avoided. On the other hand, the plasma can be utilized for the energy transfer in some cases; plasma supported energy transfer is used for all highly transparent media.

For a comprehension of the above-mentioned processes, a fundamental understanding of the underlying physical processes is of great importance. In Sect. 1.2, the interaction of electromagnetic radiation at material surfaces is treated, and the FRESNEL formulae and their applications are discussed. In Sect. 1.3, the absorption of non-electrically conducting materials, plasmas and metals is investigated. The influence of the temperature and the surface characteristics on the absorptivity of metals is discussed. Section 1.4 deals with the problem of heat conduction. Solutions of the heat conduction problem are discussed for some special cases that allow at least a qualitative understanding of the processes during material processing. In Sect. 1.5, some results of thermo-mechanics are presented. Elastic and plastic deformations are treated. In Sect. 1.6 phase transformations of steel, a still much used material, is discussed. In Sect. 1.7 the basics of flow dynamics are presented. In Sect. 1.8, several models for describing non-thermal equilibrium evaporation are outlined that allow to evaluate the density and pressure of the off-flowing vapor. In Sect. 1.9, some results of thermal equilibrium plasmas like the SAHA equation and transport processes in plasmas are compiled.

1.2 The Behavior of Electromagnetic Radiation at Interfaces

1.2.1 The FRESNEL Formula

Most of the processes that occur during the interaction of laser radiation with matter start at the surfaces. At small intensities, the interaction of the electromagnetic field with the material at the surface are determined by the FRESNEL formulae. The FRESNEL formulae describe the reflection and transmission of a plain harmonic wave incident on an infinitely extended ideal plane surface. Reflection r and transmission t of the field amplitudes are defined by the following relations:

$$r = \frac{E_r}{E_i} \tag{1.3}$$

$$t = \frac{E_t}{E_i} \tag{1.4}$$

with

E_i—electric field of the incident wave

$E_{r,t}$—electric field of the reflected and transmitted waves, respectively.

It has to be emphasized that the FRESNEL formula only describes the behavior at the surface; there is nothing said about the transmission or absorption within the specimen.

The FRESNEL formula can be deduced from the Maxwell equations considering the boundary conditions for the fields at the surface. It has to be distinguished between perpendicular ($\perp$) and parallel ($\parallel$) polarization. In the case of perpendicular polarization, the electric field vector is perpendicular to the plane that is spanned by the incident and reflected wave vectors respectively, whereas in the case of parallel polarization the field vectors are parallel to this plane. The wave vectors $\vec{k}_i$, $\vec{k}_r$ and $\vec{k}_t$ all lie in one plain. The vector of the electric field can have components perpendicular $\perp$ or parallel $\parallel$ to this plane. Reflection and transmission depend on the direction of the electric field vector relative to the plane of incidence (Fig. 1.2).

For practical applications, the polarization of the laser radiation is often chosen so that the field strength is either perpendicular ($\perp$) or parallel ($\parallel$) to the plane of incidence (in special cases, circular polarization is used). In these cases, the decomposition of the field vectors in their perpendicular and parallel components can be omitted and the mathematical treatment is simplified. Figure 1.3 shows the situation in the case of normal incidence.

The angle α that the wave vectors of the incident and reflected waves respectively make with the surface normal and the angle β of the refracted wave are connected by SNELL's law:

$$n_1 \, \sin \alpha = n_2 \, \sin \beta \tag{1.5}$$
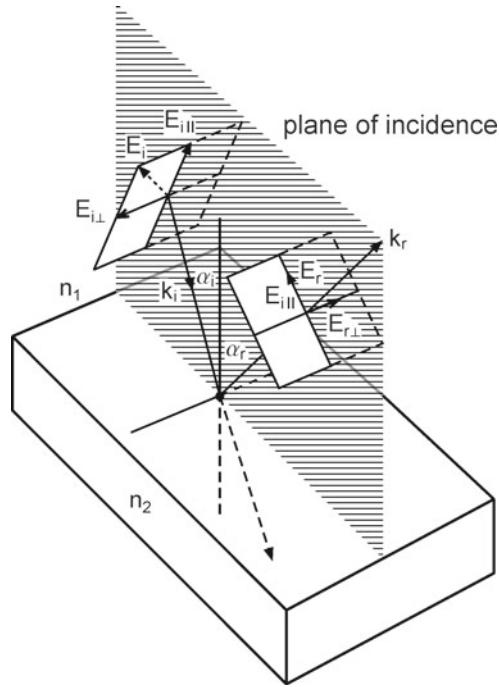
Fig. 1.2 Incident, reflected and transmitted beam lie in one plane. The electric field vector can be split into two components, one component is parallel and the other component is perpendicular to this plane
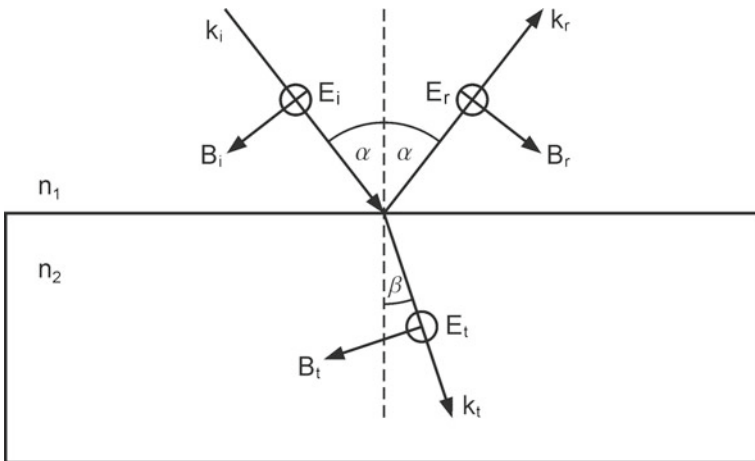
Fig. 1.3 Polarization perpendicular to the plane of incidence

n_1 and n_2 are the indices of refraction of the two media. The FRESNEL formulae for perpendicular polarization read (Jackson 1975)[1]:

$$\frac{E_r}{E_i} = r_s = \frac{n_1 \cos \alpha - \dfrac{\mu_1}{\mu_2} \sqrt{n_2^2 - n_1^2 \sin^2 \alpha}}{n_1 \cos \alpha + \dfrac{\mu_1}{\mu_2} \sqrt{n_2^2 - n_1^2 \sin^2 \alpha}} \tag{1.6}$$

$$\frac{E_t}{E_i} = t_s = \frac{2 n_1 \cos \alpha}{n_1 \cos \alpha + \dfrac{\mu_1}{\mu_2} \sqrt{n_2^2 - n_1^2 \sin^2 \alpha}} \tag{1.7}$$

with
$\mu_{1/2}$—magnetic permeability of media 1 and 2, respectively.

Figure 1.4 shows the situation for parallel polarization. The FRESNEL formulae for parallel polarization read (Jackson 1975)[2]:

$$\frac{E_r}{E_i} = r_p = \frac{\dfrac{\mu_1}{\mu_2} n_2^2 \cos \alpha - n_1 \sqrt{n_2^2 - n_1^2 \sin^2 \alpha}}{\dfrac{\mu_1}{\mu_2} n_2^2 \cos \alpha + n_1 \sqrt{n_2^2 - n_1^2 \sin^2 \alpha}} \tag{1.8}$$

$$\frac{E_t}{E_i} = t_p = \frac{2 n_1 n_2 \cos \alpha}{\dfrac{\mu_1}{\mu_2} n_2^2 \cos \alpha + n_1 \sqrt{n_2^2 - n_1^2 \sin^2 \alpha}} \tag{1.9}$$

In the case of normal incidence, i.e. $\alpha = 0$, the plane of incidents cannot be defined uniquely any more and the difference between $\perp$ and $\parallel$ polarization vanishes. In that case, Eqs. 1.6 and 1.8 as well as Eqs. 1.7 and 1.9 give the same results. The amplitudes of the reflected and transmitted waves in the case of normal incidence are given by

$$\frac{E_r}{E_i} = \frac{n_1 - n_2}{n_2 + n_1} \tag{1.10}$$

$$\frac{E_t}{E_i} = \frac{2 n_1}{n_2 + n_1} \tag{1.11}$$

When $n_2 > n_1$, the reflected wave undergoes a phase change of 180° (this holds for real indices of refraction).

---

[1] For a derivation, see Appendix A.1.

[2] For a derivation, see Appendix A.1.
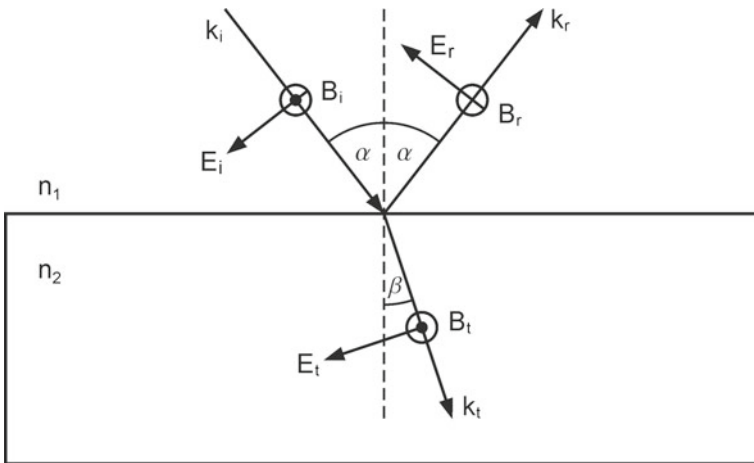
Fig. 1.4 The direction of the field vector of the reflected wave is often given in the opposite direction. In that case Eq. 1.9 has to be multiplied by -1

1.2.1.1 FRESNEL **Formulae with Absorption**

The FRESNEL formulae are valid for real as well as for complex indices of refraction. The imaginary part describes the absorption of the wave in the medium. In what follows, only the case will be discussed that n_2 is complex but n_1 is real. SNELL's law still applies but it has to be recognized that a complex value of n_2 implies that the angle β is complex-valued too[3] and so doesn't have a simple physical interpretation any more. The determination of the angle that the phase front normal makes with the surface normal in the case of complex n_2 is more complicated as in the case of real n_2.[4] For the determination of the coefficients of reflection and transmission the knowledge of this angle is not necessary, so its determination will be omitted here. The complex index of refraction can be written as

$$n_c = n + i\,\kappa \tag{1.12}$$

with
n—real part of the index of refraction n_2
κ—imaginary part of the index of refraction n_2 or absorption coefficient.

When the phase differences between the fields are not of interest, it is advisable not to use the amplitudes but the squares of the absolute values of the amplitudes:

---

[3] See Eq. 1.5.
[4] See BORN, WOLF Born and Wolf (1999).

$$R_s = |r_s|^2 \tag{1.13}$$
$$R_p = |r_p|^2 \tag{1.14}$$
$$T_s = |t_s|^2 \tag{1.15}$$
$$T_p = |t_p|^2 \tag{1.16}$$

The ratio of the squares of the absolute values of the amplitudes of two waves in the same medium equal the ratio of their intensities, R_s and R_p and thus give the ratio of the intensities of the incident and the reflected waves, respectively. Contrary to this, T_s and T_p don't equal the intensity ratio of the refracted and incident waves, respectively (a rigorous treatment of power conservation leads to the POYNTING vector which is given by the cross product of the $\vec{E}$ and $\vec{H}$ fields, respectively). For unpolarized radiation, it is as follows:

$$R = \frac{R_\perp + R_\parallel}{2} \tag{1.17}$$

Here, it is assumed that on an average the randomly distributed polarization directions are equally represented. The absorption coefficient A, defined as that part of the incident intensity that is not reflected, is given by

$$A = 1 - R \tag{1.18}$$

In the case of normal incidence and with $n_1 = 1$ and $n_2 = n + i\,\kappa$, R and T become

$$R = \frac{(n-1)^2 + \kappa^2}{(n+1)^2 + \kappa^2} \tag{1.19}$$

$$T = \frac{4}{(n+1)^2 + \kappa^2} \tag{1.20}$$

1.2.1.2 Analysis of the FRESNEL Formula and BREWSTER Effect

Because of SNELL's law, R and T as well as r and t are only functions of the angle of incidence α (with n_1, $n_2 = n + i\,\kappa$ and the radiation wavelength λ kept constant). Figure 1.5 shows $R_\perp(\alpha)$, $R_\parallel(\alpha)$ and $1/2(R_\perp(\alpha) + R_\parallel(\alpha))$ with $n = 1.5$ and $\kappa = 0$. It can be seen that $R_\perp(\alpha)$ is a monotonically increasing function of α, whereas $R_\parallel(\alpha)$ becomes zero at the BREWSTER angle α_B. At the BREWSTER angle α_B, the refracted and reflected wave vectors respectively are perpendicular to each other. The dipoles that oscillate in the direction of the incident wave vector cannot emit any power in that direction. This is the case if $\alpha + \beta = 90°$. With SNELL's law (Eq. 1.5), it is as follows:

$$\alpha_B = \arctan\left(\frac{n_2}{n_1}\right) \tag{1.21}$$
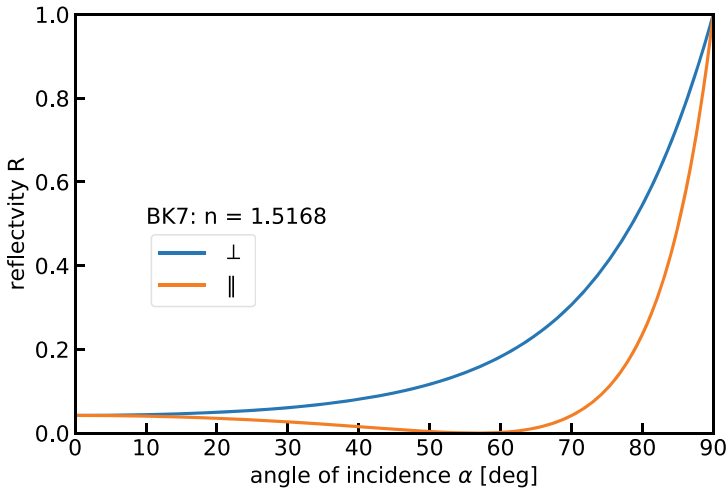
Fig. 1.5 Reflection in case of perpendicular, parallel and unpolarized light respectively as a function of the angle of incidence. $n_1 = 1$, $n_2 = 1.5$

Figure 1.6 shows the intensity reflectivity of the reflection at a metal surface for $\perp$ and $\parallel$ polarization respectively as a function of the angle of incidence. The reflectivity is much higher compared to Fig. 1.5. In the case of $\perp$, the reflectivity increases monotonically with increasing angle of incidence. Contrary to this behavior, the reflectivity in the case of $\parallel$ polarization decreases at first and only begins to increase above ca. 88°. The small reflectivity at this angle is caused by the BREWSTER effect although the reflectivity doesn't vanish as it does in case of non-dissipating media. When the real part of the index of refraction is zero, the reflectivity of $\parallel$ polarized light vanishes at the BREWSTER angle (see Fig. 1.5).

The BREWSTER effect can be utilized to polarize a light wave. Even when the angle of incidence doesn't equal the BREWSTER angle, the polarization plane is rotated in general. Figure 1.7 shows the electric field vectors before and after the reflection. The wave vectors point into the plane of the figure (in case of normal incidence, the two wave vectors are anti-parallel). The $\perp$ and $\parallel$ electric field components undergo a phase shift of 180°. In the direction of the respective wave vectors, this means that the vector of the parallel component keeps its direction whereas the vector of the perpendicular component reverses its direction. As a result the plane of polarization is rotated.

1.2.1.3   Total Reflection

When a wave is reflected at an interface with $n_2 < n_1$, the wave is totally reflected for angles of incidence greater than a limiting angle α_0 which is given by the condition $\beta = 90°$. With SNELL's law, it is as follows:
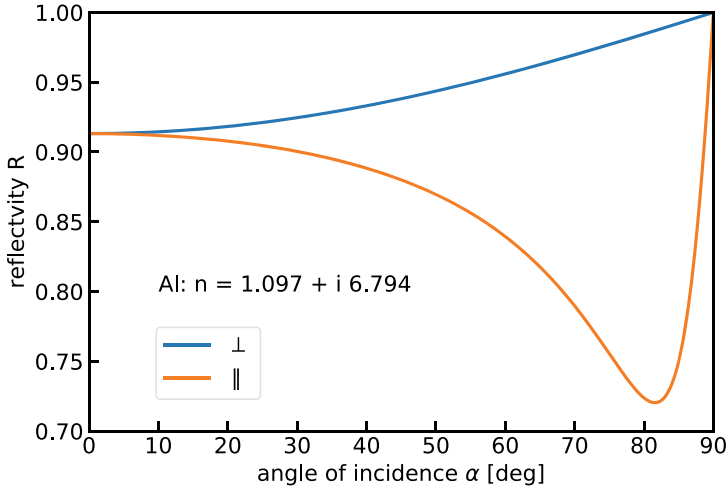
Fig. 1.6 Reflectivity in case of ⊥ and ∥ polarized light respectively as a function of the angle of incidence. $n_1 = 1$, $n_2 = 30 + i\,30$. The value of the index of refraction n_2 corresponds quite well to Al
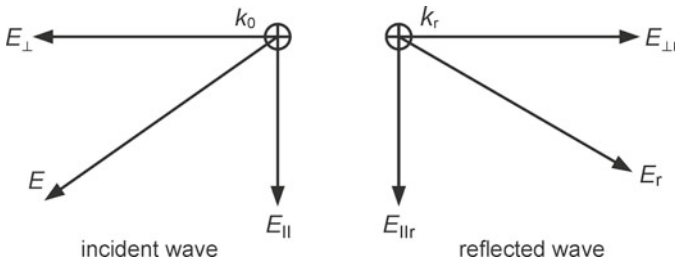
Fig. 1.7 Rotation of the plane of polarization during reflection at a denser medium

$$\sin \alpha_0 = \frac{n_2}{n_1} \tag{1.22}$$

$$\alpha_0 = \arcsin\left(\frac{n_2}{n_1}\right) \tag{1.23}$$

with $n_1 = 1.5$ (glass) and $n_2 = 1$ (air) $\alpha_0 = 42°$.

1.2.2 Applications of the FRESNEL Formulae in the Field of Laser Technology

In the field of laser technology in particular, the BREWSTER effect and total internal reflection are utilized.
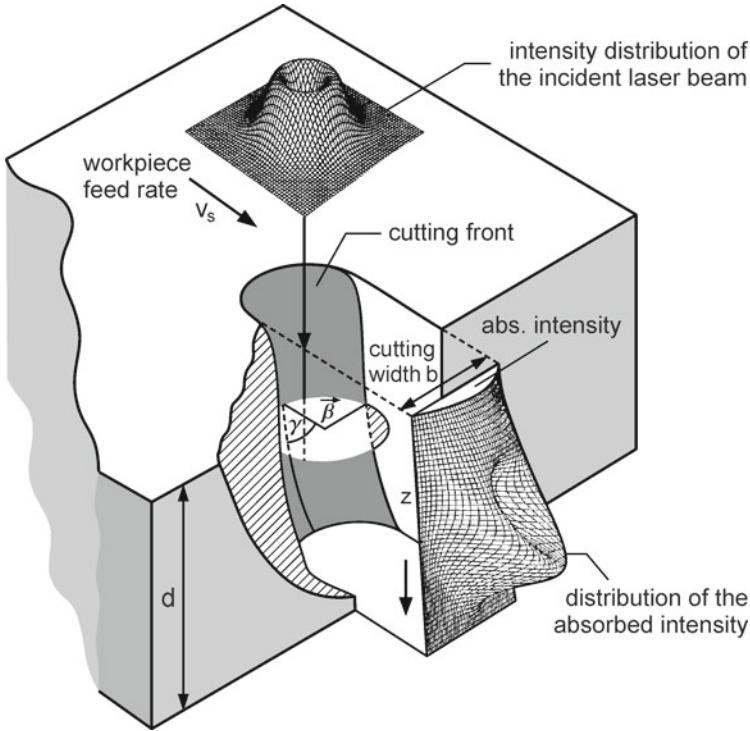
Fig. 1.8 Intensity distribution at a cutting front

1.2.2.1 BREWSTER **Effect**

The BREWSTER effect is exploited for

- polarization of the laser light
- minimizing reflection losses by the use of BREWSTER windows
- increasing the absorption during cutting, welding, etc. by the use of angles of incidence near the BREWSTER angle.

As an example for the utilization of the BREWSTER effect,[5] Fig. 1.8 shows the distribution of the absorbed intensity at the cutting front during laser cutting of Al. The distribution is the result of convolving the intensity distribution of the incident laser beam with the incident angle-dependent absorption coefficient A (Eq. 1.18).

---

[5] The BREWSTER effect occurs at the BREWSTER angle. The reduced reflectivity of ‖ polarized radiation at angles different from the BREWSTER angle often is called BREWSTER effect too.

1.2.2.2 Total Internal Reflection

Total internal reflection is predominantly used for beam guiding and shaping. Examples are

- low loss radiation transport through a fiber;
- cavity dumping.

1.3 Absorption of Laser Radiation

During material processing with laser radiation, the result of laser treatment is predominantly determined by the power that is absorbed within the workpiece. A measure of the power that is available for the material treatment process P_{abs} is the absorption A or absorptivity. The absorptivity is the ratio of power that is deposited within the workpiece and the power of the incident radiation:

$$A = \frac{P_{abs}}{P} \tag{1.24}$$

The absorptivity A can have any value between 0 and 1. The absorbed radiation energy is in general transformed to heat energy. This energy conversion can pass several stages that can possibly be utilized for material processing. The absorption of laser radiation can for example lead to the dissociation of molecules. Before this, no equilibrium state relaxes to an equilibrium state, i.e. transformation of the absorbed energy to heat energy, and the dissociated molecules can be removed. In that case material is ablated. The above-defined absorptivity is a global value that in general contains no information about where in the workpiece the radiation energy is deposited. In the case of metals, the absorption always takes place in a thin surface layer, i.e. the absorption is localized. This information is not included in A.

The absorptivity can be determined directly by measuring the power of the incident laser radiation and the temperature increase of the workpiece (with known heat capacity) or indirectly by measuring the power of the reflected light P_r and the power that is transmitted through the workpiece P_t, respectively[6]:

$$P_{abs} = P - P_r - P_t \tag{1.25}$$

If the radiation that is transmitted through the workpiece surface is totally absorbed within the workpiece, the absorptivity is given by

$$A = 1 - R \tag{1.26}$$

---

[6] Here, the transmitted power is defined as the power that is transmitted through the whole workpiece contrary to the definition in Sect. 1.2 where P_t is the power that is transmitted through the surface of the workpiece.

In the case of non-conducting materials or very thin metal films, part of the radiation that penetrates into the workpiece can leave the workpiece again. Describing this part by the transmittance T, it holds

$$A = 1 - R - T \qquad (1.27)$$

The parameters:

- index of refraction n
- index of absorption κ
- electric conductivity σ
- heat conductivity K and
- specific heat c

are material-specific parameters. They solely depend on the properties of the material at hand and the radiation wavelength, and can be calculated approximately for simple materials. The absorptivity not only depends on the material properties. Some further influencing factors are

- properties of the laser beam like wavelength, polarization, etc.
- the ambient conditions (process gas, material that surrounds the workpiece, etc.)
- the surface properties (roughness, morphology, etc.)
- the geometry of the workpiece (thickness, boundaries of the workpiece, etc.)
- the changes of the workpiece and the environment that is induced by the absorbed laser power (local heating, phase changes, laser-induced plasma).

1.3.1 Description of the Phenomena

The description of the interaction of electromagnetic radiation with matter can be done at different model levels. Matter consists of electrons and atomic kernels. For spatial dimensions $r \gg 10^{-15}$ m the atomic kernels can be considered to be point charges, and for spatial dimensions greater than the classical electron radius $r \gg r_0 \sim 2.8 \cdot 10^{-15}$ m the electrons can be considered to be point charges too. These point charges interact with electromagnetic fields and excite spatially and temporally fast fluctuating fields on their part. The interaction between electromagnetic fields and electrically charged particles is treated rigorously within the framework of quantum electrodynamics. The quantum theoretical treatment of electromagnetic fields leads to the concept of photons, i.e. there can be only an integer number of photons being emitted or absorbed. If the particles that interact with the electromagnetic fields are bound, these too can only absorb or emit certain energy quanta. In the framework of an atomistic model, this is described as the absorption of a photon and the creation of a phonon (energy quantum of lattice oscillations).

In the framework of a classical description, the spatio-temporal evolution of electromagnetic fields is described by the microscopic MAXWELL equations in vacuum interacting with point charges (positively charged atomic kernels and negatively

charged electrons). The atoms can be described as dipoles that are excited by the external radiation and that emit radiation on their part that interferes with the primary radiation. This process can be interpreted as coherent scattering. If radiation hits a surface of a solid, the radiation that is emitted by the dipoles at the solid surface consists of three parts. The first one corresponds to the reflected wave. The second one is emitted in the same direction as the incident wave. According to the EWALD-OSEEN extinction theorem (Born and Wolf 1999), modulus and phase of this wave are such that the incident wave and this wave extinct each other exactly within region 2 (see Fig. 1.3). The third part corresponds to the refracted wave.

A further level of describing electromagnetic phenomena is to average over macroscopic small but microscopic large spatial regions. In this way, one gets the macroscopic MAXWELL equations.[7] The macroscopic MAXWELL equations treat the matter as a continuum whose electromagnetic properties are described by material parameters. This parameters can either be measured or calculated using microscopic models. The macroscopic MAXWELL equations read:

$$\vec{\nabla} \times \vec{E} = \frac{\partial \vec{B}}{\partial t} \tag{1.28}$$

$$\vec{\nabla} \times \vec{H} = \vec{j} + \frac{\partial \vec{D}}{\partial t} \tag{1.29}$$

$$\vec{\nabla} \cdot \vec{D} = \rho \tag{1.30}$$

$$\vec{\nabla} \cdot \vec{B} = 0 \tag{1.31}$$

For a solution of these equations, one needs

- the relationship between $\vec{D}$ and $\vec{E}$ and $\vec{H}$ and $\vec{B}$ respectively as well as the relationship between $\vec{j}$ and $\vec{E}$ (these relationships describe the material behavior)
- the geometry of the workpiece and its environment
- the boundary conditions for $\vec{E}$, $\vec{D}$, $\vec{H}$ and $\vec{B}$.

In the following, space charges are neglected, i.e. $\rho = 0$.

1.3.1.1 Field Relationships

The relationships between $\vec{E}$ and $\vec{D}$ and $\vec{B}$ and $\vec{H}$ respectively are in general nonlinear. But in many cases of material processing with laser radiation, the relationships can be very well approximated by linear models. The relationships depend in general on the frequency of the radiation field. In case of time harmonic fields, the FOURIER transformed field quantities are related according to

$$\vec{D}(\vec{r}, \omega) = \varepsilon_0 \, \varepsilon(\omega) \, \vec{E}(\vec{r}, \omega) \tag{1.32}$$

$$\vec{B}(\vec{r}, \omega) = \mu_0 \, \mu(\omega) \, \vec{H}(\vec{r}, \omega) \tag{1.33}$$

---

[7] See JACKSON (1975), LANDAU, LIFSCHITZ (1984).

Many crystals have orientation-dependent material properties; these crystals are said to be anisotropic. In that case, the dielectric constant ε and the magnetic permeability μ are no longer scalar quantities but tensors. That means that the electric field $\vec{E}$ and the electric displacement $\vec{D}$ in general aren't collinear as is the case in vacuum and isotropic materials. This is associated with the phenomenon of birefringence. In the following anisotropic material behavior is neglected. The magnetic permeability μ only deviates significantly from the vacuum value 1 in case of ferromagnetic materials. In the following, it will be assumed that

$$\mu(\omega) = 1 \tag{1.34}$$

Inverse FOURIER transformation of Eq. 1.32 results in

$$\vec{D}\,(\vec{r}, t) = \vec{E}(\vec{r}, t) + \int_{-\infty}^{\infty} G(\tau)\,\vec{E}(\vec{r}, t - \tau)\, d\tau \tag{1.35}$$

$$G(\tau) = \frac{1}{2\,\pi} \int_{-\infty}^{\infty} [\varepsilon(\omega) - 1]\, e^{-i\omega\tau}\, d\omega \tag{1.36}$$

In Jackson (1975), it is shown that due to causality $G(\tau)$ vanishes for $\tau < 0$, i.e. the electric displacement $\vec{D}(t)$ at time t depends on the past history of the electric field $\vec{E}(t)$ but not on future values of $\vec{E}(t)$. Equation 1.35 is nonlocal in time but local in space. This local approximation only holds as long as the spatial scale of variations of the electric field are large compared to the scale of the atomic polarization. In case of dielectric materials with bound electrons, this holds as long as the wavelength of the radiation is large compared to atomic dimensions but in conductors the free path length of electrons can exceed the wavelength or penetration depth of the radiation fields.[8] This will not be considered further.

The material properties are accounted for in the MAXWELL equations by $\varepsilon(\omega)$. In case of small frequencies ε is constant. In this frequency region, the polarization of the medium instantly follows the electric field. At higher frequencies, the response of the material lags behind the temporal change of the electric field. At very high frequencies the material response vanishes. In frequency space, it holds

$$\lim_{\omega \to 0} \varepsilon(\omega) = \varepsilon_{\text{stat}} \tag{1.37}$$

$$\lim_{\omega \to \infty} \varepsilon(\omega) = \varepsilon_{\infty} \to 1 \tag{1.38}$$

---

[8] This is, for example, the underlying mechanism of the anomalous skin effect.

1.3.1.2 Wave Equation

With Eqs. 1.28, 1.29, 1.32 and 1.33, the wave equation

$$\vec{\nabla}\left(\vec{\nabla}\cdot\vec{E}\right) - \Delta\vec{E} = -\mu_0\epsilon_0\epsilon\frac{\partial^2\vec{E}}{\partial t^2} \tag{1.39}$$

results. In homogeneous media and with zero space charges, $\vec{\nabla}\cdot\vec{E} = 0$. With $\mu_0\epsilon_0 = 1/c^2$, Eq. 1.39 becomes

$$\Delta\vec{E} = \frac{\epsilon}{c^2}\frac{\partial^2\vec{E}}{\partial t^2} \tag{1.40}$$

A solution of this equation is the plane wave:

$$\vec{E} = \vec{E}_0\exp\left[i\,(k\,z - \omega\,t)\right] \tag{1.41}$$

with
k—complex wave number
ω—real angular frequency

the complex wavenumber is

$$k = k_0\sqrt{\epsilon} = k_0 n = k_r + ik_i \tag{1.42}$$

n is the complex index of refraction. The plane wave solution can also be cast into the form:

$$\vec{E} = \vec{E}_0\exp\left[i\,(k_r\,z - \omega\,t)\right]\exp\left[-k_i z\right] \tag{1.43}$$

If the imaginary part of the complex wavenumber $k_i > 0$, the wave decays exponentially within the material.

1.3.1.3 Geometry of the Workpiece

In most cases in textbooks, the temporal change of the geometry of the workpiece is neglected. In the following this approach will be adopted. But it has to be emphasized that during material processing, the geometry of the workpiece can change considerably due to melt flow and evaporation.

1.3.2 Isolators

The main difference between isolators on one side and plasmas and metals on the other side is that in isolators electrons are bound (at least as long as the incident intensities are below the threshold for ionization), whereas in plasmas and conductors the electrical properties are mostly determined by the free (or as in case of metal quasi free) electrons. The dielectric constant of isolators is composed of three parts:

- electronic polarization:
  the electrons are pulled away from their rest position at the atomic sites and oscillate around these points
- ionic polarization:
  differently charged ions are deflected with respect to each other, i.e. the effective ion charges of the crystal sub-lattices oscillate
- orientation polarization of permanent dipoles:
  permanent dipoles are aligned by the electric field (e.g. H_2O).

Orientation polarization is negligible for frequencies in the infrared region and above. Electronic polarization is the main mechanism in the near-infrared down to the X-ray region. Due to their larger mass, the oscillating frequencies of the ions are much smaller compared to the oscillating frequencies of the bound electrons. Because of this, the ionic part of the dielectric constant dominates in the infrared region. The polarization can be described by harmonic oscillators. Harmonic oscillators are characterized by their eigenfrequency ω_0 and by the damping constant δ. The deflection x of an oscillator with effective charge e^* with respect to its rest position induces a dipole moment:

$$p = e^* \, x \tag{1.44}$$

The equation of motion in frequency space of a harmonic oscillator subject to an external field reads:

$$-\omega^2 \, x(\omega) - i \, \delta \, \omega \, x(\omega) + \omega_0^2 \, x(\omega) = \frac{e^*}{m} \, E(\omega) \tag{1.45}$$

The dipole moment is thus

$$p = \varepsilon_0 \, \alpha(\omega) \, E(\omega) \tag{1.46}$$

$$\alpha = \frac{e^{*2}}{m \, \varepsilon_0} \frac{1}{\omega_0^2 - \omega^2 - i \, \delta \, \omega} \tag{1.47}$$

α is the polarizability. The polarization P is given by

$$P = \frac{N}{V} \, p \tag{1.48}$$

N/V is the density of harmonic oscillators, thus the polarization is given by

$$P = \frac{N}{V} \frac{e^{*2}}{m} \frac{1}{\omega_0^2 - \omega^2 - i\,\delta\,\omega} E(\omega) \tag{1.49}$$

The field strength in the above equation is the field strength at the atomic location. In general, this doesn't equal the average (averaged over microscopic large scales) field strength. With

$$P = \varepsilon_0 \, (\varepsilon(\omega) - 1) \, E(\omega) \tag{1.50}$$

it follows:

$$\varepsilon(\omega) = 1 + \frac{N}{V} \frac{e^{*2}}{m\,\varepsilon_0} \frac{1}{\omega_0^2 - \omega^2 - i\,\delta\,\omega} \tag{1.51}$$

The damping can be caused by different physical processes. In case of atomic excitation, the damping is due to radiation damping. In case of oscillations of sub-lattices of a crystal with respect to each other, damping is caused by the coupling of the lattice vibration to other degrees of freedom. In both cases, normally $\delta \ll \omega_0$ holds.

1.3.2.1 Electronic Polarization

Equation 1.51 applies to single oscillators. Atoms and ions in general have more than one electron and more than one eigenfrequency and damping constant. The eigenfrequencies correspond to the energy gaps between atomic levels. The transition probabilities determine the polarizability and can only be computed within a quantum mechanical framework. In doing this, the form of Eq. 1.51 remains virtually unchanged:

$$\varepsilon(\omega) = 1 + \frac{N}{V} \alpha_{el}(\omega) \tag{1.52}$$

$$\alpha_{el}(\omega) = \frac{e^2}{m\,\varepsilon_0} \sum \frac{f_{ij}}{\omega_{ij}^2 - \omega^2 - i\,\delta_{ij}\,\omega} \tag{1.53}$$

The sum runs over all transitions $(i \to j)$. The f_{ij} are the oscillator strengths of the transitions. The electronic polarizability α_{el} not only depends on the element at hand but also on the atomic or ionic environment in the solid or fluid. Equation 1.52 only holds for sufficiently rarefied gases. This is due to the fact that the field strength in Eq. 1.46 that induces the atomic dipole moment does not equal the averaged field strength at the atomic position but is affected by the polarization of the medium. The field strength E' that has to be inserted in Eq. 1.46 in the case of cubic symmetry is given by (with other symmetries the deviations are generally small) Stern and Boffy

(1990), Stern and Gautier (1986)

$$E' = E + \frac{1}{3\,\varepsilon_0}\,P \tag{1.54}$$

With this it follows:

$$P = \frac{N}{V}\,p = \frac{N}{V}\,\alpha\,\varepsilon_0\,E' = \frac{N}{V}\,\alpha\,\varepsilon_0\,\left(E + \frac{1}{3\,\varepsilon_0}\,P\right) \tag{1.55}$$

Resolving with respect to P gives

$$P = \frac{\varepsilon_0\,\alpha\,\dfrac{N}{V}}{1 - \dfrac{\alpha\,\dfrac{N}{V}}{3}}\,E \tag{1.56}$$

With

$$D = \varepsilon_0\,E + P = \varepsilon_0\,\varepsilon\,E \tag{1.57}$$

the dielectric constant is

$$\epsilon = \frac{1 + \dfrac{2}{3}\,\alpha\,\dfrac{N}{V}}{1 - \dfrac{1}{3}\alpha\,\dfrac{N}{V}} \tag{1.58}$$

and the polarizability:

$$\alpha = \frac{3}{\dfrac{N}{V}}\,\frac{\varepsilon - 1}{\varepsilon + 2} \tag{1.59}$$

This is the equation of CLAUSIUS- MOSOTTI or the LORENTZ- LORENZ law. With $N/V = 10^{29}\ \mathrm{m}^{-3}$ and $\varepsilon = 3$, the electronic polarizability is $\alpha = 1.5 \cdot 10^{-29}\ \mathrm{m}^3$.

1.3.2.2 Ionic Polarizability

In the following, only the case of a single ion resonance frequency is discussed. The resonance frequencies of the ion sub-lattices are in the infrared region. The orientation polarization can be neglected in this region and the electronic polarization is almost frequency-independent. With Eq. 1.51, $\omega_0 = \omega_T$ and the limiting cases $\varepsilon(0)$ and $\varepsilon(\infty)$, it follows:

$$\varepsilon(\omega) = \varepsilon(\infty) + \frac{\omega_T^2}{\omega_T^2 - \omega^2 - i\,\delta\,\omega}\,(\varepsilon(0) - \varepsilon(\infty)) \qquad (1.60)$$

$\varepsilon(\infty)$ contains the contribution of the hull electrons. $\varepsilon(\omega)$ is a complex quantity $\varepsilon = \varepsilon_1 + i\,\varepsilon_2$. The frequency dependence of the real and imaginary parts of $\varepsilon(\omega)$ of a single harmonic oscillator is shown in Fig. 1.9. The frequency ω_T was chosen to be $1.9 \cdot 10^{14}$ s ($\lambda = 10\mu$m) and the damping $\delta = 0.01\,\omega_T$. The dielectric constant at $\omega = 0$ is $\varepsilon = 3$; at large frequencies, it is $\varepsilon = 2$. When approaching the resonance frequency ω_T coming from small frequencies, the real and imaginary parts of ω_T increase. That is the region of normal dispersion. After exceeding the resonance frequency, $\mathrm{Re}\,[\varepsilon(\omega)]$ decreases and becomes negative. This region of decreasing $\mathrm{Re}\,[\varepsilon(\omega)]$ is the region of anomalous dispersion. In case of zero damping ($\mathrm{Im}\,[\varepsilon] = 0$) and negative real part of ε ($\mathrm{Re}\,[\varepsilon] < 0$), the real part of the complex index of refraction

$$n_c = n + i\,\kappa = \sqrt{\varepsilon} \qquad (1.61)$$

vanishes which implies that the wave cannot propagate in the medium but is totally reflected at the interface. With finite damping this behavior is attenuated. When exceeding the frequency ω_L, $\mathrm{Re}\,[\varepsilon(\omega)]$ becomes positive again. If the harmonic oscillator corresponds to a lattice vibration, the frequency ω_L at which $\mathrm{Re}\,[\varepsilon(\omega)] = 0$ is the resonance frequency of longitudinal lattice vibrations. In case of zero damping, the LYDDANE-SACHS-TELLER relation follows from Eq. 1.60:
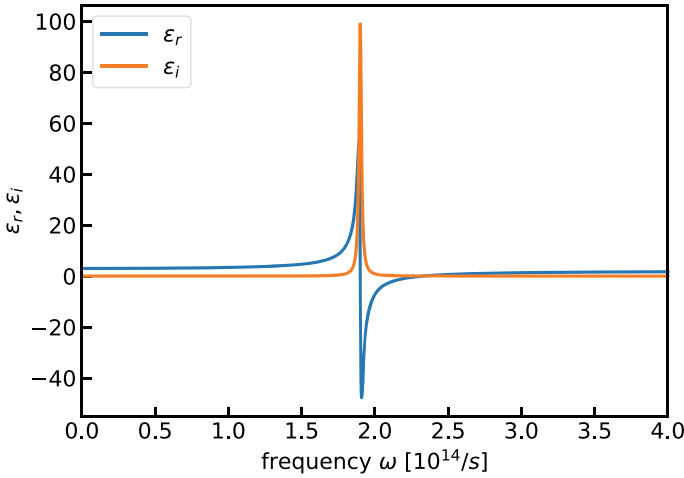
Fig. 1.9 Real and imaginary parts of the dielectric constant of a crystal with ion lattice. Computed according to Eq. 1.60 with $\omega_T = 1.9 \cdot 10^{14}$ s^{-1} which corresponds to $\lambda = 10\,\mu$m, $\delta = 0.01\,\omega_T$. The dielectric constant at $\omega = 0$ is $\varepsilon = 3$; at high frequencies, it is $\varepsilon = 2$
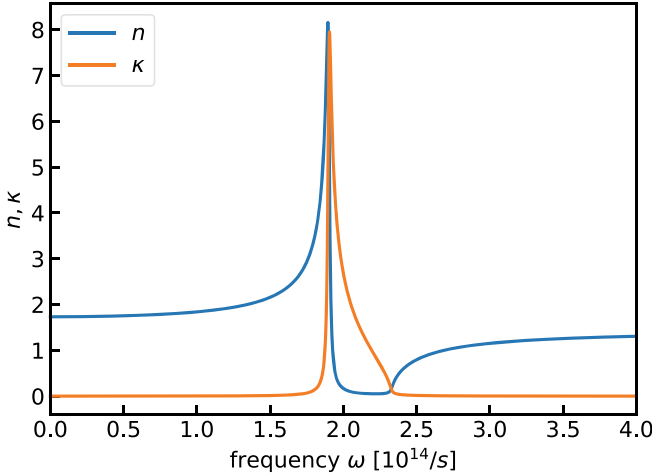
Fig. 1.10 Real and imaginary parts of the index of refraction computed using Eq. 1.61 with the dielectric constant given in Fig. 1.10

$$\left(\frac{\omega_T}{\omega_L}\right)^2 = \frac{\varepsilon(\infty)}{\varepsilon(0)} \tag{1.62}$$

The index of refraction is shown in Fig. 1.10. The reflectivity in case of normal incidence on a plane interface is

$$R = \frac{(n-1)^2 + \kappa^2}{(n+1)^2 + \kappa^2} \tag{1.63}$$

and is shown in Fig. 1.11. The reflectivity is quite large in the range of frequencies where the real part of $\varepsilon(\omega)$ is negative (in case of zero damping R approaches 1). With $\varepsilon(\omega) = 1$ and $\delta = 0$ $R = 0$.

Considering the restrictions in treating absorption mentioned above, there is a further meaningful distinction:

- the optical penetration depth δ_{opt} is small compared to the workpiece thickness s. Then there is no transmission through the workpiece and the absorption is given by Eq. 1.26, i.e. absorption can be computed using the reflectivity only. The boundary conditions at the interface between workpiece and environment determine the absorptivity A
- the optical penetration depth is large or comparable to the thickness of the material considered. The material is partially transparent. This case can be of importance in the field of surface treatment of metals when absorption-enhancing layers are used or when oxide layers exist.
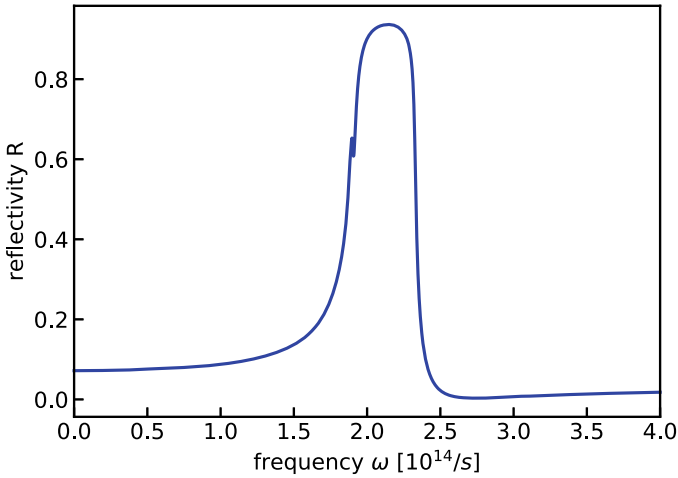
Fig. 1.11 Intensity reflectivity computed using Eq. 1.63 and the index of refraction depicted in Fig. 1.10

1.3.2.3 Supplementary Substances in Polymers

The principal optical properties of polymers are in many cases not determined by the polymer molecules but by supplementary substances such as color pigments and softeners. A polymer without supplementaries can be transparent at a certain wavelength but can be strongly absorbing with a supplementary added. Utilizing this effect makes it possible to weld polymer parts by laying them on top of each other without melting one of the outside surfaces.

1.3.3 Dielectric Properties of Plasmas

A plasma is a mixture of free electrons, positively charged ions (in some cases, also negatively charged ions are present) and neutral particles (atoms and molecules). The charged particles can interact with electric and magnetic fields. Because of their much larger masses compared to electrons, the interaction of the ions with electromagnetic fields is considerable less important, and the energy exchange between plasma and field is almost entirely due to the electrons. The free electrons in metals can with some minor modifications be treated similar to plasma electrons so that the following is also applicable to metals, at least partially. With the assumption that the photon energy is small compared to the mean electron energy the plasma conductivity is given by[9]

---

[9] See Appendix A.2.

$$\sigma = \frac{e^2 \, n_e}{m_e \, \nu_m} \, \frac{\nu_m}{\nu_m - i \, \omega} \qquad (1.64)$$

with

e—electron charge
n_e—electron density
m_e—electron mass
ν_m—momentum transfer frequency
ω—angular frequency of the electromagnetic field.

The momentum transfer frequency ν_m is defined as $1/\tau_m$ with τ_m being the mean time of transfer of electron momentum to other particles during collisions. ν_m consists of three parts; electrons collide with neutral particles, with ions and with other electrons. The consideration of electron-electron collisions makes the computations a lot more complicated. But this contribution doesn't change the conductivity considerably so that in many cases it is sufficient to only consider the electron-neutral and electron-ion collisions.[10] Because of the large range COULOMB interaction, the electron-ion collision cross section is in general much larger than the electron-neutral cross section. The dielectric constant is related to the conductivity:

$$\varepsilon = 1 - \frac{\sigma}{i \, \omega \, \varepsilon_0} \qquad (1.65)$$

With this it follows:

$$\varepsilon = 1 - \frac{\omega_p^2}{\omega^2 + \nu_m^2} + i \, \frac{\nu_m}{\omega} \, \frac{\omega_p^2}{\omega^2 + \nu_m^2} \qquad (1.66)$$

The electron plasma frequency is

$$\omega_p = \sqrt{\frac{e^2 \, n_e}{\epsilon_0 \, m_e}} \qquad (1.67)$$

The index of refraction is given by the MAXWELL relation:

$$n_c = \sqrt{\varepsilon} = n + i \, \kappa \qquad (1.68)$$

with

$$n^2 = \frac{1}{2} \sqrt{\left(1 - \frac{\omega_p^2}{\omega^2 + \nu_m^2}\right)^2 + \left(\frac{\nu_m}{\omega} \, \frac{\omega_p^2}{\omega^2 + \nu_m^2}\right)^2} + \frac{1}{2} \left(1 - \frac{\omega_p^2}{\omega^2 + \nu_m^2}\right) \qquad (1.69)$$

$$\kappa^2 = \frac{1}{2} \sqrt{\left(1 - \frac{\omega_p^2}{\omega^2 + \nu_m^2}\right)^2 + \left(\frac{\nu_m}{\omega} \, \frac{\omega_p^2}{\omega^2 + \nu_m^2}\right)^2} - \frac{1}{2} \left(1 - \frac{\omega_p^2}{\omega^2 + \nu_m^2}\right) \qquad (1.70)$$

---

[10] LORENTZ model of a plasma.

In Eq. 1.66, two limiting cases can be distinguished:

- $\nu_m = 0$:
  the dielectric constant is real
- $\nu_m \gg \omega$:
  the real part of the dielectric constant is small compared to its imaginary part, which holds for example in case of metals.

1.3.3.1   Collision-Free Plasma

In the collision-free case, the dielectric constant is given by

$$\varepsilon = 1 - \frac{\omega_p^2}{\omega^2} \tag{1.71}$$

The wave number of a plane electromagnetic wave is

$$|\vec{k}| = k_0 \, n_c \tag{1.72}$$

with

$$n_c = \sqrt{\varepsilon} = \sqrt{1 - \frac{\omega_p^2}{\omega^2}} \tag{1.73}$$

$$n_c = \sqrt{1 - \frac{\omega_p^2}{\omega^2}} \tag{1.74}$$

$$k_0 = \frac{\omega}{c} \tag{1.75}$$

with
k_0—vacuum wave number
c—vacuum velocity of light.

When ω_p/ω starting from small values approaches unity, the wave number approaches zero which means that the wavelength:

$$\lambda = \frac{2\,\pi}{k} \tag{1.76}$$

becomes infinite. If the plasma frequency exceeds the critical value ($\omega_p > \omega$), the index of refraction and the wave number become imaginary. This implies that the wave cannot propagate within the plasma any more and because of this it is totally reflected at plasma interfaces.[11] The electrical field strength decays exponentially

---

[11] See Eq. 1.63, $R = 1$ for $n = 0$ and k finite.

within the plasma:

$$\vec{E} = \vec{E}_0\, e^{-i\,\omega\,t}\, e^{-k_i\,x} \tag{1.77}$$

k_i is the imaginary part of the wave number. The time-averaged absolute value of the POYNTING vector of a plane wave in a plasma is given by (Appendix A.3)

$$I = \frac{1}{2}\frac{k_r}{k_0}\frac{|E_0|^2}{Z_0}\, e^{-2\,k_i\,x} \tag{1.78}$$

$$Z_0 = \sqrt{\frac{\mu_0}{\varepsilon_0}} \tag{1.79}$$

with
k_r—real part of the wavenumber
Z_0—wave impedance of free space.

If the wave number is purely imaginary, i.e. $k_r = 0$, then $I = 0$. That means there is no time-averaged energy transport into the plasma and the decrease of the electric field is only due to reflection. Figure 1.12 shows the reflection at a collisionless plasma computed with Eq. 1.63 and the index of refraction according to Eq. 1.74. Above $\omega_p/\omega = 1$ total reflection occurs. In the case of finite collision frequency ν_m, the decrease of the electric field within the plasma is due to reflection as well as absorption, i.e. the incident radiation is partly absorbed by the plasma. When the plasma frequency ω_p is small compared to the wave frequency ω, the imaginary part of the wave number becomes

$$k_i = \frac{1}{2}\frac{\nu_m\,\omega_p^2}{c\,(\omega^2 + \nu_m^2)} \tag{1.80}$$

1.3.3.2 Collision Dominated Plasma

If the momentum transfer frequency ν_m is large compared to the wave frequency ω and the imaginary part of the plasma dielectric constant ε_i is large compared to its real part ε_r, the dielectric constant is approximately given by

$$\varepsilon = i\,\frac{\omega_p^2}{\omega\,\nu_m} \tag{1.81}$$

With Eqs. 1.64 and 1.67 it follows:

$$\varepsilon = i\,\frac{\sigma}{\varepsilon_0\,\omega} \tag{1.82}$$
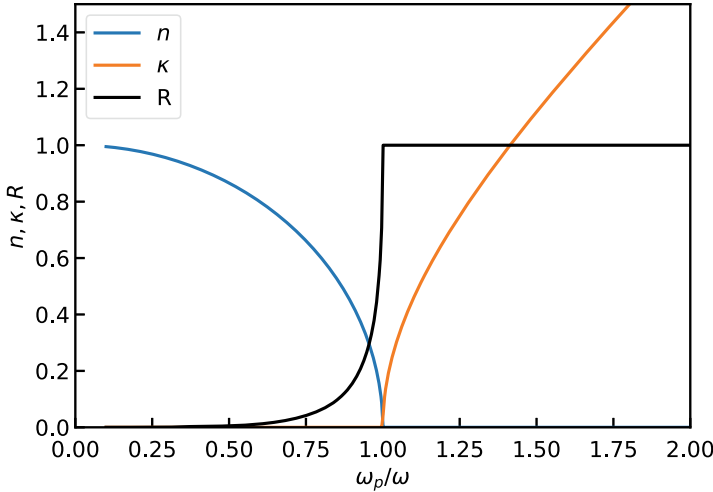
Fig. 1.12 Reflection of an electromagnetic wave at a vacuum collisionless-plasma interface. If the plasma frequency ω_p exceeds the critical value, namely the frequency ω of the electromagnetic wave, the wave is totally reflected

The index of refraction then becomes

$$n_c = \sqrt{\frac{\sigma}{2\,\omega\,\varepsilon_0}}\,(1+i) \tag{1.83}$$

which means $n = \kappa$. With this the reflectivity Eq. 1.63 is

$$R = 1 - \frac{4\,n}{(n+1)^2 + n^2} \tag{1.84}$$

With Eq. 1.84 and $n \gg 1$, the HAGEN-RUBENS relation follows:

$$R \simeq 1 - \frac{2}{n} = 1 - \sqrt{\frac{8\,\omega\,\varepsilon_0}{\sigma}} \tag{1.85}$$

The requirements are in general fulfilled in the case of metals. As an example, let $n_c = 30 + i\,30$ (according to Eq. 1.83, this corresponds to an electric conductivity of $\sigma = 3 \cdot 10^6\ \Omega^{-1}\mathrm{m}^{-1}$). With this $R = 93\%$. Despite the high collision frequency and the associated strong damping, an electromagnetic field is not completely absorbed by the plasma, but much of the incident wave energy is reflected. The complex wave number is given by

$$k = k_0\,n_c \tag{1.86}$$

With the above-given example values, the real and imaginary parts have equal values and the wave number exceeds the vacuum value by a factor of more than 30. The real part of the wave number is

$$k_r = \frac{2\,\pi}{\lambda} \qquad (1.87)$$

λ is the wavelength within the plasma and is about 30 times smaller compared to the vacuum wavelength λ_0. The imaginary part of the wave number is

$$k_i = \frac{1}{\delta_s} \qquad (1.88)$$

δ_s is the damping length of the wave in the plasma or the skin depth. With Eqs. 1.64 and 1.67 and the assumption of large collision frequency, the plasma frequency can be expressed as

$$\omega_p = \sqrt{\frac{\sigma\,\nu_m}{\varepsilon_0}} \qquad (1.89)$$

With this and with Eqs. 1.79, 1.81 and 1.83, the skin depth amounts to

$$\delta_s = \sqrt{\frac{2}{\omega\,\sigma\,\mu_0}} \qquad (1.90)$$

Using the above-given example values of the index of refraction, the skin depth is $\delta_s = \lambda_0/188$. With a vacuum wave length λ_0 of 10.6 μm, this gives $\delta_s = 53$ nm.

In addition to the above-described processes, electromagnetic fields can excite different kinds of plasma waves. This especially holds in the presence of a static magnetic field. These processes normally are not important during material processing with laser radiation, so this will not be treated here.

1.3.4 Absorption of Metallic Materials

Most metals show large reflectivity and accordingly low absorption of electromagnetic radiation. Contrary to atoms and molecules, the absorption spectra do not have discrete lines but are continuous from the far-infrared region (**FIR**) down to short wavelengths in the ultraviolet region **UV**. In the **UV**, there are also discrete bands of absorption. The explanation for this phenomenon is given by the electron theory of metals due to DRUDE (1900). Models that rely on classical physics like the DRUDE model can describe the absorption qualitatively quite well but in some cases their predictions are in conflict with experience. This holds, for example, for the contribution of the free electrons to the heat capacity. With quantum mechanical corrections,

especially with the introduction of the FERMI statistic, these contradictions can be removed and the performance of the electron theory of metals is thus improved substantially. For example, the absorption of metals in the **UV** is also determined by transitions between different energy bands.

Even today, modified versions of the DRUDE model are used to describe the absorption of electromagnetic radiation and the corresponding optical constants of metals. This is mainly due to its simplicity and its clarity. It can be shown that especially in the infrared region, even quantum mechanical results are approximately reproduced if suitable parameters are introduced into the DRUDE theory (Roberts 1959; Wieting and Schriempf 1972). The absorption of metals at a given wavelength depends mainly on four parameters:

- the optical constants of the material
- the physical condition of the surface (roughness, etc.)
- the chemical composition of the surface (oxide layers, etc.)
- the temperature that in return influences the other three parameters.

The absorption of materials that are used in production environments can in general only be computed approximately because the physical and chemical surface properties cannot be determined with the necessary precision. Computational models are thus only reasonable for materials under ideal conditions, i.e. materials that comply with the assumptions of the theory and that have an ideal surface. Because of this in practical situations, precise values of the absorption can only be determined experimentally. Despite this, the knowledge of the physical mechanisms is crucial because the measurements can only be performed within small parameter fields and thus the functional dependence of the absorption on application-specific parameters have to be extrapolated from theory. For metal specimen with a thickness large compared to the skin depth, it holds that $T \simeq 0$ and the absorption is given by

$$A = 1 - R \tag{1.91}$$

The index of refraction n and the absorption index κ depend on the wavelength and thus also A depends on the wavelength. The wavelength-dependent absorption $A(\lambda)$ as a function of the optical parameters at normal incidence is given by

$$A(\lambda) = 1 - \frac{(n(\lambda) - 1)^2 + \kappa(\lambda)^2}{(n(\lambda) + 1)^2 + \kappa^2(\lambda)} \tag{1.92}$$

The dependence of $A(\lambda)$ on the angle of incidence α and the polarization direction (parallel or perpendicular polarization) is described by the FRESNEL formulae.[12] For the computation of the optical parameters of metals, their frequency-dependent electrical conductivity has to be determined. This is done in the following chapter in the frame of the DRUDE theory. The DRUDE theory largely corresponds to the plasma model of the preceding Sect. 1.3.3.

---

[12] See Sect. 1.2.

1.3.5   The DRUDE *Model of Absorption*

Within the framework of the DRUDE model, the electrons in a metal are treated as a
free electron gas moving under the action of an electrical potential. The electrical,
thermal, combined thermo-electrical and magnetic characteristics are derived using
gas kinetic models. Under the exposure of laser radiation, the free electrons are accel-
erated and in return emit radiation corresponding to their acceleration. Free electrons
cannot absorb energy on a time-averaged basis from an electric field oscillating peri-
odically in time. The reason for this is that the electron velocity in steady state is
$\pi/2$ phase-shifted relative to the electric field. But this phase relation is distorted
by collisions of the electrons with the periodic lattice potential and with phonons.
The DRUDE model can particularly be applied to simple metals with isotropic crystal
structure, like Na and Ka, and allows to compute at least approximately the optical
constants n and κ based on the following three assumptions:

- the electromagnetic radiation only interacts with the free electrons in the conduc-
  tion band, the polarization of atomic kernels and bound electrons as well as all
  oscillations of the crystal lattice are neglected
- the free electrons in the metal obey OHM's law
- all free electrons of a given metal can be characterized by a single effective mass
  m^* and a single collision frequency ν_m (this hypothesis is based on the assumption
  that the FERMI statistic allows for unique values corresponding to m^* and ν_m, an
  assumption that is only valid in some special cases).

The optical constants n and κ of a metal are related to macroscopically measurable
electric and magnetic parameters:

$$(n + i\ \kappa)^2 = \left(\varepsilon - \frac{\sigma}{i\ \omega\ \varepsilon_0} \right) \mu \tag{1.93}$$

with
σ—electric conductivity at frequency ω
ε—dielectric constant, contribution of the bound electrons and ions
μ—magnetic permeability.
   If the interaction only takes place between radiation and free electrons, it holds
that $\varepsilon \simeq 1$ and $\mu \simeq 1$ in the **IR** region. It thus follows:

$$(n + i\ \kappa)^2 = \left(1 - \frac{\sigma}{i\ \omega\ \varepsilon_0} \right) \tag{1.94}$$

The applicability of OHM's law:

$$\vec{j} = \sigma\ \vec{E} \tag{1.95}$$

implies that the movement of the free electrons in the metal can be described by a local relation between electric field and current density. The interaction with the crystal lattice and the degeneracy of the electrons have to be treated quantum mechanically. In the frame of the model of a quasi free electron gas, the electrons can be treated as free particles if the free electron mass is substituted in the equation of motion by an effective mass that can be smaller or larger than the free electron mass. The equation of motion of the quasi free electrons in a metal conforms to the equation of motion of electrons in a plasma and reads[13]:

$$m^* \frac{d\vec{v}}{dt} + m^* \nu_m \, \vec{v} = -e \, \vec{E} \tag{1.96}$$

with
m^*—effective mass of the electrons
$\vec{v}$—mean velocity of the electrons
ν_m—momentum transfer frequency
$\vec{E}$—electric field of the laser radiation.

$\frac{1}{\nu_m}$ is the mean time for the transfer of electron momentum to phonons or lattice impurities during collisions. The velocity $\vec{v}$ of the electrons follows from Eq. 1.96:

$$\vec{v} = -\frac{e}{m^*} \frac{1}{\nu_m - i \, \omega} \vec{E} \tag{1.97}$$

The third assumption allows to use a unique electron density n_e in the expression for the current density:

$$\vec{j} = -e \, n_e \, \vec{v} \tag{1.98}$$

Combining Eqs. 1.95, 1.97 and 1.98 provides for the electric conductivity :

$$\sigma = \frac{e^2 \, n_e}{m^* \, (\nu_m - i \, \omega)} \tag{1.99}$$

Splitting into real and imaginary parts results in

$$\sigma = \sigma_1 + i \, \sigma_2 \tag{1.100}$$

$$\sigma_1 = \sigma_0 \, \frac{\nu_m^2}{\nu_m^2 + \omega^2} \tag{1.101}$$

$$\sigma_2 = \sigma_0 \, \frac{\nu_m \, \omega}{\nu_m^2 + \omega^2} \tag{1.102}$$

with the **DC** conductivity:

---

[13] See Appendix A.2.

$$\sigma_0 = \frac{e^2\, n_e}{m^*\, \nu_m} \tag{1.103}$$

With Eqs. 1.94 and 1.100–1.103, it follows for the index of refraction and the index of absorption of a metal within the frame of the DRUDE model:

$$n^2 = \frac{1}{2}\sqrt{\left(1 - \frac{\omega_p^2}{\omega^2 + \nu_m^2}\right)^2 + \left(\frac{\nu_m}{\omega}\,\frac{\omega_p^2}{\omega^2 + \nu_m^2}\right)^2} + \frac{1}{2}\left(1 - \frac{\omega_p^2}{\omega^2 + \nu_m^2}\right) \tag{1.104}$$

$$\kappa^2 = \frac{1}{2}\sqrt{\left(1 - \frac{\omega_p^2}{\omega^2 + \nu_m^2}\right)^2 + \left(\frac{\nu_m}{\omega}\,\frac{\omega_p^2}{\omega^2 + \nu_m^2}\right)^2} - \frac{1}{2}\left(1 - \frac{\omega_p^2}{\omega^2 + \nu_m^2}\right) \tag{1.105}$$

$$\omega_p^2 = \frac{e^2\, n_e}{\epsilon_0\, m_e}$$

Equations 1.104 and 1.105 correspond to Eqs. 1.69 and 1.70 of the index of refraction and the index of absorption of a plasma. In Eqs. 1.104 and 1.105, the effective electron mass m^*, the density n_e of the quasi free metal electrons as well as the momentum transfer frequency ν_m of the electrons in the metal have to be known. The momentum transfer frequency ν_m is composed of two parts, the electron transfer momentum:

- during collisions with phonons and
- during collisions with impurities.

Figure 1.13 shows the reflection coefficient of aluminum calculated according to the Drude theory and experimental values.

1.3.6 Temperature Dependence of the Absorption of Metals

Experimentally usually an increase of the absorption with increasing temperature is observed. Figure 1.14 shows the specific electric resistance and the absorption as a function of temperature of stainless steel and Fe. The similarity of the curves indicates similar causes of the temperature dependence. The DRUDE model explains both dependencies with the increase of the electron lattice collision frequency ν_m. The temperature dependence of the electric conductivity can be extracted from the law of WIEDEMANN-FRANZ (Sect. 1.4.2):

$$\frac{\sigma(T)}{K(T)} = \frac{1}{L\, T} \tag{1.106}$$

with
L—LORENZ number
$L(\mathrm{Al})$—$2.4 \cdot 10^{-8}\ \mathrm{V}^2(\mathrm{mK}^2)^{-1}$
$L(\mathrm{Fe})$—$2.8 \cdot 10^{-8}\ \mathrm{V}^2(\mathrm{mK}^2)^{-1}$.

The temperature dependence of the collision frequency follows immediately:
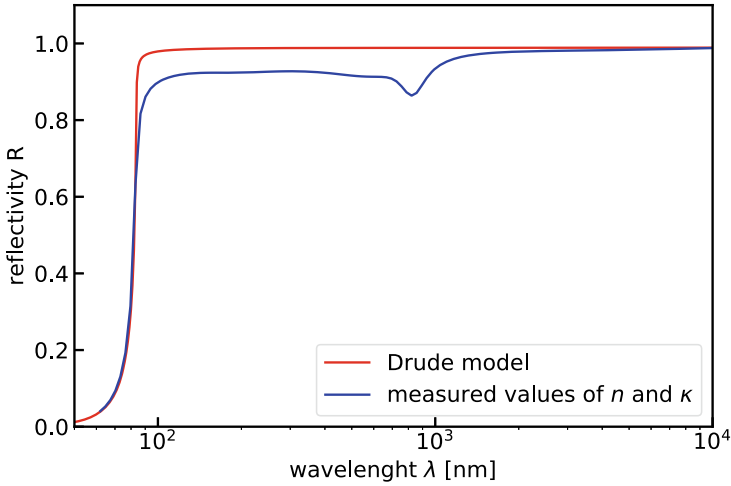
Fig. 1.13 Reflectivity of an Al surface. The theoretical curve is computed with the help of Eqs. 1.63, 1.104, 1.105 and 1.103 as well as the values $\sigma = 3.6 \cdot 10^7 \ \Omega^{-1} \mathrm{m}^{-1}$, $n = 1.8 \cdot 10^{29} \ \mathrm{m}^{-3}$ and $\nu_m = 1.3 \cdot 10^{14} \ \mathrm{s}^{-1}$. The experimental values are taken from Refractive Index (1972)
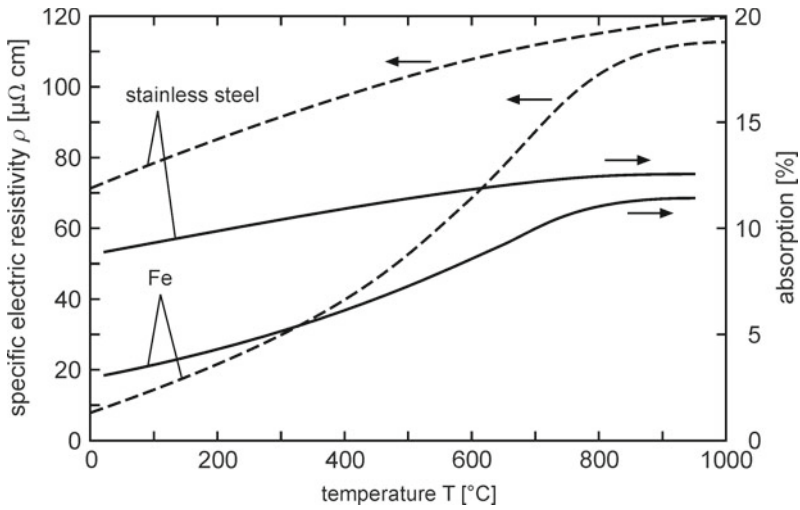
Fig. 1.14 Absorption and electric resistance as function of the temperature. Solid lines: increase of the absorption of stainless steel and of Fe with increasing temperature; broken lines: specific electric resistance of stainless steel and of Fe (Stern and Boffy 1990; Stern and Gautier 1986)
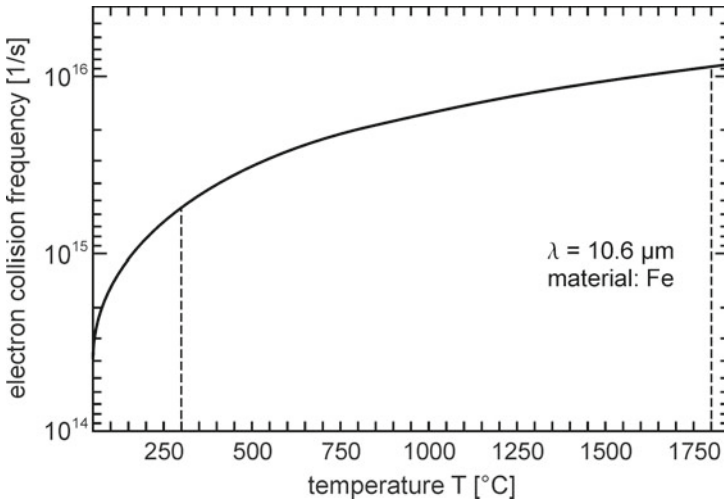
Fig. 1.15 Dependence of the electron collision frequency on the temperature (Wissenbach 1985). Here only the contribution of the electron-phonon collisions has been considered while neglecting the collisions with atomic impurities
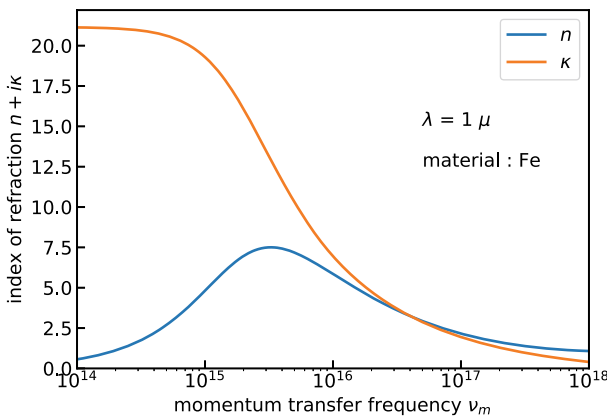
Fig. 1.16 Index of refraction and index of absorption as a function of the collision frequency (Wissenbach 1985). n is computed according to Eq. 1.104 and κ according to Eq. 1.105 (plasma approximation). The density of the quasi free electrons n_e in Fe is estimated in Wissenbach (1985) to be $\approx 6 \cdot 10^{29} \mathrm{m}^{-3}$. For the effective mass m^*, the free mass m_e is used. According to Refractive Index (1972), the values at $\lambda = 1\,\mu\mathrm{m}$ are $n = 2.93$ and $\kappa = 3.83$, respectively

$$\nu_m = \frac{e^2\, n_e}{m_e}\, \frac{L\, T}{K(T)} \tag{1.107}$$

Figure 1.15 shows the momentum transfer frequency $\nu_m(T)$ of Fe (Wissenbach 1985). Only the contribution of the electron-phonon collisions has been included in
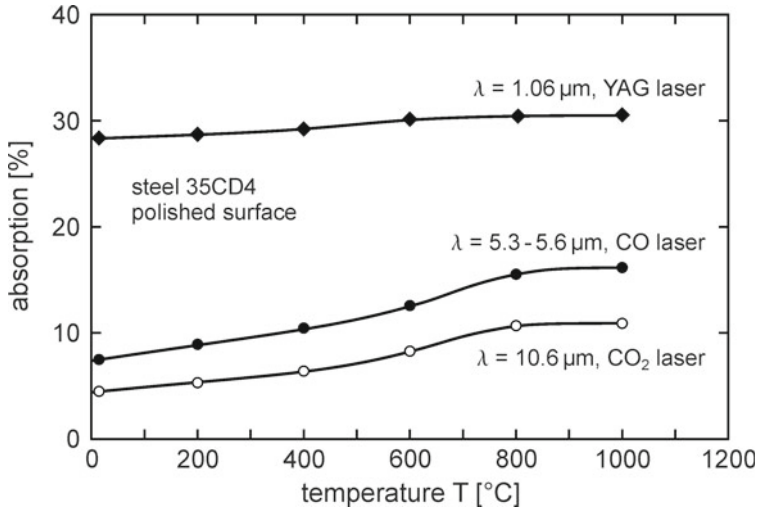
Fig. 1.17 Temperature dependence of the absorption at different wavelengths (Stern and Gautier 1986)

Fig. 1.15 neglecting the contribution of the collisions between electrons and impurities Fig. 1.15. The application of Eq. 1.107 requires the law of WIEDEMANN-FRANZ to hold, i.e. collisions of the electrons must equally contribute to the thermal and electric resistance, respectively. This prerequisite is in general valid at high temperatures.

For a given material, the index of absorption κ and the index of refraction n depend only on the electron collision frequency ν_m and the wavelength of the radiation. Figure 1.16 shows n and κ as a function of the electron collision frequency in the plasma approximation.

Because the temperature dependence of the absorption and electric conductivity can be attributed to the same underlying physical mechanisms, $A(T)$ can be determined from measurements of $\sigma(T)$ which can be measured easier and with higher precision. This means that if the electric conductivity $\sigma(T)$ and the absorptivity $A(\lambda; T))$ are known at $T = 20\,°C$, then $A(\lambda, T)$ can be calculated as a function of temperature exploiting the temperature dependence of $\sigma(T)$. Figure 1.17 shows the temperature dependence of the absorption for different materials and laser wavelengths.

1.3.7 Influence of the Surface Conditions

The roughness of surfaces has a significant influence on the spectral absorptivity of metals. In general, the absorptivity increases with increasing roughness. Figure 1.18 shows the absorptivity of a polished and a grinded surface respectively of the same
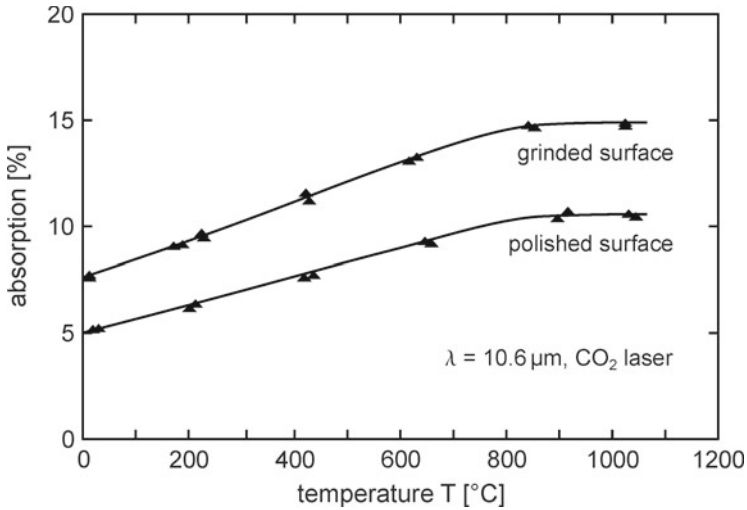
Fig. 1.18 Comparison of the absorptivity of a polished and a grinded surface of the same material (Stern and Gautier 1986)
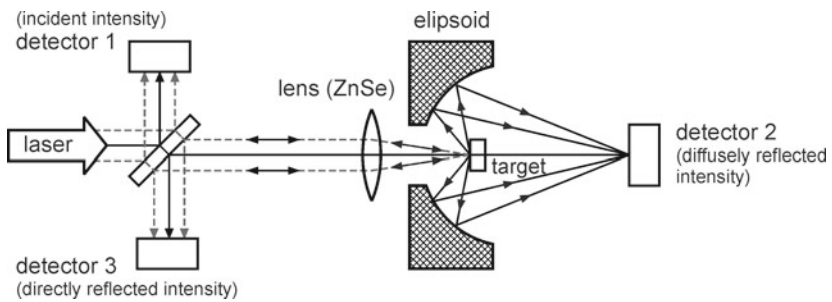
Fig. 1.19 Schematic drawing of the experimental setup for measuring the direct and diffuse reflection

material. If the temperature approaches the melting point, the higher absorptivity of the rough surface decreases to the value of the polished surface.

In treating the impact of the surface roughness quantitatively, two limiting cases can be distinguished depending on whether the ratio of the mean quadratic height of the surface h and the wavelength λ is larger or smaller than 1. The mean quadratic height of the surface roughness is given by

$$h = \sqrt{\frac{1}{L} \int_0^L y^2 \, dx} \tag{1.108}$$

with

λ—wavelength of the laser radiation.

In the limiting case $h/\lambda \ll 1$ the surface can be assumed to be ideal, then the well-known relations for reflection and refraction can be used. In the limit $h/\lambda \gg 1$, geometric optics can be applied (Kanayama and Baba 1975; Abdukadir 1973). Geometric optics allows to estimate the absorptivity as a function of the angle of incidence of a rough surface by using the FRESNEL formulae for the computation of the absorption at the ideal material surfaces and by assuming a random distribution of surface inclinations. Scalar models have been developed by BECKMANN (1963) and PORTEUS (1963). SACADURA (1980) extended these models by considering polarization phenomena and the influence of a random distribution of the surface characteristics. SACADURA developed a model (Sacadura 1972) in which the surface consists of a great number of V formed micro grooves with ideal flat walls and variable cone angles distributed according to a GAUSSian distribution. With **Nd:YAG** laser radiation ($\lambda = 1.06\,\mu m$), the limiting case $h/\lambda \gg 1$ generally applies (except when using highly polished surfaces). In the case of **CO$_2$** laser radiation ($\lambda = 10.6\,\mu m$), this doesn't equally hold in general. SARI, COHEN and SCHERKOSKE (1980) developed a model of plasma waves that are excited by surface irregularities.

In case of technical applications, a measurement of the reflectivity is indispensable for capturing the influence of the surface structure. With intensities $I \ll I_p$ (I_p: process intensity), the absorption is determined by measuring the incident, diffusely and directly reflected power (Fig. 1.19). Figure 1.20 shows the result of measurements for two different steel grades. With unpolarized radiation, measured and computed values coincide quite well. The diffuse part amounts to about 10%, except for polished surfaces. With increasing roughness, the direct reflection of sand blasted targets decreases and the diffuse reflection increases.

In case of metals, the reflectivity decreases with increasing temperature, which is attributed to the increasing electron-lattice collision frequency (Fig. 1.15). The increased reactivity at high temperatures can lead to irreversible modifications of the reflectivity by chemical reactions. Oxidation can take place when the hot surface is in contact with air. Oxide layers in general increase the absorptivity. This is of special importance when material is molten because the oxides are floating on the melt surface. On the other hand, does the original surface roughness not influence the absorptivity any more because the laser beam hits the smooth melt surface?

1.4 Energy Transport and Heat Conduction

The energy that is absorbed during laser material processing is mostly transformed to heat. The absorption within the specimen normally is not homogeneous. On metal surfaces, the thickness of the layer in which the laser radiation is absorbed is only
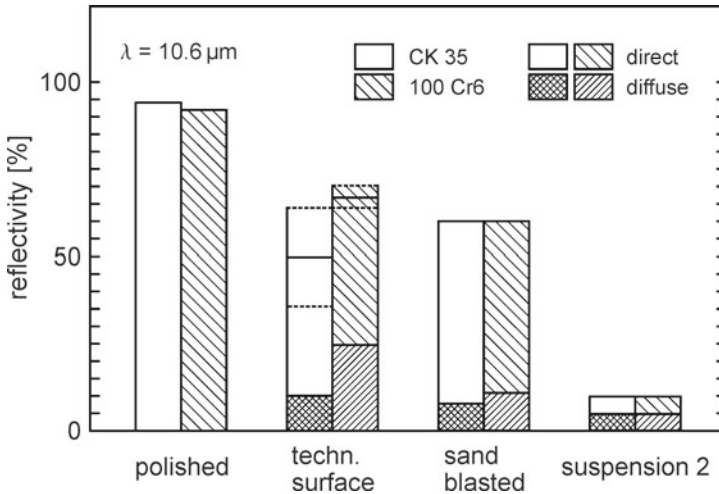
Fig. 1.20 Measured reflectivity with $I \ll I_p$ for different steel grades (Wissenbach 1985)

a fraction of the laser wavelength.[14] Because of the inhomogeneous absorption, temperature gradients develop that cause heat fluxes. Heat conduction is thus a very important physical process during laser material processing.

1.4.1 Energy Transport Equation

In molten material, energy transport is due not only to heat conduction but also to convection of melt. In many cases, during laser material processing the workpiece and the laser beam are moved relatively to each other.[15] Because of the relative movement of the laser beam and the workpiece respectively, the heat conduction problem formulated in the reference frame of the workpiece becomes time-dependent, whereas in the reference frame of the laser beam it is stationary (assuming that the laser output is time-independent) but with a conductive heat flow term added. The energy transport equation reads neglecting friction[16]:

$$\frac{\partial \rho \, c_v \, T}{\partial t} + \vec{\nabla} \cdot (\rho \, c_v \, T \vec{v}) = -\vec{\nabla} \cdot \vec{q} + w(\vec{r}) \tag{1.109}$$

$$\vec{q} = -K \, \vec{\nabla} \, T \tag{1.110}$$

---

[14] See Sect. 1.3.3.

[15] Generally, the laser beam is fixed and the workpiece is moved, but with large or heavy pieces it is often more convenient to move the laser beam using a 'flying optic'.

[16] For a derivation, see Appendix B or Carslaw and Jaeger (1959), Becker and Bürger (1975).

with

T—temperature

ρ—mass density

c—specific heat

w—absorbed energy per volume

$\vec{v}$—velocity

$\vec{q}$—heat flux density

K—heat conductivity.

In case of virtually incompressible fluids, the difference between c_v and c_p can be neglected in almost all cases of interest. The heat conductivity K is a macroscopic parameter that describes heat transport in a continuum. The microscopic mechanisms of heat conduction can be very different. Equation 1.109 is a parabolic differential equation that constitutes an initial boundary value problem, i.e. the problem is only well posed if correct initial and boundary conditions are prescribed (Fig. 1.21).

At a time instant t_0, the temperature has to be prescribed in the whole region of interest.[17] On the boundary of the region of interest for all times $t > t_0$, either the temperature has to be prescribed, i.e. DIRICHLET boundary condition, or the normal derivative of the temperature, i.e. V. NEUMANN boundary condition, which is according to Eq. 1.110 equivalent to the heat flux, or a combination of both.

The heat conduction equation is quasi-linear because ρ, c und K can in general depend on the temperature but the highest derivative is linear.[18] The velocity $\vec{v}$ is in general space-dependent. If the material is molten, the heat conduction equation has in general to be solved together with the NAVIER-STOKES equation and the mass transport equation. The solution of the quasi-linear problem as well as the solution of the linear problem[19] in case of space-dependent flow velocity can in general only be determined by means of numerical methods. With the simplifying assumption that ρ, c and K and $\vec{v}$ have constant values, Eq. 1.109 together with Eq. 1.110 become a linear differential equation with constant coefficients. In this case, general solutions can

Fig. 1.21 Initial and boundary conditions for the solution of the heat conduction equation. B is the body and ∂B its boundary

$$T(x, y, z)|_{t=0}$$

$$\frac{\partial T(t)}{\partial n}\Big|_{\partial B}$$

$$T(t)|_{\partial B}$$

---
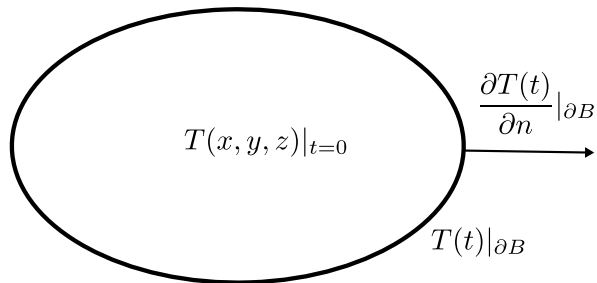
[17] In the following, $t_0 = 0$ will be assumed without loss of generality.

[18] A differential equation is only called nonlinear if the highest derivative is nonlinear.

[19] The heat conduction problem becomes linear when ρ, c and K do not depend on the temperature.

be found by means of the method of GREEN's functions, at least if simple boundary conditions can be applied.

1.4.2 Heat Conduction Mechanisms

Besides radiation heat transport, which is not going to be considered here, in solids two distinct mechanisms of heat transport occur. The first one is energy transport due to the heavy particles by lattice vibrations or phonons and the second one is due to free electrons. In non-conducting materials, only phonon heat conduction occurs whereas in metals both phonon and electron heat conduction take place. In pure metals for all temperatures, the electron heat conductivity is much larger than the phonon heat conductivity so that the latter can be neglected in metals. The highest value of heat conductivity can be observed in sapphire, a non-conductor. The strong binding forces between the atoms that are also responsible for the hardness of sapphire and, for example, diamond cause the high phonon heat conductivity. The heat conductivity of sapphire is at its maximum[20] $K = 2 \cdot 10^4 \, \text{W K}^{-1} \, \text{m}^{-1}$ at 30 K (Becker and Bürger 1975). In comparison, the heat conductivity of Cu, which has the highest heat conductivity of all metals, is only $K = 5 \cdot 10^3 \, \text{W K}^{-1} \, \text{m}^{-1}$ (at 20 K) (Becker and Bürger 1975). The exact theoretical treatment of heat conductivity in solids is quite involved so that here only a simplified treatment based on elementary gas theory will be outlined.

From elementary gas theory, the following expression for the heat conductivity of an ideal gas without excitation of inner degrees of freedom results:

$$K = \frac{1}{3} \, c \, v \, \lambda \qquad (1.111)$$

with
c—heat capacity
v—mean thermal velocity of the particles
λ—mean free path between between two consecutive collisions.

This expression can be used to approximate heat conduction in solids. In non-conductors, $\vec{v}$ is the group velocity of the phonons and λ the mean free path of the phonons. The phonon mean free path of, for example, quartz at $T = 0\,^\circ\text{C}$ is 4 nm and that of NaCl is 2.3 nm (Becker and Bürger 1975). In metals, c is the heat capacity of the degenerate electron gas (Becker and Bürger 1975):

---

[20] In general, the heat conductivities have their maximal values at low temperatures; the heat capacity in Eq. 1.111 increases with increasing temperature (c vanishes at 0 K) whereas the mean free path decreases with the temperature.

$$c_{el} = \frac{\pi^2 \, n_e \, k_B \, T}{2 \, \varepsilon_F} \tag{1.112}$$

$$\varepsilon_F = \frac{1}{2} \, m \, v_F^2 \tag{1.113}$$

with
v_F—FERMI velocity
ε_F—FERMI energy.

With the definition of the momentum transfer frequency:

$$\nu_m = \frac{v_F}{\lambda} \tag{1.114}$$

it follows:

$$K_{el} = \frac{\pi^2}{3} \, \frac{k_B^2}{e^2} \left[\frac{e^2 \, n_e}{m \, \nu_m} \right] T \tag{1.115}$$

The expression in braces on the right-hand side is the electric conductivity Eq. 1.103. With this, the WIEDEMANN-FRANZ law follows (see Sect. 1.3.6):

$$\frac{K_{el}}{\sigma_{el}} = L \, T \tag{1.116}$$

$$L = \frac{\pi^2 k_B^2}{3e^2} \tag{1.117}$$

with
L—LORENZ number.

L is not a real natural constant as Eq. 1.117 might suggest but varies slightly among different metals. The thermo-physical coefficients are functions of the temperature as well as the structure and phase of the material. The heat conductivity, for example, is much smaller in the fluid phase than in the solid phase. When a phase change occurs, the energy density is no longer a unique function of the temperature. In this case, it is more convenient not to use the temperature but the enthalpy as a dependent variable.

In the following, some heat conduction problems with temperature-independent coefficients and constant convective velocity are presented. These problems are relevant for laser material processing but don't represent a complete treatment of the subject. A more complete treatment of heat conduction problems can, for example, be found in CARSLAW and JAEGER (Carslaw and Jaeger 1959).

1.4.3 Heat Conduction Equation with Constant Coefficients and the Method of GREEN's Functions

With the assumption of constant thermo-physical coefficients ρ, c, K and constant velocity $\vec{v}$, Eq. 1.109 becomes linear. Equations 1.109 and 1.110 then result in

$$\frac{\partial T}{\partial t} = \kappa \, \Delta T - \vec{v} \cdot \vec{\nabla} \, T + \frac{w}{\rho \, c} \tag{1.118}$$

$$\kappa = \frac{K}{\rho \, c} \tag{1.119}$$

with
κ—temperature conductivity.

If the source w in Eq. 1.118 is split into several sources, then the resulting temperature distribution is given by the linear superposition of the temperature distributions that result from the individual sources. The method of GREEN's functions rests on this principle of superposition (Morse and Feshbach 1953). GREEN's function is, despite a constant, the temperature distribution that results from a DIRAC-delta source $\delta(t - t', \vec{r} - \vec{r}')$. The time t' and the location $\vec{r}'$ of the DIRAC-δ source can have any value. The theory of GREEN's functions is not going to be outlined here; a comprehensive treatment of this topic can, for example, be found in MORSE and FESHBACH (1953) or in SOMMERFELD (1977). GREEN's function of the heat conduction equation is a solution of Eq. 1.118 with a DIRAC-delta source:

$$\frac{\partial G(\vec{r}, t|\vec{r}', t')}{\partial t} = \kappa \, \Delta \, G(\vec{r}, t|\vec{r}', t') - \vec{v} \cdot \vec{\nabla} \, G(\vec{r}, t|\vec{r}', t') + \delta(\vec{r} - \vec{r}', t - t') \tag{1.120}$$

The derivatives are taken with respect to t and $\vec{r}$. With the initial condition $T(t < t') = 0$ everywhere and the boundary condition $T(t, |\vec{r}| \to \infty) = 0$, the solution reads:

$$G(\vec{r}, t|\vec{r}', t') = \frac{1}{[4 \, \pi \, \kappa \, (t - t')]^{3/2}} \, \exp\left(-\frac{[\vec{r} - (\vec{r}' + \vec{v} \, (t - t'))]^2}{4 \, \kappa \, (t - t')}\right) \tag{1.121}$$

The general solution for an arbitrary space- and time-dependent source that conforms to the same initial and boundary conditions as GREEN's function Eq. 1.121 can be computed as a convolution of GREEN's function with the source distribution:

$$T(x, y, z, t) = \int\limits_{0}^{t} \int\limits_{-\infty}^{\infty} \int\limits_{-\infty}^{\infty} \int\limits_{-\infty}^{\infty} G(\vec{r}, t|\vec{r}', t') \, \frac{w(\vec{r}', t')}{\rho \, c} \, d^3r' \, dt' \tag{1.122}$$

GREEN's function in the time-independent case reads:

surface heat source at $z = 0 + \epsilon$

T

$w = w_+ + w_- = 2w_0$

surface heat source at $z = 0 - \epsilon$

$w(z) = 2w_0\delta(z)$

$[\delta(z)] = 1/m$
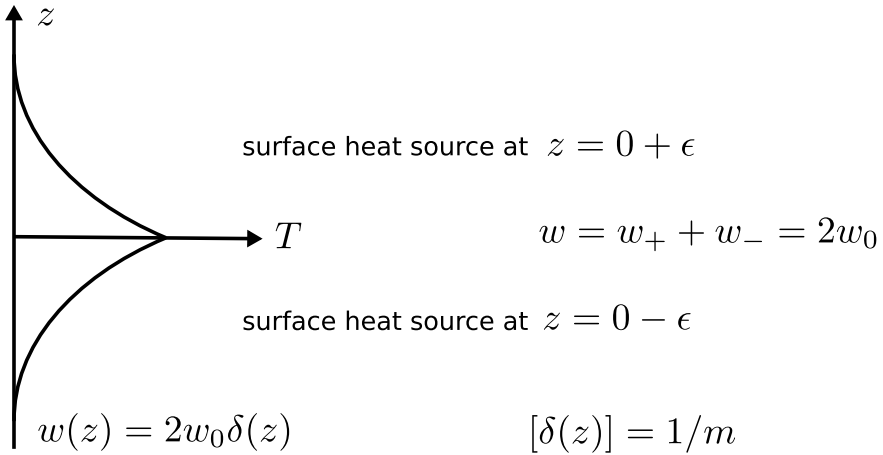
Fig. 1.22 Characterization of a surface source that applies to a half space by a DIRAC-delta volume source of the whole space

$$G(\vec{r}, \vec{r}') = \frac{1}{4 \pi \kappa} \frac{1}{|\vec{r} - \vec{r}'|} \exp\left(\frac{\vec{v} \cdot (\vec{r} - \vec{r}')}{2 \kappa}\right) \exp\left(-\frac{|\vec{v}| |\vec{r} - \vec{r}'|}{2 \kappa}\right) \quad (1.123)$$

and the general solution is given by

$$T(x, y, z) = \int\limits_{-\infty}^{\infty} \int\limits_{-\infty}^{\infty} \int\limits_{-\infty}^{\infty} G(\vec{r}, \vec{r}') \frac{w(\vec{r}')}{\rho c} d^3 r' \quad (1.124)$$

In Eqs. 1.122 and 1.124, the integration runs over the whole space. In most cases of practical importance the workpieces have finite dimensions. The first approximation to a finite workpiece is a workpiece with a plane surface that extends into half space. The solution of the half space problem can simply be derived from the solution of the whole space by mirroring the source at the plane that separates the two half spaces. If the radiation is absorbed within a thin surface layer, the absorption can be described by DIRAC-delta functions (Fig. 1.22):

$$w(x, y, z) = I(x, y) \lim_{\epsilon \to 0} \ [\delta(z + \epsilon) + \delta(z - \epsilon)] \quad (1.125)$$

$$= I(x, y) \ 2\delta(z) \quad (1.126)$$

The factor of 2 must not be omitted when using Eq. 1.122 or Eq. 1.124 for solving half space problems, because these equations apply to the whole space problem.

1.4.3.1   Point Source

In most cases of laser material processing, the laser radiation is focused onto the workpiece surface. The intensity that is absorbed at the surface is thus spatially concentrated. At distances that are large compared to the laser spot size on the surface, the details of the laser intensity distribution is inessential. In that case, the source can be assumed to be a point source. The point source is placed at the origin of the coordinate system and the power is switched from 0 to a constant value at $t = 0$:

$$w(x, y, z, t) = P_L(t)\, \delta(x)\, \delta(y)\, \delta(z) \tag{1.127}$$

P_L is the laser power that is absorbed in a half space. Without loss of generality, the velocity is set to be

$$\vec{v} = \vec{e}_x\, v \tag{1.128}$$

With Eqs. 1.121 and 1.122 after integration over the space coordinates, which is trivial because of the DIRAC-delta source distribution, the following temperature distribution results:

$$T(x, y, z, t) - T_\infty =$$
$$\int_0^t \frac{2\, P_L(t')}{\rho\, c}\, \frac{1}{[4\, \pi\, \kappa\, (t - t')]^{3/2}}\, \exp\left(-\frac{[x - v\,(t - t')]^2 + y^2 + z^2}{4\, \kappa\, (t - t')}\right) dt' \tag{1.129}$$

The term T_∞ was added because GREEN's function Eq. 1.122 holds for zero temperature at infinity. The integrand is essentially GREEN's function Eq. 1.122. A general analytical solution of the integral in Eq. 1.129 is not known. In the case of $v = 0$, one gets

$$T(r, t) - T_\infty = \int_0^t \frac{2\, P_L(t')}{\rho\, c}\, \frac{1}{[4\, \pi\, \kappa\, (t - t')]^{3/2}}\, \exp\left(-\frac{r^2}{4\, \kappa\, (t - t')}\right) dt' \tag{1.130}$$
$$r = \sqrt{x^2 + y^2 + z^2}$$

When the laser power at time $t = 0$ is switched from 0 to the constant value P_L, i.e.

$$P_L(t) = P_L\, \Theta(t) \tag{1.131}$$

with
$\Theta(t)$—HEAVISIDE step function
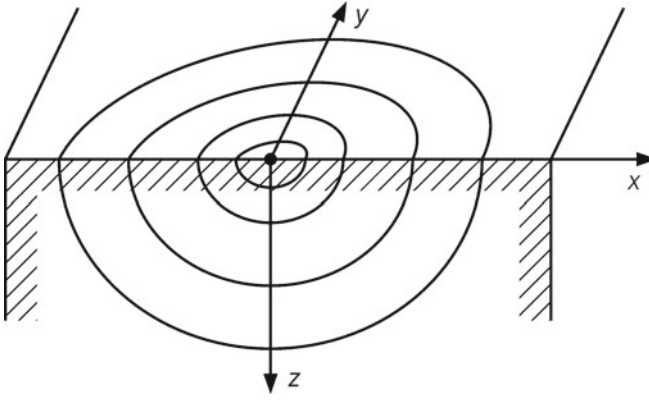
Fig. 1.23 Schematic drawing of the isotherms for a non-moving point source

the solution of the integral Eq. 1.130 reads[21]:

$$T(r, t) - T_\infty = \frac{P_L}{2\,\pi\,\rho\,c\,\kappa} \frac{1}{r} \operatorname{erfc}\left(\frac{r}{\sqrt{4\,\kappa\,t}}\right) \tag{1.132}$$

with
erfc—error function.

In Fig. 1.23 isotherms are shown schematically.

In the time-independent case and with finite velocity, the temperature distribution is given by Rosenthal (1946)

$$T(x, y, z) - T_\infty = \frac{2\,P_L}{\rho\,c} \frac{\exp\left(-\dfrac{|v|\,r - v\,x}{2\,\kappa}\right)}{4\,\pi\,\kappa\,r} \tag{1.133}$$

Figure 1.24 shows a schematic drawing of the isotherms. The temperature decreases in positive x-direction because the velocity is assumed to be negative:

$$T \sim \frac{\exp\left(-\dfrac{|v|}{\kappa}\,x\right)}{r} \tag{1.134}$$

with
$x > 0,\ y = 0,\ z = 0$.

In negative x-direction one gets

$$T \sim \frac{1}{r} \tag{1.135}$$

---

[21] See Appendix B.9.
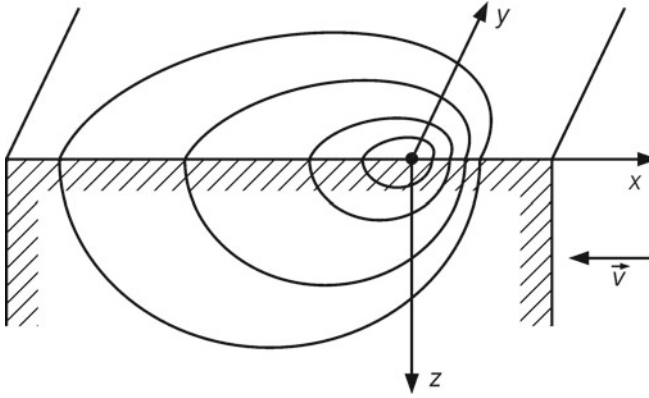
Fig. 1.24 Schematic drawing of the isotherms of a moving source

with
$$x < 0, \; y = 0, \; z = 0$$
and in transverse direction at $x = 0$:

$$T \sim \frac{\exp\left(-\dfrac{|v|\, r}{2\,\kappa}\right)}{r} \tag{1.136}$$

with
$$x = 0, \; r = \sqrt{y^2 + z^2}.$$

1.4.3.2   Line Source

The line source is a model for laser energy absorption and heat conduction in cases in which the coupling does not occur at the plane surface but within a key hole that is initially not present but is formed by processes that are induced by the laser power, like evaporation. This is the case, for example, during laser cutting and deep penetration welding. In case of cutting, a cutting front is created that moves through the workpiece and in case of deep penetration welding a vapor-filled key hole is formed that penetrates into the workpiece. In both cases, the laser energy is absorbed at the walls of the cutting front and the keyhole, respectively. Assuming that there are no temperature gradients in the direction of the incident laser beam but only gradients normal to the key hole or cutting front respectively, the heat conduction can approximately be treated 2-dimensionally. In the simplest case, the key hole is idealized to be a line. At least for distances sufficiently far away from the line source, the temperature distribution can approximately be described by this model. The line source is given by

$$w = \frac{w'(t)}{\rho c} \, \delta(x) \, \delta(y) \tag{1.137}$$

$$w' = \frac{P_L}{s} \tag{1.138}$$

with
w'—absorbed power per length.

With Eqs. 1.123 and 1.124, the temperature distribution results in

$$T(x, y, t) - T_\infty = \int_0^t \frac{w'(t)}{\rho c} \, \frac{1}{4 \pi \kappa (t - t')} \, \exp\left(-\frac{(x - v (t - t'))^2 + y^2}{4 \kappa (t - t')}\right) dt' \tag{1.139}$$

In the case of zero velocity and constant power, the temperature is given by[22]

$$T(r, t \geq 0) - T_\infty = \frac{w'}{\rho c} \, \frac{1}{4 \pi \kappa} \, E_1\left(\frac{r^2}{4 \kappa t}\right) \tag{1.140}$$

$$r^2 = x^2 + y^2$$

$$E_1(x) = \int_x^\infty \frac{e^{-\xi}}{\xi} \, d\xi \tag{1.141}$$

with
E_1—exponential integral (Abramowitz and Stegun 1984).

The isotherms are concentric circles centered at the origin ($x = 0$, $y = 0$). In the transient case and with finite velocity, the temperature is given by Rosenthal (1946)

$$T(x, y) - T_\infty = \frac{w'}{\rho c} \, \frac{1}{2 \pi \kappa} \, K_0\left(\frac{|v| \, r}{2 \kappa}\right) \exp\left(\frac{v \, x}{2 \kappa}\right) \tag{1.142}$$

with
K_0—modified BESSEL-function of the second kind.

Figure 1.25 shows isotherms computed using Eq. 1.142. The BESSEL function K_0 diverges at $r = 0$, i.e. the temperature becomes infinite at $r = 0$. For large arguments, K_0 can be expanded (Abramowitz and Stegun 1984):

$$K_0(z) \simeq \sqrt{\frac{\pi}{2 z}} \, \exp(-z) \left[1 - \frac{1}{8 z} + \frac{3^2}{2! \, (8 z)^2} - \frac{3^2 \cdot 5^2}{3! \, (8 z)^3} - \dots\right] \tag{1.143}$$

For large z, the expression in parenthesis in Eq. 1.143 approximately equals 1. The asymptotic behavior for large positive values of x and with $v < 0$ is then given by

---

[22] See Appendix B.9.
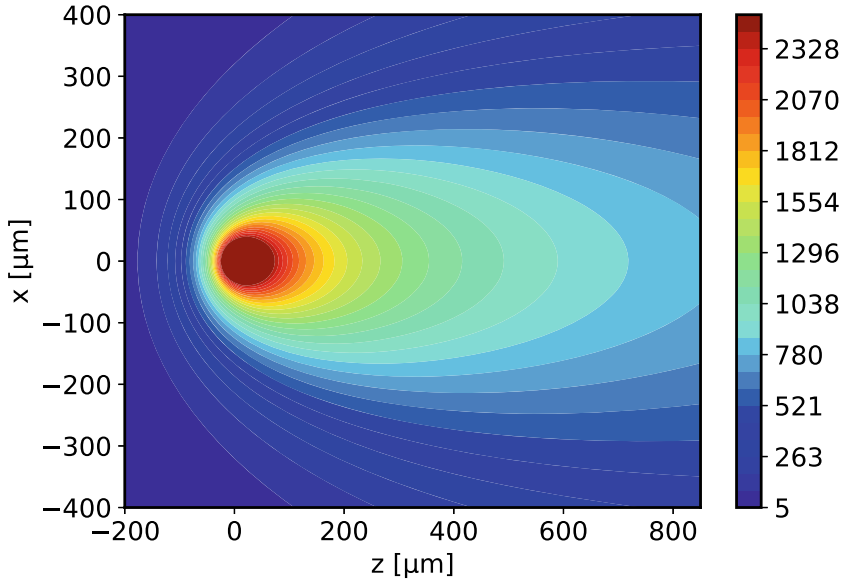
Fig. 1.25 Isotherms in case of a moving line source in Al computed with Eq. 1.142:
$T_\infty = 300$ K, $v = 0.1$ m s^{-1}, $w' = 10^6$ W m^{-1}, $\kappa = 4.9 \cdot 10^{-5}$ m^2 s^{-1}, $\rho = 2.7 \cdot 10^3$ kg m^{-3}, $c = 0.909$ kJ kg^{-1} K^{-1}

$$T \sim \frac{\exp\left(-\dfrac{|v|r}{2\kappa}\right)\exp\left(\dfrac{vx}{2\kappa}\right)}{\sqrt{r}} \tag{1.144}$$

with
$x > 0, \ y = 0.$

In negative x-direction it holds

$$T \sim \frac{1}{\sqrt{r}} \tag{1.145}$$

with
$x < 0, \ y = 0$
and in transverse direction:

$$T \sim \frac{\exp\left(-\dfrac{|v|}{2\,\kappa}y\right)}{\sqrt{r}} \tag{1.146}$$

with
$x = 0.$

1.4.3.3 Transversal Infinitely Extended Surface Source

In case of metal workpieces, the laser radiation is in general absorbed within a thin surface layer the thickness of which being much smaller than the lateral extent of the laser spot. There are cases in which also the heat penetration depth is small compared to the lateral extent of the laser beam at the surface, e.g. with large laser beam diameters and fast movement of the workpiece relative to the laser beam or with short laser pulses. In this case, it can approximately be assumed that the source is transversal infinitely extended, i.e. the general 3-dimensional problem reduces to a 1-dimensional problem. The boundary region of the laser spot however cannot be described by this model (Fig. 1.26). The laser power density is given by

$$w = 2 \, I_L(t) \, \delta(z) \tag{1.147}$$

with
I_L—absorbed laser intensity.

The factor of 2 again has to be added because Eq. 1.122 holds for the whole space (see above). Inserting this into Eq. 1.122 and spatially integrating over the whole space and assuming zero velocity results in

$$T(z, t) - T_\infty = \int_0^t \frac{2 \, I_L(t')}{\rho \, c} \, \frac{1}{\sqrt{4 \, \pi \, \kappa \, (t - t')}} \, \exp\left(-\frac{z^2}{4 \, \kappa \, (t - t')}\right) dt' \tag{1.148}$$

When the laser intensity at $t = 0$ is switched from 0 to the finite value I_L, the solution of this integral reads[23]:
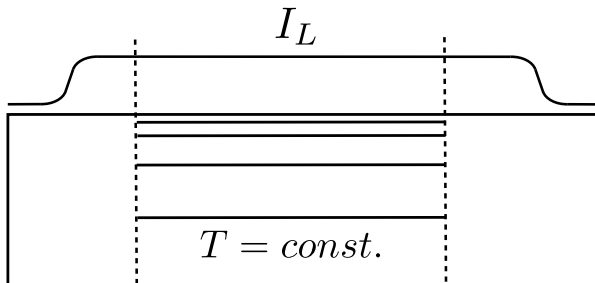
Fig. 1.26 1-dimensional heat conduction. When the diameter of the incident laser beam is large compared to the heat penetration depth, approximately a 1-dimensional heat conduction model can be adopted. The boundary regions of the laser beam however cannot be described by this simplified model

---

[23] See Appendix B.9.
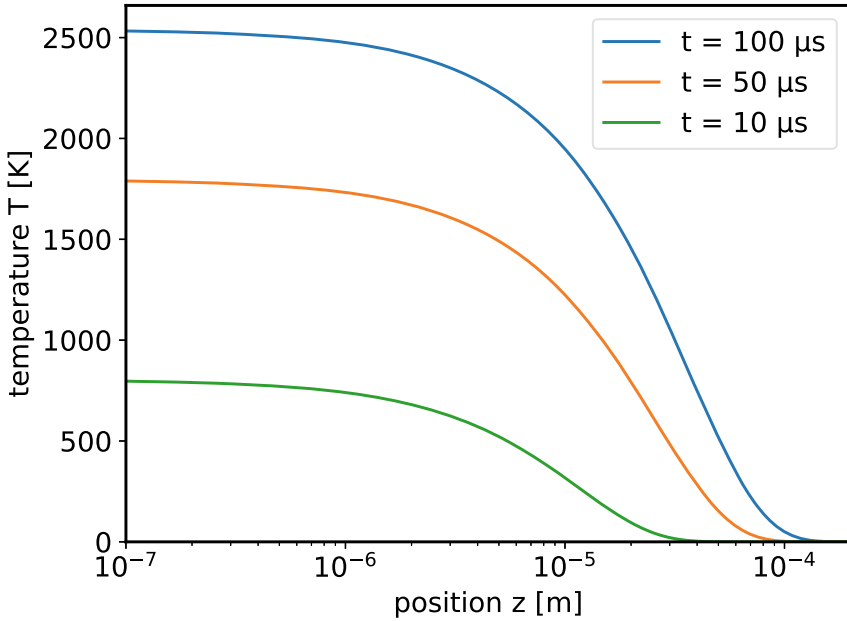
Fig. 1.27 Temperature as a function of the location at different time instances. Computed with Eq. 1.151. The material is Al, $I_L = 10^{10}$ W m^{-2}, $t_L = 10^{-5}$ s, $T_\infty = 300$ K, $\kappa = 4.9 \cdot 10^{-5}$ m^2 s^{-1}, $\rho = 2.7 \cdot 10^3$ kg m^{-3}, $c = 0.909$ kJ kg^{-1} K^{-1}

$$T(z,t) - T_\infty = \frac{2\,I_L}{\rho\,c}\sqrt{\frac{t}{\kappa}}\,\text{ierfc}\left(\frac{z}{\sqrt{4\,\kappa\,t}}\right) \tag{1.149}$$

$$\text{ierfc}(x) = \frac{1}{\sqrt{\pi}}e^{-x^2} - x\,\text{erfc}(x)$$

In the case of finite pulse duration t_L, one gets

$$w = 2\,I_L\,\delta(z)\,\Theta(t)\,\Theta(t_L - t) \tag{1.150}$$

and thus

$$T(z,t) - T_\infty = \frac{2\,I_L(t)}{\rho\,c\,\sqrt{\kappa}}$$
$$\cdot\left[\sqrt{t}\,\text{ierfc}\left(\frac{z}{\sqrt{4\,\kappa\,t}}\right) - \Theta(t - t_L)\sqrt{t - t_L}\,\text{ierfc}\left(\frac{z}{\sqrt{4\,\kappa\,(t - t_L)}}\right)\right] \tag{1.151}$$

Figure 1.27 shows the temperature distribution at different instants of time.

In the stationary case with transversal infinitely extended surface source, the differential equation can also easily be solved without using the method of GREEN's
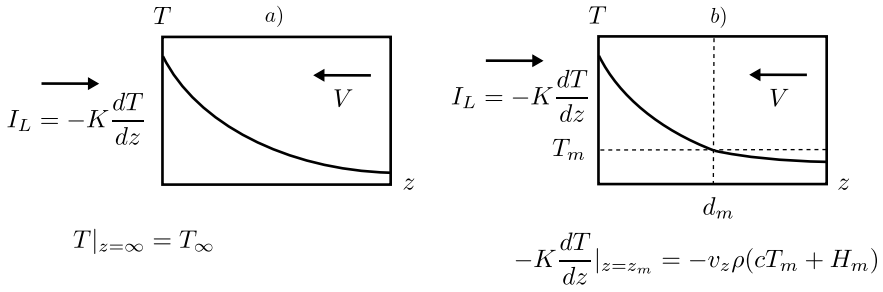
Fig. 1.28 Transversal infinitely extended surface source. Prescribed quantities: **a**: heat flux at the surface, temperature at infinity **b**: heat flux and temperature at d_m

functions. The heat conduction equation without volume source reads:

$$\frac{d^2T}{dz^2} - \frac{v_z}{\kappa}\frac{dT}{dz} = 0 \qquad (1.152)$$

At $z = 0$, the laser intensity I_L is coupled into the workpiece. In the above treated cases, the absorption at the surface was treated using DIRAC-delta volume sources. But this can also be modeled using appropriate boundary conditions: The heat flow at the surface must be equal to the absorbed intensity (Fig. 1.28a):

$$-K\left.\frac{dT}{dz}\right|_{z=0} = I_L \qquad (1.153)$$

with $v = -v_z$ and the boundary condition at infinity:

$$T|_{z=\infty} = T_\infty \qquad (1.154)$$

the solution reads:

$$T - T_\infty = \frac{I_L}{\rho c}\frac{1}{v_z}\exp\left(-\frac{v_z}{\kappa}z\right) = \frac{I_L}{K}\frac{\kappa}{v_z}\exp\left(-\frac{v_z}{\kappa}z\right) \qquad (1.155)$$

If the material is assumed to be molten in the region $0 \leq z \leq d_m$, the heat flux at $z = d_m$ has to supply the energy for heating and melting the material:

$$-K\left.\frac{dT}{dz}\right|_{z=d_m} = -v_z\,\rho\,(c\,T_m + H_m) \qquad (1.156)$$

with
ρ—mass density
c—specific heat capacity

T_m—melting temperature
H_m—melting enthalpy.

The melting enthalpy is the energy that has to be supplied in order to transform a given amount of material at constant pressure and at the melting temperature T_m from the solid phase to the liquid phase. Because part of the heat energy is consumed by the phase transformation, the heat flux at $z = d_m$ is discontinuous. With Eq. 1.156 and the further requirement:

$$T|_{z=d_m} = T_m \tag{1.157}$$

the temperature distribution is given by

$$T(z) = \left(T_m + \frac{H_m}{c}\right) \exp\left(\frac{v_z}{\kappa} d_m\right) \exp\left(-\frac{v_z}{\kappa} z\right) - \frac{H_m}{c} \tag{1.158}$$

The intensity that has to be coupled into the workpiece surface at $z = 0$ is (Eq. 1.153)

$$I_L = v_z \, \rho \, (c \, T_m + H_m) \, \exp\left(\frac{v_z}{\kappa} d_m\right) \tag{1.159}$$

Figure 1.29 shows the temperature distribution for different velocity values and a melt film thickness of $d_m = 50 \, \mu m$. This is a typical value, e.g. during laser cutting. The material constants are that of Al. The temperature at the surface increases with increasing velocity.

1.4.3.4 Transversal Infinitely Extended Volume Source

There are cases in which the penetration depth is finite and in which its impact on the energy absorption has to be taken into account. Especially plastics can have quite large absorption length. The absorbed power density is in this case:

$$w(z, t) = \alpha \, I_L(t) \, \exp\left(-\alpha \, |z|\right) \tag{1.160}$$

with
α—absorption coefficient
α^{-1}—absorption length.

In the exponential function, the absolute value of z is used because the absorbed energy density has to be symmetric with respect to the plane $z = 0$. With Eq. 1.122 and $v = 0$, the solution reads:
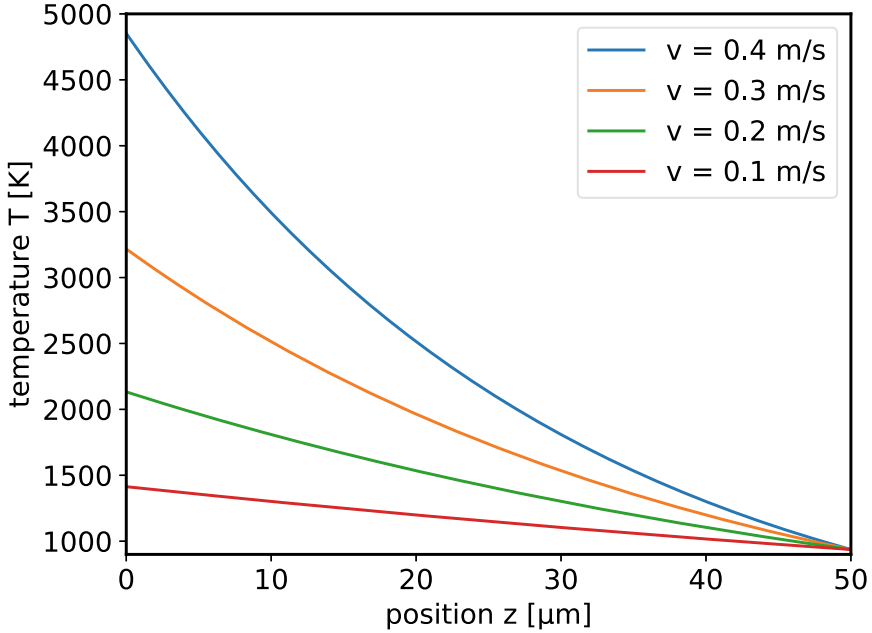
Fig. 1.29 Temperature as a function of the normalized coordinate z/d_m computed according to Eq. 1.158. The material is Al, $d_m = 50\,\mu\text{m}$, $v = 0.3,\ 0.6,\ 0.9,\ 1.2,\ 1.5,\ \text{m s}^{-1}$, $\kappa = 4.9 \cdot 10^{-5}\,\text{m}^2\,\text{s}^{-1}$, $c = 0.909\,\text{kJ kg}^{-1}\,\text{K}^{-1}$, $T_m = 937\,\text{K}$, $H_m = 3.77 \cdot 10^2\,\text{kJ kg}^{-1}$

$$T(z,t) - T_\infty = \frac{2}{\rho c} \int_0^t I_L(t') \frac{1}{\sqrt{4\,\pi\,\kappa\,(t-t')}} \exp\left(-\frac{z^2}{4\,\kappa\,(t-t')}\right) A(z,t,t',\alpha)\,dt' \quad (1.161)$$

$$A(z,t,t',\alpha) = \frac{\sqrt{\pi}}{2}\frac{\alpha\,a}{2}\left[\text{erfce}\left(\frac{\alpha\,a}{2}+\frac{z}{a}\right) + \text{erfce}\left(\frac{\alpha\,a}{2}-\frac{z}{a}\right)\right] \quad (1.162)$$

$$a = \sqrt{4\kappa(t-t')}$$

$$\text{erfce}(x) = \exp(x^2)\text{erfc}(x)$$

When the absorption coefficient tends to infinity, then $A(z,t,t',\alpha) \to 1$ and the result of Eq. 1.148 is reproduced.

1.4.3.5 GAUSSIAN **Intensity Distribution**

With a GAUSSian intensity distribution at the surface, the source is

$$w(x,y,z,t) = \frac{2\,P_L}{\rho c}\frac{2}{\pi\,w_0^2} \exp\left(-\frac{2\,(x^2+y^2)}{w_0^2}\right)\delta(z) \quad (1.163)$$

with
w_0 beam waist.

Within the beam radius w, 87% of the beam power is contained. The temperature distribution is given by

$$
T(x, y, z, t) - T_\infty = \int\limits_0^t \frac{2\,P_L}{\rho\,c}
$$

$$
\cdot \frac{1}{\sqrt{4\,\pi\,\kappa\,(t - t')}}\, \frac{1}{4\,\pi\,\kappa\,(t - t') + w_0^2/2}
$$

$$
\cdot \exp\left(-\frac{(x - v\,(t - t'))^2 + y^2}{4\,\kappa\,(t - t') + w_0^2/2}\right)\, \exp\left(-\frac{z^2}{4\,\kappa\,(t - t')}\right) dt' \tag{1.164}
$$

With $v = 0$, $(x = 0, y = 0, z = 0)$ and constant laser power which simplifies to

$$
T(0, 0, 0, t) = \frac{2\,P_L}{\rho\,c}\, \frac{1}{\sqrt{2}\,\kappa\,\pi^{3/2}\,w_0}\, \arctan\left(\sqrt{\frac{8\,\kappa\,t}{w_0^2}}\right) \tag{1.165}
$$

1.4.3.6 Finite Workpiece Thickness

In the case of finite workpiece thickness, solutions of the heat conduction problem can be found using GREEN's function Eq. 1.123, which conforms to boundary conditions at infinity, by exploiting symmetries. This is achieved by choosing the source w distribution in such a way that the boundary conditions that have to be imposed in the case of finite workpiece thickness are fulfilled automatically (method of mirror sources). Figure 1.30 shows this schematically. The heat fluxes normal to the workpiece surfaces vanish everywhere. This also holds where the laser beam hits the surface because w is modeled by two symmetric DIRAC-delta functions, so that exactly at the interface at $z = 0$ the heat flux is zero. In order to get zero heat flux at the plane $z = -d$, another source is placed at the plane $z = -2d$ and so on, and similarly for $z + 2d$ and so on. For the exact solution, an infinite number of delta sources need to be summed over

$$
w = \sum_{n=-\infty}^\infty w_n \tag{1.166}
$$

$$
w_n = 2\,P_L\,\delta(x - x_0)\,\delta(y - y_0)\,\delta(z - 2\,n\,d) \tag{1.167}
$$

In the stationary case and with a point source (infinitely many point sources), the temperature is given by
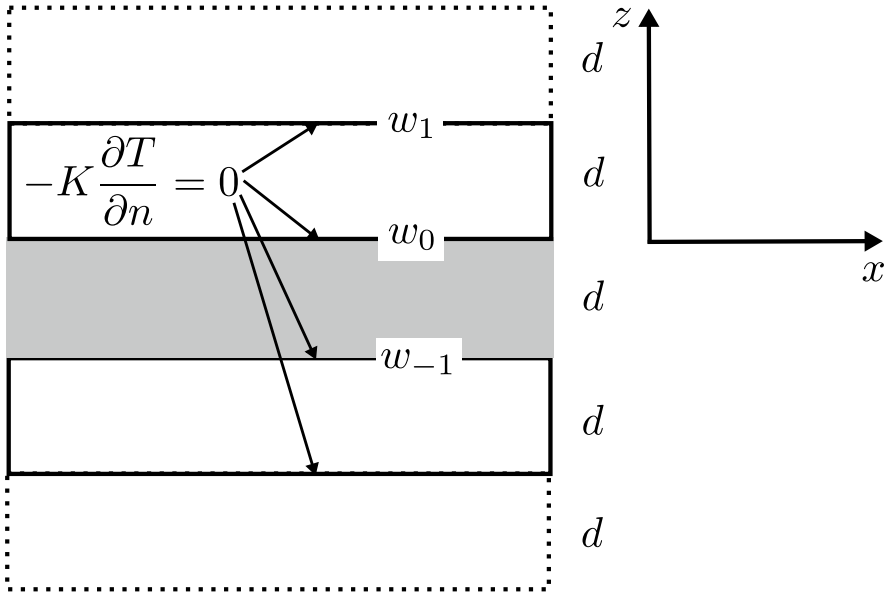
Fig. 1.30 Method of mirror sources for the calculation of temperature distributions in the case of finite workpiece thickness. The shaded region corresponds to the workpiece

$$T = \frac{2\,P_L}{\rho\,c}\,\exp\left(-\frac{v\,x}{2\,\kappa}\right)\sum_{n=-\infty}^{\infty} T_n \qquad (1.168)$$

$$T_n = \frac{\exp\left(-\dfrac{v}{2\,\kappa}\,\sqrt{x^2 + y^2 + (z - 2\,n\,d)^2}\right)}{4\,\pi\,\kappa\,\sqrt{x^2 + y^2 + (z - 2\,n\,d)^2}} \qquad (1.169)$$

For practical calculations, it is sufficient to retain only a few terms in the sum.

1.4.4 Temperature-Dependent Thermo-Physical Coefficients

In the proceeding sections constant thermo-physical coefficients had been assumed. This is an idealization; the thermo-physical coefficients in general depend on the structure, phase and temperature of the workpiece material. When phase transitions take place, the energy density is no unique function of the temperature any more so that instead of using the temperature in the heat conduction equation the enthalpy is the relevant physical quantity. When the temperature dependence of the thermo-physical coefficients is taken into account, the energy transport equation no longer
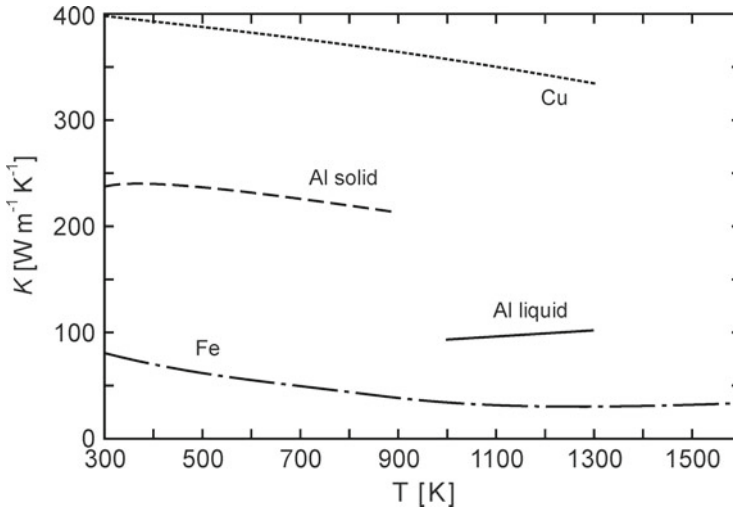
Fig. 1.31 Heat conductivity of Al, Cu and Fe as a function of temperature (Weast 1990). The sharp decrease of the Al heat conductivity occurs at the melting temperature; the heat conductivity in the liquid phase is much smaller than in the solid phase

is linear and analytical solutions are in general unavailable so numerical algorithms have to be employed. The most frequently used methods are the **F**inite **E**lement **M**ethod, the **F**inite **D**ifference and the **F**inite **V**olume **M**ethod (Törnig 1979).

Figure 1.31 shows the heat conductivity of Al, Cu and Fe. Cu shows the highest heat conductivity, Fe the smallest. The heat conductivities are highest at small temperatures. The sharp decrease of the Al heat conductivity occurs at the melting temperature. This is because the heat conductivity in the totally unordered liquid phase is much smaller than in the at least partially ordered solid phase.

1.4.5 Heat Conduction in Case of Short Laser Pulse Durations

FOURIER's law Eq. 1.110 implies that the heat flux is proportional to the temperature gradient and that heat propagates with infinite velocity. But this is an approximation that can only be applied on large time scales. On shorter time scales, heat conduction deviates from the results given by FOURIER's law. From non-equilibrium dynamics, it follows that on short time scales FOURIER's law has to be augmented by a relaxation term (Jou et al. 1982):

$$\tau_{\vec{q}} \frac{\partial \vec{q}}{\partial t} + \vec{q} = -K \vec{\nabla} T \qquad (1.170)$$

This modification leads to a finite thermal propagation speed. The relaxation time constant τ_q and the heat conductivity K depend on the microscopic properties of the material like collision frequencies of electrons and phonons. This quantities can be deduced from solutions of the BOLTZMANN equation (Kostrykin et al. 1998). The relaxation time constant τ_{qe} for the electron heat flux corresponds to the electron collision frequency and its value is in the $(1-10)$ fs range. In case of very short pulses, it also has to be considered that electron and phonon temperatures are not in equilibrium with each other. To treat this situation, a two temperature model has to be employed in which electron and phonon temperatures and their interaction have to be accounted for. If the laser beam diameter is large compared to the thermal penetration depth, the problem can be treated 1-dimensionally. With the assumption that the normal of the workpiece surface as well as the incident laser beam respectively are parallel to the z-axis, the heat conduction problem can be described by the following system of equations:

$$\frac{\partial U_e}{\partial t} \;+\; \frac{\partial q_e}{\partial z} \;=\; I(x,y,t)\,A\,\alpha \exp(-\alpha z) + h_{ex}(T_{ph} - T_e) \quad (1.171)$$

$$\frac{\partial U_{ph}}{\partial t} \;+\; \frac{\partial q_{ph}}{\partial z} \;=\; h_{ex}(T_e - T_{ph}) \quad\quad (1.172)$$

$$\tau_{q_e}\frac{\partial q_e}{\partial t} \;+\; q_e \;=\; -K_e\frac{\partial T_e}{\partial z} \quad\quad (1.173)$$

$$\tau_{q_{ph}}\frac{\partial q_{ph}}{\partial t} \;+\; q_{ph} \;=\; -K_{ph}\frac{\partial T_{ph}}{\partial z} \quad\quad (1.174)$$

α is the volume absorption coefficient. The phonon heat conductivity can in general be neglected compared to the electron heat conductivity (for metals at least) so these equations can be simplified. Because of the finite value of the relaxation time constants τ_q on short time scales, wave-like phenomena can occur with the result that within short times heat energy can be transported from colder to warmer regions. To describe the interaction of fs laser pulses with solid materials, the correction Eq. 1.170 and a two temperature model has to be used whereas in the case of ps pulses the simpler FOURIER's law can be applied.

1.5 Thermo Mechanics

1.5.1 Elastic Deformations

Within solid bodies, there can be stresses due to, e.g. deformations or thermal loadings. The force per unit area $\vec{t}$ that acts within a solid body on an area element with normal $\vec{n}$ can be expressed using the stress tensor $\hat{T}$. In components, the relation reads (Becker and Bürger 1975):

$$t_i = \tau_{ij}\, n_j \tag{1.175}$$

with

t_i—vector components of $\vec{t}$

n_j—vector components of $\vec{n}$

τ_{ij}—tensor components of $\hat{T}$.

Here, EINSTEIN's sum convention is applied, i.e. summation over double indices. The stress vector $\vec{t}$ does depend not only on the position but also on the normal $\vec{n}$, thus $\vec{t}$ is not a vector field, whereas $\hat{T}$ only depends on the position and because of this it is a tensor field. The stress-strain relation for elastic materials is given by[24]

$$\tau_{ij} = \frac{E}{1+\nu}\left(\gamma_{ij} + \frac{\nu}{1-2\nu}\gamma_{kk}\delta_{ij}\right) \tag{1.176}$$
$$\gamma_{kk} = \gamma_{11} + \gamma_{22} + \gamma_{33}$$

with

γ_{ij}—components of GREEN's strain tensor

E—YOUNG's modulus

ν—POISSON's ratio.

The components of the strain tensor in geometric linear approximation, i.e. in case of sufficiently small deformations, are given by

$$\gamma_{ij} = \frac{1}{2}\left(\frac{\partial u_i}{\partial x_j} + \frac{\partial u_j}{\partial x_i}\right) \tag{1.177}$$

The u_i are the components of the displacement vectors of the material points of the solid with respect to a reference configuration. If the position of a material point in the reference configuration is given by $\vec{x}_0$ then the position of the material point after deformation is given by

$$\vec{x} = \vec{x}_0 + \vec{u} \tag{1.178}$$

The reversal of Eq. 1.176 reads:

$$\gamma_{ij} = \frac{1+\nu}{E}\left(\tau_{ij} - \frac{\nu}{1+\nu}\tau_{kk}\delta_{ij}\right) \tag{1.179}$$
$$\tau_{kk} = \tau_{11} + \tau_{22} + \tau_{33}$$

---

[24] A derivation of this relation can be found in Appendix B.

1.5.1.1 Uniaxial Loading

It is assumed that a bar is loaded only longitudinally so that $\tau_{22} = \tau_{33} = 0$. Inserting it into Eq. 1.179 yields

$$E = \frac{\tau_{11}}{\gamma_{11}} \tag{1.180}$$

$$\nu = -\frac{\gamma_{22}}{\gamma_{11}} = -\frac{\gamma_{33}}{\gamma_{11}} \tag{1.181}$$

This clarifies the meaning of YOUNG's modulus and of POISSON's ratio. YOUNG's modulus equals the slope of the stress-elongation curve in case of uniaxial loading. E has the dimension N/m^2, i.e. that of stress. POISSON's ratio ν is the ratio of the lateral to the longitudinal strain in case of uniaxial loading. ν is dimensionless and its value typically lies between 0.2 and 0.49. For most metals, this value is about 0.3. POISSON's ratio is a measure for the compressibility of the material. With $\nu = 0.5$, the solid is incompressible, which means the solid volume doesn't change during arbitrary deformations. With $\nu = 0$, no lateral deformation occurs in case of only longitudinal loading.

1.5.1.2 Uniaxial Strain

Again, it is assumed that a bar is loaded only longitudinally. Additionally the bar is assumed to be clamped laterally. Then $\gamma_{22} = 0$ and $\gamma_{33} = 0$. Inserting it in Eq. 1.176 yields

$$\frac{\tau_{11}}{\gamma_{11}} = E\frac{(1-\nu)}{(1+\nu)(1-2\nu)} \tag{1.182}$$

$$\frac{\tau_{22}}{\tau_{11}} = \frac{\tau_{33}}{\tau_{11}} = \frac{\nu}{1-\nu} \tag{1.183}$$

1.5.2 Thermal Induced Stress

If a solid is heated it will expand in general. If the temperature is homogeneous and the expansion is not obstructed by external forces, then there will be no stresses within the body (unless there already had been stresses prior to heating). An unobstructed, isotropic expansion due to thermal heating can be described by the spherical symmetric tensor:

$$\gamma_{ij}(\theta) = \alpha\,\theta\,\delta_{ij} \tag{1.184}$$
$$\theta = T - T_0$$

with

α—coefficient of thermal expansion ($\alpha_{steel} \approx 6 \cdot 10^{-6}/K$)
T—temperature
T_0—temperature before heating.

Within the frame of a geometric and physical linear theory, the total strain tensor is given by a superposition of this tensor with the tensor Eq. 1.177:

$$\gamma_{ij} = \frac{1+\nu}{E}\left(\tau_{ij} - \frac{\nu}{1+\nu}\tau_{kk}\delta_{ij}\right) + \alpha\,\theta\,\delta_{ij} \tag{1.185}$$

The inverse relation reads:

$$\tau_{ij} = \frac{E}{1+\nu}\left(\gamma_{ij} + \frac{\nu}{1+\nu}\gamma_{kk}\delta_{ij}\right) - \frac{E}{1-2\nu}\alpha\,\theta\,\delta_{ij} \tag{1.186}$$

When the thermal induced expansion is totally obstructed, i.e. all components of the strain tensor are zero, the thermal induced stresses are given by

$$\tau_{ii} = -\frac{E}{1-2\nu}\alpha\,\theta \tag{1.187}$$
$$\tau_{ij,i\neq j} = 0$$

which is an isotropic stress state.

1.5.3 Plastic Deformation

In case of ideal elastic materials, deformations are reversible when the prescribed loadings are released. Real solids show this kind of behavior only for sufficiently small deformations. When the elasticity limit is exceeded, there remain deformations even when the loadings are released entirely. This kind of inelastic behavior can be time-independent or time-dependent. In the former case, only the order of the loadings is of importance but not the rate of the loadings. This rate-independent behavior is called plastic deformation. In the time-dependent case, the deformations not only depend on the loadings but also on their time rate. Examples are creeping and relaxation processes. Besides this cracks can occur. In the following, plastic deformations are considered in more detail.

Elastic deformations are in general accompanied by volume changes, whereas plastic deformations are generally volume preserving. A microscopic mechanism that underlies plastic deformation is the slipping of crystal layers along each other.

Fig. 1.32 Stress-strain
diagram of an ideal
elasto-plastic solid
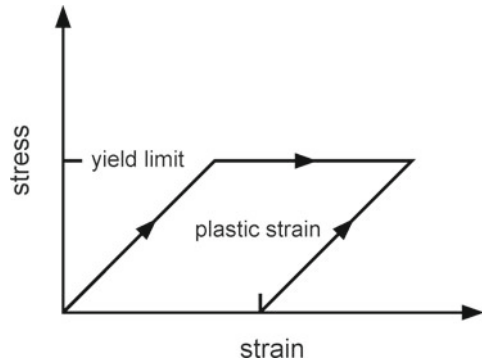
But the shear stresses that are necessary for this to take place are about 100 times larger compared to those that have been observed experimentally during plastic deformation. This is due to lattice impurities that can translocate in the presence of shear stresses. Because only single atoms have to be displaced contrary to whole crystal layers, the necessary forces are much lower. Impurities can be present before applying the loading or can be generated by the shear stresses, especially at the surfaces. Figure 1.32 schematically shows the strain-stress diagram of an ideal elasto-plastic solid in the case of uniaxial loading. Up to the yield point the material is elastic, the slope of the diagram equals YOUNG's modulus E. From the yield point the stress does not increase any further, the solid is solely deformed plastically. When releasing the loading, only the elastic contribution of the deformation is restored. This ideal behavior is not observed in general. The dislocation of impurities is partly obstructed by the plastic deformation, and the material hardens. Because of this, the stress increases even after reaching the yield point although with a smaller slope compared to the region of pure elastic deformation.

During elasto-plastic deformation, the strain tensor can be separated into an elastic and a plastic contribution:

$$\gamma_{ij} = \gamma_{ij}^e + \gamma_{ij}^p \tag{1.188}$$

The elastic part of the strain is related to the stress according to the linear stress-strain relation Eq. 1.176. Plastic deformation takes place according to the VON MISES criterion if (Betten 1993)

$$f(\tau_{ij}) = \sqrt{\frac{3}{2} S_{ij} S_{ij}} - Y(\lambda) = 0 \tag{1.189}$$

$$S_{ij} = \tau_{ij} - \frac{1}{3} \tau_{kk} \delta_{ij} \tag{1.190}$$

S_{ij} are the so-called stress deviators. They specify how much a stress state deviates from an isotropic stress state. Plastic deformations do not occur with isotropic stress

states. When $f(\tau_{ij}) < 0$ the deformation is elastic, and in case of $f(\tau_{ij}) = 0$ it is plastic. The plastic deformation takes place in such a way that the stress state always lies on the surface determined by $f(\tau_{ij}) = 0$ in the space of the stress components. λ is the integrated absolute value of the plastic deformation of the solid. The yield point depends on λ because according to the above-mentioned hardening of the material during plastic deformation, the yield point can be shifted to higher values. The strain tensor is symmetric so that a principal axis transformation can always be accomplished. In the frame of principal axis, all non-diagonal components of the stress tensor vanish. In that case, one gets

$$f(\tau_{ij}) = \sqrt{\frac{1}{2}\left[(\tau_{11} - \tau_{22})^2 + (\tau_{11} - \tau_{33})^2 + (\tau_{22} - \tau_{33})^2\right]} \qquad (1.191)$$

1.5.3.1 Examples of Plastic Deformations

Plastic deformation of solid materials is used in many areas. All metal sheet bending procedures rely on irreversible plastic deformation. But plastic deformations can also occur undesirably. During welding, part of the material is heated and even molten. During cooling and re-solidification, the material suffers volume changes which induces stresses that are partly limited by plastic deformations and partly remain as residual stresses. During heat treatment, volume changes can take place that in general are not restored entirely during cooling. In these situations residual stresses remain too.

1.6 Phase Transformations

There are many new metal alloys, ceramic materials and plastics that have become important materials in many fields of industrial production. Despite this, Fe-based materials still are widely used due to their versatile properties. Because of its low strength, pure Fe is rarely used but Fe-C alloys allow to produce steels and cast Fe grades of a great variety of desired properties. Due to the steel making process, there are besides C always other chemical elements present like Si, Mn, P and S. Further chemical elements like Cr, Ni, Mo, V, W, etc. are often added to get distinct properties. Considering additionally heat treatment which is mostly used to change mechanical properties, there is a great array of application areas for Fe-based materials.

There exist Fe-based materials of low up to the highest mechanical strengths ($340-2000$ N/mm^2), with excellent corrosion resistance, increased heat resistivity, good deformation properties even at low temperatures, high erosion resistance, good casting properties, weldability, etc. Not all of these desired properties can be realized

in a single steel grade, but in any grade there are a few of these properties that are accentuated. Principal distinctions are

- steel or cast steel
  these are Fe-C alloys that are ductile without any further treatment with less than 2.06% C
- cast Fe
  these are Fe-C alloys with more than 2.06% C (mostly between 2.5 and 5% C) which cannot be forged but only be casted.

1.6.1 Fe-C Diagram

1.6.1.1 Pure Fe

Below the melting temperature, Fe atoms compose crystals, though in the macroscopic realm no single crystals are formed but small crystallites. Fe exists in two distinct crystal structures. Below 911 °C, the crystal structure is cubic body-centered (cbc) (Fig. 1.33). There are four Fe atoms at the four corners of the equilateral cube and a further one in the center of the cube. This form of Fe is called α-Fe or ferrite. Below the CURIE temperature of 769 °C Fe is ferromagnetic, above this temperature it is paramagnetic. The crystal structure does not change when crossing this temperature. Above 911 °C, the crystal structure changes to be a cubic face-centered structure (cfc) (Fig. 1.34). In this case besides the four Fe atoms at the cube corners, there are eight Fe atoms on the eight faces of the cube. This crystal structure possesses a smaller density compared to the cubic body-centered structure and is called γ-Fe or austenite. When getting at 1392°, the cfc-structure is transformed back to form again a cbc-structure which is called δ-Fe or δ-ferrite. The reason for the transformations of

Fig. 1.33 Cubic body-centered α-Fe
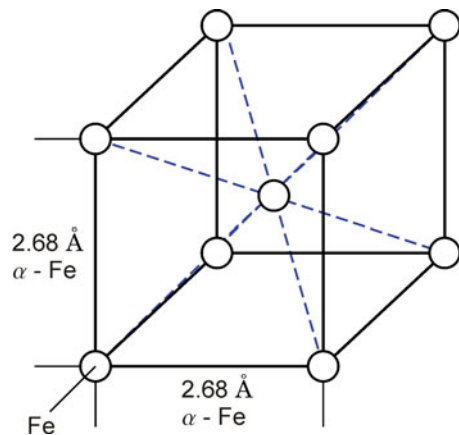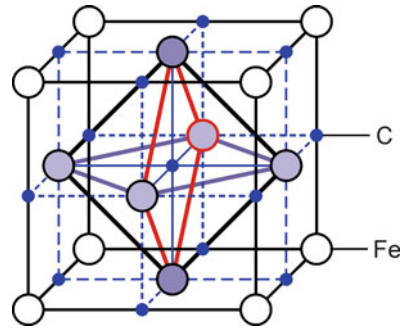
the crystal structures at 911 °C and 1392° respectively is that the newly built crystal
structures have lower total energy at the given temperatures. The transformations of
the crystal structures are called allotropic transformations because the transforma-
tion doesn't take place simultaneously within the whole solid but in the transition
region there exists a mixture of both crystal structures (Fig. 1.35). At 1536 °C, the
crystallites disintegrate and the material becomes liquid.

Commonly, the transition temperatures are specially named. The names are of
French origin:
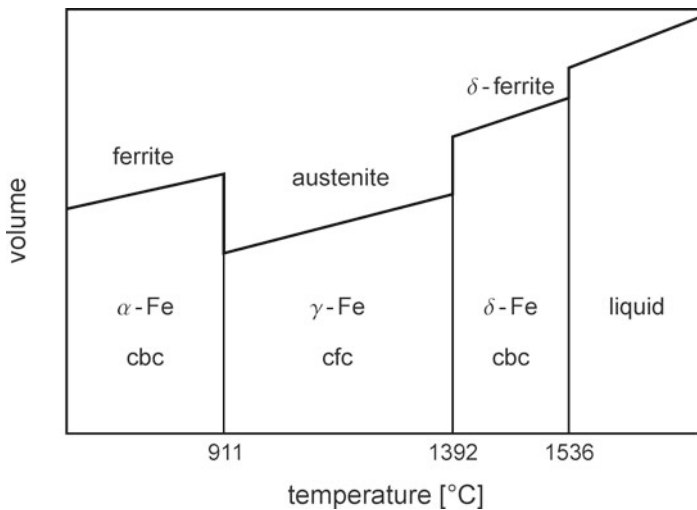
Fig. 1.35 Volume change during allotropic transformations

Transition	During heating	During cooling
melt $\rightleftharpoons \delta$	A_c	A_r
$\delta \rightleftharpoons \gamma$	A_{c4}	A_{r4}
$\gamma \rightleftharpoons \alpha$	A_{c3}	A_{r3}
$\alpha_{param} \rightleftharpoons \alpha_{ferrom}$	A_{c2}	A_{r2}
austenite $\rightleftharpoons$ perlite	A_{c1}	A_{r1}

A : arrêt
   hold temperature
c : chaffage
   heating
r : refroidissement
   cooling

1.6.1.2 Fe-C Mixtures

When there is no pure Fe but a Fe-C mixture, the situation becomes more involved. The C can exist in Fe alloys in different forms. Firstly, C can be dissolved in the Fe crystals (α, γ, δ) (Stüdermann 1967; Horstmann 1985). Solutions with different C-concentrations are called mixed crystals. The C solubility depends on the temperature and the crystal structure. The cfc-lattice (γ-Fe) has a maximal C-solubility of 2.01%, whereas the cbc-lattice (α-Fe and δ-Fe) has only a maximal solubility of 0.02%.

Besides being solved in the cfc or cbc Fe lattice, C can exist in the form of Fe_{3C}, called Fe-carbide. In some cases, C can also exist as an independent phase in the form of graphite. When the structure only consists of Fe-C mixed-crystals and carbide, the system is called metastable $Fe-Fe_{3C}$ system. This structure is preferably formed during rapid cooling. In the Fe-C diagram Fig. 1.36, the equilibrium lines are drawn through. The system consisting of Fe-C mixed crystals and C in the form of graphite is called stable Fe-C system. The equilibrium lines for this system are normally
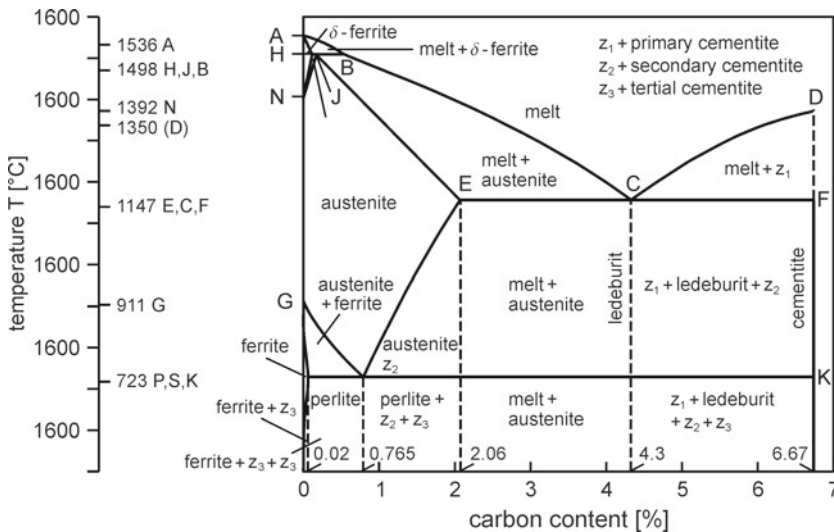
Fig. 1.36 Fe-C diagram

drawn dashed in the Fe-C diagram. In both cases, the equilibrium lines are valid only for sufficiently slow temperature changes.

Metastable System In the metastable Fe-Fe$_{3C}$ system, the C only exists in bound form up to a concentration-dependent temperature value. In the Fe-C diagram, the separation line is given by the line QPSECD. Above this line, C only exists in solved form.

Above the liquidus line ABCD the material is liquid. During cooling, Fe-C mixed crystals begin to form along the line ABC, and along the line CD primary crystallization (crystallization in the liquid phase) of Fe$_{3C}$ sets in. After primary crystallization of γ mixed crystals or Fe$_{3C}$, the melt solidifies when the line ECF (solidus line or eutectic line) is reached. Between liquidus and solidus line, a mixture of crystallites and melt coexists. Because the C concentrations of the primary melt and the crystallites differ, the concentration of the melt is shifted toward the C concentration of the eutectic point C. The transition point C at which two phases are created out of a single one is called eutecticum. The word eutecticum has its origin in Greek and means the immediate and complete transition from liquid to solid state or in other words liquidus and solidus lines coincide. Fe-C mixed crystals and carbide crystallites form simultaneously which leads to a fine-grained and uniform structure that consists of two different kinds of crystals. An eutectic alloy always has the lowest possible melting temperature and the best casting properties. In the Fe-C diagram at a temperature of 1145 °C and a C-concentration of 4.3%, there is a eutecticum. The structure that forms at this point is called LEDEBURIT (after its discoverer A. LEDEBUR). Because of the transformation of the γ mixed crystals at 723 °C to perlite (see below) at normal temperature, LEDEBURIT consists of perlite und carbide. At C-concentrations between 2.06% and 4.3% and at normal temperatures, there are besides LEDEBURIT perlite islands that originate from the primarily formed γ mixed crystals. At C-concentrations above 4.3%, there are extended carbide zones within the LEDEBURIT structure.

The Fe-C diagram shows a similar structure to the eutecticum at a C-concentration of 0.83% C and a temperature of 723 °C. At this point, the ferrite and carbide phases of the austenite structure segregate and form a structure called perlite. This 'small eutecticum' is called eutectoid. Accordingly, one speaks about eutectoidic, under eutectoidic ($< 0.83\%$ C) and over eutectoidic ($> 0.83\%$ C) steel.

During perlite formation, the homogeneous γ mixed crystal (austenite, cfc-lattice) with 0.8% C decays into a heterogeneous mixture of α-mixed crystals (0.02% C, ferrite, cbc-lattice) and Fe$_{3C}$ (6.67% C, carbide). This eutectoidic reaction is determined by diffusion which means that this process depends on the diffusion rate and thus on the temperature. The perlite formation itself happens by nucleation and crystal growth. Disk-like small carbide crystallites serve as nuclei that preferably are formed at austenite grain boundaries. In the immediate vicinity, the C-concentration in the austenite decreases and can easily be transformed to ferrite. Because of the reduced solubility of C in ferrite, the C atoms are 'squeezed out' of the ferrite regions and concentrate at the crystallite boundaries. This enhances the growth conditions for the C-rich Fe$_{3C}$ that is subsequently formed at these sites. This is the reason for the

disk-like structure of perlite. The disk width depends on the C diffusion rate which decreases with decreasing temperature. Thus, the structure of perlite becomes much finer when the transformation takes place at low temperatures.

List of the most important Fe-C **structures**:

- austenite: cfc γ-Fe
- ferrite: cbc α-Fe
- carbide: Fe_{3C}
- perlite: ferrite + carbide in the form of striations created during eutectoid decay of the austenite at 723 °C and a C-concentration of 0.8%
- LEDEBURIT I: eutectic (γ-Fe + Fe_{3C}) is created from the melt at 1147 °C and a C-concentration of 4.3%
- LEDEBURIT II: γ-Fe decays to perlite at 723 °C.

1.6.2 Hardening of Perlitic Structures

During hardening of perlite, the steel has firstly to be transformed to the austenite structure. Because of the finite diffusion rates, this make necessary a minimum holding time so that the C-concentration in the carbide filaments can decrease from 6.67% to under 2.01%, the maximum C-solubility of austenite (γ-Fe). The higher the temperature, the higher the diffusion rate and thus the lower the necessary holding time. When the material is now cooled very rapidly, no perlite can form any more because the C cannot diffuse out of the cubic face-centered ferrite (α-Fe). The C atoms that are captured in the Fe-crystal deform the crystal which makes it very hard. This structure is called martensite and besides being very hard it is also difficult to deform plastically because the C obstructs the movement of impurities and dislocations.

1.6.2.1 C-Diffusion

The atoms of a crystal lattice oscillate around their rest positions. Normally, they don't leave their position within the crystal. At sufficiently high temperatures, the energy of an atom can be large enough to be able to move within the crystal, and the atom is diffusing. The energy threshold for diffusion is called activation energy. Especially, impurity atoms that are much smaller than the host atoms can diffuse, like C in an Fe-matrix. The diffusion flux density is according to FICK's 1st law given by

$$\vec{j}_D = -D\,\vec{\nabla}c \tag{1.192}$$

with

D—diffusion coefficient

c—concentration of the diffusing species.

The diffusion coefficient D depends on the temperature and the crystal structure:

$$D = D_0 \exp\left[-\frac{E_A}{k_B T}\right] \tag{1.193}$$

with

D_0—frequency factor

E_A—activation energy.

The frequency factor D_0 describes the oscillation properties of the crystal lattice. The activation energy E_A is a measure of the energy threshold that atoms have to overcome in order to be able to move around. Figure 1.37 shows the diffusion coefficient of C in Fe as a function of the temperature. The temporal change of the concentration is according to FICK's 2. law:

$$\frac{\partial c}{\partial t} = \vec{\nabla} \cdot D \, \vec{\nabla} c \tag{1.194}$$

In the following, it will be assumed that there exists a plane carbide disk in the region given by $-z_{carbide} < z < z_{carbide}$. With this assumption and the assumption that the diffusion coefficient does not depend on the C concentration, Eq. 1.194 can be simplified:
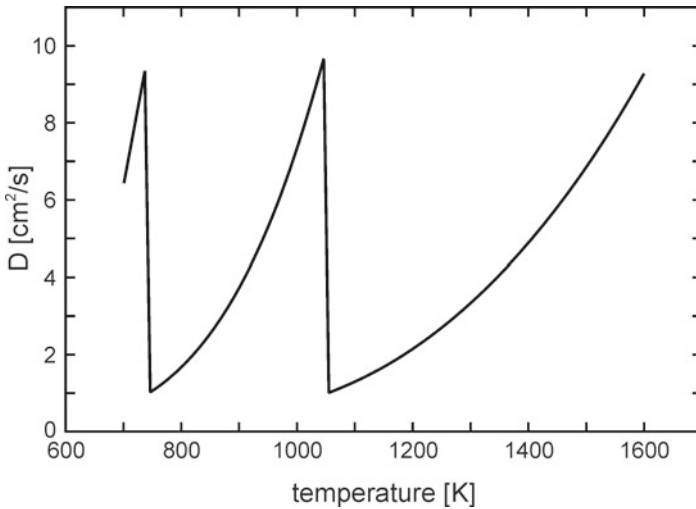
Fig. 1.37 C diffusion coefficient in Fe as function of the temperature
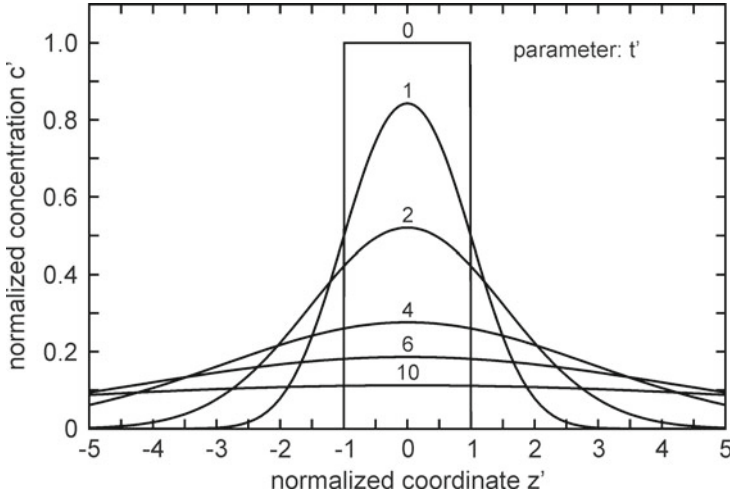
Fig. 1.38 Normalized C concentration according to Eq. 1.197 as a function of the normalized coordinate z' at different normalized time instances t'

$$\frac{\partial c}{\partial t} = D \frac{\partial^2 c}{\partial z^2} \tag{1.195}$$

The solution of Eq. 1.195 reads (see Appendix B.10):

$$c(z,t) - c_{ferrite} = \frac{1}{2}\left(c_{carbide} - c_{ferrite}\right)\left[\text{erf}\left(\frac{z + z_{carbide}}{\sqrt{4Dt}}\right) - \text{erf}\left(\frac{z - z_{carbide}}{\sqrt{4Dt}}\right)\right] \tag{1.196}$$

or in normalized form:

$$
\begin{aligned}
c'(z',t') &= \frac{c(z,t) - c_{ferrite}}{c_{carbide} - c_{ferrite}} \\
&= \frac{1}{2}\left[\text{erf}\left(\frac{z'+1}{\sqrt{t'}}\right) - \text{erf}\left(\frac{z'-1}{\sqrt{t'}}\right)\right] \\
z' &= \frac{z}{z_{carbide}} \\
t' &= \sqrt{\frac{4\,D\,t}{z_{carbide}^2}}
\end{aligned}
\tag{1.197}
$$

Figure 1.38 shows the normalized concentration c' as a function of the normalized coordinate z' at different normalized time instances t'.

The time constant τ for decay of the carbide disk follows from the requirement:

$$c(0, \tau) = c_{austenite} = c_{carbide} \; \text{erf} \left(\frac{z_{carbide}}{\sqrt{4D\tau}} \right) \tag{1.198}$$

With $c_{austenite} = 2.1\%$ and $c_{carbide} = 6.67\%$ it follows:

$$\text{erf} \left(\frac{z_{carbide}}{\sqrt{4D\tau}} \right) \approx \frac{1}{3.2} \tag{1.199}$$

and further:

$$\tau \approx 3 \; \frac{z_{carbide}}{D} \tag{1.200}$$

This time constant determines the minimum holding time for complete transformation of the perlite structure to the austenite structure. On the other hand, the material has to be cooled subsequently so rapidly that the austenite is totally transformed to martensite without forming unwanted crystal structures like perlite or beinite. This requires cooling rates of more than 10^3 K/s which implies short laser interaction times so that only that part of the workpiece is heated that has to be transformed whereas neighboring parts remain cold initially so that the heat can be transported rapidly from hot to cold regions. The necessary holding time can only be realized if the diffusion coefficient is sufficiently large which means that the transformation temperatures have to exceed by far the threshold of austenite formation. Equation 1.151 shows the time evolution of the temperature when applying a laser beam with a square pulse in time and in case that the assumption of 1-dimensional heat conduction is justified.

1.7 Melt Flow

During laser material processing, the material is often heated so strongly that it melts. In the case of laser surface alloying, the melt convection is forced by gradients of the surface tension which is utilized for the mixing of the basis material and the alloying material. During cutting and ablation, the material is expelled partly or entirely as melt, and during deep penetration welding, the melt flows around the key hole. A solution of the system of mass, momentum and energy conservation equations is, as in the case of heat conduction, only possible when appropriate initial and boundary conditions are prescribed. Boundary and initial conditions strongly depend on the specific problem at hand. In the present presentation, only simple models will be discussed that help to comprehend the main principles.

In the following, the equations governing fluid flow are presented and the boundary conditions at the interfaces liquid-solid and liquid-ambient atmosphere are discussed. Then two simple solutions are treated in more detail. The first one is plane potential flow around a cylinder. This serves as the first approximate model of the melt flow around the key hole during laser welding. The second one is boundary layer flow which occurs during cutting, drilling and ablation.

1.7.1   Mass, Momentum and Energy Conservation

Melt flow implies not only mass and momentum transport but energy transport as well. Thus in the mathematical treatment of melt flows, an energy equation has to be included besides the equations for mass and momentum transport. A derivation of these three equations can be found in Appendix B. The melt is virtually incompressible, which means the density is almost constant. The mass conservation equation Eq. 1.647 reads in this case:

$$\vec{\nabla} \, \vec{v} = 0 \tag{1.201}$$

The momentum or NAVIER-STOKES equation in case of incompressible fluids is given by

$$\frac{\partial \vec{v}}{\partial t} = -(\vec{v}\nabla) \, \vec{v} - \frac{\vec{\nabla} \, p}{\rho} + \nu \, \Delta \, \vec{v} + g \tag{1.202}$$

with
p—pressure
η—kinematic viscosity
ρ—mass density
$\nu = \eta/\rho$—dynamic viscosity
g—acceleration of gravity.

   In the energy equation Eq. 1.704, the heat generation due to friction can be neglected. With Eq. 1.705 it follows:

$$\frac{\partial \rho \, c_v \, T}{\partial t} = \vec{\nabla} \cdot (K \, \vec{\nabla} \, T) - \vec{\nabla} \cdot (\vec{v} \, \rho \, c \, T) + w \, (\vec{r}, t) \tag{1.203}$$

with T—temperature
c—specific heat capacity
K—heat conductivity
w—absorbed power density.

1.7.2   Boundary Conditions

The flow problem is only well posed if appropriate boundary conditions are prescribed. Melts that exist during laser material interaction are bound by solid material as well as by the ambient atmosphere or vapor, respectively. At the melt-solid interface, the boundary condition for the velocity field is

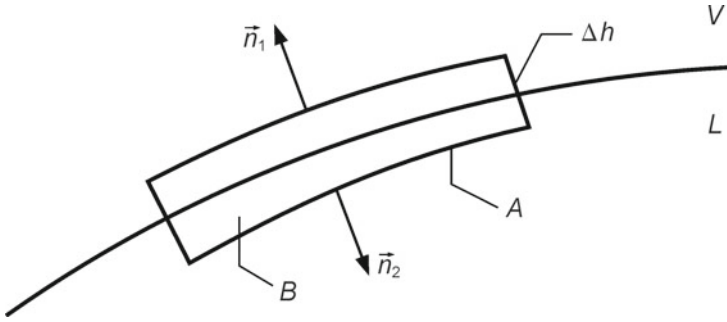$$\vec{v}_L|_{\text{boundary}} = \vec{v}_S|_{\text{boundary}} \tag{1.204}$$

Fig. 1.39 Momentum conservation at a free boundary between liquid (L) and vapor (V)

The index L designates the liquid phase and the index S the solid material. This equation implies that the velocity is continuous at the boundary. The continuity of the normal component allows solid material to enter the molten region which is transformed to the liquid phase in doing so. The continuity of the tangential component ensures the no-slip condition that applies in case of a flow involving friction.

The boundary between melt and ambient atmosphere is a free surface. In general, the contour of this surface is not fixed but adjusts itself according to the flow conditions and the ambient atmosphere. This has to be taken into account; the contour can, for example, be determined iteratively. In the case of a fixed contour of the free surface, the normal component of the velocity is

$$(\vec{v} \cdot \vec{n})|_{\text{boundary}} = 0 \tag{1.205}$$

Equation 1.205 implies that there is no mass flow through the boundary (evaporation is neglected here). The momentum flux at the surface follows from Eqs. 1.652 and 1.653. The integration volume B is shown in Fig. 1.39. If the height Δh becomes zero, the volume integral in Eq. 1.653 vanishes. The surface integral in Eq. 1.653 together with Eqs. 1.658 and 1.659 results in

$$(\hat{T}\,\vec{n}_1)_V + (\hat{T}\,\vec{n}_2)_L = -(\hat{T}\,\vec{n}_2)_V + (\hat{T}\,\vec{n}_2)_L \tag{1.206}$$
$$\vec{n}_1 = -\vec{n}_2$$

The index V designates vapor or ambient atmosphere, respectively. $\hat{T}$ is the stress tensor. The two normal vectors point in opposite directions (Fig. 1.39). The melt behaves like a NEWTONian fluid but the NEWTONian fluid stress tensor $\hat{T}$ has to be augmented by contributions that act at the surface. The surface tension σ induces the capillary pressure and gradients of the surface tension induce tangential forces (shear forces) at the boundary. This is shown schematically in Fig. 1.40. The surface forces are given by
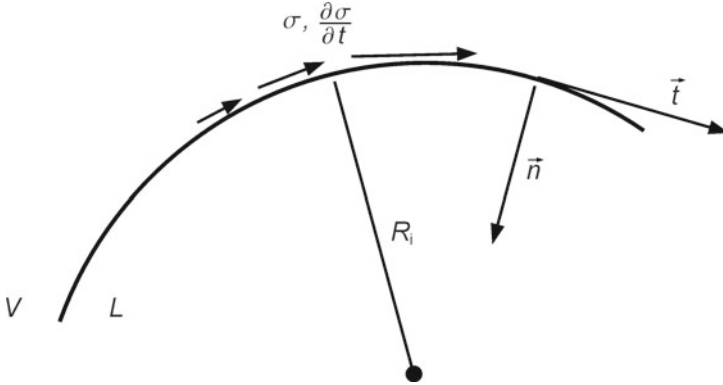
Fig. 1.40 Surface forces at boundaries between melt and gas. R_i is one of the two principal radii of curvature, σ is the surface tension and $\dfrac{\partial \sigma}{\partial t}$ is the change of the surface tension in the tangential direction. $\vec{n}$ and $\vec{t}$ are unit vectors in normal and tangential directions, respectively

$$(\hat{T}\,\vec{n})_{\partial B} = p_K\,\vec{n} + \frac{d\sigma}{dt}\,\vec{t} \tag{1.207}$$

$$p_c = \sigma \left(\frac{1}{R_1} + \frac{1}{R_2} \right) \tag{1.208}$$

with
$R_1,\ R_2$—principal radii of curvature of the boundary contour
p_c—capillary pressure.

The surface tension σ depends on the material at hand (small amounts of additives can have a significant impact) and the temperature. The interface shown in Fig. 1.40 is convex. In case of concave interfaces the radii of curvature have negative sign.

The contribution of the NEWTONian stress tensor follows from Eq. 1.679:

$$(\hat{T}\,\vec{n}) = -\bar{p}\,n_i + \eta \left(\frac{\partial v_i}{\partial x_j} + \frac{\partial v_j}{\partial x_i} \right) n_j \tag{1.209}$$

$$\bar{p} = p - \lambda \frac{\partial v_j}{\partial x_j} \tag{1.210}$$

with η—dynamic viscosity
λ—volume viscosity.

EINSTEIN summation convention is adopted (summation over double indices). The volume viscosity acts like a change of the static pressure. This volume effect vanishes in case of incompressible fluids. The component of Eq. 1.209 that is parallel to the surface normal is given by

$$(\hat{T}\,\vec{n}) \cdot \vec{n} = -\bar{p} + \eta \left(\frac{\partial v_i}{\partial x_j}\, n_i\, n_j + \frac{\partial v_j}{\partial x_i}\, n_i\, n_j \right) \qquad (1.211)$$

$$= -\bar{p} + \eta \left(\frac{\partial}{\partial x_j}(v_i\, n_i)\, n_j + \frac{\partial}{\partial x_i}(v_j\, n_j)\, n_i \right)$$

With Eq. 1.205 the second term on the right side vanishes. With Eqs. 1.206, 1.207 and 1.211 it follows:

$$(\hat{T}\,\vec{n}_2)_V \cdot \vec{n}_2 = -\bar{p}_V \qquad (1.212)$$

$$(\hat{T}\,\vec{n}_2)_L \cdot \vec{n}_2 = -p_L + p_C \qquad (1.213)$$

$$\bar{p} = p_L + p_C \qquad (1.214)$$

The component of Eq. 1.209 that is tangential to the boundary is given by

$$(\hat{T}\,\vec{n}) \cdot \vec{t} = \eta \left(\frac{\partial v_i}{\partial x_j}\, n_j\, t_i + \frac{\partial v_j}{\partial x_i}\, n_j\, t_i \right) \qquad (1.215)$$

$$= \eta \left(\frac{\partial}{\partial x_j}(v_i\, t_i)\, n_j + \frac{\partial}{\partial x_i}(v_j\, n_j)\, t_i \right)$$

The second term on the right side vanishes again because of Eq. 1.205. The first term is the derivative in normal direction of the tangential component of the velocity field. With this it follows:

$$(\hat{T}\,\vec{n}) \cdot \vec{t} = \eta\, \frac{\partial v_t}{\partial n} \qquad (1.216)$$

With Eq. 1.207:

$$(\hat{T}\,\vec{n}_2)_L \cdot \vec{t} = \eta_M \left(\frac{\partial v_t}{\partial n_2} \right)_L + \frac{d\sigma}{dt} \qquad (1.217)$$

$$(\hat{T}\,\vec{n}_2)_V \cdot \vec{t} = \eta_G \left(\frac{\partial v_t}{\partial n_1} \right)_V \qquad (1.218)$$

$$\eta_L \left(\frac{\partial v_t}{\partial n_2} \right)_L + \frac{d\sigma}{dt} = \eta_V \left(\frac{\partial v_t}{\partial n_1} \right)_V \qquad (1.219)$$

The surface tension is a function of the surface temperature T and of the concentrations c of alloying additives or impurities:

$$\sigma = \sigma(T, c) \qquad (1.220)$$

The gradient of the surface tension thus is given by

$$\frac{d\sigma}{dt} = \frac{\partial \sigma}{\partial T}\, \frac{\partial T}{\partial t} + \frac{\partial \sigma}{\partial c}\, \frac{\partial c}{\partial t} \qquad (1.221)$$

The temperature dependence of the surface tension of molten metal is quite well known (Brandes 1983). This does not equally hold for the concentration dependence. Additionally, the concentrations of the substances that are present at the boundary are often unknown. Even in the case of additives, the concentrations can differ from that in the bulk material because of selective vaporization. In the case of impurities like absorbed gases or oxides, the uncertainty is even larger.

1.7.3 Plane Potential Flow

If in a frictionless flow the curl of a velocity field is zero everywhere at a given time, then according to HELMHOLTZ's vortex theorem it will be zero for all times (Becker and Bürger 1975). With

$$\vec{\nabla} \times \vec{v} = 0 \tag{1.222}$$

the velocity field can be expressed as the gradient of a scalar potential field:

$$\vec{v} = \vec{\nabla}\phi \tag{1.223}$$

With

$$\vec{\nabla} \cdot \vec{v} = 0 \tag{1.224}$$

it follows:

$$\Delta\,\phi = 0 \tag{1.225}$$

The potential ϕ is thus a solution of LAPLACE's equation. For the solution of this kind of flow problem, standard methods of electrostatics can be used (method of conformal mapping).

1.7.3.1 Source and Dipole Flow

The velocity field of a line source is shown in Fig. 1.41. With the definition of the source

$$Q := \iint \vec{v} \cdot \vec{n}\, dA \tag{1.226}$$

 the velocity field is given by

Fig. 1.41 Velocity field of a
plane source flow
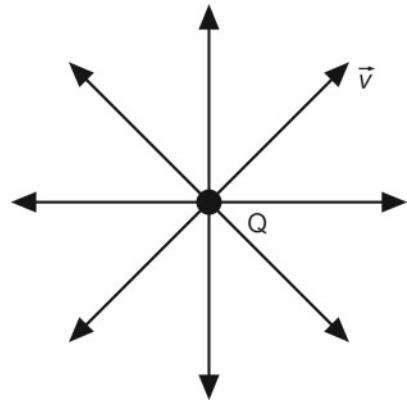
$$\vec{v} = \frac{Q}{4 \pi r^2} \, \vec{e}_r \qquad\qquad (1.227)$$

With this, the potential is

$$\phi = -\frac{Q}{4 \pi r} \qquad\qquad (1.228)$$

Figure 1.42 schematically shows the velocity field of a plane source flow. If the sign of Q is negative, Q is not a source but a drain. The superposition of the velocity field of a source and a drain results in a dipole flow whose potential is given by

$$\phi = -\frac{Q}{4 \pi} \left(\frac{1}{r} - \frac{1}{r'} \right) \qquad\qquad (1.229)$$

With the law of cosines it follows:

$$r'^2 = r^2 - 2 \, r \, \Delta x \, \cos \theta + \Delta x^2 \qquad\qquad (1.230)$$
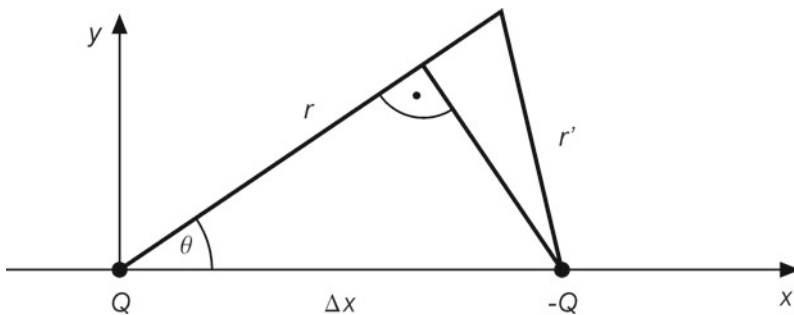
Fig. 1.42 Dipole flow

The distance Δx between source and drain is assumed to be small compared to r and r', respectively. Then it follows:

$$r' = r \left(1 - \frac{\Delta x}{r} \cos \theta\right)$$

(1.231)

and

$$\frac{1}{r'} = \frac{1}{r} \left(1 + \frac{\Delta x}{r} \cos \theta\right) + O\left(\frac{\Delta x^2}{r^2}\right)$$

(1.232)

Thus with $\Delta x \to 0$ while leaving the dipole moment M constant, the potential Eq. 1.229 approximately is given by

$$\phi = \frac{M}{4 \pi r^2} \cos \theta$$

(1.233)

With

$$\cos \theta = \frac{x}{r}$$

(1.234)

this results in

$$\phi = \frac{M}{4 \pi r^3} x$$

(1.235)

1.7.3.2 Flow Around a Cylinder

The superposition of the dipole flow Eq. 1.235 and a plane flow which has the potential:

$$\phi = v_\infty x$$

(1.236)

with the constant velocity v_∞ results in the potential:

$$\phi = v_\infty x \left(1 + \frac{a^3}{2 r^3}\right)$$

(1.237)

$$\frac{M}{4 \pi v_\infty} = \frac{a^3}{2}$$

(1.238)

With Eq. 1.223, the velocity components are given by

$$v_x = v_\infty \, x \, \left(1 + \frac{a^3}{2 \, r^3} - \frac{3}{2} \frac{a^3 \, x^2}{r^5} \right) \tag{1.239}$$

$$v_y = -v_\infty \frac{3}{2} \frac{a^3 \, x \, y}{r^5} \tag{1.240}$$

At $r = a$, it follows:

$$v_x = \frac{3}{2} \, v_\infty \, \left(1 - \frac{x^2}{a^2} \right) \tag{1.241}$$

$$v_y = -\frac{3}{2} \, v_\infty \, \frac{x \, y}{a^2} \tag{1.242}$$

The scalar product of the velocity and the position vector $\vec{r}$ at $|\vec{r}| = a$ vanishes:

$$(\vec{v} \cdot \vec{r})_{|\vec{r}|=a} = (v_x \, x + v_y \, y)_{|\vec{r}|=a} = 0 \tag{1.243}$$

The position vector is parallel to the cylinder surface normal. Equation 1.243 thus implies that the component of the velocity normal to the cylinder surface at $|r| = a$ vanishes and thus the velocity field given by Eqs. 1.239 and 1.240 constitutes a flow field around a cylinder with radius a. Figure 1.43 shows streamlines of the flow field Eqs. 1.239 and 1.240. At the points ($x = -a, y = 0$) and ($x = a, y = 0$) respectively, the velocity is zero. This two points are the front and rear stagnation points respectively. The velocity components as a function of the angle θ at the cylinder surface are given by
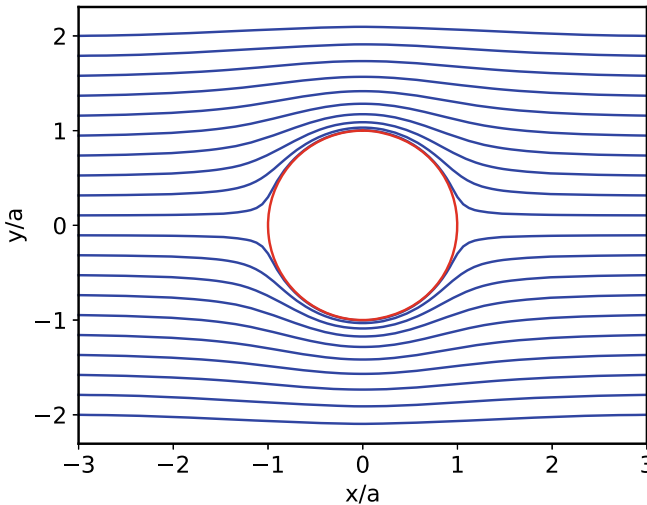
Fig. 1.43 Streamlines of a frictionless, incompressible flow around a cylinder

$$v_x = \frac{3}{2} v_\infty \, \sin^2 \theta \tag{1.244}$$

$$v_y = -\frac{3}{2} v_\infty \, \cos \theta \, \sin \theta \tag{1.245}$$

The absolute value of the velocity at the cylinder surface is thus

$$|v| = \frac{3}{2} v_\infty \, \sin \theta \tag{1.246}$$

According to BERNOULLI's law (Becker and Bürger 1975), the following relation holds along a streamline in case of a frictionless and incompressible fluid:

$$p + \frac{\rho}{2} |\vec{v}|^2 = \text{const.} \tag{1.247}$$

i.e. the sum of the static pressure and the dynamic pressure is constant along a streamline. Along the streamline that touches the cylinder surface, it thus holds

$$p_\infty + \frac{\rho}{2} v_\infty^2 = p(\theta) + \frac{9}{4} \frac{\rho}{2} v_\infty^2 \, \sin^2 \theta \tag{1.248}$$

At the stagnation points $\theta = 0$ and $\theta = \pi$ respectively, the velocity vanishes and the static pressure becomes

$$p = p_\infty + \frac{\rho}{2} v_\infty^2 \tag{1.249}$$

The static pressure is minimal at $\theta = \pi/2$:

$$p = p_\infty - \frac{5}{4} \frac{\rho}{2} v_\infty^2 \tag{1.250}$$

while the velocity has its maximum value at this point which amounts to $\frac{3}{2} v_\infty$. The force that acts on a unit area of the cylinder surface is given by

$$d\vec{f} = -\vec{e}_r \, p(\theta) \, a \, d\theta \, dz \tag{1.251}$$

$$\vec{e}_r = \cos \theta \, \vec{e}_x + \sin \theta \, \vec{e}_y \tag{1.252}$$

Integration over the total cylinder surface, i.e. from $\theta = 0$ to $\theta = \pi$, yields the total force that is exerted on the cylinder by the flow. The result shows that the total force vanishes which is in contradiction to experience. The reason for this is the idealization of a frictionless flow that was presupposed in the above derivation. Real flows aren't frictionless which especially show at boundaries. At flow-solid boundaries, the tangential flow component vanishes at the boundary due to friction

(no-slip condition). The tangential flow component increases rapidly within in a small layer away from the boundary up to (or nearly to) the value that a frictionless flow would have. Outside the boundary layer, the flow can approximately be treated as being frictionless if the contour of the solid body is assumed to include the boundary layer. Then the methods for treating plane frictionless potential flows can be applied, while the boundary layers are treated within the frame of the boundary layer theory. But this approximate solution has its limitations. The boundary layers can detach from the surface, and turbulences can emerge which cause forces on the body which is passed by the flow. In case of melt-gas (or melt-vapor) interfaces, like during laser welding, there is no no-slip condition of the melt. On the other hand during laser welding, only a small part of the material around the key hole is liquid whereas in the above-discussed case of flow around a cylinder the total region outside the cylinder was assumed to be liquid. The potential flow thus is only an approximation of the real melt flow around a key hole.

1.7.4 Laminar Boundary Layers

When a solid is passed by a fluid, then due to friction forces boundary layers evolve. Within the boundary layer thickness, the value of the tangential velocity component that is zero at the boundary increases up to (or nearly to) the value that the flow velocity would have without friction. Figure 1.44 schematically shows the boundary layer during flow around a plate.

The boundary layer theory rests on the assumption that the velocity component parallel to the surface is much larger than the component perpendicular to the surface and that the pressure gradient perpendicular to the surface can be neglected. The latter assumption makes it possible to use for the pressure gradient in x-direction the value outside the boundary. In the stationary case, the x-component of the NAVIER-STOKES equation reads:

$$v_x \frac{\partial v_x}{\partial x} + v_y \frac{\partial v_x}{\partial y} = -\frac{1}{\rho} \frac{\partial p}{x} + \nu \left(\frac{\partial^2 v_x}{\partial x^2} + \frac{\partial^2 v_x}{\partial y^2} \right) \tag{1.253}$$
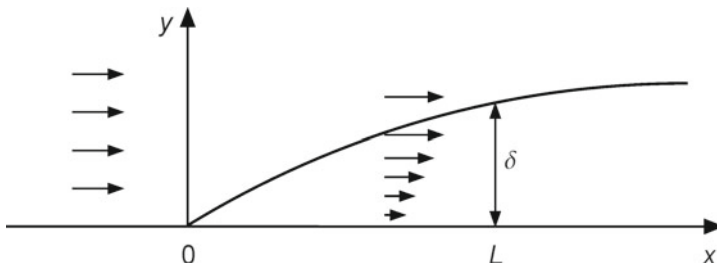
Fig. 1.44 Boundary layer at a plane plate. The plate begins at $x = 0$

with
ν—kinematic viscosity.

The boundary layer approximations are given by

$$|v_x| \gg |v_y| \tag{1.254}$$

$$\left.\frac{\partial p}{\partial x}\right|_{y=0} \simeq \left.\frac{\partial p}{\partial x}\right|_{y=\delta} \tag{1.255}$$

$$\frac{\partial v_x}{\partial x} = O\left(\frac{v_x}{L}\right) \tag{1.256}$$

$$\frac{\partial^2 v_x}{\partial x^2} = O\left(\frac{v_x}{L^2}\right) \tag{1.257}$$

$$\frac{\partial v_x}{\partial y} = O\left(\frac{v_x}{\delta}\right) \tag{1.258}$$

$$\frac{\partial^2 v_x}{\partial y^2} = O\left(\frac{v_x}{\delta^2}\right) \tag{1.259}$$

L is a characteristic length describing the extension of the boundary layer. The term

$$\frac{\partial^2 v_x}{\partial x^2} \tag{1.260}$$

can be neglected in the NAVIER-STOKES equation. On the other hand, the term

$$v_x \frac{\partial v_x}{\partial x} \tag{1.261}$$

cannot be neglected because it can have, according to Eq. 1.259, the same order of magnitude as

$$v_y \frac{\partial v_x}{\partial y} \tag{1.262}$$

With this, the boundary layer approximation of the NAVIER-STOKES equation neglecting the lifting force is given by

$$v_x \frac{\partial v_x}{\partial x} + v_y \frac{\partial v_x}{\partial y} = -\frac{1}{\rho}\frac{\partial p}{\partial x} + \nu \frac{\partial^2 v_x}{\partial y^2} \tag{1.263}$$
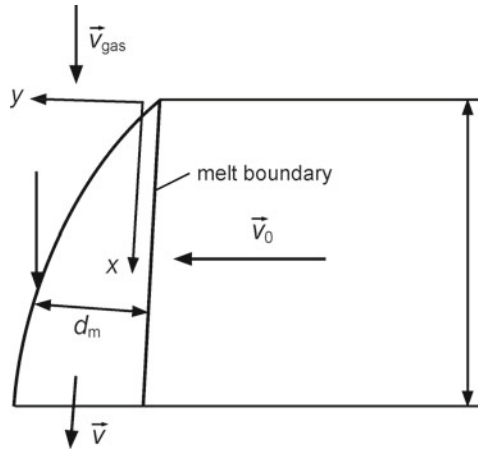
The continuity equation reads:

Fig. 1.45 Boundary layer
flow during laser material
processing

$$\frac{\partial v_x}{\partial x} + \frac{\partial v_y}{\partial y} = 0 \tag{1.264}$$

If the pressure gradient is known, these two equations are sufficient to solve the
problem. As mentioned above, the pressure gradient can approximately be deter-
mined using the solution of the flow problem outside the boundary layer with fric-
tion neglected. The pressure gradients that occur during laser material processing
are either determined by gas flows that are used to expel the melt or by the ablation
pressure that emerges during evaporation of material.

The boundary layer flows that exist during, for example, ablation and cutting are
slightly different from the one shown in Fig. 1.44. Figure 1.45 shows this schemat-
ically in case of laser cutting. The laser beam propagates from top to down and is
partially absorbed at the melt film surface. The absorbed laser intensity is used for
heating and melting of the material. The workpiece is moved to the left and the gas
flow coming from the top exerts pressure and shear forces onto the melt film that
lead to the expulsion of the melt. The material thus flows into the boundary layer at
$y = 0$ (and melts in doing so) and leaves the boundary layer region at $x = d$. The
mean velocity at $x = d$ can be determined using the work piece thickness d, the melt
film thickness d_m and the feed rate:

$$\bar{v}_x(x = d) = \frac{d}{d_m} v_0 \tag{1.265}$$

It is assumed that no melt is flowing through the melt surface. In this case, the
following kinematic condition has to be met by the melt thickness d_m (Vicanek et al.
1987):

$$\frac{d\,d_m}{dx} = \left| \frac{v_y}{v_x} \right|_{y=d_m} \tag{1.266}$$

$$d_m(0) = 0 \tag{1.267}$$

The REYNOLDS number appropriate for the problem at hand is

$$\mathrm{Re} = \frac{\rho \, v_0 \, d_m}{\eta} \tag{1.268}$$

The REYNOLDS number is a dimensionless number describing the ratio of the inertial forces to the friction forces within a flow. In the case of small REYNOLDS numbers ($\mathrm{Re} \ll 1$), the inertial term can be neglected compared to the friction term in Eq. 1.263 whereas in the case of large REYNOLDS numbers ($\mathrm{Re} \gg 1$) the friction term can be neglected.

1.7.4.1 Friction-Dominated Boundary Layer Flow

With $\mathrm{Re} \ll 1$ and neglecting the inertial term in Eq. 1.263, it follows:

$$\frac{\partial p}{\partial x} = \eta \, \frac{\partial^2 v_x}{\partial y^2} \tag{1.269}$$

The boundary condition at the melt surface is

$$-\eta \, \frac{\partial v_x}{\partial y}\bigg|_{y=d} = \tau \tag{1.270}$$

The shear stress τ that is exerted onto the melt surface by the gas jet and the pressure gradient are of the same order of magnitude (Vicanek and Simon 1987):

$$\tau = \sqrt{\frac{\eta_G \, \rho_G \, v_G^3}{d}} \tag{1.271}$$

$$\frac{\partial p}{\partial x} \simeq \frac{p_G}{d} \tag{1.272}$$

With the ansatz for the velocity v_x:

$$v_x = v_{x_0} + c_1 \, y + c_2 \, y^2 \tag{1.273}$$

the following solution results:

$$v_x = v_{x_0} - \frac{1}{\eta} \left(\tau \, y + \frac{\partial p}{\partial x} \, (d \, y - \frac{1}{2} \, y^2) \right) \tag{1.274}$$

Taking the derivative with respect to x yields

$$\frac{\partial v_y}{\partial x} = -\frac{1}{\eta} \frac{\partial v_y}{\partial x} \, y \, \frac{d \, d_m}{dx} \tag{1.275}$$

With the continuity equation:

$$\frac{\partial v_y}{\partial y} = -\frac{\partial v_x}{\partial x} \tag{1.276}$$

and Eq. 1.275, it follows for the velocity component v_y:

$$v_y = v_{y_0} + \frac{1}{\eta} \frac{\partial p}{\partial x} \, y \, \frac{d \, d_m}{dx} \frac{y^2}{2} \tag{1.277}$$

Using the kinematic condition Eqs. 1.266 and 1.274 as well as Eq. 1.277, the following determining equation for the boundary layer thickness d_m is obtained:

$$\frac{d_m^3}{d_p^3} + \frac{d_m^2}{d_\tau^2} = 1 \tag{1.278}$$

$$d_\tau^2 = \frac{2 \, \eta \, v_0 \, x}{\tau} \tag{1.279}$$

$$d_p^3 = \frac{3 \, \eta \, v_0 \, x}{-\dfrac{\partial p}{\partial x}} \tag{1.280}$$

With vanishing pressure gradient, the boundary layer thickness is given by d_τ whereas with vanishing shear stress it is given by d_p.

1.7.4.2 Inertia-Dominated Boundary Layer Flow

If the REYNOLDS number is large compared to 1 (Re $\gg$ 1), the friction in Eq. 1.263 can be neglected. Additionally, it will be assumed that

$$\frac{\partial v_y}{\partial y} = 0 \tag{1.281}$$

i.e. the melt is not accelerated in the y-direction. Hence, from the continuity equation it also follows:

$$\frac{\partial v_x}{\partial x} = 0 \tag{1.282}$$

With this, the momentum conservation Eq. 1.263 becomes

$$\frac{\partial v_x}{\partial y} = -\frac{1}{v_y \, \rho} \frac{\partial p}{\partial x} \tag{1.283}$$

The solution of this equation with $v_y = v_0$ is given by

$$v_x = v_{x_0} - \frac{1}{v_0 \, \rho} \frac{\partial p}{\partial x} \, y \tag{1.284}$$

Using the kinematic condition Eq. 1.266, the boundary layer thickness d_m follows:

$$d_m = \sqrt{\frac{2 \, \rho \, x}{-\dfrac{\partial p}{\partial x}} \, v_0} \tag{1.285}$$

1.8 Laser-Induced Vaporization

There are laser material treatment applications that are associated with the vaporization of material. Examples are laser drilling, laser welding (deep penetration welding at least), sublimation cutting and in some cases ablation.

The starting point of a physical description and mathematical treatment of evaporation processes is the evaporation in case of vapor-melt phase equilibrium. The equilibrium vapor pressure is given by the equation of CLAUSIUS-CLAPEYRON. If thermodynamic equilibrium exists there are as many particles leaving the melt surface, i.e. evaporate, as there are vapor particles that hit the melt surface and recondensate. In a state of thermodynamic equilibrium, there is no net flow of particles in either direction. This means that during material ablation, when there is a net flow of particles, the system is necessarily in a non-equilibrium state.

In what follows, approximate expressions for the net particle fluxes as a function of temperature during non-equilibrium evaporation are derived starting with the flux of particles that leave the melt surface in case of thermodynamic equilibrium vaporization. In doing so, it is assumed that the particles within the melt stay in a state of thermodynamic equilibrium. Using the derived vaporization rate as a function of temperature and the energy conservation equation, the evaporation rate as a function of the laser intensity is determined.

1.8.1 Vapor Pressure in Thermodynamic Equilibrium

A vessel partially filled with melt is assumed to be in a heat bath at the temperature T. The space above the melt is filled with vapor. In a state of thermodynamic equilibrium, it holds (Reif 1965)

$$T_V = T_M = T \tag{1.286}$$

$$p_V = p_M = p \tag{1.287}$$

$$g_V = g_M \tag{1.288}$$

with

T—temperature

p—pressure

g—free enthalpy per atom.

The saturation vapor pressure is a function of the temperature. The derivative of the saturation vapor pressure p_{SV} with respect to the temperature is given by the equation of CLAUSIUS-CLAPEYRON[25] (Adam and Hittmair 1978; Becker 1975; Reif 1965):

$$\frac{dp_{SV}}{dT} = \frac{H_V(T)}{(v_V - v_C)\,T} \tag{1.289}$$

mit:

v_V—specific volume in the vapor phase

v_C—specific volume in the condensed phase

H_V—evaporation enthalpy.

The evaporation enthalpy is the energy that has to be supplied in order to vaporize a given amount of material. The evaporation enthalpy is a function of the temperature.[26] The vapor is treated as ideal gas. With

$$v_V = \frac{1}{\rho} = \frac{R\,T}{p} \tag{1.290}$$

and Eq. 1.289, it follows:

$$\frac{dp_{SV}}{dT} = \frac{H_V(T)}{R\,T^2}\,p_{SV} \tag{1.291}$$

with ρ—mass density

R—ideal gas constant.

Integrating Eq. 1.291 with constant H_V yields

$$p_{SV} = p_0\,\exp\left(\frac{H_V}{R\,T_0}\right)\,\exp\left(-\frac{H_V}{R\,T}\right) \tag{1.292}$$

with

p_0—vapor pressure at T_0.

---

[25] See Appendix C.1.

[26] See Appendix C.2.

At $p_0 = 10^3$ hPa, the temperature T_0 corresponds to the evaporation temperature under normal conditions. With the abbreviation:

$$p_{SV,\max} = p_0 \, \exp\left(\frac{H_V}{R\,T_0}\right) \tag{1.293}$$

it follows:

$$p_{SV} = p_{SV,\max} \, \exp\left(-\frac{H_V}{R\,T}\right) \tag{1.294}$$

The saturation vapor density is given by

$$\rho_{SV} = \frac{p_{SV,\max}}{R\,T} \, \exp\left(-\frac{H_V}{R\,T}\right) \tag{1.295}$$

and the particle density by

$$n_{SV} = \frac{p_{SV,\max}}{m\,R\,T} \, \exp\left(-\frac{H_V}{R\,T}\right) \tag{1.296}$$

1.8.2 Vaporization Rate

The velocity distribution of the vapor particles in thermodynamic equilibrium is given by the MAXWELLian-distribution (Reif 1965):

$$f(v_x, v_y, v_z) = n_{SV} \left(\frac{m}{2\,\pi\,k_B\,T}\right)^{3/2} \exp\left(-\frac{m}{2\,k_B\,T}\,(v_x^2 + v_y^2 + v_z^2)\right) \tag{1.297}$$

with the saturation vapor density n_{SV} according to Eq. 1.296. The particle flux density of vapor particles hitting the melt surface and re-condensating there is given by (the x-axis is assumed to be normal to the surface)

$$j_{(V \to S)} = \int_{-\infty}^{0} v_x\,g(v_x)\,dv_x = -\frac{n_{SV}}{2}\,\frac{v_{TH}}{2} \tag{1.298}$$

$$g(v_x) = \int_{-\infty}^{\infty} f(v_x, v_y, v_z)\,dv_y\,dv_z = n_{SV}\,\sqrt{\frac{m}{2\,\pi\,k_B\,T}}\,\exp\left(-\frac{m\,v_x^2}{2\,k_B\,T}\right) \tag{1.299}$$

$$v_{TH} = \sqrt{\frac{8\,k_B}{\pi\,m}\,T} = \sqrt{\frac{8}{\pi}\,R\,T} \tag{1.300}$$

Fig. 1.46 Vapor pressure in thermodynamic equilibrium
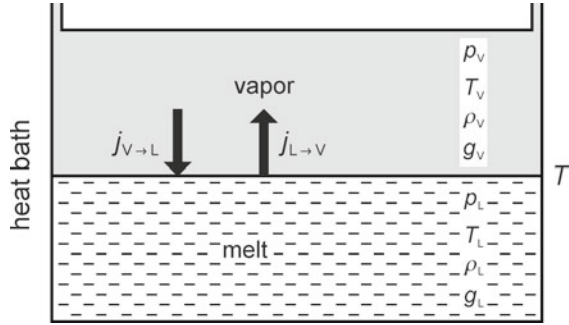
V_{TH} is the mean thermal speed. In thermodynamic equilibrium, the flux of particles emerging from the melt surface equals the flux of vapor particles hitting the melt surface and re-condensating there (see Fig. 1.46). Considering the directions of the fluxes, it holds

$$j_{(M \to V)} = -j_{(V \leftarrow M)} = \frac{n_{SV}}{2} \frac{v_{TH}}{2} \tag{1.301}$$

In thermodynamic equilibrium systems, there is no net vaporization. In case that the vapor state does not correspond to the equilibrium state, e.g. if the vapor is not enclosed but can freely expand, the particle flux density j of the particles emerging from the melt will still correspond to the equilibrium state at that temperature as long as the melt surface stays in the thermodynamic equilibrium state that corresponds to the given temperature. That means that the velocity distribution of the particles in the melt surface equals the equilibrium distribution or deviates only slightly. The velocity distribution Eq. 1.299 with $v > 0$ is the velocity distribution of the particles at the melt-vapor interface just emerging from the melt.[27] This distribution function thus does not depend on the state of the vapor phase but only on the state of the melt surface. As long as the melt stays in this thermodynamic state of equilibrium, the emerging vapor flux can be described using this velocity distribution function, which is a half MAXWELLian distribution. The distribution function is normalized so that the particle density is

$$n_V = \int\limits_{-\infty}^{\infty} g(v_x) \, dv_x \tag{1.302}$$

Because particles with velocity $v_x < 0$ do not exist in case of the half MAXWELLian distribution, the density of the particles is only half of the saturation particle density:

$$n_V = \frac{n_{SV}}{2} \tag{1.303}$$

---

[27] It is assumed here that all vapor particles that hit the melt re-condensate there.
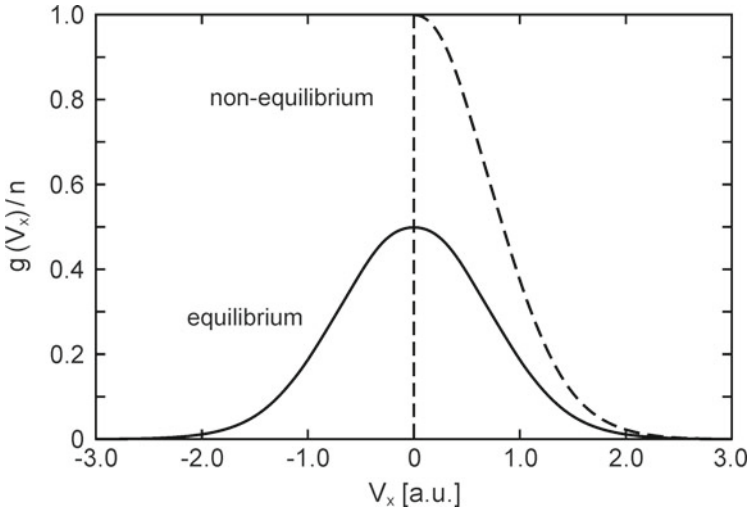
Fig. 1.47 Velocity distribution function, determined according to Eq. 1.299 (drawn through line) and Eq. 1.304 (dashed line), respectively. The distributions are normalized with respect to the densities

The probability of finding a particle velocity within a given velocity interval with $v_x > 0$ doubles in case of the half MAXWELLian because of the lack of particles with $v_x < 0$. The distribution function of the off-flowing particles is thus given by

$$g(v_x) = \frac{n_{SV}}{2} \, 2 \sqrt{\frac{m}{2 \pi k_B T}} \, \exp\left(-\frac{m \, v_x^2}{2 \, k_B T}\right) \Theta(x) \tag{1.304}$$

with
$\Theta(x)$—HEAVISIDE step function.

Figure 1.47 shows the velocity component $g(v_x)/n_V$ of the distribution function Eq. 1.304 together with the velocity component $g(v_x)/n_{SV}$ of the equilibrium distribution Eq. 1.299. The velocity of the off-flowing vapor equals the mean velocity in the x-direction. From the distribution function Eq. 1.304, it follows:

$$v_V = \frac{v_{TH}}{2} \tag{1.305}$$

which is just half the thermal speed.

Describing the non-equilibrium vaporization using the saturation vapor density Eq. 1.296 that was derived under the assumption of thermodynamic equilibrium is only justified as long as the melt surface stays in a state of thermodynamic equilibrium. The equilibrium state of the melt surface therefore may only be disturbed slightly. This holds if sufficiently few particles leave the melt surface. Sufficiently few means that the time constant of evaporation of a particle is large compared to the

time constant of relaxation toward an equilibrium state in the melt. The relaxation time constant t_{relax} amounts to a few mean collision times of the particles in the melt. The mean collision time is in the ps range so that as an upper bound it can be estimated that $t_{\text{relax}} \approx 10$ ps. The vaporization time constant $t_{\text{evaporate}}$ follows from the ratio of the number of particles per area N_{LS} on the melt surface to the flux density of evaporating particles ($n_V \, v_V$):

$$t_{\text{evaporate}} = \frac{N_{LS}}{n_V \, v_V} \tag{1.306}$$

Assuming the particle radius $r_a = 5 \cdot 10^{-10}$ m, one gets

$$N_{LS} \approx 10^{18} \text{ m}^{-2} \tag{1.307}$$

The equilibrium condition is given by

$$t_{\text{evaporate}} \gg t_{\text{relax}} \tag{1.308}$$

The maximum evaporation rate should thus obey the inequality:

$$n_V \, v_V \ll \frac{N_{LS}}{t_{\text{relax}}} = 10^{29} \frac{1}{m^2 \, s} \tag{1.309}$$

for the assumption to be justified that the melt stays in a thermodynamic state of equilibrium. The value given in Eq. 1.309 corresponds to an ablation rate of about 1 m/s. Because of collisions among vapor particles, the velocity of some of the particles can become negative so that they move back to the melt surface. The particle flux density according to Eq. 1.301 thus is an upper bound of the net particle flux off the melt surface at the temperature T.

The above-described simple model is similar to the model proposed by AFANASEV and KROKHIN (1967) that is based on the assumption that the evaporation can be described by a combustion wave. KROKHIN does not assume the velocity of the vapor particles at the melt surface be given by Eq. 1.305 but by the local velocity of sound.

The non-MAXWELLian velocity distribution of the vapor particles emerging from the melt surface is driven by collisions within a few free mean paths toward a MAXWELLian velocity distribution superimposed by a mean flow velocity. The transition layer is called KNUDSEN layer. The parameters density, temperature and mean flow velocity that determine the MAXWELL distribution have to be determined using kinetic models, which means a solution of the BOLTZMANN equation for the off-flowing particles has to be determined. The velocity distribution function can, for example, be computed by MONTE CARLO simulations (Murukami and Oshima 1974) or by approximate solutions of the BOLTZMANN equation (Ytrehus and Ostmo 1996). The parameters of the MAXWELL distribution outside the KNUDSEN layer depend on the surface temperature of the melt and the ratio of the vapor pressure at this tem-

perature to the pressure of the ambient atmosphere. If the ambient pressure equals the vapor pressure, no net evaporation takes place; this is the case of thermodynamic equilibrium. With increasing vapor pressure, the off-flow velocity increases and the temperature of the vapor particles decreases below the surface value. With further increasing vapor pressure or decreasing ambient pressure respectively, the velocity of the off-flowing vapor does only increase up to a certain value, which is given by the local value of the velocity of sound. The simple model described above mainly covers the case of strong evaporation. The predicted value of the velocity however is below the local velocity of sound and the predicted vapor temperature is too high. The deviations however are in many cases small enough to be tolerable; the vaporization rate ($n_V\ v_V$) anyway depends mainly on the absorbed laser intensity.

1.8.3 Particle and Energy Conservation During Laser-Induced Vaporization

In Sect. 1.8.2, an approximate expression for the evaporation rate as a function of the surface temperature was derived (Eq. 1.301 together with Eqs. 1.300 and 1.296). The surface temperature is determined by the laser intensity that is absorbed within a thin surface layer, by conduction of heat into the material and by the off-flowing vapor (Fig. 1.48). In the stationary 1-dimensional case, the particle conservation can be written as

$$n_V\ v_V = n_0\ v_p \tag{1.310}$$

 with
n_V—vapor density

Fig. 1.48 Schematic drawing of the ablation of metals with laser radiation
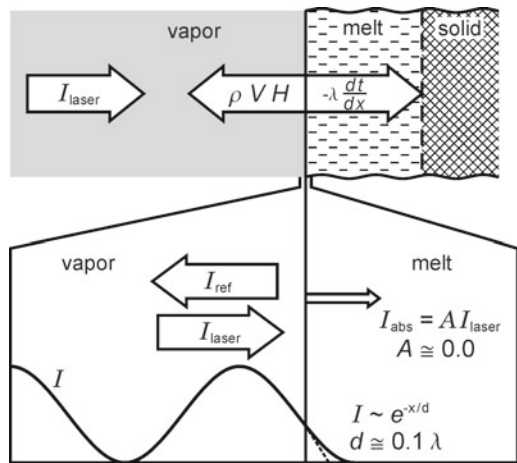
v_V—vapor velocity
n_0—density of the melt
v_p—process or ablation rate.

Energy conservation is given by Aden et al. (1990)

$$I_{abs} = m \, n_0 \, v_p \, (H_V + H_m + c_p \, T) \tag{1.311}$$

with
I_{abs}—absorbed laser intensity
c_p—specific heat capacity for constant pressure
H_V—evaporation enthalpy
H_m—melting enthalpy
m—mass of the vapor particles.

In the energy conservation equation Eq. 1.311, the kinetic energy of the vapor has been omitted. With Eqs. 1.310, 1.311, 1.296 and 1.305 and the assumption that the vapor temperature equals the surface temperature, it follows:

$$I_{abs} = I_0(T) \, \exp\left(-\frac{H_V}{R \, T}\right) \tag{1.312}$$

$$I_0(T) = \frac{p_{SV,\text{max}}}{R \, T} \, (H_V + H_m + c \, T) \, \frac{1}{4} \sqrt{\frac{8}{\pi} \, R \, T} \tag{1.313}$$

The exponential factor in Eq. 1.312 varies much stronger as a function of the temperature than $I_0(T)$ does so that $I_0(T) \approx I_0(T_V)$ can be assumed. Then Eq. 1.311 can be resolved with respect to the temperature:

$$T \simeq \frac{H_V}{R} \, \frac{1}{\ln\left(\dfrac{I_0(T_V)}{I_{abs}}\right)} \tag{1.314}$$

T_V is the temperature corresponding to the saturation vapor pressure of 1050 mbar. The temperature varies only slightly with the absorbed intensity. The particles density follows using Eqs. 1.310, 1.311 and 1.305:

$$n_V = 2 \frac{I_{abs}}{\sqrt{\dfrac{8}{\pi} \, R \, T}} \, \frac{1}{m \, (H_V + H_m + c \, T)} \tag{1.315}$$

In Eq. 1.315, the temperature according to Eq. 1.314 can be inserted. Because the temperature varies only slightly with the absorbed intensity also $T = T_V$ can approximately be used. Using the surface temperature that can be computed either by the implicit relation Eq. 1.312 or by the approximation Eq. 1.314, all thermodynamic quantities of the vapor can be determined:
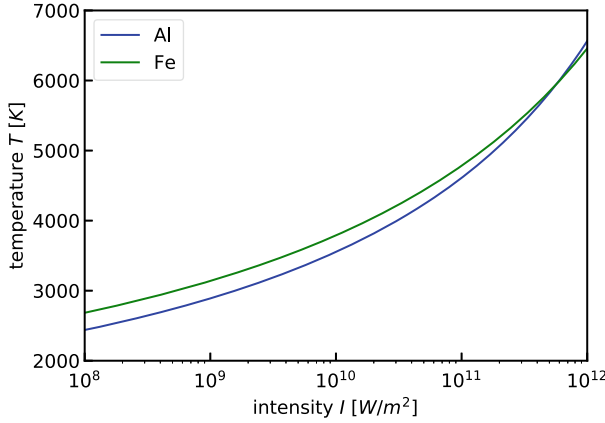
Fig. 1.49 Temperature as a function of the absorbed laser intensity determined using Eq. 1.312

$$T_V = T \tag{1.316}$$

$$p_V = \frac{1}{2} \, p_{SV,\max} \, \exp\left(-\frac{H_V}{R\,T}\right) \tag{1.317}$$

$$n_V = \frac{1}{2} \, \frac{p_{SV,\max}}{m\,R\,T} \, \exp\left(-\frac{H_V}{R\,T}\right) \tag{1.318}$$

$$v_V = \frac{1}{2} \sqrt{\frac{8}{\pi}\,R\,T} \tag{1.319}$$

The process rate follows from the energy conservation Eq. 1.311:

$$v_p = \frac{I_{abs}}{m\,n_0\,(H_V + H_m + c_p\,T)} \tag{1.320}$$

Figures 1.49, 1.50, 1.51, 1.52, 1.53 and 1.54 show T_V, p_V, n_V, v_V and v_p as a function of the absorbed intensity for Al and Fe.

The energy conservation equation Eq. 1.311 implies that in the 1-dimensional stationary case, the absorbed laser energy is used to heat and subsequently melt and evaporate the material. In the general 3-dimensional case, part of the laser energy is lost by heat conduction to regions of the material that are not going to be vaporized. These losses reduce the surface temperature compared to the 1-dimensional case or equivalently make necessary a higher laser intensity in order to get the same surface temperature. Thus in general, the effect of 3-dimensional heat conduction has to be taken into account in the energy conservation equation. This requires to solve the time-dependent 3-dimensional heat conduction equation together with the appropriate application-dependent boundary conditions. Analytical solutions can only be found in special cases. Using numerical methods makes possible to solve even very
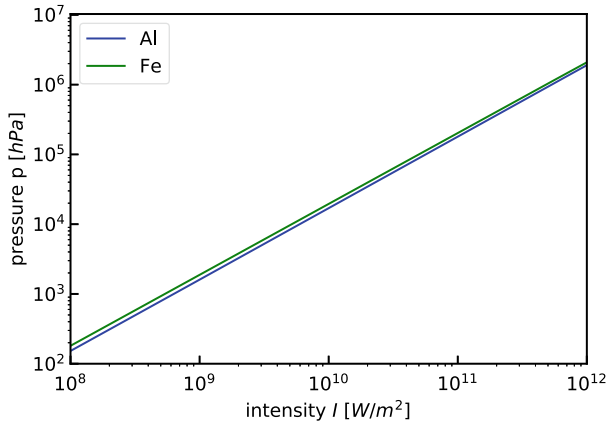
Fig. 1.50   Vapor pressure as a function of the absorbed laser intensity determined using Eq. 1.317
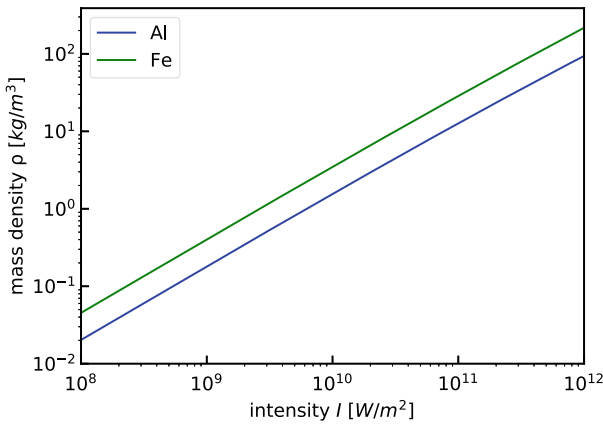
Fig. 1.51   Vapor density as a function of the absorbed laser intensity determined using Eq. 1.318

complicated problems but at the expense of large implementation and computing efforts.

1.8.4   Description of the Evaporation Process as a Combustion Wave

The above-described evaporation model is to be understood as the first approximation. The particles flowing back to the melt surface were neglected and for the temperature and the vapor velocity simple assumptions were made. If the saturation evaporation pressure only deviates slightly from the ambient pressure, the assump-
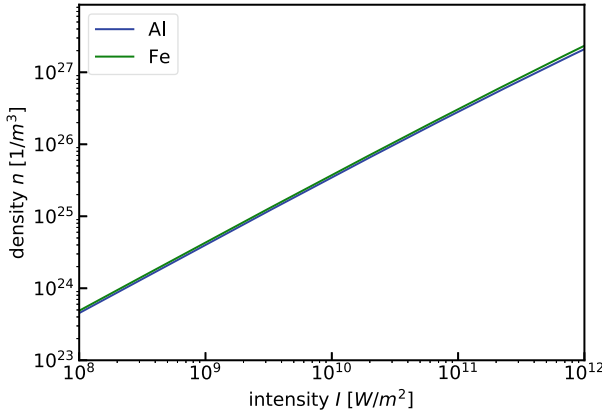
Fig. 1.52 Vapor velocity as a function of the absorbed laser intensity determined using Eq. 1.319
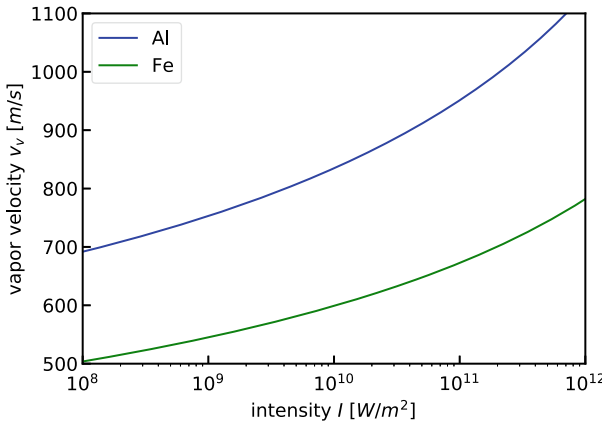
Fig. 1.53 Ablation rate as a function of the absorbed laser intensity determined using Eq. 1.320

tion that the vapor temperature equals the surface temperature is surely justified. On the other hand in this case of weak vaporization, the number of particles flowing back to the melt surface cannot be neglected and the above presupposed value of the vapor velocity derived from the half MAXWELLian distribution is too high. In the case of strong evaporation on the other hand, the temperature drops below the melt temperature due to the vapor expansion and acceleration within the KNUDSEN layer and the vapor velocity can reach the local velocity of sound (Ytrehus and Ostmo 1996). The proposal of AFANASEV and KROKHIN to describe evaporation in analogy to combustion waves marks an improvement in the modeling of evaporation processes. Originally, this model was applied to the case of strong evaporation. In the following, this idea is described in a slightly modified form.
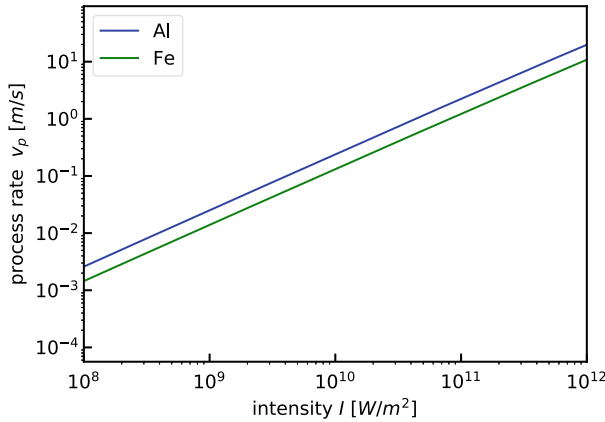
Fig. 1.54 Evaporation rate ($n_V \, v_V$) as a function of the absorbed laser intensity

In the theory of combustion waves, the combustion front is treated as a discontinuity (Fig. 1.55). The not yet combusted material flows into the discontinuity where the combustion takes place. The chemical energy that is released during combustion is transferred into heating and accelerating the material. In the case of laser-induced evaporation, the chemical energy is replaced by the absorbed laser energy. The states of the material on the left- and right-hand sides of the discontinuity respectively are related by the jump conditions of RANKINE-HUGONIOT. The absorbed laser energy has to be included in the energy conservation equation. The RANKINE-HUGONIOT jump conditions read:

$$\rho_1 \, v_1 = \rho_2 \, v_2 \tag{1.321}$$

$$\rho_1 \, v_1^2 + p_1 = \rho_2 \, v_2^2 + p_2 \tag{1.322}$$

$$I_V + \rho_1 \left(e_1 + \frac{p_1}{\rho_1} + \frac{v_1^2}{2} \right) = \rho_2 \left(e_2 + \frac{p_2}{\rho_2} + \frac{v_2^2}{2} \right) \tag{1.323}$$

The index 1 designates the quantities within the melt and the index 2 the quantities within the vapor, respectively. The intensity I_V is that part of the laser intensity that is transferred into evaporation. The total absorbed laser intensity is composed of this part and the part that is used to heat and melt the material. With this it follows:

$$I_V = I_{abs} - \rho_1 \, v_1 \, (H_v + H_m + c \, T) \tag{1.324}$$

The internal energy e_1 is

$$e_1 = c_1 \, T \tag{1.325}$$

In e_2, the evaporation energy has to be taken into account:

Fig. 1.55 Schematic drawing of a combustion front. The layer between the regions 1 and 2 is treated as an infinitely thin discontinuity. In reality, this layer has a finite thickness within which the local equilibrium state of region 1 relaxes to the local equilibrium state of region 2. Within this layer, there exists no MAXWELLian distribution of particle velocities and thus no local thermodynamic equilibrium. On the right side of region 2, it is indicated that the state of the off-flowing gas is not constant in general, but where the 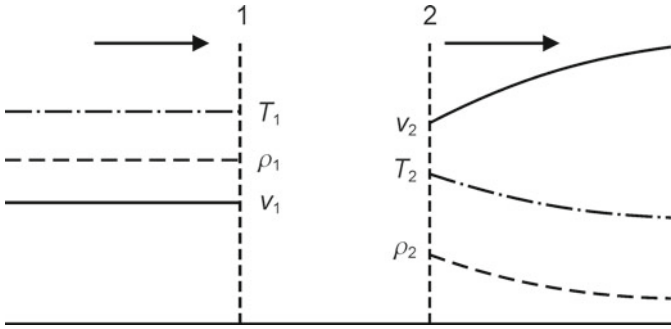states of the gas are always states of local thermodynamic equilibrium. This region is not included in the present treatment because this would make it necessary to solve the flow problem with the appropriate boundary conditions imposed by the ambient atmosphere

$$e_2 = c_2\, T + H_V \qquad (1.326)$$

It is assumed that within the vapor, the ideal gas law holds

$$p_2 = \rho_2\, R\, T_2 \qquad (1.327)$$

AFANASEV and KROKHIN (1967) assumed equal temperatures for melt and vapor and that the vapor velocity equals the local velocity of sound. ADEN (1990) proposed a different assumption. It is well known from the theory of combustion waves that the local velocity of sound is the limiting velocity that cannot be exceeded (Chorin and Marsden 1979). This is expressed by the CHAPMAN- JOUGUET condition. During weak vaporization, the vapor velocity can be below this value. If the vapor velocity is below the local velocity of sound, the ambient vapor (or gas) acts back on the vapor flow in the vicinity of the surface and by this on the evaporation process. In that case, the vapor flow has to be calculated self-consistently. This will not be done here but there can be gained some useful results even without a complete solution. In doing so, the vapor pressure is prescribed and all the other quantities, e.g. the vapor velocity, are computed using this quantity. The value of the ambient pressure at which the vapor velocity reaches local velocity of sound is the minimal pressure that can exist in front of the melt surface. Even when there is vacuum downstream, the evaporated vapor itself causes this minimal pressure. In that case, the evaporation is not influenced by the ambient atmosphere. During expansion of the vapor within the KNUDSEN layer, the temperature decreases. In order to take this into account, the following additional condition for the single particle energy is required to hold (Aden et al. 1990):

$$\frac{3}{2} k_B T_1 + \frac{m}{2} v_1^2 = \frac{3}{2} k_B T_2 + \frac{m}{2} v_2^2 \tag{1.328}$$

The sum of the thermal and the kinetic energy of a particle is conserved during evaporation. In thermodynamic equilibrium, the pressure in the melt equals the saturation vapor pressure. This is composed of the momentum that the off-flowing vapor exerts on the melt surface and the momentum transfer of the particles that flow back from the vapor region onto the melt surface. If a part of the back-flowing particles are missing, the pressure in the melt decreases. In Aden et al. (1990), this is taken into account by the following assumption:

$$p_1 = p_{SV}(T_1) - \rho_2 v_2^2 \tag{1.329}$$

The pressure within the melt is reduced compared to the saturation vapor pressure by the momentum flux density of the net number of evaporated particles. The heat capacity at constant volume of a monoatomic ideal gas is given by

$$c_V = \frac{3}{2} \frac{k_B}{m} = \frac{3}{2} R \tag{1.330}$$

In crystal solids well above the DEBYE temperature, the heat capacity is twice as large, i.e. $c_V = 6/2\ R$.[28] In fluids, the value of the heat capacity lies between these two values. Because the internal energy is much smaller than the evaporation enthalpy, the error introduced by Eq. 1.330 in the energy conservation equation Eq. 1.323 is negligible. Likewise, the pressure work p/ρ can be neglected on both sides of Eq. 1.323. With this and with Eq. 1.321 again, the energy conservation equation Eq. 1.311 follows:

$$I_{abs} = \rho_2 v_2 (H_V + H_m + c\ T) \tag{1.331}$$

Neglecting the first term on the left side of Eq. 1.322 together with Eq. 1.329 results in

$$p_{SV} = 2 \rho_2 v_2^2 + p_2 \tag{1.332}$$

The velocity v_2 is normalized with respect to the local velocity of sound c_2:

$$\hat{v} = \frac{v_2}{c_2} \tag{1.333}$$

$$c_2 = \sqrt{\kappa\ R\ T}$$

with κ—adiabatic coefficient.

---

[28] Three degrees of freedom of the kinetic energy and three degrees of freedom of the potential energy.

The vapor density is normalized with respect to the saturation vapor density:

$$\hat{\rho} = \frac{\rho_2}{\rho_{SV}} \tag{1.334}$$

$$\rho_{SV} = \frac{p_{SV}}{R\,T_1} \tag{1.335}$$

and the pressure with respect to the saturation vapor pressure:

$$\hat{p} = \frac{p_2}{p_{SV}} \tag{1.336}$$

Eq. 1.332 becomes

$$2\,\kappa\,\hat{v}^2\hat{p} + \hat{p} = 1 \tag{1.337}$$

or

$$\hat{v}^2 = \frac{1 - \hat{p}}{2\,\kappa\,\hat{p}} \tag{1.338}$$

If the vapor pressure equals the saturation vapor pressure, i.e. $\hat{p} = 1$, then $\hat{v} = 0$ and thus also $v_2 = 0$. In that case there is no net evaporation. This is again the case of thermodynamic equilibrium. The vapor velocity cannot exceed local velocity of sound which means $\hat{v}_{\max} = 1$. The minimal normalized vapor pressure is then using $\kappa = 5/3$:

$$\hat{p}_{\min} = \frac{1}{1 + 2\,\kappa} \simeq 0.23 \tag{1.339}$$

The value of the pressure within the vapor can thus not be smaller than $0.23\ p_{SV}$. Neglecting the kinetic energy of the melt in Eq. 1.328 and applying the normalizations Eqs. 1.333, 1.334 and 1.336 results in

$$\frac{3}{2}\,R\,T_1 = \frac{3}{2}\,R\,T_2 + \frac{1}{2}\,v_2^2 \tag{1.340}$$

$$\hat{v}^2 = \frac{3}{\kappa}\left(\frac{\hat{\rho}}{\hat{p}} - 1\right) \tag{1.341}$$

With Eq. 1.337, this becomes

$$\hat{\rho} = \frac{1}{6}\,(1 + 5\hat{p}) \tag{1.342}$$

With the minimal value of $\hat{p}$ (Eq. 1.339), the minimal value of the normalized density is given by

$$\hat{\rho}_{\min} = 0.358 \qquad (1.343)$$

The ratio of the temperatures T_2 and T_1 is

$$\hat{T} = \frac{T_2}{T_1} = \frac{\hat{p}}{\hat{\rho}} = \frac{6\,\hat{p}}{1 + 5\,\hat{p}} \qquad (1.344)$$

The minimal value of the normalized temperature is thus

$$\hat{T}_{\min} \simeq 0.64 \qquad (1.345)$$

The solid lines in Fig. 1.57 are the normalized velocity v_2/c_2, the normalized density ρ_2/ρ_{SV} and the normalized temperature T_2/T_1 respectively as a function of the inverse of the normalized vapor pressure p_{SV}/p_2 with p_2 being the pressure at the KNUDSEN layer-vapor interface. The pressure p_2 does not equal the pressure of the ambient atmosphere but rather depends on the evaporation rate (and itself influences it) and on the density and pressure of the ambient atmosphere. For a more exact computation of the vaporization rate the vapor density, the vapor temperature, the energy conservation within the solid, the evaporation process itself and the vapor flow downstream of the KNUDSEN layer considering the boundary conditions imposed by the ambient atmosphere have to be solved self-consistently.[29]

1.8.5 Kinetic Model of the Evaporation and the KNUDSEN Layer

In the following, a kinetic model of the evaporation is outlined (Ytrehus and Ostmo 1996). Again, the assumption is made that in case of non-equilibrium evaporation, the particles that leave the melt surface have the same velocity distribution as in the case of total thermodynamic equilibrium. Figure 1.56 schematically shows the evaporation process. The melt surface is located at $x = 0$. The distribution function of the off-flowing particles at the melt surface corresponds to a half MAXWELLian distribution. The particle density equals half the saturation density at the given surface temperature:

$$f_{SV}(0, \vec{v}) = n_{SV} \left(\frac{m}{2\,\pi\,k_B\,T_1(0)} \right)^{\frac{3}{2}} \exp\left(-\frac{m\,(v_x^2 + v_y^2 + v_z^2)}{2\,k_B\,T_1(0)} \right) \quad : \quad v_x \geq 0 \quad (1.346)$$

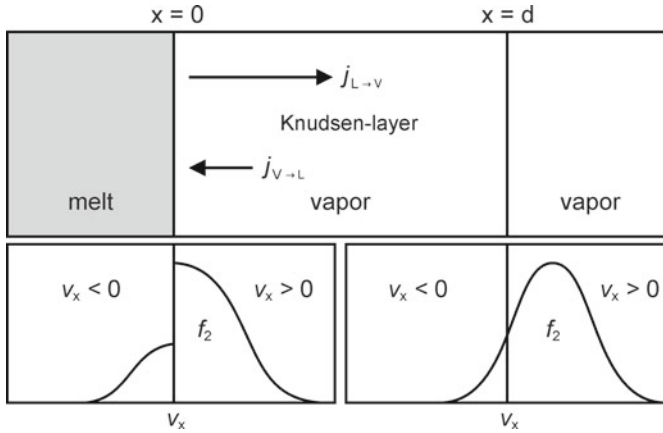---

[29] See also Aden et al. (1990).

Fig. 1.56 Schematic diagram of the velocity distribution function at the melt surface and the edge of the KNUDSEN layer. Within the KNUDSEN layer, the non-MAXWELLian distribution function of the vapor particles at $x = 0$ relaxes toward a MAXWELL distribution with superimposed mean flow velocity. The thickness d of the KNUDSEN layer amounts to a few free path lengths. The edge of the KNUDSEN layer at $x = d$ cannot be defined as sharply as it is depicted here

The distribution function of the back-flowing particles ($v_x < 0$) is not known so a reasonable assumption has to be made for this. The total distribution function of off-flowing and back-flowing particles in general is no MAXWELLian distribution.[30] The vapor particles relax on their way through the KNUDSEN layer to a MAXWELLian distribution with superimposed mean flow velocity caused by collisions among the vapor particles:

$$f_2(d, \vec{v}) = n_2(d) \left(\frac{m}{2 \pi k_B T_2(d)} \right)^{\frac{3}{2}} \exp\left(-\frac{m \left([v_x - v_2(d)]^2 + v_y^2 + v_z^2 \right)}{2 k_B T_2(d)} \right) \quad (1.347)$$

The vapor density n_2, the temperature T_2 and the vapor velocity v_2 follow from the requirement of conservation of the particle, momentum and energy flux densities. This means that the particle, momentum and energy flux densities respectively have to be equal if either computed using the velocity distribution function at the melt surface or at the point $x = d$.[31] For this, an assumption has to be made for the distribution function of the back-flowing particles at the melt surface. YTREHUS (1996) proposed the following distribution function at the melt surface:

$$v_x > 0 : f_1(0, \vec{v}) = f_{SV}(0, \vec{v}) \tag{1.348}$$
$$v_x < 0 : f_1(0, \vec{v}) = \beta \cdot (f_2(0, \vec{v}) + f_{SV}(0, \vec{v})) \tag{1.349}$$

---

[30] This only holds in case of thermodynamic equilibrium.

[31] For the computation of moments of the velocity distribution, see Appendix C.3.
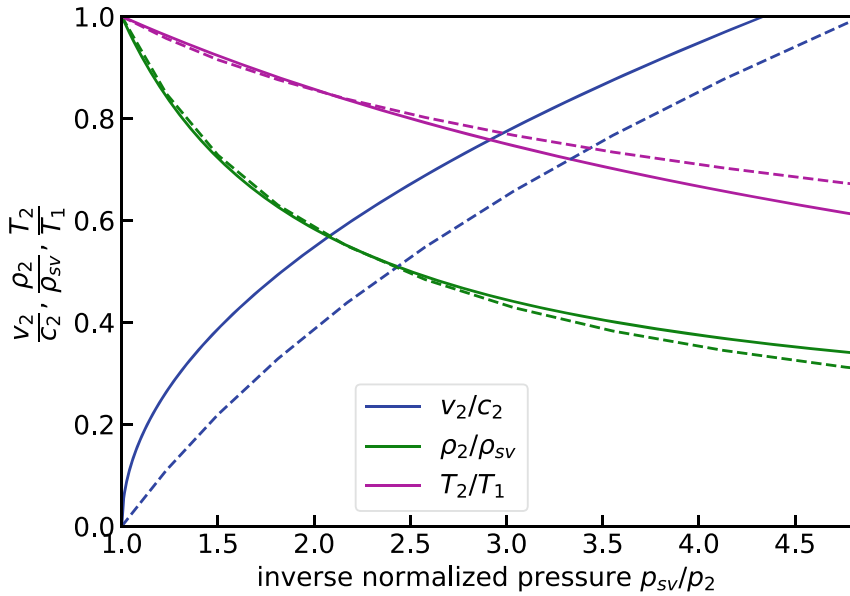
Fig. 1.57 Normalized velocity, normalized density and normalized temperature as a function of the normalized vapor pressure. Solid lines according to Eqs. 1.338, 1.342 and 1.344, respectively. Dashed line values taken from YTREHUS (1996, Table 1)

The distribution function of the back-flowing particles is the sum of the distribution function at the edge of the KNUDSEN layer Eq. 1.347 and the distribution function that corresponds to the equilibrium state (Eq. 1.346) multiplied by a factor β. Given are the surface temperature as well as another quantity at the edge of the KNUDSEN layer at $x = d$. This can be either the pressure or in the case of strong evaporation the velocity which in that case equals the local velocity of sound. The three conservation equations for particle density, momentum and energy are three equations for the three unknowns n_2, v_2 and β respectively in case that the pressure is prescribed or n_2, T_2 and β in case that the velocity is prescribed (and equals the velocity of sound). Figure 1.57 shows the normalized velocity, the normalized density and the normalized temperature as a function of the normalized pressure. Comparison with the combustion model shows that there are only minor differences between the normalized densities and temperatures, whereas the normalized velocities differ more.

1.9 Plasma Physics

The energy of the laser radiation that is applied to the workpiece during laser material processing has to be transformed effectively into usable process energy. The normal light absorptivity at those wavelengths for which high power lasers are available today is quite low in case of dielectrics and in case of metals its value lies in the 10–40% region.[32] When exceeding a critical intensity in general, an increase of the absorptivity can be observed (Kocher et al. 1972; Peschko 1981). Figure 1.58 shows this behavior in case of processing Cu using a pulsed Nd:YAG laser. At small intensities, the reflectivity corresponds to the normal reflectivity; after exceeding the critical value of the intensity, the reflectivity decreases to a value of almost zero. The decrease of the reflectivity is accompanied by an increase of the energy coupling into the workpiece. The increased coupling can be ascribed to a plasma that develops at the workpiece surface. This plasma is created by the incident laser beam. The plasma absorbs a great part of the laser energy and partly transfers the energy to the work piece (Pirri 1979). All materials with low absorption and high thermal conductivity, such as diamond and sapphire, are best processed with lasers using this plasma-assisted method (Kocher et al. 1972).

For the optimal coupling of the plasma energy into the workpiece surface, the plasma has to be located near the surface. This can be realized by short laser pulses or in vacuum. With longer laser pulses or with normal ambient atmosphere LSD (**L**aser **S**upported **D**etonation) waves are created that absorb the laser energy at the side
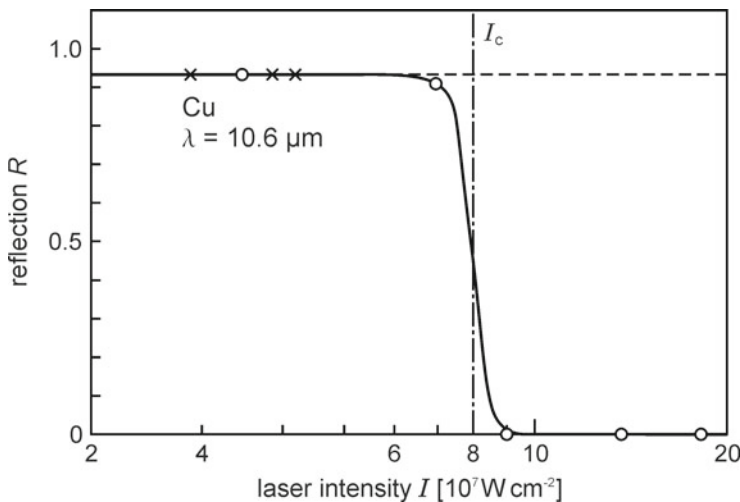

Fig. 1.58 Reflectivity R of a Cu target as a function of the laser intensity with normal incident gained from drilling experiments with pulsed Nd:YAG-lasers with a pulse length of $t_L \simeq 10^{-7}$ s (Peschko 1981)
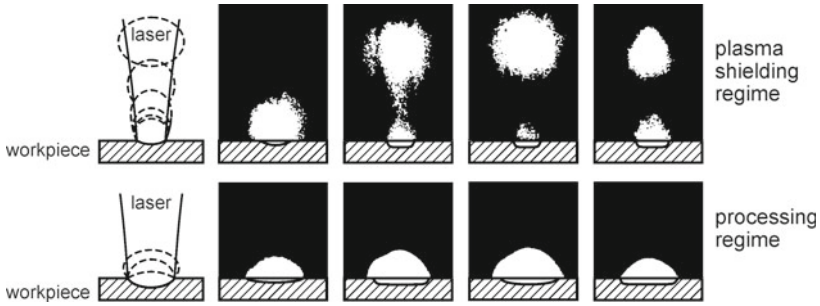
---

[32] See Sect. 1.3, Fig. 1.13.

Fig. 1.59 Framing-shoots of the laser-induced plasma above a steel specimen during processing with a pulsed CO_2-laser beam with 50 ns time gaps (Beyer et al. 1986). Upper row: plasma shielding, laser intensity $I > 2 \cdot 10^7 \, \dfrac{W}{cm^2}$, the plasma detaches from the workpiece surface. Lower row: laser processing, laser intensity $2 \cdot 10^6 \, \dfrac{W}{cm^2} < I < 10^7 \, \dfrac{W}{cm^2}$, the plasma stays in contact with the workpiece surface

remote from the specimen surface. The threshold intensity for LSD wave formation increases with the wavelength of the laser radiation. Figure 1.59 shows pictures made with a framing camera while exposing a steel specimen to CO_2-laser radiation. The individual frames are each separated in time by 50 ns. If the intensity is carefully adapted, the glowing plasma stays in contact with the workpiece surface (lower row of Fig. 1.59). The laser energy is absorbed in the plasma near the surface and is transformed into heat and radiation in the UV and visible region and is subsequently partly transferred to the specimen surface (Pirri 1979). At higher intensities, the vapor density and accordingly the absorption increase (upper row of Fig. 1.59). The laser energy is almost entirely absorbed in a thin plasma sheet at the side remote from the surface so that only a small fraction of the laser energy reaches the surface. The plasma is strongly heated and accelerated away from the workpiece. When it detaches, laser processing is interrupted. Only after expansion and sufficient rarefaction of the plasma, the laser beam can again reach the specimen surface and processing can go on.

On the one hand, the laser-induced plasma can be utilized to increase the energy coupling (this is called 'plasma- enhanced coupling'), but there can also be situations when the plasma shields the specimen so that the laser energy cannot reach the workpiece surface any more. The vapor plasma can not only absorb but also scatter the laser light, mostly due to material clusters that are either ejected from the melt surface or evolve by condensation within the vapor. A further effect of the hot plasma is the pressure force exerted onto the surface that can deform the surface so that a key hole forms that expands deeply into the workpiece.

The comprehension of all this phenomena makes necessary a knowledge of the plasma physics basics. Plasma physics is a large and complex field so here only a short introduction can be presented. First, the concept of DEBYE shielding is explained. In many cases of interest, the laser-induced plasmas are in a state of (near) thermody-

namic equilibrium. Equilibrium state variables are compiled. Of special importance is the SAHA equation that allows to calculate electron and ion densities. Furthermore, transport processes and the corresponding transport coefficients as well as the interaction of laser light with plasmas are discussed. Then some non-equilibrium processes are shortly presented. The last part covers the field of radiation that is emitted by plasmas.

1.9.1 Debye Radius and Definitions

A plasma is a many-particle system that in general consists of free electrons, neutral atoms and positively as well as in some cases negatively charged ions. A principal characteristic of plasmas is their electric neutrality, i.e. in a plasma there exist as much positive as negative charges. However, this must not be the case for an arbitrarily chosen sub-volume of the plasma. When choosing the sub-volume to just include a single electron or ion charge, neutrality obviously is violated. Even if there are several particles within the chosen sub-volume, charge neutrality need not necessarily exist. If there is a net charge within a sub-volume, ambient charges of opposite sign are attracted while those of the same sign are repelled. By this, the original net charge is compensated for. The length scale within which charge compensation takes place is called shielding length and depends on the charge density and the ratio of the COULOMB interaction energy and the mean thermal energy of the particles. In the following, the screening length in the DEBYE approximation is derived. For this, a single ion (the same holds for electrons) is considered which is treated as a point charge while the other charge carriers surrounding the ion are treated as a charged continuum. This corresponds to the self-consistent field approximation (or mean field approximation) in solid-state physics and the HARTREE-FOCK approximation in atomic physics, respectively. The electrons are attracted by the ion while the other positive ions are repelled. Due to the COULOMB interaction, the probability of finding a plasma electron closer to positive ions and farther away from electrons (and if present negative ions) is enhanced compared to the case of no COULOMB interaction. This holds correspondingly for ions too. The long distance COULOMB interaction leads to correlations among the spatial locations of the charged particles and thus enhances the order of the system compared to a system without COULOMB interaction which means that the entropy of a plasma is smaller than that of a system with no COULOMB interaction. The densities of electrons and ions surrounding the single ion are given by BOLTZMANN factors:

$$n_e = n_{e_0} \exp\left(\frac{e\,\phi}{k_B\,T}\right) \tag{1.350}$$

$$n_p = n_{p_0} \exp\left(-\frac{e\,\phi}{k_B\,T}\right) \tag{1.351}$$

with e—elementary charge
k_B—BOLTZMANN constant
T—plasma temperature.

n_{e_0} and n_{p_0} are the mean densities of electrons and ions, respectively. The distributions Eqs. 1.350 and 1.351 are equilibrium distributions. For the assumption of equilibrium to apply, the time constants for relaxation toward the equilibrium state have to be sufficiently small. In the following, it is assumed that the energy $e\,\phi$ is small compared to the mean thermal energy $k_B\,T$. Then the exponential factors in Eqs. 1.350 and 1.351 can be linearized. The density of the single ion is described by a DIRAC delta function. The electric potential obeys POISSON's equation:

$$\Delta\,\phi = -\frac{e}{\varepsilon_0}\,\delta(r) + \frac{e}{\varepsilon_0}\,(n_e - n_p) \tag{1.352}$$

Inserting the linearized densities results in

$$\Delta\,\phi = -\frac{e}{\varepsilon_0}\,\delta(r) + \frac{e^2\,(n_{e_0} + n_{p_0})}{\varepsilon_0\,k_B\,T}\,\phi \tag{1.353}$$

The solution of this equations reads:

$$\phi = -\frac{e}{4\,\pi\,\varepsilon_0\,r}\,\exp\left(-\frac{r}{r_D}\right) \tag{1.354}$$

with the DEBYE radius[33]:

$$r_D = \sqrt{\frac{\varepsilon_0\,k_B\,T}{e^2\,(n_{e_0} + n_{p_0})}} \tag{1.355}$$

The first part in Eq. 1.354 is the potential of the point charge of the single ion, while the exponential describes the contribution of the surrounding plasma particles. The potential of a point charge in a plasma decays outside a distance given by the DEBYE radius much stronger than the potential of an isolated point charge. This means that a plasma is electrically neutral on scales that are large compared to the DEBYE radius.

Figure 1.60 shows the DEBYE radius as a function of the electron density at a plasma temperature of 1 eV (11600 K). The electron densities in laser-induced plasmas during laser material processing with CO_2-laser radiation with intensities in the range of several 10^{10} W m^{-2} are between 10^{22} and 10^{23} m^{-3} and the temperatures are about 0.5–2.0 eV (Beyer 1985). With an electron density of 10^{23} m^{-3} and a temperature of 1 eV, the DEBYE radius amounts to $r_D = 16$ nm. At higher intensities, the values of electron density and temperature are in general higher too. The main assumption in deriving the above expression of the DEBYE radius was that the surrounding electrons and ions can be treated as a continuous charged cloud. This

---

[33] The generalization in case of multiple charged ions can be found in Appendix D.2.
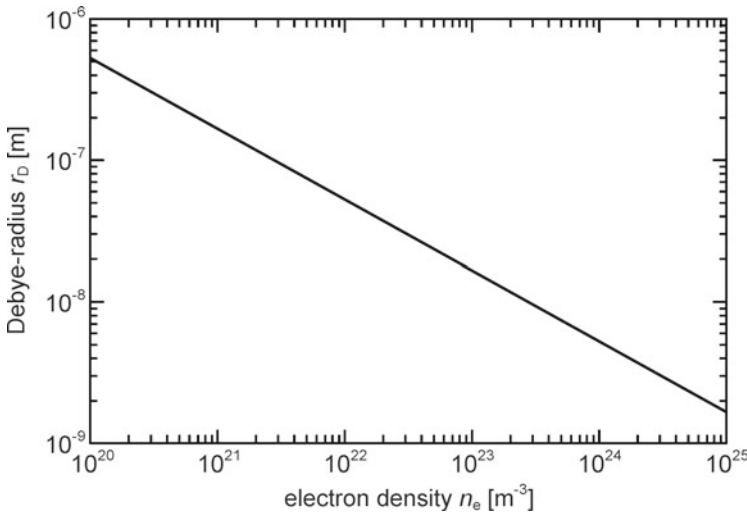
Fig. 1.60 DEBYE radius as a function of the electron density computed using Eq. 1.355 with a temperature of 1 eV (11600 K)

implies that there are many particles within a DEBYE sphere. The number of particles within a DEBYE sphere is given by

$$N_D = \frac{4}{3} \pi \, (n_e + n_i) \, r_D^3 \tag{1.356}$$

This number has to be large compared to 1 for the DEBYE approximation to hold. When this requirement is not met, the concept of shielding has to be modified. The shielding radius then becomes larger compared to the results of the DEBYE approximation (Ebeling et al. 1976). With the above-mentioned values of the electron density and the temperature $N_D = 3.4$, which means that the prerequisites of the DEBYE approximation are only met approximately. This will be further discussed in Sect. 1.9.3. Expanding the exponential in Eq. 1.354 in case of small values of r_D results in

$$\phi = -\frac{e}{4 \pi \, \varepsilon_0} \frac{1}{r} + \frac{e}{4 \pi \, \varepsilon_0} \frac{1}{r_D} \tag{1.357}$$

The first term on the right-hand side is the potential of the single ion and the second term is the potential that is caused by the other plasma particles at the single ion location.

A further important quantity in plasma physics is the LANDAU length l which is defined as the distance from a point charge at which the potential energy equals the mean thermal energy of the plasma particles:

$$l = \frac{e^2}{4 \pi \varepsilon_0 k_B T} \tag{1.358}$$

A plasma approximately behaves like an ideal gas if the mean thermal energy of the particles by far exceeds the mean COULOMB interaction energy. This requirement is met in case that the mean distance between the plasma particles is large compared to the LANDAU length. The plasma parameter:

$$\Gamma = l \, (n_e + n_i)^{1/3} \tag{1.359}$$

thus has to be small compared to 1 for a plasma to be an ideal plasma. Another important parameter is the ratio of the LANDAU length and the DEBYE radius:

$$\mu = \frac{l}{r_D} \tag{1.360}$$

This parameter too has to be small compared to 1. With Eq. 1.356 it follows:

$$\mu = \frac{1}{3N_D} \tag{1.361}$$

The last quantity mentioned here is the COULOMB logarithm:

$$\ln \Lambda_c = \ln \left[\frac{12 \pi \varepsilon_0 r_D k_B T}{e^2} \right] \tag{1.362}$$

$$\Lambda_c = 9 N_D = \frac{3}{\mu} \tag{1.363}$$

This quantity will be explained in more detail in one of the next chapters.

1.9.2 Some Results from Thermodynamics and Statistics of a Plasma

In the framework of thermodynamics, many-particle systems in thermodynamic equilibrium are treated macroscopically[34]; the microscopic nature of the systems is excluded. The equations of state either have to be determined empirically or have to be derived theoretically from 'first principles' within the framework of equilibrium statistics. The principal quantity that links the thermodynamic and the statistical treatment is the partition function. The partition function of a canonical ensemble is given by Reif (1965)

---

[34] Some useful thermodynamic relations are compiled in Appendix D.1.

$$Z = \sum_r \exp\left(-\frac{E_r}{k_B T}\right) \tag{1.364}$$

with
E_r—total energy of the system in state r.

The summation is over all states including degenerated states. The probability to find a system in state r with energy E_r is given by

$$P_r = \frac{\exp\left(-\dfrac{E_r}{k_B T}\right)}{Z} \tag{1.365}$$

Multiplying by E_r and summing over all states gives the mean or internal energy of the system:

$$E = \sum_r E_r \exp\left(-\frac{E_r}{k_B T}\right) Z^{-1} \tag{1.366}$$

or with Eq. 1.364:

$$E = k_B T \frac{\partial \ln Z}{\partial T} \tag{1.367}$$

The free energy of a system is defined by Reif (1965)

$$F = E - T S = -k_B T \ln Z \tag{1.368}$$

S is the entropy:

$$S = -\left(\frac{\partial F}{\partial T}\right)_{V,N} \tag{1.369}$$

with
N—number of particles N_1, N_2, ... of the different particle species
V—volume.

The derivative is taken with respect to T while leaving the volume and all particle densities constant. Together with Eq. 1.368 it follows:

$$\frac{E}{T^2} = -\left(\frac{\partial}{\partial T} \frac{F}{T}\right)_{V,N} \tag{1.370}$$

The chemical potential of particle species j is defined as

$$\mu_j = \left(\frac{\partial F}{\partial N_j}\right)_{T,V,N} \tag{1.371}$$

During differentiation of the right-hand side with respect to the number N_j, all other particle numbers, the volume and the temperature are kept constant. Derivation of the free energy with respect to the volume while keeping the temperature and all particle numbers fixed gives the pressure:

$$p = -\left(\frac{\partial F}{\partial V}\right)_{T,N} \tag{1.372}$$

1.9.2.1 Partition Function of an Ideal Plasma

In computing the partition function Eq. 1.364, the sum runs over all total system states with E_r being the energy of the total system state r. In case of a system of non-interacting particles, the energy E_r is given by the sum of the energies e_{r_i} of all particles. In computing the partition function, the sum runs over all states of all particles. In case of non-distinguishable particles during summation, states that are only distinguished by permutations of particles have to be counted only once:

$$Z = \sum_{r_1, r_2, \ldots} \exp\left(-\frac{1}{k_B T}(e_{r_1} + e_{r_2} + \cdots)\right) = \frac{z^N}{N!} \tag{1.373}$$

with
N—number of particles.

$N!$ corresponds to the number of possible permutations of the particles. In case of several particle species, one gets

$$Z = \prod_i^m \frac{z_i^{N_i}}{N_i!} \tag{1.374}$$

with
m—number of different particle species.

The total energy of a particle is given by the sum of its kinetic and its internal energy. With the assumption that kinetic and internal energies are independent of each other, it is possible to sum over all states of the different degrees of freedom independently. The single particle partition function is thus given by the product of the translational degrees of freedom and of the internal degrees of freedom:

$$z_i = \xi_i \, U_i \tag{1.375}$$

The partition function of the translational degrees of freedom is given by

$$\xi_i = \frac{V}{\Lambda^3} \tag{1.376}$$

with the thermal DE'BROGLIE wavelength :

$$\Lambda = \frac{h}{\sqrt{2\,\pi\,m\,k_B\,T}} \qquad (1.377)$$

with
h—PLANCK's constant.

The partition function of the internal degrees of freedom of an atom is given by

$$U_a = \sum_{j}^{\infty} g_j^a \, \exp\left(-\frac{E_j^a}{k_B\,T}\right) \qquad (1.378)$$

with
g_j^a—degeneracy.

The COULOMB potential has infinitely many bound states that all have negative energies. The continuum limit has energy 0. The ground state has the lowest energy; with increasing main quantum number, the energies increase and in the limit $n \to \infty$ become 0, i.e. the exponential factor in Eq. 1.378 becomes 1. Because of this, the partition function Eq. 1.378 diverges. But this only holds in case of an isolated atom. An atom in a gas or plasma is not isolated however. Due to the interaction of the particles with each other, the states close to the continuum cannot be attributed to the individual atoms any more; the electrons in these states are quasi-free. In computing the partition function, the summation has to be restricted to states with energies below an energy limit that depends on the particle density and the temperature.

When computing the partition function of ions, the energy zero point has to be set with care. In case that the energy of the ground state of the neutral atom is taken as the zero point, the ionization energy has to be added to the energies of the ion states when these are taken with respect to the ion ground state:

$$U_i = \sum_{j} g_j^i \, \exp\left(-\frac{E_{ion}^a + E_j^i}{k_B\,T}\right) \qquad (1.379)$$

Separation of the ionization energy gives

$$U_i = \exp\left(-\frac{E_{ion}^a}{k_B\,T}\right) U_i' \qquad (1.380)$$

With

$$U_i' = \sum_{j} g_j^i \, \exp\left(-\frac{E_j^i}{k_B\,T}\right) \qquad (1.381)$$
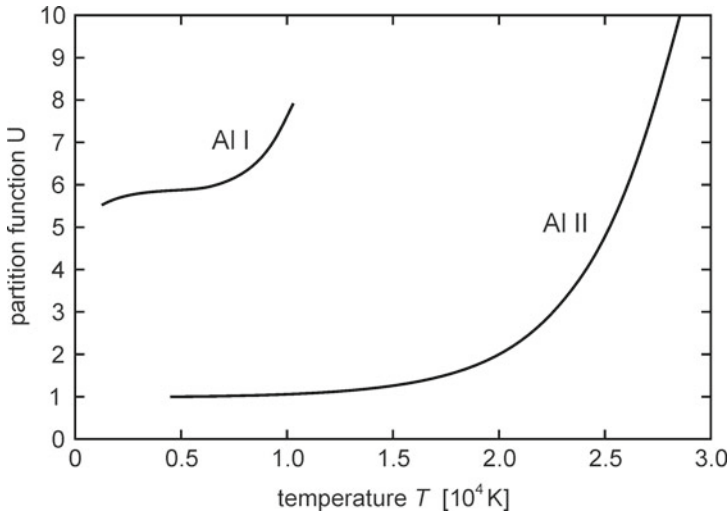
Fig. 1.61 Partition function of atomic Al (Al I) and singly charged Al (Al II) as a function of the temperature. The reduction of the ionization energy is $\Delta E_i = 0.1$ eV. The partition functions of Al and other metal plasmas are tabulated in Drawin and Felenbok (1965)

The energies and degeneracies of all states have to be known for the computation of the partition function. In case of hydrogen, these are known and the partition function can be determined quite easily. The summation must however not be performed over all (infinitely many) states of the isolated hydrogen atom. Due to the interaction with the other plasma particles, the continuum limit is shifted toward smaller energies. If the particle densities are large, this can lead to very high ionization degrees even at relatively small temperatures. This phenomenon is also called pressure ionization. The sum in the partition function must not run over all infinitely many states but has to be truncated at an energy below the continuum limit. In case of other species with more complicated level schemes, the determination of the partition function is much more difficult. For quite a lot of elements, the partition functions are tabulated in Drawin and Felenbok (1965). Figure 1.61 shows the partition function of an Al-plasma as a function of the temperature assuming a reduction of the ionization energy of 0.14 eV. The change of the ionization energy is due to the COULOMB interaction. This will be discussed in more detail below in connection with the SAHA equation. The reduction of the ionization energy gives the limit for the summation in calculating the partition function.

The partition function of the internal degrees of freedom of electrons is due to the two possible spin states equal to 2:

$$U_e = 2 \tag{1.382}$$

1.9.2.2 State Variables of an Ideal Plasma

The logarithm of the partition function Eq. 1.373 is

$$\ln Z = \sum_i^m \ln \frac{z_i^{N_i}}{N_i!} = \sum_i^m (N_i \ln z_i - ln N_i!) \simeq \sum_i^m N_i (\ln z_i - ln N_i + 1) \quad (1.383)$$

In the last step, the STIRLING formula was used:

$$\ln N! \simeq N \ln N - N \qquad (1.384)$$

For simplification in the following, only a single particle species is considered:

$$\ln Z = N (\ln \xi + \ln U - \ln N + 1) = N (\ln \frac{V}{\Lambda^3} + \ln U - \ln N + 1) \qquad (1.385)$$

In case of multiple particle species, the contributions of all particle species are added. With Eq. 1.367, the internal energy is given by

$$E = k_B T N \left(\frac{T}{\xi} \frac{\partial \xi}{\partial T} + \frac{T}{U} \frac{\partial U}{\partial T} \right) \qquad (1.386)$$

The first term in parentheses is the contribution due to the translational degrees of freedom. With Eqs. 1.376 and 1.377, this term becomes

$$\frac{T}{\xi} \frac{\partial \xi}{\partial T} = T \Lambda^3 \frac{\partial \Lambda^{-3}}{\partial T} = \frac{3}{2} \qquad (1.387)$$

The second term together with Eq. 1.378 becomes

$$\frac{T}{U} \frac{\partial U}{\partial T} = \frac{T}{U} \frac{1}{k_B T^2} \sum_j g_j E_j \exp\left(-\frac{E_j}{k_B T}\right) = \frac{\overline{E}}{k_B T} \qquad (1.388)$$

with
$\overline{E}$—mean energy of the inner degrees of freedom.

In case of the ions, the ionization energy has to be added:

$$\overline{E}^i = E_{\text{ion}}^a + E_{\text{ex}}^i \qquad (1.389)$$

with
E_{ex}^i—mean excitation energy of an ion
E_{ion}^a—ionization energy of the neutral atom.

With Eqs. 1.386, 1.387 and 1.388, the internal energy is

$$E = \frac{3}{2} N k_B T + N \overline{E} \tag{1.390}$$

For the free energy, it follows with Eq. 1.368:

$$F = -k_B T N \left(\ln \frac{U}{\Lambda^3} - \ln \frac{N}{V} + 1 \right) \tag{1.391}$$

With this, the chemical potential is given by (Eq. 1.371)

$$\mu = \left(\frac{\partial F}{\partial N} \right)_{T,V} = k_B T \ln \frac{N}{V} - k_B T \ln \frac{U}{\Lambda^3} \tag{1.392}$$

and the pressure by (Eq. 1.372)

$$p = -\left(\frac{\partial F}{\partial V} \right)_{T,N} = \frac{N k_B T}{V} \tag{1.393}$$

1.9.2.3   Coulomb Corrections

In the last two chapters, the COULOMB interaction among the plasma particles was neglected. The interaction leads to a modification of the state variables. As already mentioned above, the interaction reduces the entropy. The coulomb-interaction energy of a system consisting of free electrons and ions is given by the expression (Jackson 1975):

$$E_c = \frac{1}{2} \sum_{i(\text{Elek})} \sum_{j(\text{Elek})} \frac{e^2}{4\pi\varepsilon_0 r_{ij}} + \frac{1}{2} \sum_{i(\text{Ion})} \sum_{j(\text{Ion})} \frac{e^2}{4\pi\varepsilon_0 r_{ij}} - \sum_{i(\text{Ion})} \sum_{j(\text{Elek})} \frac{e^2}{4\pi\varepsilon_0 r_{ij}} \tag{1.394}$$

The sum in the first term on the right-hand side of Eq. 1.394 runs over all electrons, whereas in the second term it runs over all ions. If the sums run over all indices i and j, the interaction energy between two particles is counted twice. Because of this, the sum has to be multiplied by 1/2. The third term comprises the electron-ion interaction. Because in this sum the indices belong to different particles, the interaction is not counted twice. The r_{ij} are the distances between the respective particles. Performing the summations in Eq. 1.394 in a many-particle system is in general quite tedious and can only be done approximately. In the case that the distances r_{ij} are randomly distributed, i.e. the locations of the particles are not correlated, the contributions cancel and the interaction energy E_c becomes zero. But due to the interaction, there are correlations so that E_c does in general not vanish. In the following, E_c will be calculated in the DEBYE approximation.

The DEBYE approximation corresponds to the self-consistent field approximation, i.e. the summation over distinct particles is replaced by integration over particle densities or probability densities. Equation 1.394 then becomes

$$E_c = \frac{1}{2} n_{e_0}^2 \iint u_{ee} \, w_{ee}(r) \, dV \, dV \tag{1.395}$$

$$+ \frac{1}{2} n_{i_0}^2 \iint u_{ii} \, w_{ii}(r) \, dV \, dV \tag{1.396}$$

$$+ n_{e_0} n_{i_0} \iint u_{ei} \, w_{ei}(r) \, dV \, dV \tag{1.397}$$

with the interaction energies:

$$u_{ee} = u_{ii} = \frac{e^2}{4 \, \pi \, \varepsilon_0 \, r} \tag{1.398}$$

$$u_{ei} = - \frac{e^2}{4 \, \pi \, \varepsilon_0 \, r} \tag{1.399}$$

with
r—distance between particles
$w(r)$—probability.

The $w(r)$ are the probabilities to find two particles that are separated by r. These probabilities follow from the densities Eqs. 1.350 and 1.351 respectively by dividing by the mean particle densities. With this and the potential Eq. 1.354, it follows:

$$w_{ee} = w_{ii} = 1 - \frac{e^2}{4 \, \pi \, \varepsilon_0 \, k_B \, T} \frac{\exp\left(-\dfrac{r}{r_D}\right)}{r} \tag{1.400}$$

$$w_{ei} = 1 + \frac{e^2}{4 \, \pi \, \varepsilon_0 \, k_B \, T} \frac{\exp\left(-\dfrac{r}{r_D}\right)}{r} \tag{1.401}$$

The probability to find a particle in the vicinity of another particle whose charge has the same sign is reduced compared to the non-interacting case and enhanced if the two particles have opposite sign. Because every particle interacts with every other particle, the integration has to be done twice. The factor 1/2 in Eq. 1.395 again is introduced because otherwise the contribution of the interaction between two particles would be counted twice. With the condition of neutrality:

$$n_{e_0} = n_{p_0} \tag{1.402}$$

it follows:

$$E_c = -2 \, n_{e_0}^2 \iint_{V \; V} \frac{e^2}{4 \, \pi \, \varepsilon_0} \frac{e^2}{4 \, \pi \, \varepsilon_0 \, k_B \, T} \frac{\exp\left(-\dfrac{r}{r_D}\right)}{r^2} \, dV \, dV \tag{1.403}$$

With the volume element:

$$dV = 4 \pi r^2 \, dr \tag{1.404}$$

and the definition of the DEBYE radius Eq. 1.355 it results in

$$E_c = -n_{e_0} \int \frac{e^2}{4 \pi \varepsilon_0 \, r_D^2} \frac{1}{r_D^2} \int_0^\infty \exp\left(-\frac{r}{r_D}\right) dr \, dV \tag{1.405}$$

The COULOMB-interaction energy of a plasma in DEBYE approximation is thus given by

$$E_c = -\frac{1}{2} V \frac{e^2}{4 \pi \varepsilon_0 \, r_D} (n_{e_0} + n_{p_0}) \tag{1.406}$$

The COULOMB interaction reduces the internal energy of a plasma compared to a system without interaction due to the fact that the particles are not totally free. If the free electrons would be bound to the ions, the number of particles and because of this also the energy of the translational degrees of freedom would halve (in case of fully singly ionized plasma). Inserting Eq. 1.406 into Eq. 1.370 and integrating yields the COULOMB correction of the free energy:

$$F_c = -\frac{1}{3} \frac{V e^2}{4 \pi \varepsilon_0 \, r_D} (n_{e_0} + n_{p_0}) \tag{1.407}$$

The free energy of a plasma is smaller too compared to a non-interacting systems. With Eqs. 1.369, 1.371, 1.372 and 1.407, it follows for the COULOMB corrections of the entropy, the pressure and the chemical potential of the electrons and ions in the DEBYE approximation:

$$S_c = -\frac{\partial F_c}{\partial T}\bigg|_{V,N} = \frac{1}{6} \frac{V e^2}{4 \pi \varepsilon_0 \, r_D \, T} (n_{e_0} + n_{p_0}) \tag{1.408}$$

$$p_c = -\frac{\partial F_c}{\partial V}\bigg|_{T,N} = -\frac{1}{3} \frac{e^2}{4 \pi \varepsilon_0 \, r_D} (n_{e_0} + n_{p_0}) \tag{1.409}$$

$$\mu_{c_e} = -\frac{\partial F_c}{\partial n_e}\bigg|_{T,p,N_0,n_p} = -\frac{1}{3} \frac{V e^2}{4 \pi \varepsilon_0 \, r_D} \left(1 + \frac{(n_{e_0} + n_{p_0})}{2 n_e}\right) \tag{1.410}$$

$$\mu_{c_i} = -\frac{\partial F_c}{\partial n_p}\bigg|_{T,p,N_0,n_e} = -\frac{1}{3} \frac{V e^2}{4 \pi \varepsilon_0 \, r_D} \left(1 + \frac{(n_{e_0} + n_{p_0})}{2 n_p}\right) \tag{1.411}$$

As already mentioned above, the correlations among the particles reduce the entropy as well as the pressure. In case of a fully ionized plasma with an electron density of $10^{24}\,\mathrm{m}^{-3}$ and a temperature of $1\,\mathrm{eV}$, the pressure amounts to $1500\,\mathrm{kPa}$ when neglecting the COULOMB interaction, and the reduction of the pressure due to the interaction amounts to $168\,\mathrm{hPa}$. The chemical potential of the electrons and ions decrease too. The reduction of the chemical potential is equivalent to a reduction of the ionization energy which has significant consequences for the degree of ionization

of a plasma. Generalizations of some of the formulas for multiple ionized ions can be found in Appendix D.2.

1.9.2.4 Law of Mass Action and Saha Equation

The SAHA equation which describes the equilibrium ionization in a plasma is one of the most important equations in plasma physics and is a special case of the law of mass action. According to the second law of thermodynamics, the entropy of an isolated system is maximal. From this, it follows that in a system that is in contact with a heat bath and whose volume is fixed, the free energy F acquires a minimum value. The free energy contains contributions from atoms (a) (in general there can also be molecules), ions (i) and electrons (e) which is a function of the temperature, the volume and the particle densities:

$$F = F(T, V, N_a, N_e, N_i) \tag{1.412}$$

In an isolated system, the sum of all atoms and ions is constant. Because the free energy acquires a minimum value, the variation of the free energy with the particle densities while keeping temperature and volume fixed has to vanish in a state of thermodynamic equilibrium:

$$\frac{\partial F}{\partial N_a} dN_a + \frac{\partial F}{\partial N_e} dN_e + \frac{\partial F}{\partial N_i} dN_i = 0 \tag{1.413}$$

The differentials of the different particle species are not independent of each other. When a free electron is created, an ion is created too and a neutral particle is annihilated:

$$dN_a = -dN_e = -dN_i \tag{1.414}$$

Inserting yields

$$\frac{\partial F}{\partial N_e} + \frac{\partial F}{\partial N_i} = \frac{\partial F}{\partial N_a} \tag{1.415}$$

The derivative of the free energy with respect to the density of a particle species while keeping constant all other quantities is the chemical potential of the particle species considered (Eq. 1.371). Thus

$$\mu_e + \mu_i = \mu_a \tag{1.416}$$

Equation 1.416 expresses that the sum of the chemical potentials of an electron and an ion equals the chemical potential of a neutral atom. With the densities $n = N/V$, the chemical potentials are given by (Eqs. 1.392, 1.410 and 1.411)

$$\mu_a = k_B \, T \, \ln n_a - k_B \, T \, \ln \frac{U_a}{\Lambda_a^3} \tag{1.417}$$

$$\mu_e = k_B \, T \, \ln n_e - k_B \, T \, \ln \frac{U_e}{\Lambda_e^3} + \mu_{ce} \tag{1.418}$$

$$\mu_i = k_B \, T \, \ln n_i - k_B \, T \, \ln \frac{U_i}{\Lambda_i^3} + \mu_{ci} \tag{1.419}$$

$$\mu_{ce} = \mu_{ci} = -\frac{1}{2} \frac{e^2}{4 \, \pi \varepsilon_0 \, r_D} \tag{1.420}$$

Inserting it in Eq. 1.416 results in

$$\ln n_e + \ln n_i - \ln n_a = \ln \frac{U_e}{\Lambda_e^3} + \ln \frac{U_i}{\Lambda_i^3} - \ln \frac{U_a}{\Lambda_a^3} - (\mu_{ce} + \mu_{ci}) \tag{1.421}$$

With this, the SAHA equation of ionization equilibrium in a plasma reads:

$$\frac{n_e \, n_i}{n_a} = \frac{U_e}{\Lambda_e^3} \frac{\Lambda_a^3}{U_a} \frac{U_i}{\Lambda_i^3} \exp\left[-(\mu_{ce} + \mu_{ci})\right] = K(T)^{-1} \tag{1.422}$$

with
$K(T)$—equilibrium constant.

The partition function of the internal degrees of freedom of an electron is 2 (2 spin states). The DE'BROGLIE wavelength of ions and atoms respectively are almost identical:

$$\Lambda_i \simeq \Lambda_a \tag{1.423}$$

With Eqs. 1.380 and 1.377, it follows:

$$\frac{n_e \, n_i}{n_a} = \frac{2}{\Lambda_e^3} \frac{U_i'}{U_a} \exp\left(-\frac{E_{ion}^a - \Delta E_{ion}^a}{k_B \, T}\right) \tag{1.424}$$

$$\Lambda_e = \frac{h}{\sqrt{2 \, \pi \, m_e \, k_B \, T}} \tag{1.425}$$

$$\Delta E_{ion}^a = -(\mu_{ce} + \mu_{ci}) = \frac{e^2}{4 \, \pi \, \varepsilon_0 \, r_D} \tag{1.426}$$

with
m_e—electron mass
E_{ion}^a—ionization energy
ΔE_{ion}^a—reduction of the ionization energy.

The reduction of the ionization energy is due to the COULOMB interaction. With an electron density of 10^{24} m^{-3} and a temperature of 1 eV, the ionization energy is decreased by 0.29 eV. Because the DEBYE radius equation contains the electron den-

sity Eq. 1.424 is an implicit, non-linear equation for determining the electron density, which can only be solved by iterative numerical methods. Even at low temperatures ($k_B T > 0.1 E_{\mathrm{ion}}$), the degree of ionization is considerably high. This is due to the fact that the two particles electron and ion can occupy much more states than a single neutral atom. In Eq. 1.364, the sum runs over all states including the degenerate states. Even in case of small values of the exponential factors, the contributions of the higher energy levels can be large due to their great number. Equation 1.424 accordingly also applies in case of higher ionization stages. Instead of the atoms a, the corresponding values of the ions with ionization stage $(i - 1)$ have to be taken. With $i = 1$, Eq. 1.424 for the atom is reproduced.[35] Figure 1.62a–f shows solution of a system of three SAHA equations of the type Eq. 1.424 for three ionization stages in a Fe-plasma.

1.9.3 Transport Characteristics of Plasmas

In the preceding chapters, the plasma was assumed to be in a state of thermodynamic equilibrium. Transport processes arise when there are deviations from thermodynamic equilibrium. If the relevant mean free paths that govern the transport processes are small compared to the spatial dimensions over which the plasma state varies locally states of thermodynamic equilibrium exist, at least approximately. The local quantities can be determined using the equilibrium equations. Particle diffusion and heat fluxes are functions of the local density and temperature gradients. The following treatment is restricted to those cases in which the electric current densities are only functions of the local electric field. The complex electric high-frequency conductivity is derived in Sect. 1.3 and Appendix A.2 respectively (Eq. 1.64):

$$\sigma = \frac{e^2 \, n_e}{m_e \, \nu_m} \frac{\nu_m}{\nu_m - i \, \omega} \tag{1.427}$$

In Eq. 1.427 only the contribution of the electrons is included. The momentum transfer frequency ν_m is the inverse of the mean time for momentum transfer of the electrons to other particles during collisions. The momentum transfer frequency is given by[36]

$$\nu_m = n \, \overline{v \, \sigma_m(v)} \tag{1.428}$$

---

[35] The generalization in case of multiple charged ions can be found in Appendix D.2.

[36] Equation 1.427 is only strictly valid if the collision frequency $\nu_m(v)$ is constant; nevertheless Eq. 1.427 describes the conductivity also in case of non-constant $\nu_m(v)$ if an appropriate mean value of the collision frequency is used.
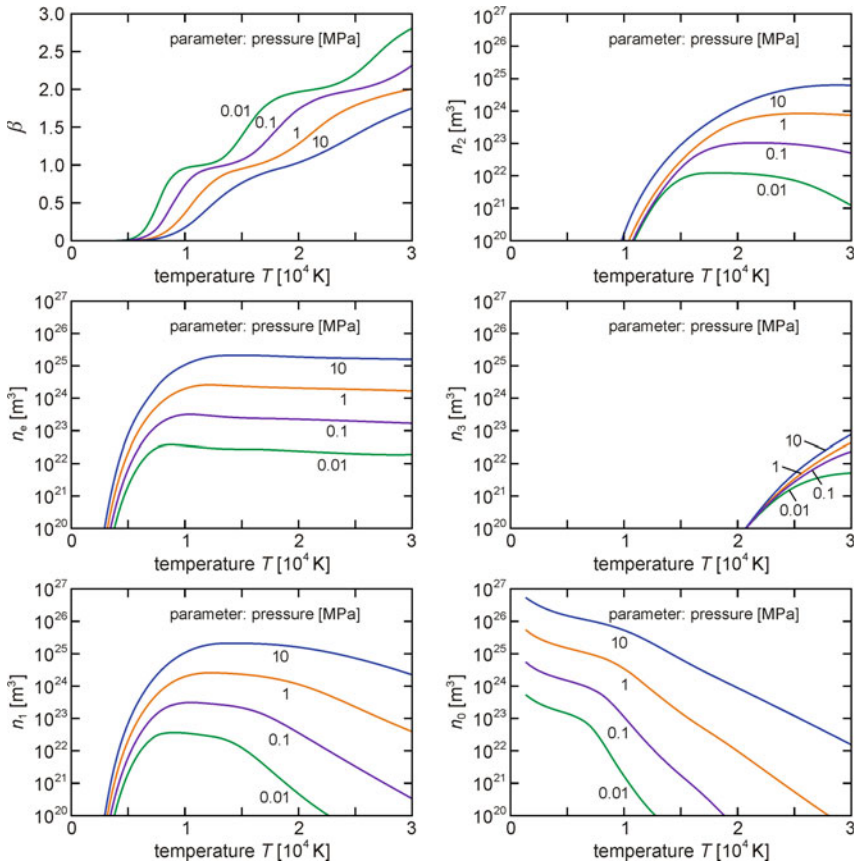
Fig. 1.62 Figures **a–f** show solutions of a system of three equations of the type Eq. 1.424 for three ionization stages of Fe. The generalization of the SAHA equation in case of multiple charged ions can be found in Appendix D.2. The ionization energies are FeI: 6.9 eV, FeII: 16.18 eV and FeIII: 30.64 eV respectively (Drawin and Felenbok 1965). The plasma is neutral, i.e. $n_e = n_1 + 2\,n_2 + 3\,n_3$. n_1, n_2 and n_3 are the densities of the singly, twofoldly and threefoldly charged ions, respectively. Parameter is the pressure, i.e. $p(n_0 + n_e + n_1 + n_2 + n_3)\,k_B\,T$. The pressures are 0.01, 0.1, 1 and 10 MPa (0.1, 1, 10, 100 bar) respectively. Figure **a** shows the electron density normalized with respect to the sum of the densities of the heavy particles as a function of temperature. At the temperature values at which β increases more sharply, the mean energy becomes high enough to ionize the next ionization stage. Figures **b–e** show the electron density, the density of the singly, twofoldly and threefoldly charged ions and figure f the density of the neutral particles as a function of the temperature

with

n—density of collision partners

v—electron speed

$\sigma_m(v)$—momentum transfer cross section.

The over-line indicates time averaging. The momentum transfer cross section is given by

$$\sigma_m(v) = \int\limits_0^{4\pi} \frac{d\sigma_c}{d\Omega}(v)\,(1 - \cos\phi)\,d\Omega \tag{1.429}$$

The product of differential cross section and the factor $(1 - \cos\phi)$ is integrated over the solid angle from 0 to 4π. The factor $(1 - \cos\phi)$ is the relative value of momentum transfer that occurs during an elastic collision with a collision partner whose mass by far exceeds the mass of the colliding particle when the colliding particle is scattered by an angle of ϕ. In case of forward scattering, i.e. $\phi = 0$, there is no momentum transfer; if the scattering angle equals $\pi/2$, the momentum transfer equals the momentum of the colliding particle and in case of backward scattering, i.e. $\phi = \pi$, twice the momentum of the colliding particle is transferred to the heavy collision partner.

The collision frequency in Eq. 1.427 in general consists of several contributions. As long as the mean electron energy is small compared to all excitation energies of the heavy particles, there are much more elastic than inelastic collisions, so it suffices to only consider the contributions of the elastic collisions to the momentum transfer frequency. In general, a plasma is not fully ionized so that the collision frequency is composed of the contributions of the neutral particles and the ions:

$$\nu_m = \nu_{m,ea} + \nu_{m,ei} \tag{1.430}$$

The differential cross section depends on the interaction potential between electron and collision partner. In case of neutral collision partners, the interaction range is short and the interaction potential depends on the atomic structure. The cross sections are either measured or calculated theoretically within the frame of quantum mechanics. In the following, only simple models of electron-neutral collisions are presented. At small energies in many cases of interest, the elastic cross section is approximately velocity-independent. With a MAXWELLian distribution of electron velocities, the collision frequency is thus given by

$$\nu_{m,ea} = n_a\,\sigma_0\,\overline{v} = n_a\,\sigma_0\,\sqrt{\frac{8}{\pi}\,\frac{k_B\,T}{m_e}} \tag{1.431}$$

The collision frequency Eq. 1.431 is a monotone function of the temperature. The collision cross section σ_0 is of the order of 10^{-19} m^2. With an electron temperature of about 1 eV it follows:

$$\frac{\nu_{m,ea}}{n_a} \simeq 10^{-13}\ \text{m}^3\ \text{s}^{-1} \tag{1.432}$$

At high energies, the collision cross sections approximately decrease inversely proportional to the velocity so that the collision frequency is independent of the velocity and thus also independent of the temperature. In case of ions and at distances that are large compared to the ion radius, the interaction potential can very well be described

by a COULOMB potential. The details of the ion potential at small distances can be neglected as long as the COULOMB potential dominates the collisions. The differential cross section for a COULOMB collision between an electron and an ion is given by Ichimaru (1973)

$$\frac{d\sigma_c}{d\Omega}(v) = \frac{Z^2\, e^4}{(4\,\pi\,\varepsilon_0)^2\,(m_e\,v^2)^2\,\sin^4(\phi/2)} \tag{1.433}$$

with

Z—ion charge
v—velocity of the electron far away from the ion
ϕ—scattering angle.

The impact parameter b is connected with the scattering angle by the relation:

$$\cot(\phi/2) = \frac{b\,m_e\,v^2\,4\,\pi\,\varepsilon_0}{Z\,e^2} \tag{1.434}$$

Inserting the differential cross section Eq. 1.433 into Eq. 1.429 together with the solid angle element:

$$d\Omega = 2\,\pi\,\sin\phi\,d\phi\,d\psi \tag{1.435}$$

results in the momentum transfer cross section:

$$\sigma_{m,ei}(v) = \frac{4\pi\,Z\,e^4}{(4\,\pi\,\varepsilon_0)^2\,(m_e\,v^2)^2}\int_{\phi_{\min}}^{\pi}\frac{(1-\cos\phi)\,\sin\phi}{\sin^4(\phi/2)}\,d\phi \tag{1.436}$$

The integral gives

$$\int_{\phi_{\min}}^{\pi}\frac{(1-\cos\phi)\,\sin\phi}{\sin^4(\phi/2)}\,d\phi = \ln\left(\frac{1}{\sin(\phi_{\min}/2)}\right) \tag{1.437}$$

Equation 1.437 has a logarithmic divergence if $\phi_{\min} \to 0$. Small scattering angles are associated with large impact parameters, i.e. the distance between the collision partners is large. The divergence is thus due to the infinite range of the COULOMB potential. As was pointed out when treating the DEBYE screening in Sect. 1.9.1, the potential of an ion in a plasma drops much faster than the pure COULOMB potential. In computing the cross section, the screened potential Eq. 1.354 should have been used, but there is no simple analytical solution for this. Another possibility to avoid the divergence is to cut off the COULOMB potential at the DEBYE radius. The maximal impact parameter then equals the DEBYE radius. With this, the minimal scattering angle is using Eq. 1.434 given by

$$\phi_{\min} = 2 \ \arctan\left(\frac{Z \ e^2}{4 \ \pi \ \varepsilon_0 \ r_D \ m_e \ v^2}\right) \tag{1.438}$$

The argument of arctan is besides a factor of 2, the ratio of the potential energy in a COULOMB-potential at the distance $r = r_D$ (r_D = DEBYE radius) and the kinetic energy of the impacting electron. When this ratio is large, the scattering angle becomes large. An essential prerequisite of the DEBYE approximation is that the mean kinetic energy is large compared to the mean potential energy. Then the argument in the arctan function is small for most of the electrons if their velocities are MAXWELLian distributed and because of this the scattering angle is small too. Expanding the arctan function in case of small arguments, inserting in Eq. 1.437 and substitute v^2 with its mean value:

$$\overline{v^2} = \frac{3 \ k_B \ T}{m_e} \tag{1.439}$$

results in

$$\ln\left(\frac{1}{\sin\left(\phi_{min}/2\right)}\right) = \ln \Lambda_c \tag{1.440}$$

$$\Lambda_c = \frac{12 \ \pi \ \varepsilon_0 \ r_D \ k_B \ T}{Z \ e^2} \tag{1.441}$$

with
$\ln \Lambda_c$—COULOMB logarithm.

In deriving this expression, the slow electrons were neglected and the cut-off of the COULOMB potential at the DEBYE radius is rather somewhat arbitrary than justified exactly. But because this only enters logarithmically, the error that is introduced by this approximation is relatively small. This holds at least as long as $\ln \Lambda_c$ is large compared to 1, which is the case if the number of particles within the DEBYE sphere is large. The ions end electrons within the DEBYE sphere can then be treated like a continuous background that shields the charge of an ion outside the region given by the DEBYE radius. This is the regime of ideal plasmas with the mean kinetic energy by far exceeding the mean interaction energy. If, on the other hand, the number of particles within the DEBYE sphere is close to 1, which implies that the interaction energy is not negligible any more, the concept of shielding has to be modified (Beyer et al. 1986; Günther et al. 1983). This is the regime of non-ideal plasmas that can be described accurately only within the frame of quantum physics. In the following, only some simple considerations are presented. In order to avoid the divergence of the COULOMB logarithm, $\ln[\Lambda_c]$ can be substituted by $\ln[1 + \Lambda_c]$. The expression for the shielding length r_s has to be modified too. One possibility is to take take the mean electron distance as the lower limit of the shielding length, i.e.:

$$r_s = \ r_D \quad : r_D > n_e^{-1/3} \tag{1.442}$$

$$r_s = n_e^{-1/3} : r_D < n_e^{-1/3} \tag{1.443}$$

GÜNTHER et al. (1983) derived the following expression for the shielding length from experiments with weakly non-ideal plasmas in the case of $N_D \geq 1$:

$$r_s = r_D \left(5 \exp\left(-\frac{2}{3} N_D\right) + 1 \right) \tag{1.444}$$

with
N_D—number of electrons and ions within a DEBYE sphere (Eq. 1.357).

The electron-ion momentum transfer cross section is using Eqs. 1.436 and 1.440 given by

$$\sigma_{m,ei}(v) = 4\pi \frac{Z^2 e^4}{(4\pi \varepsilon_0)^2 (m_e v^2)^2} \ln \Lambda_c \tag{1.445}$$

The electron-ion momentum transfer frequency is with Eq. 1.428:

$$\nu_{m,ei}(v) = 4\pi \frac{Z^2 e^4}{(4\pi \varepsilon_0)^2 m_e^2 v^3} \ln \Lambda_c\, n_i \tag{1.446}$$

The COULOMB logarithm is only valid for not too small electron velocities. Because of this, Eq. 1.446 is not averaged by integrating over all velocities but by substituting v^3 by its mean value. In case of a MAXWELLian distribution of the electron velocities, this is given by

$$\overline{v^3} = 8 \sqrt{\frac{2}{\pi}} \left(\frac{k_B T}{m_e}\right)^{3/2} \tag{1.447}$$

With this it follows:

$$\nu_{m,ei} = \left(\frac{\pi}{2}\right)^{3/2} \frac{Z^2 e^4}{(4\pi \varepsilon_0)^2 \sqrt{m_e} (k_B T)^{3/2}} \ln \Lambda_c\, n_i \tag{1.448}$$

$$\nu_{m,ei} = 1.7 \cdot 10^{-12} \, \text{s}^{-1} \, \text{m}^3 \left(\frac{k_B T}{e}\right)^{-3/2} \ln \Lambda_c\, n_i\, Z^2 \tag{1.449}$$

The DC ($\omega = 0$) electron conductivity of a fully ionized plasma without neutral particles and with only singly ionized ions is with Eq. 1.427 given by

$$\sigma_e = \left(\frac{2}{\pi}\right)^{3/2} \frac{(4\pi \varepsilon_0)^2 (k_B T)^{3/2}}{e^2 \sqrt{m_e}} \frac{1}{\ln \Lambda_c} \frac{n_e}{n_i} \tag{1.450}$$

$$\sigma_e \approx 1.646 \cdot 10^4 \frac{1}{\Omega\, \text{m}} \left(\frac{k_B T}{e} \frac{1}{V}\right)^{3/2} \frac{1}{\ln \Lambda_c} \frac{n_e}{n_i} \tag{1.451}$$

If the electron and ion densities are equal, then the conductivity is independent of the density.[37] The conductivity increases proportional to $T^{3/2}$.

In Eq. 1.450, only the electron-ion collisions are accounted for. This plasma model is called LORENTZ plasma. If electron-electron collisions are taken into account too, the electric conductivity is described by the SPITZER equation (Günther and Radtke 1984):

$$\sigma_{sp} = 1.16 \left(\frac{2}{\pi}\right)^{3/2} \frac{(4\,\pi\,\varepsilon_0)^2\,(k_B\,T)^{3/2}}{e^2\,\sqrt{m_e}} \frac{1}{\ln \Lambda_c} \tag{1.452}$$

Equations 1.450 and 1.452 only differ by the prefactor of 1.16. For the sake of completeness, the electron heat conductivity of a fully ionized plasma is given here. The heat conductivity of an ideal gas is (Reif 1965)

$$K_e = \frac{5}{2} \frac{n\,k_B^2\,T}{m\,\nu_m} \tag{1.453}$$

With Eq. 1.448, the electron heat conductivity of a fully ionized ideal plasma is then given by

$$K_e = \frac{5}{2} \left(\frac{2}{\pi}\right)^{3/2} \left(\frac{4\,\pi\varepsilon_0}{e^2}\right)^2 \frac{e^{5/2}\,k_B}{\sqrt{m_e}} \left(\frac{k_B\,T}{e}\right)^{5/2} \frac{n_e}{n_i} \frac{1}{\ln \Lambda_c} \tag{1.454}$$

$$K_e \approx 3.6 \frac{W}{m\,K} \left(\frac{k_B\,T}{e} \frac{1}{V}\right)^{5/2} \frac{n_e}{n_i} \frac{1}{\ln \Lambda_c} \tag{1.455}$$

1.9.4 Interaction Between Electromagnetic Waves and Plasmas

The absorption of electromagnetic radiation by plasma electrons is treated in Sect. 1.9.3 in the framework of the so-called microwave approximation. The absorption mechanism is also called inverse bremsstrahlung. The equation of motion of the mean electron momentum is

$$\frac{\partial \overline{v}}{\partial t} + \nu_m\,\overline{v} = -\frac{e}{m_e}\,E \tag{1.456}$$

This simple equation of motion for the mean electron momentum is only an approximation. A more exact calculation can only be done within the frame of kinetic models. But the basic relationships can also be drawn from the simple models so that kinetic models will not be discussed here. In case of time harmonic fields and using Eq. 1.456 it follows:

---

[37] Neglecting the density dependence of the COULOMB logarithm.

$$\bar{v} = -\frac{e}{m_e} E \frac{\nu_m + i\,\omega}{\nu_m^2 + \omega^2} \tag{1.457}$$

In the collision-free case, $(\nu_m = 0)$ and at steady state the electron velocity and the electric field are out of phase by $90°$. This means that no net energy is absorbed during one field cycle; the energy that is gained by the electron during one half cycle is lost again by the electron during the next half cycle. The mean energy is

$$\varepsilon = \frac{m_e}{2}\,\bar{v}^2 = \frac{e^2}{2m_e\omega^2}|E|^2 \tag{1.458}$$

With a field strength of $E = 2 \cdot 10^6$ V m^{-1} which corresponds to an intensity of 10^{10} W m^{-2} and the frequency of CO_2-lasers $\omega = 1.88 \cdot 10^{14}$ s^{-1}, the mean electron energy is 10^{-5} eV, which is far below the mean thermal energy of a hot vapor of 0.3 eV ($T \approx 3000$ K). If there are collisions things change dramatically. The collisions disturb the phase relation between electron movement and electric field. When at the instant of field reversal the electron collides such that the direction of its velocity is reversed too, and the electron can gain energy in the next half cycle as well instead of loosing energy. After the next half cycle the same holds again. The collision frequency in Eq. 1.457 does not imply that the collisions occur exactly periodically; the reciprocal of the collision frequency is just the time between two consecutive collisions (of the same electron) averaged over many collisions. Besides this, not every collision results in a reversal of the direction of the velocity, rather every angle can be realized. Equation 1.457 describes the average over many collisions. The mean value of the power absorbed by an electron is

$$\frac{1}{2}\,\mathrm{Re}\left[\bar{v}(e\,E^*)\right] = \frac{1}{2}\frac{e^2}{m_e}\frac{\nu_m}{\nu_m^2 + \omega^2}\,|E|^2 \tag{1.459}$$

In the collision-free case, the absorbed power vanishes as outlined above. In case of very large collision frequencies $(\nu_m \gg \omega)$, the absorbed power decreases inversely proportional to the collision frequency. The maximum of the power absorption is reached at $\nu_m = \omega$. This corresponds to the above sketched case of collisions that occur at the instant of field reversal. With a field strength of $E = 2 \cdot 10^6$ V m^{-1} and the frequency of CO_2-lasers, the mean absorbed power is 10^9 eV s^{-1}. The electron energies are in the 1 eV range so the time constant for energy absorption is in the 1 ns range. The intensity absorptivity of an electromagnetic wave is twice the imaginary part of the complex wavenumber[38]:

$$\alpha = 2\,\mathrm{Im}\,[k] = 2\,\frac{\omega}{c}\,\mathrm{Im}(n_c) \tag{1.460}$$

---

[38] See Sect. 1.3.3.

In the limit of small plasma frequencies (compared to the frequency of the radiation field), the absorption coefficient in the microwave approximation is given by (Eq. 1.79)

$$\alpha \simeq \frac{\omega_p^2 \, \nu_m}{c \, \omega^2} \, \frac{1}{1 + \frac{\nu_m^2}{\omega^2}} \tag{1.461}$$

$$\omega_p^2 = \frac{e^2 \, n_e}{m_e \, \varepsilon_0} \tag{1.462}$$

The second factor on the right-hand side of Eq. 1.461 describes correlations between distinct collisions. These correlations cause a reduction of the absorption (Raizer 1977). The microwave approximation is mainly based on the assumption that the photon energy $\hbar \, \omega$ is small compared to the mean thermal energy of the electrons. During interaction of electrons with electromagnetic fields, both stimulated emission and absorption take place. Equation 1.460 represents the difference of both processes. All electrons can participate in absorption but only those electrons can take part in emission whose energy exceeds the photon energy. If the photon energy is larger than the energy of a part of the electrons, these electrons cannot participate in emission and thus the net absorption, which is the difference of absorption and stimulated emission, is larger than given by Eq. 1.461.

The impact of the collisions is described above classically as a disturbance of the phase relation between electromagnetic field and electron movement. Quantum mechanically, the absorption is described as a collision process with the collision partners electron, photon and another particle. A photon has the energy $\hbar \, \omega$ and the momentum $\hbar \, \omega/c$. If the electron takes the energy of the photon, then the electron momentum increase corresponding to the energy $\hbar \, \omega$ is much larger than the photon momentum. The momentum excess has to be transferred to the third collision partner. During scattering of low energy photons at free electrons, the photon energy does not change. This scattering process is called THOMSON scattering (in case of high photon energies COMPTON-scattering takes place, which in general is accompanied by energy transfer). When the photon energy is in the range of the mean electron energy or above, not all electrons can emit photons because their energy is to low. The true absorption coefficient is given by the difference of absorption coefficient and coefficient of stimulated emission (Bekefi 1966):

$$\alpha_\omega = \alpha_{\omega A} - \alpha_{\omega S} \tag{1.463}$$

The absorption coefficient follows by averaging the velocity-dependent absorption coefficient of an electron $\eta_{\omega A}(v)$ with respect to the velocity distribution of the electrons and multiplying by the electron density (Bekefi 1966):

$$\alpha_{\omega A} = n_e \int \eta_{\omega A}(v) \, f(v) \, 4\pi \, v^2 \, dv \tag{1.464}$$

with

$\eta_{\omega A}(v)$—coefficient of absorption of a photon of energy $\bar{h}\,\omega$ by an electron of velocity v.

The electron velocity after absorption is v'. Energy conservation demands

$$\frac{m_e}{2}\,v'^2 = \frac{m_e}{2}\,v^2 + \hbar\,\omega \qquad (1.465)$$

Correspondingly, there is a similar relation for the coefficient of stimulated emission $\eta_{\omega S}(v')$. Here, v' is the electron velocity before the emission and v the electron velocity after the emission:

$$\alpha_{\omega S} = n_e \int \eta_{\omega S}(v')\,f(v')\,4\,\pi\,v'^2\,dv' \qquad (1.466)$$

From the principle of detailed balancing, a relationship follows between $\eta_{\omega A}$ and $\eta_{\omega S}$ (Bekefi 1966):

$$\eta_{\omega A}(v)\,v^2\,dv = \eta_{\omega S}(v')\,v'^2\,dv' \qquad (1.467)$$

$v^2\,dv$ and $v'^2\,dv'$ respectively are, except a constant factor, the number of states within the velocity intervals $(v + dv)$ and $(v' + dv')$, respectively. In case of a MAXWELLian distribution of the electron velocities, Eqs. 1.463–1.467 give

$$\alpha_\omega = n_e \int \eta_{\omega A}(v)\,f(v)\,4\,\pi\,v^2\,dv\,\left(1 - \exp\left(-\frac{\hbar\,\omega}{k_B\,T}\right)\right) \qquad (1.468)$$

In case of electron-ion collisions, the calculations become much more involved. Some results can be found in BEKEFI (1966). Inserting the electron-ion collision frequency Eq. 1.448 instead of the electron-atom collision frequency Eq. 1.461 approximately gives the absorption coefficient in case of electron-ion collisions.

Figure 1.63 shows the sum of the electron-atom and electron-ion collision frequencies of a Fe-plasma as a function of the temperature according to the values given in Fig. 1.62a–f with a circular frequency of $1.88 \cdot 10^{14}$ s^{-1} (CO$_2$-laser). The parameter is the total pressure without COULOMB-corrections:

$$p = (n_e + n_a + \sum n_i)\,k_B\,T \qquad (1.469)$$

Figure 1.64 shows the corresponding electron plasma frequency and Fig. 1.65 the absorption coefficient Eq. 1.460.
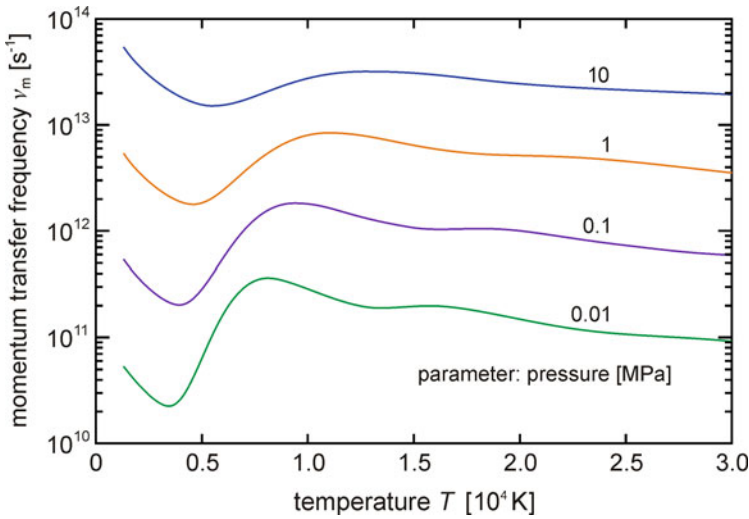
Fig. 1.63 Sum of electron-atom and electron-ion collision frequencies in a Fe-plasma as a function of the temperature computed using the values given in Fig. 1.62 a–f and Eqs. 1.431 and 1.448
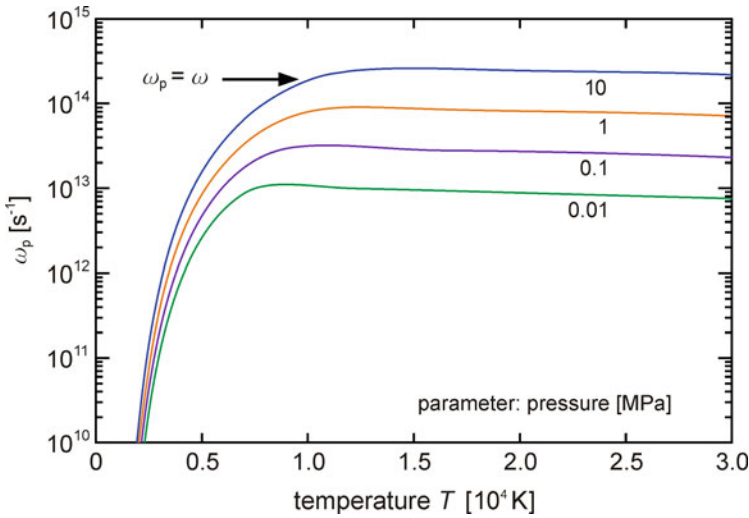

Fig. 1.64 Electron plasma frequency in a Fe-plasma as a function of the temperature computed using the values given in Fig. 1.62a–f and Eq. 1.462. The plasma frequency reaches at $p = 10$ MPa and $T \gg 1$ eV the circular frequency of the CO_2-laser radiation of $\omega = 1.87 \cdot 10^{14}$ s^{-1}
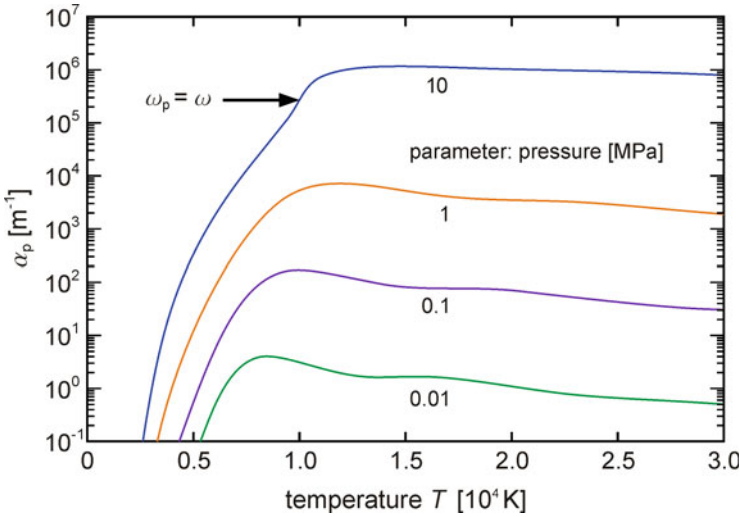
Fig. 1.65 Absorption coefficient of a Fe-plasma as a function of the temperature. Computed according to the values given in Fig. 1.62a–f with the circular frequency ω of CO_2-laser radiation. $\text{Im}(n) = \kappa$ is the imaginary part of the index of refraction of a plasma (Eq. 1.70). The strong increase of the absorption coefficient around $\omega_p = \omega$ is due to the fact that an electromagnetic wave in a collision-free plasma cannot propagate any more if the plasma frequency exceeds the circular frequency of the wave and is reflected totally (see Fig. 1.62a–f). Due to collisions, this behavior is modified but as long as the collision frequency is not too high the principal characteristic is maintained

Besides inverse bremsstrahlung, other absorption mechanisms as well as scattering can occur. Multiphoton ionization preferably occurs in the visible and ultraviolet regions and at high radiation intensities. The principal incoherent scattering process in laser-induced plasmas is RAYLEIGH scattering at small metal droplets[39] (Matsunawa 1991). THOMSON scattering at free electrons can be neglected. Besides these incoherent processes, laser radiation can be absorbed by exciting plasma waves and there can also be coherent scattering processes like stimulated BRILLOUIN scattering and stimulated RAMAN scattering. But these effects are normally unimportant at the laser intensities that are used during laser material processing.

A further effect is the modification of the collision cross sections induced by electromagnetic radiation. Of special interest is the reduction of the ionization energy in a strong laser field. The determination of the collisional ionization cross section in the presence of a strong laser field has to be performed within the frame of quantum mechanics (Cavaliere et al. 1980). A simple estimate of the upper limit of the reduction of the ionization energy due to the laser field can be obtained by investigating the DC case. The potential that acts upon an electron far away from the kernel and the other hull electrons is approximately given by the COULOMB Potential. In

---

[39] When the size of the droplets approaches the laser wavelength MIE-scattering takes place.

the presence of a DC field, the total potential is given by the superposition of both potentials:

$$\phi = -\frac{e}{4\,\pi\,\varepsilon_0\,r} - E_{DC}\,r \tag{1.470}$$

with
E_{DC}—DC electric field.

The potential has its maximum value at

$$r(\phi_{max}) = \sqrt{\frac{e}{4\,\pi\,\varepsilon_0\,E_{DC}}} \tag{1.471}$$

Inserting it into Eq. 1.470 yields

$$\phi_{max} = -2\sqrt{\frac{eE_{DC}}{4\,\pi\,\varepsilon_0}} \tag{1.472}$$

The continuum limit of the COULOMB potential is at zero energy. With this, it follows for the reduction of the ionization energy:

$$\Delta E_{ion} = 2\,e\,\sqrt{\frac{eE_{DC}}{4\,\pi\,\varepsilon_0}} \tag{1.473}$$

The electric field strength of an electromagnetic wave of intensity I is given by

$$E = \sqrt{Z_0\,I} \tag{1.474}$$

with
$Z_0 = 377\ \Omega$—vacuum wave resistance.

Equation 1.474 only applies in vacuum. But as long as the plasma does not significantly change, the wave propagation Eq. 1.474 can approximately also be used within plasmas. At an intensity 10^{10} W m^{-2}, the field strength is $E = 1.9 \cdot 10^6$ V m^{-1} and the reduction of the ionization energy is $\Delta E_{ion} = 0.1$ eV. Because Eq. 1.474 was derived in the case of a DC field, this value has to be understood as an upper bound. A more precise determination is, as already mentioned above, much more involved.

1.9.5 Non-equilibrium Processes

Up to now, it was assumed that the plasma is in a state of at least local thermodynamic equilibrium. This implies that the velocity distribution function of the particles is a
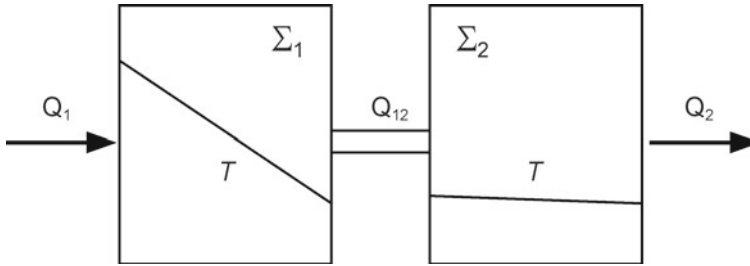
Fig. 1.66 Schematic illustration of the thermal coupling between two systems. In system 1 energy is fed into whereas energy is extracted out of systems 2. If the heat conductivity is large, the temperature within the system is almost constant. This is assumed here for system 2. When the heat contact between the systems is large, then the temperature in both systems at the point of contact will be equal

MAXWELLian, that all occupation numbers of atomic and ionic levels are given by BOLTZMANN factors and the ionization degree is governed by SAHA equations[40] and that a single temperature can be applied. But thermodynamic equilibrium is more or less a special case; lasers are an example of highly non-equilibrium systems. In the following, the conditions for thermodynamic equilibrium to exist in laser-induced plasmas will be discussed and the limits of its validity will be estimated.

The strength of coupling between subsystems and other heat baths is of principal importance. To illustrate this, a simple model is adopted (Fig. 1.66). Energy is fed into a system and extracted from another one. Both systems are assumed to be in thermal contact. When the heat conductivity within one of the systems is large, which means that the coupling between distinct regions of the system is large, the temperature will be almost constant everywhere within the system. The state of this system can then be characterized by a single temperature. When the heat contact between the two systems is large too, the temperatures of both systems will also be equal. The condition for homogeneous temperatures not only depends on the strength of the coupling but also on the values of the energy fluxes that are fed in and extracted respectively and the time scales of the processes involved. If at time $t = 0$ the energy flux into system 1 is switched on, it will take some characteristic time to reach a state of homogeneous and equal temperatures.

The subsystems within a plasma are the free electrons, the translational degrees of freedom of atoms and ions, the electronic levels of atoms and ions and the plasma radiation. Furthermore, electron-ion pairs are created and annihilated (ionization and recombination). The laser field energy is mainly fed into the plasma by inverse bremsstrahlung. The electrons collide with other electrons and with the heavy plasma particles. Due to the equal masses of the collision partners, electron-electron collisions are accompanied by large energy exchanges. With degrees of ionization above 10^{-4}, the electron-electron collisions drive the electron distribution function toward

---

[40] This applies accordingly to the dissociation equilibrium of molecules.

a MAXWELLian distribution. This applies accordingly to the heavy particles though the temperatures in general don't have the same values.

The mean electron energy is determined by the absorbed laser energy and by the energy transfer to other particle species. During elastic collisions between electrons and heavy particles, there is a large momentum transfer but only a very small energy transfer. In case of inelastic collisions during which a heavy particle is excited or ionized, the amount of energy transfer is much larger. In order to excite an atom the electron energy must exceed a threshold value, namely the excitation energy. Because of this threshold, the energy losses due to inelastic collisions increase strongly with increasing mean electron energy. The energy conservation is given by

$$\frac{d(\varepsilon\, n_e)}{dt} = \alpha\, I - P_{\text{elast}} - P_{\text{ex}} - P_{\text{ion}} - P_{\text{rad}} + P_{\text{rec}} + P_{\text{superelast}} \quad (1.475)$$

The mean energy ε of the electrons is increased by the interaction with the laser field. The first term on the right-hand side of Eq. 1.475 is the time-averaged value of the absorbed power density. The electrons lose energy by elastic-elastic collisions with heavy particles (P_{elast}), by excitation and ionization collisions (P_{ex}, P_{ion}) and by radiation (P_{rad}). The radiation losses of the electrons which are mainly due to bremsstrahlung can be neglected at the electron energies that exist in laser-induced plasmas during laser material processing. The electron gas gains energy during electron-ion recombination (P_{rec}) and during super-elastic collisions ($P_{\text{superelast}}$). The time constant of equilibration of the electron energy in laser-induced plasmas during laser material processing is in the range of 1 ns to several 100 ns. This time constant is mainly determined by the inelastic collisions, while the time constant for energy transfer from the electrons to the translational degrees of freedom of the heavy particles is determined by the elastic collisions. Due to the small mass ratio of electron and ion or atom mass respectively, the energy transfer per collision is quite low. The mean energy transfer is given by

$$\dot{\varepsilon} = \frac{2\, m_e}{M}\, \nu_m\, \varepsilon \quad (1.476)$$

with
M—mass of the heavy particles (ions, atoms)
m_e—electron mass.

In a Fe-plasma ($M \approx 10^5\, m_e$) with a collision frequency of $10^{11}\ \text{s}^{-1}$, the electron relaxation time constant approximately amounts to $\tau_\varepsilon \approx 500$ ns.

The number of electrons initially increases avalanche-like by collisional ionization of atoms and ions until the electron creation is compensated for by recombination and other loss processes like diffusion. The electron density conservation reads:

$$\frac{dn_e}{dt} = R_{\text{ion}} - R_{\text{diff}} - R_{\text{rec}} \quad (1.477)$$

Electrons are produced by ionizing collisions (R_{ion}); losses are due to diffusion (R_{diff}) and recombination (R_{rec}). These processes and especially ionization depend on the mean electron energy. For simplification, the transport processes will not be treated explicitly; the diffusion losses can be accounted for by approximate expressions. The electrons transfer energy to the heavy particles by excitation, ionization and by energy transfer to the translational degrees of freedom of the heavy particles. When the mean energies of these energy reservoirs reach the mean electron energy, the electrons gain on the average as much energy during super-elastic collisions as they lose during inelastic and elastic collisions. In case of a steady power absorption from the laser field, the mean electron energy and thus the energy of the degrees of freedom of the heavy particles continue to increase. For a stationary plasma state to exist, the plasma has to lose energy. This can be due to radiation, energy transfer to the workpiece or by transformation of the internal energy of the plasma into directional translation energy. The latter mechanism implies acceleration of the plasma. The energy transfer to the workpiece can be due to heat conduction (energy of the translational degrees of freedom) or by transfer of excitation and recombination energy which is more effective. The contribution of the radiation to the energy conservation is difficult to estimate. In case of black body radiation, the energy density of the radiation in the frequency interval ($\nu, \nu + d\nu$) is given by PLANCK's law:

$$P_\nu \, d\nu = \frac{8 \, \pi \, \nu^2}{c^3} \; \frac{h \, \nu}{\exp\left(\dfrac{h \, \nu}{k_B \, T}\right) - 1} \, d\nu \qquad (1.478)$$

The first factor on the right-hand side is the mode density in the frequency interval ($\nu, \nu + d\nu$); the second factor is the mean energy of a mode of frequency ν. The intensity is obtained by multiplying the energy density of the radiation with the velocity of light c. Integration of the intensity over all frequencies results in the STEFAN-BOLTZMANN law:

$$S = \sigma \, T^4 \qquad (1.479)$$

$\sigma = 5.7 \cdot 10^{-8} \; \text{W m}^{-2} \, \text{K}^{-4}$.

With a temperature of 11,000 K and a surface of $10^{-6} \, \text{m}^2$ $S = 834$ W. Equations 1.478 and 1.479 only apply in case of complete thermodynamic equilibrium including radiation. The PLANCK radiation spectrum is continuous. When PLANCKs law applies, the microscopic nature of the radiating system is unimportant. The region between spectral lines is filled by line broadening and by continuum radiation (bremsstrahlung and recombination radiation). The contribution of continuum radiation processes becomes comparable to the line radiation only at very high densities, which do not exist in many laser-induced plasmas that are created during laser material processing. Because of this, the radiation spectra of this plasmas are mainly dominated by line radiation. Whereas thermodynamic equilibrium in many cases of interest exists, at least approximately, among the plasma particles, this holds much

less often for the radiation. The important quantity is the mean free path of the photons. If the photon mean free path is small compared to the plasma dimension, the photons are absorbed and re-emitted quite often before they can leave the plasma. The radiation that leaves the plasma is then mainly emitted from within a thin layer at the plasma surface which is a basic assumption of Eq. 1.479.

The quantitative description of the radiation of plasmas is quite involved in general. There are mainly two models that are used. In the LTE model,[41] it is assumed that the states of the atoms and ions are populated according to the BOLTZMANN law. The prerequisite for this to apply is that there are much more transitions due to super-elastic collisions than radiation transitions. In this case, the radiation does not have a significant impact on the population densities. In the CR model[42] on the other hand, deexcitation by collisions are neglected. The excitation results from electron collisions, the deexcitation from radiation transitions. In the following, the plasma radiation in the LTE model is discussed.

1.9.6 Plasma Radiation in the LTE Model

In laser-induced plasmas, several distinct elemental species can be present each with several ionization stages. With the assumption that the particles are in local thermodynamic equilibrium, the states of atoms and ions are occupied according to the BOLTZMANN law. For the description of such systems, the following definitions are used:

a—designates the element

z—ionization stage $z = 0, 1, \ldots$

n—energy state (main quantum number)

The densities of atoms, ions and electrons are governed by a system of SAHA equations:

$$\frac{N_e N_{a,z+1}}{N_{a,z}} = \frac{2}{\Lambda_e^3} \frac{U_{a,z+1}(T, \Delta E_{a,z+1}^{ion})}{U_{a,z}(T, \Delta E_{a,z}^{ion})} \exp\left(-\frac{E_{a,z}^{ion} - \Delta E_{a,z}^{ion}}{k_B T}\right) \quad (1.480)$$

$$\Lambda_e = \frac{h}{\sqrt{2\pi m_e k_B T}} \quad (1.481)$$

subject to the constraint of constant total number of the heavy particles:

$$N_a = \sum_{z=0}^{n_{z_a}-1} N_{a,z} \qquad : z = 0, \ldots, n_{z_a} - 1 \quad (1.482)$$

---

[41] LTE = **L**ocal **T**hermodynamic **E**quilibrium.

[42] CR = **C**ollisional **R**adiative.

and of charge neutrality:

$$N_e = \sum_{a=0}^{n_a-1} \sum_{z=0}^{n_{z_a}-1} z \; N_{a,z} \qquad : a = 0, \ldots, n_a - 1 \qquad (1.483)$$

n_{z_a} is the number of relevant ionization stages of element a. If temperature and the total density of the heavy particles are given, this system of equations has a unique solution, although it can in general only be found by numerical methods. The partition functions are

$$U_{a,z}\left(T, \Delta E_{a,z}^{ion}\right) = \sum_{n=1}^{n_{max}} g_{a,z;n} \exp\left(-\frac{E_{a,z;n}}{k_B T}\right) \qquad (1.484)$$

with
n_{max}—highest excited but still bound state
and the reduction of the ionization potential of the i'th ionization stage[43]:

$$\Delta E_{a,z}^{ion} = (z+1)\frac{e^2}{4\pi\epsilon_0 r_D} \qquad (1.485)$$

with the DEBYE radius:

$$r_D = \sqrt{\frac{\epsilon_0 k_B T}{e^2\left(n_e + \sum_{a,z} z^2 N_{a,z}\right)}} \qquad (1.486)$$

The occupation numbers of ionization stage z in the excited state n is given by

$$N_{a,z;n} = N_{a,z}\frac{g_{a,z;n}}{U_{a,z}\left(T, \Delta E_{a,z}^{ion}\right)} \exp\left(-E_{a,z;n}/k_B T\right) \qquad (1.487)$$

1.9.6.1   Line Radiation

The radiation of a plasma consists of line radiation, recombination radiation and bremsstrahlung. The line radiation results from transitions between an energetically higher level n to an energetically lower level m in which a photon is emitted whose energy equals the energy difference of the two involved levels. The number of spontaneous transitions between the levels n and m respectively per volume, time and frequency interval is

$$\frac{dN_{sp}}{dt} = A_{nm} f_{nm}^L(\nu) N_n \qquad (1.488)$$

---

[43] For multiple ionized ions, see Appendix D.1.

A_{nm} is the EINSTEIN coefficient of spontaneous emission, N_n is the density of the particles in the state n, $f_{nm}^L(\nu)$ is the line shape of the transition and ν the frequency of the emitted radiation. The line shape $f_{nm}^L(\nu)$ depends on the dominant line broadening mechanism and is normalized as follows:

$$\int_0^\infty f_{nm}^L(\nu)d\nu = 1 \tag{1.489}$$

The line shape function as a function of the wavelength is with

$$\lambda = \frac{c}{\nu} \tag{1.490}$$

and

$$f(\nu)d\nu = f(\lambda)d\lambda \tag{1.491}$$

$$f(\nu) = f(\lambda)\frac{d\lambda}{d\nu} \tag{1.492}$$

given by

$$f(\nu) = f(\lambda)\frac{\lambda^2}{c} \tag{1.493}$$

Besides spontaneous emission, there is also absorption and stimulated emission. The number of absorbing transitions $m \to n$ per volume, time and frequency interval is

$$\frac{dN_{abs}}{dt} = B_{mn}f_{nm}^L(\nu)\rho(\nu)n_m \tag{1.494}$$

$$\rho(\nu) = \frac{I(\nu)}{c}, \qquad \rho(\nu) = \left[\frac{Js}{m^3}\right], \qquad I(\nu) = \left[\frac{Ws}{m^2}\right] \tag{1.495}$$

$\rho(\nu)$ is the photon energy density per frequency interval, $I(\nu)$ the intensity per frequency interval. B_{mn} is the EINSTEIN coefficient of absorption and is related to A_{nm} by

$$A_{nm} = \frac{8\pi\nu^2}{c^3}h\nu B_{nm} \tag{1.496}$$

$$B_{nm} = A_{nm}\frac{c^3}{8\pi h\nu^3} \tag{1.497}$$

$$B_{nm} = \left[\frac{m^3}{Js^2}\right] \qquad A_{nm} = [1/s]$$

The number of stimulated emissions $n \to m$ per volume, time and frequency interval is

$$\frac{dN_{stim}}{dt} = B_{nm} f_{nm}^L(\nu) \rho(\nu) N_n \tag{1.498}$$

$$B_{mn} = \frac{g_n}{g_m} B_{nm} \tag{1.499}$$

1.9.6.2 Radiation Transport

The intensity change per frequency interval and solid angle along the path element dz is given by the radiation transport equation:

$$dI(\nu) = \left(\frac{1}{4\pi} \frac{dN_{sp}}{dt} + \frac{dN_{stim}}{dt} - \frac{dN_{abs}}{dt}\right) h\nu dz \tag{1.500}$$

With Eqs. 1.488 and 1.494 it follows:

$$\frac{dI(\nu)}{dz} = S(\nu) - \kappa(\nu) I(\nu) \tag{1.501}$$

$$S(\nu) = \frac{1}{4\pi} A_{nm} N_n h\nu f_{nm}(\nu) \tag{1.502}$$

$$\kappa(\nu) = (B_{mn} N_m - B_{nm} N_n) \frac{h\nu}{c} f_{nm}(\nu) \tag{1.503}$$

In case of spatially constant $S(\nu)$ and $\kappa(\nu)$, Eq. 1.501 has the solution:

$$I(\nu) = \frac{S}{\kappa} (1 - \exp(-\kappa z)) \tag{1.504}$$

In the limiting case $\kappa z \ll 1$, the plasma is optically thin and the intensity increases linearly with the path length z:

$$I(\nu) = S(\nu) z = \frac{1}{4\pi} A_{nm} N_n h\nu f_{nm}(\nu) z \tag{1.505}$$

whereas in the limiting case $\kappa z \gg 1$ the plasma is optically thick and the intensity becomes independent of the path length z:

$$I(\nu) = \frac{S(\nu)}{\kappa(\nu)} \tag{1.506}$$

Using the equilibrium densities, PLANCK's law follows[44]:

---

[44] P_ν in Eq. 1.478 is the radiation energy density, whereas $I = Pc$ in Eq. 1.507 is the intensity per solid angle.

$$I(\nu) = \frac{1}{4\pi} \frac{8\pi\nu^2}{c^2} \frac{h\nu}{\exp\left(\dfrac{h\nu}{k_B T}\right) - 1} \tag{1.507}$$

1.9.6.3 Radiation Power of Line Radiation

The radiation power per volume and frequency interval of the transition $n \to m$ of the element a in ionization stage z is given by Griem (1964)

$$p_{a,z;nm}(\nu) = A_{a,z;nm} h \nu_{a,z,nm} N_{a,z;n} f^L_{a,z;nm}(\nu) \tag{1.508}$$

$$N_{a,z;n} = N_{a,z} \frac{g_{a,z;n}}{U_{a,z}\left(T, \Delta E^{ion}_{a,z}\right)} \exp\left(-E_{a,z;n}/k_B T\right) \tag{1.509}$$

with
$E^{ion}_{a,z}$—excitation energy with respect to the ground state.

Using

$$p_{a,z;nm}(\nu)d\nu = p_{a,z;nm}(\lambda)d\lambda \tag{1.510}$$

$$p_{a,z;nm}(\lambda)d\lambda = A_{a,z;nm} h \frac{c}{\lambda} N_{a,z;n} f^L_{a,z;nm}(\nu)d\nu \tag{1.511}$$

$$p_{a,z;nm}(\lambda)d\lambda = A_{a,z;nm} h \frac{c}{\lambda} N_{a,z;n} f^L_{a,z;nm}(\lambda)d\lambda \tag{1.512}$$

yields the power per volume and frequency interval of the transition $n \to m$ of the element a in the ionization stage z (Griem 1964):

$$p_{a,z;nm}(\lambda) = A_{a,z;nm} h \frac{c}{\lambda} N_{a,z;n} f^L_{a,z;nm}(\lambda) \tag{1.513}$$

1.9.6.4 Line Shapes

The line shapes depend on the line broadening mechanism. All transitions are subject to the natural line broadening which is determined by the finite life time of the respective states. The line shape due to the natural line broadening is given by a LORENTZ function:

$$f^L_{a,z;nm}(\nu) = \frac{2}{\pi} \frac{\Delta\nu^L_{nm}}{4(\nu - \nu_{nm})^2 + \left(\Delta\nu^L_{nm}\right)^2} \tag{1.514}$$

$$\int_0^\infty f^L_{nm}(\nu)d\nu = 1 \tag{1.515}$$

or as a function of the wavelength:

$$f_{a,z;nm}^{L}(\lambda) = \frac{2}{\pi} \frac{\Delta\lambda_{nm}^{L}}{4(\lambda - \lambda_{nm})^2 + \left(\dfrac{\lambda}{\lambda_{nm}}\Delta\lambda_{nm}^{L}\right)^2} \tag{1.516}$$

$$\int_{0}^{\infty} f_{nm}^{L}(\lambda)d\lambda = 1 \tag{1.517}$$

$\Delta\nu_{nm}^{L}$ and $\Delta\lambda_{nm}^{L}$ respectively are the frequency and wavelength full width at half maximum (FWHM), respectively.

Due to the thermal movement of the light emitting particles, the radiation is DOPPLER shifted. The superposition of many emitted photons with different DOPPLER shifted wavelengths results in a DOPPLER shape function:

$$f^{L}(\lambda) = \frac{2\sqrt{\ln 2}}{\sqrt{\pi}} \frac{1}{\Delta\lambda_{nm}^{D}} \exp\left[-4\ln 2 \frac{(\lambda - \lambda_{nm})^2}{\left(\Delta\lambda_{nm}^{D}\right)^2}\right] \tag{1.518}$$

$$\Delta\lambda_{nm}^{D} = \sqrt{\frac{8k_B T \ln 2}{M c^2}} \lambda_{nm} \tag{1.519}$$

with
$\Delta\lambda_{nm}^{D}$—full width at half maximum (FWHM).

STARK broadening is caused by collisions of the electrons with the light emitting particles, during which the potential of the impacting electrons shift the energy levels which on the average leads to a broadening of the line. Besides line broadening, the STARK effects also causes a line shift:

$$\Delta\lambda_{Stark} = w_m \frac{n_e}{n_{e,0}} \qquad : [w_m] = m \tag{1.520}$$

$$\Delta\lambda_{Shift} = d_m \frac{n_e}{n_{e,0}} \qquad : [d_m] = m \tag{1.521}$$

with
w_m—full width at half maximum (FWHM) at the electron density $n_{e,0}$
n_e—actual electron density.

Often several broadening mechanisms exist simultaneously. If there are two broadening mechanisms that both have a LORENTZian shape, the resulting line shape again is a LORENTZian shape with the total width:

$$\Delta\lambda = \Delta\lambda_1 + \Delta\lambda_2 \tag{1.522}$$

In case of two DOPPLER broadening mechanisms, the combined line width is given by

$$\Delta\lambda = \sqrt{\Delta\lambda_1^2 + \Delta\lambda_2^2} \tag{1.523}$$

In case of a LORENTZ shape and a DOPPLER shape, the combined line shape is given by the convolution of both functions:

$$f^V(\lambda) = \int\limits_{-\infty}^{\infty} f^D(\lambda') f^L(\lambda' - \lambda)\lambda' \tag{1.524}$$

This combined line shape is called VOIGT profile. The resulting line width is approximately given by

$$\Delta\lambda_V = \frac{\Delta\lambda_L}{2} + \sqrt{\frac{\Delta\lambda_L^2}{4} + \Delta\lambda_D^2} \tag{1.525}$$

1.9.6.5 Bremsstrahlung

Besides line radiation, in which bound electrons are involved, in plasmas there can also be radiation emitted by free electrons. The emitted power due to bremsstrahlung per volume and frequency interval in the hydrogen approximation is given by Griem (1964)

$$\epsilon_{ff}(\nu) = 4\pi 2\pi 16 \frac{(\alpha a_0)^3 E_H}{3 (3\pi)^{1/2}} \sqrt{\frac{E_H}{k_B T}} \exp\left(-\frac{h\nu}{k_B T}\right) N_e \sum_{az} z^2 N_{a,z} \tag{1.526}$$

With

$$\epsilon(\nu)d\nu = \epsilon(\lambda)d\lambda \tag{1.527}$$

$$\epsilon(\lambda) = \epsilon(\nu)\frac{d\nu}{d\lambda} = \epsilon(\nu)\frac{c}{\lambda^2} \tag{1.528}$$

it follows the bremsstrahlung power per volume and wavelength interval (Griem 1964):

$$\epsilon_{ff}(\lambda) = 4\pi 2\pi \frac{c}{\lambda^2} 16 \frac{(\alpha a_0)^3 E_H}{3 (3\pi)^{1/2}} \sqrt{\frac{E_H}{k_B T}} \exp\left(-\frac{hc}{\lambda k_B T}\right) N_e \sum_{az} z^2 N_{a,z} \tag{1.529}$$

1.9.6.6 Recombination Radiation

During recombination of an electron and an ion, the excess energy can be taken by a photon that is emitted. The power of recombination radiation per volume and wavelength interval in the hydrogen approximation is given by Griem (1964)

$$\epsilon_{fb}(\nu) = C \exp\left(-\frac{h\nu}{k_B T}\right) N_e \sum_{a=0}^{n_a-1} \sum_{z=1}^{n_{za}-1} \sum_{n^*}^{n^*+\Delta n_{max}} \frac{z^4}{n^3} \exp\left(\frac{z^2 E_H}{n^2 k_B T}\right) N_{a,z} \qquad (1.530)$$

$$C = 4\pi 2\pi \frac{32}{3} \frac{(\alpha a_0)^3 E_H}{3 (3\pi)^{1/2}} \left(\frac{E_H}{k_B T}\right)^{3/2}$$

$$n \ge n^* = \sqrt{\frac{z^2 E_H \lambda}{hc}}$$

$$\Delta n_{max} = 30$$

$$\epsilon_{fb}(\lambda) = C \frac{c}{\lambda^2} \exp\left(-\frac{hc}{\lambda k_B T}\right) N_e \sum_{a=0}^{n_a-1} \sum_{z=1}^{n_{za}-1} \sum_{n^*}^{n^*+\Delta n_{max}} \frac{z^4}{n^3} \exp\left(\frac{z^2 E_H}{n^2 k_B T}\right) N_{a,z} \quad (1.531)$$

1.9.6.7 Influence of the Apparatus on Measured Spectra

When measuring the radiation spectrum emitted by a plasma, the spectrum is modified by the measuring system. Two principal mechanisms can be distinguished:

- the transmission of the radiation through optical components and the detector sensitivity dependent on the wavelength
- line broadening due to the finite measuring accuracy.

The influence of the wavelength-dependent transmission and detector sensitivity can be taken into account by a wavelength-dependent multiplication factor, and the line broadening by the apparatus can be accounted for by convolving the spectrum that is emitted by the plasma by a function that describes the apparatus broadening called apparatus function:

$$I_m(\lambda) = S_{Apparat}(\lambda) \int_0^\infty f(\lambda, \lambda', \Delta\lambda_{Apparat}) I_p(\lambda') d\lambda' \qquad (1.532)$$

with
$f(\lambda, \lambda', \Delta\lambda_{Apparat})$—apparatus function
$\Delta\lambda_{Apparat}$—full half width of the apparatus
$S_{Apparat}(\lambda)$—spectral characteristic of the apparatus
$I_p(\lambda)$—spectrum emitted by the plasma
$I_m(\lambda)$—spectrum with the impact of the measuring apparatus taken into account.

Appendix Physical Basics

A Optics

A.1 *Derivation of the* Fresnel *Formulae*

Reflection and refraction of plane electromagnetic waves at interfaces are described by the Fresnel formulae. In the following, a derivation of the Fresnel formulae is presented.

Figure 1.67 shows the coordinate system that is used. For the incident, reflected and refracted waves respectively, the plane wave ansatz is made (Jackson 1975):

$$\vec{E}_i = \vec{E}_0 \, \exp\left(i\,\vec{k}_i \cdot \vec{r} - i\,\omega\,t\right) \tag{1.533}$$

$$\vec{E}_r = \vec{E}_{0_r} \, \exp\left(i\,\vec{k}_r \cdot \vec{r} - i\,\omega\,t\right) \tag{1.534}$$

$$\vec{E}_t = \vec{E}_{0_t} \, \exp\left(i\,\vec{k}_t \cdot \vec{r} - i\,\omega\,t\right) \tag{1.535}$$

The Maxwell equations yield

$$\vec{B}_i = \frac{\vec{k}_i \times \vec{E}_i}{\omega} \tag{1.536}$$

$$\vec{B}_r = \frac{\vec{k}_r \times \vec{E}_r}{\omega} \tag{1.537}$$

$$\vec{B}_t = \frac{\vec{k}_t \times \vec{E}_t}{\omega} \tag{1.538}$$

with
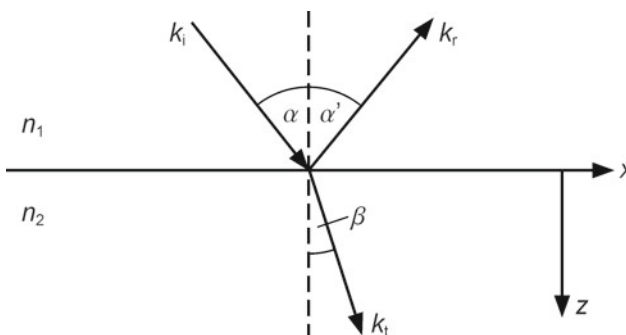
Fig. 1.67 Coordinate system and notation

$$\vec{k}_i = k_i \, \vec{e}_i = k_i \, (\cos \alpha \, \vec{e}_z + \sin \alpha \, \vec{e}_x) \tag{1.539}$$

$$\vec{k}_r = k_i \, \vec{e}_r = k_r \, (-\cos \alpha' \, \vec{e}_z + \sin \alpha' \, \vec{e}_x) \tag{1.540}$$

$$\vec{k}_t = k_i \, \vec{e}_t = k_t \, (\cos \beta \, \vec{e}_z + \sin \beta \, \vec{e}_x) \tag{1.541}$$

The absolute values of the wave vectors are given by

$$k_i = k_r = \frac{\omega}{c} \, n_1 \tag{1.542}$$

$$k_t = \frac{\omega}{c} \, n_2 \tag{1.543}$$

with the indices of refraction:

$$n_1 = \sqrt{\mu_1 \, \varepsilon_1} \tag{1.544}$$

$$n_2 = \sqrt{\mu_2 \, \varepsilon_2} \tag{1.545}$$

If the radiation is absorbed in medium 2, the field strength decays exponentially in the direction of propagation. Absorbing materials can be described using a complex dielectric constant. This implies complex index of refraction and thus a complex wave number. In the expression for the plane waves, it has to be considered that the absorption sets in at the interface $z = 0$. The planes of constant amplitude are parallel to the interface, whereas the planes of constant phase are perpendicular to the wave vectors. The wave in the absorbing medium no longer is a simple plane wave but an inhomogeneous wave. This can be accounted for if the components of the unit vectors $\vec{e}_t$ are allowed to be complex-valued. Then β becomes complex too, which implies that β no longer has a simple physical interpretation as the angle of the refracted wave with respect to the surface normal. The boundary conditions at $z = 0$ have to be fulfilled for all values of x. This implies equality of the spatial variations of the three fields at $z = 0$ and thus the equality of the phase factors:

$$\vec{k}_i \cdot \vec{r}|_{z=0} = \vec{k}_r \cdot \vec{r}|_{z=0} = \vec{k}_t \cdot \vec{r}|_{z=0} \tag{1.546}$$

$$k_i \, \sin \alpha = k_r \, \sin \alpha' = k_t \, \sin \beta \tag{1.547}$$

Because $k_i = k_r$, it follows $\alpha = \alpha'$. With Eqs. 1.542 and 1.543, SNELL's law follows:

$$n_1 \, \sin \alpha = n_2 \, \sin \beta \tag{1.548}$$

If n_2 is complex then β is complex too. Equation 1.548 comprises the kinematics of reflection and refraction.

In order to determine the amplitudes of the reflected and transmitted waves, appropriate boundary conditions have to be set up:

- normal components of $\vec{D} = \varepsilon\,\varepsilon_0\,\vec{E}$:

$$\left[\varepsilon_1\,(\vec{E}_i + \vec{E}_r) - \varepsilon_2\,\vec{E}_t\right]\cdot\vec{n} = 0 \tag{1.549}$$

- normal components of $\vec{B}$ (see Eq. 1.536):

$$\left[\vec{k}_i \times \vec{E}_i + \vec{k}_r \times \vec{E}_r - \vec{k}_t \times \vec{E}_t\right]\cdot\vec{n} = 0 \tag{1.550}$$

- the tangential components of $\vec{E}$ and $\vec{H} = \vec{H} = \dfrac{1}{\mu\,\mu_0}\,\vec{B}$ are continuous:

$$[\vec{E}_i + \vec{E}_r - \vec{E}_t] \times \vec{n} = 0 \tag{1.551}$$

$$[\frac{1}{\mu_1}\,(\vec{k}_i \times \vec{E}_i + \vec{k}_r \times \vec{E}_r) - \frac{1}{\mu_2}\,\vec{k}_t \times \vec{E}_t] \times \vec{n} = 0 \tag{1.552}$$

In case of arbitrary polarization, the wave can be split into two waves, one with perpendicular polarization and the second one with parallel polarization of the electric field vector with respect to the plane of incidence. Both cases will be treated separately. In case of perpendicular polarization, Eqs. 1.551 and 1.552 result in (Eq. 1.549 adds no further information, whereas Eq. 1.550 together with SNELL's law gives the same result as Eq. 1.552)

$$E_i + E_r - E_t = 0 \tag{1.553}$$

$$\sqrt{\frac{\varepsilon_1}{\mu_1}}\,(E_i - E_r)\,\cos\alpha - \sqrt{\frac{\varepsilon_2}{\mu_2}}\,E_t\,\cos\beta = 0 \tag{1.554}$$

With this the FRESNEL formulae in case of perpendicular polarization follow:

$$\frac{E_r}{E_i} = r_s = \frac{n_1\,\cos\alpha - \dfrac{\mu_1}{\mu_2}\,n_2\,\cos\beta}{n_1\,\cos\alpha + \dfrac{\mu_1}{\mu_2}\,n_2\,\cos\beta} \tag{1.555}$$

$$\frac{E_t}{E_i} = t_s = \frac{2\,n_1\,\cos\alpha}{n_1\,\cos\alpha + \dfrac{\mu_1}{\mu_2}\,n_2\,\cos\beta} \tag{1.556}$$

If the electric field vector is parallel to the plane of incidence, Eqs. 1.549 and 1.550 result in (Eq. 1.552 adds no further information, whereas Eq. 1.551 together with SNELL's law gives the same result as Eq. 1.550)

$$(E_i - E_r)\,\cos\alpha - E_t\,\cos\beta = 0 \tag{1.557}$$

$$\sqrt{\frac{\varepsilon_1}{\mu_1}}\,(E_i + E_r) - \sqrt{\frac{\varepsilon_2}{\mu_2}}\,E_t = 0 \tag{1.558}$$

With this the FRESNEL formulae in case of parallel polarization follow:

$$\frac{E_r}{E_i} = r_p = \frac{\dfrac{\mu_1}{\mu_2}\, n_2^2\, \cos\alpha - n_1\, n_2\, \cos\beta}{\dfrac{\mu_1}{\mu_2}\, n_2^2\, \cos\alpha + n_1\, n_2\, \cos\beta} \tag{1.559}$$

$$\frac{E_t}{E_i} = t_p = \frac{2\, n_1\, n_2\, \cos\alpha}{\dfrac{\mu_1}{\mu_2}\, n_2^2\, \cos\alpha + n_1\, n_2\, \cos\beta} \tag{1.560}$$

With the help of SNELL's law it follows for $\cos\beta$:

$$n_2\, \cos\beta = \sqrt{n_2^2 - n_1^2\, \sin^2\alpha} \tag{1.561}$$

With this the FRESNEL formulae can be written as a function of the angle of incidence alone. This also holds in case of complex n_2 in which β becomes complex too.

A.2 Dielectric Characteristics of Plasmas

A plasma is in general a mixture of free electrons, positive ions and neutral atoms (or neutral molecules). A plasma is electrically neutral; charge neutrality is only violated in the vicinity of boundaries or within spatial dimensions that are comparable or smaller than the DEBYE radius. Due to their much smaller mass, the electrons are at equal energy much faster than the ions. Thus in general, the electron current density is much higher than the ion current density, which implies that the electrons mainly determine the electric characteristics of plasmas. The electron current density is

$$\vec{j} = -e\, n_e\, \vec{v}_e \tag{1.562}$$

 with
e—elementary charge
n_e—electron density
$\vec{v}_e$—mean or drift velocity of the electrons.

The movement of electrons that are accelerated by an electric field is obstructed by collisions with other plasma particles. The impact of the collisions on the drift velocity can be modeled by a velocity proportional friction force. The equation of motion that governs electron drift velocity reads:

$$m_e\, \frac{d\vec{v}_e}{dt} + m_e\, \nu_m\, \vec{v}_e = -e\, \vec{E} \tag{1.563}$$

with

m_e—electron mass.

With the assumption that the momentum transfer frequency ν_m does not depend on the velocity, it follows in case of time harmonic electric fields:

$$\vec{\nu}_e = -\frac{e}{m_e}\,\vec{E}\,\frac{1}{\nu_m - i\,\omega} \tag{1.564}$$

The use of complex numbers in mathematically describing real physical quantities is treated in Appendix A.3. Comparison with Eq. 1.562 results in OHM's law:

$$\vec{j} = \sigma\,\vec{E} \tag{1.565}$$

with the complex plasma conductivity:

$$\sigma = \frac{e^2\,n_e}{m_e\,\nu_m}\,\frac{\nu_m}{\nu_m - i\,\omega} \tag{1.566}$$

In case of time harmonic fields, the MAXWELL equations read:

$$\vec{\nabla} \times \vec{E} = i\,\omega\,\vec{B} \tag{1.567}$$

$$\vec{\nabla} \times \vec{H} = \mu_0\,(\sigma\,\vec{E} - i\,\omega\,\varepsilon_0\,\vec{E}) = i\,\omega\,\epsilon_0\,\mu_0\,\varepsilon\,\vec{E} \tag{1.568}$$

In the second equation, the particle and the displacement currents are combined. The complex dielectric constant of the plasma is given by

$$\varepsilon = 1 - \frac{\sigma}{i\,\omega\,\varepsilon_0} \tag{1.569}$$

$$\varepsilon = 1 - \frac{\omega_p^2}{\omega^2 + \nu_m^2} + i\,\frac{\nu_m}{\omega}\,\frac{\omega_p^2}{\omega^2 + \nu_m^2} \tag{1.570}$$

$$\omega_p^2 = \frac{e^2\,n_e}{m_e\,\varepsilon_0} \tag{1.571}$$

With Eqs. 1.567 and 1.568 and the assumption of spatial homogeneity of the dielectric constant and that the plasma is electrically neutral, the wave equation follows:

$$\Delta\vec{E} + \frac{\omega^2}{c^2}\,\varepsilon\,\vec{E} = 0 \tag{1.572}$$

This wave equation is solved by plane waves with complex wave vectors $\vec{k}$:

$$\vec{E} = \vec{E}_0\,\exp\left[i\,(\vec{k}\cdot\vec{r} - \omega\,t)\right] \tag{1.573}$$

In case of propagation in the x-direction it follows:

$$\vec{E} = \vec{E}_0 \, \exp\left[i\left(k_r \, x - \omega \, t\right)\right] \, \exp\left[-k_i \, x\right] \tag{1.574}$$

k_r is the real part and k_i the imaginary part of the complex wave vector:

$$|\vec{k}| = k_0 \, n_c \tag{1.575}$$

$$n_c = \sqrt{\varepsilon} \tag{1.576}$$

$$k_0 = \frac{\omega}{c} \tag{1.577}$$

with

k_0—wave vector in vacuum

n_c—complex index of refraction of the plasma.

The time-averaged energy flux density is given by the time-averaged POYNTING vector[45]:

$$\bar{\bar{S}} = \frac{1}{2} \, \mathrm{Re}\left[\vec{E}_0 \times \vec{H}_0^*\right] \tag{1.578}$$

The star indicates the complex conjugated value. In case of a plane wave it follows in scalar form:

$$\bar{S} = \frac{k_r}{k_0} \, \frac{|E_0|^2}{Z_0} \, \exp\left(-2 \, k_i \, x\right) \tag{1.579}$$

In case of zero momentum transfer frequency ν_m, the plasma dielectric constant is given by

$$\varepsilon = 1 - \frac{\omega_p^2}{\omega^2} \tag{1.580}$$

and the index of refraction by

$$n_c = \sqrt{1 - \frac{\omega_p^2}{\omega^2}} \tag{1.581}$$

If the electron plasma frequency ω_p exceeds the frequency ω of the electromagnetic wave, the dielectric constant ε becomes negative. Then the index of refraction and the wave vector are imaginary and the intensity reflectivity R of the reflection at a plasma-vacuum interface becomes 1,[46] i.e. the wave is reflected totally and thus

---

[45] See Appendix A.3.

[46] See Eq. 1.19.

the time-averaged POYNTING vector vanishes. $k_r = 0$ means that the wave cannot propagate within the plasmas and decays exponentially:

$$\vec{E} = \vec{E}_0 \, \exp\left(-i \, \omega \, t\right) \, \exp\left(-k_i \, x\right) \tag{1.582}$$

The electron density at which the plasma frequency equals the circular frequency of the electromagnetic wave is called critical density. The exponential decay of the field strength above the critical density in case of vanishing collision frequency is not due to absorption but solely due to reflection. In case of finite collision frequency, the wave vector is no longer purely imaginary and the POYNTING vector has a finite value. The damping of the wave within the plasma is then due to both reflection and absorption.

A.3 Description of Electromagnetic Fields by Complex Quantities

Physical observables like the electric and magnetic fields are real quantities. But in many cases of interest, it is advantageous to use complex quantities to mathematically describe electromagnetic fields. In this case, it has to be kept in mind that only real quantities are physically meaningful. The description by complex numbers is possible because the MAXWELL equations are linear in the field quantities and thus real and imaginary parts are independent of each other. In computing products of field quantities, e.g. the POYNTING vector, it has explicitly to be accounted for that fields are real quantities. The real field of a plane wave that propagates in z-direction can be written as

$$\vec{E} = \text{Re}\left[\vec{E}_0 \, \exp\left[i\left(k \, z - \omega \, t\right)\right]\right] \tag{1.583}$$

$$= \frac{1}{2}\left(\vec{E}_0 \, \exp\left[i\left(k \, z - \omega \, t\right)\right] + \vec{E}_0^* \, \exp\left[-i\left(k \, z - \omega \, t\right)\right]\right) \tag{1.584}$$

$$\vec{H} = \text{Re}\left[\vec{H}_0 \, \exp\left[i\left(k \, z - \omega \, t\right)\right]\right] \tag{1.585}$$

$$= \frac{1}{2}\left(\vec{H}_0 \, \exp\left[i\left(k \, z - \omega \, t\right)\right] + \vec{H}_0^* \, \exp\left[i\left(k \, z - \omega \, t\right)\right]\right) \tag{1.586}$$

As long as the fields only enter linearly, the complex quantities can be used. This makes the computations often much easier because the exponential functions are in general easier to handle than the sin and cos functions. Inserting this into the MAXWELL equations results in an equation for the complex amplitudes $\vec{E}_0$ and $\vec{H}_0$. When determining physical quantities, the expressions Eqs. 1.583, 1.583 have to be used:

$$\vec{E} = \vec{E}_{0_r} \, \cos\left(k \, z - \omega \, t\right) - \vec{E}_{0_i} \, \sin\left(k \, z - \omega \, t\right) \tag{1.587}$$

with
r—indicates the real part of $\vec{E}$
i—indicates the imaginary part of $\vec{E}$.

$$\vec{E} = \vec{e}_x \left[E_{0_{rx}} \cos (k\, z - \omega\, t) - E_{0_{ix}} \sin (k\, z - \omega\, t) \right. \tag{1.588}$$
$$+ \vec{e}_y \left[E_{0_{ry}} \cos (k\, z - \omega\, t) - E_{0_{iy}} \sin (k\, z - \omega\, t) \right.$$
$$+ \vec{e}_z \left[E_{0_{rz}} \cos (k\, z - \omega\, t) - E_{0_{iz}} \sin (k\, z - \omega\, t) \right.$$

This can be cast into the form:

$$\vec{E} = \vec{e}_x \left[|E_{0_x}| \sin (k\, z - \omega\, t + \phi_x) \right] \tag{1.589}$$
$$+ \vec{e}_y \left[|E_{0_y}| \sin (k\, z - \omega\, t + \phi_y) \right]$$
$$+ \vec{e}_z \left[|E_{0_z}| \sin (k\, z - \omega\, t + \phi_z) \right]$$

with
$$\tan \phi_x = -\frac{E_{0_{ix}}}{E_{0_{rx}}}, \; \tan \phi_y = -\frac{E_{0_{iy}}}{E_{0_{ry}}}, \; \tan \phi_z = -\frac{E_{0_{iz}}}{E_{0_{rz}}}.$$

While computing the POYNTING vector, the real parts of the fields have to be taken:

$$\vec{S} = \mathrm{Re}(\vec{E}_0 \exp [i\,(k\, z - \omega\, t)]) \times \mathrm{Re}(\vec{H}_0 \exp [i\,(k\, z - \omega\, t)]) \tag{1.590}$$

The real parts can be written as the sum of the complex quantity and its complex conjugated value:

$$\vec{S} = \frac{1}{2} \left(\vec{E}_0 \exp [i\,(k\, z - \omega\, t)] + \vec{E}_0^* \exp [-i\,(k\, z - \omega\, t)] \right) \tag{1.591}$$
$$\times \frac{1}{2} \left(\vec{H}_0 \exp [i\,(k\, z - \omega\, t)] + \vec{H}_0^* \exp [-i\,(k\, z - \omega\, t)] \right)$$

This gives

$$\vec{S} = \frac{1}{4} \left(\vec{E}_0 \times \vec{H}_0^* + \vec{E}_0^* \times \vec{H}_0 \right. \tag{1.592}$$
$$+ (\vec{E}_0 \times \vec{H}_0) \exp [2\, i\,(k\, z - \omega\, t)]$$
$$+ (\vec{E}_0^* \times \vec{H}_0^*) \exp [2\, i\,(k\, z - \omega\, t)] \left. \right)$$

With this it follows:

$$\vec{S} = \frac{1}{2} \left(\mathrm{Re}(\vec{E}_0 \times \vec{H}_0^*) + \mathrm{Re}((\vec{E}_0 \times \vec{H}_0) \exp [2\, i\,(k\, z - \omega\, t)]) \right) \tag{1.593}$$

The POYNTING vector consists of a constant part and an oscillating part. The oscillating part vanishes in taking the time average. The time-averaged POYNTING vector is the intensity of the wave and reads:

$$\bar{\bar{S}} = \frac{1}{2} \left[\text{Re}(\vec{E}_0 \times \vec{H}_0^*) \right] \tag{1.594}$$

In vacuum, the $\vec{E}$ and $\vec{H}$ vectors are perpendicular to each other and their absolute values are related by

$$|H_0| = \frac{|E_0|}{Z_0} \tag{1.595}$$

with
Z_0—vacuum wave resistance.

With this it follows:

$$\bar{S} = \frac{1}{2} \frac{|E_0|^2}{Z_0} \tag{1.596}$$

In the literature, the fields are often defined omitting the factor $1/2$ in Eqs. 1.583 and 1.585. Then Eq. 1.596 becomes

$$\bar{S} = 2 \frac{|E_0|^2}{Z_0} \tag{1.597}$$

B   Continuum Mechanics

The following is mainly based on the excellent book Becker and Bürger (1975).

B.1   Coordinate Systems and Deformation Gradient

In the field of continuum mechanics, matter (solids, fluids, gases) is treated as a continuum in 3-dimensional space. The points that constitute the continuum are called **material points**. The **material points** can be identified uniquely by their coordinates at a reference time. At later times, the positions of the **material points** will in general no longer coincide with the reference values. The change of position of the **material points** can be described using a time-dependent point transformation. The coordinates ξ_1, ξ_2, ξ_3 that the **material points** are assigned to at the reference time τ are called material coordinates. The coordinates x_1, x_2, x_3 of the 3-dimensional physical space are called space coordinates. It holds

$$\vec{\xi} = \vec{\xi}(\vec{x}, t; \tau) \tag{1.598}$$

$$\vec{\xi}(\vec{x}, \tau; \tau) = \vec{x} \tag{1.599}$$

as well as

$$\vec{x} = \vec{x}(\vec{\xi}, t; \tau) \tag{1.600}$$

$$\vec{x}(\vec{\xi}, \tau; \tau) = \vec{\xi} \tag{1.601}$$

The differentials of the spatial coordinates are given by

$$dx_i = \frac{\partial x_i(\vec{\xi}, t)}{\partial \xi_k} d\xi_k = F_{ik} d\xi_k \tag{1.602}$$

Double indices are summed over. The matrix

$$\hat{F} = (F_{ik}) = \frac{\partial(x_1, x_2, x_3)}{\partial(\xi_1, \xi_2, \xi_3)} = \begin{pmatrix} \dfrac{\partial x_1}{\partial \xi_1} & \dfrac{\partial x_1}{\partial \xi_2} & \dfrac{\partial x_1}{\partial \xi_3} \\[2mm] \dfrac{\partial x_2}{\partial \xi_1} & \dfrac{\partial x_2}{\partial \xi_2} & \dfrac{\partial x_2}{\partial \xi_3} \\[2mm] \dfrac{\partial x_3}{\partial \xi_1} & \dfrac{\partial x_3}{\partial \xi_2} & \dfrac{\partial x_3}{\partial \xi_3} \end{pmatrix} \tag{1.603}$$

is called deformation gradient. The determinant of this matrix is the JACOBI determinant Δ of the coordinate transformation $\left(\vec{\xi} \leftrightarrow \vec{x} \right)$:

$$\Delta = \det \left(\frac{\partial(x_1, x_2, x_3)}{\partial(\xi_1, \xi_2, \xi_3)} \right) \tag{1.604}$$

It always holds that $\Delta > 0$. Now it is assumed that the three material coordinate vectors $d\vec{\xi}_a$, $d\vec{\xi}_b$, $d\vec{\xi}_c$ with lengths a, b and c respectively are perpendicular to each other (Fig. 1.68). The volume element $dV_0 = (d\vec{\xi}_a \times d\vec{\xi}_b) \cdot d\vec{\xi}_c$ is then $(a\,b\,c)$. With this and Eq. 1.602, the coordinates of the vectors $d\vec{x}_i$ are given by

Fig. 1.68 Material coordinate system
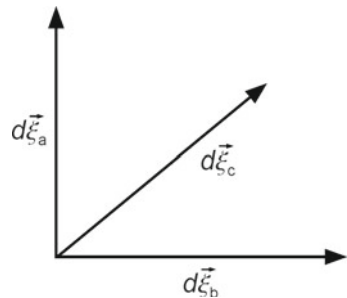
$$x_{1a} = F_{11}\, a \qquad x_{2a} = F_{21}\, a \qquad x_{3a} = F_{31}\, a$$
$$x_{1b} = F_{12}\, b \qquad x_{2b} = F_{22}\, b \qquad x_{3b} = F_{32}\, b$$
$$x_{1c} = F_{13}\, c \qquad x_{2c} = F_{23}\, c \qquad x_{3c} = F_{33}\, c$$

With this it follows:

$$
\begin{aligned}
d\vec{x}_a \times d\vec{x}_b &= (F_{11}a, F_{21}a, F_{31}a) \times (F_{12}b, F_{22}b, F_{32}b) \\
&= ab\,[(F_{21}F_{32} - F_{31}F_{22}), (F_{31}F_{12} - F_{11}F_{32}), (F_{11}F_{22} - F_{21}F_{12})] \\
(d\vec{x}_a \times d\vec{x}_b) \cdot d\vec{x}_c &= abc\,[(F_{21}F_{32} - F_{31}F_{22}), (F_{31}F_{12} - F_{11}F_{32}), (F_{11}F_{22} - F_{21}F_{12})] \\
&\qquad (F_{13}, F_{23}, F_{33}) \\
(d\vec{x}_a \times d\vec{x}_b) \cdot \vec{x}_c &= dV \\
&= dV_0[(F_{21}F_{32}F_{13} - F_{31}F_{22}F_{13}), \\
&\qquad (F_{31}F_{12}F_{23} - F_{11}F_{32}F_{23}), \\
&\qquad (F_{11}F_{22}F_{33} - F_{21}F_{12}F_{33})]
\end{aligned}
$$

or:

$$dV = dV_0\,\Delta \tag{1.605}$$

Scalar as well as vector functions can be formulated in material as well as in spatial coordinates:

$$\phi(\vec{\xi}(\vec{x}, t; \tau)) = \tilde{\phi}(\vec{x}, t) \tag{1.606}$$
$$\vec{V}(\vec{\xi}(\vec{x}, t; \tau)) = \tilde{\vec{V}}(\vec{x}, t) \tag{1.607}$$

It holds

$$\frac{\partial \phi}{\partial x_i} = \frac{\partial \phi}{\partial \xi_j} \frac{\partial \xi_j}{\partial x_i} \tag{1.608}$$

B.2 Deformation

When considering three material points at a reference time $t = \tau$ and at a later time instance $t = t_0$ then in general the relative positions of these three points will have changed. If the relative positions did not change, rigid body motion took place. If the points are infinitely close to each other, then the vectors connecting the points are given by (see Fig. 1.69)[47]

$$d\vec{x}^T \cdot \delta\vec{x} - d\vec{\xi}^T \cdot \delta\vec{\xi} = (\hat{F}d\vec{\xi})^T \cdot (\hat{F}\delta\xi) - d\xi^T \cdot \delta\vec{\xi} \tag{1.609}$$

---

[47] T denotes the transposed matrix.

Fig. 1.69 Deformation in material and spatial coordinates respectively
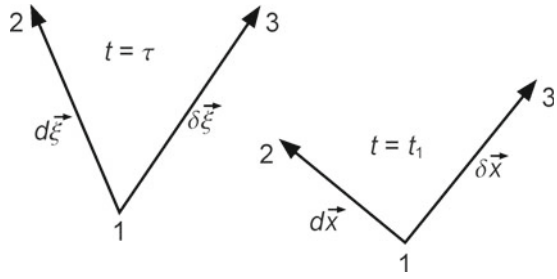
With

$$(\hat{F}d\vec{\xi})^T = d\vec{\xi}^T\,\hat{F}^T \tag{1.610}$$

it follows:

$$d\vec{x}^T \cdot \delta\vec{x} - d\vec{\xi}^T \cdot \delta\vec{\xi} = d\vec{\xi}^T\,\hat{F}^T\,\hat{F}\,\delta\vec{\xi} - d\vec{\xi}^T \cdot \delta\vec{\xi}$$
$$= 2\,d\vec{\xi}^T\left[\frac{1}{2}(\hat{F}^T\,\hat{F} - 1)\right]\delta\vec{\xi} \tag{1.611}$$

The expression in braces is GREEN's strain tensor:

$$\hat{G} = \frac{1}{2}\left(\hat{F}^T\,\hat{F}\,-\,\hat{1}\right) \tag{1.612}$$

GREEN's strain tensor is symmetrical. With the definition of the displacement vector $\vec{u}$:

$$\vec{x} = \vec{\xi} + \vec{u}(\vec{\xi}) \tag{1.613}$$

the deformation tensor $\hat{F}$ is given by

$$F_{ik} = \frac{\partial x_i}{\partial \xi_k} = \delta_{ik} + \frac{\partial u_i}{\partial \xi_k} \tag{1.614}$$

or in short:

$$\hat{F} = \hat{1} + \vec{\nabla}_\xi\,\vec{u} \tag{1.615}$$

Inserting this into Eq. 1.612 yields

$$\hat{G} = \frac{1}{2} \left[\left(1 + \vec{\nabla}_{\xi}\,\vec{u} \right)^T \left(1 + \vec{\nabla}_{\xi}\,\vec{u} \right) - 1 \right]$$

$$\hat{G} = \frac{1}{2} \left[\left(1 + \vec{\nabla}_{\xi}^T\,\vec{u} \right) \left(1 + \vec{\nabla}_{\xi}\,\vec{u} \right) - 1 \right]$$

$$\hat{G} = \frac{1}{2} \left[1 + \vec{\nabla}_{\xi}^T\,\vec{u} + \vec{\nabla}_{\xi}\,\vec{u} + \vec{\nabla}_{\xi}^T\,\vec{u}\ \vec{\nabla}_{\xi}\,\vec{u} - 1 \right]$$

$$\hat{G} = \frac{1}{2} \left[\vec{\nabla}_{\xi}^T\,\vec{u} + \vec{\nabla}_{\xi}\,\vec{u} + \vec{\nabla}_{\xi}^T\,\vec{u}\ \vec{\nabla}_{\xi}\,\vec{u} \right] \tag{1.616}$$

In components GREEN's strain tensor reads:

$$\gamma_{ik} = \frac{1}{2} \left[\frac{\partial u_k}{\partial \xi_i} + \frac{\partial u_i}{\partial \xi_k} \right] + \frac{1}{2} \sum_l \frac{\partial u_l}{\partial \xi_i} \frac{\partial u_l}{\partial \xi_k} \tag{1.617}$$

With the assumption:

$$\left| \frac{\partial u_i}{\partial \xi_k} \right| \ll 1 \tag{1.618}$$

quadratic terms in Eq. 1.617 can be neglected and the geometrically linearized GREEN's strain tensor follows:

$$\gamma_{ik} = \frac{1}{2} \left[\frac{\partial u_k}{\partial \xi_i} + \frac{\partial u_i}{\partial \xi_k} \right] \tag{1.619}$$

With this Eq. 1.611 reads in components:

$$d\vec{x} \cdot \delta\vec{x} - d\vec{\xi}^T \cdot \delta\vec{\xi} = 2 \sum_i \sum_k \gamma_{ik}\, d\xi_i\, \delta\xi_k \tag{1.620}$$

B.2.1   Physical Meaning of the Components of GREEN's Strain Tensor

With

$$d\vec{\xi} = \delta\vec{\xi} = (dl_0, 0, 0) \tag{1.621}$$

it follows from Eq. 1.620 (see Fig. 1.70):

$$dl^2 - dl_0^2 = 2\gamma_{11}dl_0^2$$
$$dl = \sqrt{1 + 2\gamma_{11}}\,dl_0 \tag{1.622}$$

Fig. 1.70 Physical meaning of the components of G

With the assumption $|\gamma_{11}| \ll 1$, the square root can be expanded:

$$dl = (1 + \gamma_{11})\, dl_0$$

or:

$$\gamma_{11} = \frac{dl - dl_0}{dl_0}$$

This implies that the diagonal elements of GREEN's strain tensor describe the elongation. With

$$d\vec{\xi} = (dl_0, 0, 0)$$
$$\delta\vec{\xi} = (0, dl_0, 0)$$

it follows from Eq. 1.620:

$$d\vec{x}^T \cdot \delta\vec{x} - d\vec{\xi}^T \cdot \delta\vec{\xi} = 2\,\gamma_{12}\, dl_0^2$$

and because $d\vec{\xi} \cdot \delta\vec{\xi} = 0$ it follows:

$$d\vec{x}^T \cdot \delta\vec{x} = 2\,\gamma_{12}\, dl_0^2$$

The scalar product on the right-hand side is

$$d\vec{x}^T \cdot \delta\vec{x} = |d\vec{x}^T||\delta\vec{x}|\cos\phi$$

With the vector length Eq. 1.622 it follows:

$$d\vec{x}^T \cdot \delta\vec{x} = dl_0\,\sqrt{1 + 2\gamma_{11}}\,dl_0\,\sqrt{1 + 2\gamma_{22}}\,\cos\phi$$

and thus

$$\cos\phi\sqrt{1 + 2\gamma_{11}}\sqrt{1 + 2\gamma_{22}} = 2\gamma_{12}$$
$$\gamma_{12} = \frac{1}{2}\frac{\cos\phi}{\sqrt{1 + 2\gamma_{11}}\sqrt{1 + 2\gamma_{12}}} = \frac{1}{2}\frac{\sin\alpha}{\sqrt{1 + 2\gamma_{11}}\sqrt{1 + 2\gamma_{12}}}$$

In case of $|\gamma_{ii}| \ll 1$, it approximately holds

$$\gamma_{12} \approx \frac{1}{2} \sin \alpha$$

and in case of small angles:

$$\gamma_{12} \approx \frac{\alpha}{2} \tag{1.623}$$

The non-diagonal elements of GREEN's strain tensor thus describe the changes of angles.

B.3 Derivation with Respect to Time

Time derivatives can be defined for material as well as spatial coordinates:

- material derivative

$$\frac{D\phi}{Dt} := \frac{\partial \phi(\vec{\xi}, t)}{\partial t} \tag{1.624}$$

- spatial derivative

$$\frac{\delta \phi}{\delta t} := \frac{\partial \phi(\vec{x}, t)}{\partial t} \tag{1.625}$$

The velocity and acceleration of a particle are defined as

$$\frac{D\vec{x}}{Dt} = \vec{v} \tag{1.626}$$

$$\frac{D\vec{v}}{Dt} = \vec{a} \tag{1.627}$$

If a scalar field function ϕ is given in spatial coordinates:

$$\phi(x_1, x_2, x_3, t) = \phi(x_1(\xi_2, \xi_2, \xi_3, t), x_2(\xi_2, \xi_2, \xi_3, t), x_3(\xi_2, \xi_2, \xi_3, t), t) \tag{1.628}$$

then it follows for the material time derivative:

$$\frac{D\phi}{Dt} = \frac{\partial \phi(x_1, x_2, x_3, t)}{\partial t} + \frac{\partial \phi(x_1, x_2, x_3, t)}{\partial x_k} \frac{\partial x_k(\vec{\xi}, t)}{\partial t} \tag{1.629}$$

With Eqs. 1.624 and 1.626 it follows:

$$\frac{\partial x_k(\vec{\xi}, t)}{\partial t} = \frac{D x_k}{D t} = v_k \tag{1.630}$$

and with Eq. 1.625 one gets in components:

$$\frac{D\phi}{Dt} = \frac{\delta\phi}{\delta t} + (\vec{\nabla}\,\phi) \cdot \vec{v} \tag{1.631}$$

The same applies to vector functions. With the definition of the gradient of a vector function:

$$(\vec{\nabla}\,\vec{f}) = \left(\frac{\partial f_i}{\partial x_j}\right) \tag{1.632}$$

it follows:

$$\frac{D\vec{f}}{Dt} = \frac{\delta\vec{f}}{\delta t} + (\vec{\nabla}\,\vec{f})\vec{v} \tag{1.633}$$

and especially for $\vec{v}$:

$$\frac{D\vec{v}}{Dt} = \vec{a} = \frac{\delta\vec{v}}{\delta t} + (\vec{\nabla}\,\vec{v})\vec{v} \tag{1.634}$$

B.4   REYNOLDS's *Transport Theorem*

While integrating a function of time and spatial coordinates $\phi(\vec{r}, t)$ over a moving material body B:

$$\psi(t) = \iiint\limits_{B(t)} \phi(\vec{r}, t)\, dV \tag{1.635}$$

the integration region will in general be time-dependent. This has to be accounted for when performing the time derivative. When transforming the integral to material coordinates, the integration region B_0 is time-independent. With Eq. 1.605 it follows:

$$\psi(t) = \iiint\limits_{B(t)} 0\, \phi(\vec{x}(\vec{\xi}, t), t)\, \Delta(\vec{\xi}, t)\, dV_0 \tag{1.636}$$

The time derivative then is

$$\frac{D\psi}{Dt} = \iiint\limits_{B_0} \left[\frac{D\phi}{Dt}\Delta + \phi\frac{D\Delta}{Dt}\right] dV_0 \tag{1.637}$$

With (Becker and Bürger 1975):

$$\frac{D\Delta}{Dt} = \Delta \vec{\nabla} \cdot \vec{v} \tag{1.638}$$

one gets

$$\frac{D\psi}{Dt} = \iiint\limits_{B_0} \left[\frac{D\phi}{Dt} + \phi \vec{\nabla} \cdot v\right] dV_0$$

$$= \iiint\limits_{B(t)} \left[\frac{D\phi}{Dt} + \phi \vec{\nabla} \cdot v\right] dV \tag{1.639}$$

This is REYNOLDS's transport theorem. With Eq. 1.631 it follows:

$$\frac{D\psi}{Dt} = \iiint\limits_{B(t)} \left[\frac{\delta\phi}{\delta t} + (\vec{\nabla}\phi)\cdot\vec{v} + \phi\,\vec{\nabla}\cdot\vec{v}\right] dV \tag{1.640}$$

or:

$$\frac{D\psi}{Dt} = \iiint\limits_{B(t)} \left[\frac{\delta\phi}{\delta t} + \vec{\nabla}\cdot(\phi\vec{v})\right] dV \tag{1.641}$$

Using GAUSS's theorem:

$$\iiint\limits_{B(t)} \vec{\nabla}(\phi\vec{v}) = \iint\limits_{\partial B(t)} (\phi\vec{v})\cdot\vec{n}dA \tag{1.642}$$

it follows:

$$\frac{D\psi}{Dt} = \iiint\limits_{B(t)} \frac{\delta\phi}{\delta t} dV + \iint\limits_{\partial B(t)} (\phi\vec{v})\cdot\vec{n}\, dA \tag{1.643}$$

$\partial B(t)$—boundary of the body

B.5 Mass Conservation

The mass M of a body B is given by integrating its mass density over the volume of the body:

$$M = \iiint\limits_{B(t)} \rho \, dV \tag{1.644}$$

When the body B is moving, the integration volume changes with time, whereas the mass of a body is conserved, which implies that its time derivative vanishes. With Eq. 1.639:

$$\frac{DM}{Dt} = 0 = \iiint\limits_{B(t)} \left[\frac{D\rho}{Dt} + \rho \, \vec{\nabla} \cdot \vec{v} \right] dV \tag{1.645}$$

B can be chosen arbitrarily so that the integrand (assuming sufficient continuity of the integrand) must be zero:

$$\frac{D\rho}{Dt} + \rho \, \vec{\nabla} \cdot \vec{v} = 0 \tag{1.646}$$

With Eq. 1.631 it follows:

$$\frac{\delta\rho}{\delta t} + \vec{\nabla} \cdot (\rho \vec{v}) = 0 \tag{1.647}$$

This is the differential form of mass conservation. The time derivative of the integral of the product of an arbitrary field function ϕ with the mass density using Eq. 1.639 is given by

$$\frac{D}{Dt} \iiint\limits_{B(t)} \rho\phi \, dV = \iiint\limits_{B(t)} \left[\frac{D(\rho\phi)}{Dt} + \rho\phi \, \vec{\nabla} \cdot \vec{v} \right] dV$$

$$= \iiint\limits_{B(t)} \left[\frac{D\rho}{Dt}\phi + \rho\frac{D\phi}{Dt} + \rho\phi \, \vec{\nabla} \cdot \vec{v} \right] dV \tag{1.648}$$

With Eq. 1.646 one gets

$$\frac{D}{Dt} \iiint\limits_{B(t)} \rho\phi \, dV = \iiint\limits_{B(t)} \rho\frac{D\phi}{Dt} \, dV \tag{1.649}$$

This relation was deduced for scalar functions but it also applies in case of vector functions:

$$\frac{D}{Dt} \iiint\limits_{B(t)} \rho \vec{a} \, dV = \iiint\limits_{B(t)} \rho \frac{D\vec{a}}{Dt} \, dV \tag{1.650}$$

B.6 Momentum Conservation

The momentum of a body is defined as

$$\vec{P} := \iiint\limits_{B(t)} \rho \vec{v} \, dV \tag{1.651}$$

Let $\vec{K}$ be the sum of all forces acting on the body B, then the time evolution of the momentum $\vec{P}$ of the body is given by

$$\frac{D\vec{P}}{Dt} = \vec{K} \tag{1.652}$$

A basic theorem of continuum mechanics states that the forces $\vec{K}$ that act on a body can be split into a contribution that act on the surface and a part that act on the volume (e.g. gravity):

$$\vec{K} = \iint\limits_{\partial B(t)} \vec{t} \cdot \vec{A} + \iiint\limits_{B(t)} \rho \, \vec{f} dV \tag{1.653}$$

with
$\partial B(t)$—boundary of the body
$\vec{t}$—surface forces.

The vector $\vec{t}$ is called stress vector and has the unit force per area. With Eq. 1.650, momentum conservation becomes

$$\iiint\limits_{B(t)} \left[\rho \frac{D\vec{v}}{Dt} - \rho \, \vec{f} \right] dV = \iint\limits_{\partial B(t)} \vec{t} \, dA \tag{1.654}$$

$\vec{t}$ can be described using CAUCHY's stress tensor $\hat{T}$:

$$\vec{t} = \hat{T} \cdot \vec{n} \tag{1.655}$$

or in components:

$$t_i = \tau_{ij} n_j \tag{1.656}$$

$\vec{n}$ is the normal of the area element that $\vec{t}$ acts on. Thus the force that acts on an area element not only depends on the stress tensor, which is a function of space only, but also on the unit vector. This implies that $\vec{t}$ is not a vector field whereas the stress tensor $\hat{T}$ is a tensor field. The quantities τ_{ii} are called normal stresses and the quantities $\tau_{ij}, i \neq j$ are called shear stresses. From angular momentum conservation it follows that CAUCHY's stress tensor is symmetric (Becker and Bürger 1975):

$$\tau_{ij} = \tau_{ji} \tag{1.657}$$

The surface integral in the momentum equation Eq. 1.654 can be cast to a volume integral:

$$\iint_{\partial B(t)} \hat{T}\,\vec{n}\,dA = \iiint_{B(t)} \vec{\nabla} \cdot \hat{T}\,dV \tag{1.658}$$

The divergence of a tensor as defined in Eq. 1.658 is a vector:

$$\vec{\nabla} \cdot \hat{T} = \frac{\partial \tau_{ij}}{\partial x_j} \tag{1.659}$$

Again double indices are summed over. Momentum conservation thus reads:

$$\iiint_{B(t)} \left(\rho \frac{D\vec{v}}{Dt} - \vec{\nabla} \cdot \hat{T} - \rho\,\vec{f} \right) dV = 0 \tag{1.660}$$

Because B is arbitrary the integrand must vanish (assuming continuity of the integrand). With Eqs. 1.631 and 1.625, it follows:

$$\rho \frac{D\vec{v}}{Dt} = \rho \frac{\partial\vec{v}}{\partial t} + \rho\,(\vec{\nabla}\,\vec{v})\,\vec{v} = \vec{\nabla} \cdot \hat{T} + \rho\,\vec{f} \tag{1.661}$$

This is the momentum conservation in differential form. In components it reads:

$$\rho \frac{\partial V_i}{\partial t} + \rho \frac{\partial V_i}{\partial x_j}\,V_j = \frac{\partial \hat{T}_{ij}}{\partial x_j} + \rho\,f_i \tag{1.662}$$

Double indices are summed over. Multiplication of the mass conservation equation Eq. 1.647 by V_i:

$$V_i \frac{\partial \rho}{\partial t} + V_i\,V_j \frac{\partial \rho}{\partial x_j} + V_i\,\rho \frac{\partial V_j}{\partial x_j} = 0 \tag{1.663}$$

and adding Eq. 1.662 yields

$$\frac{\partial(\rho \, V_i)}{\partial t} + \frac{\partial(\rho \, V_i \, V_j)}{\partial x_j} = \frac{\partial \hat{\tau}_{ij}}{\partial x_j} + \rho \, f_i \qquad (1.664)$$

This is the conservative form of the momentum conservation.

B.7 Material Equations

In case of pure mechanical material properties, material equations relate stresses and strain. In case of solids, the movement of the solid body is described by the strain tensor, whereas in case of fluids the strain velocity tensor applies.

B.7.1 Elastic Solids

Stress and strain of a solid are related by the general relation:

$$\hat{T}(\vec{\xi}, t) = f(\hat{G}(\vec{\xi}, t)) \qquad (1.665)$$

In case of small strain:

$$|\gamma_{ij}| \ll 1$$

i.e. in the geometric linear case, it holds

$$\hat{T}_{ij} = f_{ij}(\gamma_{11}, \gamma_{12}, \gamma_{13}, \gamma_{22}, \gamma_{23}, \gamma_{33}) \qquad (1.666)$$

If the functions f_{ij} are linear homogeneous in γ_{ij} (physical linear model), generalized HOOKE's law follows:

$$\tau_{11} = c_1 \, \gamma_{11} + \cdots + c_6 \, \gamma_{33}$$
$$\tau_{12} = c_7 \, \gamma_{11} + \cdots + c_{12} \, \gamma_{33}$$
$$\tau_{33} = c_{31} \, \gamma_{11} + \cdots + c_{36} \, \gamma_{33}$$

The 36 constants $c_1, c_2, ..., c_{36}$ reduce to 21 due to symmetry considerations (Becker and Bürger 1975). Assuming complete isotropy of the solid, these 21 constants reduce to only 2 (there are crystals that make it necessary to keep all 21 constants). In case of isotropic materials, HOOKE's law applies:

$$\hat{T} = 2\mu \hat{G} + \lambda (\text{Tr} \, \hat{G}) \hat{I} \qquad (1.667)$$

Tr $\hat{G}$ is the trace of the strain tensor and μ and λ are the LAMÉ constants. $\hat{I}$ is the identity tensor. In the field of continuum mechanics often alternative constants are used:

- YOUNG's modulus E
- POISSON's ratio ν
- compressibility κ.

The two sets of constants are related by

$$\mu = \frac{E}{2(1 + \nu)}$$

$$\lambda = \frac{E\,\nu}{(1 + \nu)(1 - 2\nu)}$$

$$\kappa = \frac{3}{3\lambda + 2\mu}$$

and the inverse expressions:

$$E = \frac{\mu(3\lambda + 2\mu)}{\lambda + \mu}$$

$$\nu = \frac{\lambda}{2(\lambda + \mu)}$$

λ must not be negative which implies that $0 \leq \nu < 0.5$. Using these constants, Eq. 1.667 can be written as

$$\tau_{ij} = \frac{E}{1 + \nu}\left(\gamma_{ij} + \frac{\nu}{1 - 2\nu}\left(\gamma_{11} + \gamma_{22} + \gamma_{33}\right)\delta_{ij}\right) \tag{1.668}$$

The components of the strain tensor as a function of the stresses are

$$\gamma_{ij} = \frac{1 + \nu}{E}\left(\tau_{ij} - \frac{\nu}{1 + \nu}\left(\tau_{11} + \tau_{22} + \tau_{33}\right)\delta_{ij}\right) \tag{1.669}$$

B.7.2 NEWTONIAN Fluids

In case of flows with friction, the stress tensor is composed of a spherical symmetric and a friction contribution:

$$\hat{T} = -p\hat{I} + \hat{T}_r \tag{1.670}$$

with

p—hydrostatic pressure.

Because in fluids there is no distinguished configuration, it can always be assumed that the deformation gradient is given by $\hat{I}$ which implies that GREEN's stress tensor vanishes. In fluids the deformation gradient is replaced by the deformation velocity:

$$\dot{\hat{F}} = \frac{\partial^2 x_i(\vec{\xi}, t)}{\partial \xi_k \partial t} = \frac{\partial}{\partial \xi_k} \frac{\partial x_i(\vec{\xi}, t)}{\partial t} \tag{1.671}$$

With Eqs. 1.625 and 1.626, it follows:

$$\dot{\hat{F}} = \frac{\partial V_i}{\partial \xi_k} = \frac{\partial V_i}{\partial x_l} \frac{\partial x_l}{\partial \xi_k} \tag{1.672}$$

Using short-hand notation, this reads:

$$\dot{\hat{F}} = \left(\vec{\nabla}\vec{v}\right) \hat{F} \tag{1.673}$$

Because in fluids there is no distinguished configuration, every configuration can be taken as reference configuration. This implies that $\hat{F}$ can be set to be the unit tensor for all times. Thus it follows:

$$\dot{\hat{F}} = \vec{\nabla}\vec{v} = \frac{\partial V_i}{\partial x_j} \tag{1.674}$$

The matrix Eq. 1.674 can be split into a symmetric and an antisymmetric part:

$$\vec{\nabla}\vec{v} = \hat{D} + \hat{W} \tag{1.675}$$

$$D = \frac{1}{2}\left(\vec{\nabla}\vec{v} + \vec{\nabla}^T\vec{v}\right) = \frac{1}{2}\left(\frac{\partial V_i}{\partial x_j} + \frac{\partial V_j}{\partial x_i}\right) \tag{1.676}$$

$$W = \frac{1}{2}\left(\vec{\nabla}\vec{v} - \vec{\nabla}^T\vec{v}\right) = \frac{1}{2}\left(\frac{\partial V_i}{\partial x_j} - \frac{\partial V_j}{\partial x_i}\right) \tag{1.677}$$

T indicates the transposed tensor. The antisymmetric part $\hat{W}$ describes a rigid body rotation (Becker and Bürger 1975); in case of fluids, this contribution vanishes. The friction part of the stress tensor of fluids is postulated to be of the form:

$$\hat{T}_r = f(\hat{D}), \quad f(0) = 0 \tag{1.678}$$

In case of NEWTONian fluids, the following relation applies (Becker and Bürger 1975):

$$\hat{T}_r = 2\,\eta\,\hat{D} + \lambda(Sp\,\hat{D}) \tag{1.679}$$

with
η—shear viscosity
λ—volume viscosity.

Equation 1.664 then becomes

$$\frac{\partial(\rho\,V_i)}{\partial t} + \frac{\partial(\rho\,V_i\,V_j)}{\partial x_i} = -\frac{\partial p}{\partial x_i} + \lambda\,\frac{\partial}{\partial x_i}\frac{\partial V_j}{\partial x_j} + \eta\,\frac{\partial}{\partial x_j}\left(\frac{\partial V_i}{\partial x_j} + \frac{\partial V_j}{\partial x_i}\right) + \rho\,f_i \quad (1.680)$$

In case of incompressible fluids, the mass conservation Eq. 1.647 yields

$$\frac{\partial V_j}{\partial x_j} = \vec{\nabla}\cdot\vec{v} = 0 \tag{1.681}$$

The divergence of $\hat{D}$ is thus given by

$$\vec{\nabla}\hat{D} = \frac{\partial d_{ij}}{\partial x_j} = \frac{1}{2}\frac{\partial^2 V_i}{\partial x_j^2} = \frac{1}{2}\,\Delta\vec{v} \tag{1.682}$$

The momentum conservation in case of incompressible NEWTONian fluids thus reads:

$$\rho\frac{\partial V_i}{\partial t} + \frac{\partial(\rho\,V_i\,V_j)}{\partial x_i} = -\frac{\partial p}{\partial x_i} + \eta\,\frac{\partial^2 V_i}{\partial x_j^2} + \rho\,f_i \tag{1.683}$$

or in short:

$$\rho\,\frac{\partial\vec{v}}{\partial t} + \rho\,(\vec{v}\,\vec{\nabla})\,\vec{v} = -\vec{\nabla}\,p + \eta\,\Delta\,\vec{v} + \rho\,\vec{f} \tag{1.684}$$

B.8   Energy Conservation

With the assumption that the energy of a body B can uniquely be split into a part that does not depend on the movement, namely its internal energy, and its kinetic energy, the total energy E of the body is given by

$$E = \iiint\limits_{B(t)} \rho\,\varepsilon\,dV \tag{1.685}$$

with
$\varepsilon = e + \dfrac{1}{2}\,\vec{v}^2$—specific total energy density

e—specific internal energy
v—velocity.

The integration runs over the material body B. If the body moves, the integration region changes. According to the first law of thermodynamics, the time change of the internal energy equals the power of the external forces that act on the body and the heat flux through the boundary of the body:

$$\underbrace{\frac{D}{Dt} \iiint\limits_{B(t)} \rho\, \varepsilon\, dV}_{1} = \underbrace{\iint\limits_{\partial B(t)} (\vec{t} \cdot \vec{v} - \vec{q} \cdot \vec{n})\, dA}_{2,3} + \underbrace{\iiint\limits_{B(t)} (\rho\, \vec{f} \cdot \vec{v} + w)\, dV}_{4,5} \qquad (1.686)$$

with
1—total energy
2—power of the stresses acting on the boundary of the body
3—heat flux through the boundary ($\vec{n}$ is directed outward)
4—power of the volume forces
5—volume heat source.

With REYNOLDS's transport theorem, Eq. 1.639 results in the energy conservation equation:

$$\iiint\limits_{B(t)} \left(\frac{\partial \rho \varepsilon}{\partial t} + \vec{\nabla} \cdot (\rho\, \varepsilon\, \vec{v}) \right) dV = \iint\limits_{\partial B(t)} (\vec{t} \cdot \vec{v} - \vec{q} \cdot \vec{n})\, dA + \iiint\limits_{B(t)} (\rho\, \vec{f} \cdot \vec{v} + w)\, dV \quad (1.687)$$

With

$$V_i\, t_i = V_i\, (\tau_{ij}\, n_j) = (\tau_{ji}^T\, V_i)\, n_j \qquad (1.688)$$

it follows:

$$\iint\limits_{\partial B(t)} \vec{v} \cdot \vec{t}\, dA = \iint\limits_{\partial B(t)} \vec{v} \cdot \hat{T}\, \vec{n}\, dA = \iint\limits_{\partial B(t)} (\hat{T}^T\, \vec{v}) \cdot \vec{n}\, dA = \iint\limits_{\partial B(t)} \vec{\nabla} \cdot (\hat{T}^T\, \vec{v})\, dV \qquad (1.689)$$

and with

$$\iint\limits_{\partial B(t)} \vec{q} \cdot \vec{n}\, dA = \iiint\limits_{B(t)} \vec{\nabla} \cdot \vec{q}\, dV \qquad (1.690)$$

Eq. 1.687 yields

$$\iiint\limits_{B(t)} \left(\left[\frac{\partial \rho \varepsilon}{\partial t} + \vec{\nabla} \cdot (\rho\, \varepsilon\, \vec{v}) \right] - \vec{\nabla} \cdot (\hat{T}^T\, \vec{v}) - \rho\, \vec{f} \cdot \vec{v} + \vec{\nabla} \cdot \vec{q} - w \right) dV \qquad (1.691)$$

Because B is arbitrary, the integrand has to vanish (assuming continuity of the integrand):

$$\frac{\partial \rho \varepsilon}{\partial t} + \vec{\nabla} \cdot (\rho \varepsilon \, \vec{v}) = \vec{\nabla} \cdot (\hat{T}^T \, \vec{v}) + \rho \, \vec{v} \cdot \vec{f} - \vec{\nabla} \cdot \vec{q} + w \qquad (1.692)$$

This is the differential form of the energy conservation of the total energy. In components this reads:

$$\frac{\partial \rho \varepsilon}{\partial t} + \frac{\partial \rho \varepsilon V_i}{\partial x_i} = \frac{\partial}{\partial x_j} (\tau_{ij} \, V_i) + \rho \, f_i \, V_i - \frac{\partial q_i}{\partial x_i} + w \qquad (1.693)$$

In case of a frictionless fluid, the first term on the right-hand side becomes using Eq. 1.670:

$$\frac{\partial}{\partial x_j} (\tau_{ij} \, V_i) = \frac{\partial}{\partial x_j} (-p \, \delta_{ij} \, V_i) = -\frac{\partial (p \, V_i)}{\partial x_i} \qquad (1.694)$$

This is the compression work. Equation 1.693 applies to the total energy. Expanding the terms on the left-hand side yields

$$\frac{\partial \rho e}{\partial t} + \frac{\partial \rho e V_i}{\partial x_i} + \rho \, V_i \, \frac{\partial V_i}{\partial t} + \frac{1}{2} \, (V_i \, V_i) \frac{\partial \rho}{\partial t} + \frac{1}{2} \, (V_i \, V_i) \frac{\partial \rho V_j}{\partial x_j} + \frac{1}{2} \, \rho (V_i \, V_j) \frac{\partial V_i}{\partial x_j} =$$
$$\frac{\partial}{\partial x_j} (\tau_{ij} \, V_i) + \rho \, f_i \, V_i - \frac{\partial q_i}{\partial x_i} + w \qquad (1.695)$$

Double indices are again summed over. The fourth and fifth terms on the left-hand side equal the left-hand side of the mass conservation Eq. 1.647 multiplied by $\frac{1}{2} \, (V_i \, V_i)$ and thus are zero. The third and sixth terms equal the left-hand side of the momentum conservation Eq. 1.662 multiplied by V_i. With Eq. 1.662 and

$$\vec{\nabla} \cdot (\hat{T}^T \, \vec{v}) - \vec{v} \cdot (\vec{\nabla} \cdot \hat{T}) = \frac{\partial}{\partial x_j} (\tau_{ij} \, V_i) - V_i \frac{\partial \tau_{ij}}{\partial x_j} = \tau_{ij} \frac{\partial V_i}{\partial x_j} = \mathrm{Tr}(\hat{T} \, \vec{\nabla} \, \vec{v}) \qquad (1.696)$$

Eq. 1.695 becomes

$$\frac{\partial \rho e}{\partial t} + \frac{\partial \rho e V_i}{\partial x_i} = \tau_{ij} \frac{\partial V_i}{\partial x_j} - \frac{\partial q_i}{\partial x_i} + w \qquad (1.697)$$

In short:

$$\frac{\partial \rho e}{\partial t} + \vec{\nabla} \cdot (\rho \, e \, \vec{v}) = \mathrm{Tr}(\hat{T} \, \vec{\nabla} \, \vec{v}) - \vec{\nabla} \cdot \vec{q} + w \qquad (1.698)$$

Using the stress tensor of NEWTONian fluids Eqs. 1.670 and 1.679, the first term on the right-hand side becomes

$$\tau_{ij} \frac{\partial V_i}{\partial x_j} = -p \, \delta_{ij} \frac{\partial V_j}{\partial x_i} + 2 \, \eta \, d_{ij} \frac{\partial V_i}{\partial x_j} + \lambda \frac{\partial V_j}{\partial x_j} \delta_{ij} \qquad (1.699)$$

and with this:

$$\tau_{ij} \frac{\partial V_i}{\partial x_j} = -(p - \lambda) \frac{\partial V_j}{\partial x_j} + \eta \left(\frac{\partial V_i}{\partial x_j} + \frac{\partial V_j}{\partial x_i} \right) \frac{\partial V_i}{\partial x_j} \tag{1.700}$$

The internal energy is a function of the temperature and the volume so that the differential of the internal energy can be written as

$$de = \left(\frac{\partial e}{\partial T} \right)_v dT + \left(\frac{\partial e}{\partial v} \right)_T dv \tag{1.701}$$

with
$v = V/\rho$—specific volume.

The expression in parentheses in the first term on the right-hand side is the specific heat capacity at constant volume:

$$\left(\frac{\partial e}{\partial T} \right)_v = c_v \tag{1.702}$$

The second term in Eq. 1.701 describes the dependency of the internal energy on the volume. In case of ideal gases this term vanishes; in case of fluids and solids respectively this term can be neglected in comparison with the first one. The energy thus is

$$e = \int_{T_0}^{T} c_v(T') \, dT' + e_0 \simeq c_v \, (T - T_0) + e_0 \tag{1.703}$$

If the second term on the right-hand side can be neglected, the energy conservation reads:

$$\frac{\partial \rho \, c_v \, T}{\partial t} + \vec{\nabla} \cdot (\rho \, c_v \, T \vec{v}) = -\vec{\nabla} \cdot \vec{q} + \tau_{ij} \frac{\partial v_i}{\partial x_j} + w(\vec{r}) \tag{1.704}$$

In case of fluids and solids, c_v and c_p respectively only differ marginally, so a unique value can be used. In case of constant velocity, the second term on the right-hand side of Eq. 1.704 vanishes. But also in case of the velocity not being constant, this term can be neglected when dealing with incompressible fluids. The heat flux is according to FOURIER's 1st law proportional to the negative gradient of the temperature:

$$\vec{q} = -K \, \vec{\nabla} \, T \tag{1.705}$$

Eq. 1.705 expresses that heat flows from warm to cold regions. The proportionality constant K is the heat conductivity.

B.9 Compilation of Mathematical Formulas Used in Energy Transport Computations

In Sect. 1.4.2, the method of GREEN's functions is employed to compute temperature distributions. The method of GREEN's functions makes it necessary to solve integrals. GREEN's function Eq. 1.121 reads:

$$G(\vec{r}, t | \vec{r}', t') = \frac{1}{[4\,\pi\,\kappa\,(t - t')]^{3/2}}\,\exp\left(-\frac{[\vec{r} - (\vec{r}' + \vec{v}\,(t - t'))]^2}{4\,\kappa\,(t - t')}\right) \quad (1.706)$$

or with $\vec{v} = v\,\vec{e}_x$:

$$G = \frac{a^{3/2}}{\pi^{3/2}}\,\exp\left(-a\,(x - [x' + v\,(t - t')])^2\right)\,\exp\left(-a\,(y - y')^2\right)\,\exp\left(-a\,(z - z')^2\right) \quad (1.707)$$

$$a = \frac{1}{4\,\kappa\,(t - t')}$$

B.9.1 Integration Over Space

With a point source:

$$w = \frac{2\,P_L}{\rho\,c}\,\Theta(t')\,\delta(x')\,\delta(y')\,\delta(z') \quad (1.708)$$

the spatial integration in Eq. 1.122 over the space yields

$$T = \frac{2\,P_L}{\rho\,c}\,\int_0^t \frac{a^{3/2}}{\pi^{3/2}}\,\exp\left[-a\,\left((x - v\,(t - t'))^2 + y^2 + z^2\right)\right]\,dt' \quad (1.709)$$

With a line source:

$$w = \frac{w'}{\rho\,c}\,\Theta(t')\,\delta(x')\,\delta(y') \quad (1.710)$$

with
w'—absorbed power per length
and

$$\int_{-\infty}^{\infty} \exp\left(-a\,\xi^2\right)\,d\xi = \sqrt{\frac{\pi}{a}} \quad (1.711)$$

it follows:

$$T = \frac{w'}{\rho c} \int_0^t \frac{a}{\pi} \exp\left(-a (x - v (t - t')])^2 - ay^2\right) dt' \tag{1.712}$$

And in case of a surface source:

$$w = 2 I_L(t) \delta(z) \tag{1.713}$$

and velocity $\vec{v} = v\vec{e}_z$:

$$T = \frac{2 I_L}{\rho c} \int_0^t \sqrt{\frac{a}{\pi}} \exp\left(-a (z - v (t - t'))^2\right) dt' \tag{1.714}$$

A GAUSSian source:

$$w(x', y', z', t') = \frac{2 P_L}{\rho c} \frac{2}{\pi w_0^2} \exp\left(-\frac{2 (x'^2 + y'^2)}{w_0^2}\right) \delta(z') \Theta(t') \tag{1.715}$$

$$\int_{-\infty}^{\infty} \int_{-\infty}^{\infty} \frac{2 P_L}{\rho c} \frac{2}{\pi w_0^2} \exp\left(-\frac{2 (x'^2 + y'^2)}{w_0^2}\right) dx' dy' = \frac{2 P_L}{\rho c}$$

leads while integrating over y' to

$$\int_{-\infty}^{\infty} \exp\left[-b y'^2 - a (y - y')^2\right] dy' =$$

$$\int_{-\infty}^{\infty} \exp\left[-(a + b)(y'^2 - 2 y' \frac{a}{a + b} y) - ay^2\right] dy' \tag{1.716}$$

$$a = \frac{1}{4 \kappa (t - t')}$$

$$b = \frac{2}{w_0^2}$$

Quadratic supplement together with Eq. 1.711 yields

$$\int_{-\infty}^{\infty} \exp\left(-(a+b)(y'^2 - 2\,y'\,\frac{a}{a+b}\,y + \left[\frac{a}{a+b}\right]^2 y^2) + \left[\frac{a}{a+b}\right]^2 y^2 - a\,y^2\right) dy' =$$

$$\int_{-\infty}^{\infty} \exp\left(-(a+b)(y' - \frac{a}{a+b}\,y)^2\right) \exp\left(-\frac{y^2}{\frac{1}{a}+\frac{1}{b}}\right) dy' =$$

$$\sqrt{\frac{\pi}{\frac{1}{4\,\kappa\,(t-t')}+\frac{2}{w_0^2}}} \; \exp\left(-\frac{y^2}{4\,\kappa\,(t-t')+w_0^2/2}\right) \tag{1.717}$$

Together with the integration over x' (quadratic supplement like above) and z' (simple integration over a DIRAC-δ function) it follows:

$$\frac{P_L}{\rho\,c} \exp\left(-\frac{(x - v\,(t-t'))^2}{4\,\kappa\,(t-t')+w_0^2/2}\right) \exp\left(-\frac{y^2}{4\,\kappa\,(t-t')+w_0^2/2}\right) \exp\left(-\frac{z^2}{4\,\kappa\,(t-t')}\right) \tag{1.718}$$

With this, the temperature is

$$T(x, y, z, t) - T_\infty = \int_0^t \frac{2P_L}{\pi\,\rho\,c} \frac{1}{\sqrt{4\,\pi\,\kappa\,(t-t')}} \frac{1}{4\,\kappa\,(t-t')+w_0^2/2} \tag{1.719}$$

$$\cdot \; \exp\left(-\frac{(x - v\,(t-t'))^2 + y^2}{4\,\kappa\,(t-t')+w_0^2/2}\right) \exp\left(-\frac{z^2}{4\,\kappa\,(t-t')}\right) dt' \tag{1.720}$$

B.9.2 Integration Over Time

With $v = 0$, the integrals Eqs. 1.709, 1.712 and 1.714 have the form:

$$\int_0^t \frac{1}{[4\,\pi\,\kappa\,(t-t')]^{n/2}} \exp\left(-\frac{r^2}{4\,\pi\,\kappa\,(t-t')}\right) dt' \tag{1.721}$$

with
$n = 1, 2, 3.$

With the substitution:

$$\frac{r^2}{4\,\pi\,\kappa\,(t-t')} = \xi^2 \tag{1.722}$$

it follows:

$$\frac{1}{\pi^{n/2}} \frac{1}{2\,\kappa}\, r^{(2-n)} \int\limits_{\frac{r}{\sqrt{4\kappa t}}}^{\infty} \xi^{(n-3)}\, \exp(-\xi^2)\, d\xi \tag{1.723}$$

Case $n = 3$: With

$$\int\limits_{a}^{\infty} \exp(-\xi^2)\, d\xi = \frac{\sqrt{\pi}}{2} \mathrm{erfc}(a) \tag{1.724}$$

it follows[48]:

$$\frac{1}{4\,\pi\,\kappa} \frac{1}{r}\, \mathrm{erfc}\left(\frac{r}{\sqrt{4\,\kappa\,t}}\right) \tag{1.725}$$

Case $n = 2$: With Eq. 1.723 it follows:

$$\frac{1}{\pi} \frac{1}{2\,\kappa} \int\limits_{\frac{r}{\sqrt{4\kappa t}}}^{\infty} \exp(-\xi^2)/\xi\, d\xi \tag{1.726}$$

With

$$\int\limits_{a}^{\infty} \exp(-\xi^2)/\xi\, d\xi = \frac{1}{2} \int\limits_{a^2}^{\infty} \exp(-\xi)/\xi\, d\xi = \frac{1}{2}\mathrm{E}_1(a^2) \tag{1.727}$$

one gets[49]:

$$\frac{1}{4\,\pi\kappa}\, E_1\left(\frac{r^2}{4\,\pi\kappa}\right) \tag{1.728}$$

Case $n = 1$: With Eq. 1.723 it follows:

---

[48] For erfc, see Appendix B.9.3.
[49] For E_1, see Appendix B.9.4.

$$\frac{1}{\pi^{1/2}} \frac{1}{2\,\kappa}\, r \int\limits_{\frac{r}{\sqrt{4\kappa t}}}^{\infty} \exp(-\xi^2)/\xi^2 \, d\xi \tag{1.729}$$

With

$$\int\limits_{a}^{\infty} \exp(-\xi^2)/\xi^2 \, d\xi = \frac{1}{a} \exp(-a) - \sqrt{\pi}\,\mathrm{erfc}\,(a) = \frac{a}{\sqrt{\pi}}\,\mathrm{ierfc}\,(a) \tag{1.730}$$

it follows[50]:

$$\sqrt{\frac{t}{\kappa}}\,\mathrm{ierfc}\left(\frac{r}{\sqrt{4\,\kappa\,t}}\right) \tag{1.731}$$

The solution of the integral in Eq. 1.719 with $v = 0$ and $x = 0$, $y = 0$, $z = 0$ yields

$$T(0, 0, 0, t) = \frac{2\,P_L}{\rho\,c} \frac{1}{\sqrt{2}\,\kappa\,\pi^{3/2}\,w_0}\,\arctan\left(\sqrt{\frac{8\,\kappa\,t}{w_0^2}}\right) \tag{1.732}$$

B.9.3   Error Functions

$$\mathrm{erf}(x) = \frac{2}{\sqrt{\pi}} \int\limits_{0}^{x} \exp(-\xi^2)\, d\xi \tag{1.733}$$

$$\mathrm{erfc}(x) = \frac{2}{\sqrt{\pi}} \int\limits_{x}^{\infty} \exp(-\xi^2)\, d\xi \tag{1.734}$$

$$\mathrm{ierfc}(x) = \frac{1}{\sqrt{\pi}} \exp(-x^2) - x\,\mathrm{erfc}(x) \tag{1.735}$$

$$\mathrm{erfce}(x) = \exp(x^2)\,\mathrm{erfc}(x) \tag{1.736}$$

---

[50] For ierfc, see Appendix B.9.3.

B.9.4 Exponential Integral

$$E_1(x) = \int_x^\infty \frac{e^{-\xi}}{\xi}\, d\xi \tag{1.737}$$

B.10 Diffusion in Metals

Equation 1.195 reads:

$$\frac{\partial c}{\partial t} = D\frac{\partial^2 c}{\partial z^2} \tag{1.738}$$

A new dimensionless variable is introduced:

$$\eta = \frac{z - z_0}{\sqrt{4Dt}} \tag{1.739}$$

With

$$\frac{\partial c}{\partial t} = \frac{\partial c}{\partial \eta}\frac{\partial \eta}{\partial t} \tag{1.740}$$

$$= -2D\frac{\eta}{4Dt}\frac{\partial c}{\partial \eta}$$

and

$$\frac{\partial c}{\partial z} = \frac{\partial c}{\partial \eta}\frac{\partial \eta}{\partial z} \tag{1.741}$$

$$\frac{\partial^2 c}{\partial z^2} = \frac{\partial}{\partial z}\left(\frac{\partial c}{\partial \eta}\frac{\partial \eta}{\partial z}\right)$$

$$= \left(\frac{\partial}{\partial z}\frac{\partial c}{\partial \eta}\right)\frac{\partial \eta}{\partial z} + \frac{\partial c}{\partial \eta}\frac{\partial^2 \eta}{\partial z^2}$$

$$= \left(\frac{\partial}{\partial z}\frac{\partial c}{\partial \eta}\right)\left(\frac{\partial \eta}{\partial z}\right)^2$$

$$= \frac{\partial^2 c}{\partial \eta^2}\,4Dt \tag{1.742}$$

Equation 1.738 becomes

$$\frac{d^2c}{d\eta^2} + 2\eta\frac{dc}{d\eta} = 0 \tag{1.743}$$

With

$$a = \frac{dc}{d\eta} \tag{1.744}$$

it follows:

$$\frac{da}{d\eta} + 2\eta a = 0 \tag{1.745}$$

which has the solution:

$$a = \exp(-\eta^2) \tag{1.746}$$

Inserting it into Eq. 1.744 and integrating over the concentration results in

$$c(\eta) = \tilde{C}_1 \int_0^\eta \exp\left(-\eta'^2\right) d\eta' + \tilde{C}_0 \tag{1.747}$$

or:

$$c(z, t) = C_1 \mathrm{erf}\left(\frac{z - z_0}{\sqrt{4Dt}}\right) + C_0 \tag{1.748}$$

The solution complying to the initial conditions:

$$c(z < -z_{carbide}) = c_{ferrite}$$
$$c(-z_{carbide} > z < z_{Karbid}) = c_{carbide}$$
$$c(z_{carbide} > z) = c_{ferrite}$$

can be constructed by the superposition of two solutions of the form Eq. 1.748:

$$c_1(z, t) = C_{11}\mathrm{erf}\left(\frac{z - z_{Karbid}}{\sqrt{4Dt}}\right) + C_{01} \tag{1.749}$$

$$c_2(z, t) = C_{12}\mathrm{erf}\left(\frac{z + z_{Karbid}}{\sqrt{4Dt}}\right) + C_{02} \tag{1.750}$$

with the initial conditions:

$$c(z < -z_{carbide}) = c_{ferrite} - \frac{1}{2}c_{Karbid}$$
$$c(z > -z_{carbide}) = \frac{1}{2}c_{carbide}$$

Fig. 1.71 C concentration
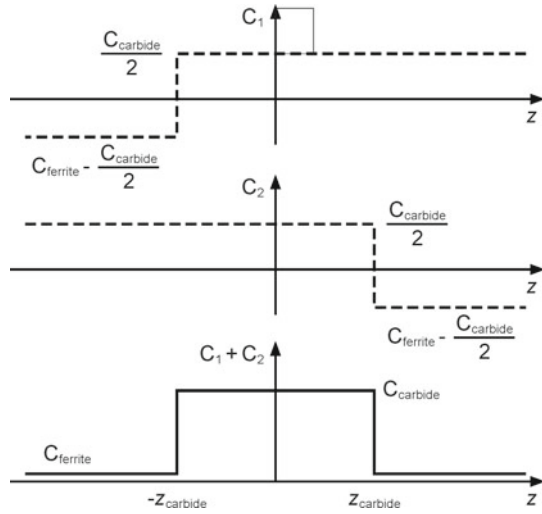
and

$$c(z < z_{carbide}) = \frac{1}{2} c_{carbide}$$

$$c(z > z_{carbide}) = c_{ferrite} - \frac{1}{2} c_{carbide}$$

(see Fig. 1.71).

C Laser-Induced Vaporization

C.1 *Equation of* CLAUSIUS-CLAPEYRON

The free enthalpy of a thermodynamic equilibrium system with pressure and temperature kept constant is minimal (Becker 1975):

$$G = E - T S + p V = \text{Minimum} \tag{1.751}$$

This implies that if the system consists of two phases, the specific free enthalpies of both phases are equal:

$$g_1 = g_2 \tag{1.752}$$

$$g = e - T s + p v \tag{1.753}$$

with
e—specific internal energy
s—specific entropy
v—specific volume.

Because in case of phase equilibrium this applies for any temperature and the corresponding pressure, it follows:

$$dg_1 = dg_2 \tag{1.754}$$

With Eq. 1.753 and the fundamental equation of thermostatics:

$$de = T\,ds - p\,dv \tag{1.755}$$

it follows:

$$dg = -s\,dT + v\,dp \tag{1.756}$$

and with Eq. 1.754:

$$(s_2 - s_1)\,dT = (v_2 - v_1)\,dp \tag{1.757}$$

This yields the equation of CLAUSIUS-CLAPEYRON:

$$\frac{dp}{dT} = \frac{\Delta s}{\Delta v} \tag{1.758}$$

Setting

$$\Delta s = \frac{H_V}{T} \tag{1.759}$$

with
H_V—evaporation enthalpy.

Equation 1.289 follows.

C.2 Temperature Dependence of the Evaporation Enthalpy

The assumption that the evaporation enthalpy does not depend on the temperature is only met approximately. The total energy that is needed to evaporate melt or solid respectively at $T = 0\,\text{K}$ and subsequently heat the vapor up to the temperature T while keeping the pressure constant equals the energy that is needed to first heat the melt or solid up to the temperature T and then evaporate the material (Adam and Hittmair 1978):

$$H(0) + \int_0^T c_p^{(D)}(T)\, dT = \int_0^T c_p^{(C)}(T)\, dT + H(T) \qquad (1.760)$$

with

$c_p^{(V)}$—heat capacity of the vapor for constant pressure

$c_p^{(C)}$—heat capacity of the condensated material (melt or solid) for constant pressure.

In case of an ideal gas $c_p^{(D)} = 5/2\, R$. With this, the vaporization enthalpy is given by

$$H(T) = H(0) + \frac{5}{2}\, R\, T - \int_0^T c_p^{(C)}(T)\, dT \qquad (1.761)$$

With $c_p = 5/2\, R$, it follows $H(T) = H(0)$ and the saturation pressure is given by (see Eq. 1.292)

$$p_{SV} = p_{SV,\text{max}} \exp\left(-\frac{H_V}{R\,T}\right) \qquad (1.762)$$

In a solid $c_p^{(C)} = 6/2\, R$ approximately holds.[51] Inserting this into Eq. 1.291 and integrating yields

$$p_{SV} \propto \frac{1}{\sqrt{T}} \exp\left(-\frac{H_V(0)}{R\,T}\right) \qquad (1.763)$$

In case of thermal electron emission, $c_p^{(C)}$ is the heat capacity of the conduction band electrons of the metal which has a very small value (Becker 1975). With $c_p^{(C)} = 0$ and the assumption that the electrons outside the metal behave like an ideal gas Eq. 1.291 yields

$$p_{SV} \propto T^{5/2} \exp\left(-\frac{H_V(0)}{R\,T}\right) \qquad (1.764)$$

The saturation electron density is given by

$$n_{SV} \propto T^{3/2} \exp\left(-\frac{H_V(0)}{R\,T}\right) \qquad (1.765)$$

The mean velocity of the electrons leaving the metal is proportional to $\sqrt{T}$. With the particle current density:

---

[51] Three degrees of freedom of the kinetic and three degrees of freedom of the potential energy respectively.

$$j = n_{SV} \, v \tag{1.766}$$

this yields the RICHARDSON equation (Becker 1975):

$$j \propto T^2 \, \exp\left(-\frac{H_V(0)}{R \, T}\right) \tag{1.767}$$

C.3   Velocity Moments

The mean value of a velocity-dependent quantity is computed by integrating the product of this quantity and the velocity distribution function over the velocity space. The density, e.g. follows by integrating the velocity distribution function. The momentum density in x-direction is determined by integrating the product of $m \, v_x$ and the velocity distribution function. Velocity moments are built generally according to

$$p_{ikl}(f) = \int\limits_{-\infty}^{\infty} \int\limits_{-\infty}^{\infty} \int\limits_{-\infty}^{\infty} v_x^i \, v_y^k \, v_z^l \, f(v_x, v_y, v_z) \, dv_x \, dv_y \, dv_z \tag{1.768}$$

In case of a MAXWELLian distribution, the particle density, momentum density and the energy density are given by

$$p_{000}(f(\vec{v})) = n \tag{1.769}$$

$$p_{100}(f(\vec{v})) = m \, n \, v \tag{1.770}$$

$$\frac{m}{2} \, [p_{200}(f(\vec{v})) + p_{020}(f(\vec{v})) + p_{002}(f(\vec{v}))] = \frac{3}{2} \, m \, n \, R \, T + \frac{m \, n}{2} \, v \tag{1.771}$$

The conservation of density, momentum and energy flux respectively while crossing the KNUDSEN layer leads to

$$p_{100}(f(\vec{v})) = n_2 \, v_2 \tag{1.772}$$

$$p_{200}(f(\vec{v})) = n_2 \, v_2^2 \tag{1.773}$$

$$p_{300}(f(0, \vec{v})) + p_{120}(f(0, \vec{v})) + p_{102}(f(0, \vec{v})) = n_2 \, v_2 \, (\frac{5}{2} \, R \, T_2^2 + v_2^2) \tag{1.774}$$

The left-hand sides result from determining the appropriate velocity moments[52] using the MAXWELLian distribution Eq. 1.347, whereas the moments on the right-hand side are built using the non-MAXWELLian distribution Eq. 1.348. The results can be found in Ytrehus and Potter (1977).

---

[52] Particle, momentum and energy density respectively have to be multiplied by v_x for determining the respective fluxes.

D   Plasma Physics

D.1   Some Results of Thermodynamics

The entropy is a function of the energy, the volume and the particle numbers:

$$S = S(E, V, N_1, ...N_m) \tag{1.775}$$

The total differential of the entropy is

$$dS = \left(\frac{\partial S}{\partial E}\right)_{V,N} dE + \left(\frac{\partial S}{\partial V}\right)_{E,N} dV + \sum_{i=1}^{m} \left(\frac{\partial S}{\partial N_i}\right)_{E,V,N} dN_i \tag{1.776}$$

In case of constant particle numbers, the differential of the entropy is given by the first law of thermodynamics (Reif 1965):

$$dS = \frac{\delta Q}{T} = \frac{dE + p\, dV}{T} \tag{1.777}$$

Comparison with Eq. 1.776 yields

$$\left(\frac{\partial S}{\partial E}\right)_{V,N} = \frac{1}{T} \tag{1.778}$$

$$\left(\frac{\partial S}{\partial V}\right)_{E,N} = \frac{p}{T} \tag{1.779}$$

The chemical potential is defined as

$$\mu_j = -T \left(\frac{\partial S}{\partial N_j}\right)_{E,V,N} \tag{1.780}$$

With this, Eq. 1.776 becomes

$$dS = \frac{dE}{T} + \frac{p\, dV}{T} - \sum_{i=1}^{m} \frac{\mu_i}{T}\, dN_i \tag{1.781}$$

Multiplication with T and rearranging leads to

$$dE = T\, dS - p\, dV + \sum_{i=1}^{m} \mu_i\, dN_i \tag{1.782}$$

When the energy E is given as a function of S, V and N_i, Eq. 1.782 becomes

$$\left(\frac{\partial E}{\partial S}\right)_{V,N} = T \tag{1.783}$$

$$\left(\frac{\partial E}{\partial V}\right)_{S,N} = -p \tag{1.784}$$

$$\left(\frac{\partial E}{\partial N_j}\right)_{S,V,N} = \mu_j \tag{1.785}$$

Taking the derivative of Eq. 1.783 with respect to the volume V and of Eq. 1.784 with respect to the entropy S and equating the respective results yields because the order of the partial derivatives doesn't matter:

$$\left(\frac{\partial T}{\partial V}\right)_{S,N} = \left(\frac{\partial p}{\partial S}\right)_{V,N} \tag{1.786}$$

The free energy is defined as

$$F = E - T\,S \tag{1.787}$$

Thus

$$d(E - T\,S) = dF = -S\,dT - p\,dV + \sum_{i=1}^{m} \mu_i\,dN_i \tag{1.788}$$

Comparison of coefficients results in

$$\left(\frac{\partial F}{\partial T}\right)_{V,N} = -S \tag{1.789}$$

$$\left(\frac{\partial F}{\partial V}\right)_{T,N} = -p \tag{1.790}$$

$$\left(\frac{\partial F}{\partial N_j}\right)_{T,V,N} = \mu_j \tag{1.791}$$

From the first two equations it follows:

$$\left(\frac{\partial S}{\partial V}\right)_{T,N} = \left(\frac{\partial p}{\partial T}\right)_{V,N} \tag{1.792}$$

The enthalpy is defined as

$$H = E + p\,V \tag{1.793}$$

Thus

$$dH = T\, dS + V\, dp + \sum_{i=1}^{m} \mu_i\, dN_i \tag{1.794}$$

with

$$\left(\frac{\partial H}{\partial S}\right)_{p,N} = T \tag{1.795}$$

$$\left(\frac{\partial H}{\partial p}\right)_{S,N} = V \tag{1.796}$$

$$\left(\frac{\partial H}{\partial N_j}\right)_{S,p,N} = \mu_j \tag{1.797}$$

$$\left(\frac{\partial T}{\partial p}\right)_{S,N} = -\left(\frac{\partial V}{\partial S}\right)_{p,N} \tag{1.798}$$

The free enthalpy is given by

$$G = F + p\, V = E - T\, S + p\, V \tag{1.799}$$

Thus

$$d(E - T\, S + p\, V) = dG = -S\, dT + V\, dp + \sum_{i=1}^{m} \mu_i\, dN_i \tag{1.800}$$

with

$$\left(\frac{\partial G}{\partial T}\right)_{p,N} = -S \tag{1.801}$$

$$\left(\frac{\partial G}{\partial p}\right)_{S,N} = V \tag{1.802}$$

$$\left(\frac{\partial G}{\partial N_j}\right)_{T,p,N} = \mu_j \tag{1.803}$$

$$\left(\frac{\partial S}{\partial p}\right)_{T,N} = -\left(\frac{\partial V}{\partial T}\right)_{p,N} \tag{1.804}$$

Equations 1.786, 1.792, 1.798 and 1.804 are the MAXWELL relations.

D.2   Generalization in Case of Multiple Ionized Ions

In the following, some equations are generalized in the case of plasmas consisting of electrons and single as well as multiple ionized ions. The DEBYE radius is

$$r_D = \sqrt{\frac{\varepsilon_0 \, k_B \, T}{e^2 \, (n_e + \sum_i Z_i^2 \, n_i)}} \qquad (1.805)$$

with
Z_i—ion charge number
n_i—ion density.

The COULOMB correction of the internal energy is

$$E_c = -\frac{1}{2} \, V \, \frac{e^2}{4 \, \pi \, \varepsilon_0 \, r_D} \left(n_e + \sum_i Z_i^2 \, n_i \right) \qquad (1.806)$$

The COULOMB correction of the free energy is given by

$$F_c = -\frac{1}{3} \, V \, \frac{e^2}{4 \, \pi \, \varepsilon_0 \, r_D} \left(n_e + \sum_i Z_i^2 \, n_i \right) \qquad (1.807)$$

In a state of thermodynamic equilibrium with constant temperature and pressure, the free energy is minimal:

$$dF(V, T, n_e, n_0, n_i, n_{i+1}, ldots) = 0 \qquad (1.808)$$

It is assumed that the densities of all particle species are constant except the density of electrons, i-fold ionized ions and $(i + 1)$-fold ionized ions. Particle density variations are not independent of each other. When an electron and a $(i + 1)$-fold ionized ion are created, a i-fold ionized ion is annihilated. Thus

$$dn_e = dn_{i+1} = -dn_i \qquad (1.809)$$

With this it follows:

$$\frac{\partial F}{\partial n_e} - \frac{\partial F}{\partial n_i} + \frac{\partial F}{\partial n_{i+1}} = \mu_e - \mu_i + \mu_{i+1} = 0 \qquad (1.810)$$

with
μ—chemical potential.

The reduction of the ionization energy of the i-fold ionized ions is

$$\Delta E_i = -\left(\frac{\partial F_c}{\partial n_e} - \frac{\partial F_c}{\partial n_i} + \frac{\partial F_c}{\partial n_{i+1}}\right) = \tag{1.811}$$

$$- (\mu_{c,e} - \mu_{c,i} + \mu_{c,i+1}) = (Z_i + 1)\,\frac{e^2}{4\,\pi\,\varepsilon_0\,r_D} \tag{1.812}$$

With Eq. 1.810 the SAHA equation in the general case of multiple ionized ions follows:

$$\frac{n_e\,n_{i+1}}{n_i} = \frac{2}{\Lambda_e^3}\,\frac{U'_{i+1}(T)}{U_i(T)}\,\exp\left(-\frac{E_i - \Delta E_i}{k_B\,T}\right) \tag{1.813}$$

with
U'_{i+1}—partition function of the $i+1$-fold ionized ion
U_i—partition function of the i-fold ionized ion.

The energy zero point in computing the partition function is the ground state of the respective ion. The energy E_i is the ionization energy of the i-fold ionized ion. Λ_e is the thermal DE'BROGLIE wavelength of the electrons Eq. 1.425.

E   Glossary of Symbols and Constants

The developments in the field of laser technology are highly characterized by their interdisciplinary character. In describing the basic phenomena, descriptions and nomenclatures are taken from a great array of physical and engineering disciplines. Due to this, a confusing diversity of notations and descriptions has evolved. The composition presented in this book follows as much as possible the norms "…Normen über einheitliche Begriffsbestimmungen, Benennungen und Formelzeichen für physikalische Grssen, über Einheiten und Einheitenzeichen sowie über mathematische Zeichen und Begriffe" that were elaborated by the *Normenausschuss Einheiten und Formelgrössen* (DIN 1990).

The units used in this book are either SI-units or in exceptional cases other commonly used units. The SI-units ("Système International d'Unités", international system of units) can be divided into basic units (Table 1.1) and derived units (Table 1.2), respectively (Table 1.3).

Table 1.1 SI—basic units (DIN 1990, [S. 1])

Quantity	SI-basic unit	
	Name	Symbol
Length	Meter	m
Mass	Kilogram	kg
Time	Second	s
Electric current	Ampere	A
Thermodynamic temperature	Kelvin	K
Amount of substance	mol	mol
Illumination	Candela	cd

Table 1.2 Derived SI-units with their special names and symbols (DIN 1990, [S. 2])

Quantity	SI-unit		Relation
	Name	Symbol	
Plane angle	Radiant	rad	$1\,\text{rad} = 1\,\frac{\text{m}}{\text{m}}$
Solid angle	steradiant	sr	$1\,\text{sr} = 1\,\frac{\text{m}^2}{\text{m}^2}$
Frequency of a periodic process	Hertz	Hz	$1\,\text{Hz} = 1\,\frac{1}{\text{s}}$
Force	Newton	N	$1\,\text{N} = 1\,\frac{\text{kg m}}{\text{s}^2}$
Pressure, mechanical stress Pascal	Pa	Pa	$1\,\text{Pa} = 1\,\frac{\text{kg}}{\text{m s}}$
Energy, work, heat	Joule	J	$1\,\text{J} = 1\,\frac{\text{kg m}^2}{\text{s}^2}$
Power, heat flux	Watt	W	$1\,\text{W} = 1\,\frac{\text{kg m}^2}{\text{s}^3}$
Electric charge	Coulomb	C	$1\,\text{C} = 1\,\text{A s}$
Electric voltage	Volt	V	$1\,\text{V} = 1\,\frac{\text{J}}{\text{C}} = 1\,\frac{\text{kg m}^2}{\text{s}^3\,\text{A}}$
Electric capacity	Farad	F	$1\,\text{F} = 1\,\frac{\text{C}}{\text{V}} = 1\,\frac{\text{s}^4\,\text{A}^2}{\text{kg m}^2}$
Electric resistance	Ohm	Ω	$1\,\Omega = 1\,\frac{\text{V}}{\text{A}} = 1\,\frac{kg \cdot m^2}{s^3 \cdot A^2}$
Magnetic flux	Weber	Wb	$1\,\text{Wb} = 1\,\text{V s} = 1\,\frac{\text{kg m}^2}{\text{s}^2\,\text{A}}$
Magnetic induction	Tesla	T	$1\,\text{T} = 1\,\frac{\text{Wb}}{\text{m}^2} = 1\,\frac{\text{kg}}{\text{s}^2\,\text{A}}$
Inductivity	Henry	H	$1\,\text{H} = 1\,\frac{\text{Wb}}{\text{A}} = 1\,\frac{\text{kg m}^2}{\text{s}^2\,\text{A}^2}$

Table 1.3 Units not belonging to SI (DIN 1990, [S. 3])

Quantity	SI-unit		Definition
	Name	Symbol	
Pressure	Bar	bar	$1 \text{ bar} = 10^5 \text{ Pa}$
Energy in atom physics	Electron volt	eV	1 electron volt is the energy that an electron gains within a potential difference of 1 V in vacuum: $1 \text{ eV} = 1.6021892 \cdot 10^{-19} \text{ J}$

E.1   Used Symbols

Symbol	Meaning	Einheit
a	Cylinder radius	m
a	Index: atom	–
A	Area	m^2
A	Absorptivity	%
A_T	Expansion factor	–
Ac	Phase change temperature	°C
b	Mode order	–
b	Impact parameter	m
B	Magnetic field	$\frac{\text{V s}}{\text{m}^2}$
$B(t)$	Volume of a material body	m^3
b_c	Cutting groove width	m
c	Velocity of sound	$\frac{\text{m}}{\text{s}}$
c	Specific heat capacity	$\frac{\text{J}}{\text{g K}}$
c_p	Heat capacity for constant pressure	$\frac{\text{J}}{\text{g K}}$
c_v	Heat capacity for constant volume	$\frac{\text{J}}{\text{g K}}$
D	Diffusion coefficient	$\frac{\text{cm}^2}{\text{s}}$
D	Dielectric displacement	$\frac{\text{A s}}{\text{m}^2}$
d	Workpiece thickness	m
d_m	Melt film thickness	m
e	Elementary charge	A s
e	Specific internal energy	$\frac{\text{J}}{\text{m}^3}$
e	Index: electron	
E	Electric field	$\frac{\text{V}}{\text{m}}$

E	Internal energy	J
E_{ion}	Ionization energy	J, eV
E_r	Energy of state r	J, eV
f	Focal length	M
$\vec{f}$	Volume force	$\frac{N}{m^3}$
f_1	Focus length of the first telescope optic	M
f_2	Focus length of the second telescope optic	m
f_{ij}	Oscillator strength	
f_{HL}	Heat loss factor	–
F	Free energy	J
F_p	Pressure force	N
$F_{r,G}$	Friction force of the gas	N
$F_{r,W}$	Friction force of the melt	N
G	Enthalpy	J
G	Index: gas	
h	Surface roughness depth	m
H	Magnetic induction	$\frac{A}{m}$
h_M, H_m	Specific melting enthalpy	$\frac{J}{g}$
h_V, H_V	Specific evaporation enthalpy	$\frac{J}{g}$
$\Delta_R H$	Reaction enthalpy	$\frac{kJ}{g}$
i	Index: ion	
I	Intensity	$\frac{W}{m^2}$
I_0	Maximal intensity	$\frac{W}{m^2}$
I_P	Processing intensity	$\frac{W}{m^2}$
I_c	Threshold intensity for plasma creation	$\frac{W}{m^2}$
I_s	Threshold intensity for plasma shielding	$\frac{W}{m^2}$
j	Current density	$\frac{A}{m^2}$
k	Wave number	$\frac{1}{m}$
k_0	Vaccum wave number	$\frac{1}{m}$
k_i	Imaginary part of the wave number	$\frac{1}{m}$
K	Heat conductivity	$\frac{W}{m\,K}$
K_e	Electron heat conductivity	$\frac{W}{m\,K}$
K	Normalized beam quality number	–
l	LANDAU-length	m
$\dot{m}_{ein}$	Material mass inflow	$\frac{g}{s}$
$\dot{m}_{aus}$	Material mass outflow	$\frac{g}{s}$
$\dot{m}_c$	Fugenmaterialmassenstrom	$\frac{g}{s}$
$\dot{m}_V$	Vapor mass flow	$\frac{g}{s}$
M	Beam transfer matrix	–
m	Mass	kg

m_e	Electron mass	kg
M	Mass of heavy particles (atoms, molecules)	kg
M	Dipole moment	$\frac{m^4}{s}$
M_S	Martensite starting temperature	°C
n	Index of refraction	–
n	Particle density	$\frac{1}{m^3}$
n	Real part of the index of refraction	–
n_e	Electron density	$\frac{1}{m^3}$
n_i	Ion density	$\frac{1}{m^3}$
n_a	Atom density	$\frac{1}{m^3}$
n_c	Komplex index of refraction	–
n_{SD}	Saturation vapor density	$\frac{1}{m^3}$
$\vec{n}$	Normal unit vector	–
N	Particle number	
N_D	Number of electrons within a DEBYE-sphere	
p	Dipole moment	A s m
p	Static pressure	$\frac{N}{m^2}$
p_K	Capillary pressure	$\frac{N}{m^2}$
p_{SD}	Saturation vapor pressure	$\frac{N}{m^2}$
P	Polarization	$\frac{A\,s}{m^2}$
P_r	Probability of a state	–
p_{Fl}	Mean static melt pressure	$\frac{N}{m^2}$
p_u	Ambient pressure	$\frac{N}{m^2}$
p_0	Cutting gas pressure	$\frac{N}{m^2}$
$\widehat{p}$	Impact pressure	$\frac{N}{m^2}$
$\overline{p}$	Mean static pressure in cutting groove	$\frac{N}{m^2}$
P_c	Cutting power	W
P_{HL}	Heat loss by het conduction	W
P_c	Capillar power	W
P_L	Laser power	W
$P_{L,\text{in}}$	Impinging laser power	W
P_R	Reaction power	W
P_V	Power loss	W
P_c	Welding power	W
q	Complex beam parameter	–
Q	Source strength of a source flow	$\frac{m^3}{s}$
$\dot{q}$	Heat flux	$\frac{W}{m^2}$
r	Amplitude reflection factor	–
r	Radius	m

r_D	DEBYE-radius	m
r_{DR}	Drilling hole radius	m
r_s	Effective shieldung length	m
R	Reflectivity	%
s	Processing depth	m
s	Specific entropy	$\frac{\text{J}}{\text{g}}$
s_c	Cutting groove depth	m
s_{DR}	Drilling hole depth	m
s_w	Weldseam depth	m
$\vec{S}$	POYNTING vector	$\frac{\text{W}}{\text{m}^2}$
S	Entropy	J
S	Index: melt	–
t	Time	s
t	Amplitude transmission factor	–
$\vec{t}$	Tangential unit vector	–
$\vec{t}$	Surface forces	$\frac{\text{N}}{\text{m}^2}$
t_h	Holding time	s
t_k	Cooling time	s
t_L	Pulse duration	s
$\hat{T}$	Stress tensor	$\frac{\text{N}}{\text{m}^2}$
T	Temperature	K
T_H	Hardening temperature	°C
T_M	Melting temperature	K
T_P	Process temperature	K
T_V	Evaporation temperature	K
T_0	Rest temperature of the gas	K
T_∞	Ambient temperature	K
T_z	Ignition temperature	K
u	Interaction energy	J, eV
U	Partition function of the inner degrees of freedom	–
V	Index: vapor	–
v	Velocity	$\frac{\text{m}}{\text{s}}$
v	Specific volume	$\frac{\text{m}^3}{\text{kg}}$
v_c	Cutting velocity	$\frac{\text{m}}{\text{s}}$
v_{DR}	Drilling velocity	$\frac{\text{m}}{\text{s}}$
v_F	FERMI velocity	$\frac{\text{m}}{\text{s}}$
v_{TH}	Mean thermal velocity	$\frac{\text{m}}{\text{s}}$
v_G	Gas velocity	$\frac{\text{m}}{\text{s}}$
v_H	Feed rate during hardening	$\frac{\text{m}}{\text{s}}$

v_{krit}	Critical cooling rate	$\frac{{}^\circ\mathrm{C}}{\mathrm{h}}$
v_w	Welding velocity	$\frac{\mathrm{m}}{\mathrm{s}}$
V_W	Volume of the heat affected zone	m^3
$\bar{v}_M$	Mean melt expulsion velocity	$\frac{\mathrm{m}}{\mathrm{s}}$
w	Laser beam radius R	m
w	Power density	$\frac{\mathrm{W}}{\mathrm{m}^3}$
w_0	Laser beam waist	m
w_F	Laser beam focal radius	m
w_L	Laser beam radius at the processing optic	m
x	Vapor density to saturation vapor density ratio	–
x_v	Laminar Vorstrecke	M
y_H	Width of the hardening groove	Mm
z_D	Diffusion length	μm
z_H	Hardening depth	Mm
z_p	Vapor density to saturation vapor density ratio	–
z_R	RAYLEIGH length of the laser beam	m
Z	Partition function	–
α	Heat-transfer coefficient	$\frac{\mathrm{W}}{\mathrm{m}^2\,\mathrm{K}}$
α	Absorption coefficient	$\frac{1}{\mathrm{m}^1}$
α	Atomic polarizability	m^3
α	Energy factor	–
α_B	BREWSTER-Winkel	–
β	Momentum factor	–
β	Absorption index	–
δ	Damping constant	$\frac{1}{\mathrm{m}}$
δ_M	Melt film thickness	m
δ_{opt}	Optical penetration depth of the laser radiation	Nm
δ_w	Heat penetration depth	mm
ε	Dielectric constant	–
ε	Mean electron energy	J, eV
ε	Specific total energy	$\frac{\mathrm{J}}{\mathrm{m}^3}$
ε_F	FERMI-energy	J, eV
η	Dynamical viscosity of the melt	$\frac{\mathrm{g}}{\mathrm{m}\,\mathrm{s}}$

Γ	Plasma parameter	–
κ	Temperature conductivity	$\frac{m^2}{s}$
κ	Imaginary part of the complex index of refraction	–
λ	Wave length	m
λ	Mean free path	m
λ	Volume viscosity	$\frac{N\,s}{m^2}$
Λ	DE'BROGLIE-wave length	m
Λ_c	COULOMB-logarithm	–
μ	Magnetic permeability	–
μ	Chemical potential	J
μ	Plasma parameter	–
ν	Frequency	$\frac{1}{s}$
ν_m	Momentum transfer frequency	$\frac{1}{s}$
ρ	Mass density	$\frac{g}{m^3}$
ρ	Volume charge density	$\frac{A\,s}{m^3}$
σ	Surface tension	$\frac{N}{m}$
σ	Electrical conductivity	$\frac{A}{V\,m}$
σ_e	Electron conductivity	$\frac{A}{V\,m}$
σ_m	Momentum transfer cross section	m^2
σ_{sp}	SPITZER-conductivity	$\frac{A}{V\,m}$
τ	Shear stress	$\frac{N}{m^2}$
τ_W	Normal stress of the melt	$\frac{N}{m^2}$
τ_G	Normal stress of the cutting gas	$\frac{N}{m^2}$
ϕ	Electrical potential	V
ϕ	Potential of a potential flow	$\frac{m^2}{s}$
φ	Angel of incidence	rad
φ_B	BREWSTER angle	rad
θ	Divergence angle	rad
ω	Angular frequency	$\frac{1}{s}$
ω_p	Plasma frequency	$\frac{1}{s}$
ξ	Partition function of the translational degrees of freedom	–

E.2 Physical Constants

Symbol	Meaning	Value	
c	Vacuum velocity of light	$2.998 \cdot 10^8$	$\frac{m}{s}$
e	Elementary charge	$1.602 \cdot 10^{-19}$	C
g	Local acceleration of gravity	9.81	$\frac{m}{s^2}$
h	PLANCK's constant	$6.626 \cdot 10^{-34}$	J s
$\hbar$	$\frac{h}{2\pi}$	$1.05456 \cdot 10^{-34}$	J s
k	BOLTZMANN's constant	$1.381 \cdot 10^{-23}$	$\frac{J}{K}$
L	LORENZ number		
$L(\text{Al})$	LORENZ number of Al	$2.4 \cdot 10^{-8}$	$\frac{V^2}{K^2}$
$L(\text{Fe})$	LORENZ number of Fe	$2.8 \cdot 10^{-8}$	$\frac{V^2}{K^2}$
m_e	Electron mass	$9.10956 \cdot 10^{-31}$	kg
m_p	Proton mass	$1.67261 \cdot 10^{-27}$	kg
R	Molar gas constant	8.3143	$\frac{kJ}{kmol\,K}$
Z_0	Vacuum wave impedance	$3.767 \cdot 10^2$	$\frac{V}{A}$
ϵ_0	Vacuum dielectric constant	$8.854 \cdot 10^{-12}$	$\frac{A\,s}{V\,m}$
μ_0	Magnetic permeability	$4\,\pi \cdot 10^7$	$\frac{V\,s}{A\,m}$
σ	STEFAN- BOLTZMANN constant	$5.670 \cdot 10^{-8}$	$\frac{W}{m^2\,K}$

E.3 Characteristic Numbers

Number	Name	Formula
Nu	NUSSELT number	$\frac{\alpha\,l}{\lambda_{fl}}$
Pe	PÉCLET number	$\frac{v\,l}{a} = \text{Re} \cdot \text{Pr}$
Pr	PRANDTL number	$\frac{\nu}{a}$
Re	REYNOLDS number	$\frac{v\,l}{\nu}$

with
λ_{liquid}—heat conductivity of the liquid
l—characteristic length.

E.4 Reference State

In practice, there are quite a lot of reference states being used that accordingly have to be indicated or cited appropriately. Such a state of a solid, liquid or gaseous substance is characterized by a reference temperature T_{ref} and a reference pressure p_{ref}. As an example, the norm state and the norm volume according to DIN 1343 (DIN 1990, [S. 142]) are given here: In the norm state, a substance has the norm temperature of $T_n = 273.15$ K ($t_n = 0\,°C$) and the norm pressure $p_n = 1.01325$ bar. One mol of an ideal gas has the norm volume:

$$V_{m,0} = (22.41410 \pm 0.00019) \cdot 10^{-3} \; \frac{\text{m}^3}{\text{mol}} \tag{1.814}$$

with
$V_{m,0}$—molar norm volume.

E.5 Material Constants

Temperature values given in Celsius or Kelvin respectively are related by

$$273.2 \text{ K} = 0\,°C \tag{1.815}$$

The temperature dependence of the dynamical viscosity can be determined using

$$\eta(T) = \eta_0 \, \exp\left(E/T\right) \tag{1.816}$$

The material parameter values listed below for Al and Cu are taken from Brandes (1983), Mende and Simon (1976) and Weast (1990). If not stated explicitly, the values for Fe, steel and stainless steel respectively are taken from Mende and Simon (1976).

If not otherwise stated, the material parameter values used in the text are those compiled below.

Al	Temperature	Value	Unit
Melting temperature T_M		933	K
Evaporation temperature T_V		2793	K
Melting enthalpy h_M		$3.77 \cdot 10^5$	$J\,kg^{-1}$
Evaporation enthalpy h_V		$1.172 \cdot 10^7$	$J\,kg^{-1}$
Mass density ρ	293 K	$2.7 \cdot 10^3$	$kg\,m^{-3}$
	933 K, liquid	$2.385 \cdot 10^3$	$kg\,m^{-3}$
Specific heat capacity c	293 K	900	$J\,kg^{-1}\,K^{-1}$
	673 K	1076	$J\,kg^{-1}\,K^{-1}$
Heat conductivity K	293 K	238	$W\,m^{-1}\,K^{-1}$
	673 K	238	$W\,m^{-1}\,K^{-1}$
	933 K, liquid	94.03	$W\,m^{-1}\,K^{-1}$
	1273 K, liquid	105.35	$W\,m^{-1}\,K^{-1}$
Electrical conductivity σ	293 K	$3.74 \cdot 10^7$	$\Omega^{-1}\,m^{-1}$
	673 K	$1.46 \cdot 10^7$	$\Omega^{-1}\,m^{-1}$
	1273 K, liquid	$3.45 \cdot 10^6$	$\Omega^{-1}\,m^{-1}$
Surface tension σ	933 K, liquid	0.914	$N\,m^{-1}$
$\frac{d\sigma}{dT}$		$-0.35 \cdot 10^{-3}$	$N\,m^{-1}\,K^{-1}$
Dynamic viscosity η	933 K, liquid	$1.3 \cdot 10^{-3}$	$N\,s\,m^{-2}$
η_0		$0.453 \cdot 10^{-3}$	$N\,s\,m^{-2}$
YOUNG's modulus E		$2.67 \cdot 10^3$	$N\,m^{-2}$
POISSON's ratio ν		0.3	

Cu	Temperature	Value	Unit
Melting temperature T_M		1357	K
Evaporation temperature T_V		2833	K
Melting enthalpy h_M		$2.07 \cdot 10^5$	$J\,kg^{-1}$
Evaporation enthalpy h_V		$4.65 \cdot 10^6$	$J\,kg^{-1}$
Mass density ρ	293 K	$8.96 \cdot 10^3$	$kg\,m^{-3}$
	1356 K, liquid	$8.0 \cdot 10^3$	$kg\,m^{-3}$
Specific heat capacity c	293 K	385	$J\,kg^{-1}\,K^{-1}$
	1273 K	473	$J\,kg^{-1}\,K^{-1}$
Heat conductivity K	293 K	394	$W\,m^{-1}\,K^{-1}$
	1310 K	244	$W\,m^{-1}\,K^{-1}$
	1356 K, liquid	165.6	$W\,m^{-1}\,K^{-1}$
	1873 K, liquid	180.4	$W\,m^{-1}\,K^{-1}$
Electrical conductivity σ	293 K	$5.9 \cdot 10^7$	$\Omega^{-1}\,m^{-1}$
	1250 K	$1.2 \cdot 10^7$	$\Omega^{-1}\,m^{-1}$
	1356 K, liquid	$5.0 \cdot 10^6$	$\Omega^{-1}\,m^{-1}$
	1873 K, liquid	$3.95 \cdot 10^6$	$\Omega^{-1}\,m^{-1}$
Surface tension σ	1356 K, liquid	1.285	$N\,m^{-1}$
$\frac{d\sigma}{dT}$		$-0.13 \cdot 10^{-3}$	$N\,m^{-1}\,K^{-1}$
Dynamic viscosity η	933 K, liquid	$4.0 \cdot 10^{-3}$	$N\,s\,m^{-2}$
η_0		$0.3009 \cdot 10^{-3}$	$N\,s\,m^{-2}$
YOUNG's modulus E		3666.8	$N\,m^{-2}$
POISSON's ratio ν		0.3	

Fe	Temperature	Value	Unit
Melting temperature T_M		1673 (1803 (Gieck 1984))	K
Evaporation temperature T_V		3008 (3003 (Kuchling 1985))	K
Melting enthalpy h_M		$2.7 \cdot 10^5$ ($3 \cdot 10^5$ (Gmelin 1978))	J kg^{-1}
Evaporation enthalpy h_V		$6.370 \cdot 10^6$	J kg^{-1}
Mass density ρ	293 K	$7.87 \cdot 10^3$	kg m^{-3}
Specific heat capacity c	293 K	456 (Gieck 1984)	J kg^{-1} K^{-1}
	1073 K	791	J kg^{-1} K^{-1}
	T_M	$754 - 838$ (Gmelin 1978)	J kg^{-1} K^{-1}
Heat conductivity K	293 K	74 (Kuchling 1985)	W m^{-1} K^{-1}
	T_M	40	W m^{-1} K^{-1}
	1073 K	29.7	W m^{-1} K^{-1}
Electrical conductivity σ	293 K	$9.9 \cdot 10^6$	Ω^{-1} m^{-1}
	1073 K	$9.45 \cdot 10^6$	Ω^{-1} m^{-1}
	1809 K, liquid	$7.22 \cdot 10^5$	Ω^{-1} m^{-1}
Surface tension σ	T_M	1.872	N m^{-1}
$\frac{d\sigma}{dT}$		$-0.49 \cdot 10^{-3}$	N m^{-1} K^{-1}
Dynamic viscosity η	1809, liquid	$5.5 \cdot 10^{-3}$	N s m^{-2}
η_0		$0.453 \cdot 10^{-3}$	N s m^{-2}
YOUNG's modulus E		$4.979 \cdot 10^3$	N m^{-2}
POISSON's ratio ν		0.3	

Steel	Temperature	Value	Unit
Melting temperature T_M		1744 (Gieck 1984)	K
		1673 (Treusch 1985)	K
Evaporation temperature T_V		2773 (Gieck 1984)	K
		2945 (Treusch 1985)	K
Melting enthalpy h_M		$2.05 \cdot 10^5$ (Gieck 1984)	J kg^{-1}
		$2.81 \cdot 10^5$ (Treusch 1985)	J kg^{-1}
Evaporation enthalpy h_V		$6.246 \cdot 10^6$ (Treusch 1985)	J kg^{-1}
Mass density ρ	293 K	$7.900 \cdot 10^3$ (Gieck 1984)	kg m^{-3}
Specific heat capacity c	293 K	510 (Kuchling 1985; Treusch 1985)	J kg^{-1} K^{-1}
	293 K	490 (Gieck 1984)	J kg^{-1} K^{-1}
	T_M	$754 - 838$ (Gmelin 1978)	J kg^{-1} K^{-1}
Heat conductivity K	293 K	45 (Kuchling 1985)	W m^{-1} K^{-1}
Surface tension σ	T_M	1.7	N m^{-1}
η_0		$0.453 \cdot 10^{-3}$	N s m^{-2}

Stainless steel	Temperature	Value	Unit
Melting temperature T_M		1723 (Gieck 1984)	K
		1801 (Ruge 1980)	*K*
Evaporation temperature T_V		2673 (Ruge 1980)	K
Melting enthalpy h_M		$2.32 \cdot 10^5$ (Ruge 1980)	J kg^{-1}
		$2.81 \cdot 10^5$ (Treusch 1985)	J kg^{-1}
Evaporation enthalpy h_V		$6.229 \cdot 10^6$ (Ruge 1980)	J kg^{-1}
Mass density ρ	293 K	$7.9 \cdot 10^3$ (Gieck 1984)	kg m^{-3}
	293 K	$7.8 \cdot 10^3$ (Ruge 1980)	kg m^{-3}
Specific heat capacity c	293 K	504 (DVS 1990)	J kg^{-1} K^{-1}
	T_M	$570 - 680$ (Hervey 1982)	J kg^{-1} K^{-1}
Heat conductivity K	293 K	$14 - 16$ (Hervey 1982; Thyssen-Edelstahlwerke et al. 1987; Gieck 1984)	W m^{-1} K^{-1}
	900 K	18 (Hervey 1982)	W m^{-1} K^{-1}
	800 K	29.7	W m^{-1} K^{-1}
	800 K	15 (DVS 1990)	W m^{-1} K^{-1}

References

Abdukadir A (1973) Spectral directional emittance of roughned metal surfaces

Abramowitz M, Stegun IA (1984) Pocketbook of mathematical functions. Harri Deutsch, Thun

Adam G, Hittmair O (1978) Wärmetheorie. Vieweg

Aden M, Beyer E, Herziger G (1990) Laser induced vaporization of a metal surface. J Appl Phys D 23

Afanasev Y, Krokhin ON (1967) Vaporisation of matter exposed to laser emission. Sov Phys JETP 35:639

Becker R (1975) Theorie der Wärme. Springer-Verlag

Becker E, Bürger W (1975) Kontinuumsmechanik. Teubner, Stuttgart

Beckmann P, Spizzichino A (1963) The scattering of electromagnetic waves. Pergamon Press, New York

Bekefi G (1966) Radiation processes in plasmas. Wiley, New York

Betten J (1993) Kontinuumsmechanik. Springer

Beyer E (1985) Eunfluss des laserindizierten Plasmas beim Schweissen mit CO$_2$-Lasern. Dissertation, TH darmstadt

Beyer E, Behler K, Petschke U, Sokolowski W (1986) Schweißen mit CO$_2$-Lasern. Laser Optoelektron 18:35–46

Born M, Wolf E (1999) Principles of optics. Cambridge University Press

Brandes AE (1983) Smithells metals reference book. Butterworths, London

Carslaw HS, Jaeger JC (1959) Conduction of heat in solids, 2nd edn. Oxford University Press

Cavaliere P, Ferrante G, Leone C (1980) Particle-atom ionising collisions in the presence of a laser radiation field. J Phys B 13:4495

Chorin AJ, Marsden JE (1979) A mathematical introduction to fluid mechanics. Springer-Verlag, New York

DIN (1990) Einheiten für Begriffe und physikalische Größen: Normen, 7th ed. Beuth Verlag

Drawin HW, Felenbok P (1965) Data for plasmas in local thermodynamic equilibrium. Gauthier-Villars, Paris

Drude P (1900) Zur Elektronentheorie der Metalle. Annalen der Physik 566:1

DVS (1990) Handbuch der Kennwerte von metallischen Werkstoffen zur FEZEN–Werkstoff–Datenbank; Bd.: 2: Hochlegierte Stähle und Nichteisenmetalle, DVS-Verlag, Oberhausen

Ebeling W, Kraeft WD, Kremp D (1976) Theory of bound states and ionization equilibrium in plasmas and solids. Akademie-Verlag, Berlin

Gieck K (1984) Technische Formelsammlung. Gieck-Verlag, Heilbronn

Gmelin D (1978) Metallurgie des Eisens. Springer-Verlag, Berlin

Griem HR (1964) Plasma spectroscopy. Mc-Graw-Hill

Günther K, Lang S, Radtke R (1983) Electrical conductivity and charge carrier screening in weakly non-ideal plasmas. J Phys D Appl Phys 16:1235

Günther K, Radtke R (1984) Electrical properties of weakly nonideal plasmas. Birkhäuser, Basel

Hervey PD (1982) Engineering properties of steel. American Society for Metals

Horstmann D (1985) Das Zustandsschaubild Eisen-Kohlenstoff. Stahleisen

Hummel RE (1971) Optische Eigenschaften von Metallen und Legierungen, vol 22. Springer-Verlag, Berlin

Ichimaru S (1973) Basic principles of plasma physics. Benjamin/Cummings Publishing Company, London

Jackson JD (1975) Classical electrodynamics. Wiley, New York

Jou D, Liebot J, Casas-Vazques J (1982) Irreversible-thermodynamics approach to nonequilibrium heat fluctuations. Phys Rev A 36:508

Kanayama K, Baba H (1975) Directional monochromatic emittances of the random rough surfaces of metal and nonmetals. Tr J S M E Trans 41

Kocher E et al. (1972) Dynamics of laser processing in transparent media. IEEE J-QE-8

Kostrykin V, Nießen M, Jandeleit J, Schulz W, Kreutz EW (1998) Picosecond laser pulses induced heat and mass transfer. In: SPIE conference on high-power laser ablation, vol 3343

Kuchling H (1985) Taschenbuch der Physik. Hari Deutsch, Thun

Landau LD, Lifschitz EM (1984) Elektrodynamik der Kontinua, vol VIII. Akademie-Verlag, Berlin

Linlor WI (1963) Ion energies produced by giant-pulse. Appl Phys Lett 3:210

Lompre LA, Mainfray G (1985) Interaction of an intense laser pulse with a many-electron atom: fundamental processes in fundamentals of laser interactions. Springer, Berlin

Maiman TH (1960) Optical and microwave-optical experiments in Ruby. Phys Rev Lett 94:564

Matsunawa A (1991) Beam—plasma interaction in laser materials processing by different wavelength. In: Proceedings of the 10th international congress LASER 91

Mende D, Simon G (1976) Physik: Gleichungen und Tabellen. Wilhelm Heine, München

Morse PM, Feshbach H (1953) Methods of theoretical physics. McGraw-Hill, New York

Murukami M, Oshima K (1974) Rarefied gas dynamics. DFVLR Press

Peschko W (1981) Abtragung fester Targets durch Laserstrahlung

Petring D (1993) Anwendungsorientierte Modellierung des Laserstrahlschneidens zur rechnergestützten Prozessoptimierung. Dissertation RWTH Aachen, Shaker

Pirri AN (1979) Plasma energy transfer to metal surfaces irradiated by pulsed lasers. IAAJ 16

Porteus JO (1963) Relation between height distribution of rough surface and the reflectance at normal. J Opt Soc Am 53:1394

Raizer YuP (1977) Laser-induced discharge phenomena. Consultants Bureau, New York

Ready JF (1963) Development of plume of material vaporized by giant pulse laser. Appl Phys Lett 3:11

https://refractiveindex.info/?shelf=main&book=Fe&page=Johnson

Reif F (1965) Fundamentals of statistical and thermal physics. Mcgraw Hill

Roberts S (1959) Optical properties of nickel and tungsten and their interpretation according to Drude's formula. Phys Rev 114:104

Rosenthal D (1946) The theory of moving sources of heat and its application on metal treatments. Trans ASME 48:849–866

Ruge J (1980) Handbuch der Schweißtechnik. Springer-Verlag, Heidelberg

Sacadura JFO (1972) Influence de la rugosité sur le rayonnement thermique émis par les surfaces opaques. J Heat Mass Transfer 15:1451

Sacadura JFO (1980) Modélisation et étude expérimentale du rayonnement thermique de sufaces métalliques microrugueuses

Sari SO, Cohen DK, Scherkoske KD (1980) Study of surface plasma-wave reflectance and roughness induced scattering in silver foils. Phys Rev B 21:6

Sommerfeld A (1977) Theoretische Pysik, vol IV. Harri Deutsch, Thun

Stern G, Boffy B (1990) Mesure de l'absorbtivite spectrale de materiaux metalliques par calorimetrie multilaser. Rapport ISL R102/90

Stern G, Gautier B (1986) Influence de la temperature et de l'etat de surface sur l'absorption spectrale $\lambda = 10.6\mu$ de differents alliages metalliques, Application au traitement thermique par laser CO_2. Rapport ISL R106/86

Stüdermann H (1967) Wärmebehandlung von Stahl. Carl-Hanser

Thyssen-Edelstahlwerke AG (1987) Remanit-Werkstoffblätter. Thyssen-Edelstahlwerke A.G

Törnig W (1979) Numerische Mathematik für Ingenieure und Physiker. Springer-Verlag, Berlin

Treusch HG (1985) Geometrie und Reproduzierbarkeit einer plasmaunterstützten Materialabtragung durch Laserstrahlung

Vicanek M, Simon G (1987) Momentum and heat transfer of an inert gas jet to the melt in laser cutting. J Phys D Appl Phys 20:1191–1196

Vicanek M, Simon G, Urbassek HM, Decker I (1987) Hydrodynamical instability of melt flow in laser cutting. J Phys D Appl Phys 20:140–145

Weast RC (1990) Handbook of chemistry and physics. CRC Press

Wieting TJ, Schriempf JT (1972) Free-electron theory and laser interactions with metals. Report of NRL Progress

Wissenbach K (1985) Härten mit CO_2-Laserstrahlung. Dissertation TH Darmstadt

Ytrehus T, Potter JL (ed) (1977) Theory and experiments on gas kinetics in evaporation. In: International symposium on rarefied gas dynamics 1976, 10 Snowmass-at-Aspen Col

Ytrehus T, Ostmo S (1996) Kinetic theory approach to interphase processes. Int J Multiphase Flow 22(1):133–155

Part II
Industrial Laser System

Chapter 2
Industrial Laser Systems

Hans-Dieter Hoffmann

2.1 Introduction

The basic components of a laser system are the optical resonator with the laser medium, the laser pump, the cooling unit, and the beam guiding and shaping units (Fig. 2.1).

The individual components of the laser determine the characteristics of the emitted laser radiation. The wavelength, for example, is primarily predefined by the laser medium. The resonator determines the longitudinal and transversal mode structure of the laser radiation and thereby the spectral and spatial properties of the emitted light.

The laser pump provides the energy transformed into laser radiation and controls the laser output power. The cooling system enables efficient operation and ensures that the laser's operating conditions remain stable over time.

With the types of lasers available today, a large wavelength and power range can be covered. Laser wavelengths range from a few nm to μm and can be generated with average output powers up to MW range. The capability of laser media to store energy allows for peak output powers in the PW range and even higher.

The differences between individual laser systems are accordingly large. They differ with reference to the laser media used and their aggregate states, their resonator configuration, and the pump process applied.

Laser systems are classified according to the aggregate state or the material type of the laser medium. Commonly, the categories *gas laser*, *solid-state laser*, *dye laser,* and *semi-conductor laser* are used. How the individual laser systems are named is based, as a rule, on the material of the active medium: In a CO_2 laser, the active medium is carbon dioxide gas (other gases such as Ne, He, etc., are added), in a HeNe laser, a gas mixture out of helium and neon and in a ruby laser, a ruby crystal.

H.-D. Hoffmann (✉)
Fraunhofer ILT, Aachen, Germany
e-mail: hans-dieter.hoffmann@ilt.fraunhofer.de
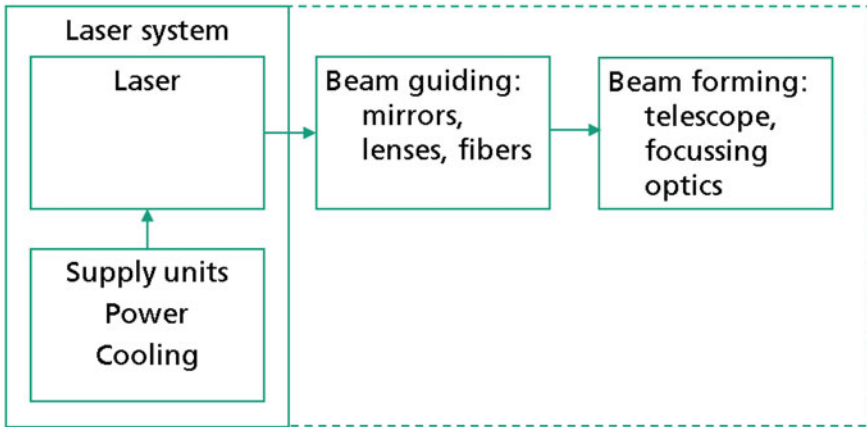
Fig. 2.1 Schematic of a laser system

Despite the fact that semiconductor lasers and fiber lasers are based on solid-state media, in some literature only lasers based on optically pumped crystals are called solid-state lasers.

A Brief History of Lasers and Their Applications

While historically the first laser that has been demonstrated was a flash lamp pumped solid-state laser based on a Ruby crystal, gas lasers dominated the commercial market for a long time. Helium–Neon lasers have been used for various fields from ultra-precise measurement of distances to mass applications like reading of barcodes. Beside the high stability of the spectral emission, the capability of generating stable continues wave output with passive cooling has been a major advantage. In materials processing applications, CO_2 lasers have been the workhorse in the past decades. Applications like cutting and welding of metals require power in the multi-kW class. The power scalability and the comparably high efficiency of CO_2 lasers in combination with efficient cooling techniques enabled economical production processes. While CO_2 lasers are now more and more substituted by ThinDisk, Fiber, InnoSlab, and Diode lasers, they will remain relevant in applications requiring the spectral properties of far infrared (FIR) emission around 10 μm wavelength. Examples are cutting and structuring of organic materials, carbon-reinforced composites and other plastics or the efficient excitation of plasma for generation of extreme ultraviolet light for semiconductor lithography. Another class of gas lasers, the Excimer lasers provide J class pulse energy at ns pulse duration and average power in the ultraviolet range. Applications driving the development of Excimer lasers are Semiconductor Lithography with structure sizes of down to about 10 nm and the annealing of silicon layers for high resolution displays. Another important application for Excimer lasers is an eye surgery process called LASIK (Laser in situ keratectomy). The benefit of gas lasers for UV generation is the low absorption of UV in gases and the capability of continuous regeneration of the gain medium. Solid-state media suffer under

comparably high absorption of UV light and have to be replaced in more or less short intervals depending on the generated wavelength and power.

Around 1990 lamp pumped solid-state lasers based on cylindrical laser rods became a source for industrial welding applications. The capability to deliver the light by a fiber-enabled easier process integration and provided a long-term stable beam shape, widely independent of aging effects of the laser source. Despite the low wall plug efficiency of about 3%, about 3 times lower compared to CO_2 lasers, the lamp-pumped solid state laser was well accepted in industrial applications like spot welding in the electronics industry or welding and brazing of metal parts in the automotive industry. With the development of high-power diode laser arrays in a first step lamps have been replaced by laser diodes as a pump source. This generation of diode pumped solid state lasers outperformed high-power CO_2 lasers in efficiency and the improved beam quality allowed novel, more flexible cutting applications. The latest generation of ThinDisk-, Fiber-, and InnoSlab-based solid-state lasers makes full use of the spectral and spatial characteristics of high-power laser diodes. Continuous wave solid-state lasers based on ThinDisk and Fiber designs entered the large cutting market and are substituting CO_2 lasers in many applications. Output power up to multi 10 kW level is available at about 40% wall plug efficiency.

Today the brightness of high-power laser diodes allows for an increasing number of materials processing applications with direct diode lasers. Examples are heat treatment, soldering, brazing, and welding. By dense wavelength combining methods, the spatial brightness has been increased to a level that allows even for efficient metal cutting. Whether diode lasers will replace other solid-state lasers in continuous wave operation is a question of aspects like efficiency, reliability, and costs. In high-peak power-pulsed operation diodes seem to be no replacement for crystal and fiber-based lasers. The main reason for this is the low upper state lifetime of semiconductor materials in the order of 100 ps which does not allow for storing a relevant amount of energy. Q-switched and mode-locked lasers including linear or regenerative amplifiers need crystals or glasses as a gain medium.

Fast and ultrafast laser pulses allow for processing with extremely low or even no heat-affected zones. In order to reduce the wavelength sensitivity of the process, multi-photon and extreme plasma absorption enables new processes like filament cutting of glasses and crystals. Currently, the largest individual application with several thousands of femtosecond lasers in the field is femto-LASIK. This eye surgery process requires very precisely localized absorption of laser energy in the human cornea. On the other hand, industrial ultrafast processes require increasing average power. While industrial ps and fs lasers are available at 100 W level today, amplifiers based on InnoSlab and ThinDisk concepts have demonstrated more than 1 kW average output power at pulse durations in the sub ps range. Fiber lasers are close to this performance but require compressed pulse amplification (CPA) for the peak power and pulse energy required by most production processes. The large bandwidth of some gain media can also be used to generate emission with tunable wavelength. Today variable wavelengths are mainly applied for addressing specific fluorescence or absorption lines in measurement applications.

The fundamental properties of the laser radiation generated by laser systems can be split into four groups and are described by the following parameters:

1. Energetic: Power and energy.
2. Spatial: Number of transversal modes, M^2, beam parameter product (BPP).
3. Spectral: Center wavelength, bandwidth, number of longitudinal modes.
4. Temporal: Pulse duration, pulse repetition rate, and pulse shape.

The following chapters present selected laser types relevant to applications of modern high-power lasers.

2.2 Semiconductor Lasers

2.2.1 Light Generation in Semiconductors

High-Power Diode Laser

Diode lasers are built up by epitaxial layers of semiconductor media.

A schematic band gap profile along the vertical cavity direction for a double-hetero-structure with three QWs is displayed in Fig. 2.2.

To realize semiconductor diode lasers, an optical resonator is necessary. Therefore, edge-emitting diodes are cleaved and mirror-coated at the front- and rear end to provide high-reflective and low-reflective sides for optical feedback and out-coupling of radiation. For vertical-cavity surface-emitting laser (VCSEL) Bragg mirrors built by alternating layers of semiconductor media with high and low refractive indexes are utilized. Due to stimulated recombination, the emitted photons contribute to the light field inside the resonator. When the number of injected carriers exceeds a certain value (threshold-current injection density), the device emits laser radiation.

The main design target for the development of high-power diode lasers is the combination of power and beam quality, alias the brightness.[1] The brightness (Traub et al. 2003) of a laser source in the paraxial approximation is defined as

$$B = \frac{P}{A\Omega} = \frac{P}{\lambda_0^2 M^2}$$

where P is the optical power, A the emission area, and Ω is the solid angle into which the power is emitted. M^2 is the beam propagation parameter and λ_0 is the wavelength in vacuum.

Broad-area laser diodes (BA-LDs) show an astigmatic output beam profile with a large divergence angle in fast axis (FA) in combination with high beam quality in the vertical direction and a small divergence angle in SA together with small beam

---

[1] "Brightness" is commonly used for the description of high power laser emission. The DIN/ISO conformal nomenclature is "radiance".
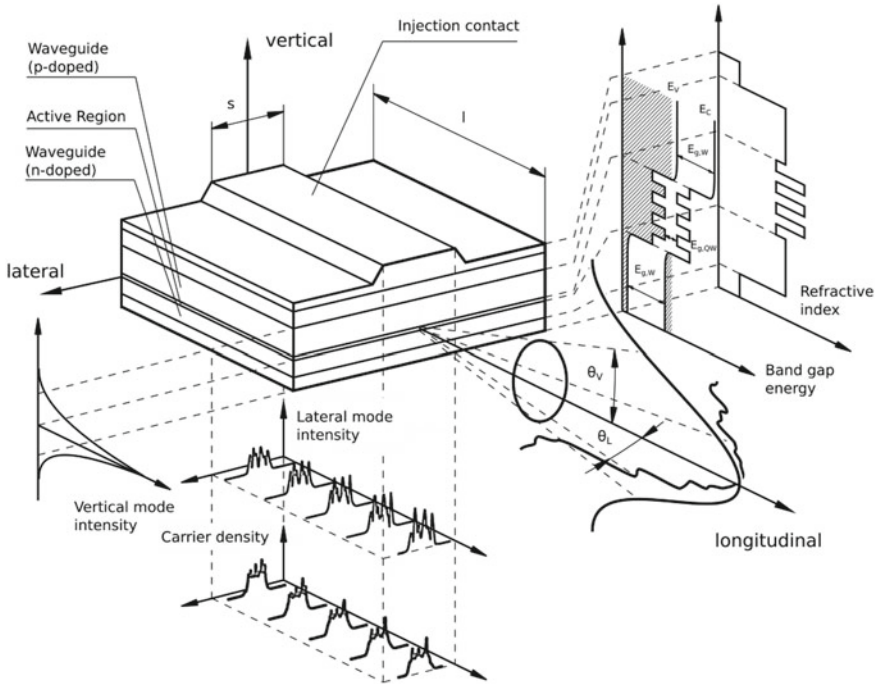
Fig. 2.2 Principle drawing of a broad-area diode laser: epitaxial grow, band gap energy profile, refractive index profile, vertical mode intensity, lateral mode intensity evolution, carrier density evolution, lateral and vertical far-field profiles, and axis names (lateral, vertical, longitudinal) convention

quality in the lateral direction (illustration in Fig. 2.2). Typical SA divergence angles (full angle) are around 10 degrees; typically, FA divergence angles (full angle) are around 30 degrees and higher (Traub et al. 2003).

The gain of semiconductor medium is broad around tens of nm and the wavelength difference in the Fabry–Perot cavity is small so that the devices operate in multi-longitudinal modes. BA-LDs tend to chaotic operation at high powers and consequently require mechanisms for modal discrimination from internal or external resonators to achieve the desired high brightness for industrial applications.

Output Characteristics of High-Power Laser Diodes

High-power diode lasers have been established in a wide range of applications from lighting to materials processing. These applications have different requirements in power, spatial and spectral properties of the laser emission. Concerning spatial and spectral brightness, high-power diodes range between light-emitting diodes (LED) and solid-state lasers. In the last decade, a significant improvement in average laser output power has been achieved. The increase in output power per emitter is a main
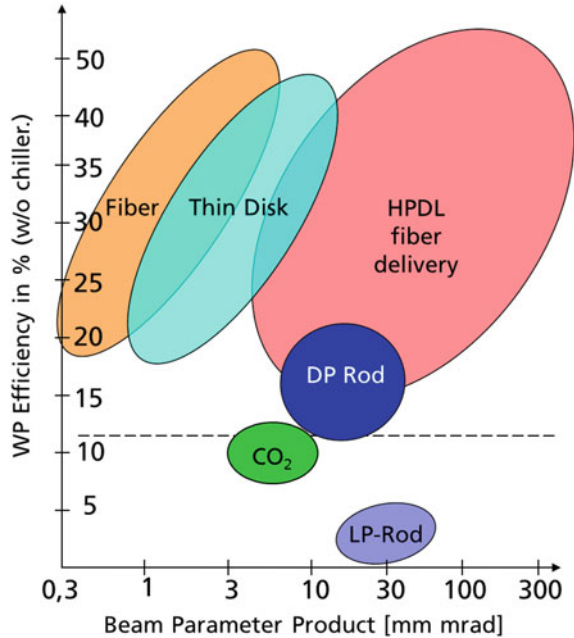
driver of the expanding range of applications of high-power diode lasers (Nilsson
et al. 2003).

High-power diode lasers show the best efficiency of all known lasers concerning
the conversion of electrical power into optical power. An internal E/O efficiency of
about 75% has been demonstrated by different research groups. Depending on the
emission wavelength, the output power and the transversal beam properties typical
industrial laser diodes can be operated at E/O efficiencies between 50 and 70% today.
In parallel to these improvements, the main activities were focusing on the extension
of reliability and lifetime. While, for most medical lasers, some 100 h of operation are
sufficient, industrial lasers require reliable operation over several 10,000 h (Fig. 2.3).

2.2.2 Beam Combination for Power Scaling

As the output power of single-laser diode emitters is limited, for further power scaling
the emission of several single emitters has to be combined. State-of-the-art commer-
cial 100 μm emitters allow for about 15 W average power corresponding to the order
of 10^6 W/cm^2.

Combining methods can be fundamentally divided into coherent and incoherent
combining. **Coherent combining** by coupling of N emitters leads to $(N * E)^2 \sim$
N^2-times the intensity of the individual emitter as the E-vector of the individual
fields is superposed. This requirement in precise control of the polarization state, the

transversal mode, and the phase of the diode emission could be achieved in different setups by sophisticated control schemes (Hergenhan 2002).

The basic methods of **incoherent beam combining** are spatial multiplexing, polarization multiplexing, and wavelength multiplexing.

Spatial combining by geometrically overlaying the emission of individual emitters offers power scaling at degrading beam quality. In an ideal case, the brightness ($\sim P/BPP$) could be kept constant. In reality, there will be some loss in brightness because of manufacturing and alignment tolerances as well as diffraction losses at edges of components. **Fused fiber combiners** offer a waveguide-based method of **spatial beam combination**. The general rules for power scaling and brightness are similar to the rules for free space spatial combining. For technical realization, a bundle of fibers with a large core and a thin cladding is fused together at one end. In most cases, a dense package of fibers of similar diameter is required leading to fixed numbers of fibers per bundle (for example, 7:1 or 19:1). It has to be kept in mind that the beam quality described by the beam parameter product allows for exchanging core diameter and numerical aperture which is equivalent to beam diameter and far-field angle in the case of free space propagation (Geiger et al. 2007). Depending on details of the realization, fused combiners can also be operated in the reverse direction as fused splitters. The figure visualizes the concept of fused combiners (Fig. 2.4).

Polarization combining offers doubling of brightness by superposition of two orthogonally polarized beams. The output of an incoherent polarization combination is not linearly polarized.

Spectral combining offers superposition of potentially a large number of beams which is limited mainly by the spectral properties of the diode emission: the emission bandwidth and drift of the center wavelength as well as the steepness and contrast ratio of the spectral filters used for combining. The center wavelength of free running GaAs-based laser diodes shifts typically about 0.3 nm/K and 1 nm/10 A of operating current. A lower estimate for the minimum wavelength spacing is given by total the shift of the center wavelength within the nominal range of output power of about 15–20 nm.
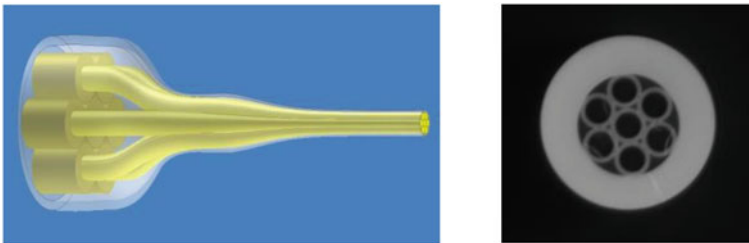
Fig. 2.4 Left: Schematic of a fused fiber combiner (Vytran). Center: Microscope image of a fused bundle (ILT)
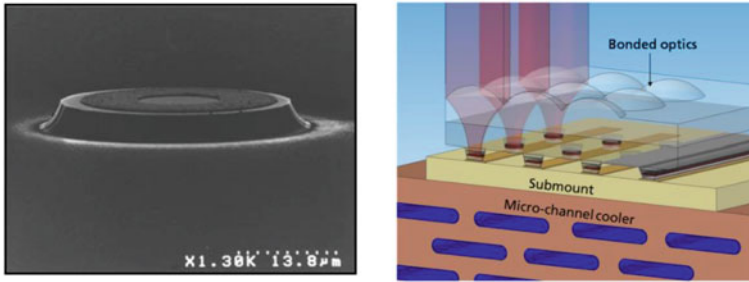
Fig. 2.5 Vertical emitter array on cooler, with collimating optics array (by Trumpf photonic components)

2.2.3 Vertical Emitting Arrays

After a long time evolution, in the communication market, high-power vertical emitting arrays (VCSEL) have been demonstrated in the past few years. Single emitters with diameters between about 3 and 100 μm are capable to generate 5–500 mW output power (Fig. 2.5). Power scaling by arrays is easy. Single-chip arrays provide power in the range of 1–100 W. For further power scaling to the range between 10 and 10,000 W, multi-chip modules are required.

The structure of the vertical emitter allows for wafer-scale processing without the additional effort for dicing and coating as known from the edge-emitting diodes. The drawback of VCSEL is the lower e/o efficiency up to about 40% which is significantly lower compared to the current state of edge emitters but shows a fast improvement over the last years.

The basic structure of vertical emitters and the symmetrical beam profile allow for comparably simple beam forming elements. External optical cavities enable power scaling at high beam quality. Tailored intensity distributions can be easily achieved by adapted array structures.

2.2.4 Application of High-Power Diode Lasers

The main application of high-power diode lasers is still pumping of solid-state and fiber lasers. Solid-state lasers range from single W lasers for inter-satellite communication over kW class lasers for material processing up to high energy lasers for fusion research (Fig. 2.6).

Direct Materials Processing

The power and brightness improvement of diode lasers in the past decade was a key for enlarging the number of industrial applications for direct materials processing with high-power diode lasers.
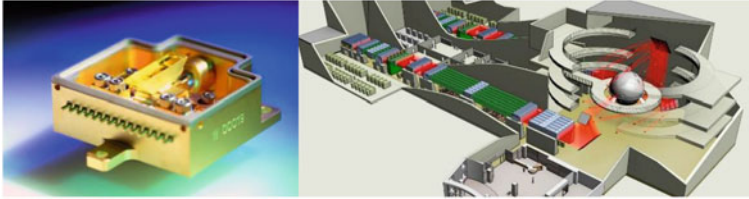
Fig. 2.6 Left: Pump module for a solid-state laser-based homodyne inter-satellite link with 2 diode bars. Right: European fusion plant HiPER requiring about 100,000 diode bars

Figure 2.7 shows the increasing number of applications in materials processing that could be addressed by high-power diode lasers in the past decade.

The most recent diode laser generation of companies like Laserline and Trumpf achieve the performance of lamp-pumped solid state lasers. Figure 2.8 shows a direct comparison of lamp-pumped lasers versus diode lasers and the demonstration of identical performance in welding of steel.
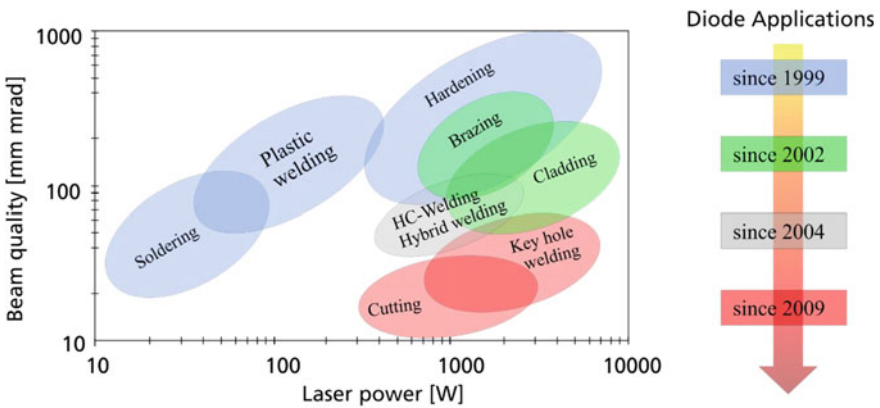
Fig. 2.7 Process requirement: beam parameter product versus laser output power
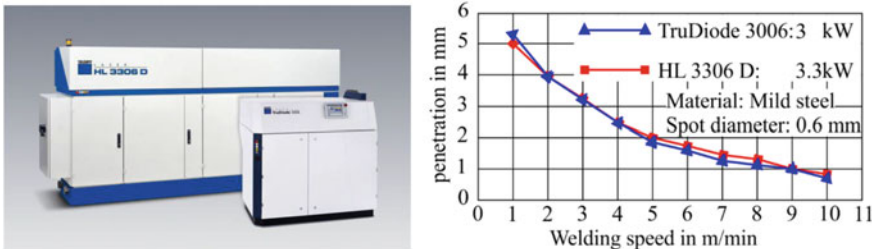
Fig. 2.8 Left: Lamp-pumped solid state laser in comparison to direct diode laser. Right: Comparison of welding results
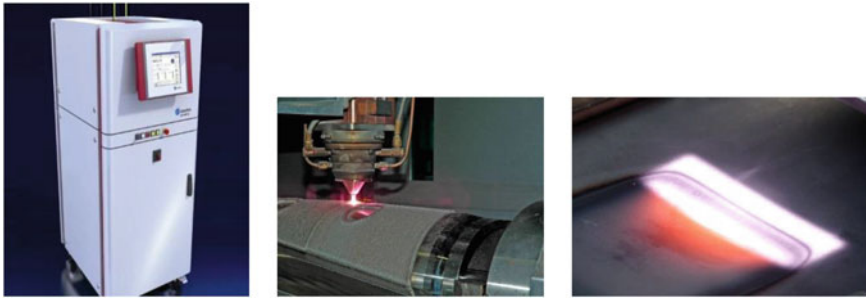
Fig. 2.9 Left: 20 kW average power fiber-coupled diode laser (Laserline). Center: Powder cladding of tungsten carbide layers for wear protection. Right: Laser heat treatment for deep drawing

Compared to lamp-pumped solid state lasers, high-power diode lasers offer significantly better wall plug efficiency (diode laser >40%, lamp-pumped solid-state laser = 2–3%) and multi-10,000 h of operation without changing lamps.

The availability of fiber-coupled output power beyond 10 kW is a driver to use high-power diode lasers for processes like laser cladding (Fig. 2.9).

Local heat treatment by laser emission allows for deep drawing of ultra-high strength steel in order to reduce weight of steel components, for example, in the automotive industry.

Thermal processing of materials like sintering of thin oxide layers require multi 10 kW output power with line-shaped intensity distribution (Fig. 2.10). Laser-controlled heating is used to improve the efficiency of thin film solar cell significantly. Conventional heat sources cannot be used because of the sensitive substrate material.
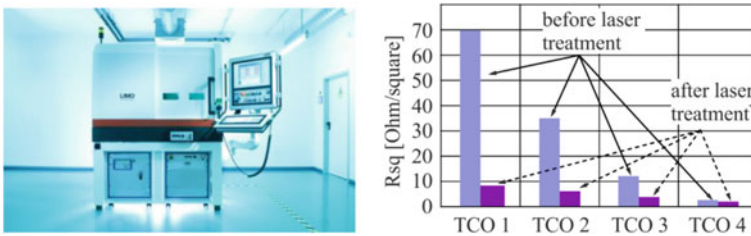
Fig. 2.10 Left: Pilot production unit for Sintering of TCO by a line-shaped beam with 20 kW average output (LIMO). Right: Results after processing

2.3 Solid-State Lasers

2.3.1 Introduction

Solid-state lasers have been established as a versatile tool in industry, medicine, and science. They cover a large range of parameters, e.g., average laser power from single mW for laser pointers up to powers beyond 10 kW for welding of thick steel sheets and thermal processing. Based on a large number of crystals and glasses with different properties as host for a wide range of active ions, solid-state lasers allow for generation-tailored beam properties. Wavelength from visible to far IR and pulse durations down to single femtoseconds can be generated. The generation of high-peak power pulses is based on the capability of storing pump energy in solid-state media. As solid-state media are manufactured with dimensions from single mm to multi-10 cm, solid-state lasers are capable to generate pulse energy in the kilojoule range at ns pulse duration out of a single beamline.

Despite the fact that diode lasers and fiber lasers are also based on solid-state media, "Solid State Laser" is commonly used for lasers based on optically pumped crystals.

2.3.1.1 Selected Crystal Types and Their Properties

Nd3+ was the first of the trivalent rare earth ions to be used in a laser, and it remains by far the most important element in this group. Stimulated emission has been obtained with this ion incorporated in at least 100 different host materials, and a higher power level has been obtained from Nd lasers than from any other four-level material. Very usual host materials are YAG and glass. In these hosts, stimulated emission is obtained at a number of frequencies within three different groups of transitions centered at 0.9, 1.06, and 1.35 μm (Koechner 2006).

Beside conventional growing techniques in recent years, Nd:YAG ceramics have been produced with good optical quality. Lasers that have incorporated Nd:YAG ceramic as active element have achieved power outputs and efficiencies comparable to conventionally grown Nd:YAG lasers. Compared to Nd:YAG single crystals, Nd:YAG ceramics can be produced with a more homogeneous and very high Nd concentration and larger size.

2.3.1.2 Basic Configurations

If the direction of pump light and generated laser light is codirectional the configuration is named "end pumped" or "longitudinally" pumped. Configurations with orthogonal direction of pump light and laser light are called "side pumped" or
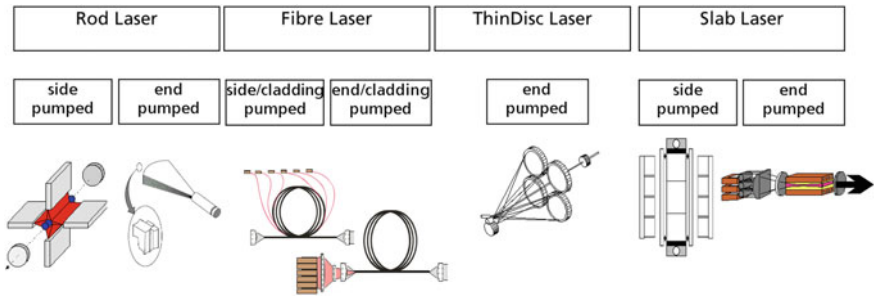
Fig. 2.11 Basic configurations of solid-state lasers

Table 2.1 Comparison of basic properties of solid-state laser amplifier concepts

	Rod	Fiber	Innoslab	Thin-disk	
				Regenerative	Multi-pass
Fundamental mode avg. power	−	++	+	++	++
Amplification factor	+	++	+	+	−−
Average power scaling	+	++	+	−	++
Pulse energy	+	−−	+	+	++
Nonlinearity	−	−−	+	+	++
Dispersion	−	−−	+	−	++

"transversally pumped". In fiber lasers, the pump light usually is guided in a waveguide limited by an outer cladding and passes the doped core several times. All laser concepts shown in Fig. 2.11 have been demonstrated up to kW average output power.

Beside the direction of pumping, the direction of laser emission and heat removal are fundamental design aspects and are crucial for the laser characteristics. The ThinDisk laser is close to the "ideal" configuration as pump light, generated laser light and heat flow ideally have the same direction thus not generating any transversal distortions. However technical implementation leads to residual effects. All laser concepts have some strong and weak points.

A general comparison of some basic properties of the different laser concepts is shown in Table 2.1. Dependent on the laser medium, the mode of operation, average output power, pulse power, pulse duration, and wavelength individual laser concepts may provide a best solution for a required parameter configuration.

2.3.2 Rod Lasers

The first laser which has been developed by T. Maiman in 1960 was based on a rod, i.e., a cylindrically shaped ruby crystal surrounded by a flash lamp for pumping. The

rod laser became a workhorse for scientific, military, medical, and industrial applications for several decades. Efficiency and output power were significantly improved by optimized cavities for improved pump light absorption and the development of laser crystals like Nd:YAG. Direct water cooling of the rod and the use of arc lamps enabled cw operation at multi 100 W laser output power level for industrial materials processing. Despite all improvements, the average output power of diffraction-limited rod lasers is typically limited to multi-10 W level. Industrial multi-rod lasers up to typically 4 kW level were the workhorse for applications like laser welding. The laser emission is delivered by high-order multimode fibers with 300–800 µm core diameter and a numerical aperture of 0.1 leading to M^2 of 45–120. These limitations in average output power and beam quality are very fundamental and mainly caused by thermo-optical effects in the laser rod.

The high brightness of diode emission in comparison to lamp emission enables new fundamental pumping schemes like longitudinal pumping through the small end faces of the rod.

Today CW lamp-pumped rod lasers have been widely replaced by new laser designs like direct diode lasers, ThinDisk, and Fiber lasers. Reasons are the higher reliability, reduced maintenance effort, and nearly one order of magnitude higher efficiency of these new laser types. Even pulsed lamp-pumped lasers, which had the benefit of low costs per Watt of pump power (a flash lamp generates about one order of magnitude more power compared to an arc lamp) are now being replaced by Fiber lasers. Fiber and ThinDisk lasers offer better beam quality which may reduce the required pulse power and benefit from the strong drop in diode costs caused by the scaling of production numbers.

Industrial Rod Lasers

Replacing the flash lamps in industrial high-power lasers for welding and cutting applications the transversally pumped rod laser shown in Fig. 2.12 has been developed from 1996 to 2000. Single rod modules generate an average power of 550 W or 1 kW, depending on rod diameter and the number of pump diodes.

For further power scaling up to eight modules are placed in a resonator–amplifier configuration. Power scaling is based on lens guide technology. This concept allows for power scaling without drop in beam quality. Today high power CW rod lasers are being replaced by disc, fiber, and diode lasers. The high average power rod laser
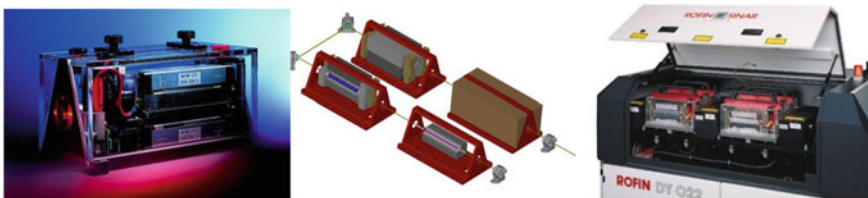
Fig. 2.12 Left: Diode-pumped laser head [Rofin], Center: Power scaling with 4 laser heads. Right: Fiber-coupled industrial 2.2 kW CW multi-rod laser [Rofin]
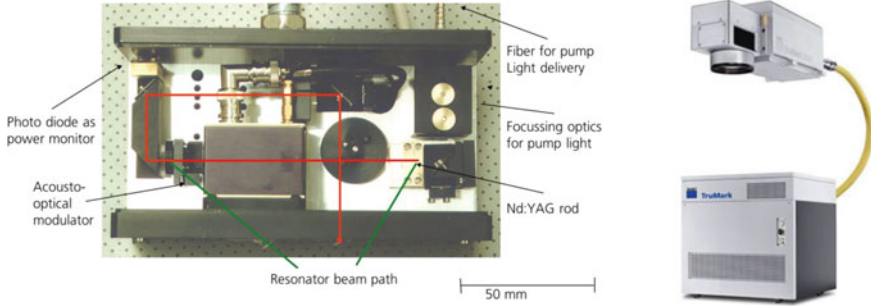
Fig. 2.13 Early prototype of an end-pumped laser for marking [ILT]. Right: Industrial laser marker including power supply and scanner [Trumpf]

is still of interest for generation of pulses by Q-switching for applications like laser cleaning.

At low average output power starting from a few Watt up to multi-10 W, the end-pumped rod laser is widely used for applications like marking and micro-machining. These lasers are usually CW-pumped and acousto-optically Q-switched in order to generate pulses with durations in the range of about 10–50 ns. An early prototype with a folded, very compact beam path is shown in the left picture of Fig. 2.13.

A state-of-the-art industrial system including supply unit and beam deflector is shown in the right picture of Fig. 2.13.

2.3.3 Thin Disk Lasers

2.3.3.1 Basic Design

Laser Crystal

The ThinDisk laser is based on a cylindrically shaped laser crystal of typically 50–200 μm thickness. The disk is pumped through one surface with circular cross section and cooled through the opposite surface. This surface represents a high reflective mirror for pump light and laser light. In a linear resonator configuration, only one additional mirror for out-coupling is required. To achieve efficient pumping, crystals with high absorption are required. Ytterbium-doped crystals like Yb:YAG, Yb:KGW, or Yb:KYW are a good choice. Yb:YAG, for example, can be doped up to a level of about 10% compared to about 1% doping level of Nd:YAG without deterioration of laser performance (Fig. 2.14).

Fig. 2.14 ThinDisk set up: blue: heat sink, yellow: laser crystal, orange: fiber-coupled pump radiation, and brown: generated laser emission
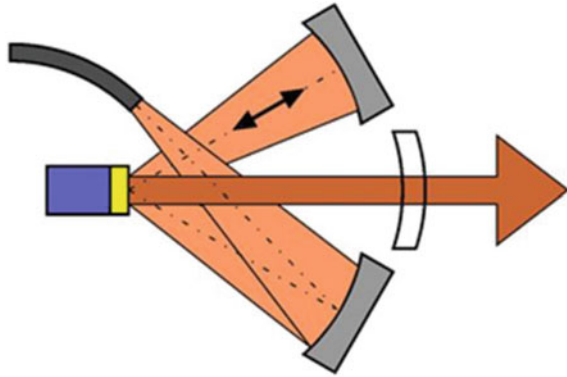
2.3.3.2 Examples of Industrial and Scientific ThinDisk Lasers

Examples of commercial low-power disk lasers are the CW frequency-doubled ThinDisk laser used in ophthalmology and projection systems with power level in the range of about 2–10 W (Fig. 2.15 left). The right picture shows a semiconductor-based ThinDisk laser (OPSL) with internal frequency conversion for operation with a CW output power of several W.

The following picture shows a kW class ThinDisk laser (Fig. 2.16). The laser power is delivered by step-index fibers with core diameters between 50 and 300 μm dependent on output power and application. For efficient and economical use of the system, the emission can be switched to 4 fibers. The right picture shows a multi-disc configuration for power scaling with 4 disks arranged in one oscillator.

Fig. 2.15 Left: Frequency-doubled ThinDisk laser [Jenoptik]. Right: Optically pumped Disk Laser [Coherent]
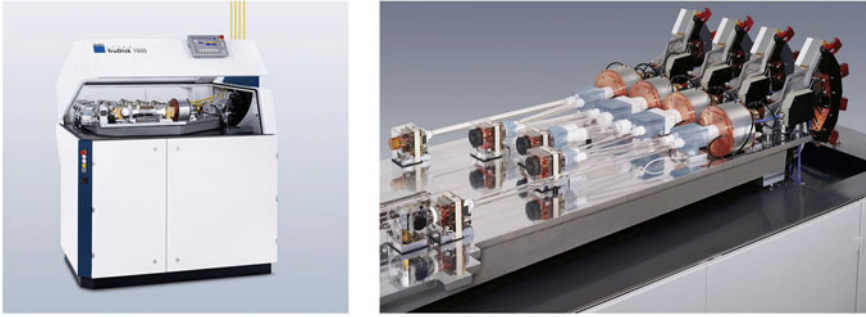
Fig. 2.16 Left: Industrial muti-kW ThinDisk laser. Right: Multi-disk configuration (by Trumpf)

2.3.4 Slab Lasers

Slab lasers are based on a crystal plate with rectangular shape. The basic geometry is adaptable to the emission characteristics of edge-emitting diode lasers. The slab geometry is typically used for lasers with simplified pump geometry or for scaling the output power compared to rod designs. Various slab-based solid-state concepts have been demonstrated in the past years. A selection of these is shown on the following pages, focusing on compact setups with high efficiency.

2.3.4.1   Transversally Pumped Slab Laser

The advantages of transversely pumped lasers, where the direction of incident pump power and laser emission are essentially perpendicular are the scalability to high power with relatively simple configurations of the diode pump lasers. However, there is a geometric challenge to overlapping the deposited pump power with a TEM_{00} mode. To match the pumped volume created by side pumping, a laser crystal with diode laser bar emission a multi-pass slab design (MPS, Fig. 2.17) is proposed in Moulton et al. (1998). In the design, a pumped region in the form of a thin sheet is created by diode laser bars collimated in fast axis.

Comprehensive investigations with various kinds of laser crystals have been carried out and discussed in Dergachev et al. (2007). Power scaling at high beam quality and efficiency has been demonstrated to up to multi 10 W level. For further power scaling, multi-slab configurations are an option.

2.3.4.2   Partially End Pumped Slab Laser

For the generation of multi-100 W or even kW average output power at high beam quality, a new end-pumped slab laser concept (INNOSLAB) has been proposed and discussed in Du et al. (1998) and Russbueldt et al. (2015). A **hybrid resonator** for
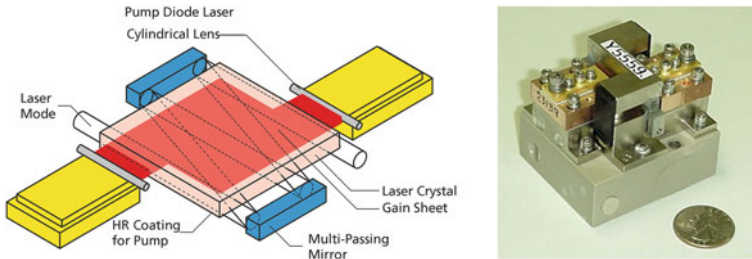
Fig. 2.17 Left: Schematic of multi-pass slab (MPS) laser design. Right: Photo of an MPS amplifier
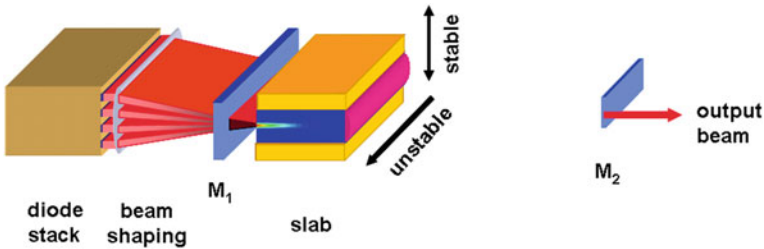
Fig. 2.18 Schematic of the end-pumped INNOSLAB laser with a hybrid resonator

direct generation of diffraction-limited beam quality at high efficiency out of the strongly elliptical gain sheet is configured as follows:

- a stable/instable resonator concept (= hybrid resonator) is utilized. The resonator is stable in the plane of the small dimension and is off-axis unstable in the plane of large dimension of the gain cross section (Fig. 2.18).
- a beam propagation straight through the gain sheet without any zig-zag path (e.g., no bounces to the slab faces) inside the slab crystal leads to reduced crystal fabrication effort and decreased tendency to parasitic oscillation.

2.3.4.3 Examples of Industrial and Scientific Slab Lasers

The INNOSLAB concept seems to be currently by far the most prominent slab laser concept that is used in numerous industrial and scientific applications. In Fig. 2.19, selected INNOSLAB-based lasers are shown. The main driver for the use of INNOSLAB lasers in the industrial market is the capability to generate or amplify short pulses from single ns down to fs pulse duration at average power levels in the range of multi-10–multi-100 W very efficiently in comparably compact setups. For scientific applications, new parameter ranges for ultrafast lasers are required. INNOSLAB lasers for scientific applications offer, for example, up to kW average power at a pulse duration of around 600 fs and pulse energy up to the multi-10 mJ range or pulse durations in the 100 ps range at a pulse energy of several 100 mJ at

Fig. 2.19 Left: Q-switched ns laser [Edgewave], center: 400 W fs amplifier [AMPHOS]. Right: LIDAR source for space operation [ILT, Airbus Defense and Space]

kHz repetition rate. An extensive overview on the INNOSLAB research is provided in Russbueldt et al. (2015).

Using **LIDAR** (light detection and ranging) technique, 3D density profiles of trace gas concentrations of, for example, CH_4, CO_2, H_2O, aerosols, or wind speed profiles, can be measured with unprecedented data quality. On board of a helicopter, an airplane, or a satellite, this technique can provide high resolution and high spatial coverage at the same time. Consequently, there is a great demand for the appropriate measurements in the field of atmospheric research. Furthermore, this technology is already used by industry for remote detection of pipeline leakage on board of a helicopter. Due to the high efficiency, the power scaling capability, and the very compact design, the INNOSLAB concept has been selected by ESA and DLR as a platform for future LIDAR systems (Löhring et al. 2014).

2.3.5 Fiber Lasers

The progress in the development of fiber lasers has accelerated in the past 10 years. Initially, only a means to enhance the performance of optical telecommunication networks in the beginning, these lasers have enjoyed increasing output power, thus making them a common tool for industrial applications such as materials processing, marking, or metrology. Due to their excellent beam quality as well as the simple and robust construction, fiber lasers complement well-established industrial lasers like CO_2 and Nd:YAG lasers, even replacing them in some areas. As sources for pulsed output, fiber laser systems can be used for metrology, e.g., Light Detecting and Ranging (LIDAR), as well as micromaterials processing or for applications in life sciences. The fiber laser's properties allow for very small focus sizes, thus potentially optimizing processes such as cutting and welding of sheet metals. Cw lasers with a single-mode output power of 5 kW and multi-mode fiber lasers with output powers up to more than 100 kW are commercially available.

The basic concepts of light guidance in optical fibers, fiber lasers, and some remarks about fundamental limitations and setups will now be introduced.
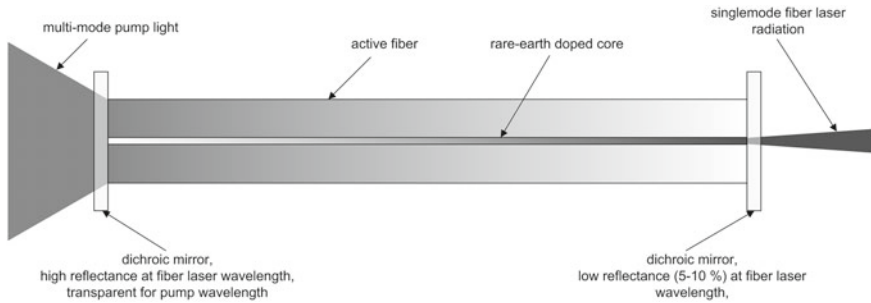
Fig. 2.20 The basic principle of a fiber laser. Highly multi-mode pump radiation is transformed to few-mode or even single-mode fiber laser radiation

2.3.5.1 Principle of the Fiber Laser

A fiber laser is often described as a brightness converter. Its principle is depicted in Fig. 2.20. The energy which is used for pumping usually comes from laser diodes which often have a multi-mode output. This pump light is then converted into fiber laser radiation, often with a single-mode beam quality, at very high efficiencies.

Figure 2.20 shows the principle of a fiber laser. The pump light is coupled into the cladding of the active fiber. In every fiber increment, a certain amount of the pump light is absorbed by the active ions in the core to create an inversion. Due to total internal reflection, light that is spontaneously emitted from the excited dopants and within the acceptance angle of the core will be guided and amplified in the core.

2.3.5.2 Examples of Industrial Fiber Lasers

During the past years, fiber lasers have replaced other lasers for several applications and become a standard tool, for example, for sheet metal cutting where the fundamental mode operation in combination with high average output powers in the multi-kW range helped increase the throughput of the processing plant while maintaining superior processing quality, or for marking applications, for which the relatively low cost of q-switched fiber lasers helped the fiber laser to its breakthrough.

Continuous wave and QuasiCW fiber lasers are available with fundamental mode beam quality up to about 10 kW and more than 120 kW multi-mode output (Fig. 2.21).

A typical and widely spread example of pulsed fiber lasers are q-switched lasers with pulse durations in the 100 ns regime whose main applications are marking and microprocessing. By introducing fiber-coupled acousto-optic modulator into the cavity, the laser output can be modulated. Typical lasers of this class (Fig. 2.22) have average output powers in the range of several 10 W and pulse energies in the mJ regime, resulting in pulse peak powers in the 10 kW class. Fiber lasers are available with pulse duration in the ps and fs regime up to about 100 μJ pulse energy and multi 10 W average power (22).

Fig. 2.21 Left: 6-kW TruFiber laser series (www.trumpf.com). Right: YLS 1-120+ kW Series (www.ipg.com)

Fig. 2.22 Left: One example of a commercial Q-switch laser is the IPG YLPN series. (www.ipg photonics.com). Right: TruMicro 2000 series ps and fs fiber lasers (www.trumpf.com)

2.4 Gas Lasers

Lasers based on gas as the active laser medium provide superior performance concerning high average power in CW and pulsed operation in the mid- and far infrared and the deep ultraviolet wavelength regimes. While the average power performance of solid state sources based on glasses and crystals is currently limited by increasing absorption beyond about 2 μm and below about 300 nm gas lasers provide multi-kW or even multi-10 kW operation at industrially relevant efficiency.

2.4.1 CO_2 Laser

The first CO_2 laser was realized by Patel in the year 1964. The laser transitions take place between vibrational and rotational states of the electronic ground state of the CO_2 molecule. The wavelengths are in the IR region around 10 μm. Today CO_2 lasers

Table 2.2 Efficiency and typical power densities of different excitation techniques. η_D and η_{PS} are the efficiency of energy deposition in the laser gas and of the power supply unit respectively, $\eta_{tot} = \eta_D \eta_{PS}$ is the total efficiency

	η_D (%)	η_{PS} (%)	η_{tot} (%)	p_D [W/cm^3]
DC	25	95	24	25
AC (200 kHz)	22	95	21	25
AC (2.5 MHz)	19	92	18	60
RF (13/27 MHz)	20	70	14	70

are important tools in the field of manufacturing technology. This is mainly due to their relative simple construction, the high efficiency of about 25%, which however reduces to some 10% in the case of high-power lasers, and the high realizable output powers. Commercially available CO_2 lasers today reach powers of up to about 40 kW.

2.4.1.1 Excitation and Construction of CO$_2$ Lasers

The excitation of the N_2 buffer gas in the CO_2 laser gas mixture is accomplished by electron collisions. The electrons can be injected by an electron gun through a thin metal foil into the CO_2 laser gas vessel or can be produced by ionizing electron collisions in a gas discharge. Both methods can be used in combination in an electron beam sustained discharge. Electron beam pumping is employed only for the excitation of large volume high-pressure pulsed CO_2 lasers.

The most frequently employed CO_2 laser excitation technique is electron collisional excitation in self-sustained gas discharges. The discharges can be driven by direct currents or by high-frequency fields with a variety of frequencies. The discharges can be longitudinal with respect to the optical axis or transversal. The discharge types differ in efficiency and realizable power densities: Whereas the efficiency decreases with increasing excitation frequency, the attainable power density increases with increasing excitation frequency (Table 2.2). Because of this today high power CO_2 lasers are mostly excited by high-frequency discharges.

CO_2 lasers can be separated into two distinct pressure regimes:

- High-pressure CO_2 lasers are operated at pressures of about 1 bar or above. The necessary power density for efficient excitation exceeds 10^4 W/cm^3 so that the gas is heated up beyond the maximum allowable temperature within a few ms. Figure 2.23 schematically shows the construction of a TEA[2] laser. Pressures beyond 1 bar are necessary if the objective is to continuously tune the emission wavelength.
- Low-pressure CO_2 lasers (Fig. 2.24) can be operated continuously as well as in pulsed mode. The pressure ranges from about 10 mbar up to 200 mbar. Build-up

---

[2] TEA stands for Transversely Excited at Atmospheric pressure.
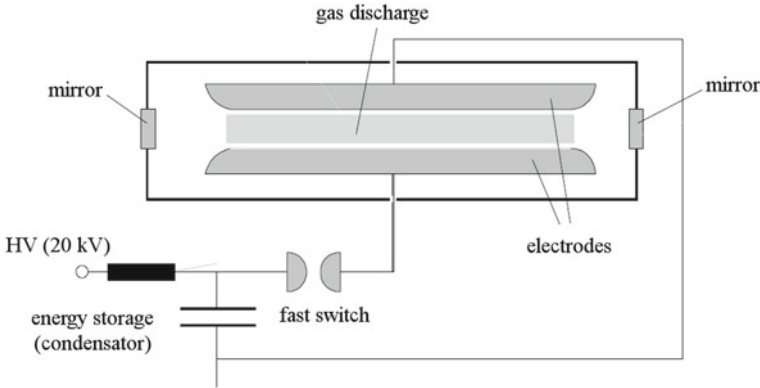
Fig. 2.23 Schema of a diffusion-cooled TEA CO_2 laser. TEA lasers are operated at atmospheric pressures and hence can only be excited in pulsed mode

and decay times are much longer compared to high-pressure CO_2 lasers due to the lower particle collision rates.

Today, direct current discharge excitation is mostly replaced by high-frequency discharges. HF frequencies of 13.6 or 27 MHz are most frequently used with the exception of waveguide lasers that are generally operated at about 100 MHz.

Because CO_2 lasers can only be operated efficiently up to a temperature of about 600 K the gas has to be cooled effectively in the case of continuous excitation as well as in repetitive pulsed mode. Diffusion cooling and convective cooling, which are the two possible cooling mechanisms, already were mentioned in the last paragraph.

With diffusion cooling the dissipated energy is transported by energy diffusion (heat conduction) to the liquid-cooled walls of the discharge vessel where the energy is transferred to the wall. The maximum power density is limited by the heat conductivity of the gas. In the stationary case and with cylindrical discharge tubes, the heat conduction equation in cylindrical coordinates reads

$$\frac{d^2T}{dr^2} + \frac{1}{r}\frac{dT}{dr} = -\frac{p}{K}$$

r—radial coordinate.

p—dissipated energy density.

K—heat conductivity of the gas.

The energy density p is assumed to be homogeneous within the discharge vessel. The solution of this equation is given by:

$$T(r) = \frac{p}{4K}(R^2 - r^2) + T_w$$

R—discharge tube radius.
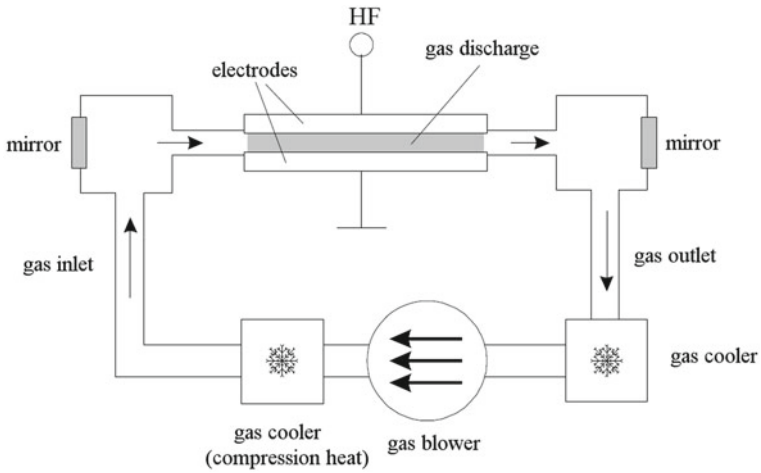
Fig. 2.24 Schema of a high-frequency excited low-pressure CO_2 laser with fast axial gas flow. The second heat exchanger behind the gas recirculating fan is used to extract the compression heat that was added to the gas by the compression work of the fan

$T_w = T(R)$—wall temperature.

The maximum allowable power density p_{max} with a given temperature difference ΔT_{max} between wall and tube axis is given by (Fig. 2.25)

$$p_{max} = \frac{4K}{R^2} \Delta T_{max}$$
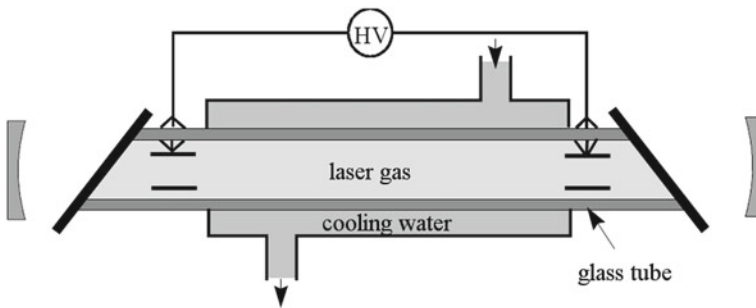
Fig. 2.25 Schematic drawing of a sealed-off CO_2 laser

2.4.1.2 Characteristics and Field of Applications

In Table 2.3, characteristic data of pulsed and continuous wave CO_2 lasers are summarized. CO_2 lasers are a very important type of laser in the field of commercial use. The main advantages are the ability to deliver powers of up to 40 kW (Fig. 2.26) in the 1ß μm wavelength range at comparably high efficiency. CO_2 lasers particularly are the working horse of production technology. Its great popularity is mainly due to the availability of mature and robust systems in the power range of 1–10 kW. Up to now, this power range could not be made accessible by any other type of laser. CO_2 lasers also play an important role in laser surgery. This is because the water contained in living tissue strongly absorbs the 10 μm radiation so that small powers suffice and surrounding tissue is not damaged.

Table 2.3 Characteristic data of pulsed and continuous wave CO_2 lasers

Parameter	Pulsed CO_2-laser	CW CO_2-laser
Wavelength [μm]	10.6	10.6 (9–11)
Power [kW]	10^{-1}–10^9	10^{-2}–10^2
Efficiency	5–25%	5–25%
Beam quality K	0.1–1	0.2–1
Pulse duration [ns]	>100	–
Pulse energy [J]	10^{-1}–10^3	–
Repetition frequency [kHz]	1–2	–
Gas pressure [mbar]	10^2–10^3	10^2–10^3
Gas temperature [K]	<600	<600
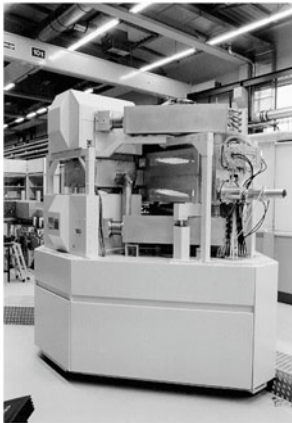
Fig. 2.26 Left: 40 kW CO_2 laser which is designed for welding of thick steel plates of 20–40 mm thickness (ILT). Right: High-Power Amplification Chain (HPAC) consisting of four main amplifiers for generation of EUV emission at 13.5 nm (TRUMPF)

2.4.2 Excimer Lasers

Excimer lasers make up a special class of molecule lasers. *Excimers* are bonds out of two atoms whose interaction potential is repulsive in the electronic ground state, but is attractive in certain, electronically excited states. The electronic ground state is, therefore, instable and degrades through collisions of the atoms within approx. 10^{-12} s, while the excimer molecules have a specific lifetime of about 10^{-8} s in electronically excited states through the radiation degradation time. The laser transitions take place between the electronically excited states and the instable electronic ground state. The great advantage of this type of laser is that the lower laser state is practically unpopulated, since the relaxed molecules degrade in a short period of time. Therefore, a high population inversion can be attained in excimer lasers.

Excimers were proposed as a laser medium in 1960, but the first excimer laser was realized in 1970 by BASOV. Excimer lasers were initially pumped by means of electron radiation excitation. Subsequently, discharge arrangements, as they were originally developed to excite nitrogen lasers, were also used for excimer laser excitation. Before excimer lasers became reliable industrial tools, substantial improvements were necessary to prolong gas lifetime and the reliability of components. Great efforts were made to optimize the layout of the pulse power circuitry, the discharge tube design and to provide optical materials capable of withstanding high doses of UV radiation. These developments qualified excimer lasers as reliable light sources for fabrication processes and for lithography in the semiconductor industry.

2.4.2.1 The KrF Molecule and Laser Transition

Excimer stands for *excited dimer*, thus an excited molecule consisting of two of the same atoms. To this group belong noble gas dimers such as Ne_2 or Xe_2. In addition to dimers, or symmetrical molecules, there are molecules made of two different atoms or of three atoms, which only undergo bonding in excited states. These molecules are called exciplexes, (excited state polymers); as a rule, however, no difference is made between symmetrical and unsymmetrical molecules, and the general name, excimer, is used.

Laser transitions have been observed in a multitude of excimers. Some of them are listed in Table 2.4. Due to their high potential power, the noble gas halogen systems are the most important excimer lasers for applications. The most powerful excimer laser is the KrF laser. Figure 2.27 shows the potential–energy curve of the KrF molecule as a function of the interatomic distance for different electronic states. By means of the curves, it can be seen that the potential curve of the ground state does not exhibit a minimum, but rather level off toward larger atom distances. This characterizes the instability of the bond in the ground state.

The laser transition occurs from the electronically excited $B^2\Sigma 1/2$ state to the $X^2\Sigma 1/2$ ground state. Transitions appear from differing oscillation states of the upper level; the transition from the oscillation ground state has the largest amplification.

Table 2.4 Compilation of excimer molecules, commercially realized lasers are in bold

Compounds	Molecules
Rare gas excimers	Ne2, Ar2, Kr2, Xe2
Rare gas halide excimers	*ArF, KrF, XeCl, XeF*
Rare gas metal excimers	NaXe, HgXe, HgKr, HgXe, TlXe
Rare gas halide trimeres	Ar2F, Kr2F, Xe2F, Xe2Cl, Xe2Br
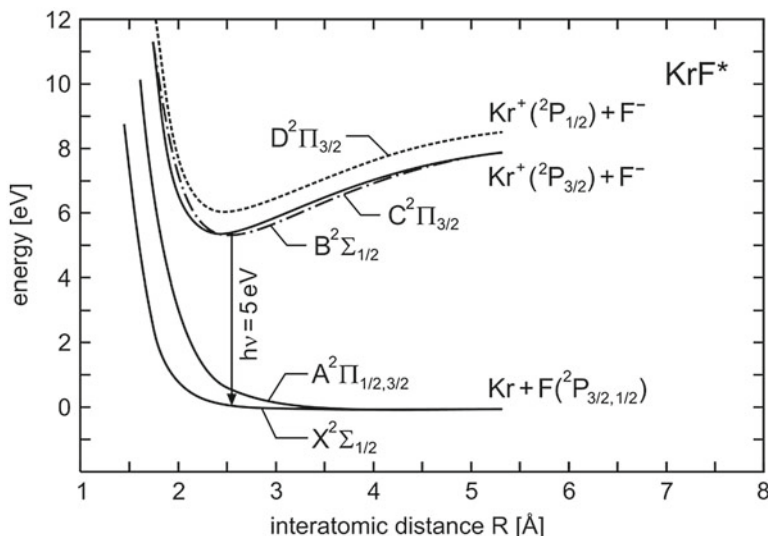
Fig. 2.27 Binding energy and intermolecular distance for the KrF molecule; in the excited state, a stable molecule is formed, whereas after the electronic transition, the ground state is repulsive

The wavelength of this transition lies at 248.5 nm. The laser transition between both electronic states occurs very quickly in comparison to the time constant of the relative movement of both atoms. In this way, a dependency occurs—of the transition energy upon the atom distance at the time of the transition. The consequence is a significant line broadening: The fluorescence linewidth lies at about 5 nm and the linewidth of the laser radiation is about 1 nm.

2.4.2.2 Kinetics of the KrF Laser

Since the excimer molecules are instable, they have to be formed in active volumes. Noble gas halogen excimer lasers contain, in addition to the noble gas and a halogen donor, an additional *buffer gas*, which is also a noble gas. As a rule, fluorine gas F_2 is admixed as a fluorine donor for KrF lasers, but nitrogen trifluoride NF_3 can also be used. As a buffer gas, helium or argon is used. The buffer gas atoms absorb energy and impulse excesses as collision partners for three-body collisions.

The large linewidth of the laser transitions means a short effective lifetime in the upper laser level and, therefore, a small amplification. For this reason, high minimum pump power densities are required in order to reach the laser threshold. They lie typically in the magnitude of 10^{12} W/m^3, which means that a required pump power of 1 GW results for discharge volumes of $1 \, \mathrm{l} = 10^{-3}$ m^3. Such values are only attainable in pulsed operation.

2.4.2.3 Excitation of Excimer Lasers

Excimer lasers can be pumped either by an intensive, pulsed electron beam or by a pulsed high-voltage discharge. In commercial systems, the discharge excitation method has established itself due to the lower technical complexity. The principal configuration of a transversally excited atmospheric pressure discharge gas laser (TEA laser) is depicted in Fig. 2.28. Typically, the discharge unit ("tube") consists of two long extended main electrodes, spark gaps for pre-ionization, a tangential blower for gas exchange, a gas cooler, and dust filter. The electrical energy from a high-voltage power supply is stored in a capacitor bank and transferred to the main electrodes when a high-voltage switch is triggered. If the pre-ionization circuit is properly timed, then a high-pressure glow discharge develops.

The gas mixture in the discharge tube normally contains 5–10% krypton (Kr), 0.1–0.5% fluorine (F$_2$), and the buffer gas, which, as a rule, is helium (He). The total pressure typically amounts to 1.5–4 bar. Gas discharges with the above-mentioned, high power density cannot be kept stable in this pressure range over a longer period of time. After several 10 ns, instabilities lead to the collapse of the homogeneous discharge into individual, narrow discharge channels. These discharge channels are called *filaments*. In these areas, the discharge crosses over from a glow discharge into an arc discharge. Above all, the filaments originate from the electrode material evaporating on the cathode as a consequence of the high discharge currents at individual points. These *hot spots* deliver much more electrons than their surroundings and form the base point of filaments. On account of these instabilities, only a pulsed

Fig. 2.28 Schematics of the main components of excimer lasers; the electric discharge current and the gas flow are perpendicular to the optical axis

dust filter
rear mirror
discharge electrodes
storage capacitors
power supply
HV switch
output coupler
gas circulation
fan
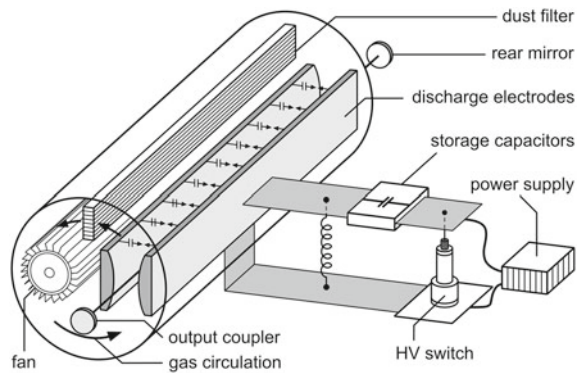
excitation with pulse lengths of a few 10 ns is possible. In pulsed operation, very high amplifications, however, are attained, up to 10%/cm. The total efficiency from excimer lasers moves in the range of about 1% (wall-plug efficiency).

2.4.2.4   Laser Resonators

Local fluctuations of gas and electron densities inside the "homogenous" glow discharge stimulate the formation of ionization waves ("streamers"), which tend to end up in a number of sparks. This situation is typically reached in an excimer discharge after 50 ns of electrical pumping, and thus the resulting optical pulse duration is limited to about 30 ns FWHM. Most of the industrial and scientific lasers are designed for an optical resonator length of about 1 m. Within a pulse duration of 30 ns, there are only five roundtrips possible before the laser pulse ceases. For the rear mirror and the output coupler, a planar resonator of Fabry–Perot type is usually chosen with a high-reflecting end mirror. The reflectivity of the output coupler is set for maximum power extraction; depending on discharge length and power density of the gas discharge, the optimum reflectivity is between 10 and 25%. Due to the small saturation energy density of 2 mJ/cm^2 and the high value of the small signal gain of ~0.1 cm^{-1} (Taylor et al. 1988) is sufficient to stimulate laser emission in excimer gases.

The typical bandwidth obtained in excimer lasers is 0.5 nm for KrF and 0.3 nm for ArF (http://www.coherent.com/Lasers/index.cfm?fuseaction=forms.Downloads File&DLID=6459). Then the temporal coherence length is rather low, typically shorter than 150 μm for a small excimer laser of 0.5 m discharge length. When line-narrowing optics, such as prisms, are inserted into the optical resonator, the bandwidth can be reduced to <0.35 pm resulting in a temporal coherence length of about 3 mm. That is adequate for writing of fiber Bragg gratings in optical fibers for telecommunications applications, but the situation is more demanding in lithography. To achieve the ultimate feature size, the bandwidth of the light source has to be limited to 0.35 pm to avoid chromatic aberrations of the imaging system. State-of-the-art lasers for lithography consist of an oscillator and an amplifier section and sophisticated optical equipment to measure and adjust the bandwidth and the center wavelength (Kumazaki et al. 2008; Brown et al. 2007).

For micro-machining applications the low coherence length of broadband laser emission is favored; otherwise, diffraction pattern will blur the image quality. Scattering effects from masks can be minimized even further by using a beam homogenizer, which generates multiple beamlets with various angles to the optical axis to illuminate the mask. These beams overlap at the mask plane, are fed through the imaging optics, and then combine in the image plane. Because of the varying optical path length and mixing up of different angular modes, the degree of coherence becomes very low and speckle patterns are minimized.

2.4.2.5 Applications and Laser Performance

Excimer lasers are the most powerful and intense light sources available in the near (~350 nm) and the deep UV (~200 nm) range. Their applications can be found in optical lithography, manufacturing, industrial R&D, science, and medicine. Since the performance of semiconductor circuits is related to the density of transistors and capacitors, the size of these elements has been shrinking over the last few decades, while the transistor count nearly has doubled every 2 years. This trend was predicted in 1965 by Moore (1965) from Intel Corp. and therefore is called "Moores law"—the prediction has held until now. Today, optical lithography relies on ArF excimer lasers. Single patterning and 193 nm immersion with water enable critical structures (CDs) of 45 nm. To reach the next "node" of 32 nm, CD immersion double patterning using two masks with offset structures and two exposure steps is required. According to the ITRS roadmap for lithography (The International Technology Roadmap for Semiconductors 2009) in 2009, the first CPUs with 32 nm structures are brought to the market in 2009. Probably, the 22 nm node will mark the end of the line for optical lithography, introducing resolution enhancement techniques as phase-shifting masks, optical proximity corrections, liquid immersion imaging with high NA <1.35, and advanced mask features for multiple patterning (The International Technology Roadmap for Semiconductors 2009). The investments in new laser sources have slowed down due to the growing interest of industries to gain more return of investment than to reach the next "node", which may require more sophisticated excimer sources. Therefore, the revenues dropped in 2009 to $135 mio. compared to $399 mio. in 2007, but are expected to increase again (Sullivan & Frost 2004).

Outside semiconductor industries, excimer lasers are used in production processes to drill printed circuit boards (Bachmann 1989; Lankard and Wolbold 1992), anneal thin film transistor circuits for flat panel displays (308 nm) (Choi and Han 1996), drill ink jet nozzles (248 nm) (Endert et al. 1997), and mark glasses (193 nm) (Endert et al. 1995). Typically, excimer lasers are employed in three-shift production cycles with scheduled intermissions for maintenance. The ablation of polymer or plastic materials has sometimes been termed "cold ablation", which means that material is vaporized without heating the sample. That was attributed to a pure photochemical decomposition, but later investigations showed that thermal effects were present for most materials. The important point is the very steep temperature gradient which is caused by the high absorption of the UV radiation (optical penetration depth ~μm) and the short pulse duration (<30 ns). Therefore, the deposited pulse energy is concentrated in a layer of approximately 1 μm thickness which defines the extension of the heat-affected zone. In practice, machining of structures requires several pulses to achieve a certain depth and, therefore, the effect of heat accumulation has to be considered.

High-pulse energy lasers are employed for pulsed laser deposition (PLD) to prepare thin films of superconducting (Auciello et al. 1988) or ferro-electric materials for fabrication of ultrafast electronics, magnetic sensors (squids), and data storage (Masterson et al. 1992; Setter and Waser 2000). The main advantage of excimer laser PLD is that materials composed of elements with different thermal properties—e.g.,

heat of sublimation and evaporation, melting, and vaporization temperature—can be vaporized, keeping the stoichiometry at the substrate's surface. This process is often referred to as laser-induced congruent evaporation. Preparation of thin films of optical materials like $LiNbO_3$, TiN, or ZnO is investigated for applications in integrated optics, light-emitting diodes, and telecommunications (Lowndes et al. 1996). Writing of diffractive structures on optical fibers (fiber Bragg gratings, FBGs) is used to produce ultra-narrowband filters and multiplexers for telecommunications (Hill et al. 1993). FBG fiber sensors are cheap and robust devices to measure stress and strain or temperature in high-voltage or noisy environments. Sensing fibers can be embedded in critical infrastructure like bridges to monitor anomalous burden and aging effects (Kersey et al. 1997).

Furthermore, medium-power excimer lasers are employed in a great variety of industrial R&D and scientific research projects. Combustion processes in car engines are studied by laser-induced fluorescence to help develop more efficient and environment-friendly cars. For monitoring of the upper atmosphere, water vapor and ozone concentrations are measured by LIDAR (Light Detection and Ranging) at distances ranging from ground up to 40 km in height approaching the stratosphere (Ansmann et al. 1992).

Excimer laser vision correction has emerged as the most prominent application of lasers in medicine. The number of laser units sold in the US market reached 2,933 units in 2003, which accounts for revenues of \$210 mio. of total \$546 mio. for the medical laser market (Sullivan & Frost 2004). LASIK (laser in-situ keretec-tomileusis) is now used to correct myopia and mild hyperopia and routinely employed (Pérez-Santonja et al. 1997). In the LASIK procedure, first, a precision cutting instrument (keratom) is used to cut a thin sheet ("flap") of the cornea tangentially to the surface. Then, the lamella is flapped to expose the inner structure of the cornea to an ArF excimer laser beam. The laser spot is swept across the surface and fired in predefined manner to reshape the thickness of the cornea. By each pulse, a layer of 0.5–1 μm thickness is removed. Then the flap is brought back into its former position to cover the surface of the lesion. This procedure has turned out to show a better wound healing than the previously employed photorefractive keratectomy (PRK) (Diamond 1995), where the ablation is performed at the outer surface of the cornea after peeling off the thin epithelium layer. Recent vision correction systems employ wavefront-guided LASIK to correct for higher order aberrations to attain perfect vision of the eye. However, success is dependent on the surgeon's experience and the condition of the patient (Table 2.5 and Fig. 2.29).

Table 2.5 Applications and performance of excimer lasers, data derived from Coherent Inc., Cymer Inc., and Gigaphoton Inc.

Application	Lithography	Fiber Bragg gratings	Ink jet nozzles, PLD, patterning	Annealing	Scientific, R&D	Vision correction, marking
Excimer	ArF line narrowed <0.35 pm	ArF, KrF line narrowed <15 pm	KrF	XeCl	ArF, KrF, XeCl, XeF	ArF
Wavelength [nm]	193	193, 248	248	308	193, 248, 308, 351	193
Pulse energy [mJ]	10	0.5–2	500	1000	200–400	5
Pulse rate [pps]	6.000	1.000	200	600	100	500
Pulse duration [ns]	70	15	20	30	20	5
Pulse power* [MW]	0.14	0.033–0.133	25	33	10	1
Average power [W]	60	0.5–2	100	600	20–40	2.5

* Pulse power calculated from pulse energy and pulse duration

Fig. 2.29 Left: High-power excimer laser for annealing (COHERENT). Right: Excimer laser optimized for lithography (GIGAPHOTON)

References

Ansmann A et al (1992) Combined Raman elastic-backscatter LIDAR for vertical profiling of moisture, aerosol extinction, backscatter, and LIDAR ratio. Appl Phys B Lasers Opt 55(1):18–28

Auciello O et al (1988) Spectroscopic analysis of electronically excited species in XeCl eximer laser-induced plasma from the ablated high temperature superconductor YBa2Cu3O7. Appl Phys Lett 53(1):72–74

Bachmann F (1989) Excimer lasers in a fabrication line for a highly integrated printed circuit board. Chemironics 4(149)

Brown DJW, O'Keeffe P, Fleurov V (2007) Recirculating ring ArF light source for immersion lithography optical microlithography. Proc SPIE, Opt Microlith 6520(3):652020.1–652020

Choi KY, Han MK (1996) Two-step annealed polycrystalline silicon thin-film transistor. J Appl Phys 80(3):1883–1890

Dergachev A, Flint JH, Isyanova Y, Pati B, Wall KF, Slobodtchikov E, Moulton PF, Review paper, published in IEEE JSTQE PSSFTS #2255 (2007)

Diamond S (1995) Excimer laser photorefractive keratectomy (PRK) for myopia–present status: aerospace considerations. Aviation Space Environ Med 66(7):690–693

Digonnet MJF (2001) Rare-earth-doped fiber lasers and amplifiers. s.l., Marcel Dekker, Inc. 0-8247-0458-4

Du K, Wu N, Xu J, Giesekus J, Loosen P, Poprawe R (1998) Opt Lett 23(5)

Endert H, Patzel R, Basting D (1995) Excimer laser: a new tool for precision micromachining. Optical Quantum Electron 27(12):1319–1335

Endert H et al (1997) Excimer lasers in manufacturing. Proc SPIE 2993:46–53

Geiger J, Erben B, Hoffmann D, Altmeyer S (2007) Characterization of high power multimode combiners. In: CLEO/Europe and IQEC 2007 conference digest 'CLEO/Europe and IQEC conference digest', Optical Society of America, Munich, Germany, pp CJ–21

Giesen A (2004) Results and scaling laws of thin disk lasers. In: Scheps R, Hoffmann HJ (eds) Solid state lasers XIII: technology and devices. Proc SPIE 5332, p 212

Hergenhan G (2002) Coherent Combining of vertical emitters – system concept and experimental verification. IFSW Stuttgart, Herbert Utz Verlag

Hill KO et al (1993) Bragg gratings fabricated in monomode photosensitive optical fiber by UV exposure through a phase mask. Appl Phys Lett 62(10):1035–1037

Kersey AD et al (1997) Fiber grating sensors. J Lightwave Technol 15(8):1442–1463

Koechner W (2006) Solid state laser engineering, 6th edn. Springer, Berlin, Heidelberg, New York

Kumazaki T et al (2008) Reliable high power injection locked 6 kHz 60W laser for ArF immersion lithography. SPIE 6924(198)

Landolt Börnstein (2011) Laser physics and applications, subvolume B: laser systems. Springer, p 229

Lankard JR, Wolbold G (1992) Excimer laser ablation of polyimide in a manufacturing facility. Appl Phys A 355–359

Löhring J, Luttmann J, Kasemann R, Schlösser M, Klein J, Hoffmann D, Amediek A, Büdenbender C, Fix A, Wirth M, Quatrevalet M, Ehret G (2014) INNOSLAB-based single-frequency MOPA for airborne LIDAR detection of CO2 and methane. Proc SPIE 8959:89590J–1–89590J-8

Lowndes DH et al (1996) Synthesis of novel thin-film materials by pulsed laser deposition. Science 273(5277):898–903

Marcuse D (1977) Loss analysis of single-mode fiber splices. Bell Syst Tech J 56:5

Masterson HJ et al (1992) Iron-oxide thin-films produced by laser ablation deposition. J Magent Magn Mater 115(2–3):155–162

Mende J, Schmid E, Speiser J, Spindler G, Giesen A, Thin-disk laser—power scaling to the kW regime in fundamental mode operation. Proc SPIE 7193V-12

Moore GE (1965) Cramming more components onto integrated circuits. Electronics 38(8)

Moulton PF, Harrison J, Martinsen RJ (1998) U.S. Patent 5,774,489

Neuhaus J, Bauer D et al, Subpicosecond thin-disk laser oscillator with pulse energies of up to 25.9 microjoules by use of an active multipass geome-try 16(25):20530. Optics Express

Nighan WL Jr (1995) Laser Focus World 32(5):97

Nilsson J et al (2003) High power fiber lasers: new developments. SPIE

Othonos A (1999) Fiber Bragg Gratings. s.l., Artech House Publishers. ISBN 0-89006-344-3

Pérez-Santonja JJ et al (1997) Laser in situ keratomileusis to correct high myopia. J Cataract Refract Surg 23:372–385

Russbueldt P et al (2015) Innoslab amplifiers. IEEE J Select Top Quantum Electron 21(1):17. Art. 3100117. ISSN: 1077-260X

Setter N, Waser R (2000) Electroceramic materials. Acta materialia 48(1):151–178

Snitzer E (1961) Optical maser action of Nd3+ in a barium crown glass. Phys Rev Lett 7

Sullivan & Frost (2004) U.S. Medical Lasers Markets

Taylor AJ, Gibson RB, Roberts JP (1988) Picosecond gain dynamics in KrF amplifiers. Appl Phys Lett 52:773

The International Technology Roadmap for Semiconductors (2009) Lithography [Online]. http://www.itrs.net/Links/2009ITRS/Home2009.htm

The typical bandwidth obtained in excimer lasers is 0.5 nm for KrF and 0.3 nm for ArF [Online], 13 September 2010. http://www.coherent.com/Lasers/index.cfm?fuseaction=forms.DownloadsFile&DLID=6459

Traub M, Plum H-D, Hoffmann H-D, Loosen P, Poprawe R (2003) Homogenized high power diode laser systems for material processing and illumination. In: Proceedings of the 2nd international WLT-conference on lasers in manufacturing, vol 2, pp 29–32

Voges E, Petermann K (2002) Optische Kommunikationstechnik. Springer, Berlin. ISBN 3-540-67213-3

Part III
Laser Beam Shaping

Chapter 3
Beam Shaping for Laser Material Processing

Martin Traub

Besides output power, pulse shape and wavelength, the intensity distribution on the workpiece is one of the main parameters to optimize laser processes. For the simple case of a diffraction limited Gaussian beam, the only parameter to adapt its intensity distribution to the process requirements is the beam diameter. It depends on the wavelength and the f number of the aberration-free focusing optics, i.e. the ratio of the focal length of the focusing optics and the diameter of the collimated beam entering this optics. Typically, applications like laser powder bed fusion, cutting and marking require very high intensities or small spot sizes, so that they benefit from Gaussian intensity distributions (Fig. 3.1a).

Due to the rotational symmetry of the intensity distribution, the laser process is independent of the orientation of the beam. For applications that do not require the highest intensity but depend on a homogeneous intensity distribution, either a one- or two-dimensional top hat intensity distribution is beneficial. For simultaneous welding of polymers, the whole weld seam is illuminated, so that a homogeneous intensity over the entire weld seam is achieved (Petring et al. 2006). The complete intensity profile is typically formed by rectangular-shaped segments (Fig. 3.1b). If a higher intensity is necessary for the process, a combination of a top hat and a Gaussian intensity distribution as shown in Fig. 3.1c) is beneficial. Typical applications include coating removal, hardening and pumping of slab shaped solid-state laser media (Russbueldt et al. 2015; Traub et al. 2003, 2006). If a comparably low intensity is sufficient, a two-dimensional top hat intensity distribution can be used e.g. for mask illumination (Fig. 3.1d).

The intensity profile $I(x, y)$ can be calculated by

M. Traub (✉)
Fraunhofer ILT, Aachen, Germany
e-mail: martin.traub@ilt.fraunhofer.de
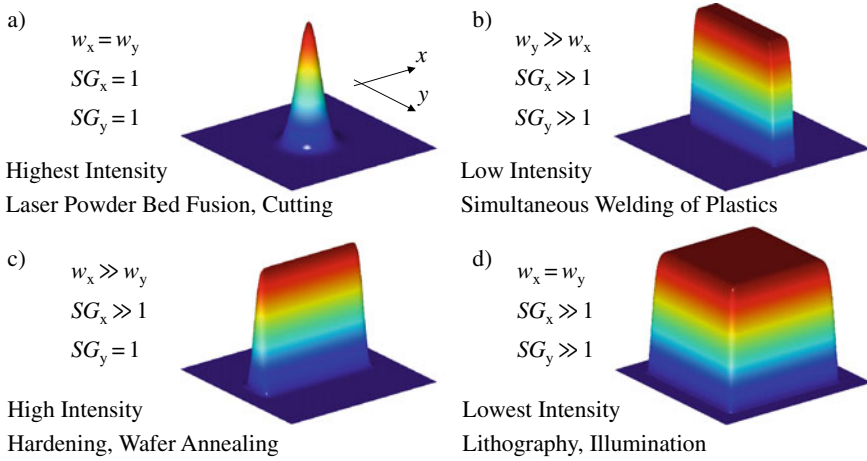
Fig. 3.1 Typical intensity profiles and applications

$$\frac{I(x,\,y)}{I_0} = e^{-2\left(\left(\frac{x}{w_x}\right)^{2SG_x} + \left(\frac{y}{w_y}\right)^{2SG_y}\right)}, \tag{3.1}$$

where $SG_{x,y}$ is the super-Gaussian factor for the x and y direction. For $SG = 1$, the intensity distribution is Gaussian, and for very large values of SG, the intensity distribution corresponds to a top hat distribution. Therefore, the typical shapes of the intensity distributions shown in Fig. 3.1 can be described by a set of four parameters ($w_{x,y}$ and $SG_{x,y}$).

The transformation of an arbitrary to a top hat intensity distribution is called homogenization. For homogenization of multimode high-power lasers, typically two approaches are applied, each based on the segmentation of the far field or near field intensity distribution and overlaying the resulting sub-apertures in the target plane (Traub 2020). The first concept uses either one or two micro-lens arrays for segmentation and a subsequent optical system for overlaying the segments.

The second concept is based on a cuboidal light mixing rod, typically made of a low index and highly transparent material like fused silica. The laser radiation is coupled into the light mixing rod, and it is guided by total internal reflection inside the rod (Fig. 3.2). Alternatively, the light mixing rod can be formed by high-reflective coated substrates or ultra-precision machined copper parts if no sufficiently transparent material is available for the wavelength of the laser to be homogenized.

With every reflection, a segment of the far field is folded back on the central segment. The number of reflections and thus the number of segments overlaid depends on the length and the width of the light mixing rod, the difference between its index of refraction and the index of the surrounding medium, and the divergence of the laser beam coupled into the light mixing rod. As shown in Fig. 3.2, light mixing rods can be used for one- and two-dimensional homogenization of laser beams.

1D:

Beam Source

Coupling Optics

2D:
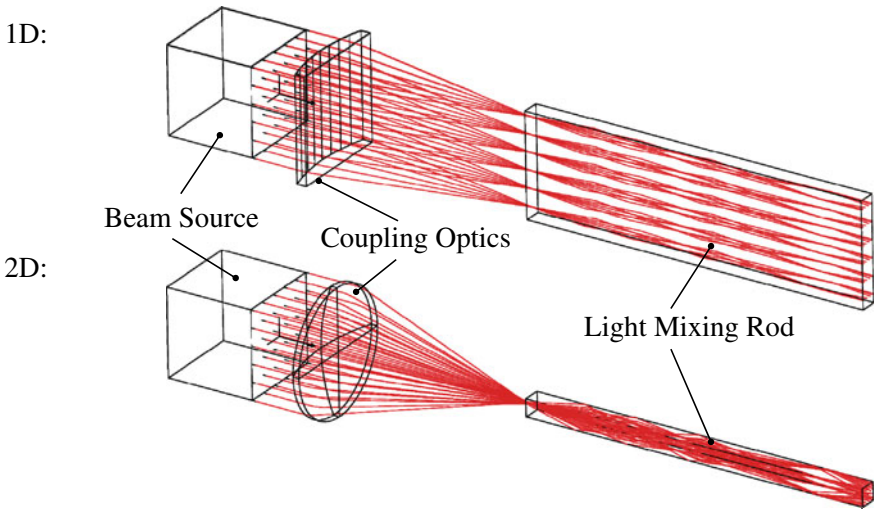
Light Mixing Rod

Fig. 3.2 Homogenization of high-power laser beams based on light mixing rods

For most applications, the exit surface of the light mixing rod is imaged on the work piece by an optical system to maintain a sufficiently large working distance. By using an anamorphic optics, the aspect ratio of the intensity distribution can be adapted.

Figure 3.3 shows the change of the intensity distribution as a function of the length of the light mixing rod for a super-Gaussian (left) and a segmented far field intensity distribution (right). The achieved homogeneity strongly depends on the input far field intensity distribution, thus the dimensions of the light mixing rod have to be thoroughly adapted to the laser beam to be homogenized. The design process is based on non-sequential raytracing. To calculate the intensity distribution inside the light mixing rod, a point source with an either super-Gaussian or segmented far field intensity distribution is placed in front of the entrance surface (Fig. 3.3). Therefore, the intensity distribution on the entrance surface of the light mixing rod corresponds to the far field intensity distribution of the source. While the given setup allows the homogenization of the super-Gaussian far field intensity distribution, the segmented distribution is converted to a modulated distribution at the exit surface of the light mixing rod. The concept is limited to spatially incoherent laser beams to avoid modulations with high spatial frequencies caused by interference.

For applications that benefit from line-shaped intensity distributions with a high aspect ratio, e.g. high-speed cleaning applications as described in Traub et al. (2003), optical setups consisting of scanners, segmented mirrors or cylindrical lenses are used to generate the desired intensity distribution on the workpiece. Typically, scanner-based approaches are too slow to avoid significant overlap of the single laser pulses which decreases the efficiency of the process. In addition, scanning devices based on moving parts usually cannot withstand high mechanical loads like shock or vibration.
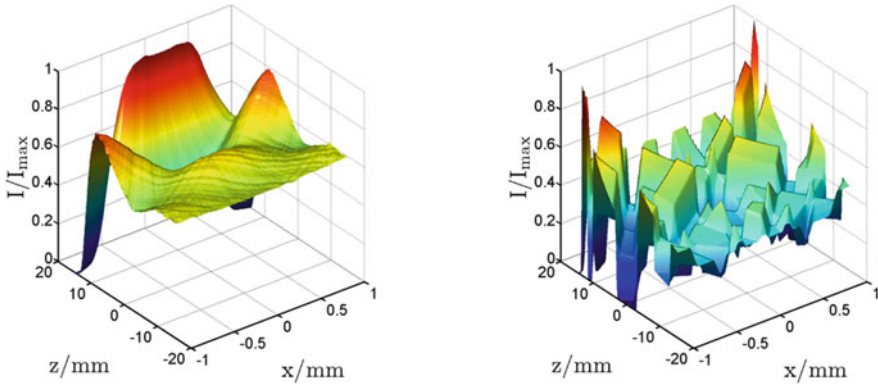
Fig. 3.3 Homogenization of high-power laser beams based on light mixing rods. For a super-Gaussian intensity distribution, an aspect ratio of 20 is sufficient for the given divergence (left), while for the segmented intensity distribution, a residual modulation is observed at the exit surface (right)

Therefore, it is desired to transform the rotationally symmetric intensity distribution to an asymmetric one. For low aspect ratios (typically <10), cylindrical lenses or prisms can be used to generate the line shaped intensity distribution. The limitation is caused by the fact that for constant intensity, the angle of divergence is roughly scaled by the square root of the aspect ratio in the direction where the intensity distribution is small, so that the optical setup gets comparably large for a constant back focal length of the setup, while the depth of focus is also decreased by the same factor.

To overcome this limitation, it is necessary to not only adapt the beam shape in the focal plane, but also to modify the beam parameter product ($BPP = \theta \cdot w_0$) in the two lateral directions x and y. Numerous concepts have been developed for the inverse application of efficiently coupling a highly asymmetric laser beam emitted by a laser diode bar into an optical fiber. The adaption of the BPP is achieved by dividing the laser radiation into n sub-beams which are either rearranged or rotated by 90°. One approach based on a so-called micro-step mirror is shown in Fig. 3.4. The micro-step mirror consists of n steps, each tilted by 45° around the x axis and offset in the z direction, and the offset typically corresponds to the width of the individual step. A second micro-step mirror rearranges the sub-beams generated by the first one.

The laser beam typically exiting an optical fiber is collimated and focused in the y direction on the first micro-step mirror by a cylindrical lens. The height of the beam as well as the depth of focus of the system defined by the fiber, the collimating and the focusing lens have to be adapted to the geometry of the micro-step mirror. For a beam focused in the y direction, the BPP is not affected by the optical system. After the reflection of the sub-beams at the second micro-step mirror, the size of the beam remains nearly constant, while the angle of divergence is swapped by the reflection at the second micro-step mirror. Therefore, the BPP in the x' and y' direction is changed acc. to
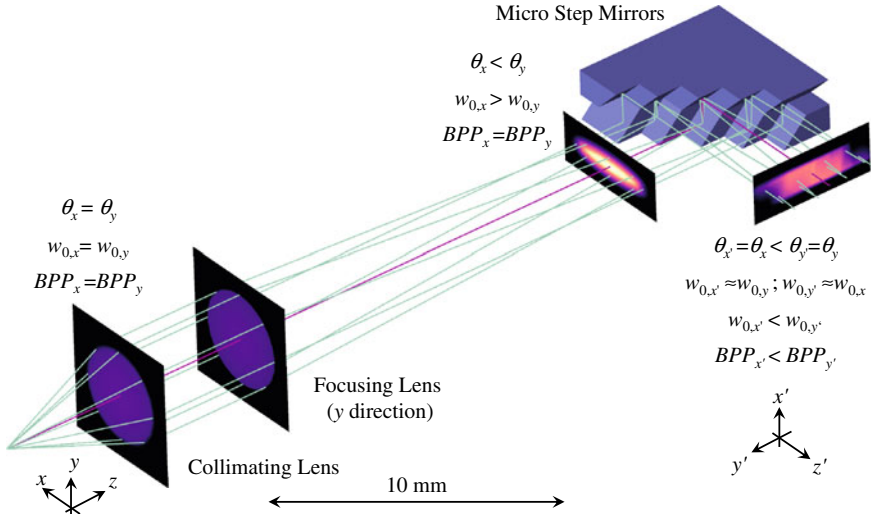
Fig. 3.4 Concept of beam asymmetrization based on micro step mirrors

$$BPP_{x'} \approx \frac{1}{n} BPP_x; \; BPP_{y'} \approx n BPP_y; \; n \approx \sqrt{\frac{BPP_{y'}}{BPP_{x'}}}. \tag{3.2}$$

The number of steps n for a given aspect ratio can be calculated by Eq. (3.2).

The near and far field intensity distributions at different planes of the beam transformation setup based on micro-step mirrors with 5 steps each are shown in Fig. 3.5. Following the pair of micro-step mirrors, a cylindrical telescope is placed to equalize the size of the near field intensity distribution in the x' and y' direction. By focusing the beam with a spherical group, the line-shaped intensity distribution on the work piece is generated. The aspect ratio of the line (Fig. 3.5d) amounts to 22, calculated based on the 2nd moment method.

In addition to the discussed approach based on micro-step mirrors, refractive optical elements can be used for moderate aspect ratios as introduced in Traub et al. (2014). Another setup consisting of plano parallel mirrors is discussed in Huneus et al. (2019). This setup generates a line with a very high aspect ratio of approx. 20,000, suitable for debonding flexible OLED displays. For high-power laser beam sources in the multi-kW regime, the micro-step mirror-based approach offers the advantage of efficient heat removal if the elements are monolithically manufactured of copper. The reflectivity can be increased by applying a suitable HR coating on the reflecting facets of the device.

Spatial Intensity Distribution

Angular Intensity Distribution
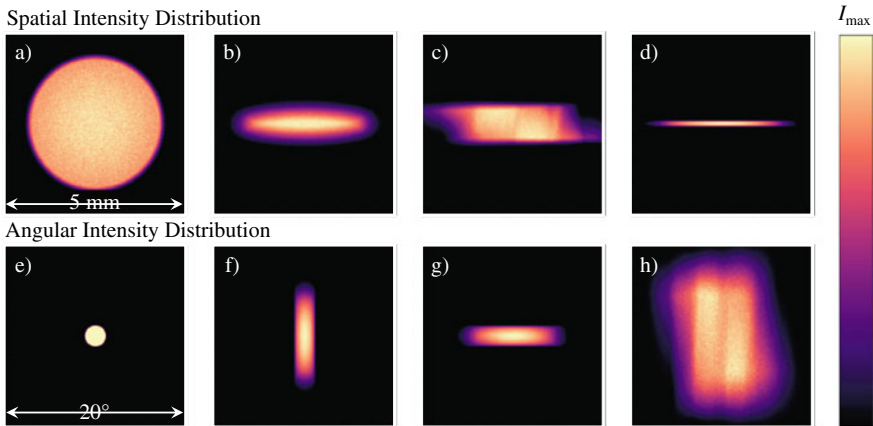
Fig. 3.5 Near field (top row) and far field (bottom row) intensity distribution at different planes of the beam transformation setup based on micro-step mirrors; **a** and **e** show the intensity distribution behind the collimating lens, **b** and **f** in the entrance surface of the first micro step mirror, **c** and **g** in the exit surface of the second micro step mirror, and **d** and **h** on the workpiece after expanding the beam in the x' direction and focusing it with a spherical group

References

Huneus F, Lingel C, Zeller T, Heimes A, Tillkorn C, Janami K (2019) Compact line focus system for laser-based debonding of flexible electronic components. In: Proceedings of the SPIE 10906, Laser-based micro- and nanoprocessing 2019, p 109060G. https://doi.org/10.1117/12.2513763

Petring D, Polzin R, Becker M (2006) Applications. In: Bachmann F, Loosen P, Poprawe R (eds) High power diode lasers. Technology and application. Springer, p 369

Russbueldt P, Hoffmann D, Hoefer M, Loehring J, Luttmann J, Meissner A, Weitenberg J, Traub M, Sartorius T, Esser D, Wester R, Loosen P, Poprawe R (2015) Innoslab amplifiers. IEEE J Sel Top Quantum Electron 21(1):447–463. https://doi.org/10.1109/JSTQE.2014.2333234

Traub M (2020) Erzeugung prozessangepasster Leistungsdichteverteilungen für die Lasermaterialbearbeitung. PhD thesis, RWTH Aachen University

Traub M, Meyer R, Hoffmann H, Loosen P, Poprawe R (2003) High speed cleaning of railheads with a fiber-coupled Nd:YAG laser. In: Chen X, Duley WW, Farson D, Ostendorf A (eds) Proceedings of the 22nd international congress on applications of lasers and electro-optics, Orlando, LIA, pp 1504-1-6

Traub M, Hoffmann H, Plum D, Wieching K, Loosen P, Poprawe R (2006) Homogenization of high power diode laser beams for pumping and direct applications. In: Proceedings of the SPIE 6104, High-power diode laser technology and applications IV, p 61040Q. https://doi.org/10.1117/12.645260

Traub M, Hoffmann D, Hengesbach S, Loosen P (2014) Automatic design of multi-lens optical systems based on stock lenses for high power lasers. In: Proceedings of the SPIE 9293, International optical design conference 2014, p 92931I. https://doi.org/10.1117/12.2074508

Chapter 4
Adapted Beam Shaping Using Free-Form Optics

Annika Völl

As has been shown in Sects. 2.3 and 2.4, the laser beam energy is thermalized in a processed material and, when no phase transitions occur, the induced temperature distribution can be calculated using a heat conduction equation. Therein, a relevant quantity with influence on the temperature distribution is the laser beam's intensity distribution. In the subsequent chapters, it will further be described for various thermal treatment applications that the process results on the other hand strongly depend on the realized temperature distribution. Consequently, the process quality and efficiency can be increased by adapting the laser beam's intensity distribution to the particular process. To realize a given optimal temperature distribution, this requires two steps: At first, the necessary intensity distribution must be derived from the desired temperature distribution and afterwards the obtained intensity distribution must be realized in an experimental setup through an adapted optical system.

For the derivation of the necessary intensity distribution, the situation can be formulated as an inverse heat conduction problem (see Fig. 4.1). *Inverse* here refers to the fact that—instead of calculating the resulting temperature distribution from a known heat source (which is a *direct* heat conduction problem)—the required intensity distribution is derived from information on the necessary temperature distribution. This information usually does not include the complete temperature distribution—in this case the intensity distribution can be calculated straightforward using equation 2.109—but only some parts of it. For example, a homogeneous temperature distribution within the irradiated area might be advantageous to obtain a homogeneous heat treatment result.

Because in the inverse heat conduction problem the cause must be calculated from its effect, this problem is a lot more elaborate than the equivalent direct heat conduction problem. In fact, it has been shown that the problem is *ill-posed* which here means that the problem's solution is very unstable and it is necessary to apply sophisticated

A. Völl (✉)

Chair for Technology of Optical Systems, RWTH Aachen University, Aachen, Germany
e-mail: annika.voell@tos.rwth-aachen.de
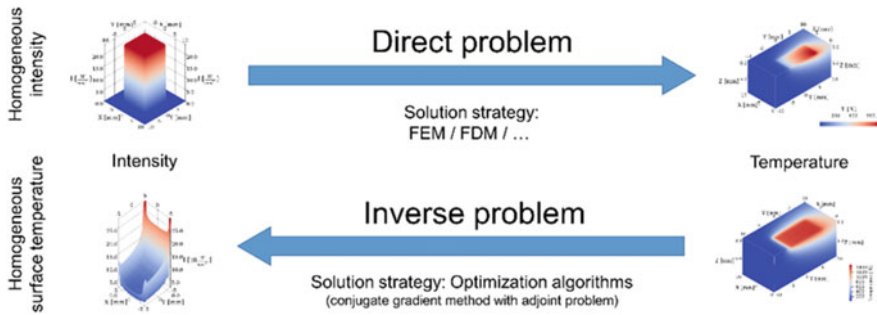
Fig. 4.1 Definition of the inverse heat conduction problem for the examples of homogeneous intensity and temperature distributions respectively

numerical optimization algorithms (Völl et al. 2018). However, the benefit of using numerical strategies is that complexities such as temperature-dependent thermophysical and optical material properties or different workpiece geometries can be taken into account easily.

The intensity distributions that are obtained in such a way usually are very inhomogeneous and often exhibit strong variations. In its lower part, Fig. 4.1 shows exemplarily the intensity distribution that is necessary to obtain a homogeneous intensity distribution within the irradiated area on a steel workpiece assuming that the laser is moving with a feed rate of 10 mm/s. The intensity distribution is not rotational symmetric and shows strong peaks on its edges. Thus, to realize such intensity distributions in an experimental setup optical designs are necessary that go beyond conventional beam shaping strategies. Especially, it is not possible to use spherical or other rotational symmetric optical components. From the different beam shaping strategies that can be applied so-called free-form optics have been proven appropriate. In comparison with conventional spherical or aspherical components, free-form optics provide many more degrees of freedom that can be adapted to form the surfaces of the components nearly arbitrarily. By specifically adapting the surface curvature locally, each incident ray is thus deflected by the optical surface in a particular way so that in total the combination of all rays form a certain intensity pattern on the target surface (see Fig. 4.2). As an example, a free-form optics can be designed that forms the intensity patterns from Fig. 4.1 when illuminated with a conventional diode laser beam. As the prediction of the geometric form that is required for an optical surface to provide such a functionality is rather sophisticated the design of free-form optics is again performed using numerical strategies. Here, different design algorithms depending on the characteristics of the light source, e.g. the beam quality or the degree of coherence, can be implemented. One exemplary algorithm is described in Bäuerle et al. (2012).

Free-form optics present of course not the only possible strategy to realize application adapted intensity distributions. As their surfaces are fixed, it is especially not possible to realize time-dependent intensity distributions using free-form optics. In these cases, other beam shaping objects such as deformable mirrors or VCSELs can
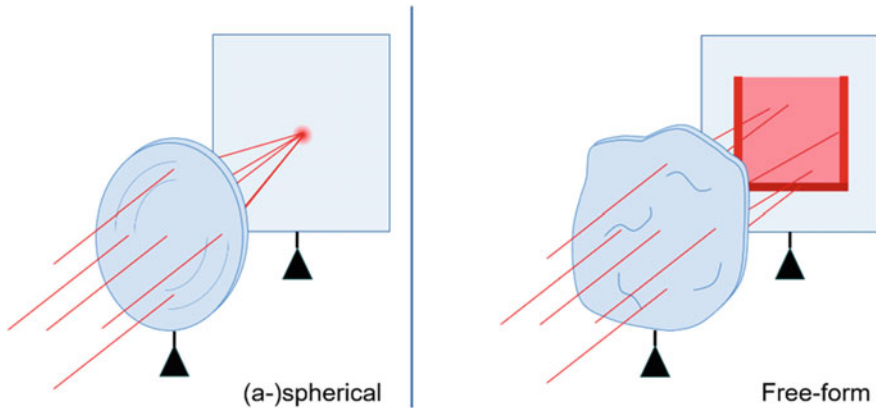
Fig. 4.2 Difference between a conventional optics and a free-form optics for laser applications: A conventional optical system usually consists of spherical or aspherical lenses and is designed to e.g. generate the smallest possible laser spot. With a free-form optics, the light of the laser source is deflected to generate a prescribed intensity distribution

be applied. Deformable mirrors can be realized in the form of a so-called LCoS (*liquid crystal on silicon*) wherein a layer of liquid crystals is pixelated and the liquid crystals in each pixel are oriented independently through an applied voltage. In consequence, light reflected by different pixels obtains specific phase shifts which results in total in a defined phase profile of the laser beam. Through focussing, this can be transformed into an intensity distribution. VCSELs (*vertical surface emitting lasers*) on the other hand are special realizations of laser diodes where the light is emitted perpendicularly to the layer structure. In this way, different emitters are arranged in plane and can be addressed individually. Using this, temporal and spatial varying intensity distributions can be realized. However, at the moment, only a 1D spatial variation is available in commercial high-power VCSEL products.

Combining these two steps of deriving and realizing such intensity distributions application adapted beam shaping is enabled for various heat treatment applications. In 1988 (Burger 1988), an application adapted intensity distribution has been realized for the first time for the process of laser hardening (see also Sect. 5.2). This intensity distribution (see Fig. 4.3) is designed to obtain a homogeneous temperature distribution of 1450 °C within the irradiated area of 10 mm × 10 mm on the surface of a steel workpiece. In this case, the intensity distribution is realized with a scanner that is deflecting the beam with a varying speed fast enough so that the deposited energy can in a first approximation be integrated over time. Using this intensity distribution broader, more homogeneous heat tracks and thus a higher process efficiency are obtained when compared to other beam shaping strategies. More recently, intensity distributions have been derived for further applications as, for example, for the laser-based softening of high strength steels (Völl et al. 2018; Vogt et al. 2019). Here, the challenge is that a thin steel sheet shall be softened using a high feed rate. Using conventional beam shaping strategies such as a tophat-intensity no constant

Fig. 4.3 Application
adapted intensity distribution
for laser hardening
generating a constant
temperature distribution
within the irradiated surface
area. The distribution has
been calculated using the
method from Burger (1988)
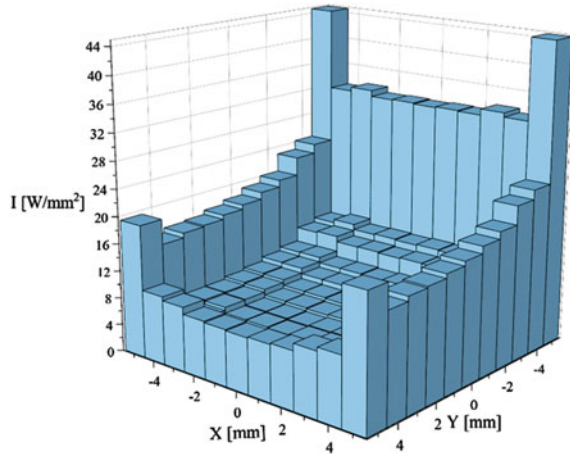
Fig. 4.4 Hardness
measurement comparison for
two different intensity
distributions: a
tophat-intensity and an
application adapted intensity
that has been realized with a
free-form optics. The
development of the hardness
throughout the sheet is very
homogeneous for the
application adapted intensity
distribution. Reproduced
from Vogt et al. (2019), with
the permission of the Laser
Institute of America
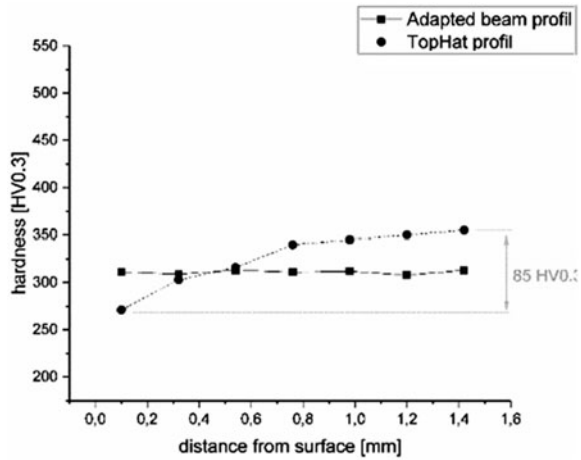
hardness throughout the thickness of the sheet can be obtained, especially as the surface temperature becomes too high. Thus, an application adapted intensity distribution is calculated that keeps the surface temperature constant for a comparatively long time so that the heat can diffuse throughout the sheet. This intensity distribution is comparable to the one in Fig. 4.3 and has been realized experimentally with a free-form optics. As a result, it is possible to obtain a homogeneous hardness over the complete thickness even for a feed rate as high as 10 m/s (see Fig. 4.4). Further application adapted intensity distributions have been realized for laser-assisted tape placement and—under certain assumptions—for the functionalization of thin layers.

To what extent these strategies can be transferred to processes where the material undergoes a phase transition is currently under investigation.

References

Bäuerle A, Bruneton A, Wester R, Stollenwerk J, Loosen P (2012) Algorithm for irradiance tailoring using multiple freeform optical surfaces. Opt Express 20:14477–14485

Burger D (1988) Beitrag zur optimierung des Laserhärtens, Ph.d Thesis, Univ Stuttg

Vogt S, Völl A, Wollgarten S, Freese T, Stollenwerk J, Weisheit A, Loosen P (2019) Local laser softening of high-strength steel with an adapted intensity. J Laser Appl 31(1):012007. https://doi.org/10.2351/1.5052147

Völl A, Vogt S, Wester R, Stollenwerk J, Loosen P (2018) Application specific intensity distributions for laser materials processing: tailoring the induced temperature profile. Opt Laser Technol 108:583–591

Part IV
Surface Treatment

Chapter 5
Laser Softening of High-Strength Steels

Sabrina Vogt, Andreas Weisheit, and Konrad Wissenbach

5.1 Motivation

Considering climate change as a result of human malpractice through greenhouse gas emissions, amongst others in road traffic, the automotive industry is striving to optimize energy efficiency by reducing the general fuel consumption of automotive vehicles. At the same time, crash safety specifications are constantly being tightened. A lever to satisfy both issues is the net mass reduction of a car through new lightweight construction strategies by high-strength steels.

Cold forming steels (International Iron Steel Institute; Bleck 2012) and press-hardened steels (Overrath et al. 2010; Merklein and Lechler 2006) are used in car body construction. Depending on the elongation at fracture and the yield strength, the cold forming steels are subdivided into different groups. IF steels have the highest elongations at fracture (40–50%) at low yield strengths (<250 MPa), PM steels have the lowest elongations at fracture (5–15%) and the highest yield strengths (>1200 MPa). In between are bake hardening, micro alloyed, dual-phase, TRIP and CP steels.

Press hardening makes it possible to achieve good formability during pressing with minimal springback and excellent strength through martensite transformation by controlled cooling. In the initial state, manganese-boron steels have a ferritic-perlitic microstructure and yield strengths between 350 and 550 MPa and an elongation at a fracture of up to 20%. After hot forming—or press hardening—the steel has a martensitic microstructure with a yield strength between 1000 and 1200 MPa and an elongation at fracture of approx. 5% (Weber 2008).

Typical widely used representatives of these steels are the press-hardened manganese-boron steel MBW® 1500 (manufactured and press-hardened by Thyssenkrupp Steel Europe) (22MnB5) and the cold-rolled strip ZE 1100 (developed and cold rolled by BILSTEIN GROUP). Offering superior mechanical properties

S. Vogt · A. Weisheit (✉) · K. Wissenbach
Fraunhofer ILT, Aachen, Germany
e-mail: andreas.weisheit@ilt.fraunhofer.de

and thus crash performance, press-hardened steels allow the construction of thinner components e.g. B-pillars and side sills. With hot stamping, complex geometries can be formed while high strength is achieved when the part is hardened in a cooled die. In the case of the manganese-boron steel MBW® 1500, the tensile strength is 1500 MPa after hot stamping (Overrath 2010; Merklein and Lechler 2006).

On the other hand, cold forming steels can be hardened by means of cold rolling. A tensile strength up to 1200 MPa can be achieved by this process for low alloyed steels. Typical components for cold forming steels are e.g. seat rail and safety components, such as airbag parts or buckles of seat belts.

However, the high strength of these steels also require changes in further processing steps, such as joining and cold forming (when used in the cold-rolled state). For mechanical joining of hot stamped parts with aluminum parts using rivets, the maximum allowed strength is 600 MPa using standard tools (Abe et al. 2009). In Burget and Sommer (2012), it was shown that after spot welding of hot stamped parts, the heat-affected zone around the welded spot reduces the strength of the joint. During the cold forming of cold-rolled steel strips, critical degrees of deformation can occur locally which causes crack formation during the forming process. Thus, it is necessary to integrate softening steps in the process chain of such workpieces. Here, a laser based heat treatment hereinafter referred as laser softening offers the possibility to process areas locally and thus create areas with defined strength profiles (Bergweiler 2013; Vogt 2019; Vogt et al. 2018, 2019). This targeted integration of localized areas in the workpieces then allows mechanical joining, avoiding the formation of metallurgical notches during spot welding and improving the forming properties during cold forming.

5.2   Process Description and Materials

The process management for laser softening is very similar to that of laser hardening. During softening, the workpiece is also exposed to a defined temperature–time curve. The heat input is achieved by absorption of the laser radiation and thermalization of the optical energy. The movement of the laser beam over the steel plate produces individual tracks (Fig. 5.1). Fiber-coupled diode lasers with wavelengths between 940 and 1060 nm and output powers >10 kW are predominantly used as laser beam sources. Homogenization optics (zoom homogenizer type), which generate a rectangular laser beam with a homogeneous intensity distribution, are mainly used for softening.

As in laser hardening, the softening process is usually temperature-closed-loop controlled, whereby the emitted heat radiation is measured with a pyrometer. Depending on the material, the sheet thickness, the required softening geometry and the process parameters, in particular the beam geometry and the processing speed, a set value for the relative temperature of the pyrometer is determined, from which the laser power is calculated as a manipulated variable. Since the absorptivity and thus also the emissivity change during the softening process, e.g. due to oxidation
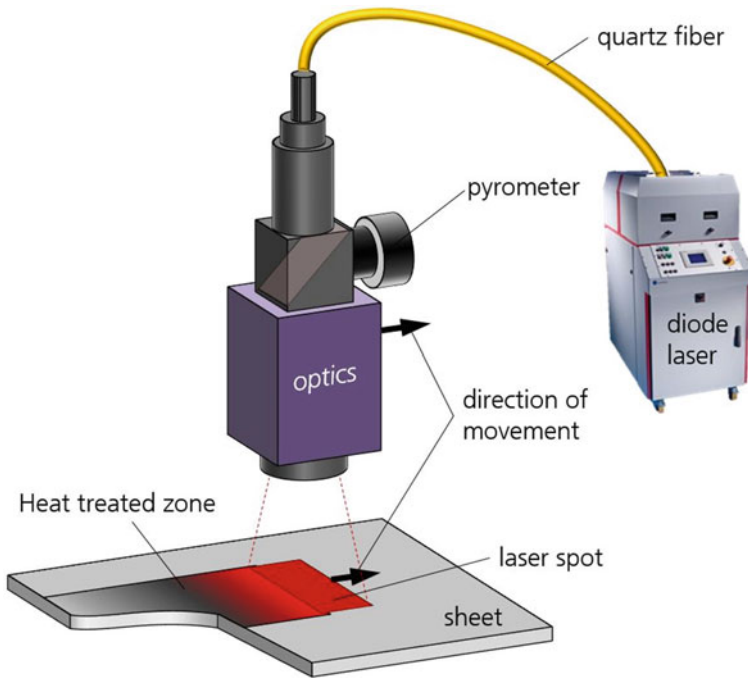
Fig. 5.1 Experimental setup for local laser heat treatment of high-strength steel sheets

of the sheet surface, the calibration of the pyrometer cannot be carried out via the emissivity. Calibration is performed by measuring the temperature with thermocouples on the back side of the sheet and correlating it with the measured pyrometer values during softening on the sheet surface. By varying the temperature set value of the pyrometer and thus the laser power, calibration curves are determined that show the relationship between the pyrometer value and the maximum value of the thermocouple measurements (Bergweiler 2013; Vogt 2019). These calibration curves are correlated with the microstructural changes resulting from laser softening and the associated hardness values.

As already mentioned above, results for the two materials MBW® 1500 and ZE 1100 are presented below. Both materials are available in sheet form with a thickness of 1.5 mm. Table 5.1 shows the mechanical properties and the coating state of the materials.

After hot stamping the microstructure of MBW® 1500 (Fig. 5.2, left) is fully martensitic, with a hardness of around 505 HV 0.3. The MBW® 1500 is coated with an aluminum–silicon (AS) coating to prevent oxidation during press hardening and

Table 5.1 Material properties of the press-hardened steel MBW® 500 and cold-rolled strip ZE 1100

Material	MBW® 1500 (22MnB5)	ZE 1100
Steel type	Press-hardened	Cold-rolled strip
Coating	AS 150	Uncoated
Tensile strength [MPa]	1470 ± 8	1132 ± 26
Elongation A_{80} [%]	4.6 ± 0.3	2.5 ± 0.2
Hardness [HV 0.3]	505 ± 8	360 ± 7

provide corrosion protection in use. For laser heat treatment, this layer exhibits the following optical characteristics:

- High absorptivity (~83%) for the wavelengths emitted by the diode laser (940–1060 nm)
- Oxidation resistance up to 900 °C: During the laser heat treatment process no oxidation occurs and the absorptivity for the laser radiation remains constant
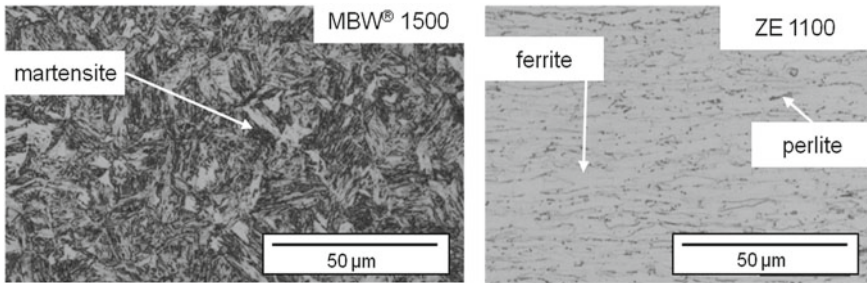
Fig. 5.2 Microstructure in the initial state of MBW® 1500 (left) and ZE 1100 (right)

ZE 1100 exhibits a ferritic-perlitic microstructure (Fig. 5.2, right) and shows lines, stretched and work-hardened rolled structure, with a hardness of around 360 HV 0.3. The material is not coated. This material has the following optical properties:

- Medium absorptivity (~41%) for the wavelengths emitted by the diode laser (940–1060 nm)
- Oxidation occurs during the laser heat treatment and the absorptivity is increased (~82%)

5.3 Experimental and Simulation Results

The following procedure is usually applied to determine the process parameters for a rectangular beam geometry generated by a zoom optics (Vogt 2019): First, a beam width s_B is specified which results, for example, from the width of the area to be softened. The beam length s_L in the feed direction and the feed speed v_S are used to determine the interaction time t_W:

$$t_W[ms] = (s_L[mm]/vs\,[mm/\min]) * 60 * 10^3 \qquad (5.1)$$

The depth of the softened zone is determined by the interaction time in combination with the specified surface temperature. The beam length is limited by the zoom optics used or by the available laser power in order to achieve the required intensity in combination with the specified beam width. The feed speed then remains as the process parameter to be adjusted. For different combinations of beam width, beam length and feed speed, the measured maximum temperatures on the backside of the sheet varied between 500 and 1000 °C. In process engineering, these maximum temperatures are varied by varying the setpoint values of the closed-loop temperature control in 50 °C steps. The process parameters are varied in order to determine their influence on the microstructure and the mechanical characteristic values.

Using the Finite Element Method (FEM), the temperature differences between the top and back side of the sheet can be calculated by simulating heat conduction (Pirch et al. 2017). The larger the interaction time, the smaller the temperature difference between the top and back side of the sheet. This relationship is shown in Fig. 5.3. If the feed speed is too high, the interaction time becomes too short for a homogeneous temperature distribution over the sheet thickness during the process. With an interaction time of less than 1000 ms, the temperature difference is larger than 50 °C between the top and back side of the sheet. The influence of the temperature differences between the top and back side of the sheet on the mechanical properties is shown below.

The influence of different process parameters on the ZE 1100 is illustrated below. Figure 5.4 shows the average hardness (averaged over 20–30 hardness values in the width and depth of the heat treated zone) of ZE 1100 for different parameter sets (different laser spot dimensions and feed speeds and thus different interaction times) over the maximum temperature on the back side of the sheet. Below 700 °C, the average hardness corresponds approximately to the hardness of the initial state.

Below a maximum temperature of 750 °C, the microstructure has a linear, elongated rolling structure identical to the initial state (Fig. 5.5a). A reduction of work hardening induced by rolling is not observed. Above 750 °C significant softening is achieved down to below 200 HV 0.3 (190 HV 0.3 at approx. 820–840 °C). The reduction in hardness can be explained by the reduction in dislocation density by short-term recrystallization, since the microstructure is formed completely new. In contrast to the initial state, the globular microstructure has no preferred orientation and contains both ferritic and pearlitic phase fractions (Fig. 5.5b). At maximum
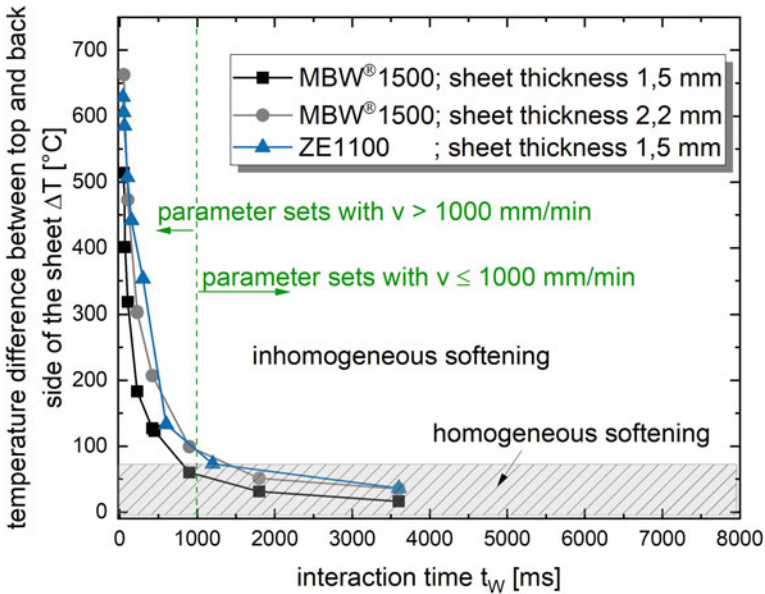
Fig. 5.3 With FEM simulation calculated temperature difference between top and back side of the sheet in dependence of the interaction time

temperatures above 840 °C, both ferritic and local bainitic phase fractions can be detected in the microstructure, resulting from partial austenitisation during laser heat treatment. Due to high cooling rates, which are larger than 30 K/s (measured on the basis of the gradient in the temperature–time curve from 800 to 500 °C), needle-like bainite structures are formed (Fig. 5.5c). The hardness increases to approx. 250 HV 0.3.

Below the maximum temperatures of 700 °C, the hardness exhibits small standard deviations (Fig. 5.4), since no short-term recrystallization takes place in this temperature range. The large standard deviations of the hardness in the temperature range between 700 and 780 °C can be explained by the fact that with these process parameters there are temperature differences over the sheet thickness of approx. 50 °C (Bergweiler 2013) and the upper area of the sheets has reached the recrystallization temperature. In the lower area of the sheet, the temperature is not high enough to cause recrystallization. These hardness fluctuations correlate with the local microstructure (Fig. 5.6). For a maximum temperature of 740 °C, recrystallization is only achieved in the upper area, while the elongated rolled structure is still visible in the middle and bottom of the sheet. At a maximum temperature of 840 °C, however, recrystallization takes place over the entire thickness of the sheet. In order to achieve a homogeneous softening over the sheet thickness of 1.5 mm, the maximum temperature on the top side of the sheet must be approx. 50 °C above the starting recrystallization temperature (approx. 0.4 of the melting temperature) of the material.
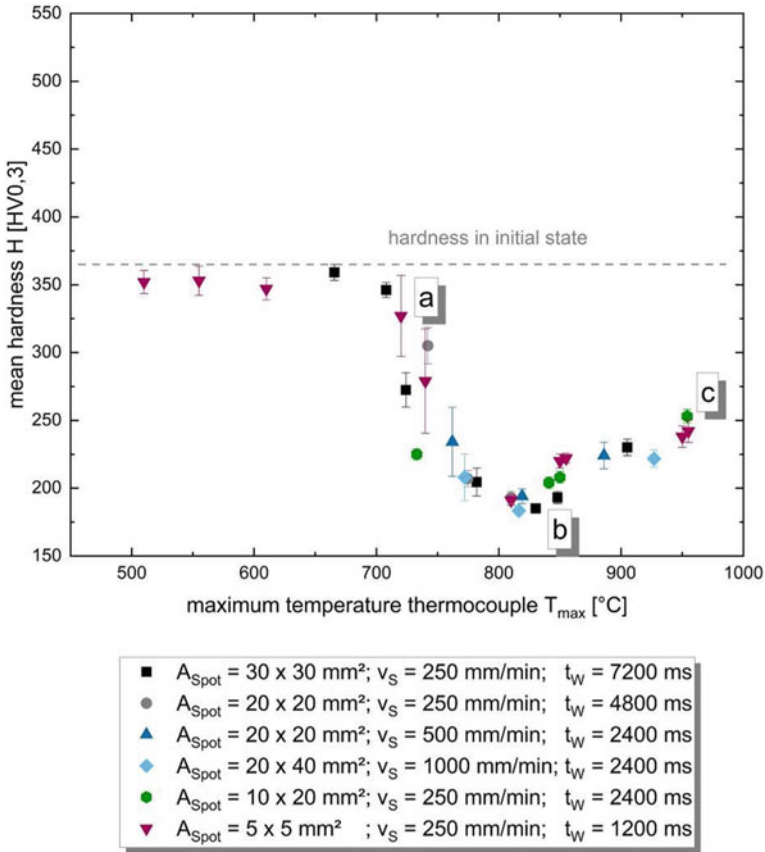
Fig. 5.4 Mean hardness in dependence of maximum temperature (measured with thermocouples at the back side of the sheet) after laser heat treatment of ZE 1100 (sheet thickness: 1.5 mm), with closed-loop temperature control
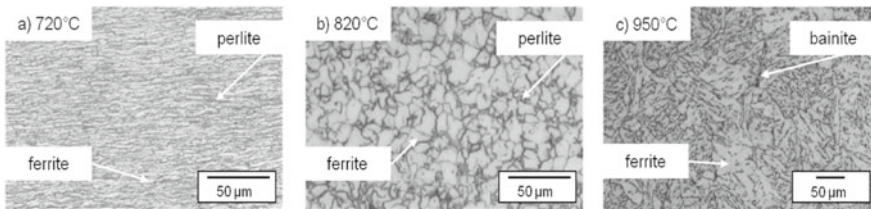
Fig. 5.5 Microstructure (in the middle of the sheet) of ZE 1100 at different maximum temperatures (measured with thermocouples at the back side of the sheet) after laser heat treatment, processing parameters: $v_S = 250$ mm/min, $A_{Spot} = 5 \times 5$ mm^2, with closed-loop temperature control
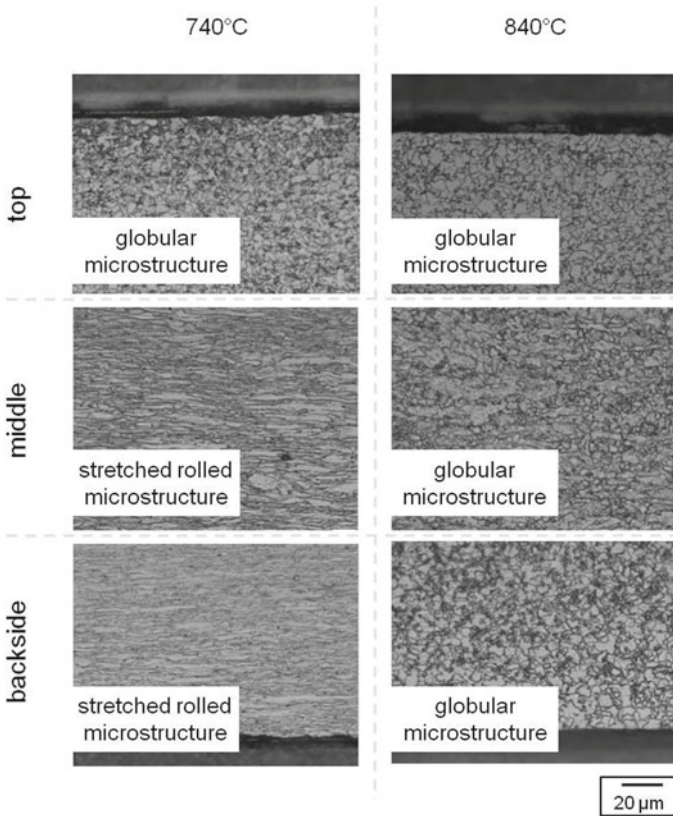
Fig. 5.6 Microstructure at the top, middle and backside of the sheet for two different maximum temperatures (measured with thermocouples at the backside of the sheet) after laser heat treatment of ZE 1100; processing parameters: $v_S = 250$ mm/min, $A_{Spot} = 5 \times 5$ mm^2, with closed-loop temperature control

Figures 5.7 and 5.8 show the mechanical characteristic values obtained from tensile tests as a function of the maximum temperature for ZE 1100. The tensile strength shows a similar temperature dependence as the hardness (Fig. 5.4). The tensile strength is reduced by short-term recrystallization from 1132 ± 26 MPa in the initial state with increasing maximum temperature to 556 ± 7 MPa at approx. 850 °C. The yield strength is reduced from 1123 MPa $\pm$ 27 MPa to 518 MPa $\pm$ 9 MPa. The tensile strength and yield strength have no significant difference in the values and, depending on the maximum temperature, have almost the same characteristics. Ductility (uniform elongation and elongation at break) increases with decreasing strength (Fig. 5.8) due to recrystallization accompanied by the globular microstructure. The elongation at break is increased from $2.5 \pm 0.2\%$ to $19 \pm 1.5\%$. The maximum softening is achieved in the temperature range between 800 and 850 °C. At maximum temperatures above 850 °C, smaller elongations and larger strengths
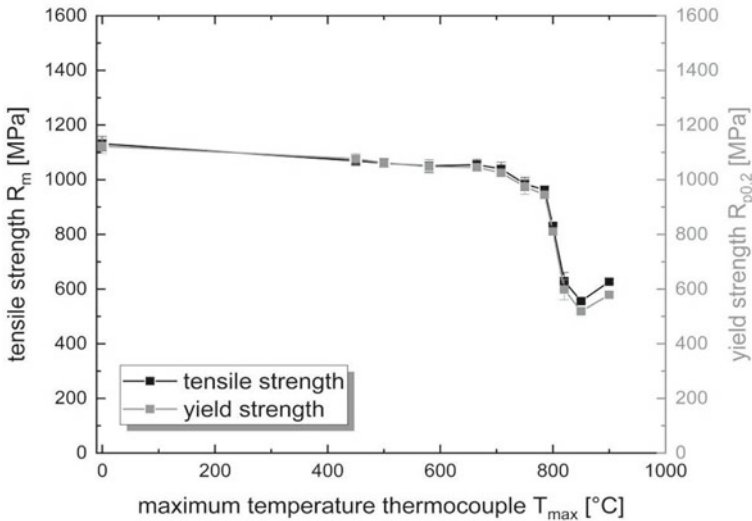
Fig. 5.7 ZE 1100: tensile and yield strength in dependence of maximum temperature, process parameters: spot dimensions: 30×30 mm^2, $v_s = 500$ mm/s, with closed-loop temperature control

are achieved analogous to the hardness curve, since needle-like bainite structures are formed in the microstructure.

The same procedure was applied for the material MBW® 1500 + AS. But only selected results are presented below.

Depending on the temperature, two different softening effects are observed for MBW® 1500 + AS (Bergweiler 2013; Vogt 2019):

- $T = 200$–723 °C: Tempering of martensite
- $T > 723$ °C (A_{c1}): Partial austenitisation and formation of a ferrite/perlite microstructure during cooling (provided that the cooling rate is less than 27 K/s)

Cross sections of samples with interaction times of 3600 and 1800 ms, respectively, are shown in the Fig. 5.9. The microstructure of the top, center and bottom area of the sample sheet is depicted. Samples exposed at an interaction time of 3600 ms (right) show maximum softening. The maximum temperature at the bottom of the sheet is 775 °C and thus above austenitisation temperature. The resulting microstructure consists predominantly of ferrite and cementite. The microstructure is homogeneous across the complete sheet thickness. The shorter interaction time of 1800 ms (left) results in an inhomogeneous microstructure. The temperature at the bottom of the sheet is 650 °C and therefore no ferritic/perlitic transformation has occurred resulting in a tempered martensitic microstructure. The maximum temperature at the top of the sheet is approx. 720 °C. In the heat treated zone a minimum hardness of about 200 HV 0.3 can be achieved.

Due to high feed speeds and the resulting temperature difference over the thickness of the sheet, different microstructures result and accordingly a difference in hardness
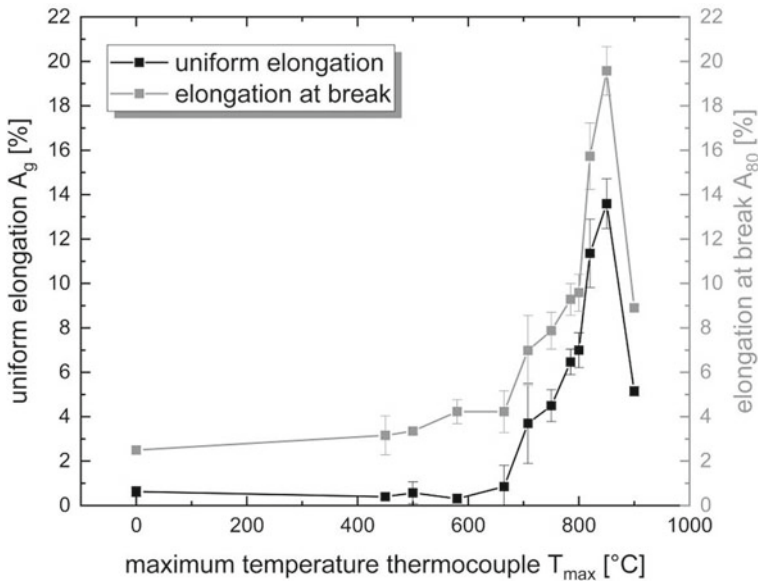
Fig. 5.8 ZE 1100: uniform elongation and elongation at break in dependence of maximum temperature; process parameters: spot dimensions: 30×30 mm^2, $v_s = 500$ mm/s, with closed-loop temperature control

over the thickness of the sheet can be observed.

$$\Delta H = H_{PU} - H_{PO} \tag{5.2}$$

ΔH is the difference in hardness over the thickness of the sheet, H_{PU} is the hardness on the back side and H_{PO} the hardness on the top side of the sheet. Figure 5.10 shows the relationship between hardness difference and interaction time for both materials. A qualitatively identical course as in Fig. 5.3 can be observed for both materials. The temperature difference correlates directly with the hardness differences. In order to achieve a homogeneous hardness distribution ($\leq \pm 10$ HV 0.3), the process parameters laser spot length and feed speed must be adapted so that the interaction time is larger than 1000 ms for a sheet thickness of 1.5 mm. Consequently, it can be stated from Fig. 5.3 that a maximum temperature difference of 50 °C must be achieved for a sheet thickness of 1.5 mm in order to achieve a homogeneous hardness distribution.

In Fig. 5.11 the hardness distribution of five specimens treated with different interaction times are shown for MBW® 1500 + AS. Five tensile tests were carried out per parameter set. The influence of the hardness on the interaction time (Fig. 5.11) correlates with the hardness and interaction time from Fig. 5.10. Macroscopically, all of the specimens are showing a ductile fracture behavior with a characteristic 45° fracture angle. This is the case even for the non-treated specimens, which can
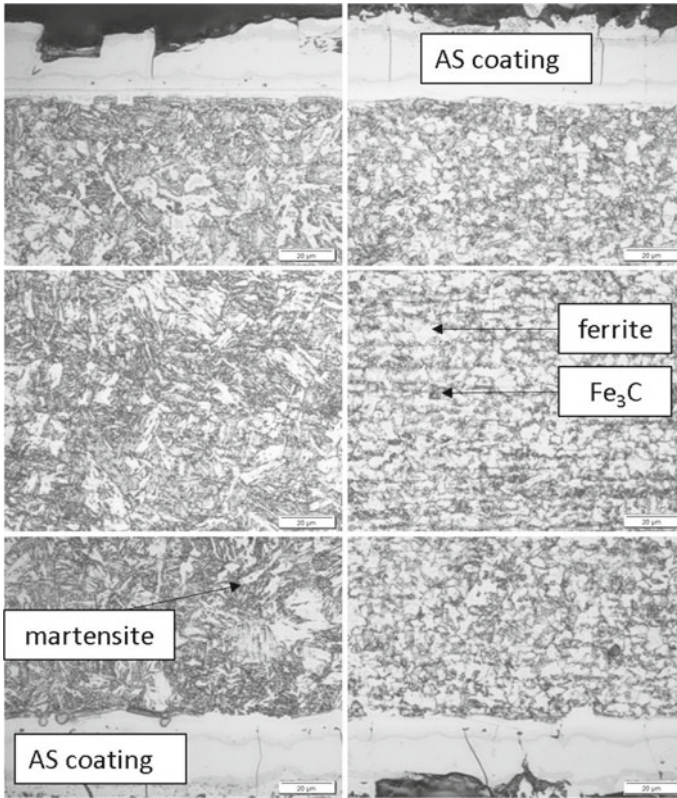
Fig. 5.9 Micro sections after laser heat treatment of MBW® 1500 + AS with interaction time 1800 ms (left) and 3600 ms (right)
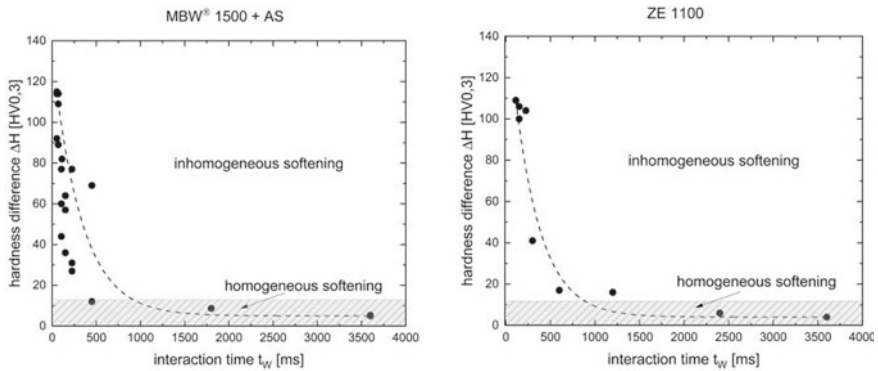
Fig. 5.10 Hardness difference between top and back side of the sheet with a thickness of 1.5 mm in dependence of the interaction time; hatched area represents the area of homogeneous softening left: MBW® 1500 + AS, right: ZE 1100
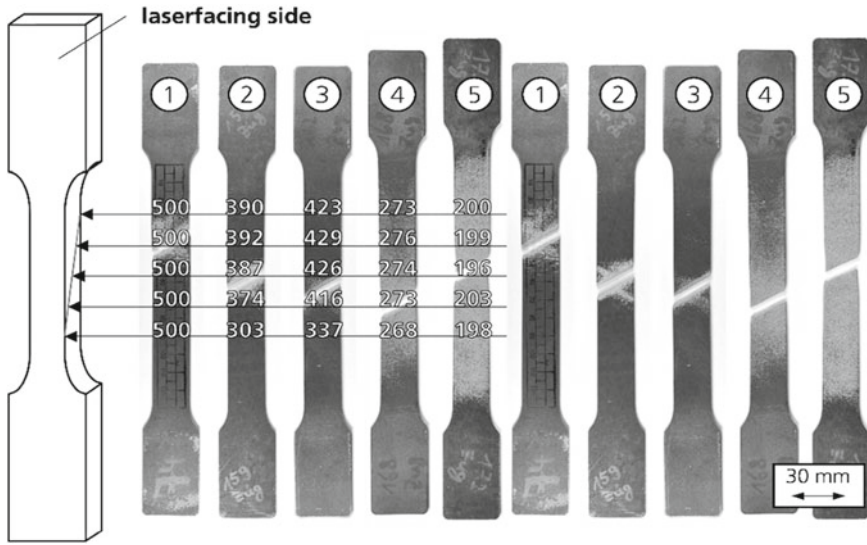
Fig. 5.11 Tensile test specimens with hardness distribution [HV 0.3] across the thickness, the parameters of specimens are: 1: initial state MBW® 1500 + AS; 2: $t_W = 70$ ms; 3: $t_W = 52.5$ ms; 4: $t_W = 1800$ ms; 5: $t_W = 3600$ ms

be attributed to the reasonable plastic strain of 4.6% until fracture. The brittle AS coating spalls when the sample is deformed.

In Fig. 5.12 the reduction of tensile and yield strength (left) and increase of elongation at break (right) in dependence of the interaction time is shown. In correspondence to the hardness the tensile strength is decreased almost linearly. The smaller the exposure time, the larger the hardness difference and the tensile strength. The tensile strength of 1500 MPa in the initial state can be reduced to a minimum of 640 MPa and the yield strength of 1130 MPa to 470 MPa, which is directly connected to the ferrite/perlite microstructure. The elongation at break of 4.6% in the press hardened MBW® 1500 + AS can be increased to a maximum of 17%.
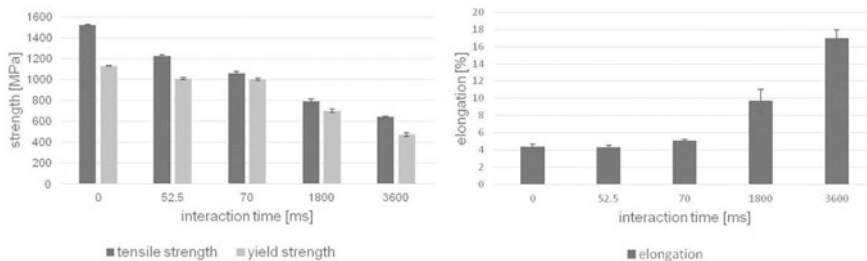
Fig. 5.12 Mechanical properties of MBW® 1500 + AS in dependence of interaction time
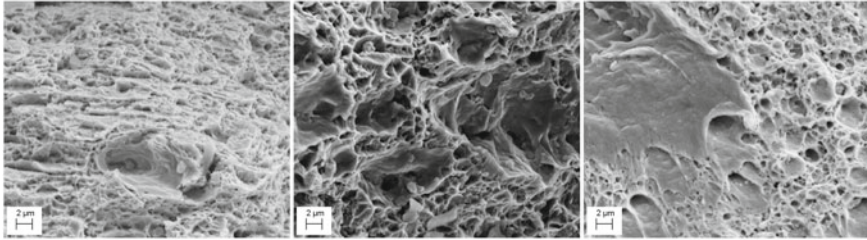
Fig. 5.13 SEM images of the fractured surface of the tensile test specimens made of MBW® 1500, Left interaction time 3600 ms, middle: interaction time 1800 ms, right: interaction time 70 ms

The fracture surfaces of all tested specimens exhibit a ductile dimple fracture mode (Fig. 5.13 left and middle). Brittle fracture (cleavage mode) could only be observed locally (Fig. 5.13 right) attributed to residual martensite.

Plate bending tests according to VDA 238–100 were performed in order to investigate the bending behavior of the laser heat treated sheets. The results are shown in Fig. 5.14. The abort criterion for this test is a reduction of the bending force of 30 N. The material in the press hardened state exhibits a maximum bending angle of about 50°. All investigated heat treated specimens show superior maximum bending angle compared to non-heat treated specimens. The specimens with the lowest hardness (interaction time: 1800 and 3600 ms) could be bended to a maximum bending angle of 120°. The specimens with a low hardness difference across the sheet thickness were bended in one direction since homogeneous mechanical properties across the sheet are expected. The specimens with a pronounced hardness difference (e.g. exposure time of 70 ms) have been bended with the top side under compression and under tension. When the softer top side is under tension a higher angle (103°) is achieved compared to the case when the harder side is under tension (74°) (Vogt 2019). In this case failure occurs earlier. For the specimens with hardness differences across the sheet thickness the standard deviation of the bending radius increases. This is due to inhomogeneous properties across the sheet thickness.

Figure 5.15 shows a micro section of a plate bending specimen with 1800 ms interaction time. Along the neutral fiber no stress will occur from the plate bending test. Due to the deformation on both sides (compression and tension) the AS coating is damaged. On the tension side it is teared apart and on the compressed side it is partially flacked off (Fig. 5.15). Cracks can be observed in the coating. These cracks can be initiated by pores or other defects. The pores may be attributed to the Kirkendall-effect.

Table 5.2 summarizes the conditions for homogeneous and inhomogeneous softening for both materials. For homogeneous softening, the process parameters feed speed and laser spot length must be selected so that the interaction time is larger than or equal to 1000 ms and for inhomogeneous softening less than 1000 ms. The maximum temperature must be selected so that it initiates the softening mechanism of the respective material.
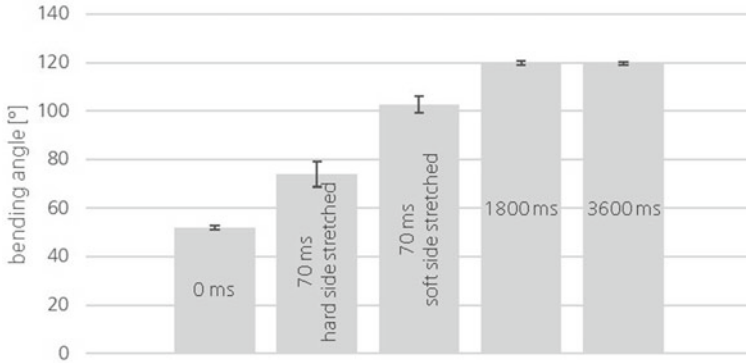
Fig. 5.14 Bending angle in dependence of interaction time and direction of loading for MBW®
1500
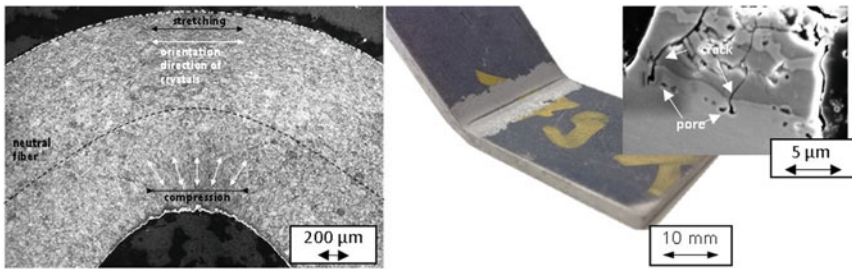
Fig. 5.15 Cross section of bended specimen in micro section with explanation of orientation direction of crystals (left), flaked off coating from a specimen in the bending radius (middle); SEM images of the interdiffusion and alloyed coating layers; interaction time 1800 ms

Table 5.2 Process parameters for homogeneous and inhomogeneous softening for ZE 1100 and MBW® 1500 + AS with sheet thickness of 1.5 mm

Steel grade	Homogeneous softening $\leq \pm 10$ HV 0.3	Inhomeous softening $> \pm 10$ HV 0.3
ZE 1100	$\Delta T \leq 50\ °C$ $T_{max} = T_{Recrystallization}$ or $T_{Phase\ transformation}$ $t_W \geq 1200\ ms$	$\Delta T > 50\ °C$ $T_{max} = T_{Recrystallization}$ or $T_{Phase\ transformation}$ $t_W < 1200\ ms$
MBW® 1500 + AS	$\Delta T \leq 50\ °C$ $T_{max} = T_{Tempering}$ or $T_{Phase\ transformation}$ $t_W \geq 1000\ ms$	$\Delta T > 50\ °C$ $T_{max} = T_{Tempering}$ or $T_{Phase\ transformation}$ $t_W < 1000\ ms$

Examples for process parameters for homogeneous softening:

- MBW® 1500 + AS: v_S = 500 mm/min; A_{Spot} = 10 × 10 mm^2; T_{max} = 800 °C
- ZE 1100: v_S = 1000 mm/min; A_{Spot} = 20 × 20 mm^2; T_{max} = 800 °C

Examples for process parameters for inhomogeneous softening:

- MBW® 1500 + AS: v_S = 1000 mm/min; A_{Spot} = 5 × 5 mm^2; T_{max} = 800 °C
- ZE 1100: v_S = 8000 mm/min; A_{Spot} = 20 × 20 mm^2; T_{max} = 800 °C

5.4 Double-Side Processing and Tailored Intensity Distribution

In order to increase the process speed and quality for homogeneous softening, two approaches are presented for a sheet thickness of 1.5 mm below (Vogt 2019; Vogt et al. 2018, 2019):

1. Simultaneous double-side processing of the sheet
2. Tailored intensity distribution

(1) In the case of processing on both sides simultaneously, the sheet is exposed to laser radiation from the top and bottom side. Two almost identical laser beam sources and processing heads are used for this purpose. The laser heat treatment is closed-loop temperature-controlled on both sides. The processing on both sides leads to a more homogeneous temperature distribution over the thickness of the sheet, because the required heat penetration depth is halved and thus higher feed speeds are possible.

    Figure 5.16 shows the average hardness for MBW® 1500 as a function of the distance from the sheet surface for three cases: When softening on one side at a feed speed of 12000 mm/min and a laser spot length of 25 mm, a softening depth of approx. 0.3 mm is obtained. A homogeneous softening of approx. 350 HV 0.3 at a feed speed of 12 m/min is achieved by double-side processing. In order to achieve a homogeneous softening with a laser spot size of 5 × 25 mm^2 on one side, the maximum feed speed is limited to 3000 mm/min.

    Figure 5.17 shows a comparison of the maximum feed speeds achieved for single- and double-side processing for MBW® 1500. Through simultaneous processing on both sides, the feed speed can be increased sevenfold for the MBW® 1500 + AS with a laser spot size of 5 × 5 mm^2. With increasing spot length, the increase of feed speed for double-side processing compared to single-side processing is reduced.

(2) Processing speed and quality can be significantly improved by using tailored intensity distributions to generate optimal temperature distributions in the sheet. By solving an inverse heat conduction problem to calculate an intensity distribution that induces this tailored temperature profile in the laser heat treatment process, a tailored intensity distribution can be developed (Völl et al. 2016).
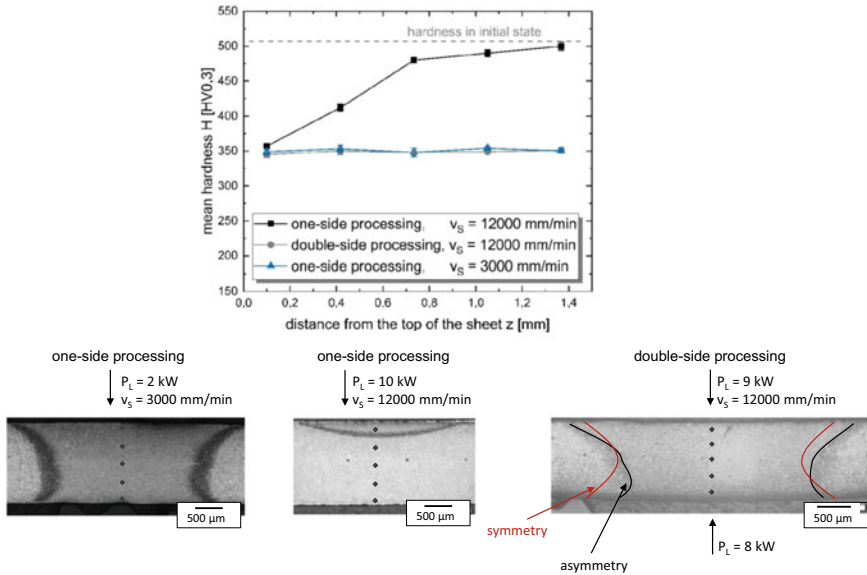
Fig. 5.16 Mean hardness across the thickness of the sheet and corresponding cross sections for one- and double-side processing for MBW® 1500 + AS

Using a combination of the conjugate gradient method with FEM (Völl et al. 2016), the intensity distribution shown in Fig. 5.18, left was calculated which creates a homogeneous temperature profile over the spot size on the surface of MBW® 1500 assuming a feed speed of 10000 mm/min. Afterwards, state-of-the-art design algorithms for free-form optics (Bäuerle et al. 2012) was applied to derive the shape of a free-form mirror that can generate this "chair" intensity distribution. This mirror was manufactured using diamond turning.

Figure 5.18, right shows a measurement of the intensity distribution. Compared to the simulated intensity distribution (Fig. 5.18, left), the intensity peaks at the corners of the transition from the front to the sides are missing. Furthermore, the intensity distribution is slightly displaced to one side, which probably results from the inaccurate adjustment of the free-form mirror inside the optical alignment.

Since the sheet is irradiated from one side, a characteristic temperature difference across the thickness of the sheet is inevitable during heat treatment. A homogeneous intensity profile, induced by a top-hat beam profile, produces an inhomogeneous temperature profile on the sheet material. The induced temperature distribution has a maximum in the center and decreases at the edges. Furthermore, the temperature on the sheet surface increases across the beam axis parallel to the movement direction (Burger 1988). In deeper regions of the sheet, the maximum temperatures are significantly smaller, resulting in inhomogeneous microstructure transformation. Homogeneous softening across the sheet thickness can only be achieved with low process feed speeds of (<1000 mm/min). As the feed speeds increase (up to 10000 mm/min),
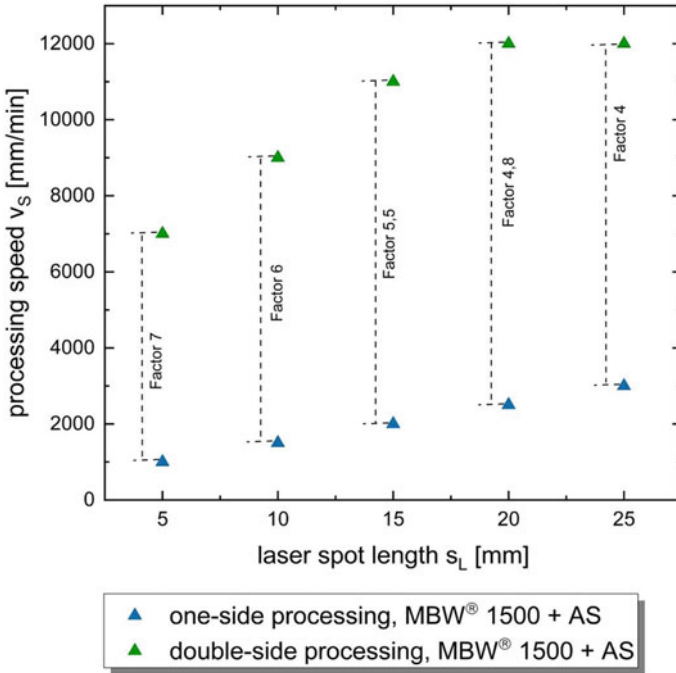
Fig. 5.17 Comparison of maximum processing speeds for one- and double-side processing in dependence of spot length for MBW® 1500 + AS
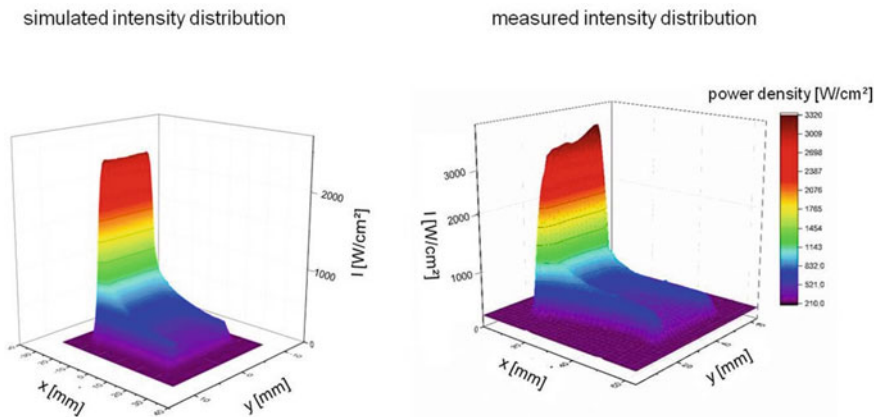
Fig. 5.18 Left: Simulated "chair" intensity distribution of a beam profile for efficient laser softening; Right: Measured caustics of free-form optic with BeamMonitor (PRIMES), intensity distribution over the symmetry axes x and y of the focal plane, spot size 10×40 mm^2
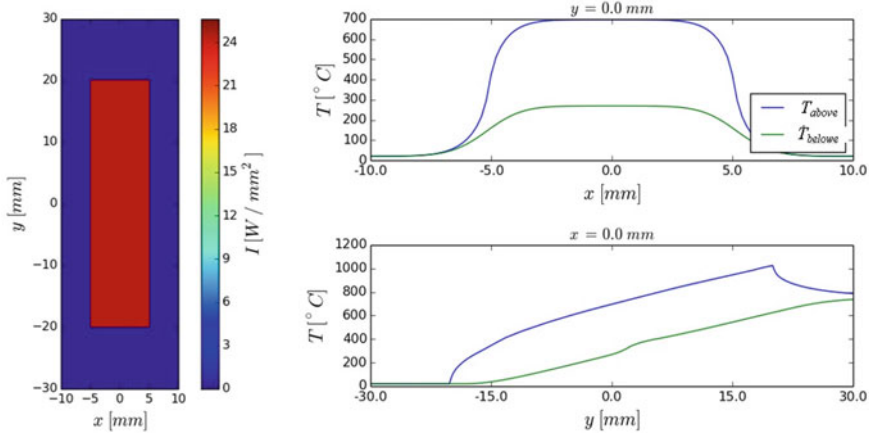
Fig. 5.19 Achieved temperature distribution using a top-hat intensity distribution on steel out of MBW® 1500; Left: Top-hat intensity with a spot size of 10×40 mm^2 and a feed speed of 10 m/min. The power required is 10 kW; Right: Temperature profile across the sheet thickness of 1,5 mm. The difference of the temperature between top and bottom is about 62% in x = 0.0 mm

the temperature distribution across the thickness of the material becomes more inhomogeneous (Fig. 5.19). The variation of the temperature from the top to the bottom is about 62% at a feed speed of 10000 mm/min.

The intensity distribution of the free-form optics has a maximum on the front, which leads to a rapid increase of the sheet temperature. On the sides of the beam, an increased intensity is required in order to equalize the heat conduction losses transversely to the feed direction. This allows a more homogeneous temperature field (Fig. 5.20) over the sheet thickness, compared to a top-hat distribution.

A typical hardness distribution after laser heat treatment with a top-hat profile and feed speeds of 0.5 and 6 m/min are shown in Fig. 5.21. In the heat-treated zone, a minimum hardness of around 205 HV 0.3 can be achieved, which is in accordance with Fig. 5.4. While increasing the feed rate, the laser power must be also increased from 0.9 to 6 kW. Owing to the lateral heat flow during laser heat treatment, a transition zone of several millimeters (approx. 5–8 mm) is formed at the edges of the irradiated area until the initial hardness (approx. 500 HV 0.3) of the hot stamped sheet is reached (Fig. 5.21, left). There is no hardness difference over the sheet thickness for low feed speeds (Fig. 5.21, right). With increasing feed speed the irradiation time of the laser radiation of the heat-treated zone is reduced. In the case of excessively high feed speeds, the irradiation timeframe is reduced, resulting in an inhomogeneous heat distribution inside the sheet. Owing to the resulting temperature difference over the sheet thickness, the bottom of the sheet is less softened than the top of the sheet. The hardness difference from the top to the bottom of the sheet at a feed speed of 6 m/min and a laser spot length of 40 mm is 75 HV 0.3 (Fig. 5.21, right).

Figure 5.22 shows the hardness profiles across the sheet thickness for MBW® 1500 + AS for a feed speed of 10 m/min and constant laser power of 12 kW for both
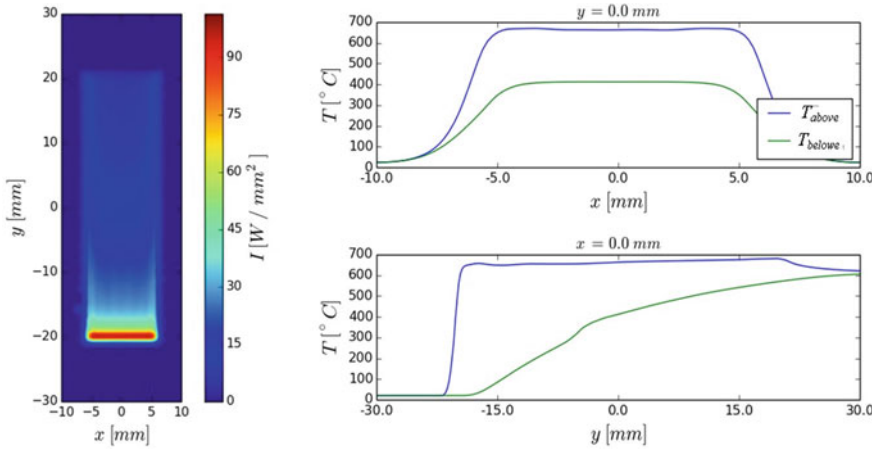
Fig. 5.20 Achieved temperature distribution using a tailored intensity distribution; Left: Intensity which induces a homogeneous temperature distribution on the surface of steel out of MBW® 1500 with a spot size of 10×40 mm^2 and a feed speed of 10000 mm/min. The power required is 10 kW; Right: Temperature profile across the sheet thickness of 1.5 mm. The difference of the temperature between top and bottom is about 40% in x = 0.0 mm
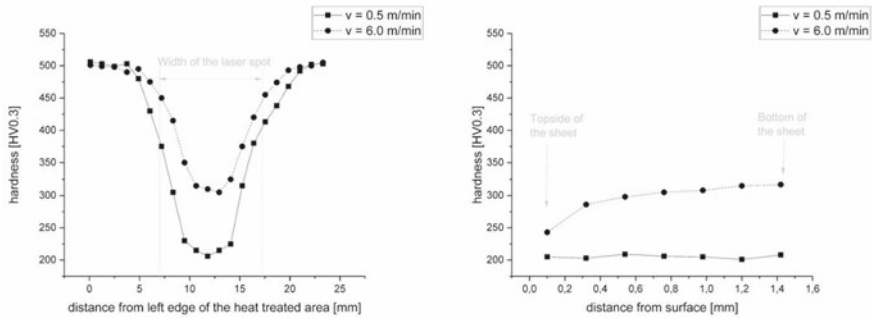
Fig. 5.21 Hardness distribution in a cross section (left) and across the thickness of the sheet (right) after laser softening of MBW® 1500 + AS using top-hat intensity distribution, 10×40 mm^2 laser spot size. The laser power is 0.9 kW at v = 0.5 m/min. The laser power is 6 kW at v = 6.0 m/min, sheet thickness of 1.5 mm

beam profiles. The tailored beam profile results in a more homogeneous temperature distribution and increased energy input into the workpiece. Due to larger energy input, shorter irradiation time is required than in the case of the top-hat beam profile. Homogeneous softening is thus achieved over the entire sheet thickness at feed speeds of up to 10 m/min. With the tailored beam profile, the hardening difference top to bottom within the sheet is only 5 HV 0.3. It is significantly smaller than in the case of the top-hat beam profile where it has a value of 85 HV 0.3.

Fig. 5.22 Comparison of hardness distribution across the thickness of the sheet after laser softening of MBW® 1500 + AS between top-hat profile (laser power 9.5 kW) and tailored beam profile (free-form optic) (laser power 12 kW). Laser spot size: 10 × 40 mm², feed speed: 10 m/min
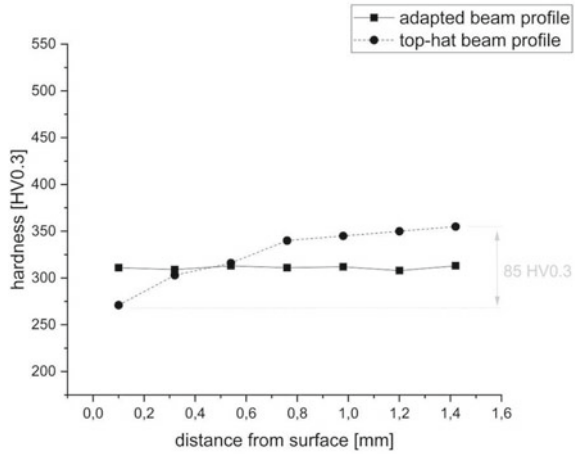
Figure 5.23 shows the hardness profiles across the width of the sheet in the center of the sheet for the process parameters used in Fig. 5.22. Due to the homogeneous intensity distribution of the top hat beam profile, the heat losses caused by conduction at the edge of the heat-treated zone are larger than for the free-form optical system. Owing to the tailored beam profile, the temperature is increased at the sides of the heat-treated zone, and the heat loss due to conduction is partly compensated. Therefore, the width of the treated zone has increased by 33%.

The local microstructure is in accordance with the hardness. For both intensity distributions a tempered martensitic structure can be observed across the sheet thickness (Fig. 5.24).

Table 5.3 shows the process parameters of the best softening results with processing on both sides and chair distribution compared to one-side softening and

Fig. 5.23 Hardness distribution in a cross section (middle of the sheet) after laser softening of MBW® 1500 + AS in the comparison top-hat profile (laser power 9.5 kW) to the adapted beam profile (free-form optic) (laser power 12 kW). Laser spot size 10 × 40 mm², feed speed 10 m/min
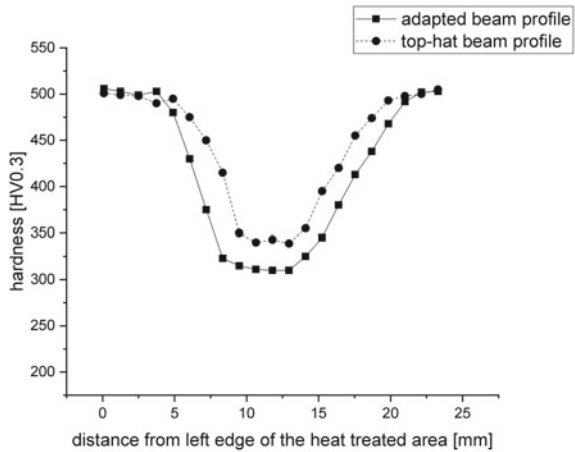
Fig. 5.24 Microstructure of MBW® 1500 + AS after laser softening; Left: top-hat profile with a laser power of 9.5 kW; Right: Tailored beam profile with laser power 12 kW. Laser spot size 10×40 mm², feed rate 10 m/min
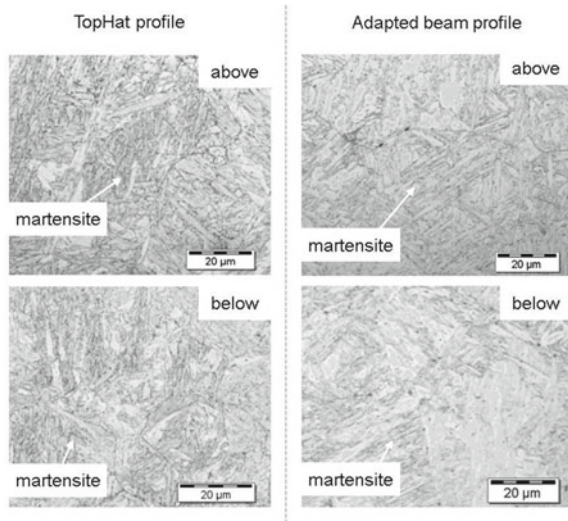
top-hat distribution. The criteria are the maximum softening with regard to hardness, the homogeneity of hardness over the thickness of the sheet and the maximum feed speed.

Table 5.3 Comparison of processing parameters for a homogeneous softening across the sheet thickness (1.5 mm) for one- and double-side processing for MBW® 1500 and comparison of processing parameters for top-hat and adapted intensity distribution for MBW® 1500 + AS and ZE 1100

Steel grade	Laser heat treatment	Processing parameters for homogeneous softening ($\Delta H \leq 10$ HV0,3) across sheet thickness			Hardness [HV0,3]
		A_{Spot} [mm²]	P_L [kW]	v_S [mm/min]	
MBW® 1500 + AS	One-side processing	5×5	0.9	1000	250
	Double-side processing		4.5 + 5.0	7000	
MBW® 1500 + AS	Top-hat-intensity distribution	10×40	6,5	2500	320
	Adapted intensity distribution		12	10,000	
ZE 1100	Top-hat-intensity distribution	10×40	9.2	3000	240
	Adapted intensity distribution		12	4000	

The feed speed can be increased sevenfold (Table 5.3 for MBW® 1500) by means of simultaneous processing on both sides to achieve homogeneous softening over the thickness of the sheet.

By laser softening with a tailored beam profile, a more homogeneous softening can be achieved over the thickness of the sheet, the lateral dimension of the softened zone can be increased by more than 50% and the transition area of the softened zone to the initial material can be reduced accordingly.

The two approaches show the potential of increasing the feed speed and, accordingly, the increase in productivity and economic efficiency of laser softening.

5.5 Application

The characteristic high strength of press-hardened components can deteriorate their joinability and crash performance (chapter "Motivation") (Burget and Sommer 2012; Vogt 2019; Meschut et al. 2014). Locally softened areas in the vicinity of the joints can reduce the initiation of cracks and their propagation into the component and have a positive effect on the spot welds initiating failure during crash (Zimmermann et al. 2013).

Two softening stages for the MBW® 1500 + AS were investigated with the following process parameters:

Spot dimensions: 20×20 mm^2, $v_S = 500$ mm/min, $t_W = 2400$ ms,

- Medium softening (softening stage 1), approx. 270 HV 0.3 (tensile strength 750 MPa), $T_{max} = 700$ °C
- Maximum softening (softening stage 2), approx. 200 HV 0.3 (tensile strength 650 MPa), $T_{max} = 850$ °C

The softening is homogeneous over the thickness of the sheet. For softening stage 1 the tensile strength is 750 MPa for softening stage 2 650 MPa.

In order to investigate the influence of the softening zones on spot-welded joints of stressed sheets, five tensile specimens are prepared and tested in each case. Figure 5.25 shows the measurement sequences of the quasi-static tensile tests of MBW® 1500 + AS with weld spot (without softening) compared to MBW® 1500 + AS with weld spot (left: softening stage 1, right: softening stage 2). This shows that the maximum force of the softened samples is reduced. At softening stage 1 the maximum force is reduced from 26 to 19 kN and at softening stage 2 to 17 kN. In the lower part of Fig. 5.25 a welded tensile sample without softening is depicted.

Based on these results, the critical areas for a B-pillar were determined by a Finite Element model (Schlussbericht zum Teilvorhaben 2018), which predicts the failure of the material and joining points. These are the starting points for crack initiation (Fig. 5.26, left). These two areas are heat treated with the above mentioned softening stages. The striking plate is made of the dual-phase steel DP 600 (plate thickness 1.0 mm) with a hot-dip galvanised coating Z100 and the insert consists of a MBW® 1500 with an AS coating. These joining partners are joined with the B-pillar by
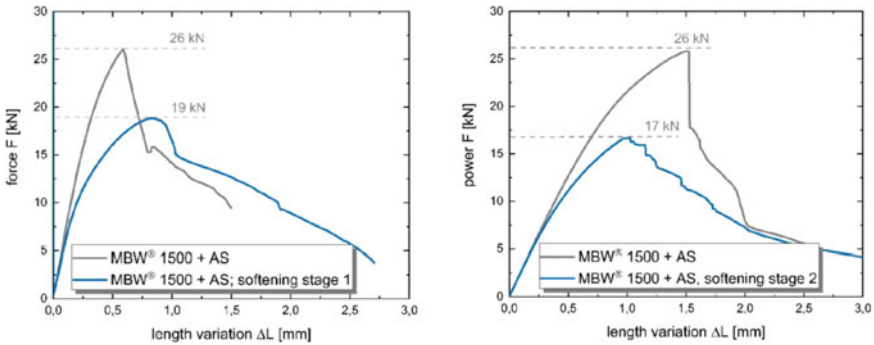
Tensile test specimen with spot weld joint

Fig. 5.25 Comparison of force–length change curves of tested tensile samples made of MBW® 1500 with spot welds without softening and softening stage 1 (left) and softening stage 2 (right); spot welded sample made of MBW® 1500 without softening (below)

resistance spot welding with 24 welding points (Fig. 5.26 right). On this basis, and further FE calculations a B-pillar test rig (Fig. 5.27 top left) is realized in order to specifically provoke material failure or to prevent material failure with softened flanges. By means of the component tests the simulation method can be verified, calibrated and the predictive capability for failure cases can be iteratively improved. These models can then be integrated into the full vehicle crash simulation.

In Fig. 5.27 the measured force–displacement curves of a 3-point bending test of not softened and softened B-pillars are shown. B-pillars without softening fail during
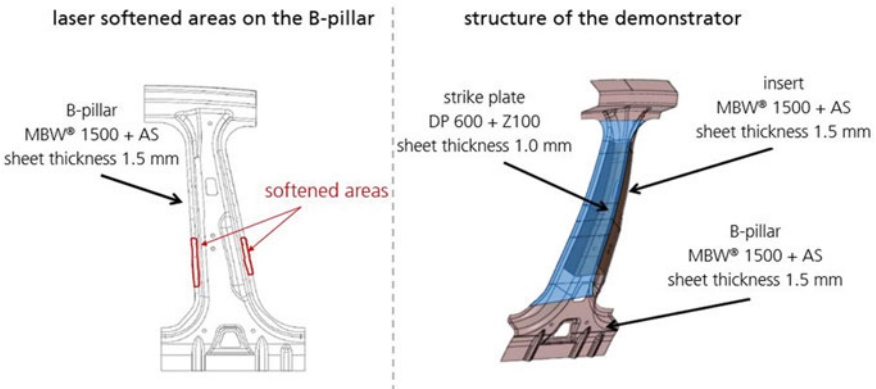
Fig. 5.26 Design of a B-pillar demonstrator for a 3-point-bending test bench; left: softening areas on the B-pillar, right: joining partners: striking plate, insert and B-pillar
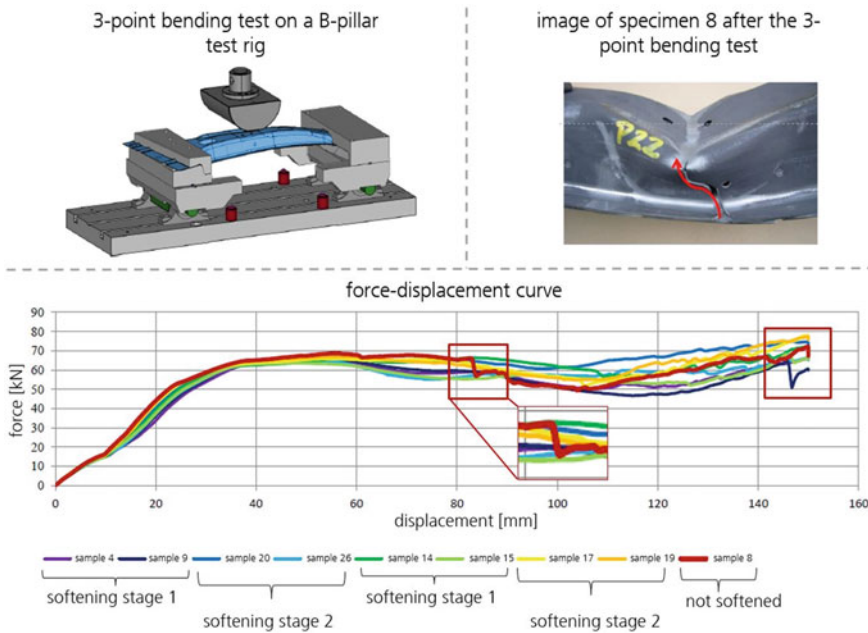
Fig. 5.27 3-point-bending test on a B-pillar test bench; above/left: scheme of the bending test bench; above/right: crack initiation after a test of a B-pillar without softening; below: force–length diagram of a 3-point bending test

loading in the flange area, starting from the welding spot (Fig. 5.27, top right). Failure can be recognised by the force–displacement curve through a drop at approx. 82 mm (Fig. 5.27, bottom, red curve). The softened B-pillars show such a course only after approx. 145 mm. The high deformations due to the mechanical load can lead to crack initiation (Sommer and Burget 2012; Sommer et al. 2013). As the deflection of the B-pillar increases, crack propagation occurs in the base material. Locally softened B-pillars exhibit improved crash behaviour, since all quasistatically tested B-pillars with softened flange show no crack initiation. The force–displacement curves of the tested locally softened B-pillars are similar, although different softening stages are set (Fig. 5.27).

The results of the 3-point bending tests were used for a full vehicle crash simulation for a "side crash" (Schlussbericht zum Teilvorhaben 2018). The simulations show that the B-pillar fails at the flange starting from the welding spot for the stages "without softening" and with softening stage 2 (Fig. 5.28, left and middle). The crack initiation started earlier for the B-pillar without softening than for the B-pillar with softening stage 2. At softening stage 1, no crack is initiated due to a side crash during loading (Fig. 5.28, right). The tensile strength at softening stage 2 is lower than at softening stage 1, which may be the reason for crack initiation as the overall component shows a lower strength. The results thus show that the highest softening level does not necessarily lead to the best crash result. But it shows that a softening at
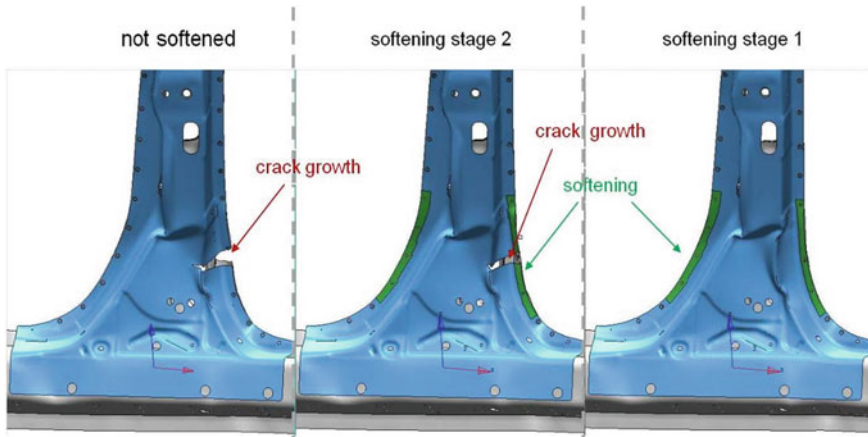
Fig. 5.28 B-pillar after a full vehicle crash simulation; left: B-pillar without softening; middle: B-pillar with softening stage 1; right: B-pillar with softening stage 2

the flange of a B-pillar shows an improved crash behaviour compared to an untreated B-pillar. A further improvement can be achieved by optimizing the position of the softening and the softening stage. The next step is the verification or validation of the softened B-pillars in a real full vehicle side crash test.

References

Abe Y, Kato T, Mori K (2009) Self-piercing riveting of high tensile strength steel and aluminum alloy sheets using conventional rivet ad die. J Mater Process Technol 209(8):3914–3922

Bäuerle A, Bruneton A, Wester R, Stollenwerk J, Loosen P (2012) Algorithm for irradiance tailoring using multiple freeform optical surfaces. In: Opt Express 20:14477–14485

Bergweiler G (2013) Lokale Wärmebehandlung mit Laserstrahlung zur Verbesserung der Umform- und Funktionseigenschaften von hochfesten Stählen. PhD thesis, RWTH Aachen University

Bleck W (2012) Spezielle Werkstoffkunde der Stähle für Studium und Praxis; 2. Aufl. Aachen: Mainz

Burger D (1988) Beitrag zur Optimierung des Laserhärtens. PhD thesis, University of Stuttgart

Burget S, Sommer S (2012) Characterization and modeling of fracture behavior of spot welded joints in hot-stamped ultra-high strength steels, LS-DYNA Forum, Ulm

International iron & steel institute: Advanced High Strength Steel (AHSS) Application Guidelines—version 3

Merklein M, Lechler J (2006) Investigation of the thermo-mechanical properties of hot stamping steels. J Mater Process Technol 177:452–455

Meschut G, Matzke M, Olfermann T, Maier H-J, Reimche W, Mroz G, Drossel W-G, Ahnert M, Broschwitz E, Kraus C, Meschut G (2014) Lokale Konditionierung von presshartem Vergü-tungsstahl für das Hybridfügen von Mischbaustrukturen : Ergebnisse eines Vorhabens der industriellen Gemeinschaftsforschung (IGF) gefördert über die Arbeitsgemeinschaft indus-trieller Forschungsvereinigungen e.V. (AIF) aus Mitteln des Bundesministerium für Wirtschaft

und Energie. Hannover : Europäische Forschungsges. für Blechverarbeitung, 2014 (EFB-Forschungsbericht 391)

Overrath J et al (2010) Aktuelle Entwicklung der Warmumformung im automobilen Fahrzeugbau; Bauteile der Zukunft: Methoden und Prozesse; 30. EFB-Kolloquium Blechverarbeitung, Hannover

Pirch N, Linnenbrink S, Gasser A, Wissenbach K, Poprawe R (2017) Analysis of track formation during laser metal deposition. J Laser Appl 29(2):022506–022511

Schlussbericht zum Teilvorhaben (2018) "Simulationsgestützte Optimierung des Crashverhaltens laserentfestigter Warmumformkomponenten" des Verbundprojektes "Kombinationsverfahren zum Laserschneiden und zur lokalen Laserentfestigung von Bauteilen aus hochfesten pressgehärteten Stählen (KLASSE, Projektnummer 13N12914)"

Sommer S, Burget S (2012) Charakterisierung und Modellierung von Punktschweißverbindungen in pressgehärteten Bauteilen für die Crashsimulation. 16. Kongress SIMVEC Berechnung, Simulation und Erprobung im Fahrzeugbau, Düsseldorf, VDI-Verlag

Sommer S, Wink H-J, Klokkers F et al (2013) Charakterisierung und Ersatzmodellierung des Bruchverhaltens von Punktschweißverbindungen an ultrahochfesten Stählen für die Crashsimulation unter Berücksichtigung der Auswirkung der Verbindung auf das Bauteilverhalten. Forschungsvorhaben P 806/A 262 der AVIF

Vogt S, Bechheim L, Banik J, Flaischerowitz M, Weisheit A, Schleifenbaum JH (2018) Local laser softening of press-hardened steel at high feed rates. J Laser Appl 30(3):031201

Vogt S, Völl A, Wollgarten S, Freese T, Stollenwerk J, Weisheit A, Loosen P (2019) Local laser softening of high-strength steel with adapted intensity. J Laser Appl 31(1):012007

Vogt S (2019) Local laser softening of semi-finished products and components of high- strength steels. PhD thesis, RWTH Aachen University

Völl A, Stollenwerk J, Loosen P (2016) Computing specific intensity distributions for laser material processing by solving an inverse heat conduction problem. In: Proceedings of the SPIE, vol 9741, pp 974105 9

Weber M (2008) Karosserieleichtbau durch neue Stähle und verbesserte Bauweisen. DVM-Bericht 675:173–182

Zimmermann F, Spörer J, Schwarzbauer T, Volk W (2013) Indirect press hardened car body parts with tailored properties by partial tempering, using a premixed oxygen-methane flame jet proceedings. Herrsching

Chapter 6
Laser Transformation Hardening

Konrad Wissenbach, Marko Seifert, Norbert Pirch, and Andreas Weisheit

6.1 Motivation

Laser beam hardening produces hard, wear-resistant surface layers on tools and components made from steel and cast iron. Especially on small and/or complex shaped components where conventional hardening processes cause problems regarding distortion or achievement of required hardening geometries, laser beam hardening offers advantageous solutions.

Comparable to conventional methods of hardening (e.g. induction hardening, flame hardening, and furnace hardening), transformation hardening with laser radiation is characterized by a well-defined temperature–time sequence in the solidus range (Amende 1990; Beyer and Wissenbach 1998; Schmitz-Justen 1986; Willerscheid 1990; Vitr et al. 1995). In comparison to other methods of hardening, the entire temperature cycle runs in a relatively short time, i.e. a few tenths of a second up to several seconds. Thus, laser beam hardening is considered as a short-time hardening process.

In comparison to most of the conventional methods of hardening, laser beam hardening generally does not require the use of external cooling agents. The high thermal conductivity of metals causes rapid self-quenching which means that the laser radiation heats up near-surface layers only. Absorbed optical energy in the surface layers is thermalized and transported into the bulk of the part via thermal conduction. The bulk material remains almost unchanged due to the low amount of

---

Definitions in these lecture notes: transformation hardening equals martensitic surface layer hardening equals laser hardening.

K. Wissenbach · N. Pirch · A. Weisheit (✉)
Fraunhofer-Institut fuer Lasertechnik, Aachen, Deutschland
e-mail: andreas.weisheit@ilt.fraunhofer.de

M. Seifert
Fraunhofer-Institut fuer Werkstoff- und Strahltechnik, Dresden, Germany

total energy used during the process. This enables surface hardening even on small components. The most important advantages of laser beam hardening are:

- Minimal distortion of the processed parts saving post machining or straightening
- High geometrical precision of the hardened zone
- Short process time
- Option of hardening partial surface areas and generation of hardening patterns respectively
- Usually no external cooling agents required
- Easy integration into automated flexible manufacturing
- Suitable for on-line process monitoring and control

With the development of efficient high-power diode lasers at the end of the 1990s, laser beam hardening as a surface hardening process experienced a boom. Over the past 10 years, numerous systems have been installed in the industry. These systems replace or supplement conventional heat treatment processes (e.g. furnace or induction hardening) in many industrial applications. Process advantages such as high precision and reproducibility, short process times as well as minimal heat input into the components and the resulting low distortion come into operation.

6.2 Process Description

Figure 6.1 shows a scheme of laser beam hardening in case of relative movement between laser beam and component. Areas 1–3 represent a spatial allocation of the transformation processes during laser beam hardening. Area 1 comprises austenite formation, area 2 martensite formation and area 3 the hardened track. As depicted in Fig. 6.2, the resulting temperature–time cycle of a volume element of a component results from the optical and thermo-physical material properties, the material volume available for self-quenching, the geometry of the work piece, the intensity distribution of the laser beam on the component surface and the speed v_H of the component surface relative to the optical axis. The temperature–time cycle of transformation hardening is divided into three phases:

- Heating-up the work piece above the A_{c3}–temperature
- Dwell time to achieve the austenitic microstructure
- Cooling-down with a material-specific minimum cooling rate below the martensite start temperature

Figure 6.2 shows a diagram of the transformation of the microstructure constituents during transformation hardening with a predefined temperature–time cycle (Schmitz-Justen 1986). After exceeding the A_{c1}-temperature (start of austenite formation), the austenite formation sets in (see Chap. 2.6). The volume to be hardened has to stay above the transformation temperature (A_{c3}-temperature (end of austenite formation)) for a certain time in order to ensure the diffusion driven transformation
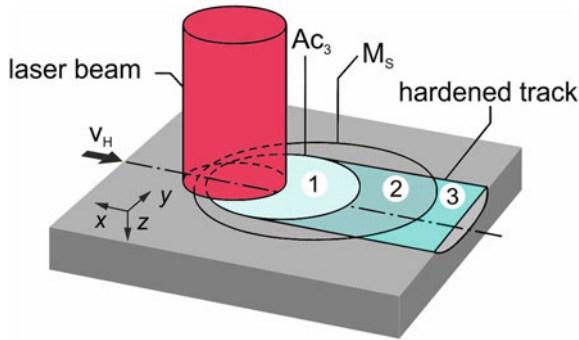
Fig. 6.1 Scheme of transformation hardening with laser radiation; A_{c3}: Temperature where austenite formation is finished; M_S: Temperature where martensite foramtion starts
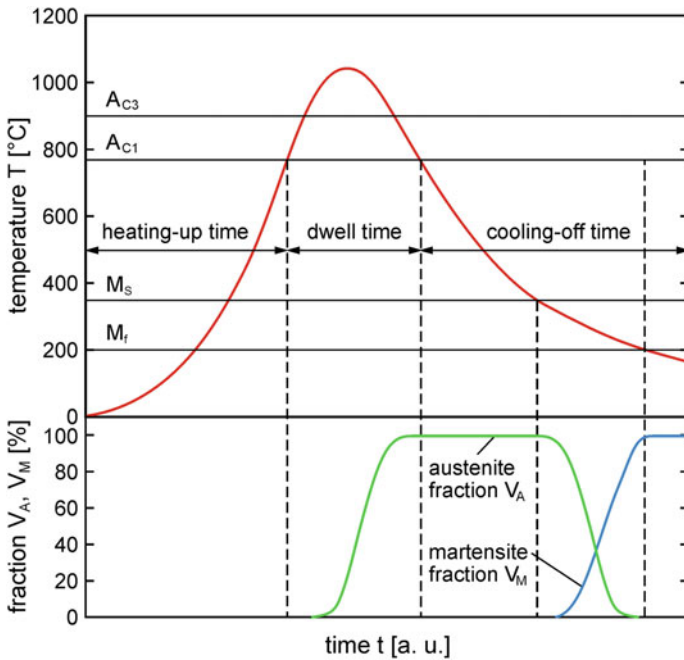
Fig. 6.2 Temperature–time cycle during transformation hardening with laser radiation; A_{c1}: Temperature where austenite formation starts; M_f: Temperature where martensite formation is finished

into austenite as complete as possible. The actual time necessary does not only depend on the individual process parameters but also on the initial microstructure. Subsequent self-quenching with a minimum quenching rate by means of heat conduction into the surrounding material suppresses ferrite, pearlite and bainite transformation

and initiates martensite formation as soon as the temperature falls below the M_s-temperature (start of martensite formation) (see Chap. 2.6) Martensite formation ends when the M_f-temperature (end of martensite formation) is reached.

In general, all materials that can be hardened with conventional methods are suitable for transformation hardening with laser radiation, i.e. steel and cast iron with a carbon content $\geq 0.3\%$.

Due to the short temperature–time sequences (typical: 0.1–10 s) materials with a fine-grained structure, a high proportion of pearlite or quenched and tempered materials are better suited for laser hardening than materials with a high proportion of ferrite and stable carbides (Amende 1990). The time–temperature-austenitization diagrams (TTA) and the time–temperature-transformation diagrams (TTT) (Ohrlich et al. 1973; Ohrlich and Pietrzeniuk 1976) provide important indications for the process management as well as for the austenitization process and for the required minimum cooling rate. The TTA diagrams allow to determine the transformation temperatures for materials with different heat treatment conditions in dependence on the heating-up speed as well as the dwell time necessary for the generation of homogeneous austenite. As an example, Fig. 6.3 shows the TTA diagram for steel DIN Ck45 (AISI 1045). The pearlite-austenite transformation runs above the A_{c1}-temperature while the homogenization of the austenite runs above the A_{c3}-temperature. The progression of the A_{c1}-temperature and the A_{c3}-temperature in relation to the heating-up rate can be seen in Fig. 6.3.

The austenitization temperature depends on the heating rate, the state of heat treatment, the carbon content and the alloying elements. It is therefore necessary to determine individual TTA diagrams for each material, which display the dependence of the austenitization temperature and time on the heating rate. Figure 6.3 comprises
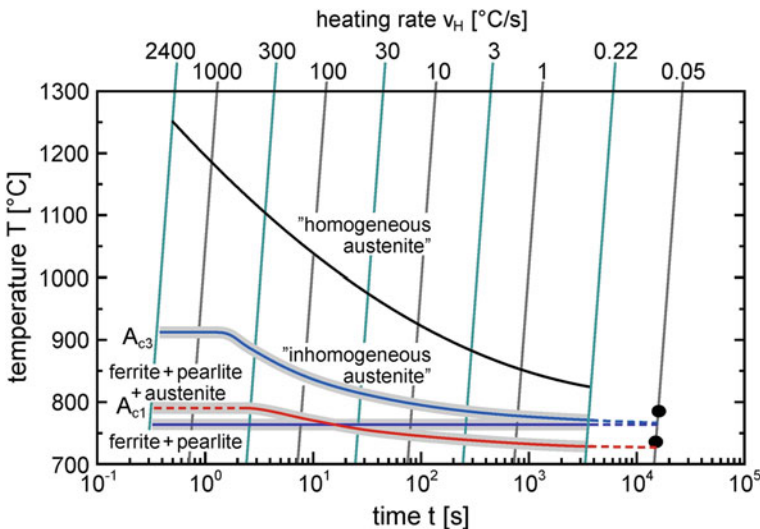
Fig. 6.3 Time-temperature-austenitization diagram (TTA) for DIN Ck45 (AISI 1045)

the temperatures necessary for complete austenitization. Typical heating rates for laser beam hardening are between 300 and 3000 °C/s. Consequently, steel DIN Ck45 (AISI 1045) has an A_{c1}-temperature of 790 °C and an A_{c3}-temperature of 911 °C.

The minimum cooling rate necessary for the generation of a fully martensite microstructure can be found in the TTT diagrams. Figure 6.4 shows the TTT diagrams for two austenitization temperatures of steel DIN Ck45 (AISI 1045). The cooling curves and the domains of the different microstructure types are presented. Depending on its cooling curve, the microstructure contains ferritic, pearlitic, bainitic and martensitic fractions that are proportionate to the percentages displayed on the individual cooling curves. Predictions about the transformation of the microstructure are only possible on the basis of their cooling curves. The cooling-down time starts as soon as the temperature falls below the A_{c1}-temperature. TTT diagrams are solely exact valid for a given austenite grain size and a predefined heating-up and dwell time during the stated austenitization temperature.

Depending on the cooling curve, the austenite transforms at certain temperatures into the structures listed in Fig. 6.4. In order to achieve a martensitic microstructure, it is necessary to select a cooling rate that avoids passing through regions of ferrite, pearlite and bainite structures. These structures possess a considerably lower hardness than martensite. When all diffusion controlled phase transformations have been passed the whole carbon content is trapped in the austenite. At a certain temperature (M_S) the undercooled austenite starts transforming into the tetragonal body-centered
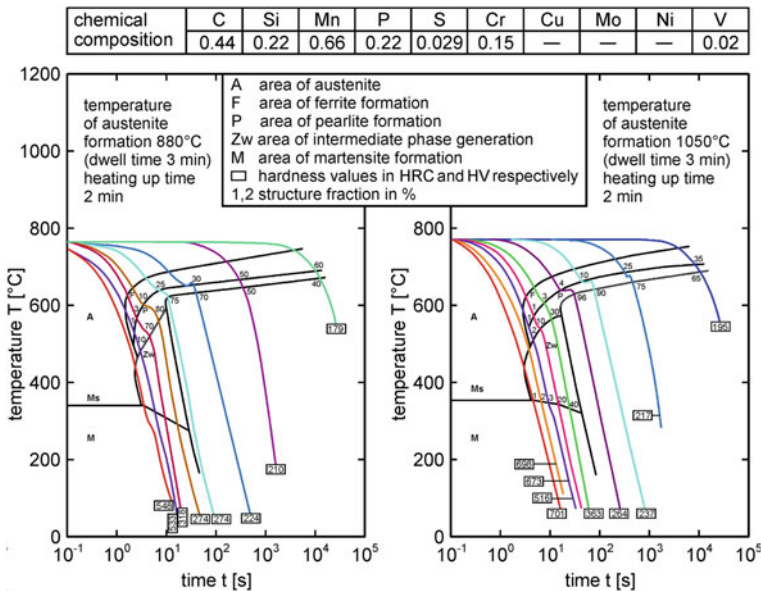
Fig. 6.4 Time-temperature-transformation diagrams for steel DIN Ck45 (AISI 1045) austenitization temperature 880 and 1050 °C

martensite. The formation of the martensite is finished when the M_f-temperature is reached.

6.3 Physical Background

The physical processes relevant for transformation hardening are:

The <u>absorption</u> of laser radiation on technical steel surfaces (see Chap. 2.3).

The absorbed optical energy is transformed into thermal energy and transported into the component through <u>heat conduction</u> (see Chap. 2.4). Depending on the process parameters and the thermo-physical material properties, a time- and location-dependent temperature distribution results in the workpiece.

<u>Transformation kinetics</u> (see Chap. 2.6) deals essentially with austenite and martensite formation and depends on the microstructure and the temperature–time cycle. Austenite formation is a diffusion process largely determined by nucleation and grain growth. The diffusion of carbon (which depends on temperature and time) is crucial for the process. In contrast to austenite formation, martensite formation is <u>not</u> a diffusion process. The formation of martensite starts abruptly and occurs cascade-like in fractions of a second with further cooling below the M_s-temperature. The formation of the martensite is triggered by a collective change of location of atomic groups in a coordinated movement. The face-centered cubic austenite lattice (FCC) turns into the body-centered cubic martensite lattice (BCC), which is distorted tetragonally due to the trapped carbon.

Depending on the component geometry, the thermo-physical material properties, the temperature distribution and the resulting transformation processes a three-dimensional transient tension field is formed that is decisive in determining the deformation and the residual stress behavior of the component after the hardening process (Müller et al. 1996) (see Chap. 2.5).

6.4 Beam Guiding and Shaping Optics

For transformation hardening a homogeneous intensity distribution is advantageous in order to avoid local remelting of the component surface and also to achieve a uniform hardness penetration depth across the track width. Numerous beam guiding and shaping optics are available in order to use the advantage of laser hardening as a highly flexible process for hardening different geometries. When designing such optics the following aspects have to be taken into account:

- Changes in the properties of the laser radiation (e.g. laser power, intensity distribution, polarization state) due to the optical components

- Minimization of the number of optical components to minimize power losses

Figure 6.5 shows a subdivision of beam shaping systems into static and dynamic systems. In static systems, intensity distributions are generated with temporally constant dimensions. Since laser hardening often requires homogeneous intensity distributions, the variants "imaging of the fiber end" and "homogenization optics" using microlens arrays are preferred. These systems produce circular or rectangular beam cross-sections. For special applications, ring-shaped power density distributions can be generated, e.g. by using an axicon. Thus, e.g. ring-shaped beam geometries with diameters in the mm-range can be processed in a "spot heating" without movement of the laser beam. The use of transmissive and reflective free-form optics enables the generation of application-specific, complex intensity distributions. The desired intensity distribution is the input variable required to calculate the corresponding surface structure of the free-form optics by design algorithms as a first step. In a second step, the free-form optics are manufactured by ultra-precision machining. The best known example for laser heat treatment is the so-called chair distribution. With this intensity distribution, both the undesired lateral heat dissipation is compensated and rapid heating above the A_{c3}-temperature in the feed direction is achieved (see chapter Laser Softening). With diffractive optical elements (DOE, glass carriers with a microstructure), the incident laser beam can be shaped or divided into multi beams. The beam splitting enables the simultaneous hardening of several areas of one component or several components. DOEs can also be used to generate almost any beam geometry and can be used for laser powers in the kW-range.

With dynamic beam shaping optics, the intensity distribution can be changed over time. The best known systems are scanners (polygon scanners and galvanometer scanners) and zoom optics. Polygon scanners consist of a round body which rotates around its axis. On its surface plane mirrors are located. If a laser beam hits one of the mirrors, it is reflected and guided over the workpiece by the rotary motion. With polygon scanners, significantly higher scan speeds in the range of >100 m/s can be achieved than with the galvanometer (galvo) scanner (up to 30 m/s). The disadvantage of polygon scanners is the one-dimensional deflection. Galvo scanners are the preferred choice for laser hardening because they offer greater flexibility with regard to beam shaping (deflection in 2 axes) and the typical feed rates for laser hardening do not permit deflection rates in the range of several m/s due to the transformation kinetics. By varying the amplitude and the scanning frequency, both the geometry of the track and the temperature can be set in a defined way.

With zoom optics, the automatic shifting of optical elements (e.g. lenses) changes the focal length of the optics, which changes the beam dimensions.

The other dynamic optical systems shown in Fig. 6.5 (Digital Mirror Device, DMD; acoustic optical modulator; Liquid Crysal on Silicon, LCoS) are not yet used for laser hardening. DMDs usually consist of individual elements arranged in matrix form, where each individual mirror consists of a tilting reflecting surface. The movement is caused by the force of electrostatic fields. Each mirror can be adjusted individually in its angle and usually has two stable end states, between which it can

static

Focusing optics

Picture of a fiber end

Ring beam distribution by axicon

Homogenization by multi-lens array

Freeform optics

Beam splitting and shaping by diffractive optical element

dynamic

Polygon scanner

Galvanometer scanner

Zoom optics

Digital mirror device

Acousto-optic modulator

Liquid Crystal on Silicon
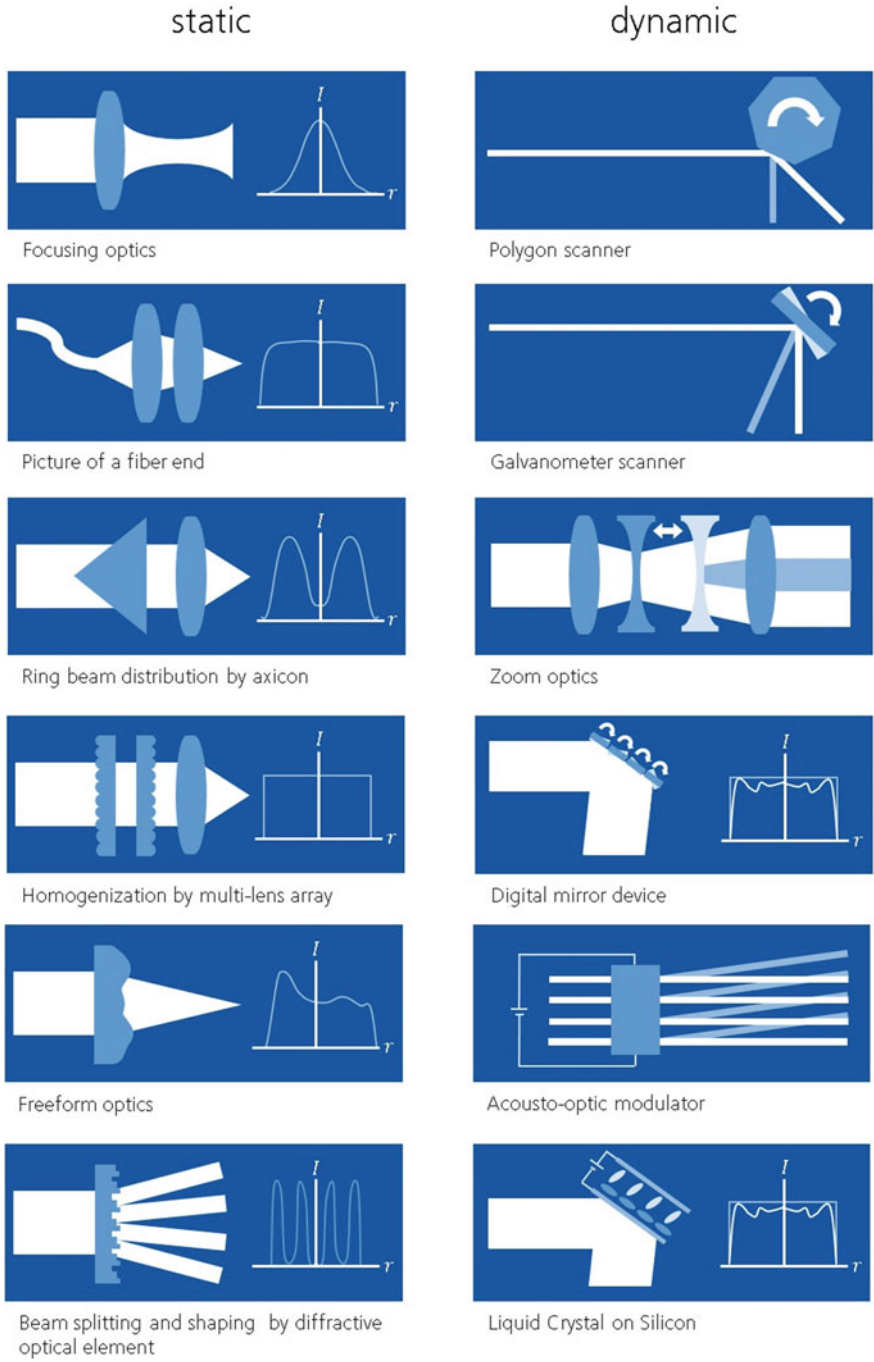
Fig. 6.5 Static and dynamic beam guiding and shaping optics

change up to 5000 times per second. This makes it possible to generate homogeneous intensity distributions. Acousto-optical modulators are mainly used for fast switching (5–100 ns) of laser radiation. LCoS displays are used for projectors and consist of a silicon foil, a thin layer of liquid crystals on it and a thin glass pane. The incident laser beam is directed onto the LCoS display via a special polarizing mirror, where the liquid crystal molecules are aligned by electric voltage in such a way that the light is reflected in the desired brightness. The fill factor of the display is very high (>90%), which results in a high optical efficiency. In contrast to DMD technology, the light must be polarized so that it can be modulated by a LCoS display. This requires a higher power. The most important reason that DMDs and LCoSs are not yet used for macro laser material processing is the limitation of the systems to laser powers in the range of 100 W.

6.5 Modelling and Experimental Results

Today diode lasers are mainly used for transformation hardening. But also Nd:YAG and fiber lasers are suitable for transformation hardening due to their wavelength in the range around 1 μm. Due to the low absorptivity A of CO_2 laser radiation ($\lambda =$ 10.6 μm) on technical steel surfaces (A < 10%), the use of absorption-increasing coatings (e.g. graphite, phosphate, metal oxides) is necessary to increase energy coupling. This requires additional work steps for the application and removal of the coatings. In particular, the low reproducibility of the properties of the applied coatings are critical. For these reasons, CO_2 lasers are no longer used for transformation hardening. The main advantages of hardening with diode, Nd:YAG, and fiber laser radiation are

- Relatively high absorptivity on technical steel surfaces (30–35%)
- Increased absorptivity of the laser radiation (>80%) when hardening is performed in air due to the formation of a thin oxide layer during processing
- Possibility of transmitting the laser radiation using optical fibers improving flexibility of processing
- Process control by temperature measurement

Modelling of Laser Hardening

As shown above, the hardening geometry is determined by the local temperature–time cycles and the transformation kinetics of the material. For predicting the hardening geometry simulation tools have been developed, which can calculate the spatial-resolved temperature time cycles as a solution of the heat conduction equation with suitable boundary conditions and with the aid of the TTT- and TTA-diagrams. Essential input variables for the models are on the one hand the absorptivity depending on the surface condition of the workpiece (e.g. ground, milled, oxidized), the wavelength of the laser radiation as well as the angle of incidence of the laser radiation
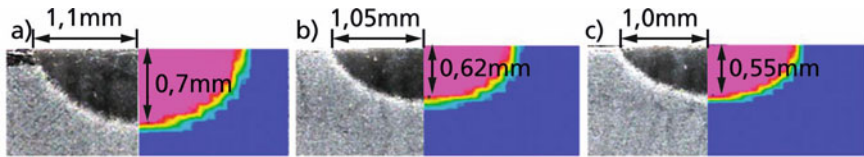
Fig. 6.6 Comparison of experimental and calculated hardening geometries (Babu et al. 2014)

and on the other hand the laser power and intensity distribution of the laser radiation. The transformation temperature is determined from the TTA-diagrams as a function of the heating rate. The course of the A_{c3}-isotherms is calculated from the 3D-temperature field and compared with the experimentally determined hardening geometry (e.g. from micrographs). Figure 6.6 shows as an example a comparison of experimentally determined hardening geometries in cross sections with the calculated geometries (Babu et al. 2014). The good agreement can be clearly seen. The degree of agreement of such models with the experimental results depends on the one hand on the quality of the model (e.g. consideration of real intensity distributions used in the experiments, the spatial resolution of the finite element mesh in the area of interaction with the laser radiation) and on the other hand on the quality of the input data for the model. In particular, the absorptivity, the approximation of the intensity distribution, the temperature-dependent thermo-physical material properties as well as the transformation temperatures are to be mentioned here.

In (Hung et al. 2018) the finite element method is used to calculate process diagrams for single tracks in a rectangular workpiece geometry ($100 \times 12 \times 6$ mm^3) for the materials C45 and 42CrMo4. The same absorptivity of A = 40% is assumed for both materials. The transformation temperatures ($760\,°C$ for C45, $850\,°C$ for 42CrMo4), the different melting temperatures of the materials ($1520\,°C$ for C45, $1410\,°C$ for 42CrMo4) as well as the temperature dependence of the thermal conductivity and the specific heat capacity are considered. A Gaussian intensity distribution is used in the model.

Figure 6.7 shows the hardening width and depth for a beam diameter of 3 mm as a function of the scanning speed for laser powers of 200, 350 and 500 W for both materials. Both the hardness track width and the hardness track depth decrease with increasing feed speed. With increasing laser power, the same hardening widths and depths are achieved at higher speeds. Due to the lower transformation temperature for C45 compared to 42CrMo4, larger hardness geometries result for C45 than for 42CrMo4.

Figure 6.8 shows the calculated hardening width at a hardening depth of 1 mm as a function of the laser power for different beam shapes. Analogous to Fig. 6.7, the track width increases with increasing laser power. The smallest track widths result for the Gaussian intensity distribution, since for this distribution the highest intensity is located in the center and due to the steep flanks in the intensity distribution the heat quickly flows radially outwards. The largest track widths are achieved with rectangular beam distributions, whereby the track width increases with increasing

Fig. 6.7 Calculated hardening depth and width in dependence of the scanning speed for C45 and 42CrMo4 (Hung et al. 2018)
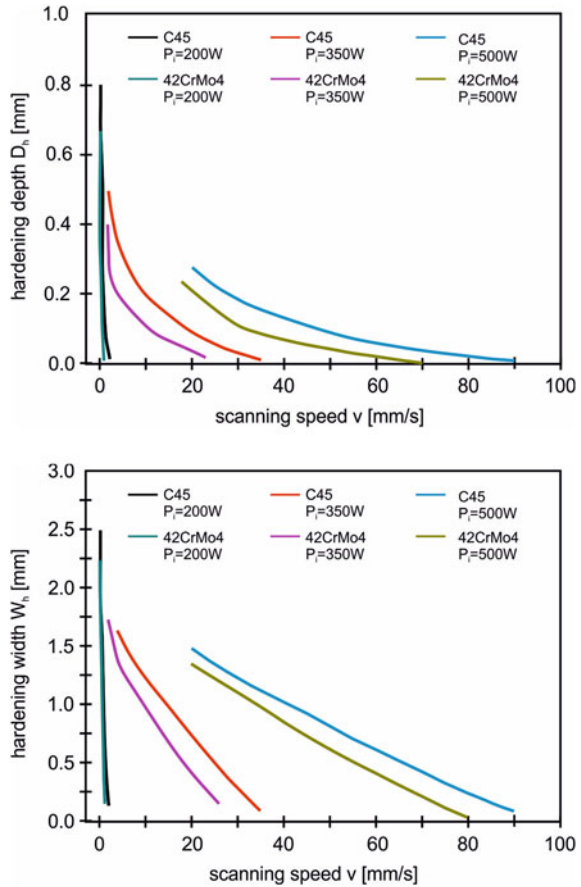
aspect ratio of width to length in the feed direction. If the aspect ratio is increased by a factor of 2, it can be seen that the increase in track width for the larger aspect ratio is less than a factor of 2 due to the lower intensity at the same laser power.

With such process diagrams, the user can be provided with a tool to preselect process parameters.

Experimental results

Typical characteristics of laser beam hardening are:

Laser output power: 100 W–10000 W
Beam cross sections: 1 mm^2 (1 × 1 mm^2) – 500 mm^2 (100 × 5 mm^2)
Incident intensity: $1 \times 10^3 - 10^4$ W/cm^2
Hardening depth: <0.1 – 1.5 (typical, 3 mm possible for certain materials)
Hardening width: <1 – Y>100 mm
Scanning speed: 0.1 – 4 m/min (up to 100 m/min for thin sheet metal or edges)

Figure 6.9 shows in the upper portion a cross-section of a laser beam hardened track on a hollow profile made from Ck45 (AISI 1045). The hardening depth is uniform across the entire track width. On the left, the related photos of the microstructure show an overview including the hardening geometry and the heat affected zone (HAZ), on the right they show the martensitic microstructure in the hardened zone. The hardness as a function of depth shows maximum values of 700 HV 0.3 and a hardening depth of 0.8 mm.

The maximum temperature during hardening has a crucial influence on hardness and wear properties. Figure 6.10a shows the surface hardness for the tool steel X155CrMoV12.1 as a function of the maximum surface temperature (Bonss et al. 2016). Up to a maximum temperature of about 1200 °C the hardness increases continuously up to values of about 900 HV. Furthermore, it can be seen that hardness values >700 HV are only achieved in a narrow temperature range of 1200 °C ± 30 °C. At higher temperatures residual austenite is formed, which reduces the hardness. At further increasing temperature undesired melting occurs. If the temperature is below the above mentioned region, the microstructure is not completely transformed into martensite, resulting in a lower hardness. Figure 6.10b shows the depth of the heat treatment zone (defined as the depth at which an increase in hardness occurs compared to the base material) as a function of temperature. Above the austenitic start temperature (>900 °C) the hardening of the material begins. With increasing temperature, the hardening depth increases almost linearly with temperature.

Quality assurance in laser hardening (Bonss et al. 2016; Seifert et al. 2014, 2013)

Since laser hardening is determined by the temperature–time cycle, non-contact temperature measuring instruments such as pyrometers or thermal imaging cameras are suited for process control and quality assurance. Typical temperature ranges for laser hardening are between 1000 and 1500 °C, so that a wavelength range from approx. 650–2500 nm is used for signal acquisition. In order to achieve the lowest possible sensitivity to changes in emissivity or signal attenuation, a measuring wavelength as short as possible is generally recommended. This is often not feasible

Fig. 6.9 Example of laser hardening of steel Ck45
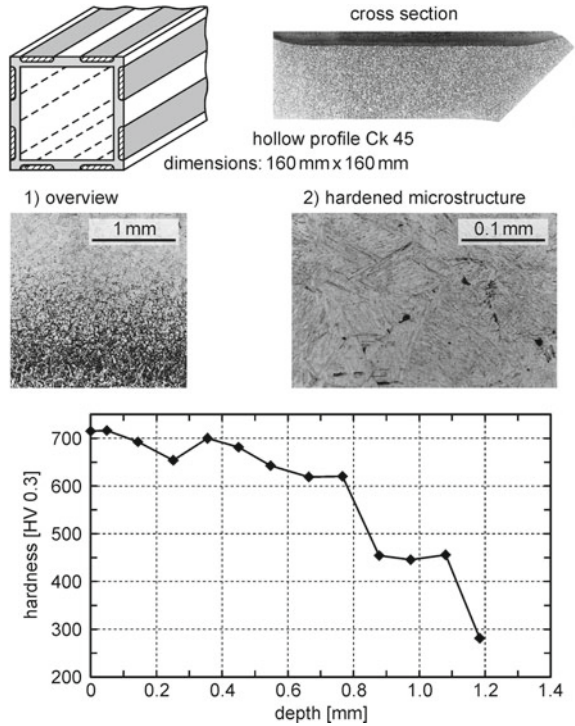
since the signal strength decrease exponentially in the direction of short wavelengths and the signal-to-noise ratio deteriorates as a result. It is important to note that the temperature measurement is also influenced by back reflected laser radiation. With high-power diode lasers of certain wavelengths, the signal superposition is added by the so-called LED background radiation, which also has a broadband effect outside the core laser wavelengths. This problem can be solved by installing special filters in the laser device and between the process and the temperature measuring device.

The temperature measuring instruments can be arranged laterally or coaxially with respect to the laser beam axis (Fig. 6.11). The coaxial arrangement with integration of the temperature measuring device in the laser optics has become increasingly established, since the lateral arrangement has several decisive disadvantages. For example, if the working distance or beam angle of the laser optics to the component surface changes, the measuring spot can move within the interaction zone. This can result in considerable temperature measurement errors. One advantage of lateral measurement is that the measurement detector is not looking through optical devices, which makes calibration much easier (Seifert et al. 2014).

Pyrometers and thermal imaging cameras measure the thermal radiation emitted from the surface. While pyrometers measure the mean temperature over a measuring spot, thermal imaging cameras measure the temperature of each pixel of an image. Pyrometers offer the advantage of higher time resolution (up to 100 kHz) in addition

Fig. 6.10 **a** Surface
hardness as a function of
maximum surface
temperature for the tool steel
X155CrMoV12.1. **b** Depth
of heat treatment zone as a
function of maximum
surface temperature for the
tool steel X155CrMoV12.1
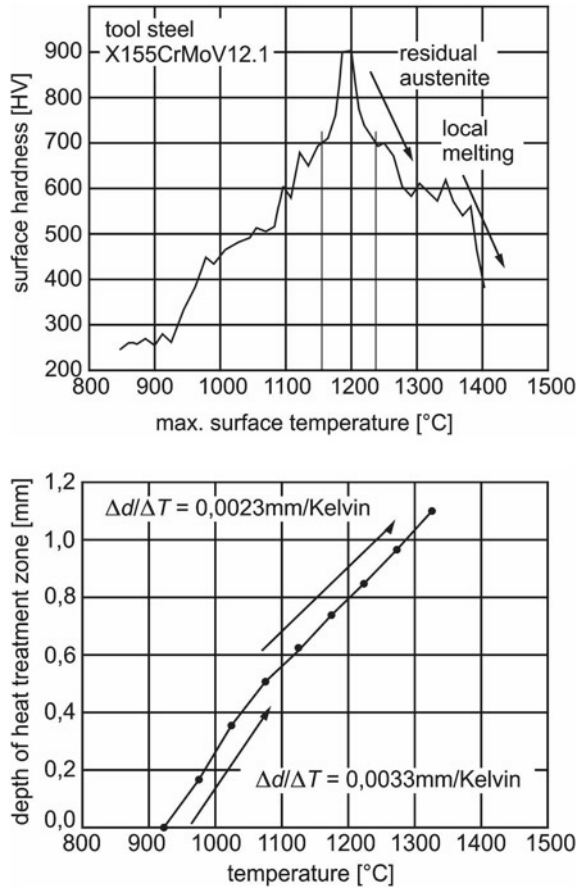
to lower investment costs (5–30 T€). Thermal imaging cameras allow a spatial
resolution in the submillimeter range and a time resolution between 0.2 and 1 kHz.
The investment costs are significantly higher (25–100 T€).

For many applications the measurement of the relative temperature is sufficient.
In series hardening of identical parts, for example, the temperature–time curves
measured with a pyrometer can be evaluated (e.g. maximum temperature or mean
value of the temperature signal). These characteristic values are correlated with the
hardening result (e.g. the hardening depth) and a process window is determined.
Outside this process window, the hardness depths are too small or the surface melts.
Thus it can be concluded from the temperature signals whether a component is OK
or not OK. For absolute temperature measurement, the calibration of the measuring
instruments is necessary. In addition, the calibration must always be carried out
in combination with the processing optics, because when viewed through the laser
optics, each optical assembly between the measuring device and the process absorbs
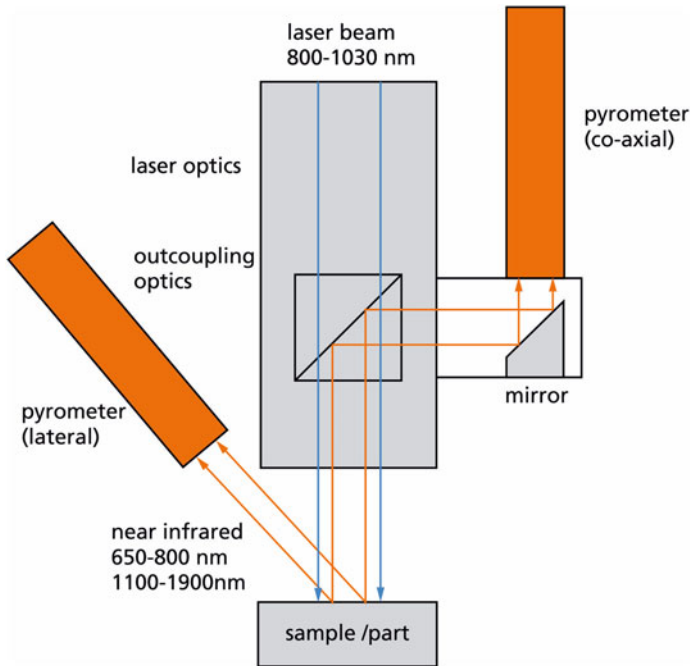
Fig. 6.11 Lateral and co-axial arrangement of the temperature measurement instruments

or reflects the back part of the temperature signal. Suited calibration devices are available (Seifert et al. 2013).

Figure 6.12 shows a closed-loop controlled hardening process for spot hardening (no movement of the beam) of an impact screw made of 100Cr6. The temperature is measured with a calibrated pyrometer so that the temperature is given in absolute figures. At the beginning of the hardening process, the laser power is high to rapidly heat up the surface to the target value (here 1200 °C). Then the target value is held for a certain time. During that time the laser power is continuously reduced since heat accumulation requires less heat input to keep the temperature constant. After shut down of the laser radiation self-quenching starts.

System technology for laser hardening

In the following, selected system components are presented which can be used for process monitoring and quality control in laser hardening (Bonss et al. 2016).

E-MAqS

"E-MAqS" is a camera based temperature measuring system. An industrial grey scale CCD camera with a frequency up to 300–600 Hz is used with sufficient sensitivity in the near infrared. Limited by the signal-to-noise-ratio of the sensor the system can measure temperatures above 700 °C. The visible light and the laser light are cut

Fig. 6.12 Temperature and laser power as a function of time for a closed-loop process control in spot hardening
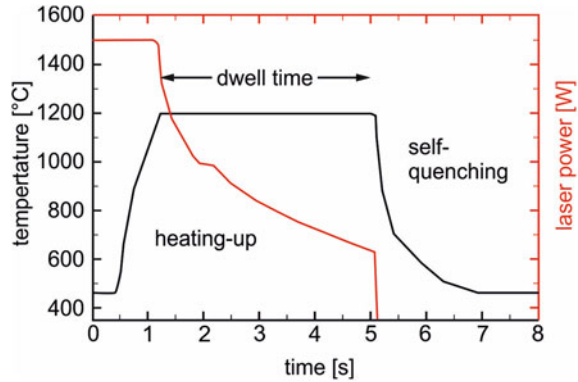
off from the incoming radiation with special filters. A typical measuring wavelength is 740 nm. The nonlinear correlation between temperature and grey scale values is realized by calibration with black body devices or LED-based calibrators. Having a lateral resolution of maximum 640×480 pixel even very small hot spots can be measured if necessary, but in temperature controlled processes typically an averaged measurement by integration over a certain amount of pixels is used to measure the core process temperature.

E-FAqS

"E-FAqS" is a fast pyrometric system with InGaAs sensor, sensitive in the range of about 1.2–1.7 µm, to get temperature information about very fast processes. This system is able to measure low temperatures from 160 °C and above with a sample rate of 20 kHz. The measuring spot size is adaptable.

LompocPro (Digital Software Controller)

"LompocPro" is a Windows-based digital software controller for control of laser processes like laser hardening or laser cladding. Different temperature measuring equipment (pyrometers, cameras) can be connected, depending on the application. Laser power, being the controlled value, is regulated following a suitable set value. This set value can be the surface temperature for laser hardening, but also the area or size information to control liquid phase processes. For quality control all measured variables are stored, visualized and can be monitored.

LASSY

"LASSY" is a dynamic scanner based beam shaping system for flexible adjustment of laser beam width and intensity distribution to the needs of the application. Typically the laser beam is scanned perpendicular to the feed direction. The scanning optics is suited for lasers in the wavelength range from 808 to 1070 nm (diode, Nd:YAG; Yb:YAG) and has no focusing component. A laser optics with a rectangular or circular focal spot with minimum focal length of 300 mm is necessary in front of the input of the scanner optics. Typical suitable spot dimensions are in the range of 4–16 mm. All

sensitive components of the scanning head are cooled with water or compressed air to prevent heating-up, caused by absorbed laser power or back reflected laser or heat radiation. The optics have been designed and tested for laser powers up to 10 kW. The size of the scanning head is approx. 190 mm × 195 mm × 120 mm. Change of scanning width and intensity profile can be done during a running process manually or via the machine bus interface. Adaption to local different hardening track size and especially to local different heat flow conditions is possible.

6.6 Industrial Applications

In the following, three applications are presented.

Hardening of Brake Levers

Figure 6.13 shows the truck brake lever made of 42CrMo4 to be hardened.

The area to be hardened has a diameter of about 15 mm and the hardening depth should be >0.6 mm. For this application a special rotating mirror optics is used, which generates a conical beam profile. The hardening of the brake lever is temperature controlled using a 5 kW diode laser, whereby the camera-based system E-MAqS was integrated coaxially into the rotating beam path (Fig. 6.14).

Figure 6.15 shows the temperature–time curve and the closed-loop controlled laser power during the hardening process. The measurement of the temperature (black curve) starts after a heating-up phase of >2 s, if the lower temperature limit of the camera sensor (in this case 900 °C) is exceeded. During the next 3 s the process

Fig. 6.13 Truck brake lever made of 42CrMo4
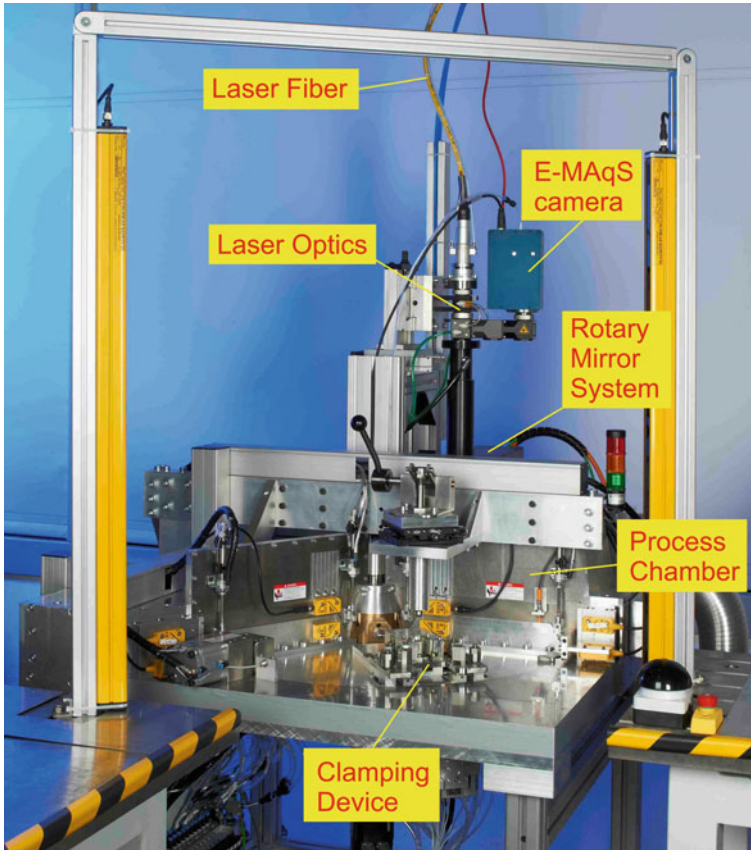
Fig. 6.14 Setup for laser hardening of truck brake levers

zone is heated to a hardening temperature of about 1200 °C. By decrease of the laser power (red curve) the LompocPro process controller automatically holds the peak temperature at a constant level for about 2 s to ensure a 100% austenitization, high heat penetration and to avoid local melting. The oscillations in the signal curves are caused by the geometry of part. During the fast conical rotation the laser beam is scanning over areas of different local heat flow conditions. Inspite of the temperature control remaining temperature fluctuations with an amplitude of several 10 K are visible.

The result of hardening is shown in Fig. 6.16 in the form of cross sections. The maximum hardening depth is 1.5–2 mm and a maximum hardness of 60 HRC is achieved.

Fig. 6.15 Temperature and corresponding laser power during closed-loop hardening of the truck brake levers
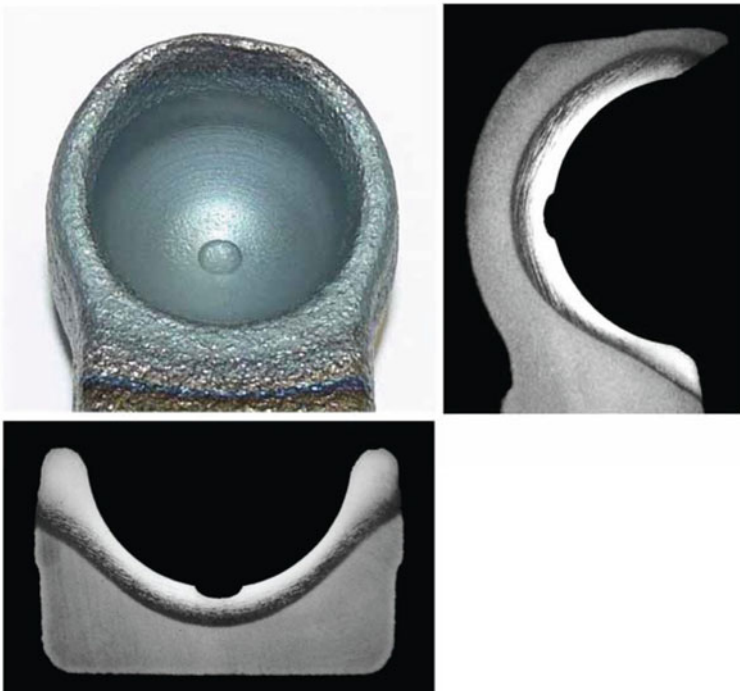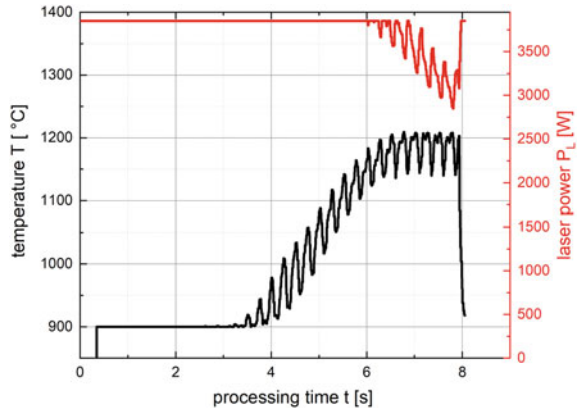
Fig. 6.16 Longitudinal and cross section of a laser hardened truck brake lever

This application has been implemented in industry, where up to half million parts are hardened per year. Laser hardening has substituted the previously used conventional hardening process due to the following advantages:

- Shell-like hardening zone reduces the risk of breakage under full load

- Short process time
- Single part process enables improved quality control
- Reduced energy consumption and costs
- Low distortion—no mechanical post treatment of hardening zone required

Hardening of Ball Grooves on Ring Joints (Vitr et al. 1995)

Ring joints are a component of the slip joint assembly group. The ball groove areas of the ring joints made from DIN Cf53 (AISI 1050) are to be hardened (Fig. 6.17). Induction hardening hardens the entire interior of the joint with a maximum hardness penetration depth of about 1.7 mm. During the process, large distortion is created in the area of the drillings and ball grooves. A subsequent finishing (grinding) is required to eliminate these distortion. Nd:YAG laser radiation hardens only the area of the ball grooves with specified hardening penetration depths of about 1 mm, hardness penetration widths of about 3–6 mm and a length of the treatment area of about 20 mm. This way, distortion is minimized and subsequent finishing can be avoided.

Figure 6.17 shows the treatment with laser radiation. Due to the given geometry of the ring, the minimum angle of incidence of the laser beam is 30° (angle between optical axis and ring joint radius on the xz-plane) when transmitted into the area to be hardened (ball groove). The process gas nozzle is a circular nozzle with a diameter
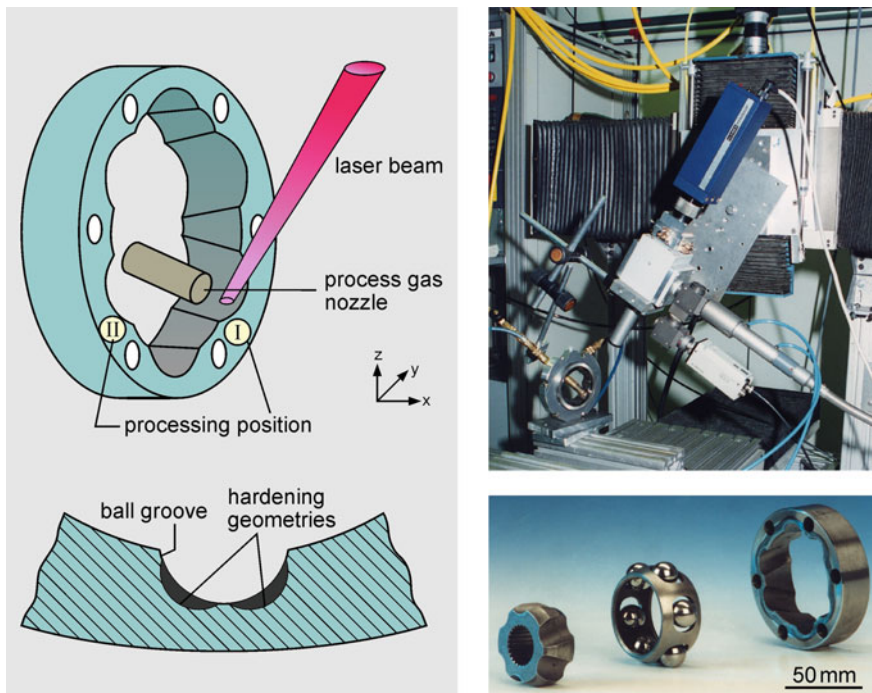
Fig. 6.17 *Laser hardening of ring joints*

of 10 mm that has been positioned under an angle of 30° in the xz-plane onto the ball groove relative to the interaction zone.

In order to harden the 12 ball grooves of a ring, two processing positions (I and II) and a 180° rotation of the joint ring become necessary. This is due to the ball grooves being tilted towards each other under the angle α (xy-plane). Figure 6.17 shows on the right hand side a cross-section of the positions of the two zones of the ball track to be hardened. Figure 6.17, center, displays the experimental set-up with ring joint fixture, process gas nozzle, as well as beam guiding and beam shaping optics.

A laser power of 1950 W and a feed speed of about 600 mm/min produces the required hardness penetration depth of about 1 mm and hardness penetration widths of about 6.3 mm. Based on these feed speeds, the process takes about twice as long as induction hardening, excluding the set-up time for a ring joint. Figure 6.18 shows a fully hardened ring joint in overview (a) and a detail of the ball groove (b). On the right hand side, a cross-section as well as a longitudinal section are presented. The ring joint geometry before and after laser hardening is measured and translated into a distortion coefficient. The evaluation of the distortion coefficients demonstrates that the distortion during laser beam hardening of ring joints (distortion coefficient 8) is half the amount of the distortion that takes place during induction hardening (distortion coefficient 15–17).

Hardening of Forming Tools

Laser hardening of large forming and cutting tools (with tool dimensions in the range of several meters) is meanwhile established as a standard process in industrial
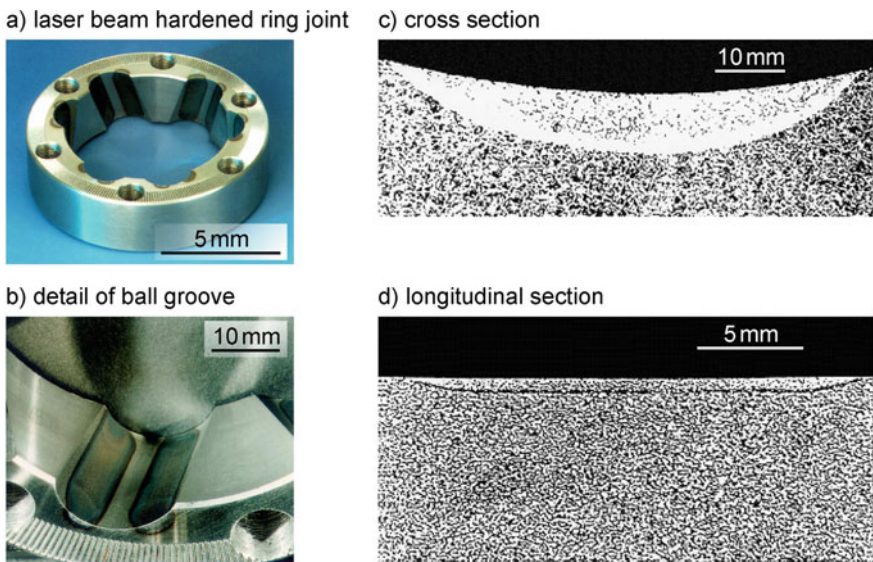
Fig. 6.18   Laser hardened ring joint
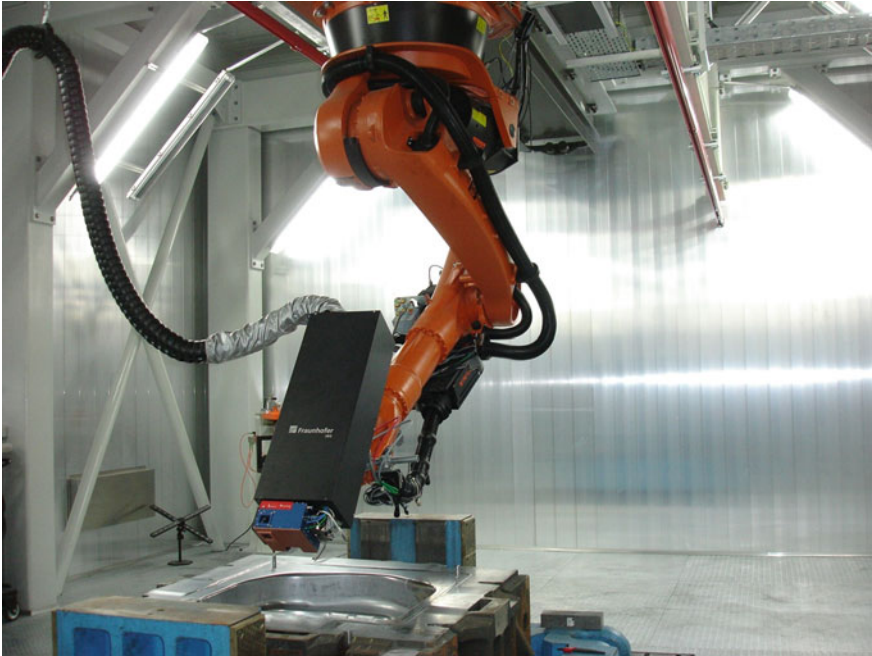
Fig. 6.19 Roboter-based laser hardening of a tool using the scanner system "LASSY"

manufacturing technology. In most cases, robot-based systems with fiber-coupled diode lasers with output powers between 6 and 10 kW are used (Fig. 6.19).

Due to the large variety of tool geometries to be hardened, flexible beam shaping systems such as the scanner-based module "LASSY" are suitable for this application. In Fig. 6.19 such a module is mounted on a robot arm. In most cases the hardening process is closed-loop temperature controlled. The hardening of a tool can be seen in Fig. 6.20. With the LASSY beam shaping system and 6 kW high power diode laser, hardening widths of up to approx. 60 mm can be achieved (see Fig. 6.21).

Fig. 6.20 Laser hardening of a tool using the system technology depicted in Fig. 6.19
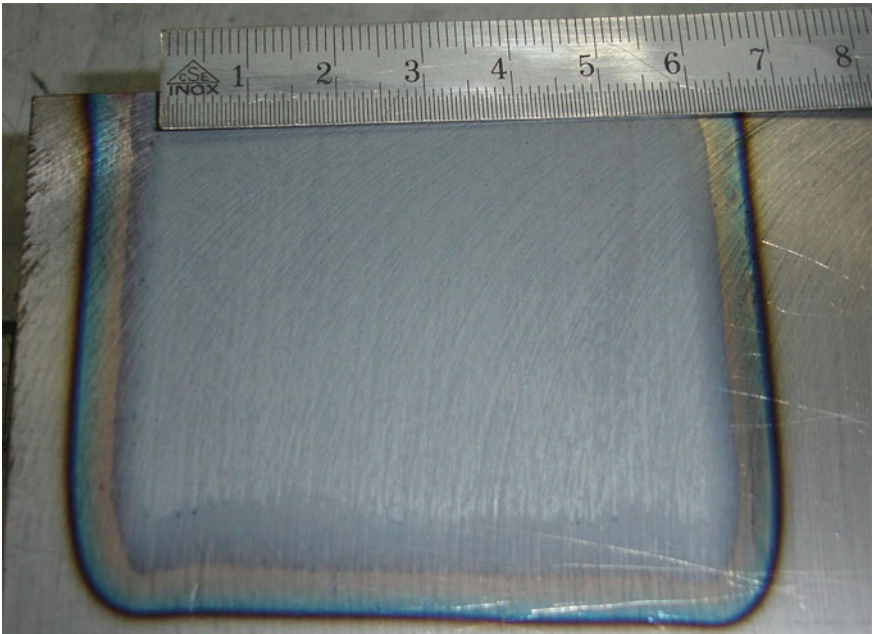
Fig. 6.21 Top view of a laser hardened single track with a width of approx. 60 mm

References

Amende W (1990) Oberflächenbehandlung mit Laserstrahlung. In: Treiber H (ed) Der Laser in der Fertigungstechnik. Hoppenstedt Technik, Darmstadt

Babu P, Buvanashekaran G, Balasubramanian KR (2014) Numerical analysis and experimental validation of hardness and microstructural changes during laser transformation hardening of low alloy steel plates. J Mater Design Appl 228(3):217

Beyer E, Wissenbach K (1998) Oberflächenbehandlung mit Laserstrahlung. Springer

Bonss S, Seifert M, Hannweber J, Karsunke U, Kühn S, Pögen D, Beyer E (2016) Precise contact-free temperature measurement is the formula for reliable laser driven manufacturing processes. In: Proceedings 9th LANE conference

Hung T, Shi H, Kuang J (2018) Temperature modeling of AISI 1045 steel during surface hardening processes. Materials 11:1815

Müller K, Körner C, Bergmann H-W (1996) Numerische Simulation der Eigenspannungen und Deformationen beim Laserrandschichthärten. HTM 51(1):19–28

Ohrlich J, Pietrzeniuk H-J (1976) Atlas zur Wärmebehandlung der Stähle, Bd. 4, Stahleisen

Ohrlich J, Rose A, Wiest P (1973) Atlas zur Wärmebehandlung der Stähle, Bd. 3, Stahleisen

Schmitz-Justen C (1986) Einordnung des Laserstrahlhärtens in die fertigungstechnische Praxis. Dissertation RWTH Aachen

Seifert M, Brenner B, Bonss S (2013) Qualitätsgesichertes Laserstrahlhärten durch mobile Temperaturkalibrierung. Konferenzbeitrag zur Fachtagung Temperatur 2013, Physikalisch-Technische Bundesanstalt Berlin 5/6:161–170

Seifert M, Anhalt K, Baltruschat C, Bonss S, Brenner B (2014) Precise temperature calibration for laser heat treatment. J Sensor Sensor Syst 3:47–54

Vitr G, Ollier B, Küpper F, Wissenbach K (1995) Umwandlungshärten komplizierter Werkstückgeometrien mit Nd:YAG-Laserstrahlung. In: Laser in der Materialbearbeitung, Band 4, Präzisionsbearbeitung mit Festkörperlasern, VDI Verlag

Willerscheid H (1990) Prozessüberwachung und Konzepte zur Prozessoptimierung des Laserstrahlhärtens. Dissertation RWTH Aachen

Part V
Additive Manufacturing

Chapter 7
Laser Powder Bed Fusion (LPBF)

S. Bremen, F. Eibl, Ch. Gayer, D. Heußen, Tim Lantzsch, L. Masseling, J. Munk, A. Vogelpoth, T. Pichler, N. Pirch, J. Risse, T. Schmithüsen, M. Schniedenharn, A. Such, Ch. Tenbrock, U. Thombansen, Ch. Weiß, and K. Wissenbach

Overview on Additive Manufacturing

In accordance with DIN EN ISO/ASTM 52900 (2018) Additive Manufacturing (AM) is a process of joining materials to make parts from computer-aided design (CAD) data, usually layer upon layer, as opposed to subtractive manufacturing and formative manufacturing methodologies such as casting, forging or milling. No tooling and material removal are required. Since the first technique for AM became available in the late 1980s and was used to fabricate models and prototypes (Beaman and Deckard 1990; Bourell et al. 1991; Koch and Mazumder 2000) AM technology has experienced more than 30 years of development and is presently one of the rapidly developing advanced manufacturing techniques with high disruptive potential (Gibson et al. 2010). In combination with Industry 4.0, AM opens up the ability to manufacture or print industrial products directly on the basis of digital data. In this way, industrial value chains can be sustainably changed within the entire production technology. Overviews about the different AM processes are found e.g. in Gibson et al. 2010; Gebhardt 2016). Additive Manufacturing is subdivided into the following process categories (Draft ISO/ASTM 52900, 2018):

- binder jetting, a process in which a liquid bonding agent is selectively deposited to join powder materials; example of AM-process: binder jetting
- directed energy deposition, a process in which focused thermal energy is used to fuse materials by melting as they are being deposited; examples of AM-processes: Laser or Electron Beam Metal Deposition (LMD or EMD)
- material extrusion, process in which material is selectively dispensed through a nozzle or orifice; example of AM-process: Fused Deposition Modeling (FDM)

S. Bremen · F. Eibl · Ch. Gayer · D. Heußen · T. Lantzsch (✉) · L. Masseling · J. Munk ·
A. Vogelpoth · T. Pichler · N. Pirch · J. Risse · T. Schmithüsen · M. Schniedenharn · A. Such ·
Ch. Tenbrock · U. Thombansen · Ch. Weiß · K. Wissenbach
Fraunhofer ILT, Aachen, Germany
e-mail: tim.lantzsch@ilt.fraunhofer.de

- material jetting, process in which droplets of feedstock material are selectively deposited; examples of AM-processes: ink or aerosol jetting
- powder bed fusion, process in which thermal energy selectively fuses regions of a powder bed; examples of AM-processes: Laser or Electron Beam Powder Bed Fusion (LPBF or EPBF), Laser Sintering
- sheet lamination, process in which sheets of material are bonded to form a part; example of AM-processes: Laminated Object Manufacturing (LOM), Cutting and Joining of metal sheets
- vat photopolymerization, process in which liquid photopolymer in a vat is selectively cured by light-activated polymerization; examples of AM-processes: Laser-stereolithography, polymer jetting

The initially developed AM processes include stereolithography apparatus (West et al. 2001), laminated object manufacturing (Park et al. 2000), fused deposition modeling (Gray et al. 1998), three-dimensional printing (Ribeiro 1998) and selective laser sintering (Bourell et al. 1992; Childs et al. 1999; Pham et al. 1999). These AM processes are typically applied for the fabrication of prototypes made from low melting point polymers (Gu et al. 2012).

The capability of producing physical objects in a short time directly from CAD models helps to shorten the production development steps. Nevertheless, the production of prototypes made from polymers has no longer been the current research focus of AM, because it enters a mature development stage. The next natural development of AM techniques was to produce complex shaped functional metallic parts, including metals, alloys and metal matrix composites (MMCs) that cannot be easily produced by the conventional methods, in order to meet the demanding requirements from different industrial sectors (e.g. turbomachinery, automotive, mechanical engineering, medical technology) (Gu et al. 2012).

In Draft ISO/ASTM 52900 (2018), AM is further structured into material (e.g. metals, polymers), initial state (e.g. powder, wire, foil, sheet metal), material distribution (e.g. powder bed, deposition nozzle), basic AM principle (e.g. melting, sintering, extrusion, reactive curing) and process category (see above).

Although AM processes share the same layer upon layer philosophy, each AM process has its specific characteristics in terms of usable materials, processing procedures and applications. In this book/chapter, the focus is on single step AM processes for processing metallic materials. The capability of obtaining high performance metallic parts with controllable microstructural and mechanical properties also shows a distinct difference for various AM processes. The prevailing AM processes for the fabrication of metallic parts addresses three process categories: powder bed fusion, binder jetting and directed energy deposition (Gu et al. 2012).

The powder bed fusion and binder jetting process categories are suitable for the manufacturing of complex parts with sufficient mechanical technological properties. Both process categories take place in a powder bed and the typical size of the process chambers of standard machines is in the range of 250–300 mm in x- and y-direction and 300–400 mm in height (z-direction). While powder bed fusion processes use laser (Laser Powder Bed Fusion, LPBF) and electron radiation (Electron beam powder

bed fusion, EPBF) for partial or complete melting of powder materials, in binder jetting a print head matrix is moved over the build surface. In this process, the binder is added dropwise by the print head to the powder to be bonded, so that the powder particles glue together. The parts have a high porosity and low mechanical properties. Therefore, in subsequent process steps, the binder is removed and the green part is sintered in a furnace. Therefore Powder Bed Fusion processes are single step processes while binder jetting is a multi-step process. The main advantage of binder jetting is the high build-up rate, which is up to a factor of 50 higher than LPBF. For this reason, the importance of binder jetting has increased significantly in recent years. In this chapter, binder jetting is not discussed further and reference is made to the relevant literature (Gebhardt 2016; Wohlers 2019). This chapter "LPBF" addresses the processing of metallic materials. An exception to this is the manufacture of patient-specific implants made from a composite material (polylactide PLA and calcium carbonate), which is presented in Sect. 7.3.8.

From the process category "directed energy deposition", the Laser Metal Deposition (LMD) process with powder and wire additive materials is discussed in Chap. 14 As an alternative to lasers, electron and plasma beams can be used as energy sources for this process category. The main advantage of the LMD process is its high flexibility in terms of application. Thus, the process can be used for cladding, the repair of especially high-priced parts, but also for the additive manufacturing of new parts. The extreme high-speed metal deposition (EHLA) process is a promising process variant of conventional LMD that offers both technical (e.g. processability of materials that are difficult to weld) and economic (e.g. high process speeds) advantages (Chap. 12).

In the chapter "Additive Manufacturing of Embedded Sensors" (Chap. 16), multi-layer coatings are deposited and functionalized. Various coating and printing processes are used. The printing processes can be assigned to the process categories "material jetting" and "material extrusion" and include ink or aerosol jetting, dispensing and screen printing.

The materials used differ in a wide range, based on precursor solutions, sol gels, nano-particulate dispersions, or micro-particulate pastes, depending on the desired functionality and deposition method.

Chapter 17 deals with biofabrication based on AM. Stereolithography (SL) and multi-photon polymerization (MPP) belong to the vat photopolymerization processes and laser-induced forward transfer (LIFT) is a laser-based droplet-on-demand process, which can be assigned to the category "material jetting". The 3D-bioprinting focusses on biocompatible polymers e.g. hydrogels and cells as well as mixtures thereof, so called bioinks. The described techniques are nozzle-free with many advantages for cell printing/cell deposition. Examples for 3D printing of scaffolds for tissue engineering and sorting and transfer of single cells are given.

7.1 Fundamentals of LPBF

7.1.1 Laser Sintering and Laser Powder Bed Fusion

In laser-based powder bed processes for metallic materials, a distinction is made between processes with partial and complete melting. Processes with partial melting are summarized under the term laser sintering (LS), complete melting under the term laser powder bed fusion (LPBF). Equivalent terms for LPBF are Selective Laser Melting (SLM), Laser Cusing, Laser Metal Fusion, and Direct Metal Printing. The machine technology for both processes consists of the same components: Laser beam source, optical system for beam guidance and focusing, computer for controlling the process, process chamber with inert gas guidance, movable build platform, powder reservoir and powder deposition unit (see Sect. 7.3.7.1) (Gu et al. 2012; Meiners 1999).

In laser sintering of metallic materials, special multi-component powders are processed, using a low-melting point and a high-melting point material. In some cases, the high-melting powder particles are also coated with the low-melting component. Under the action of the laser radiation, only the low-melting component is melted. This acts as a binder for the high-melting powder particles, which remain in the solid phase. In this process, densification of the powder layer takes place by rearrangement of the high-melting powder particles in the liquid phase. A well-known powder system is CuSn/CuP–Ni, where copper phosphate together with bronze act as the binder phase. The parts produced by laser sintering have a density of about 75%. To improve the functional properties, the parts are infiltrated after LS. The melting temperature of the infiltrate must be lower than that of the binder phase. Capillary forces cause the liquid infiltrate to penetrate the pores, which increases the density (Gu et al. 2012).

In summary, LS of pre-alloyed powders leads to, for example, low density, heterogeneous microstructures and properties. Therefore, post-processing treatment such as furnace post-sintering, hot isostatic pressing (HIP), or infiltration with a low melting point material is normally necessary to improve the mechanical properties. Driven by the demand to produce fully dense parts with mechanical properties comparable to those of bulk materials, LPBF has been developed.

7.1.2 Process Principle and Process Parameters of LPBF

The manufacturing in LPBF takes place in a sequential manner consisting of: (1) selective melting of the powder according to the defined scan path, (2) lowering of the build platform about the defined layer thickness and (3) powder deposition with a recoater (Fig. 7.1). This sequence is repeated until the manufacturing process is completed. All processes start on a base plate or preform, which are placed on the
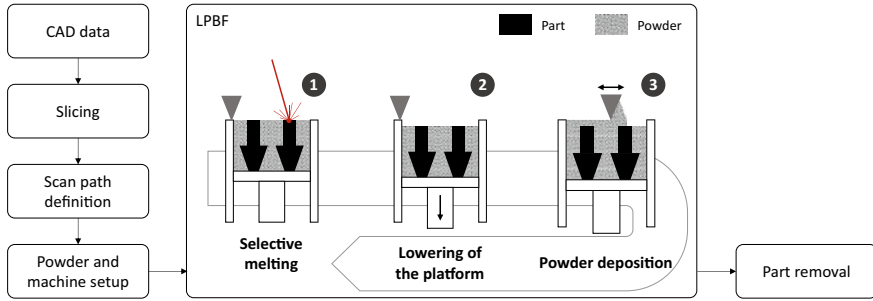
Fig. 7.1 Schematic diagram of the main steps in the LPBF process, reprinted from Risse (2019)

moveable build platform. The part size is limited by the available build space, defined by size and range of travel of the build platform (Risse 2019).

LPBF takes place in a process chamber with an inert gas atmosphere at small overpressures in the range of several mbar. Argon is mainly used as the inert gas and oxygen levels of <200 ppm are typically achieved. Metals are mainly processed using solid state lasers, e.g. fiber lasers, with a wavelength $\lambda = 1{,}030$ bis $1{,}080$ nm and energy absorption takes place in the first nanometers below the surface. Laser beam deflection is done by mirrors mounted on galvanometer scanners and the resulting scan speeds are limited by the inertia of the scanners. Smaller beam diameters and smaller layer thickness, as well as finer powder sizings, lead to a lower surface roughness and higher geometrical resolution in comparison to EPBF (Risse 2019).

Process parameters and scan strategies are introduced based on Fig. 7.2. The beam diameter d_S is mainly determined by the optical system of the LPBF machine and is 70–100 μm for standard machines. In most cases, a constant beam diameter is used. The scan strategy defines the pattern of vectors which the laser beam scans with the scan speed v_S and the laser power P_L in order to melt the powder material in a specific area. The area to be processed is derived by slicing the part in layers with the thickness D_l. The most common strategies, which define the pattern of vectors in each layer, are (Fig. 7.2b) (Risse 2019):

- Meander strategy: no further division, scan vector length l_S is infinite
- Stripe strategy: division in stripes, width defined by scan vector length
- Chess board strategy: division in squares, edge length defined by scan vector length

The resulting segments are filled with vectors using the hatch distance Δy_h. In most cases, the vectors follow a meander-like pattern so that a bidirectional scan pattern within a segment is achieved. Alternatively, identical vector orientations can be used, known as unidirectional scan pattern (Fig. 7.2a). A segment overlap Δy_0 can be defined in order to ensure a sound metallurgical bonding between adjacent segments. The scan vector orientation, and thus the segment orientation as well, is rotated about a specific angle α_{rot} between adjacent layers. Typical rotation angles are for instance 90° or 67° (Risse 2019).
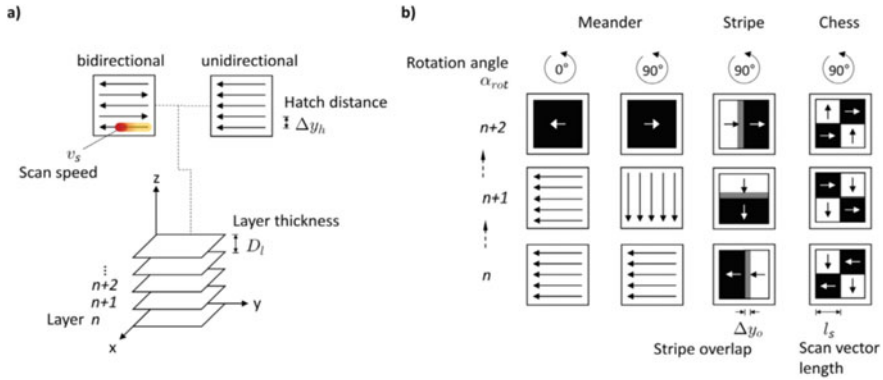
Fig. 7.2 **a** Main process parameters and **b** schematic diagram of the most relevant scan strategies, reprinted from Risse (2019)

In order to compare the energy input of different process parameters combinations, the volume energy density E_V and the line energy density E_L are defined according to Eqs. (7.1) and (7.2) (Risse 2019; Tenbrock et al. 2020):

$$E_V = P_L/(v_S \times \Delta y_h \times D_l) \quad [J/mm^3] \tag{7.1}$$

$$E_L = P_L/v_S \quad [J/mm] \tag{7.2}$$

Furthermore the intensity I_L is an important characteristic of the LPBF process (Tenbrock et al. 2020):

$$I_L = P_L/F_L \text{ with } F_L = \pi(d_S/2)^2 \text{ for a circular beam} \quad [W/cm^2] \tag{7.3}$$

Next to the energy input, the productivity of a process parameter is a relevant economic factor. One possibility to describe this is an analytic description of the build rate, which is defined according to Eq. (7.4). This description neglects machine and geometry dependent impact factors and resembles a theoretical upper limit. Thus, it is known as theoretical build-up rate (Risse 2019).

$$V_{th} = v_S \times \Delta y_h \times D_l \quad [mm^3/s] \tag{7.4}$$

7.1.3 Methods for the Determination of Process Parameters

There are literature references (Yadroitsev 2009) that list more than 130 influencing parameters that affect the process and thus the final quality of the part. This vast

parameter space illustrates how complex and challenging it is to optimize the process in terms of density, dimensional accuracy, roughness, microstructure, building cost, and build rate with a low or tolerable number of defects. Such defects are cracks, pores and bonding defects. In addition, it must be considered that the results achieved cannot usually be transferred one-to-one to another machine, but that the transfer to another machine may require fine-tuning of existing process windows. And this leads to the fact that process optimization usually first concentrates on the parameters that can be varied on the machine. The very first goal of such an optimization is a process window in which densities >99.5% with as few or tolerable defects as possible are achieved in a robust process. The starting point for process development is in most cases a commercial LPBF machine with a laser power range $P_{min} < P_L < P_{max}$ and a given beam diameter d_S. This determines the available intensity range (Eq. 7.4). Depending on the material, a certain processing regime has proven to be effective for a stable process without balling (Li et al. 2012; Cunningham 2018; Liu et al. 2016) and humping (Tang et al. 2020; Tang et al. March 2020; Gunenthiram et al. 2017). The processing regimes are distinguished between heat conduction, transition (weld-in) and deep welding regimes. The occurrence of the respective regime is significantly determined by the intensity. In the heat conduction regime, no vapor capillary occurs. The geometry of the melt is determined by heat conduction and, if present, Marangoni convection. The depth-to-width ratio (aspect ratio) of the remelted zone/geometry after solidification in a plane perpendicular to the scan direction is typically <1:2. As the intensity increases, vapor capillary formation occurs. When the aspect ratio is less than 2:1, the transition regime is present; for larger ratios, deep welding is present. In deep welding, the absorbed energy within the vapor capillary increases due to multiple reflection. The deep welding regime is avoided in LPBF due to the formation of pores in the lower region of the vapor capillary. The most common processing regime in LPBF of metallic materials is the transition regime (Schniedenharn 2020).

There are a number of approaches to determine the optimal parameters for generating additively manufactured parts with desired characteristics (see, for example, the summary in Kamath et al. 2014). The magnitude of the influence of the various process parameters, such as powder quality, layer thickness, laser power, scanning speed, hatch distance, scan vector length and scan strategy on the properties, such as density and surface roughness, are investigated in carefully designed experiments. For this purpose, small cubes are built and their properties are evaluated (Kruth et al. 2010; Spierings and Levy 2009). In practice-relevant parts, however, the scan vector lengths used in the process window are often significantly undercut in thin-walled part areas. This causes deviations in the resulting time–temperature cycles and melt pool geometries from the results in the solid material on the cubes. Likewise, upside and downside regions of the part are not addressed. This should indicate at this point that these sensitive part areas may require part specific fine tuning of the parameters. Because the effort for specimen preparation is the same, rectangular cuboids with a projection of 60° are used in recent studies (Ferrar et al. 2012), which allow an analysis on the characteristics of the up-skin and down-skin surfaces in addition to the top surface of the samples. The experimental designs are prepared according to the methods of statistical design of experiments DOE. However, the experimental

effort for full factorial designs grows very fast with the number of parameters and the chosen levels of each parameter. To counter this, the so-called Taguchi method is often used in practice, in which the full factorial experimental design is reduced to a partial factorial experimental design. In a partial factorial experimental design, there are too few support points to determine all development coefficients for the polynomial approach, and so interaction terms that are estimated to be small on the basis of expert knowledge are set to zero.

The test specimens which are produced for this purpose, are then analyzed metallographically with regard to remelting geometry, occurrence of defects and microstructure. Usually, a layer thickness (typical layer thicknesses 30–100 µm) and a hatch distance (e.g. $\Delta y_h = 0.7 \times d_S$) are first selected as reference points.

Another approach takes as a starting point for parameter determination a parameter set for an already investigated material with similar thermophysical properties. Here, too, the laser power and beam diameter of the parameter set already available should approximately correspond to those of the LPBF machine used because of the transferability.

In Bosio ([2019](#)) a method for the determination of process parameters for a commercial LPBF machine is applied, in which in a first step single tracks for a defined layer thickness are produced under variation of laser power and scanning speed. These tracks are characterized in terms of track uniformity (stable and unstable tracks) and remelt geometry (irregular and regular melt pools). Thus, the parameters for P_L and v_S are narrowed down. The width of the single tracks is used to define values for the hatch distance in the case of overlapping processing. In the next step, cuboids are fabricated using different scanning strategies (see Fig. [7.2](#)b). For this purpose, DOE methods are applied varying the parameters P_L, v_S, Δy_h and the scanning strategy. The samples are evaluated in terms of density metallographically. In this way suitable process windows are determined.

However, further investigations have shown that not only the continuously varying parameters such as laser power, scan speed, overlap and powder layer thickness, but also the process conditions determined by the fixed machine architecture, such as the arrangement of the shielding gas flow, have a significant influence e.g. the porosity of the produced parts (Schniedenharn [2020](#); Ferrar et al. [2012](#); Ladewig et al. [2016a](#); Reijonen et al. [2020](#)). For the mechanism to what extent the gas flow and the orientation of the part or the scan vectors to the gas flow have an influence on e.g. the porosity Schniedenharn ([2020](#)) and Ladewig ([2016a](#)) attribute two different phenomena: (1) increased absorption and/or scattering of the laser radiation by the metal vapor and condensate particles ejected from the melt pool, and (2) large spatters and/or removed powder particles landing on the unprocessed powder bed when the gas flow is insufficient to remove the vapor plume and/or spatters.

The inert gas loaded with by-products is exhausted from the process chamber, cleaned and fed back into the process chamber via a nozzle. The most commonly used shielding gas flow in LPBF machines is the lateral flow. In the lateral flow, the shielding gas flows parallel to the build plane and thus has the same preferred direction at any point on the build plane. The shielding gas flow must be designed in such a way that, as far as possible, all process by-products are transported away from

the interaction zone (interaction zone: area in which laser beam—process by-product interaction can occur) and, at the same time, any influence on the powder bed (e.g. swirling up of powder) is avoided. Ideally, the flow velocity should be the same over the entire build plane. The flow direction should be in the direction of the emission direction of the process by-products. This must be taken into account when orienting the scan vectors relative to the shielding gas flow (Schniedenharn 2020).

As already mentioned before, it must be considered that process parameters developed for the production of simple test specimens are not suitable for the production of parts without further modification. For this purpose, process parameters must be developed, e.g., for contour exposure, for fabrication of support structures and of overhangs. Furthermore, the scanning strategy and the orientation of the part in the process chamber have to be adapted to the part geometry.

Due to the rapid development of the LPBF process in recent years, process parameters have been determined for numerous materials. The most important material classes for metallic materials are

- Various steels (e.g. tool steel, stainless steel, tempered steel)
- Aluminum alloys (e.g. AlSi10Mg)
- Pure titanium and titanium alloys (e.g. TiAl6V4)
- Nickel-based alloys (e.g. Inconel 718)
- Cobalt-chromium alloys (e.g. Wirobond C+)

The material-specific aspects of processing the various classes of materials with LPBF and LMD are discussed in Chap. 14. Many of these materials can be processed with high quality using standard LPBF machines from different machine manufacturers (see Sect. 7.3.7.1). The machine manufacturers also specify machine-specific process parameters for numerous materials. Some material classes, such as copper and copper alloys, difficult-to-weld nickel-based alloys such as IN738 (Risse 2019) or titanium aluminides or magnesium alloys (Jauer 2018), cannot be processed with standard LPBF machines or can only be processed with low quality. Specific measures are necessary for their processing, such as adapted laser beam sources, integration of preheating modules or modification of the shielding gas flow. Some of these measures are described in more detail in Sects. 7.3.4 and 7.3.7.2.

7.2 Vertical and Horizontal Process Chain

Manufacturing processes and value chains with maximum flexibility and simultaneous consistency in data transfer and material flow can significantly shorten product development cycles. LPBF is such a manufacturing method. The reasons are the fast transfer of geometry data into real products as well as the enormous flexibility and short reaction time. However, only the integration of LPBF manufacturing into established production chains enables shorter innovation cycles and continuous improvements in development, production and maintenance. In addition, new opportunities for material development, function- and resource-oriented product design arise.
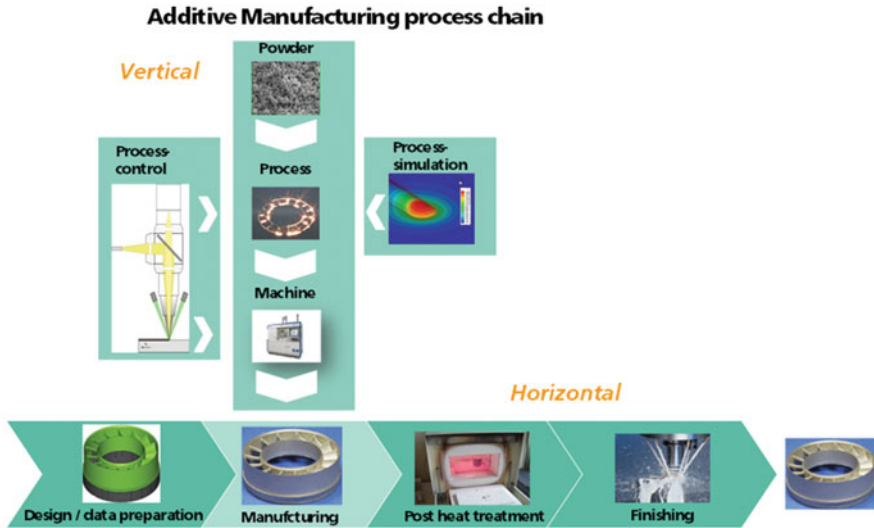
Fig. 7.3 Vertical and horizontal process chain for LPBF

Against this background, this chapter considers both the LPBF-specific vertical process chain and its integration into a continuous horizontal process chain (Fig. 7.3).

The vertical process chain comprises the development and provision of suitable powder materials, the actual LPBF process, and the implementation of the LPBF processes with robust machine technology. Other important aspects in the vertical chain are quality assurance for on-line monitoring and defect detection during the process as well as the support of process development and optimization through the development of simulation tools on different size scales. The horizontal process chain starts with the AM-compatible design of parts and tools in order to take advantage of the enormous degrees of design freedom offered by LPBF. After manufacturing, post heat treatment is often performed both to improve part quality (e.g. HIP) and to adjust the desired microstructures. The final step in the horizontal chain is usually the finishing of the parts. This includes, for example, the removal of the support structures as well as the separation of the parts from the substrate plate and the final machining of the part to achieve the required dimensional accuracy and surface topography.

The elements of the two process chains are presented in more detail in the following chapters.

7.3 Vertical Process Chain

7.3.1 Powder Materials for LPBF

The properties of the powder material have a significant influence on the properties of the powder layer after deposition, the LPBF process and the final part properties (DebRoy et al. 2018). In Vock et al. (2019), the relationships between the powder and part properties are presented in four levels.

The lowest level describes the pure physical or chemical property of the individual particles (named: powder properties). The second level describes the behavior of the powder ensemble as a whole (named: bulk powder behavior). The third level describes the behavior of the powder under process-specific conditions (named: in-process performance). Finally, the sum of various aspects of each level influences the final part properties, such as density, surface quality, defects and mechanical properties (Vock et al. 2019).

Major powder properties are the morphology, particle size distribution (PSD), chemical composition, impurities, moisture content, density of individual particles (e.g. hollow particles), and material-specific thermophysical properties. These properties influence both the flowability of the powder bulk and thus the properties of the powder bed (e.g. apparent and tap density, Hausner ratio) as well as the final part properties. The properties of the first two levels influence the LPBF process with respect to the formation of a homogeneous, reproducible powder layer after deposition and the interaction of the laser radiation with the powder bed (e.g. absorption behavior of the powder, formation of process by-products (see above)) (Vock et al. 2019).

In addition to the properties of the powders, their costs are also of great importance. Depending on the LPBF system configuration, the powder costs account for between 14 and 41% of the part costs. This means that the powder material costs are still the second largest cost driver after the machine costs (investment costs) in the LPBF technology (Schrage 2016).

The following requirements and relationships of the powder properties can be taken from the literature (Vock et al. 2019; Sutton et al. 2016; Brandt 2017; DebRoy et al. 2018):

Morphology

Morphological parameters are particle size, shape, and surface roughness. Particle sizes between 10 and 60 μm are mainly used for LPBF. Spherical particles are beneficial for flowability. Non-spherical particles tend to mechanically interlock and become entangled with each other. In the case of coarse particles, smooth and spherical particles flow better than rough, sharp-edged, non-spherical particles. But in the case of fine particles, which are cohesive and between which adhesive forces play a major role, rough particles may exhibit a more favorable flow behavior. Fine and smooth particles tend to agglomerate, which must be avoided (Vock et al. 2019).

Particle Size Distribution (PSD)

In Liu et al. (2011), the influence of the PSD on both the properties of the powder bed and the properties of test specimens is investigated. Two PSDs (PSD1: 0–45 µm, PSD2: 15–45 µm) of the 316L material are used for this purpose: The apparent density, tapped density and powder bed density are larger for the wider PSD1 than for PSD2. The reason for this is that with a wider PSD, the smaller particles can fill the voids between the coarser ones. However, the Hausner factor for PSD1 is larger than for PSD2, so the flowability for PSD1 is lower than for PSD2. It is found that powder 1 tends to achieve larger densities of the test specimens for the same process parameters. The roughness of the test specimens is also lower for powder 1 than for powder 2. The tensile strength and elongation at break, on the other hand, are greater for powder 2. However, this result is valid only when, as in this publication, the wider PSD is obtained by smaller particles. If the proportion of small particles becomes too large, the influence of interparticle forces increases and the flowability decreases.

Moisture

A high moisture content in the powder has a negative effect on both the flowability and the laser-powder bed interaction. The interaction of the laser radiation with the moisture can lead to an irregular remelting process combined with increased formation of defects (e.g. pores). An example is the processing of aluminum alloys, where moisture leads to an increased formation of hydrogen pores (Weingarten et al. 2015). Therefore, in many cases, it is recommended to dry the powder before the LPBF process.

Chemical Composition

The chemical composition of the powder must be in accordance with the specifications of the respective material. The specification limits for the chemical composition can be taken from certain standards, for example. For AlSi alloys, these are compiled in DIN 1706. Depending on the material, the powder should be further analyzed with regards to the presence of trace elements, e.g. oxygen, hydrogen, nitrogen, as well as with regards to impurities. The trace elements can have a negative effect both on the processability (e.g. increased oxide formation in the case of oxygen) and on the functional properties of the parts (e.g. hydrogen pores).

Density of Powder Particles

The density of the powder particles is an important input variable for the LPBF process. If the powder has a large number of hollow particles (porosity), this can also lead to an increased formation of defects (pores, binding defects) in the final part.

The above representation shows that spherical powders with good surface quality and well-defined PSD that are preferably suitable for LPBF. However, such powders are expensive to produce and therefore represent a major cost driver for LPBF.

In this context, the selected powder atomization method significantly influences the properties of the powder produced and the cost at which it can be purchased
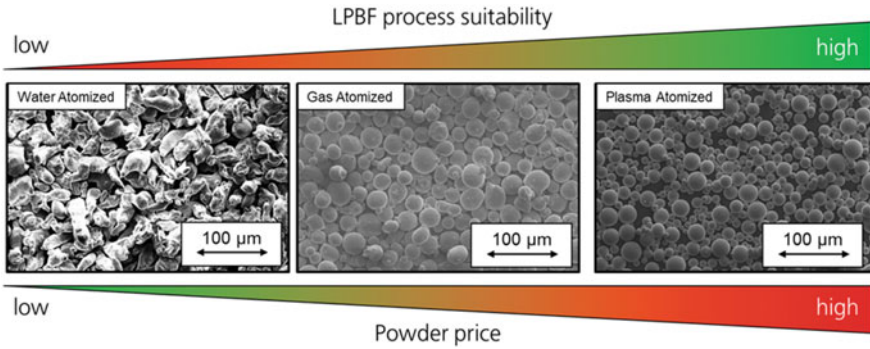
Fig. 7.4 SEM images of the particle morphology produced by water atomization (left, 316L), gas atomization (middle, 316L) and plasma atomization (right, IN 718)

(Anderson et al. 2018; Dawes et al. 2015). These powders are usually produced via gas atomization (EIGA (electrode induction melting gas atomization), VIGA (vacuum induction melting gas atomization)) or, less frequently, via plasma atomization (PREP (plasma rotating electrode process)). The output rate of the desired particle fraction depends on the raw material and the atomization process used.

However, in terms of volume and in case of non-reactive metals, the most widely used atomization method for the production of powder materials is water atomization, which is used, for example, for the production of approx. 93% of all steel powders (Beiss et al. 2003). Although these powders can be purchased at significantly lower prices than gas atomized powders, they have aspherical particle shapes and are thus limited in their flowability for processing by LPBF (Neikov 2009) (see Fig. 7.4).

The use of water-atomized powders offers the potential to reduce material costs by a factor of 2–3 (R. Berger Strategy Consultants GmbH 2018). Using gas-atomized powders, the material cost share in the LPBF process can take a share of about 23% for single-laser systems and up to 40% for new, more efficient multi-laser systems (Schrage 2016).

Quality control of the powder used is mandatory. For this purpose, the quality parameters particle morphology, particle size distribution, flowability, chemical composition and moisture content are frequently measured. Various methods are available for measuring these parameters (Vock et al. 2019; Sutton et al. 2016).

Since powder is a major cost driver in the LPBF process (Schrage 2016), powder that is not used during manufacturing is partially recycled. However, the proportion of recycled powder can have a negative influence on powder quality and thus on part properties and quality. The reasons for the poorer powder properties are oxidation, changes in the particle size distribution and the deposition of process by-products (e.g. spatters) in the powder. In order to achieve a high powder quality for reuse, preparation and monitoring of the powder are necessary (Lutter-Günther 2020).

The following is a comparison between water-atomized and gas-atomized powder of the stainless steel 316L. Aim is to illustrate the relationship between the powder particle properties (particle sizes and morphology) resulting from different powder

production processes on the in-process powder properties (powder layer density) and on the part quality (part density, surface roughness) (Pichler et al. 2018).

The powder batches are subdivided into different fractions by sieving. A fine (mesh size 37–25 µm), a medium (mesh size 53–37 µm) and a coarse fraction (mesh size 74–53 µm) of each powder manufacturing route is used. As expected, the gas atomized powder fractions are of spherical shape and the water atomized ones have a spattered and irregular shape (Pichler et al. 2018).

The particle size distribution of the water atomized powder fractions are wider than those of the gas atomized ones. The flowability of the gas atomized powder fractions is better than those of the water atomization.

The investigation of LPBF process parameters is performed by building up test specimens (cubic samples with 5 mm edge length). The parameters laser power $P_L = \{250, 370\}$ W, scanning speed $v_S = \{400, 800, 1,200\}$ mm/s and hatch distance $\Delta y_S = \{0.10, 0.12\}$ mm at constant laser beam diameter $d_S = 0.070$ mm and constant powder layer thickness $D_l = 0.06$ mm are varied. The relative density of the test specimens is examined by analyzing the cross-sections with a light microscope. The target values are relative densities of >99.5%.

Figure 7.5 shows an example of the density as a function of the scanning speed for both laser powers for the grain fraction 37–53 µm. While a density >99.5% is achieved for the gas atomized powder at 250 W and 800 mm/s and at both hatch distances, this is only possible for the water atomized powder at a hatch distance of 100 µm. At a laser power of 370 W, the density criterion is achieved with the gas atomized powder at least up to a scanning speed of 1,200 mm/s. With water atomized powder, the density criterion is only achieved at a scanning speed of 800 mm/s.

A reduced density of <99.5% can be noted for scan speeds of $v_S = 400$ mm/s for all gas atomized powder batches, both for a laser power $P_L = 250$ W and $P_L = 370$ W. The increased energy input results in a reduced density and an increased formation of spatters that can be observed during the LPBF processing. Comparing the densities for the three different powder size distributions for $P_L = 250$ W and $v_S = 1,200$ mm/s, it can be noted that the relative density decreases from fine to coarse powder size distributions. This is valid for gas atomized as well as for water atomized powder.
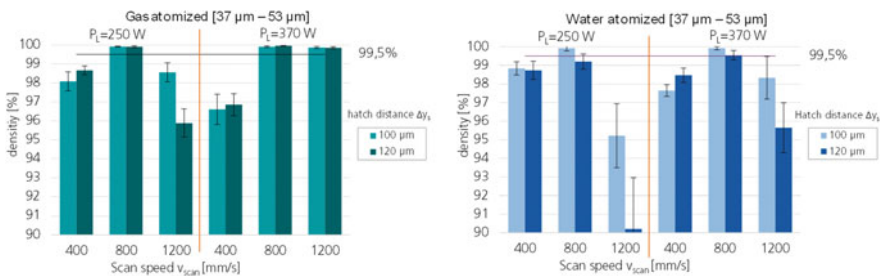
Fig. 7.5 Density in dependence of scan speed for two laser powers, left: gas atomized powder, right: water atomized powder, reprinted from Pichler et al. (2018)
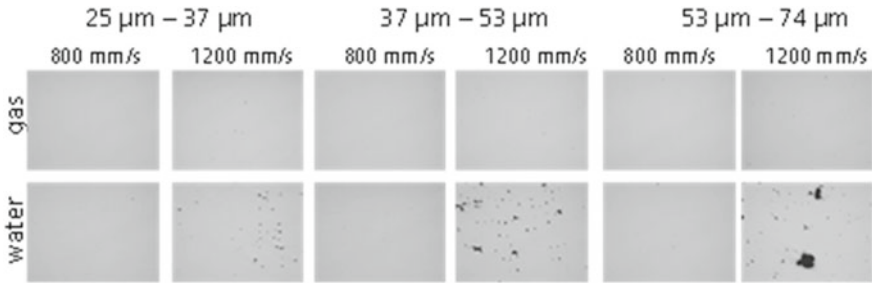
Fig. 7.6 Cross sections of test samples for the same process parameters for gas and water atomized powder, reprinted from Pichler et al. (2018)

Figure 7.6 shows the cross sections of specimens processed with $P_L = 370$ W, and $v_S = 800$ mm/s $v_S = 1,200$ mm/s and $\Delta y_S = 120$ µm. The desired relative density can be achieved for a scan speed of 800 mm/s for gas and water atomized powder, whereas for a scan speed of 1,200 mm/s only for the gas atomized powders. Lack of fusion defects can be observed for water atomized powders for a scan speed of 1,200 mm/s.

In summary, the following statements can be made (Pichler et al. 2018):

- The desired density of >99.5% can be achieved with all powder types by adaption of processing parameters.
- For both gas and water atomized powders the density decreases with increasing powder grain size for constant processing parameters. Larger powder particles seem to require more energy in order to melt completely and form dense specimens.
- Beside the absolute energy input, the interaction time between laser and powder/ melt pool seems to have an influence on processability, especially for water atomized powders, where increased interactions times (lower scan speeds) are required in order to form dense specimens.

Weiß and Schleifenbaum (2020) comes to similar results: the author compares gas- and water-atomized 316L powder and fabricates test specimens with different layer thicknesses (40, 80, 120 µm), different laser powers (120, 240, 360 W), a hatch distance of 100 µm and under a variation of the scan speed. The density and pore morphology of the specimens are analyzed. The author also finds that lower scan speeds are needed in case of water-atomized powders than for gas-atomized powders in order to meet the density criterion. For the same process parameters, the sphericity of the pores is lower for water atomized powder than for gas atomized.

7.3.2 Process Managements for LPBF

In recent years, various process managements (hereinafter also referred to as process strategies) have been developed that address part quality in addition to the productivity. Different process managements and the motivations for their development are:

- Increasing the build-up rate and thus the productivity of the process → High Power LPBF and Adaptive LPBF.
- Improvement of part quality → Geometry-adapted process management
- Processing of materials that cannot be processed with sufficient quality using standard LPBF machines → LPBF with preheating and LPBF with other wavelengths
- Manufacturing of small parts with higher detail resolution → Micro LPBF

The implementation of the process managements usually also requires a modification of the machine technology. Examples include the use of different beam diameters, the use of laser beam sources with other wavelengths, the integration of preheating modules into LPBF machines or the adaptation of the control software. Therefore, these developments can be assigned to the area of LPBF process as well as to the area of machine technology in the vertical process chain. Depending on which aspect is predominant, the developments presented below are shown either in one or the other area of the vertical process chain.

Conventional, High Power (HP) and Adaptive LPBF

In conventional LPBF management (Fig. 7.7), the part is divided into layers of equal thickness, regardless of its geometry and regardless of the required surface quality. The layer thicknesses are often in the range 30–50 μm and the scanning strategy also remains constant for the entire part. The process parameters are selected to achieve a density >99.5% and low surface roughness. As a consequence, low build-up rates and thus long processing times result, which considerably reduce the productivity and thus also the economic efficiency of the process.

Increasing the productivity is a key issue in LPBF development. This can be realized by several measures:

1. Increasing the laser power, thus increasing scan speed and/or layer thickness. Processing with larger beam diameters thereby to also increase the hatch distance. According to Eq. 1.2.3, these measures lead to an increase of the build-up rate.
2. Enlargement of the process chamber. This allows more parts to be manufactured in one build job and increases productivity.
3. Parallelization of the LPBF process by using multiple laser beam sources and multiple scanner systems in one machine.

Measures 2 and 3 are presented in the Sect. 7.3.7.
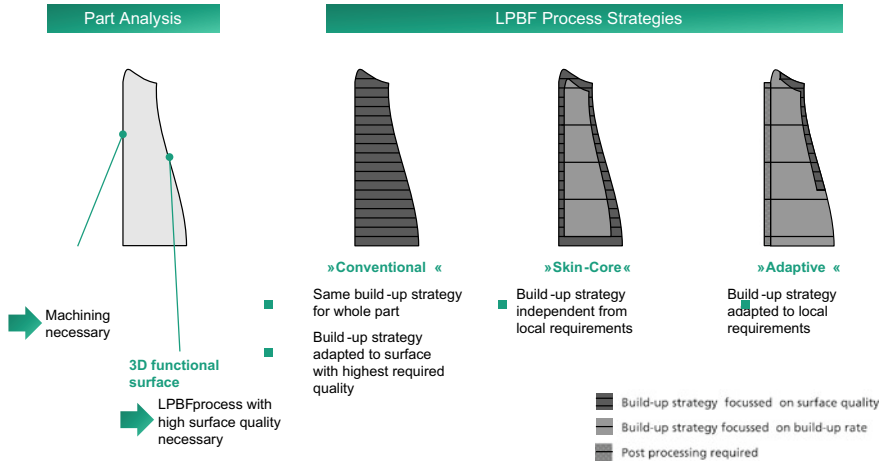
Fig. 7.7 Schematic representation of different process strategies for LPBF

High Power LPBF

High Power LPBF works with laser powers in the kW-range. With a constant beam diameter, this means an increase in intensity. Depending on the thermal conductivity of the materials to be processed, different process strategies can be used. For materials with high thermal conductivity (e.g. Al alloys), the build-up rate can be increased at a constant beam diameter by increasing the scan speed (Buchbinder 2013). For materials with low thermal conductivity (e.g. IN 718), increasing the intensity can lead to an unstable remelting process with deep penetration welding in combination with increased pore and spatter formation. Schleifenbaum (2010) developed the skin–core principle as a solution. In this case, the part to be produced is divided into a skin and a core area (Fig. 7.8). In order to achieve high detail resolution and low surface roughness, the skin area is fabricated with laser beam diameters of 70–120 µm at laser powers of 200–400 W and low layer thicknesses of 30–50 µm. Since the core area has low requirements in terms of detail resolution and roughness, it can be processed with beam diameters of 500–1,000 µm and layer thicknesses of 60–300 µm. Critical in the process management is the overlapping area between the skin and the core. For this purpose, a specific overlapping area is defined. There are two strategies for this area:

- The core volume is increased so that part of the skin volume is also melted during exposure of the core.
- After each exposure of the core volume, contour offset scans are performed in the overlapping area between the skin and the core.

By increasing the beam diameter and adapting the process parameters the cooling and solidification conditions change significantly in comparison to the conventional LPBF process. Therefore, the microstructure and mechanical properties also change.

Fig. 7.8 Skin–core build-up strategy for High Power LPBF, reprinted from Bremen et al. (2017, Fig. 1), with the permission of Springer
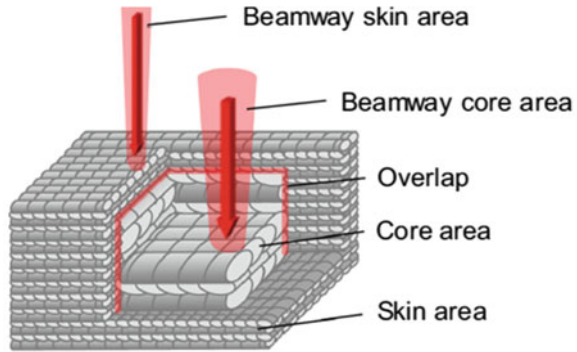
Using IN 718 as an example, the High Power LPBF process is presented below. The investigations were conducted using a LPBF machine SLM280HL (SLM Solutions). The machine is equipped with two laser sources, a single mode fiber laser with a maximum laser power $P_L \leq 400$ W (beamway 1) and a multimode fiber laser with a maximum laser power $P_L \leq 2$ kW. The beam diameter for beamway 1 is $d_{S1} = 80$ µm and $d_{S2} = 730$ µm for beamway 2. The machine allows the active fiber to be changed during the process by using a beam-switching unit. For parameter development test samples $(20 \times 20 \times 20$ mm$^3)$ were manufactured and the density was measured by light microscopy (Bremen et al. 2017).

For the development of a HP-LPBF process window, beamway 2 with a beam diameter $d_S \approx 730$ µm and increased laser power $(P_L = 2$ kW) was employed to manufacture test samples. For a laser power of $P_L = 1$ kW, cubic test cubes with a density $\geq 99.5\%$ can be produced with a layer thickness of $D_l = 90$ µm $(v_S = 350$ mm/s, $\Delta y_h = 500$ µm) and $D_l = 150$ µm $(v_S = 250$ mm/s, $\Delta y_h = 500$ µm) (see Fig. 7.9). The theoretical build-up rate can be calculated to $V_{th} = 15.75$ mm^3/s $(D_l = 90$ µm) and $V_{th} = 18.75$ mm^3/s, which is a significant increase compared to the theoretical build-up rate achieved for the conventional LPBF process $V_{th} = 3$–4 mm^3/s (Fig. 7.9). An increase of the layer thickness and a reduction of the scanning velocity leads to an increased theoretical build-up rate, and a lower volume energy is needed $(E_V$ $(D_l = 90$ µm$) = 63.5$ J/mm$^3 | E_V$ $(D_l = 150$ µm$) = 53.3$ J/mm^3).

The results show that, when the laser power is further increased for $D_l = 150$ µm, the scanning velocity can be increased by up to $v_S = 300$ mm/s $(P_L = 1.5$ kW) and $v_S = 400$ mm/s $(P_L = 2$ kW), which, in turn, leads to theoretical build-up rates of $V_{th} = 22.5$ mm^3/s and $V_{th} = 30$ mm^3/s (see Fig. 7.10). Compared to $P_L = 1$ kW, the build-up rate can be further increased with increasing laser power. However, the corresponding energy density also increases $(66.7$ J/mm$^3)$ with increasing laser power. This means that the process efficiency decreases for a laser power >1 kW. These results can be explained by the formation of spatters from the increased laser power. With increasing laser power, the number of spatters and the size of spatters increase. These spatters are deposited on the molten layer and have a size between 50 and 200 µm. Therefore, these spatters are not completely melted in the following scanning step, thus resulting in binding defects.
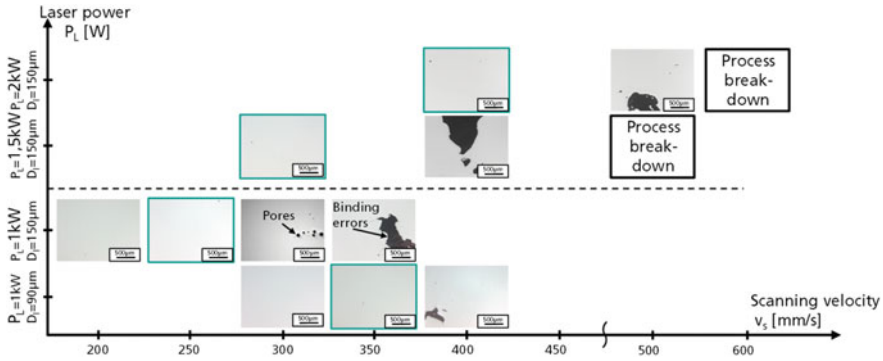
Fig. 7.9 Cross sections of test samples manufactured by HP-LPBF. The cross sections marked in green represent the maximum scan speed for a parameter set, reprinted from Bremen et al. (2017, Fig. 3), with the permission of Springer
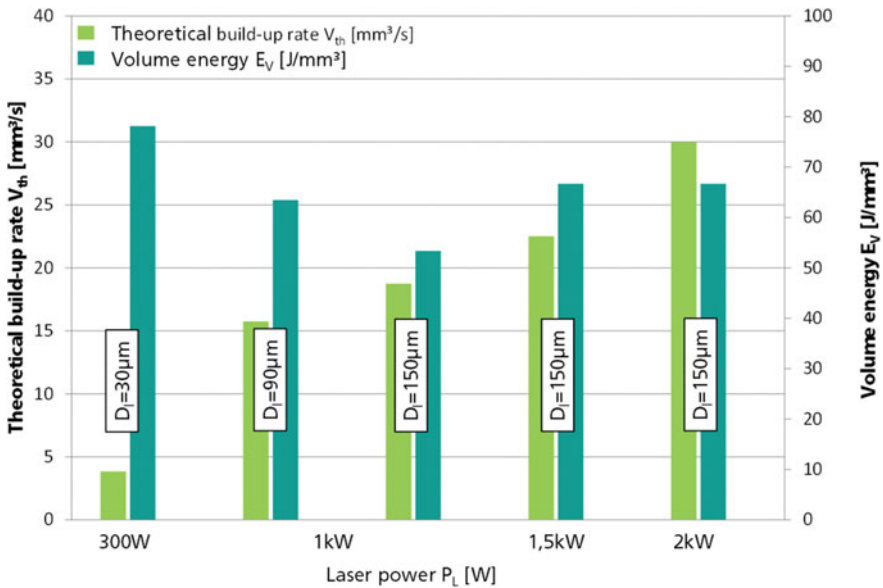
Fig. 7.10 Build-up rate and volume energy for parameter sets with different laser power, reprinted from Bremen et al. (2017, Fig. 4), with permission of Springer

Grain size, shape, and orientation for the both process windows were investigated by EBSD (Fig. 7.11). It can be observed that small grains exist with a mean diameter of $d_K = 25\ \mu m$ for the LPBF process according to the state of the art. These grains grow over two to ten layers and are elongated in the build-up direction. Most of the grains have an angle of 35°–40° according to build-up direction. In comparison, for test cubes generated with $P_L = 1\ kW$ at $D_l = 90\ \mu m$, the EBSD shows grains with
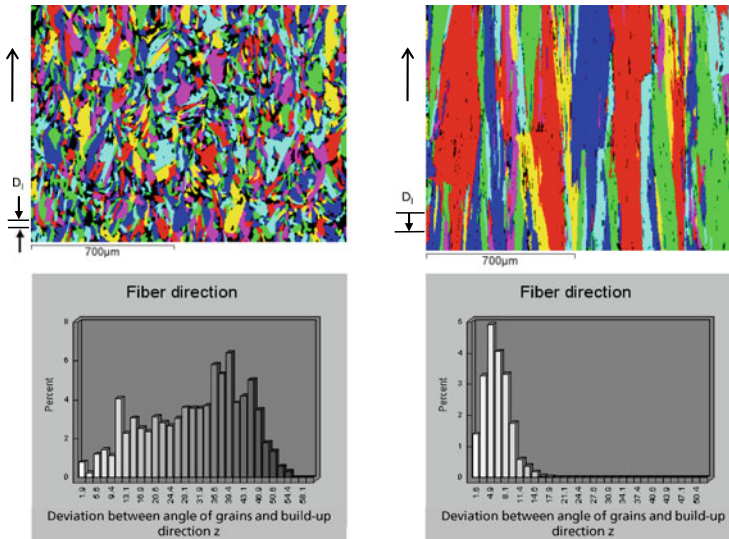
Fig. 7.11 EBSD analysis of the grain structure. Left: conventional LPBF process (300 W), Right: HP-LPBF (1 kW), $D_l = 90\,\mu$m, $v_S = 350$ mm/s, reprinted from Bremen et al. (2017, Fig. 5), with the permission of Springer

a mean diameter of $d_K = 97\,\mu$m. The grains grow over the whole height of the test cube and are strictly directed in the build-up direction.

The mechanical properties of conventional and HP processed samples with and without heat treatment are presented in Sect. 7.4.3.

The process management developed is applied to the part pylon-bracket (Bremen 2017). The pylon bracket is part of the engine mounting of the A 320 and is made of the material IN 718. It has a length of 272 mm, a width of 35 mm and a height of 38 mm (Fig. 7.12 left). Due to the limited build chamber size of the used LPBF machine, the part is manufactured in reduced size of a factor of 2. The pylon bracket is manufactured both completely with the above presented conventional parameter set and with the skin–core strategy. For this purpose, the skin is manufactured with the conventional parameter set and the core with different parameter sets of the HP-LPBF at laser powers of 1 and 1.5 kW (Fig. 7.12 right). The main times (laser-on) can be reduced by 23–28% compared to conventional LPBF fabrication, depending on the parameters of the core strategy. However, the auxiliary times (laser-off) increase significantly due to the increasing delay times for the fabrication of the skin (short scan vectors), so that the total fabrication time does not scale with the increased build-up rates.

Adaptive LPBF

Adaptive process management is similar to the skin–core process management. In contrast to skin–core process management, the part is not divided into an inner and outer area, but is individually adapted to the requirements of the respective part
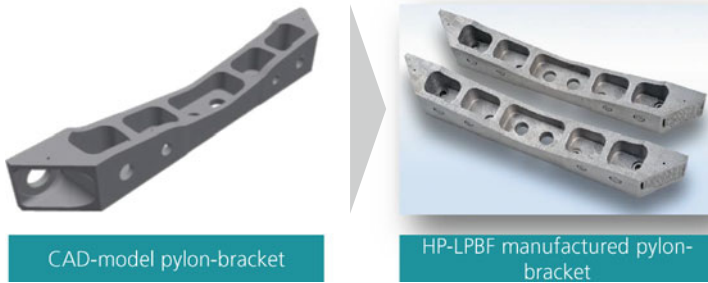
Fig. 7.12 Left: CAD-model of pylon-bracket, right: pylon-bracket manufactured with HP LPBF, reprinted from Bremen (2017, Fig. 92), with the permission of Apprimus

(see Fig. 7.7). With regard to the entire process chain and taking into account the post-processing methods, the part is analyzed in advance and divided into areas. In adaptive process management, part areas with functional surfaces that cannot be post-processed or can only be post-processed at great effort are exposed with process parameters that are tailored to high surface quality. Edge areas whose surfaces require post-processing or areas inside the part are exposed with process parameters that are tailored to a high build-up rate.

In the following, adaptive process management is presented using the example of a guide vane segment (see also Sect. 7.4.1) and this is compared with conventional and skin–core process management. Adaptive process management is discussed using the six-row guide vane segment (Fig. 7.13; Sect. 7.4.1) with six twin vanes made of the material IN 718. The 3D CAD model of the guide vane segment is shown in Fig. 7.13, top left. The part consists firstly of a root with a groove as a fitting surface and secondly of the blades attached to the root. The LPBF manufacturing of the guide vane segment requires an adaptation of the part geometry: To connect the vane cluster to the substrate plate, the geometry of the root area is adapted. For the machining of the groove, a finishing oversize is added in the root area (Fig. 7.13, top right). Different requirements are specified for the part areas. The functional surfaces of the blades must have a high surface quality. Manufacturing by conventional LPBF or with skin–core process management is tailored to a small surface roughness and thus low post-processing. In contrast, adaptive process management is designed for optimization across the entire process chain. Here, the root area is manufactured with process parameters tailored for a large build-up rate. This area is subsequently post-processed by milling.

The adaptive process management is implemented with two beam diameters (Fig. 7.13): The process parameters for the small beam are: Beam diameter: 200 μm, Layer thickness: 30 μm, Laser power: 200 W and adjusted scan strategy with hatch distance and scan speed. The parameters for the large beam are: Beam diameter: 1,000 μm, Layer thickness: 300 μm, Laser power: 920 W as well as adapted scan strategy with hatch distance and scan speed. With the parameters for the large beam, build-up rates of up to 15 mm^3/s are achieved. In the transition area from the root to the
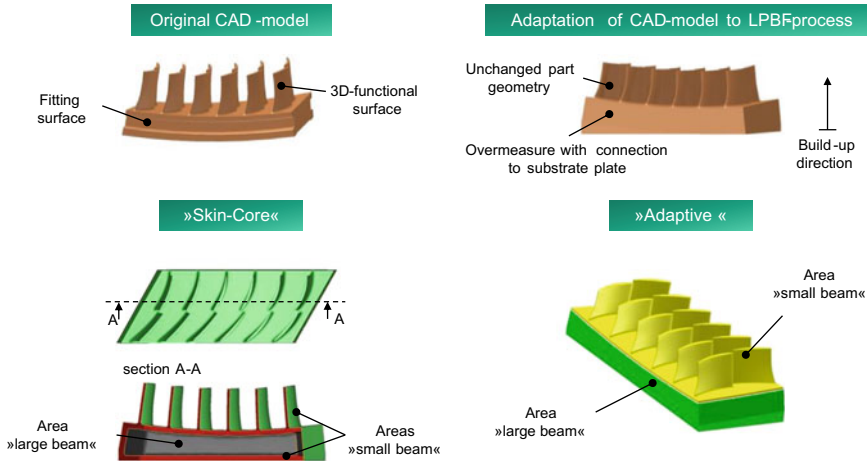
Fig. 7.13 Original CAD-model and adapted CAD-model for the guide vane and schemes of skin–core and adaptive process management

blades, the layer thickness is reduced in 3 steps for the large beam diameter and then the small beam diameter with a layer thickness of 30 μm is used. Figure 7.14 shows the processing times for different process managements. The longest processing time is required for conventional process management with the small beam diameter. The least one with the large beam diameter. However, the quality of the part is insufficient for the large beam diameter in terms of roughness and density at the blades and in terms of roughness at the root. The processing time for adaptive processing is a factor of 1.9 smaller than for conventional processing and a factor of 1.6 smaller than for skin–core processing. Part densities in the range of 99.5% are achieved for all process managements.

7.3.3 Geometry-Specific Adaptation of LPBF Process Management

For parameter development of a specific material, simple test samples (e.g. cubes) are typically used to identify suitable process parameters (see Sect. 7.1.3). However, the challenge arises in transferring these parameters to parts with high geometric complexity. This often results in deficits in both process efficiency and part quality, e.g. due to local overheating in filigree structures.

After CAD design, parts to be manufactured by LPBF are prepared for manufacturing by slicing the CAD model into layers, rasterizing the areas of each layer to be remelted with vectors (hatching) and saving the data in a machine-specific format. For this, geometric characteristics at a global level of the part are taken into account, as shown in Fig. 7.15. Within a layer, a distinction is made between the part interior
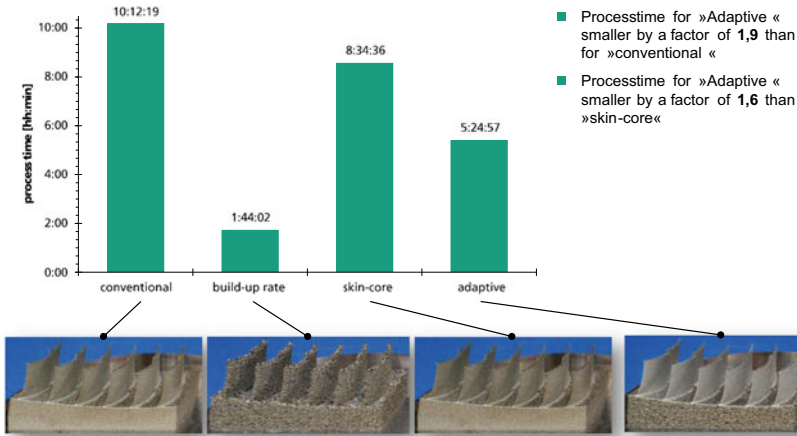
Fig. 7.14 Process times for manufacturing the 6-row guide vane cluster with different process managements

Fig. 7.15 Global areas of a part, reprinted from Pichler (2019, Fig. 2-1) with the permission of Hanser
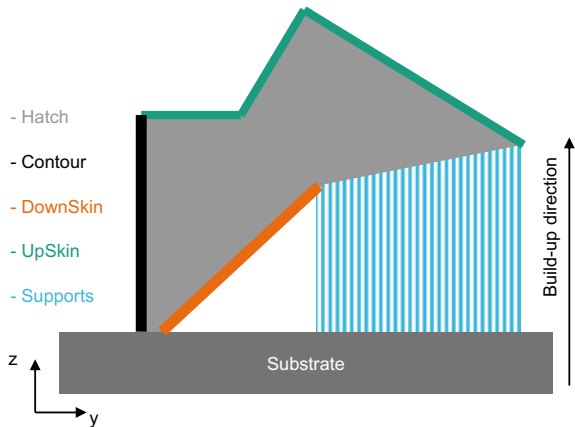
(hatching) and the part exterior (contour). In addition, overhang areas (DownSkin) and cover areas (UpSkin) as well as support structures are identified. For each of these areas, the user can define parameters for data preparation (e.g. hatch distance, hatch pattern) and parameters for the fabrication (e.g. laser power, scanning speed). Within these global part areas, however, the process parameters remain constant.

In conventional LPBF process, the laser power applied is always constant, independently of the length of the scan vectors. Particularly with shorter scan vectors, this leads to overheating effects which can have a negative impact on part quality. In geometry-adapted process management, on the other hand, the process parameters are adapted as a function of the scan vector length.

For the implementation of the geometry-specific process control, extended information is required in the manufacturing data sent to the LBPF machine. In particular, this includes the vector-specific adaptation of the process parameters.

Since the existing data formats do not support dynamic adaptation of process parameters as described above, the development of novel data formats is necessary. The manufacturing data are generated with a software on the basis of the geometry-specific parameter sets. A special data format has been established for transferring the layer data, which contains all the relevant information for carrying out the LPBF process. This includes the scan paths generated layer by layer for the parts to be manufactured, the corresponding local process parameters and metadata, such as information on the build strategy used.

Figure 7.16 shows an example of a table with allocation of the laser power according to the vector length and a prepared build job in false color representation as well as the manufactured parts. With the help of the table, the process parameters of the individual scan vectors of the samples are adjusted as a function of the vector length. Linear interpolation is performed between the respective interpolation points. In the example shown, the laser power is adjusted as a function of the scan vector length. For short vectors, the laser power is reduced to avoid overheating effects. For longer vectors larger laser powers are allocated. In the same way, for example, the scan speed can be adjusted. Similarly, scanner settings such as jump speed or SkyWriting parameters can be adjusted.

Due to the geometry-adapted process management, a significant reduction of shape deviations can be achieved by the locally adapted energy input. Figure 7.17 shows an example of the vector data with the corresponding laser power and the surface topography of a triangular specimen. When standard parameters are used, material elevations always occur in filigree areas as well as during track changes in massive exposure areas. In Fig. 7.17, the local elevation in the tip of the triangular specimen is particularly noticeable when standard parameters are used. By adjusting the laser power within individual scan vectors, the material elevation could be reduced from about 140 µm to about 35 µm.

Vector length l_v [mm]	Laser Power P_L [Watt]
$l_v \leq 2$	150
$2 < lv \leq 5$	200
$l_v > 5$	275
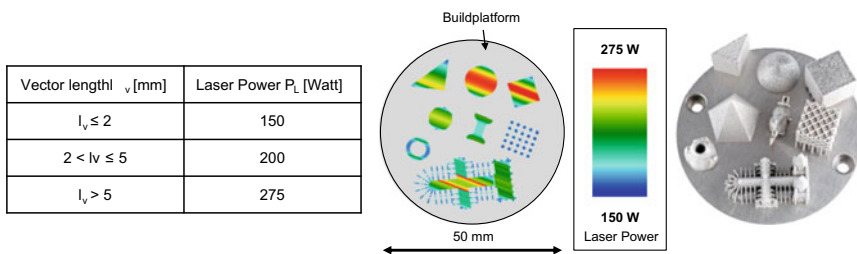
Fig. 7.16 Allocation of laser power to the scan vector length, false color representation of the build job and fabricated samples, reprinted from Pichler (2019, Fig. 4-2), with the permission of Hanser
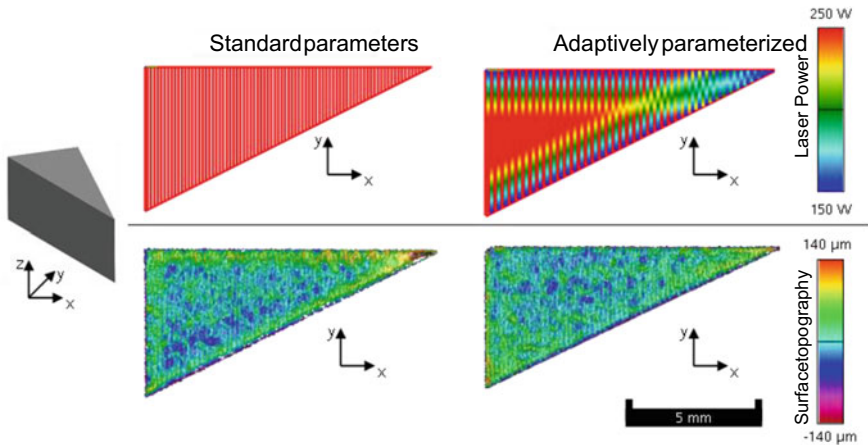
Fig. 7.17 Vector data and allocated laser power (top) and surface topography (below) of fabricated test samples, reprinted from Pichler (2020)

7.3.4   LPBF of Copper with Green Laser Radiation

Due to their high conductivity, copper materials are of particular importance for the realization of thermal and electrical functions in many applications. Parts with particularly high requirements in terms of electrical and/or thermal conductivity are often realized in conventional manufacturing using pure copper. An important area of application for copper materials are inductors, e.g. for inductive hardening systems. Therefore, there is an increasing demand to manufacture copper materials with LPBF, in particular to utilize the geometric freedom of LPBF (see Sect. 7.4.1).

As described in Sect. 7.1.2, laser radiation in the infrared spectral range at approx. $\lambda = 1,030$ to $1,080$ nm is usually used for LPBF. In recent years, low-alloyed copper materials have been processed with LPBF (Becker 2014). Densities of 99.9% have been achieved for the copper materials CuCrNb (Gradl et al. 2019), CuCrNi2Si (Becker 2014), and CuCr1Zr (Becker 2014) when processing with infrared laser radiation. Depending on the material, the electrical conductivities range between 40 and 80% IACS (the unit of specific electrical conductivity is given in IACS% ("International Annealed Copper Standard"), a unit of measurement normalized to the conductivity of Cu-ETP at 58 MS/m).

The high thermal conductivity of pure Cu (approx. 400 W/mK) and the low absorptivity (approx. 5%) for wavelengths in the range of 1 μm are the reasons why until now no satisfactory results have been achieved when processing pure Cu with infrared laser radiation. The reasons for this are explained below. Although Stoll et al. (2020) achieve a density of max. 99.8% as well as a conductivity of 97 IACS% by using a very small beam diameter of 35 μm with an infrared laser beam source and a layer thickness of 30 μm. However, the volume energies applied to achieve the maximum density are very high, ranging from about 790–950 J/mm^3. The build-up

rates of 0.4–0.5 mm³/s, on the other hand, are very small, so that productivity is very low.

An alternative approach is to use laser radiation in the green spectral range (λ = 515 and 532 nm). For this purpose, different laser sources (pulsed and cw) are investigated (Heußen 2020): With these laser sources, process parameters are determined at beam diameters of 72, 180 and 440 µm, at which a density >99.5% is achieved. The most suitable laser source operates in the cw-mode and emits a maximum laser power of 1 kW at a wavelength of λ = 515 nm. The focus diameter with the selected optical set-up (f-theta lens with focal length f = 160 mm) is about 180 µm.

Compared to the wavelength at λ = 1 µm, the absorptivity for λ = 515 nm increases from 5% to about 60% for a blank sheet material made of pure Cu. For powder made of pure Cu, values of 23% for λ = 1 µm and 78% for λ = 515 nm are obtained. These are spectroscopically measured values, i.e. the values represent the "powerless" case. With increasing temperature, the absorptivity increases. At a temperature of 980 °C, the absorptivity of pure Cu increases to about 15% at λ = 1 µm (Blom et al. 2003).

Figure 7.18 shows a comparison of the remelting behavior for the two wavelengths both schematically and in the form of a single track without powder.

The high thermal conductivity of pure copper of approx. 400 W/mK and the associated thermal losses due to self-quenching require an increased energy input for the wavelength of λ = 1 µm compared to other materials in order to generate a stable melt pool of sufficient size. This is usually realized by increasing the irradiated laser power, when the beam diameter is constant. The increase of intensity in the beam focus leads to reach the boiling temperature and initiate evaporation. The recoil pressure of the metal vapor jet leads to the formation of a capillary (deep welding regime, see Sect. 7.1.3). Due to high energy losses through the capillary walls, the capillary becomes unstable, a change to the heat conduction regime takes place. This
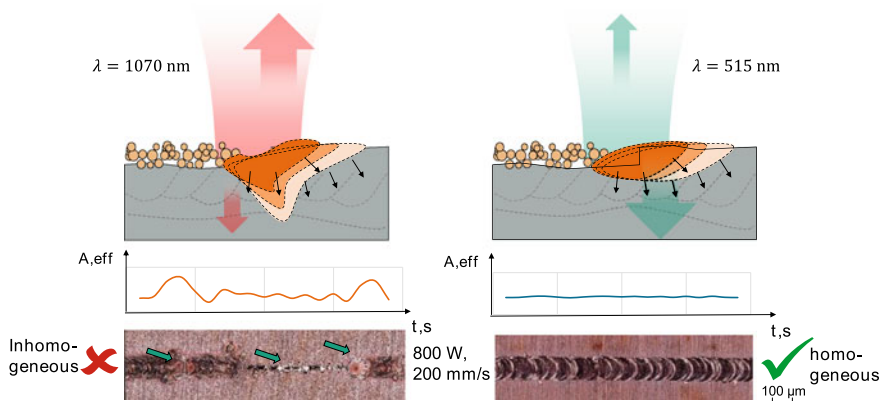
Fig. 7.18 Remelting behavior of pure copper for the wavelength of λ = 1 µm and λ = 0.515 µm: above: Scheme of typical melt pool geometry, middle: Time dependent absorption behavior, below: top-view of remelting tracks

is associated with a change from high to low absorption. At lower energy inputs, the formation of the melt is insufficient due to the high reflectivity of copper for the infrared laser radiation. The resulting remelting behavior is sensitive to changing boundary conditions (e.g. quality of the powder layer, beam incidence angle, …). As a result, the temporal absorptivity changes (Fig. 7.18 center left) and, as a consequence, a non-uniform remelting track is produced. In comparison, alternation between high and low absorptivity is avoided with green laser radiation (heat conduction regime), whereby the temporal absorptivity remains nearly constant (Fig. 7.18 center right) and a homogeneous remelting track is achieved.

The results for process development show that densities >99.5% can be realized over a wide parameter range with a beam diameter of 180 μm. In addition to high scanning speeds of up to 3,000 mm/s at 30 μm layer thickness, parameter combinations with a layer thickness of 60 and 90 μm in particular also allow comparatively high build-up rates (Fig. 7.19). The higher the build-up rate that can be realized and the lower the volume energy, the greater the productivity and economy of the process. Figure 7.19 shows the results of the test specimens with a relative density >99.5%. Also shown are the parameter combinations from the state-of-the-art when infrared laser radiation is used. The results generated with green laser radiation at a beam diameter of 180 μm range from very low volume energies (66 J/mm^3) and high build-up rates (15.12 mm^3/s) to very high volume energies (2,000 J/mm^3) at comparatively low build-up rates (0.3 mm^3/s).

The maximum build-up rate at 30 μm layer thickness for a beam diameter of 180 μm is achieved with 5 mm^3/s at a volume energy of 119 J/mm^3. With 60 μm layer thickness, a maximum build-up rate of 10.08 mm^3/s is achieved with an energy input of 79.3 J/mm^3. At 90 μm layer thickness, a maximum build-up rate of 5.4 mm^3/s is achieved with an energy input of 148 J/mm^3. This shows that with a layer thickness of 60 μm both a larger build-up rate and a lower volume energy is achieved compared to the smaller and larger layer thickness. This means that at a layer thickness of 60 μm and for the beam diameter of 180 μm the process efficiency is highest, i.e. the irradiated energy density is used in the best possible way for the process. Figure 7.20 shows examples of cross sections for selected parameters. The orientation of the grains in the build-up direction can be clearly seen. For these parameters, high densities in the range of 99.9% are achieved.

The specific electrical conductivity is measured by means of a phase-sensitive eddy current method (approved according to DIN EN 2004-1) on the cross sections of the test specimens. The values are obtained in the "as built" condition without any additional post heat treatment.

The electrical conductivity increases with the relative density. One explanation for this is a reduction in the conductive cross-section due to pores and binding defects for the electric current. Furthermore, dislocations and grain boundaries, for example, influence the electrical conductivity. Some test specimens show significantly lower conductivities despite a high measured relative density. This is especially the case for specimens generated at large scan speeds >2,000 mm/s. A relative density of nearly 100% therefore appears to be a necessary precondition for achieving the maximum conductivity, but not a sufficient precondition. The specimens with a relative density
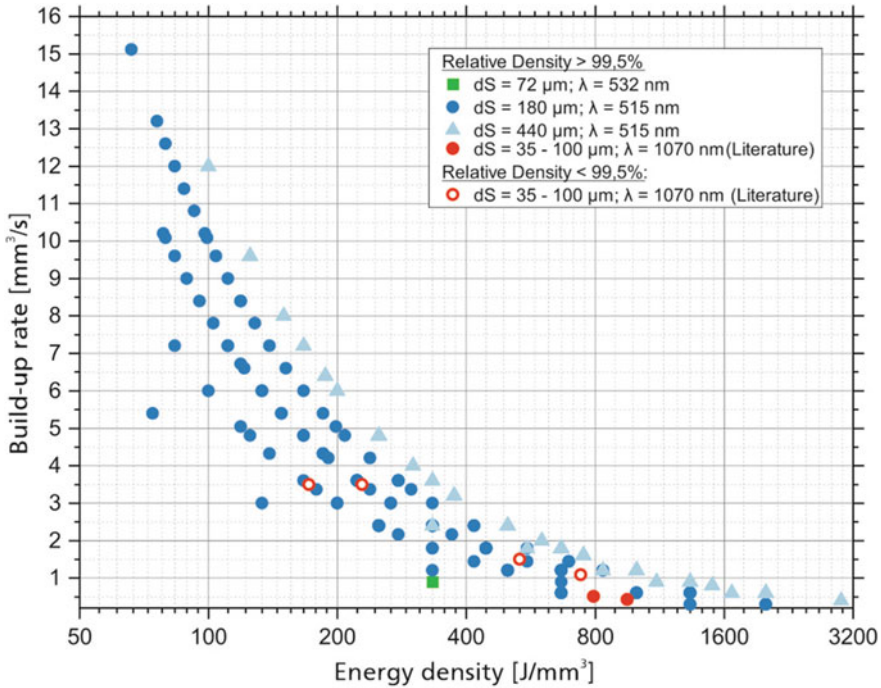
Fig. 7.19 Build-up rate as a function of the volume energy for different beam diameters and different wavelengths
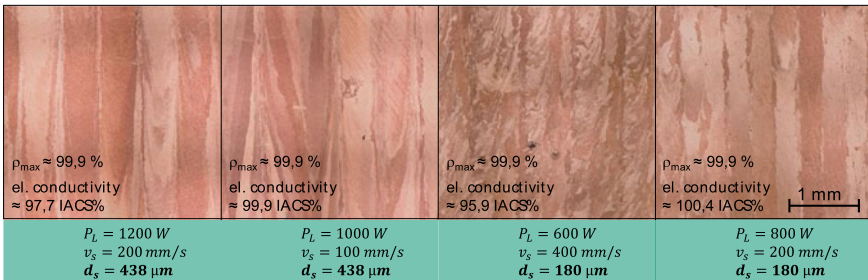
Fig. 7.20 Cross sections (x–z) of pure copper fabricated with different process parameters

above 99.5% have an electrical conductivity of at least 93.5 IACS%. For a relative density greater than 99.8%, the electrical conductivity is at least 95 IACS%. The highest conductivity measured is 102.6 IACS%.

In order to use the results of the process development for the manufacturing of parts, an adapted contour exposure is being developed in addition to the development of the process management for the volume area ("Hatch"). This makes it possible to

Fig. 7.21 Demonstrator parts manufactured with green (left) and IR laser radiation (right)
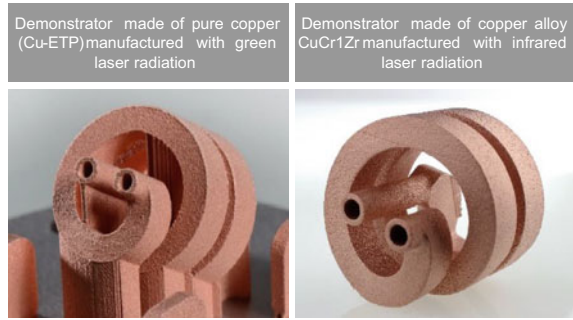
reduce the roughness on vertical surfaces from Sa = approx. 50 µm to Sa = approx. 21 µm and to build near-net-shape geometries.

A demonstrator manufactured with the developed process is shown in Fig. 7.21. The hollow tube geometry shown on the left is based on inductors for inductive heat treatment and is a challenge from a manufacturing point of view with regard to internal overhang surfaces, which have to be built up without support structures. Shown on the right is the identical demonstrator, made of CuCr1Zr with infrared laser radiation. With a roughness of Sa = approx. 21 µm, the demonstrator manufactured from pure copper using green laser radiation has a higher roughness than the inductor on the right, which has a roughness of Sa = approx. 10 µm.

7.3.5 Review of LPBF Simulation

Introduction

Process simulation is used to derive improved process strategies and parameters with reduced experimental effort based on a deeper understanding of the process. The simulation tools developed for this purpose address the preparation of the powder layer, the thermalization of the optical energy in the powder bed and the substrate or the part, the heat transport taking into account convective contributions during melting and solidification and the distortion due to residual stresses in the part and the substrate plate caused by the process.

In addition, simulation tools are being developed to predict the microstructure of the part based on the local temperature time cycles associated with the process strategy. A phase field model is usually used to simulate the microstructure formation during the LPBF process (Acharya et al. 2017). Here, the behavior of the phase field variables in the domain is determined by phase field equations coupled with the heat and solvent diffusion equations. The interface between the solid and the liquid is determined by a uniform but rapid change in the phase field variables. MICRESS—the MICRostructure Evolution Simulation Software—is a software package that enables the calculation of microstructure formation in time and

space during phase transformations, especially in metallurgical systems (https://micress.rwth-aachen.de/). The software is based on the multiphase-field concept. The software addresses e.g. dendrite formation, segregation in the interdendritic region, carbide precipitation, grain formation, recrystallisation phenomena. For a computational prediction of the grain texture, the cellular automaton method is also often used (Lian et al. 2019; Rai et al. 2017).

An alternative but also in some ways complementary approach to modelling is the use of artificial intelligence modelling approaches, with which the identification and quantification of the high-dimensional influence-effect relationships in the LPBF process can be used to derive indications of process windows. However, this approach will not be discussed here, nor will model approaches for optimization of the topology or the design of support structures in the LPBF process. Not discussed but not unmentioned are simulation tools for optimizing manufacturing costs (Schrage 2016; Barclift et al. 2016; Barclift 2018; Fritz and Kim 2020) as a function of part orientation, whereby this influences the number of layers, the required support structures and the areas with overhangs.

Powder Layer

Whether the LPBF process is carried out in heat conduction or keyhole mode (see Sect. 7.1.3), the correct powder layer height and packing density in a single layer are crucial for the simulation results. The levelling height of the build platform does not generally correspond to powder layer height. The powder layer height increases in the first layers due to the difference in volume of the powder and solidified material. The powder layer height in the process is then equal to the levelling height of the build plate divided by the powder layer density of the powder (Meiners 1999). Due to the waviness of the last layer, there may also be local deviations from the powder layer height in the process, which are not insignificant, possibly leading to bonding errors and increased spatter formation.

The rheology of powders is influenced by many different factors (see Sects. 7.3.1) (Spierings et al. 2015). These include the powder form, the powder grain fraction and the surface texture of the powder particles. All these factors can influence the behavior of the powder particles during powder deposition to the last layer. External influences such as humidity, temperature and pressure can also affect the rheology of the powder.

The discrete element method (DEM) is a numerical method for the time-resolved calculation of particle motion-flow, considering the interaction of the particles on contact (Manne and Satyam 2015). This method calculates the particle flow based on displacements and rotations of the discrete bodies of different types of particle shapes (Harthong et al. 2009). The particle motion is based on a solution of Newton's second law of motion and the Rigid Body Dynamics equation in combination with special time-stepping algorithms (Parteli and Pöschel 2016). LIGGGHTS (Kloss et al. 2012), for example, is such a software tool that can be used for the model-theoretical investigation of powder spreading. The extent to which particle spreading behavior is affected by disturbances, such as spatters, is shown by Ng's work (2020). The analysis shows that the local powder layer density is measurably disturbed

when particles interact with elevations on the build plane such as may be caused by spattering. Gaps form directly behind the elevation because the flow of particles is impeded.

The physics-based DEM simulations are extraordinarily computationally intensive, especially when considering a sufficiently high number of particles in the model for a representative result. In order to reduce the overall computational effort, a physics model-based machine learning in the form of a feed-forward neural network with feedback was programmed to interpolate the highly non-linear results, with which a minimum accuracy of the trained neural network of 96% was realized (Desai and Higgs 2019).

Melt Pool Computations

If you look in the literature regarding melt pool calculations in the LPBF process considering the particle layer, you will find papers using either the ALE3D (2017), Flow3D (Cheng et al. 2018) or Open Foam (Gürtler et al. 2013) software tools. All three tools are based on the volume of fluid method and solve the free boundary value problem in the LPBF process, i.e. calculate the melt pool surface as part of the solution. This also includes for the transition region the formation of a depression of the melt in the laser beam material interaction region when the process temperature reaches the boiling temperature. If the laser power is increased further, a keyhole is then formed, but it can form pores because of the possible fluctuations in the root region. Figure 7.22, for example, shows a snapshot of the temperature distribution and the track geometry for IN718 with standard parameters for an EOS machine as calculated with the software tool Flow 3D. At the beginning of capillary formation, the melt is pressed backwards against the direction of travel and remains as an elevation in the track after solidification. A depression forms in the laser-irradiated zone, as is typical for the transition mode (weld-in mode) in the transition region.

With the help of these software tools, it was possible, for example, to reproduce the time-resolved development of pores in the root area of the keyhole and to identify the physical causes. The spatters observed experimentally at the front of the keyhole could also be physically reproduced with these models. However, one criticism remains: The degrees of freedom of movement of the particles are limited and do not represent the real process as it is observed with high-speed cameras. Experimentally, it is observed that the particles are carried away by the vapor jet. The metal vapor jet generates a flow vortex in the atmosphere above the powder layer which is directed towards the keyhole. This boundary layer flow entrains the particles on both sides of the melt in the trailing area, thus thinning the powder layer in this area, but feeding the melt with the entrained particles, which ultimately contribute to the track build-up (Chen and Yan 2020). The software tools mentioned above model a flow of particles, but that is not what happens in the process. The tools basically simulate the remelting of a pre-sintered layer, and perhaps the melt instabilities calculated by the tools are a consequence of this. This mechanism, that the melt is essentially fed by the particles only in the trail, is shown in a paper by Chen and Yan (2020), in which a stream jet is moved below the powder layer with plausible assumptions for the temperature and velocity of the vapor jet Fig. 7.23.
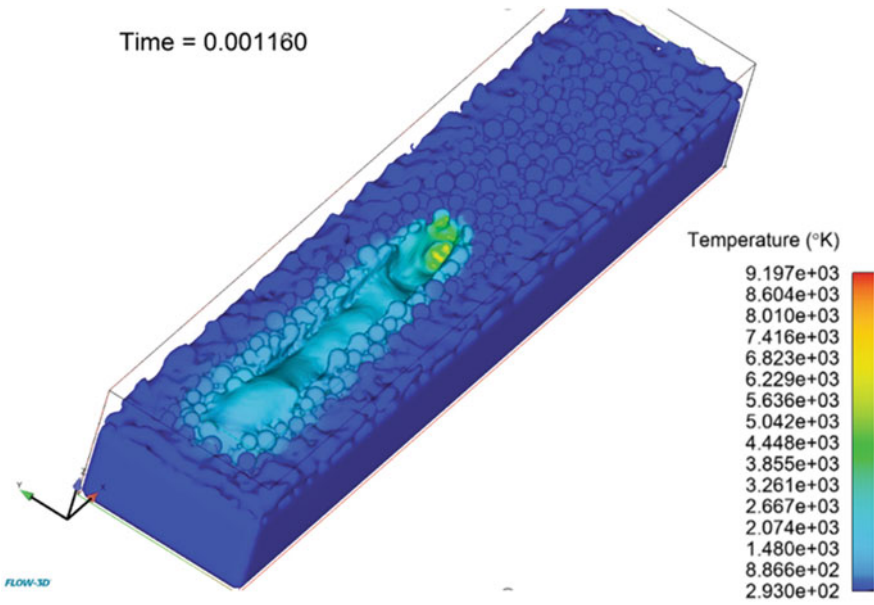
Fig. 7.22 Snapshot of a single track, $P_L = 280$ W, $v_S = 1,000$ mm/s, IN718, Gauss, $d_S = 0.18$ mm; computed with Flow 3D
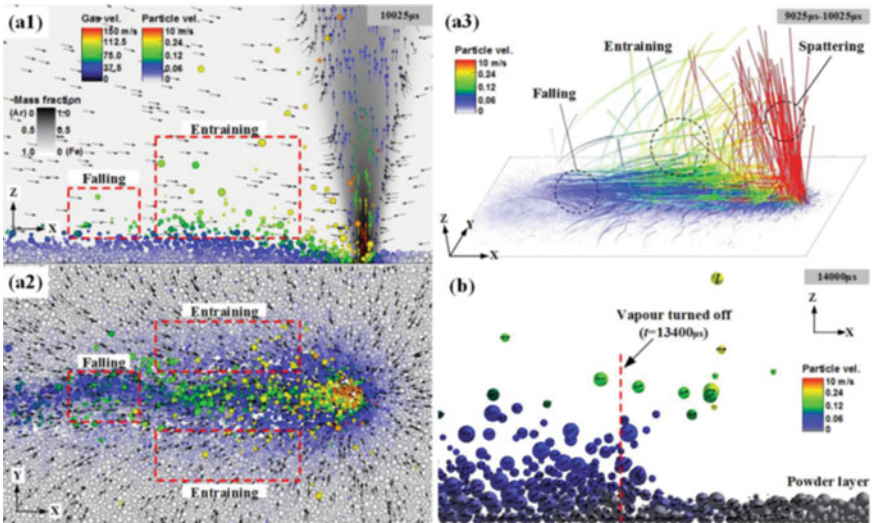
Fig. 7.23 Spattering phenomenon: **a1** side view and **a2** top view of the velocity field, where the velocity of the gas phase is represented by the arrow colour and the velocity of each particle is represented by its colour; **a3** particle trajectories; **b** particle motions after the metal vapour is off, where the arrows represent the velocity directions of particles, reprinted from Chen and Yan (2020, Fig. 6), with the permission of Elsevier

The paper demonstrates how, based on these assumptions, a vortex is generated in the atmosphere that generates particle transport from both sides of the melt trail into the melt. Despite all the progress in process understanding, none of the tools has yet succeeded in predicting a process window purely by calculation and thus reducing the experimental effort required for process development. It does not need to be mentioned that on this microscopic level only single tracks or a few tracks in overlap and several layers up to a track length of approx. 2 mm can be calculated, because due to the required grid resolution, the number of nodes grows very quickly and the models are no longer computable. This means that with the help of the software tools, it is possible to gain an understanding of the geometry formation process for short track lengths for single tracks, tracks in overlap and multiple layers and to prioritize process parameters with regard to their influence. But the computing capacities are not yet sufficient to define a window for the process parameters in advance for a part.

Distortion, Residual Stress

The thermal stresses induced in LPBF usually reach the yield point, plastic deformations occur in the part, which remain in the part after temperature homogenization and lead to residual stresses and deformations (Pirch et al. 2018). In the worst case the distortion can lead to cracks and part failure during or after the manufacturing process. Process strategy, material properties, part stiffness and the type of fixturing and orientation used on the build plate can all affect the amount of residual stresses created in a part. Identifying and quantifying these factors through trial and error is both expensive and time consuming. An alternative way to develop process strategies that significantly reduce distortion and prevent part failure is to use simulation tools that simulate the thermomechanical behavior of the part during and after the process and when it is removed from the build plate.

A thermomechanical analysis based on a micromodel (Dunbar et al. 2016) is not applicable to models in the cubic centimeter range. In order to simulate larger geometries, it is necessary to drastically reduce the size of the numerical problem. Two different techniques can be found in the literature.

1. Representative substitute heat sources: Instead of individual trajectories, complete scan vectors, hatch areas or complete layers are exposed at once. Furthermore, instead of the nominal layer heights on the build platform, several layers are combined into one layer in the model, which is then exposed to a volume density for the heat source, whose height and exposure time results from the parameters such as laser power, scan speed and overlap (Amine et al. 2014; Michaleris 2014).
2. Inherent strain: In this method, the deformation is calculated based on a plastic strain (intrinsic strain) that is activated layer by layer in the model. The strain must first be calibrated for the material on a model geometry for the process parameters. This method originated in the simulation of welding processes and was rediscovered for the LPBF process due to significantly lower numerical effort compared to coupled thermomechanical models (Keller and Ploshikhin 2014; Li et al. 2015).

Despite some good results in predicting part distortion, the inherent strain method has limitations that have been systematically investigated (Bugatti and Semeraro 2018).

In a benchmark, 5 of the most commonly used software tools for the calculation of residual stresses and distortion in the LPBF process (Atlas 3D Sunata 2018, Additive Works Amphyon 2018, MSC Simufact Additive 3.1, Autodesk Netfabb Simulation 2019, Ansys Additive Print 19.1) were tested for their predictive accuracy of part distortion for different model geometries (Peter et al. 2020). The different tools use the inherent strain method as well as the representative substitute heat sources method. It is not possible to select a single software that offers a universal solution based on the results. Rather, these tests have shown several strengths and disadvantages for each software. It should also be remembered that the results obtained were specific to IN718 produced on the EOS M290 and can therefore only be generalized to other materials or other additive manufacturing machines with limitations (Peter et al. 2020). Nevertheless, the results show that the simulation tools have successfully predicted process strategies and negative distortion to the part before the build job resulting in significantly reduced distortion of the part after the build job.

Conclusion

The software tools available today allow the LPBF to be simulated in advance on a model-theoretical basis close to practice and the various process parameters to be prioritized in terms of their influence on the process. This is used to advantage in the design of the statistical test plans when it comes to fine-tuning the process parameters.

Despite the significant progress made, for example, in the time-resolved calculation of the melt pool formation and its dynamics, considering the flow dynamics, the degrees of freedom of movement for the particles are only insufficiently represented in the simulation tools currently available. The physics of the metal vapor, the propagation of the laser beam into the keyhole is not yet addressed in the LPBF process model at the microscopic level and remains a task for the future in order to develop a complete self-consistent model. About the thermomechanical models at the microscopic level, the reference remains to the usually missing temperature-dependent material properties such as the yield point, Young's modulus and Poisson's ratio, which should be known up to the vicinity of the melting temperature. Since a texture with respect to the grain structure is often found in the LPBF microstructure, the assumption of isotropic material properties should also be abandoned. The models with the shortest times are of course particularly interesting, as the preparation time for a build job does not really allow much time for model calculations. Since the part stiffness is included in the thermomechanical stress and this changes specifically with the geometry of the part height, there are approaches in the literature to take this influence into account in the inherent strain method by adjusting the inherent strain as a function of the part height.

7.3.6 Process Control in Laser Powder Bed Fusion

Introduction

In LPBF, a multitude of parameters (see Sect. 7.1.3) influence the result of the melting process and thus the final quality of a part. One group of parameters is external from the perspective of the process chamber with powder properties being a key factor (see Sect. 7.3.1). Prior to introducing the powder into the manufacturing machine, most of these properties can be controlled through practical measures such as certification of the powder supplier for standardized powder properties. The grain size distribution can be controlled by sieving and the humidity by a drying furnace. Other external parameters are the quality of the gas supply to the manufacturing machine. While gas from industrial suppliers is well standardized, the piping between gas tank and manufacturing machine sometimes is not. Still, this can be controlled through professional planning and installation. The same is true for the environment conditions of the manufacturing machine with respect to temperature and humidity on the shop floor.

Things become more critical inside the manufacturing machine. It is equipped with a laser source, optical components for the beam delivery, protective windows, gas circulation nozzles and a build platform (see Sect. 7.3.7). All these elements need to be in the defined condition, calibrated, adjusted, clean and fully operational. Especially optical systems tend to change properties when metal vapor precipitates on protective windows or when lenses catch dust. Still, all these properties can be measured and adjusted as needed. Another critical point is powder deposition. For the task of transporting the powder and depositing the powder layer with a precise and homogeneous amount of powder, each provider of a LBPF manufacturing machine has its own approach. Here, the interaction of the actual powder particles and the built part surface influence the process significantly. Deviation in powder volume per area and local particle size distribution is difficult to control and cannot be determined in-situ. Companies such as SLM Solutions have implemented a layer control system to detect uncoated or warped areas of the part (https://trendkraft. io/wirtschaft-geschaeft/slm-solutions-enthullt-weltneuheit-auf-der-euromold-slm-500-hl-fur-metallische-additive-fertigungsverfahren/; https://www.trumpf.com/en_GB/products/services/services-machines-systems-and-lasers/monitoring-analysis/monitoring-truprint/process-monitoring/). But none of these can measure the density of the powder in a specific area. The laser-based melting process needs to be tolerant against this variation or it needs sensors to detect such deviations. Laser, powder and the substrate or part finally interact to melt the powder under the current atmosphere inside the process chamber. Figure 7.24 gives a diagram of this input/output relationship. As a result, new material solidifies and builds onto the substrate or part.

The observation of this process can provide an insight into the heating and cooling of the material but also indicate events such as the ejection of molten material from the melt pool. Illumination enables the generation of images that provide additional information about events on the powder bed. The more information is collected, the
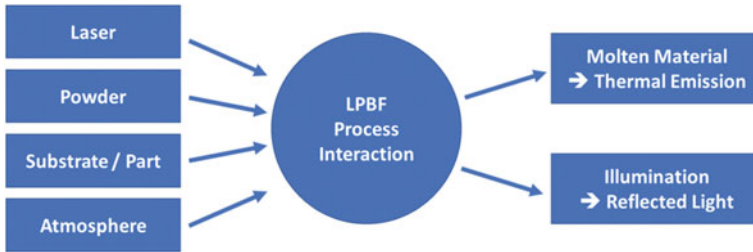
Fig. 7.24 Input/output relation of the LPBF process with respect to process observation

better the basis for an analysis of the course of the melting process. However, the information that can be collected during the process depends on the construction principle of the manufacturing machine and the sensor selection.

Sensor Design for Process Observation

Concept Laser for example used a camera system to observe the melt pool area coaxially in its machines (Kolb et al. 2018). SLM Solutions employs a pyrometer to monitor the thermal radiation in the center of the melt pool with its Melt Pool Monitoring system (MPM) (https://www.slm-solutions.com/products-and-solutions/machines/slm-280/; Alberts et al. 2017). This selection of sensors has effects not only on the type of information per sampled data set but also on the sampling rate. A camera system has typical framerates of 1,000 Hz where a pyrometer at comparable price has 100,000 Hz sampling rate. This means that the designer of the sensor system needs to decide to monitor the process with the underlying question on dynamics of the melt pool, or on spatial distribution of the thermal emission from the melt pool area. Figure 7.25 visualizes this difference. While a 1,000 Hz camera system with 8bit resolution and 100×100 pixels delivers a data at 10 Mbyte/s, a pyrometer with 100 kHz@12bit transfers 0.2 Mbyte/s. Albeit higher data rate of the camera system, it cannot monitor the dynamics of the process.
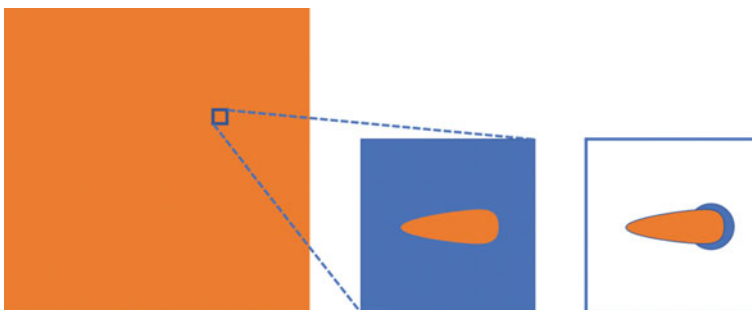
Fig. 7.25 Sensor selection: **a** process area, **b** camera image with interaction zone, **c** pyrometer spot with interaction zone

Optical systems for beam delivery need to be modified to serve the purpose of process observation (Thombansen et al. 2014). For high level signals at minimum sensor readout noise, coatings of the lenses need to be adapted and beam splitters are needed to separate the power laser beam from the sensor beam. But the design of the laser optics also has a significant impact on any coaxially coupled sensor system. High power optics usually are made solely from silica lenses which gives them low absorption and thus a good thermal stability. However, an optical system made from a single material cannot correct wavelength-dependent aberrations. The transmission of different wavelengths however is the basis for monitoring laser-based manufacturing processes. The construction principle of a f-theta lens in combination with the employment of a single optical material is the reason why this optics cannot monitor the thermal emission from the center of a melt pool by means of a pyrometer. Figure 7.26 shows the effect of two chromatic aberrations. The focus point of a beam with the observation wavelength shifts upwards with increase in scan angle due to axial aberration, thus leading to a defocused observation and it shifts sideways due to lateral aberration which means that the sensor observes at a displaced location.

For a LPBF machine that is equipped with a 400 mm silica f-theta lens, the lateral displacement between the processing spot and the observation spot can be as much as 3 mm in a 150 mm scan field for a processing laser at 1,070 nm and an observation wavelength of 1.9 μm. As a reference, a typical spot size of the processing laser in such a setup is about 100 μm which is 1/30 of the aberration related displacement.

In contrast to the f-theta system, Fig. 7.27 shows an optical system that focuses the laser beam into the processing plane through an actively moved pre-focusing unit. The convex lens is motorized and positioned to adjust the focus position according to the position of the mirrors. An appropriate design of the imaging optics for the process observation signal only needs to correct the axial aberration which can be achieved with lenses of different materials.

Fig. 7.26 Aberrations of f-theta optics caused by different wavelengths of processing laser and observation wavelengths axial aberration and lateral aberration
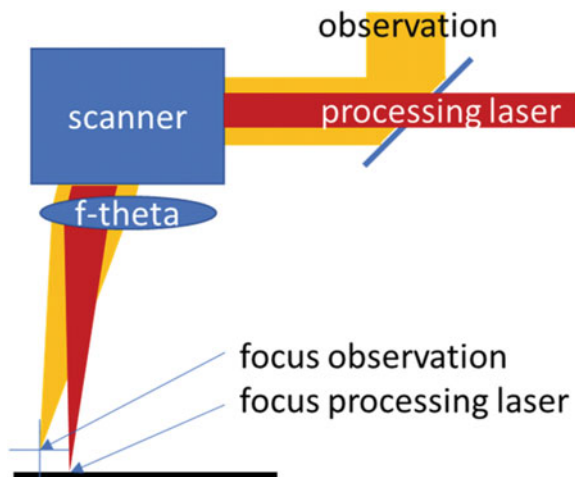
Fig. 7.27 Coaxial sensor system based on retrofocus principle
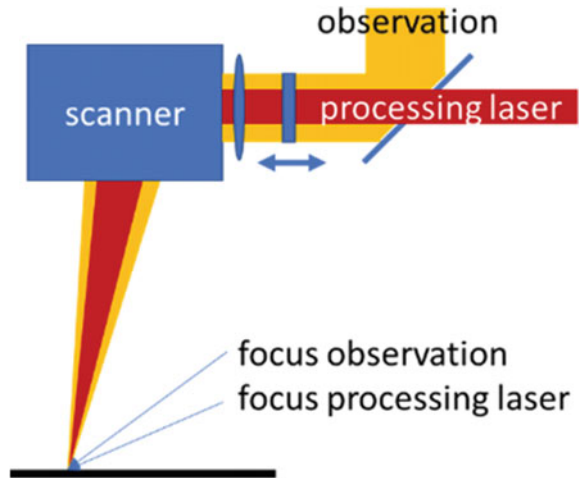
Fig. 7.28 Principle of an OT system with a camera system to observe the build plane from a lateral position
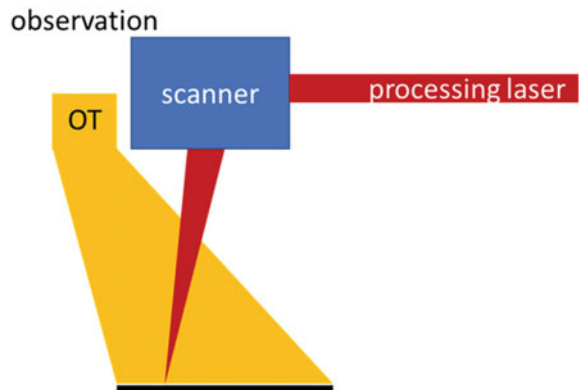
Sensor systems without coaxial coupling do not encounter such aberrations and are not influenced by attenuation of lens coatings and beam splitters. Their optical system is fixed and does not move with melt pool through the scanner mirrors. The term Optical Tomography (OT) is used for systems that employ such a laterally installed camera system for an observation of the entire build area with long exposure time to produce a 3D data set layer by layer (see Fig. 7.28).

The camera system of an OT system is positioned at the top of the process chamber right next to the scanning optics. Its optical system is coupled into the process chamber through a glass window that separates the camera from the atmosphere that is inside the chamber and allows transmission of wavelengths from the visible spectrum up to the infrared. In a typical setup, this allows a camera system with 4 million pixels to observe a build plane of 200 by 200 mm what results in a spatial resolution of 100 μm. Cameras with this number of pixels typically are based on CMOS technology which limits the detectable wavelength on the upper bound to 900 nm

depending on make and model. While this is advantageous for the design of a suitable optical system and for the blocking of the laser-wavelength, it puts the requirement of long integration times as the thermal emission in this spectral band is less intense compared to larger wavelengths as used for the pyrometric systems (Table 7.1). In addition to this obstacle, camera systems typically have a short blackout when the image is read by the acquisition electronics (10 ms at 400 mm/s scan speed result in 4 mm scan length). This means that there is no continuous observation of the process.

The technical principles of an OT system make it ideal to monitor the build process from the perspective melting conditions across the build plane and across all layers. Due to its long exposure time and the lateral view, it is capable of detecting local thermal emissions integrated over time and to stack subsequent layers to a final data set in three dimensions. Coaxially coupled camera systems monitor the interaction zone with more detail. They offer information with local and temporal resolution. Coaxially coupled pyrometric systems monitor a single small area. This provides information of transient events in the melt pool.

Signal Analysis

Application of pyrometers

Retro-focus optics with coaxially coupled pyrometers enable the monitoring of thermal emission from the center of the melt pool at high sampling rates of 100 kHz and more. Figure 7.29 shows a work piece that was processed with a laser while the thermal emission was recorded by a coaxially coupled pyrometer (principle depicted in Fig. 7.27). The left image shows the melt tracks one to six which show defects at the two positions marked with "A" and "B". At these two positions is less material resulting in a void. The image on the right displays the readings from the pyrometer which are mapped against the positions where they were sampled. Here, at the marked positions "A" and "B", an excessive reading of thermal emission is detected. The signal reading and the void at the same position suggest an ejection of the material during the melting process.

Application of camera systems

Table 7.1 Typical values for process observation sensors systems that use individual optics in combination with the manufacturing machine (values vary by manufacturer, model and price); * in some applications, systems record a full layer with a few images at long exposure times

Type	Lateral resolution (μm)	Temporal resolution (μs)	Spectral band (μm)	Continuous sampling
Pyrometry (coaxial)	50	5	1.2–1.7	Yes
OT (lateral)	100	5,000*	0.6–0.9	No
IR camera (coaxial)	50	100	1.1–1.9	No
CMOS camera (coaxial)	10	500	0.6–0.9	No
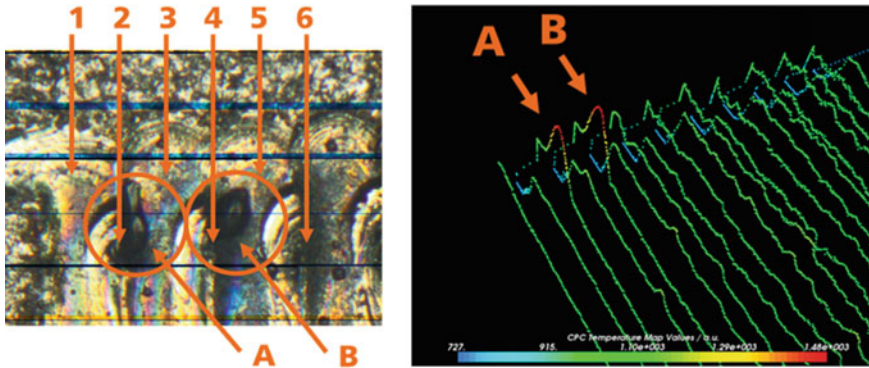
Fig. 7.29 Occurrence of ejection of material on a sample (left) and in the temperature map (right); CC BY 3.0 (Thombansen et al. 2014)

Camera systems in process observation often face situations where both low intensities and wide spectral range of the emitted radiation challenge the acquisition of information about the manufacturing process. Such camera systems often use sensors with 8bit resolution which does not provide sufficient dynamics. Peak intensities of silicon sensors range in the area of 550 nm which makes them a bad choice for the detection of infrared radiation. On the other hand, cameras based on InGas sensors have low sampling rates and high noise which again impacts information content of the images.

Figure 7.30 shows long time exposures where ejected portions of the material are visible as a trace but where the melt pool itself is overexposed. At shorter exposure times, Fig. 7.31 shows the melt pool with its trace and a localized material ejection of larger particles (Thombansen et al. 2015).

Camera systems that observe the process interaction zone are also capable of detecting the amount of powder that is being processed in the respective layer (Thombansen et al. 2015). Figure 7.32 shows the first step of this approach with images that have been acquired by both illuminating the powder surface during processing with a light source at 808 nm and by acquiring the thermal emission from the melt pool (Thombansen and Ungers 2014). The spot in the center of the image results

Fig. 7.30 Coaxial images from a CMOS imaging system at long exposure times (256 pixel * 256 pixel, 1 kHz)
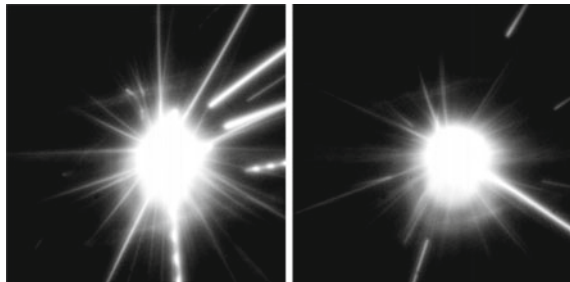
Fig. 7.31 Images that visualize the ejection of a large particle which is seen on the camera image
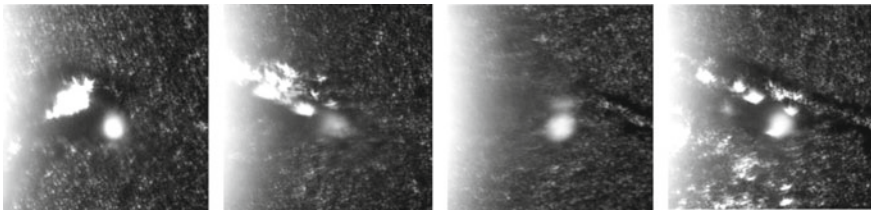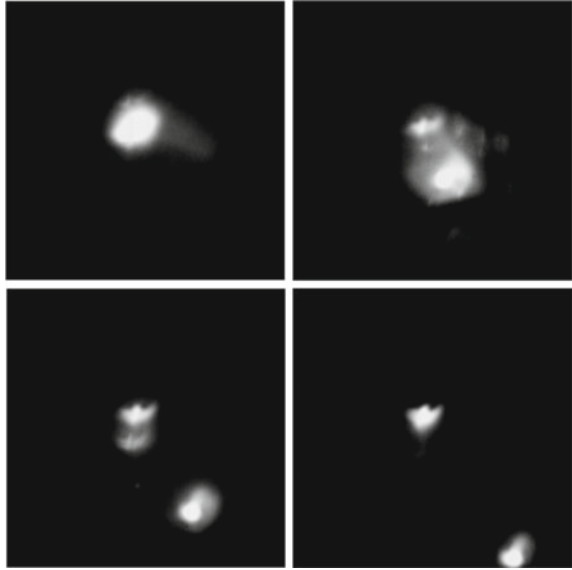
Fig. 7.32 Coaxial images from the illuminated powder bed surface where the processing laser is melting powder (CMOS sensor, 256 × 256 pixels) (Thombansen and Ungers 2014)

from the thermal emission of the melt pool, dark areas result from the reflections of illuminated powder while some light areas on the left result from reflections from the material surface. The combination of reflected light caused by the illumination and from the thermal radiation caused by the interaction of the laser with the powder produces images with two parts of information: The four images show a different intensity in the area of the melt pool and different size; if the full sequence of images is viewed, then the motion of particles in the vicinity of this area that is caused by the interaction of the laser with the powder and melt pool can be seen to change as well.

To use these images for powder layer thickness indication, a sequence of algorithms has been developed. Figure 7.33 shows the result of extracting two criteria from a single track image sequence, the amount of motion of powder particles calculated by motion detection algorithms (blue) and the amount of thermal emission from the melt pool calculated by intensity detection algorithms (red). The combination of both
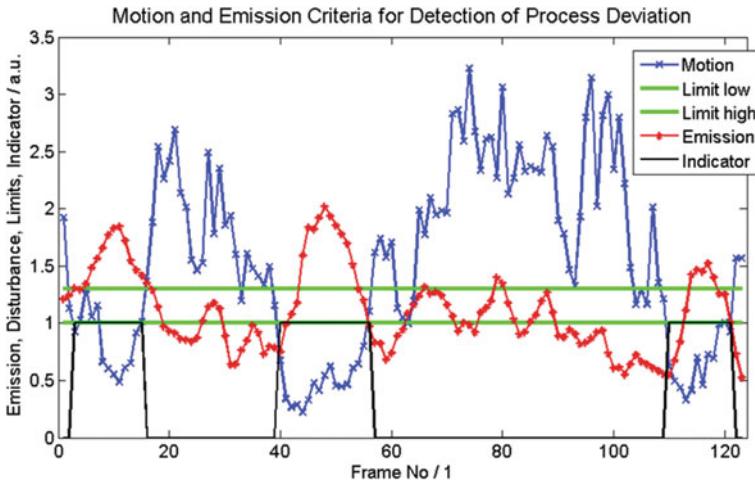
Fig. 7.33 Detection of powder thickness through motion detection algorithms applied to camera images (Thombansen et al. 2015)

signals enables a differentiation between the default amount of powder and excessive amount of powder, denoted by the indicator signal (black). Along the processed track, it indicates a state where there is both a high amount of powder motion (blue) and comparatively low thermal emission (red) (Thombansen et al. 2015). And this state represents a mismatch between setting parameters (laser power/scan speed) and boundary conditions (amount of powder/material) which leads to a process deviation. The approach shows how a single sensor is capable of monitoring two different properties based on process observation in two different spectral regions at the same time and location. It shows how algorithms can extract two criteria from one image and how to combine those criteria towards a signal for a cause-effect relationship.

Camera systems in lateral perspective setup are mostly used for the so-called optical tomography (see Fig. 7.28). A key feature of such systems is the continuous integration of all thermal emissions that occur on the build plane, layer by layer. In doing so, it does not differentiate between thermal emission events over time and location, but it registers the integrated thermal emission for each location.

Figure 7.34 shows a characteristic example of a part where the build process has been monitored with OT. The OT images show increased thermal emission in some areas of the part for a number of layers. The post processed part breaks with a defect pattern that correlates to those areas where the OT indicated excess thermal radiation compared to the normal amount of emission.

Early works on lateral thermography observation have employed long wave infrared cameras to identify the influence of scan parameter variation on the detection of pores and flaws (Krauss et al. 2012). Here criteria were found to differentiate changes in scan speed of 16% by the evaluation of acquired images, changes in laser power in the range of 10% were reported not to be detectable. Artificial defects
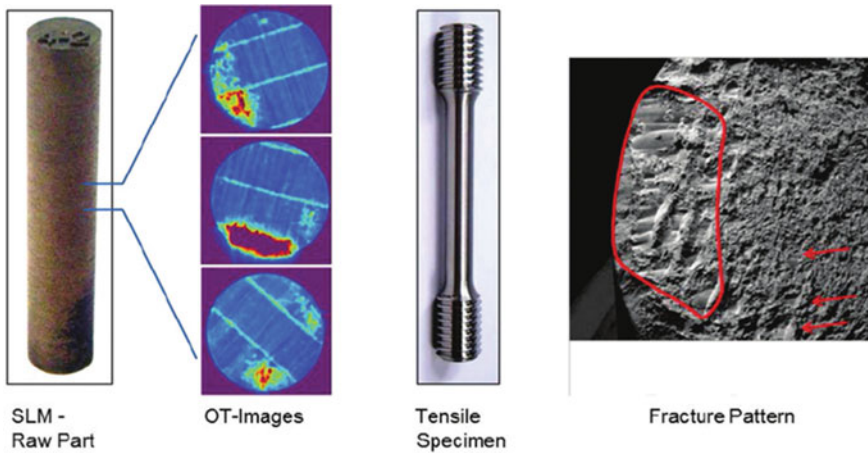
Fig. 7.34 Sequence of using OT from produced part with image per layer to post processed part and destructive tensile test, reprinted from Zenzinger et al. (2015, Fig. 8), with the permission of AIP publishing

in height and width in the range of $140 \times 300\ \mu m$ were reported to be detectable with low confidence in this setup. With changes to more affordable sCMOS sensors (https://www.pco.de/de/scientific-kameras/#section-39) and full build plate observation, similar results are achieved. Changes in laser power, scan speed and hatch distance are reported to be detectable. Even combined deviations such as 105% laser power, 104% scan speed, 100% hatch distance, 100% layer thickness and 111% focus diameter can be distinguished from the 100% seed point with a confidence of $R^2 = 99.4\%$, even in the case of 3% tolerance per value (Ladewig 2019). Most prominently, agreements between defects detected by CT scans and failure in tensile testing in about the same area are reported (Zenzinger et al. 2015; Ladewig 2019; Ladewig et al. 2016b). Figure 7.35 shows a comparison of such a CT scan and the analyzed thermal emission from the OT system. A general resume of this comparison reads such that the OT result shows an increased probability of the occurrence of defects. Thus, although direct cause-effect relationships have not been published, the OT seems to be capable of indicating process conditions that most probably will lead to defects in the final part.

Table 7.2 lists the main process monitoring systems by monitored object and sensor. Where all systems build on well-known sensor principles, they differ significantly in software that analyses the sensor data.

Whilst the implementation of suitable sensor systems for quality control in additive manufacturing is a challenge, the implemented solutions have demonstrated the feasibility. All mentioned applications however show that the analysis of acquired data remains a challenge. Innovative approaches look at multi-layer analysis with an in depth analysis along the time axis taking the evolution of the process and melt pool into account (Montazeri and Rao 2018). Fresh ideas from the area of Artificial
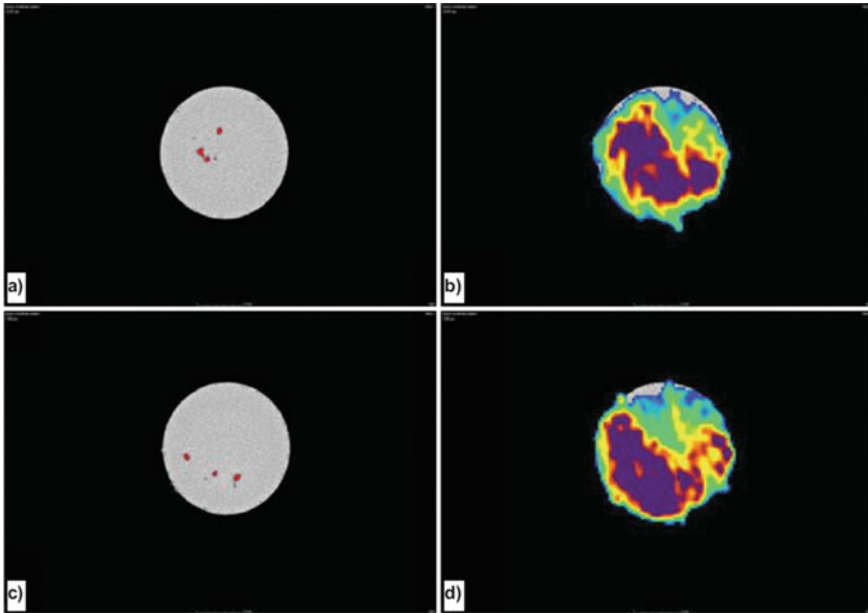
Fig. 7.35 Comparison of two indicators of a delamination defect: CT scan data showing voids in red color (left) and OT data showing regions of high thermal radiation in violet color (right), reprinted from Ladewig (2019)

Table 7.2 List of commercially available monitoring systems

Product	Manufacturer	Monitoring object	Sensor
QM meltpool 3D	GE (former Concept Laser)	Melt pool	Coaxial photodiodes or coaxial camera
EOSTATE MeltPool	EOS	Melt pool	Coaxial and lateral sensors
EOSTATE exposure OT	EOS	Powder bed	Lateral camera
Melt pool monitoring (MPM)	SLM Solutions	Melt pool	Coaxial photodiodes
Layer control system (LCS)	SLM Solutions	Powder bed	Lateral camera
InfiniAM Spectral	Renishaw	Melt pool	Coaxial photodiodes
Truprint monitoring	Trumpf	Melt pool	Coaxial photodiodes
Truprint monitoring	Trumpf	Powder bed and part geometry	Lateral camera
PrintRite3D	Sigma Labs	Melt pool	Coaxial photodiodes

Intelligence (AI) are also both promising and questioned (Yadav et al. 2020) while the combination of today's process knowledge seems to be of major importance to describe the relation of process events and defects.

Resumee

Process control in laser powder bed fusion requires a sensor system that is well integrated into the optical design of the manufacturing machine. For coaxial monitoring, the sensor selection needs to match the concept of the focusing optics to deliver information about the course of the process. A clear distinction needs to be made between monitoring dynamics of the melt pool, monitoring the shape of the melt pool and monitoring of the entire processing area. Examples like material ejections from the melt pool, overheating of the melt pool and powder thickness demonstrate that algorithms are well capable of detecting single events and general deviations from the planned course of the process. It is essential to remember that results of a single layer might not indicated failures in the build process as the re-melting in subsequent layers will heal a significant amount of deviations. If processing is continued, defects such as voids or different powder thicknesses are most often compensated. Still, the reported results arise from deviations of the process. Thus, an increase in deviations can be used as an indicator for instabilities and needs to be addressed to ensure part quality. From that angle, process observation is a valuable tool to monitor the course of the process towards product quality. Future work in this area will need to address the cause-effect relationship such that today's deviation diagnosis will eventually be replaced by forward looking identification of causes from a classically combined process and data analysis knowledge and AI approaches.

7.3.7   Machine Technology

7.3.7.1   Set-Up of LPBF Machines

The current set-up of commercially available LPBF machines is shown schematically in Fig. 7.36 (without control system and without laser beam source). An LPBF system essentially consists of the following subsystems (Schniedenharn 2020).

- Laser beam source,
- Beam guidance and shaping,
- build chamber (including build platform, powder supply and powder deposition unit),
- inert gas guidance and
- control system.

Laser beam source, beam guidance and beam shaping: State-of-the-art laser beam sources currently in use are cw (continuous wave) ytterbium single-mode fiber lasers with a wavelength λ of 1.06 μm. An exception is the use of green laser radiation
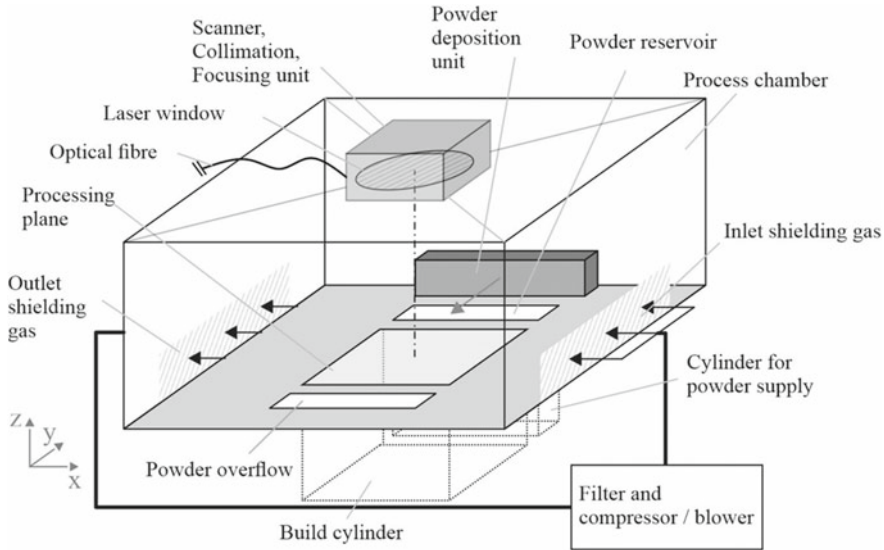
Fig. 7.36 Schematic representation of a LPBF system (shown without control system and without laser beam source), reprinted from Schniedenharn (2020), with the permission of Apprimus

with wavelengths of 515 or 525 nm for processing highly reflective materials e.g. copper materials (see Sect. 7.3.4). Beam guidance and shaping consist of collimation, scanner and focusing unit. The scanner is used to position the laser beam in the build plane, the focusing unit generates a defined beam diameter and compensates the scan field curvature. This unit is designed either as an F-Theta objective behind the scanner or as a dynamic focusing unit in front of the scanner. In the case of an F-Theta objective, the focusing is realized via a rigid lens package, and in the case of a dynamic focusing unit, via a movable lens. To avoid contamination of the optics by dust or process by-products, they are mounted outside the build chamber. The laser radiation is transmitted through an optical window (laser window), into the process chamber (Schniedenharn 2020).

Process chamber: The process chamber is designed as a gas-tight sealed chamber, which is flooded with inert gas during the process, in order to prevent an undesired reaction (oxidation, nitration) of the melt and the solidified material with the surrounding atmosphere. The build cylinder is moved downwards layerwise during the process, the powder supply is realized either from above through the process chamber ceiling or by an additional cylinder from below through the chamber floor.

The powder deposition is usually adjusted so that not all of the powder conveyed is required to cover a layer. Excess powder is fed into the overflow and, analogous to the powder not remelted in the build cylinder, is prepared for reuse after the process. For powder deposition, a defined quantity of powder is deposited in front of the powder deposition tool and moved translationally (in rare cases also rotationally) over the

build platform. Rigid metal or ceramic blades as well as flexible carbon fiber brushes or silicone lips are used as powder deposition tools (Schniedenharn 2020).

Protective gas guidance: The task of the protective gas guidance is to remove process by-products from the interaction zone. The shielding gas guidance is designed as a closed system. After leaving the process chamber, the shielding gas is cleaned of process by-products through a filter unit via the outlet, compressed by means of a blower or compressor, and fed back into the process chamber via the inlet (Schniedenharn 2020).

Control system: The process automation (control of all axes and the inert gas guidance system) as well as the transfer of the exposure data to the driver card of the scanner are performed by the control system during the process. The laser beam source is controlled by the scanner's driver card. Depending on the configuration, the user has the possibility to set process parameters independently before or during the process (Schniedenharn 2020).

Despite the basically identical design, different machines are now commercially available. Machine providers are the companies Aconity 3D (GE), Additive Industries (NL), AddUp (Fr), DMG MORI former Realizer (GE), 3D Systems (US), EOS GmbH Electro Optical Systems (GE), GE Additive former Concept Laser (GE), Renishaw (GB), SISMA S.p.A. (IT), SLM Solutions (GE), TRUMPF (GE), and Velo3D (US).

The machines can be divided into standard machines, machines with large and small build space, as well as special machines.

Standard machines have laser beam sources with maximum laser powers between 200 and 500 W and build space sizes of approx. $250 \times 250 \times 300$ mm^3. These machines allow the manufacturing of a wide range of parts with numerous materials.

Small machines have build spaces in the range of 50–100 mm^3 (see μ-LPBF below) and use laser beam sources with powers of less than 200 W. Typical beam diameters are below 50 μm. This allows the manufacturing of filigree parts with structure sizes <50 μm (see Sect. 7.3.7.3).

Special machines have, in addition to the actual LPBF machine, additional machine components for automated set-up, heat treatment, separation of the parts from the substrate plate, powder handling, etc.

The build spaces of large machines range from $500 \times 280 \times 325$ to $800 \times 400 \times 500$ mm^3. In these machines, two approaches are being used to increase productivity, whereby both approaches are often used at the same time: First, the use of laser powers in the kW range (High Power LPBF) and second, the use of multiple laser beam sources and optical systems (see Sect. 7.3.7.6). Figure 7.37 shows schematically the different processing strategies for a 2-laser-scanner system:

Strategy 1: Both scan fields are positioned next to each other with a slight overlap. This results in a doubling of the build area. By using two laser beam sources and two scanning systems both scan fields can be processed at the same time. In this case the build-up rate is doubled.
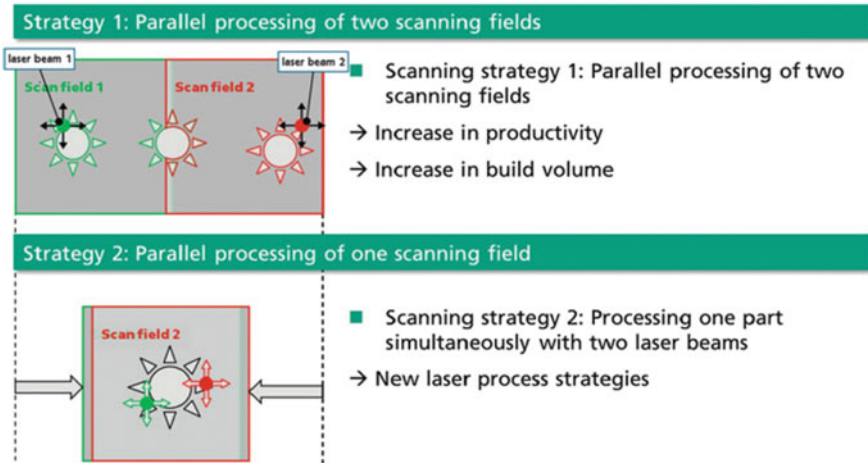
Fig. 7.37 Processing strategies with two lasers and two scanning systems, reprinted from Poprawe et al. (2015, Fig. 5.7), with the permission of Springer

Strategy 2:   The two laser beam sources and the two scanning systems expose the same build area. Again, a doubling of the build-up rate is achieved.

In the following, both machine modifications and newer machine concepts are presented: The machine modifications include, on the one hand, various preheating concepts in order to be able to process materials that are difficult to weld with the LPBF, for example, and, on the other hand, systems with which parts with structure sizes in the micrometer range can be manufactured.

Newer machine concepts pursue different goals: On the one hand, the system costs are to be reduced and, on the other hand, the build-up rate as well as the build space size are to be increased. The scalability of the systems in terms of build space and productivity is also a goal of these new concepts.

7.3.7.2   Preheating in LPBF

Difficult-to-weld high-temperature materials such as nickel-based superalloys (e.g. IN 738, MAR-M 247) and intermetallic alloys (e.g. titanium aluminides) cannot be processed crack-free with commercially available LPBF systems. Due to the high cooling rates of 10^4–10^6 K/s during the LPBF process, residual stresses are induced. If these stresses locally exceed the ductility of the material cracking can occur during the process or subsequent post-heat treatment (Risse 2019; Gussone et al. 2015; Vogelpoth et al. 2019). In addition to the formation of cracks, distortion induced by the residual stresses is another problem for LPBF manufactured parts.

Analogous to conventional welding processes, preheating can also be used in LPBF to reduce the cracking tendency and distortion (Risse 2019; Vogelpoth et al.
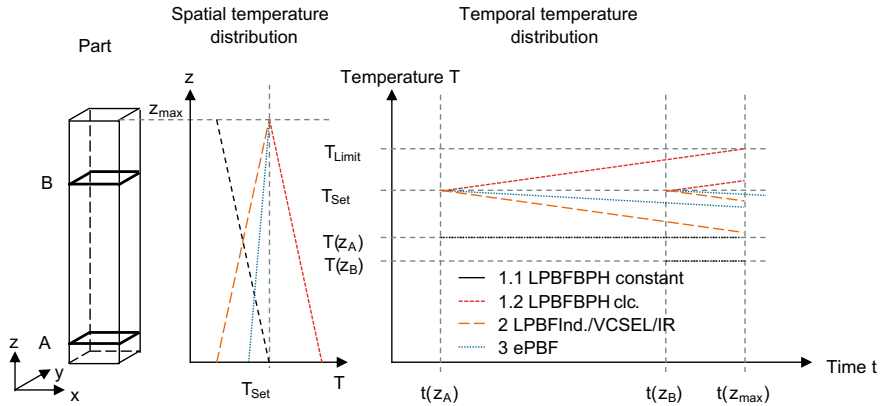
Fig. 7.38 Schematic representation of the estimated temperature curves in a preheated LPBF process over the part height and over the process duration for two exemplary part levels. Shown are the concepts of a base plate preheating with a constant base plate temperature (BPH constant), a base plate preheating closed-loop controlled (clc) to reach the required limit temperature in the working plane (BPH clc), the preheating of the working plane by means of induction heating, vertical cavity surface emitting lasers or infrared emitters (Ind/VCSEL/IR) and for the ePBF process, reprinted from Risse (2019)

2019). Preheating in the part both ensures in-process stress-relief annealing and reduces the material-specific causes of crack formation. The required limit temperature above which these effects occur depends on the material. For example, a preheating temperature of 1,050 °C (Risse 2019) was determined for IN738LC and even a preheating temperature of 1,200 °C for MAR M-247 (Hagedorn et al. 2013) for crack-free processing with LPBF.

Key characteristics of any preheating technology are the resulting spatial and temporal temperature distribution in parts during manufacturing. Temperature distributions for the hereafter described technologies are shown qualitatively on the example of a cubic-shaped geometry in Fig. 7.38 (Risse 2019).

In LPBF, preheating in commercial systems is restricted to resistance heating of the base plate and temperatures of up to 550 °C (Fig. 7.38, case 1) (SLM Solutions). R&D systems with inductive preheating of the base plate allow for preheating temperatures of up to 1,200 °C (Aconity3d GmbH; Hagedorn et al 2014). The heat is distributed from the base plate into the part by thermal conduction. The main drawback of the base plate preheating is the increasing distance between heat source and working plane with increasing build heights. This leads to a continuously decreasing temperature in the working plane, respectively to a negative spatial temperature gradient in build direction (Fig. 7.38, case 1.1). The maximum temperature is located in the first layers of the part at the base plate. This temperature decrease can be compensated by an increasing temperature in the base plate, so that a constant temperature in the working area is maintained (Fig. 7.38, case 1.2). The tolerable temperature (T_{Limit}) in the base plate and the previously built up layers is limited by their melting temperature and the sintering temperature of the powder. If the powder sintered, the

LPBF process cannot be continued and the process is terminated. The maximum tolerable temperature in the base plate limits then the achievable build height for a corresponding designated preheating temperature. Next to the temperature gradient in build-direction, a temperature gradient in x/y-direction typically exists, due to the heat dissipation at the lateral surface of the build envelope (Risse 2019).

In order to be able to realize a preheating in the LPBF process that is independent of the part height, direct preheating of the working plane is necessary. Induction heating can be used for this purpose. The use of Vertical Cavity Surface Emitting Laser (VCSEL) and infrared emitters are the subject of current research (Fig. 7.38 case 2) (Vogelpoth 2018, 2019). In case of an inductive heating, the energy is absorbed in the volume but close to the surface of the part (skin effect) and temperatures of more than 1,000 °C can be achieved. Heating rates can be very high (>100 °C/s), so that it is principally possible to apply the heating only directly before and during the melting phase. In case the base plate is not actively heated or insulated, a temperature gradient in z-direction evolves, which points against the build direction (Risse 2019).

For the radiation-based preheating processes (VCSEL, IR), in addition to the parts, areas of the powder bed that are not remelted are also preheated. Due to the higher absorption of radiation in the powder and the significantly lower thermal conductivity compared to remelted material, uncontrolled powder aging and sintering of powder particles occur at higher temperatures, which can lead to the termination of the LPBF process. Part temperature ranges <800 °C are currently achieved with VCSEL (Vogelpoth 2018).

In EPBF (Fig. 7.38, case 3), preheating is a side effect of the necessity to sinter the powder before melting but is deliberately used to improve the part quality. The fast-moving electron beam scans the powder bed in the working area without melting the powder and generates a quasi-planar heat source. The energy is absorbed on the surface of the powder particles and distributed in the part by thermal conduction. Thus, the maximum temperature is in the working plane and the minimum in the first layers of the part at the base plate. The maximum preheating temperature is limited by the sinter tendency of the used materials. In case the sintering level is too high, produced parts and sintered powder cannot be separated. Currently, the maximum preheating temperature is limited to 1,100 °C in commercially available EPBF machines. For these EPBF machines, the whole build envelope is designed to heat up due to dissipated heat from the powder bed. Consequently, the spatial gradients are assumed to be lower than in the other preheating technologies (Risse 2019).

In all described technologies, the heat dissipation takes place through the powder bed into the sidewalls of the build envelope via thermal conduction, and in the working area via radiation and convection (LPBF only, due to inert gas flow). Next to the heat input from the preheating and the high energy beam, this heat dissipation defines in combination with the thermal conductivity of the used material (powder and bulk) the spatial temperature distribution in the part. Thus, temperature distributions are also geometry and material dependent (Risse 2019).

Two examples are shown below, one using inductive preheating and one using VCSEL preheating of the working plane.

Example 1: LPBF of titanium aluminide

With only half the density of nickel-based alloys, but comparable mechanical properties of up to 800 °C, intermetallic titanium aluminides (TiAl, $\rho = 3.9$–4.1 g/cm^3) are a material class that could replace common engine materials. Advantageous properties like high strength and creep resistance combined with high corrosion and wear resistance increase their attractiveness, especially for turbomachinery applications (Vogelpoth et al. 2019).

Titanium aluminides exhibit a brittle-to-ductile transition (BDTT) above a temperature of 750–900 °C, at which ductility increases strongly. Studies on the processing of TNM™ titanium aluminides by LPBF at preheating temperatures between 800 and 1,000 °C have shown that TNM™ can be manufactured crack-free with densities >99.9% (Gussone et al. 2015, 2017; Vogelpoth et al. 2019; Löber et al. 2011). With a tensile strength of up to 900 MPa, LPBF fabricated TNM™ is comparable to conventionally fabricated titanium aluminides. However, LPBF manufactured TNM™ exhibits a smaller ductility. Reasons for this are a too high oxygen content >1,000 ppm and/or the very fine microstructure after LPBF, which has to be adjusted by a post heat treatment.

The alloy TNM™-B1 is processed on a laboratory-scale LPBF system using a multi-mode fiber laser at a maximum laser power of 500 W and a Gaussian intensity distribution. The beam was focused to 100 μm in diameter. With argon as a shielding gas and a gas purification system, an oxygen concentration $O_2 < 10$ ppm and moisture concentration $H_2O < 20$ ppm could be achieved. These contents are sufficient to prevent visible oxidation of powder or parts during the LPBF process. The LPBF system is equipped with an inductive substrate plate heater, with which substrate temperatures of T = 1,200 °C are possible (Vogelpoth et al. 2019).

Figure 7.39 shows the temperature–time curves for a LPBF process with controlled base plate preheating (Fig. 7.38 case 1.2). In order to be able to process this alloy without cracking, the temperature must be >800 °C (Vogelpoth 2018; Sauthoff 1995). In addition to the measured variables of the base plate temperature (green) and the pyrometer signal (gray), the specified control temperature (orange) and the temperature in the working plane (red) are shown over the process duration.

In order to be able to maintain the specific temperature of 850 °C for TNM™-B1 in the working plane over the entire process duration and the total part height, the base plate temperature must be increased step by step to over 1,100 °C. This is the maximum tolerable base plate temperature. At this temperature, the first powder particles in the vicinity of the base plate begin to sinter, so that this is the maximum tolerable base plate temperature. In this example, the overall height for the part made of TNM™-B1 is thus limited to 19 mm.

Example 2: Preheating with VCSEL

An innovative preheating concept uses a VCSEL module for additional heating of the working plane (case 2 in Fig. 7.38). For this purpose, an array of six vertical-cavity surface-emitting laser bars (VCSEL) with 400 W each is installed in a LPBF machine. With infrared radiation at 808 nm, this array can heat the device from the top
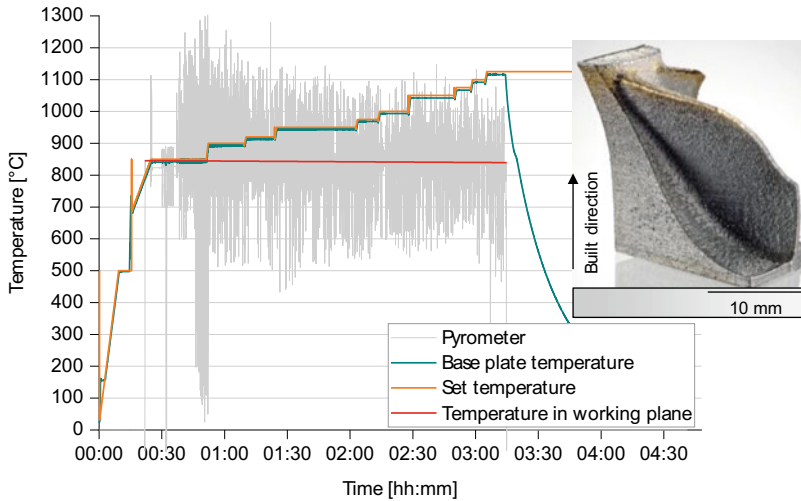
Fig. 7.39 Left: temperature–time-curves of a LPBF process with controlled inductive base plate preheating device, right: with this system manufactured blade made of the titanium aluminde alloy TNM™-B1.

to several 100 °C during the building process. The bars can be controlled individually so that sequences of different patterns are possible. The process is monitored with an infrared camera to ensure a homogeneous temperature in the processed layer.

Figure 7.40 shows temperature–time curves for a VCSEL preheated process for TiAl. The substrate plate heating is not active, only thermocouples are used to measure the substrate plate temperature (base plate temperature, analogous to Fig. 7.39). The target temperature in this example is 800 °C. The temperature in the working plane is measured with an IR camera. The red curve represents the temperature averaged from the camera signal. On the right axis the irradiated laser power of the VCSEL module is shown. The laser power of the module is manually controlled. Two areas are shown in the diagram: Until about 01:20, the substrate is only preheated by the VCSEL to reach the set temperature of 800 °C. After that, the VCSEL power is manually controlled down and the LPBF process starts (unstable IR camera signal). The end of the LPBF process is reached at about 02:20. Due to the manual control of the laser power of the VCSEL module, the temperature temporarily drops below the required 800 °C.

In the lower part of Fig. 7.40, an exposure in the working plane is shown on the left. The area preheated by the VCSEL module from above is clearly visible. In addition, the processing of a specimen with the "LPBF laser" is visible. In the right part of Fig. 7.40, the specimens of the alloy TNM™-B1 manufactured with this preheating concept are shown. All specimens could be manufactured crack-free.
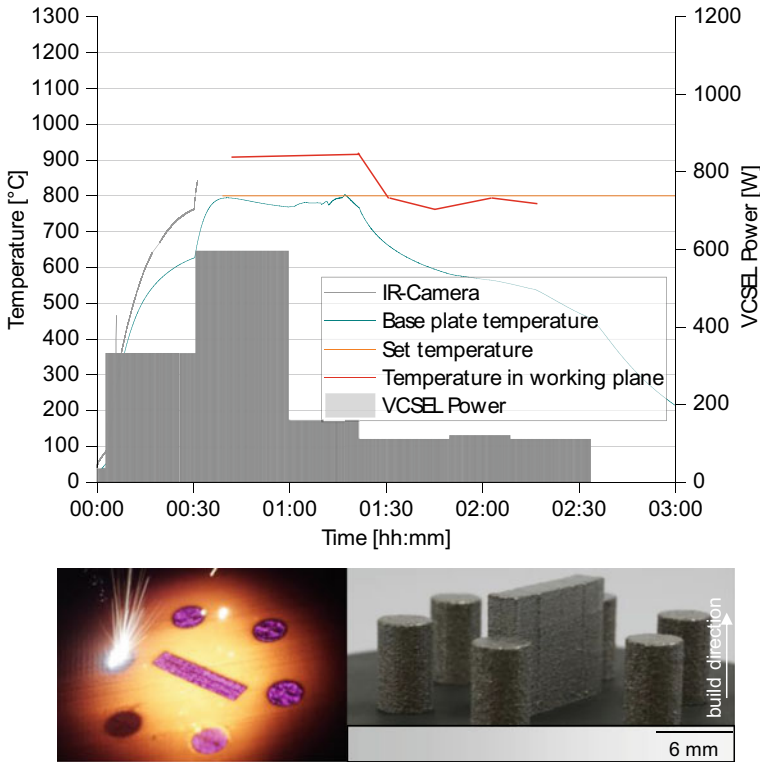
Fig. 7.40 Above: temperature–time-cycles of a VCSEL-based preheating process, below left: exposure in the working plane during VCSEL preheating, right: crack free test samples fabricated of TNM™-B1 with VCSEL preheating

7.3.7.3 Micro-Laser Powder Bed Fusion (μ-LPBF)

In the field of micro technology there is an increasing demand for small, highly complex parts. In order to expand the capabilities of LPBF and to meet this demand, the Micro-Laser Powder Bed Fusion (μ-LPBF) was developed at Fraunhofer ILT.

In comparison to the conventional LPBF-process with powders with particle sizes of 15–50 μm, layer thicknesses of 30–100 μm, and laser spot diameters of 70–100 μm (see Sects. 7.1.2 and 7.1.3) the μ-LPBF approach uses powders with smaller particle sizes ($d_{90} \leq 10$ μm), smaller layer thicknesses (10 μm) and smaller laser spot diameters (20–25 μm). An important characteristic of this process is that the laser does not operate in the continuous wave (cw) mode but in the pulsed wave (pw) mode. In this mode, thin melt tracks can be generated whose widths approximately correspond to the diameter of the focused laser beam (Masseling and Gayer 2018; Oosterhuis 2018).

Materials that have been successfully processed with μ-LPBF are stainless steel (316L), nickel base superalloys (IN 718, IN 625), aluminum alloys (AlSi10Mg), 18 k

gold and Ni–Ti with d_{90}-values smaller than 10 and 15 μm. Since the small particles agglomerate easily, a special powder coating unit was developed for use in μ-LPBF machines. With this unit, the above-mentioned powder materials can be prepared in uniform layers of the desired thickness.

The μ-LPBF process was developed on a modified SLM-50 machine from Realizer. The system is equipped with an air-cooled single mode ytterbium fiber laser yielding a maximum output power of 120 W in continuous wave (cw) mode. The focus spot diameter is approximately 25 μm. For μ-LPBF, the machine was modified: First, a custom-made vibrating unit was integrated, which supports powder deposition and enables even powder spreading for particle sizes $d_{90} < 10$ μm. Second, an altered inert gas supply was applied for improved inert gas atmosphere of O_2 < 30 ppm. Third, a laser controller was applied in order to trigger the laser signal, yielding modulated laser radiation. The laser on/off signal is provided by the machine control and forwarded to the frequency generator, which provides the trigger signal, superimposed with the initial on/off command of the machine control. The triggered on/off command then yields modulated laser radiation, which is guided through the optical components to the powder bed. The pulse lengths are in the range of 50–300 μs and the pulse frequencies are between 0.5 and 5 kHz.

In the following some applications are presented:

Figure 7.41 shows a stent with a complex hollow tube design (4 mm diameter and 12 mm height) that was built using a Ni–Ti shape memory alloy with a particle size of $d_{50} = 4.4$ μm. Single-track experiments were performed to develop a process parameter set that resulted in small wall thicknesses down to 32 μm. It was found that when the laser pulse length and laser power were reduced, the width of the melt track also decreased. For the material Ni–Ti a minimal surface roughness of Sa = 1.3 μm was achieved, while for other materials the following values are achieved: For nickel base alloys a minimal roughness of Sa = 0.8 μm, for steel and titanium Sa values between 1.2 and 2 μm and for gold and copper, Sa values are between 5 and 15 μm.

Figure 7.42 illustrates a monolithic demonstrator in the "as built" state that was manufactured in one piece without subsequent assembly. Such parts can be produced with tolerance deviations as low as approx. 20 μm.

In Fig. 7.43 left an example for manufacturing of jewelry made of gold is presented while in Fig. 7.43 right a complex part made of 316L is manufactured via μ-LPBF.

7.3.7.4   3D Laser Printing (3DLP)

A reduction of the costs of LPBF machines can be achieved by the application of cost-efficient diode laser systems. However, their combination with galvanometer scanners results in insufficient scan field and/or laser spot sizes due to their lower beam quality in comparison to fiber lasers. Therefore, this machine concept does not use scanner systems. Instead, several fiber-coupled diode lasers are combined with a working head moved by a gantry system with linear axes to realize the so-called 3DLP ("3D Laser Printing") process (Fig. 7.44) (Eibl et al. 2017; Eibl 2017).
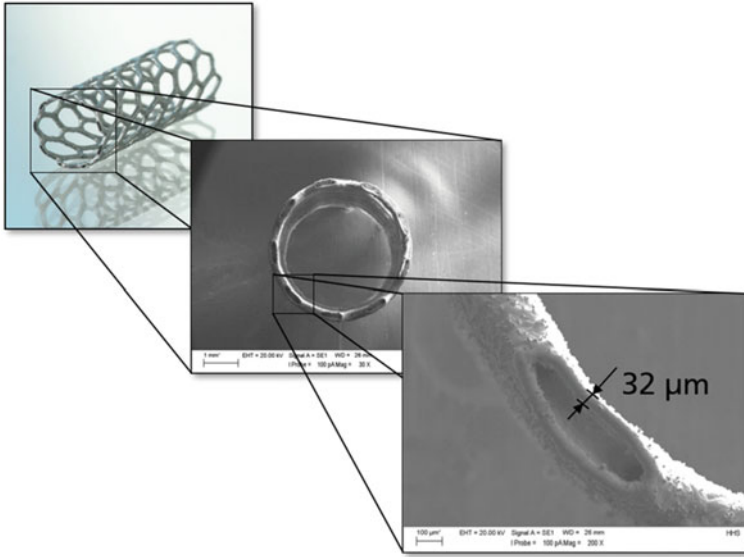
Fig. 7.41 Stent with complex hollow tube structure made of Ni–Ti. The minimal structure size is about 32 μm
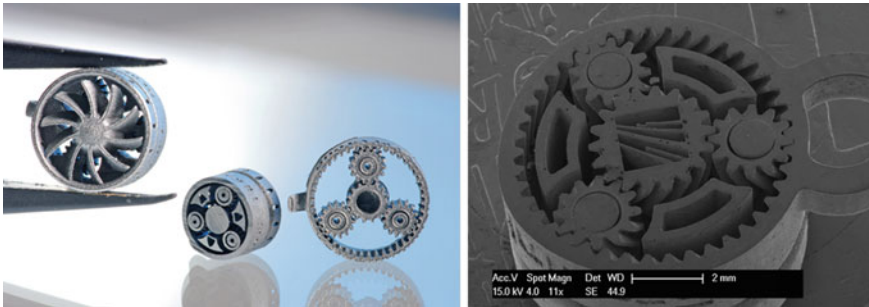
Fig. 7.42 Planetary gear made of 316L, manufactured in one piece without the need for assembly

In this case, five individually controllable diode laser spots with a diameter of approx. 200 μm each are arranged in a multi-spot array (processing head). The control of the individual spots (modulation according to the desired part geometry) is carried out via a proprietary spatially resolved exposure control system. The five individual spots can be arranged in different configurations (e.g. as line-array, arrow-array or W-array (Eibl 2017)). The output power of each diode laser is 200 W. The build space of the prototype machine was $150 \times 150 \times 150$ mm^3. Another important component of this machine concept is a local shielding gas system. With increasing build space, it becomes more difficult to ensure complete removal of the process by-products by the inert gas. Therefore, a local shielding gas system was developed

Fig. 7.43 Left: jewelry parts made of gold after micro bead blasting, right: castle made of stainless steel 316L in the "as built" state
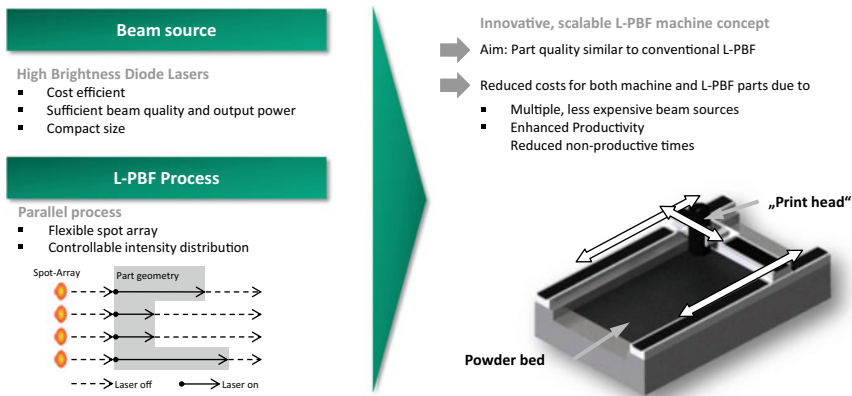
Fig. 7.44 Multi-spot array for 3DLP, reprinted from Eibl (2017, Fig. 1), with the permission of Apprimus

and mounted to the processing head. The principle of an open process chamber with local shielding gas flow as shown in Fig. 7.45 enables a significant increase of build envelope while maintaining the processing conditions locally. Due to the symmetrical design, the flow direction can be inversed depending on the exposure direction. The local shielding gas inlet ("Argon Curtain") reduces the demands on the surrounding process atmosphere.

Figure 7.46 schematically shows the arrangement of two individual tracks in different processing directions. Each track is generated by the five individual laser beams. In addition to the offset of the individual beams, the offset of the tracks is also adjusted.

Exemplary demonstrator parts manufactured with the line-array are shown in Fig. 7.47. Due to a local shielding gas system mounted to the working head, part densities of 99.98% are achieved for the material 316L (Eibl 2017). Main advantage of the 3DLP process is the increased scalability of both melting rate and build
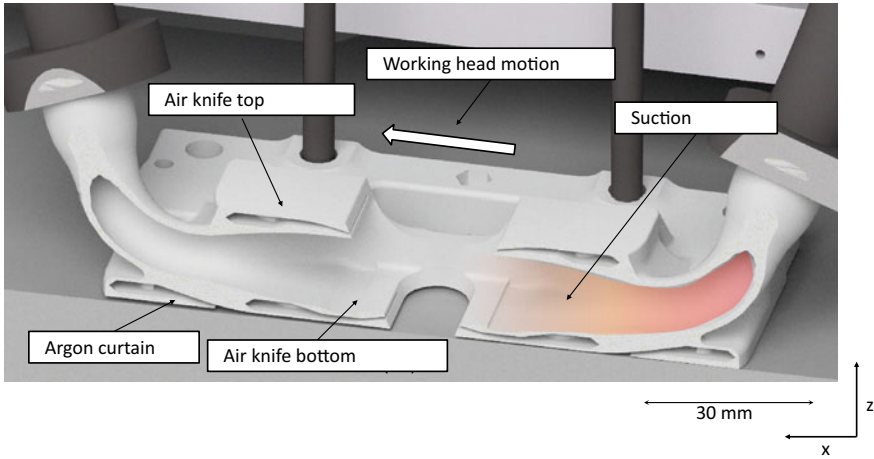
Fig. 7.45 Schematic side view of a movable LPBF process chamber. The optical system is mounted to the chamber and moved over the powder bed, while the required shielding gas atmosphere is maintained within the chamber, reprinted from Eibl (2017, Fig. 39), with the permission of Apprimus

Fig. 7.46 Schematic representation of two melting lines with the line-array as basic structural unit of the part, each line generated by simultaneous operation of five spots, reprinted from Eibl (2017, Fig. 27b), with the permission of Apprimus
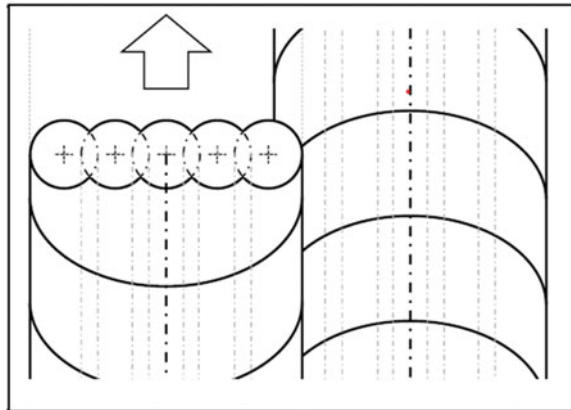
envelope. By increasing the number of spots within the array, the melting rate can be increased without the requirement of parameter adaption, while the build envelope can be adapted via the axis system independently from the optical unit.

In general, 3DLP allows for greater melting rates due to the application of multiple spots, while beam positioning via axis systems leads to less dynamic positioning compared to scanner-based processes. Therefore, the greater melting rates can be utilized in particular for large, predominantly solid parts, i.e. for geometries that require less non-productive beam positioning (Eibl 2017). An evaluation of the economic benefits of the system requires knowledge of the initial cost of a production system. An estimate based on the laboratory system described above showed that the
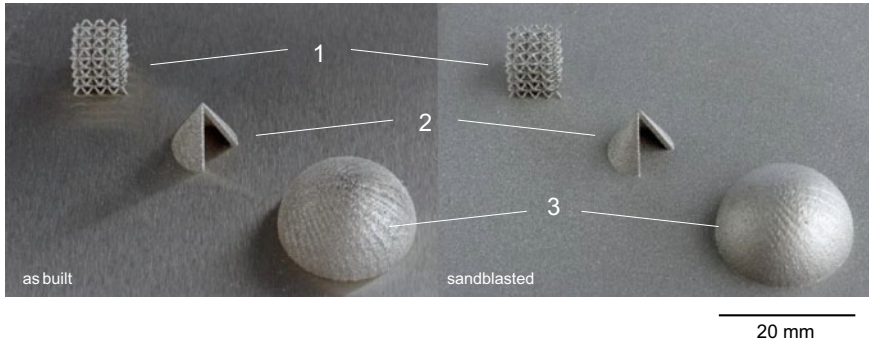
1: Lattice structure 10 x 10 x 10 mm³, strut thickness ~300 µm

2: Hollow cone, wall thickness 1 mm

3: Semisphere, Ø 20 mm

Fig. 7.47 Demonstrator parts (stainless steel 316L) generated via 3DLP with multi-spot-array with five individually controllable fiber-coupled diode lasers

number of spots is the main factor influencing productivity. Furthermore, a part cost reduction of 50% is already possible with 10 installed laser spots.

7.3.7.5 Low Cost LPBF Machine

In order to reduce the investment costs for a standard LPBF machine and thus to facilitate access to LPBF for small and medium-sized companies in particular, a new system concept was developed.

The concept of the low-cost LPBF machine avoids cost-driving components such as classic laser-scanner systems. The use of a Cartesian axis system in combination with a diode laser as the beam source results in the greatest potential savings. In a first step, a prototype system was built with the following main components:

- 2-axis system
- Build space: Ø 80 mm × 90 mm
- Diode laser >100 W with 160 µm focus diameter

Process parameters were determined for the materials 1.4404, tool steels and nickel-based alloys IN 625 and IN 718, with which a density of over 99.5% can be achieved. Various parts were manufactured with the machine. In the meantime, this machine concept has been further developed into a commercially available machine (https://www.lm-innovations.com/de-de/anlagen/alpha-140/). This machine has a build space of Ø 140 mm × 200 mm, a diode laser with an output power of 140 W and a focus diameter of 140 µm.

7.3.7.6 Scalable LPBF Machine Concept

The aim of the concept is the scalability of build-up rate and build space size. To this purpose, the required machine technology, suitable exposure concepts and the associated process management are being developed. Like the 3DLP, this machine concept is also based on a gantry system. The use of a movable processing head with a base area of 500 × 200 mm with local inert gas guidance creates locally controllable, constant process conditions. Five laser-scanner systems arranged in a line are integrated into the processing head. Single mode fiber lasers with a maximum output power of 400 W and Gaussian intensity distribution are used as beam sources. The beam diameter of the individual modules is about 100 μm. The laser radiation is guided into the processing head via optical fibers. Both the deviations of the focus positions of the five modules and the alignment of the five scan fields were eliminated by suitable measures and the required positioning accuracy of the scanner systems of below 20 μm was achieved (Tenbrock 2020).

A nozzle system for the new processing head is being developed to ensure effective removal of the resulting process by-products (e.g. metal condensate; spatters). The nozzle system must be very compact, because it is mounted on the processing head and therefore the traversability of the processing head and the resulting limited build space must be taken into account. With this nozzle system, a sufficiently homogeneous flow distribution is achieved independent of the position of the processing head in the build space (Tenbrock 2020).

Figure 7.48, left shows the 5-scanner processing head integrated into a prototype machine. The machine control is adapted to allow simultaneous machining with 5 scanners. With this system, part sizes of up to 1,000 × 800 × 400 mm can be manufactured. To increase productivity, a CAM system is being developed to optimize the utilization of the scanners in the process and minimize the manufacturing time (Tenbrock 2020).

With regard to process management, process strategies for simultaneous multi-scanner processing are being investigated (Fig. 7.48). One challenge here is the avoidance of mutual impairment of adjacent remelting processes, e.g. as a result of
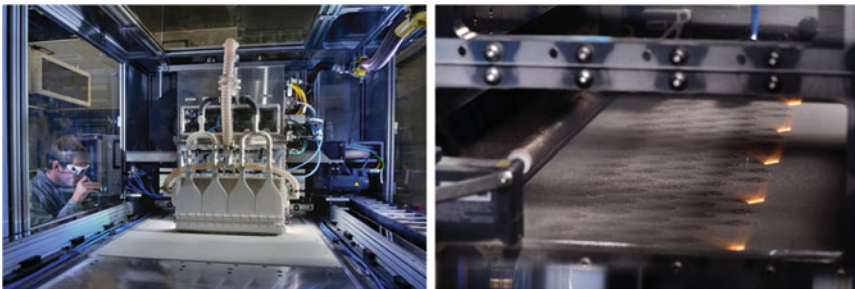
Fig. 7.48 Multi-scanner processing head (left) and simultaneous processing with five laser beams
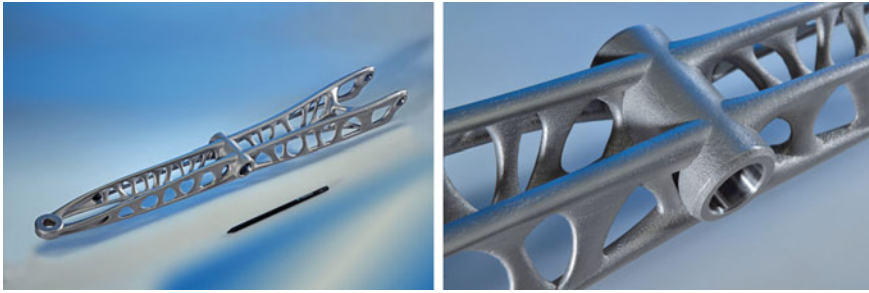
Fig. 7.49 Demonstrator part made of 316L manufactured in the prototype machine

laser-condensate interaction (Tenbrock et al. 2021). In addition, a process management for on-the-fly processing is being developed. By synchronized movement of the scanner drives and the linear axis system, the exposure and the deposition process can be parallelized and non-productive times can be eliminated. In manufacturing trials, it can be shown that the developed approaches to multi-scanner and on-the-fly processing enable a significant increase in productivity with consistently high relative part density. Using layer thicknesses of 100 μm, a theoretical build-up rate of 45 mm^3/s can be achieved for the multi-scanner system, which is a significant increase compared to the reference value of about 3 mm^3/s with standard machines. This prototype system was used to manufacture the demonstrator part shown in Fig. 7.49 (Tenbrock 2020).

7.3.8 Laser Sintering of Polylactide-Based Composites for Biodegradable Implants

As an example of a non-metallic material, the processing of polylactide-based composites for bioresorbable patient-specific implants will be presented.

LPBF is widely used in biomedical engineering, especially for the fabrication of implantable medical devices and bone tissue engineering scaffolds (Gayer et al. 2019; Gayer 2017; Youssef et al. 2017). LPBF enables the manufacture of patient-specific implants (PSI) with complex interconnected pore structures to promote bone ingrowth. Typical materials are titanium and polyetherketoneketone (PEKK). Titanium and PEKK implants have the disadvantage that they permanently remain in the patient's body, which could cause late complications. Biodegradable implants, which can be resorbed by the human body in a timeframe of months to years, are a promising alternative. These implants avoid revision surgeries and bone grafting. Among the biodegradable polymers, polylactide has the highest mechanical strength (Gayer et al. 2019).

Polylactide (PLA) decomposes into lactic acid in the human body, which can create an acidic environment around such an implant. This acidic environment can

lead to inflammatory reactions, which can impair healing. To avoid the formation of an acidic environment, buffering filler materials, such as calcium phosphate (CP) or calcium carbonate (CC), are added to the polylactide matrix. Due to its greater basicity, CC is more suitable for neutralizing the acidic degradation products than CP. In addition to the buffering effect, CP and CC have the advantage of being more bone-like compared to polylactide. For example, bone consists of about 50% calcium phosphates and about 5% calcium carbonate (Gayer 2021).

Against this background, a composite material suitable for processing with LS should be developed. One powder production method that is frequently used by research groups is solvent evaporation (Yan et al. 2020). However, biodegradable polymers such as PLA are only soluble in toxic organic solvents such as chloroform or dichloromethane. Those toxic solvents are a severe health hazard and pose a problem for medical application as well as for the upscaling of the powder production. To avoid those problems, a composite powder is developed through a solvent-free method based on good manufacturing practice (GMP) standards. A large variety of different polymer/filler combinations can be produced with this process. This includes a newly developed composite material that is made of PLA and precipitated calcium carbonate (PCC) (Gayer et al. 2019, 2018; Gayer 2017) (Fig. 7.50).

The specifically designed PCC particles are a source of precious Ca^{2+} ions that are needed for proper bone formation. In addition, the PCC particles are supposed to improve the degradation behavior of the composite material by buffering the acidic degradation products of PLA. PCC particles also offer a suitable surface structure that improves the adhesion to the PLA matrix.

Nearly all powder particles are smaller than 100 μm so that thin powder layers with about 100 μm thickness can be realized. This is important, as particle fusion can be achieved faster and more homogeneously for thin powder layers than for thicker layers. Additionally, smaller layer thicknesses enable a higher detail resolution (Gayer 2017).

In accordance to the Sect. 3.1 the newly developed PLA-based composite particles have a rounded shape that results in good flowability, which is a precondition for
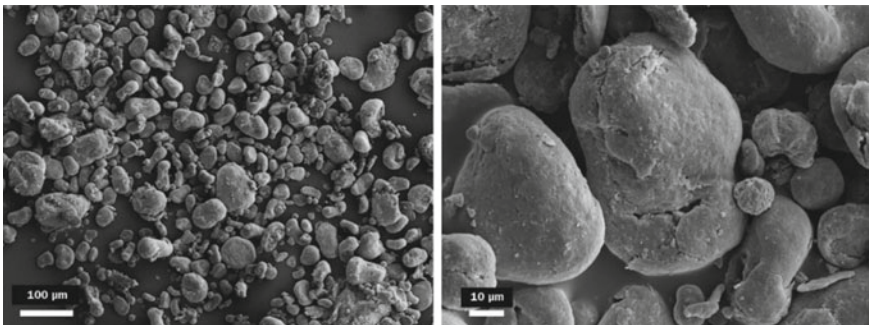
Fig. 7.50 SEM images of the newly developed biodegradable polylactide/calcium carbonate composite powder, reprinted from Gayer (2017), Schaefer Kalk GmbH & Co. KG

homogeneous powder deposition. Another crucial material property is melt viscosity. In comparison to metal melts, polymer melts are approx. 5–8 orders of magnitude more viscous than metal melts. Usually they require a long time to achieve complete fusion of the polymer particles. The suitable polymer chain length results in a melt viscosity small enough to enable fast fusion.

The developed composite material shows little absorption for a wavelength of about 1 μm (see Sect. 2.3). Therefore, CO_2 lasers with 10.6 μm wavelength are used for processing. At this wavelength, the molecular bonds of polymers are excited, resulting in molecular vibrations so that significant absorption occurs. For LS a customized EOS Formiga P 110 laser sintering machine including a CO_2 laser with 30 W optical power is used. The laser beam was focused to a spot diameter of about 450 μm, which gives a typical intensity of up to 19 kW/cm^2 (Gayer 2017).

The process parameters for the LS process must be carefully adjusted in such a way that the PLA matrix melts completely to achieve a high density with high mechanical strength. At the same time, thermal degradation must be avoided as far as possible. The filler material, on the other hand, should be completely retained in the solid state. Therefore, this process is very similar to the process described for metallic materials in Sect. 7.1.1, where special multi-component powders are processed, using a low-melting point and a high-melting point material.

Figure 7.51 shows the results of a series of tests in which the laser power was varied. With increasing laser power, the surface texture of the specimens (6 × 6 × 4 mm) changed from rough and porous to smooth and dense (Fig. 7.51a, b). The formation of a flat surface coincided with a yellow discoloration. For low laser power (0.30 W), the polished cross-section revealed lack of fusion in the form of many irregular shaped voids (Fig. 7.51c). As the laser power was increased, the number of irregular shaped voids decreased resulting in a lower micro-porosity. The best results were observed at 0.40 W resulting in the lowest micro-porosity of approximately 2%. While lower laser powers led to lack of fusion, higher laser powers caused yellowing and increased gas pore formation. The CC was observed both in the form of spherulites (12 μm diameter) as well as in the form of their fragments. During SLS processing, the PLA was melted and the CC remained as a solid filler material that was homogeneously dispersed throughout the PLA melt. The CC spherulites were visible as light dots in the light microscope (LM) and SEM images. The CC fragments appeared as thin strip-like structures that appeared dark in the LM and light in the SEM images. A close-up of the polished cross-section of the 0.40 W specimen gives information about the CC distribution in the PLA matrix (Fig. 7.51d) (Gayer et al. 2019).

A narrow processing window was determined that yields optimum strength (biaxial bending strength of about 80 MPa) and minimum degradation (<10% decrease of the inherent viscosity). In addition, the test specimens showed good cell compatibility with osteoblast-like MG-63 cells.

The key to successful manufacturing of a patient-specific implant demonstrator (Fig. 7.52) is to control the complex interplay between powder material, machine and process. The interconnected pore structure was designed using Autodesk's Within software, which allows integration of a pore structure that follows the implant's
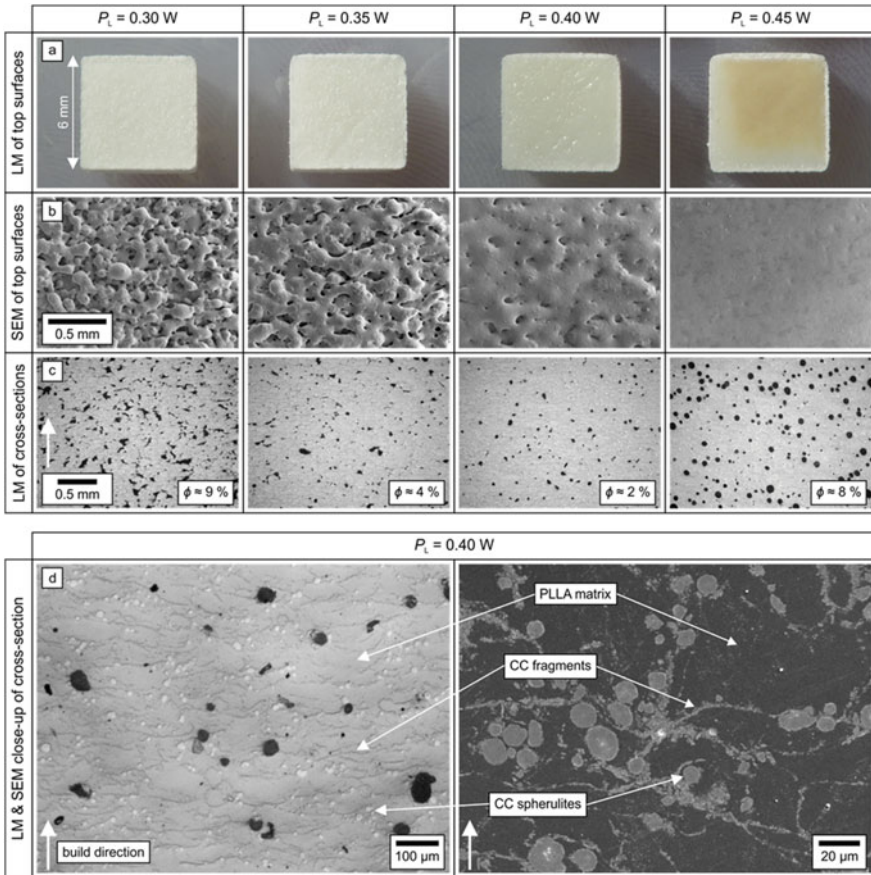
Fig. 7.51 Analysis of SLS specimens ($6 \times 6 \times 4$ mm) manufactured from a PLA/CC composite: **a** light microscope (LM) images of the top surfaces as a function of laser power P_L, **b** SEM images of these top surfaces, **c** LM images of polished cross-sections parallel to the build direction (indicated by arrow) including the micro-porosity ϕ determined from these cross-sections, and **d** LM close-up (left) and SEM close-up (right) of the polished cross-section for $P_L = 0.40$ W, reprinted from Gayer et al. (2019)

surface contour so that a smooth global surface without off-standing struts is achieved. The strut diameter was about 1 mm. The build process took only about two hours, and the implant offers a perfect fit to the cranial defect (Gayer 2017).

Therefore it could be shown that manufacturing of biodegradable patient-specific implants by laser sintering is feasible. The next step will be thorough in vitro and in vivo testing of the novel scaffolds. In the future, such biodegradable PSIs made by laser sintering could significantly improve the medical treatment of bone defects.
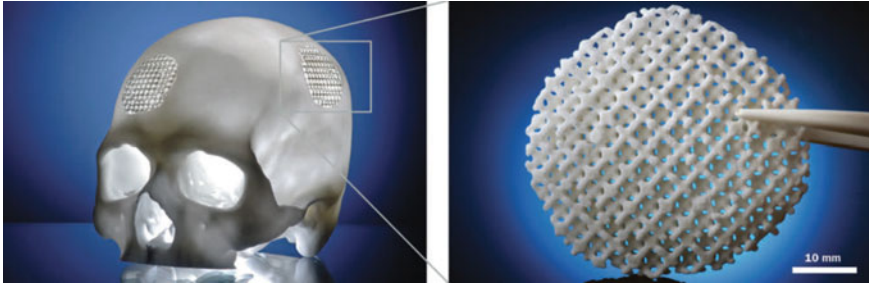
Fig. 7.52 A biodegradable patient-specific cranial implant demonstrator was made by laser sintering from polylactide/calcium carbonate composite powder on the customized Formiga P 110 machine, reprinted from Gayer (2017), KLS Martin Group

7.4 Horizontal Process Chain

7.4.1 Design

At the beginning of the horizontal process chain is the design. First, tools with integrated cooling channels are considered. From a design point of view, conformal cooling channels are the best solution for achieving homogeneous heat transfer of the processed molding compound via the mold walls to the cooling medium. The cooling channels can be designed using simulation tools. Such conformal cooling channels can have intertwined 3D channels and therefore cannot be manufactured by conventional manufacturing processes (e.g. milling, EDM). With the LPBF process, such conformal cooling channels can be manufactured, but the manufacturing restrictions of LPBF have to be taken into account (see below).

Therefore, the question arises at the very beginning whether functional or performance improvements can be achieved for given part applications by using the LPBF process, with which the usually higher manufacturing costs can be justified. In the application described, it must be decided whether the potential added value from improved cooling (e.g. reduced cycle time, improved quality of the injection molded part) justifies the higher manufacturing costs of LPBF.

When asking whether a part is suitable for manufacturing with LPBF, selection criteria should be applied and the possible added value through additive manufacturing should also be considered. Examples of selection criteria are the dimensions and complexity of the part, the required surface quality, the number of pieces to be manufactured, possible LPBF manufacturing restrictions, the costs for manufacturing, the mechanical requirements in the part operation and the consideration of the entire process chain up to the final part. The possible added value results from function optimization, weight reduction, integral design, longer service life, reduced lifecycle time between design, manufacture and validated part delivery, short-term and demand-oriented spare parts production or shorter process chains.

A major advantage of the LPBF is the extensive design freedom. This advantage can be used especially in the following applications:

1. the part to be manufactured cannot be produced using conventional manufacturing processes due to its geometry.
2. additive manufacturing allows parts to be manufactured monolithically, thus saving time-consuming joining and assembly processes for the individual parts.
3. topology optimization and integration of lattice structures can drastically reduce part weight and improve functional properties.

In the following, these aspects are discussed in more detail:

Ad 1: Complex Parts

The tool- and mold-making industry is a typical example of a branch producing final parts in small batches (typically less than 10). As already described above, tools with conformal cooling channels are predestined for manufacturing with LPBF. Due to the layer-by-layer fabrication, almost any cooling channel geometries can be produced. Thanks to LPBF, an improved tool cooling can be attained, resulting in reduced cycle times and improved part quality.

Figure 7.53 on the left shows schematically a mold insert for the pot of a kitchen machine with spiral-shaped conformal cooling channels. The mold insert is made of tool steel 1.2343. Figure 7.53 right shows the mold insert manufactured with LPBF. The tool insert was post processed by grinding and spark erosion. In Fig. 7.54, two mold inserts are installed in a cooling fixture to investigate the cooling performance. One tool insert is made of the copper alloy Ampco 940 with standard cooling channels and the other tool insert was made of 1.2343 tool steel with LPBF and conformal cooling channels. Figure 7.54 on the right shows the temperature distribution of both inserts after 2 s recording with an infrared camera. Despite the Cu material with its high heat conductivity, the LPBF manufactured tool insert shows a significantly better cooling performance (lower temperature) due to the conformal cooling channels. The example demonstrated that the manufacturing of complex parts using LPBF can significantly increase part performance.

Ad 2: Monolithic Manufacturing

As an example of a monolithic part design, a guide vane cluster of a gas turbine is discussed below. The guide vane cluster is a design variant of a compressor stator. For this purpose, the part is considered along the design and manufacturing chain (see Fig. 7.55).

In the conventional manufacturing route, individual blade segments with two blades each (twin segment) have so far been milled from the solid material and later assembled in the gas turbine casing to form a stator ring. Due to the small gap distance between the blades, milling the guide vanes as a cluster is technically very demanding and not economically viable. In a first evolution stage (Fig. 7.56 center), a six-row guide vane segment results that can be monolithically manufactured with LPBF. In LPBF manufacturing, adaptive process management can be advantageously applied for this part (see Sect. 7.3.2). Design adjustments result in the twelve-row vane cluster
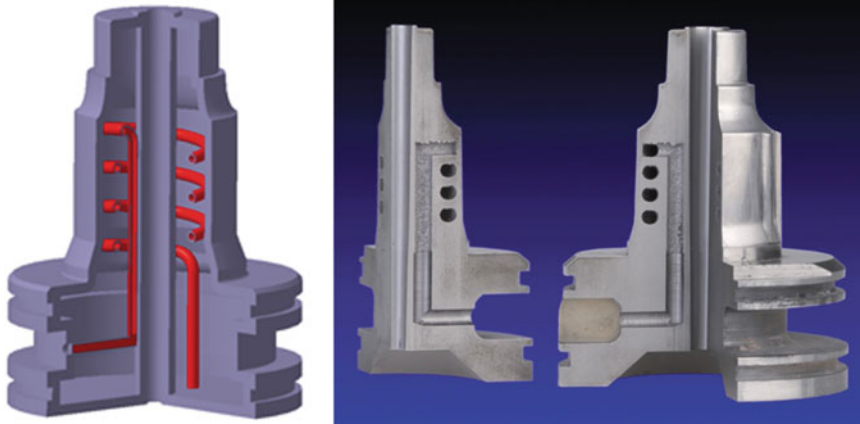
Fig. 7.53 Left: scheme of a mold insert with conformal cooling channels, right: LPBF manufactured mold insert after post processing
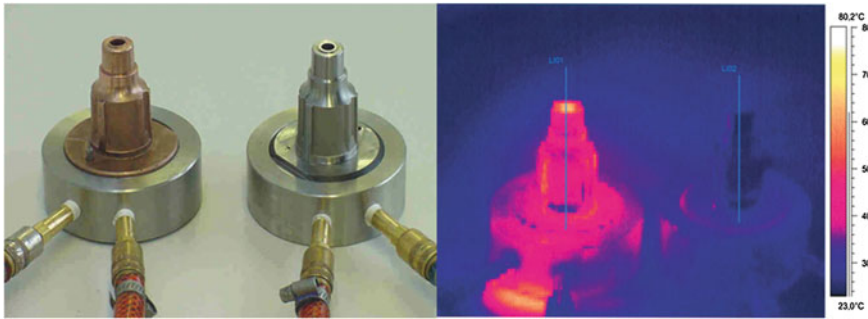
Fig. 7.54 Left: mold inserts made of a cooper alloy and steel in a cooling device, right: temperature distribution in both mold inserts
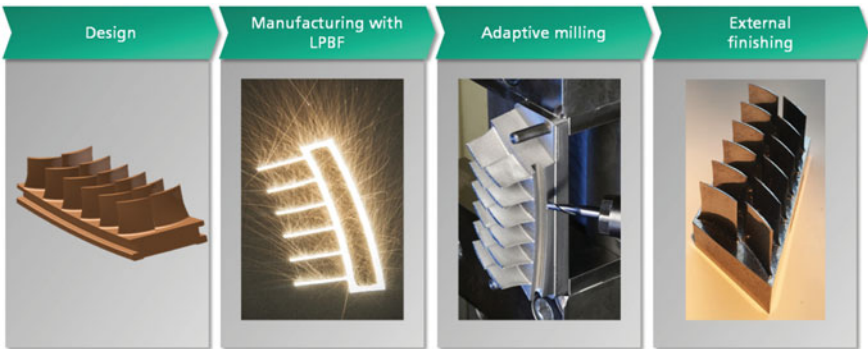
Fig. 7.55 Design and manufacturing chain for the guide vane cluster
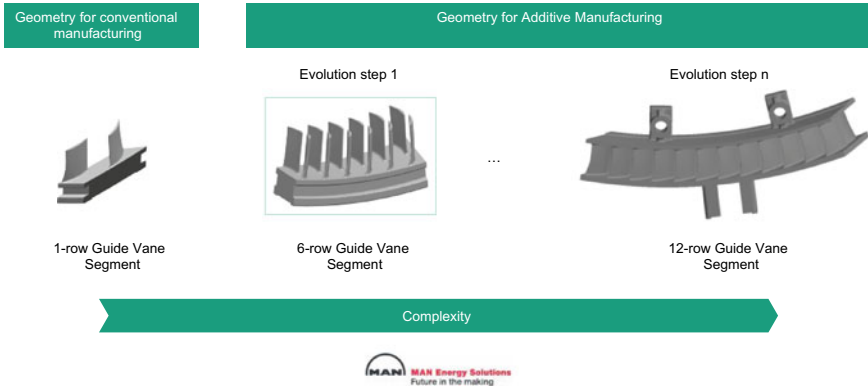
Fig. 7.56 Design variants for conventional and additive manufacturing of the guide vane cluster

with shroud shown on the right in Fig. 7.56. This design enables a reduction from 13 individual parts to one part. A further advantage is, that the part holders can be manufactured directly as well, thus saving a part package. The monolithic design reduces the gap losses and thus improves aerodynamics and part functionality. This reduces production costs compared to the conventional manufacturing route.

The manufacturing of the twelve-row guide vane segment with a shroud using the LPBF process can be carried out in good quality (minimum defects, high dimensional accuracy) if the part orientation and support design are optimal. The finishing of fitting surfaces (e.g. of the blade root) is done by milling. Due to the high demands on the surface quality and the shape tolerance of the flow and functional surfaces, subsequent post-processing of the LPBF manufactured part is necessary. In principle, various processes can be used for this purpose (see Sect. 7.4.2). Figure 7.57 shows a guide vane segment that has been finally post-processed using the Micro Machining Process (MMP, Sect. 7.4.2). The roughness is lower than 0.8 μm. The part is used in series production on MAN ES.

Ad 3: Topology Optimization

Topology optimization describes a mathematical method for finite element analysis (FEA) to determine the optimum distribution of material in a design space for a given set of loading and boundary conditions. The result of topology optimization can be complex free-form geometries, bionic or lattice structures that cannot be manufactured using conventional manufacturing processes. With LPBF, a method is nowadays available with which such structures can be manufactured (Orme et al. 2018).

In Orme et al. (2018), a process chain is proposed that must be followed in order to manufacture topology optimized parts with reliable and reproducible properties. The process chain includes the steps: 1. selection of the part, 2. topology optimization for the LPBF considering LPBF manufacturing constraints (e.g. minimum feature size, surface angle, see below) and LPBF specific boundary conditions (e.g. removal

Fig. 7.57 12-Row guide vane cluster manufactured with LPBF and post-processed with MMP

of support structures, powder removal, residual stresses and distortion of the part) 3. FE-based design verification, 4. the additive manufacturing process, and 5. the technological properties of the manufactured part. Two feedback loops are integrated into this chain: Between steps 2 and 3, it must be ensured that the topology-optimized design withstands the specific part loads, and between steps 4 and 5, it must be ensured that the part performance of the additively manufactured part satisfies the in-service loads of the part.

In order to raise this potential, design methods (e.g. topology optimization, lattice structures) have to be adapted to the potential of LPBF manufacturing or even new design methods have to be developed (e.g. Generative design) to be implemented in the context of "Design for Additive Manufacturing (DfAM). Two positive effects are achieved through topology optimization and lattice structures: On the one hand, the part volume to be manufactured is reduced, which increases productivity, and on the other hand, a reduction in weight is achieved. An important prerequisite for topology optimization is the proper specification of the load cases and the clamping. In an iterative process the topology optimization algorithm calculates the stress level of each FEA element. Elements with low stresses are deleted until the optimization criterion (e.g. weight fraction) is achieved. The topology optimization that can be performed by several commercial software solutions (e.g. Ansys Mechanical (www. ansys.com), Altair Optistruct (www.altair.de) usually results in very complex parts with 3D freeform surfaces and hollow and filigree structures. Additionally, lattice structures can be integrated into topology-optimized parts by the use of software solutions like nTopology (www.ntopology.com), ParaMatters (www.paramatters.com), ELISE (www.elise.de; www.elise/industries/aeospece), Autodesk Generative Design (www.autodesk.com) and many more. These so created complex geometries cannot
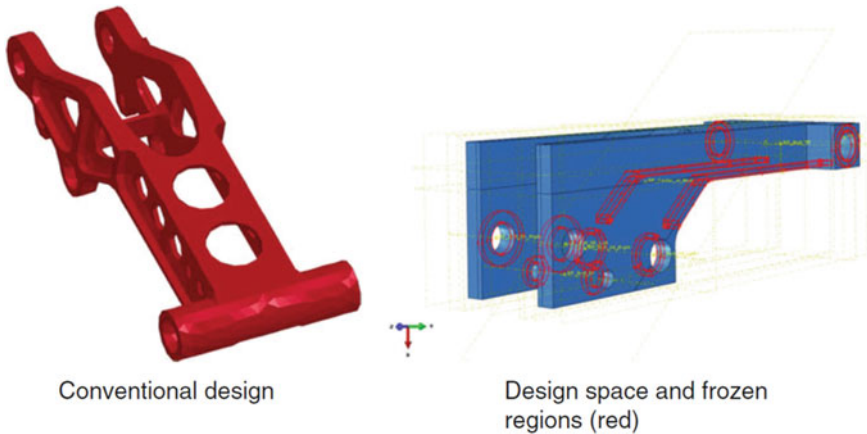
Fig. 7.58 Kinematics lever of a business class seat, reprinted from Poprawe et al. (2015, Fig. 5.12), with the permission of Springer

be manufactured by conventional manufacturing but with LPBF under consideration of LPBF-specific manufacturing restrictions (e.g. minimum feature size, surface angle) directly in the design process.

One part of the seat assembly, a kinematics lever (Fig. 7.58 left), was selected for topology optimization. In a first step the maximum design space and connecting interfaces to other parts in the assembly were defined (Fig. 7.58 right) to guarantee the fit of the optimization result to the seat assembly. Interfacing regions are determined as frozen regions, which are not part of the design space for optimization (Poprawe et al. 2015).

The kinematics lever is loaded if the passenger takes the sleeping position. The load profile is defined and statically represented by various maximum forces during part operation. Current topology optimization software is limited to static load cases. Therefore the dynamic load case is simplified to five static load cases, which consider the maximum forces at different times of the dynamic seat movement. The objective criterion of the optimization is a volume fraction of 15% of the design space. The part is optimized regarding stiffness. In Fig. 7.59 the optimization result as a mesh structure and an FE analysis for verification of the structure are shown. The maximum stress is approx. 300 MPa, which is below the limit of Yield Strength of 410 MPa of the aluminum alloy 7075.

Before the manufacturing of the optimization result via LPBF, the surfaces get smoothened to improve the optical appearance of the part and to minimize stress concentrations. Compared to the conventional part (90 g) a weight reduction of approx. 14% (final weight 77 g, Fig. 7.60) was achieved.

Weight reduction plays a key role in the aerospace industry. Therefore, drastic weight reductions are achieved with topology optimization in combination with LPBF manufacturing. Two parts where weight reductions of 56 and 80% are achieved are shown in www.elise.de and www.elise/industries/aeospece. In Orme et al. (2018)
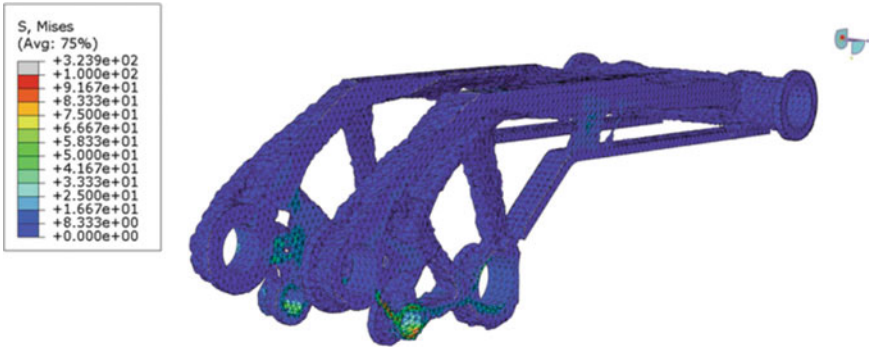
Fig. 7.59 Mesh structure of optimization result including stress distribution, reprinted from Poprawe et al. (2015, Fig. 5.13), with the permission of Springer

Fig. 7.60 Final light-weight part manufactured by LPBF, reprinted from Poprawe et al. (2015, Fig. 5.14), with the permission of Springer

three case studies from the field of space technology are presented, where weight reductions of about 25, 40 and 80% are achieved.

Ad 3: Functional Adapted Lattice Structures

Additive manufactured lattice structures belong to the material class of cellular materials. Cellular materials are classified by the type of cell arrangement (periodic or stochastic) and the cell structure (open or closed cell types). Additive lattice structures have a periodic and open cell structure. In Rehme (2009), different cell types are compared. The cell type f2cc,z is ranked highest due to its high strength, high

energy absorption, low anisotropy and low build-up time, making it suitable for a wide range of applications (Merkt 2015; Rehme 2009).

Good stiffness-to-weight ratio and great energy absorption are the unique properties of lattice structures on one hand and their low volume on the other hand make them to a suitable tool for developing functionally optimized parts. Lattice structures or cellular materials are used in various fields such as lightweight construction, as energy and sound absorbers, vibration dampers, in-heat exchangers and implants.

Depending on the stress or on particular functions of part areas, lattice structures are substituting solid materials. Compared to a topology optimization where the part areas are either kept or removed according to the load paths, graded properties can be created with lattice structures. Homogeneous transitions between the solid material and the lattice structure can be realized, e.g. by varying the lattice strut diameters. The material requirement of the load case can thus be fine-tuned.

The main challenges in designing these types of customized parts are the intricate modeling of the macroscopic behavior, the mostly unknown mechanical properties, the absence of a design methodology for parts with customized part functions and knowledge about the influence of different scan strategies and scan parameters on the mechanical properties.

When manufacturing lattice structures via LPBF, both process- and material-specific boundary conditions must be taken into account:

The process-specific boundary conditions include the determination of the limits of the achievable structure sizes as well as the stability of the lattice structures, which in turn depends on the stability of single struts and the lattice dimension.

The minimum structure size is mainly determined by the focus diameter of the laser beam in the working plane. In addition to the purely geometric limitation, process errors can also occur with small structures as a result of the mechanical influence of the powder deposition unit. In addition to the strut size, the overhanging length is limited. Structures can only be built up to a defined overhanging length without additional support structures. If the critical overhang length is exceeded, sintering of powder or complete failure of the structure can occur. In addition to the free minimum overhanging length, there is a material-specific critical angle (minimum overhanging angle), which must not be undercut if overhanging geometries are to be built up without support structures. Experience shows that this angle is in the range of $\alpha = 35°$–$45°$, depending on the material (Schmithüsen et al.).

Another important aspect is the scanning strategy for manufacturing the lattice structure. Two scan strategies are commonly used for the manufacturing of lattice structures: Contour-Hatch scan strategy and Pointlike exposure strategy (Fig. 7.61). Contour-Hatch scan strategy is the most used scan strategy, which causes many scan vectors and jumps between scan vectors, resulting in a high amount of scanner delays. Pointlike exposure strategy reduces the complex geometry to a set of points of exposure and less jumps and scanner delays are caused. To investigate the influence of the two scan strategies on the geometry of the lattice structures, different types of f2ccz structures were manufactured. The material used in this study was stainless steel 316L (1.4404) (Poprawe et al. 2015).
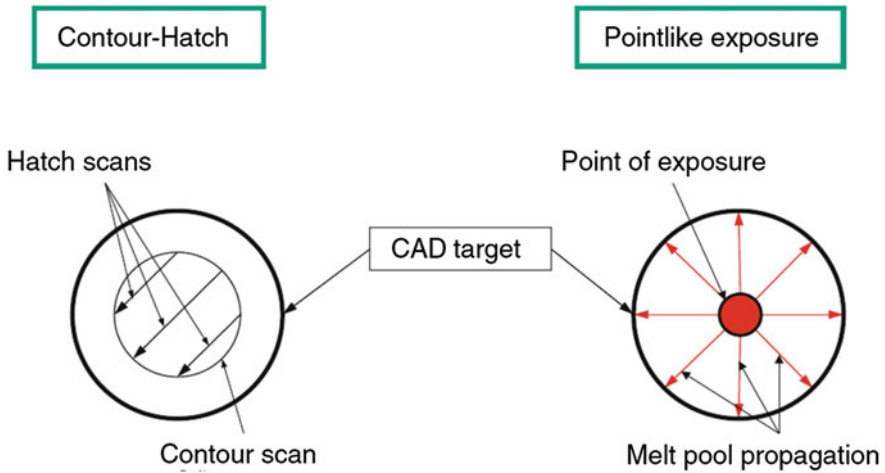
Fig. 7.61 Commonly used scan strategies for the fabrication of lattice structures, reprinted from Poprawe et al. (2015, Fig. 5.17), with the permission of Springer

The parameters were iteratively adapted regarding a low geometric deviation from the CAD model. A measurement of the relative density of the lattice structures by Archimedean density measurement was performed. The relative density is the filling degree of the structure and can be used to determine geometric deviations of the structure. Three different kinds of Contour-Hatch parameters (Laser power: 100–130 W, scan speed: 700–900 mm/s) and one parameter set for Pointlike exposure (Laser power: 182 W) were investigated. Figure 7.62 shows the deviations of the relative density to the CAD model target for the investigated parameters. For Pointlike exposure strategy the relative density is 4% higher than the CAD model target. All in all, the CAD model target can be reached with low deviations (Poprawe et al. 2015).

To further investigate the geometry lattice structures were investigated by micro CT measurement. Figure 7.63 shows a reconstruction based on these CT images. Lattice structures manufactured by Contour-Hatch scan strategy show no visible build-up errors and vertical and diagonal struts have the same diameter. In contrast pointlike exposure strategy shows light contractions at knots and deviations between vertical and diagonal strut diameter (Poprawe et al. 2015).

The material-specific boundary conditions include the determination of the mechanical properties for the respective lattice structure for a given material. For this purpose, lattice tensile specimens are manufactured with the respective lattice parameters (strut width, lattice dimension). In order to represent the connection of the lattice structures to the part shell and the different orientations of the lattice cells in the part, the lattice tensile specimens are manufactured at different angles of inclination and with cover surfaces (Schmithüsen et al.).

The process- and material-specific results are used to design a part with lattice structures. Different lattice parameters (cell shape, cell spacing, strut width) allow
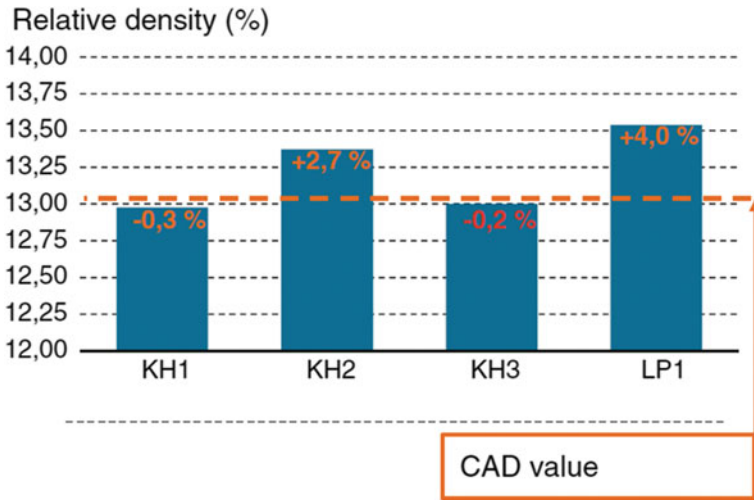
Fig. 7.62 Deviations of relative density to the CAD model target for both scanning strategies, reprinted from Poprawe et al. (2015, Fig. 5.18), with the permission of Springer
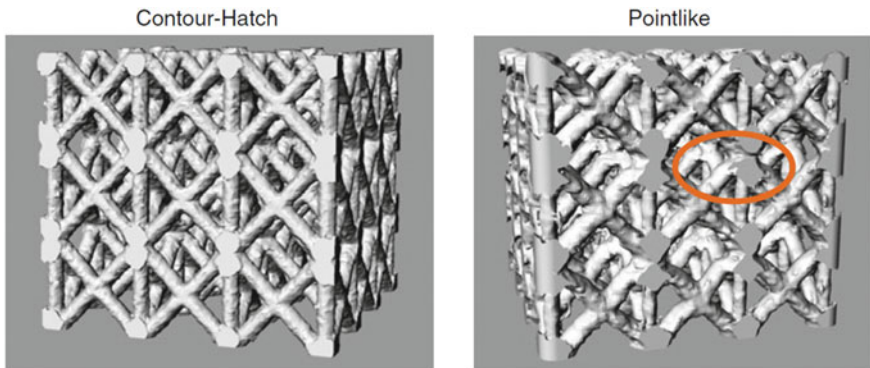
Fig. 7.63 Micro CT reconstructions to investigate the dimensional accuracy of lattice structures, reprinted from Poprawe et al. (2015, Fig. 5.19), with the permission of Springer

locally different mechanical properties to be monolithically fabricated to manufacture parts with increased functionality.

This is demonstrated below using the example of a stub axle made of the tempered steel 1.7734 in which locally adapted mechanical properties are generated by integrating different lattice structures. This results in a weight reduction of 25% compared to the conventionally manufactured stub axle. Figure 7.64 left shows the stub axle on the substrate plate after LPBF fabrication. The following post-processing steps were then performed: Removal of the powder, stress relieving, removal from the substrate plate and of the support structures and machining post-processing. Figure 7.64 right
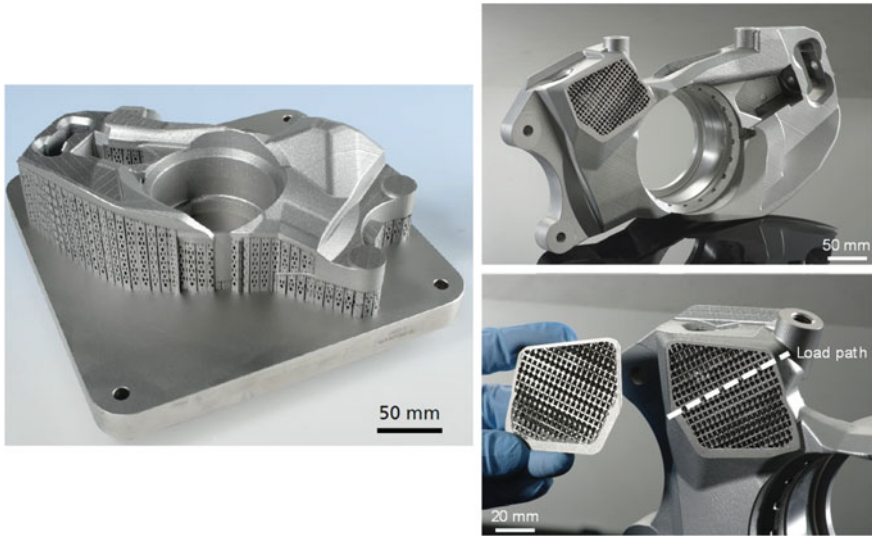
Fig. 7.64 Left: stub axle with support structures after the LPBF process, right: post-processed stub axle (above) and graded lattice structures with indicated load path, reprinted from Schmithüsen et al.

shows the final machined stub axle and a detailed view of the load matched graded lattice structures with the indicated load path. Along the main load paths, the struts of the lattice structures are dimensioned thicker accordingly (Schmithüsen et al.).

7.4.2 Post-processing

After the LPBF process, the parts are usually placed on the substrate plate and, depending on the part geometry, the parts also have support structures. Furthermore, in most cases the parts do not have the required properties (e.g. mechanical properties, surface quality). The surface roughness, for example, has a dominant influence on the mechanical properties of additively manufactured parts (see Sect. 7.4.3). Therefore, different post-processing steps are necessary depending on the requirements of the part. These are discussed in more detail below.

Removal from the Substrate Plate

After LPBF manufacturing, the part is removed from the substrate plate by sawing or metal cutting. For more filigree parts, the removal is done by wire spark erosion.

Heat Treatment

As described in Sect. 7.4.3, heat treatment is used both to reduce residual stresses and to adjust the microstructure and thus to achieve the required mechanical properties.

Heat treatment is carried out either immediately after the LPBF process with existing support structures or at the very end of the finishing processes.

Removal of Support Structures

Support structures fulfill several functions during the LPBF process:

- In the case of critically inclined surfaces of the part with angles <45° to the substrate plate, they ensure that the part can be manufactured with high dimensional accuracy
- Avoidance or reduction of distortion of the part by absorbing thermally induced stresses arising during the LPBF process
- Transport of process heat to the substrate plate to avoid an unstable LPBF process

Depending on the part geometry and the support structures, these are removed manually with hand tools (e.g. pliers) or automatically with milling or turning. Another approach is the use of a wet-chemical etching process. The basic principle of the process is based on the dissolution of the support structures by an etching agent. The process can be used for the complete removal of both external and internal support structures, independently of their geometry. Further advantages are the processing time, which is independent of the number of pieces and the surface smoothing effect, which may eliminate the need for further finishing steps (Schmithüsen et al. 2017).

The process has so far been investigated for aluminum materials (Schmithüsen et al. 2017). The etching agent used is sodium hydroxide (NaOH), which reacts strongly chemically with aluminum, although other etching agents (e.g. hydrofluoric acid) have been used. But with regard to industrial implementation of the process, such etching agents are excluded for reasons of occupational safety and environmental protection. Sodium hydroxide, on the other hand, is used industrially as a cleaning agent (Schmithüsen et al. 2017).

During the development of the process, various concentrations of sodium hydroxide, the etching time and the temperature of the etching agent were investigated. For efficient use of the process, it makes sense that the support structures are first dissolved as selectively as possible at the junction of the part and the support structure (target separation point). This ensures that both the etching agent and the support material, is minimized and that the support structures are completely removed from the part. A possible support structure that meets this criterion is, for example, a tree-like structure with a conical transition between support structure and part, as shown in Fig. 7.65. The process was applied, for example, to the AlSi10Mg geometries shown in Fig. 7.65. The L-profile (Fig. 7.65 right) represents an example of a part firmly fixed to the substrate plate with easily accessible support structures in the overhang. The ring profile represents a part that is fixed to the substrate plate only by the support structures. Furthermore, the support structures are only accessible to a limited extent (internal, on curved surfaces) (Schmithüsen et al. 2017).

The shortest processing time was achieved with 50% sodium hydroxide (50% NaOH,) and a starting temperature of the etching agent of 80 °C. Figure 7.66 shows an example of the specimens processed with 50% sodium hydroxide.
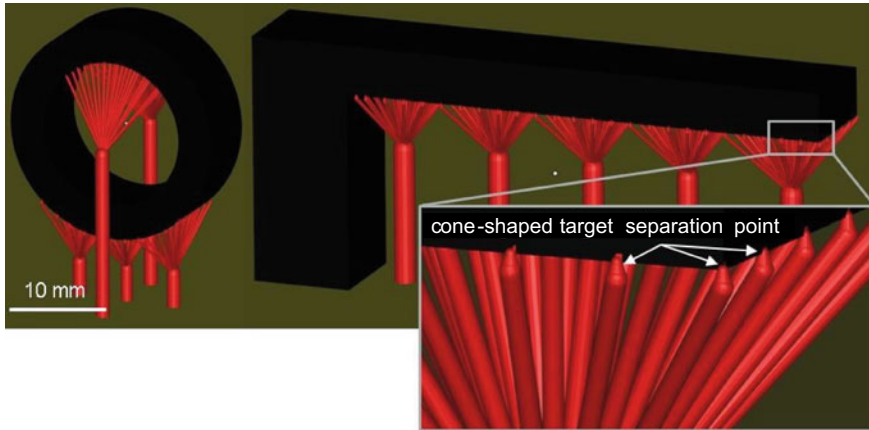
Fig. 7.65 Test geometries with a tree-like support structure and cone-shaped target separation points, reprinted from Schmithüsen et al. (2017)
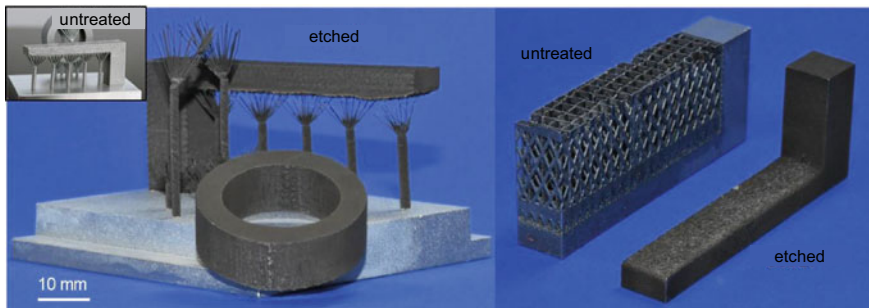
Fig. 7.66 Left: untreated and etched test geometry (ring and L-profile) with tree structure, right: untreated and etched test geometry (L-profile) with block structure, reprinted from Schmithüsen et al. (2017)

As can be seen in Fig. 7.66, a brownish brittle layer (lamellar silicon layer) is formed on the surface of the etched specimens during processing. However, this layer can be removed by ultrasonic cleaning, so that the specimen after the wet-chemical process again looks optically very closely to the untreated specimen (Fig. 7.67).

In order to investigate the influence of different sodium hydroxide concentrations and exposure times on material removal and surface roughness, LPBF-fabricated cuboid specimens are examined. As a result, an almost linear dependence of the material removal rate on the exposure time is determined. The removal rate for a 50% concentration is about 0.061 mm/min and for a 10% concentration is about 0.012 mm/min, indicating that the removal rate increases linearly with etching agent concentration to a good approximation. Since chemical ablation occurs uniformly

Fig. 7.67 Left: etched and ultrasonically cleaned test geometry, right: untreated test geometry (ring profile), reprinted from Schmithüsen et al. (2017)

over the surface, a constant oversize of the part can be used to compensate for the ablation (Schmithüsen et al. 2017).

The surface roughness Sa is also reduced by etching. With the 10% concentration of NaOH, Sa values between 7 and 13 µm are achieved, with the 50% concentration values between 6 and 29 µm are achieved with etching durations of up to 10 min. The reference roughness of "as built" specimen is 17.8 µm. This means that the roughness can be specifically adjusted via concentration of the etching agent and etching duration.

The wet-chemical process has also been successfully applied to the aluminum materials AlSi12 and AlSi9Cu3 (Schmithüsen and Schleifenbaum 2019).

Another aspect is the type of support structures. Usually, a combination of single melt tracks (so-called vector supports) and bulk material (so-called volume supports) is used. While vector supports are very well suited for the wet-chemical process, volume supports can only be dissolved with a delay due to their small surface area in relation to the volume. However, they are essential for the LPBF process to reduce distortion and allow process heat transport.

In order to achieve the same dissolution times for both support structures, the volume supports were provided with a porosity of up to 26%. For this purpose, appropriate process parameters (e.g. layer thickness, hatch distance) were developed for the material AlSi10Mg (Schmithüsen et al. 2019). These parameters lead to a reduction in processing time. With increasing porosity the etching effect is also increasing. The sample with the highest porosity (26%) was completely dissolved
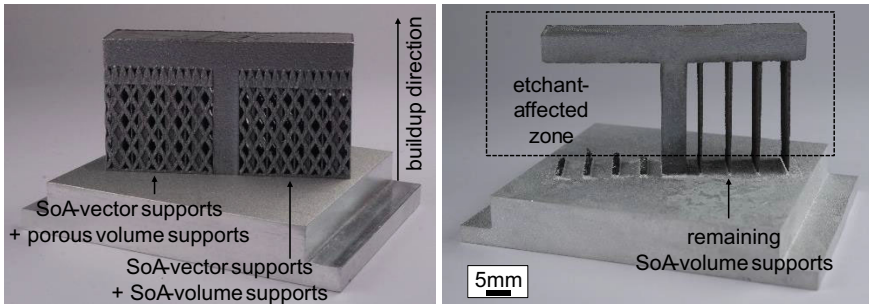
Fig. 7.68 Left twincantilever after LPBF process with different support structures, right: twincantilever after etching treatment (t = 10 min), reprinted from Schmithüsen et al. (2019, Fig. 12), with the permission of Hanser

after etching treatment (t = 45 min). The strength of the porous volume supports is in the range of the vector supports. During the etching tests, the largest removal rate was observed at the highest porosity of the samples. This approach was successfully demonstrated on a twincantilever (see Fig. 7.68). The twincantilever is manufactured with vector supports and volume supports with and without porosity. The vector supports and the volume supports without porosity are named state-of-the-art (SoA) supports, because they are manufactured with standard LPBF parameters.

As can be seen in Fig. 7.68 on the left, the demonstrator part was manufactured without defects using LPBF. After the etching treatment of t = 10 min (cf. Fig. 7.68 right), only the remnants of the SoA volume supports are still present on the demonstrator part, and the SoA vector supports and the porous volume supports have been completely dissolved. It could thus be shown that by adjusting the LPBF process parameters, volume supports can be produced which can be dissolved at a similar rate to vector supports (Schmithüsen et al. 2019).

Figure 7.69 shows two parts before and after wet-chemical post-treatment. The part at the rear was manufactured with the newly developed support structures. After wet-chemical treatment, internal and external support structures are completely removed.

Rough- and Fine-Machining

For rough machining (up to about 0.5 mm overmeasure to the final contour) CNC turning, CNC milling and CNC drilling are used.

CNC turning, CNC milling, wire EDM, slide grinding, grinding, honing, shot blasting, Micro Machining Process (MMP), flow grinding, lapping, polishing are available for fine machining.

When post-processing complex parts, a distinction is made between three categories:

Post-processing of accessible surfaces (Fig. 7.70a): Accessible surfaces are those areas of the part that can be post-processed using tools (e.g. by milling). Post-processing of surfaces that are difficult to access (Fig. 7.70b): Part areas where

Fig. 7.69 Parts before and after wet-chemical etching

tool-based post-processing is not possible due to limited accessibility are referred to as surfaces that are difficult to access. However, these part areas can usually be reached with fluids or particles, so that post-processing can be carried out here using processes that are not tool-based. Reworking of inaccessible surfaces (Fig. 7.70c) is not possible and will therefore not be considered further in the following.

When selecting finishing processes for difficult-to-access geometries, their effects on surface quality (roughness, defects or chemical changes in the near-surface microstructure), shape accuracy and mechanical properties must be evaluated.

a) »accessible«
- accessibility for machine tools
- accessibility for particles and fluids

a) »not accessible«
- no accessibility for machine tools
- no accessibility for particles and fluids

b) »difficult accessible«
- no accessibility for machine tools
- accessibility for particles and fluids
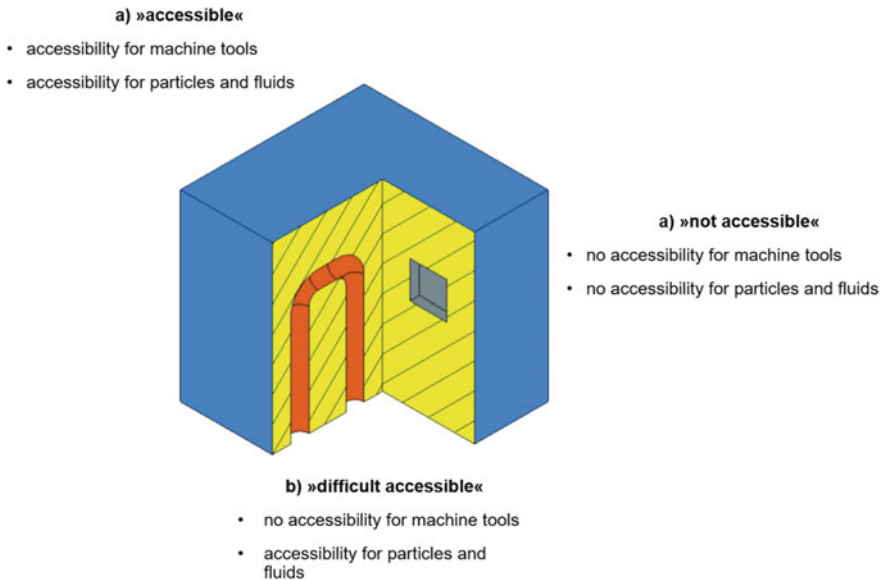
Fig. 7.70 Schematic representation for categorizing accessibility for additively manufactured geometries

Depending on the application, these criteria have different priorities. For example, the requirements in the jewelry and aesthetics sectors focus on optics and haptics. Therefore, the reduction of surface roughness is in the foreground. Geometric accuracy (shape deviation) and mechanical properties have a secondary role from the point of view of the finishing process. With regard to accessibility, also for particles and fluids, lattice structures represent a particular challenge due to shadowing, turbulence and similar effects. There is also a high requirement for surface roughness in flow surfaces. For example, rough surfaces can lead to turbulence in the flow and thus increase the pressure loss or reduce the efficiency of the flow. The area of flow surfaces can be divided into internal channels and flow guiding structures/vanes. Inner channels are typically used for cooling purposes (e.g. tooling). To fulfill the cooling function, the surface roughness is of key importance. Shape deviation and mechanical properties, on the other hand, play a secondary role. In contrast, low surface roughness, low shape deviation and very good mechanical properties are essential for flow-conducting blades.

In the following, manufacturing processes for tool-free finishing are discussed in more detail. These include, for example, shot blasting and slide grinding. The processes can be differentiated according to the type of material removal.

One possibility is mechanical removal. This mechanism is used in blasting or slide grinding. In blasting, a blasting medium is accelerated in blasting systems and brought to impact on the surface of a workpiece to be machined. In slide grinding, irregular relative movements take place between the workpiece and a large number of loose chips, which cause chip removal. Slide grinding can be further subdivided depending on the relative motion applied and the abrasive used.

Other processes include abrasive flow machining and the so-called MMP Technology®. The latter is marketed under a registered trademark by BinC Industries SA, where the acronym MMP stands for the Micro Machining Process. In pressure flow lapping, a lapping agent is forced through the workpieces under pressure. Another option for tool-less machining is electrochemical ablation with an external electrical power source. A distinction is made between electropolishing and plasma polishing.

Various post-processing processes are investigated using the guide vane cluster as an example. The functional surfaces of the guide vane cluster are divided into accessible (vane root) and inaccessible surfaces (vanes). For post-processing of the accessible fitting surfaces of the blade root, milling is an option due to economic and technical advantages. For the blades, the non-tool processes sandblasting, slide grinding, abrasive flow machining, MMP Technology® and plasma polishing are investigated. Before and after finishing, the vane segments are inspected with regard to surface roughness and shape deviation. The target value for the surface roughness, which has a value of Ra > 8 µm before post-processing, is Ra < 0.8 µm. Furthermore, the shape deviation should be minimal. In addition, any influence on the near-surface microstructure should be as low as possible.

The MMP Technology® was the only process, which achieved a surface roughness of Ra < 0.4 µm (Fig. 7.71) after 24 h of treatment, which was below the required target value. The lowest roughness reduction was achieved by sandblasting (Ra >
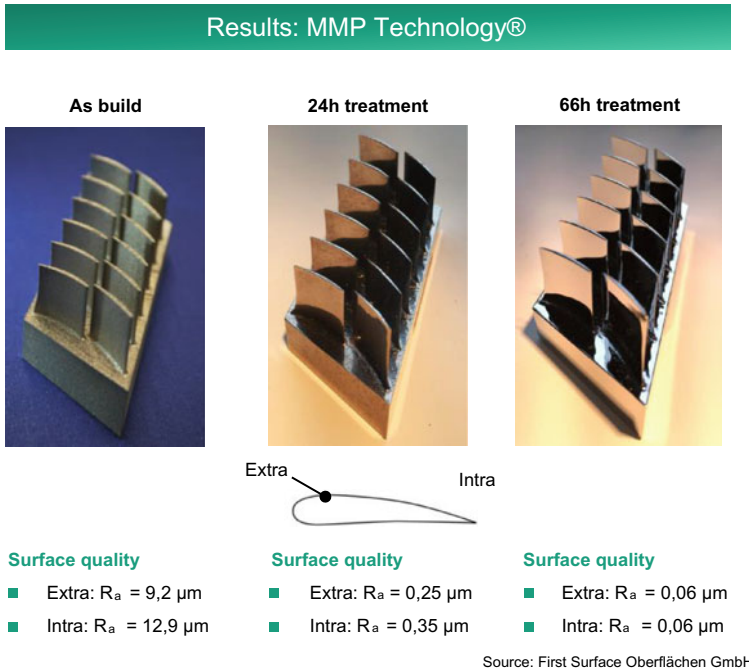
Fig. 7.71 Guide vane cluster in "as built" condition and after post-processing with MMP

5 μm). None of the other three processes reached the target roughness value (slide grinding 2.5 μm ≤ Ra ≤ 3.5 μm, abrasive flow machining 2.5 μm ≤ Ra ≤ 3.5 μm, plasma polishing 3 μm ≤ Ra ≤ 4.5 μm). An influence of residues or chemical changes on the surface is not observed with all the processes. In plasma polishing, however, a pronounced influence on the surface due to deposits of oxide and carbide layers occurs. The shape deviation in sandblasting, MMP Technology® and plasma polishing is in the range of the shape deviation already induced in LPBF.

7.4.3 Mechanical Properties of LPBF Manufactured Samples/Parts

In addition to numerous process-related aspects (e.g. increasing productivity, improving part quality, especially in the manufacture of complex geometries), the investigation and analysis of the mechanical properties of additively manufactured samples/parts represents an important task. The aim is to adjust the mechanical properties in accordance with the standards and guidelines of conventionally processed materials (e.g. by casting, forging). Previous work has mainly investigated the static mechanical properties of tensile strength, yield strength and elongation at break for

AM manufactured specimens. Both static and dynamic testing are mostly performed on specimen geometries specified in standards (e.g. DIN 50125 for tensile testing). The transfer of results from specimens to parts is often not given, since the manufacturing process, depending on the part geometry and its position in the build chamber, can lead e.g. to different microstructures, but especially also to the appearance of different defects.

The following presentation only gives some basic tendencies for the mechanical properties. Since these properties depend on a large number of influencing variables (e.g. quality of the feedstock powder, process strategy, position of the specimens in the build chamber, heat treatment cycle), the comparability of the results of different authors must be critically examined and it is difficult to derive general statements. The most frequently investigated materials are various steels (e.g. 316L), titanium alloys (e.g. TiAl6V4), aluminum alloys (e.g. AlSi10Mg) and nickel-based alloys (e.g. IN 718). Depending on the process management (e.g. different process parameters, build-up strategies, with and without preheating) tensile specimens with different build-up directions (e.g. vertical, horizontal, 45° inclined) are fabricated. An overview of the mechanical properties of the above-mentioned materials produced with different additive processes is given in DebRoy et al. (2018).

The mechanical properties are decisively determined by the microstructure (microstructure, defects) and this in turn depends on the melting and solidification conditions during the LPBF process. The melting behavior includes, for example, the size and geometry of the melt pool, the solidification conditions are given by the temperature gradient G, solidification rate R and cooling rate $\dot{T}$, where $\dot{T} = G \times R$. The melting and solidification conditions are largely determined by the process parameters. The LPBF process is characterized by rapid solidification with a commonly dendritic solidification structure. For example, as the energy input decreases, the melt pools become smaller, resulting in larger temperature gradients and higher cooling rates. Higher cooling rates and solidification rates lead to a finer microstructure (smaller grains), resulting in higher yield strengths and tensile strengths due to the Hall–Petch relationship. In addition to the fine grain structure, a high dislocation density at the grain boundaries due to rapid solidification and high residual stresses and/or defects such as binding defects, unfused powder particles and pores are characteristic of the LPBF process. Common defects encountered in LPBF are elongated bonding defects that contain unfused powder particles. These are often elongated defects perpendicular to the build-up direction (Brandt 2017). Depending on the direction of the applied tensile stress during mechanical testing, different failure limits result: If the tensile stress is applied perpendicular to the longitudinal direction of the binding defects, excess stress occurs at the sharp corners of the binding defects. For this reason, the failure limits are greater when the tensile stress is applied in the longitudinal direction of the binding defects than when the tensile stress is applied perpendicular to the binding defects.

Another characteristic of the mechanical properties of specimens fabricated by LPBF is their anisotropy in relation to their build-up direction, depending on the material. As a rule, the mechanical properties perpendicular to the build-up direction show larger values than in the build-up direction. A possible reason for this is

that defects such as bonding defects, pores or oxide inclusions in the bonding zone between the layers can reduce the strength when loaded perpendicular to the layers. However, the grain size and orientation and thus the number of grain boundaries also have a material-dependent influence on the mechanical properties of additively manufactured samples/parts (Bremen 2017). For austenitic steels (DebRoy et al. 2018) and IN 718 (Bremen 2017), for example, depending on the process strategy, elongated grains are found in the build-up direction, which extend over many layers. This grain structure is due to the fact that the component of the temperature gradient in the build-up direction (z-direction) is dominant on the solidification front. This grain structure results in a larger number of grain boundaries in the direction of loading in specimens manufactured lying down than in specimens manufactured standing up (Fig. 7.72 below), where the tensile load acts in the direction of grain orientation. Grain boundaries represent weak points in the microstructure where microcracks can be initiated, leading to failure of the specimen. Therefore, in this case, lower mechanical properties are to be expected for specimens fabricated horizontally than for those fabricated vertically (Bremen 2017). If a nearly isotropic grain structure is present (Fig. 7.72 above), the number of grain boundaries for both loading directions are approximately the same and therefore no differences in the mechanical properties should be present. Depending on which influence predominates (defects or grain size or orientation), different results are obtained for specimens manufactured lying down or standing up.

In the following, the static mechanical properties of IN718 are shown for different process managements (parameters for small beam and HP parameters for large beam, see Sect. 7.3.2) without and with post heat treatment.

The mechanical properties at static load were investigated for the two process windows ($P_L = 300$ W|$P_L = 1$ kW, $D_l = 90$ μm). Therefore, ten bars per process window with cylindrical shape, were manufactured with an inclination angle of 90° to the substrate and then machined to final dimensions. Afterwards, one half of the test specimens were heat treated according to AMS 5662 with an additional hipping

Fig. 7.72 Influence of grain structure on the mechanical properties for different build-up orientations, reprinted from Bremen (2017, Fig. 78), with the permission of Apprimus
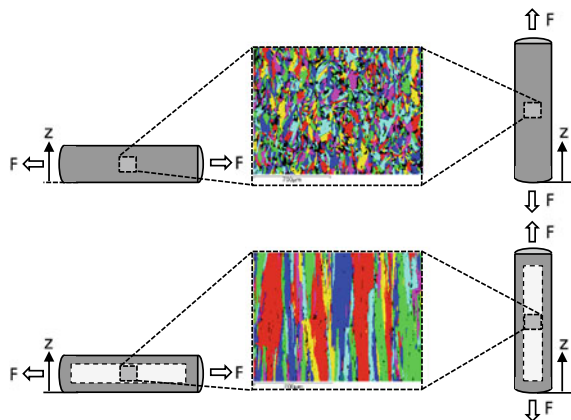
process before the solution annealing (T = 965 °C, t = 1 h, p = 2,000 bar). The results for the tensile tests are shown in Fig. 7.73. The mechanical properties for the low power LPBF process show a tensile strength of R_m = 983 N/mm^2 and a yield strength $R_{p0.2}$ = 632 N/mm^2 with a breaking elongation of A = 22.8%. In contrast, the mechanical properties for HP-LPBF (P_L = 1 kW, D_l = 90 µm) show slightly reduced tensile strength of R_m = 930 N/mm^2 and yield strength $R_{p0.2}$ = 549 N/mm^2. But the breaking elongation (A = 26.4%) is higher in comparison to low power LPBF (A = 22.8%). After heat treatment, the tensile strength and yield strength are increased and the breaking elongation was lower. For low power LPBF a tensile strength of R_m = 1,391 N/mm^2, a yield strength of $R_{p0.2}$ = 1,150 N/mm^2 at A = 14.9% can be observed. For HP-LPBF, the tensile strength is in the same range (R_m = 1,340 N/mm^2) as well as the yield strength ($R_{p0.2}$ = 1,136 N/mm^2). Thus, both process windows show values that exceed the requirements for heat-treated and forged IN718 (Special Metals Corporation 2016). The requirements demand a tensile strength of R_m = 241–1,275 N/mm^2, a yield strength of $R_{p0.2}$ = 862 N/mm^2, and a breaking elongation of A = 6–12%.

Only the breaking elongation for the HP-LPBF manufactured test specimen does not exceed the requirements but is within the given range between A = 6–12%. These results show that IN718 can be manufactured by HP-LPBF with increased laser power $P_L \leq 2$ kW (Bremen et al. 2017).

The influence of the surface roughness on the mechanical properties is also investigated in many cases, since the specimens manufactured by LPBF are characterized by a high degree of roughness. For this purpose, the specimens are comparatively investigated, e.g. in the surface states "as build", chip-machined, abrasively blasted, ground, MMP (Micro Machining Process) (http://mmptechnology.com/site/) machined and polished. As the surface roughness increases, the mechanical properties generally decrease, since a rough surface exerts notch effect with local stress concentration, causing failure to occur sooner. The best mechanical properties are obtained when
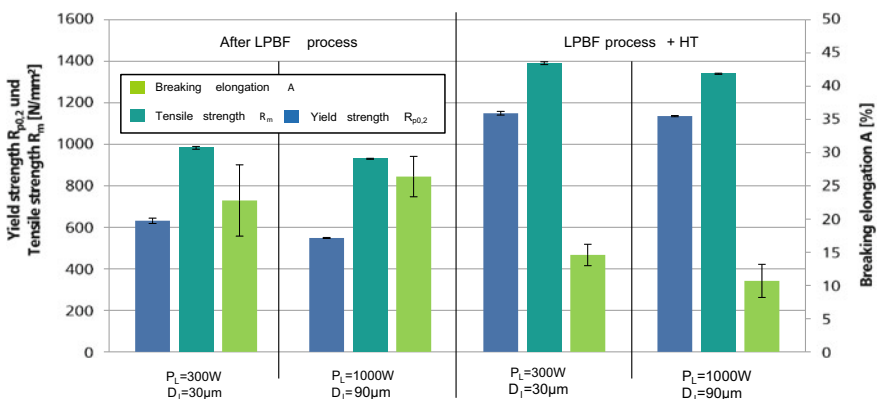
Fig. 7.73 Static mechanical properties for conventional and HP-LPBF in the as built state and after heat treatment, reprinted from Bremen et al. (2017, Fig. 6), with the permission of Springer

the top surface layer of the specimens is completely removed. The influence of the surface roughness on the dynamic properties of IN 718 in particular is investigated in Bürger (2020).

The mechanical properties of LPBF-manufactured specimens often achieve a similar or even higher level than conventionally produced specimens. However, the elongation at break is lower in many cases. Possible causes are, on the one hand, microdefects such as pores and oxide inclusions, which lead to the formation of larger cracks more quickly by microplastic flow and thus to faster material separation. On the other hand, the higher ductility expected with a fine-grained isotropic microstructure is reduced by the grain texture in the build-up direction during additive manufacturing, resulting in lower elongations at break.

The number of publications on the dynamic properties of specimens manufactured by means of AM is significantly smaller than that of the static properties, since dynamic testing is associated with a significantly greater effort. In dynamic testing, the specimen is subjected to a cyclic load consisting of tensile or a combination of tensile and compressive stresses. The number of cycles is determined as a function of the applied stresses until failure of the specimen. In particular, steels (DebRoy et al. 2018; Spierings et al. 2013; Röttger et al. 2016), the titanium alloy TiAl6V4 (Amsterdam and Kool 2009; Brandl et al. 2011; Sterling et al. 2015), the aluminum alloy AlSi10Mg (Buchbinder 2013; Meixlsperger 2019), and the nickel-base alloy IN718 (Bremen 2017; Bürger 2020) were investigated. As with the static mechanical properties, the dynamic properties depend on the microstructure, the stress state and occurring defects such as pores, bonding defects and cracks, as well as on the surface roughness. Again, elongated defects with sharp corners (see above) and the stress peaks occurring there are very critical.

Measures to improve the mechanical properties include post heat treatment (application of defined temperature–time cycles), hot isostatic pressing (HIP) (application of temperature and pressure) and post-processing of the "as-built" surface to reduce roughness. Post-heat treatment results in a reduction of stresses introduced by the additive process, homogenization of the microstructure, grain growth, microstructural modifications and precipitation, depending on the temperature–time curve and the material. Often the heat treatment cycle consists of several stages. For IN 718, for example, the cycle consists of a solution annealing and two aging stages (Bremen 2017). The known heat treatment cycles for conventionally manufactured specimens are often applied in the first step. Depending on the resulting microstructure, these temperature–time cycles are adapted (e.g. duration of heat treatment) for LPBF-produced samples. Hipping also leads to heat treatment effects, but the main goal of such treatment is to eliminate pores and small bonding defects inside the samples. For the dynamic properties, the surface roughness due to the notch effect and defects near the surface have the biggest influence.

The main results obtained in dynamic testing can be summarized as follows:

- With a nearly defect-free microstructure with high density, dynamic properties are achieved that are often above those of cast materials but below those of forged materials.

- Defects such as pores, spatter, bonding defects between layers, and unfused powder particles are the main causes of crack initiation and, consequently, deterioration of dynamic properties (Brandt 2017; Amsterdam and Kool 2009).
- Compared to the static properties, the above-mentioned defects have a much stronger effect under dynamic loading (Bremen 2017).
- The surface roughness has a significant influence on the dynamic properties (DebRoy et al. 2018). This is investigated for the materials 316L and 15-5PH in DebRoy et al. (2018), Spierings et al. (2013) and for the material IN 718 in Bürger (2020) and Bremen (2017). A similar tendency is observed for AlSi10Mg in Buchbinder (2013).
- Brittle phases between the layers (e.g. oxides in AlSi10Mg (Buchbinder 2013) reduce the dynamic strength by providing starting points for cracks. Using AlSi10Mg as an example, it was shown in Tang and Pistorius (2017) that different oxides (large oxides (μm-range) from the process and small oxides (sub μm-range) already present in the powder) negatively influence the properties. With the larger oxides, there is an increased formation of pores.
- Preheating during the production of the samples has an influence on the microstructure refinement and thus on the dynamic properties (Buchbinder 2013).

In summary, it can be stated that the dynamic properties of additively manufactured specimens in particular are in many cases lower than those of conventionally manufactured specimens. The main reasons for this are defects and the high surface roughness of LPBF-fabricated specimens.

References

Acharya R, Sharon JA, Staroselsky A (2017) Prediction of microstructure in laser powder bed fusion process. Acta Mater 124:360–371

Alberts D, Schwarze D, Witt G (2017) Proceedings of the 28th annual international solid freeform fabrication symposium, Austin, TX, USA, vol 7

ALE3D (2017) An arbitrary Lagrangian-Eulerian multi-physics code. Technical report, LLNL-TR-732040

Amine T, Newkirk JW, Liou F (2014) An investigation of the effect of direct metal deposition parameters on the characteristics of the deposited layers. Case Study Therm Eng 3:21–34

Amsterdam E, Kool GA (2009) High cycle fatigue of laser beam deposited Ti-6Al-4V and Inconel 718. In: 25th ICAF symposium Rotterdam, pp 27–29

Anderson IE, White EMH, Dehoff R (2018) Feedstock powder processing research needs for additive manufacturing development. Curr Opin Solid State Mater Sci 22(1):8–15

Aconity3d GmbH (2016) Aconity LAB. http://aconity3d.com/equipment.html

Barclift MW (2018) Cost modeling and design tools for additive manufacturing with laser powder bed fusion. Thesis, 2018, Pennsylvania State University, The Graduate School Department of Mechanical and Nuclear Engineering

Barclift M, Joshi S, Simpson T, Dickman C (2016) Cost modeling and depreciation for reused powder feedstocks in powder bed fusion additive manufacturing. In: Proceedings of the 26th annual international solid freeform fabrication symposium—an additive manufacturing conference

Beaman JJ, Deckard CR (1990) Selective laser sintering with assisted powder handling. US patent no. 4938816

Becker D (2014) Selektives Laserschmelzen von Kupfer und Kupferlegierungen. Doctoral thesis, Aachen University, Apprimus Verlag. ISBN 978-3-86359-217-2

Beiss P, Behrens V, Landolt H, Börnstein R, Martienssen W, Madelung O (2003) Group VIII: advanced materials and technologies, vol 2: materials—powder metallurgy data. Electronic version. Springer, Berlin

Blom A, Dunias P, van Engen P, Hoving W, Kramer J (2003) Process spread reduction of laser microspot welding of thin copper parts using real-time control. In: SPIE proceedings, photon processing in microelectronics and photonics II, vol 4977, p 493

Bosio F et al (2019) A time saving and cost-effective method to process alloys by laser powder bed fusion. Mater Des 181

Bourell DL, Marcus HL, Barlow JW, Beaman JJ (1992) Int J Powder Metall 28:369–381

Bourell DL, Marcus HL, Barlow JW, Beaman JJ, Deckard CR (1991) Multiple material systems for selective beam sintering. US patent no. 5076869

Brandl E, Leyens C, Palm F (2011) Mechanical properties of additive manufactured Ti-6Al-4V using wire and powder-based process. Mater Sci Eng 26

Brandt M (2017) Laser additive manufacturing, materials, design, technologies, and applications. Elsevier

Bremen S (2017) Korrelation der High Power SLM Prozessführung mit der Produktivität, Effizienz und den Materialeigenschaften für den Werkstoff Inconel 718. Doctoral thesis, Aachen University, Apprimus Verlag. ISBN 978-3-86359-516-6

Bremen S, Meiners W, Wissenbach K, Poprawe R (2017) Correlation of the high power SLM process with resulting material properties for IN 718. Berg-und Hüttenmännische Monatshefte 5(162):170–185

Buchbinder D (2013) Selective laser melting von Aluminiumgusslegierungen. Dissertation RWTH Aachen, Shaker Verlag

Bugatti M, Semeraro Q (2018) Limitations of the inherent strain method in simulating powder bed fusion processes. Addit Manuf 23:329–346

Bürger L (2020) Charakterisierung der Oberflächentopografie beim Laserstrahlschmelzen von IN 718. Doctoral Thesis Aachen University

Chen H, Yan W (2020) Spattering and denudation in laser powder bed fusion process: multiphase flow modelling. Acta Mater 196:154–167

Cheng B, Li X, Tuffile C, Ilin A, Willeck H, Hartel U (2018) Multi-physics modeling of single-track scanning in selective laser melting: powder compaction effect. In: Proceedings of the 29th annual international solid freeform fabrication symposium—an additive manufacturing conference

Childs THC, Berzins M, Ryder GR, Tontowi A (1999) Proc Inst Mech Eng B 213B:333–349

Cunningham R (2018) Defect formation mechanisms in powder-bed metal additive manufacturing. Carnegie Mellon University

Dawes J, Bowerman R, Trepleton R (2015) Introduction to the additive manufacturing powder metallurgy supply chain. Johnson Matthey Technol Rev 59(3):243–256

DebRoy T, Wei HL, Zuback JS, Mukherjee T, Elmer JW, Milewski JO, Beese AM, Wilson-Heid A, De A, Zhang W (2018) Additive manufacturing of metallic components—process, structure and properties. Prog Mater Sci 92:112–224

Desai PS, Higgs CF (2019) Spreading process maps for powder-bed additive manufacturing derived from physics model-based machine learning. Metals 9:1176. https://doi.org/10.3390/met9111176

Draft ISO/ASTM 52900 (2018) Additive manufacturing—general principles—terminology; German and English version

Dunbar AJ, Denlinger ER, Gouge MF, Michaleris P (2016) Experimental validation of finite element modeling for laser powder bed fusion deformation. Addit Manuf 12:108–120

Eibl F (2017) Laser powder bed fusion of stainless steel with high power multi-diode-laser array. Doctoral thesis, Aachen University, Apprimus Verlag. ISBN 978-3-86359-587-6

Eibl F, Tenbrock C, Pichler1 T, Schmithüsen T, Heussen D, Schleifenbaum JH (2017) Alternative beam sources and machine concepts for laser powder bed fusion. In: IEEE high power diode lasers and systems conference 2017

Ferrar B, Mullen L, Jones E, Stamp R, Sutcliffe CJ (2012) Gas flow effects on selective laser melting (SLM) manufacturing performance. J Mater Process Technol 212(2):355–364

Fritz K, Kim IY (2020) Simultaneous topology and build orientation optimization for minimization of additive manufacturing cost and time. Int J Numer Methods Eng 121:3442–3481

Gayer C (2017) Laser sintering moves into medical market. Industrial Photonics, pp 16–19

Gayer C et al (2018) Influence of the material properties of a poly (D, L-lactide)/β-tricalcium phosphate composite on the processability by selective laser sintering. J Mech Behav Biomed Mater 87:267–278

Gayer C et al (2019) Development of a solvent-free polylactide/calcium carbonate composite for selective laser sintering of bone tissue engineering scaffolds. Mater Sci Eng C 101:660–673

Gayer C (2021) Laser sintering of polylactide-based composites. Doctoral Thesis Aachen University (to be published in 2021)

Gebhardt A (2016) Additive Manufacturing: 3D-Drucken für Prototyping—Tooling—Produktion, 5th edn. Carl Hanser, München

Gibson I, Rosen DW, Stucker B (2010) Additive manufacturing technologies. Springer US, Boston, MA

Gradl PR, Protz CS, Ellis DL, Greene SE (2019) Progress in additively manufactured copper-alloy GRCop-84, GRCop-42, and bimetallic combustion chambers for liquid rocket engines. In: 70th international astronautical congress (IAC), Washington D.C., United States, 21–25 October 2019

Gray RW, Baird DG, Bohn JH (1998) Rapid Prototyp J 4:14–25

Gu DD, Meiners W, Wissenbach K, Poprawe R (2012) Laser additive manufacturing of metallic components: materials, processes and mechanisms. Int Mater Rev 57(3):133–164

Gunenthiram V, Peyre P, Schneider M, Dal M, Coste F et al (2017) Analysis of laser–melt pool–powder bed interaction during the selective laser melting of a stainless steel. J Laser Appl 29(2)

Gürtler F-J, Karga M, Leitza K-H, Schmidt M (2013) Simulation of laser beam melting of steel powders using the three-dimensional volume of fluid method. Phys Procedia 41:881–886. Open Foam

Gussone J, Hagedorn Y-C, Gherekhloo H, Kasperovich G, Merzouk T, Hausmann J (2015) Microstructure of γ-titanium aluminide processed by selective laser melting at elevated temperatures. Intermetallics 66:133–140

Gussone J, Garces G, Haubrich J, Stark A, Hagedorn Y-C, Schell N, Requena G (2017) Microstructure stability of γ-TiAl produced by selective laser melting. Scr Mater 130:110–113

Hagedorn Y-C et al (2014) Processing of nickel-based superalloy MAR M-247 by means of high temperature—selective laser melting (HT - SLM). In: High value manufacturing: advanced research in virtual and rapid prototyping—proceedings of the 6th international conference on advanced research and rapid prototyping, VR@P 2013

Harthong B et al (2009) Modeling of high-density compaction of granular materials by the discrete element method. Int J Solids Struct 46(18–19):3357–3364

Heußen D (2020) Additive Fertigung von Bauteilen aus Rein-Kupfer mittels SLM und "grüner" Laserstrahlung. Final report of the IGF project Nr. 19.549 N

Jauer L (2018) Laser powder bed fusion von Magnesiumlegierungen. Doctoral thesis Aachen University, Apprimus Verlag. ISBN 978-3-86359-682-8

Kamath C, El-Dasher B, Gallegos GF, King WE, Sisto A (2014) Density of additively-manufactured, 316L SS parts using laser powder-bed fusion at powers up to 400W. Int J Adv Manuf Technol 74:65–78

Keller N, Ploshikhin V (2014) New method for fast predictions of residual stress and distortion of AM parts. In: Solid freeform fabrication symposium, Austin, Texas, pp 1229–1237

Kloss C et al (2012) Models, algorithms and validation for opensource DEM and CFD–DEM. Prog Comput Fluid Dyn Int J 12(2–3):140–152

Koch J, Mazumder J (2000) Apparatus and methods for monitoring and controlling multi-layer laser cladding. US patent no. 6122564

Kolb T, Gebhardt P, Schmidt O, Tremel J, Schmidt M (2018) Procedia CIRP 74:116. https://doi.org/10.1016/j.procir.2018.08.058

Krauss H, Eschey C, Zaeh MF (2012) Thermography for monitoring the selective laser melting process. In: Proceedings of the 23rd solid freeform fabrication symposium, Austin TX, USA

Kruth J, Badrossamay M, Yasa E, Deckers J, Thijs L, Van Humbeeck J (2010) Part and material properties in selective laser melting of metals. In: Proceedings of 16th international symposium on electro machining (ISEM XVI, 2010), Shanghai

Ladewig A, Schlick G, Fisser M, Schulze V, Glatze U (2016a) Influence of the shielding gas flow on the removal of process by-products in the selective laser melting process. Addit Manuf 10:1–9

Ladewig A, Schlick G, Fisser M, Schulze V, Glatzel U (2016b) Addit Manuf 10:1. https://doi.org/10.1016/J.ADDMA.2016.01.004

Ladewig A (2019) Optische Tomographie. Shaker, Düren

Li R, Liu J, Shi Y, Wang L, Jiang W (2012) Balling behavior of stainless steel and nickel powder during selective laser melting process. Int J Adv Manuf Technol 59:1025–1035

Li C, Fu CH, Guo YB, Fang FZ (2015) Fast prediction and validation of part distortion in selective laser melting. Proc Manuf 1:355–365

Lian Y, Gan Z, Yu C, Kats D, Liu WK, Wagner GJ (2019) A cellular automaton finite volume method for microstructure evolution during additive manufacturing. Mater Des 169:107672

Liu B, Wildman R, Tuck Ch, Ashcroft I, Hague R (2011) Investigation the effect of particle size distribution on processing parameters optimization in Selective Laser Melting process. In: Solid freeform fabrication (SFF) symposium

Liu X, Boutaous M, Xin S, Siginer D (2016) Numerical simulation of balling phenomenon in metallic LASER melting process. In: Proceedings of the ASME 2016 heat transfer summer conference, the ASME 2016 fluids engineering division summer meeting, and the ASME 2016 14th international conference on nanochannels, microchannels, and minichannels HTFEICNMM 2016, Washington, DC, USA

Löber L, Biamino S, Ackelid U, Sabbadini S, Epicoco P, Fino P, Eckert J (2011) Comparison of selective laser and electron beam melted titanium aluminides. In: 22nd annual international solid freeform fabrication symposium—an additive manufacturing conference, SFF 2011

Lutter-Günther M (2020) Qualitätsorientiertes und modellbasiertes Pulverrecycling beim Laserstrahlschmelzen. Doctoral thesis TU München

Manne A, Satyam N (2015) A review on the discrete element modeling of dynamic laboratory tests for liquefaction assessment. EJGE 20(21–46)

Masseling L, Gayer C (2018) Micro-powder bed fusion (μ-PBF)—extremely high resolution for small-scale applications. In: Laser powder bed fusion, conference proceedings, ASPE/euspen 2018 Summer topical meeting on advancing precision in additive manufacturing

Meiners W (1999) Direktes Selektives Laser Sintern einkomponentiger metallischer Werkstoffe. Dissertation RWTH Aachen, Shaker Verlag, Aachen

Meixlsperger M (2019) Anwendungsspezifische Prozessführung des Selective Laser Melting am Beispiel von AlSi-Legierungen im Automobilbau. Doctoral thesis Aachen University

Merkt SJ (2015) Qualifizierung von generativ gefertigten Gitterstrukturen für maßgeschneiderte Bauteilfunktionen. Doctoral thesis, Aachen University

Michaleris P (2014) Modeling metal deposition in heat transfer analyses of additive manufacturing processes. Finite Elements Anal Des 86:51–60

Montazeri M, Rao P (2018) J Manuf Sci Eng 140. https://doi.org/10.1115/1.4040264

Neikov OD (2009) Handbook of non-ferrous metal powders: technologies and applications, 1st edn. Elsevier, Amsterdam

Ng P (2020) Simulating particle packing during powder spreading for selective LASER melted additive manufacturing using the discrete element method in ABAQUS. Thesis 2020, California Polytechnic State University, San Luis Obispo

Oosterhuis G (2018) Additive manufacturing maturing with the aid of precision engineering. Dutch Soc Precis Eng J Mikroniek 4

Orme M, Madera I, Gschweitl M, Ferrari M (2018) Topology optimization for additive manufacturing as an enabler for light weight flight hardware. Designs 2:51

Park J, Tari MJ, Hahn HT (2000) Rapid Prototyp J 6:36–49

Parteli EJR, Pöschel T (2016) Particle-based simulation of powder application in additive manufacturing. Powder Technol 288:96–102

Peter N, Pitts Z, Thompson S, Saharan A (2020) Benchmarking build simulation software for laser powder bed fusion of metals. Addit Manuf 36

Pham DT, Dimov S, Lacan F (1999) Proc Inst Mech Eng B 213B:435–449

Pichler T (2019) Geometry-specific process control to increase the efficiency of laser powder bed fusion (LPBF), Rapid.Tech 3D Fachkongress 2019, Erfurt Germany

Pichler T (2020) Final report of the Fraunhofer internal project "Future Additive Manufacturing"

Pichler T, Schrage J, Schleifenbaum JH (2018) Increasing productivity of laser powder bed fusion (L-PBF) by qualifying and processing different powder qualities and application of intelligent processing strategies. In: Fraunhofer direct digital manufacturing conference 2018, pp 322–328

Pirch N, Niessen M, Linnenbrink S, Schopphoven T, Gasser A, Poprawe R, Schöler C, Arntz D, Schulz W (2018) Temperature field and residual stress distribution for laser metal deposition. J Laser Appl 30:032503

Poprawe R, Hinke C, Meiners W et al (2015) SLM production systems: recent developments in process development, machine concepts and component design. In: Brecher C (ed) Advances in production technology. Springer, Berlin, pp 49–65

R. Berger Strategy Consultants GmbH (2018) Advancements in metal 3D printing

Rai A, Helmer H, Körner C (2017) Simulation of grain structure evolution during powder bed based additive manufacturing. Addit Manuf 13:124–134

Rehme O (2009) Cellular design for laser freeform fabrication. Doctoral thesis, Technical University Hamburg-Harburg

Reijonen J, Revuelta A, Riipinen T, Ruusuvuori K, Puukko P (2020) On the effect of shielding gas flow on porosity and melt pool geometry in laser powder bed fusion additive manufacturing. Addit Manuf 32:101030

Ribeiro F (1998) Comput Control Eng J 9:31–38

Risse J (2019) Additive manufacturing of nickel-base superalloy IN738LC by laser powder bed fusion. Doctoral thesis, Aachen University

Röttger A, Geenen K, Windmann M, Binner F, Theisen W (2016) Comparison of microstructure and mechanical properties of 316L austenitic steel processed by selective laser melting with hot-isostatic pressed and cast material. Mater Sci Eng A 678:365–376

Sauthoff G (1995) Intermetallics. VCH, Weinheim, New York

Schleifenbaum JH (2010) Individualized production by means of high power selective laser melting. CIRP J Manuf Sci Technol 2(3):161–169

Schmithüsen T, Schleifenbaum JH (2019) Wet-chemical support removal for additive manufactured metal parts. In: Solid freeform fabrication 2019: proceedings of the 30th annual international solid freeform fabrication symposium, pp 2051–2063

Schmithüsen T, Eibl F, Meiners W (2017) Untersuchungen zum automatisierten Entstützen SLM-gefertigter Bauteile. RTE journal - Forum für Rapid Technologie 1–13

Schmithüsen T, Laag T, Schleifenbaum JH (2019) Mikroskopisches Stützendesign für die nass-chemische Nachbearbeitung von LPBF-gefertigten Bauteilen aus AlSi10Mg, RapidTech + FabCon 3.D: Erfurt. In: Proceedings of the 16th Rapid.Tech conference, pp 318–334

Schniedenharn M (2020) Einfluss von Fokusshift und Prozessnebenprodukten auf den Laser Powder Bed Fusion Prozess. Doctoral thesis, Aachen University, Apprimus. ISBN 978-3-86359-910-2

Schrage J (2016) Maschinenspezifische Kostentreiber bei der additiven Fertigung mittels Laser-Strahlschmelzen (LBM): Rapid.Tech—international trade show & conference for additive manufacturing

17. Special Metals Corporation (2016) Datenblatt Inconel 718: http://www.specialmetals.com/documents/Inconel%20alloy%20718.pdf. Accessed 11 Jul 2016

Spierings AB, Starr TL, Wegener K (2013) Fatigue performance of additive manufactured metallic parts. Rapid Prototyp J 18(2):88–94

Spierings AB et al (2015) Powder flowability characterization methodology for powder-bed-based metal additive manufacturing. Prog Addit Manuf 1(1–2):9–20. https://doi.org/10.1007/s40964-015-0001-4

Spierings A, Levy G (2009) Comparison of density of stainless steel 316L parts produced with selective laser melting using different powder grades. In: 20th annual international solid freeform fabrication symposium, an additive manufacturing conference. University of Texas at Austin, Austin, pp 342–353

Sterling A, Shamsaei N, Torries B, Thompson SM (2015) Fatigue behavior of additively manufactured Ti-6Al-4V. Procedia Eng 133:576–589

Stoll T, Trautnitz P, Schmiedeke S, Franke JE, Travitzky N (2020) Process development for laser powder bed fusion of pure copper. In: Helvajian H, Gu B, Chen H (Hrsg.) Laser 3D manufacturing VII: SPIE, 2020, p 46

Sutton AT, Kriewall CS, Leu MC, Newkirk JW (2016) Powders for additive manufacturing processes: characterization techniques and effects on part properties. In: Solid freeform fabrication 2016: proceedings of the 26th annual international solid freeform fabrication symposium—an additive manufacturing conference, p 1004

Schmithüsen T, Meiners W, Eibl F (2017) Schlussbericht ToPoLight: Topologieoptimierte Leichtbaustrukturen für nachhaltige Ressourceneffizienz im Automobilsektor. FKZ: 131857 KMUi

SLM Solutions (2016). Hochtemperaturheizung SLM 280. https://slm-solutions.de/produkte/maschinen/hochtemperaturheizung-slm-280

Tang M, Pistorius PC (2017) Oxides, porosity and fatigue performance of AlSi10Mg parts produced by selective laser melting. Int J Fatigue 94:192–201

Tang C, Le KQ, Wong CH (2020) Physics of humping formation in laser powder bed fusion. Int J Heat Mass Transf 149:119172

Tang P, Wang S, Duan H, Long M, Li Y, Fan S, Chen D (2020) The formation of humps and ripples during selective laser melting of 316l stainless steel. JOM (The Minerals, Metals & Materials Society). https://doi.org/10.1007/s11837-019-03987-7

Tenbrock C (2020) Final report of the Fraunhofer internal project "Future Additive Manufacturing"

Tenbrock C, Kelliger T, Praetzsch N, Ronge M, Jauer L, Schleifenbaum JH (2021) Effect of laser-plume interaction on part quality in multi-scanner laser powder bed fusion. Addit Manuf 38:101810

Tenbrock C, Fischer F, Wissenbach K, Schleifenbaum JH, Wagenblast P, Meiners W, Wagner J (2020) Influence of keyhole and conduction mode melting for top-hat shaped beam profiles in laser powder bed fusion. J Mater Process Technol 278:116514

Thombansen U, Ungers M (2014) Phys Procedia 56:1286. https://doi.org/10.1016/j.phpro.2014.08.053

Thombansen U, Gatej A, Pereira M (2014) Opt Eng 54:11008. https://doi.org/10.1117/1.OE.54.1.011008

Thombansen U, Abels P (2015) SPIE LASE 2015, 0277-786X, 93560R. https://doi.org/10.1117/12.2079475

Vock S, Klöden B, Kirchner A, Weißgärber T, Kieback B (2019) Powders for powder bed fusion: a review. Prog Addit Manuf

Vogelpoth A (2018) VCSEL-based preheating for LPBF. In: TCT conference @ formnext. Messe Frankfurt

Vogelpoth A (2019) Direkte Pulverbettvorwärmung mittels NIR-Modul beim LPBF, Annual report Fraunhofer ILT 2019, p 57

Vogelpoth A, Schleifenbaum JH, Rittinghaus SK (2019) Laser additive manufacturing of titanium aluminides for turbomachinery applications. In: Proceedings of ASME Turbo Expo 2019: turbomachinery technical conference and exposition, June 17–21. Phoenix, Arizona, USA

Weingarten C, Buchbinder D, Pirch N, Meiners W, Wissenbach K, Poprawe R (2015) Formation and reduction of hydrogen porosity during selective laser melting of AlSi10Mg. J Mater Process Technol 221:112–120

Weiß C, Schleifenbaum JH (2020) Densification behavior and pore morphology at high layer thicknesses for LPBF processing of gas- and water-atomized 316L powders. In: Fraunhofer direct digital manufacturing conference. ISBN 978-3-8396-1521-8

West AP, Sambu SP, Rosen DW (2001) Comput Aid Des 33:65–79

Wohlers T (2019) Wohlers report

Yadav P, Rigo O, Arvieu C, Le Guen E, Lacoste E (2020) Crystals 10:524. https://doi.org/10.3390/cryst10060524

Yadroitsev I (2009) Selective laser melting: direct manufacturing of 3D-objects by selective laser melting of metal powders. LAP Lambert Academic Publishing

Yan D et al (2020) Preparation and laser powder bed fusion of composite microspheres consisting of poly (lactic acid) and nano-hydroxyapatite. Addit Manuf 34:101305

Youssef A, Hollister SJ, Dalton PD (2017) Additive manufacturing of polymer melts for implantable medical devices and scaffolds. Biofabrication 9(1):12002

Zenzinger G, Bamberg J, Ladewig A, Hess T, Henkel B, Satzger W (2015) AIP conference proceedings, vol 1650, p 164. https://doi.org/10.1063/1.4914606

http://mmptechnology.com/site/

https://micress.rwth-aachen.de/

https://trendkraft.io/wirtschaft-geschaeft/slm-solutions-enthullt-weltneuheit-auf-der-euromold-slm-500-hl-fur-metallische-additive-fertigungsverfahren/

https://www.lm-innovations.com/de-de/anlagen/alpha-140/

https://www.pco.de/de/scientific-kameras/#section-39

https://www.slm-solutions.com/products-and-solutions/machines/slm-280/

https://www.trumpf.com/en_GB/products/services/services-machines-systems-and-lasers/monitoring-analysis/monitoring-truprint/process-monitoring/

www.altair.de

www.ansys.com

www.autodesk.com

www.elise.de and www.elise/industries/aeospece

www.ntopology.com

www.paramatters.com

Chapter 8
LMD Introduction

Check for
updates

Andres Gasser and Thomas Schopphoven

During the last decades **L**aser **M**etal **D**eposition LMD (also known as laser cladding or **D**irect **E**nergy **D**eposition DED) has become an established technique in many applications for applying wear and corrosion protection layers on metallic surfaces as well as for the repair of high added value components. Application fields are dye and tool making, turbine components for aero engines and power generation, machine components such as axes, gears and oil drilling components. Continuous wave lasers with power ranges of more than 20 kW are used on automated machines with 3 or more axes, enabling 3D processing. LMD is also used as an additive manufacturing technique, where it stands out among other processes due to its versatility, especially to deposit material onto complex shapes such as free-form, 3D surfaces and to manufacture multi-material parts. In LMD, the laser radiation is used to create a melt pool on the surface of the substrate. At the same time, a metallic powder or wire filler material is fed to the processing area or into the melt pool. In order to produce a defect-free, metallurgically bonded layer, the process parameters (laser power, feed rate, feed rate of the filler material, etc.) must be adapted so that the process heat provided is sufficient to initiate a suitable temperature–time cycle for the base material and the filler material. This should both create a melt pool on the substrate surface and ensure complete melting of the filler material.

Typical powder grain sizes used for LMD range between 20 and 100 µm and typical wire diameters from 0.4 mm to 1.8 mm. The powdered filler material is fed into the interaction area with a carrier gas, usually Argon or Helium. The carrier gas also acts as shielding gas. The laser melts a thin layer of the surface (some tenths of mm) and the filler material leading to a layer with high density (100%) and metallurgical bonding. Due to the local heat input given by the focussed beam a low thermal load is achieved, resulting in a small heat affected zone. Typical values for

A. Gasser (✉) · T. Schopphoven
Fraunhofer ILT, Aachen, Germany
e-mail: andres.gasser@ilt.fraunhofer.de
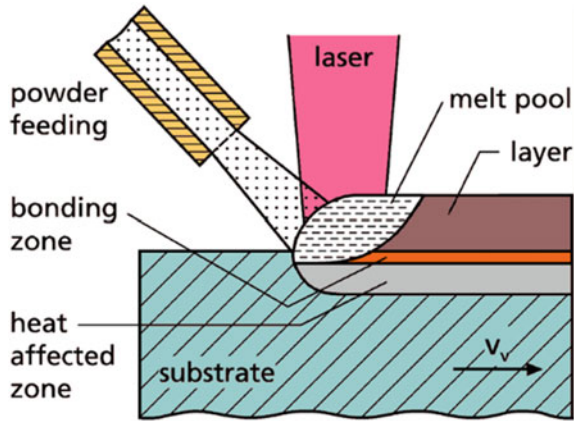
Fig. 8.1 Schematic representation of the LMD process with lateral powder feeding

Fig. 8.2 Pulsed laser LMD process with manual wire feeding (left) and automated LMD processes with cw laser radiation and continuous powder feeding (middle) and coaxial wire feeding (right)

the heat affected zone range from some tenths of mm up to 1 mm. Figure 8.1 shows a schematic representation of the LMD process with a lateral powder feeding nozzle.

CO_2 lasers, Solid State lasers SSL (fibre, disc or diode lasers) are used for LMD. Due to the higher absorptivity and the higher process efficiency of the shorter wavelengths of the SSL these lasers are commonly used today in LMD. Furthermore, these lasers can be guided through fibres which offer higher flexibility in the beam guiding system. Additionally, fibre lasers, disc lasers and diode possess a high wall-plug efficiency leading to an improved economic efficiency.

For repair applications also small pulsed lasers using manual wire feeding are established. The manual wire feeding offers high flexibility without the need of complex programming. These machines have limited deposition rates due to the low average power of the lasers (typically up to 200 W).

Figure 8.2 shows the manual pulsed LMD process with wire feeding (left side) and the automated LMD processes with cw laser radiation and continuous powder feeding (middle) and coaxial wire feeding (right side).

Table 8.1 Most important parameters in LMD and typical values

Parameter	Typical values for LMD
Laser power	200–20,000 W
Beam diameter	0,6–10 mm
Speed	200–5000 mm/min
Powder/wire feeding rate	0,5–150 g/min
Feeding gas rate (powder)	2–15 l/min Ar or He
Shielding gas rate (powder/wire)	2–15 l/min Ar or He
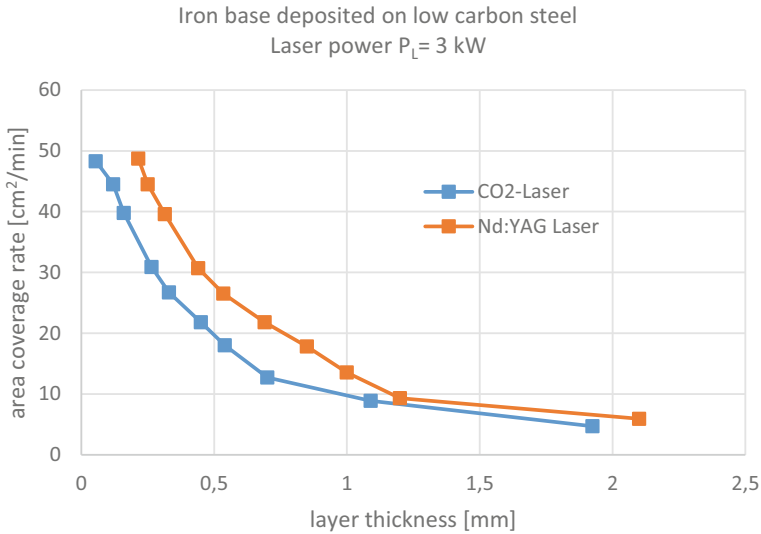
Fig. 8.3 LMD area coverage rates (cm^2/min) at different layer thickness h (mm) achieved with CO_2- and Nd:YAG laser radiation at a laser power of 3 kW

The most important parameters in LMD with typical values are given in Table 8.1.

Figure 8.3 shows the achieved LMD layer thickness versus the area coverage rate for two different wavelengths (CO_2-laser 10.6 μm and Nd:YAG laser 1064 nm) at 3 kW laser power. A low carbon steel was chosen as the base material, and the additive material is a Fe-based alloy. The higher absorptivity of the Nd:YAG laser leads to higher LMD rates (about 50% higher area coverage rate).

Figure 8.4 shows the overall absorptivity in LMD processes with CO_2-laser radiation compared to diode and solid-state laser radiation. On the right side two LMD results (cross sections) are shown, which were produced with CO_2-laser and Nd:YAG laser radiation. For achieving the same geometrical results (layer width and thickness) about 2.5 times more laser power is required for the CO_2-laser. The overall energetic efficiency is given by η.
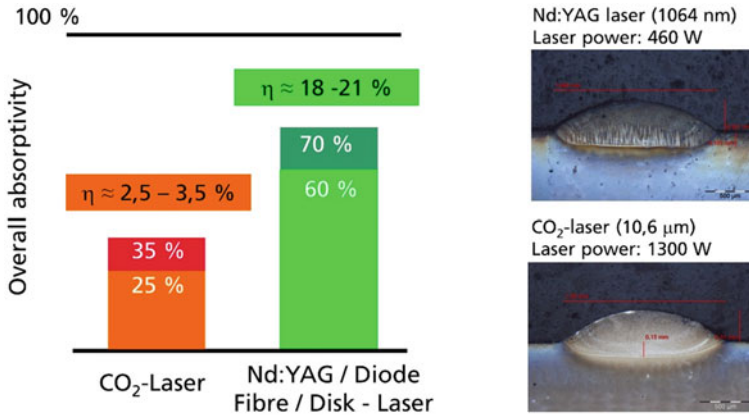
Fig. 8.4 Overall absorptivity and energetic efficiency achieved for LMD with different wavelengths

$$\eta = abs \times \eta_{wall-plug}$$

Introducing typical values for the wall-plug efficiency of about 10% for the CO_2-laser and of about 30% for solid state lasers (not lamp pumped Nd:YAG) results in an energetic efficiency of:

$$\eta_{CO_2} = 2.5 - 3.5\%$$

$$\eta_{SSL/diode} = 18 - 21\%$$

Figure 8.5 shows different layers achieved by LMD. Singles layers up to 1–1,5 mm thickness as well as multiple layers up to several cm thickness are feasible. On the right hand of Fig. 8.5 typical material combinations are shown. Depending on the application different filler materials can be applied resulting in different hardness ranges.

Figure 8.6 shows the hardness distribution of two Stellite 6 (Cobalt base alloy) layers, one single layer and one layer out of three single layers. The layers were deposited on a low carbon steel (0,45% C). The hardness values achieved range between 500 HV 0.3 und 650 HV 0.3, the thickness from 1,2 up to 3,7 mm. The heat affected zone (HAZ) is in the range of 1 mm. Usually the HAZ ranges in the measure of the layer thickness and can be reduced by reducing the thickness of the deposited layer (e.g. by applying less laser power during the LMD process).

Laser metal deposition has diverse advantages like (Gasser et al. 1997):

- Metallurgical bonding between deposited material and substrate material
- Very low porosity and no bonding defects and undercuts
- Nearly no oxidation, even for oxidation sensitive materials
- Layer thickness ranging between 0,05 mm and 1,5 mm for a single layer
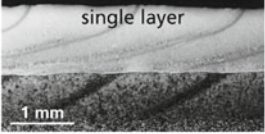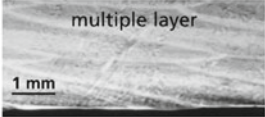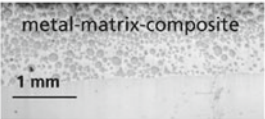
Base material	Additive material	Hardness of layer
Fe-Base: tool steel, stainless steel, low carbon steel, ...	Cobalt-, Nickel and Fe-Base-alloys Metal-matrix-composites (Carbides + Ni-,Co- or Fe-alloys	200 - 800 HV 0.3 20 - 63 HRC
Aluminium alloys	Aluminium aloys	75 - 170 HV 0.3
Nickel and Titanium alloys	Nickel and Titanium alloys	250 – 450 HV 0.3
Copper alloys	Copper alloys, Co- and Ni-alloys	50 HV -350 HV 0.3

Fig. 8.5 Different layers produced by LMD
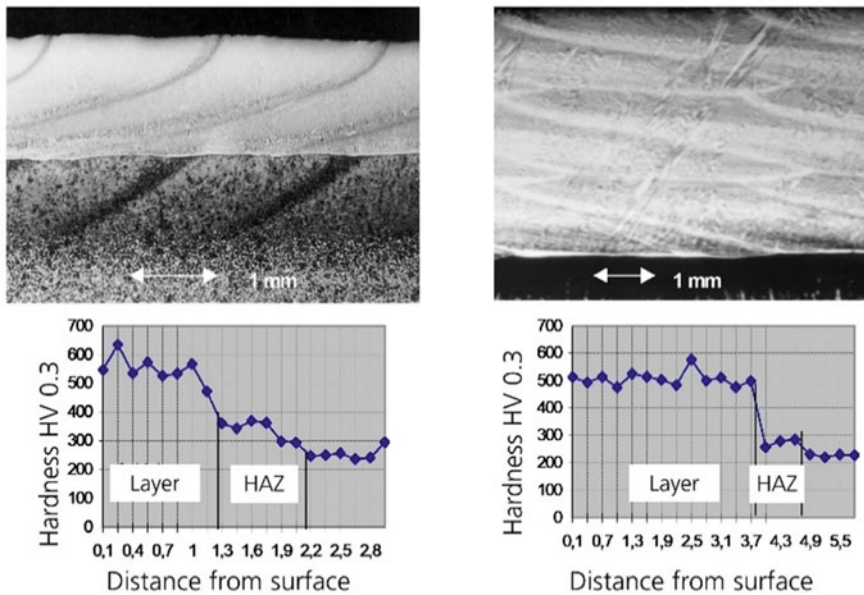
Fig. 8.6 Cross sections of single and multiple Stellite 6 layer (3 layers) on low carbon steel and corresponding hardness profiles

- Minimised heat input and distortion
- Highly automated and reproducible production of high precision layers

Compared to the total workpiece volume, LMD generally involves melting small volumes, so that the dominant process for cooling is heat conduction into the

surrounding material (self-quenching). Characteristics of this are the high heating and cooling rates in the range of 10^3 to 10^4 Ks^{-1}, whereby fine microstructures in the micrometre range are produced (Beyer and Wissenbach 1998; Poprawe 2005; Arrizubieta et al. 2017). The relationship between the temporal and spatial change of the temperature field in the base and filler material, i.e. the solidification conditions and the resulting residual stress state can be described by mathematical models, see Sect. 6.2.2.

Different concepts exist for the material supply to the processing area, depending on the application. In the case of powdered materials, nozzle concepts adapted to the application (accessibility, precision requirements, etc.) are used: lateral, coaxial or multi-jet nozzles, see Sect. 6.2.3. For wire-shaped filler materials special beam shaping optics are used, see Sect. 6.2.5.

As filler materials, various commercially available, predominantly metallic alloys based on nickel (e.g. NiCrMo, C276, NiCr, NiCrAl, NiBSi, NiCrBSi), cobalt (e.g. CoCrC, CoCrWC, CoCrMoNiC, CoCrMoWNi) or iron (e.g. FeNiCr, FeWMoC) or metal matrix composites consisting of a ductile metal matrix and embedded hard materials, such as WC, Cr3C2, TiC or SiC, are used (Majumdar and Mann 2013; Vuoristo et al. 2005; Zhong and Liu 2010), see Sect. 6.2.4.

In LMD with powder materials, part of the laser beam is absorbed by the powder particles above the melt pool. The radiation absorbed by the powder particles leads to a heating of the powder particles. The non-absorbed part is (repeatedly) re-reflected or transmitted. The molten pool is created by the transmitted radiation portion. Depending on the particle temperature before entering the melt pool, two different process regimes are distinguished: the conventional LMD with particle temperatures that are predominantly lower than the melting temperature, and the extremely high-speed laser metal deposition EHLA, in which a large proportion of the particles are completely melted by the laser radiation before entering the melt pool. This eliminates the time required to melt the particles in the molten pool, thus enabling increasing the feed rate from a few metres per minute to several hundred metres per minute (Poprawe et al. 2018; Schopphoven et al. 2017, 2016; Schopphoven 2020), see Sect. 6.2.5.

Wire feeding offers diverse advantages where the powder filler material cannot be applied, e.g. when safety, health or technical reasons apply, see Sect. 6.2.6.

The relative movement between laser radiation and substrate results in a dense and metallurgically bonded weld bead after solidification of the melt. By superimposing several weld beads laterally, a flat coating can be produced. If several layers are build-up-welded over one another, the process can also be used for repair, additive manufacturing or for hybrid additive manufacturing, i.e. the additive manufacturing of volumes on existing conventionally manufactured (e.g. casting, forging) basic geometries, e.g. for geometric modification, see Sect. 6.2.7.

Section 6.2.8 shows some application areas of the conventional LMD approach using powder filler materials as well as the extreme high-speed LMD process (EHLA).

References

Arrizubieta JI, Lamikiz A, Klocke F, Martínez S, Arntz K, Ukar E (2017) Evaluation of the relevance of melt pool dynamics in laser material deposition process modeling. Int J Heat Mass Transf 115:80–91

Beyer E, Wissenbach K (1998) Oberflächenbehandlung mit dem Laserstrahl. Springer, Berlin Heidelberg. https://doi.org/10.1007/978-3-642-58726-9, S 7, 243–251

Gasser A, Backes G, Wissenbach K, Hoffmann E, Poprawe R (1997) Maßgeschneiderte Oberflächen durch Laserstrahl-Oberflächenbehandlung mit Zusatzwerkstoffen—eine Übersicht, Laser und Optoelektronik 3/97

Majumdar JD, Mann I (2013) Laser assisted fabrication of materials. Springer, Heidelberg, pp 226–230

Poprawe R (2005) Lasertechnik für die Fertigung. Springer, Berlin, Deutschland

Poprawe R, Hinke C, Meiners W, Eibl F, Zarei O, Voshage M, Willenborg E et al (2018) Digital photonic production along the lines of industry 4.0. In: Laser applications in microelectronic and optoelectronic manufacturing (LAMOM) XXIII (Vol. 10519, p. 1051907). International Society for Optics and Photonics

Schopphoven T, Gasser A, Wissenbach K, Poprawe R (2016) Investigations on ultra-high-speed laser material deposition as alternative for hard chrome plating and thermal spraying. J Laser Appl 28(2):022501

Schopphoven T, Gasser A, Backes G (2017) EHLA: extreme high-speed laser material deposition: economical and effective protection against corrosion and wear. Laser Tech J 14(4):26–29

Schopphoven T (2020) Experimentelle und modelltheoretische Untersuchungen zum Extremen Hochgeschwindigkeits-Laserauftragschweißen. Fraunhofer Verlag

Vuoristo P, Tuominen J, Nurminen J (2005) Laser coating and thermal spraying—process basics and coating properties. In: Conference proceedings: ITSC 2005. International Thermal Spray Conference & Exposition, Basel, Switzerland

Zhong M, Liu W (2010) Laser surface cladding the state of the art and challenges. In: Proceedings of the institution of mechanical engineers, part c journal of mechanical engineering science

Chapter 9
Modelling of Laser Metal Deposition

Norbert Pirch and Markus Nießen

9.1 Introduction

Laser metal deposition (LMD) has become an established processing technique for the repair and manufacture of metal parts and the functionalization of metal surfaces. The LMD-process is used on complex geometries, durable and high-valued components e.g. for aero engines, turbo machinery and tooling industry.

In the powder-based LMD process (Fig. 9.1), a focused laser beam is used to generate melt tracks onto the substrate. Powder particles are injected into the melt through a powder nozzle and lead to an increase in melt volume. A welding bead is generated by the movement of the laser beam. A layer is built up by overlap machining and a volume by several layers.

The powder particles attenuate the incident laser beam and only the transmitted portion into the process zone is available for direct heating of the substrate. By selecting the relative position of the substrate surface to the laser beam focus, the power density distribution in the process zone can be varied according to the beam caustic and thus influence the melt pool width and process temperature. Only particles which hit the surface of the molten pool contribute to the track structure. The others are reflected from the substrate surface or adhere when the particle temperature is sufficiently high. When the particles come into contact with the melt, there is a temperature exchange because the local temperature on the surface of the molten pool is different from the particle temperature. Depending on the difference, this can lead to a local heat sink or heat source and must be considered as a boundary condition in the heat balance. The heating of the individual particle until it comes into contact with the melt depends on its individual trajectory and its speed with which it passes the laser beam. The particle temperatures at a position of the melt pool surface can vary considerably depending on the path they have taken through the

N. Pirch (✉) · M. Nießen
Fraunhofer ILT, Aachen, Germany
e-mail: norbert.pirsch@ilt.fraunhofer.de
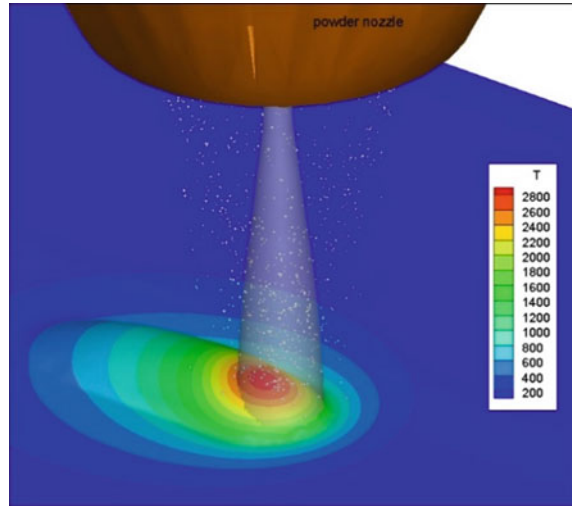
laser beam and the particle volume they have. Despite the small heat-affected zone,
the LMD process suffers from welding distortion like all other welding processes,
although not to the same extent. Various approaches are pursued in the literature to
counter this. A frequently used approach in this context is that of preheating, for the
whole component or a local preheating (Aggarangsi and Beuth 2006). Alternatively,
the approach is also pursued in which the component warpage to be expected on
the basis of model calculations is entered into the CAD model as negative warpage
(Biegler et al. 2020). The idea behind this is to design the negative warpage in such
a way that the sum of the negative warpage and the warpage caused by the process is
compensated in such a way that the contour deviation from the CAD model remains
within predefined limits.

According to the state of the art, no methodology exists at present for the LMD
process to determine in advance a suitable process strategy including the process
parameters for a component and material specific task. By this the experimental
expenditure of time could be reduced significantly. Besides, the process simulation
should enable a detailed physical understanding of the involved physical processes
it should enable to calculate a process window in advance in such a way that
experimentally only a fine adjustment is necessary.

In the following chapters we will give a short review about the state of the art and
describe a model developed at Fraunhofer ILT. The structural analysis is based on
a developed three-dimensional time-dependent finite element model for laser metal
deposition (LMD) with coaxial powder feeding supply (Pirch et al. 2017). This model
encompasses the powder stream, his interaction with the laser radiation and the melt
pool computation. The thermal model has been validated by a comparison between
experimental and computed shape of the melt pool surface concerning cross section
and longitudinal section. To solve the thermo-elastoplastic equations a massively

parallelized solver characterized by a low memory requirement and a high calculation speed for large systems of equations was developed.

9.2 State of the Art

In terms of model theory, LMD is a free boundary value problem. This means that the track geometry or the melt pool surface is part of the time-dependent solution. The first analytical models assumed quasi-stationary conditions and elliptical formed melt pool surfaces (Fathi et al. 2006). More recent models rely on the so called element activation ("death/birth") methodology (Patel and Patel 2012) but still the geometry of the melt pool surface is assumed and is approximated by brick elements. As a consequence the thermalization of the optical energy can't be modeled physically correct as a von Neumann boundary condition on the melt pool surface, because the normal vector flips at the edges of the bricks between the three directions of the coordinate system. By default the thermalization of the optical energy is modeled as a volume source with the result that the process temperature is underestimated significantly by this method. In the review article by Pinkerton (Pinkerton 2015), literature references are given that have addressed the free boundary value problem with the level set method (Qia et al. 2006). By using the level set method the interface tracking problem can be transformed into a partial differential equation. It is assumed that the motion of the liquid free surface of the molten pool is caused by mass addition and local fluid flow. Capillary forces are not taken into account. But these laser-generated melt in the LMD process with dimensions smaller than 1 mm and a process control below the evaporation temperature, where the geometry of the melt pool surface is essentially determined by the capillary forces. Earlier investigations concerning the melt pool dynamics and formation of the melt pool surface with the laser beam surface layer melting have shown that the impulse transfer of the induced Marangoni flow to the formation of the melt pool surface is negligible compared to the capillary forces (Pirch et al. 1990). In addition, studies on the influence of Marangoni flow on the distribution of alloying elements in laser boundary layer alloying show that the flow causes microsegregation (He et al. 1994, 1995). The capillary length for nickel base alloys is approx. 4.8 mm (Amore et al. 2016). A capillary surface that has a characteristic length smaller than the capillary length is the solution to the Young–Laplace equation with gravity completely absent. This means that the Marangoni flow and gravitation can be neglected for the calculation of the geometry of the melt pool surface with melt pool dimensions lower than 1 mm. Based on these assumptions, a good match could be achieved between an experimentally determined and a calculated track geometry (Pirch et al. 2017). Depending on the choice of the process parameters, a Marangoni flow can be established in the melt, which has a significant influence on the melt pool geometry and the solidification conditions (DebRoy et al. 2018). However, it is also possible to adjust the particle density on the surface of the melt bath in such a way that the free surface necessary for the formation of the flow is not given and thus suppress the flow as far as possible. The

background to this measure is that the Marangoni flow promotes the formation of micro-segregations in the mushy zone (Pirch et al. 1998).

DebRoy gives a very good overview of the different modeling approaches known from literature, their numerical implementation and their features (DebRoy et al. 2018).

9.3 Powder Gas Stream Characteristics

To determine the laser beam caustic the laser intensity distribution (LID) is measured with the Primes Focus Monitor in parallel planes with a distance of 1 mm to each other. For each plane a Super Gauß Fit (Decker 1994) is performed for the LID with a Least Square Method. By this the data are released from noise and can be interpolated arbitrarily, which is necessary to compute the temperature evolution of the particles along their trajectories.

In Fig. 9.2 the image-based particle density measurement system is shown. A laser line is positioned in the focus range of the camera and illuminates the powder gas stream from the side. The camera monitors the reflections of the illumination laser from the particles coaxially through the nozzle.

A high frame rate allows the individual powder particles to be captured in number and position at a defined point in time. Through step-by-step movement along the powder gas stream, individual layers are recorded. The particle densities per plane
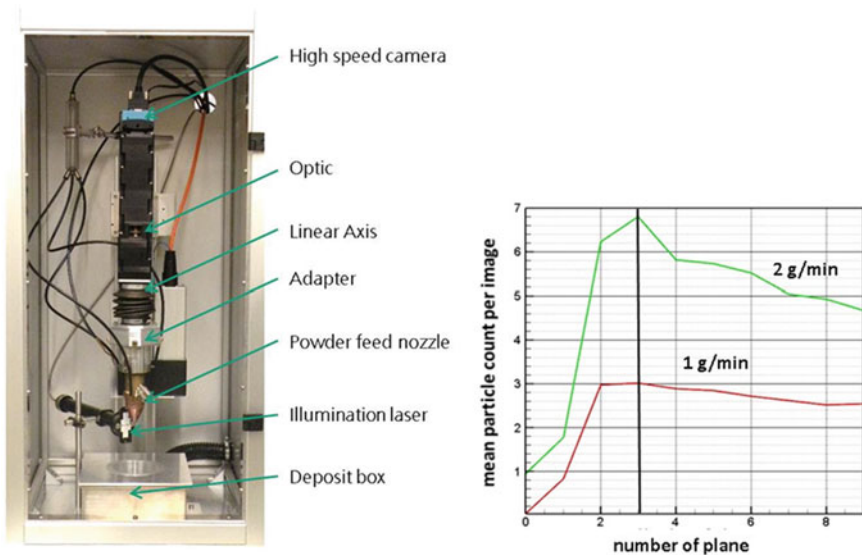
Fig. 9.2 Left: Particle density measurement system/3/. Right: Mean particle count per image (carrier gas Ar 2.2 L/min, shielding gas Ar 5 L/min, particle size 45–90 mm)
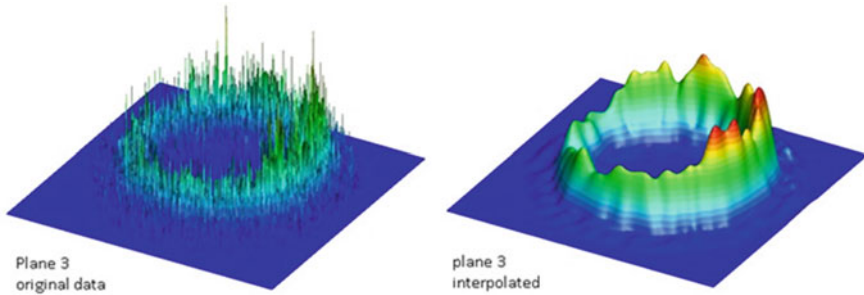
Fig. 9.3 Original data of empiric particle density distribution (PDD) and Nurbs interpolated PDD

are computed by averaging the particle positions from all relevant single images. The mean particle number per image is not constant along the particle propagation direction (Fig. 9.2 right). Just beneath the nozzle outlet not all particles are detected by the camera, and in the focus area not all particles are counted individually due to the high particle density. The curves show a local maximum at plane 3 for both powder mass rates, whereby the characteristic of the local maximum is more obvious at higher powder mass rates (Fig. 9.2 right).

The settings for the gas supply are chosen in such a way that the diameter of the powder focus and the residual oxygen content are suitable for the process in the working plane. The particle density distribution (PDD) of plane 3 is chosen as reference PDD for the statistical model. The noise of the data is eliminated by Nurbs interpolation (Fig. 9.3) of the data obtained after the Least Square Method.

The trajectories of the particles are assumed as straight lines between the nozzle outlet and the working plane. The particles are assumed with regard to their grain diameters as equal sized. The connection of the statistical model (Fig. 9.4) is given by the selection of only these trajectories which results in the reference particle density.

The mean particle velocity is according to the formula above about 770 mm/s for a powder mass rate of 1 g/min and about 682 mm/s for a powder mass rate of 2 g/min. The shadowing of the laser radiation is computed spatially resolved by averaging about 106 snapshots of the shadow image of the particles (Fig. 9.5).

The shadowing depends on the propagation length of the laser radiation through the powder cloud. For the given configuration the loss of laser radiation from the nozzle outlet down to the working plane $z = -8$ mm has a maximum value of 16% (Fig. 9.6).
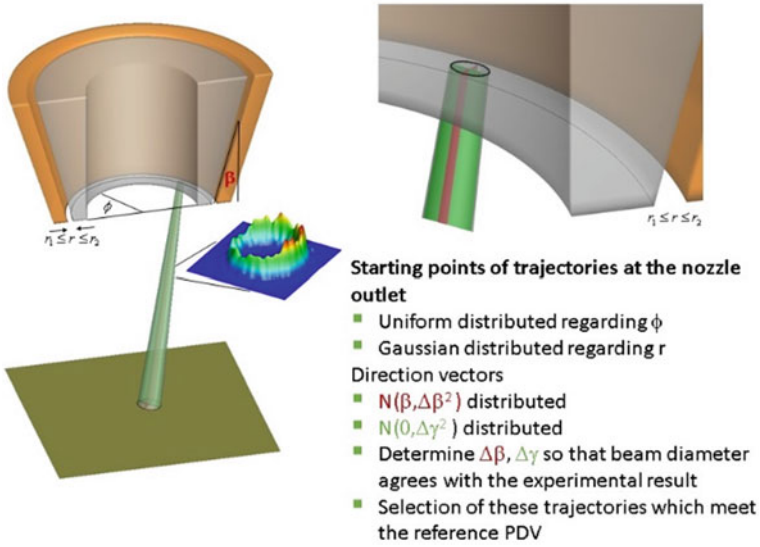
Fig. 9.4 Assumptions of the statistical model regarding the particle trajectories
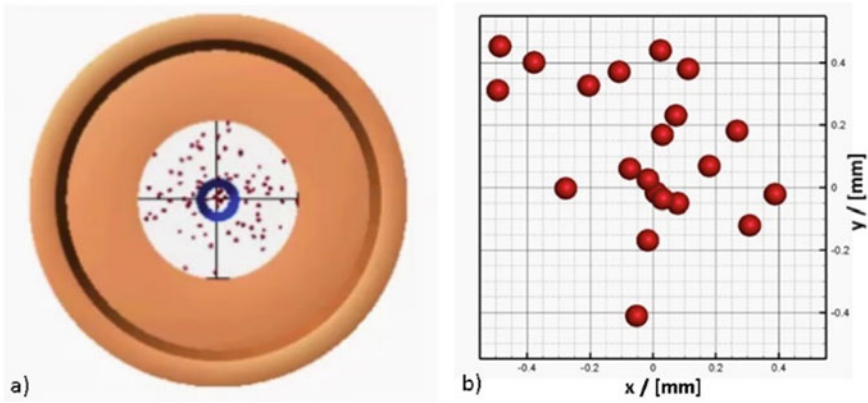
Fig. 9.5 **a** Snapshot of particles from the nozzle outlet down to the working plane $z = -8$ mm; **b** detail view within the laser propagation area

9.4   Particle Beam Interaction

The LIV data from the Primes Focus Monitor are approximated per plane with a Super Gauss Fit:

Fig. 9.6 Transmission function for the laser radiation for $z = -8$ mm
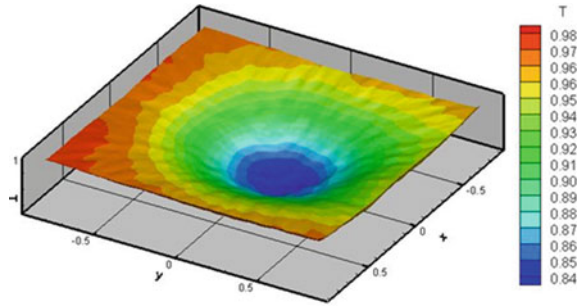
$$f(r) = \begin{cases} I_o \cdot \left(\exp\left(-f(n) \cdot \left(\frac{r}{r_o}\right)^n\right) - f_{rm} \right) & for \quad r < r_{max}, \quad r = \sqrt{x^2 + y^2} \\ 0 & for \quad r > r_{max} \end{cases}$$

with

$$f_{rm} = \exp\left(-f(n) \cdot \left(\frac{r_{max}}{r_o}\right)^n\right)$$

and

$$1 = 2 \cdot \pi \cdot \int f(r) \cdot r \, dr$$

$$(9.1)$$

The LID of the laser beam changes from a Gaussian intensity distribution just beneath the nozzle outlet along the propagation direction to a top hat distribution in the focus area and then changes again to a Gaussian distribution (Fig. 9.7).
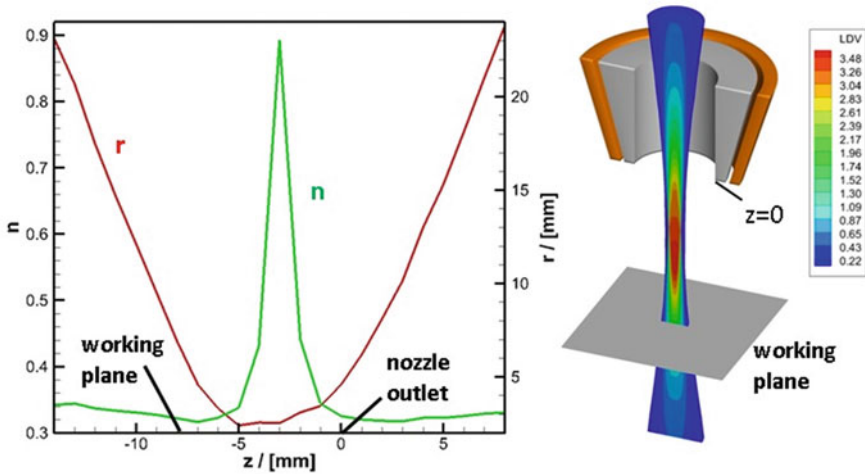
Fig. 9.7 Laser beam radius r and LID steepness coefficient n along the propagation direction z
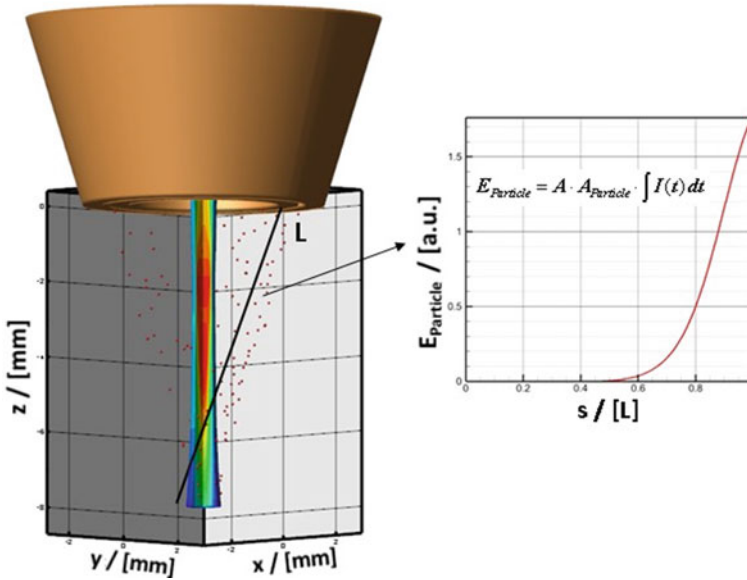
Fig. 9.8 Energy absorption along the particle trajectory L

For each particle the absorbed energy is calculated in this way from the outlet nozzle to the working plane (Fig. 9.8). About 50% of the particles reach the melting temperature for a laser power of 300W and an absorbance A of 30%.

The conversion of the particle energy into temperature (Fig. 9.9) PDD was carried out based on the enthalpy function of Inconel 718. Particles which exceed the evaporation temperature are identified as a splash and are considered as a loss for the process. The relevance of the particle temperature is derived from the boundary condition for the thermalization of the optical energy at the melt pool surface.

9.5 Thermal and Track Geometry Analysis

The geometry of the molten pool surface can be determined as a solution to the Young–Laplace equation. This represents a balance of the normal forces and requires a calculation of the mean curvature. This is numerically sensitive. A more numerically robust and physically equivalent alternative for the calculation of the melt pool surface is a minimization of the surface tension weighted melt pool surface (Pirch et al. 2019). The boundary condition is a three-phase line at which the surface of the molten pool is clamped. In addition, the time-resolved volume increases by the entry of the particles into the melt must be taken into account as volume constraint during minimization.

Fig. 9.9 Frequency distribution of particle temperature ($P_L = 300$ W, A = 30%, material: IN718)
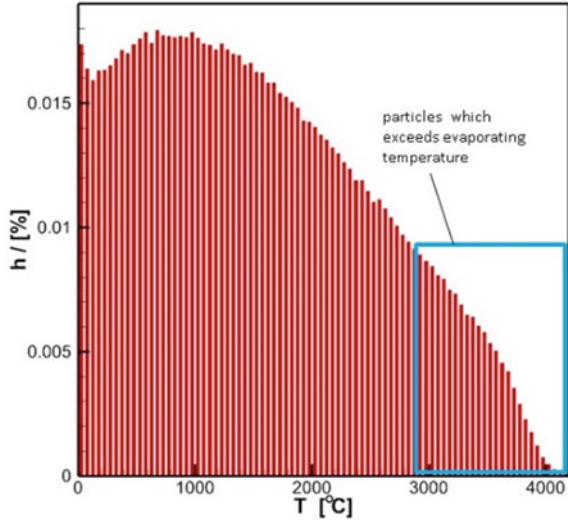
The numerical tool created using this approach allows a computational prediction of the track geometry along component edges which is a prerequisite for a near-contour design. Basis for the calculation of the geometry of the molten pool surface is the time-dependent heat conduction equation

$$\frac{\partial(\rho \cdot c_P \cdot T)}{\partial t} = \text{div}(\lambda \cdot \text{grad}T)$$

$$\text{with} : \quad \rho : \text{density}$$

(9.2)

with the boundary condition for the thermalized optical energy, the heat loss by radiation and the heat exchange between the particles and the melt

$$\lambda \cdot \langle \vec{n}, \nabla T \rangle = \underbrace{A \cdot \langle \vec{n}, \vec{I}_{\text{trans}} \rangle}_{\text{transmitted LID}} - \underbrace{\varepsilon \cdot \sigma \cdot T^4}_{\text{radiation}}$$

$$+ \underbrace{\rho_{\text{Particle}} \cdot \dot{m}_P \cdot c_P \cdot (\hat{T}_{Particle} - T_S)}_{\substack{\text{energy demand for temperature balance} \\ \text{between particle melt pool surface}}}$$

T : temperature, λ : heat conductivity, ρ_{Particle} : particle density distribution

c_p : heat capacity, ε : emissivity, σ : Boltzmann radiation constant

Depending on the sign of the difference of particle and surface temperature of the melt pool surface, the particles act as gain or a loss in the balance equation for the heat flux. In order to avoid a local new meshing after each time step, the continuous track formation is modeled by the method of the immersed boundary condition (Gornak 2013). With this method, the calculation is performed on a Cartesian mesh that

contains the complete component. In order to include the boundary conditions on the freeform surfaces areas of the component, all elements are identified that have a non-empty intersection with the freeform surface areas.

The element size is dimensioned so that the resulting temperature gradient is oscillation-free and the track geometry can be represented with sufficient resolution. The mesh is divided into a part on which the welding tracks are built up (Fig. 9.10, yellow part) and a part that remains unchanged during the process (gray part). For the calculation of the melt pool surface, each node can move in the direction of the surface normal (Fig. 9.11).

With respect to these degrees of freedom, the melt pool surface is calculated at a certain point in time as the minimum of the surface energy. The time dependent

Fig. 9.10 Triangular surface mesh of the component including the normal vectors in the edge area
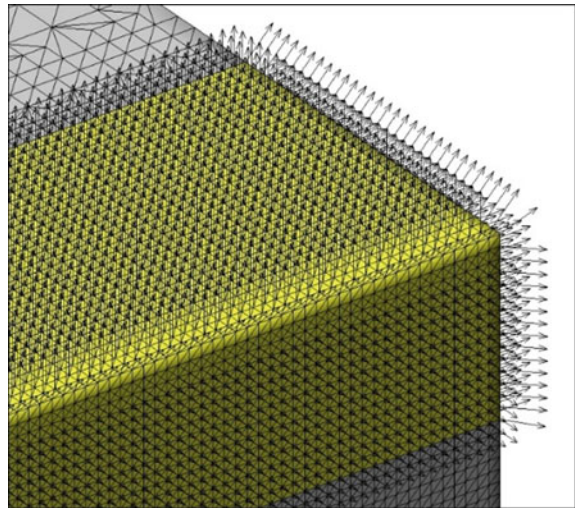
Fig. 9.11 Triangle variation along normal direction at nodes

$$\text{Triangle } (i_1, i_2, i_3) \text{ movement with}$$
$$\vec{x}'_{i_j} = \vec{x}'_{i_j} + t_{i_j} \cdot \vec{n}_{i_j}, \quad j = 1, 2, 3$$
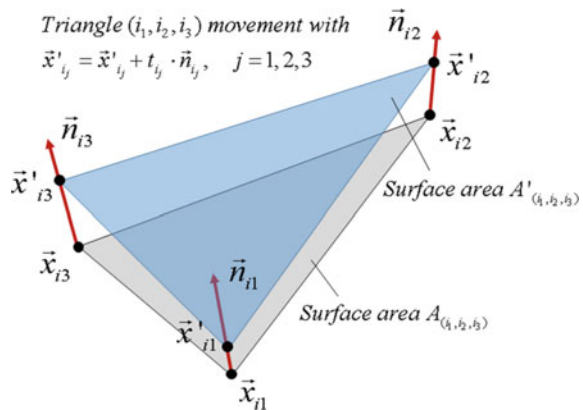
three-phase line is given as a Dirichlet condition and the variation of the melt volume is taken into account as a constraint.

If the surface of the component does not correspond to one of the three Cartesian planes in all surface areas, it is possible to triangulate the free-form surfaces via a common CAD system and to read them into the simulation tool as a start surface via an interface. For the initial Finite element mesh, a hexadecimal mesh will be used, which just envelops the component.

The capillary melt bath surface without volume constraint is derived as a minimum of the energy functional

$$
\begin{aligned}
\Pi_{Energy}(t_{i1}\dots t_{im}) &= \sum\nolimits_{Triangles} \sigma \cdot A'_{(i_1,i_2,i_3)}(\vec{t}'_{(i_1,i_2,i_3)}) \\
&= \frac{1}{2} \cdot \sum\nolimits_{Triangles} \sigma \cdot \|(\vec{x}'_{i2} - \vec{x}'_{i1}) \times (\vec{x}'_{i3} - \vec{x}'_{i1})\|
\end{aligned}
\tag{9.3}
$$

The movement of the nodes along the local normal directions leads to a volume change per triangle,

$$
\Delta V_{\text{Triangle}} = \int\limits_{\text{Triangle}} \langle \vec{n}, \vec{n}_{\text{Triangle}} \rangle dA
$$

with local displacement, $0 \le \xi \le 1, 0 \le \eta \le 1 - \xi$

$$
\vec{n}(\xi, \eta) = t_{i1} \cdot \vec{n}_{i1} + \xi \cdot (t_{i2} \cdot \vec{n}_{i1} - t_{i1} \cdot \vec{n}_{i1}) + \eta \cdot (t_{i3} \cdot \vec{n}_{i3} - t_{i1} \cdot \vec{n}_{i1})
$$

and triangle normal vector

$$
\vec{n}'_{\text{Triangle}} = (\vec{x}_{i2} - \vec{x}_{i1}) \times (\vec{x}_{i3} - \vec{x}_{i1}), \quad \vec{n}_{\text{Triangle}} = \frac{\vec{n}'_{\text{Triangle}}}{\|\vec{n}'_{\text{Triangle}}\|}
\tag{9.4}
$$

which can be calculated as an integral of the local projection of the displacement on the triangle normal (Eq. 9.4). The superscript r denotes quantities referring to the reference configuration. The total volume change is the sum of all triangles involved in the movement of the melt pool surface and must be identical to that volume change $\Delta V_{\text{Particle}}$ resulting from the particles adsorbed in the time increment. The geometry of the molten pool surface considering the change of the volume of the melt results from the addition of the constraint with a Lagrange parameter λ from the minimum of the functional (Eq. 9.5).

$$
\Pi(t_{i1}\dots t_{im}, \lambda) = \Pi_{\text{Energy}}(t_{i1}\dots t_{im}) + \lambda \cdot \left(\sum\nolimits_{\text{Triangles}} \Delta V_{\text{Triangle}} - \Delta V_{\text{Particle}} \right)
\tag{9.5}
$$

The increase in volume during a time increment between two consecutive time steps by the particle flow results as an integral of the powder mass flow over the melt pool surface.

$$\Delta V_{\text{Particle}} = \frac{\Delta_{\text{time}}}{\rho} \cdot \dot{m}_P \cdot \int\limits_{T > T_{\text{melt}}} f^{PD} dA \qquad (9.6)$$

This means in particular that the powder efficiency in the model presented here, like the track geometry, is part of the solution. The surface of the molten pool is then finally computed as solution of the equations

$$\Pi(t_{i1} \ldots_{im}, \lambda) = \Pi_{\text{Area}}(t_{i1} \ldots t_{im}) + \lambda \cdot \left(\sum_{\text{Triangles}} \Delta V_{\text{Triangle}} - \Delta V_{\text{Particle}} \right)$$

$$\frac{\partial \Pi(t_{i1} \ldots t_{im}, \lambda)}{\partial t_{i1}} = 0$$

$$\vdots \qquad\qquad\qquad\qquad\qquad (9.7)$$

$$\frac{\partial \Pi(t_{i1} \ldots t_{im}, \lambda)}{\partial t_{im}} = 0$$

$$\frac{\partial \Pi(t_{i1} \ldots t_{im}, \lambda)}{\partial \lambda} = 0$$

The simulation tool is to be used to calculate in advance the process strategy for welding traces along edges so that an overhang is generated along the edge. As one example the influence of laser beam offset to the edge on tracking the formation can be analyzed.

For the simulation a temperature dependence for the surface tension for pure IN 718 (Eq. 9.8) according to literature (Quested et al. 2009) has been used.

$$\sigma(T) = 1.842 - 0.11 \cdot 10^{-3}(T - T_{\text{melt}}), \quad [\sigma] = N \cdot m^{-1} = J \cdot m^{-2} \qquad (9.8)$$

The calculations are performed for a Super Gaussian intensity distribution (1) with $r_o = 0.6$ mm, $r_{\text{max}} = 0.9$ mm and $n = 2.3$ in the process plane. The pre-factor $f(n)$ is determined such that the integration of the LID up to r_o contains 86% of the laser power. A laser power P_L of 250 W and an absorptivity A of 45% are assumed. The absorption coefficient was determined by adapting calculated remelting depths to measured ones during remelting tests. The maximum intensity in the beam center is 174 W/mm^2 for the Gaussian-like LID. The scanning speed for simulations and experimental investigations is 500 mm/min and the powder feed rate is 1 g/min. Using these process parameters a temperature of approximate 2000 °C is reached for the quasi-stationary state (Fig. 9.12). On half the length of the welding track, a cross section has been created to perform a comparison with experimental results.

For experiment and simulation an edge offset of 0 mm has been used. Since the experimental welding track shows fluctuations, several cross sections were created along the track (Fig. 9.13, left) for comparison with the calculated result and these were compiled together with the model theoretical results in one diagram ((Fig. 9.13, right). The comparison shows that the calculated cross-section forms a smaller
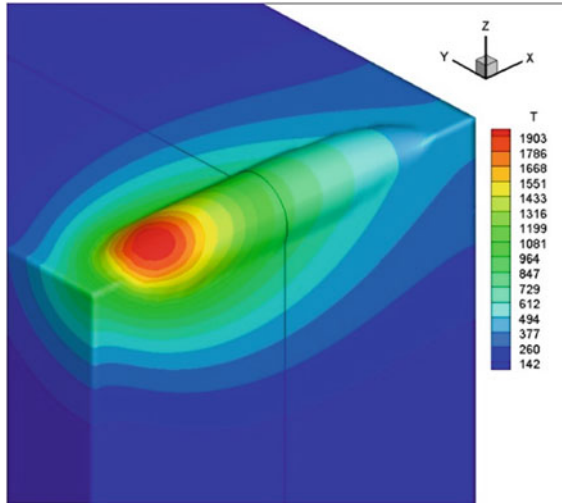
Fig. 9.12 Calculated snapshot of the track formation

overhang, shows a higher curvature in the area below the laser beam and shows a significantly smaller deep melting out at the vertical surface.

The powder particles are typically covered with homogeneous oxide layers formed by nickel oxide/hydroxide in case of Ni-based superalloys (Hryha et al. 2018). The thickness of the oxide layers are between 1 and 4 nm, depending on alloy composition, powder manufacturing method and powder handling. This means that after contact with the melt and melting, the particles locally enrich the surface of the molten pool with oxygen. Wherein the enrichment is not uniformly distributed over the melt pool surface but correlates with the local particle flow into the melt. Oxygen is a surface-active element whose presence can cause the surface tension coefficient negative for pure IN 718 to become positive. But in the presence of surface active elements, a "boomerang shape" temperature dependence surface tension is the most
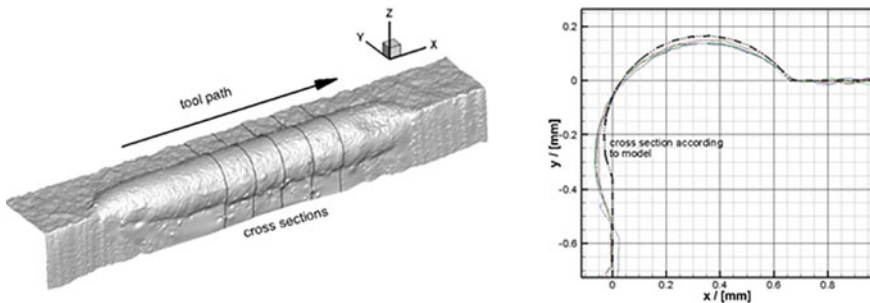
Fig. 9.13 Digitized surface of a track with 0 mm edge offset (left), cross sections including model result with a temperature dependence of the surface tension according to the Eq. 9.10 (right)

realistic (Ozawa et al. 2011; Lee and Farson 2016). But basically, for IN 718, there are currently no concrete reliable data in the literature regarding the temperature dependence of surface tension in the presence of oxygen. Furthermore, there are no quantitative assumptions about the extent to which and to what extent the oxide layers of the particles enrich the melt pool surface with oxygen. However, there is agreement on the boomerang similar shape of the function. The change from an initially positive to a negative surface tension coefficient with increasing temperature at a sufficiently high oxygen partial pressure is physically justified by the fact that at a limit temperature the oxygen is no longer able to adsorb to the surface of the molten bath (Ozawa et al. 2011). Therefore, we have tried to derive an approximation of the temperature dependence of the surface tension by comparing the track cross section according to experimental and model theoretical data.

$$\sigma(T) = \begin{cases} \sigma_{\max} + \sigma'_{\text{neg}} \cdot (T - T_c) & T_c \leq T \\ \sigma_{\max} + \sigma'_{\text{pos}} \cdot (T - T_c) & T_{\text{melt}} \leq T \leq T_c \end{cases} \tag{9.9}$$

Good consistency has been achieved by using the following data, $\sigma_{\max} = 1.754$ N/m, $\sigma'_{\text{neg}} = 1.1 * 10^{-4}$ N/m, $\sigma'_{\text{pos}} = 6.0 * 10^{-4}$ N/m, $T_c = 2100\ °C$ for the model equation (Eq. 9.9).

The increased surface tension for higher temperatures leads to a lower mean curvature in the high temperature range. The melt surface flattens in this range and pushes a part of the melt to the outside. A slightly larger overhang forms. The visible surface for the powder and the laser beam becomes larger. The powder efficiency increases and lowers thereby the processing temperature (Fig. 9.14, left) compared to the simulation with a complete negative surface tension coefficient. The increased absorption of the laser radiation in the overhang area leads to a deeper melting at the vertical surface. The comparison with the experimental cross sections shows a very good agreement ((Fig. 9.14, right). However, one must be aware that considerably more comparisons need to be made in order to consolidate the model approach and limit the scope of application. It is conceivable, for example, that the powder mass flow or the powder particle fraction is dependent on the powder particles, since they are the cause of oxygenation.

Increasing the distance between the laser beam center and the edge of the component leads to an increase in powder efficiency, whereas the overhang decreases (Fig. 9.15).

The robustness of the numerical method can be demonstrated by tool paths along the edges including turning points. The algorithm also works reliably under these conditions. Due to heat accumulation at the turning point a larger extent of the melt can be observed. This leads to a significant rounding of the contour and thus to an undersize in this area (Fig. 9.16).
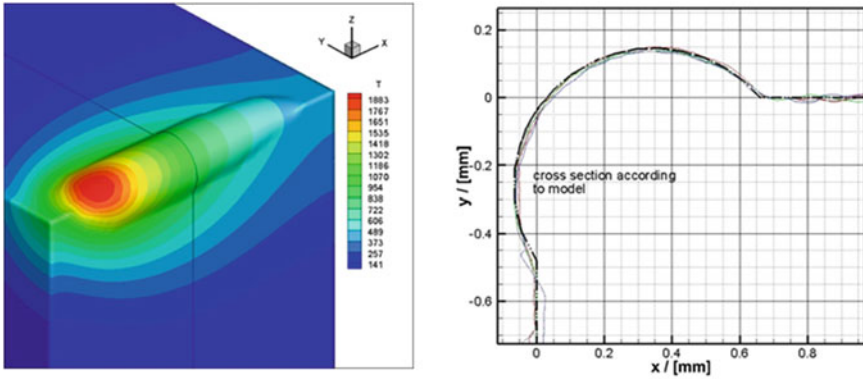
Fig. 9.14 Digitized surface of a track with 0 mm edge offset (left), cross sections including model result with a temperature dependence of the surface tension according to Eq. 9.11 (right)

Fig. 9.15 Cross sections for three different edge offsets
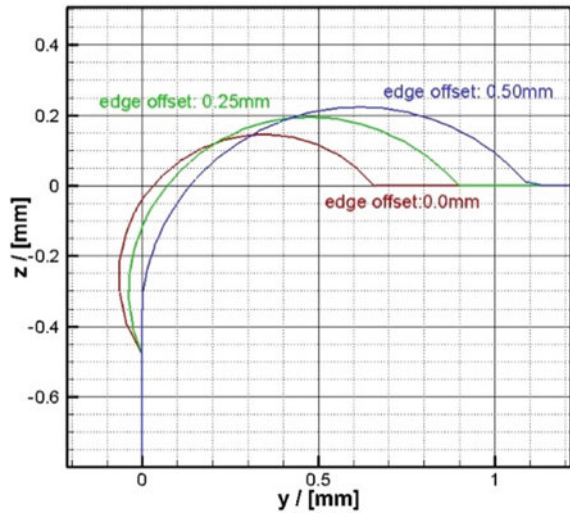
9.6 Structural Analysis

The residual stress results in general from strains generated by expansion and contraction due to temperature changes and phase transformations, and inelastic effects from plasticity and creep. Due to the short time spent at high temperature and high cooling rate creep effects and phase transformation play a secondary role. The total incremental strain vector is therefore given as a superposition of elastic, thermal, and plastic components in the form

$$\Delta\varepsilon_{ij}^{tot} = \Delta\varepsilon_{ij}^{el} + \Delta\varepsilon_{ij}^{th} + \Delta\varepsilon_{ij}^{pl} \tag{9.10}$$
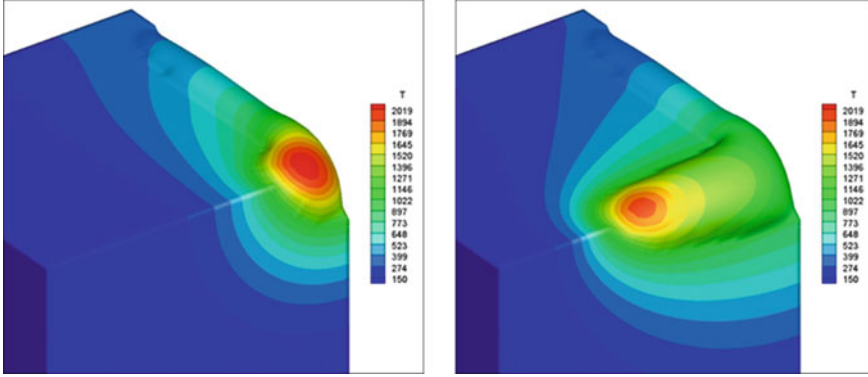
Fig. 9.16 Snapshots of the track formation at 2 different times with 0 mm edge offset

The stress increment for a given elastic strain increment is given by Hookes law

$$
\begin{aligned}
\Delta\sigma_{ij} &= C_{ijlm} \cdot \Delta\varepsilon_{ij}^{el} \\
C_{ijlm} &= \frac{E}{1+\nu} \cdot \left(\frac{1}{2}(\delta_{il} \cdot \delta_{jm} + \delta_{ij} \cdot \delta_{lm}) + \frac{\nu}{(1-2\nu)}\delta_{ij} \cdot \delta_{lm} \right)
\end{aligned}
\tag{9.11}
$$

with the Young's Modulus E, the Poisson ration and the Kronecker symbol Δ_{ij}. A combination of the last three equations yields the basis of the structural analysis

$$
\Delta\sigma_{ij} = C_{ijlm} \cdot \left(\Delta\varepsilon_{lm}^{tot} - \Delta\varepsilon_{lm}^{th} - \Delta\varepsilon_{lm}^{pl} \right)
\tag{9.12}
$$

The material is assumed to adopt a thermo-elasto-plastic behavior using rate independent plasticity with a von Mises flow rule. The elastic modulus, Poisson's ratio, coefficient of thermal expansion, and yield stress are considered as temperature dependent (Pottlacher et al. 2002; https://www.jahm.com/pages/about_mpdb.html). An inhouse simulation tool (StrucSol) was developed for the rapid solution of thermo-elastoplastic equations. The resulting system for the calculation of thermo-elasto-plastic equations are poorly conditioned. Poorly conditioned systems of equations are difficult to solve. Therefore direct solution methods are usually applied. Direct solvers require a large amount of memory, which increases quadratically with the number of degrees of freedom. This leads to a severe limitation in the possible number of elements for direct solution methods. To overcome this drawback a sparse iterative solution method based on Petsc (http://www.mcs.anl.gov/petsc) is used. This solver is massively parallelized and characterized by a low memory requirement and a high calculation speed for large systems of equations.

Computations are performed for the IN 625 (Pottlacher et al. 2002; http://www.jahm.com/pages/about_mpdb.html) as substrate and as additive material. The thickness of the substrate is 10 mm. Single tracks were deposited with a laser power of $P_L = 250$ W, a feed rate of 500 mm/min, a powder mass rate of 1 g/min and an

overlap of the tracks of $r_a = 300$ mm which is half the beam diameter. The steepness coefficient n of the laser intensity distribution (LID) is determined from the data of the Primes Focus Monitor in the working plane with a Super Gauss Fit to 2.5 (Pirch et al. 2019). The profile of the LID is compared to a Gaussian LID in the center flatter and steeper outside. The width of a single track is with 750 mm 25% greater than the beam diameter (Fig. 9.17). The track height increases from 174 mm for the single track to 272 mm for the third track for overlapping processing (Fig. 9.17). The numerical solution of the thermomechanical model equations are usually based on temperature fields that still contain the melt. However, the melt cannot carry any mechanical load. To overcome this issue the modulus of elasticity is significantly reduced in a range around the melting temperature. It is not set to zero, because the resulting stiffness matrix would be no longer regular. This numerical singularity can be avoided by extracting the molten region from the temperature fields and performing the mechanical analysis only in the solid phase [15, Figs. 9.4 and 9.5].

At each time step the subsolidus domain is determined and surface adapted meshed for the structural analysis (Fig. 9.17, right) is generated, such that no artificial extension of the E modulus above the solidus temperature is necessary. The maximum

Fig. 9.17 Snapshots of the temperature field on the track geometry and the sub solidus domain ($P_L = 250$ W, bidirectional processing, $m_P = 1$ g/min, $v_v = 500$ mm/min, base material and additive material IN 625)
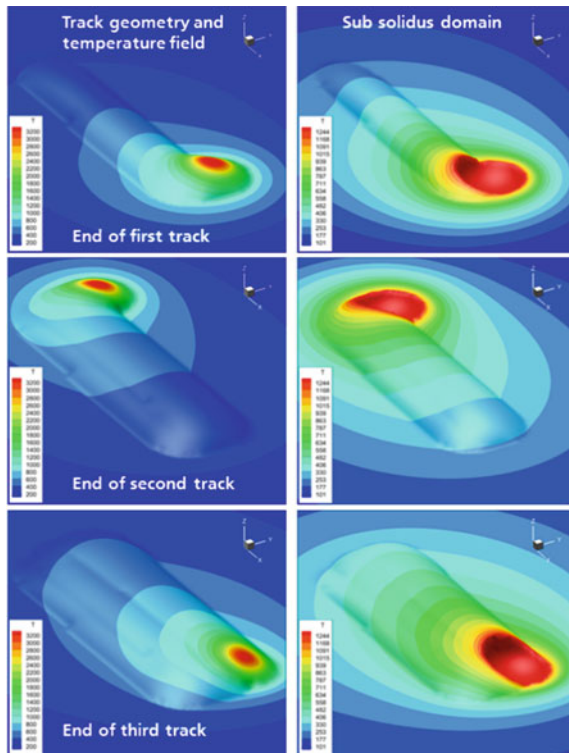
Fig. 9.18 Snapshots of the stress components σ_{xx} and σ_{yy} on the sub solidus domain at the end of the first track (Parameters see Fig. 9.17)
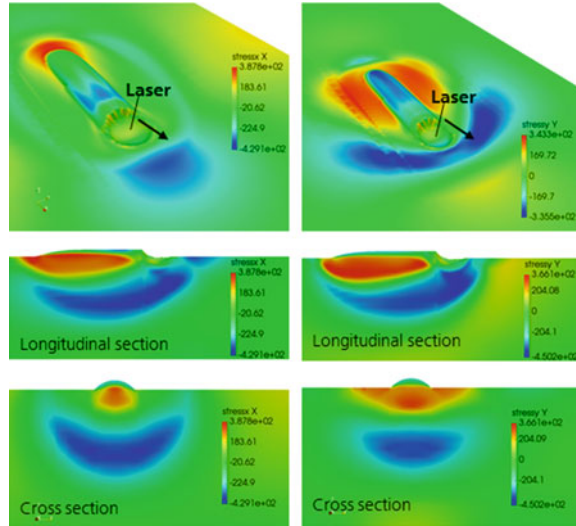
process temperature is about 3200 °C (Fig. 9.17). In front of the solid liquid interface there is a compressive stress field for the two stress components σ_{xx} and σ_{yy} (Fig. 9.18) which is continued under the track as shown by the longitudinal and cross sectional view (Fig. 9.18).

Behind the solid liquid interface a tensile stress state develops just beneath the track surface and changes to the previously mentioned compressive stress state located in deeper regions. A thin layer of the track just beneath the track surface is approximately stress free. This may be the reason for the fact that often cracks in the weld metal do not reach the surface. A comparison of the cross section for the first layer (Fig. 9.18) and after 3 tracks (Fig. 9.19) shows that the tracks 2 and 3 reduce the tensile stress state in the first layer.

The stress components σ_{xx} and σ_{yy} for the three overlapping tracks are inhomogeneous and show no symmetry concerning the position of tracks or the center of the tracks.

Figures 9.20 and 9.21 show the stress components σ_{xx} and σ_{yy} after one and two layer processing with 3 overlapping tracks for each layer but half of the powder mass used previously. A comparison of stress states after the first and the second layer shows that the maximum tensile and compressive stresses for both components σ_{xx} and σ_{yy} are increased (Figs. 9.20 and 9.21).

The comparison of the stress states after three overlapping tracks with 1 g/min and 0.5 g/min shows that the process with half of the powder feed rate,

Figures 9.20 and 9.21, results in significantly lower tensile and compressive stress states. For two layers with 0.5 g/min powder feed rate (Figs. 9.20 and 9.21) approximately, the same weld metal geometry is generated as for one layer with 3 tracks and 1 g/min powder feed rate (Figs. 9.19 and 9.22). For these two configurations the stress σ_{xx} component (Fig. 9.19) is similar but for the two layer configurations the

Fig. 9.19 Stress
components σ_{xx} and σ_{yy}
after three tracks and cooling
down to 440 °C maximum
temperature (Parameters see
Fig. 9.17, longitudinal
section in the center of the
first track)
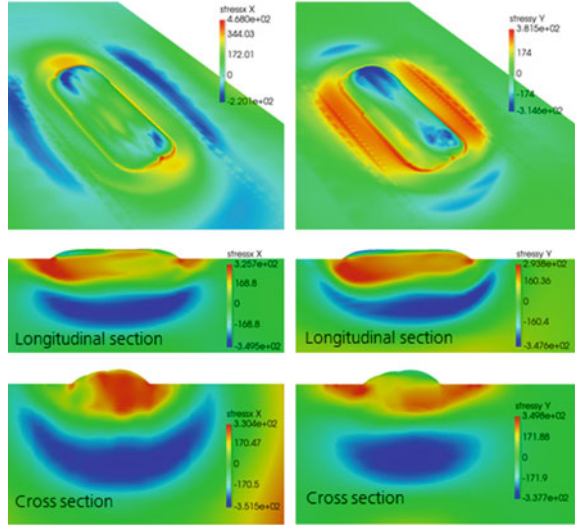
Fig. 9.20 Stress
components σ_{xx} for one and
two layers with three tracks
and cooling down to 440 °C
maximum temperature
(Parameters see Fig. 9.17,
but $m_P = 0.5$ g/min)
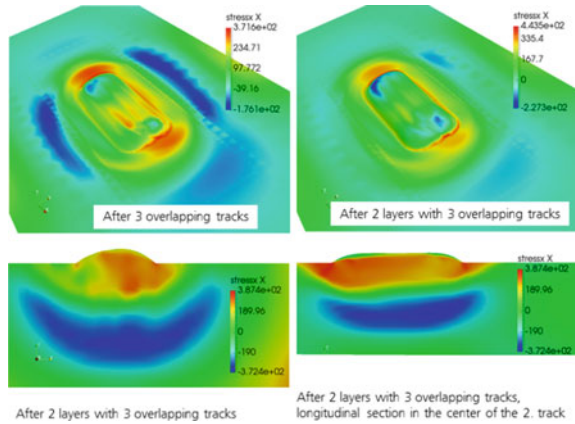
compressive stress outside the track (Fig. 9.20) is much smaller compared to the one
layer configuration

Fig. 9.21 Stress components σ_{yy} for one and two layers with three tracks and cooling down to 440 °C maximum temperature (Parameters see Fig. 9.17, but $m_P = 0.5$ g/min)
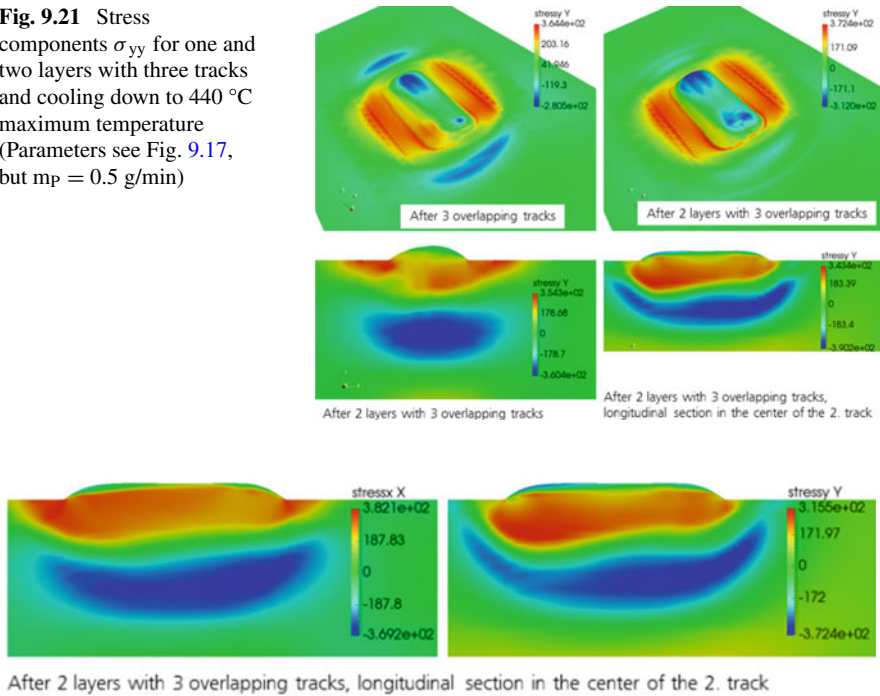
Fig. 9.22 Stress components σ_{xx} and σ_{yy} after three tracks and cooling down to 440 °C maximum temperature (Parameters see Fig. 9.17)

References

Amore S, Valenza F, Giuranno D, Novakovic R, Dalla Fontana G, Battezzati L, Ricci E (2016) Thermophysical properties of some Ni-based superalloys in the liquid state relevant for solidification processing. J Mater Sci 51(4). https://doi.org/10.1007/s10853-015-9452-8

Aggarangsi P, Beuth JL (2006) Localized preheating approaches for reducing residual stress in additive manufacturing. In: Bourell DL, Beamann JJ et al (Hrsg) Proceedings of the 17th solid freeform fabrication conference, University of Texas at Austin

Biegler M, Elsner BAM, Graf B, Rethmeier M (2020) Geometric distortion-compensation via transient numerical simulation for directed energy deposition additive manufacturing. Sci Technol Weld Join. https://doi.org/10.1080/13621718.2020.1743927

DebRoy T et al (2018) Additive manufacturing of metallic components Process, structure and properties. Prog Mater Sci 92:112–224

Decker F-J (1994) Beam distributions beyond RMS. SLAC-Pub-6684

Fathi A, Toyserkani E, Khajepour A, Durali M (2006) Prediction of melt pool depth and dilution in laser powder deposition. J Phys D 39:2613–2623

Gornak T (2013) A goal oriented survey on immersed boundary methods. Berichte des Fraunhofer ITWM, Nr. 235

Hryha E, Shvab R, Gruber H, Leicht A, Nyborg L (2018) Surface oxide state on metal powder and its changes during additive manufacturing: an overview. La Metallurgia Italiana 3:34–39

He X, Mordike BL, Pirch N, Kreutz EW (1994) Model for calculation of concentration distribution in laser alloyed pool, ECLAT '94. In: 5th European conference on laser treatment of materials. Proceedings Düsseldorf: DVS-Verlag (DVS Berichte 163), pp 260–265. ISBN: 3–87155–468–5

He X, Pirch N, Kreutz EW, Mordike BL (1995) Laser surface alloying of metallic materials. Lasers in Engineering 4:291–316

Lee YS, Farson DF (2016) Surface tension-powered build dimension control in laser additive manufacturing process. Int J Adv Manuf Technol. https://doi.org/10.1007/s00170-015-7974-5

Material Property Data Base. www.jahm.com/pages/about_mpdb.html

Ozawa S, Suzuki S, Hibiya T, Fukuyama H (2011) Influence of oxygen partial pressure on surface tension and its temperature coefficient of molten iron. J Appl Phys 109:014902

Patel CP, Patel RI (2012) 3d heat transfer analysis and numerical modeling of LENSTM process for one end stepped cylindrical wall by using stainless steel 304. Int J Mod Eng Res 2(2):1736–1740

Pinkerton AJ (2015) Advances in the modeling of laser direct metal deposition. J Laser Appl 27:S15001

Pirch N, Kreutz EW, Möller L, Gasser A, Wissenbach K (1990) Melt dynamics in surface processing with laser radiation, ECLAT '90, EMS Europ. Media Service, pp 56–61

Pirch N, Linnenbrink S, Gasser A, Wissenbach K, Poprawe R (2017) Analysis of track formation during laser metal deposition. J Laser Appl 29:022506

Pirch N, Kreutz EW, He X, Mordike B (1998) 3D modeling of heat, momentum and solute transport in laser surface alloying. In: Modelling of casting, welding and advanced solidification processes VIII, San Diego, CA

Pirch N, Linnenbrink S, Gasser A, Schleifenbaum H (2019) Laser-aided directed energy deposition of metal powder along edges. Int J Heat Mass Trans 143. Art. 118464, ISSN: 0017-9310

Pirch N, Niessen M et al (2018) Temperature field and residual stress distribution for laser metal deposition. J Laser Appl 30:032503. https://doi.org/10.2351/1.5040634

Pottlacher G, Hosaeus H, Kaschnitz E, Seifter A (2002) Thermophysical properties of solid and liquid Inconel 718 Alloy. Scand J Metall 31:161–168

Portable, Extensible Toolkit for Scientific Computation PETSc. http://www.mcs.anl.gov/petsc

Qia H, Mazumder J, Ki H (2006) Numerical simulation of heat transfer and fluid flow in coaxial laser cladding process for direct metal deposition. J Appl Phys 100:024903

Quested PN, Brooks RF, Chapman L, Morrell R, Youssef Y, Mills KC (2009) Measurement and estimation of thermophysical properties of nickel based superalloys. Mater Sci Technol 25(2):154–162

Chapter 10
LMD Filler Material Feeding Systems

Andres Gasser and **Thomas Schopphoven**

The system technology components required for LMD consist of a handling system, a laser beam source, a feed unit for the filler material (wire or powder), a processing head for laser beam shaping and focusing with integrated guidance of the filler material (wire head or powder feed nozzle), a local inert gas supply and a laser safety enclosure. To simplify the path planning for geometrically demanding tool paths, e.g. for repair and additive manufacturing, a suitable CAM module for automated path generation based on CAD data and, if necessary, a global protective gas atmosphere is additionally required. Optional are systems for process diagnosis and/or monitoring, e.g. based on non-contact measuring methods such as triangulation, spectroscopy and pyrometry. In this chapter, different approaches to material feeding are presented.

10.1 Powder Feeders

Since even small deviations in the powder mass flow can have a negative effect on the processing result, continuous and uniform powder conveying is of particular importance (Majumdar and Mann 2013; Toyserkani et al. 2005). For precise, pulsation-free powder conveying, pneumatic powder conveyors with volumetric dosing principle or with a vibrating conveyor are state-of-the-art (Bitragunta et al. 2015); see Fig. 10.1. The design of a disk powder feeder consists of a powder container, an agitator, a dosing disc and a drive in which the powder is conveyed with a conveying gas from a rotating dosing disc with a groove through a powder hose to the powder nozzle. Conveying gas volume flow and rotation speed of the dosing disc are independently

A. Gasser (✉) · T. Schopphoven
Fraunhofer Institute for Laser Technology, Steinbachstr. 15, 52074 Aachen, Germany
e-mail: andres.gasser@ilt.fraunhofer.de

T. Schopphoven
e-mail: thomas.schopphoven@ilt.fraunhofer.de
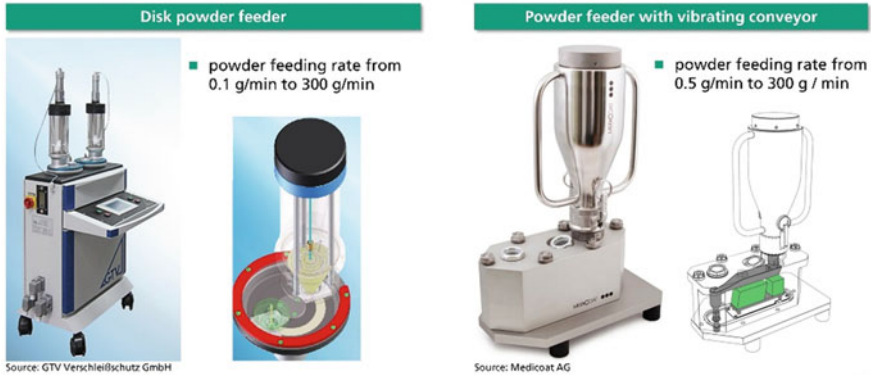
Fig. 10.1 Different powder feeding principles: rotating disk (left) and vibrating conveyor (right)

adjustable. In addition to the transport task, the conveying gas also partly fulfils the function of a protective gas, i.e. it serves to shield against oxidation at the processing point. For this reason, inert gases such as argon or helium are generally used (Gasser et al. 2010). In a powder feeder with vibrating conveyor the powder is transported through vibration from a powder hose to the outlet, where the powder is conveyed with an inert gas similar to the rotating disk.

10.2 Powder Feeding Nozzles

Depending on the LMD application, different nozzle concepts are available for the targeted material supply to the machining point: lateral, coaxial or multi-jet nozzles. Water-cooled, lateral powder nozzles are often used where accessibility is limited, e.g. repair of grooves with a large aspect ratio (ratio of groove depth/width), or for coating simple geometries such as cylinders (see Fig. 10.2, left). The powder jet cross-section area is comparatively large (approx. 2–3 mm). Furthermore, the coating result depends on the feed direction and the process equipment is complex due to the high precision requirements regarding adjustment (Majumdar and Mann 2013). In case of higher requirements regarding the accuracy of the material application or the processing of more complex geometries, powder feed nozzles are used, which enable direction-independent build-up. A distinction is made between a coaxial nozzle (see Fig. 10.2, center) and a multi-jet nozzle (see Fig. 10.2, right). With coaxial nozzles, a hollow powder-gas cone is created which encloses the laser beam. The tip of the cone is the area on which the powder-gas jet is focused (powder focus). With this concept, particularly small powder focus diameters (up to approx. 0.3–1.5 mm depending on the parameters for powder delivery) can be achieved (Majumdar and Mann 2013; Schopphoven 2020). However, tilting of the nozzle from the vertical is only possible up to about 20°.
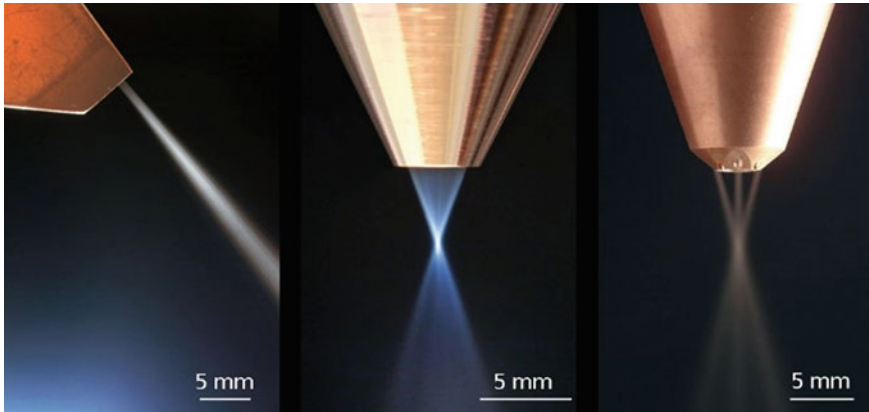
Fig. 10.2 Different nozzle variants for powder based LMD. Left: lateral powder feed nozzle, center: coaxial nozzle, right: multi-jet nozzle

At larger angles of tilt, the powder-gas jet hollow cone is distorted by the effect of gravity, resulting in an asymmetrical layer structure. With multi-jet powder feed nozzles, the influence of gravity on the powder-gas jet is less pronounced, making this concept particularly suitable for 3D machining (Majumdar and Mann 2013). Here, two or more separate powder-gas partial jets are used to achieve powder focus diameters of approx. 1.5–2.5 mm (Fraunhofer-Institut für Lasertechnik 2015). To improve the shielding at the machining point, an additional inert gas (shielding gas) flows out of the central nozzle opening in coaxial and multi-jet powder feed nozzles. The processing optics are sealed against contamination by a protective glass integrated either in the optics or in the nozzle holder. In addition to the above-mentioned powder supply nozzles, there are also lateral wide-jet nozzles for the application of material over a large area and concepts for the internal coating of pipes.

10.3   Wire Feeding

Commercial wire conveyors are used for wire feeding. These consist of different components such as the wire reel from which the wire is unwound, the straightening unit which is used to eliminate the curvature of the wire and the wire conveyor. Typical wire diameters in laser applications range from 0.4 to 1.8 mm.

Table 10.1 Advantages and disadvantages of powder and wire feeding techniques

Powder LMD	Characteristics	Wire LMD
• Atomization of nearly every metallic material is possible • Material gradients possible • MMCs possible	Availability of additive materials	• Welding material for each material class available • Wire diameter <0.6 mm for small structures not available for some materials
• Reduced material efficiency, depending on powder feeding nozzles	Material efficiency	• Nearly 100%
• Powder handling required (contamination, safety)	Contamination of the Machine	• Material loss and contamination of the machine are very low
• Wider process window • Less sensitive to deviations • Low risk of collision	Process reliability Process guidance	• Wire feeder prone to errors • Adjustment is more important • Process guidance more difficult, especially for 3D processing
• Wall thickness ≥ 0.2 mm, layer thickness ≥ 0.02 mm (EHLA)	Resolution	Smallest resolution not known yet

MMC: Metal Matrix Composite

10.4 Powder Versus Wire

Table 10.1 lists the advantages and disadvantages of each filler material feeding technique.

References

Bitragunta VS, Sparks T, Liou F (2015) Performance metric for powder feeder systems in additive manufacturing. Missouri University of Science and Technology, M.S. Missouri University of Science and Technology

Fraunhofer-Institut für Lasertechnik (2015) Jahresbericht, Dreistrahl-Pulverzufuhrdüsen mit verbesserter Performance, Aachen

Gasser A et al (2010) (2010) Maßgeschneiderte Oberflächen und Bauteile – Der Einsatz von Laserstrahlung in der Oberflächentechnik und im Rapid Manufacturing – Teil 1. Laser-Technik-J 7(4):47–53

Majumdar JD, Mann I (2013) Laser assisted fabrication of materials. Springer, Heidelberg, pp 226–230

Schopphoven T (2020) Experimentelle und modelltheoretische Untersuchungen zum Extremen Hochgeschwindigkeits-Laserauftragschweißen. Fraunhofer Verlag

Toyserkani E et al (2005) Laser cladding. CRC Press LLC, Florida, pp 68–81

Chapter 11
Extreme High-Speed Laser Material Deposition—EHLA

Thomas Schopphoven

Abstract Extreme high-speed laser material deposition, known by its German acronym EHLA, is a new variant of laser material deposition (LMD) with powdered additives. This variant's process control is unlike that of LMD, where the powder melts as it contacts the melt pool. In the EHLA process, the laser beam melts the powder above the surface of the substrate to deliver a liquid to the melt pool. Saving time otherwise required to melt the particles in the melt pool, this can increase the achievable feed rate from a few meters per minute to up to several hundred meters per minute. The EHLA process enables metal layers measured in tenths of a millimeter to be applied to large areas in a very quick, efficient way that conserves resources.

To produce a metallurgically bonded layer that is free of defects, the laser power, feed rate, powder mass flow and other process parameters have to be configured so as to apply sufficient process heat to trigger a suitable temperature-time cycle for the base material and additive. According to a heat flow balance at the surface of the melt pool, the heat flux results from the thermalized, transmitted radiation reduced by the heat flux due to the temperature equalization between the powder particles and the melt pool surface, and the heat loss due to radiation. The mathematical description of the heat balance at the melt pool surface with the fraction of transmitted radiation I_{trans}, the powder mass flow rate $\dot{m}_p$, the temperature-dependent specific heat capacity c_p, the material density ρ_p, the emissivity ε, the Stefan-Boltzmann constant σ, the temperature compensation between the temperature at the melt pool surface T_S and the mean particle temperature T_P, is given by formula 1 (Pirch et al. 2017, 2018):

$$\lambda \langle \nabla T, \vec{n} \rangle = \left\langle \vec{I}_{trans}[x(t), y(t)], \vec{n} \right\rangle - \dot{m}_p \rho_p c_p \left(T_s - T_p \right) - \varepsilon \sigma T^4 \qquad (11.1)$$

Depending on the difference between particle temperature and melt pool temperature $(T_s - T_p)$, the second term is a source or loss term for which, in the case of particle temperatures lower than the melting temperature T_M, a corresponding heat

T. Schopphoven (✉)

Fraunhofer ILT, Aachen, Germany

e-mail: thomas.schopphoven@ilt.fraunhofer.de

of fusion must be taken into account (Pirch et al. 2017). Depending on the particle temperature before entering the melt pool, two different process strategies are distinguished: the conventional LMD with particle temperatures that are predominantly lower than the melting temperature $T_p < T_M$, resp. $(T_s − T_p) > 0$, and the EHLA process, in which a large proportion of the particles should be completely melted by the laser radiation before entering the melt pool $T_p > T_M$, resp. $(T_s − T_p) < 0$ (Poprawe et al. 2018; Schopphoven et al. 2016, 2017; Schopphoven 2020).

11.1 Laser Metal Deposition LMD $(T_s − T_p) > 0$

Figure 11.1 shows the process principle of conventional LMD with a continuous coaxial powder feeding nozzle. With the conventional process, the interaction time between powder particles and laser radiation is comparatively short. Thus, the particle temperature before entering the melting pool is usually significantly lower than the melting temperature so that the particles are only completely melted in the melting pool (Lin 1999; Liu and Lin 2003; Ibarra-Medina and Pinkerton 2010). Thus, the particles are heated by the melt and the melt is heated by the transmitted laser radiation. In order to provide the latent heat for melting the powder particles, the temperature of the melt pool must be significantly higher than the melting temperature of the filler material, exist for a sufficiently long time to completely melt the particles, and be sufficiently large (melt pool depth and width) to be able to absorb the particles.

Due to the time dependence of heat conduction, a certain amount of time is required for fully melting the particles. This time is shorter the higher the melt pool temperature and/or the smaller the grain size of the powder. This results in a relatively large heat-affected zone with dimensions in the range of a few tenths to a millimeter (Zhang et al. 2012; Gasser et al. 2010; Beyer and Wissenbach 1998; Ibarra-Medina and Pinkerton 2010; Partes et al. 2005; Peyre et al. 2008).

Fig. 11.1 Schematic representation of the process principle of LMD

1	Powder nozzle	5	Deposited layer
2	Powder particles	6	Dilution zone
3	Laser beam	7	Heat-affected zone
4	Melt pool	8	Substrate

Conventional LMD
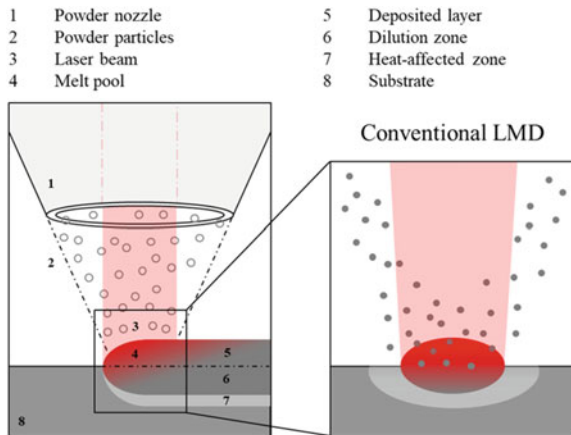
11.2 Extreme High-Speed Laser Material Deposition EHLA $(T_s - T_p) < 0$

Figure 11.2 shows the principle of the EHLA process. In the EHLA process, the powdered filler material is melted above the substrate surface and melt pool by inter-action with the laser radiation and fed into the melt pool in the liquid state (Poprawe et al. 2018; Schopphoven et al. 2016, 2017; Schopphoven 2020). This eliminates the time required for the particles to melt in the melt pool, enabling an increase in the achievable feed rates to several hundred meters per minute (Schopphoven 2020).

The molten particles are deformed or pressed against the substrate surface as a result of their kinetic energy and thermal contact is established. This can initiate a heat exchange of the particles with the solid substrate surface. The substrate is therefore heated by molten particles in addition to the energy input by the transmitted laser radiation. The temperature increase at the contact point of the particle to the substrate is time dependent due to heat conduction. The larger the particle size and temperature, the greater the temperature increase. In Fig. 11.3 left side, the temperature increase dT caused by a molten powder particle in the substrate at the contact point is shown. In Fig. 11.3 right, the time taken to reach the maximum temperature $\Delta t_{max,s}$ at the substrate surface at the contact point as a function of the particle radius and particle temperature is shown (Schopphoven 2020).

The time required to reach the maximum temperature in the substrate depends on the particle size and only to a lesser extent on the particle temperature. The larger the powder particle, the higher the temperature. A sufficient energy input for melting or the formation of a metallurgical bond at the contact point of the particles to the substrate when the substrate is not preheated can therefore only be achieved by larger particles with a particle diameter greater than about 30 µm at a temperature close to the vaporization temperature. For smaller particles, the substrate must already be sufficiently preheated by the transmitted laser radiation to locally

Fig. 11.2 Schematic representation of the process principle of EHLA

1	Powder nozzle	5	Deposited layer
2	Powder particles	6	Dilution zone
3	Laser beam	7	Heat-affected zone
4	Melt pool	8	Substrate

Temperature increase in the substrate depending
on particle radius and particle temperature

Time to reach max. temperature on the contact point of
particle and substrate
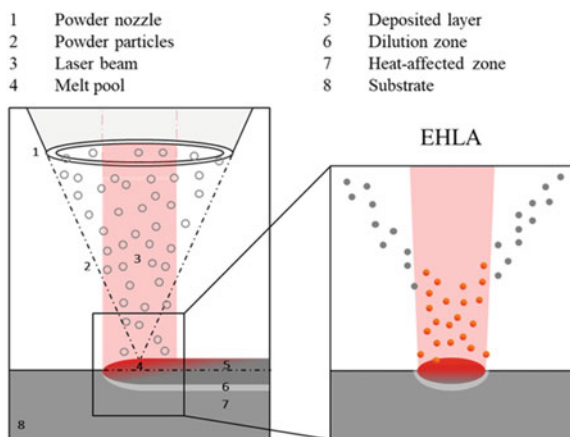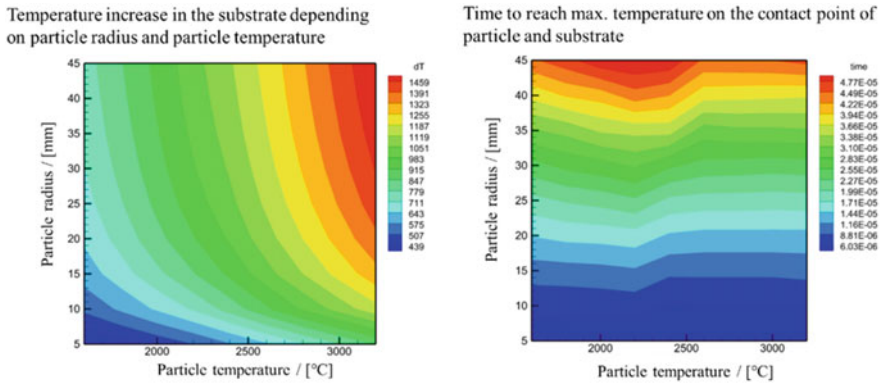
Fig. 11.3 Left: Temperature increase dT in the substrate at the contact point as a function of the particle temperature induced by a heated powder particle. Right: Time to reach the maximum temperature in the substrate at the contact point as a function of the particle temperature (Schopphoven 2020)

reach the melting temperature at the contact point. As a result, even particles that encounter the preheated substrate surface outside the melt can form a metallurgical bond and thus contribute to track formation. Therefore, unlike conventional LMD, the EHLA process does not require a specific size of the melt pool, which means that the achievable feed rate can be increased.

The developments of the EHLA process focus on rotationally symmetrical components for applications such as shafts, cylinders or brake discs. The high feed rates required, in the range of several hundred meters per minute, are realized by rotating the components. The basis for the handling system can be, for example, a conventional lathe into which the corresponding components (cf. Sect. 6.2.3.) are integrated. By adjusting the process parameters, homogeneous, high-quality, dense and fusion-bonded coatings of a variety of wear- and corrosion-resistant alloys with thicknesses of 10–250 µm can be produced by EHLA at feed rates of 25–500 m/min and area rates of up to 1000 cm^2/min. Figure 11.4 shows examples of coatings with Inconel 625 for feed rates from 25 m/min (left) to 200 m/min (right) and a powder mass flow rate of 15 g/min. For these coatings, the laser radiation was defocused so that the laser beam diameter is approximately 1 mm on the workpiece surface. The layer thicknesses produced range from approx. 250 µm at a feed rate of 25 m/min to approx. 10 µm at a feed rate of 200 m/min.

Due to the low energy input into the base material, defect-free processing of material combinations which are considered non-weldable or difficult to weld due to the formation of brittle inter-metallic phases, e.g. iron-aluminum or iron–titanium compounds or the coating of cast iron is possible. Figure 11.5, left, shows as an example the coating of a passenger car brake disc by EHLA with a thin, metallurgically bonded wear and corrosion resistant metal matrix composite coating. Brake discs are made of cast iron with graphite embedded in lamellar form. In conventional welding processes, a clearly visible mixing and heat-affected zone forms in the cast
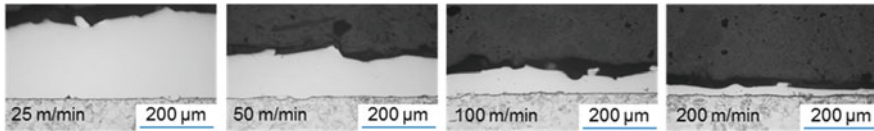
Fig. 11.4 Light microscope images of etched cross sections. Inconel 625 on 1.4301 (stainless steel) for feed rates from 25 to 200 m/min, powder mass flow rate: 15 g/min
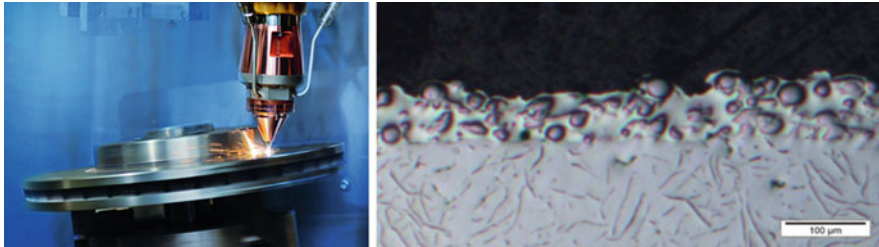
Fig. 11.5 Left: Brake discs coating with EHLA. Right: Cross-section of a coated brake disc made of EN-GJL with metal matrix composite coating consisting of 50% by volume Inconel 625 and 50% by volume tungsten carbide

iron due to the greater energy input. In the mixing zone, the lamellar carbon partially dissolves in the surrounding iron matrix and the filler metal, forming brittle phases. With EHLA, the energy input in the base material can be reduced to such an extent that the dissolution of the carbon in the base material is almost completely avoided and the formation of brittle phases is suppressed; see Fig. 11.5, right.

References

Beyer E, Wissenbach K (1998) Oberflächenbehandlung mit dem Laserstrahl. Springer, Berlin, Heidelberg. https://doi.org/10.1007/978-3-642-58726-9, S 7, pp 243–251

Gasser A et al (2010) Maßgeschneiderte Oberflächen und Bauteile – Der Einsatz von Laserstrahlung in der Oberflächentechnik und im Rapid Manufacturing – Teil 1. Laser-Technik-J 7(4):47–53

Ibarra-Medina J, Pinkerton AJ (2010) A CFD model of the laser, coaxial powder stream and substrate interaction in laser cladding. Phys Procedia 5:337–346

Lin J (1999) Temperature analysis of the powder streams in coaxial laser cladding. Opt Laser Technol 31(8):565–570

Liu CY, Lin J (2003) Thermal processes of a powder particle in coaxial laser cladding. Opt Laser Technol 35(2):81–86

Partes K (2008) Hochgeschwindigkeitsbeschichten mit dem Laserstrahl, Dissertation, Bremer Institut für Angewandte Strahltechnik, Bremen

Partes K, Seefeld T, Sepold G, Vollertsen F (2005) Increased efficiency in laser cladding by optimization of beam intensity and travel speed. In: Workshop on laser applications in Europe, vol 6157, S 615700. International Society for Optics and Photonics

Peyre P, Aubry P, Fabbro R, Neveu R, Longuet A (2008) Analytical and numerical modelling of the direct metal deposition laser process. J Phys D Appl Phys 41(2):025403

Pirch N, Linnenbrink S, Gasser A, Wissenbach K, Poprawe R (2017) Analysis of track formation during laser metal deposition. J Laser Appl 29(2):022506

Pirch N, Niessen M, Linnenbrink S, Schopphoven T, Gasser A, Poprawe R, Schulz W (2018) Temperature field and residual stress distribution for laser metal deposition. J Laser Appl 30(3):032503

Poprawe R, Hinke C, Meiners W, Eibl F, Zarei O, Voshage M, Willenborg E et al (2018) Digital photonic production along the lines of industry 4.0. In: Laser applications in microelectronic and optoelectronic manufacturing (LAMOM) XXIII, vol 10519. International Society for Optics and Photonics, p 1051907

Schopphoven T, Gasser A, Wissenbach K, Poprawe R (2016) Investigations on ultra-high-speed laser material deposition as alternative for hard chrome plating and thermal spraying. J Laser Appl 28(2):022501

Schopphoven T, Gasser A, Backes G (2017) EHLA: extreme high-speed laser material deposition: economical and effective protection against corrosion and wear. Laser Tech J 14(4):26–29

Schopphoven T (2020) Experimentelle und modelltheoretische Untersuchungen zum Extremen Hochgeschwindigkeits-Laserauftragschweißen. Fraunhofer Verlag

Zhang K et al (2012) Influences of processing parameters on dilution ratio of laser cladding layer during laser metal deposition shaping. Adv Mater Res 549:785–789

Chapter 12
Wire Laser Metal Deposition

Check for
updates

Jana Kelbassa and Andres Gasser

Laser Metal Deposition (LMD) operates using both, powder and wire additives. The last one present a series of advantages, as lower price per kilogram, lower porosity on the deposited material, lower health risks for users and lower contamination of the LMD machine. For some applications, the overspray that occurs in powder LMD (powder not used for the process, powder efficiencies between 50 and 90%) and the fluctuating quality of the available powders (contaminations/pore inclusions) are exclusion criteria.

An alternative is to use wire-shaped filler materials. According to the state of the art, the wire is fed laterally (Klocke et al. 2017) so that direction-independent processing is not possible (Fig. 12.1, left). However, the complexity of the parts and the increasing use of this process in additive manufacturing requires direction-independence. Processing heads with coaxial wire feed allow a direction-independent processing (Fig. 12.1, right).

A closed annularly shaped laser beam surrounding the wire is one of the distinguishing features of the coaxial wire LMD processing head. The laser beam and wire are arranged coaxially to each other, with the wire being fed through the inside of an annularly shaped laser beam without any shadowing (Fig. 12.2). The annularly shaped intensity profile leads to a significant improvement in wire based LMD. Furthermore, in contrast to lateral wire feeding, two substantial technological advantages, namely the independence of the feed direction and the processing of complex 3D geometries can be identified.

The processing head can be integrated into cartesian or robotic systems (Fig. 12.3) and can be operated with industrially available laser beam sources and wire feeders. iron, aluminum, nickel and titanium-based alloys can be processed. To achieve higher deposition rates, arc or hot wire can be integrated in addition to the laser beam. The

J. Kelbassa (✉) · A. Gasser
Fraunhofer ILT, Aachen, Germany
e-mail: jana.kelbassa@ilt.fraunhofer.de
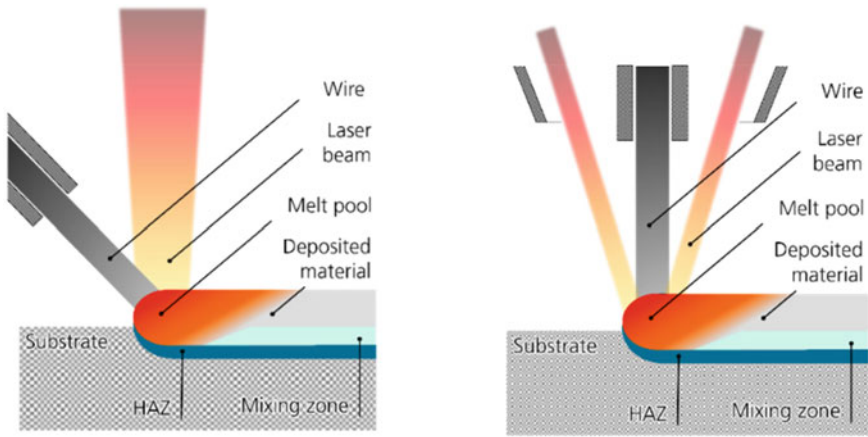
Fig. 12.1 Schematic of the wire LMD processes (left: lateral wire feeding, right: coaxial wire feeding)
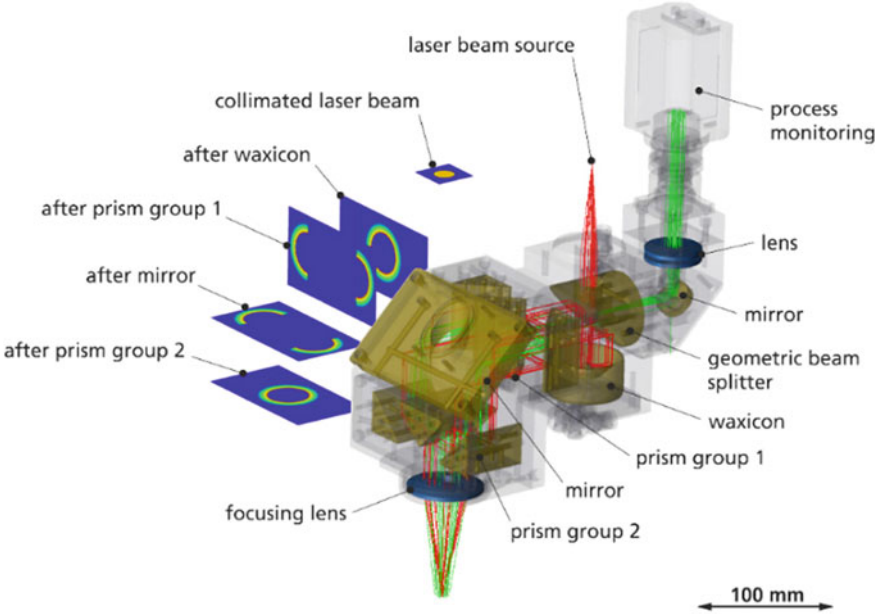
Fig. 12.2 Schematic of the laser beam shaping in the coaxial wire feed processing head
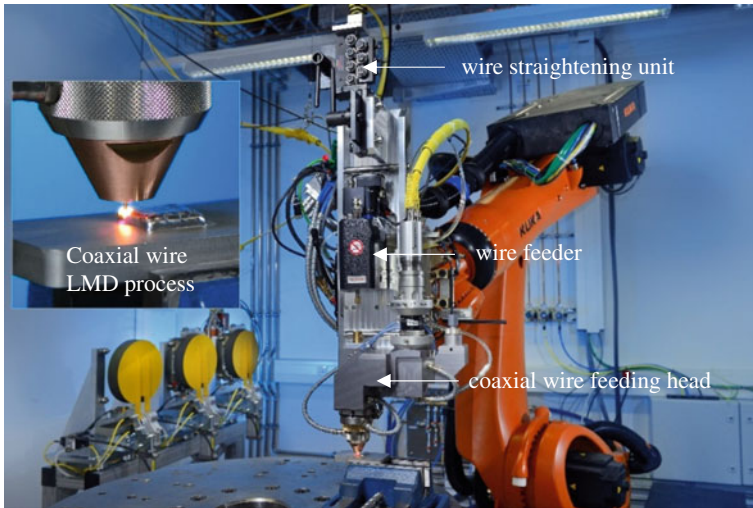
Fig. 12.3 Coaxial wire feed processing head integrated in a robotic system

Fig. 12.4 Cross sections of single tracks out of Inconel 718 produced with different laser power P_L

system technology is also suitable for direction independent welding and soldering processes.

Depending on the wire diameter, the additively producible structures range from approx. 1 mm to several millimeters and the production of near net shape components is possible.

Figure 12.4 shows 3 cross sections of deposited tracks out of Inconel 718. Well bonded layers with low dilution can be achieved. With increasing laser power, the dilution increases. Figure 12.5 shows a deposited rectangular parallelepiped out of Ti64 and a cross section.

Also, complex shapes can be applied with the coaxial wire LMD technology, as shown in Fig. 12.6. The material and geometry simulate a feature that can be additively applied to a turbine casing.
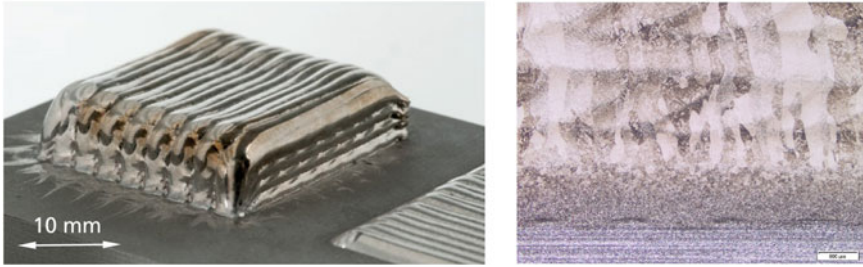
Fig. 12.5 Parallelepiped out of Ti64 and cross section

Fig. 12.6 Part out of Inconel 718 built with the coaxial wire LMD process

Reference

Klocke F, Arntz K, Klingbeil N, Schulz M (2017) Wire-based laser metal deposition for additive manufacturing of TiAl6V4: basic investigations of microstructure and mechanical properties from build up parts. In: Proceedings of SPIE 10095, Laser 3D manufacturing IV, vol 100950U. https://doi.org/10.1117/12.2251336

Chapter 13
Hybrid AM and Process Chains

Jan Bremer and Andres Gasser

The concept of Hybrid Additive Manufacturing (Hybrid AM) finds a broad definition throughout different applications. For metal-based additive manufacturing the concept often refers to a combination of material deposition, e.g. through Laser Material Deposition (LMD) or other Directed Energy Deposition (DED) processes such as wire arc deposition or cold spray, with machining through milling. Multiple manufacturers have introduced machines implementing both milling and deposition processes based on different technologies (Andreas Gebhardt 2017; Xichun Luo and Yi Qin 2018).

Combinations of additive processes and other processing steps outside of an integrated machine system are also commonly considered as Hybrid AM. Such combinations can, for example, be multiple additive processes (Shin et al. 2018), conventionally manufactured precursors onto which features are added (Jan Bremer 2018) or serial processing steps similar to the integrated approach in multiple machines. Due to the wide range of combinable processes in such process chains (Michael P. Sealy et al. 2017), automation approaches are commonly customized to a selected range of processing steps and component types.

Benefits of Hybrid Additive Manufacturing range from lower cost due to smaller required raw components and reduced machining efforts to the possibility of local material combinations. Manufacturing components using Hybrid AM, especially to implement component features which differentiate otherwise identical components, also offers additional supply chain benefits (Fig. 13.1).

Flexible processing using both highly efficient conventional processes and additive processes where best suited permits a significantly reduced number of part variants during initial processing, reducing investment and logistics cost. As components are differentiated at a later stage of the process chain, lead times can be reduced and variant complexity can be reduced throughout the supply chain.

J. Bremer · A. Gasser (✉)

Additive Manufacturing, Hybrid AM and Process Chains, Fraunhofer ILT, Aachen, Germany
e-mail: andres.gasser@ilt.fraunhofer.de
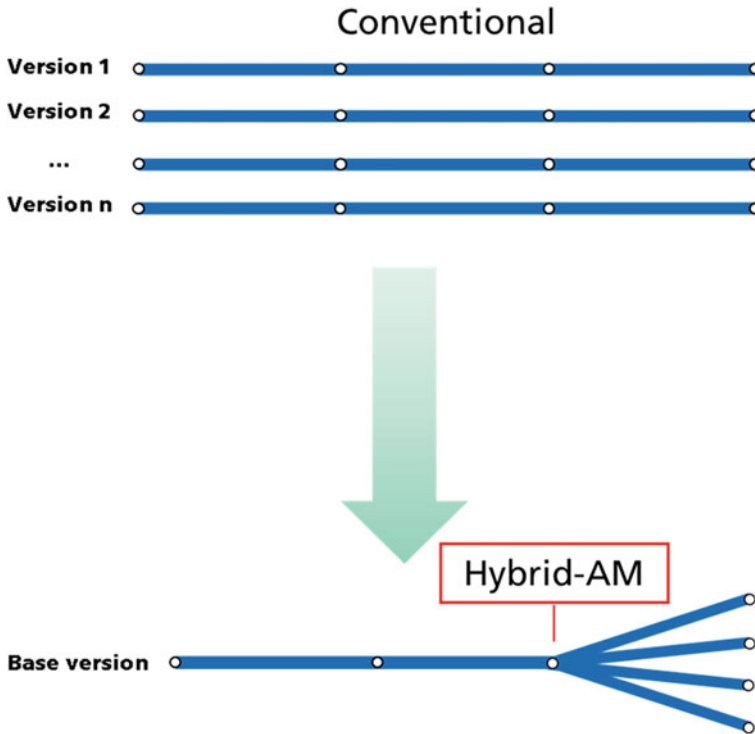
Fig. 13.1 Principle of supply chain impacts through hybrid additive manufacturing

A wide range of technologies applicable in Hybrid Additive Manufacturing originate from the currently well-established applications of coating and repair using LMD. In different applications the combination of different processing steps to re-establish original performance is a regular occurrence, as for example in turbine blade repair. (Daniel Schraknepper and Marco Göbel 2015) In coating applications material combinations are used to achieve locally differing material properties (Fig. 13.2).

Due to the characteristics of welding processes and, in repair applications, the unknown condition of individual components, robustness of all processes along the process chain is required to achieve automation. So-called adaptive processes are enablers to achieve robust automated processes. This is commonly implemented through implementation of external (Jian Gao et al. 2005) or machine-integrated sensors (Bremer, Claus 1988) which measure component geometry and other properties to automatically adapt CNC programs to the individual component to be processed. Systems to adapt both the additive as well as other processes such as milling and grinding are available, mostly originating from repair applications. Solutions for stabilization of the individual processes through closed-loop control are also commonly applied (Gujin Bi 2004).

Fig. 13.2 Exemplary process chain for automated adaptive turbine blade repair (TurPro 2013)

Research and development towards industrial implementation of Hybrid AM can be subdivided into two approaches regarding integration in process chains: horizontal process integration and vertical process integration, with horizontal process integration focusing on the implementation of multiple processing steps into one solution. Vertical integration of processes in Hybrid AM process chains focusses on the development of process solutions which can be integrated horizontally in a flexible manner through robust processes and suitable interfaces to neighboring processes both on physical and data layers.

Integration of the horizontal LMD-based Hybrid AM process chain into a single machine was investigated in the EU-funded research Project HyProCell (Juan Carlos Pereira et al. 2020).

Resulting benefits are high possible levels of automation, simpler component handling as well as a compact footprint for a given process chain. Integration of LMD processing, geometric measurement as well as machining capabilities and suitable software solutions in a commercial machine tool was demonstrated. A turbocharger component was manufactured using Hybrid AM. Based on a turned base ring, guide vanes were additively built using LMD. After machining of the top surface of the vanes, a laser-cut top ring was welded onto the component using laser-based heat transmission welding, completing the part. The component as well as the machine used in the project are depicted below (Fig. 13.3).

Integration of additive processes into distributed horizontal process chains for Hybrid AM requires high levels of robustness to permit high processing quality irrespective of variances from previous processes. Examples of such influences can be differing raw material quality or geometric deviations from nominal shape of the component to be processed.
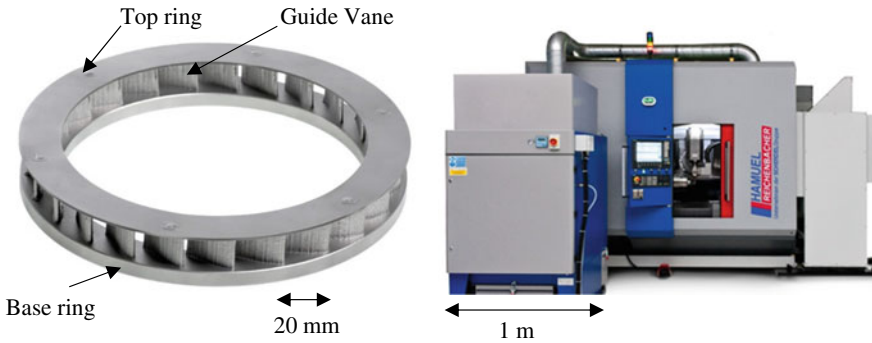
Fig. 13.3 LMD-based Hybrid AM component from HYPROCELL project (left) (Jan Bremer 2018), Machine used for horizontal process chain integration (right) (Juan Carlos Pereira et al. 2020)

Robust and cost-efficient vertical integration and automation of LMD processes was investigated in the BMBF-funded ProLMD project using robot-based system technology (Günter Neumann et al. 2021). Aspects such as raw material quality, effects of different shielding gas concepts, different robotic cell configurations and a digital process chain based on machine-integrated measurement of component geometry data were investigated.

Process stability and build quality in LMD processing is significantly influenced by geometric process parameters such as a correct working distance between laser beam, powder or wire nozzle and the substrate. By implementing machine-integrated component measurements and a toolpath planning algorithm based on measurement data of the component precise adherence to the geometrical process parameters can be ensured, increasing process stability and weld quality. Geometric data acquisition with a laser line scanner in one of the robotic LMD cells used in the ProLMD project is shown in Fig. 13.4.

Added process stability and geometric precision of the LMD-built volume were achieved by developing and implementing an intermittent geometry control approach in the ProLMD software package. Suitable process windows were investigated for layer height variation over feed rate variation with good weld quality. System-integrated geometry acquisition was used to automatically calculate localized feed rate adaption. Verification of the approach was conducted on a flat substrate with milled grooves of different depth and a cuboid target geometry. Resulting specimens and geometry measurements are depicted in Fig. 13.5.

Implementation of the vertically integrated Hybrid AM process chain was verified on different robotic cells with varying payload, size, shielding gas concepts and cost. Local component modification, reinforcement and repair was demonstrated on components ranging from tooling through aerospace structures to aeroengine components. Materials ranging from Iron- and Nickel-base alloys to Titanium alloys were processed.
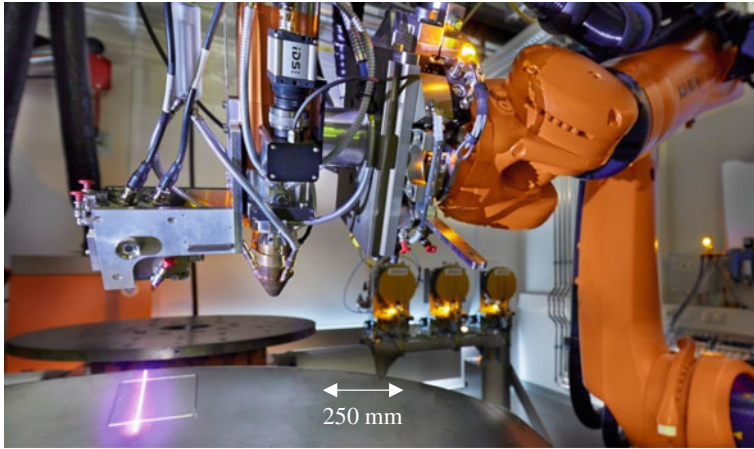
Fig. 13.4 Robotic LMD cell during geometric measurement of welded layer and substrate for calculation of tool paths for the next layer. *Copyright* Fraunhofer ILT / Ralf Baumgarten
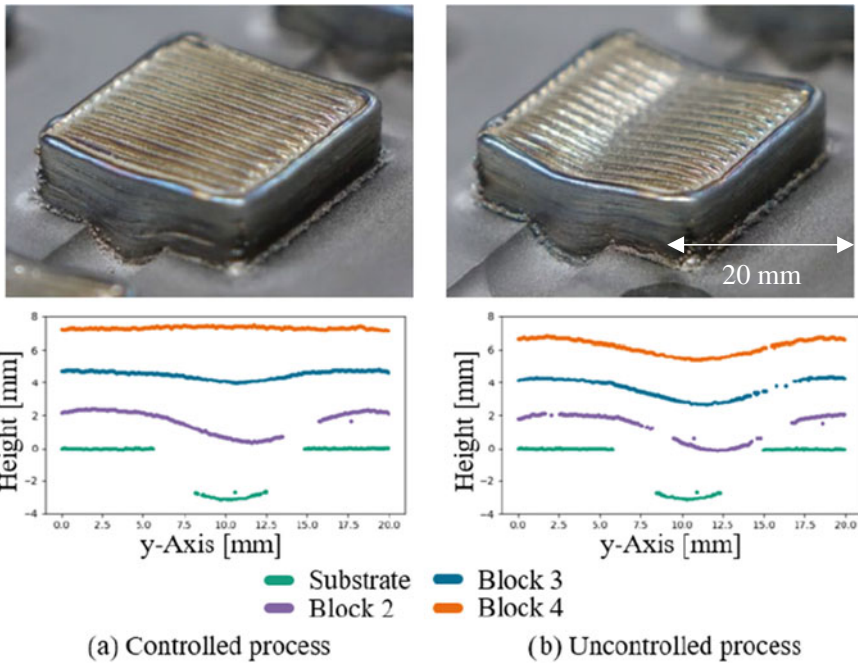
Fig. 13.5 LMD specimens built using geometric intermittent process adaption and measurement of resulting geometries during built (left) and without adaption (right) (Jan Bremer et al. 2020)

Fig. 13.6 Aerospace component with locally reinforced areas manufactured by Hybrid AM (Günter Neumann et al. 2021)

An example for such an application of local reinforcements to form openings on an aeroengine component is shown in Fig. 13.6 next to conventionally manufactured inspection openings. Through utilizing local build-up with Hybrid AM on forged blanks and subsequent post-machining cost savings of 13 to 26% were projected for such aerospace applications depending on process deposition rates (Günter Neumann et al. 2021).

Increasing innovation in process automation and digitalization as well as control and sensorics are enablers to more time- and cost-efficient approaches toward Hybrid AM. Robust processes and integration of suitable interfaces on component, process and data level permit efficient and reconfigurable process chains. A growing range of industrially implemented examples of Hybrid AM is enabled by successful past and ongoing advances in research and development. Significant time and cost savings can be realized while giving increasing design and manufacturing freedom with significantly shortened lead times for derived variant manufacturing.

References

Andreas Gebhardt (2017) Additive Fertigungsverfahren: Additive Manufacturing und 3D-Drucken für Prototyping - Tooling – Produktion, Carl Hanser Verlag GmbH Co KG, 10.07.2017

Bremer Claus (1998) Automatic blade repair system based on reverse engineering strategies. American Society of Mechanical Engineers (Paper)

Daniel Schraknepper and Marco Göbel (2015) Fachlicher Abschlussbericht Aachener Innovationscluster AdaM – Adaptive Produktion für Ressourceneffizienz in Energie und Mobilität

Gujin Bi (2004) Identifizierung und Qualifizierung von prozessrelevanten Kenngrößen zur Überwachung und Regelung beim Laserauftragschweißen, Shaker Verlag

Günter Neumann et al. (2021) Prozess- und Systemtechnik zur Hybrid-Fertigung großer Bauteile mit dem Laser-Material-Deposition-Verfahren - Ergebnisbericht des BMBF Verbundprojektes ProLMD, Fraunhofer Publica, https://doi.org/10.24406/ilt-n-633180

Jan Bremer (2018) Overview of current research topics in (Hybrid-) Additive Manufacturing using LMD. International Laser Technology Congress Aachen

Jan Bremer et al. (2020) Adaptive manufacturing with laser material deposition using intermittent machine-integrated line scanning, CAMX Virtual Conference Proceedings, September 21–24

Jian Gao et al. (2005) Investigation of a 3D non-contact system based blade repair integration system. Aircraft Eng Aerospace Techn

Juan Carlos Pereira et al. (2020) Final Report HYPROCELL project - Development and validation of integrated multiprocess HYbrid PROduction CELLs for rapid individualized laser-based production, V8.00

Michael P Sealy et al. (2017) Hybrid processes in additive manufacturing. J Manuf Sci Eng 140(6)

TurPro (2013) – Fraunhofer-Innovationscluster Integrative Produktionstechnik für energieeffiziente Turbomaschinen, Fraunhofer ILT und Fraunhofer IPT, https://www.youtube.com/watch?v=2wmXVu5718Q

Xichun Luo and Yi Qin (2018) Hybrid Machining: Theory, Methods, and Case Studies, Academic Press, 27.06.2018

You Shin et al. (2018) Hybrid additive manufacturing of Al-Ti6Al4V functionally graded materials with selective laser melting and cold spraying. J Mater Proc Tech 255:650–655

Chapter 14
LMD Applications

Andres Gasser

Today's most important applications for LMD are the repair, wear and corrosion protection of high added value, high precision machine components. For serial production LMD is used for the cladding of valves and valve seats and the wear protection of oil drilling, agricultural, mining and other components. (Schutzauftrag xxxx; http xxxx; Eimann and Drach 2000). Emerging applications are in the area of Additive Manufacturing.

14.1 Moulds and Dyes

LMD is a well-established technique for the repair and modification of plastic injection moulds (Eiman and Drach 2000; Eiman et al. 2003). Also, the repair and modification of dyes for metal sheet forming is well established (Nagel 2004).

LMD allows the repair of critical areas also near polished or grained (chemically etched) surfaces. Figure 14.1 shows the repair of a car lamp mould. This mould is worn out in the front area, and a layer of 0.15 mm thickness has been applied. No damage was observed even in the proximity of the polished surface. This type of repair cannot be performed with any other welding technique (e.g. TIG welding).

A. Gasser (✉)
Fraunhofer ILT, Aachen, Germany
e-mail: andres.gasser@ilt.fraunhofer.de

Fig. 14.1 Repair of worn
out areas in a car lamp mould

Laser deposited area

2 cm
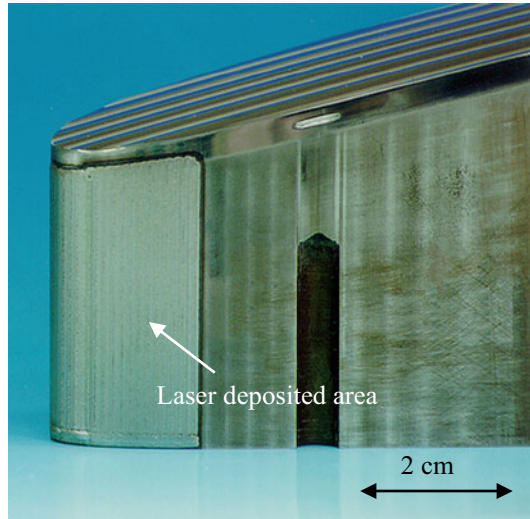
14.2 Modification of Moulds

LMD offers the unique property to add material on sensitive surfaces and materials
without damaging them. This can be used to add material to high added valued
components during the manufacturing process, especially when design changes are
required. Short term changes during the manufacturing of moulds usually lead to time
consuming repair processes. With LMD the missing material can be added precisely.
Also, moulds and inserts can be modified when the plastic injection process requires a
change in the design of the mould. Figure 14.2 shows an example for the modification
of a car lamp mould. A several mm thick layer has been applied onto the top of the
mould.

Fig. 14.2 Modification of a
car lamp mould
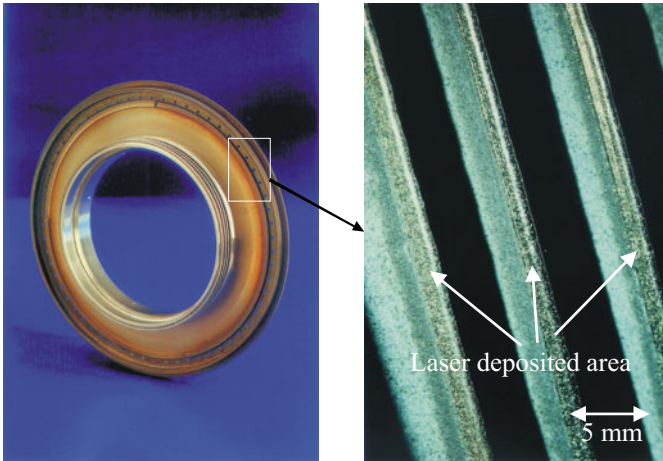
Fig. 14.3   Repairing of rotating seals of a cooling plate

14.3   Turbine Components for Aero Engines and Power Generation

The refurbishment of turbine components is performed with conventional techniques like TIG welding (Tungsten-Inert-Gas-Welding), PTA welding and thermal spraying. LMD has been established for the repair of aero engine components and offers several advantages like higher process speeds, near-net-shape deposition and low heat input (Gasser et al. 2007). Figure 14.3 shows the repair of rotating seals on a cooling plate from a helicopter. Multiple layers are applied on the sealing geometry with a width of 0.6 mm.

14.4   Gears and Axes

In the areas of petrochemical industry, offshore drilling, shipping, storage and trans-shipment, sugar industry, steel and energy industry machine components like shafts, gears, gearboxes and drilling components are being repaired or protected by means of LMD. Figure 14.4 shows a repaired axis of a centrifuge and Fig. 14.5 the repair process during LMD of a gear component.
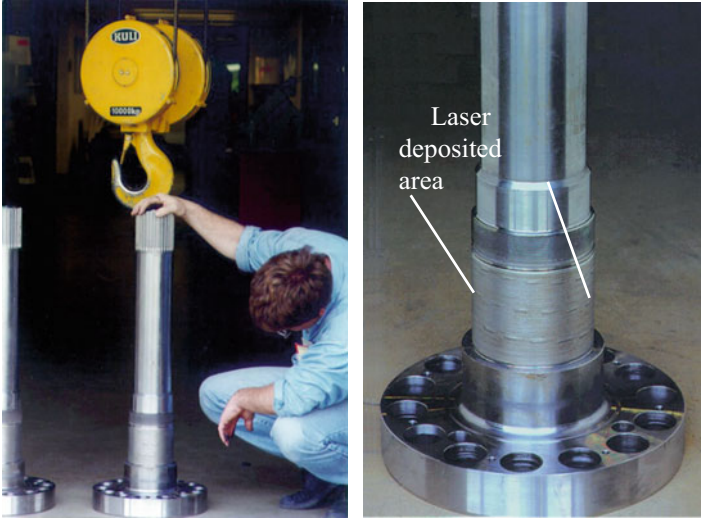
Fig. 14.4 Repair of centrifuge axis
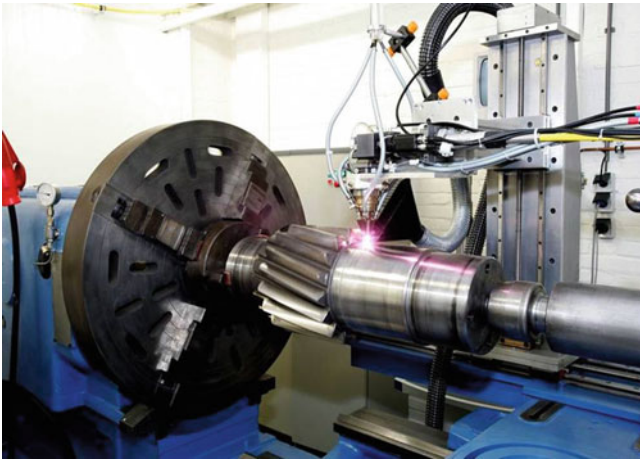
Fig. 14.5 Repair of gear components with LMD (*Source* Stork Gears and Services)

14.5 Micro Laser Metal Deposition

Laser offer the possibility to produce LMD structures below 10 μm thickness and widths below 100 μm. In the last years much effort has been made to downscale the LMD process. For such structures, powder grain sizes in the range of 10 μm have to be fed and suited powder nozzles have been built. Possible application areas for Micro LMD are medical science, electronic industry and energy sector as shown in
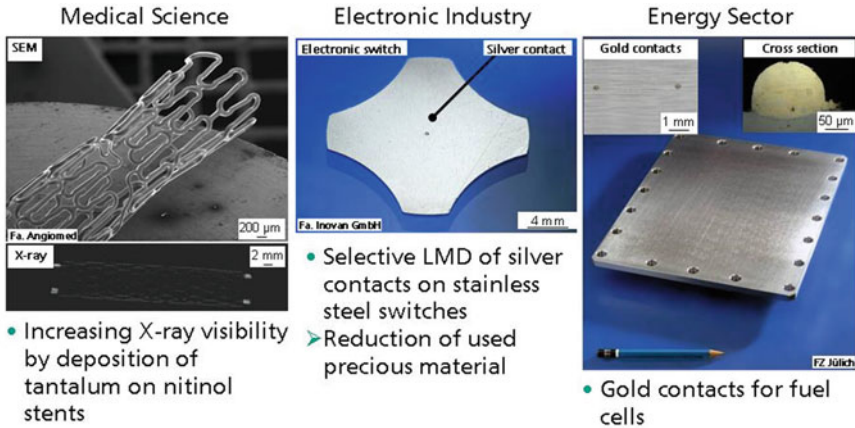
Fig. 14.6 Micro LMD applications

Fig. 14.6. These applications include the increasing of the X-ray visibility of stents and the selective deposition of silver and gold contacts for switches and fuel cells.

14.6 Laser Metal Deposition in AM

By applying single deposited tracks or layers one on top of the other three-dimensional structures can be achieved. This can be used for example for repairing turbine blades or even to build up completely new blades. Figure 14.7 shows blades that have been deposited on a shaft directly from CAD data. Recent development includes the implementation suited tools into LMD machines for closed chain repair and build-up based on CAD data or data acquired from digitalization.

As second example for the build-up of a complete component is shown in Fig. 14.8, where a mould insert out of tool steel is built based on CAD data.

14.7 Extreme High-Speed Laser Metal Deposition EHLA

Main applications for the EHLA process are axes, hydraulic cylinders, oil-drilling components and brake discs. One example of a cladded hydraulic cylinder is shown in Fig. 14.9. Inconel 625, a corrosion resistant material, has been applied.

20 mm
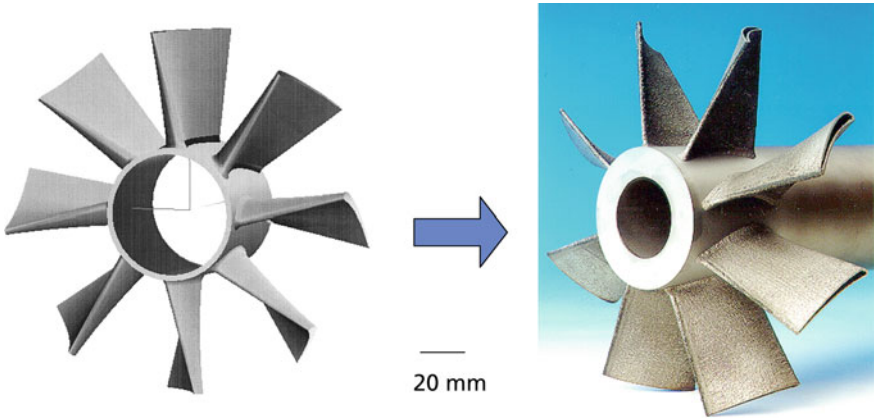
Fig. 14.7 Deposition of blades on a shaft starting from CAD data
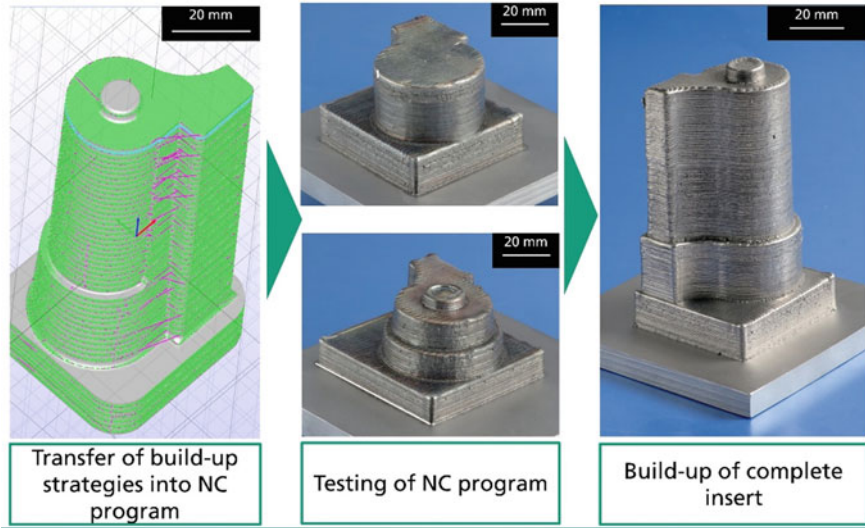
Fig. 14.8 Deposition of mould insert out of tool steel based on CAD data

Fig. 14.9 Hydraulic cylinder coated with the EHLA process (Inconel 625). *Source* IHC VREMAC Cylinders

References

Eimann K, Drach M (2000) Instandsetzung von Werkzeugen mit Laserstrahlung, Tagungsband Aachener Kolloquium Lasertechnik AKL 2000, pp 29–31

Eimann K, Drach M, Wissenbach K, Gasser A (September 2003) Lasereinsatz im Werkzeug- und Formenbau, In: Proceedings Stuttgarter Lasertage, pp 25–26

Gasser A, Wissenbach K, Kelbassa I, Backes G (2007) Aero engine repair. Ind Laser Solut, 15–20

https://www.technogenia.com/en/industries/oil-and-gas-drilling/

Kawasaki M et al. (1992) The laser cladding application at automotive parts in Toyota. In: Proceedings ISATA 92

Nagel J (2004) Laserhärten und Laser-Pulver-Auftragschweißen von Umformwerkzeugen. Tagungsband Aachener Kolloquium Lasertechnik AKL 295–305:2004

Mission Protect, Laser Community, The Laser Magazine from TRUMPF, 03/07

Chapter 15
Materials for Additive Manufacturing

Andreas Weisheit

15.1 Introduction

Today, the term additive manufacturing, also known as 3D printing, covers numerous processes. For metallic materials, the laser-based processes powder bed fusion (Laser Powder Bed Fusion, LPBF) and with powder or wire feed nozzle (Direct Energy Deposition - Laser Beam, DED-LB, also known as Laser Material Deposition, LMD) are the most important, which are also summarized as Laser Additive Manufacturing (LAM). In both processes the material is completely melted and built up layer by layer to form a component. This tool-less manufacturing offers a high degree of individualization and (almost) unlimited design possibilities. LAM has undergone rapid development over the last two decades. In the beginning, only prototypes were produced using this manufacturing process. This was quickly followed by the production of unique (e.g. implants) and individual parts (e.g. tool inserts). Today the process is moving towards series production of up to several ten thousand parts per year. Research and industry are currently working intensively on the necessary prerequisites for this, such as increasing productivity, quality assurance and integration into process chains. While there is a wide range of adapted alloys for established manufacturing processes such as casting or forging, the selection of alloys for LAM is still small and, in addition, almost exclusively limited to alloys developed for other manufacturing processes. This chapter will high light the specific conditions of LAM regarding the processing of metal based materials, summarizes the state-of-the-art of available alloys and will give an outlook on material development for LAM.

A. Weisheit (✉)
Fraunhofer ILT, Aachen, Germany
e-mail: andreas.weisheit@ilt.fraunhofer.de

15.2 Characteristics of LAM

The way materials are deposited during LAM is quite different from conventional manufacturing methods e.g. in terms of heating and quenching rates, melting conditions, exposure to gases in the environment. This creates profound challenges, since not every material lends itself easily to LAM, but it also offers opportunities: LAM can for example be employed to synthesize new, previously inaccessible materials owing to the high quenching rates that can be achieved (e.g. metallic glasses, massively oversaturated solid solutions, high entropy alloys). The unique set of requirements associated with the LAM process need to be taken into account in order to identify materials that can be easily processed by LAM and show good properties after consolidation.

From a basic materials science perspective, there are two main characteristics of the LAM processes, which on the one hand have to be considered when conventional alloys are processed and on the other hand enable material optimization and material design that go beyond what is possible with conventional manufacturing techniques:

- **Local metallurgy in combination with high cooling rates**: LAM involves rapid melting and solidification with only a small melt pool volume existing at any time during the manufacturing process. Typical cooling rates encountered in LAM range from 10^3 to 10^8 Ks^{-1}. Such high cooling rates lead to rapid solidification of the melt, yielding beneficial, very fine solidification microstructures, in contrast to the usually coarse casting microstructures obtained after the first step of conventional processing. Essentially, the melt pool in LAM is the equivalent of the crucible in conventional casting: alloying, solidification and other reactions such as precipitation occur on a local scale. The combination of high cooling rates and local metallurgy enables synthesis of materials that are not accessible by conventional casting. Rapid solidification allows quenching-in of microstructures that are far from thermodynamic equilibrium, e.g. supersaturated solid solutions or even metallic glasses. On the other hand high cooling rates lead to high thermal stresses, which can cause cracking. Furthermore, the heat dissipation into the solid material is strongly directed which leads for many alloys to directional grain growth and crystallographic orientation resulting in anisotropic properties.
- **Unique thermal history**: The time–temperature profile experienced by a part produced by LAM is very different from the one produced by conventional manufacturing. During LPBF, for example, a thin powder layer is melted by the laser beam. When the laser beam moves away, the material in the melt pool cools down at very high cooling rates due to rapid heat conduction into the underlying layers and the substrate material. During the deposition of subsequent layers, the consolidated material gets re-heated by the laser beam. It experiences a series of temperature pulse cycles up to temperatures close to the melting point (decaying in intensity with every additional layer). This "Intrinsic Heat Treatment" (IHT) is unlike any annealing conducted in conventional processing. On the one hand it can be exploited e.g. for in-situ precipitation hardening. On the other hand it can

lead to a locally and globally inhomogeneous microstructure of materials which are very sensitive to solid state phase transformation, e.g. heat treatable steel.

15.3   Alloys for LAM

15.3.1   Conventional Alloys for LAM

Conventional alloys are those that were originally developed for other manufacturing processes but are also used in additive manufacturing. In principle, the alloys that are best suited are those that are also conventionally processed by metallurgical processes, i.e. by casting or deposition welding.

However, despite whether a cast or wrought alloy is considered to be used in LAM the choice is limited, among other things, by the high cooling rates in LAM, which lead to crack formation in many of these materials. A distinction is made between stress cracks and hot cracks. Stress cracks are caused by induced residual tensile stresses, which in turn can result from local temperature gradients, shrinkage processes and phase transformations. If the material exhibits insufficient ductility and the stresses exceed the rupture stress, a crack occurs. Brittle materials are therefore particularly susceptible to this type of crack. By adjustment of the process parameters towards lower cooling rates or a preheating the risk of stress cracks can be reduced. The second type of cracks are so-called hot cracks (Carter et al. 2012). Here again a distinction is made between solidification cracks, which occur in the solidifying volume and liquation cracks which occur in the heat affected zone (HAZ). The mushy, two-phase liquid–solid region experiences tensile stresses and the high fraction of solid present (typically $f_\mathrm{solid} > 0.9$) restricts the flow of liquid metal to backfill the interdendritic regions. Solidification crack formation is promoted by a wide solidification range, micro segregation leading to reduction of the solidification temperature of the residual melt in between the grains and a high viscosity of the molten material. Liquation cracking occurs within the HAZ adjacent to the deposited layer as a consequence of local dissolution of low melting point grain boundary phases. A liquid film forms on grain boundaries within the HAZ, which fails under the tensile thermal stresses.

Another type of crack are strain age cracks, which occur particularly in nickel super alloys (see below). Strain age cracking occurs not during processing but during post weld heat treatment or high temperature service. The cracks are characterized by intergranular micro cracking as a consequence of precipitation and hardening of the alloy during thermal exposure and transfer of solidification strains onto the grain boundaries.

Transformation hardening materials such as carbon steels are also critical in processing. Here, brittle martensite is formed in every layer. As a result the usually high induced thermal stresses lead to stress cracks. Furthermore, tempering caused by the heat input of subsequently deposited layers create an inhomogeneous microstructure.

Physical properties can also restrict processing. A high reflectivity for laser radiation and a high thermal conductivity make it difficult to produce dense volumes, since only a small part of the laser energy is absorbed and the heat quickly dissipates into the solid volume. An example is pure copper (Colopi et al. 2019). Elements with a low vaporization temperature like Mg, Zn or Mn can cause also problems, namely burn-off (change in the final chemical composition) and pore formation.

The oxygen affinity is also an important criterion, mainly for DED, where only the melt pool is shielded from the surrounding atmosphere and the solidified but still hot material is exposed to air. This can result in significant formation of oxide layers which can contaminate the following layers either in form of entrapped oxide particles or solution of oxygen in the matrix.

In the following, the most important classes of alloys are discussed and some alloys are mentioned which are used in industry or at least are well investigated. In addition, reference is made to literature that provides a more or less broad overview of materials used or under investigation (Aversa et al. 2019; Bajaj et al. 2020; Bourell et al. 2017; Herzog et al. 2016; Ngo et al. 2018; Lewandowski and Seifi 2016; Zadi-Maad and Basuki 2018; Zhang et al. 2019a).

Only in individual cases will the two variants of LAM be dealt with. However, these differ not only in the way the filler material is applied, but also in the melting and solidification process. Whereas with LPBF a layer thickness of 30–50 μm is applied per layer, this value varies typically between 100 and 2000 μm with DED-LB. This results in significantly larger melt pools and lower feed rates during deposition, which in turn leads to lower cooling rates (10^3–10^4 K/s compared to 10^4–10^6 K/s). As a result, LPBF processed parts tend to have a finer microstructure, the growth of the grains is more directional (increased anisotropy in the properties) and the tendency towards stress and hot cracking is more pronounced. In addition, since the laser beam diameter in the processing plane is generally much smaller in LPBF than in DED-LB (around 100 μm compared to 300–4000 μm), the power density of the beam is greater, which means that deep penetration welding and, compared to DED-LB, increased burn-off of alloying elements can occur.

15.4 Steels

Despite numerous steels in use only very few are used or in deep investigated for LAM. This small group includes some stainless steels as well as hot working and maraging tool steels. Stainless steels serve in a variety of engineering applications such as aerospace and oil & gas but also in food processing and medical. Hot work tool steels are used for dies e.g. in injection molding machines. Maraging steels are suitable for many tooling applications (injection molding, die casting of light metal alloys, punching and extrusion) but also for various high performance industrial and engineering parts (aerospace, high strength airframe parts and motor racing applications). A very good review about the state-of-the-art regarding microstructure and properties is given in Bajaj et al. (2020).

Literature on LAM of stainless steels is almost exclusively restricted to 316L austenitic stainless steel (1.4404, X2CrNiMo17-12-2) (Suryawanshi et al. 2017; Yasa and Kruth 2011; Zhong et al. 2016). The microstructure evolving is fully austenitic. During solidification fine cells are formed with diameters of 1 μm or less. Numerous cells with very similar crystallographic orientation form one columnar grain with high angle boundaries to the neighboring grains still much finer than the ones in conventional produced material (Blinn et al. 2018; Suryawanshi et al. 2017; Riemer et al. 2014). LAM produced 316L display higher yield and tensile strength than their conventionally produced counterparts but still retain ductility. Especially the yield strength can even be increased by 100% (Shamsujjoha et al. 2018; Suryawanshi et al. 2017). The high strength is related to the finer microstructure and a high dislocation density (Shamsujjoha et al. 2018).

Another group of stainless steels which is well investigated are precipitation-hardened (PH) stainless steels. The two PH steels in use in LAM today are 17-4 PH (1.4542, X5CrNiCuNb16-4) and 15-5 PH (1.4545, X5CrNiCo15-5). Also these alloys are known as fully martensitic grades, as-produced LAM samples always contain austenite or even can be fully austenitic, depending on the process conditions. The reason for this is not fully understood. Several explanations are proposed in literature for this phenomenon which are summarized in Bajaj et al. (2020). The different fractions of martensite and austenite in 17-4 PH steel have a strong impact on the mechanical properties, which show a large range of values (Cheruvathur et al. 2015; Martinez et al. 2011; Meredith et al. 2018).

Since tools are high value parts, they are ideal applications for LAM. Among the numerous tool steels on the market, only two are used in LAM, namely the maraging steel 18Ni-300 (1.2709, X3NiCoMoTi 18-9-5) (Bajaj et al. 2020; Casati et al. 2017; Jägle et al. 2014, 2017; Tan et al. 2018) and the carbon-bearing hot work steel H13 (1.2344, X40CrMoV 5–1) (Choi and Hua 2006; Krell et al. 2018; Mertens et al. 2016). Due to the high cooling rates in LAM, martensite forms in both tool steels during processing. While the maraging steel with a ductile martensitic microstructure can be processed very easily, the carbon-bearing steel with brittle martensite tends to crack as a result of the induced thermal stresses. Cracking can be prevented by preheating (>100 °C). Both steels require a post heat treatment to achieve the desired mechanical properties. 1.2344 must be tempered to regain some ductility and 1.2709 must be aged to reach the final strength by precipitation of intermetallic phases (Sha and Guo 2009; Tan et al. 2018). The mechanical properties of LAM-produced 1.2344 and 1.2709 after post heat treatment are comparable to conventionally produced material, but not entirely identical (Bai et al. 2017; Casati et al. 2017).

The potential of maraging steels for triggering precipitations by an intrinsic heat treatment (IHT) was demonstrated via DED-LB for the alloy Fe19Ni5Ti (wt%) (Fig. 15.1) (Kürnsteiner et al. 2020). Process pauses of suitable length allow the material to cool below the M_s temperature to create martensite (first phase transformation) and the IHT of the subsequent layers triggers precipitation of $(Ni,Fe)_3Ti$ η-phase resulting in hardened regions (second phase transformation). Keeping the
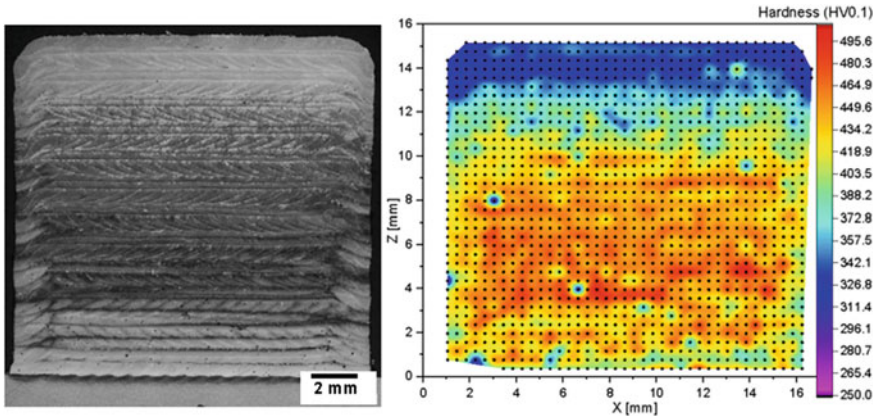
Fig. 15.1 Intrinsic heat treatment in an as-built block of Fe19Ni5Ti leads to different hardness levels depending on the thermal history of each layer

material above this critical temperature results in a softer region without precipitates as the material only transforms to martensite at a later stage in the process when there is no subsequent IHT to trigger precipitation. The interplay of two phase transformations can be controlled locally in a fully digital way through the process parameters.

15.5 Aluminum

Additive manufacturing of aluminum and its alloys were of interest since LAM became a manufacturing process for prototypes and later real parts. However, the number of Al alloys available for LAM today is still rather limited (Zhang et al. 2019b). Al is easy to machine which makes a near net-shape manufacturing less attractive from a commercial point of view (Herzog et al. 2016). But the main reason arises from the fact, that Al alloys—especially those with high strength—are difficult to weld. Since LAM is similar to welding the same difficulties occur, mainly solidification cracking due to micro segregation at grain boundaries.

Up to now, the casting alloy AlSi10Mg has been used almost exclusively for the production of parts (Aboulkhair et al. 2015; Brandl et al. 2012; Buchbinder 2013; Thijs et al. 2013). Due to the higher cooling rates, the microstructure is one to two orders of magnitude finer than in cast iron (10–20 μm compared to 100–200 μm grain size) (Fig. 15.2). As a result, yield strength and tensile strength can be increased by 5–10%. At the same time, elongation is also improved (up to 10% compared to 1% in the cast) (VDI-Richtlinie 2017). Both are due to the grain refining effect (Buchbinder 2013). The mechanical properties are only slightly anisotropic: compared to the load in the build-up direction and perpendicular to it, there are differences of 1–3%.
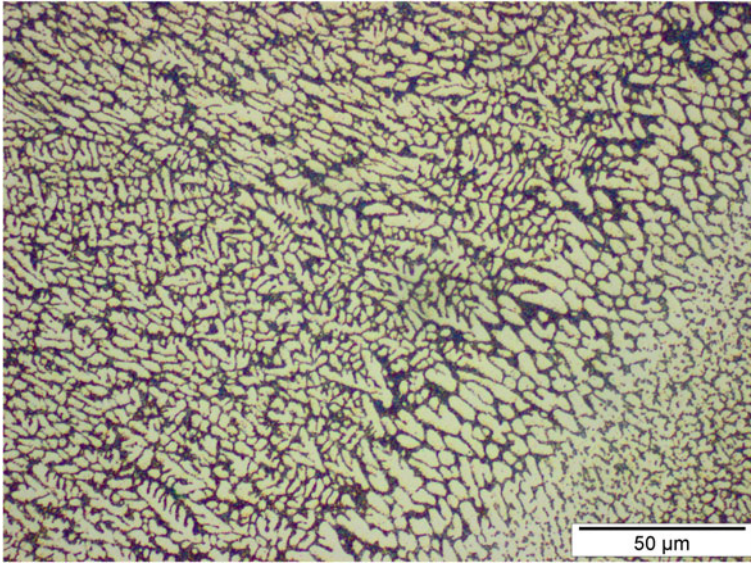
Fig. 15.2 Microstructure of AlSi10Mg processed via DED-LB; Bright dendritic phase is α-Al solid solution, dark regions are α-Al + Si eutectic; Hardness 90 HV03 (as-cast around 60 HV0.3)

The characteristic values perpendicular to the build-up direction tend to be higher (VDI-Richtlinie 2017).

Among the wrought alloys, alloys of the 2xxx series can be processed without defects by LAM (e.g. 2024, 2219, 2618) (Ahuja et al. 2014; Ding et al. 2016; Zhang et al. 2019a). For industrial applications (ground based vehicles, aerospace) the high strength alloys of the 6xxx and 7xxx series are much more interesting. However, these alloys cannot yet be processed without cracks. Hot cracks occur parallel to the direction of build-up (Belov et al. 2017; Martin et al. 2017; Montero Sistiaga et al. 2016). Since a robust and/or economic process window for crack-free processing does not exist, a chemical modification is necessary to avoid cracking. In (Montero Sistiaga et al. 2016) it is shown that crack-free processing of the high-strength wrought alloy 7075 is achieved by adding 5 wt% silicon, but strength is reduced at the same time. The authors in Martin et al. (2017) reported that the addition of Zr nanoparticles as grain refiners also leads to a crack-free structure in high strength alloys (6061, 7075).

An alloy specially developed for LPBF is Scalmalloy® (Al4.5Mg0.37Zr0.17Si0.66Sc) (Aversa et al. 2019; Schmidtke et al. 2011; Spierings et al. 2016b). This alloy is based on the weldable wrought aluminum alloy 5083 (Al–Mg system). The rapid solidification leads to the forced solid solution of Sc in the Al matrix. During ageing, fine Al_3Sc precipitates are formed which are enclosed in a temperature-stable shell of Al_3Zr ("core–shell structure"). This shell offers an effective diffusion barrier and thus counteracts diffusion-controlled coarsening effects (Radmilovic et al. 2008). At RT, the alloy achieves a strength of up to

500 MPa at approx. 8% elongation. Fatigue strength and high-temperature strength have not yet been investigated.

15.6 Titanium

Titanium and its alloys are of particular interest for additive manufacturing (Dutta and Froes 2017). This results on the one hand from the difficult machinability, which leads to high costs in component production. A near net-shape process such as LAM can lead to considerable cost reductions. LAM also offers great potential for weight reduction due to the high degree of design freedom. On the other hand, titanium is a biocompatible material with high strength and is therefore used for implants (including hip and knee). Since these are always individual parts, a tool-free process offers advantages.

Of interest for industrial and medical applications are primarily pure titanium (cp, commercial purity) (Attar et al. 2014) and TiAl6V4 (Xu et al. 2015). For both materials, solidification takes place in LAM via the β phase. During rapid cooling in the solid, β transforms into the martensitic phase α′. Typical is a stem-like epitaxial growth of the β grains across the boundaries of the layers (Fig. 15.3). The martensite then precipitates within these grains in the form of plates or needles. Due to the martensitic transformation, LAM processed volumes achieve higher strength than those conventionally processed. However, this results in a significant reduction in ductility. Ductility can be regained by heat treatment (Seyda et al. 2015) or HIP (Qiu et al. 2013).

While the build-up rate is of secondary importance for implant manufacturing, it plays an important role in terms of cost-effectiveness for aerospace applications, because LAM competes with established processes such as casting or forging. Increasing the build-up rate is therefore a key challenge. DED-LB offers the better conditions compared to LPBF, provided that restrictions in design freedom and accuracy are accepted. However, high build-up rates can hardly be achieved with local shielding alone, since the volume already built up remains hot for a long time and therefore oxidizes. Since titanium can dissolve a great amount of oxygen, this leads to a solution in the metallic matrix, which is associated with severe embrittlement. Therefore, manufacturing must be carried out in a protective gas chamber. Due to the high oxygen affinity of titanium, wire cladding is also of particular interest (Kelbassa et al. 2019), since, in contrast to the use of powder, the contamination of the filler material is already significantly reduced.

Other Ti alloys of interest include Ti–24Nb–4Zr–8Sn (Zhang et al. 2011) and Ti–6Al–7Nb (Chlebus et al. 2011) for biomedical applications, and Ti–6.5Al–3.5Mo–1.5Zr–0.3Si for aerospace applications (Zhu et al. 2014). But these investigations are so far only on a laboratory level.
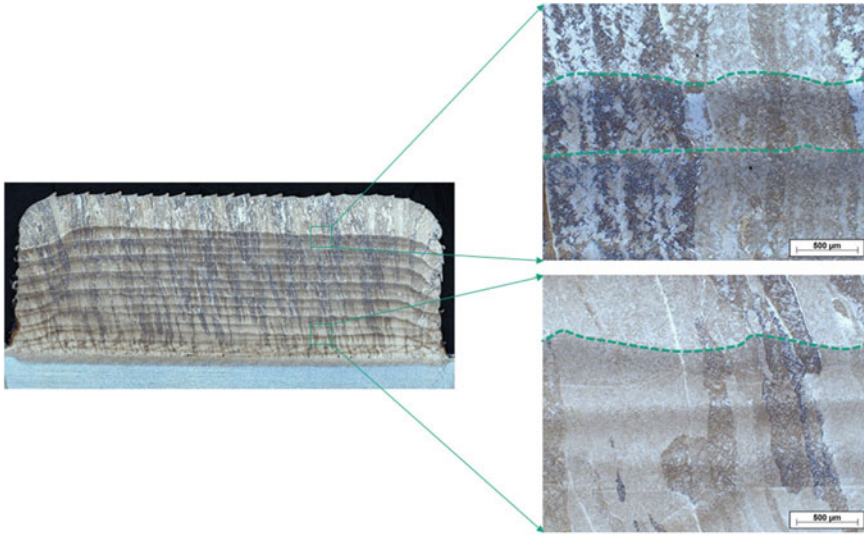
Fig. 15.3 Additively manufactured block of TiAl6V4 (DED) showing epitactic growth of large Beta-grains across single layers

15.7 Nickel

From the group of nickel-base alloys, it is almost exclusively the superalloys that are of interest (Zadi-Maad and Basuki 2018), especially those used in turbine technology (aero turbines and stationary turbines). The focus is on the repair of high-quality components such as casings and turbine blades. For production LAM is not yet economical.

Nickel superalloys—among other things—are classified according to their weldability. Since LAM is similar to the welding process, this classification can also be used as a first criterion for suitability (Carter et al. 2012). A distinction is made between solidification cracks, liquation cracks and strain age cracks (see chap. 15.3.1). Especially for the phenomenon of strain age cracking, a weldability assessment diagram has been developed, whereby the Al and Ti content is taken as a criterion. Both elements promote gamma-prime precipitation (Cam and Kocak 1998), a phase which increases strength and creep resistance. At the same time, however, this phase is brittle and in combination with the volume change during transformation and induced residual stresses, cracks can occur during heat treatment. When the total Al + Ti level for a particular alloy exceeds a critical value (often taken as 4 wt%) an alloy is considered to be difficult to weld and increasingly unweldable with increasing Al + Ti content. Solidification and liquation cracks are favored by elements like S and B.

With regard to their use for LAM, the alloys IN625 (Fig. 15.4) (Tian et al. 2020) and IN718 (Wang et al. 2017) are considered to be uncritical with regard to crack

formation (also classified as weldable according to Cam and Kocak (1998)) and are in use. According to Cam and Kocak (1998), the alloy IN738 is not weldable and also tends to crack in LAM (Engeli et al. 2016; Risse 2019). In tests with various powder batches, it was found that the crack density depends very much on the actual content of certain elements. Si (Engeli et al. 2016; Risse 2019) and Zr (Risse 2019) were identified as critical elements, which, if reduced within the range of the nominal composition, leads to a significant decrease in crack frequency. Cracks can be avoided completely by preheating to 1050 °C. At this temperature the equilibrium volume fraction of the γ/γ′-phase is reduced by more than 50% and strain age cracking is avoided. For MAR M 247 a sensitive influence of certain elements was also found. The combination of a reduction in C and Hf contents, with control of S content and the introduction of Nb to provide additional gamma-prime strengthening prevents cracking without compromising strength (Rolls-Royce 2018). The suitability of nickel superalloys for LAM must therefore be considered in a differentiated manner and examined for each alloy.

15.8 Other Conventional Metals and Alloys

Further materials with relevant industrial applications in AM are alloys of Mg, Co, and Cu.

Due to their low density, magnesium alloys are mainly used in lightweight construction. Magnesium alloys are also finding applications in medical technology (Bär et al. 2019; Jauer 2018; Karunakaran et al. 2020). Here, resorbable implants made of magnesium alloys are produced, which dissolve in the body being replaced by the body's own bone. An alloy with potential in this respect is WE43. Figure 15.5 (left) shows an EBSD picture of WE43 manufactured by LPBF. Rapid cooling leads to as fine grain structure inside a single layer. Grain growth occurs in underlying layers due to cyclic reheating (Bär et al. 2019). The processing of magnesium alloys with additive manufacturing processes offers advantages in terms of individualization and design (Fig. 15.5, right).

Co–Cr–Mo alloys have excellent mechanical properties and outstanding resistance to wear and corrosion. Due to their biocompatibility, these alloys are used for dental and orthopedic implants (Koutsoukis et al. 2015).

Copper alloys are of interest where thermal conductivity in combination with sufficient strength and hardness are required, e.g. for tool inserts in injection molding or for bearing shells (Singer et al. 2017). The materials in use are tin bronze (CuSn10) for maximum strength (Deng et al. 2018a) and low alloyed CuNi2SiCr or CuCr1Zr for medium strength (Becker 2014). Due to the rapid solidification, the alloying elements in the later alloys remain dissolved in the Cu matrix. The desired strength is then achieved with a subsequent aging treatment. Interesting alloys for the good performance at high temperatures are those of the type Cu–Cr–Nb. Cr and Nb are almost insoluble in Cu and precipitate during solidification as the Laves phase Cr_2Nb (Gradl et al. 2019). Thus the conductivity of the Cu matrix is retained to a large
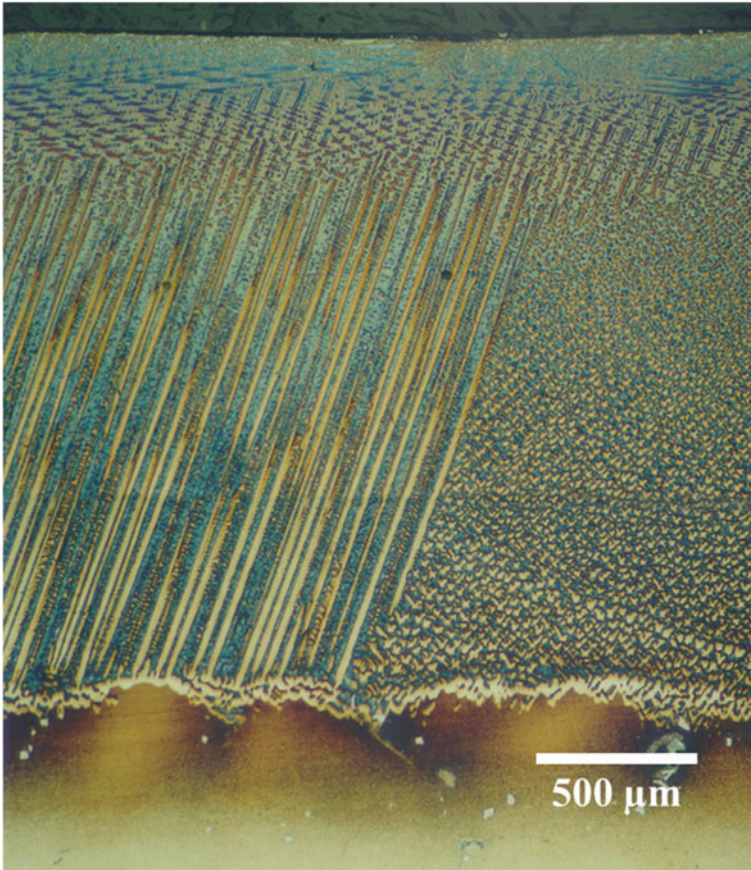
Fig. 15.4 Longitudinal section of a layer of IN 738 on parent alloy showing strongly directed growth of primary dendrites: process DED-LB

extend and the thermodynamically stable precipitates improve strength even at higher temperatures. However, the particles only develop their optimum effect if they are finely distributed in the matrix. This can only be achieved by high cooling rates during solidification, so the casting process is not suitable for production. Conventionally, this material is processed by thermal spraying, spark plasma sintering, extrusion or hot isostatic pressing. Compared to these processes, LAM opens up significantly greater design possibilities. Alloys of this type have been successfully tested for the production of rocket engine combustion chambers (Gradl et al. 2019). A challenge so far has been the processing of pure copper for electrical applications. Due to the high reflectivity for commercial multi-kW lasers with wavelengths around 1 μm, it has not been possible to produce volumes with a technical density (>99.5%) (Colopi et al. 2019). The development of blue and green laser beam sources with output powers greater than 1 kW opens up new possibilities here. Using green laser light
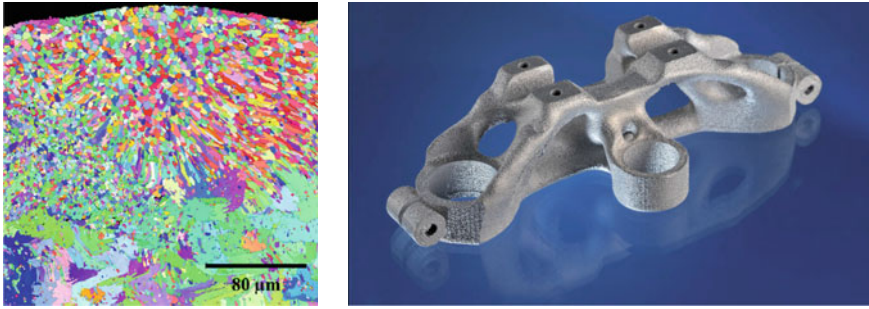
Fig. 15.5 Left: EBSD picture of WE43 manufactured by LPBF showing columnar grains along the former liquid–solid interface of a single track and equiaxed grains in the center of the track; grain growth in the underlying layers due to reheating (Bär et al. 2019); Right: Bionic motorcycle fork bridge, scale 1:4, material AZ91 (Jauer 2018)

with a wavelength of 515 nm the absorptivity of pure copper is much higher than for infrared lasers, allowing the manufacturing of dense volumes (Fraunhofer ILT 2017).

15.9   Advanced Metal Based Materials

15.9.1   Bulk Metallic Glasses

Bulk metallic glasses are materials that have attractive properties like high hardness, good corrosion resistance and a large elastic strain limit. When the first alloy types were investigated during the eighties of the last century only thin sheets could be formed restricting their application as engineering material and therefore these materials did not arise much interest in industry. However, material research during the last decades has led to alloys based on Zr and Cu which allow the manufacturing of bulk volumes (Axinte 2012; Busch et al. 1998) by reducing the required cooling rates to freeze in the amorphous structure. The parts can be produced conventionally by casting or thermoplastic forming. With LAM, a further manufacturing process has been added, which expands the limits of design (Williams and Lavery 2017). Today Zr- and Cu-based alloys are on the market for LAM (Stolpe and Elsen 2016), Ti-based alloys are under development (Deng et al. 2018b). Low cost Fe-based alloys are also of interest but require higher cooling rates and exhibit extreme brittleness (Li et al. 2018) which hinders their industrial use until today.

15.10   Particle Reinforced Composites

The addition of mostly hard ceramic particles is mainly aimed at improving mechanical properties at elevated temperatures such as tensile strength or creep resistance. Besides the quantity of particles, their size is of decisive importance. As the size of the particles decreases, their effect on the mechanical properties increases. The greatest effect is achieved with nanoscale particles. An example of this are ODS materials (Oxide Dispersion Strengthened) (Czyrska-Filemonowicz and Dubiel 1997). The particle size here is in the range of 10–50 nm. Even with additions of 1–3% by volume, the number of particles is so large and their spacing so small that they effectively impede dislocation movement—and thus plastic flow and creep. The production of particle-reinforced composites is conventionally carried out mostly by powder metallurgy (Czyrska-Filemonowicz and Dubiel 1997), but the effort and thus the costs are high due to the numerous process steps (powder production—mixing/milling—compacting—sintering—heat treatment—finishing). Any approach allowing manufacturing of ODS steels without prior mechanical alloying would bring down the cost for these materials significantly and open the door for a wide variety of high-temperature applications. LAM represents a promising variant for the production of particle-reinforced composites. The uniform distribution of nano and micro scaled particles is achieved by mixing/milling. Rapid solidification during LAM ensures the entrapment of the fine particles in the matrix and at the grain boundaries with only a slight increase of size.

The feasibility of LAM as a manufacturing methods for ODS steels has been demonstrated (Al-Mangour et al. 2017; Kenel et al. 2017; Spierings et al. 2016a). A typical strengthening material is nano-scaled Y_2O_3 (Spierings et al. 2016a). The nano particles are deposited on the micro particles of the ferritic steel either by ball milling (Spierings et al. 2016a) or a novel powder synthesis route, consisting of laser processing of a colloid containing the agglomerated nano particles and subsequent electrophoretic deposition on the micro particles (Doñate-Buendía et al. 2018; Streubel et al. 2018). Powder composites, which are characterized by a homogenous distribution of Y_2O_3-nanoparticles on the surface of micrometer-sized stainless steel particles, could be synthesized. The powder composites were successfully processed by DED-LB and LPBF, leading to bulk specimens with low porosities and homogenous distribution of nanoscale dispersoids. Compression tests at elevated temperatures demonstrate the superior performance of reinforced material compared to raw stainless steel specimens.

15.11   Others

Research into new materials is not only about the material itself, but also about suitable production methods. That is why new materials such as High Entropy Alloys (HEA), fine eutectics or silicides today are being tested for processing by LAM long

before the first industrial applications are realized. Alloys with promising properties are high entropy alloys (Brif et al. 2015; Zhang et al. 2014; Haase et al. 2017), eutectic alloys (Requena et al. 2020) and silicides (Schmelzer et al. 2020). While HEA and fine eutectic alloys exhibit high strength at moderate ductility, silicides such as Mo-Si-B show excellent high temperature properties with the potential to replace nickel superalloys.

15.12   Alloy Development for LAM

Almost all alloys which are used today in LAM are conventional alloys developed for other manufacturing technologies. To exploit the benefits of LAM towards a manufacturing technology not only for niche applications requires further progress in robustness, reliability and efficiency of the process but also the availability of new alloy which fit to the process conditions of LAM (e.g. rapid cooling) as well as for the addressed application. An example is the alloy Scalmalloy® which has been developed especially for LAM reaching mechanical properties in the range of high strength wrought Al alloys. However, alloy development today is associated with a long term process of many years until a new alloy enters the market. Therefore, industry is rather restrained to invest in alloy development because the return of invest is uncertain or far in the future. As a consequence the research into new alloy is mainly driven by the scientific community with no strong link to industrial needs. Such fundamental research is a key factor for progress, however, it also requires industrial participation to bring parts made from new alloys into service. Again Scalmalloy® is a good example. While the mechanical properties are outstanding the high price and low availability of Sc hinders the spreading of this alloy for LAM applications.

One tool to overcome this situation is Rapid Alloy Development (RAD). This term refers not to a special method but to an acceleration of alloy development by high throughput methods. In this respect LAM allows rapid alloy development by quickly iterating through a series of materials compositions to identify the optimum one. This is due to the powder metallurgical nature of the process. By introducing a mixture of two or more powders into the melt pool, homogeneous materials of varying chemistry can be produced (Fig. 15.6). In contrast to conventional processing, where producing castings with varied alloy composition takes considerable time and material, LAM makes it possible to produce parts of different composition in one production run (Knoll et al. 2017). Even production of graded parts, i.e. with a composition varying within the part, is possible. This rapid alloy development ability can be used in the development of materials employed in conventional manufacturing as well as in the development of materials suitable for LAM itself. Once a promising alloy is identified, it is easy to build a variety of sample geometries for testing of strength, fatigue, corrosion, wear etc. A further acceleration is possible when RAD is combined with digital material development based on thermodynamic and phase field models (predicting phases and microstructure) and atomistic models (predicting properties)
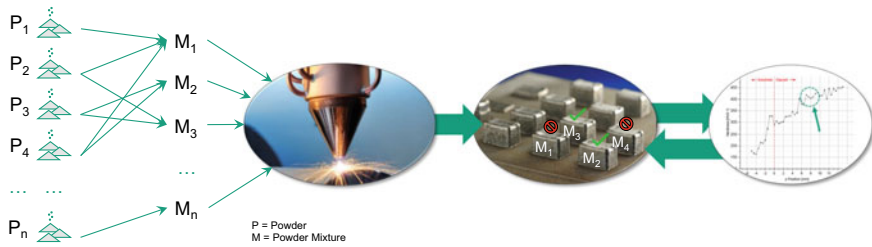
Fig. 15.6 Rapid Alloy Development (RAD) using DED; Build-up of specimens from powder mixtures ($M_1 = P_1 + P_2$, …), characterization and selection of promising compositions

and the use of machine learning (Liu et al. 2017). The later can help to deal with loads of data to discover correlations which might otherwise take month or years for scientists to find.

Innovations from materials research are a key factor for solving future tasks. New materials help to increase material and energy efficiency, improve the quality of life and enhance the competitiveness of industry. According to the Gartner Hype Cycle LAM has passed the peak of inflated expectations. To climb up the slope of enlightenment and to reach the plateau of productivity tailored alloys will be a valuable and required contribution.

References

Aboulkhair NT, Tuck C, Ashcroft I, Maskery I, Everitt NM (2015) On the precipitation hardening of selective laser melted AlSi10Mg. Metall Mater Trans A 46A(8):3337–3341. https://doi.org/10.1007/s11661-015-2980-7

Ahuja B, Karga M, Yu KN, Schmidt M (2014) Fabrication and characterization of high strength Al-Cu alloys processed using laser beam melting in metal powder bed. Phys Procedia 56:135–146. https://doi.org/10.1016/j.phpro.2014.08.156

Al-Mangour B, Grzesiak D, Yang JM (2017) In-situ TiC particle reinforced 316L stainless steel matrix nanocomposites: powder preparation by mechanical alloying and selective laser melting behavior. Powder Tech 326. https://doi.org/10.1016/j.powtec.2017.11.064

Attar H, Calin M, Zhang LC, Scudino S, Eckert J (2014) Manufacture by selectivelaser melting and mechanical behavior of commercially pure titanium. Mater Sci Eng A 593:170–177. https://doi.org/10.1016/j.msea.2013.11.038

Aversa A, Marchese G, Saboori A, Bassini E, Manfredi D, Biamino S, Ugues D, Fino P, Lombardi M (2019) New aluminum alloys specifically designed for laser powder bed fusion: a review. Materials 12:1007. https://doi.org/10.3390/ma12071007

Axinte E (2012) Metallic glasses from '"alchemy"' to pure science: present and future of design, processing and applications of glassy metals. Mater Des 35:518–556. https://doi.org/10.1016/j.matdes.2011.09.028

Bär F, Berger L, Jauer L, Kurtuldu G, Schäublin R, Schleifenbaum JH, Löffler JF (2019) Laser additive manufacturing of biodegradable magnesium alloy WE43: a detailed microstructure analysis. Acta Biomater 98:36–49. https://doi.org/10.1016/j.actbio.2019.05.056

Bai Y, Yang Y, Wang D, Zhang M (2017) Influence mechanism of parameters process and mechanical properties evolution mechanism of maraging steel 300 by selective laser melting. Mater Sci Eng A 703:116–123. https://doi.org/10.1016/j.msea.2017.06.033

Bajaj P, Hariharan A, Kini A, Kürnsteiner P, Raabe D, Jägle EA (2020) Steels in additive manufacturing: a review of their microstructure and properties. Mater Sci Eng A 772(20):138633. https://doi.org/10.1016/j.msea.2019.138633

Becker D (2014) Selektives Laserschmelzen von Kupfer und Kupferlegierungen. Dissertation, RTWH Aachen

Belov N, Naumova E, Akopyan T (2017) Eutectic alloys based on the Al–Zn–Mg–Ca system: microstructure, phase composition and hardening. Mater Sci Technol 33(6):656–666. https://doi.org/10.1038/nature23894

Blinn B, Klein M, Gläßner C, Smaga M, Aurich JC, Beck T (2018) An investigation of the microstructure and fatigue behavior of additively manufactured AISI 316L stainless steel with regard to the influence of heat treatment. Metals 8:220. https://doi.org/10.3390/met8040220

Bourell D, Kruth JP, Leu M, Levy G, Rosen D, Beese AM, Clare A (2017) Materials for additive manufacturing. CIRP Ann Manuf Technol 66:659–681. https://doi.org/10.1016/j.cirp.2017.05.009

Brandl E, Heckenberger U, Holzinger V, Buchbinder D (2012) Additive manufactured AlSi10Mg samples using selective laser melting (SLM): microstructure, high cycle fatigue, and fracture behavior. Mater Des 34:159–169. https://doi.org/10.1016/j.matdes.2011.07.067

Brif Y, Meurig T, Todd T (2015) The use of high-entropy alloys in additive manufacturing. Scripta Mater 99:93–96. https://doi.org/10.1016/j.scriptamat.2014.11.037

Buchbinder D (2013) Selective laser melting von Aluminiumgusslegierungen. Diss, RWTH Aachen, Shaker

Busch R, Bakke E, Johnson WL (1998) Viscosity of the supercooled liquid and relaxation at the glass transition of the Zr46.75Ti8.25Cu7.5Ni10Be27.5 bulk metallic glass forming alloy. Acta Mater 46(13):4725±4732. https://doi.org/10.1016/S1359-6454(98)00122-0

Cam G, Kocak M (1998) Progress in joining of advanced materials. Int Mater Rev 43(1):1–44. https://doi.org/10.1179/imr.1998.43.1.1

Carter LN, Attallah MM, Reed RC (2012) Laser powder bed fabrication of nickel-base superalloys: influence of parameters; characterisation, quantification and mitigation of cracking. In: Superalloys 2012—Proceedings of the 12th international symposium on superalloys. https://doi.org/10.1002/9781118516430

Casati R, Lemke J, Vedani M (2017) Microstructural and mechanical properties of as built, solution treated and aged 18 Ni (300 grade) maraging steel produced by selective laser melting. Metall Ital 109:11–20

Chlebus E, Kuźnicka B, Kurzynowski T, Dybała B (2011) Microstructure and mechanical behaviour of Ti-6Al-7Nb alloy produced by selective laser melting. Mater Charact 62:488–495. https://doi.org/10.1016/j.matchar.2011.03.006

Cheruvathur S, Lass EA, Campbell CA (2015) Additive manufacturing of 17–4 PH stainless steel: post-processing heat treatment to achieve uniform reproducible microstructure. JOM (J Occup Med) 68:930–942. https://doi.org/10.1007/s11837-015-1754-4

Choi J, Hua Y (2006) Dimensional and material characteristics of direct deposited H13 tool steel by CO_2 laser. J Laser Appl 16:245–251. https://doi.org/10.2351/1.1809638

Colopi M, Demir AG, Caprio L, Previtali B (2019) Limits and solutions in processing pure Cu via selective laser melting using a high-power single-mode fiber laser. Int J Adv Manuf Technol 104:2473–2486. https://doi.org/10.1007/s00170-019-04015-3

Czyrska-Filemonowicz A, Dubiel B (1997) Mechanically alloyed, ferritic oxide dispersion strengthened alloys: structure and properties. J Mater Proc Tech 64:53–64. https://doi.org/10.1016/S0924-0136(96)02553-8

Deng C, Kang J, Feng T, Feng Y, Wang X, Wu P (2018a) Study on the selective laser melting of CuSn10 powder. Materials 11:614. https://doi.org/10.3390/ma11040614

Deng L, Wang S, Wang P, Kühn U, Pauly S (2018b) Selective laser melting of a Ti-based bulk metallic glass. Mater Lett 212:346–349. https://doi.org/10.1016/j.matlet.2017.10.130

Ding Y, Muniz-Lerma JA, Trask M, Chou S, Walker A, Brochu M (2016) Microstructure and mechanical property considerations in additive manufacturing of aluminum alloy. MRS Bull 41. https://doi.org/10.1557/mrs.2016.214

Doñate-Buendía C, Frömel F, Wilms MB, Streubel R, Tenkamp J, Hupfeld T, Nachev M, Gökce E, Weisheit A, Barcikowski S, Walther F, Schleifenbaum JH, Gökce B (2018) Oxide dispersion-strengthened alloys generated by laser metal deposition of laser-generated nanoparticle-metal powder composites. Mater Des 154:360–369. https://doi.org/10.1016/j.matdes.2018.05.044

Dutta B, Froes FH (2017) The additive manufacturing (AM) of titanium alloys. Metal Powder Rep 72(2). https://doi.org/10.1016/j.mprp.2016.12.062

Engeli R, Etter T, Hövel S, Wegener K (2016) Processability of different IN738LC powder batches by selective lasermelting. J Mater Process Technol 229:484–491. https://doi.org/10.1016/j.jmatprotec.2015.09.046

Fraunhofer ILT (2017) Green light for new 3D printing process, press release, 30.07.2017

Gradl PR, Protz C, Cooper K, Garcia C, Ellis D, Evans L (2019) GRCop-42 development and hot-fire testing using additive manufacturing powder bed fusion for channel-cooled combustion chambers. In: 55th AIAA/SAE/ASEE joint propulsion conference 2019

Haase C, Tang F, Wilms MB, Weisheit A, Hallstedt B (2017) Combining thermodynamic modeling and 3D printing of elemental powder blends for high-throughput investigation of high-entropy alloys—towards rapid alloy screening and design. Mater Sci Eng A. https://doi.org/10.1016/j.msea.2017.01.099

Herzog D, Seyda V, Wycisk E, Emmelmann C (2016) Additive manufacturing of metals. Acta Mater 117:371–392. https://doi.org/10.1016/j.actamat.2016.07.019

Jägle EA, Choi P, Van Humbeeck J, Raabe D (2014) Precipitation and austenite reversion behavior of a maraging steel produced by selective laser melting. J Mater Res 29. https://doi.org/10.1557/jmr.2014.204

Jägle EA, Sheng Z, Kürnsteiner P, Ocylok S, Weisheit A, Raabe D (2017) Comparison of maraging steel micro- and nanostructure produced conventionally and by laser additive manufacturing. Materials 10. https://doi.org/10.3390/ma10010008

Jauer L (2018) Laser powder bed fusion von Magnesiumlegierungen. Dissertation, RWTH Aachen

Karunakaran R, Ortgies S, Tamayol A, Bobaru F, Sealy MP (2020) Additive manufacturing of magnesium alloys. Bioactive Mater 5:44–54. https://doi.org/10.1016/j.bioactmat.2019.12.004

Kelbassa J, Gasser A, Bremer J, Pütsch O, Poprawe R, Schleifenbaum JH (2019) Equipment and process windows for laser metal deposition with coaxial wire feeding. J Laser Appl 31(2). https://doi.org/10.2351/1.5096112

Kenel C, Dasagyri G, Bauer T, Colella A, Spierings AB, Leinenbach C, Wegener K (2017) Selective laser melting of an oxide dispersion strengthened (ODS) γ-TiAl alloy towards production of complex structures. Mater Des 134:81–90. https://doi.org/10.1016/j.matdes.2017.08.034

Knoll H, Ocylok S, Weisheit A, Springer H, Jägle E, Raabe D (2017) Combinatorial alloy design by laser additive manufacturing. Steel Res Int 88(8). https://doi.org/10.1002/srin.201600416

Krell J, Röttger A, Geenen K, Theisen W (2018) General investigations on processing tool steel X40CrMoV5-1 with selective laser melting. J Mater Process Technol 255:679–688. https://doi.org/10.1016/j.jmatprotec.2018.01.012

Koutsoukis T, Zinelis S, Eliades G, Al-Wazzan K, Rifaiy M, Al Jabbari YS (2015) Selective laser melting technique of Co-Cr dental alloys: a review of structure and properties and comparative analysis with other available techniques. J Prosthodont 24:303–312. https://doi.org/10.1111/jopr.12268

Kürnsteiner P, Wilms MB, Weisheit A, Gault B, Jägle EA, Raabe D (2020) High-strength Damascus steel by additive manufacturing. Nature 582:25. https://doi.org/10.1038/s41586-020-2409-3

Lewandowski JJ, Seifi M (2016) Metal additive manufacturing: a review of mechanical properties. Annu Rev Mater Res 46:151–186. https://doi.org/10.1146/annurev-matsci-070115-032024

Li N, Zhang J, Xing W, Ouyang D, Liu L (2018) 3D printing of Fe-based bulk metallic glass composites with combined high strength and fracture toughness. Mater Des 143:285–296. https://doi.org/10.1016/j.matdes.2018.01.061

Liu Y, Zhao T, Ju W, Shi S (2017) Materials discovery and design using machine learning. J Materiomics 3:159e177. https://doi.org/10.1016/j.jmat.2017.08.002

Martinez L, Medina F, Wooten J, Ciscel D, Ackelid U, Wicker RB (2011) Microstructural architecture, microstructures, and mechanical properties for a nickel-base superalloy fabricated by electron beam melting. Metall Mater Trans A Phys Metall Mater Sci 42:3491–3508. https://doi.org/10.1007/s11661-011-0748-2

Martin JH, Yahata BD, Hundley J-M, Mayer JA, Schaedler JA, Pollock TM (2017) 3D printing of high-strength aluminium alloys. Nature 549(7672):365–369. https://doi.org/10.1038/nature23894

Mertens R, Vrancken B, Holmstock N, Kinds Y, Kruth JP, Van Humbeeck J (2016) Influence of powder bed preheating on microstructure and mechanical properties of H13 tool steel SLM parts. Phys Procedia 83:882–890. https://doi.org/10.1016/j.phpro.2016.08.092

Meredith SD, Zuback JS, Keist JS, Palmer TA (2018) Impact of composition on the heat treatment response of additively manufactured 17–4 PH grade stainless steel. Mater Sci Eng A 738:44–56. https://doi.org/10.1016/J.MSEA.2018.09.066

Montero Sistiaga M, Mertens R, Vrancken B, Wang X, Van Hooreweder B, Kruth JP, Van Humbeeck J (2016) Changing the alloy composition of Al7075 for better processability by selective laser melting. J Mater Process Technol 238:437–445.https://doi.org/10.1016/j.jmatprotec.2016.08.003

Ngo TD, Kashani A, Imbalzano G, Nguyen KTQ, Hui D (2018) Additive manufacturing (3D printing): a review of materials, methods, applications and challenges. Compos B 143:172–196. https://doi.org/10.1016/j.compositesb.2018.02.012

Qiu C, Adkins NJE, Attallah MM (2013) Microstructure and tensile properties of selectively laser-melted and of HIPed laser-melted Ti-6Al-4V. Mater Sci Eng A 578:230–239. https://doi.org/10.1016/j.msea.2013.04.099

Radmilovic V, Tolley A, Marquis EA, Rossell MD, Leea Z, Dahmen U (2008) Monodisperse Al3(LiScZr) core/shell precipitates in Al alloys. Scripta Mater 58:529–532. https://doi.org/10.1016/j.scriptamat.2007.11.012

Requena G, Bugelnig K, Sket F, Milenkovic S, Rödler G, Weisheit A, Gussone J, Haubrich J, Barriobero-Vila P, Pusztai T, Gránásy L, Theofilatos A, Silva JC, Hecht U (2020) Ultrafine Fe-Fe2Ti eutectics by directed energy deposition: insights into microstructure formation based on experimental techniques and phase field modelling. Addit Manuf 33. https://doi.org/10.1016/j.addma.2020.101133

Riemer A, Leuders S, Thöne M, Richard HA, Tröster T, Niendorf T (2014) On the fatigue crack growth behavior in 316L stainless steel manufactured by selective laser melting. Eng Fract Mech 120:15–25. https://doi.org/10.1016/J.ENGFRACMECH.2014.03.008

Risse J (2019) Additive manufacturing of nickel-base superalloy IN738LC by laser powder bed fusion. Dissertation, RWTH Aachen

Rolls-Royce (2018) Nickel-base superalloy and the use of thereof, EP 3 293 276 A1

Schmidtke K, Hawkins A, Emmelmann C (2011) Process and mechanical properties: applicability of a scandium modified al-alloy for laser additive manufacturing. Phys Procedia 12. https://doi.org/10.1016/j.phpro.2011.03.047

Schmelzer J, Rittinghaus SK, Gruber K, Veit P, Weisheit A, Krüger M (2020) Printability and microstructural evolution of a near-eutectic three-phase V-based alloy. Addit Manuf 34:101208. https://doi.org/10.1016/j.addma.2020.101208

Seyda V, Herzog D, Emmelmann C, Jahn S, Sändig S, Straube C (2015) Einflussfaktoren auf die Qualit€at von Ti-6Al-4V-Bauteilen in der laseradditiven Fertigung. In: Proceedings of DVS Congress, Nuremberg, No 4460

Sha W, Guo Z (2009) Maraging steels: modelling of microstructure, properties and applications. Elsevier

Shamsujjoha Md, Agnew SR, Fitz-Gerlad JM, Moore WR, Newman TA (2018) High strength and ductility of additively manufactured 316L stainless steel explained. Met Mat Trans A 49A:3011. https://doi.org/10.1007/s11661-018-4607-2

Singer F, Deisenroth DC, Hymas DM, Dessiatoun SV, Ohadi MM (2017) Additively manufactured copper components and composite structures for thermal management applications. In: 16th IEEE Intersociety conference on thermal and thermomechanical phenomena in electronic systems (ITherm). https://doi.org/10.1109/ITHERM.2017.7992469

Spierings AB, Bauer T, Dawson K, Colella A, Wegener K (2016a) Processing ODS modified IN625 using selective laser melting. In: Proceedings of the SFF2015

Spierings AB, Dawson K, Voegtlin M, Palm F, Uggowitzer PJ (2016b) Microstructure and mechanical properties of as-processed scandium-modified aluminium using selective laser melting. CIRP Ann Manuf Technol 65:213–216. https://doi.org/10.1016/j.cirp.2016.04.057

Stolpe M, Elsen A (2016) Additive Fertigung metallischer Gläser. Lasermagazin 4

Streubel R, Wilms MB, Doñate-Buendia C, Weisheit A, Barcikowski S, Schleifenbaum JH, Gökce B (2018) Depositing laser-generated nanoparticles on powders for additive manufacturing of oxide dispersion strengthened alloy parts via laser metal deposition. Jpn J Appl Phys 57. https://doi.org/10.7567/JJAP.57.040310

Suryawanshi J, Prashanth KG, Ramamurty U (2017) Mechanical behavior of selective laser melted 316L stainless steel. Mater Sci Eng A 696:113–121. https://doi.org/10.1016/j.msea.2017.04.058

Tan C, Zhou K, Kuang M, Ma W, Kuang T (2018) Microstructural characterization and properties of selective laser melted maraging steel with different build directions. Sci Technol Adv Mater 19:746–758. https://doi.org/10.1080/14686996.2018.1527645

Thijs L, Kempen K, van Kruth JP, Humbeeck J (2013) Fine-structured aluminium products with controllable texture by selective laser melting of pre-alloyed AlSi10Mg powder. Acta Mater 61:1809–1819. https://doi.org/10.1016/j.actamat.2012.11.052

Tian Z, Zhang C, Wang D, Liu W, Fan W, Wellmann D, Zhao Y, Tian Y (2020) A review on laser powder bed fusion of Inconel 625 nickel-based alloy. Appl Sci 10:81. https://doi.org/10.3390/app10010081

VDI-Richtlinie (2017) VDI 3405 Blatt 2.1 Additive Fertigungsverfahren, Laser-Strahlschmelzen metallischer Bauteile - Materialkenndatenblatt Aluminiumlegierung AlSi10Mg

Wang X, Gong X, Chou K (2017) Review on powder-bed laser additive manufacturing of Inconel 718 parts. J Eng Manuf 231(11):1890–1903. https://doi.org/10.1177/0954405415619883

Williams E, Lavery N (2017) Laser processing of bulk metallic glass: a review. J Mater Process Tech 247:73–91. https://doi.org/10.1016/j.jmatprotec.2017.03.034

Xu W, Brandt M, Sun S, Elambasseril J, Liu Q, Latham K, Xia K, Qian M (2015) Additive manufacturing of strong and ductile Tie6Ale4V by selective laser melting via in situ martensite decomposition. Acta Mater 85:74–84. https://doi.org/10.1016/j.actamat.2014.11.028

Yasa E, Kruth JP (2011) Microstructural investigation of selective laser melting 316L stainless steel parts exposed to laser re-melting. Procedia Eng 19:389–395. https://doi.org/10.1016/J.PROENG.2011.11.130

Zadi-Maad A, Basuki A (2018) The development of additive manufacturing technique for nickel-base alloys: a review. AIP Conf Proc 1945:020064. https://doi.org/10.1063/1.5030286

Zhang LC, Klemm D, Eckert J, Haod YL, Sercombe TB (2011) Manufacture by selective laser melting and mechanical behavior of a biomedical Ti–24Nb–4Zr–8Sn alloy. Scripta Mater 65:21–24. https://doi.org/10.1016/j.scriptamat.2011.03.024

Zhang Y, Zuo TT, Tang Z, Gao MC, Dahmen KA, Liaw PK, Lu ZP (2014) Microstructures and properties of high-entropy alloys (HEA). Prog Mater Sci 61:1–93. https://doi.org/10.1016/j.pmatsci.2013.10.001

Zhang C, Chen F, Huang Z, Jia M, Chen G, Ye Y, Lin Y, Liu W, Chen B, Shen Q, Zhang L, Lavernia EJ (2019a) Additive manufacturing of functionally graded materials: a review. Mater Sci Eng A 764:138209. https://doi.org/10.1016/j.msea.2019.138209

Zhang J, Song B, Wei Q, Bourel D, Shi Y (2019b) A review of selective laser melting of aluminum alloys: processing, microstructure, property and developing trends. J Mater Sci Technol 35:270–284. https://doi.org/10.1016/j.jmst.2018.09.004

Zhu Y, Liu D, Tian X, Tang H, Wang H (2014) Characterization of microstructure and mechanical properties of laser melting deposited Ti–6.5Al–3.5Mo–1.5Zr–0.3Si titanium alloy. Mater Des 56:445–453. https://doi.org/10.1016/j.matdes.2013.11.044

Zhong Y, Liu L, Wikman S, Cui D, Shen Z (2016) Intragranular cellular segregation network structure strengthening 316L stainless steel prepared by selective laser melting. J Nucl Mater 470:170–178. https://doi.org/10.1016/j.jnucmat.2015.12.034

Chapter 16
Additive Manufacturing of Embedded Sensors

Christian Vedder

16.1 Motivation

Excessive temperature increase or static and dynamic overload can impair the function and the service life of mechanical parts leading to down times and reduced productivity of machines. To prevent greater damage to the parts within such machines, to optimize their functionality and efficiency or to get data for creating a digital twin (Ünal-Saewe et al. 2020), sensors are applied onto their surface. A common way for measuring mechanical stress, for example, includes the installation of prior manufactured, standardized body sound sensors or strain gauges and the electrical read-out of stress dependent electrical voltage or resistivity (Keil 2017). While these sensors have been developed and improved over decades they sometimes lack the possibility to be easily adapted to individual measuring tasks or be applied in automated processes, resulting in reduced sensing performance and high personnel costs for the manual installation. Furthermore, some environmental circumstances exceed the chemical or thermal threshold of common sensor solutions.

Modern approaches include a wet chemical deposition of functional coatings to components and a thermal post treatment, often achieved via oven processes, to obtain a certain coating functionality, such as electrical conductivity or chemical resistance among others. A major drawback of this approach is the thermal impact on the component as well as the massive energy consumption during treatment, since the whole component including the coating has to be heated up while only the coating requires thermal treatment. This sometimes excludes thermosensitive parts from being coated.

The laser overcomes these disadvantages by achieving high heating and cooling rates in a locally selective heat treatment. Using laser radiation, high coating temperatures that exceed the critical temperature of a temperature-sensitive substrate (e.g.

C. Vedder (✉)
Fraunhofer ILT, Aachen, Germany
e-mail: christian.vedder@ilt.fraunhofer.de

477

30 mm

Fig. 16.1 Printed and laser sintered strain gauge on various temperature-sensitive polymers (Fraunhofer ILT 2020)

decomposition temperature for polymers, tempering temperatures for hardened steels) can be achieved in a very short time without affecting the substrate material (Vedder 2013). Figure 16.1 shows laser-sintered silver nano-particulate coatings on different temperature-sensitive polymer foils.

What's more, the ability to treat layers locally and selectively opens up new possibilities in the creation of customized surface properties. Furthermore laser-based techniques are ideal for inline processing.

The process chain for the additive manufacturing of embedded sensors using print and laser processes is shown in Fig. 16.2. In a first step, the substrate can be cleaned from residual oil, dirt, rust, oxides etc. and pre-treated, using laser radiation as an alternative to plasma treatment, to obtain certain required surface conditions and improve wetting behavior or adhesion.

In the following steps, functional coatings are deposited using spray, dip coating or print processes such as ink or aerosol jetting, dispensing, screen printing etc. The materials used differ in a wide range, based on precursor solutions, sol gels, nano-particulate dispersions, or micro-particulate pastes, depending on the desired functionality and deposition method. A thermal post treatment step is needed to evaporate solvents or binders and to 'functionalize' the coating, by sintering or melting the remaining particles. Sensors are built up in multi-layers from different materials, thus, further printing and treatment steps are following the application of the first layer.

While the process chain is mostly identical, the materials and layer configurations can widely differ, depending on the desired sensor design and function. For most sensors, an electrical insulation is required as a first layer when being installed on an electrically conductive substrate like metal (Fig. 16.3).
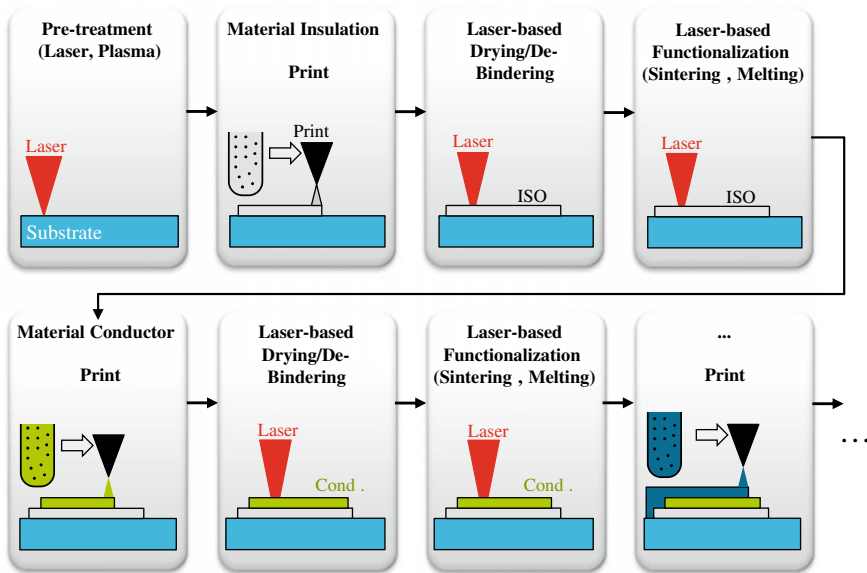
Fig. 16.2 Process chain for additively manufacturing multilayer sensors (Vedder et al. 2017)
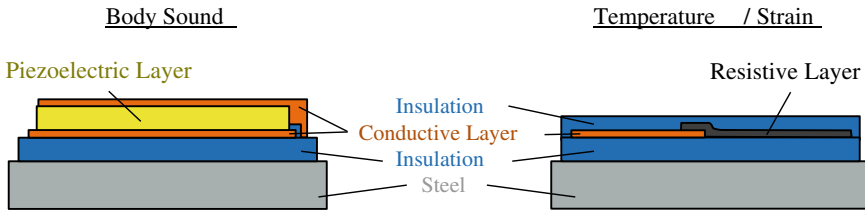
Fig. 16.3 Cross-section sketches of a simplified body sound sensor (left) and strain sensor (right) (Vedder et al. 2017)

A simple body sound sensor consists of an additional conductive layer, a piezo-electric layer and another conductive layer while a strain gauge includes a conductive and a resistive layer. The conductive and resistive layer can be combined and made of the same material; in this case, the resistivity can be increased by printing smaller cross-sectional areas of the conductor. Another possibility is the adaption of the sintering degree by a stronger or weaker selective laser treatment to achieve a higher or lower electrical conductivity within the layer. Most designs close with an encapsulation layer, made from an insulating material.

Challenges lie in the selection of suitable materials regarding chemical compatibility, adapted coefficient of thermal expansion etc., of suitable printing methods to obtain the required layer thickness, edge sharpness of printed structures, thickness uniformity etc. and of suitable laser systems as well as process parameters, e.g. laser wavelength, power, spot diameter, scanning strategy and speed, track distance, etc.

16.2 Laser Pre-treatment and Wetting Behavior

Pre-treatment with laser radiation can be used to clean surfaces from residual materials like oil or grease, native oxides or rust, unrequired coatings like paints, etc. It can also be used to modify the surface conditions for the following manufacturing steps and obtain a suitable set of surface properties (e.g. defined surface roughness and oxidation state). These can influence not only the wetting behavior of solvent-based coatings on the substrate surface (Dyckerhoff and Sell 1972) during the printing process (Fig. 16.4) but also of the molten material on the substrate surface during the laser process (Fig. 16.5) (Vedder et al. 2017).

For laser-based pre-treatment, mainly pulsed laser sources are utilized. If the surface energy of substrate and coating do not match well, a dewetting behavior called balling occurs during wet chemical deposition or during the laser melting process. Wetting behavior can be positively influenced by matching interface materials (substrate surface and coating material), adapting surface roughness and/or surface temperature, among other things.
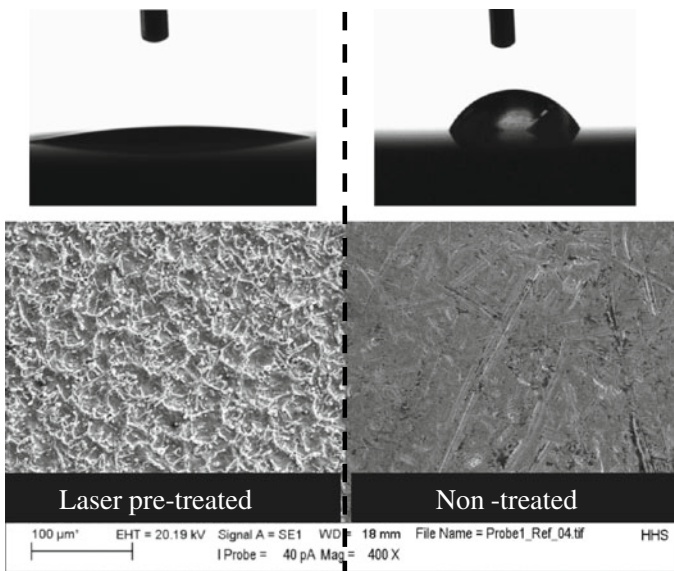
Fig. 16.4 Comparison of the wetting behavior (top row) of solvent-based fluids on a non-treated (right) and laser pre-treated (left) 100Cr6 metal surface (top row) as well as microscopic pictures of the substrate surfaces (bottom row) (Vedder et al. 2017)
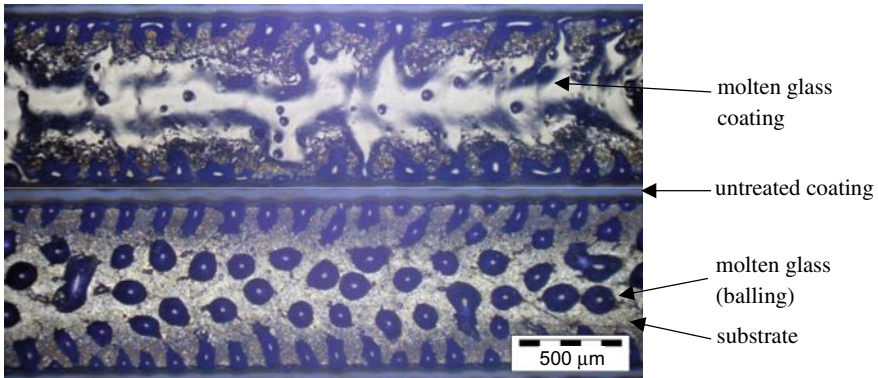
Fig. 16.5 Comparison (top view) of the wetting behavior of laser molten glass on a non-treated (bottom) and on a laser pre-treated 100Cr6 metal surface (top) (Vedder et al. 2017)

16.3 Wet Chemical Coating Methods—Thick and Thin Films

Apart from full area coating methods like dip, spin, spray coating etc. there are alternatives such as screen printing, dispensing, ink jet and aerosol jet printing for direct application of structured coatings onto substrates. Digital printing methods (e.g. ink jetting, aerosol jetting, dispensing) can alter the selectively applied coating structure by adapting the digital model without modifying the hardware (e.g. masks/screens in screen printing).

Using conventional thermal treatment (oven), structures within the coating will have to be created during the coating process (selective application + oven process). Using a defined laser radiation spot and a scanning head instead, a structure can be created within a full area coating during the laser treatment process (full area application + selective laser process). The non-irradiated parts of the coating can often be washed off while the irradiated parts will remain (Fig. 16.6). As the laser process is digitally controlled, too, adaptations to the desired design can be made by modifying the digital model. To improve resource and energy efficiency both selective application and laser treatment can be combined (selective application + selective laser process).

A classification of sensor manufacturing methods can be made by differentiating between thin film sensors (layer thickness approx. <1 μm) and thick film sensors (usually layer thickness range of 10 μm and more). Ink or aerosol jetters are commonly used to digitally print thin films, using solutions or nano-particulate dispersions (inks). Lateral structure sizes of down to about 50 μm (ink jet) and 20 μm (aerosol) can be achieved, depending on the used machines, materials and the wetting behavior of the substrate. Dispensers or screen printers, among others, are used to print thick films with lateral structure sizes of down to 100 μm (dispenser) and 50 μm (screen printer) using micro-particulate pastes or dispersions. These—as

Printed layer

Laser treated
structure

30 mm
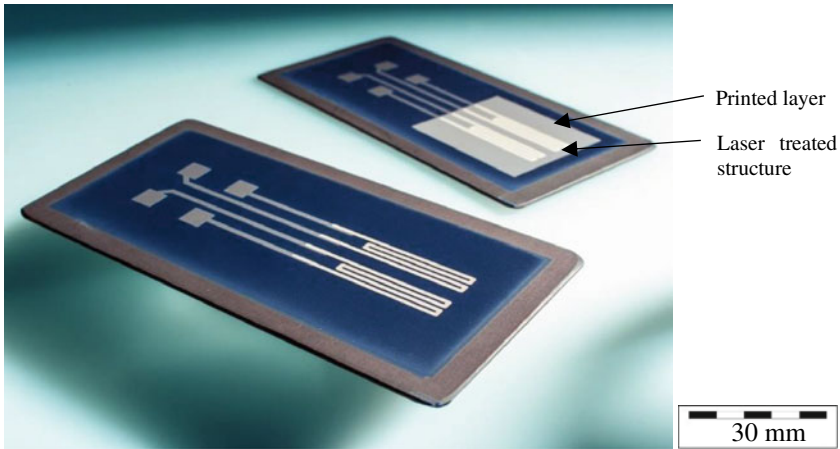
Fig. 16.6 Printed and laser treated layers of temperature sensors on a metal plate (back: pre-wash state with printed layer (grey square), front: post-wash state with remaining temperature sensing structure) (Vedder et al. 2017)

well as the inks—consists of the functional material (particles, that will be sintered, for example, and remain to achieve a desired coating functionality) and the auxiliary material (solvents and stabilizing materials that are necessary for the printing process and will be removed from the coating during the thermal treatment process).

16.4 Laser-Based Drying/Debindering

The functionalization step usually requires high coating temperatures for sintering or melting of the functional particles, for example. In case of a glass-based insulation material, processing temperatures lie between 650 and 850 °C. Using a furnace for the thermal treatment of printed layers with rather low heating and cooling rates of 10–100 K/min and treatment times of several minutes to hours, auxiliary materials like solvents and organic binder materials are evaporated in the process. Laser processes on the other hand reach very high heating and cooling rates of up to several 10,000 K/min within short radiation-material interaction times of one second and far below. This leads to instantaneous evaporation of the solvents and burning of the organic binders, destroying the functional coating. Thus, a drying step is needed for a comparably slower evaporation of the auxiliary materials at lower temperatures (100–450 °C). Figure 16.7 shows the laser functionalization (sintering) of a printed piezoelectric layer without a prior drying step, resulting in a burning of the material (left) and destruction of the coating, and after a laser drying step (right), achieving an intact coating.
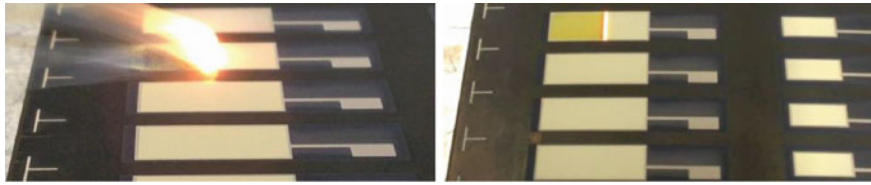
Fig. 16.7 Laser sintering of printed piezoelectric coatings without (left) and with a prior laser drying step (right), laser treatment direction: left to right (Vedder et al. 2022)

16.5 Laser-Based Sintering

The main step in the laser-based thermal treatment is the functionalization after which the coating shows its desired functionality (insulation, electrical conductance, etc.). Functional particles are sintered or molten at high temperatures of several 100 °C. The conversion of optical energy into thermal energy is based on the absorbance of a material. If a material is rather transparent for most of the available laser wavelengths, the material can be modified using additives that show a higher absorbance. In the case of a glass-based insulation material for the additive production of high temperature sensors, tungsten carbide is used in varying concentrations to adapt the optical properties of the coating (Fig. 16.8). Adding up to 5 wt% of tungsten carbide raises the absorbance at a wavelength of 980 nm from about 4 to 55%.

Apart from the substrate surface roughness and oxidation state, the surface temperature of the coated metal substrate has a high impact on the wetting behavior of
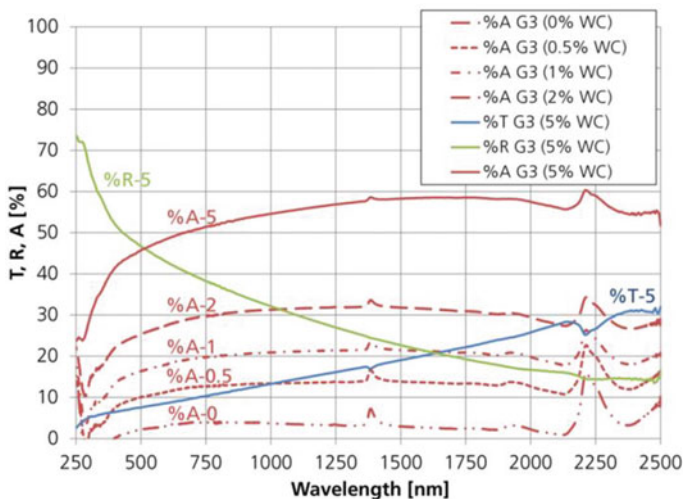
Fig. 16.8 Transmittance (T), reflectance (R) and absorbance (A) spectra of a micro-particulate glass layer with 5 wt% tungsten carbide particles as radiation absorbers (full lines) as well as absorber concentration dependent absorbance spectra (broken and dotted lines) (Vedder et al. 2017)
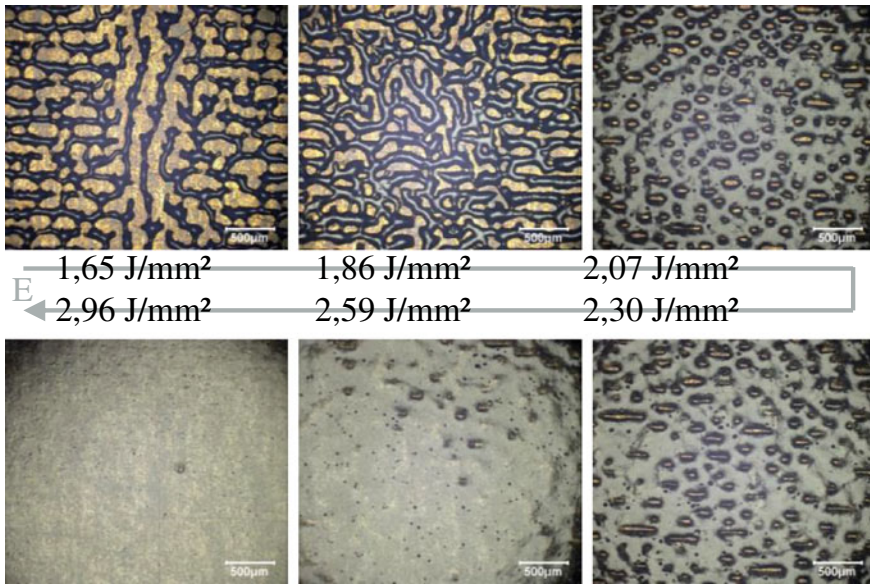
Fig. 16.9 Improved wetting behavior of glass-based insulation layer on metal substrate with increasing laser fluence (top view) (Vedder et al. 2017)

molten materials. The temperature can either be raised by pre-heating, using a heating element to increase the substrate surface temperature, or by raising the laser fluence in the melting process (Fig. 16.9).

In this specific case, raising the applied laser energy per area from 1.65 to 2.96 J/mm^2 leads to a full wetting of the surface with molten glass and, therefore, to a fully functional insulation. Figure 16.10 shows the cross-sections of two different insulating materials such as pure glass (left) and glass with added absorbing particles (middle) as well as a multi-layer coating including an additional conductive layer (right) as part of a temperature sensor on a metal substrate. Still, some single pores remain in the insulation layer, which is common also after conventional oven treatment. The solution is a multi-layer coating process to prevent open pores to impair electrical insulation.

16.6 Applications

As already motivated, sensors are used to monitor mechanical and thermal load or stress of components to prevent further damage and optimize machine operating points (machine efficiency, accuracy etc.).

While conventional strain gauges, for example, are highly developed and well established, there is still a great amount of time-consuming and manual work needed
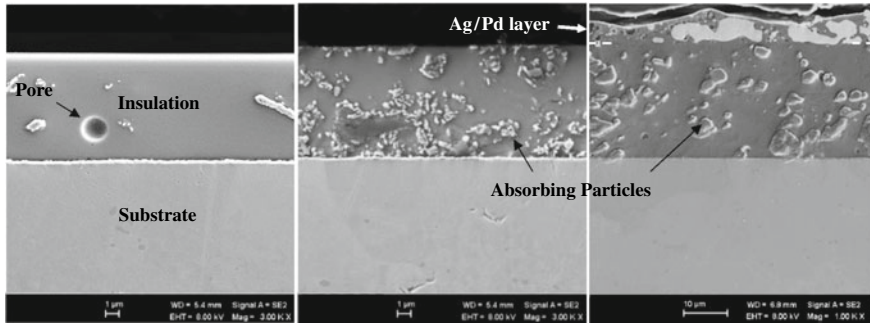
Fig. 16.10 Cross-section of laser-molten single and multi-layers on a metal substrate: Pure glass-based insulation (left), glass-based insulation layer with light absorbing particles (middle), with additional Ag/Pd conductive layer on top (right) (Gradmann et al. 2016; Vedder et al. 2017)

for the application of the sensors to the components with high risks for manufacturing errors and little flexibility in adaptation to special measuring tasks. Inline-capable and automatable approaches such as the laser-based additive manufacturing of sensors show high potential for the reproducible production of embedded sensors. A comparison of a conventionally applied (left) and a printed and laser treated strain gauge sensor on a metal part (right) is shown in Fig. 16.11.

Figure 16.12 shows additively manufactured thick film body sound and strain gauge sensors on roller bearing chassis, made from hardened steel, at different steps in the manufacturing process (left). Most of the shown sensor areas include a double insulating as well as a conducting layer. Some also show the black resistive elements in a full bridge strain gauge assembly. On the right side an additively manufactured thin film strain gauge sensor (also full bridge) is combined with a wireless telemetry system for data acquisition on a structural metal component.

A logical step further is the integration of thin film applied strain gauges into 3D printed components: The additive manufacturing of the component using laser powder bed fusion (LPBF) is interrupted for the integration of the sensor, which is
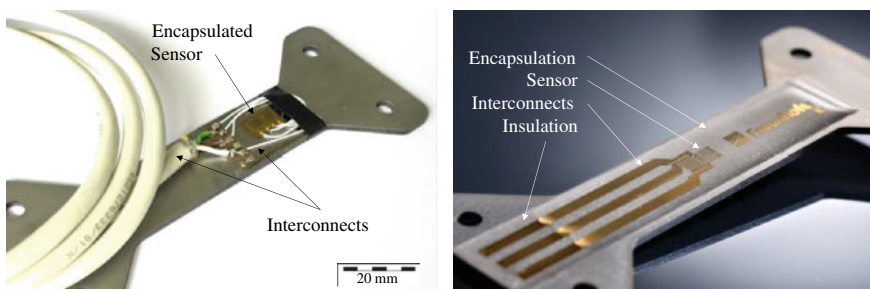
Fig. 16.11 Comparison of a conventional strain gauge (left) and an additively manufactured strain gauge (half bridge) on a metal component (right) (Vedder 2021)

Fig. 16.12 Additively manufactured thick film strain and body sound sensors on roller bearings (varying production steps) through print and laser process (left) (Vedder et al. 2017), Additively manufactured thin film strain gauge (full bridge) with wireless telemetry on metal component (right) (Vedder 2021)

Fig. 16.13 Printed and laser treated thin film strain gauge (insulation layer, sensor grid and interconnect, encapsulation) on a 3D printed component before further embedding using laser powder bed fusion (LPBF) (Fraunhofer ILT 2020)
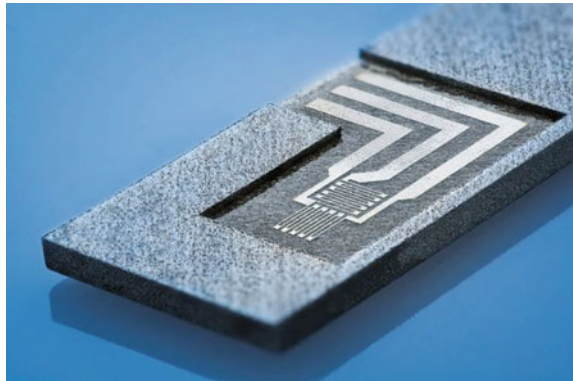
additively manufactured with thin film processing technology. Here, the different materials and structures are printed directly onto the component layer by layer and then functionalized (sintered, melted, hardened, etc.) using laser radiation. For the production of strain gauges, the insulation layer, the measuring grid and the encapsulation are applied one after the other. The LPBF building process is then continued, closing the cavity and thus fully integrating the sensor into the component (Fig. 16.13) (Fraunhofer ILT 2020).

References

Dyckerhoff GA, Sell P-J (1972) Über den Einfluß der Grenzflächenspannung auf die Haftfestigkeit. Die Angewandte Makromolekulrare Chemie 21:169–185
Fraunhofer ILT (2020) Annual report 2019. Aachen

Gradmann R, Seuthe T, Vedder C, Eberstein M, Partsch U (2016) Adaption of functional ceramic materials for the laser sintering process in integrated sensor applications. J Microelectron Electron Packag 13(4):176–181. https://doi.org/10.4071/imaps.515

Keil S (2017) Dehnungsmessstreifen. Springer Vieweg, Wiesbaden. ISBN 978-3-658-13611-6

Ünal-Saewe T, Vedder C, Vervoort S, Schleifenbaum JH (2020) Digitaler Zwilling im Produktlebenszyklus additiv gefertigter Komponenten. In: Frenz W (ed) Handbuch Industrie 4.0: Recht, Technik, Gesellschaft. Springer, GmbH Deutschland, Berlin. ISBN 978-3-662-58473-6

Vedder C (2013) Hochgeschwindigkeits-Laserfunktionalisierung gedruckter, nanopartikulärer Schichten am Beispiel von Indium-Zinn-Oxid. Shaker Verlag, Aachen

Vedder C (2021) Thermal laser post-treatment of functional layers. In: Proceedings to Lasersymposium Elektromobilität LSE '21', Aachen

Vedder C, Mertin J, Fink S, Steinhoff M, Stollenwerk J (2022) Laser-Based Production of Electrical Functional Layers. In: Proceedings to eHarsh Seminar, Aachen

Vedder C, Wollgarten S, Gradmann R, Stollenwerk J, Wissenbach K, Eberstein M (2017) Laser-based functionalization of electronic multi-material-layers for embedded sensors. J Laser Appl 29(2):226031–226037. https://doi.org/10.2351/1.4983267

Chapter 17
Laser Induced Forward Transfer—LIFT

Richard Lensing

The rise of additive manufacturing technologies has led to an acceleration of the development in the field of biofabrication. Various bioprinting methods are investigated for the research in and production of artificial tissue and organs. A promising method is the laser induced forward transfer (LIFT). This method utilizes laser pulses as the driving force for the transfer of drops or pieces of a thin donor film onto a receiver substrate. Initially developed for the transfer of solid donor films (Bohandy et al. 1986), the LIFT method has been expanded to using pastes and liquids as donor material, with few limitations regarding the rheological properties. Compared to other printing techniques, like inkjet printing, LIFT is a nozzle-free technique. Therefore, the commonly accepted limit for printable particle sizes of 1/100th of the nozzle diameter does not apply to LIFT (Serra and Piqué 2019). Hence LIFT can transfer a variety of functional materials and inks loaded with large biological structures. In the field of biofabrication mainly liquid donor LIFT is used for the transfer of inks with cells or bio-active components, also called bio-inks.

17.1 Fundamentals

In general a LIFT donor is a three layered system composed of a support layer, which is transparent for the laser radiation, an absorber layer where the laser energy is deposited and a donor film which is transferred. In liquid donor printing the transfer proceeds as depicted in Fig. 17.1. (1) A laser pulse is tightly focused onto the absorbing layer leading to an evaporation of the absorber and an expulsion of absorber material in form of a plasma plume. (2) A vapour bubble forms, displacing the surrounding ink and deforming the ink-air-surface. When the restoring forces

R. Lensing (✉)
Fraunhofer ILT, Aachen, Germany
e-mail: richard.lensing@ilt.fraunhofer.de
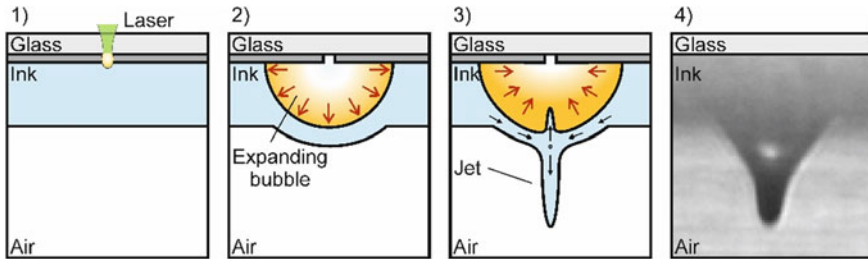
Fig. 17.1 Sketch of a LIFT process. (1) Laser evaporation of the absorber layer. (2) Resulting, expanding vapor bubble which displaces the surrounding ink. (3) The bubble collapses, the back flowing liquid forms a jet which expands perpendicular to the ink-air-interface. (4) Picture of the jet formation at the point of a starting bubble collapse

exceed the internal forces the bubble collapses and (3) the back flowing liquid forms a jet perpendicular to the surface. The jet expands towards the receiver substrate dragging any material inside the ink with it. Depending on the distance the ink jet either reaches the receiver depositing the ink directly or it breaks mid-air due to Rayleigh-Plateau instabilities creating droplets.

In both cases the transferred material forms a droplet-shaped "pixel" on the receiver substrate. A time sequence of the jet formation is depicted in Fig. 17.2. The dimensions of the deposited droplet are strongly influenced by the rheological properties of the donor ink, the properties and size of the particles inside the ink, and the composition of the receiver substrate. The droplet size can be adjusted by the laser parameters (laser fluence, laser spot size, pulse width) and the donor film thickness. With increasing laser fluence and donor film thickness larger droplets are transferred. At the lower end droplet sizes as small as 10 µm diameter (droplet volume 10 fL) have been realized with donor films of 5 µm thickness and less (Duocastella et al. 2007).

In addition to the controlled droplet sizes LIFT shows a high spatial resolution which is mainly influenced by the moving axis or scanner used in the machine setup as
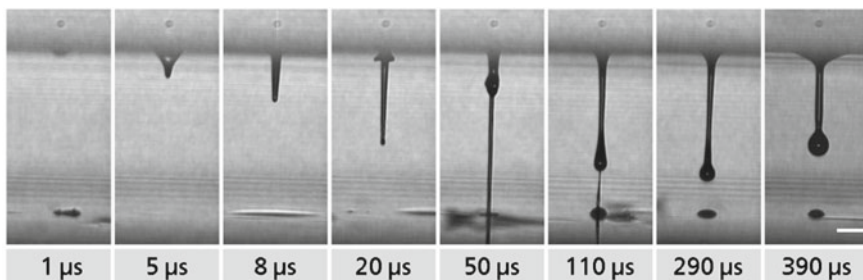
Fig. 17.2 Time sequence of the jet formation in a LIFT process using a nanosecond laser source with 12 µJ pulse energy and a 5% gelatin ink layer with a thickness of 130 µm. The distance between transfer and receiver slide is 1.1 mm. Scalebar 200 µm

well as the receiver substrate. Riester showed a positioning accuracy with a standard deviation of 2–10% of the droplet diameter (Riester 2015). Which leads to a spatial accuracy on a scale of single-digit microns.

17.2 Applications

The ability to print living cells and biomaterials in 2D and 3D structures opens new opportunities for the research of cell–cell and cell-environment interaction as well as for creating tissue-like structures. As a nozzle-free printing technique LIFT avoids issues like clogging and orifice induced shear stress. The high spatial resolution and the few limitations regarding the rheological properties of the ink allows for the printing of high cell densities for tissue engineering as well as enabling the transfer of single cells. The transfer of a large variety of cells such as Chinese hamster ovary cells (Wu et al. 2001), rat cardiac cells (Barron et al. 2005), and human stem cells (Gruene et al. 2011), among others (Serra and Piqué 2019; Riester 2015), has been demonstrated with cell viabilities close to 100% and little to no influence on cell functionality.

The field of laser assisted bioprinting for tissue engineering is well described and can be found elsewhere (Bishop et al. 2017; Guillotin et al. 2013; Koch et al. 2012). This chapter focuses on LIFT for single cell selection which is helpful for a combination with other optical analysis technologies.

17.2.1 Transfer of Single Cells

As an optical contact-free method with the capability of transferring single cells LIFT can be combined with optical setups like Raman spectroscopy, fluorescence microscopy or other imaging processes to identify and isolate cells.

One application of such a combined process is the laser assisted cell sorting (LACS) of high-producer cells for the production of monoclonal cell lines used in the production of proteins for biopharmaceuticals. The process is composed of three steps: cell identification, analysis of the functionality, and isolation of the cell. For cell identification an imaging system detects the cells on the transfer slide. Then the Raman spectrum is taken and analysed using a machine learning software to distinguish e.g. producer cells and non-producer cells. The producer cells are then transferred directly into microtiter plates via LIFT. In order to traverse the gap between donor and bottom of the individual wells on the receiving microtiter plate the LIFT-Jets have to reach a transfer distance of at least 6.5 mm. Figure 17.3a shows the rate of successful transfers for different transfer distances at 6.4 µJ, 11.1 µJ, and 13.6 µJ pulse energies. The cell viability of single cells after transfer into microtiter plates stays close to 100% as shown in Fig. 17.3b. Furthermore the production of proteins has been shown to be largely unaffected by the transfer process (Jaeckle et al. 2020).
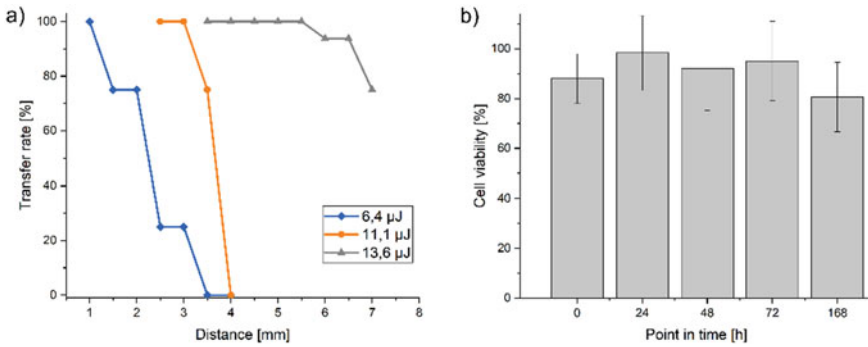
Fig. 17.3 a Rate of successful transfer for different transfer distances and laser pulse energies. **b** Cell viability for LACS Transfer into microtiter plates

This combination of optical processes allows for the automation of one of the most time-consuming steps in the development of monoclonal high-producer cell lines.

References

Barron JA, Krizman DB, Ringeisen BR (2005) Laser printing of single cells: statistical analysis, cell viability, and stress. Ann Biomed Eng 33(2):121–130

Bishop ES et al (2017) 3-D bioprinting technologies in tissue engineering and regenerative medicine: current and future trends. Genes Dis 4(4):185–195

Bohandy J, Kim BF, Adrian FJ (1986) Metal deposition from a supported metal film using an excimer laser. J Appl Phys 60(4):1538–1539

Duocastella M et al (2007) Study of the laser-induced forward transfer of liquids for laser bioprinting. Appl Surf Sci 253:7855

Gruene M et al (2011) Adipogenic differentiation of laser-printed 3D tissue grafts consisting of human adipose-derived stem cells. Biofabrication 3(1):015005

Guillotin B et al (2013) Laser-assisted bioprinting for tissue engineering. Biofabrication, William Andrew Publishing, pp 95–118

Jaeckle B et al (2020) Towards automation in biologics production via Raman micro-spectroscopy, laser-induced forward cell transfer and surface-enhanced Raman spectroscopy. J Biotechnol 323:313–321

Koch L et al (2012) Skin tissue generation by laser cell printing. Biotechnol Bioeng 109(7):1855–1863

Riester D (2015) Ortsselektives, Präzises Laserdrucken Von Biomaterialien Und Zellen, 1. Apprimus, Aufl. Aachen

Serra P, Piqué A (2019) Laser induced froward transfer: fundamentals and applications. Adv Mater Technol 4:1800099

Wu PK et al (2001) The deposition, structure, pattern deposition, and activity of biomaterial thin-films by matrix-assisted pulsed-laser evaporation (MAPLE) and MAPLE direct write. Thin Solid Films 398:607–614

Chapter 18
3D Photopolymerization for Biofabrication

Nadine Nottrodt and Elke Bremus-Köbberling

The chemical process of photo-induced polymerization has found widespread applications in the field of 3D printing. A special field of applications is biofabrication where photopolymerization is used for 3D bioprinting, e.g., for tissue engineering. In brief, a photopolymerization reaction uses the energy of light to initiate the cross-linking of monomers or pre-polymers to form polymeric networks. The prevalent mechanism of chain growth is radical polymerization of acrylic monomers. This reaction is typically started via UV-irradiation (< 400 nm) and requires a photoinitiator (PI) to produce the reactive species. Nowadays other mechanisms like cationic or "living" polymerizations or thiol-ene click reactions come more and more into focus (Bagheri et al. 2019; Chatani et al. 2014). In academic as well as in industrial research and development 3D photopolymerization-based technologies like stereolithography (SL), digital light processing (DLP), and multiphoton polymerization (MPP) are widely applied to fabricate components and devices with special mechanical, optical, chemical, or biological properties. For biofabrication additional properties like cytotoxicity of monomers and photoinitiators as well as UV radiation being harmful for cells have to be taken into account. New materials and technologies for biofabrication purposes have to be elaborated.

18.1 Stereolithography (SL)

Stereolithography is one of the first rapid prototyping technologies using a photo resin to build three-dimensional structures by layer-wise UV light irradiation. In 1984, Chuck Hull invented the first stereolithographic machine (US patent US4575330A)

N. Nottrodt (✉) · E. Bremus-Köbberling
Fraunhofer Institute for Laser Technoloy ILT, Steinbachstrasse 15, 52074 Aachen, Germany
e-mail: nadine.nottrodt@ilt.fraunhofer.de

which was able to fabricate 3D printed components. A very promising field of application for SL is the evolving field of biofabrication. In 2009, Mironov et al. gave a definition on Biofabrication, which explains that Biofabrication means the production of complex living and non-living biological products from raw materials such as living cells, molecules, extracellular matrices, and biomaterials (Mironov et al. 2009). As a production tool for three-dimensional structures, SL is very promising for tissue engineering by using materials like cells and tissue-relevant photo-cross linkable materials to build scaffolds for cell embedding.

The general setup of a stereolithographic machine (Fig. 18.1) contains a vat, a building platform, and a light source. The vat is the reservoir for the photo resin and the building chamber at the same time. Photo resins consist of monomers with either photo-reactive side chains, e.g., moieties like acrylate groups in combination with a special photoinitiator (PI) sensitive for a chosen UV light or thiol-ene moieties which can be polymerized directly by UV light (266 nm) (Hoffmann, et al., 2017). Typical PIs react at wavelengths in the range of 350 to 400 nm, e.g., Irgacure 2959 or 369 (Stampfl et al. 2008; Gauvin et al. 2012). For biofabrication application, the cytocompatibility of PIs is highly important. The mentioned Irgacure materials have been positively tested for their cell compatibility, nevertheless UV light is harmful for the cell DNA. Therefore other PIs working in the near UV (400–490 nm) like lithium phenyl-2,4,6-trimethylbenzoylphosphinate (LAP) or even visible light sensitive PIs are also under investigation and show promising results for biofabrication.

Two different setups for SL can be distinguished; one is a bottom up, the other one a top-down approach. In a bottom-up approach, the UV light comes from the top of the vat, while the light in a top-down approach is coupled into the vat through a transparent window in the bottom of the vat. During a bottom-up printing process,
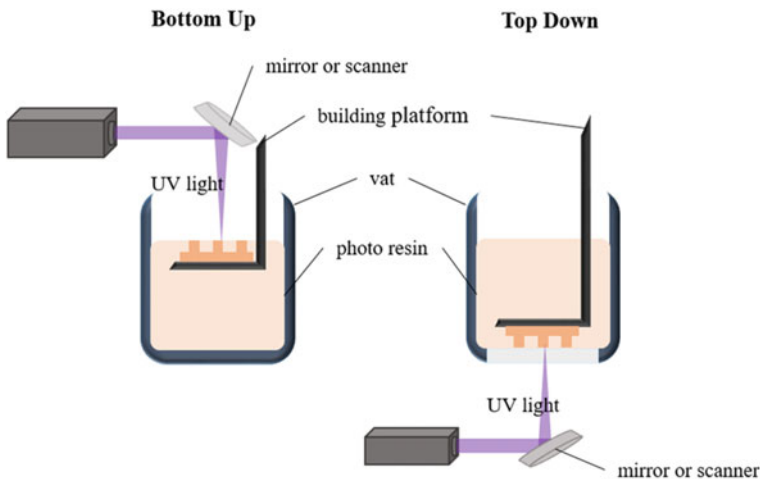
Fig. 18.1 The general stereolithographic setup consists of a vat, a building platform, and a light source. The main difference between the bottom-up and top-down approach for stereolithography is determined by the direction of irradiation

the building platform is positioned several micrometers below the surface of the resin. During the next step, the photo resin is exposed to the UV light and the material starts to polymerize. Afterward the platform lowers to allow the resin to cover the surface equally either by surface tension or a coating setup and irradiation continues. This procedure is repeated several hundreds of time to allow for a layer-by-layer 3D printing. Within the top-down approach, the platform is allocated at the bottom of the vat. The distance between the platform and the bottom defines the layer thickness. After irradiation the platform lifts up from the bottom, resin can fill the gap and another irradiation process can start to build the 3D object. The latter has the advantage that oxygen inhibition is prohibited.

While classical SL uses laser irradiation to induce single photon induced photo cross-linking with the limitations of being restricted to the surface due to low penetration depth into the liquid monomer mixture and consecutive polymerization steps with uncontrolled dark reactions, two further processes will be described. Digital light processing (DLP) to increase the building rate and multiphoton polymerization (MPP) for direct laser writing (DLW) to increase the printing resolution.

18.2   Digital Light Processing (DLP)

The main idea of DLP technology follows the top-down approach of SL taking the advantage of an illumination system at 405 nm wavelength using projection to illuminate the printing platform. The light is guided on a digital mirror device (DMD) which is a dynamic mask consisting of microscopically small mirrors on a semiconductor chip, which can be switched on and off rapidly and guide the light on small lenses focusing on the building platform. Doing so, a whole layer can be photocured in once and not point-by-point compared to SL. Therefore the building rate is enhanced. Since the projector uses a screen for projection, each voxel has cubic shape, which decreases the resolution of the printing product in x–y-direction. The resolution in z-direction depends on the layer thickness independent from SL or DLP process.

18.3   Multiphoton Polymerization (MPP)

Multiphoton lithography or multiphoton polymerization for direct laser writing (DLW) describes a method able to write structures in polymerizable resins with a resolution < 100 nm. The first idea of two photon absorption (TPA)—i.e., simultaneous absorption of two photons of a longer wavelength is effective to overcome the same energy barrier as one photon of twice the energy—was depicted by Maria Göppert-Mayer in the early 1930s (Herzfeld and Göppert-Mayer 1931). However, it took until solid-state femtosecond lasers became available (Moulton 1982) that a wider scientific community received the feasibility of two photon processes. Since

then this topic is being extensively investigated which can be seen from current reviews and papers (Ovsianikov et al. 2012; Whitby et al. 2017; Stokker-Cheregi et al. 2018).

The multiphoton polymerization process in DLW is based on two effects: first ultrashort laser pulses in the femtosecond (fs) range and second a tight focusing of the laser beam (NA > 1). These simultaneous effects allow for very high photon density in the focus causing non-linear effects (Miwa et al. 2001).

When focusing a UV laser onto a photo resin each single photon can start the polymerization reaction during SL immediately, resulting in polymerization beginning at the surface and continuing along the beam path into the photo resin limited by the optical penetration depth. The resolution also depends on the polymer layer thickness. In comparison (Fig. 18.2) in MPP, a tightly focused laser beam with ultrashort laser pulses at a wavelength in the visible region of the spectrum is focused on the volume of the transparent photo resin. Only the intensity in the focus is high enough to excite the resin by multiphoton absorption. The absorption causes a chemical change in a small volumetric pixel (voxel). The size of the voxel is determined by laser power and focal width and defines the resolution. By moving the laser focus a second voxel is produced next to the first one. An overlapping distance between the voxels results in a line. Diffusion effects in the irradiated polymer allow the voxels to grow together even without irradiation in the upper and lower part of the voxel. By moving the focal point following a Computer Aided Design/ Computer Aided Manufacturing (CAD/ CAM) model micro and nanostructures can be written (Selimis et al. 2015).

18.4   Applications

Even though the described processes of SL, DLP, and DLW via MPP are widely applied in technical applications for academia and industry, we restrict this overview to applications in the field of biofabrication like microfluidics, biomedical devices, tissue engineering, and drug delivery. (Pereira et al. 2015). An example for successful biofabrication is the photopolymerization of hydrogel networks that can be performed even in the presence of cells and bioactive molecules. Generation of 3D microenvironments with precise polymer architectures and varying compositions via SL and MPP provides control over cell functions by mimicking the natural environment on cellular and sub-cellular scale (Lutolf 2012; Torgersen et al. 2013). Bashir lab, for example, produced cell-laden hydrogels from PEGDA pre-polymers containing two cell types (skeletal muscle myoblasts and primary hippocampus neurons) at different locations via bottom-up stereolithography to study successfully the effects of co-encapsulation (Zorlutuna et al. 2011). Parkatzidis et al. produced grid-like structures from novel photocurable hydrogels mimicking the Extracellular Matrix (ECM) by means of MPP for 3D culturing of dental pulp stem cells (Parkatzidis, et al., 2019).
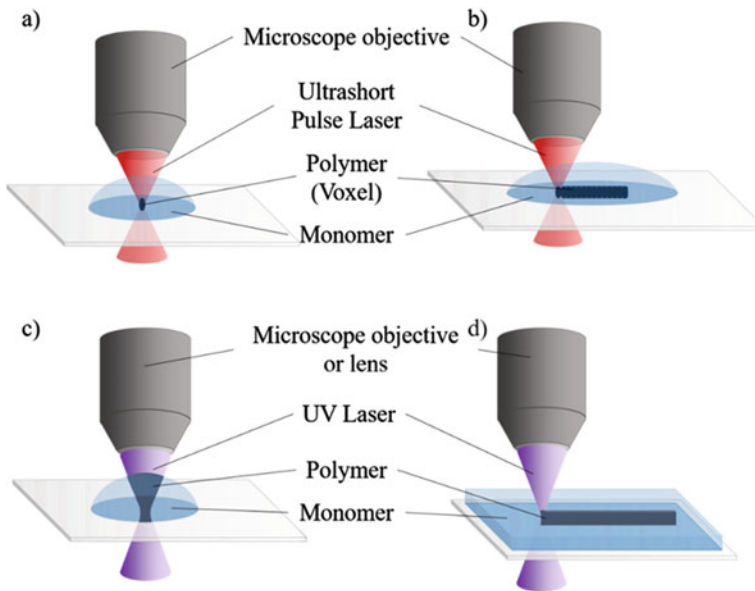
Fig. 18.2 Differences in digital laser writing via MPP and stereolithography. **a-b** DLW, **a** in a monomer solution. A polymer voxel is built in the focal plane of the ultrashort pulsed laser beam. **b** by moving the focus in the monomer volume voxels are formed next to each other and grow together by radical diffusion effects. **c-d** single photon stereolithography. **c** the monomer cross-links from the surface along the whole beam caustic according to the optical penetration depth, **d** by moving the beam over the liquid surface the monomer polymerizes in the whole monomer layer

Typical applications for single photon-based stereolithography are in the field of scaffold production for tissue engineering. The focus of these scaffolds is on the design to provide structures optimized for cell seeding and growth (Hoffmann et al. 2017) (Fig. 3a, b). Providing the right mechanical properties to allow cells to mature into a fully functional tissue. Within the human body tissue ranges, e.g., from soft and elastic fatty tissue to hard, load-bearing mandibular bone. Moreover, from relatively thin cell layers like epidermis to complex vascularized heart tissue or full-thickness skin. 3D Printing technologies allow for the systematic investigation of scaffold design. (An et al. 2015) An example is the design of branched vascular structures for full-thickness skin development, which provides optimized geometry for blood flow (Han et al. 2018) (Fig. 3c). While SL produces structures in the size of several micrometers, MPP allows the production in the range of nanometers. Nanometers correspond to the feature sizes of cell adhesion points, meaning that MPP allows for mimicking surface structure to analyze the process of cell adhesion and the mechanical load of cells on those structures (Engelhardt et al. 2011).
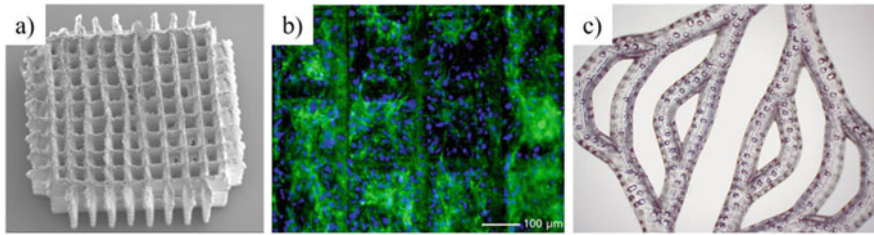
Fig. 18.3 Scaffolds produced by stereolithography: **a** Wood pile scaffold; **b** scaffold shown in **a** seeded with fibroblast cells stained with GFP and DAPI; **c** branched porous scaffold for following calculations for optimized branching angle

References

An J, Teoh JEM, Suntornnond R, Chua CK (2015) Design and 3D printing of scaffolds and tissues. Special section: advanced materials and materials. Engineering 1:261–268

Bagheri A, Jin J (2019) Photopolymerization in 3D Printing. ACS Appl Polym Mater 1:593–611. https://doi.org/10.1021/acsapm.8b00165

Chatani S, Kloxin CJ, Bowman CN (2014) The power of light in polymer science: photochemical processes to manipulate polymer formation, structure, and properties. Polym Chem 5:2187–2201. https://doi.org/10.1039/C3PY01334K

Engelhardt S, Hoch E, Borchers K, Meyer W, Krüger H, Tovar GEM, Gillner A (2011) Fabrication of 2D protein microstructures and 3D polymer–protein hybrid microstructures by two-photon polymerization. Biofabrication 3:25003. https://doi.org/10.1088/1758-5082/3/2/025003

Gauvin R, Chen Y-C, Lee JW, Soman P, Zorlutuna P, Nichol JW, Bae H, Chen S, Khademhosseini A (2012) Microfabrication of complex porous tissue engineering scaffolds using 3D projection stereolithography. Biomaterials 33:3824–3834. https://doi.org/10.1016/j.biomaterials.2012.01.048

Han X, Courseaus J, Khamassi J, Nottrodt N, Engelhardt S, Jacobsen F, Bierwisch C, Meyer W, Walter T, Weisser J, Jaeger R, Bibb R, Harris R (2018) Optimized vascular network by stereolithography for tissue engineered skin. Int J Bioprint 4:134. https://doi.org/10.18063/IJB.v4i2.134

Herzfeld KF, Göppert Mayer M (1931) Energieübertragung an adsorbierte Moleküle 1931A:669–678. https://doi.org/10.1515/zpch-1931-s172

Hoffmann A, Leonards H, Tobies N, Pongratz L, Kreuels K, Kreimendahl F, Apel C, Wehner M, Nottrodt N (2017) New stereolithographic resin providing functional surfaces for biocompatible three-dimensional printing. J Tissue Eng 8. https://doi.org/10.1177/2041731417744485

Lutolf MP (2012) Cell environments programmed with light. Nature 482:477–478. https://doi.org/10.1038/482477a

Mironov V, Trusk T, Kasyanov V, Little S, Swaja R, Markwald R (2009) Biofabrication: a 21st century manufacturing paradigm. Biofabrication 1:22001. https://doi.org/10.1088/1758-5082/1/2/022001

Miwa M, Juodkazis S, Kawakami T, Matsuo S, Misawa H (2001) Femtosecond two-photon stereolithography. Appl Phys A 73:561–566. https://doi.org/10.1007/s003390100934

Moulton P (1982) Ti-doped sapphire: tunable solid-state laser. Opt News 8(6):9–9

Ovsianikov A, Li Z, Torgersen J, Stampfl J, Liska R (2012) Selective functionalization of 3D matrices via multiphoton grafting and subsequent click chemistry. Adv Funct Mater 22:3429–3433. https://doi.org/10.1002/adfm.201200419

Parkatzidis K, Chatzinikolaidou M, Kaliva M, Bakopoulou A, Farsari M, Vamvakaki M (2019) Multiphoton 3D printing of biopolymer-based hydrogels. ACS Biomater Sci Eng 5:6161–6170. https://doi.org/10.1021/acsbiomaterials.9b01300

Pereira RF, Bártolo PJ (2015) 3D bioprinting of photocrosslinkable hydrogel constructs. J Appl Polym Sci 132. https://doi.org/10.1002/app.42458

Selimis A, Mironov V, Farsari M (2015) Direct laser writing: principles and materials for scaffold 3D printing. Microelectron Eng 132:83–89. https://doi.org/10.1016/j.mee.2014.10.001

Stampfl J, Baudis S, Heller C, Liska R, Neumeister A, Kling R, Ostendorf A, Spitzbart M (2008) Photopolymers with tunable mechanical properties processed by laser-based high-resolution stereolithography. J Micromech Microeng 18:125014. https://doi.org/10.1088/0960-1317/18/12/125014

Stokker-Cheregi F, Palla-Papavlu A, Paun IA, Lippert T, Dinescu M (2018) Laser structuring of soft materials: laser-induced forward transfer and two-photon polymerization. In: Ossi PM (ed) Advances in the application of lasers in materials science. Springer International Publishing, Cham, pp 247–273

Torgersen J, Qin X-H, Li Z, Ovsianikov A, Liska R, Stampfl J (2013) Hydrogels for two-photon polymerization: a toolbox for mimicking the extracellular matrix. Adv Funct Mater 23:4542–4554. https://doi.org/10.1002/adfm.201203880

Whitby R, Ben-Tal Y, MacMillan R, Janssens S, Raymond S, Clarke D, Jin J, Kay A, Simpson MC (2017) Photoinitiators for two-photon polymerisation: effect of branching and viscosity on polymerisation thresholds. RSC Adv 7:13232–13239. https://doi.org/10.1039/C6RA27176F

Zorlutuna P, Jeong JH, Kong H, Bashir R (19/2011) Tissue engineering: stereolithography-based hydrogel microenvironments to examine cellular interactions. Adv Funct Mater 21:3597. https://doi.org/10.1002/adfm.201190080

Part VI
Functionalization and Modification

Chapter 19
Thin and Thick Film Processing

Christian Vedder

19.1 Motivation

Ever since people build things, a great deal of effort has also gone into enhancing or changing the surface properties, be it the decoration of pots, the production of waterproof layers or the hardening of metals. With the progress of technical development, the modification and coating methods have become increasingly complex. Hardening of steel parts (see Chap. 6) has been one of the earlier approaches in laser-based treatment of surfaces which falls into the category of enhancing the basic properties of the part's surface (Fig. 19.1).

Other approaches are based on the coating of surfaces to enhance the basic properties, e.g. the deposition of hard coatings to further increase the surface hardness of above mentioned parts, or to add other surface properties such as resistance against chemicals, reflection of light in different colours (decoration), conductance of electricity (see also Chap. 6.3), and much more, by applying functional layers. In this chapter, the terms 'layer', 'coating' and 'film' are used synonymously.

19.2 Approaches for Laser-Based Processing of Surfaces and Coatings

Approaches for the laser-based modification of surfaces (Fig. 19.2A) such as hardening and softening are discussed in Chaps. 5 and 6. Apart from laser-based coating methods like pulsed laser deposition (PLD), laser-induced forward transfer (LIFT) and many more, this chapter will focus on the laser-based modification and functionalization of layers. Modification, in this chapter, is defined as the treatment of layers

C. Vedder (✉)
Fraunhofer ILT, Aachen, Germany
e-mail: christian.vedder@ilt.fraunhofer.de
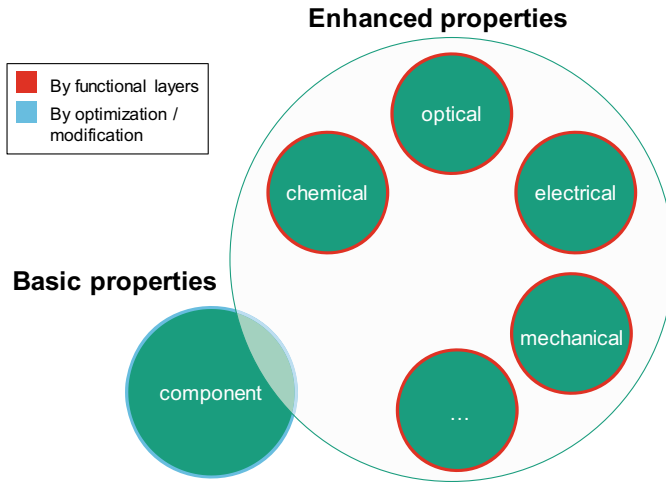
Fig. 19.1 Enhanced basic properties by surface modification in comparison to enhanced additional properties through added functional layers (Vedder 2021)

to increase or alter an already existent functionality, such as the annealing of via physical or chemical vapour deposited (PVD, CVD) coatings on glass, e.g. indium tin oxide as a transparent conducting material, to increase the electrical conductivity (Fig. 19.2B). Functionalization is the creation of a coating functionality, such as electrical conductance through the laser treatment of the coating (Fig. 19.2C). This can be achieved, for example, by printing a silver-based nano-particulate dispersion onto glass and laser treating the coating to evaporate the solvents, needed for the printing process, as well as to sinter the nanoparticles to obtain a conducting layer. While the printed layer is not electrically conducting, the laser-treated is.

In most cases, the modification or functionalization is based on a thermal treatment of the coatings which is conventionally done using oven processes (Fig. 19.3A). Coating and substrate are heated in a controlled scenario, achieving a comparably slow thermal treatment of the whole part, which can last for minutes up to hours at heating and cooling rates of 10–50 K/s. Other approaches are based on rapid thermal processing/annealing (RTP/RTA, Fig. 19.3B), still lasting for several seconds to minutes while heating up the whole part, or photonic/flash sintering (Fig. 19.3C), typically lasting for milliseconds while mainly heating up a wide area of the coating using a broad range of radiation wavelengths. With laser radiation (Fig. 19.3D), not only interaction times can be reduced further to the sub-millisecond regime with heating rates of up to several thousand K/s to decrease the thermal impact on the substrate and inter-material or inter-layer diffusion processes, but treating the coating selectively (instead of substrate and coating) as well as locally (in the range of the laser spot size) can further reduce the required energy.
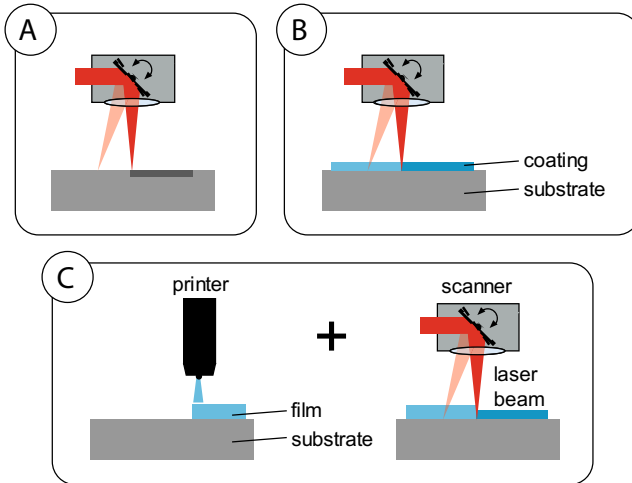
Fig. 19.2 Comparison of laser-based approaches: **A** modification of a part's surface, **B** modification of already coated substrates, **C** additive manufacturing of coatings using wet chemical deposition and laser-based thermal post-treatment (Vedder 2021)
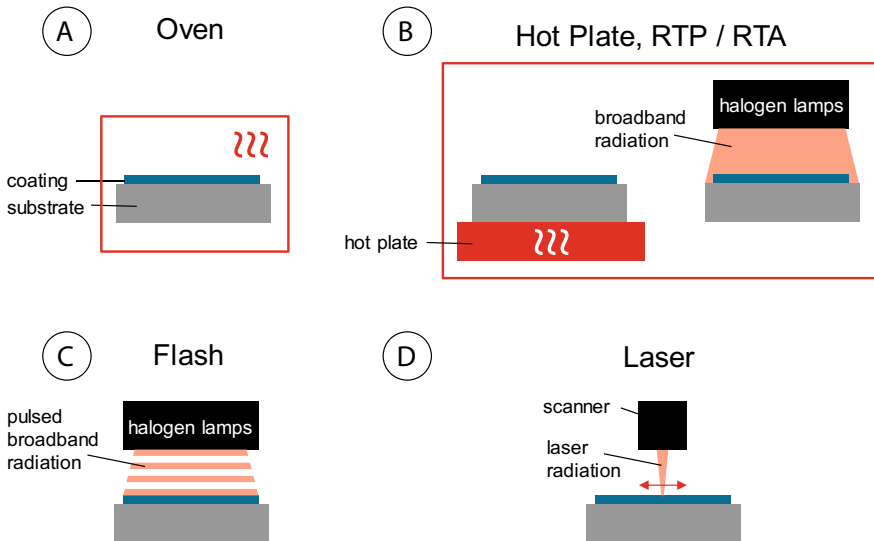
Fig. 19.3 Comparison of thermal treatment approaches: **A** oven, **B** hot plate or rapid thermal processing, **C** flash sintering, **D** laser treatment

19.3 Laser-Based Modification of Coatings

The laser-based modification of coatings is used to alter or enhance coating properties in a short thermal process. One example is the laser-based annealing of indium tin oxide (ITO), a transparent conducting oxide (TCO) which is used in many modern electronic devices such as organic light emitting diodes (OLED), displays and touch-screens. ITO combines qualities like high electrical conductivity as well as high visual transparency, and still is the most suitable material for thin film anodes in the afore-mentioned devices (OLED: Fig. 19.4, left). Nevertheless, due to the (in comparison to metals) high electrical resistance of ITO and the OLED-specific lateral electrical connection to the anode, bigger OLEDs in early stages of the development tended to show reduced luminosity towards the middle of the light emitting panel area (Fig. 19.4, right) (Vedder 2013).

In this example, the via physical or chemical vapour deposition (PVD/CVD) applied, approximately 130 nm thick layers show a typical sheet resistance of 21–22 Ω/sq after deposition. It can be decreased by more than 25% down to 16 Ω/sq (Fig. 19.5) via fast NIR laser annealing using a continuous wave fibre laser emitting at a wavelength of 1070 nm (top hat intensity distribution). Lower sheet resistances can be achieved by using higher radiation intensities at higher scanning velocities while applying a meandric scanning strategy. This process is limited, since cracking in the ITO layer occurs at higher laser intensities due to mechanical stress in the ITO layer which is thermally induced at high heating and cooling rates. The interaction time is approx. 90 μs at an areal rate of 4.5 cm^2/s.

The reduction of electrical resistance is caused by an increase of ITO oxygen vacancies through laser treatment (measured by X-ray photoelectron spectroscopy), leading to a higher charge carrier concentration. Additionally, a cure of crystal lattice defects or dislocations (detected by X-ray diffractometry) leads to higher charge carrier mobility. Both increases of carrier concentration and mobility are also shown in simulations on laser processed nano-particulate ITO layers, performed with the

light emission

lateral electrical connection of ITO

□ substrate (glass)
□ transparent conductive layer (ITO)
■ hole transport layer

■ emitting layer
■ electron transport layer
■ metal cathode

10 mm
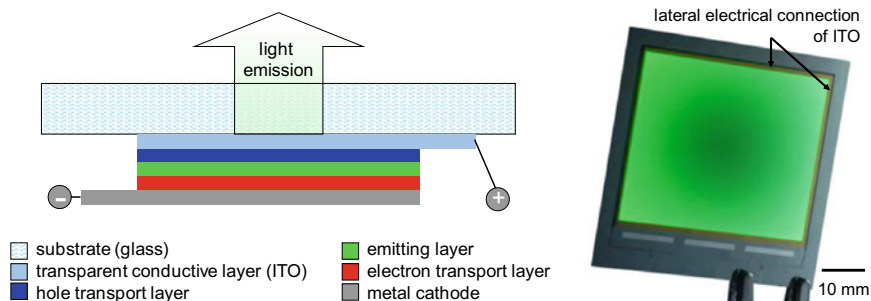
Fig. 19.4 Cross-sectional scheme of an OLED (left), mock-up of a reduced luminosity in the centre of a green OLED panel (right) (Vedder 2013)
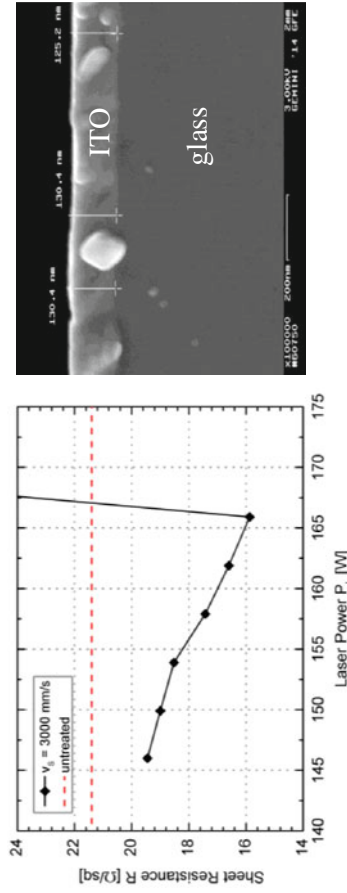
Fig. 19.5 Dependence of the sheet resistance R on the used laser power P_L, the red dotted line represents the sheet resistance before laser treatment (left). Cross section of an ITO layer on glass

SCOUT software by W. Theiss, based on the Extended Drude and OJL-Models (Vedder 2013).

19.4   Laser-Based Functionalization of Coatings

Unlike the laser-based modification of already applied functional coatings, the laser-based functionalization of coatings is used to obtain a certain coating functionality which is not existent prior to laser treatment. Modern approaches include a wet chemical deposition of coatings onto parts and a thermal post-treatment, typically conducted in an oven process, to obtain a certain coating functionality, such as electrical conductivity or chemical resistance among others. A major drawback of this approach is the high thermal impact on the whole part as well as the massive energy consumption during treatment, since the part including the coating has to be heated up while only the coating requires thermal treatment. This sometimes excludes thermosensitive parts from being coated.

The laser overcomes these disadvantages by achieving high heating and cooling rates in a locally selective heat treatment. Using laser radiation, high coating temperatures that exceed the critical temperature of a temperature-sensitive substrate (e.g. decomposition of polymers, softening of hardened steels) can be achieved in a very short time without affecting the substrate material (Vedder 2013). In addition, the ability to treat layers locally and selectively opens up new possibilities in the creation of customized surface properties. Furthermore, laser-based techniques are ideal for inline processing and digital workflow.

An exemplary process chain for the laser-based inline manufacturing of functional layers is shown in Fig. 19.6.

A mechanical, chemical or laser-based pre-treatment can be used to clean the surface from dirt, oxides or residual oil/grease of upstream manufacturing processes and to apply desired surface conditions (roughness, oxides) for the following deposition process (step 1). The result is a pre-treated surface for further processing. In step 2, functional materials, such as nano- or microparticle pastes, inks and sol-gels are deposited onto the substrate surface. Pastes, for example, consist of functional particles (gold, silver, etc.), solvents (alcohol, water, etc.) and stabilizers, which are necessary to prevent particle agglomeration and support the deposition process. Deposition methods can be dip or spin coating, spraying, knife or slot die coating, screen printing, etc. or digital printing techniques such as ink jetting, aerosol jetting and dispensing. The result is a wet coating. Usually this step is followed by an oven processing for thermal treatment. In the case of laser-based thermal treatment, the following steps are divided into laser drying (step 3) and laser functionalization (step 4). In step 3, the solvents and auxiliary ingredients like organic binders are evaporated. To prevent the coating from being destroyed due to an instant, explosive-like evaporation of the solvents or burning of the organics, laser drying is usually conducted with lower intensities and heating rates at temperatures from 60 up to 450 °C. In an inert atmosphere, the thermal decomposition of organic materials is
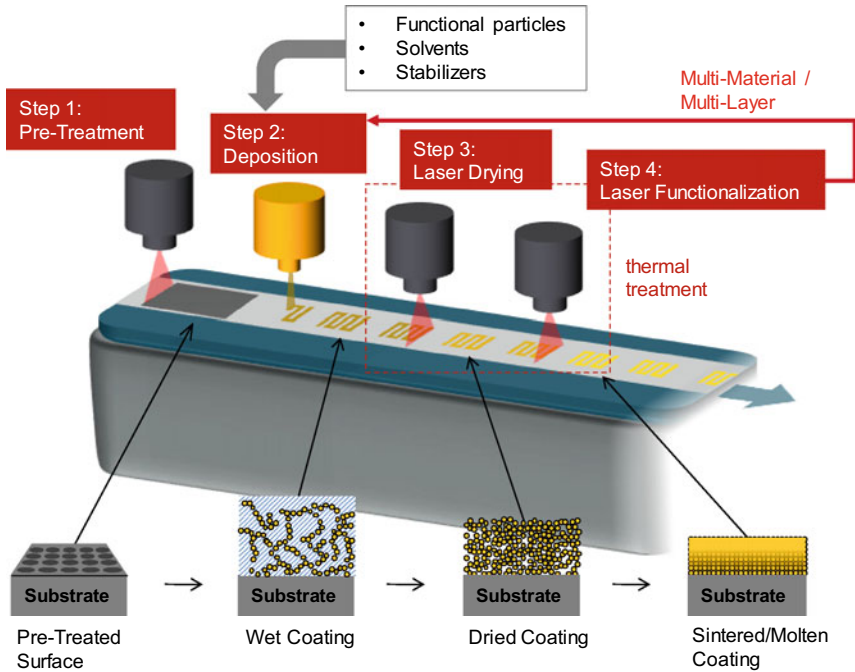
Fig. 19.6 Process chain for inline laser-based deposition of thin (<1 μm) or thick films (>1 μm) (Vedder 2021)

also often called pyrolysis. The result is a dry coating, ideally consisting only of the remaining functional particles. In step 4, higher laser radiation intensity/energy is used to obtain higher temperatures (200–1000 °C or above) in short time scales for sintering, melting, crystallization, etc. of the remaining particles/material. By repeating the deposition and thermal treatment steps, multi-layers can be produced. This way, sensors on parts can be additively manufactured (see also Chap. 16).

An exemplary machine set-up for dispensing and laser curing of polymer-based insulating and conducting materials on metal parts is shown in Fig. 19.7.

19.4.1   Laser-Based Drying

Laser-based drying can not only be used as a pre-step for the functionalization process, but also as a stand-alone process to substitute energy-intensive oven processes. The drying process of slurries, for example, is a key element in the manufacturing of battery electrodes since, on the one hand, it shows great energy saving potential and, on the other hand, it has a significant influence on the performance of battery cells. Electrode slurries are conventionally dried in continuous furnace

processes. The low efficiency of these processes is attributed to the indirect heat input via convection as well as to the great thermal mass of the machines themselves. In contrast to these processes, laser drying shows a higher efficiency of the thermal energy input (only the layer and small areas of the substrates are heated up) and enables the reduction of installation spaces.

The main goal is to evaporate the water of slot-die coated films (Fig. 19.8) while conserving the active as well as the binder materials, which are destroyed at temperatures beyond 180–240 °C (material-dependent). Typical coating thickness can be in the range of 10–200 μm. Further goals are the achievement of coating adhesion to the substrate and the preservation of the porous character of the layer to allow the electrolyte to infiltrate the electrode later on (Vedder et al. 2016).

There are several approaches for the laser-based drying: Two exemplary set-ups for roll-to-roll processing are shown in Fig. 19.9. Approach A includes the scanning of focused radiation from a fibre-guided diode laser, for example, while approach B includes a fixed vertical cavity surface emitting laser (VCSEL) or, alternatively, a diode laser with focusing optics to achieve a large irradiation area of 40 mm × 300 mm or more, for example. Both approaches include a closed-loop control of the laser power to obtain a constant drying temperature, based on a pyrometric data measurement in the drying zone.

In the application field of battery electrodes, graphite-based anodes as well as cathodes made from LiFePO4-slurries have proven to be easily laser dryable. The cross sections of laser and conventionally oven-dried cathodes are compared in Fig. 19.10. There is no significant difference in the layer's morphology detectable (Vedder et al. 2016).

The inline-capability and compatibility of the laser process with conventional manufacturing lines has been demonstrated. Energy savings of up to 50%—compared to conventional oven drying processes—can be achieved, since only the electrode
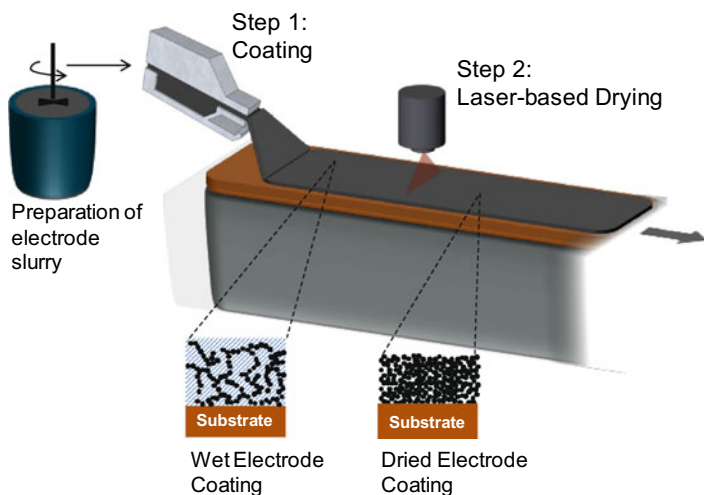
Fig. 19.8 Process chain used for the laser-based, additive production of battery electrodes (Vedder et al. 2016)
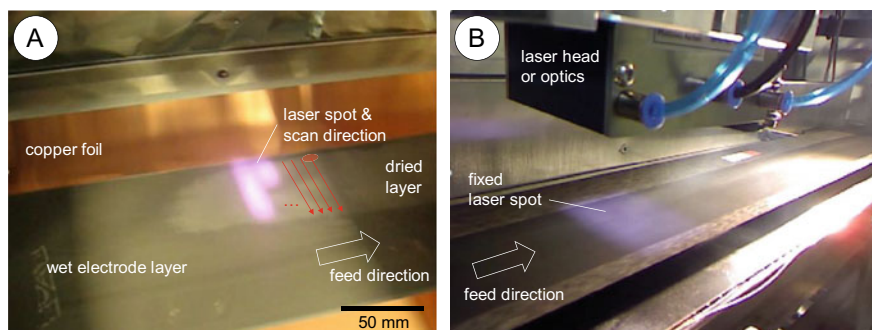
Fig. 19.9 Comparison of two laser drying approaches and set-ups: **a** scanned laser spot, **b** fixed area irradiation (Vedder 2021)

layer is thermally processed. Furthermore, the installation footprint can be reduced drastically in comparison to oven-based processing (Vedder et al. 2016). An early-stage laser set-up is compared to the length of an oven-based line in Fig. 19.11. Further set-ups are investigated to increase the feed speed to industrial scales of 80 m/min and more.
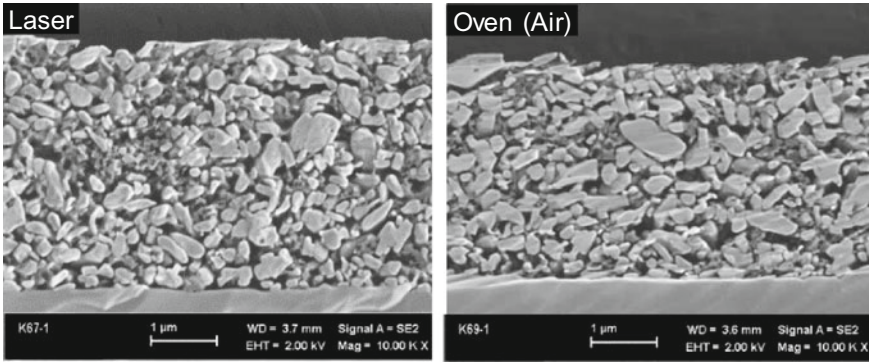
Fig. 19.10 SEM cross section of a laser-dried cathode in comparison to a conventionally dried cathode (Vedder et al. 2016)
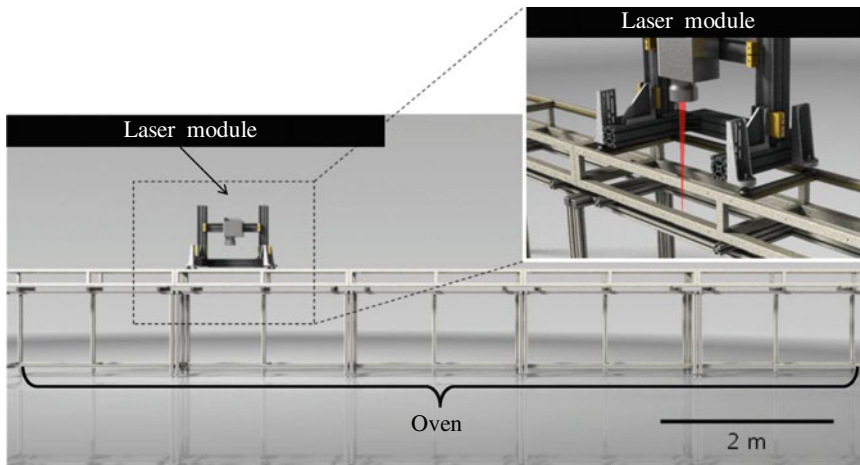
Fig. 19.11 Size of a laser module for drying of battery electrodes compared to the installation space of an oven (Vedder 2021)

19.4.2 Laser-Based Sintering

Laser-based sintering in coating processes is a powerful tool to locally fuse particles within a layer. Conventionally, a laser beam is deflected by mirrors within a scanning head in order to be moved across a surface of a substrate. Focusing optics are used to increase the power intensity on the surface (Fig. 19.12) to melt the whole or parts of the irradiated particles which re-solidify after the laser treatment and build a cohesive, often porous layer.

Conventional (e.g. oven-based) sintering is categorized into solid phase sintering at temperatures below the melting point of the lowest melting component and liquid
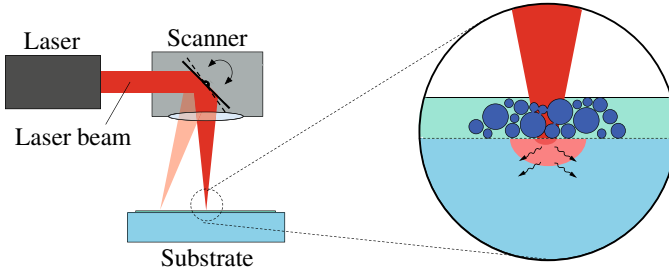
Fig. 19.12 Thermal treatment of particulate layers by laser radiation (process principle) (Vedder 2013)

phase sintering at temperatures above the melting point of prior added low-melting components (sintering additives), used as matrix material for the high-melting particles. The sintering process is divided into three sintering stages: (1) Initial stage with forming of necks between the particles based on gas diffusion, surface diffusion, grain boundary diffusion and volume diffusion, (2) intermediate stage with neck growth and gradual formation of grain boundaries and (3) end stage with further grain growth and further pore reduction or elimination (Salmang et al. 2007).

Compared to conventional oven sintering, laser sintering is a rather selective and fast process with high heating rates of up to several thousand K/s. Because of the short interaction times in the sub-second regime, laser sintering is merely considered a liquid phase sintering process: the particle surface is molten while the core merely stays solid. The transition between sintering and melting a particulate layer is fluid. If the particle crystallinity must be preserved, using low-melting components as embedding matrix material is another approach. The reduction of interaction times also leads to a decrease of material diffusion in multi-material layers which offers new possibilities in joining otherwise incompatible materials (Hoff et al. 2022).

Laser sintering of wet chemical deposited layers (via spraying, dip-coating or printing) has strongly developed over the past years and is highly resource and energy efficient since only the required material can be deposited without masks and downstream stripping processes, and only the deposited layer can be thermally treated using laser radiation which is a main advantage to conventional oven processes. The manufacturing of layers using print and laser processes often can be done in ambient atmosphere, which is a huge benefit in energy savings, compared to vacuum-based coating processes such as chemical or physical vapour deposition. Furthermore, large as well as temperature-sensitive parts can easily be coated, the desired temperature can be adapted in milliseconds via pyrometric control and the process is highly automatable and easily able to be integrated into digital workflows.

Advantages, among others, are (Vedder et al. 2008):

- High temperature, fast treatment of the particle-based coating with coinstantaneous low thermal load on the substrate.
- Adaptable local degree of sintering.
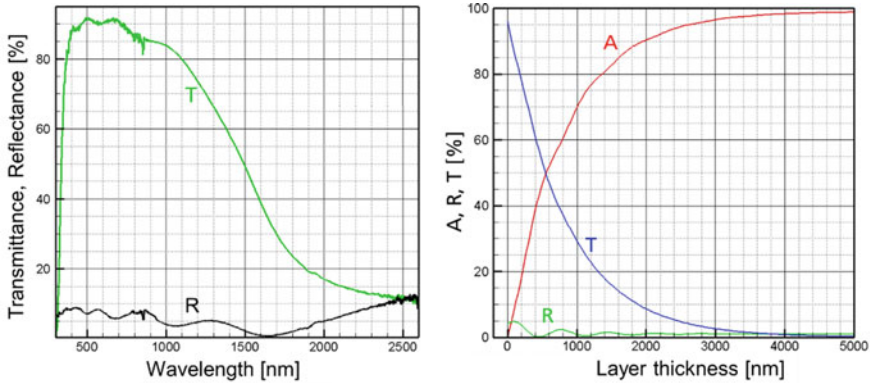
Fig. 19.13 Measured optical properties of a 0.6 µm thick, nano-particulate ITO layer (left), simulated layer thickness-dependent optical properties of nano-particulate ITO (right, wavelength: 1550 nm), T: transmittance, R: reflectance, A: absorbance (Vedder 2013)

- Avoidance of extensive grain growth, reduction of loss of porosity (thus reduced decrease of accessible surface area and concomitant drop in e.g. catalytic activity).

One challenge in laser sintering of coatings is the choice of a suitable laser wavelength. Optical properties are highly dependent on the material and particle size. Indium tin oxide (ITO), for example, is a transparent conductive oxide, mainly transparent in the visual spectrum (Fig. 19.13, left) and still transmissive in the near infrared spectrum.

Using simulation software, the complex refraction index for ITO as well as the layer thickness-dependent optical properties of nano-particulate ITO layers are calculated (Fig. 19.13, right). With increasing layer thickness more radiation is absorbed in the layer, leading to a higher layer temperature at constant laser process parameters. Inconsistent layer thickness can be a result of deviations in the printing process or movement of solid particles during the drying of a nano-particulate wet layer (so-called 'coffee stain effect'), leading to thicker edges of the coating. To counteract the higher absorbance in the thicker parts of the layer, the laser radiation energy has to be adapted. A closed-loop temperature control, based on pyrometric data from the processing zone, is a possible approach (Vedder 2013).

This way, inkjet printed ITO layers can be laser sintered (Fig. 19.14) to reduce the electrical sheet resistance of several mega ohms per square after printing and drying to less than 100 Ω/sq after laser treatment. These layers can be used as transparent electrodes in small scale OLEDs or individually printed electroluminescence lamps on glass or polymer substrates (Fig. 19.15) (Vedder 2013).
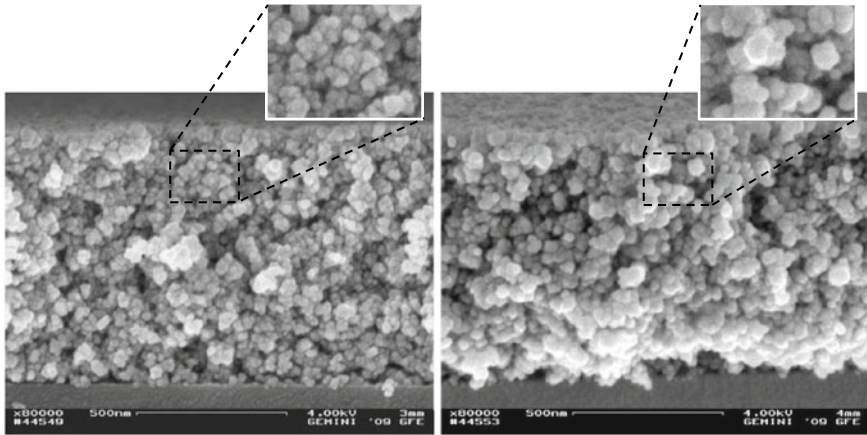
Fig. 19.14 SEM pictures of a printed and untreated (left) as well as laser-treated (right) ITO coating on glass (Vedder 2013)

Fig. 19.15 Electroluminescence lamps with printed and laser-treated ITO layers on glass and polymer substrates (Vedder 2013)

19.4.3 Laser Crystallization

In the course of miniaturization and the increasing integration of electrical circuits, microelectromechanical systems (MEMS) continue to become more important. Piezoelectric materials are used for microactuators; these materials mechanically deform when an electric field is applied. Sol–gel-based systems out of lead zirconate titanate (PZT) are characterized by their pronounced dielectric and piezoelectric properties with thinly applicable layer thicknesses, but have to be crystallized by means of thermal post-treatment. In contrast to conventional furnace processes, laser processes can heat small volumes for a short period of time in a location-selective
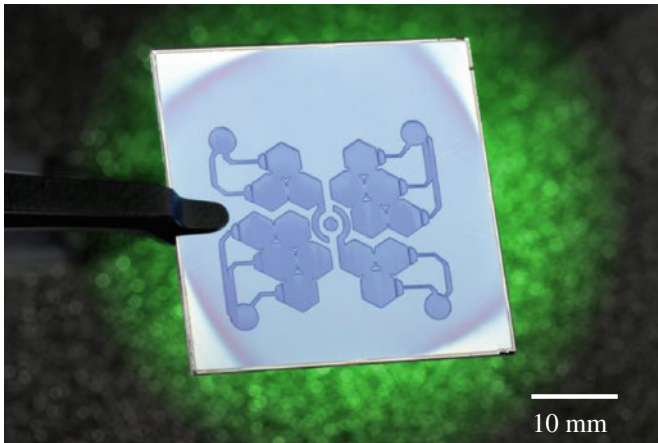
Fig. 19.16 Selectively laser-crystallized PZT layer on a silicon substrate (Fink and Vedder 2018)

manner, thus reducing the thermal impact on the coated substrate. Sol–gel-based PZT precursor solutions are spin-coated onto specially prepared silicon wafers. Subsequently, in a laser-based process, the organic layer components are removed (pyrolysis) at 300–400 °C and the layers crystallized (functionalization) at 700–800 °C (Fig. 19.16) (Fink and Vedder 2018).

Wet-chemical application and laser post-treatment are performed several times to obtain thicker layers. The process development is supported by simulations of the laser-induced time–temperature sequences. Laser radiation can be used to crystallize single layers with thicknesses of about 50 nm as well as multiple layers with a total thickness of up to 200 nm. The columnar microstructure can be controlled by adjusting the laser process parameters. The laser-crystallized layers show almost the same ferro- and piezoelectric properties ($2P_r \approx 60$ μC/cm^2, $d_{33} \approx 100$ pm/V) as those from the furnace process. The applications of highly efficient piezoelectric layers range from sensor technology, for example, to measure structure-borne noise, and actuator technology in micropumps and relays, to inkjet printers all the way to use in communications technology (Fink and Vedder 2018).

References

Fink S, Vedder C (2018) Additive, laser-based manufacture of piezoelectric layers. In: Fraunhofer ILT: annual report 2017, Aachen

Hoff LC, Scheld WS, Vedder C, Stollenwerk J (2022) Laser sintering of ceramic-based solid-state battery materials. In: Proceedings SPIE 11989, Laser-based Micro- and Nanoprocessing XVI, 119890E (4 March 2022). https://doi.org/10.1117/12.2607752

Salmang H, Scholze H, Telle R (2007) Keramik, 7. Auflage. Heidelberg

Vedder C, Stollenwerk J, Pirch N, Wissenbach K (2008) Production technology for transparent and conducting nano layers. In: Proceeedings to ICALEO 2008, 27th International congress on applications of lasers & electro-optics, Temecula, CA, USA, Paper N303

Vedder C (2013) Hochgeschwindigkeits-Laserfunktionalisierung gedruckter, nanopartikulärer Schichten am Beispiel von Indium-Zinn-Oxid. Shaker, Aachen. ISBN: 978-3-8440-2231-5

Vedder C (2021) Thermal laser post-treatment of functional layers. In: Proceedings to 'Lasersymposium Elektromobilität LSE '21', Aachen

Vedder C et al (2016) Laser-based drying of battery electrode layers. In: International congress on applications of lasers & electro-optics 2016, N501. https://doi.org/10.2351/1.5118636

Chapter 20
Bending

A. Olowinsky

20.1 Introduction

Material processing with laser radiation is characterized by the fact that the energy required in a particular process can be delivered spatially and temporally with high accuracy over the surface of the material (Steen 1998; Schuocker 1999). An interesting machining process is laser bending, which has become an important research activity in recent years (Steen 1998; Schuocker 1999; Chan et al. 2000; Magee et al. 1998a). It is a laser-based process that bends sheet metal, semi-finished products, or final components by thermally induced stresses and, in contrast to mechanical methods, offers a "tool-less" forming process. Here, the spectrum of applications ranges from shipbuilding to use as an alignment process in microelectronics (Magee et al. 1998a). Even high-strength steels or titanium-based materials have been successfully formed using the process (Magee et al. 1998b). Recently, the process has been investigated in conjunction with conventional forming processes to improve the accuracy of the geometries that can be achieved. One of the main issues that still needs to be addressed and solved is the influence that the material properties have on the resulting bending angle (Sprenger et al. 1995). Despite these facts, rapid prototyping of complex-shaped objects such as engine mounts and air outlets using laser bending has already been reported. A comprehensive review of recent advances and investigations in the field of sheet forming can be found in Safari et al. (2020) where different studies on the prediction of the bending angle and the achieved accuracy are reported.

For a better understanding, the use of laser bending as an alignment method in microtechnology will be particularly discussed in the following, and the different mechanisms as well as various possible applications will be pointed out.

A. Olowinsky (✉)
Fraunhofer ILT, Aachen, Germany
e-mail: alexander.olowinsky@ilt.fraunhofer.de

Smaller, more intelligent and more complex—this is the aim of multifunctional components which introduce more autonomy into machines and tools. Indicators such as functionality, quality, and production costs are heavily influenced by these components. Thus micro system technology plays an important role in the technological development of the 21 century (Safari et al. 2020). Micromechanical sensors such as gear rate sensors, acceleration sensors, or RADAR distance sensors with highly integrated electronics claim neu safety standards in automotive (Miller 1998). Micro-optical components in growth markets such as the ICT are gaining enormously in importance (Bosch and AG: Geschäftsbericht 1998; Kopka et al. 1999). Miniaturized endoscopes and catheter systems as well as intelligent implants are demonstrating the potential of microtechnological solutions in the field of medical devices (Safari et al. 2020). All these products have one thing in common: they are all based on miniaturization and integrated intelligence, hence are asking for microtechnology—actuators, sensors, intelligence, and communication—and are reflecting the character of a cross-sectional technology.

Due to the high requirements in accuracy and the sensitivity to damage of the fragile parts, the assembly of MEMS is challenging for a lot of producers in terms of manufacturing problems. Especially tools and methods for handling and high-accuracy positioning and joining are required. The increasing level of integration raises new requirements for the assembly technology. In particular in automation the conventional methods for adjustment are limited. The stroke of electrical relays is indeed adjusted by screws nowadays, but by reducing the production cycle times this procedure can no longer be applied. Here a new method has been established. By means of pulsed laser irradiation thermal stress is induced inside the relay spring, which leads to a movement of the spring's end and thus to an adjustment of the stroke (Bishop and Giles 1998).

The forming by laser radiation is influenced by several parameters which are partly depending on each other. A part of the relevant process parameters is displayed in an ISHIKAWA diagram (see Fig. 20.1).

The laser radiation as a dominant process parameter is described primarily by wavelength, power, and pulse duration. In combination with the machine parameters beam shaping and feed rate, the method of Forming is developed.

Depending on the used laser beam parameters, two fundamental types of forming can be distinguished (Fig. 20.2).

20.2 Process Models

In the literature, several mechanisms for laser beam forming are mentioned (Vollertsen 1994; Vollertsen and Holzer 1994). The main difference between them lies in the temperature development during the laser treatment. The mechanisms can be divided into several groups (see Fig. 20.3).

In the following three methods, the thermal mechanisms will be investigated exemplarily.
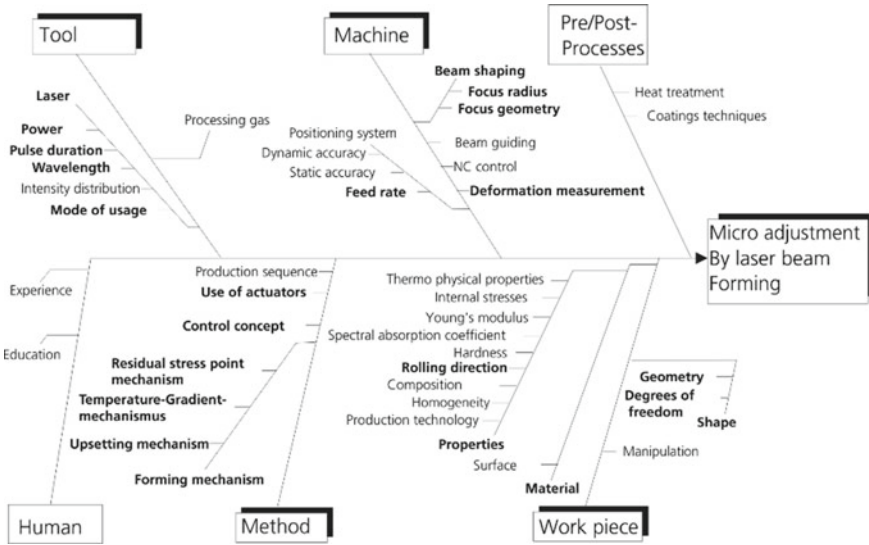
Fig. 20.1   ISHIKAWA diagram with impacts and influences on the forming result

Fig. 20.2   Principal differentiation on the basis of directions of movement
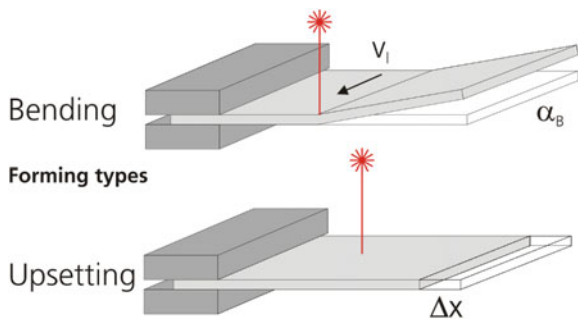
20.3   Internal Stress Point Mechanism

The easiest case of simple bending by laser irradiation can be made by single point irradiation without relative movement between laser beam and part. The part is locally heated in the region of the zone of interaction of beam and matter and expands. The developing compressive stresses are converted into plastic compressive strain due to the decreasing yield stress as the surrounding material can be seen as rigid. According to the ratio between hindering section modulus and the induced compressive stresses a counter bending away from the laser beam may occur. As soon as the tensile strength is reached all additional thermal stresses are converted to plastic deformations so that the counter bending angle remains constant. After the irradiation stops the heated and compressed area cools down which is combined with a thermal contraction.
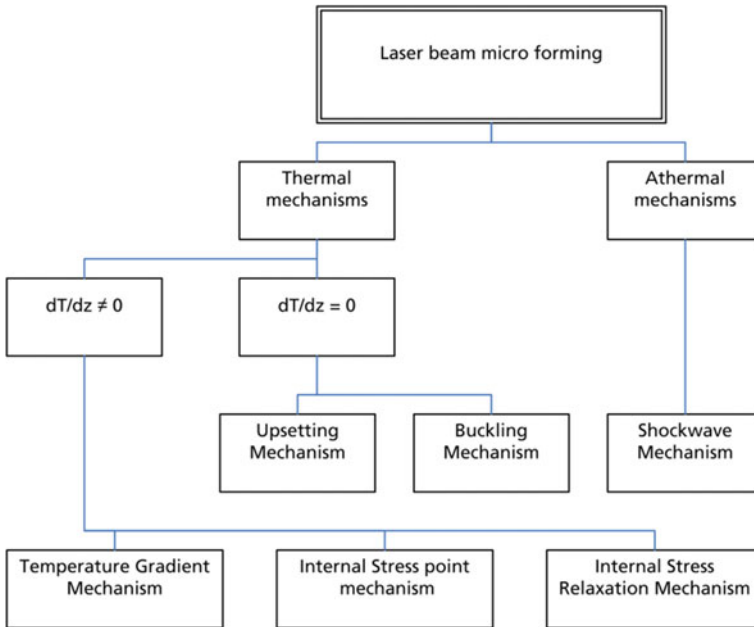
Fig. 20.3 Classification of the mechanisms of laser-induced forming (Sprenger et al. 1995) dT/dz describes the temperature distribution over the sheet thickness

The residual compressive stresses are relieved and residual tensile stresses develop. These tensile stresses lead to a bending toward the laser beam.

These stresses also reach the yield stress in maximum which in the cooling phase is higher due to the lower temperature compared to the heating phase. The residual stresses increase in the same degree as the yield stress with decreasing temperature. The thermal contraction is compensated by local plastic strain. After complete cooling, only a small residual stress source remains which creates a slight bending. The bending edge is determined by the component itself and runs through the point of irradiation. The orientation of the bending edge follows the minimum geometrical moment of inertia. Therefore the position of the point of irradiation relative to the edges of the part does not play an important role.

Multiple irradiations at the same position do not lead to an increase in the bending angle as at first the elastic deformations are relieved due to the residual stresses in the upper layer of the part before the above-described process phases are run through. Larger bending angles can be achieved by placing several spot side by side.

20.4 Temperature Gradient Mechanism

The transition from residual stress point mechanism to TGM is caused by the relative movement between the laser beam and the component (Vollertsen 1994). Shows the elementary model: A symmetrical 2-layer model calculates the bending angle via the difference of the thermal expansion of the two layers (Fig. 20.4).

The laser power is absorbed in the upper layer and transformed into heat. The thermal expansion is hindered by the lower layer and transformed into plastic compression. The lower layer stays thermally and geometrically unchanged.

$$\alpha_B = 4 \cdot \frac{\alpha_{th}}{\rho \cdot c_p} \cdot \frac{A \cdot P_L}{v_f} \cdot \frac{1}{s_0^2} \ [\text{rad}] \tag{20.1}$$

The bending angle increases linearly with the energy introduced into the part and decreases with the reciprocal of the square of the sheet thickness. The following section tries to explain the sequence of the process steps which are illustrated in Fig.

The sheet is irradiated by the laser beam. The upper layer facing the laser beam is heated and expands. During the heating melting temperature can be exceeded but this is not a precondition for the process.

The thermal expansion causes a counter bending. This counter bending depends on the width b of the sheet and is pure elastic deformation (Vollertsen and Holzer 1994).

The yield strength decreases due to the increasing temperature in this area. The section modulus of the non-heated lower layer and the area ahead of the laser beam in feed direction work against this counter bending. The developing compressive stresses are increasing up to the yield stress. Beyond this point a plastic deformation occurs. As the temperature is still increasing the elastic stresses are partially converted to plastic compression.

After the irradiation the cooling phase starts. The heat is dissipated in the surrounding material. By heat conduction the temperature in the lower layer increases. The thermal contraction of the upper layer which was plastically compressed during the heating phase leads to bending toward the laser beam. The

Fig. 20.4 Elementary model of laser beam bending
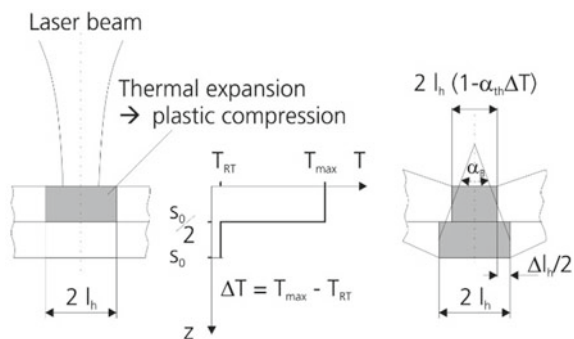
Fig. 20.5 sequence of
forming states

Start heating

Thermally induced expansion
pure elastic deformation (counter bending)

Thermally induced expansion
plastic deformation of irradiated layer

Heat flow from irradiated layer
thermally induced contraction
Heating of lower layer

Thermally induced contraction
plastic expansion of lower layer

Cooling of component under reformation
of elastic deformations

lower layer expands and it is plastically deformed. As the temperature is uniformly distributed, the cooling takes place without further changes of the geometry. The single steps are displayed in Fig. 20.5.

For the TGM, a model has been developed giving the bending angle α_B in dependence of the laser power and the sheet thickness. This model is given in the following equation:

$$\alpha_B = 3 \cdot \frac{\alpha_{th}}{\rho \cdot c_p} \cdot \frac{A \cdot P_L}{v_f} \cdot \frac{1}{s_0^2} \ [\text{rad}] \tag{20.2}$$

α_B Bending angle
α_{th} coefficient of thermal expansion CTE.
ρ Density.
c_p specific heat capacity.
A Absorption.
P_L Laser power.
v_f feed rate.
s_0 sheet thickness.
The main differences to the residual stress point mechanism are as follows:

- The bending edge is not given by the minimum section modulus but follows the line of irradiation. Therefore also non-linear deformations can be realized.
- The deformation can be increased by multiple irradiations of the same line.

20.5 Upsetting Mechanism

The upsetting mechanism is based on a nearly homogeneous temperature distribution over the sheet thickness. Thus the thermal expansion is transformed uniformly to plastic deformation without bending of the part. As mentioned in the previous section, the asymmetric compression leads to an out-of-plane deformation. Using an appropriate process parameter set and an adapted temperature profile, a stress distribution can be created which is symmetric to the neutral fiber of the component. The deformation runs in 3 phases. These phases are illustrated in Fig. 20.6, showing a cross section of a sheet which is not clamped.

In the first step, the component is heated locally. The diameter of the laser beam on the surface is smaller than the width of the component. Heat conduction creates a homogeneous temperature field over the thickness of the sheet. The thermal expansion in-plane is hindered by the surrounding not heated material. Only the expansion perpendicular to the surface remains as degree of freedom.

With increasing temperature, the yield strength of the material decreases. The thermally induced stresses are exceeding the yield stress and material is plastically deformed.

During the cooling after the laser pulse the plastically compressed area contracts. But due to the plastic compression the initial state cannot be reached. The surrounding material hinders the shrinkage during cooling and the expansion during heating likewisely. The again decreasing temperature makes the yield stress rise. The increasing shrinkage forces lead to compressive stresses in the non-irradiated area. The stress state is not homogeneous and ranges just below the yield strength. Therefore mechanical loads are provoking deformation of the component.

Fig. 20.6 Schematic of the upsetting mechanism

Irradiation Heating of component

Expansion of heated area

Cooling and thermally induced contraction
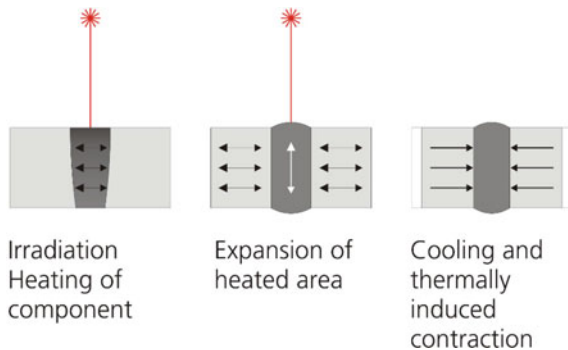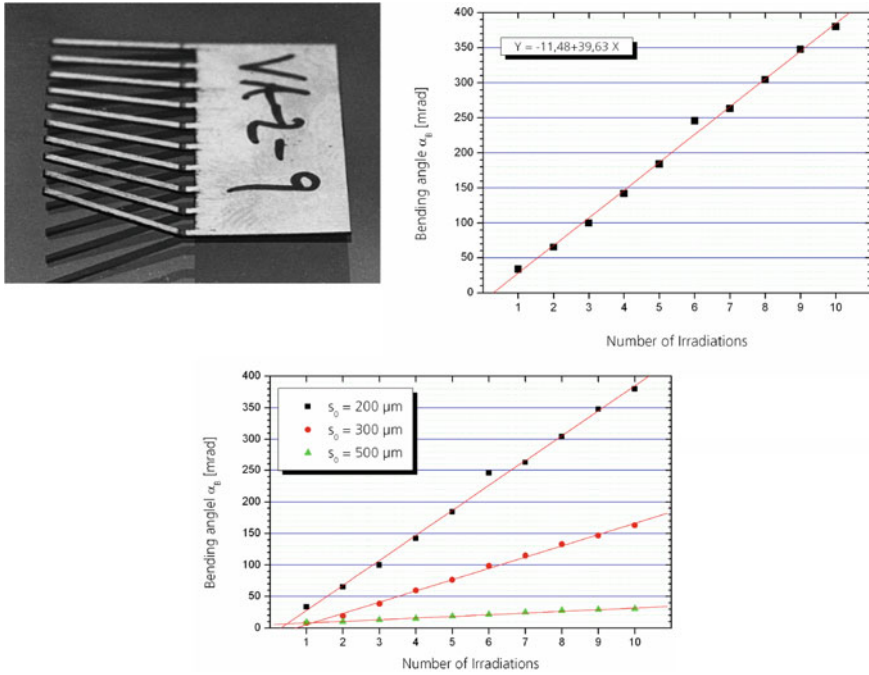
Fig. 20.7 Bending behavior of stainless steel with repeated irradiation. Thickness $s_0 = 200\,\mu$m. Laser parameters:$P_P = 260$ W, $\square_H = 0{,}3$ ms, $f_P = 20$ Hz, v_L 100 mm/min, $2w = 100\,\mu$m

20.6 Forming Results

On the basis of comb-like structures the bending behavior of narrow parts is investigated. The influence of the sheet thickness plays an important role besides the number of irradiations. The two-layer model shown in Fig. 20.4 will be used for explanation. The development of the temperature gradient over the sheet thickness and thus the thickness of the upper and lower layer are influencing the achieved bending angle. The thicker material the smaller the upper heated layer and the connected tensile stresses will be. Accordingly the resulting bending angle will be smaller (Fig. 20.7).

20.7 Applications of Laser Beam Forming for Actuators

The mechanisms of laser beam forming can be used to manufacture various actuators. Here the different mechanisms lead to different actuator types (see Fig. 20.8).

In principle two occurrences of actuators according to the mechanisms can be distinguished: The actual bending occurs with the out-of-plane method, whereas with the in-plane method all deformations take place in the plane of the component.

Fig. 20.8 Basics of the laser beam micro forming as adjustment tool
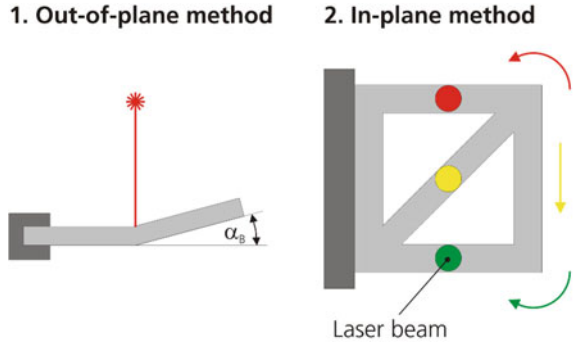
Out-of-plane characterizes a movement in the direction of the incident laser beam, the deformation or displacement occurs out of the principal plane of the actuator. However in-plane indicates a movement perpendicular to the laser beam but in the principal plane.

20.8 Framework Actuator

The framework actuator consists of a square with a crossbeam. With an appropriate irradiation of the actuator, several movements can be realized. The upsetting mechanism is used as forming mechanism. The laser parameters have to be chosen in a way that a movement out of the plane caused by the residual stress point mechanism is suppressed. The framework actuator shown in Fig. 20.9 gives the unit cell to assemble quite complex adjustment structures. The different movements can be assigned to the different irradiation points:

Fig. 20.9 Framework actuator. The result of the irradiation at the different points in the upper row is shown below
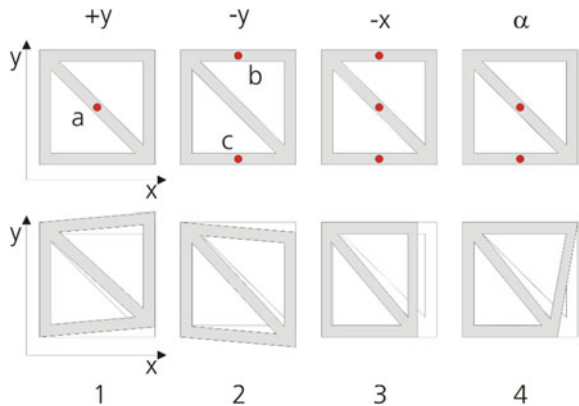
- An irradiation at point a causes a lateral movement of the right-hand side in positive y-direction because the crossbar is compressed. (Fig. 9.1)
- A simultaneous irradiation of point b and c leads to a shortening of the upper and lower bar of the square. The crossbeam suppresses the displacement in negative x direction and a movement of the right-hand side in negative y-direction occurs. (Fig. 9.2)
- Irradiation of all points a, b, and c simultaneously leads to a shortening of the complete actuator. (Fig. 9.3)
- An angular change at the right side can be achieved by irradiating point a and c, as shown in Fig. 20.8 or alternatively a and b for a rotation in the other direction. (Fig. 9.4)

20.9   Two Bridges Actuator

For the Two Bridges Actuator TBA, the upsetting mechanism is used to change the length of the actuator. The shortening of the actuator can be divided into different phases (Fig. 20.10).

In the first step, the laser is heating at position 1. The thermally induced compressive stresses are balanced by tensile stresses at position 2. At the transition to the molten state at position 1, all stresses at this position as well as at position 2 are released. The molten pool can only expand in the direction perpendicular to the part (Table 20.1).

The procedure can be repeated until the desired displacement is reached. The repetitions are only limited by the fact that the two shoulders of the actuators are touching each other and the actuator cannot be compressed anymore. This actuator can be seen as a basic cell to realize more complex movements.

The tube actuator with three Two Bridges Actuators gives a simple structure to adjust mirrors and lenses in optical instruments. The rigid construction and the compact arrangement of the double bridges allow very small units that can exactly be adapted to the application. Fig. 20.11 shows the measurement setup to display the behavior of the actuator and the movement of the center of gravity of a deflected laser beam. With treating the first double bridge the COG moves toward the lower left corner. The irradiation of the second TBA results in an upward movement, whereas the last TBA causes a nearly horizontal displacement to initial point.

Fig. 20.10 Two bridges actuator
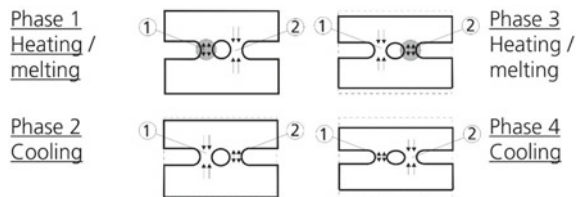
Table 20.1 Phases of treatment of the unidirectional two bridges actuator

	Position 1	Position 2
Phase 1 Heating	Heating	
	Thermal Expansion (compressive stresses)	Obstruction of the thermal expansion (tensile stresses)
	Reaching the melting point: Relaxation of compressive stresses	Relaxation of tensile stresses
Phase 2 Cooling	Thermal contraction (tensile stresses)	Obstruction of the thermal contraction (compressive stresses)
	⇨ Shortening of the component	
Phase 3 Heating	Heating	
	Obstruction of the thermal expansion (tensile stresses)	Thermal Expansion (compressive stresses)
	Relaxation of tensile stresses	Reaching the melting point: Relaxation of compressive stresses
	⇨ Shortening of the component	
Phase 4 Cooling	Obstruction of the thermal contraction (compressive stresses)	Thermal contraction (tensile stresses)
	⇨ Shortening of the component	

Hence all points within the measurement area can be reached by a combination of all three TBAs. This means that within the maximum deflection any tilt angle can be realized.

Fig. 20.11 Top:
measurement setup bottom:
Movement of the center of
gravity of the measurement
beam
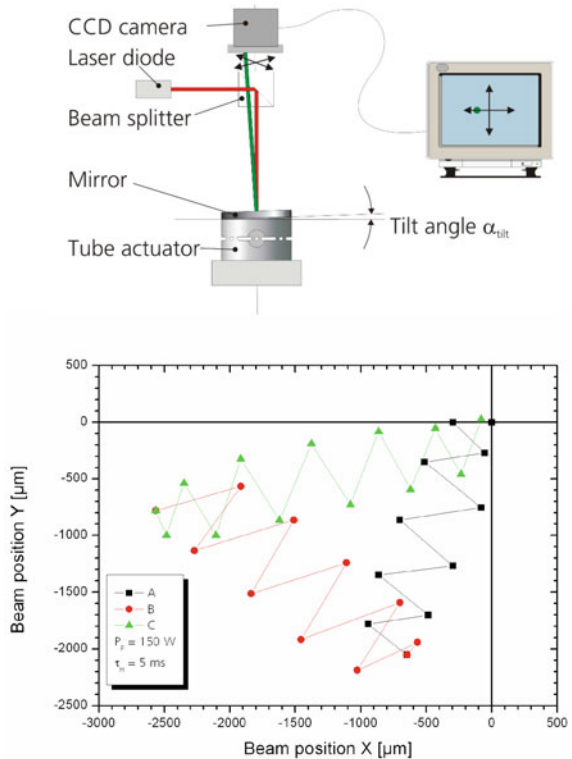
20.10   Conclusion

Laser beam forming offers a variety of tools and methods to be used in adjusting
microcomponents. The combination of different actuators gives room for the real-
ization of very complex adjustment structures. The stroke and the accuracy of the
adjustment can be adapted to the application. As the result of the forming is depending
mainly on the laser parameters automated adjustment procedures can be set up.

References

Bishop DJ, Giles R (1998) Silicon micromechanics takes on ligth-wave networks, Ind Phys, S.
    39–40
Robert Bosch AG (1998) Geschäftsbericht, Pressebild-Nr. 2-K8–10516
Chan KC, Yau CL, Lee WB (2000) Laser bending of thin stainless steel sheets, J Laser Appl, 12(1)
Geiger M, Becker W, Rebhan T, Hutfless J (1995) Microbending and precision straightening by
    the aid of excimer laser radiation, In: Proceedings LANE 95. Meisenbach Verlag, Bamberg, pp
    306–309

Hamann Chr., Rosen H-G (1990) Relaisfederjustierung mittels gepulster Nd:YAG-Laser, Laser/Optoelektronik in der Technik, Hrsg. W. Waidelich, Berlin: Springer Verlag

Huber A (2001) Justieren vormontierter systeme mit dem Nd:YAG-Laser unter Einsatz von Aktoren aus der Reihe Fertigungstechnik—Erlangen (114), Meisenbachverlag Bamberg

Klocke F, Demmer A, Dietz C (1997) Laser assisted metal forming, In: Laser Assisted Net Shape Engineering 2, Proceeding of the LANE'97, 2, pp 81–92

Kopka P, Hoffmann M, Voges E (1999) Bistable 2x2 and mulstistable 1X4 micromechanical fibre-optic switches on silicon, In: Proceedings 3rd International Conference on MOEMS, Mainz

Magee J, Watkins KG, Steen WM, Calder N, Sidhu J, Kirby J (1998b) Laser forming of high strength alloys. J Laser Appl 10(4):149–155

Magee J, Watkins KG, Steen WM (1998a) Advances in laser forming, J Laser Appl, 10(6)

Miller F (1998) Mikrotechniken, Fraunhofer Magazin, Zeitschrift für Forschung, Technik und Innovation, 4, Fraunhofer Gesellschaft, München

Olowinsky A, Gillner A, Poprawe R (1997) Mikrojustage durch Laserstrahlumformen, In: Proceedings of the Sensor'97, 4, pp 133–137

Olowinsky A (2003) Laserstrahlmikroumformen—neues Justageverfahren in der Mikrotechnik, Dissertation RWTH Aachen, Shaker

Ramos J, Magee J, Noble F, Watkins K, Steen WM (1998) The microstructure of laser bent aluminium alloy AA2024-T3. In Proceedings of the 17th International Congress of lasers and Electro Optics (ICALEO 98), Orlando

Safari M, Alves de Sousa R, Joudaki J (2020) Recent advances in the laser forming process: A Review. Metals, 10, 1472. https://doi.org/10.3390/met10111472

Schuocker D (1999) High power lasers in production engineering. Imperial College Press, London

Sprenger F Vollertsen, Steen WM, Watkins KG (1995) Influence of strain hardening on laser bending, Manuf Syst 24, pp 215–221

Steen WM (1998) Laser material processing, 2nd edn. Springer-Verlag, London

Vollersten F (1996) Laserstrahlumformen, lasergestützte formgebung: verfahren, mechanismen, modellierung. Meisenbach Verlag, Bamberg

Vollertsen F (1994) Mechanisms and models for laser forming, In: Proceedings LANE 94. Meisenbach verlag, Bamberg, pp 345–359

Vollertsen F, Holzer S (1994) Laserstrahlumformen - Grundlagen und Anwendungsmöglichkeiten, VDI-Z 136 Nr 1\2 Januar/Februar

Part VII
Joining

Chapter 21
Heat Conduction Mode Welding

Martin Dahmen

21.1 Intro

Heat conduction mode welding is a technique of fusion welding used for joining materials. The text following describes some basic features and applications of this joining method. Starting with an historical overview the fundamentals necessary for the understanding of the process are outlined. Specific parameters controlling weld quality are mentioned as well as the weldability of metallic materials is scratched. As fusion welding is considered the description is limited to metals. Joining of polymers follows a similar approach but the mechanism of joining differs from welding of metals. Some remarks on equipment and application close the section.

21.2 Historical Remarks

Heat conduction mode welding is the mother of all fusion welding processes. Joining by fusion is said to be invented in ancient Egypt around 4000 B.C. for joining metals with comparably low melting temperature, such as copper and bronze, and progressed to silver and gold. Prominent examples are a brazed goblet of queen Pu-Abi made from a gold silver alloy, dating from about 2500 B.C (Roberts 1973) and the famous death mask from Tut-Ench-Amun from 1300 B.C. The joining method was rather brazing and soldering instead of welding. The latter came up with the sculpture of big bronze statues by the ancient Greeks and Romans. First fusion welding processes are reported to be performed during the early fifth century B.C. Statues were cast in several pieces by an indirect lost-wax process and joined by a flow fusion welding process. The principle of ancient flow fusion welding consists of pouring molten

M. Dahmen (✉)
Fraunhofer Institute for Laser Technology, Steinbachstrasse 15, 52074 Aachen, Germany
e-mail: martin.dahmen@ilt.fraunhofer.de

bronze between the bronze pieces to be joined (Azéma and Mille 2010). The welding heat in the base metal was produced by conductive heat transfer by the flowing liquid bronze.

Welding of iron/steel has its roots in processing sponge iron. This natural hot forging became forge welding of welding in the eastern Mediterranean and Egypt at about 1000 B.C. From these early beginnings through the middle ages, the blacksmith trade developed the art of welding by hammering to a high level of maturity (Zhang and Yang 2020). This technique was in use until mid-nineteenth century and was then replaced by riveting and later fusion welding. It survives in diffusion friction welding and still can be found in niche applications.

With the advent of weldable steels on the one hand, and more powerful or localised heat sources on the other hand, fusion welding of iron-base alloys became possible from the third quarter of the nineteenth century on. Two energy sources have been applied, oxyacetylene flames and electric arcs, developing from 1836 and 1801, respectively. The first one is still used for welding of thin to medium sheets. The mode of operation is kind of a pinhole process where the so-called welding eye is surrounded by the melt coming from the workpiece and the consumable. In this regard, it is related to modern beam welding processes. Arc welding has developed from its beginnings to a vast variety of processes. They all have in common that an electric arc is used for superficial melting of the surface or the workpiece and the consumable. It resembles the ancient flow fusion welding but is much more efficient due to the highly concentrated energy.

Beam welding processes represent a relatively young class of manufacturing technologies. The story of electron beam welding started in 1879 when the physicists Hittorf and Crookes used cathode rays to melt metals. Further experiments and developments led to the first electron beam processing machine in 1952 and the discovery of the 'deep welding effect' in 1958 by Karl-Heinz Steigerwald. Lasers emerged rapidly since the discovery of their principle in 1960. First welding applications with a ruby laser were already implemented in the late sixties. The discovery of alternative active materials led to the development of Nd:glass and CO_2 lasers around 1970 and their industrial application in the following years (Ready 1997). Both processes allow versatile joining applications by the application of the processes of heat conduction mode welding at lower power densities and deep penetration welding at greater intensities.

21.3 Fundamentals

21.3.1 Absorption in Solid State

When light strikes a material surface part of it will be reflected from the interface due to the change of the index of refraction, and part will be transmitted into the material. The fraction of the reflected energy depends on the polarisation, the angle of incidence

and the indices of refraction. The reflection coefficients for both polarisations are described by the Fresnel equations. Reflectivity of a given material depends on the frequency of the light through the dispersion relation of its index of refraction. For metals their value ranges between 0.4 and 0.95 in the near UV and visible range and between 0.9 and 0.99 in the infrared range.

Inside the material absorption causes a decay of the intensity of the light with the length of travel. The Lambert–Beer law describes an exponential decay with an absorption coefficient dependent on wavelength and temperature. The magnitude of the gradient of intensity yield the volumetric energy deposition rate. In the interesting region of wavelengths from (approx. 450–11,000 nm) metals are opaque for electromagnetic radiation. The specific mechanism of absorption is that photons couple into the available electronic or vibrational states in the material depending on the photon energy. In metals, this is dominated by the free electrons and transferred to lattice phonons by collisions. The time it takes for the excited states to transfer energy to phonons and thermalisation is in the order of 10^{-12} to 10^{-10} s depending on the material. In case of a low excitation rate compared to the thermalisation rate processes are regarded as photo-thermal (Ursu et al. 1990). This is the case for laser processing with long laser pulses above nano-seconds pulse durations.

The absorptivity of laser radiation by metals is determined by the intensity of the incident radiation, the space–time characteristics of the radiation pulses and the wavelength of the electromagnetic wave. On the material side different parameters such as the material composition, surface finish and the properties of the ambient medium affect the amount of absorbed energy. Intensities of 10^5–10^6 Wm^{-2} in general lead to heating of the material, an effect which is used in transformation hardening or the introduction of local thermally induced stress. The absorptivity depends on the material and its properties. Pure aluminium at room temperature has an absorptivity of around 0.025 in the infrared range showing a relative maximum of 0.14 at a wavelength 808 µm and 0.08 in the visible range. In most other alloys, a steady rise of absorptivity with decreasing wavelength can be observed. For 10.6 µm (CO_2 laser) absorptivity of metals and alloys usually amounts to a few percent. Decreasing the wavelength leads to an increase in absorptivity (Coblentz 1910). The relative increase depends on the material. Upon changing the wavelength from 1064 to 450 nm in technical alloys on the base of aluminium, iron and nickel absorptivity rises by a factor of 1.5 to 3. For metals like platinum, copper and gold absorptivity is increased by a factor of 2, 13 and 66, respectively (Pelarpat et al. 2020). For titanium absorptivity ranges from 0.27 at 1000 nm to 0.5 at 500 nm.

With increasing temperature the absorptivity rises. For aluminium a linear rise of the emissivity, averaged over a wavelength band from 0.1 to 10 µm from 0.008 at 50 K to 0.062 at 800 K was measured (Bartl and Baranek 2004; Sainte-Catherine et al. 1991). In carbon steels there is also a rise until the austenitic transformation takes place. For a AISI 1045 a steep drop from about 0.3 to 0.1 at 800 °C followed by an increase from 1100 °C on (Wang et al. 2000). Temperature effects often cannot be seen independent from the surface conditions as formation of oxides during heating affects the absorption of laser radiation, which in turn leads to a sharp increase of energy deposited (Ursu et al. 1990; Xie et al. 1997).

21.3.2 Absorption in Liquid State

Although historical experiments on absorption at the onset of melting led to the conclusion that absorptivity increases by a factor of about 1.4 for stainless steel and titanium to 3.3 for aluminium and copper (Xie and Kar 1997), in more recent studies no such changes have been reported. At 1064 nm wavelength, the absorptivity of steel ranges between 0.3 and 0.4 for target temperatures less than or equal to the fusion temperature. When the metal becomes liquid, the absorptivity is modified and increases by about 5% (Lazov and Angelov 2010). Measurement of the energy coupling efficiency in 304 stainless steel yielded constant behaviour over temperature for 10.6 and 1.07 μm at 7 and 27%, respectively, and a slight decrease at 515 μm from 33 to 28%. At melting temperature no change was observed. Oxidation causes a sharp rise to an efficiency of about 65% at melting temperature. Beyond melting the value stays constant (Hipp et al. 2019a).

Absorptivity on liquid surfaces considering angle of incidence and surface roughness can be estimated by the Fresnel approach. At grazing incidence (1°–3°), CO_2-laser radiation has high overall absorptance on a molten steel surface, owing to its low Brewster angle, in contrast to the high reflectivity experienced by shorter wavelength lasers (532–1070 nm) due to their relatively high Brewster angles. This trend is reversed for higher angles of incidence (6°–8°). Strong surface waviness enhances the absorptivity and the overall absorption for wavelengths between 532 and 1070 nm (Kaplan 2012).

21.3.3 Heat Conduction/Conductive Heat Transfer

The absorbed part of the energy is transported into the material by conduction and is dependent on material parameters such as heat conductivity and heat capacity. As consequence, the temperature at the location of the laser spot starts to rise. At an intensity of typical 2–5 · 10^9 W m^{-2} melting occurs when the heat supplied by the laser beam exceeds the heat that is dissipated by heat conduction and the temperature is greater than melting temperature of the material. Time-to-melt ranges from 0.6 ms for the lower intensity to less than 0.1 mm for the higher one at feed rate 'zero' (Simonds et al. 2018). The fusion front moves deeper into the material and comes to a hold at a depth which is determined by the power density of the beam, the feed rate and the material's thermal diffusivity of the material. At a power density of approximately 10^{10} W m^{-2} evaporation occurs. The melt surface shows a vapour-induced depression, and the process enters the transition to deep penetration welding.

21.3.4   Enhancement of Absorption

Surface conditions most metal surfaces are rough to some extent, and oxide layers are more of a rule than an exception. Reference values for the absorptivity for pure metal surfaces are of limited validity. Surface roughness may result in multiple reflections and can involve absorption at large angles of incidence, close to Brewster angle. Absorption by oxide layers depend on the characteristic optical properties of may cause multiple reflections or wave-guiding. Additionally the surface may be contaminated with material that has a higher absorptivity than the base material. For smooth surfaces, absorption can be described by the optical properties of the materials and the Fresnel equations. This changes for rough surfaces. If the ratio of the laser wavelength and the roughness depth ranges between 0.46 and 1.36, as obtained in sanded or sandblasted surfaces absorptivity becomes independent from the behaviour predicted by Fresnel's equations (Hipp et al. 2019b). When the roughness depth and the wavelength of the roughness profile is in the order of magnitude of the laser wavelength absorptivity is maximised (Bergström et al. 2007; Bergström 2008).

Metals processed under industrial conditions most often have an oxide layer on the surface. Its chemical and optical properties differ substantially from the material underneath. The structure as well as the thickness of the oxide layer determine its contribution to absorptivity. In the case of thick layers absorptivity can be increased as much as an order of magnitude (Bartl and Baranek 2004; Bergström 2008). If the oxide layer is thin, in the order of magnitude of the wavelength of the incoming radiation the increase of absorption is driven by interference effects. Under circumstances oxide layers are formed during processing, when increase temperature leads to a reaction of the metal with oxygen. This effect may cause a so-called thermal runaway which makes it difficult to control processing (Ursu et al. 1990), such as welding.

Defects and impurities may cause a local increase in absorptivity. Dust particles residuals of abrasives represent sharp centres of absorption. These particles can be wiped off or removed by other cleaning techniques. Inclusions and (micro) cracks are another source of disturbance when they are present at the surface processed. Especially inclusions, when clustered, may react at the temperature increased leaving surface defects at a larger scale behind. Consequences of welding are uneven heating and melting. In terms of welding this leads to uneven weld penetration and a decrease in quality. The same holds true for soilings on the surface, which should be removed prior to welding. The use of absorptive coatings, as used, e.g. in transformation hardening, is not recommended for welding because residuals can enter the molten material and have a negative effect on metallurgy and strength of the joint produced.

21.4 Melt Flow/Convective (Heat) Transfer

In the fused zone two flow effects occur, Marangoni convection (Tsai and Kou 1989) and buoyancy-driven flow. An estimation of the significance of the regimes yield, e.g. for stainless steel a ratio of Marangoni to Grashoff-number of 3.84×10^5, hence, the flow is driven mainly by Marangoni convection (He et al. 2005). A non-uniform heat influx a thermal gradient, for steel of typical 10^5–10^8 K m^{-1} is induced leading to a gradient of the surface tension. Another source of surface tension gradients are variations in surface active elements (Mills et al. 1998). The dependence of surface tension on temperature and element concentration result in a spatial variation of surface tension, manifested in thermocapillary forces at the free surface which must be balanced by shear stresses due to the liquid metal viscosity. By shear stresses from regions of low to high surface tension, a weld pool flow is driven. The flow is regarded as laminar due to the small time interval between melting and solidification. Turbulent flows are not desired because they lead to an unstable melt pool and poor surface quality of the weld (Kidess et al. 2016).

Marangoni-driven flow has a profound impact on the final weld shapes. In most metals this flow is directed outward at the free surface, deflected into the fused material at the fusion boundary and returning at the weld centre. In the case of steels the direction and magnitude of these forces are determined by the sulphur content, since the temperature coefficient of surface tension is negative when the sulphur content is less than 30 ppm, leading to a radially outward flow with shallow penetration, whereas at a content greater than 60 ppm the gradient becomes positive, producing a radially inward flow resulting in an increase of weld penetration, weld cross section and process efficiency (Zhao et al. 2010). Other surfactants that increase surface activity are oxygen and selenium. Reactive elements such as Al, Ca and Ce can have an adverse effect on penetration by reducing the soluble content of the active elements (Zhao et al. 2010; Aidun and Martin 1997; Pitscheneder et al. 1996).

21.5 Controlling Weld Shape

Due to the nature of the process of heat conduction welding ratio of depth to width of the seam is approximately 0.5 and can be enhanced to about 1 by convective transport inside the fused zone. The shape approximates a segment of an ellipsoid.

The intensity distribution has an impact on the energy transport mechanisms. Using standard beam shaping beam with Gaussian or top-hat intensity distribution is achieved. At very thin material this may lead to an over-heating at the weld centre possibly causing burn-through. This can be overcome by using ring-shaped intensity distributions (Funck et al. 2014) or twin spots (Kidess et al. 2016). By these a more homogenous temperature profile can be generated. An enhancement of process window in terms of material thickness and material combination can be attained.

Furthermore the flow can be reversed just by controlling the power density distribution on the surface (Daub et al. 2010). Elliptic beams may also increase process efficiency regarding the penetration depth when the long axis is oriented parallel to the feed direction (Ayoola et al. 2019). Rectangular-shaped foci are not recommended because they produce regions of undefined flow in the corners (Rasch et al. 2019).

Experimental observation of the weld pool is difficult because of the limited size of the molten area, the short duration of the liquid state and the opaque nature of molten metals. Theoretically it is possible to use tracer methods for the observation of the liquid surface. Due to the small dimensions the applicability is limited. Also X-ray-based methods can be applied X-ray (Aucott et al. 2018) but are challenging for the same reason. The significance of these methods is limited because of the limitations in resolution of the observation optics.

Due to the opaque nature of liquid metals, the effects on melt flow can be assessed only by simulation (Bag and De 2010; Tong et al. 2013). Full-scale simulations require the solution of the full set of transport equations, whereas for the prediction of parameters for manufacturing simplified models or phenomenological models can be utilised. Some knowledge can be drawn from simulative approaches in arc, especially TIG, welding. Regarding the smaller dimensions of the laser-induced melt pool, it is necessary to adopt the appropriate discretisation and the application of the laws of similarity (Bag and De 2010). Multiscale approaches can help to avoid these bottlenecks, and multiphysics tools present an easy access to simulation of complex processes. (Tong et al. 2013; Kidess 2016).

Depending on the individual approach specific issues of the welding process can be extracted and can be investigated isolated from the rest of the process. Examples are the effect of tramp elements on the flow behaviour or the effect of intensity and its spatial distribution on the seam shape. Coupled models (Hu and Eberhard 2017) allow a holistic view on the welding process including heat effect in the solid phase.

21.6 Materials

Weldable are in principle all materials which show a distinct melt phase on heating. This holds true for metals and metallic alloys, but also for some ceramic materials, such as quartz glass and aluminium nitride. For joining glass far-infrared lasers still are applied, for other materials solid state lasers in different wavelength ranges come under consideration. Heat conduction welding can be applied for materials sensitive to evaporation of burn-off of volatile alloying elements, e.g. zinc in brasses, or metals with small melting temperature and/or liquid section which are sensitive against evaporation. The general rules guiding weldability with other processes remain valid by the large (Hrivňák 1991; Kou 2002; Lippold 2015). In some cases, rapid heating and cooling and their effects on the metallurgy have to be taken into account. Some examples are described in the following paragraphs.

Aluminium alloys are covered by a thin oxide layer with a melting temperature of 2200 °C, which is quite high compared to the melting point of about 660 °C for the bulk material. It may remain intact while the material beneath is molten hence, a metallurgical bond will not be established. Therefore aluminium alloys require a thorough cleaning procedure prior to welding. Metals and alloys based on titanium and zirconium have great affinity to nitrogen and oxygen. Welding require a carful shielding against atmospheric gases. For laser beam welding of titanium and its alloys argon with a purity class of 4.6 is sufficient, whereas zirconium requires higher purity (5.0) and, if possible, a full shielding.

Pure titanium or near-alpha titanium alloys have an excellent weldability. Due to a high absorptivity and a small heat conductivity, the weld zone can be confined to a small area. This also enables a good control of the weld shape. An oxide layer is also present but its melting temperature is close to that of the metal. Because of the affinity to oxygen and nitrogen, a proper shielding is mandatory.

Mild steels with low carbon content from 0.05 to 0.2% carbon are weldable in both continuous and pulsed mode. With increasing carbon content welding becomes more difficult. In medium carbon steels with up to 0.6% carbon, the heat effects of the joining process lead to embrittlement by the formation of untempered martensite. These steels require pre-heating to about martensite start temperature and post-weld heat treatment in order to avoid cold cracking in weld and heat-affected zone. High carbon steels with up to 1% carbon require specific techniques and also a post-weld heat treatment. For medium and high carbon steels, welding is only possible in continuous wave mode.

Welding of austenitic stainless steels is a complex matter due to the great variety of available grades. The standard (metastable) grades, e.g. 304 and 316, normally show excellent weldability if continuous laser beam welding is applied. In pulsed mode welding, the variations 304 and 316 L shall be applied. These steels show an increase in ferrite after welding that has to be taken into account when corrosion is an aspect of application. For avoiding hot cracking, a predominant solidification as ferrite is advantageous. A certain ratio of the chromium and equivalents marks this critical transition. This threshold is 1.52–1.675 for slow solidification as in TIG welding and 1.6 for faster solidification as achieved in laser beam welding (Lienert and Lippold 2003). The alloy composition should be tuned to this ratio.

21.7 Equipment

Beam sources applied are CO_2 lasers which are nowadays mostly replaced by solid state lasers diode, Nd:YAG, disk and fibre lasers due to the increased absorptivity at wavelengths around 1 μm. With the advent of lasers with emission spectra in the green to blue spectrum at beam power beyond 100 W with high brightness a big leap forward in productivity was done. Especially in the blue range, the process windows can be significantly increased. Light in the near infrared and visible range can be easily transported by glass fibres, making beam handling much more reliable. The

shorter wavelengths pose high requirement on the surfaces of optical elements in order to maintain a stable a good optical imaging.

Beam shaping is mostly achieved by focusing a collimated laser beam resulting in Gaussian or top-hat intensity distribution. Dual spots have been produced by step or roof-top mirrors at far-infrared wavelengths. Nowadays for near-infrared or visible radiation the beam is split by prisms ahead of focusing. Ring-shaped profiles can be produced by axicons (Pitscheneder et al. 1996). Elliptical spots are achieved by inclination of a circular beam or more sophisticated by optical imaging through cylinder lenses or specially shaped lenses. More fancy patterns are generated by diffractive optical elements (Katz et al. 2018). The latter approach suffers from high optical losses decreasing the efficiency of the imaging.

Because of the absence of evaporation there is no disturbance by vapour plumes. This enables a reliable supply of shielding gas. Nevertheless, a laminar flow of gas should be assured. When it comes to welding reactive materials trailing shroud equipped with laminarisers, multi-weave or porous metal are suited candidates, should be applied.

21.8 Applications in Joining

In a joining context, a number of processes is possible based on the power modulation. Single spot welding with or without beam weaving is mainly used for contacting applications or in joining wires. Pulse duration are range typically between milliseconds and a few tenths of a second. With a superposed movement of the beam relative to the work-piece pulsed seam welding becomes possible. This technique is used for joining thermally sensitive parts or components where a specified inside temperature must not be exceeded. Welding results in a more or less rough surface where traces of the single spots remain visible at the surface. Some materials react sensitive on repeated melting and solidification, as some stainless steels with primary austenitic solidification. When the ration of pulse duration and feed rate equals seam length, or if continuous wave laser radiation is applied, continuous welds can be produced. This process results in the best surface qualities and is used for producing smooth weld beads. The aim is to iron discontinuities, e.g. of former welds or to improve the surface quality in order to improve corrosion resistance or for other technical as well as aesthetic reasons.

The direct use of heat conduction welding in joining is found mostly found in welding thin sheet metal parts. Applications are mainly found in the field of micro welding, where small gauge sheet metal with up to 0.5 mm thickness has to be joined. Compared to deep penetration welding large cross-sections of the weld in the joining plane for great load capacity and current carrying capacity (electrical contacts) in lap joints. The limited heat input makes an upscaling of the cross section by the use of scanners easier. The most classical application was, and is, welding of pacemakers made from titanium alloy. Thanks to a good absorptivity and a uncomplicated metallurgy they are sealed hermetically by pulsed welding. Aluminium foils

are welded for the application in compound tubes for floor heaters. They consist of an inner PEX tube and an outer sealing made from PE. Here deep penetration welding should be avoided in order not to damage the inner tube. Applications in steel are found in welding of casings for electronic packaging, but also for transport and storage boxes. Especially for thin gauge sheets a strong and decorative weld can be produced economically and fast. If the sheet thickness increases a kind of 'borderline' process can be applied using the effect of the vapour depression.

References

Aidun DK, Martin SA (1997) Effect of sulphur and oxygen on weld penetration of high-purity stainless steels. J Mater Eng Perform 4(4):497–502

Aucott L, Dong H, Mirihanage W, Atwoold R, Kidess A, Gao S, Wen S, Marsden J, Feng S, Tong M, Conolley T, Dragopoulos M, Kleiin C, Richardson I, Browne D, Mathiesen R, Atkinson H (2018) Revealing internal flow behaviour in arc welding and additive manufacturing of metals. Nat Commun 9:5414. https://doi.org/10.1038/s41467-018-07900-9

Ayoola WA, Suder WJ, Williams SW (2019) Effect of beam shape and spatial energy distribution on weld bead geometry in conduction welding. Opt Laser Technol 117:280–287

Azéma A, Mille B (2010) La grande sculpture antique en bronze assemblée par soudage par fusion. Soudage et techniques connexes, Mars-Avril, Institut de Soudure, pp 20–22

Bag S, De A (2010) Computational modelling of conduction mode laser welding process. In: Na X (ed) Laser welding, pp 133–160. https://doi.org/10.5772/265

Bartl J, Baranek M (2004) Emissivity of aluminium and its importance for radiometric measurement. Measure Phys Quantit 4:31–36

Bergström D, Powell J, Kaplan A (2007) Absorptance of nonferrous alloys to Nd:YLF and Nd:YAG laser light at room temperature. Appl Opt 46(8):1290–1301

Bergström D (2008) The absorption of laser light by rough metal surfaces, PhD thesis, Luleå University of Technology

Coblentz WW (1910) The reflecting power of various metals. J Franklin Inst 170(3):169–193

Daub R, Wiedemann R, Mahrle A, Duong J, Zäh M (2010) Influence on the efficiency of the heat conduction mode laser beam welding process regarding different laser spot geometries. In: Proceedings of the 29th international conference on lasers and electro-optics, September 26–30, Anaheim, CA, paper #505

Funck K, Nett R, Ostendorf A (2014) Tailored beam shaping for laser spot joining of highly conductive thin films. Phys Procedia 56:750–758

He X, Elmer JW, DebRoy T (2005) Heat transfer and fluid flow in laser microwelding. J Appl Phys 97:084909

Hipp D, Mahrle A, Beyer E (2019a) Energy coupling of laser radiation on AISI 304 stainless steel: effect of high temperatures and surface oxidation. Materials 12:2802

Hipp D, Mahrle A, Beyer E (2019b) Beyond Fresnel: absorption of fibre laser radiation on rough stainless steel surfaces. J Phys D Appl Phys 52:355302

Hrivňák I (1991) Theory of weldability of metals and alloys. Elsevier, Amsterdam

Hu H, Eberhard P (2017) Thermomechanically coupled conduction mode laser welding simulations using smoothed particle hydrodynamics. Comp Part Mech 4:473–486. https://doi.org/10.1007/s40571-016-0140-5

Kaplan AFH (2012) Absorptivity modulation on wavy molten steel surfaces: the influence of laser wavelength and angle of incidence. Appl Phys Lett 101:151605

Katz S, Kaplan N, Grossinger I (2018) Using diffractive optical elements. Laser Tech J 2(2018):29–32

Kidess A (2016) Multiscale modeling of mesoscale phenomena in weld pools. PhD thesis, TU Delft

Kidess A, Kenjereš J, Righolt BW, Kleijn CR (2016) Marangoni driven turbulence in high energy surface melting processes. International Journal of Thermal Sciences 104, doi:https://doi.org/10.1016/j.ijthermalsci.2016.01.015

Kou S (2002) Welding metallurgy

Lazov L, Angelov N (2010) Physical model about laser impact on metals and alloys. Contemp Mater I−2:124−128

Lienert, Lippold (2003) Sci Technol Join Weld 8(1):1−9

Lippold JC (2015) Welding metallurgy and weldability. Wiley, Hoboken

Mills KC, Keene BJ, Brooks RF, Sirali A (1998) Marangoni effects in welding. Phil Trans R Soc A 356:911−925

Pelarpat JM, Finuf M, Boese E, Zediker M (2020) Blue lasers add power and brightness. Ind Laser Solut, May/June, 10−12

Pitscheneder W, DebRoy T, Mundra K, Ebner R (1996) Role of sulphur and processing variables on the temporal evolution of weld pool geometry during multikilowatt laser beam welding of steels. Weld J Res Suppl, pp 71s−80s

Rasch M, Roider C, Kohl S, Strauß J, Maurer N, Nagulin KY, Schmidt M (2019) Shaped laser beam profiles for heat conduction welding of aluminium-copper alloys. Opt Lasers Eng 115:179−189

Ready JF (1997) Applications of laser welding. In: Ready JF (ed) Industrial applications of lasers. Dan Diego, pp 343 ff

Roberts PM (1973) Gold brazing in antiquity. Gold Bull 6:112−119. https://doi.org/10.1007/BF03215024

Sainte-Catherine C, Jeandin M, Kechemair D, Ricaud JP, Sabatier L (1991) Study of dynamic absorptivity at 10.6 μm (CO_2) and 1.064 μm (Nd:YAG) wavelengths as a function of temperature. J de Physique IV Colloque 01(C7):151−157

Simonds BJ, Sowards J, Hadler J, Pfeif E, Wilthan B, Tanner J, Harris C, Williams P, Lehman J (2018) Time-resolved absorptance and melt pool dynamics during intense laser irradiation of a metal. Phys Rev Appl 10:044061. https://doi.org/10.1103/PhysRevApplied.10.044061

Tong M, Duggan T, Liu J, Xie Y, Dodge M, Aucott L, Dong H, Davidchak R, Dantzig J, Barrera O, Cocks A, Kitaguchi H, Lozano-Perez S, Zao C, Richardson I, Kidess A, Kliejn C, Wen S, Barnett R, Browne D (2013) Multiscale, multiphysics numerical modeling of fusion welding with experimental characterization and validation. J Miner Metals Mater Soc 65(1):99−106. https://doi.org/10.1007/s11837-012-0499-6

Tsai MC, Kou S (1989) Marangoni convection in welds with a free surface. Int J Numer Meth Fluids 9:1503−1516

Ursu I, Mihaelescu N, Prokhorov AM, Konov VI (1990) Laser heating of metals. CRC Press, Boca Raton, Fl

Wang J, Weng C, Chang J (2000) The influence of temperature and surface conditions on surface absorptivity in laser surface treatment. J Appl Phys 87(7):3245−3253

Xie J, Kar A (1997) Mathematical modelling of melting during laser materials processing. J Appl Phys 81:3015−3022

Xie J, Kar A, Rothenflue JA, Latham WP (1997) Temperature-dependent absorptivity and cutting capability of CO_2, Nd:YAG and chemical oxygen-iodine lasers. J Laser Appl 9:77−85

Zhang C, Yang J (2020) A history of mechanical engineering. Springer Nature, Singapore, p 56f

Zhao CX, Kwakernaak C, Pan Y, Richardson IM, Saldi Z, Kenjeres S, Kliejn CR (2010) The effect of oxygen on transitional Marangoni flow in laser spot welding. Acta Mater 58:6345−6357

Chapter 22
Laser Beam Welding of Thermoplastics

S. Behrens, M. Brosda, C. Engelmann, N. P. Nguyen, K. van der Straeten, A. Olowinsky, A. L. Boglea, A. Roesner, and U. A. Russek

22.1 Motivation

Plastics play an important role in almost every facet of our lives and constitute a wide variety of products, from everyday products such as food and beverage packaging, over furniture and building materials to high-tech products in the automotive, electronics, aerospace, white goods, medical and other sectors. Today, advanced plastics have already replaced other materials (such as metals for stiff components, glass in optical industry and even silicon in low cost electronics) and have determined drastic changes in the design and set up of almost all products in terms of weight reduction and cost saving. These are crucial factors for the success of both disposable and long-lasting products in manufacturing and use.

The plastics compared to the metals have a lower weight, a high manufacturability and corrosion resistance and can be easily recycled. The use of plastic materials covers almost all the application fields from packaging, construction, automotive, electronic devices, consumer goods to agriculture (Fig. 22.1) (PlasticsEurope 2020).

Successful (plastic) products are based on the optimal balance between:

- careful selection of the plastic material,
- proper construction (Design for Manufacturing),
- appropriate manufacturing and subsequently joining method.

Although polymers provide unattained manufacturing capabilities (e.g. large parts can be produced by injection moulding with high reproducibility) they require assembly technologies, which must enable massive production of components, even if made by complex parts. In the global market driven by reduced production costs in low-wage countries, Europe's industry needs to achieve higher quality and higher

S. Behrens · M. Brosda · C. Engelmann · N. P. Nguyen · K. van der Straeten · A. Olowinsky (✉) · A. L. Boglea · A. Roesner · U. A. Russek
Fraunhofer ILT, Aachen, Germany
e-mail: alexander.olowinsky@ilt.fraunhofer.de
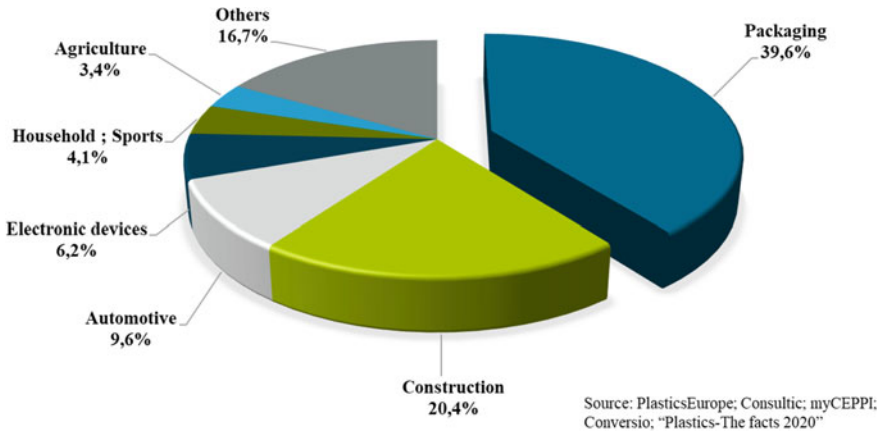
Fig. 22.1 Application fields of plastic materials in west Europe 2019 (PlasticsEurope; Consultic; myCEPPI; Conversio; "Plastics-The facts 2020")

flexibility of product assembly with reduced costs in order to remain competitive, since assembly costs have a large share of product manufacturing costs. Transparency Market Research estimates the globally laser plastic welding market at around 950 Million US $ in 2019 and the market is projected to register a CAGR of 8.4% during the forecast period 2020–2025 (Laser plastic welding market, Transparency Market research 2021).

To this end, compared to conventional plastic joining (like adhesive bonding, mechanical crimping, hot plate welding, vibrational welding and ultrasonic welding), laser polymer welding technology offers significant advantages, such as low cost, power scalability, flexible geometry and contour shaping, joining capability without additional material, and process stability combined with the possibility for online process control, which have already established laser polymer welding as a versatile process for high-quality assembly in many industrial applications.

Through the specific characteristics of all laser processes such as contactless and locally defined energy deposition the thermal damage of the joining partners is avoided. The mechanical stress is also being reduced or avoided since during the joining process the components experience no relative movement to each other. For optimal plastic material combination, the welding strength is close to the one of the base materials. Furthermore, tight, pore-less and optical high-quality weld seams can be achieved through laser beam welding of plastic materials. The idea of laser beam welding of polymers was developed in the 60 s. However, this process gained importance mainly due to the development of the high power diode lasers in the early 90 s. The previously used laser systems based on CO_2 and Nd:YAG-lasers were replaced by the diode lasers due to the significantly reduced price and increased efficiency (Russek et al. 2001; Bachmann and Russek 2002). Due to the good focusability, nowadays even fibre lasers are used for polymer welding.

The quality of the welding as well as the various applications that can be covered by the laser beam welding reveal its great market potential. At present, the laser beam welding can be considered for approximately 20% of the plastic processing market in fields like electronics, automotive or packaging.

22.2   Process Basics

22.2.1   The Joint Configuration

For the laser welding of polymers with high power diode lasers (HPDL) the overlap joint (Fig. 22.2, left) enjoyed a greater success than the butt joint (Fig. 22.2, right) and became the most used joint configuration.

The principle of the laser beam welding of plastic materials is based on the absorption of the electro-magnetic radiation in the material.

In the case of the overlap joint the process is called laser transmission welding, because one of the joining partners is transparent for the wavelength of the laser beam so it can pass through this joining partner depositing the necessary energy for the welding process in the joining area. The area is represented by the contact surface between the two joining partners. Here, the electro-magnetic energy is converted by the absorbing joining partner with almost no losses into thermal energy. Through heat conduction, the transparent joining partner is also melted. To guarantee an efficient heat transfer a firm contact between the joining partners is required. In the case of transmission welding a thin film of molten material in the range of 30–300 µm is generated in the welding zone.
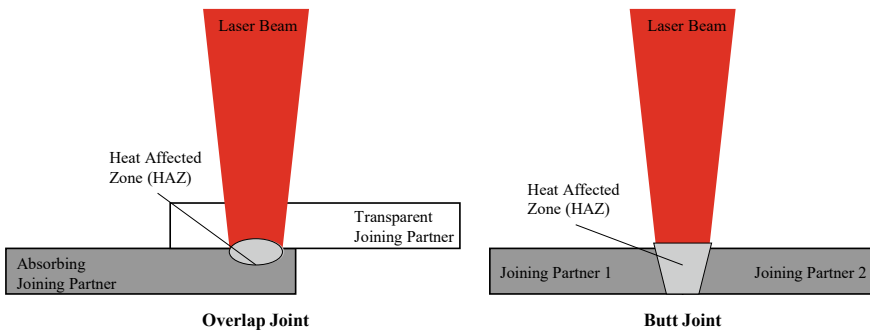
Fig. 22.2   Typical joint configurations for the laser beam welding of plastics

22.2.2 Irradiation Methods

To benefit from the specific advantages of the laser process, it is important to observe or generate boundary conditions that are conducive to the process. This includes having a part design and a weld geometry that are suitably tailored to the laser process. Due to the optical properties of the polymer, diode laser, Nd:YAG lasers and fibre lasers can be used for laser transmission welding. A suitable laser should be selected based on the welding configuration employed. There are five main irradiation methods to distinguish (Fig. 22.3).

The standard method is called 'contour welding'. In this case, the focused laser beam is moved over the materials surface, following the weld seam geometry. The laser source might be a diode or fibre laser, either with fibre coupling or without, dependent on the application and the typical laser power is in the range of 10 to 100 W. The movement along the desired welding contour can be performed using an x–y handling system to move the joining partners under a fixed laser beam or by the use of galvanometer scanners in order to move the laser beam while holding the joining partners fixed. Welding speeds typically range from 2 to 5 m/min, in some cases up to 25 m/min. This method provides a simple, very flexible, easy controllable and cost-efficient method for laser transmission welding of polymers.

Guiding the laser beam by means of fast galvano-scanning mirrors system over an arbitrary two-dimensional weld seam contour within a limited scanning field is called quasi-simultaneous welding. An F-Theta-Optic ensures the focal spot of the laser beam lying at each point of the scanning field plane within this plane. If the power is sufficiently high (several 100 W) and the scanning speed is fast enough, in fact so fast that the heat loss is so little, that no re-solidification occurs, the entire irradiated seam is softened as well, so that a quasi-simultaneous weld procedure
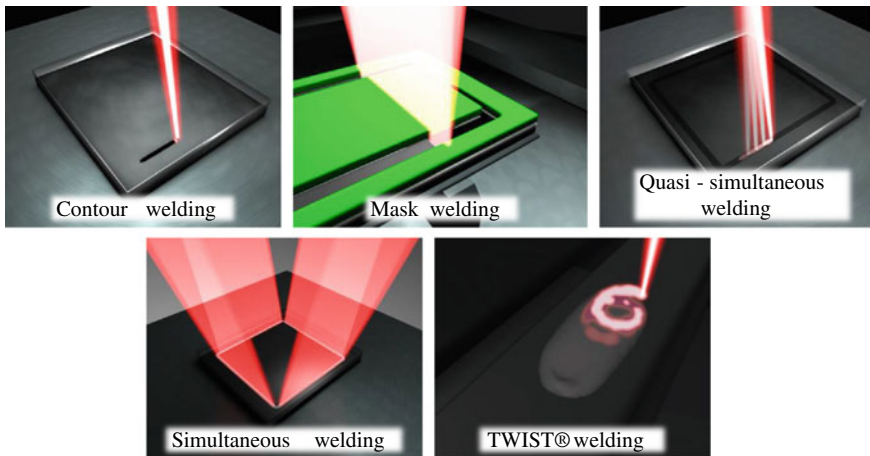
Fig. 22.3 Process variants based on different irradiation strategies

is realized. Because of plastifying, the entire weld seam part tolerances may be compensated.

To generate narrow weld seams ($\approx$100 µm) and complex seams designs in microtechnology, biology and life science employment of mask welding is preferred. A mask between laser beam source and joining partners guarantees an irradiation only of areas to be welded. This mask is conformal with the weld seam, so those places, which shall not be exposed to the laser radiation, are protected. High power diode lasers with a collimated, homogeneous, line-shaped intensity distribution are preferred for this irradiation method (Chen 2000). The resolution or the smallness, respectively, depends on the thickness of the transparent joining partner, the optical and thermal properties of both joining partners, the intensity distribution as well as on the arrangement of the laser source, clamping device and mask. The process efficiency however is reduced by the fact that the laser power is blocked from the mask and thus, not used for the process.

The compact and modular set up of high-power diode lasers permits simultaneous laser welding. By means of appropriate beam forming and guiding a homogeneous intensity distribution fitting to the entire weld seam geometry must be generated (Becker 2003; Russek 2003a). There are different strategies possible to realize simultaneous welding, such as direct irradiation of the weld seam contour, using classic optical components, employing mask technology or application of fibre bundles. During the welding process, the entire weld seam is irradiated as a whole and welded with one single laser pulse. Apart from short process times, which are of interest for big lot production, simultaneous welding allows a more moderate irradiation of the parts to be welded. It offers wider process windows, marked bridging capability as well as enhanced weld strength compared to contour welding. Similar to quasi-simultaneous welding, component tolerances can be compensated as the whole contour is irradiated simultaneously.

TWIST is an acronym for Transmission Welding by an Incremental Scanning Technique. The process superimposes the feed movement of the beam with a highly dynamic oscillation pattern in order to achieve a uniform energy input (Boglea 2013). In contour welding of the conventional material combination (transmittent/absorbent), especially when high brilliance lasers are used the seam centre tends to overheat due to the Gaussian intensity distribution of the beam. By oscillating the beam more energy is deposited at the edges leading to a more homogeneous seam.

22.3 Process Management

The process management is an essential aspect in order to achieve a high-quality joining. A detailed process insight reveals that the weld strength has a typical evolution for different laser energy levels (Klein et al. 1987; Hänsch et al. 1998; Russek et al. 2003). Therefore, the graphical representation of the weld seam strength versus laser energy represents the so-called 'characteristic curve' of the laser beam welding process (Fig. 22.4). On this characteristic curve the different stages or situation of a

laser transmission welding process can be identified. In the first situation (Fig. 22.5), a low energy input leads to the melting of the absorbing joining partner and just to a heating of the transparent joining partner. For this case the weld seam has a poor strength. With the increase of the energy (Fig. 22.5), a sufficient molten volume will be produced and a strong weld seam can be achieved. The optimal process parameters for achieving the strongest weld seam are within this domain of the characteristic curve. A further increase in the energy will lead to thermal decomposition of the absorbent joining partner and reduces the strength of the weld (Fig. 22.5). However, in particular cases an increase in the weld strength can be noticed but the process instability will rise, too. One of the most common consequences of such a situation is the formation of pores in the weld seam, which will eventually cause the failure of the weld seam or will compromise the leakage tightness of the assembly.

In addition to the laser energy coupled in the material, the weld strength also depends on the time of interaction between energy and material. A short interaction time prevents the plastification of the transparent joining partner. With increasing irradiated energy, the absorbent joining partner decomposes while the heat flow into the transparent joining partner is still too small to plastify the transparent material sufficiently. If the interaction time between laser beam and material is too long, the
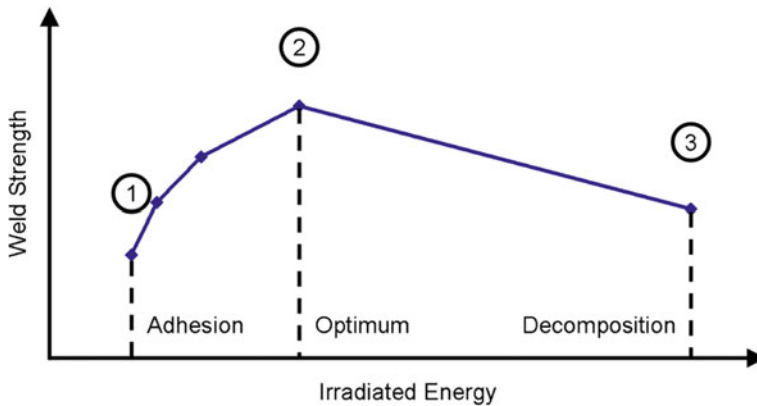
Fig. 22.4 The characteristic curve for a laser beam transmission welding process
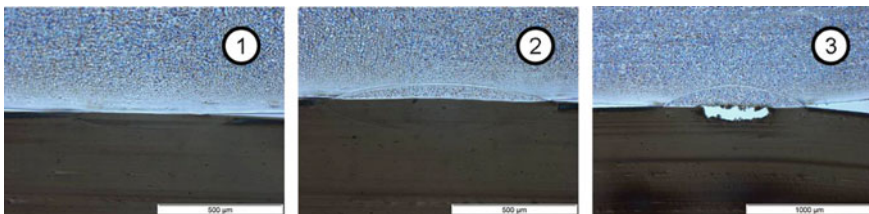
Fig. 22.5 Different states of the welding process (heat-affected zone)

heat-affected zone reaches the surface of the joining partner and a surface distortion can be observed (Russek 2003b).

22.4 Light-Material Interaction

For materials to be joined, a heat source is generated in the joining zone by absorption of the laser radiation. Thus, the parts can fuse together by means of the generated melt that forms the heat-affected zone. Therefore, the underlying basis for machining or processing materials with laser light depends on the way in which the laser reacts with the specific material involved (Atanasov 1995; Menges et al. 2002). The different light material interactions are displayed in Fig. 22.6 (neglect of the second boundary reflection).

If light hits the material surface it is reflected and penetrated into the material. Surface reflection is represented as R_G in Fig. 22.6. The part of the light that is not reflected at the surface enters the material. As the light passes through the medium, its intensity decreases according to Lambert–Beer's law:

$$I(x) = I_0 \cdot e^{C_{ex} \cdot x}$$

$I(x)$ is the intensity at the point x, I_0 denotes the intensity of the entering light and C_{ex} represents the extinction coefficient, which depends on the material, wavelength, additives and other parameters. C_{ex} consists of two parts. The first one is the absorption coefficient C_{abs}, which indicates the absorbed energy A in Fig. 22.7. In fact, the absorption coefficient C_{abs} can cover values from nearly zero (transparent) over a medium range (volume absorber) up to high numbers (surface absorber). The

Fig. 22.6 Light-material interaction
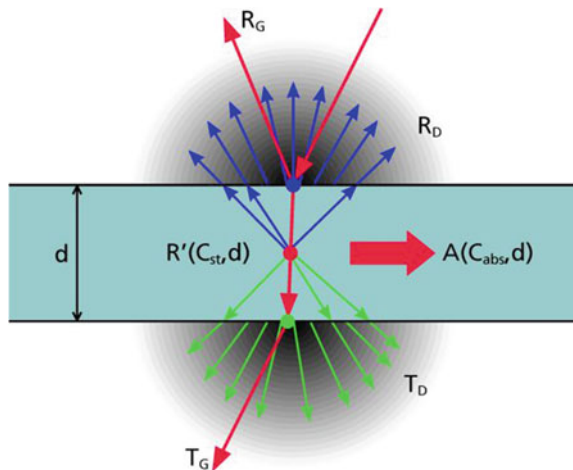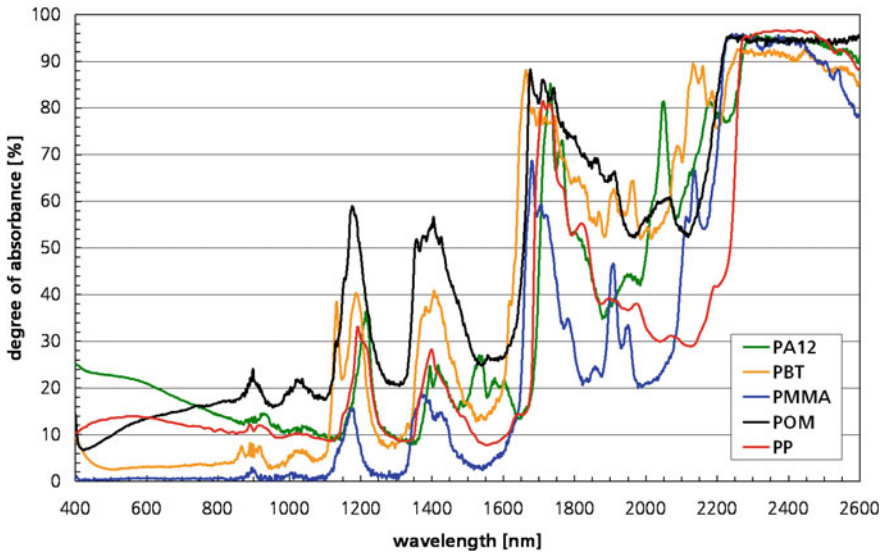
Fig. 22.7 Spectra of different polymers (PA 12, PBT, PMMA, POM and PP)

absorbed energy is transformed into heat and, thus, leads to a temperature increase, which may cause melting or even thermal decomposition (Nonhof 1994).

The second part of the extinction coefficient C_{ex} is the scattering coefficient C_{st}, which indicates the deflection of the light. Scattering (R') deflects the light out of its original propagation direction. This can take place by, e.g. particles, crystals or grain boundaries, but the overall energy of the light is not transferred into the material and, thus, does not affect the state of the matter. The deflected light which leaves the material can be measured as diffuse reflectance (R_D) on top of the material or diffuse transmittance (T_D) below the material.

The light that is propagated through the material is indicated by the transmittance (T). T consists of two components. The first component is the directed transmittance (T_G). This component has the same direction as the entering light. The second component is the diffusive transmittance (T_D), which is characterized by all directions except the one of the directed light.

22.5   Optical and Thermal Properties of Thermoplastics

22.5.1   Optical Properties

The optical properties of the material influence the laser transmission welding process significantly. The top layer has to be sufficiently transparent for the wavelength used. The more transparent the material is, the more energy can be transmitted into the

welding area. For the bottom layer, the absorption is the important parameter for the welding process. The interaction of material and radiation only takes place in the top area of the bottom welding partner.

The extinction of the original radiation flux is caused by scattering and absorption. Since both physical phenomena appear at the same time it is difficult to separate them. Loss of laser power due to scattering and absorption within the transparent joining partner causes an increased original laser power to guarantee sufficient laser energy for plastification within the joining area. Furthermore, the more laser energy is absorbed per length (volume) within the transparent joining partner, the larger the risk of burning the transparent thermoplastic. Due to these coherences, the process window becomes smaller. Therefore, knowledge concerning influencing the optical properties, while adapting them to the laser beam process is a crucial point of laser beam welding of thermoplastics. Dyes, crystallinity, additives and other ingredients added to the basic thermoplastic influence the optical properties. Therefore, they allow adapting the optical properties to the process technical needs.

From the physical point of view, absorption is the damping of electro-magnetic waves while propagating through a spatially extended media. Here, absorption takes place because of the interaction of electro-magnetic laser radiation and matter (thermoplastic). Due to dielectric and magnetic losses of the media absorbed energy is transformed into heat energy. Absorption of the laser power in the infrared (IR) range occurs by excitation of vibrations in molecules. The light is absorbed in the ultraviolet range (UV) by excitation of electrons. Polymers show characteristically strong absorption in the deep IR or deep UV range. The strength and structure of the absorption in the IR range is governed by molecular groups, with absorption coefficients for radiation at 10 μm wavelength typically lying in the range 100–1000 cm^{-1}.

The optical penetration depth is the reciprocal value of the absorption coefficient and depends on the actual utilized thermoplastic (chemical compound, chemical ingredients), the morphology of the thermoplastic (e.g. degree of crystallinity) and the processing of the thermoplastic, the used laser wavelength and furthermore, it depends on the nature, quantity (concentration), size and distribution of the added substances, such as colour additives as well as flame retardant, filling and reinforcement materials.

In the IR wavelength range, most materials show decent absorbance without additives at special wavelength, which correlates to the chemical structure of the polymer. In Fig. 22.7, this behaviour can be seen for different polymers. At several wavelengths (1200, 1450, 1700, 1900 and >2400 nm), the absorption reaches a sufficient value for melting by stimulation of radiation at this wavelength. If the laser wavelength is chosen according to the results of the spectra, no further IR-absorber has to be added.

In the visible and near IR range, most non-pigmented thermoplastics are transparent or show an opaque translucent behaviour. Therefore, the extent to which the laser radiation is absorbed is usually adjusted by IR-absorbers such as carbon black, pigments or dyes and not by the polymer matrix itself. Due to its broad band absorbing abilities and its low price carbon black is the standard IR-absorber for applications in which the optical properties of the welding partners are from minor interest. By changing the amount of added carbon black, the optical penetration depth can be
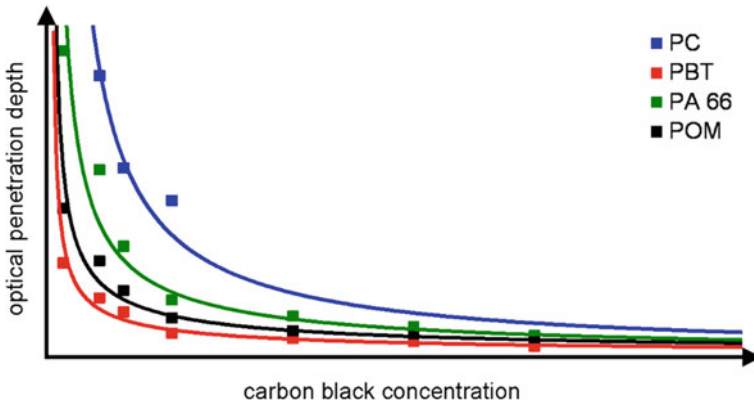
Fig. 22.8 Optical penetration depth over the amount of added carbon black

adapted. In Fig. 22.8, the optical penetration depth is depicted over the amount of added carbon black for a few standard plastics. The optical penetration depth governs the molten volume created in the welding area. Higher molten volume allows higher gap bridging capabilities but the managed process speed is lowered. Therefore, a trade-off for the desired application has to be found.

Combinations with a higher degree of complexity could be realized with special laser additives. But as such absorbing additives usually have an intrinsic colour of their own in the visible range (e.g. a slight green for an IR-absorber), a compromise has to be found between technical design and the demands on the colouring.

> In contrast to absorption scattering causes a change of the original intensity distribution due to an interaction between laser radiation and matter. The scattering means a change of the original beam propagation behaviour of the laser radiation. While scattering is negligible within amorphous thermoplastics, it is of relevance within partially crystalline thermoplastics. Crystalline super structures (spherulites) cause the scattering (a sort of multiple reflection). The original optical path becomes changed, while the optical path within the scattering medium becomes lengthened. This again causes an increased absorption. Therefore, the absorption increases either with growing degree of crystallinity or at the same degree of crystallinity but smaller (and therefore more) spherulites. Together both effects (absorption and scattering) cause a broadening of the original intensity distribution and a decrease of the original intensity. Due to scattering, a broadened intensity distribution may cause broader weld seams. The more transparent the material is, the more energy can be irradiated into the welding area. The higher the amount of additives (e.g. glass fibres, etc.), the degree of crystallinity and the thickness of the top layer, the lower is the amount of direct transmitted laser energy into the welding area.

In Fig. 22.9, the behaviour of the laser spot for a natural PA is shown for different thicknesses d.
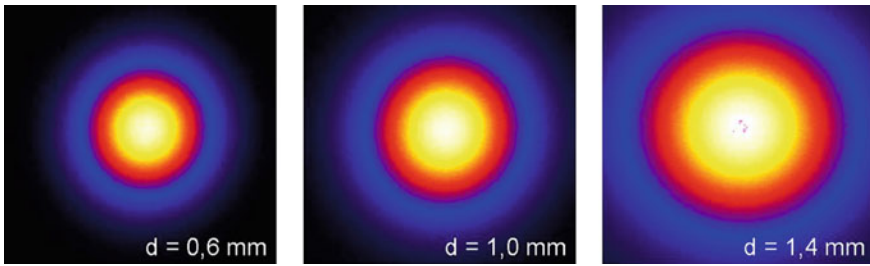
Fig. 22.9 Increase of the laser beam diameter due to scattering for Polyamide (PA 6) and different material thicknesses d

22.5.2 Thermal Properties

While considering thermal properties of thermoplastics, such as melting and decomposition behaviour, mechanical strength versus temperature, phase transition, heat conductivity, thermal expansion coefficient as well as the viscosity, welding of thermoplastics is quite different from welding metals. The temperature within the joining area has to be kept over melting and below decomposition temperature. Therefore, this temperature range may be very small. The mechanical strength vs. temperature for thermoplastics is different for amorphous and partial crystalline thermoplastics. Especially, there are no distinct phase transitions for amorphous thermoplastics as in metals. Considering the short interaction times of laser radiation with the thermoplastic material as well as the low heat conductivity of polymers in the order of 0.1–1 W/(m K), the intensity distribution is imaged into an energy density profile corresponding to a temperature profile within a layer of the dimension of the optical penetration depth. The large thermal expansion coefficients of thermoplastics do not only support the mixing and diffusion of the thermoplastics to be welded, but also may cause inherent tensions because of shrinkage, even after long periods of time after solidification. Viscosity of plastified (molten) thermoplastics is much larger than for molten metals, therefore, molten thermoplastics do not flow and mix sufficiently within the available interaction time without any external force, such as inherent pressure. In summary, fulfilling optical and thermal process requirements is mandatory for obtaining high-quality welds.

22.5.3 Further Physical Properties

Alongside the physical properties, such as transmission, absorption and melting point, there are also other aspects to be borne in mind in respect of weldability. On the one hand, the polymer compatibility (Fig. 22.10) of the parts to be joined must be ensured if dissimilar thermoplastics are to be used. On the other hand, it must be borne in mind that the modification of one type of polymer generates new polymer

Material-Mix	ABS	ASA	MABS	PA 6	PA 6.6	PA 12	PBT	PBT/ASA	PC	PC/ABS	PE-LD	PE-HD	PEEK	PES	PET	PMMA	POM	PP	PPS	PS	PSU	PVC	SAN
ABS	●	●	●				●	●	●	●				○	●	●				○	○		●
ASA	●	●					●	●	●	●						●							●
MABS	●		●																				
PA 6				●	●	●																	
PA 6.6				●	●	●																	
PA 12				●	●	●																	
PBT	●	●					●	●	●	●				○	●					○			●
PBT/ASA							●	●	●	●					●								
PC	●	●					●	●	●	●				●	●	○					○		
PC/ABS	●	●					●	●	●	●													
PE-LD											●	●						●		○			
PE-HD											●	●						●					
PEEK											○	○	●									○	
PES	○						○		●					●	●						○		
PET							●	●	●					●	●								○
PMMA	●	●							○							●							○
POM																	●						
PP											●							●					
PPS																			●				
PS	○						●													●			
PSU	○						●		●					○							●	○	
PVC	●	●					●		●												○	●	
SAN	●	●					●							○	○	○				○			●

● High strength   ○ Low strength   ☐ No connection
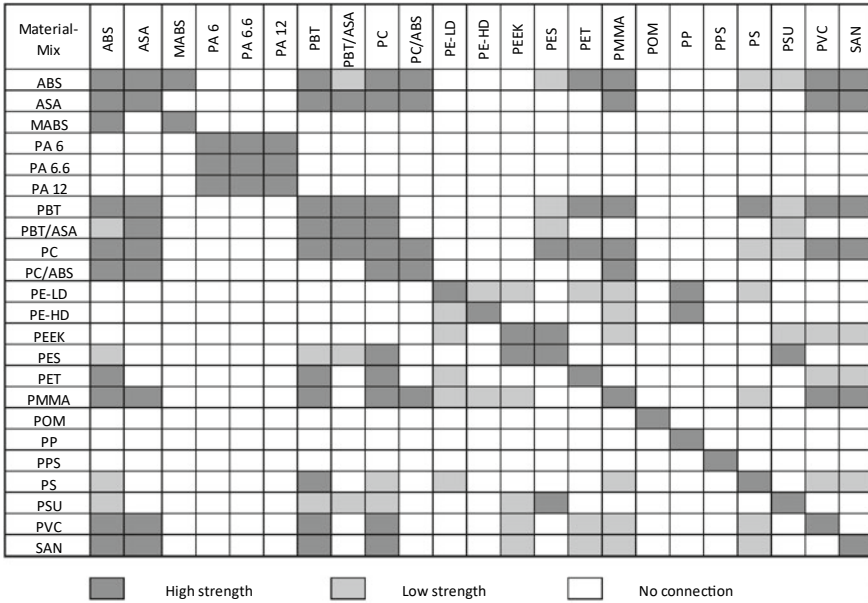
Fig. 22.10 Polymer compatibility matrix (Klein; Laser Welding of Plastics: Materials, Processes and Industrial Applications; Wiley–VCH, Weinheim 2011)

types which can have very different joining behaviour. The joining of identical-type thermoplastics has already become established in industry over the past few years. In future, development work will focus especially on the joining of dissimilar material types, since this will permit the targeted selection and alignment of the material to the specific conditions that prevail in the application. This will go hand in hand with increased functionality and enhanced added value for new, innovative products.

Plastics contain a large number of additives that are incorporated in order to achieve specific product properties for the application in question. A number of these are visually perceptible additives, while others are not. Problems that impair or even prevent laser welding and which have their origins in the additives employed are not always recognized immediately on account of the complex way in which they act.

Laser beam welding adapted design

In obtaining high-quality welds different design and technical aspects have to be considered compared to conventional welding technologies, while certain requirements have to be fulfilled, such as.

- constructional or laser adapted design of the joining partners
- demands on the product reconcile with laser adapted design of the joining partners
- guaranteeing clamping and positioning of joining partners during irradiation process

- considering joining partners are welded in their final position
- avoiding or minimizing gaps between the joining partners
- ensuring accessibility, avoiding beam obstructing parts between laser and joining area
- polymer specific design of the joining partners
- guaranteeing welding suitability of the joining partners (polymer compatibility)
- considering influence of processing conditions on crucial demands for laser process
- matching the physical properties to the laser beam process
- considering type, concentration, distribution and size of additives
- avoiding impurities and moisture (especially for PA)
- method depending factors of process influence:
- irradiation method and joint geometry
- laser beam source (i.e. wavelength, power)
- joining parameters as well as their clamping strategy, parts supply and removal

If intending to apply laser beam welding for an existing or new product the laser beam adapted design must be considered early, in order to use the process technical opportunities and advantages.

Laser sources for the polymer welding

In principle for the laser welding of thermoplastics usual laser sources are represented by the CO_2, Nd:YAG and the diode lasers. The wavelength of the CO_2 laser leads to very short optical penetration depths. Therefore, the CO_2 lasers are used more for the welding of thin foils rather than for the overlap welding of thicker plastic components (Duley and Mueller 1992). The diode lasers due to the lower investment cost and possibility for fibre delivery of the laser beam enjoyed a greater industrial acceptance. However, the low beam quality of these laser systems and the high expansion of the welding area are some drawbacks for their use. The optical penetration depth can be assured for the relevant process window through carbon black pigments for example.

The laser beam welding of thermoplastics with high power diode lasers generates optically high valuable weld seams and leads to several process specific advantages such as contactless deposition of the joining energy, no process induced vibrations, no thermal stress of the entire joining components, no particle release during the welding as well as a high industrial integration and automation potential. The impact on working environment compared to alternative processes like the development of vapours in the case of gluing is for the laser transmission welding negligible. The dimensions of the possible joining partners reach from Macro-components, e.g. hermetically sealed liquid recipients from the Automotive industry to the Micro-components, e.g. housings for electronic components or medical products.

For such applications, the diode lasers due to their compactness and reliability (lifetime of about 10,000 h under optimal working conditions) are the most suitable laser sources. The emission wavelengths for these laser systems are in the range of approximately 800 to 1940 nm. For this domain, the laser beam can be guided through optical fibres allowing the easy integration of the laser source in processing

heads or robot systems. Furthermore, the optical properties of the polymers in this wavelength range make the high-power diode lasers most suitable for the laser beam welding.

Laser source	CO_2	Diode	Nd:YAG	Fibre
Wavelength (μm)	9.6–10.6	0.8–1.9	1.06	1.03–2.0
Beam quality M^2	1.1	47	1.1	1.05
Efficiency (%)	10	30	3–10	20
Beam delivery	Free beam	Optical fibre	Optical fibre	Optical fibre
Compactness	+	+	−	+ +
Scanner beam manipulation	+	(+)	+	+ +
Spot diameter (μm)	50	~200	20	10

The industrial acceptance of the laser beam welding increased also due to the higher cost-effectiveness in the range of high-power diode and fibre lasers.

This innovative technology enables the achievement of high-quality assembling of mechanical and electronic high sensitive micro-components as well as of reliable, tight and high strength joining of macro-components. For the technical realization of the process there are several concepts available, concepts that can be adapted to the specific requirements of individual applications.

Amorphous as well as partly crystalline thermoplastics can be welded by means of laser radiation. Even though the glass reinforcements lead to the scattering of the laser beam depending on the concentration and dimensions of the glass fibres and of the dimensions of the joining partners such materials can be successfully laser welded as well. Through the addition of the base polymer of pigments or additives, the plastic material properties can be suited to match the requirements of the laser beam welding.

22.6 New Approaches for the Polymer Welding

The recent technological advances enabled the development of miniaturized polymeric components starting from simple geometries up to high levels of complexity. The low cost of these materials and their cost-effective manufacturing have brought simultaneously opportunities and challenges for the development of hybrid Microsystems or larger products containing plastic materials (Sieffert 2003; Russek 2016). Since such devices usually involve the assembly of multiple components with different functions, one of the main challenges for their complete realization is represented by the joining process. The real growth of the laser transmission welding of polymers and the increase of the industrial acceptance started with the development of the high-power diode lasers (HPDL). The development of such laser sources allowed a considerable improvement of the initial investment costs, an easier integration into manufacturing systems due to their reduced constructive dimensions

and an increase of the wall-plug efficiency (~30%) compared to the alternative laser sources, represented at that moment by the Nd:YAG and CO_2 lasers.

Nowadays, due to the development of new laser sources for the materials processing with an almost ideal beam quality, e.g. fibre or disk lasers new possibilities are given to the welding of polymers. The high beam quality enables the achievement of a laser spot of only a few micrometres or working with a long focusing length while still having a small laser spot. New concepts like remote welding of polymers for joining large components or maskless achievement of weld seams as narrow as 100 μm could be now considered. The attractive investment costs, the extremely reduced constructive dimensions and an attractive wall-plug efficiency of the fibre lasers as well as the availability of new wavelengths like 1.55 mm or 1.9 μm raised the interest of the research and industrial community and subsequently, their performance for the material processing is currently subject of intensive research. If in the case of metallic materials concrete positive results were already reached demonstrating the high potential of these new lasers, for the case of polymeric materials the investigations are still at their infancy. Therefore, the current research is focused on evaluating the applicability of fibre lasers for the transmission welding of thermoplastics. In the following chapters, two of the latest research results related to this topic are presented in detail.

22.6.1 TWIST®—A New Approach for the High-Speed Welding of Polymers

The high beam quality of the single mode fibre lasers ($M^2 \approx 1.05$) offers the advantage that very small laser focal spots can be achieved fulfilling the theoretical prerequisites to perform narrower weld seams. However, when using such a high-quality laser beam focused into a very small focal spot, the power density is in the order of $I = 10^5$–10^6 W/cm^2. Such laser intensities might be ideal for cutting or welding of metals but in the case of polymer contour welding, where the commonly used laser intensities are in the range of $I = 10^2$–10^3 W/cm^2, they would lead to overheating and instantaneous material degradation even for low laser power levels.

To overcome these aspects and to achieve a thermally optimized laser welding process an innovative strategy for the coupling of the laser energy into the materials was developed. According to this approach the laser beam has to be moved with a high dynamic to avoid the overheating of the material, but simultaneously through adequate overlap of the laser spot passing over the material for consecutive increments of the weld seam, to assure the required time for the heat transfer between joining partners and the sufficient diffusion of the polymeric chains to obtain a high-quality weld seam. The new approach was called TWIST®—Transmission Welding by an Incremental Scanning Technique because it keeps the incremental weld seam forming characteristic of the contour welding while the high dynamic movement and the effect of this movement are typical to the quasi-simultaneous welding technique.

(a)   (b)   (c)
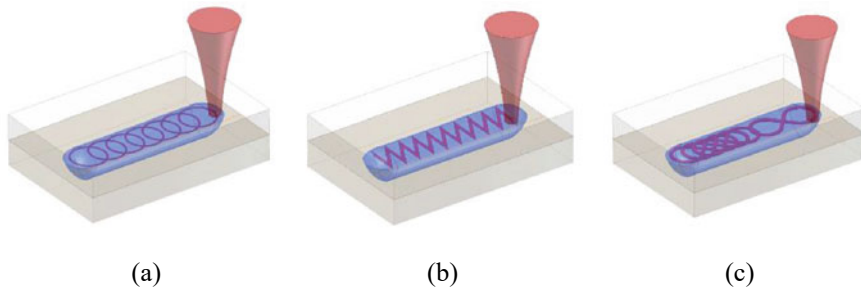
Fig. 22.11 Different possibilities for the high dynamic movement of the TWIST® approach

Furthermore, such a complex, accurate and fast movement of the laser beam can be realized only by elements from the field of high-speed scanning technology like galvanometric, polygon or resonance scanners (Boglea et al. 2007a, b).

There are multiple possibilities to perform such a weld seam. In a simplified manner, as shown in Fig. 22.11a–c, we can consider, for example, a circle, a line or even the Lemniscate of Bernoulli as individual elements of the weld seam (Boglea 2013). If the laser beam is moved with high speed along such an individual element and if in the same time the element is shifted with the desired feed rate from one increment of the weld contour to the consecutive one, the weld seam can be achieved. Nevertheless, a corresponding correlation between the laser spot, feed rate and the high-speed movement of the laser beam has to be carefully taken into consideration in order to get a homogeneous and high valuable weld seam. Such an approach has been already applied in the past for the electron beam welding of metals for achieving different properties of the weld seam or to achieve wider weld seams. Nevertheless, here independently of the chosen geometry for the individual elements of the weld seam the aim is not to broaden the weld seam but to achieve a thermally optimized welding process.

For a better understanding of the advantages of such an approach, computer simulations were performed for the case of the circular beam movement and for the movement along a Lemniscate. The results are shown in Fig. 22.12. The first simulation results reveal that for the circular beam movement an overheating at both sides of the weld seam can occur. A more homogeneous temperature distribution without overheating areas can be achieved for the high dynamic movement of the laser beam along a Lemniscate.

Experimental results show the viability of the TWIST® approach and the possibility to weld polymers with fibre lasers even when high laser intensities are involved. The high dynamic movement considered by the TWIST® approach has the benefit that a homogeneous laser energy distribution in the absorbing joining partner takes place. The effect is like the result followed by the top hat shaping of the laser intensity distribution, but without necessitating any beam shaping operation. Compared to the results achieved for the laser welding of Polypropylene, where the maximum weld strengths were in the range of 25–30 N/mm^2, the weld strength achieved through
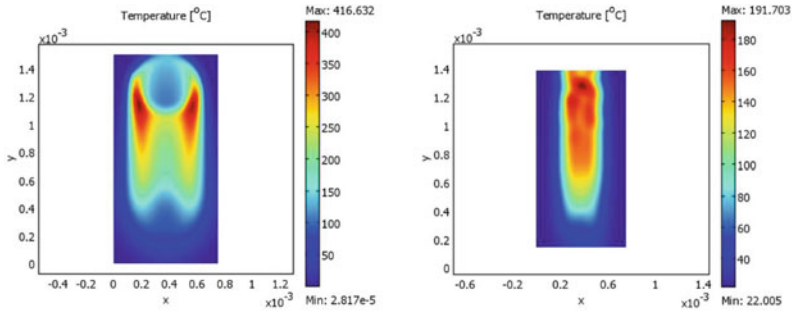
Fig. 22.12 Top view of the welding zone for a computer simulation of the temperature gradients developed for the circular beam movement (left) and for the movement along a Lemniscate (right)

TWIST® were reaching higher values in the range of 35 N/mm². The higher strength achieved through the proposed method can be the result of reduced surface tensions at the weld seam's interfaces with the joining partners.

The reduced HAZ achieved might represent a successful solution for welding of polymeric components where no distortion on the back side of the components is allowed or where a minimum distortion of the welded structures is required. For the last situation, an eloquent example is given by the recently developed microfluidic chips, where channels with a width of less than 50 µm must be sealed. Through the 'conventional' laser welding the HAZ is still too high and causes the collapse of the channel walls closing it and compromising its functionality. Also the welding of thin foils or membranes could be considered. Figure 22.13 shows the welding using the TWIST® approach of 100 µm thick Polypropylene foils with weld seams having a thickness starting from 500 µm down to 130 µm. The feed rate was varied up to 12 m/min.
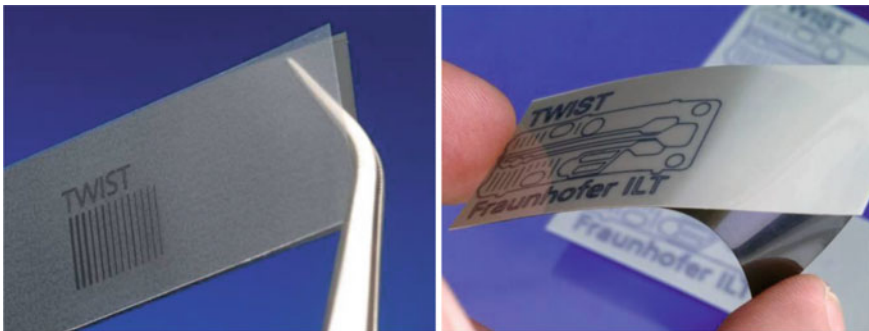
Fig. 22.13 TWIST® welding of Polypropylene foils with a thickness of 100 µm

22.7 Absorber-Free Laser Beam Welding of Transparent Thermoplastics

The optical properties of the welding partners play an important role for the welding process. One problem is the energy deposition in the welding area as soon as the material does not match the desired optical requirements. Difficulties occur when materials of the same optical properties are to be welded. To overcome these difficulties carbon black is usually used for the absorbing joining partner. But the black colour is not always desired. One solution is the usage of a colour that is IR-transparent for the transparent joining partner or a visually transparent IR-absorber for the absorbing joining partner. This IR-absorber can be an additive that is incorporated into the plastic mould or a coating applied directly onto the surface layer between the welding partners.

In this field several developments have been made, so that nearly all different colours are weldable. From the cost-efficient point of view, there is the problem of high cost for the absorbing additives. To reduce costs, especially for large-scale parts, a two-component injection moulding process can be used. With this process, the absorber is only placed in the welding area of the absorbing part.

The use of an IR-absorber is not always a desired method, especially when medical applications are concerned. The use of an additional chemical product can lead to problems in the approval of the product in terms of biological compatibility.

A new approach is the usage of tailored lasers. The wavelength of these lasers is adapted to the absorption spectra of the material. In combination with optics with high numerical apertures the welding of similar thermoplastics without an IR-absorber is feasible.

To weld similar thermoplastics in the overlap geometry, several circumstances must be considered. First, there has to be an intrinsic absorption by the polymer at the chosen wavelength. In the other way round, the wavelength of the laser system used can be chosen by the spectra of the material. If the degree of the absorption coefficient is high enough, the corresponding wavelength is suitable. In Fig. 22.14 a spectra of a PC is given. A peak in the absorption line at 1940 nm can be identified. Therefore, the material is suitable for a laser welding process at this wavelength.

Since both joining partners have the same optical properties, the laser radiation is absorbed inside the irradiated material volume. The intensity progression inside the polymer is determined by two contrary effects. First, the intensity decreases due to absorption which can be described by the lambert–beer law which depends on the absorption behaviour of the polymer as well as the thickness (Aden et al. 2018):

$$I(z) = I_0 * e^{-\alpha * z}$$

where α is the absorption coefficient, I_0 is the maximum intensity at the surface and z is the coordinate in beam propagation direction. On the other hand, the laser intensity increases due to focusing. The intensity propagation is proportional to Aden et al. (2018):
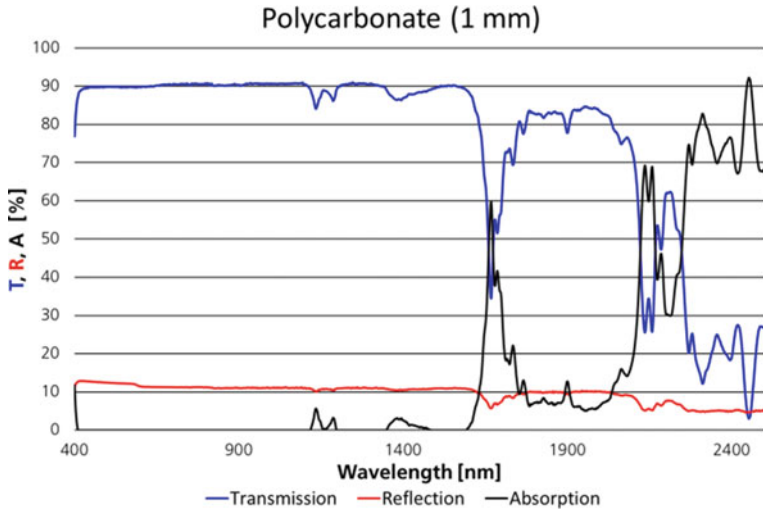
Fig. 22.14 Measured transmission, reflection and absorption of PC with 1 mm thickness

$$I(z) \sim \left(\frac{w_0}{w(z)} \right)^2$$

where w_0 is the focal diameter and z is the coordinate in beam propagation direction. Here, the intensity maximum is reached in the beam focus. The Fig. 22.15 shows the two intensity progressions.

In order to selectively melt the polymer, the decrease of the intensity has to be compensated by strongly focusing the laser beam so that the necessary intensity for

Fig. 22.15 Effects on the intensity due to absorption and focusing
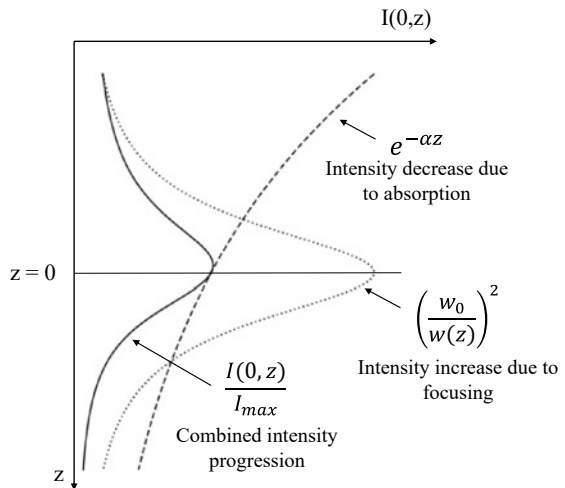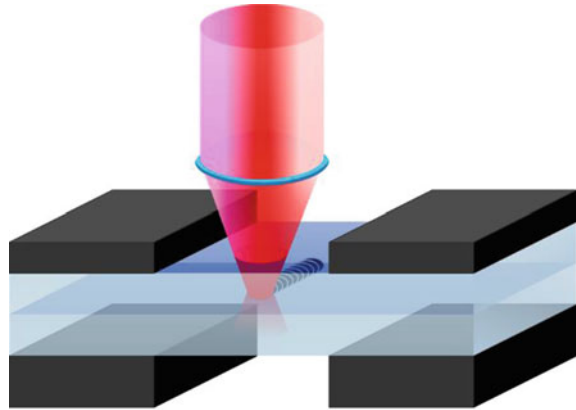
melting the polymer is only exceeded in the focal area. Otherwise, the intensity and temperature maximum are on the surface of the upper joining partner which leads to a melting of the entire material cross section. Even with strong focusing, it can be recognized that the maximum intensity and by implication, the highest temperature is not in the welding area, but slightly above in the upper welding partner. And for that reason, the focal position has to be updated and adjusted (Aden et al. 2018).

An optic with high numerical aperture is needed to achieve the desired intensity progression inside the material (Fig. 22.16). With this setup, small focal diameters are achieved which enable the generation of micro joints.

Another strategy to generate a spatially confined HAZ is quasi-simultaneous welding. Here, the laser beam is moved along the entire welding contour at high scanning speeds multiple times which leads to a nearly simultaneous heating of the entire welding contour. The advantages compared to contour welding are the higher gap bridging ability as well as the short process time which leads to an increasing interest especially for mass production. As it can be seen in the following Fig. 22.17, the heating curve can be divided into a heating and a cooling phase. Here, the line energy and laser power are kept constant whilst the number of passes and scanning speed are increased (Nguyen et al. 2020).

The HAZ is generated due to heat accumulation in both joining partners due to the low thermal conductivity of polymers. After each irradiation pass, heat is also dissipated from the upper and lower surface of the sample. With increasing number of passes and scanning speed, a reduction of both HAZ height and width can be achieved and the increase in temperature becomes lower which leads to a smoother heating process. The Fig. 22.18 shows the microscopic pictures of the HAZ in quasi-simultaneous welding (Nguyen et al. 2020).

Due to the high process dynamics and therefore the higher demands on the equipment, the total investment costs for a quasi-simultaneous welding system are higher which is one of the main drawbacks of this method. Another aspect is the limitation of the maximum seam length which depends on the scanning field of the optic as well as the maximum laser power output (Nguyen et al. 2020).
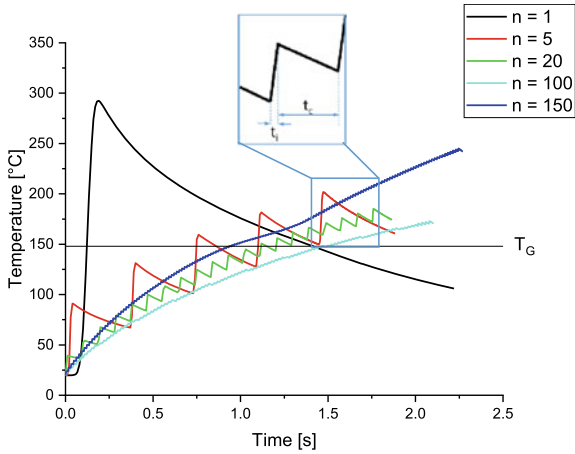
Fig. 22.17 Temperature progression in quasi-simultaneous welding for different number of passes (Nguyen et al. 2020)
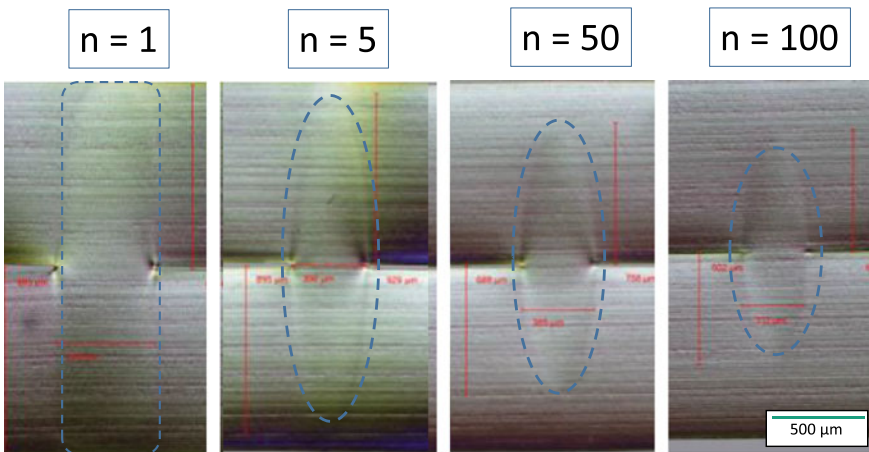
Fig. 22.18 Reduction of the HAZ geometry at increasing number of passes and constant line energy (Nguyen et al. 2020)

In several experiments, the feasibility has been shown for both thin foils and thicker bulk material. Especially for medical applications like a microfluidic device, where transparent materials have to be used to allow spectroscopy and IR-absorber is no choice because of the costs, this welding technique shows remarkable opportunities. In Fig. 22.19 a microfluidic device is shown, where the channels are sealed with a thulium-fibre laser at 1.94 µm (Nguyen et al. 2019).
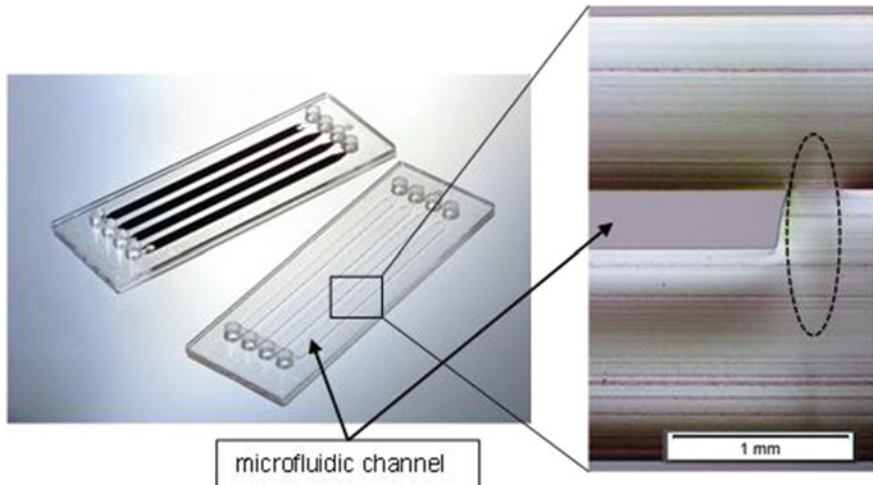
Fig. 22.19 Microfluidic device made of PC (samples provided by microfluidic ChipShop GmbH, Jena, Germany) (Nguyen et al. 2019)

The above-mentioned examples show the high potential of an absorber-free laser welding process. The aim of future works is to increase the productivity of the welding process or by establishing an online-process control.

References

Aden M, Gillner A, Otto G, Mamuschkin V (2018) Laserdurchstrahlschweißen transparenter Kunststoffe - Teil 1: Betrachtung des Energieeintrags. Joining Plastics-Fügen von Kunststoffen 12(3):166–172

Atanasov PA (1995) Laser welding of plastics—theory and experiment. Optical Eng 34(10):2976–2980

Bachmann FG, Russek UA (2002) Laser welding of polymers using high power diode lasers. Proceedings Photonics West

Becker F (2003) Einsatz des Laserdurchstrahlschweißens zum Fügen von Thermoplasten. Dissertation Universität Paderborn, Institut für Kunststofftechnik

Boglea A, Olowinsky A, Gillner A (2007a) Fibre laser welding for packaging of disposable polymeric microfluidic-biochips. J Appl Surf Sci 254:p1174-1178

Boglea A (2013) Laser transmission welding of thermoplastics using local laser beam modulation. Dissertation RWTH Aachen

Boglea A, Olowinsky A, Gillner A (2007b) TWIST—a new method for the micro-welding of polymers with fibre lasers. In the proceedings of the ICALEO, October 29–November 1, 2007b, Orlando, USA, pp 136–142

Chen JW (2000) Mit der Maske in die Mikrowelt – Neues Laserschweißverfahren für Kunststoffe, Zeitschrift TAE-Aktuell, S. 2–4, Heft 12

Duley WW, Mueller RE (1992) CO_2 laser welding of polymers. Polym Eng Sci 32(9):582–585

Hänsch D, Pütz H, Treusch HG (1998) Harte und weiche Kunststoffe mit Diodenlaser verbinden. Kunststoffe 88, Carl Hanser Verlag

Klein R, Poprawe R, Wehner M (1987) Thermal processing of plastics by laser radiation; proceedings laser 87. Springer, Heidelberg

Laser plastic welding market. Transparency Market research. https://www.transparencymarketres earch.com/pressrelease/laser-plastic-welding-market.htm. Retrieved 24 Sept 2021

Menges G, Haberstroh E, Michaeli W, Schmachtenberg E (2002) Werkstoffkunde Kunststoffe, 5. Auflage, Kapitel. 12, Carl Hanser Verlag, München Wien

Nguyen N-P, Brosda M, Olowinsky A, Gillner A (2019) Absorber-free quasi-simultaneous laser welding for microfluidic applications. JLMN 14(3):255–261. https://doi.org/10.2961/jlmn. 2019.03.0009

Nguyen N-P, Behrens S, Brosda M, Olowinsky A, Gillner A (2020) Modelling and thermal simulation of absorber-free quasi-simultaneous laser welding of transparent plastics. Weld World 69. https://doi.org/10.1007/s40194-020-00973-5

Nonhof CJ (1994) Laser welding of polymers. Polym Eng SCI 34(20):1547–1549

PlasticsEurope (2007) Consultic; myCEPPI; Conversio; Plastics-The facts 2020, p 25 (2020), pp 11

Russek UA, Otto G, Poggel M (2001) Verbindliche Nähte – Automatisiertes Fügen von Kunststoffen mit Hochleistungs-Diodenlasern. Laser Praxis 1(2001):14–16

Russek UA (2003a) Simultaneous laser beam welding of thermoplastics—innovations and challenges. ICALEO 2003a, Jacksonville, Florida, USA, Paper ID 604, October 13th–16th

Russek UA (2003b) Innovative trends in laser beam welding of thermoplastics. In: Proceedings of the second international WLT-conference on lasers in manufacturing, Munich, Germany, pp 105–112

Russek UA (2006) Prozesstechnische Aspekte des Laserdurchstrahlschweißens von Thermoplasten. Dissertation RWTH Aachen University, Shaker Verlag: Aachen

Russek UA, Palmen A, Staub H, Pöhler J, Wenzlau C, Otto G, Poggel M, Koeppe A, Kind H (2003) Laser beam welding of thermoplastics. Proceedings Photonics West

Sieffert M (2003) Farbstoffe und Pigmente- von schwarz bis weiß zu kunterbunt. Aachener Laser Seminare: Aachen

Chapter 23
Laser Transmission Bonding

F. Sari, A. Wissinger, and A. Olowinsky ⓘ

23.1 Introduction

The miniaturization in semiconductor industry shows that the temperature stress during packaging of front-end processed wafers with sensitive micro-chips is becoming more important. The state of the art for Wafer Level Packaging is the sealing of those processed wafers with cap-wafers (back-end process) in bond stations. A bond station mostly consists of a wet chemical cleaning device, a bond aligner, and a bonding device. In a standard procedure, the wafers will be cleaned with wet chemical sample preparation methods like RCA (Kern 1993), then fixed and pressed (prebonding) on each other in a bond aligner and in a last step mostly bonded in a bond-chamber through a heat treatment (tempering process) supported with diverse gas atmosphere. The tempering process (increasing the temperature) has an influence on the bonding energy which in turn influences, e.g., the mechanical strength. On the other hand, the limits of thermal load of the components integrated in a chip have a decisive influence on the temperature limit which can be applied to ensure a packaging.

A new trend is the chip-to-wafer packaging. This process enables three-dimensional chips with multiple functions by packaging of two front-end processed chips without wire bonding.

Silicon direct bonding (Lasky 1986; Shimbo et al. 1986; Schmidt 1998) is one the most applied bonding techniques. Depending on the temperature limits and wafer treatment it is differentiated between high-temperature bonding (>800 °C) and low-temperature bonding (<450 °C) (Schmidt 1998).

Laser transmission bonding (LTB) is a laser-based bonding method for processes in the semiconductor industry, for example, for wafer-level packaging of MEMS devices (Haberstroh et al. 2006; Sari et al. 2005, 2008; Witte et al. 2002; Park and

F. Sari · A. Wissinger · A. Olowinsky (✉)
Fraunhofer-Institut Für Lasertechnik ILT, Steinbachstr. 15, 52074 Aachen, Germany
e-mail: alexander.olowinsky@ilt.fraunhofer.de

Tseng 2005). While conventional bonding processes such as anodic bonding (Wallis and Pomerantz 1969; Ziaie et al. 1996) or eutectic bonding (Lin et al. 1998; Wolffenbuttel and Wise 1994) are accompanied by a global temperature increase, laser transmission bonding deposits energy only in the interaction zone of laser radiation and workpiece. This leads to a significantly reduced heat-affected zone (HAZ) and thus reduces the thermal stress during the bonding process. Increasingly higher packaging densities in electronics for the production of integrated circuits make this packaging process interesting due to the lower thermal load. The flexible adaptation of the laser radiation to different bond geometries shows the potential of this technology (Wild et al. 2001a).

Figure 23.1 gives an overview about current bond methods. Laser Transmission Bonding is shown as an alternative method to the conventional bonding techniques. Disadvantage of Silicon Direct Bonding is the high thermal input (>800 °C) which, e.g., has a negative influence on the functions of the integrated, sensitive sensors. Low-Temperature Bonding is an alternative to Silicon Direct Bonding. The wafers can be prepared with RCA-Cleaning (Kern 1993), applying plasma enhanced surface treatment with various gases like O_2 (Wiegand 2001) or using a spin-on glass (Dragoi et al. 1999) as an intermediate layer. This preparation helps to bond under 450 °C but with a long process period. Applying metallic intermediate layers like gold or aluminum between two silicon wafers leads to low-temperature bonding by formation of low-temperature eutectic bonds (Wolffenbuttel 1994). The eutectic point for silicon-gold is at 363 °C and for silicon-aluminum at 577 °C which are suitable processing temperatures to achieve strong bonding strength. Glass frit bonding is based on the application of seal glass with low softening temperature between two wafers. The Bonding temperature for this thermo-compressive process is between 400 and 450 °C (Knechtel 2005) (Fig. 23.1).

23.2 Thermochemistry of Bonding

The process of bonding needs flat and clean surfaces to activate the chemical reactions at atomic level between two surfaces. Silicon has under room temperature an oxide layer. This layer reacts with water (air humidity) and forms silanol groups (Si–OH) on the surface. It is important to use a surface preparation method to achieve a homogenous and reproducible surface condition free from any organic and metallic contamination. There are some preparation methods which can be applied. The most common method is the application of wet chemical surface cleaning method RCA. Through RCA cleaning the generation of hydrophilic surfaces can be achieved by applying two RCA cleaning steps: SC1 (NH_4OH: H_2O_2: DI–H_2O with a vol. composition 1:1:5; 10 min at 75–85 °C) and SC2 (HCl: H_2O_2: DI–H_2O; with a vol. composition 1:1:6; 10 min at 75–85 °C). The result is a surface with homogeneous chemical oxide layer and silanol groups (Fig. 23.2). Some bonding methods like eutectic bonding needs a hydrophobic surface. A hydrophobic surface can be formed by applying third cleaning steps with hydrofluoric acid.
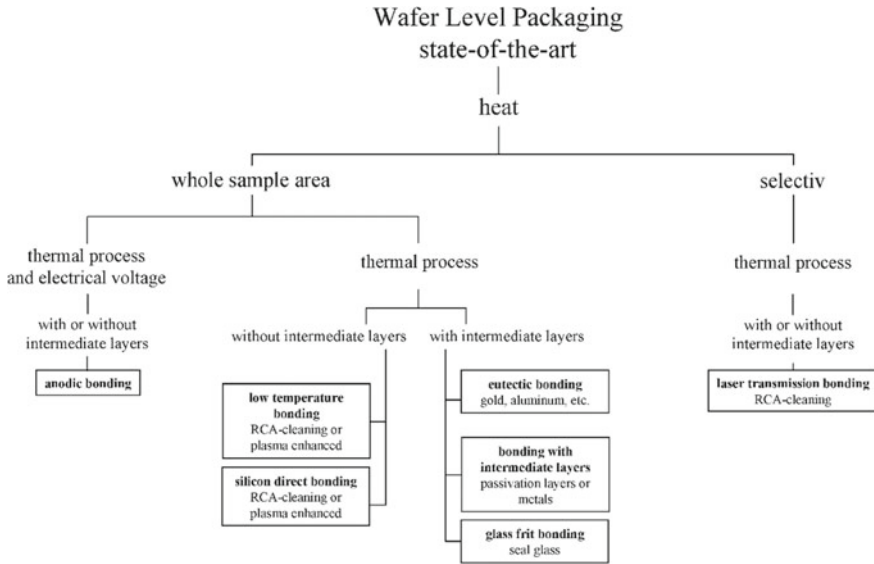
Fig. 23.1   Bonding methods
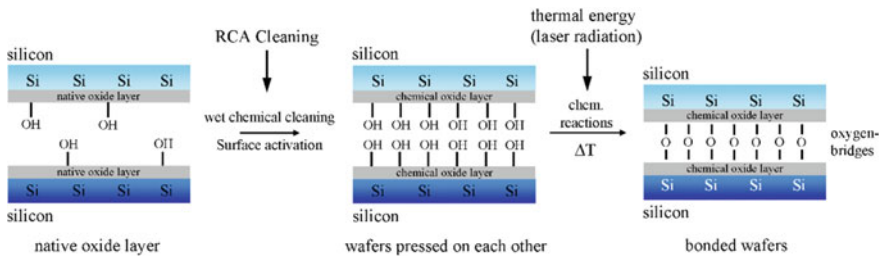
Fig. 23.2   Surface prepaparation and joining principle

After cleaning, the samples will be dried and put on each other and annealed. Primarily the thermochemistry of a hydrophilic wafer bonding procedure can be explained in 4 stages as explained in Tong and Gösele (1996):

Room temperature to 110 °C: at room temperature two wafers bond to each other through formation of hydrogen bonds (prebonding). Rearrangement of water molecules and formation of new silanol groups by fracture of Si–O–Si (23.1) is observed up to 110 °C.

$$Si-O-Si + H_2O \rightarrow Si-OH + Si-OH \qquad (23.1)$$
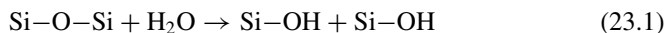
From 110 *to* 150 °C: diffusion of water molecules along the bonding interface and also through the oxide layer to silicon atoms brings the silanol groups of both

surfaces closer by formation of siloxane (23.2)

$$Si-OH + Si-OH \rightarrow Si-O-Si + H_2O \tag{23.2}$$
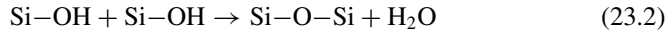
and the bond energy is increasing.

Water reaches the wafer edge through the diffusion along the bonding interface and evaporates. The diffusion of water through the oxide layer to deeper silicon atoms results in formation of new SiO_2 (23.3) which in turn is also involved in the thermo-chemical process.

$$Si + 2H_2O \rightarrow SiO_2 + 2H_2 \tag{23.3}$$
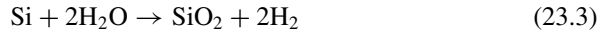
From 150 *to* 800 °C: the saturated surface energy reaches at 150 °C a value of approx. 1200 mJ/m^2. This value is constant up to 800 °C. It is believed that all silanol groups have converted to siloxane bonds at 150 °C.

Over 800 °C: the reached viscosity of SiO_2 allows oxide flow. The contacted area between the wafers is increasing by this viscous flow.

23.3 Principle of Laser Transmission Bonding

Laser Transmission Bonding (LTB) is based on transmission heating of the interface of the sample pairs to be joined (Wild 2002) and following thermo-chemical reactions (Tong and Gösele 1996) between the surfaces. The optical energy is transmitted through the upper sample (e.g., glass) and absorbed by the lower sample (e.g., silicon) at the silicon-glass interface (Fig. 23.3, left). The main part of the optical energy will be converted into heat energy and the bonding zone at the interface heated. This enables localized chemical reactions between the surfaces and leads to covalent bonds between silicon atoms by formation of siloxane (Tong and Gösele 1996).

The application of a suitable wavelength is important to join similar materials like silicon-to-silicon and glass-to-glass. The transmission of the laser radiation must be guaranteed by the upper sample. At the same time, it is important to apply a metallic interlayer at the interface which absorbs the laser radiation to activate
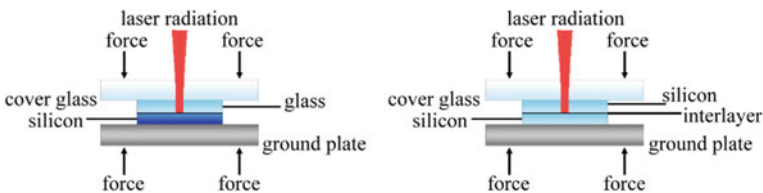
Fig. 23.3 Schematics of the joining process

thermo-chemical reactions (Fig. 23.3, right). A pressure device with integrated pneumatic cylinder assures homogeneous physical contact between the sample pairs at atomic level.

23.4 Laser Transmission Bonding of Silicon-to-Glass

A cw-Nd:YAG laser at $\lambda = 1064$ nm is suitable for bonding of silicon-to-glass along continuous lines. A pyrometric sensor which enables a thermal process control has been installed into the laser processing head (Fig. 23.4) to assure a constant temperature level at the bond front online. The evaluation of the resulting pyrometer signals during the bond process gives information of the online temperature development at the bond front. To enable a dynamic thermal process control, a labview® based software with integrated closed-loop control (PID Controller) has been developed. In Fig. 23.5, a signal flow plan of the used closed loop with the transfer behavior is shown. During the bond process, the heat development at the bond front is recorded using the pyrometric sensor. The difference between set point value (pyrometer set point value) and actual value (actual pyrometric value) is multiplied with the PID parameters in the PID Controller (proportional plus integral plus derivative controller) and an output signal (diode current control value) is sent to the laser source, so the laser power can be re-adjusted online. The control frequency is given with approximately 1000 Hz.

The coefficient of thermal expansion for single crystal silicon is $\alpha_{20\text{-}300} = 2.5 \times 10^{-6}$ K^{-1} and for Borofloat® 33 $\alpha_{20\text{-}300} = 3.25 \times 10^{-6}$ K^{-1}. The few difference between the expansion coefficients of these material allows a stress-free bonding and a stress-poor cool down process after joining.

Fig. 23.4 Laser processing head
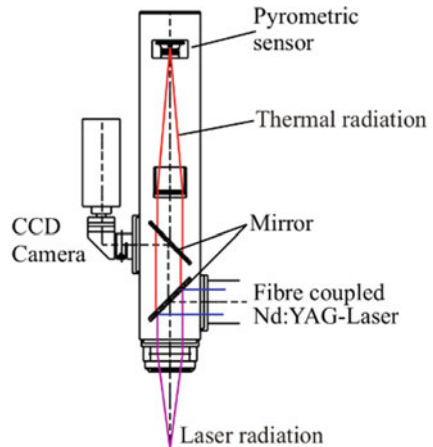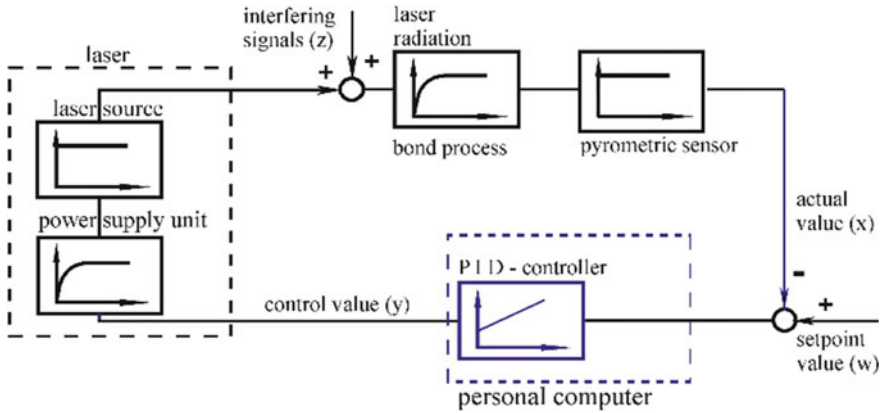
Fig. 23.5 Signal flow plan of the closed loop

Borofloat® 33 shows over 90% transmittance (thickness d $=$ 500 µm) at $\lambda =$ 1064 nm (Fig. 23.6) and silicon samples (thickness of 525 µm) have an absorbing capacity of 36–38% at $\lambda =$ 1064 nm (Fig. 23.7).

The application of laser for selective laser bonding of silicon-to-glass and the results for these using cw Nd:YAG laser sources at a wavelength of $\lambda =$ 1064 nm have been published (Wild 2002; Wild et al. 2001b, c). As a further development
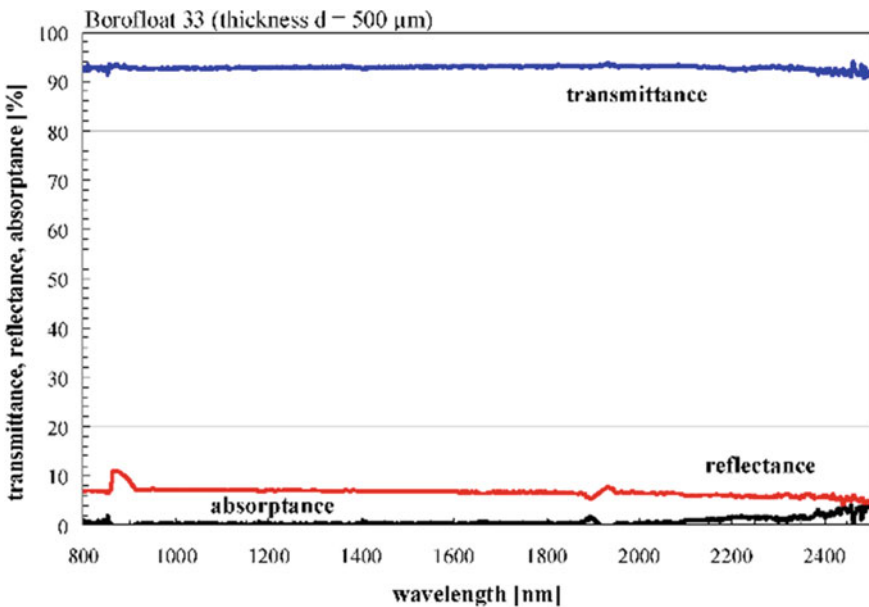
Fig. 23.6 Optical properties of a borosilicate glass (thickness 500 µm)
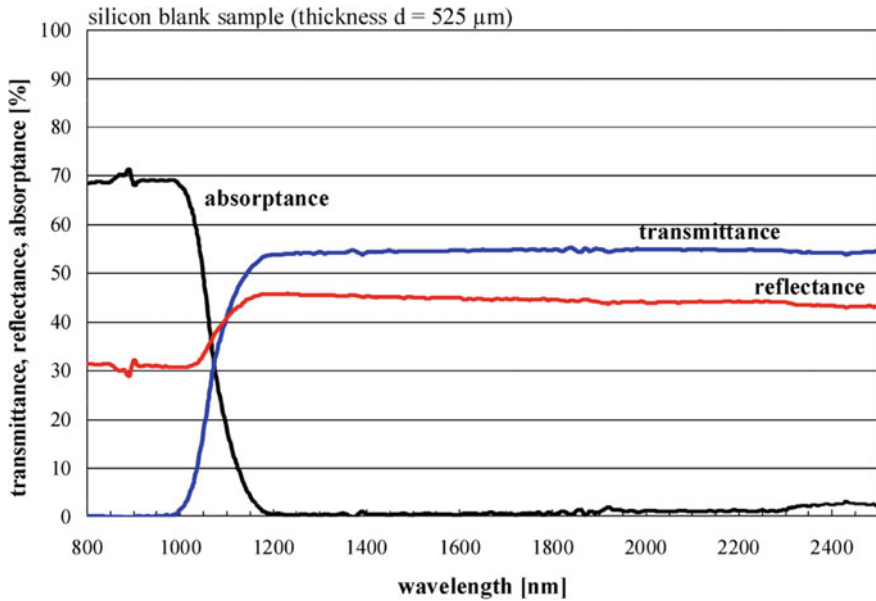
Fig. 23.7   Optical properties of single-crystal silicon (thickness 525 μm)

to these works, first bonding results of a current study by applying a fast oscillating galvanometric scanner combined with a fiber laser (wavelength of $\lambda = 1090$ nm) will be introduced here.

Compared to a laser processing head which is mostly integrated to a 3-axes machining system to enable a flexible movement of the laser radiation over the samples, scanners with integrated mirrors achieves also a flexible movement of laser radiation. The intention of this work is to show the joinability of silicon-to-glass by using fast oscillating scanners in dependence of the applied laser power and of the wobble frequency of the scanner. The bond quality is determined by evaluating the bond seam using a microscope.

The demonstrated experiments below are performed on small 5×5 mm^2 silicon and glass samples; hence the wafers were diced beforehand. 4-inch Borofloat® 33 wafers (borosilicate glass, Schott Glass, polished on both sides, thickness of 500 ± 25 μm, surface roughness <1.5 nm, total thickness variation TTV <10 μm) and silicon wafers (4-in., (100), p-doped, polished on both sides) with a thickness of 525 ± 10 μm, surface roughness <1 nm and TTV ≤3 μm are generally used for LTB.

A fiber laser (SPI, SP100C, max. power 100 W, fiber diameter of 8 μm, single mode) with a wavelength of $\lambda = 1090$ nm and a laser spot of approx. 30 μm and a scanner (Scanlab, SK1020, f-theta lens with a focal length of 80 mm) with a scan field of 35×35 mm^2 were applied. The application of scanners allows a local power modulation through special geometries over wobble function by quickly scanning the laser radiation perpendicular to the bond line. It is possible to generate bond seams by overlapping the feed rate with oscillating figures (Fig. 23.8, e.g., here circles).

Fig. 23.8 Feed motion with overlapping oscillating circular motion
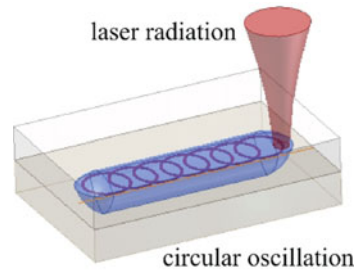
The variation of the bond seam width can be also adjusted. In addition, a further advantage of the wobble function is that melting can be avoided at the heat-affected zone during the joining process.

The results of the joining experiments show that the laser power and the wobble frequency have a direct influence on the bond seam and on the bond seam width. Figure 23.9 shows the influence of the laser power. Two sample pairs of a test series with constant process parameters are bonded with two different laser power values. It can be seen that the bond seam width is increasing by higher laser power values from approx. 130–180 μm (Fig. 23.9 left) to 180–236 μm (Fig. 23.9 right). The variation of the bond seam width within a sample pair can be explained by applying coaxial illumination method by microscopy, whereas the light dispersion is not always homogeneous. The determination of the exact bond seam width will be carried out by application of chemical etching methods like KOH for silicon.

To show the influence of the wobble frequency, the frequency was varied between 500 and 6000 Hz by constant parameters for a laser power of 41.5 W within a test series. The Examination of the bond seams regarding closed, continuous, and tight bonds is shown for four sample pairs with increasing wobble frequency in Figs. 23.10
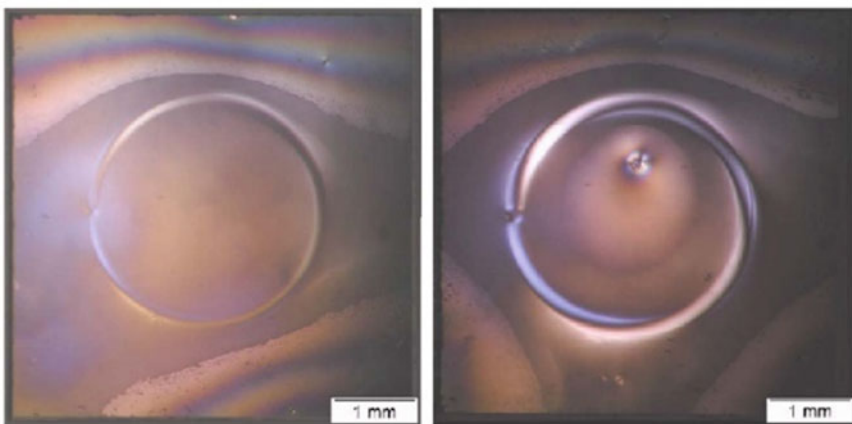
Fig. 23.9 Influence of the laser power on the bond quality

and 23.11. For wobble frequency f_W < 1500 Hz the bond seam is instable (Fig. 23.8 left). Closed, continuous, and tight bond seams could be achieved for $f_W \geq$ 2000 Hz (Fig. 23.9). A correlation between wobble frequency and bond seam width could not be seen. A possible reason is that the applied laser power was too low to show a relationship.

The achieved bond results show in general the applicability of scanners combined with fiber lasers for silicon-glass bonding process. In addition, it is possible to achieve bonding results free of cracks and free of melt and without any application of a thermal process control for feed rates values up to 8.33 mm/s and laser power values up to
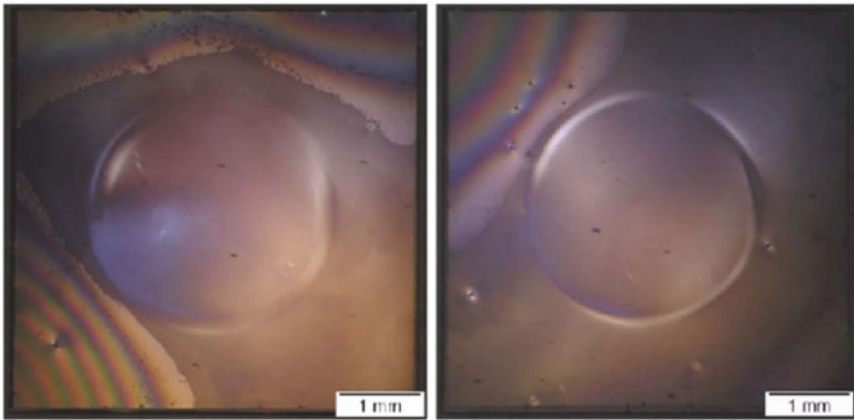
Fig. 23.10   Influence of the wobble frequency (f_W = 500 and 1500 Hz) on the bond quality
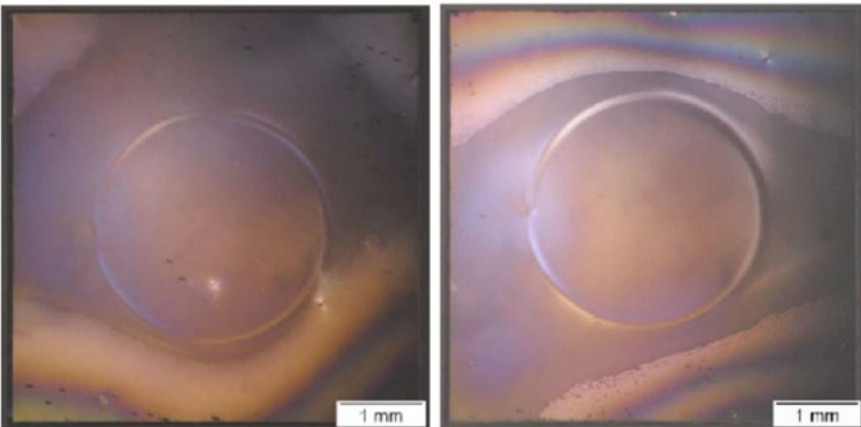
Fig. 23.11   Influence of the wobble frequency (f_W = 2000 Hz and 3000 Hz) on the bond quality

52 W. This is possible through the spatial power modulation by means of fast laser scanning.

There are some published works to selective laser transmission bonding. The common usage is the application of short-pulsed laser sources. Tseng et al. are reporting and discussing in Park and Tseng (2004, 2005, 2006), Tseng and Park 2006a, b, c, d), Tseng et al. (2007) the characterization of mechanical strength of bonded sample pairs and the investigation of the bond-interface to identify the diffusion process. Additionally, the influence of surface roughness, oxides (several thicknesses), and contact pressure is discussed. Tseng et al. apply a nanosecond Nd:YAG laser (pulse duration 6.5 ns to 7.0 ns, repletion rate 10 Hz) at $\lambda = 532$ nm. The generated bonds are punctual. It is also reported about line contours applying overlapped punctual bonds. Tan et al. discuss in Tan and Tay (2005) and Tan et al. (2006) about eutectic bonding of single crystal quartz to silicon under application of gold and tin as intermediate layer. A Q-switched Nd:YAG laser at $\lambda = 355$ nm (repetition rate up to 20 kHz) with a laser spot of 25 μm and max. laser power of 2 W is used. The eutectic bonds are generated under variation of the laser power between 0.08 and 0.83 W with a scanning speed of 0.1–0.5 mm/s. Mescheder et al. report in Mescheder et al. (2002) and Mescheder et al. (2001) about the application of Q-switched Nd:YAG laser at $\lambda = 1064$ nm to bond silicon-to-glass. In Theppakuttai et al. (2004) Thjeppakuttai is reporting about generated silicon–pyrex bonds applying Q-switched Nd:YAG laser at $\lambda = 1064$ nm with a pulse duration of 12 ns.

The reported works are applying laser sources in pulsed operation mode. The application in pulse mode allows the laser to operate in thermal diffusion mode to melt a small region of the surface, e.g., silicon as Tseng et al. report. The glass sample is indirectly melted so a diffusion bonding can be generated.

In difference to the presented works, the application of laser operation systems in cw-mode leads to bonding results in solid state. The application of laser radiation in cw-mode ensures continuous selective bonds along a line. Wild reports in Ziaie et al. (1996) that by application of laser sources in cw-operation mode bonding results without any melt phase is achievable. An additional advantage is the controllable warm up and cool down bonding process without any very intensive heat input compared to pulsed bonding with very intensive laser power in a few milliseconds. Formation of cracks can be avoided.

23.5   Laser Transmission Bonding of Silicon-to-Silicon

In difference to silicon-to-glass bonding process, the bonding of similar materials like silicon-to-silicon and glass-to-glass needs an intermediate metallic layer to absorb the laser radiation at the interface.

A cw-thulium fiber laser at $\lambda = 1908$ nm (single mode, laser spot 41–50 μm) with max. laser power of $P = 52$ W is applied. The collimated end of the fiber laser with focusing optics is integrated to a 3-axes machining system to enable a flexible
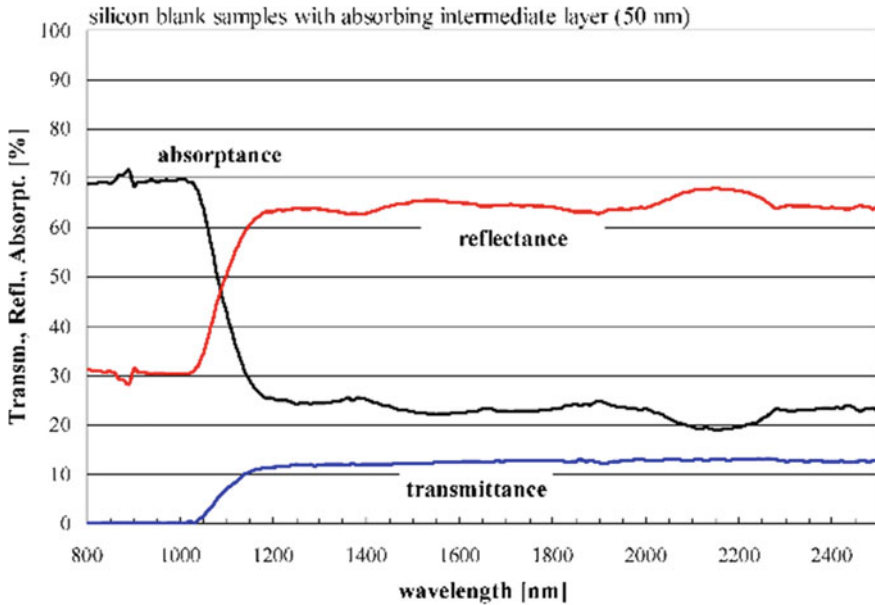
Fig. 23.12 Optical properties of a silicon sample pair with intermediate absorbing metallic layer

movement of the laser radiation over the samples. The feed rate v of the machining system defines the speed that the focused laser moves.

A metallic absorbing intermediate layer (50 nm, sputtered) is applied. The metallic intermediate layer shows an absorbing capacity of approx. 25% between two silicon samples at $\lambda = 1908$ nm (Fig. 23.12).

Experimental tests show that an absorbing capacity of 25% of the interlayer at $\lambda = 1908$ nm is enough to activate the chemical reactions at the interface to achieve bond results. Bond seams are generated applying spiral-shaped contours. IR-transmission method (Fig. 23.13a) is applied to visualize and evaluate the quality of the selective bond contours. To support the identification of the bond contours SEM analyses are performed. Figure 23.13 also shows a cross-sectional picture of a bonded sample pair after being etched with 15% KOH for 30 min. Non-bonded areas in the interface are etched. The width of the bonded areas is measured as 35–65 μm, and the width of the gaps is between 110 and 150 μm.

The mechanical strength of the silicon–silicon bonds is determined by applying micro-chevron tests (Bagdahn 2001). For this purpose, micro-chevron contours are generated on 5×5 mm^2 sample pairs. Figure 23.14 shows a sample pair after micro-chevron test. At the beginning the crack grows in the interface. In the one half the crack bends into the bulk material. This can be seen as evidence of high mechanical strength of the bonding result, so the crack is digressing from the interface to the bulk material. Maximum fracture loads up to $F_{max} = 6.35$ N could be measured.
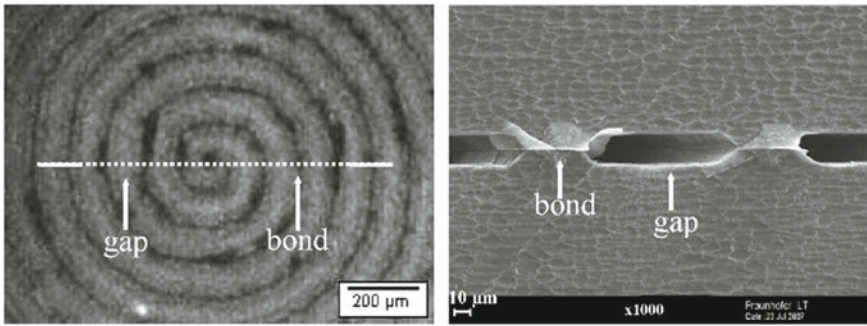
Fig. 23.13 IR-Transmission picture of a bonded sample pair. SEM pictures of a sample pair bonded with same parameters
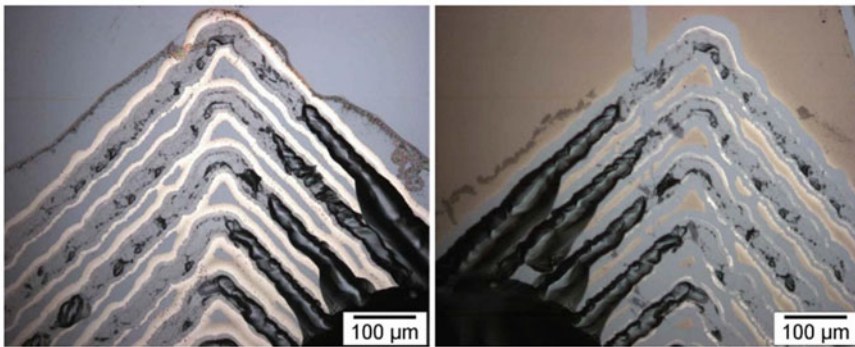
Fig. 23.14 Silicon samples after Micro-Chevron test. Left: upper sample. Right: lower sample with absorbing intermediate layer

Selective laser-assisted bonding results can also be generated by applying intermediate absorbing layers between borosilicate glass and borosilicate glass samples. Figure 23.15 shows a pair bonded applying intermediate absorbing metallic layers.

For packaging of silicon components with low thermal load and high spatial selectivity laser transmission bonding (LTB) of silicon–silicon compounds with intermediate layers using a cw-thulium fiber laser (wavelength 1,940 nm) can be used. Gold and Titanium metallic layers can be used for the interface where the combination of two Gold layers leads to the highest shear strength results (Wissinger et al. 2013).

The LTB process with the combination of low thermal stress and high spatial selectivity has been successfully demonstrated for silicon–silicon interconnects with titanium and gold layers. Metallic interlayers allow the joining of the same materials. Packaging applications in the semiconductor industry as well as hybrid microsystem technology can now make use of this new process.
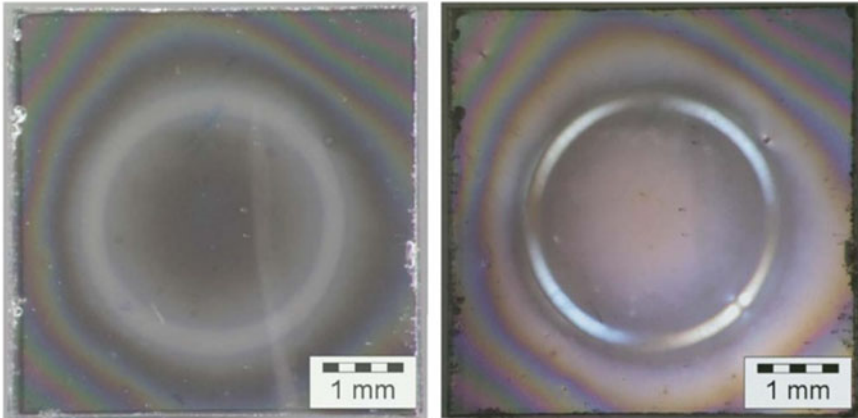
Fig. 23.15 Bonded borosilicate glass samples. Left: Sample under light-optical microscope. Right: coaxial illumination of the same sample by microscopy

References

Bagdahn J (2001) Festigkeit und Lebensdauer direkt gebondeter Siliziumwafer unter mechanischer Belastung: Der Micro-Chevron-Test (MC-Test), p. 58, Dissertation, VDI Fortschrittsberichte, VDI Reihe 9, Nr. 334, VDI Verlag Düsseldorf

Dragoi V, Alexe M, Reiche M, Gösele U (1999) Low temperature direct wafer bonding of silicon using a glass intermediate layer. In: Proceedings of the 22nd annual conference on semiconductors (CAS'99), vol 2, pp 443–446 IEEE Cat. No. 99TH8389, Sinaia, Romania

Haberstroh E, Hoffmann WM, Poprawe R, Sari F (2006) Laser transmission joining in microtechnology. https://doi.org/10.1007/s00542-006-0096-0

Kern W (1993) Handbook of semiconductor wafer cleaning technology: conventional RCA-type hydrogen peroxide mixtures. Noyes Publications, New Jersey, p 19

Knechtel R (2005) Dissertation, Halbleiterwaferbondverbindungen mittels strukturierter Glaszwischenschichten zur Verkapselung oberflächenmikromechanischer Sensoren auf Waferebene, TU Chemnitz, Fakultät für Elektrotechnik und Informationstechnik, Verlag Dr. Hut München

Lasky JB (1986) Wafer bonding for silicon-on-insulator technologies. Appl Phys Lett 48:78–80

Lin L, Cheng YT, Najafi K (1998) Formation of silicon-gold eutectic bond using localized heating method. Jpn J Appl Phys Part II 11B:1412–1414

Mescheder U, Alavi M, Hiltmann K, Lizeau Ch, Nachtigall Ch, Sandmaier H (2001) Local laser bonding for low temperature budget. In: Digest of technical papers of the transducers '01, Eurosensors XV, pp 620–623, Munich, Germany

Mescheder UM, Alavi M, Hiltmann K, Lietza Ch, Nachtigall Ch, Sandmaier H (2002) Local laser bonding for low temperature budget. Sens Actuators A Phys 97–98:422–427

Park J-S, Tseng AA (2004) Transmission laser bonding of glass with silicon wafer. In: Proceedings of 2004 Japan-USA symposium on flexible automation, paper no. UL-073. American Society of Mechanical Engineers, New York

Park J-S, Tseng AA (2005) Development and characterization of transmission laser bonding technique. In: Proceedings of IMAPS international conference on exhibition device packaging, paper no. TA15. International Microelectronics and Packaging Society

Park J-S, Tseng AA (2006) Line bonding of wafers using transmission laser bonding technique for microsystem packaging. In: ITherm 2006 proceedings, IEEE, thermal and thermomechanical phenomena in electronics systems, pp 1358–1364

Sari F, Rupf M, Gillner A, Poprawe R (2005) Advances in selective laser radiation bonding of silicon and glass for microsystems. LIM 2005:791–796

Sari F, Wiemer M, Bernasch M, Bagdahn J (2008) Laser transmission bonding of silicon-to-silicon and silicon-to-glass for wafer-level packaging and microsystems. ECS Trans 16(8):561–568. https://doi.org/10.1149/1.2982911

Schmidt MA (1998) Wafer-to-wafer bonding for microstructure formation. Proc IEEE 86(8):1575–1585

Shimbo M, Fukukawa K, Fukuda K, Tanzawa K (1986) Silicon-to-silicon direct bonding method. J Appl Phys 60:2987–2989

Tan AWY, Tay FEH (2005) Localized laser assisted eutectic bonding of quartz and silicon by Nd:YAG pulsed-laser. Sens Actuators A Phys 120(2):550–561

Tan AWY, Tay FEH, Zhang J (2006) Characterization of localized laser assisted eutectic bonds. Sens Actuators A Phys 125(2):573–585

Theppakuttai S, Shao D, Chen SC (2004) Localized laser transmission bonding for microsystem fabrication and packaging. J Manuf Process 6(1):24–31

Tong Q-Y, Gösele U (1996) A model of low-temperature wafer bonding and its application. J Electrochem Soc 143:1773

Tseng AA, Park J-S, Vakanas G-P, Wu H, Raudensky M, Chen TP (2007) Influences of interface oxidation on transmission laser bonding of wafers for microsystem packaging. Microsyst Technol 13(1):49–59

Tseng AA, Park J-S (2006a) Using transmission laser bonding technique for line bonding in microsystem packaging. IEEE Trans Electron Packag Manuf 29(4):308–318

Tseng AA, Park J-S (2006b) Mechanical strength and interface characteristics of transmission laser bonding for wafer-level packaging. IEEE Trans Electron Packag Manuf 29(3):191–201

Tseng AA, Park J-S (2006c) Effects of surface roughness and oxide layer on wafer bonding strength using transmission laser bonding technique. In: ITherm 2006c proceedings, IEEE, thermal and thermomechanical phenomena in electronics systems, pp 1349–1357

Tseng AA, Park J-S (2006d) Effects of surface roughness and contact pressure on wafer bonding strength using transmission laser bonding technique. J Microlith Microfab Microsyst 5(4):043013 (11 pp)

Wallis G, Pomerantz D (1969) Field assisted glass-metal sealing. J Apl Phys 40:3946–3949

Wiegand M (2001) Dissertation, Auswirkungen einer Plasmabehandlung auf die Eigenschaften des Niedertemperatur-Waferbondens monokristalliner Siliziumoberflächen, Mathematisch-Naturwissenschaftlich-Technischen Fakultät der Martin-Luther-Universität Halle-Wittenberg, Der Andere Verlag

Wild MJ (2002) Dissertation RWTH Aachen, Lokal selektives Bonden von Silizium und Glas mit Laser, Shaker Verlag, Aachen

Wild MJ, Gillner A, Poprawe R (2001a) Advances in silicon-to-glass bonding with laser. https://doi.org/10.1117/12.425293

Wild MJ, Gillner A, Poprawe R (2001b) Locally selective bonding of silicon and glass with laser. Sens Actuators A 93:63–69

Wild MJ, Gillner A, Poprawe R (2001c) Advances in silicon to glass bonding with laser. Proc SPIE 4407 135–141

Wissinger A, Olowinsky A, Gillner A et al (2013) Laser transmission bonding of silicon to silicon with metallic interlayers for wafer-level packaging. Microsyst Technol 19:669–673. https://doi.org/10.1007/s00542-012-1636-4

Witte R, Herfurth H, Heinemann S (2002) Laser joining of glass with silicon. Proc SPIE 4637:487–495

Wolffenbuttel RF (1994) Low-temperature silicon wafer-to-wafer bonding using gold at eutectic temperature. Sens Actuators A 43:223–229

Wolffenbuttel RF, Wise KD (1994) Low temperature silicon wafer-to-wafer bonding using gold at eutectic temperature. Sens Actuators A 43:223–229

Ziaie B, Von Arx J, Dokmeci M, Najafi K (1996) A hermetic glass-silicon micropackage with high-density on-chip feedthroughs for sensors and actuators. J Microelectromech Syst 5:166–179

Chapter 24
Soldering

F. Schmitt

24.1 Introduction

Soldering is one of the most important joining processes in addition to welding and gluing. Soldering is a thermal process for substance-to-substance bonds and coating of materials, whereas a liquid phase is formed by melting an additional solder alloy or by diffusion at the interfaces. The solidus temperature of the basic material is not being exceeded. During the soldering process, a liquid phase is caused by melting of a solder alloy or by diffusion processes within the intermediate layer. In principle, the joining process is based on interaction reactions between the joining partners and the melted solder. Therefore, a direct, oxide- and contamination-free contact between the metal surfaces of the joining partners and the solder alloy is one of the most important process requirements. If the melting temperature of the additional material is below 450 °C (840 °F) the process is called soldering, while when above 450 °C the process is called brazing.

A process adapted heating cycle is necessary for the energy input during the soldering process. This heating cycle has to perform the processes surface activation, melting of the solder alloy, wetting of the surfaces, spreading, and filling of the gap. The heating cycle involves four important parameters: the heating period with heating rate and dwell time for heating, the peak soldering temperature, the dwell time above the melting point of the solder alloy, and the cooling rate (DIN8505 1979a, b). In general, it is desirable to use a high heating rate but the maximum heating rate is normally constrained by the form of the energy input. By means of laser energy and its high energy density, it is possible to realize a maximum heat rate. The dwell time for heating is necessary for the evaporation of vapors and constituents of the flux and for the uniform heating of the joining partners up to the wetting temperature. This temperature is below the melting temperature of the solder alloy. The soldering

F. Schmitt (✉)
Fraunhofer ILT, Aachen, Germany
e-mail: felix.schmitt@rwth-aachen.de

temperature should be such that the solder alloy is certain to melt, but at the same time the solder alloy should not be overheated so that it degrades through the loss of constituents. The peak temperature is normally set at about 20–30 °C above the melting point. The minimum time that the joint geometry is held at this temperature must be sufficient to ensure that the solder alloy has melted over the entire area of the joint. Extended holding times tend to result in excessive spreading of the molten solder alloy, possible oxidation gradually taking place, and deterioration of the properties of the parent materials. The cooling stage of the cycle is not controlled by the operator but normally governed by the thermal mass of the joint geometry. For laser processing it is very fast because of the instantaneous switch-off of the laser power, resulting in a fine-grained microstructure of the joint (Fig. 24.1).

In contrast to other conventional selective soldering techniques laser beam soldering features a contactless, temporally, and spatially well-controllable energy input. Because of these characteristics laser beam soldering is predestined for joining tasks where miniaturization and reduced thermal and mechanical stresses are required. Special features of laser beam soldered joints are fine-grained microstructure and the low amount of intermetallic phases due to the fast heating and cooling rates of this process. In principle laser beam soldering is characterized by temporally and spatially selective energy input by surface absorption in the joining area,
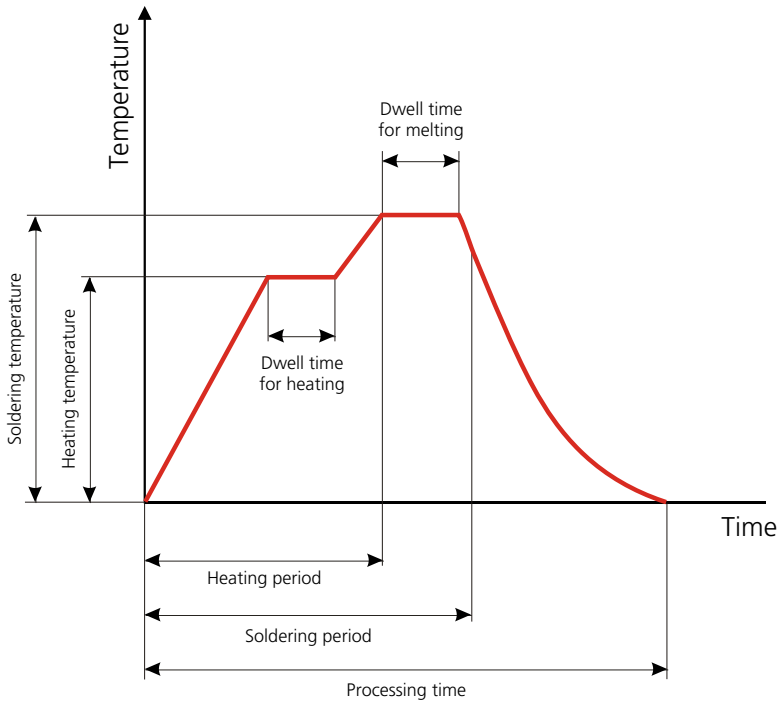
Fig. 24.1 Heating cycle for soldering

Fig. 24.2 Simulated
temperature distribution of
an electrical contact during
laser irradiation
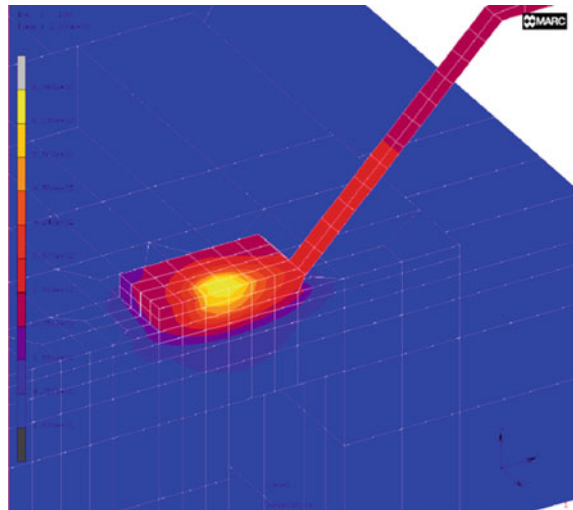
successive heat conduction, and interface processes. The joining process is deter-
mined by characteristics of the laser beam source, chosen process parameters, and
thermo-physical properties of the joining partners.

Cross-sectional view is given in Fig. 24.2 of a simulated temperature distribution
for an electrical contact during laser beam soldering. Computation of the temper-
ature distribution is done by finite element software. The commutated temperature
distribution is showing spatially selective energy input and furthermore temperature
gradients in the joining area.

24.2   Physical-Technical Fundamentals

Wetting of the surfaces is an important requirement for a good solder joint (Klein
Wassink 1991). Wetting is defined as reaction between the liquid droplet and the
solid substrate. Wetting will happen if the liquid solder alloy has a direct contact
with the surface of the metal substrate. All adherent contaminations or oxides on the
joining area form a barrier layer and reduce wetting (Fig. 24.3, left).

If the metal substrate is cleaned, correspondingly the metal atoms are direct on
the surface, solder alloy wets the surface. Contacting between atoms of solder alloy
and metal substrate leads to alloying and resulting in a good electrical conductivity
and adhesion.

Wetting of the solid metal substrate by the liquid solder alloy is an interfacial
process in which the contact angle Θ a measure of the quality of wetting provides.
If $\Theta < 90°$, a liquid droplet will wet the substrate. The contact angle is defined by
metal substrate, solder alloy, and atmosphere.
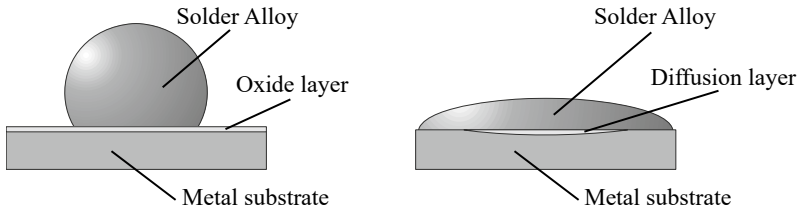
Fig. 24.3 (Left) Liquid solder alloy on oxidized substrate. Solder alloy does not wet the surface. (Right) Liquid solder alloy on clean substrate. The solder alloy wets the surface and a diffusion layer is formed at the interface

Three surface tension forces σ_{12}, σ_{13}, and σ_{23} are in balance as shown in Fig. 24.4. Following equation is applied between surface tension forces and contact angle Θ (Wetting or Young equation):

$$\cos \Theta = \frac{\sigma_{13} - \sigma_{23}}{\sigma_{12}}$$

Difference between surface tension forces σ_{13} and σ_{23} is known as adhesion tension force σ_H. The contact angle Θ is commonly used as an estimation for adhesion tension force σ_H. The surface tension forces are the important parameters for wetting. A good wetting is if

$$\sigma_{13} \geq \sigma_{23} + \sigma_{12}$$

In this case, the contact angle reaches zero and the liquid solder alloy spreads entirely on the solid substrate. Fluxing agents enhance the wetting of the substrate. In principle, fluxing agents fulfill following three functions:

- Physical: removal of oxides and other films as well as soldering reaction products off the surface to provide direct contact between solder alloy and substrate
- Chemical: removal of tarnish on the surfaces and protection from reoxidation of these surfaces during the soldering process
- Thermal: enhancement of heat flow between heat source and solder area.
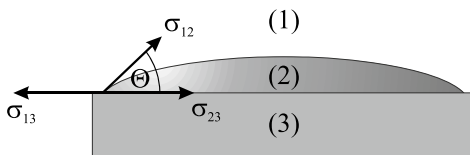
σ_{12}: Surface tension forces vapour - liquid

σ_{13}: Surface tension forces vapour - solid

σ_{12}: Surface tension forces liquid - solid

Fig. 24.4 Surface tension forces for wetting of solid substrate and liquid solder alloy

Selection of fluxes follows two criteria but these criteria efficiency and corrosiveness are opposed to each other. The efficiency of a flux is rated according to its ability to wet a surface in a certain time. On the other hand, corrosion by fluxes can lead to a non-desired chemical reaction on the joining partners.

The more active a flux is the more corrosive it is, while a non-corrosive flux will not enhance—or only restricted—wetting of solder alloy on the substrate. Because many parts in electronic industries are corrosion-sensitive selection of flux is constricted to less active fluxes.

24.3 Process Description

There are numerous different application-specific solutions available commercially for laser beam soldering machines. In principle, they are based on flexible beam shaping and guidance using galvanometric scanners or axis systems. For fiber-guided systems, the processing optics are moved but there are also systems where the entire laser beam source is being moved. In Fig. 24.5, a production cell and a laser processing optics are shown based on a galvanometric scanner.

The machine is designed for the laser beam soldering of an automotive microelectronic module (an alternator regulator realized in thick-film technology) with solder pads printed on an alumina substrate (Fig. 24.6). The housing has seven terminal leads to be soldered to the substrate. The entire alumina substrate is glued by a heat conducting adhesive to an aluminum base plate (Fig. 24.6).
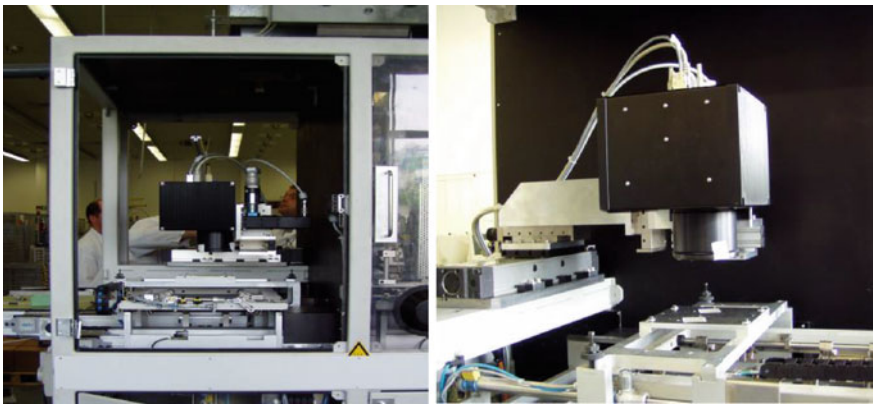
Fig. 24.5 System design for laser beam soldering based on galvanometric scanners: production cell (left) and laser processing optics (right)

Fig. 24.6 Automotive
micro-electronic module in a
plastic housing—alternator
regulator
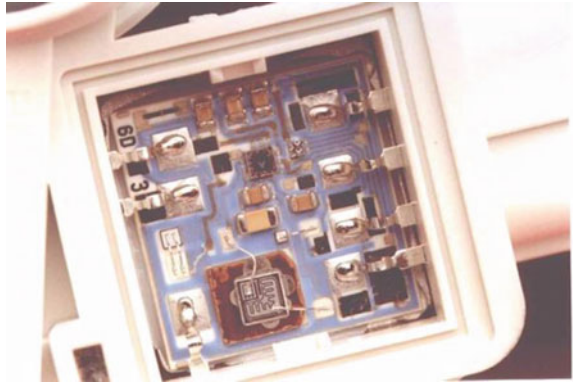
Major components of the production cell are a fiber coupled, continuous wave
(cw) diode laser system and a processing head with integrated pyrometric and power
sensors.

The diode laser system has a maximum optical output power of 250 W, which
can be modulated by controlling the pump current. The collimated laser beam passes
through a galvanometer scanner and is focused by a f-Theta lens on the lead/solder
pad area to generate the joint. The circular focus geometry of the laser beam is aligned
to the center of the semicircle at the end of the terminal lead (Fig. 24.7). The working
distance between the optics and the laser beam interaction area is about 80 mm. With
an image projection ratio of 1:2 the minimum focal diameter is 1.2 mm, which is
double the fiber core diameter of 0.6 mm.

Thermal radiation emitted from the surface follows the beam delivery system of
the galvanometer scanner and passes through a dichroic mirror, which is transparent

Fig. 24.7 Solder joint
configuration (dimensions:
mm)
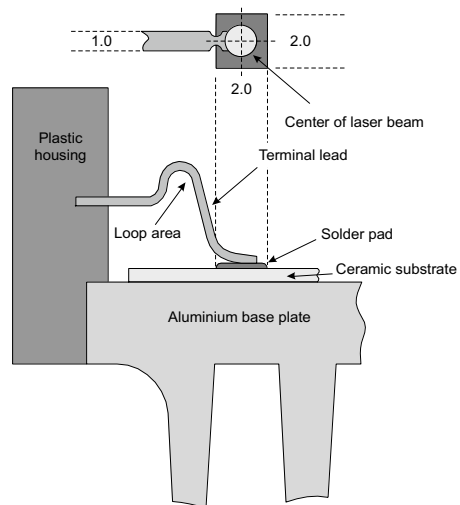
for this wavelength range. After passing the dichroic mirror the thermal radiation is focused by a lens on a photodetector (Ex. InGaAs, peak wavelength 2.3 µm). The output signal of the detector is conditioned by a logarithmic amplifier circuit. The integrated pyrometric sensor is conditioned for laser beam applications with process temperatures in the range of 150 °C, e.g., welding of plastics or soldering. The pyrometric sensor is calibrated by means of a standardized black body and the response time of the sensor is about 1 ms at 150 °C.

The surface of the lead/solder pad area is imaged onto a CCD camera via a deflecting mirror.

Apart from interconnection requirements, a high production rate has to be ensured for the process to remain attractive for mass production. For this reason the total process period, especially the irradiation time, has to be as short as possible. However, to achieve an adequate solder joint with reduced irradiation time the laser power has to be increased. To avoid the hazard of superheating, the laser power has to be limited and controlled. Therefore the thermal radiation from the interaction zone is detected and analyzed in more detail. In a series of experiments, the following features could reproducibly be observed in the recorded pyrometric signal (Bosse et al. 2002). A typical profile is presented in Fig. 24.8, where the laser is switched on at time $t = 0.2$ s. At point [A], the reduction of the ascending slope indicates the initial activation of the applied adipic acid. The second change in the pyrometric signal at point [B] is related to the onset of localized melting of the solder pad and out-gassing of volatile components. Due to the continued energy input by the laser beam, the terminal lead reaches the wetting temperature (point [C]). In the next phase there is a sudden improvement in heat dissipation due to the wetting of the terminal lead, which often results in a temperature decrease (point [C] to [E]). At point [D], a gas bubble consisting of volatile components leaves the molten solder. The variation of the signal curve following point [E] is induced by self-optimization of the surface tension and by superheating of the molten solder pool. After the laser beam is switched off at $t = 1.2$ s, very high cooling rates are observed. This high rate is caused by the optimized heat transfer into the aluminum base plate. At point [F], the solder solidifies. The change of the descending slope in the signal curve at the crystallization point [F] is known from the thermal analysis of solidification reactions in literature (Fig. 24.8).

Based on a set of characteristic curves, benchmarks can be determined and by changing specific process parameters a thermal and temporal optimized profile can be generated. Using these analytic profiles as set point settings for a closed-loop control system, the energy input can be controlled individually for each joining application or product (Fig. 24.9).

Figure 24.10 shows a detailed view of two solder joints and a cross section of a laser-soldered joint.
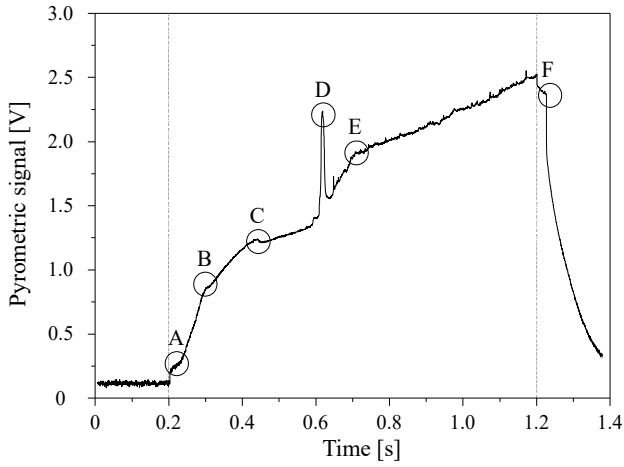
Fig. 24.8 Pyrometric signal detected during soldering; irradiation time: 1000 ms
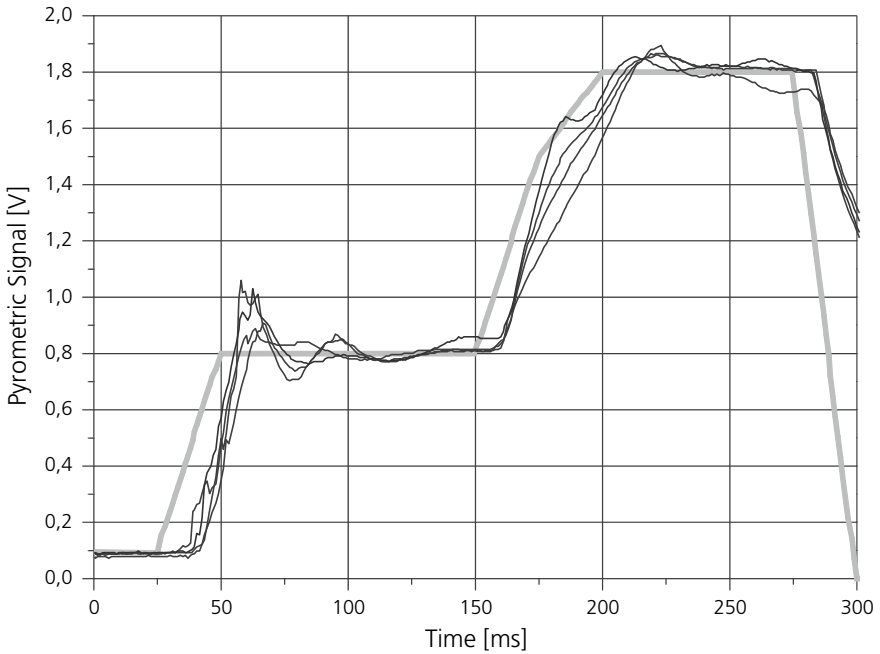
Fig. 24.9 Array of pyrometer signals recorded during different closed-loop controlled LBS processes. The gray curve represents the defined set point settings
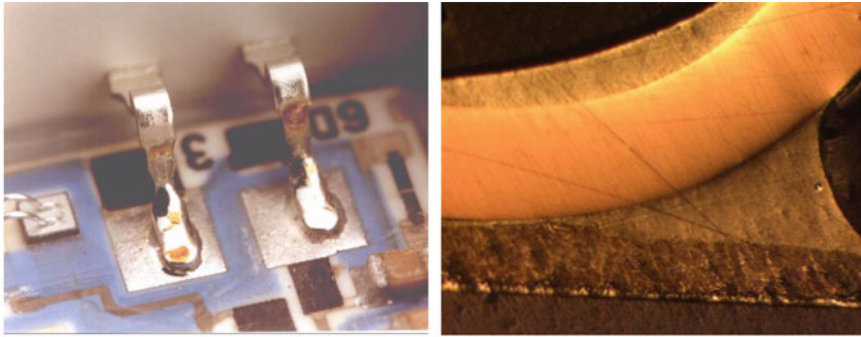
Fig. 24.10 Detailed view of two solder joints (left), cross section of a laser-soldered joint (right)

24.4 Applications

The described application shows that there is a huge potential for laser beam soldering in automotive industry. Here, electronic sensors and control systems based on ceramic substrates are used in many cases. Ceramic substrates offer superior characteristics regarding the environmental conditions in the engine compartment. These electronic systems withstand thermal loads reliable and durable mounted on active or passive heat sinks. Unfortunately, in combination with these heat sinks the assembly of such systems is complicated. Electronic and mechanical joints between the terminal lead and the corresponding connecting area on the ceramic substrate can only be realized by joining methods with high energy densities (Bosse et al. 2003).

An innovative application for laser beam soldering is the electrical contacting of solar cells for photovoltaic module production (Fig. 24.11). Due to the decreasing thickness of the solar cells, today 220 μm but in future below 150 μm, the demand for a soldering method without any mechanical contact has led to the development of the laser beam soldering process. The process is being controlled by pyrometric sensors to avoid thermal damage of the thin silicon wafer.

Laser soldering is playing an increasingly important role as an alternative to the gluing or clamping of micro-optical components into metallic mountings. In contrast to laser soldering, the energy input by induction is difficult for miniaturized optics with a diameter smaller than 1 mm and mounting widths below 50 μm because of the smaller amount of material for heating. Similarly, manual soldering using a soldering iron raises problems because of the small dimensions and therefore the resulting insufficient reproducibility. An alternative to these processes is soldering by using a high-power diode laser or a fiber laser. For these experiments the joining components consist of a gold metallized stainless steel mounting and sapphire optics, which is also metallized with gold. An AuSn solder alloy with a melting temperature of 280 °C is used. By using a fluxing agent, the surfaces are cleaned of oxides before soldering and the joining area is prevented from oxidation during the soldering process. This flux causes pores in the soldering joint and therefore pores can be detected. By means
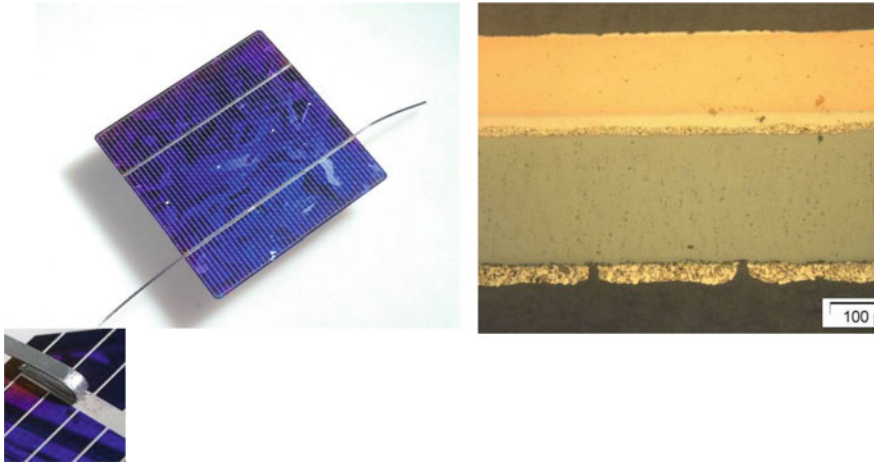
Fig. 24.11 Electrical contacting for solar cell interconnection

of a pyrometer it is possible to set a controlled process and a two-step temperature profile, as recommended in the literature for soldering. At the beginning of the laser soldering process the flux is activated at a lower temperature (~150 °C), while in the second step the necessary energy for the melting of the solder alloy is applied. This process management reduces the number of pores within the soldered joint significantly (Fig. 24.12).

The gap is filled homogeneously with the solder by capillary forces excessive solder does not wet the surfaces of the sapphire but wets the mounting on the laser facing side. Both diode lasers focused to 1 mm and fiber lasers collimated to 1 mm diameter or lower can be used as laser sources. The advantage of the fiber laser is that the focus position does not have to be aligned because the Rayleigh length is greater than 1600 mm.
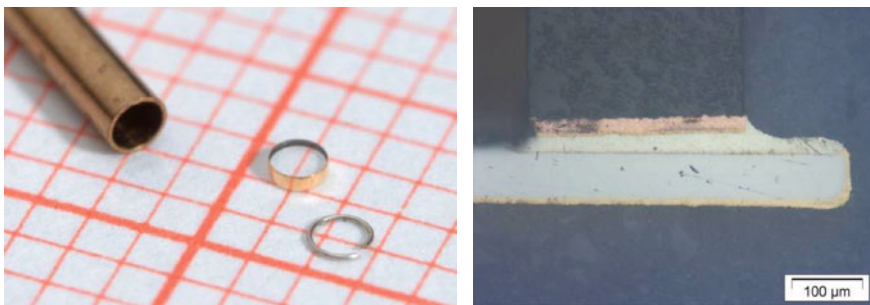
Fig. 24.12 Joining components: bushing, sapphire optics, solder preform (left). Cross section of a soldering joint (right)

Application areas of selective laser beam soldering using high-power diode lasers are manifold and are not confined to a special branch of industry. Currently industrial applications are focused on electronics assembly, especially for the automotive sector. Discrete mounting of critical components, soldering of cable strands, soldering, and brazing of micro-electronic and micro-mechanical components and cable assemblies are industrial applications of laser beam soldering.

Because of the good focusability, the accurate control of the energy input and the huge power potential laser beam soldering has the best preconditions to carry out these joining tasks reliable and reproducible. Combining diode laser systems with precise positioning systems based on fast galvanometric scanners user-defined joint configurations can be carried out product specific and with a high production rate. Here, substance-to-substance bonds are generated with a high quality in combination with minimal thermal loads for the substrate. Because of the high intensities laser beam soldering offers process durations in the range of some 100 ms per contact, depending on the joint configuration and the choice of the solder alloy. The decreasing price for diode laser systems is enabling laser beam soldering as an attractive alternative to other soldering methods even under economical aspects. In combination with the possibility to control the temperature within the joining area laser beam soldering is dedicated for automated production.

Laser soldering is a clean, non-contact joining process in which the energy is transferred to the solder joint with a precisely controlled beam. The absorption of the radiation mainly takes place in the solder, thus high-quality solder joints can be realized with short process times. The very short heating and cooling times result in a fine-grained structure of the intermetallic joint.

Applications range from electronic components in the assembly of electronic circuit carriers to photovoltaics in the manufacture of solar modules (Ogochukwu 2013). With the further development of beam sources up to diode lasers in the visible wavelength range, the range of applications for this non-contact joining process will also expand greatly in the future.

References

Bosse L, Schildecker A, Gillner A, Poprawe R (2002) High quality laser beam soldering. J Microsyst Technol 7

Bosse L, Koglin A, Olowinsky A, Kolauch V, Nover M (2003) Laser beam soldering—an attractive alternative to conventional soldering technologies. In: Laser and applications in science and technology, Proceedings of SPIE, San Jose (USA)

DIN8505 (1979a) Löten; Allgemeines, Begriffe. Teil 1, Normausschuss Schweißtechnik (NAS) im DIN Deutsches Institut für Normung e.V.

DIN8505 (1979b) Löten – Einteilung der Verfahren, Begriffe. Teil 2, Normausschuss Schweißtechnik (NAS) im DIN Deutsches Institut für Normung e.V.

Klein Wassink RJ (1991) Weichlöten in der Elektronik, 2. Auflage. Eugen G. Leuze Verlag ISBN: 3874800660

Further Reading

Ogochukwu ES (2013) Laser soldering, materials science—advanced topics. Yitzhak Mastai, IntechOpen. https://doi.org/10.5772/51527. https://www.intechopen.com/books/materials-science-advanced-topics/laser-soldering

Chapter 25
Laserbeam Microwelding

André Häusler, Johanna Helm, Soören Hollatz, Alexander Olowinsky, Woo-Sik Chung, and Marc Hummel

25.1 Introduction

With the increasing electrification of vehicles and other conventional devices in everyday use, such as bicycles, lawn mowers, or chainsaws, the global demand for engineering materials with highly electrically and thermally conductive properties, such as copper or aluminum, is rising. Undoubtedly, the future tripling of annual copper consumption goes hand in hand with the demand for an automatable, process-reliable, and reproducible joining technology for joining these very engineering materials, for example, for applications in electromobility.

Laser beam welding offers the greatest potential in this respect and is an established process for welding battery cells. By using beam sources of high brilliance, it is possible to realize a predominantly stable and reproducible joining process of metals with an increased reflection ($\approx$95%) in the wavelength range of the beam source ($\lambda \approx 1 \ \mu m$) (YOU 2017; Grupp 2017). By using fiber lasers, which are reaching ever new price and power classes due to development, laser powers > 1 kW can be concentrated to a few 10 μm focal diameters (Schmitt 2012; Gedicke 2011). As a result, an intensity can be achieved with which pure copper can also be heated to the vaporization temperature required for the deep welding process.

The resulting new application areas for fiber lasers lead to a steadily growing market of this kind of laser beam sources. According to Next Move Strategy Consulting, the global fiber laser market is projected to more than double in size between 2019 and 2030. Sized at some 2.36 billion U.S. dollars in 2019, the market is expected to reach the size of around 5.79 billion U.S. dollars in 2030.

The disadvantageous effect of these high intensities and consequently small beam diameters when using fiber lasers is the generation of a slender and deep weld with a small attachment cross section, which is disadvantageous for an electrically

A. Häusler · J. Helm · S. Hollatz (✉) · A. Olowinsky · W.-S. Chung · M. Hummel
Fraunhofer ILT, Aachen, Germany
e-mail: soeren.hollatz@ilt.fraunhofer.de

conductive application, for example. As a possible compensation method to achieve a higher cross section and to influence the weld geometry in the sense of a "tailored joint", beam oscillation in laser beam welding is increasingly in the focus of research (Häusler 2021). In this process, an additional motion is superimposed on the linear feed motion, which transforms the conventional straight-line course of the laser beam. Through this local power modulation, it is possible to influence the welding process in terms of geometry, efficiency, and precision through additional process parameters (Schmitt 2012).

Another tool for controlling geometry, quality, and functionality in laser beam welding is the use of modulated laser power in the sense of the earlier approaches of pulse shaping (Katayama et al. 1995). Thus, this temporal power modulation shows further potential to increase precision in joining by laser radiation by continuously adjusting the laser power (Schmitt 2012). By using a spatially and temporally combined power modulation, there is the possibility to fundamentally expand the design framework in laser beam welding. In conventional laser joining, for example, only the parameters laser power, feed rate, focus position, and focus diameter are available for adapting the process to technical requirements. Influencing the process with new compensation methods offers the user the possibility to design the process with new degrees of freedom and thus to significantly influence both the process design and the precision.

25.2 High-Brilliance Laser Beam for Low Energy Input

The application field for the laser beam microwelding process has been vastly expanded in various industrial sectors. The recent development of the fiber laser beam source allows a high-power output range combined with a small emission area which offers advanced processability for the microwelding. This means that they are easy to focus, which results in small focal-spot diameters ($<50\ \mu$m) and thus high-intensity value ($>>10^6$ W/cm^2).

Currently, diverse type of laser beam sources with different beam properties and wavelength are commercially available. However, due to the definition, the comparison of different laser beam sources with the beam propagation ratio or laser beam quality is only permissible for the equal wavelength. Therefore, beyond the beam parameter product, the definition "brilliance B" is used to classify laser beam sources. The brilliance is introduced since the introduction of diode-pumped high-power solid-state lasers. The beam density, which is also referred to as brilliance B in laser technology, describes the laser power P_L per emission area F$_L$ and solid angle Ω as describe in Eq. 25.1. Here, the average power and the beam propagation ratio of a beam source can be summarized by the term Brightness L (Eichler and Eichler 2003; Schmitt 2012).

$$B = \frac{P_L}{F_L \cdot \Omega} \tag{25.1}$$

with

$$F_L = \pi \cdot w_0^2 \text{ and } \Omega = \frac{A_k}{R_k^2} = \frac{\pi \cdot (R \cdot \theta_0)^2}{R_k^2} = \pi \cdot \theta_0^2 \tag{25.2}$$

results

$$B = \frac{P_L}{\pi^2 \cdot w_0^2 \cdot \theta_o^2} = \frac{P_L}{\pi^2 \cdot BPP^2} \tag{25.3}$$

B: Brilliance [W/(mm^2·sr)]; P_L: Laser power [W]; F_L: Emission area [mm^2]; Ω: Solid angle [sr]; A_k: Partial surface of a sphere [mm^2]; R_k: Radius of sphere [mm]; θ_0: Divergence [mrad]; w_0: Focal-spot diameter [mm]; BPP: Beam parameter product [mm·rmad].

Equation 25.3 shows that the brilliance B refers to the beam parameter product BPP and thus refers to the beam quality of the applied laser beam source. The classification of the commercially available beam sources for microwelding is considered based on their brilliance and shown in Table 25.1.

Based on the classification in Table 25.1, single-mode fiber lasers are considered as a high-brilliance beam source. Conditionally, disc and multi-mode fiber lasers can be also considered as high-brilliance beam sources. There is, however, no certain value known to qualify the laser beam source as a high-brilliance laser beam source.

Table 25.1 Classification of the commercially available laser beam source based on their Brilliance (Heinen 2020)

Beam source	Beam source model	BPP (typical value) [mm·mrad]	Power [W]	Brilliance [W/(mm^2·sr)]
CO_2-Laser	TruFlow 2000	6,14*	2000	5,4
Diode laser	TruDiode 301	8	300	0,5
Diode pumped pulsed Nd:YAG rod laser	TruPulse 62	8	3000	4,7
Disc laser	TruDisk 1000	2	1000	25,3
Multi-mode fiber laser	YLS-1000-MM	2	1000	25,3
Single-mode fiber laser	YLR-1000-SM	0,37**	1000	740,1

* Calculated with $\lambda = 10,6\ \mu$m, $M^2 = 1,82$
** Calculated with $\lambda = 1070$ nm, $M^2 = 1,1$

The high-brilliance laser provides a high focusability at high average laser power and following advantages can be counted for the laser beam microwelding (Schmitt et al. 2010):

– small focus-spot size enables welding of thin metal sheets.
– high intensity leads to stable incoupling of laser beam even into the high-reflective material.
– smaller required aperture leads to an increase in beam deflection scanning frequencies.

The small spot diameter enables welding of thin metal sheets. A single-mode cw laser beam with a focal-spot diameter with 22 µm is used to weld a 25 µm thin stainless steel 1.4031. At the welding velocity v = 833 mm/s, a narrow but smooth and homogeneous weld seam is generated (Okamoto et al. 2007). A top-view of a welding seam in a thin metal foil with a thickness of 25 µm is shown in Fig. 25.1.

The stable energy incoupling can be illustrated by comparing the welding results on copper components. Two different laser beam sources are used to demonstrate two focal-spot diameters ($w_{0,1} = 40$ µm and $w_{0,2} = 100$ µm) at equal optical setup, respectively. The difference of the energy incoupling is clearly observed during welding process on a high-reflective copper material. A large focal-spot ($w_{0,2} = 100$ µm) results in a spontaneous transition between the heat conduction welding to deep-penetration welding and vice versa. For intensity values below a critical level, the welding is performed in the heat conduction regime and for higher intensity value in the deep-penetration regime. In addition, spatters are clearly observed at the weld
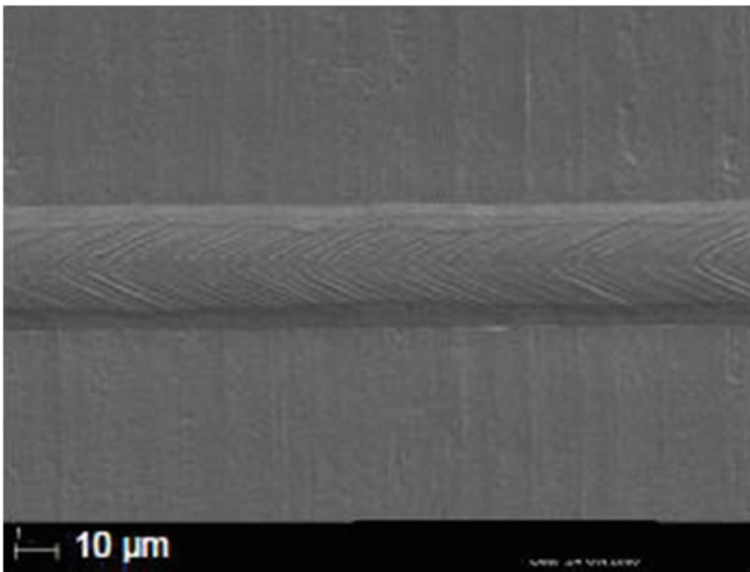
Fig. 25.1 Laser beam micro-welding of thin foil (Okamoto et al. 2007)
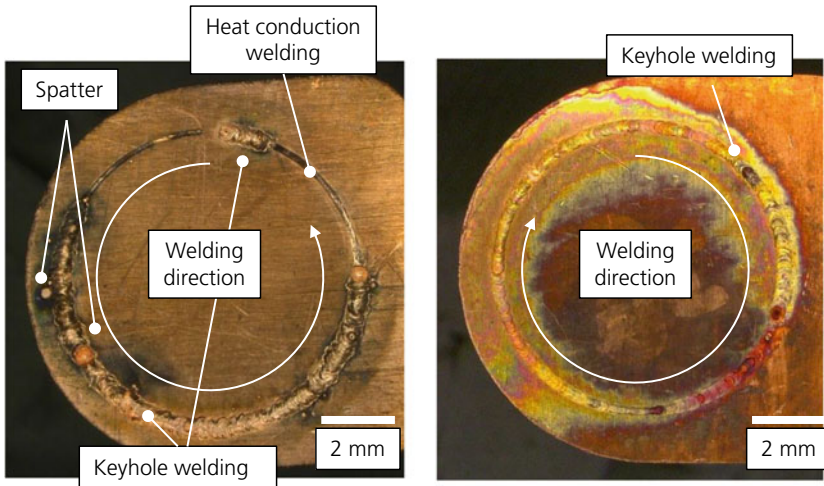
Fig. 25.2 Weld result on a copper plate with $w_{0,2} = 100\,\mu m$ (left); Weld result on a copper plate with $w_{0,2} = 40\,\mu m$ (right) (Heinen 2020)

seam (Fig. 25.2 left). However, the welding process with a small focal-spot diameter ($w_{0,1} = 40\,\mu m$) allows a continuous deep-penetration welding with only limited spatter (Fig. 25.2 right).

When the welding process is conducted in deep-penetration regime, the laser-induced vaporization forms a cavity in the melt which is called a "keyhole." Inside the keyhole, the laser beam is multi-reflected at its wall and absorbs a significant amount of the emitted laser beam. Therefore, even for the high-reflective copper material, the laser beam is converted efficiently to heat during the deep-penetration welding regime. As a result, the energy input into a material can be minimized.

25.3 Beam Guiding and Focusing

For microwelding applications small spots sizes are needed to achieved small weld seams. The applied laser sources with their high beam quality can reach focal diameters in the 10 micro range depending on the beam guiding system. Besides the conventional optical setup with a fixed optics more and more galvanometer scanners are used to focus the beam and to move it according to the desired welding geometry. The fixed optics are often used in applications where the incident beam has to be tilted with respect to the surface of the component to be welded or the parts have to be rotated for radial welds. Whenever a planar weld geometry is aimed for galvanometer scanners are used offering higher flexibility and welding speeds.
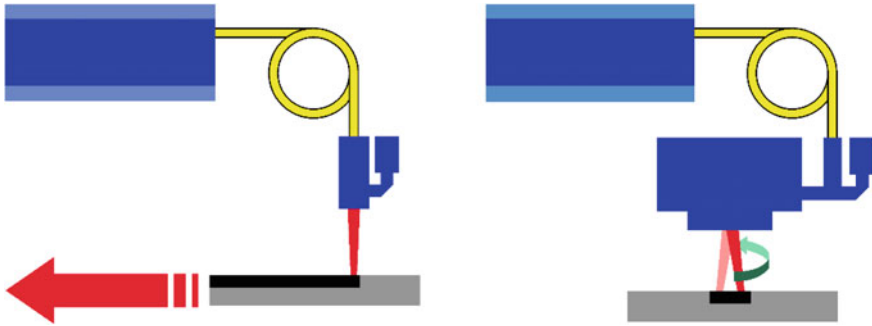
Fig. 25.3 Movement of laser beam for microwelding: fixed optics (left) and galvanometer scanner (right)

In galvanometer scanners, the beam movement is generated by rotating two mirrors arranged in the collimated beam. Special focusing lenses, so-called f-theta lenses, whose focal lengths depend on the angle of incidence on the lens, are used for this purpose. If plane-field lenses are used, the laser beam also strikes the workpiece at different angles depending on the deflection angle. By using telecentric lenses, it is possible to ensure that the laser beam hits the component surface at right angles. However, the maximum area to be processed is determined by the diameter of the lens. Another possibility is to place the focusing lens in front of the two deflecting mirrors. These so-called pre-focusing systems usually have larger scan fields and exhibit the lowest chromatic aberrations, which is particularly advantageous when using cameras or wavelength-specific process observation equipment (Rodenstock 1999) (Fig. 25.3).

25.4 Power Modulation in Laser Beam Welding

In laser beam welding, a fundamental distinction is made between spatial and temporal power modulation for further influencing the melting dynamic process. While temporal power modulation considers the power output of the beam source without including the feed motion, local power modulation is understood as a relative motion superimposed on the feed direction. In the following, the two forms of modulation investigated in this thesis are considered in laser beam welding.

25.5 Spatial Power Modulation

Smaller focal diameters are generally considered advantageous for deep-penetration welding, since the intensity threshold for deep-penetration welding can already be reached with comparatively small laser power. The disadvantage here is the smaller attachment cross section resulting from the smaller focal diameter. With appropriate beam guidance systems, local power modulation can be implemented to compensate for this disadvantage. In this case, the linear feed motion is superimposed with a second independent oscillating motion. Thereby, the oscillation movements can basically be distinguished into two types: Harmonic and non-harmonic oscillatory motions. Examples of non-harmonic oscillatory motions are present in sawtooth, rectangular, or triangular geometries (Schmitt 2012).

Harmonic oscillatory motions, in contrast, can be described by sine or cosine functions (Eq. 2.19).

$$A_{s,x}(t) = A_{s,x} \cdot \sin\left(2\pi \cdot f_{s,x} \cdot t + \varphi_x\right)$$
$$A_{s,y}(t) = A_{s,y} \cdot \sin\left(2\pi \cdot f_{s,y} \cdot t + \varphi_y\right) \tag{25.4}$$

[1] $A_{s,x}/A_{s,y}$: oscillationamplitude x/y-axis [mm]; $f_{s,x}/f_{s,y}$: oscillation frequency x/y-axis [Hz]; t: time [s]; φ_x/φ_y: phase difference of the oscillation x/y-axis [-].

The parameters of oscillation amplitude, oscillation frequency, and phase difference determine the geometry of the resulting motion. Thus, a rational ratio of the oscillation frequencies leads to periodic Lissajous figures, while the oscillation amplitudes describe the scaling of the figure in x- and y-direction and the phase difference determines the running direction and the geometry. Thus, in addition to the asymmetric motion shapes of the line and the circle, it is also possible to represent, for example, eight-shaped oscillation geometries, which, due to their shape, can achieve a symmetrical energy input related to the seam width (Thiel et al. 2012).

In laser beam microwelding, the use of a circular oscillation has gained acceptance. Experiments show that compared to conventional and other oscillation strategies, the molten pool ejections are reduced (Franco 2017). Therefore, the use of a superimposed circular oscillation will be exclusively considered in the following. The trajectory (see Fig. 25.4) is described with the introduction of the additional parameters oscillation amplitude As and oscillation frequency fs according to

$$\begin{pmatrix} x(t) \\ y(t) \end{pmatrix} = \begin{pmatrix} v_f \cdot t + A_s \cdot \cos(2\pi \cdot f_s \cdot (t - t_s)) \\ -A_s \cdot \sin(2\pi \cdot f_s \cdot (t - t_s)) \end{pmatrix} \tag{25.5}$$

[SCH12, S.33] x: spatial coordinate in feed direction [mm]; y: spatial coordinate transverse to the feed direction [mm]; v_f: feed rate [mm/s]; A_s: oscillation amplitude of the spatial power modulation [mm]; f_s: oscillation frequency of the spatial power modulation [1/s]; t: time [s]; t_s: phase difference [s].

Fig. 25.4 linear feed with a superimposed oscillation. A_s = 0,1 mm fs = 1000 Hz v_f = 100 mm/s
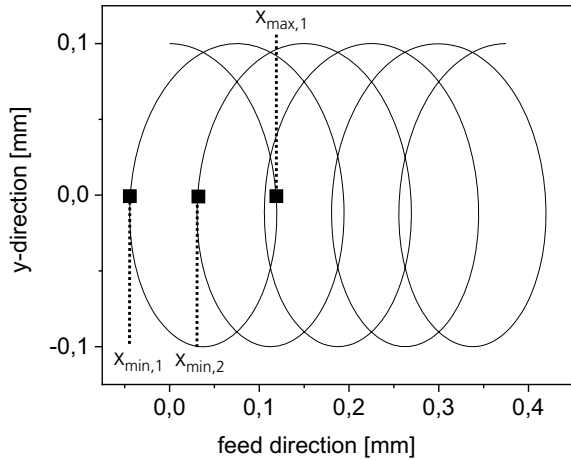
These two additional parameters together with the feed rate result in the degree of overlap U. This parameter indicates the distance between two successive oscillations in relation to the expression in the feed direction (see Fig. 25.4) and can be expressed in the form

$$U = \frac{x_{max,1} - x_{min,2}}{x_{max,1} - x_{min,1}} = \frac{\sqrt{4A_s^2 - \left(\frac{v_f}{\pi \cdot f_s}\right)^2} - \frac{v_f}{2 \cdot \pi \cdot f_s} \cdot \left(3\pi + 2 \cdot arcsin\left(-\frac{v_f}{2\pi \cdot f_s \cdot A_s}\right)\right)}{\sqrt{4A_s^2 - \left(\frac{v_f}{\pi \cdot f_s}\right)^2} - \frac{v_f}{2 \cdot \pi \cdot f_s} \cdot \left(\pi + 2 \cdot arcsin\left(-\frac{v_f}{2\pi \cdot f_s \cdot A_s}\right)\right)}$$
(25.6)

[SCH12, S.37] U: degree of overlap [-]; $x_{max,1}$: maximum of the first oscillation in x-direction [mm]; $x_{min,1}$: minimum of the first oscillation in x-direction [mm]; $x_{min,2}$: minimum of the second oscillation in x-direction [mm]; A_s: oscillations amplitude of the spatial power modulation [mm]; f_s: oscillation frequency of the spatial power modulation [Hz]; v_f: feed rate [mm/s].

Can be displayed. The superimposed oscillating motion considerably expands the design scope when forming the weld seam. In conventional laser beam welding, the design freedom of the seam is limited and can only be influenced by the parameters feed rate, power, and beam diameter. Due to the locally variable energy input, certain properties such as geometry, function, or seam quality can now be addressed in an application-specific manner (Schmitt 2012).

The beginnings of local power modulation can be traced back to electron beam welding. Here, local power modulation has already led to an increase in welding speed with a simultaneous decrease in defects in the seam. Thus, in addition to the possibility of increasing the joint cross section through rapid beam deflection, local power modulation also offers an increase in process stability (Thiel et al. 2012).

25.6   Temporal Power Modulation

Another option for influencing the laser beam welding process is temporal power modulation. The possibility of an application-specific adaptation of the temporal energy input to the properties of the materials to be welded is in the foreground here. Basically, a distinction is made between pulse shaping with pulsed beam sources and temporal variation of the laser power in laser beam processes with continuous beam sources. The different possibilities of power modulation are shown in Fig. 25.5 (Schmitt 2012).

Two approaches are described for temporal pulse forming: Thermal and metallurgical pulse forming. In thermal pulse forming, the material is first preheated at low power to remove possible impurities from previous process steps. This is followed by an increase in power above the actual threshold power to form the keyhole characteristic of deep welding. Subsequent reduction of the laser power to the threshold power determines the size of the weld pool. Gradual cooling toward the end of the pulse allows the vapor capillary to close without collapsing, reducing defect formation (Gedicke et al. 2007).

The difference to metallurgical pulse shaping consists of an additional superposition of the pulse shaping by a modulation of the laser power in the kHz range. The resulting cyclic undercooling of the molten bath can be used to influence metallurgical properties, such as mixing (Dürr et al. 2003).

Furthermore, temporal power modulation is also used in continuous seam welding. Here, too, modulation can be divided into two different categories. On the one hand, the boundary conditions of heating and cooling at the start and end of the weld can be specifically influenced with the aid of power ramps for finite welds, similar to pulse welding. On the other hand, the power can be continuously changed during the joining process. Here, the laser power is modulated by using a process-specific geometry (Schmitt 2012). An improvement of the weld quality and a stabilization of

Fig. 25.5 Differentiation of the forms of appearance of temporal power modulation
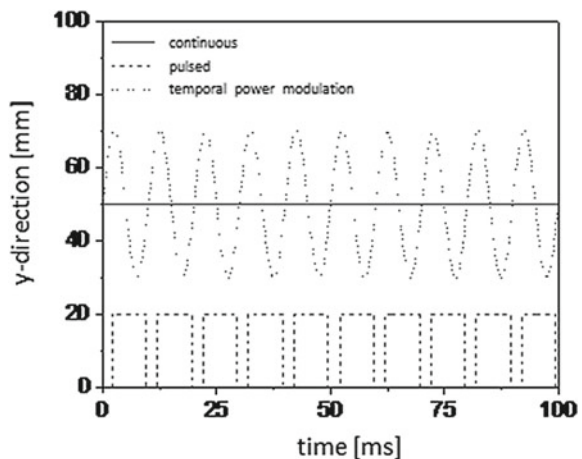
the process behavior are observed in high-speed welding with CO2 laser radiation by using a temporal power modulation.

25.7 Laser Beam Microwelding for Electromobility Applications

Johanna Helm, Sören Hollatz

Due to the high electrical and thermal conductivity of copper and aluminum, these materials are particularly suitable for electromobility applications. One of the main requirements is the conduction of high currents with a simultaneously low contact resistance. The available design space often limits the available connection area. Melt-based connections enable optimum use of the available space regarding current carrying capacity and dissipation of thermal energy from the joining zone.

Due to the high precision and the high-power intensities that can be achieved, laser beam sources with high brilliance are suitable for joining the electrical connections. The connection cross section can be increased by using spatial power modulation (see Sect. 8.5.4).

25.8 Battery Cells

An essential component of electrified vehicles is the energy storage system. This basically consists of battery cells that are assembled into modules and interconnected to form a complete pack, a battery management system, a cooling system, and a housing. Mainly Li-ion cells in three different shapes are used: Cylindrical cells, pouch cells, and prismatic cells. These cell types offer different challenges for joining with laser radiation.

Cylindrical cells of type 18,650 or 21,700 usually consist of a steel housing with a low wall thickness (0.2—0.3 mm), which is the negative pole. The positive pole is separated from the housing by a plastic seal. Both the seal and the electrolyte inside the cell are thermally sensitive. When joining a copper connector for the electrical contacting of the cell, the thermal damage threshold of the cell components must be taken into account. Laser beam welding is suitable for joining this cell type due to very short process times. Figure 25.6 shows a cross section of the top of a cylindrical cell (left). A 0.2 mm thick copper (CuSn6) sheet is welded to the battery shoulder around the positive pole to achieve a liquid-tight sealing and an electrical connection to the negative pole. The resulting battery module demonstrator is shown in the picture on the right.

Pouch cells are characterized by high shape variance and a foil coating. The poles are led out of the housing as connection tabs. These generally consist of electrode materials made of thin aluminum and copper (0.2—1 mm). The resulting dissimilar
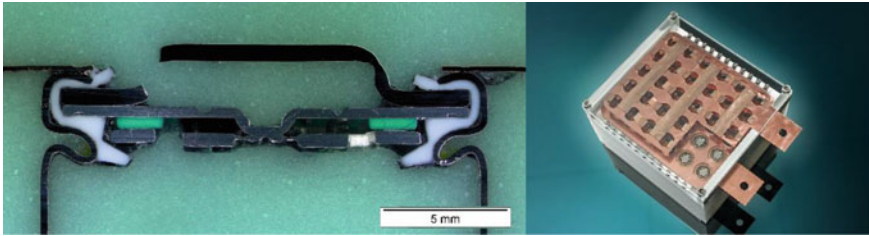
Fig. 25.6 Cross section of cylindrical cell with laser welded copper connector (left), battery module with cylindrical cells (right)
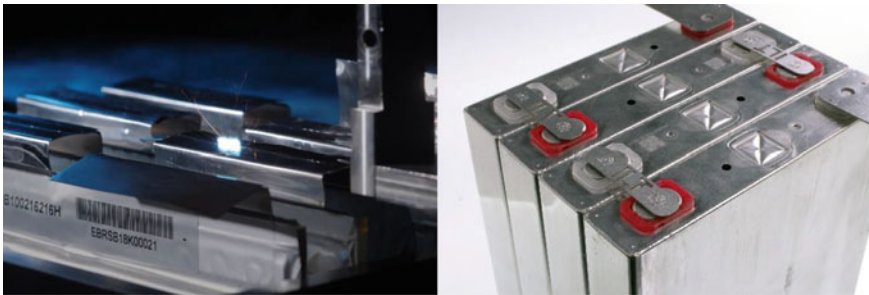
Fig. 25.7 Laser welding of pouch cells (left), laser welded prismatic cells (right)

joint of these materials is challenging for melt-based joining processes. By using spatial power modulation in laser beam microwelding, the welding depth and thus the mixing of copper and aluminum can be reduced. Intermetallic phases, which cause a reduction of the electrical and mechanical properties, can be reduced by a lesser degree of mixing. The laser welding process of pouch cells is shown in Fig. 25.7 left.

Prismatic cells consist of a solid aluminum housing with two aluminum or copper poles separated from the housing. The thickness of the poles is usually several millimeters. The challenge in contacting the cells is to join a connector with the highest possible electrical cross section in order to reduce losses due to heat dissipation. A possible arrangement of prismatic cells is shown in Fig. 25.7 right.

25.9 Power Electronics

Another important element of electrified vehicles is power electronic components for controlling the electric engine and communicating with the vehicle control system. Requirements on these components are a low contact resistance in order to keep the resulting heat generation and thus the necessary cooling power low during the high switching cycles.
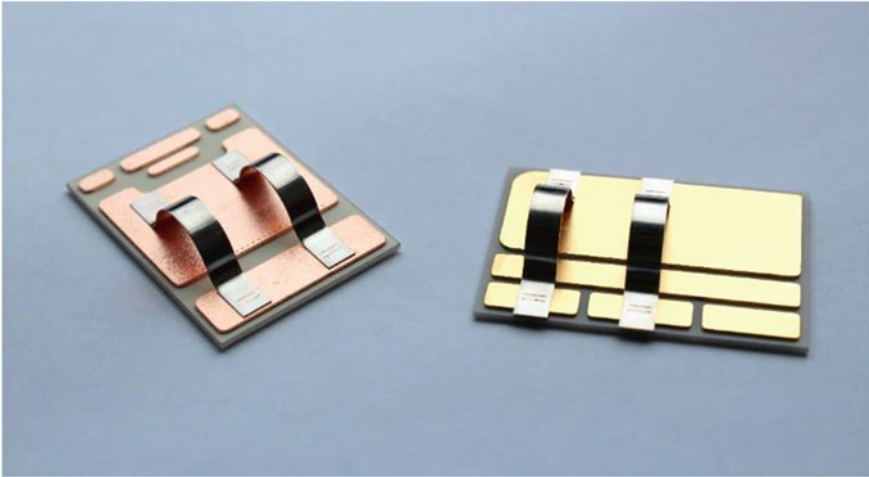
Fig. 25.8 Laser welded copper and aluminum ribbons on DCB and DAB

Laser beam microwelding is a suitable joining technology for the production of power electronic components, see Fig. 25.8. The precise energy input for many individual joints enables joining on thin and temperature-sensitive layers. The resulting melt-based connection of copper or aluminum has a low contact resistance and thus reduced heat losses.

25.10   Laser Beam Sources in the Visible Wavelength Range

The light absorption spectrum of copper in the visible region is largely influenced by interband transitions giving rise to its characteristic salmon-red color. The first absorption edge lies at 590 nm (2.1 eV) and is caused by direct interband transitions from the highest, flat d bands to the p-like states on the Fermi surface near the L point (Segall 1962). Hence, the absorptivity in the yellow-orange spectrum increases rapidly with a difference of approximately 40% between the values at 515 nm and 1030 nm at room temperature (c.f. Figure 25.9). In the infrared region absorption is dominated by damping of the free electrons due to electron–phonon collisions, even though an influence of the absorption edge persists. The measured absorption curves with a spectrometer in solid state at room temperature are shown in Fig. 25.9.

The absorption spectrum of copper furthermore depends on the surface conditions of the sample, ambient conditions, and temperature (Pells and Shiga 1969). At a wavelength of 1030 nm it has also been shown that there is a jump in absorptivity of about 5% upon melting, followed by a further increase in absorptivity with rising temperatures, which can be related to the electrical conductivity of the material (Blom et al. 2003). In the metal vapor produced during the welding process, the copper atoms
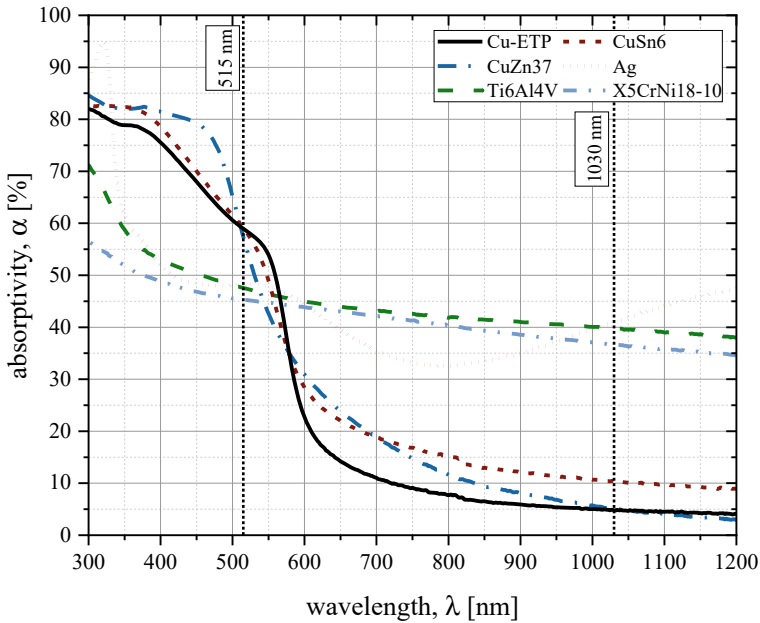
Fig. 25.9 Absorptivity of metallic materials depending on the wavelength (measured)

can absorb the green laser light because of a persistent line at 515 nm between the $3d^{10}(^1S)4p_{1/2}$ and the $3d^{10}(^1S)4d_{3/2}$ states (Sansonetti and Martin 2005). Those three effects prove the newly developed laser beam sources in the visible wavelength range as an alternative for commonly used IR-lasers.

The curves show that especially in welding applications with copper, the use of laser beam sources with shorter wavelengths in the range of 450 nm and 515 nm has a higher degree of absorption at ambient temperature and an increased absorption in the process can also be experimentally evaluated (Hummel et al. 2020; Engler et al. 2011).

Typical laser beam sources available on the market today for application with laser beam wavelengths between 450 and 532 nm are listed in Table 25.2.

The main field of application for these industrially available laser beam sources is the welding of copper. Cu-ETP and CuSn6 as alloys are in the focus of the industry. These alloys are used for the electrical contacting of power electronics and battery modules due to their high electrical conductivity. The increased absorption of 515 nm laser radiation compared to 1030 nm laser radiation results in a fundamentally changed behavior with respect to the laser parameters and the process windows that can be used for welding. This is illustrated in Fig. 25.10.

From the graphs, it can be seen, that the weld seam depth for relatively small feed rates is greater for welds at a wavelength of 1030 nm than for 515 nm wavelength. The average reduction of the weld seam depth with increasing feed rate (negative slope) is greater at a wavelength of 1030 nm compared to 515 nm. Also, the average reduction

Table 25.2 Typical Specifications of laser beam sources emitting at visible wavelengths

Laser Parameter	Unit	450 nm	515–532 nm
Laser medium	[–]	diode	disc or fiber—frequency doubled
Operation mode	[–]	cw	cw/pulsed
Average power	[W]	200–2000	500 - 2000 / 400
Pulse power	[W]	–	- / 4000
Pulse energy	[J]	–	- / 40
Beam quality	[mm*mrad]	< 11 - 60	< 1 - 4
Fiber diameter	[μm]	125–600	14–200
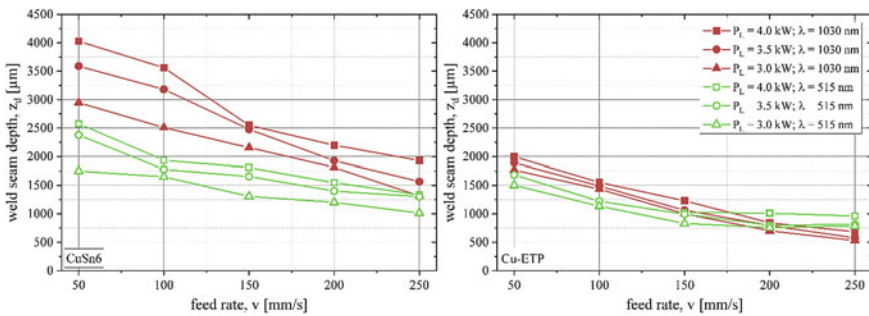
Fig. 25.10 Weld seam depth over feed rate for CuSn6 (left) and Cu-ETP (right)

of the keyhole depth with increasing feed rate with a wavelength of 515 nm is higher for CuSn6 in comparison to Cu-ETP. It can be concluded from the experimental results that welds with 515 nm wavelength in copper react less sensitive to the change in the feed rate.

In a representation of the weld seam cross sections for both laser wavelengths and materials are shown (Fig. 25.11).

In the case of CuSn6, very sharply tapered weld seams are produced at the seam base with low feed rate. With increasing feed rate, the welding depth decreases for both. However, the weld seam becomes wider at the seam base. It can also be seen that weld seams with the 515 nm laser beam source have stronger pore formation than with the 1030 nm wavelength.

Laser beam sources with a larger spot diameter due to the lower beam quality can be used preferentially for heat conduction welding. This refers specifically to the diode lasers with a wavelength of 450 nm (Fig. 25.12).

It can be seen that the laser beam source with 450 nm wavelength in particular can achieve a very low surface roughness, which is even lower than the average surface roughness of the starting material, even though two specimens were butt-jointed.

The combination of 450 nm and 1070 nm enables new methods for laser welding of highly reflective materials commonly welded with IR-lasers only. A qualitative example is shown in Fig. 25.13.
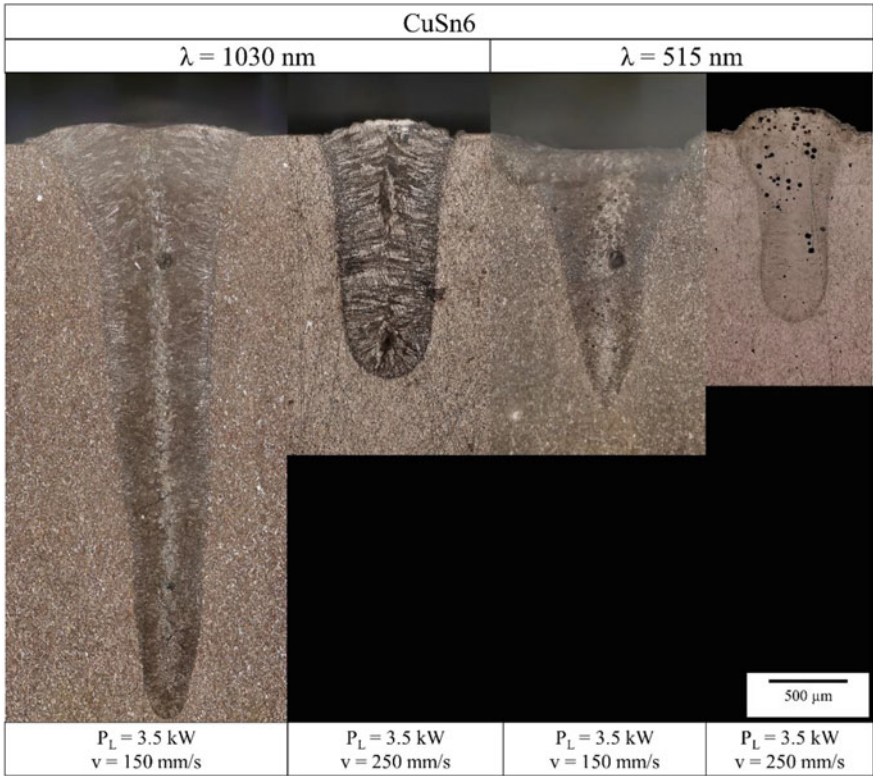
Fig. 25.11   Weld seam cross sections of CuSn6 for 1030 nm laser (left) and 515 nm laser (right)

The advantages of the very low surface roughness with the laser beam source of 450 nm wavelength in heat conduction welding mode can be combined with a deep welding process by an infrared laser with 1070 nm wavelength. Depending on the relative arrangement of the two lasers to each other in the feed direction, the surface quality and the welding depth can thus be variably adjusted as required.

surface roughness R_a

$\emptyset R_{a,1064nm} = 0.87\ \mu m$

$\emptyset R_{a,515nm} = 0.47\ \mu m$

$\emptyset R_{a,450nm} = 0.094\ \mu m$

$\emptyset R_{a,surface} = 0.18\ \mu m$

factor ~9.25
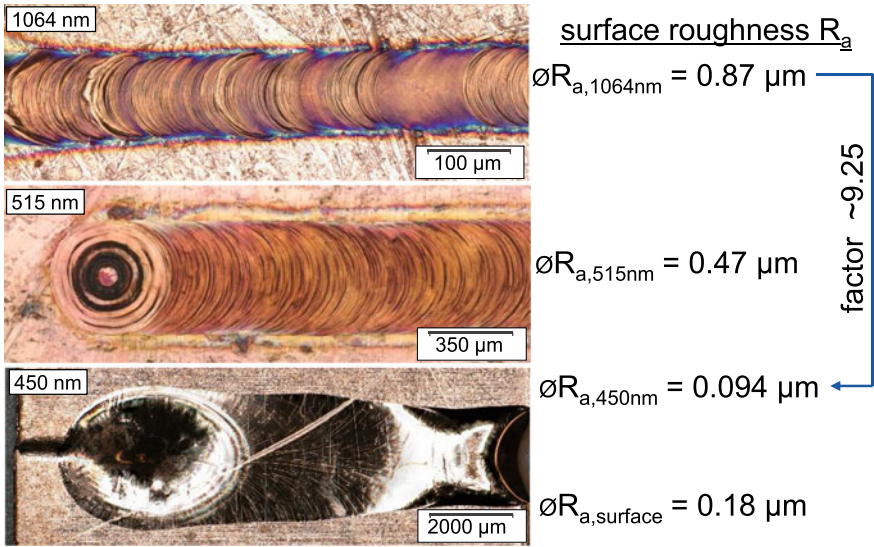
Fig. 25.12 Surface roughness of heat conduction welds with different laser wavelengths

Schweißrichtung

1 mm

A

B

C

B-300

C-300
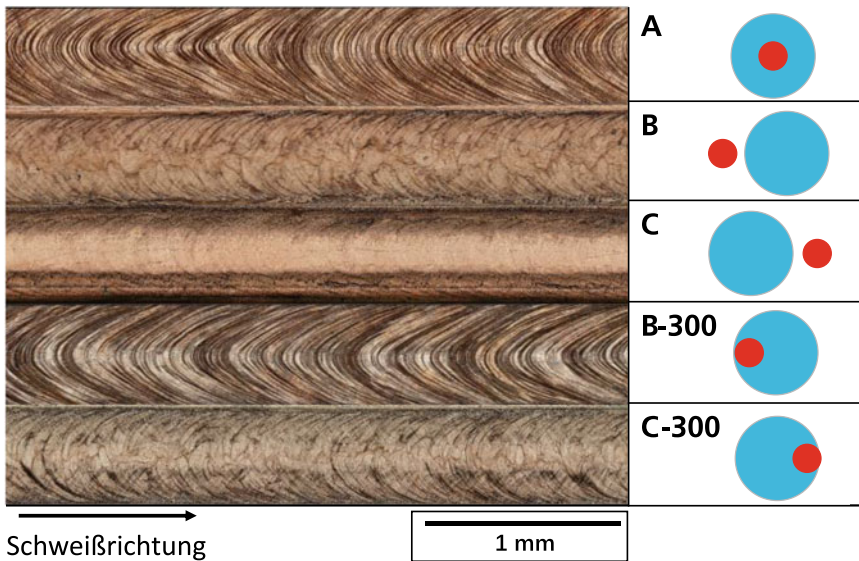
Fig. 25.13 Surface roughness depending on the relative position of laser beams in the feed direction

References

Blom A, Dunias P, van Engen P, Hoving W, de Kramer J (2003) Process spread reduction of laser microspot welding of thin copper parts using real-time control. Photon Processing in Microelectronics and Photonics II. CA, SPIE, San Jose, p 493

Dürr U, Holtz R, Westphäling T (2003) Materialspezifische pulsleistungsmodulation beim Laserstrahl-Mikroschweißen. In: Tagunsband Laser in der Elektronikproduktion und Feinwerktechnik (LEF)

Eichler J, Eichler H-J (2003) Laser: Bauformen, Strahlführung. Anwendungen. Springer, Berlin

Engler S, Ramsayer R, Poprawe R (2011) Process studies on laser welding of copper with brilliant green and infrared lasers. Phys Procedia 12:339–346. https://doi.org/10.1016/j.phpro.2011.03.142

Franco, Diana (2017): Wobbling laser beam welding of copper. Dissertation. Lissabon

Gedicke J, Olowinsky A, Artal J, Gillner A (2007) Influence of temporal and spatial laser power modulation on melt pool dynamics. In: Yongfeng Lu (Hg.): ICALEO 2007 Congress Proceedings Congress proceedings. October 29 - November 1, 2007, Hilton in the Walt Disney World Resort, Orlando, FL, USA ; [including] Laser Materials Processing Conference, Laser Microprocessing Conference [and] Nanomanufacturing Conference. [Orlando, Fla.]: Laser Institute of America (610 = 100), S. 816–822

Gedicke, Jens (2011): Robuste Prozessführung beim Laserstrahl-Mikroschweißen mit hochbrillanten Strahlquellen. Aachen: Shaker (Berichte aus der Lasertechnik). Online verfügbar unter http://www.worldcat.org/oclc/748694636

Grupp, Michael; Reinermann, Nils (2017): Copper Welding with High-Brightness Fiber Lasers. In: LTJ 14 (3), S. 25–29. https://doi.org/10.1002/latj.201700014

Häusler A (2021) Präzisionserhöhung beim Laserstrahl-Mikroschweißen durch angepasstes Energiemanagement. Apprimus Verlag, Aachen

Heinen P (2020) Prozessfähigkeitserhöhung und Fehlerreduktion beim Laserstrahl-Mikroschweißen mit örtlicher Leistungsmodulation. Apprimus Verlag, Aachen

Hummel M, Schöler C, Häusler A, Gillner A, Poprawe R (2020) New approaches on laser micro welding of copper by using a laser beam source with a wavelength of 450 nm. J Adv Join Process 1:100012. https://doi.org/10.1016/j.jajp.2020.100012

Katayama S, Takemoto T, Matsunawa A (1995) Effect of pulse shape on melting characteristics in pulsed laser spot welding. In: Proc. ICALEO

Okamoto Y, Gillner A, Olowinsky A, Gedicke J, Uno Y (2007) Fine micro-welding of thin stainless steel sheet by high-speed laser scanning, Proc. of LPM

Pells GP, Shiga M (1969) The optical properties of copper and gold as a function of temperature. J Phys c: Solid State Phys 2:1835–1846. https://doi.org/10.1088/0022-3719/2/10/318

Rodenstock: Strahlen im optischen Zentrum, Laser Magazin, 1, (1999)

Sansonetti JE, Martin WC (2005) Handbook of basic atomic spectroscopic data. J Phys Chem Ref Data 34:1559–2259. https://doi.org/10.1063/1.1800011

Schmitt, Felix (2012) Laserstrahl-Mikroschweißen mit Strahlquellen hoher Brillanz und örtlicher Leistungsmodulation. Dissertation. Aachen: Shaker (Berichte aus der Lasertechnik)

Schmitt F (2012) Laserstrahl-Mikroschweißen mit Strahlquellen hoher Brillanz und örtlicher Leistungsmodulation, Berichte aus der Lasertechnik. Shaker, Aachen

Schmitt F, Mehlmann B, Gedicke J, Olowinsky A, Gillner A, Poprawe R (2010) Laser beam micro welding with high brilliant fiber lasers, JLMN 5(3)

Segall B (1962) Fermi Surface and Energy Bands of Copper. Phys Rev 125:109–122. https://doi.org/10.1103/PhysRev.125.109

Thiel, Christiane; Axel, Hess; Weber, Rudolf; Graf, Thomas (2012) Stabilization of laser welding processes by means of beam oscillation. In: Proceedings of SPIE

YOU, Young-Tae; KIM, Jin-Woo (2017) Fiber Laser Welding Properties of Copper Materials for Secondary Batteries. In: ms 23 (4). https://doi.org/10.5755/j01.ms.23.4.16316

Chapter 26
Hybrid Lightweight Components

Kira van der Straeten

26.1 Motivation

In automotive and aerospace industry lightweight construction is a central issue due to the need to reduce CO_2 emissions. One way to achieve weight reduction is to use different materials adapted to functions and local loads. The multi-material lightweight approach enables minimizing dead weight while maintaining and preferably boosting the components' performance. The combination of different materials, such as plastics, especially fiber reinforced plastics (FRP) and metals, adapted to local loads, opens up new paths for weight reduction. While metals can withstand high loads due to their mechanical properties, polymers are characterized by low weight, attractive price, and nearly endless shaping possibilities (Fig. 26.1).

Though, a direct joint between both materials, e.g., by welding, fails due to their different physical and chemical properties. Up until now, joining of FRP and metals is usually based on mechanical fastening, riveting or adhesive joining. But these processes have their specific disadvantages. Mechanical joining requires drilling holes into the material which destroys fiber bundles inside the FRP and weakens the materials mechanical properties. Additionally, the punctual load transfer creates stress concentrations that are not suitable for FRP. On the other hand adhesive joints require extensive surface pretreatments and hardening times which results in high process times. Furthermore, a suitable adhesive material must be available for the material combination to be joined. That is the reason why new, reliable joining techniques are required.

Thermal direct joining of plastics and metals is a novel approach to join plastics and metals, which has been developed over the last decade. Because specific adhesion between polymers and metals is weak, a surface pretreatment is essential to achieve high joint strengths. The energetic state, electrical potential, morphology,

K. van der Straeten (✉)
Fraunhofer ILT, Aachen, Germany
e-mail: kiramartina@web.de
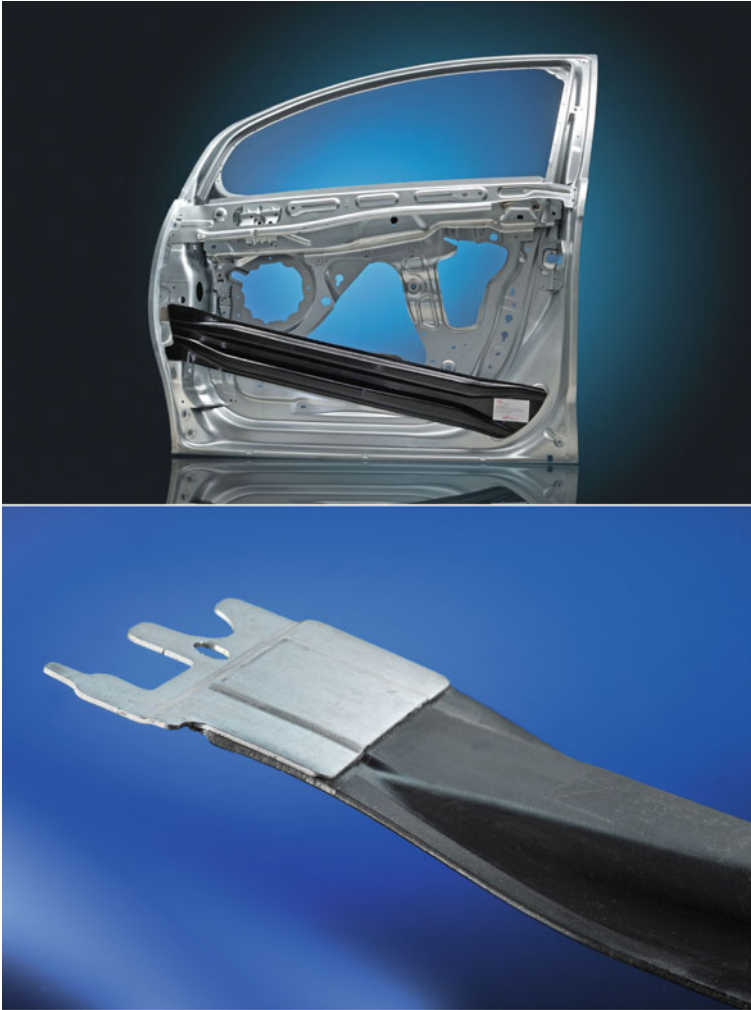
Fig. 26.1 Top: Car door with FRP reinforcement bar; Bottom: Hybrid roof bow (Spancken et al. 2018b) (©Fraunhofer ILT, Aachen)

geometry, and chemical structure have a decisive influence on the bond strength. Commonly used techniques are sandblasting, plasma pretreatment, or etching, but these techniques rarely enable mechanical interlocking between the materials.

A new approach to overcome these problems is a two-staged laser-based joining process, which consists of a microstructuring process of the metal surface and a thermal joining process.
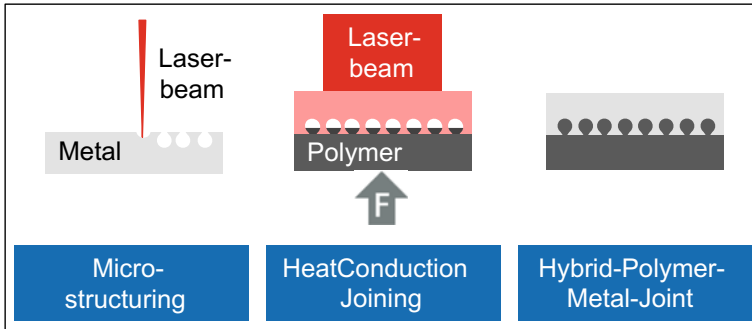
Fig. 26.2   Process chain of laser-based plastic-metal joining

26.2   Process Basics

The process principle of the laser-based process chain is shown in Fig. 26.2 (Engelmann et al. 2016; Rösner 2014; Straeten et al. 2018a). Within the first process step, the metal surface is microstructured with laser radiation in order to create undercut structures for the interlocking of polymer into the metal and to enlarge the boundary surface to increase specific adhesion. In the second heat conduction joining process step, the metal is heated up and due to thermal contact of polymer and metal the matrix of the thermoplastic composite material melts. The plasticized material flows into the cavities by applying an external joining force. After hardening a strong and durable connection is formed, which is mostly based on mechanical interlocking.

The aim of surface pretreatment using laser radiation is to modify the metal surface by sublimation and remelting in such a way that the surface is enlarged and defined undercuts are created for mechanical bonding. Different structuring approaches are pursued, which differ with regard to the beam source used, pulse duration and processing strategy, and the resulting structural geometry (Heckert et al. 2016; Rodríguez-Vidal et al. 2018; Straeten et al. 2018a).

26.3   Laser Microstructuring Approaches

When using continuous wave (cw) single-mode fiber laser beam sources, the material is ablated in a linear fashion at high scanning speeds by a combination of sublimation and melt removal (Engelmann et al. 2016; Rodríguez-Vidal et al. 2018). Due to the high beam quality of the beam source, the laser power can be focused on a very small area of ~ 40 μm focal diameter. The laser radiation is deflected on the metal surface by a scanner system consisting of two movable mirrors. Due to the high intensity, the metal is partially vaporized and the resulting sublimation pressure presses the melt from the base of the structure to the edge of the structure, where part of the melt solidifies as it is expelled (see a). The depth of the structure can be increased by

repeated passes of the laser beam and at the same time an undercut is formed by the material solidified at the neck of the structure (see b). The cavities with a drop-shaped cross section enable a reproducible bonding of the plastic in the subsequent joining process. The structure sizes are typically in the range of structure depths from 100 to 150 μm and structure widths between 30 and 50 μm. Due to the combination of sublimation and melting, the process speed is much faster compared to conventional structuring processes (Fig. 26.3).

The arrangement and alignment of the linear structures enables to influence the hybrid joint properties (Engelmann et al. 2016). The higher the structure density, the higher the resulting bond strength. However, the structural density is limited by the fact that the structures influence each other and an undercut is no longer present if the distance between the structures is too small (Fig. 26.4).

Depending on structure density and material properties, tensile shear strengths up to 25 MPa can be achieved. In general the joint strength is strongly depending on
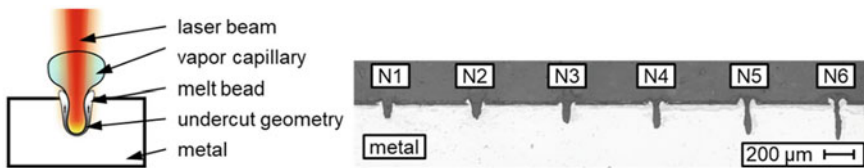
Fig. 26.3 Left: Process principle of laser microstructuring with cw laser radiation; right: Formation of undercuts with an increasing number of passes
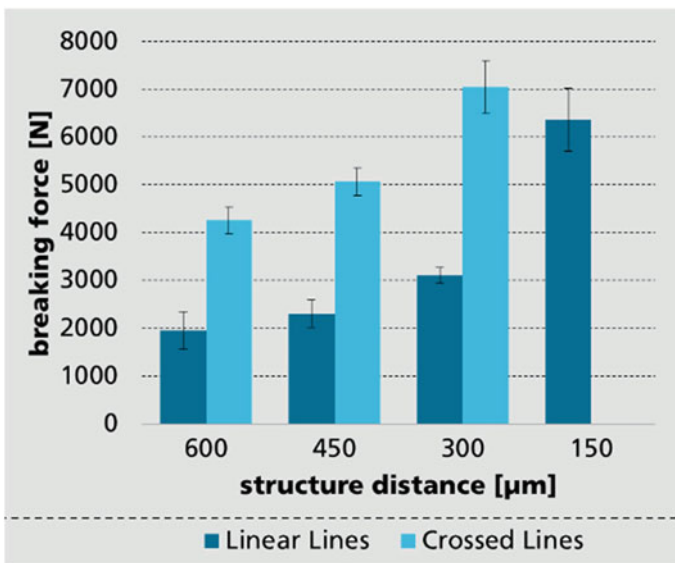
Fig. 26.4 Influence of structure distance and pattern on the joint strength

the load direction. The highest loads can be transferred for shear load. Tensile load reduces the joint strength and shear load should be avoided.

Another microstructuring approach is the formation of spongy self-organizing microstructures using ultrashort pulsed lasers (Straeten et al. 2016, 2018b). During the ablation of metals with ultrashort laser pulses the formation of numerous self-organized microstructures can be observed, e.g., mounds, spikes, micro-, nanoripples, or cone-like protrusions (CLP). The formation of CLP is a growth process, which usually starts at scratches or inhomogeneities after a few layers of ablation with high-energy ultrashort pulses in the ablated area (Eifel 2015; Tsukamoto et al. 2007). At first some dots and holes appear which grow into small clusters with increasing number of layers until the surface is completely covered with spongy structures. Visually the growth of the CLP can be monitored by a blackening of the surface. The structure is characterized by a random orientation and an extremely enlarged surface with a high surface roughness due to nano-substructures covering the microstructures (Fig. 26.5).

In contrast to the microstructuring approach with fiber lasers, the achievable joints' strengths are even higher due to the higher structure density (see Fig. 26.6). Depending on the material combination, loads of more than 25 MPa are achievable for the tensile shear load. For pure shear load joint strengths of nearly 50 MPa are possible (Spancken et al. 2018b). But currently processing and ablating with ultrashort laser pulses is a slow process due to the availability of high-power laser sources, suitable equipment und processing strategies. At this point, the ultrashort pulsed microstructuring approach is only suitable for applications where high process speeds are not required but the priority is set to achieve extremely high joint strengths.

26.4 Laser Joining Process

Whereas in the widely used welding process both joining partners melt and are joined together in the joining zone, this is not possible with plastic-metal hybrids due to the very different melting temperatures and the chemical incompatibility of the materials. In the thermal joining process of plastic-metal hybrids, a thermoplastic polymer is plasticized by applying heat and the metal surface and its cavities are wetted with molten plastic by applying joining pressure. When the plastic solidifies, a connection is formed which is based on a form fit or chemical and physical interaction.

The energy input can take place via different methods, e.g., ultrasonic joining, induction joining, heating element joining, and laser joining. When the process is optimized, the type of heating has a negligible influence on the achievable composite strengths and should be adapted to the respective application.

During laser joining of plastic-metal hybrids, the energy is introduced into the joining zone via laser radiation, absorbed on the metal surface, and converted into heat. A distinction can be made between two different irradiation strategies (see Fig. 26.7) (Rösner 2014).

Fig. 26.5 Cone-like protrusions at different magnifications (SEM-pictures) (Straeten et al. 2016)
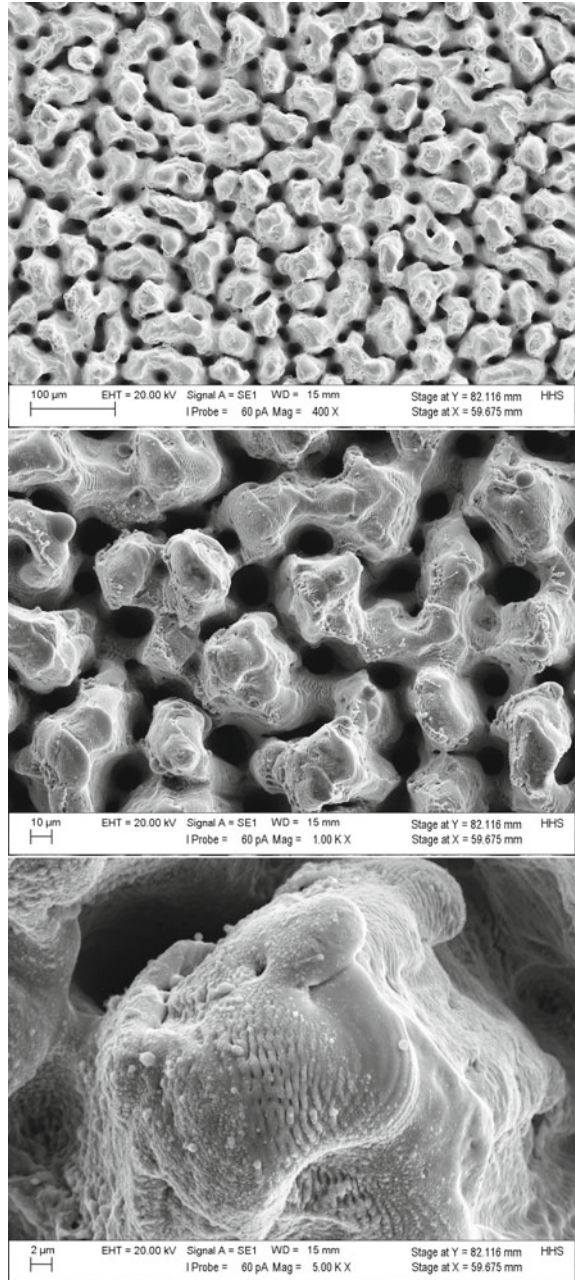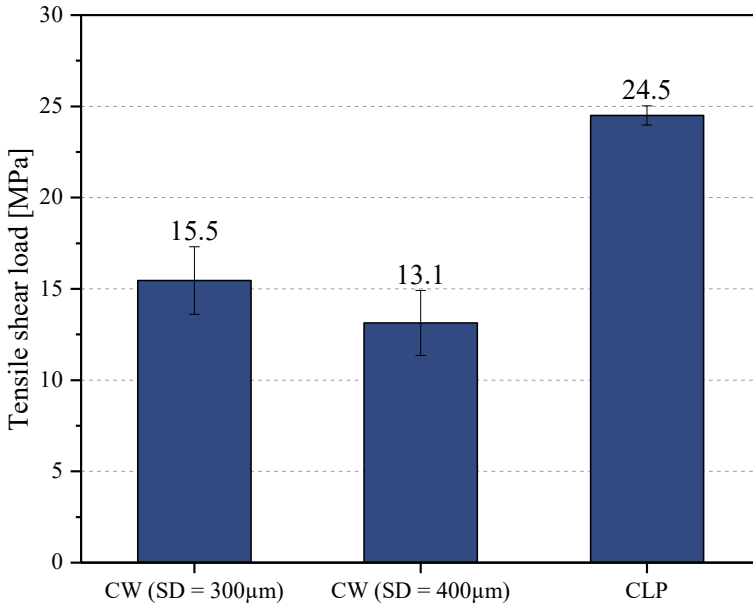
Fig. 26.6 Comparison of the tensile shear strength of hybrid joints with cw fiber laser microstructures and CLP-structures (Straeten et al. 2018b)
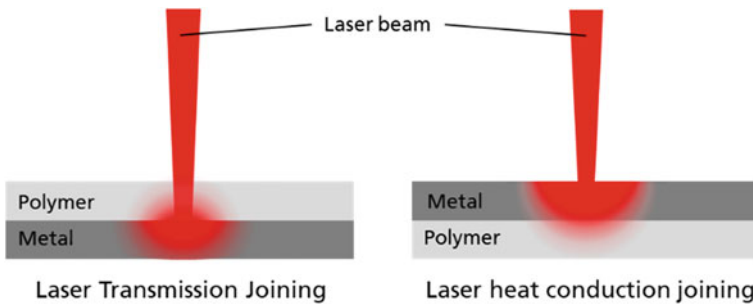
Fig. 26.7 Irradiation strategies for laser joining of plastic-metal-hybrids

For laser transmission joining, a laser-transparent plastic material faces the beam source and is transmitted. The transmitted radiation is then absorbed on the metal surface. The heat output in the metallic joining partner is proportionally transferred into the plastic by heat conduction at the interface. The plastic melts, wets the metal surface, and can flow into any existing surface structures by the applied joining pressure. This process is only applicable for laser-transparent plastics with a transparency of at least 20% and therefore not suitable for most FRP.

Alternatively, for laser heat conduction joining, the metallic joining partner is irradiated directly and the plastic component is melted by heat conduction through

the metal. It is advantageous that the optical properties of the plastic have no influence on the joining process, but the process is dependent on the heat conduction properties and the material thickness of the metal. For both irradiation approaches, sufficient thermal contact between both joining partners is necessary.

Besides direct thermal joining processes, it is also to include the joining process into the forming part of the polymer component, e.g., injection molding or compression molding. Therefore microstructured metal parts can be placed into the molding tool and the joining takes place as molten plastic penetrates the structures during the forming process. In order to guarantee the filling of the microstructures the metal parts need a certain temperature, to avoid solidification of the melt on the cold metal surface (Spancken et al. 2018a).

26.5 Applications

The laser-based approach for hybrid joining of plastics and metals is a fast and reliable process with high joint strengths without the use of any additional adhesives or fasteners. These properties make the process particularly suitable for various lightweight construction applications especially in the automotive and aeronautical industry. But due to the high process speeds and the possible combination with other forming processes the technique can not only be used for structural body parts but also for smaller parts like housings, valves, or bearings.

References

Eifel S (2015) Effizienz- und Qualitätssteigerung bei der Lasermikrobearbeitung mit UKP-Lasern durch neue optische Systemtechnik. Zugl.: Aachen, Techn. Hochsch., Diss., 2015. Ergebnisse aus der Lasertechnik. Apprimus-Verl., Aachen

Engelmann C, Eckstaedt J, Olowinsky A, Aden M, Mamuschkin V (2016) Experimental and simulative investigations of laser assisted plastic-metal-joints considering different load directions. Phys Procedia 83:1118–1129

Heckert A, Singer C, Zaeh MF, Daub R, Zeilinger T (2016) Gas-tight thermally joined metal-thermoplastic connections by pulsed laser surface pre-treatment. Phys Procedia 83:1083–1093

Rodríguez-Vidal E, Sanz C, Lambarri J, Quintana I (2018) Experimental investigation into metal micro-patterning by laser on polymer-metal hybrid joining. Opt Laser Technol 104:73–82

Rösner A (2014) Zweistufiges, laserbasiertes Fügeverfahren zur Herstellung von Kunststoff-Metall-Hybridbauteilen. Zugl.: Aachen, Techn. Hochsch., Diss., 2014. Fraunhofer Verlag, Stuttgart

Spancken D, van der Straeten K, Beck J, Stötzner N (2018b) Laser structuring of metal surfaces for hybrid joints. Light Worldw 11(4):16–21

Spancken D, Laveuve D, Beck J, Stötzner N, van der Straeten K, Büter A, Henning F (2018a) Hybrid materials—joining of polymers and metals. In: Proceedings of ECCM18

van der Straeten K, Engelmann C, Olowinsky A., Gillner A (2018a). Comparison of Laser-based Joining Approaches for Plastic-Metal-Hybrids - Strength vs. Process Speed. In: Proceedings of Hybrid Materials and Structures 2018a.

Tsukamoto M, Kayahara T, Nakano H, Hashida M, Katto M, Fujita M, Tanaka M, Abe N (2007) Microstructures formation on titanium plate by femtosecond laser ablation. In: Journal of Physics: Conference Series 59, 666–669

van der Straeten K, Burkhardt I, Olowinsky A, Gillner A (2016) Laser-induced Self-organizing microstructures on steel for joining with polymers. Phys Procedia 83:1137–1144

van der Straeten K, Olowinsky A, Gillner A (2018b) Laser-based plastic-metal-joining with self-organizing microstructures considering different load directions. J Laser Appl 30(3):32401

Chapter 27
Laser-Based Glass Frit Bonding

Heidrun Kind

27.1 Motivation

Laser-based low temperature glass frit bonding is used as a long-term encapsulation method for a wide range of products in consumer market and industrial application. Conventional frit bonding is currently done in a convection oven with peak temperatures up to 500 °C. For many applications, this overall thermal load is too high and not acceptable since temperature sensitive components have to be encapsulated. The most temperature sensitive component of the entire system defines the maximum possible temperature for the joining process.

Laser-based glass frit bonding has the unique feature that the energy input required for bonding is spatially limited to the joining area because the energy necessary for melting and wetting the parts to be joined is based on the absorption of the laser radiation applied in the glass frit material. The laser process can be controlled in such a way that the glass frit is only heated to such an extent that a reliable wetting process can take place and an evaporation of frit components is avoided. The joint achieved in this way is characterized by a hermetic barrier that prevents moisture and gas from entering. This joining process is predestined for encapsulation tasks in electrical engineering and electronics where hermetically tight electrical feedthroughs and housings are required.

H. Kind (✉)
Fraunhofer ILT, Aachen, Germany
e-mail: heidrun.kind@ilt.fraunhofer.de

Fig. 27.1 Process chain for laser-based glass frit bonding (Kind et al. 2014)

27.2   Process Chain for Glass Frit Bonding

Before the actual glass frit bonding process could be realized several steps of preparatory work have to be realized. Every single step of the process chain has an important influence on the seam quality (Fig. 27.1).

First of all, the glass frit material has to be selected. For a successful bonding process, the matching of coefficient of thermal expansion (CTE) of glass frit and material that has to be joined is mandatory. Only adapted CTEs enable a reliable joint formation.

Next step is the printing process. The frit material, which is very often supplied in paste form, must be applied to the parts to be joined. A good glass frit application quality can be guaranteed by a screen printing process. The printing process is based on using a woven mesh which is coated with an impermeable substance everywhere a frit transfer is not desired. Uncoated areas allow a glass frit transfer. A squeegee is moved across the screen mesh forcing the paste into the mesh openings. Printing thicknesses are typically in the range of 15–25 μm.

The following vitrifying process includes several procedures which transfer the glass frit paste to a compact glass without voids. To this effect, an evaporation of the organic components has to be realized at first. After that, a strong connection between glass frit material and substrate surface is formed. For this procedure, a furnace process is required.

Depending on the glass frit material a temperature–time profile ensures the requested transformation. Incomplete transformation procedures cause voids and pores during the bonding process. These defective spots result in a decrease of joint strength and an increase of the probability of leakage through the glass frit material.

After that the assembly of the parts to be joined is done in a clamping device which enables an accurately positioning of the parts. As the final step, the actual joining process is performed using the laser beam that follows the glass frit contour (Kind et al. 2014).

27.3   Principle of Laser-Based Glass Frit Bonding

As the most laser-induced processes laser glass frit bonding is based on the conversion of optical into thermal energy. To obtain the processing temperature of the glass frit the laser radiation is first of all absorbed in the frit. The result is a locally limited
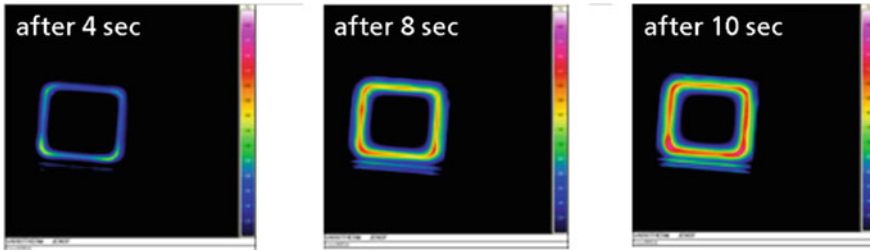
Fig. 27.2 Temperature propagation during the quasi-simultaneous heating process of a vitrified glass frit frame applied on a 20×20 mm^2 glass sample captured with a thermal imaging camera

temperature rise in the area of the laser processing zone, which ultimately leads to melting of the glass frit (Fig. 27.2).

The transparency or partial permeability of at least one joining part in the wavelength range of the laser radiation used is a precondition for the process. Laser-based glass frit bonding uses laser beam sources that emit radiation in the near infrared range mostly between 800 and 1100 nm. The following spectra (Fig. 27.3) show the optical properties of borosilicate glass, silicon, and a glass frit material as common representatives of materials suitable for a laser-based glass frit bonding process using laser sources emitting in a wavelength range from 800 to 1100 nm.

Uncoated and uncolored glasses of any kind generally have a very high transparency in almost the whole near infrared range, even with very large material thicknesses. For example, 2.2 mm thick Borofloat® transmits almost 92% of the laser radiation in the wavelength range between 800 and 1100 nm. Silicon, on the other hand, absorbs radiation in the near infrared approximately up to a wavelength of 1200 nm. A 540 µm thick sample absorbs between 65 and 68% of the emitted radiation in the range of the laser wavelengths used for glass frit bonding. In order to realize an effective bonding process, the optical properties of the frit material are particularly important. The glass frit used should absorb at least 70% of the laser radiation. The frit shown in Fig. 27.3 corresponds to this specification in the relevant wavelength range.
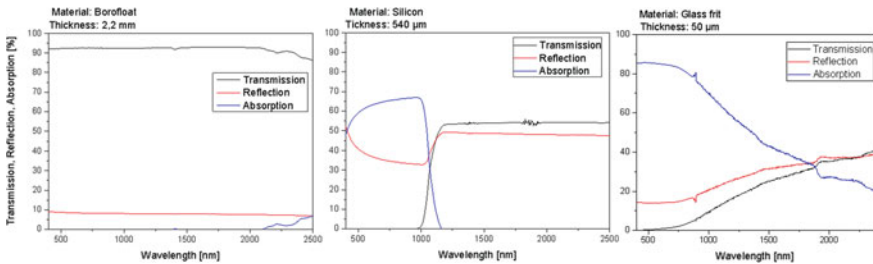
Fig. 27.3 Optical properties for different materials such as Borofloat®, silicon and a representative glass frit whose optical properties enable the laser-based glass frit bonding process
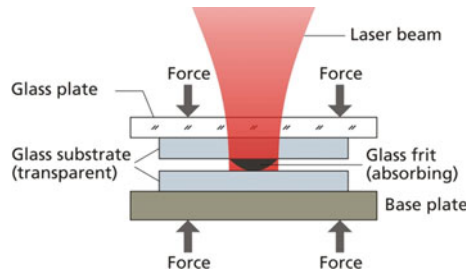
A reliable, tough joint formation requires the wetting of both joining surfaces with the molten glass frit material. A defined compressive force is used to establish the contact required to form a strong joint (Fig. 27.4).

Due to the contact between glass frit and joining parts heat is diffused into the parts. This process is driven by heat conduction. The heat flow into the joining parts is on one hand a loss process in the energy balance of the glass frit. On the other hand, it leads to a smoothing of the temperature gradients in the parts. Depending on the thermo-mechanical properties of the joining partners, the temperature gradients induced by the laser process can lead to thermal stresses that can result in cracking and breakage. Especially sudden extreme temperature fluctuations should be avoided, especially with thermal shock sensitive glasses such as soda-lime glass. For comparison, the thermal shock resistance of borosilicate glass is more than 6 times higher than that of soda-lime glass (thermal shock resistance of soda-lime glass: 40 K, thermal shock resistance of borosilicate glass: 260 K (Glas Trösch Holding AG, 2012).

27.4 Irradiation Methods

There are actually two different methods for the laser-based glass frit bonding process (Fig. 27.5). A distinction is made between a quasi-simultaneous and a contour bonding process.

Fig. 27.5 Schematic
illustration of different
laser-based glass frit bonding
methods
a quasi-simultaneous
bonding; **b** contour bonding
(Kind et al. 2014)
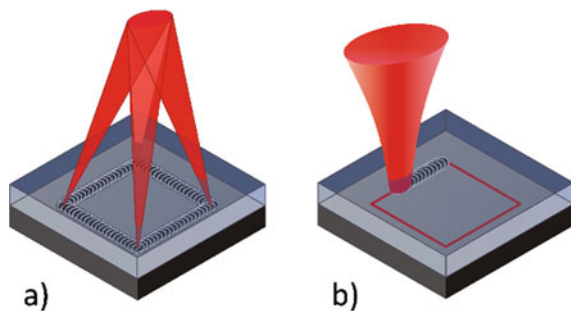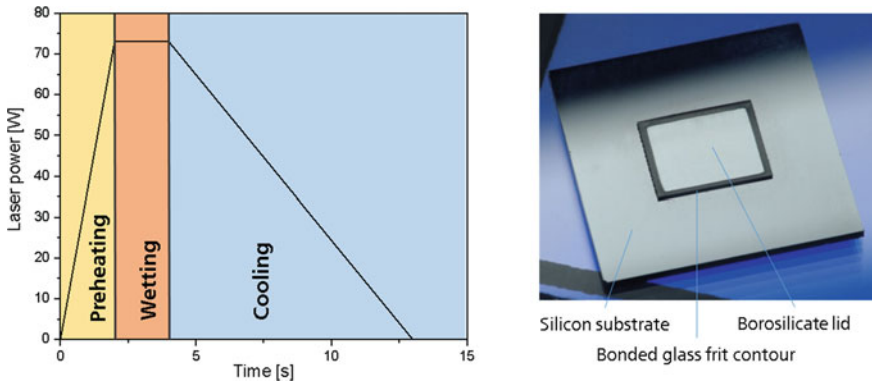
Fig. 27.6 Laser power profile divided into a preheating, wetting, and cooling phase for bonding a borosilicate glass lid to a silicon substrate. The size of the lid is 5×6 mm^2

27.4.1 Quasi-Simultaneous Laser-Based Glass Frit Bonding Process

The quasi-simultaneous bonding process is characterized by homogeneous and simultaneous heating, melting, and wetting of the whole glass frit contour. This impact is realized by multiple irradiations (some 100 times) of the glass frit contour with high feed rates. Only a scanner unit is able to realize the required but for the quasi-simultaneous process essential feed rates of minimum 1000 mm/s (Fig. 5a). Exactly this fact is the disadvantage of the process because the scanning field of the scanner optic limits the joining part dimension and makes the quasi-simultaneous bonding process impossible to use for large scale applications. Usually quasi-simultaneous laser-based bonding process is employed for part dimensions up to 30 x 30 mm^2.

The joint quality by means of a perfect form fit of the joining parts without voids or cracks depends on a smooth simultaneous heating and cooling of the whole glass frit contour. Thermal stresses must be avoided. Therefore, the duration time of the process is divided into three phases: heating, wetting, and cooling. Depending on the glass frit and its absorption properties as well as the thermo-mechanical characteristics and the size of the components to be bonded, the length and the applied laser power of each phase can vary (Olowinsky and Kind, 2010). Figure 27.6 shows the laser power profile for the bonding of a borosilicate glass lid to a silicon substrate. The size of the lid is 5×6 mm^2. The entire bonding process takes a total of 13 s.

27.4.2 Contour Laser-Based Glass Frit Bonding Process

In case of contour-based bonding process, the laser beam follows a programmed path along the glass frit contour (Fig. 5b). Heating, melting, and joining are locally
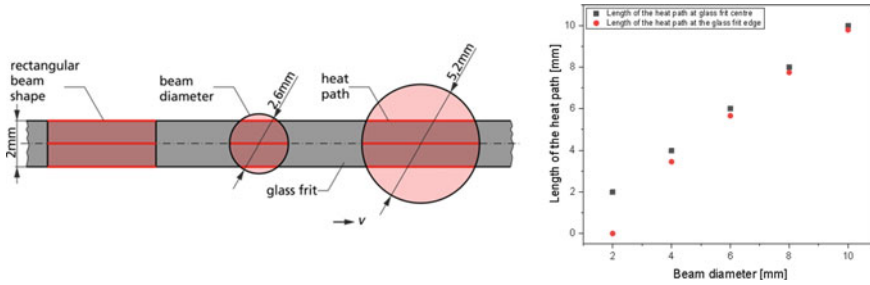
Fig. 27.7 Influence of beam shape and beam diameter on the heat path (for the calculations a glass frit width of 2 mm was assumed) (Kind et al. 2014)

limited to the dimensions of the laser spot hitting a volume element of material only once. The feed rate of the laser beam is typically in the range of several mm/s for thin materials (substrate thickness ≤ 1 mm) that are insensitive to temperature shocks, such as borosilicate glass, safety glass, or chemically toughened glass.

Due to the high local power input, the reduction of thermal stresses is more difficult with the contour bonding process than with quasi-simultaneous processing. Therefore, the demand for crack free bonding is more difficult to meet for sensitive materials because contour bonding enables only one interaction of laser beam and material. These materials require an adapted thermal management of the process where the formation of significant temperature gradients could be avoided. A variation of the beam diameter already influences the thermal management.

When using round laser spots, even a large beam diameter compared to the glass frit width can have a positive effect on thermal management and on the induced thermal stresses. Because for moving laser spots the amount of heat released in the glass frit is proportional to the length of the heat path (Aden et al. 2013) marked as red lines in Fig. 27.7

In contrast to rectangular beam shapes for circular spots, the length is maximal at frit center and minimal at the edges. As seen from the diagram in Figure 27.7, an increasing of the spot diameter makes the difference between the length of the heat path at the glass frit center and the length of the heat path at the glass frit edge smaller (for the calculations a glass frit width of 2 mm was assumed). Therefore, the released heat is more homogeneously distributed with respect to the width of the frit and thus reduces the thermal stresses.

For the float glass substrate shown in Fig. 27.8, the 2 mm width glass frit contour was continuously irradiated with a beam diameter of 5.5 mm. In this way, a homogeneous energy input was achieved, which finally led to a strong and tight connection of both glass substrates.

Material: Float glass
Thickness: 0,7 mm

Substrate size 340x340 mm²   Bond speed: 150 mm/min
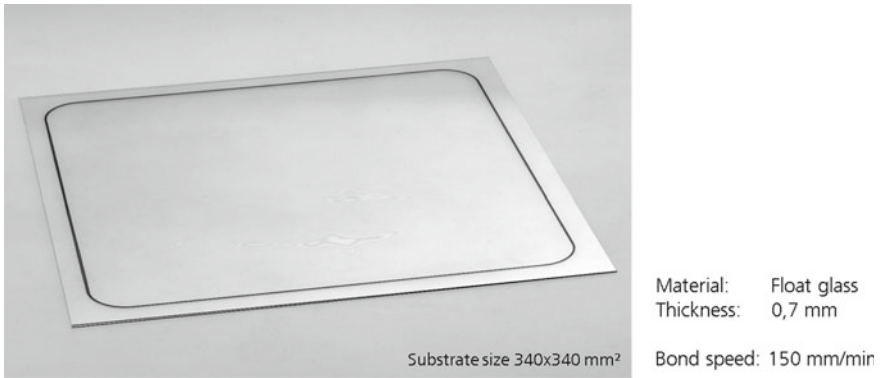
Fig. 27.8 Contour laser-based glass frit bonded float glass substrates

27.4.3   Laser-Based Glass Frit Bonding for the Production of Glass/Metal Joints

Laser-based glass frit bonding is not only suitable for the production of glass/glass, glass/silicon, and glass/ceramic combinations, but also for the production of glass/metal or ceramic/metal joints.

A major challenge for the production of these material combinations is the difference in the thermo-mechanical properties. The coefficient of thermal expansion of ceramic materials is usually significantly lower than that of metals. This difference leads to stresses which reduce the strength of the joint or, if the stresses exceed a critical limit, make a permanent joint impossible. High stresses lead to cracks in the area of the joining zone already during the cooling process. The choice of materials and glass frit is of crucial importance for the production of a tough and hermetically tight joint. The coefficient of thermal expansion (CTE) of all materials involved should be matched to each other. In the field of metallic materials, alloys with a low CTE are available which have been specially developed as joining partners for glass or ceramics.

Kovar®, for example, is a nickel–cobalt ferrous alloy that was designed to have substantially the same thermal expansion characteristics as borosilicate glass (~5 × 10^{-6}/K). If the material selection of the joining partners and the glass frit are matched to each other, a reliable joining can be realized as shown in Fig. 27.9.

Figure 27.9 shows Kovar® sleeves joined with a 400 µm thick borosilicate glass lid. Within a process time of 10 s, the glass lid with a diameter of 11 mm is joined to the metal sleeve using the quasi-simultaneous laser-based process.

Fig. 27.9 Kovar® sleeves covered with glass lid joined by a glass frit
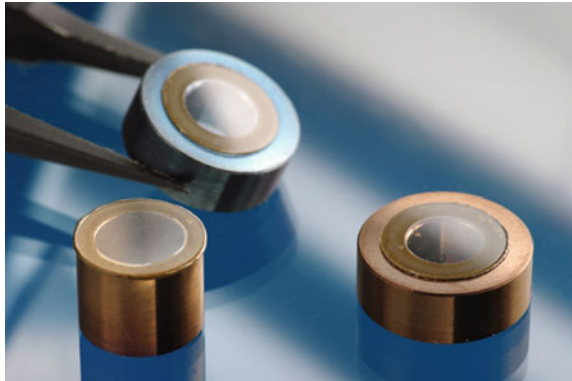
27.5 Conclusion

For laser-based glass frit bonding, the glass frit ideally has the optical properties required for the process. The absorbed radiation energy, which is spatially limited to the joining zone, is converted into thermal energy. The energy input leads to a local temperature rise exactly where the laser radiation is applied and absorbed. The energy is supplied to the process either quasi-simultaneously or continuously sequentially. The process, which is divided into a heating, wetting, and cooling phase, is suitable for many applications in which materials such as glass in uncoated and coated form as well as material combinations of glass/silicon, glass/ceramic, and glass or ceramic with CTE adapted metals have to be produced.

References

Aden M, Otto G, Duwe C (2013) Irradiation strategy for laser transmission welding of Thermplastics using high brilliance laser source. Int Polym Proc 3:300–305

Glas Trösch Holding AG (2012) Glas und Praxis - Kompetentes Bauen und Konstruieren mit Glas. Bützberg

Kind et al (2014) Laser glass frit sealing for encapsulation of vacuum insulation glasses. Phys Proc 56:673–680

Olowinsky A, Kind, H (2010) Laser glass frit bonding for hermetic sealing of glass substrates and sensors. In: Proceedings of LPM2010—the 11th International Symposium on Laser Precision Microfabrication

Part VIII
Ablation

Chapter 28
Transparent Materials

Christian Kalupka

Abstract The processing of materials like glass, which shows a high transparency in the visible regime, is possible when the laser pulse is sufficiently absorbed. Focused ultrashort laser pulses with pulse durations <10 ps can lead to such high intensities in the focal volume that nonlinear phenomena enable the necessary absorption of the laser pulse energy. Thus, a processing of transparent dielectric materials is possible with ultrafast lasers. The properties of ultrashort laser pulses enable different processing techniques to manufacture surface or in-volume modifications. By this, laser processing can be used for processes like cutting of glass or waveguide generation for integrated optics. This chapter discusses the laser processing of transparent dielectrics with ultrashort laser pulses.

The processing of materials like glass, which shows a high transparency in the visible regime, is possible when the laser pulse is sufficiently absorbed, so that modification or heating is induced. On the one hand side absorption can be realized by a beam source that emits laser radiation with a wavelength in the deep-UV regime (<250 nm), so that the single photon energy exceeds the band gap of the dielectric. On the second-hand side, the use of ultrashort laser pulses with a pulse duration <10 ps leads to nonlinear phenomena that enable an absorption even though the single photon energy is well below the band gap (Stuart et al. 1995, 1996). Thus, a processing of transparent dielectric materials is possible with ultrafast lasers. The properties of ultrashort laser pulses enable different processing techniques to manufacture surface or in-volume modifications. By this, laser processing can be used for processes like cutting of glass or waveguide generation for integrated optics (Kalupka et al. 2019; Schäfer 2012). This chapter discusses the laser processing of transparent dielectrics with ultrashort laser pulses.

C. Kalupka (✉)
Bosch Sensortec GmbH, 72770 Reutlingen, Germany
e-mail: christian.kalupka@rwth-aachen.de

28.1 Fundamentals: Ionization Mechanisms in Transparent Materials

Ultrafast lasers typically emit laser radiation with a wavelength in the infrared (e.g., Nd:YAG laser, $\lambda = 1064$ nm) or visible regime. In this case, absorption of the laser pulse energy by a transparent, dielectric workpiece can be realized by nonlinear mechanisms, which are enabled for high intensities in the order of 10^{13} W/cm^2 due to the short pulse duration typically below 10 ps (Vogel et al. 2005).

Initially, a valence electron can absorb multiple photons almost simultaneously when the total energy gain exceeds the band gap of the dielectric material. Consequently, a free electron is generated. The band gap for fused silica is 9.0 eV, thus for a laser wavelength of 1064 nm or a single photon energy of 1.2 eV, respectively, eight photons have to be absorbed to generate a free electron in the conduction band (Sudrie et al. 2002). Beside multiphoton ionization, tunnel ionization can generate free electrons, which describes the quantum tunneling of a valence electron into the conduction band as a consequence of a distortion of the atomic potential induced by the high electro-magnetic field of the laser radiation.

Both photoionization mechanisms are described by the Keldysh formalism (Keldysh 1965). Here, the photoionization rate is estimated and the interplay of multiphoton and tunnel ionization can be estimated by the Keldysh parameter γ_K.

$$\gamma_K = \frac{\omega}{e}\sqrt{\frac{c_0 \varepsilon_0 \mathrm{n} m^* E_{\mathrm{Gap}}}{I}}$$

Here, ω describes the laser angular frequency, e the coulomb constant, c_0 the speed of light in vacuum, ε_0 the dielectric constant, n the refractive index of the material, m^* the reduced mass, E_{Gap} the band gap energy and I the intensity of the laser radiation. For fused silica ($n = 1.45$, $m^* = m_e/2$, $E_{\mathrm{Gap}} = 9$ eV) and a laser wavelength of $\lambda = 1064$ nm, the photoionization rate is shown in Fig. 28.1 as a function of the Keldysh parameter γ_K or the applied intensity, respectively (Sudrie et al. 2002). Moreover, the rate for multiphoton ionization is calculated by the Kennedy approximation (Kennedy 1995), therefore, by a comparison of the overall photoionization with the multiphoton ionization rate, the role of tunnel ionization can be estimated.

For $\gamma_K \gg 1$ photoionization is dominated by tunnel ionization. The photoionization rate is less efficient compared to multiphoton ionization only, since the atomic potential is distorted in such a way, that the effective band gap increases and the absorption of an additional photon is necessary. For $\gamma_K \ll 1$, multiphoton ionization is the dominant mechanism to generate free electrons.

Subsequent to photoionization, the generated free electrons gain kinetic energy by inverse Bremsstrahlung absorption of additional photons. When the kinetic energy exceeds the critical energy $E_{\mathrm{crit}} = 1.5 E_{\mathrm{Gap}}$, collision with a valence electron is possible, which leads to a further increase of number of free electrons (impact ionization) (Kaiser et al. 2000). The ongoing impact ionization leads to an exponential increase of free electrons, which is referred to as avalanche ionization.
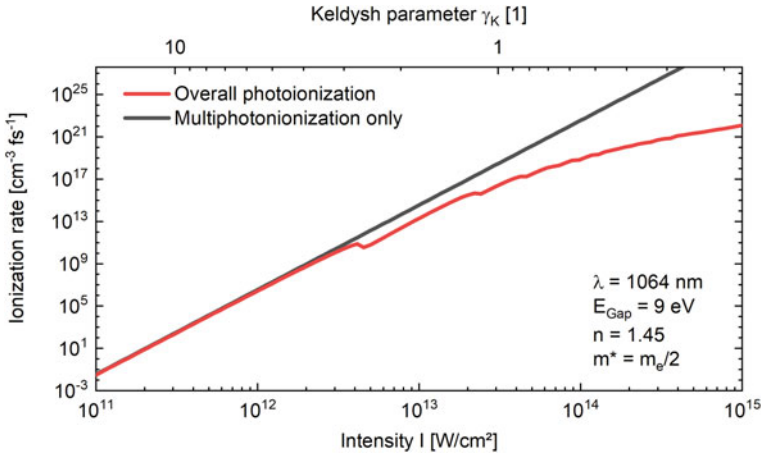
Fig. 28.1 Photoionization rate and multi-photoionization rate only for fused silica in dependency on the applied intensity I of the laser radiation or Keldysh parameter γ_K, respectively. Used parameters for fused silica $n = 1.45$, $m^* = m_e/2$, $E_{Gap} = 9$ eV and a laser wavelength of $\lambda = 1064$ nm

The free electrons transiently change the optical properties of the material, which can be approximated by the Drude formalism (Fox 2001). Typically, the high number of free electrons leads to a quasi-metallic state with increased reflectivity and a high linear absorption. Thus, the absorbed energy can be sufficiently high to induce material modification by non-thermal or thermal processes. Non-thermal processes are changes in the lattice or molecular structure which lead, e.g., to refractive index or density changes (Streltsov and Borrelli 2002; Little et al. 2010; Lin et al. 2011). Thermal processes generally describe the transfer of the optical energy to the lattice which leads to heating of the lattice followed by melting and vaporization of the material (Saliminia et al. 2006; Mishchik et al. 2013).

28.2 Processing Strategies

To achieve the sufficiently high intensities to induce nonlinear ionization and subsequent absorption of the laser pulse energy, the laser radiation is typically focused by spherical, aspherical, f-theta lenses or microscope objectives. Modification or ablation is localized in the focal volume. Depending on the applied focusing optic, the focal diameter results generally in the range from 1 to 10 µm.

For transparent dielectrics, three general processing strategies are shown in Fig. 28.2 can be realized with ultrashort laser pulses. First, by focusing the laser radiation onto the surface of the workpiece, ablation of a small surface layer can be realized. Second, focusing the laser radiation on the back side of the workpiece
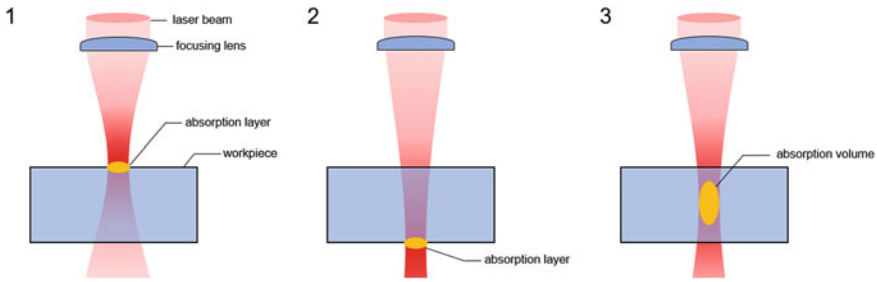
Fig. 28.2 Different techniques for processing transparent materials by ultrashort laser pulses

leads to the ablation of a small layer at the back side. To achieve back side abla-
tion, the beam must be able to propagate through the bulk with minor disturbance,
high absorption, or scattering. Third, when the focal volume is located in the bulk,
absorption can be localized in the bulk volume, which leads to modification without
any ablation at the front or back side of the workpiece.

28.3 Applications

28.3.1 Ablation Cutting and Drilling of Glass

Transparent materials like glass can be cut or drilled by gradual removal of material
from the front or back side. Since the typical ablation depth for a single laser pulse
is in the order of 100 nm, multiple pulses are necessary to realize a cutting process
of a glass substrate. For a specific cutting geometry, the laser radiation is moved
relatively to the workpiece by a galvanometer scanner, so that, e.g., a cutting line
is generated. By repeating the scanner movement, a groove is generated and further
deepening of the groove leads to a final cut of the workpiece.

For front side ablation, the surface profile exhibits a "U"-shape after the abla-
tion of several micrometer, see Fig. 28.3. The surface profile leads to refraction of
subsequent laser pulses. Thus, the local intensity is distorted and the ablation volume
decreases. Moreover, interference of refracted beams may lead to local intensity and
thus absorption spikes in the surrounding bulk material, which is shown in Kalupka
et al. (2017); Grossmann et al. 2017). Increasing the ablation depth, a "V"-shape of
the crater evolves. Here, refraction of the radiation is significantly increased so that
the ablation process is stopped.

Cutting or drilling processes can also be realized by a gradual ablation starting at
the back side of the workpiece and moving the focal position toward the front side,
see Fig. 28.4. By positioning of the focal spot on the back side, material is ablated on
the back side. Since the front surface is unmodified, refraction of the laser radiation
is avoided. A relative movement of focal position with regard to the workpiece is
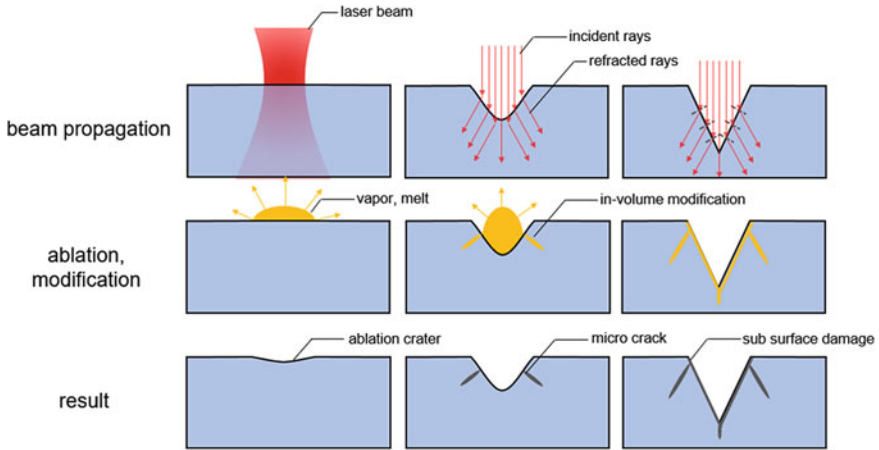
Fig. 28.3 Scheme of front side ablation process of a transparent material with ultrashort laser pulses. The columns correspond to different stages of the ablation process. The first row shows the beam distribution, second row the ablation or modification process, and the third row the ablation or modification result

necessary to ensure a stable ablation process. During the process, ablated material will be redeposited inside the groove. To ensure constant processing conditions, these contaminations have to be flushed off by process gas or a fluid.
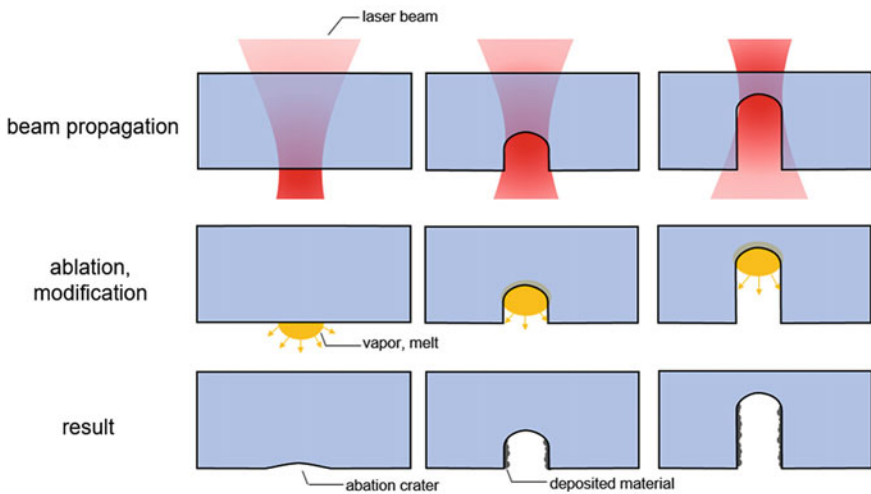
Fig. 28.4 Scheme of back side ablation process of a transparent material with ultrashort laser pulses. The columns correspond to different stages of the ablation process. The first row shows the beam distribution, second row the ablation or modification process, and the third row the ablation or modification result
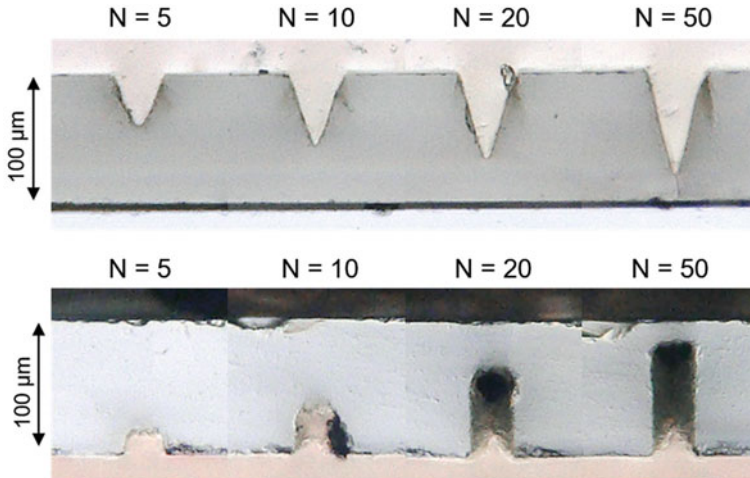
Fig. 28.5 Cross sections of grooves in 100 µm thin glass manufactured by front side (first row) and back side ablation (second row) in dependency on the number of scanned lines N

Microscope images of generated grooves in 100 µm thin glass for both front and back side ablation process are shown in Fig. 28.5. The grooves are generated by movement of the laser radiation into the image plane. Ablation was performed with a Nd:YAG ultrafast laser source with a central wavelength $\lambda = 1064$ nm, pulse duration $\tau = 10$ ps, pulse repetition rate $f_{\text{Rep}} = 200$ kHz, focal diameter $2w_0 = 30$ µm and a scanning speed of $v_{\text{Scan}} = 2$ m/s. The number of scanned lines N was increased gradually to investigate the evolution of the ablation crater and defects.

For the front side ablation, bulk modifications are observed in the vicinity of the ablation crater for $N = 5$. Increasing the number of scanned lines N, micro-cracks inside the bulk evolve as well as the "V"-shaped surface profile. Micro-cracks occur in the surrounding area of the ablation crater which reduce the mechanical strength of the glass. For back side ablation, a straight hole geometry is achieved for an increased number of pulses. Moreover, micro-cracks in the bulk can be avoided. The minimum achievable groove width corresponds to the focal diameter of the laser radiation.

Both techniques can be used for cutting or drilling of glass or other transparent materials. A manufactured array of micro holes in 200 µm thin glass by front side ablation is shown in Fig. 28.6. Each hole has an entrance edge length of 150 µm and is generated by a movement of the laser radiation with a galvanometer scanner on rectangular trajectories. Applications are via holes in thin dielectric substrates for microelectronics. Moreover, filter applications are possible for small hole diameters in the order of 10 µm or smaller. Cutting of cover glass can be used for consumer electronics.
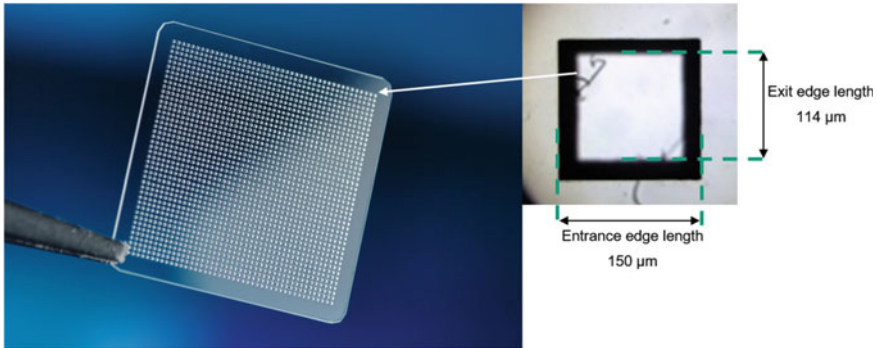
Fig. 28.6 Micro hole array in 200 μm thin glass manufactured by front side ablation with ultrashort laser pulses. The entrance edge length of each hole is 150 μm

28.3.2   In-Volume Modifications for Integrated Optics

For focusing the ultrashort laser pulses into the volume of a transparent material, in-volume modifications like refractive index changes or density changes are induced. For a Gaussian beam, the modification is generally located above the focal position as described in Grossmann et al. (2016). For a proper selection of the processing parameters, induced modifications show negative as well as a positive refractive index change as a consequence of density changes (Schäfer 2012; Beckmann 2011). For a positive refractive index change, beam guidance of light is enabled for total reflection of the input beam (Schäfer 2012; Streltsov and Borrelli 2002). A cross section of a modification in fused silica is shown in Fig. 28.7. Outside of the focal volume densification of material leads to an increase of the refractive index, which enables the guidance of visible light with $\lambda = 532$ nm. By the generation of a modification line by moving the laser radiation relative to the workpiece, waveguides in the bulk of the workpiece can be manufactured. Integrated waveguides show high stability and can be miniaturized, which can be used in applications like telecommunication (Eaton et al. 2006). Moreover, in-volume modifications can be aligned next to each other to manufacture gratings. Incident light is diffracted by these gratings and enables safety markings, beam splitters, or frequency filters in integrated optics.
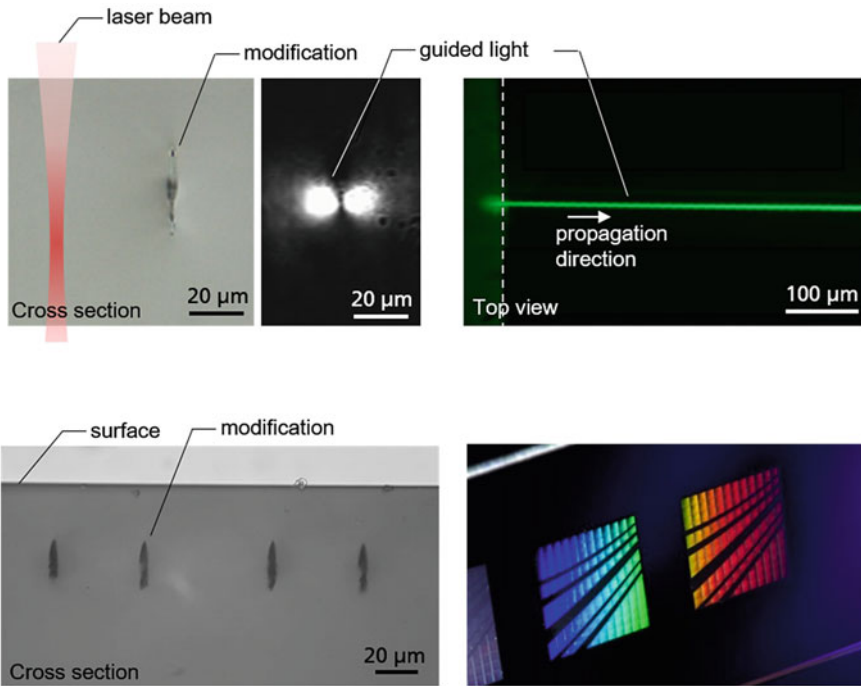
Fig. 28.7 Top row: Cross section of a single modification line in the bulk of fused silica generated with ultrashort laser pulses. The scanning speed was in the image plane. The modifications are used as waveguides. Bottom row: Cross sections of modification lines in the bulk of LiNbO$_3$, which can act as a grating

References

Beckmann D (2011) Spannungsinduzierte Volumenwellenleiter in Kristallen mittels Femtosekunden-Laserstrahlung (No. RWTH-CONV-143063). Lehrstuhl für Lasertechnik

Eaton SM, Chen W, Zhang L, Zhang H, Iyer R, Aitchison JS, Herman PR (2006) Telecom-band directional coupler written with femtosecond fiber laser. IEEE Photonics Technol Lett 18(20):2174–2176

Fox M (2002) Optical properties of solids Oxford University Press

Grossmann D, Reininghaus M, Kalupka C, Kumkar M, Poprawe R (2016) Transverse pump-probe microscopy of moving breakdown, filamentation and self-organized absorption in alkali aluminosilicate glass using ultrashort pulse laser. Opt Express 24(20):23221–23231

Grossmann D, Reininghaus M, Kalupka C, Jenne M, Kumkar M (2017) In-situ microscopy of front and rear side ablation processes in alkali aluminosilicate glass using ultra short pulsed laser radiation. Opt Express 25(23):28478–28488

Kaiser A, Rethfeld B, Vicanek M, Simon G (2000) Microscopic processes in dielectrics under irradiation by subpicosecond laser pulses. Phys Rev B 61(17):11437

Kalupka C, Großmann D, Reininghaus M (2017) Evolution of energy deposition during glass cutting with pulsed femtosecond laser radiation. Appl Phys A 123(5):376

Kalupka C, Nolte S, Poprawe R (2019) Energiedeposition von ultrakurz gepulster Laserstrahlung in Gläsern (No. RWTH-2019–04495). Lehrstuhl für Lasertechnik

Keldysh LV (1965) Ionization in the field of a strong electromagnetic wave. Sov Phys JETP 20(5):1307–1314

Kennedy PK (1995) A first-order model for computation of laser-induced breakdown thresholds in ocular and aqueous media. I. Theory. IEEE J Quant Electron 31(12):2241–2249

Lin G, Luo F, He F, Chen Q, Chen D, Cheng Y, Zhao Q (2011) Different refractive index change behavior in borosilicate glasses induced by 1 kHz and 250 kHz femtosecond lasers. Opt Mater Express 1(4):724–731

Little DJ, Ams M, Dekker P, Marshall GD, Withford MJ (2010) Mechanism of femtosecond-laser induced refractive index change in phosphate glass under a low repetition-rate regime. J Appl Phys 108(3):033110

Mishchik K, Ferrer A, de la Cruz AR, Mermillod-Blondin A, Mauclair C, Ouerdane Y, Boukenter A, Solis J, Stoian R (2013) Photoinscription domains for ultrafast laser writing of refractive index changes in BK7 borosilicate crown optical glass. Opt Mater Express 3(1):67–85

Saliminia A, Nguyen NT, Chin SL, Vallée R (2006) Densification of silica glass induced by 0.8 and 1.5 μm intense femtosecond laser pulses. J Appl Phys 99(9):093104

Schäfer D (2012) Ursächliche Prozesse der Brechungsindexmodifikation bei der Femtosekunden-Laserstrukturierung von Wellenleitern in Dielektrika (No. RWTH-CONV-143252). Lehrstuhl für Lasertechnik

Streltsov AM, Borrelli NF (2002) Study of femtosecond-laser-written waveguides in glasses. JOSA B 19(10):2496–2504

Stuart BC, Feit MD, Rubenchik AM, Shore BW, Perry MD (1995) Laser-induced damage in dielectrics with nanosecond to subpicosecond pulses. Phys Rev Lett 74(12):2248

Stuart BC, Feit MD, Herman S, Rubenchik AM, Shore BW, Perry MD (1996) Nanosecond-to-femtosecond laser-induced breakdown in dielectrics. Phys Rev B 53(4):1749

Sudrie L, Couairon A, Franco M, Lamouroux B, Prade B, Tzortzakis S, Mysyrowicz A (2002) Femtosecond laser-induced damage and filamentary propagation in fused silica. Phys Rev Lett 89(18):186601

Vogel A, Noack J, Hüttman G, Paltauf G (2005) Mechanisms of femtosecond laser nanosurgery of cells and tissues. Appl Phys B 81(8):1015–1047

Chapter 29
Thin Film Ablation

Andreas Brenner, Patrick Gretzki, Karsten Lange, Ludwig Pongratz, and Martin Reininghaus

29.1 Properties of Thin Film Materials

The range of industrial applications for thin film layers extends from LC displays, touch sensors, and biosensors to organic solar cells and flexible electronics (Fig. 29.1). The thickness of such layers typically ranges from a few nanometers to several 100 μm (Colligon and Vishnyakov 2020). In most cases, such layers are applied using processes such as plasma vapor deposition (PVD), chemical vapor deposition (CVD), or similar. For the electrical functionalization of surfaces mainly transparent conductive oxides (TCO), organic compounds, or pure metals are used, but not exclusively. An upcoming research topic is the possibility of building ceramic fuel cells using such processes (Cho et al. 2018).

Due to its high conductivity ($\sigma \approx 104$ S/cm) and high transparency of more than 80% in the visible spectral range, indium tin oxide (ITO) is currently the most frequently used TCO coating material. The TCOs are particularly important in the industry, as they can be used to produce flat, transparent field electrodes for displays.

Thin film ablatio is applied in order to isolate individual areas or to expose them for contacting. So far, etching methods or lithographic processes have been used for this purpose, but selective laser structuring has been established as an alternative, non-chemical technology (Granlund et al. 2000; Kagan et al. 2001; Cosseddu and Bonfiglio 2007; Zhang et al. 2002). The advantage of laser processing is the high flexibility and the possibility of selective processing. With an appropriate laser processing machine setup and it is possible to apply laser-based thin film ablation processes even on curved, free-form surfaces, which pushes conventional lithographic methods to their limits. In addition, individual layers can be selectively removed via a precisely adjusted intensity, even in the case of multi-layer structures. Consequently, the material properties of oxide layers and the basics of the ablation mechanisms are described in detail in the literature (Raciukaitis 2008; Yavas and Takai 1999; Brikas et al. 2007).

A. Brenner · P. Gretzki (✉) · K. Lange · L. Pongratz · M. Reininghaus
Pulsar Photonics GmbH, 52134 Herzogenrath, Germany

Fig. 29.1 Different examples of thin films coatings in industrial applications. (AbleTarget 2019)

However, the exact mechanisms and interactions involved in the ablation of thin layers are still the content of ongoing research. In particular, the fundamental background of debris formation at the edges, crack formation, and detachment mechanisms has not yet been fully clarified (Hellmann and Moorhouse 2014).

29.2 Mechanism of Thin Film Ablation

The earliest studies of laser-induced ablation of thin ITO layers were performed with Q-switched lasers and pulse durations in the nanosecond range. On transparent substrates, complete delamination of the ITO layers was realized, but this was associated with the appearance of burr at the edges of the ablated area and a pronounced thermal heat affected zone (Cabalin and Laserna 1998; Molpeceres et al. 2005). The formation of burr with a high profile of several 100 nm leads to defects in multilayer stack systems like in thin-film solar cells. Here, the burr penetrates the subsequent coatings and can thus trigger short circuits (see Fig. 29.2).
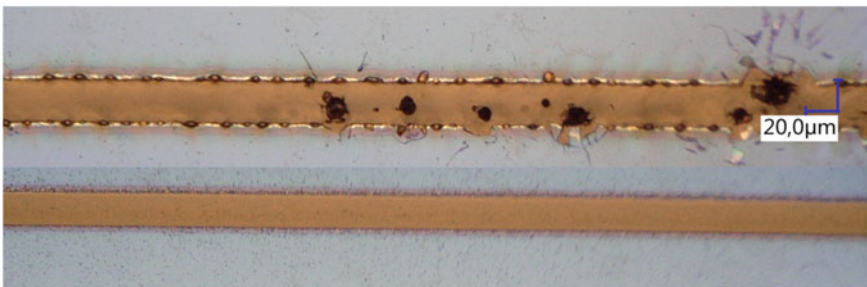
Fig. 29.2 Microscope images of ITO ablation on polycarbonate for different process regimes
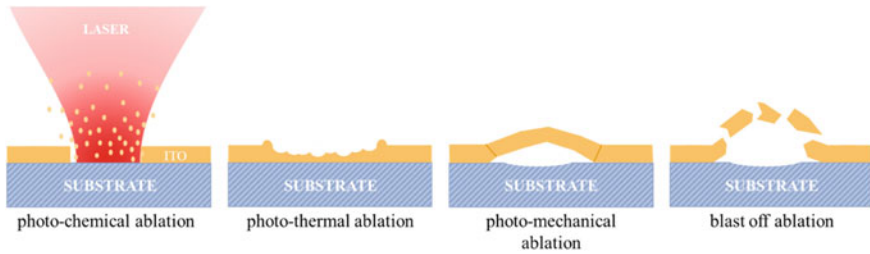
Fig. 29.3 Fundamental mechanisms of thin film ablation

For ultrashort pulsed laser radiation (USP) with typical pulse durations in the range of fs-ps, both burr formation and the thermal heat affected zone can be significantly reduced (Risch and Hellmann 2011; Park et al. 2006). In Fig. 29.2 the ablation of a 300 nm thick ITO layer with a USP laser source applying two different process regimes is shown. The formation of melt beads and the flaking of the surface layer due to thermal stress is clearly visible in the upper ablated track. The colored edges are formed by interference effects at the interface between substrate and the partially detached layer. The ablated track below is characterized by a significant reduction of burr formation to 20 nm and a strongly restricted thermal heat affected zone by adjustment of process parameters.

In Fig. 29.3 different fundamental thin film ablation processes are presented. The underlaying fundamental ablation mechanism strongly depends on the applied laser parameters (wavelength, pulse duration, focus diameter), the material properties, the layer thicknesses and the adhesion energy at the interface of layers to be separated.

In the photochemical processes, the absorbed optical energy exceeds the bond strength of material and the molecules are broken. This ablation process is usually observed when ultra violet (UV) laser radiation is applied to polymers or biological tissue. In this case, the combination of low bond strength of the molecules and the high photon energy of the UV laser radiation providing an energetic disbalance beneficial for the photochemical ablation process. For ultrashort pulsed UV laser radiation the wavelength and the pulse duration lead to reduced penetration depth of a few 10 nm and therefore to a strong confinement of the deposited energy. The resulting ablation process shows low heat conduction into the substrate and burr formation can be neglected in consequence. A dominant absorption in the thin film is the relevant prerequisite.

Photo-thermal processing is characterized by pulse duration of 10 ns or longer. The pulse duration significantly exceeds the electron–phonon interaction time of the material resulting in a thermal relaxation process and an increased energy penetration depth of several μm. When the lattice temperature reaches the melting temperature of the material, the formation of a liquid phase on the surface of the material begins. The resulting melt, several 10 nm thick, propagates at the speed of sound from the surface into the volume of the bulk material. This process is called "heterogeneous melting" (Rethfeld et al. 2002). Followed by additional energy deposition, the molten phase is

heated up to the vaporization temperature, and second phase transition to the gaseous phase takes place (Momma et al. 1996, 1997). This model is largely applicable for description of pulsed laser ablation processes with laser pulse durations in the range of ns up to µs. The material is mainly ejected by gas pressure. This generally leads to redeposition of molten material and heat-affected zones.

Photo-mechanical ablation or "spallation" takes place at pulse energies just above the ablation threshold. For metals, the electron–phonon interaction time is a few picoseconds and thus much smaller than the time period required for thermal expansion. Consequently, the heating of the irradiated volume can be assumed as "isochoric." The fast heating of a confinement volume results in significant stresses in the material. In the following, these stresses relax by deformation at the surface. At applied energies just above the ablation threshold, this phenomenon leads to material removal, called "spallation" or "photo-mechanical ablation" (Perez and Lewis 2002; Zhigilei 2003; Zhigilei et al. 2009). Here, the shock wave in the material causes the acceleration and removal of a thin, molten layer.

Many technical materials, such as ITO, belong to the class of ceramics. These brittle materials show high transparency and low ductility. Hence, for very thin layers only an insufficient amount of energy is absorbed in the thin film to be ablated. The incoming laser radiation is transmitted and absorbed at the underlying interface or substrate. If the deposited energy is high enough the substrate is evaporated at the interface. The resulting ablation products in form of a gaseous phase stretch the thin film. Subsequent pulses will increase the pressure at the interface until it exceeds the mechanical strength of the covering layer and the thin film is literally blasted off. This regime is mainly characterized by a pronounced formation of burr and chipped edges. Depending on the process regime and the material being processed, the thin film can break up into a large number of small ablated fragments. These fragments may be redeposited on the surrounding surface and impair the functionality. Due to their size, very small particles cannot be sufficiently removed by means of a cross jets or an suction unit. Therefore, in many cases a sacrificial layer is applied. The ablation products are redeposited on these soluble gel, plastic, or organic cover layers and can be removed in a subsequent cleaning process. Especially in the semiconductor and display industry, this is a necessary measure to avoid defects (Nagel et al. 2008).

29.3 Example Applications for Laser Thin Film Ablation

Safety and assistance systems such as adaptive distance control, lane departure warning, and emergency braking assistants are becoming increasingly important in the context of autonomous driving. Radar detection of objects is a fundamental detection technology that enables reliable object recognition in the distance. Current developments deal with an integration of a radar module into the headlamp that offers a variety of advantages: utilize unused space, extension of the radar field of view, temperature regulated area. One innovation thin film ablation process aims for the generation of functional microstructures on coated, light-transparent glasses or

plastics by means of ultrashort pulsed laser radiation (Figs. 29.4, 29.5). The 220 nm coating is electrically conductive (e.g., ITO) in order to obtain a beam-shaping function through a defined structural pattern with a structure resolution below 2 μm. The generated structure allows for the manipulation of the direction and the shape of the radar radiation in a transmissive or reflective manner. The structured optical module is designed to realize a tailormade beam shaping for a long-range radar (LRR), focusing the radar at a small angle of 5° with a gain of 20 dBi. This allows for the detection of obstacles at distances of 200–300 m.

Highly productive USP laser ablation is also applied for battery cell production. As a result of the heterogenic applications for lithium-ion batteries (wearables, consumer goods, etc.) there is a challenge to produce a wide variety of cell formats in a productive and flexible manner. Coating the metallic carrier substrate, which is only a few micrometers thick, with graphite-based material is a key production step. Due to the subsequent electrical contacting of the electrodes via tabs, parts of the metal foil must remain uncoated or have to be removed after a complete coating process. Utilizing a high-power ultrashort pulse laser source the graphite-based active layer can be ablated selectively with 1760 mm^3/min in a highly productive and residue-free way without
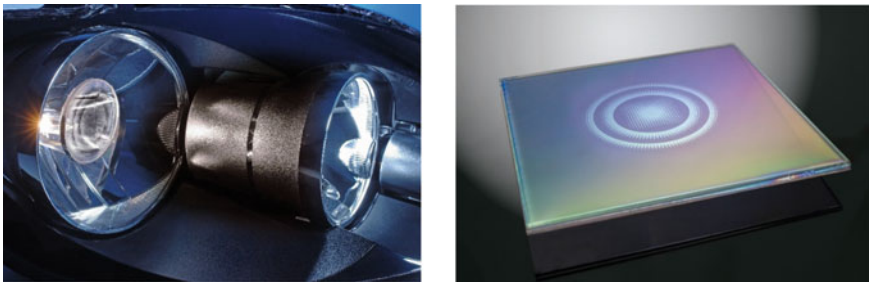
Fig. 29.4 Radar reflector that 220 nm ITO coating is selectively structured by ultrashort pulsed laser radiation for manipulating the direction and shape of radar radiation
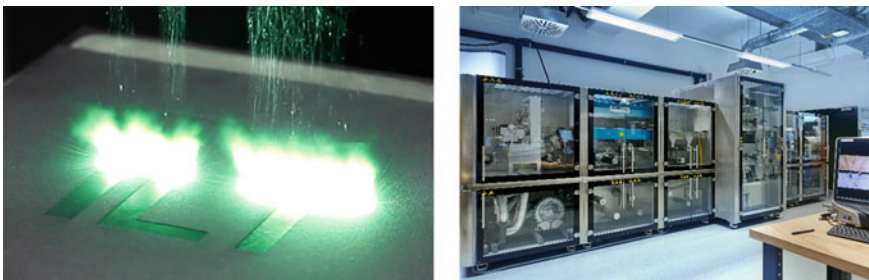
Fig. 29.5 Left: Using a tailored process anode material from very thin copper foils can be ablated at up to 1760 mm^3/min with a powerful USP laser source to expose surfaces for electrical contacts. Right: Roll-to-roll production line for structuring battery active layer in a continuous process with parallel laser beams

damaging the 10 μm thick underlying copper foil. In conjunction with today's usual active material layer thicknesses, this corresponds to an area rate of approximately 4 cm²/s. The quality of the laser ablated tab meets the high demands for a contact point that could be welded well in a subsequent process step. Due to the flexible laser manufacturing process, even non-standard cell formats that have to be adapted to the individual device design can be manufactured in an extremely productive manner. Current developments foresee roll-to-roll production with a belt feed of up to 60 m/min, where the laser beam is split into multiple beams for parallel processing to further increase productivity in a continuous process for industrialization.

Besides the classic silicon photovoltaics, organic photovoltaics (OPV) are becoming increasingly important due to their bendability and lightweight properties and the low-cost PET film that serves as substrate. The active medium consists of organic substances with a thickness of a few nanometers. A continuous roll-to-roll process with belt speeds of up to 5 m/min is suitable for mass production of those solar films (Fig. 29.6). After wet coating of several layers with a thickness in the nanometer range (10–250 nm) cw laser sources are used for uniform drying. Afterward, the nanometer-thick multilayer system is separated into individual cells by an ultrashort pulsed laser source with a pulse duration of 200 fs and a wavelength of 515 nm. This kind of laser scribing process ensures the suppression of burr at the edges or damages of adjacent layers avoiding short circuits in the layer stack. The productivity of the ablation process is increased by the use of multibeam optics, which split the laser beam into 11 parallel beamlets. Finally, edge deletion with a cw-laser source and encapsulation with a tailored laser welding process is used to capsulate the produced photovoltaic cells.
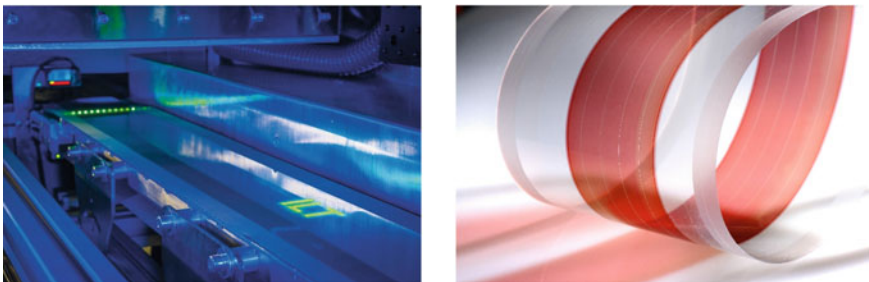
Fig. 29.6 Left: Ablation process of nanometer layers in a roll-to-roll setup by an ultrashort pulsed laser source with 11 multi-beams. Right: Final organic solar cell

References

AbleTarget (2019) Thin film coating application. https://www.abletarget.com/sliders/sputtering-targets-applications/thin-film-coating-application/

Brikas M, Gedvilas M, Rakickas T, Raciukaitis G (2007) Patterning of indium-tin oxide on glass with picosecond lasers. Appl Surface Sci, Bd 253

Cabalin LM, Laserna JJ (1998) Experimental determination of laser induced breakdown thresholds of metals under nanosecond Q-switched laser operation. Spectrochim Acta, Part B 53(5):723–730

Cho G, Lee YH, Cha S (2018) Thin film process for thin film solid oxide fuel cells—a review. J Korean Soc Prec Eng 35:1119–1129

Colligon J, Vishnyakov V (2020) Thin films. 1–55

Cosseddu P, Bonfiglio A (2007) A comparison between bottom contact and top contact all organic field effect transistors assembled by soft lithography. Thin Solid Films, Bd 515

Granlund T, Nyberg T, Stolz Roman L, Svensson M, Inganäs O (2000) Patterning of polymer light-emitting diodes with soft lithography. Adv Mater, Bd 12, Nr 4, 269–273

Hellmann R, Moorhouse C (2014) Laser patterning of transparent electrode films, from solar panels through high-end display. Ind Laser Solut Mag, Nr 11

Kagan C, Carmichael T, Kosbar L (2001) Patterning organic-inorganic thin-film transistors using microcontact printed templates. Appl Phys Lett 79:3536–3538

Lovell D, Hunt T, Laser ablation method for patterning a thin film layer. USA Patent US6838038B2

Molpeceres C, Lauzurica S, Ocaña JL, Gandía JJ, Urbina L, Cárabe J (2005) Microprocessing of ITO and a-Si thin films using ns laser sources. J Micromech Microeng 15(6):1271–1278

Momma C, Chichkov B, Nolte S, von Alvensleben F, Tünnermann A, Welling H, Wellegehausen B (1996) Short-pulse laser ablation of solid targets. Opt Commun 129:134–142

Momma C, Nolte S, Chichkov BN, Alvensleben FV, Tünnermann A (1997) Precise laser ablation with ultrashort pulses. Appl Surf Sci, Bde %1 von %2109–110, 15–19

Nagel M, Fardel R, Feurer P, Häberli M, Nüesch F, Lippert T, Wokaun A (2008) Aryltriazene photopolymer thin films as sacrificial release layers for laser-assisted forward transfer systems: study of photoablative decomposition and transfer behavior. Appl Phys A 923840:781–789

Park M, Chon BH, Kim HS, Jeoung SC, Kim D, Lee J-I, Chu HY, Kim HR (2006) Ultrafast laser ablation of indium tin oxide thin films for organic light-emitting diode application. Opt Lasers Eng 44(2):138–146

Perez D, Lewis LJ (2002) Ablation of solids under femtosecond laser pulses. Phys Rev Lett Bd 89

Raciukaitis G (2008) Laser structuring of conducting films on transparent substrates for electronics devices. Proc SPIE—Int Soc Opt Eng 7142:6

Rethfeld B, Sokolowski-Tinten K, von der Linde D, Anisimov SI (2002) Ultrafast thermal melting of laser-excited solids by homogeneous nucleation. Phys Rev B, Bd 65

Risch A, Hellmann R (2011) Picosecond laser patterning of ITO thin films. Phys Procedia 12:133–140

Ruffino F, Grimaldi MG (2019) Nanostructuration of thin metal films by pulsed laser irradiations: a review. Nanomaterials

Shelton BS (1998) Semiconductor wafer protection and cleaning for device separation using laser ablation. USA Patent US6849524B2

Yavas O, Takai M (1999) Effect of substrate absorption on the efficiency of laser patterning of indium tin oxide thin films. J Appl Phys 85(8):4207–4212

Zhang F, Nyberg T, Inganas O (2002) Conducting polymer nanowires and nanodots made with soft lithography. Nano Lett—NANO LETT, Bd 2

Zhigilei L (2003) Dynamics of the plume formation and parameters of the ejected clusters in short-pulse laser ablation. Appl Phys A, Bd 76:339–350

Zhigilei LV, Lin Z, Ivanov DS (2009) Atomistic modeling of short pulse laser ablation of metals: connections between melting, spallation, and phase explosion. J Phys Chem C 113:11892–11906

Chapter 30
Cleaning

C. Johnigk

In the last years beside conventional chemical, mechanical, or thermal cleaning techniques, laser cleaning has become more and more important. The reasons are advantages in process engineering (e.g., contactless, careful and damage free, high precision, low heat influence of the base material) as well as tightening legislation concerning hygiene observance and waste and/or pollutant avoidance (Wissenbach et al 2002).

Laser cleaning offers a new range of opportunities and processing techniques for coating and surface layer removal that can often overcome current processing limitations. This chapter discusses the basics of laser cleaning, e.g. laser material interaction, laser characteristics, and processing strategies for laser cleaning. Out of the wide field of applications of laser cleaning from micro-technology up to the cleaning of large buildings and constructions as well as new developments like mobile laser cleaning systems and specific applications are presented.

30.1 Basics of Cleaning with Laser Radiation

Cleaning/removal is based on locally confined, contactless interaction of pulsed or continuous laser radiation with the surface layer. Depending on the surface layer composition, thickness and the processing parameters, different cleaning mechanisms can be distinguished.

The content of this chapter largely corresponds to chapter 15.2 in Poprawe (2011) and has been supplemented with current examples.

C. Johnigk (✉)
Fraunhofer ILT, Aachen, Germany
e-mail: Carsten.Johnigk@ilt.fraunhofer.de
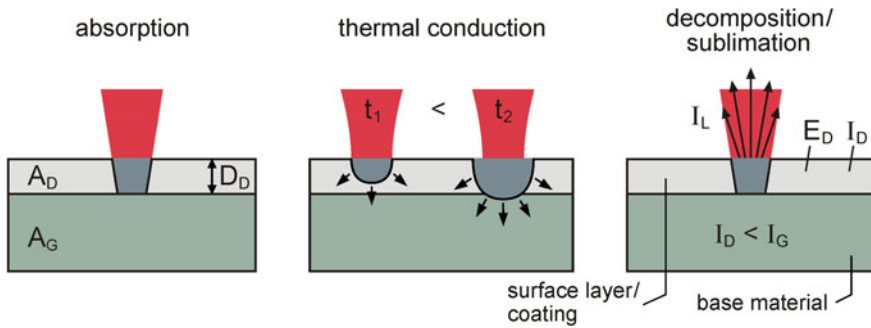
Fig. 30.1 Scheme of the ablation/cleaning process

The most important mechanisms are:

- Ablation by evaporation or decomposition of the surface layer (sublimation),
- Removal through thermally induced stress or by laser beam induced shock waves.

On technical surface layers, several mechanisms often appear at the same time, whereby the dominant mechanism depends on the material properties and the processing parameters, in particular wavelength, power density, and interaction time.

If the surface layer absorbs the laser radiation of the selected wavelength well and if the underlying base material has a small absorption $A_D > A_G$ (cf. Fig. 30.1), the cleaning process is called "self-limiting." At the beginning of the process a large amount of the incident laser radiation is absorbed and converted into thermal energy. Due to thermal conduction the base material heats up with rising interaction times $(t_2 > t_1)$. To avoid damage to the base material interaction time must be short. If the threshold power density for reaching the evaporation temperature of the surface layer is exceeded $(I_L > I_D)$, this leads to the evaporation of the surface layer. If the surface layer is completely removed, laser radiation interacts with the base material and is reflected to a large amount, so that the cleaning process terminates and no damage to the base material occurs (Fig. 30.1).

If the wavelength of the laser radiation cannot be selected in such a way that the process is self-limiting, then either the processing parameters have to be adapted accurately or process control and/or regulation measures are necessary, in order to avoid damage to the base material.

Two different processing strategies are used to clean larger areas (Fig. 30.2). When the mask image strategy is used, a mask with the desired pattern is projected onto the surface. With this strategy, special patterns can be produced or when using a square formed mask, large-scale cleaning can be performed. Care must be taken when designing the projection ratio to ensure the power density is exceeded in the desired cleaning area, which may limit the pattern size.

When the alternative scanning strategy is used, the laser beam is deflected with rotatable mirrors (galvanometers) and afterward the beam is focused with a special designed lens (e.g. F-Theta objective) onto the surface. Typical spot diameters are

mask image strategy
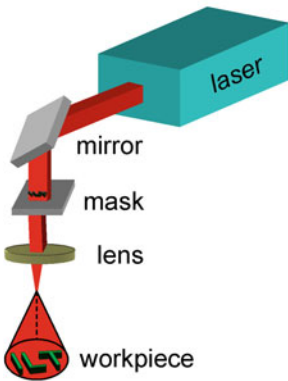
scanning strategy
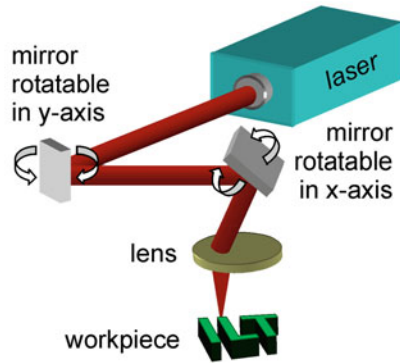
Fig. 30.2   Scheme of the processing strategies

in the range of 0.1–1.0 mm. Typically two perpendicular oriented galvanometers are integrated into a scan-head; this makes it possible to move the beam in an X-Y plane. Advantages of galvanometers are high speed movement of the laser beam with speeds up to several meters per second while having a high position accuracy and position repeatability. The dimensions of the X-Y plane (scan field) depend on the focal length of the F-Theta objective. With rising focal length the dimensions of the scan field will increase, but also the laser spot diameter, which leads to a decrease in power density. Therefore, F-Theta objectives with very long focal length which allow scan field dimensions in the range of meters can only be used when less power density is needed, or in combination with laser sources with high peak output power or excellent beam quality.

30.2   Example Applications for Laser Cleaning

Micro-technical applications. With increasing miniaturization and integration density of many micro-technical products the cleaning methods must fulfill higher requirements. Tendencies are a reduction of the surface areas to be cleaned into the μm^2 range, the increasing use of sensitive functional surfaces, the rising requirements to the cleaning quality (residual layers and/or particles with smaller dimensions and/or smaller concentrations must be removed) and quality control measures. During production, post-treatment and/or final assembly of these parts and assembly, groups a large number of cleaning and activation processes are necessary. Soldering stop lacquers, contamination, residues of plastics, lacquers, and oxide coatings must be removed. In particular for subsequent junction processes (welding, soldering, adhesive bonding) and coating processes (e.g., galvanizing), the appropriate part surfaces must fulfill the necessary purity requirements.

For the cleaning of micro-technical parts mainly short pulse lasers with wavelengths of $\lambda = 10.6\ \mu m$ (CO_2), $\lambda = 1.06\ \mu m$ (Nd:YAG), $\lambda = 532$ nm, 355 nm (Nd:YAG frequency-converted) $\lambda = 248$, 193 nm (excimer) are used with pulse durations between 5 and 250 ns. Due to the high power densities and the short interaction times the coatings are removed completely without damaging the base material.

An example of from micro-technology is the cleaning of molds, which are used in the micro system engineering as tools for the production of structured microparts. The molds are manufactured by galvanically filling up the female molds, which are made out of polymers. After the galvanic structure of the mold has been formed the female mold must be removed. This is achieved in a two-step laser cleaning process. In the first step more than 99 % of the polymers are removed in a rough cleaning process, with a TEA-CO_2- or CW-CO_2-laser (cf. Fig. 30.3) at high speed. After this cleaning process, a residual layer with a thickness of less than 1 μm remains on the surface. This layer is removed in a fine cleaning process with an excimer laser. After this two-step cleaning process the polymers have been removed completely without damaging the very sensitive surface with its structures.

The alternative cleaning process for removing the polymer by chemical etching leads to the destruction of the microstructures, which are present as single structure with aspect ratio (height to width) of more than 50 and lateral dimensions of less than 20 μm.
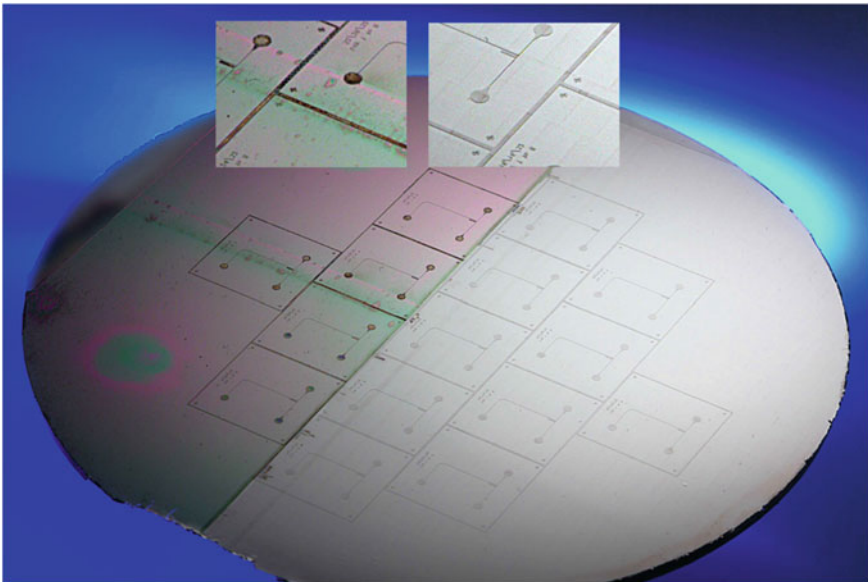
Fig. 30.3 Laser-cleaned mold for micro system engineering. Left side after rough cleaning with a CO_2-laser. Right side after fine cleaning with excimer laser

Cleaning of complex 3D geometrical shapes. Particularly in the case of safety-critical components, where any material changes due to thermal damage must be ruled out, this requires automated processes with precise path planning. The cleaning of a compressor rotor is listed here as an example (Johnigk 2020).

Within the scope of regular turbine engine maintenance, combustion residues must be removed from compressor rotors (including blades). Up to now, these rotors have been cleaned with wet-chemical processes. Due to tightening legislation, such as REACH & RoHS (Restriction of Hazardous Substances), this cleaning method is coming under increasing scrutiny and is to be replaced by a laser-based process. As disassembling the compressor rotor into its individual parts is costly and should be avoided, the complex component should be cleaned in its assembled state.

This maintenance faces a particular challenge since the components to be cleaned are complex and there is limited access to the surfaces of the individual parts. In particular cases, the CAD component data is also missing, e.g., due to the age of the component, so that this data has to be re-engineered by scanning the component in 3D and transferring the measurement points to mathematical surfaces. This data is then used to simulate the accessibility, to break down the processing into scannable segments by means of path planning (Fig. 30.4), and then to clean the component automatically in a multi-axis processing machine using the adapted laser parameters. The laser beam focus is tracked while the part geometry is processed.

Pulsed laser radiation can be used to automatically clean both blade and rotor surfaces in the assembled compressor rotor. The path planning for the laser treatment takes into account the dynamics of the axes as well as the required high processing speeds—in the range of several m/s. A 5 + 3 axis system (5 mechanical axes + 3 scanner axes) was used for this purpose. Figure 30.5 shows the compressor rotor automatically cleaned with laser radiation. For comparison, two unprocessed blades are shown in their initial state.

In-line cleaning. A further interesting application for laser cleaning which is getting more and more important is the integration of the process into production lines for mass production (Stollenwerk et al 1999). An important industry is the automotive and/or automotive supply industry, with the following potential applications:

- Local pre-treatment of pre-coated materials. The layers consist of KTL, water-based lacquers, powder coatings, or other plastic coatings. Laser cleaning can also be used for 3D parts.
- Removal of grease and oil residues
- Preparation of adhesive surfaces by removal of oxides and grease
- Partial lacquer removal from galvanized steel sheets for contacting the electrical mass without damage to the zinc layer

Other applications are the in-line cleaning of cylinder rolls or belt conveyors. In these applications, laser cleaning is carried out simultaneously to the production process. As an example, Fig. 30.6 shows the cleaning of a rotogravure cylinder, the residual "old" paint in the engraving must be removed.

The cleaning with excimer laser radiation (wavelength $\lambda = 248$ nm) is suitable due to the high absorption of ultraviolet laser radiation for the removal of thin paint
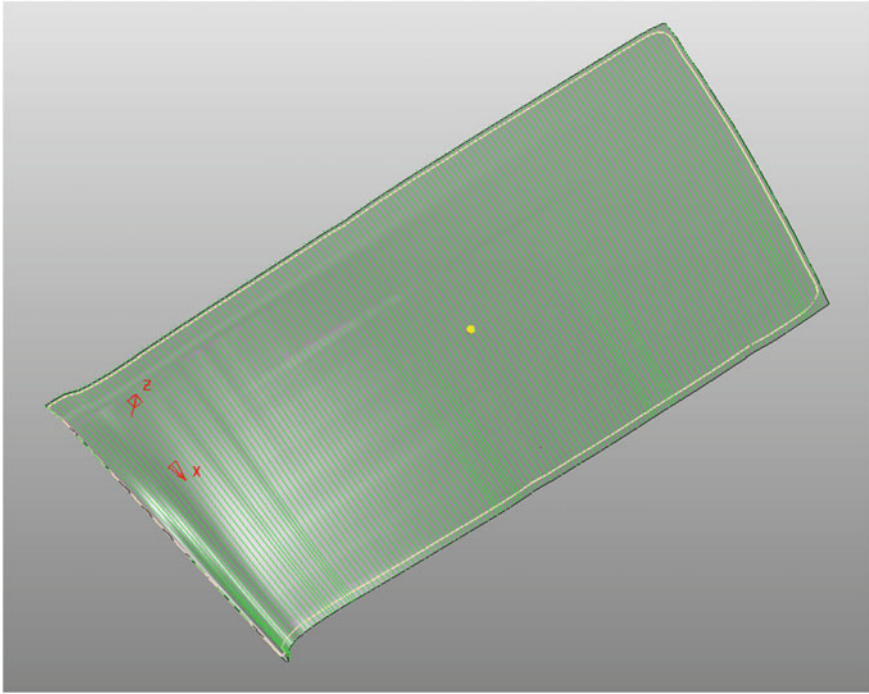
Fig. 30.4 Surface model of a single blade from a compressor stage with the individual laser trajectories (in green) from the path planning

layers in the range of a few micrometers. The chromium layer and the engraving of the rotogravure cylinder are not damaged if suitable laser beam parameters are used.

The beam delivery and shaping system consists of a cylinder lens telescope for beam shaping, reflective and/or transmissive beam homogenizer for the generation of a homogeneous power density distribution as well as zoom optics for adjustment of the square-shaped beam size. The laser beam is directed parallel to the cylinder axis.

Within a linear moving unit a deflection module causes the laser beam to be directed perpendicularly onto the cylinder surface. The linear moving unit can be moved over the complete length of the rotogravure cylinder ("flying optics"). As the rotogravure cylinder rotates the whole surface can be treated.

Figure 30.6 shows on the left the zoom optic and exhaust system as well as the surface of the rotogravure cylinder which has to be cleaned, on the right it shows a partly cleaned area of the rotogravure cylinder. The residual "old" paint is completely removed without affecting the engraving.

Cleaning of large buildings and constructions. In addition to the spatially limited cleaning of parts, new applications where large surfaces have to be cleaned get more and more important for laser cleaning. The probably most well-known
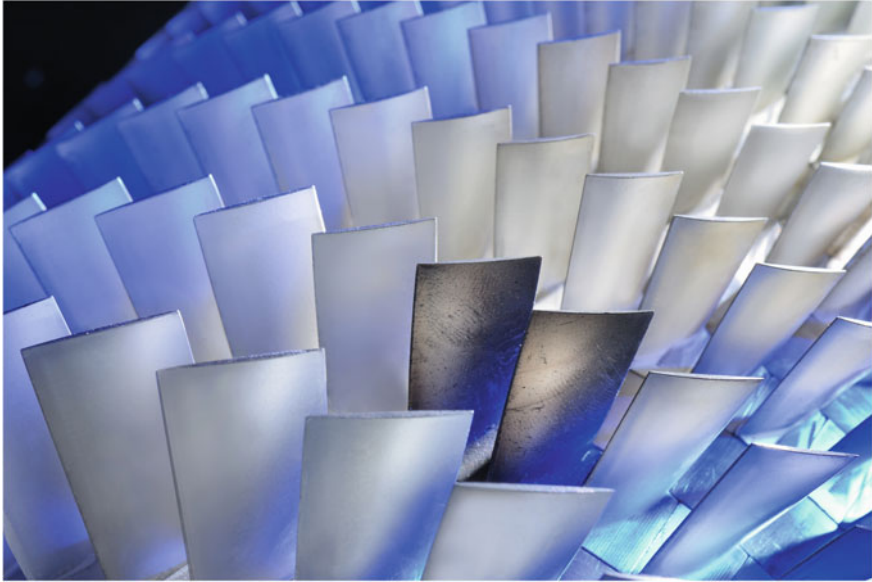
Fig. 30.5 Compressor rotor cleaned with laser radiation, two blades are in the uncleaned state
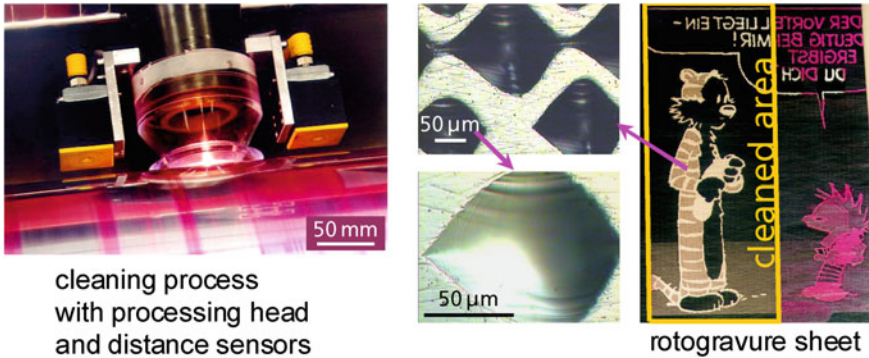
Fig. 30.6 Laser cleaning of a rotogravure sheet

application is the cleaning of historic monuments. The tasks which have to be solved are very different and show the large potential of the application.

Applications are:

- Cleaning of wood surfaces of lime, gypsum, color, wallpaper, and dirt layers without damaging the original wooden base material.
- Removal of crusts and films from weather-worn stone-surfaces, in order to remove stone-damaging deposits and to open the pores.

- Removal of corrosion crusts on bronze surfaces while conserving the natural patina.
- Removal of contamination and fungal attack, e.g., on paper.
- Opening and removal of paint designs, e.g., on wood.

But the previous work also shows that many fundamental investigations are still necessary for the determination of the parameter fields and to investigate the optical and thermal material properties, in order to fulfill the high requirements when restoring and conserving monuments.

Removal of paint coatings plays a dominant role if large surfaces of technical constructions and buildings have to be cleaned. In many of these applications multi-layer coatings with different compositions and layer thicknesses must be removed from sensitive substrates. One of the most examined applications is the paint removal from airplane components, which are submitted to regular maintenance.

When using chemical or blasting processes a large amount of secondary and sometimes hazardous waste results. Laser cleaning is used in particular for composite materials, whereby a selective paint removal down to the primer or a complete removal down to the base material is possible. Examples are the robot-supported paint removal of radomes and engine casings from the company SLCR.

In the above applications, the careful decoating without damaging the base material is of main interest. In contrast to this goal, the paint removal on large steel constructions (e.g., ships, bridges, large tanks, and high voltage transmission pylons) requires mobile laser systems, easy and flexible handling, robustness of the components, the complete collection of the waste products for environmental protection reasons and high cleaning speeds.

In a joint project Brünninghoff (2002), a mobile laser cleaning system was developed that fulfills all of the above requirements (Fig. 30.7). A Q-switch Nd:YAG laser is used providing pulses with pulse durations in the range of 100–150 ns. Best cleaning results are obtained with peak power densities in the range of 80–110 MW/cm^2. During the last decade of development, the output power of the laser source rose from 100 W to nearly 2000 W which leads to an increase of cleaning speed on the same factor (20). The laser beam is guided within a flexible fiber with a length of 50 m and a core diameter of 400 μm. The fiber connects the laser source with the hand-guided processing head. The processing head with integrated suction nozzle and integrated optical system (collimating optics, galvanometer scanner, and focusing lens) weighs about 2 Kg. The galvanometer scanner deflects the laser beam in such a way that the focused beam moves on a line. Perpendicular to this direction the processing head is moved by the operator so that large-scale cleaning with a high cleaning speed can be realized.

This system opens a wide range of new applications especially when coating thicknesses and the dimensions of the surfaces rise. A system with modified optics was successfully tested for the cleaning of railway rails. It works by directing a laser beam at the rail, where it rapidly heats up and ablates any contamination, including leaves and their residues, which may cause low adhesion. The special designed optic aligns and focuses the laser to a 20 mm wide stripe transverse to the longitudinal

average power: 2000 W
peak power: ~500 kW
pulse frequency: ~ 30 kHz
pulse duration: ~ 110 ns

laser source

resonator with antivibration elements
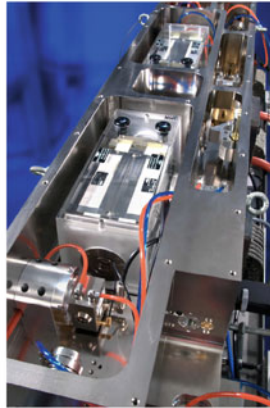
processing head

Fig. 30.7 Mobile laser cleaning system

direction of the rail. The whole device is mounted on a train. For each rail two laser systems with a respective output power of 1000 W are used, providing cleaning speeds of up to 60 km/h.

The future of laser cleaning will manly depend on further development of the laser source (e.g., increasing output power, more and shorter wavelength and shorter pulse durations) as well as further component development (e.g., processing heads in the multi-kW range with high processing speeds). This will offer new applications that will stimulate further development.

References

Brünninghoff H (2002) Reinigen von Hochspannungsmasten Konferenzbericht AKL

Johnigk C (2020) Reinigen Komplexer 3D-Geometrien mit Laserstrahlung Fraunhofer-Institut für Lasertechnik ILT Jahresbericht

Poprawe R (Hg.) (2011) Tailored light 2. Laser application technology. Springer-Verlag Berlin Heidelberg (RWTHedition), Berlin, Heidelberg

Stollenwerk J, Hoffmann H-D, Ortmann J, Schmidt G, Wissenbach K, Poprawe R (1999) High speed removal and structuring of surfaces in the automotive industry with a new diode pumped solid state laser source. Proceedings of the ICALEO 1999, San Diego, CA

Wissenbach K, Johnigk C, Willenborg E (2002) Innovative Entwicklungen im Bereich des Laserstrahl-Reinigens – Ein Überblick Proceedings Aachener Kolloquium Lasertechnik, S. 498

Chapter 31
Drilling

Check for updates

S. Janssen and D. Haasler

31.1 Introduction

Laser drilling is one of the most developed and industry-applied laser processes. In spite of being well understood and being applied in various technical and medical fields, the necessity for research and development has not diminished. Nowadays product specifications demand more precise geometries and tight tolerances, defect-free production, and productivities up to a few ten thousand holes per second. Laser-based machine tools are used for single pieces, small batches, series, and mass production. The development of high average power lasers in the multi-kilowatt range and pulse durations down to femtoseconds for ultrashort pulse lasers opens new fields for fundamental research despite being state-of-the-art in numerous mass production processes.

The mechanical contactless and thus wear-free drilling by means of laser radiation allows high-precision and materialographical quality, geometrical freedom, flexibility in production, and the possibility for automation. A great variety of technical relevant materials such as metals, alloys, ceramics, multi-layer systems, semiconductors, carbon compounds, fiber-reinforced composites, wood, paper, concrete, glass, diamond, or plastics can be drilled by means of laser radiation. Further advantages are high reproducibility, high drilling velocity, and the achievable aspect ratio. Thus, laser drilling is an alternative for classical drilling techniques such as mechanical drilling and milling, water jet drilling, electro discharge machining (EDM), electrochemical machining (ECM), and electron beam drilling.

Depending on the application and the requirements regarding geometrical and materialographical quality and productivity, laser drilling is the only applicable technique for drilling of holes with high inclination angles in e.g., turbine blades or combustion chambers with ceramic thermal barrier coatings (TBC). Nowadays,

S. Janssen · D. Haasler (✉)
Fraunhofer ILT, Aachen, Germany
e-mail: dennis.haasler@ilt.fraunhofer.de

laser drilling is applied in the industry due to the small achievable hole diameters (< 1 μm), the easy integration into existing production chains as well as the flexibility which means, for example, fast change of hole diameters or inclination angles or quick adaption to different materials without tool change. With short drilling times and an "on-the-fly" material machining, short cycle times and low machining costs can be achieved.

In laser drilling, the material removal process can be classified into two regimes: laser melt-dominated drilling and laser vapor-dominated drilling (Fig. 31.2). In the laser melt-dominated regime, the intensity of the laser radiation is approx. $\leq 10^8$ W/cm^2. The absorbed pulse energy leads to the formation of a melt pool in the drill base and only a small fraction of the material is vaporized.

This process can be divided into three key aspects (Fig. 31.1) (Schulz and Eppelt 2017; Yilbas and Sami 1997):

(I) **Melting and vaporization at the bottom of the hole:** The material is heated to such an extent that a distinctive molten bath is formed. As soon as the evaporation temperature is reached, a metal vapor forms. Due to the recoil pressure of the vapor, the melt is accelerated at the bottom of the hole.

(II) **Widening of the hole:** From the melt pool at the drill base, the melt front moves radially outwards along the hole wall and is expelled out of the hole. By lateral heat convection from the melt to the hole wall, the hole is widened. The longer the pulse duration the more pronounced is this effect.

(III) **Solidification of the melt at the hole wall**. The melt is decelerated on its way out of the hole due to friction with the solid hole wall. With sufficient recoil pressure, the melt is expelled out of the hole. However, a fraction of the

Fig. 31.1 Schematic overview of the key aspects of laser drilling including the case of hole closure in deep holes (Schulz and Eppelt 2017)
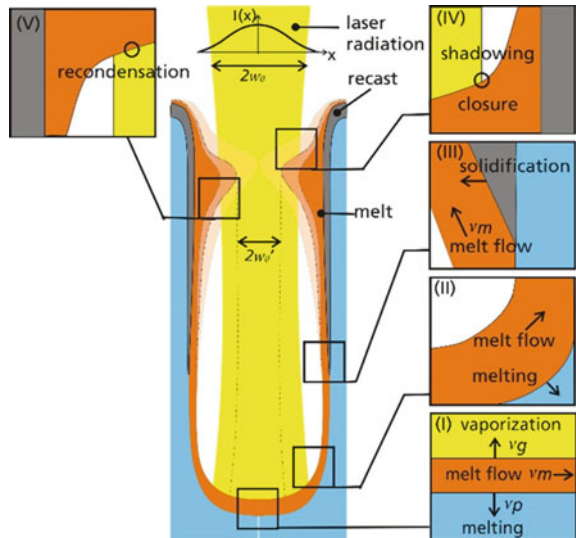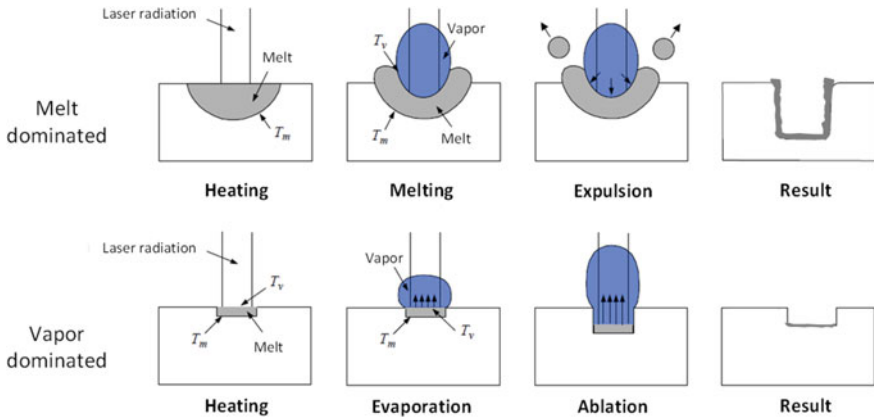
Fig. 31.2 Drilling with laser radiation: sketch of the material removal process for a melt-dominated drilling process (top row) and a vapor-dominated drilling process (bottom row)

decelerating melt cools down and solidifies on the hole wall inside the hole. This solidified melt layer remains in the drill hole and is called the recast layer.

In case of reaching drilling depths so that the decelerating melt at the hole wall stays within the hole two more effects take place. These effects can occur within a single laser pulse (single pulse drilling) or in a sequence of pulses (percussion drilling).

(IV) **Shadowing of the laser radiation and closuring of the hole:** If the peak intensity of the laser radiation is too low at the hole depth, the acceleration of the melt can be insufficient to expel it out of the hole. As the decelerating melt comes to a stop at the hole wall, the thickness of the recast layer grows to such as extent that results in a closure of the hole and therefore to a shadowing of the laser radiation. In case of closure, the laser radiation is reflected, diffracted, and absorbed in the closing cap, and the solidified mass is re-melted.

(V) **Recondensation:** Recondensation of vapor and plasma at the hole wall can occur. This results in an additional energy transfer to the hole wall.

The hole depths and diameters that can be drilled, the drilling speed and the speed of the melt front depend on numerous parameters relating to the laser radiation and the material being drilled. These include the spatial intensity distribution in the caustic curve, the temporal pulse shape, pulse energy, pulse duration, focus position, type and pressure of the process gas used, and thermal and optical properties of the material.

For minimizing melt creation the material is removed by means of laser vapor-dominated drilling. In this case, the irradiated intensity is much higher ($\sim 10^{12}$ W/cm^2), therefore, most of the material is directly evaporated and only a negligible fraction is molten. These high intensities are obtained by pulse durations in the

picosecond and femtosecond range. This results in higher precision at the expense of a highly decreased drilling rate compared to the melt-dominated drilling (Fig. 31.2).

For laser drilling, pulsed laser beam sources are utilized. There are mainly three reasons for the use of pulsed laser radiation:

- During the initial drilling process, only a blind hole is present. Thus, the ablated material has to be removed from the drill base through the hole entry, forcing the particles and the material vapor to be transported within the laser beam along the hole. With the laser radiation still being present, both the ablated material and the laser radiation are affected. The vapor is further heated up and might create a plasma while the particles are partly evaporated. Local evaporation pressure accelerates the molten particles back down into the hole. The laser radiation is absorbed and scattered by this interaction and less intensity is available at the drill base. This eventually decreases drilling speed and also the hole quality. Therefore, short interruptions of the laser irradiation are required to reduce or even avoid the aforementioned effects.
- In order to manufacture cylindrical holes with high aspect ratios, the energy transfer into the hole wall has to be minimized. If continuous wave (cw) laser radiation is utilized, the energy transfer and thus heat penetration depth is significantly increased which leads to melting of the hole and hence causes widening of the hole.
- The third reason is of a more technical nature. To take advantage of different effects in laser drilling such as the acceleration of melt or the evaporization of the material, particular intensity thresholds of the laser radiation have to be surpassed within a very limited time frame. In most of the cases, utilizing (shorter) pulses is the only way to increase the intensity to the required values.

In laser drilling, four different laser drilling techniques are used (Fig. 31.3), depending on the requirements concerning geometrical specifications (e.g., diameter, depth, conicity), geometrical quality (e.g., precision), materialographical quality (e.g., burr, debris, cracks, heat affected zone), and productivity (e.g., drilling time, drill rate):

- Single pulse drilling
- Percussion drilling
- Trepanning
- Helical drilling

Single pulse drilling is used in applications that require a large number of holes with diameters ≤ 1 mm and depths ≤ 3 mm. Each hole is created by means of a single pulse and a pulse duration in the range of 100 μs–10 ms. This drilling technique is often used in combination with "on-the-fly" (OTF) drilling, in which the drilling optic moves with a constant speed along the surface of the workpiece while the holes are drilled.

Percussion drilling is applied for holes with diameters ≤ 1 mm and depths up to 20 mm. The laser pulses are applied without relative movement between the laser
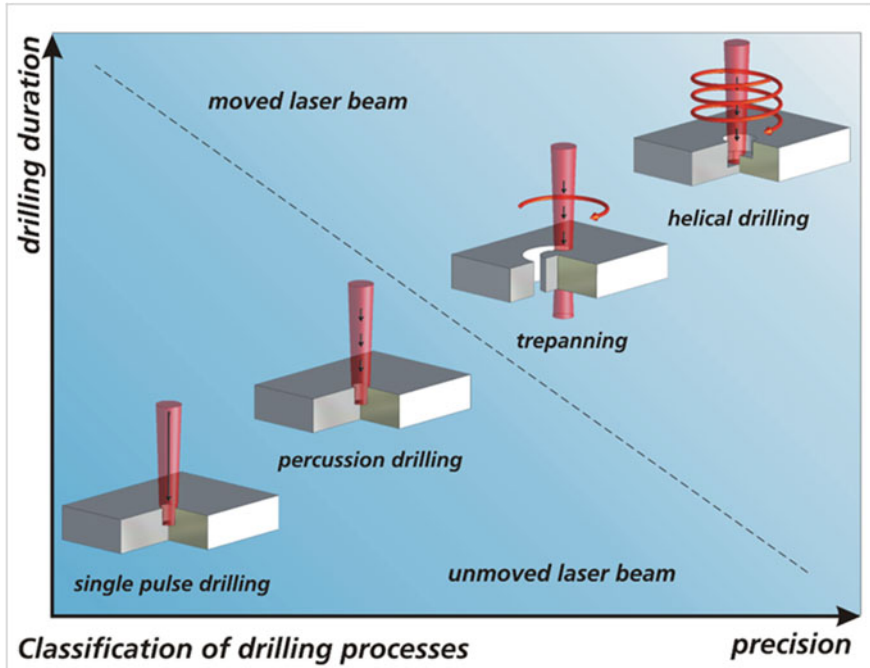
Fig. 31.3 Classification of drilling processes—drilling duration vs. precision

beam and the workpiece. Laser radiation with pulse durations from femtoseconds to milliseconds is used. The achievable hole quality differs with the pulse duration, intensity, fluence, temporal and spacial pulse shape, and the laser wavelengths in terms of recast layer formation, aspect ratio, conicity or cracks in the recast layer, and the base material.

Trepanning is a hybrid of drilling and cutting with pulsed laser radiation. Firstly, a through-hole is machined by a single pulse or by percussion drilling as a starting point (pilot hole). It is followed by a relative movement between the laser beam and the workpiece to cut out the contour of the hole. Providing the appropriate equipment (e.g., 5 axes positioning system), the machining of freeform holes with different shapes, contours, and different diameters for the hole entry and exit is possible. Pulse durations of the laser radiation used for trepanning are in the range of microseconds to milliseconds.

For *helical drilling*, the laser radiation is rotated relatively to the workpiece. Typically, pulse duration in the femto- to nanosecond regime is used. The drilling process is dominated by the vaporization of the workpiece material. This prevents the formation of a melt layer in the hole during laser drilling. Holes drilled by means of helical drilling are very precise with tolerances in the low micrometer range and exhibit a good microstructural quality of the hole wall and the area around the entry and exit.

31.2 Single Pulse Drilling

31.2.1 Process Description

Single pulse drilling is the most productive of all laser drilling methods and is used if a high drilling productivity is required, e.g., to produce filters and screens. The hole is drilled by the radiation of a single laser pulse. Yb:YAG fiber laser systems are mainly used for single pulse drilling as they provide pulse durations in the microsecond to millisecond range and intensities up to 1 MW/cm^2. Hole diameters of approx. $30 - 1,000\ \mu$m are attainable with drilling depths of up to 3 mm.

Single pulse drilling is often used in combination with an "on-the-fly" (OTF) process. In this case, a relative movement between the drilling head and the workpiece along the surface is realized and the holes are drilled during the movement. A productivity of several hundred holes per second can be obtained by this process as the positioning time can be eliminated for each individual hole. The pitch between two holes is determined by the combination of the pulse frequency and the relative speed. To prevent the creation of an elongated hole due to the movement of the laser during the pulse, the following inequation has to be respected:

$$d_{hole} \gg s_{hole} = t_p \cdot v_{rel}$$

with the hole diameter d_{hole}, hole displacement s_{hole}, pulse duration t_p and the relative movement velocity v_{rel} between the workpiece and the laser beam.

In general, a short pulse duration and low speed of movement are beneficial in an OTF-drilling process. However, process requirements especially in terms of high drilling rates often represent a contradiction with respect to the above-stated inequation.

High pulse-to-pulse stability of the laser radiation is required in single pulse drilling to maximize the reproducibility as fluctuations cannot be statistically evened out as in percussion drilling, trepanning, and helical drilling. Nevertheless, variations of the hole entry and exit diameter in the range of 10% are to be taken into account as the ablation is based on a melt-driven process. (Rodden et al. 2000).

31.2.2 Influence of Process Parameters

Based on the desired hole diameter and hole shape, the beam quality (M^2) should ideally be adaptable. When a small hole or a hole with a high aspect ratio shall be created, an M^2 close to 1 is desirable (Rohde 1999). A minimum focal diameter can be achieved or the divergence is minimal for the required spot size. When aiming to drill a larger hole with a diameter of a few hundred micrometers, a high M^2 is often favorable. Due to the increased spot diameter both the intensity and the divergence are at least one order of magnitude lower. Thus, the projected intensity on the hole

wall is too low to create a cylindrical hole. In such cases an increase of M^2 helps to increase the divergence and therefore the projected intensity. The same measure can be taken to create negative conical holes. Modern, fiber-based laser beam sources typically have an M^2 below 10. An adaption of this value is then easily possible by coupling the laser beam into a second fiber with a bigger core diameter. By this measure an increase of M^2 by a factor up to 10 is achievable.

For a given focal diameter, an increasing pulse peak power leads to a series of effects: The drilling speed increases and results in a deeper hole. Also, the entry and exit diameter increase roughly in a linear manner. An increase of the pulse duration at a constant peak power results in a deeper hole and slightly increasing hole diameter. (Rohde 1999).

The process gas pressure has not a direct effect on the material removal process during the pulse. As described in the introduction, a fraction of the material which is irradiated also evaporates. The recoil pressure of the vapor that accelerates the melt is in the range of (several) 10 MPa. The maximum static pressure on the surface of the workpiece obtained by the process gas on the other hand is only in the range of ~ 0.4 MPa and therefore not able to greatly affect the melt movement. However, the process gas pressure can still have a significant influence on the final hole shape. If the pressure is (too) high, it can prevent the melt from leaving the hole which will then accumulate around the hole entry and eventually close it. If the process gas pressure is (too) low, two effects can occur. Expelled melt can accumulate at the nozzle and on the optical elements, leading to the destruction of the optical elements or a stop of the drilling process at some point. Also, the melt might not be fully expelled from the hole after breakthrough but remains at the exit and forms droplets. A trade-off is usually required between the two mentioned effects when defining a process gas pressure for a specific process. (Rohde 1999).

31.2.3   Application Examples

Single pulse drilling is used in medical engineering, automobile manufacturing, aviation, and toolmaking. In medical engineering, one application of single-pulse drilling is to produce suture holes on surgical needles (Fig. 31.4) (Dürr 2003). The hole entry diameter is between 50 and 600 μm. Aspect ratios of 4:1 to 12:1 are achieved. Up to six needles per second are drilled.

In automobile manufacturing, conical holes with an exit diameter of 50–100 μm are drilled in 0.95 mm thick stainless steel in fuel filters (Fig. 31.5). On the fuel exit side, the holes have to be burr-free. A productivity rate of 110 holes per second is achieved by means of OTF processing (Dürr 2003; Rapp 2003).

In the aviation industry, the perforation of specific surfaces of an aircraft has a series of applications that are already found in series production and also in current research. With the aid of the perforated areas, the flow along the surface is manipulated for different purposes. Most of the applications have in common that a very high number of tiny holes (range of 1,000,000 holes/m^2) with a diameter of well
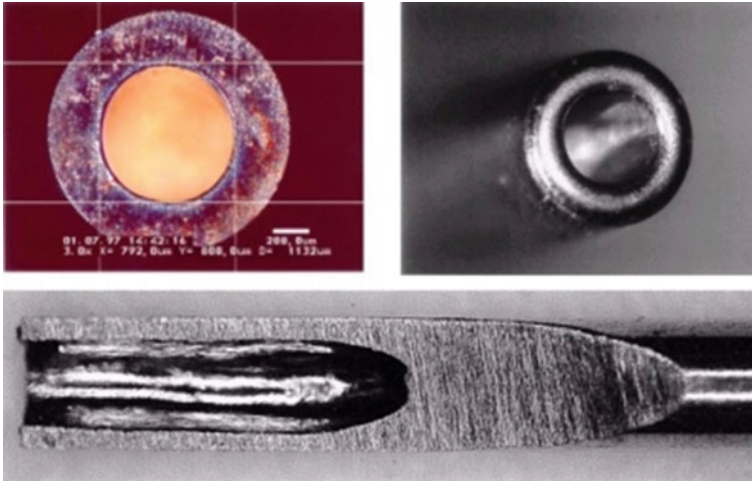
Fig. 31.4 Top view and longitudinal section of a single pulse drilled surgical needle (Dürr 2003)

Fig. 31.5 Microholes in fuel filter for automotive applications (Rapp 2003)

below 100 µm need to be manufactured in 3D-shaped surfaces. Only an OTF-based laser drilling process can achieve the required production rate of several hundred holes per second in combination with small hole diameters to enable an economic production of such parts. One function of the drilled components is to suck in a part of the boundary layer through the holes to decrease the air flow drag. In combination with a special design of the airfoil shape, this application is known as hybrid laminar flow control (HLFC). Since 2014, this technology is implemented in the vertical and horizontal tail plane of Boeings 787–9 model. Current research projects as the European Clean Sky program investigate how this technology can also be implemented

on the wings (Uchtmann et al. 2017; Ocana et al. 2019). This would reduce the fuel consumption up to 10%. In another application, if applied at the tail plane, the rudder efficiency can be increased by blowing out air on one side of the rudder. The holes can also be utilized to blow (hot) air or liquid onto the airplane surfaces for anti-icing purposes (Uchtmann et al. 2017). For the mentioned applications, typically 1 mm thick titanium sheets are drilled with a pitch of less than 1 mm.

Another application for OTF-drilling in the aviation industry is acoustic liners which can be found at the internal wall of engine nacelles at the intake. They are implemented to damp the engine noise and are composed of a porous or perforated top layer and an underlying cavity. In this case, bigger and deeper holes need to be manufactured. Hole diameters of a few $100\,\mu$m need to be drilled into the aluminum with a few millimeter thickness (NASA 2002).

31.3   Percussion Drilling

31.3.1   Process Description

In percussion drilling material is removed by means of consecutive pulses of laser radiation to create a hole. Higher aspect ratios compared to single pulse drilling (approx. up to 50:1 compared with 20:1) can be achieved as a series of pulses is applied on a single spot. The diameters of the holes produced typically range from $10\,\mu$m to 1 mm with drilling depths of up to 25 mm. Percussion drilling can be utilized for the entire range of pulse durations from femtoseconds to milliseconds based on the application. The pulse duration, fluence respectively intensity distribution, and temporal pulse shape of the laser radiation have a direct effect on the quality of the drill hole in terms of the melt film thickness (recast), aspect ratio, conical tapering or cracks in the melt film and the substrate material. For a melt-dominated drilling process, the depth of the drill hole increases with each pulse as does the required recoil pressure to expel the melt from the drill base during drilling. The recast on the drill hole wall can accumulate until the melt forms a closure. This happens especially if the pulse peak power and thus the intensity at the drill base is too low in order to accelerate the melt out of the hole. The velocity of the liquid melt at the hole wall is mainly dependent on the absorbed intensity at the drill base (Schulz and Eppelt 2017). During percussion drilling, this process of closure and re-opening recurs at different points in the drill hole due to the increase of the drilling depth, loss of intensity at the drill base, and the accelerated melt which accumulates at the hole wall. Single or multiple closures can also form during a single pulse with a pulse duration in the millisecond range or longer.

31.3.2 Influence of Process Gases

During percussion drilling with pulse durations in the microsecond and millisecond range, most of the material is expelled from the drill hole in its molten state. Depending on the type of material involved, different process gases are used to influence or support the drilling process. The use of oxygen triggers chemical reactions that lead to an increase in temperature during the drilling process and cause the material on the drill hole wall to oxidize. Nitrogen can be used to nitrate the material, while argon serves to block additional chemical reactions during the process. The driving forces generated by the gas stream can lead to either increased or reduced expulsion of the melt. If argon is applied with too much pressure, the melt is not fully expelled out of the hole (Fig. 31.6a). In the case of oxygen the pressure has almost no effect on expulsion (Fig. 31.6b) (Walther et al. 2008).

Studies on spatter (debris) formation when processing NIMONIC 263 and on the influence of process gas on the drilling process (Low et al. 1999, 2000) have shown that, with oxygen as process gas, the occurring spatter is only 10% to 20% as thick as with compressed air, nitrogen, or argon. During experiments with oxygen as process gas, the debris accumulating around the entry of the drill hole was less adhesive than that which accumulated while using the other gases (Low et al. 1999). This has been observed for many different types of metals. The exothermal reaction of oxygen with the molten material causes the melt to overheat. When using the process gas argon, the melt has a higher cooling rate (Low et al. 2000) and solidifies in multiple layers that can be metallographically detected by means of longitudinal sections of the drill hole (Low et al. 2000). Additionally, the influence of process gas on the average drilling speed was investigated (Schneider et al. 2005). The use of
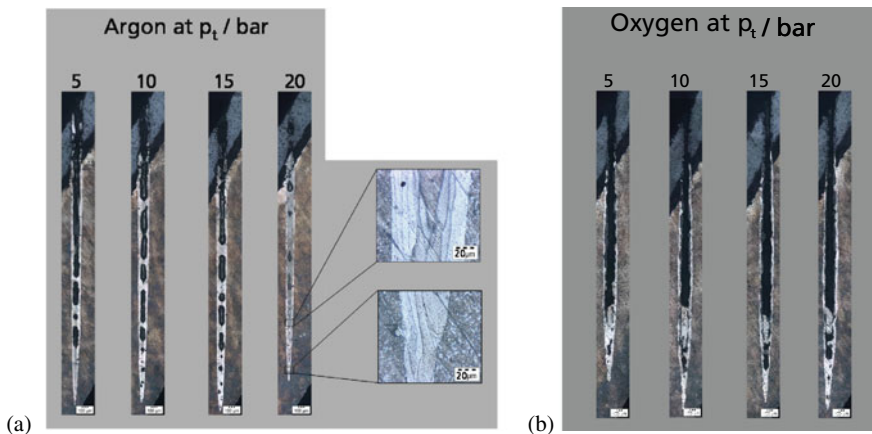
Fig. 31.6 Blind drill holes in a multi-layer system, each produced with the same number of pulses. **a** Incomplete expulsion of the melt due to too much pressure while using argon as the process gas. **b** No influence by the pressure of the process gas on the expulsion of the melt while using oxygen (Walther et al. 2008)

nitrogen results in a greater average drilling speed and a larger diameter at the hole exit than the use of oxygen. Flow visualization is used to investigate the development of the gas stream after leaving the nozzle, as a function of the recoil pressure and the distance between the nozzle and the surface of the workpiece (Schneider et al. 2005, 2007). The gas stream slows and laterally diverts the melt expelled from the drill hole. A part of the vaporized material is locked in between the shock wave of the gas stream and the surface of the drill hole (Schneider et al. 2005, 2007). Further investigations have been carried out on the effects of oxidation during the drilling process using oxygen and argon as process gases (Patel and Brewster 1990, 1991a, 1991b). The developing oxide layer influences the drilling result through changes in the absorption characteristics, the melting temperature and the additional reaction enthalpy.

31.3.3 Influence of Beam Parameters

In drilling materials for aerospace applications using a 10 kW Nd:YAG laser, it has been demonstrated that pulse shaping can help to control the taper of the hole and thus to produce a variety of drill hole geometries (Low et al. 2001; French et al. 2003; Low and Li 2002). Likewise, it has been exhibited how modulating the temporal intensity curve of the laser beam in the microsecond range influences the taper of the drill hole (Low and Li 2002).

Investigations on percussion laser drilling with pulse durations in the femtosecond to millisecond range show that a higher quality in terms of the thickness of the melt film can be achieved (Chen 2000; Karnakis et al. 2005). The plasma generated during the drilling process with shorter pulse durations can either shield the surface of the material from the incident laser beam or support the drilling process (Bugayev et al. 2005; Paul et al. 2007; Forsman et al. 2005; Treusch 1985; Haasler and Finger 2019). Studies on drilling in heat-resistant alloys demonstrate the applicability of modulated laser radiation with multiple ns pulses (bursts) as an alternative to established systems with pulse durations in the ms range for processing such objects as turbine components (Serebryakov et al. 2005).

The ablation rate decreases with increasing drilling depth under otherwise constant process parameters (Kononenko et al. 2002). The changing ablation rate can be explained by the developing conical geometry of the drill hole. The absorption of laser radiation at the base and on the wall of the drill hole is largely determined by the projected intensity and the local Poynting vectors (Hermanns 2018; Janssen et al. 2019). If the radius of curvature at the base of the drill hole is less than the thermal penetration depth, the heat losses and the minimum intensity required for ablation are greater. If the intensity is lower than the threshold intensity, no more material is ablated.

The temporal pulse shape of the laser radiation influences the geometry of the drill hole. Tapering can be reduced by modulating the laser radiation (Low and Li 2002). Various working groups have achieved an increase in the ablation rate by using

Fig. 31.7 Formation of multiple recast layers during percussion drilling: **a** 1 pulse, **b** 2 pulses, **c** 3 pulses, **d** 4 pulses
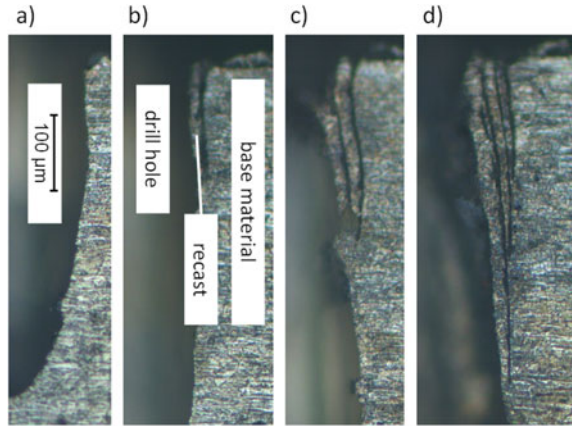
double and multiple nanosecond and picosecond pulses with pulse distances in the ns range (Forsman et al. 2005; Hartmann et al. 2005; Lapczyna et al. 1999). When applying bursts of ns pulses with pulse distances in the µs range, the ablation rate increases with shorter pulse distances and a higher number of pulses per burst at a constant level of burst energy. In the case of nanosecond pulse bursts, pulse distances between 20 and 90 µs result in the highest ablation rate. Further division of the pulses into a picosecond substructure leads to no further increase in ablation (Ostermeyer et al. 2005). The superposition of pulsed (millisecond range) or cw laser radiation on laser radiation with a shorter pulse duration and therefore greater intensity results in increased expulsion of the melt and a faster drilling speed (2019).

During percussion drilling at low pulse repetition rates, the recast is composed of multiple layers (Fig. 31.7). These can fuse to form a single layer if the repetition rate is high enough to prevent the melt from re-solidifying between pulses.

At high repetition rates, the laser radiation is additionally coupled into the vapor or plasma, depending on the pulse intensity, generated by the preceding laser pulse. By temporally modulating the laser radiation, the plasma interaction can be reduced and it is possible to produce a variety of drill hole geometries. The hole geometry can be influenced by temporally modulating the laser radiation at a constant pulse output and pulse energy (Fig. 31.8).

31.3.4 Applications

Percussion drilling is used in areas such as tool and die making, medical engineering, automotive engineering, aviation, and tool manufacturing. Applications include the drilling of cooling holes in turbine blades of aircraft engines and stationary turbines, holes in filters, sieves and nozzles for ink-jet printers, and feed-through holes for solar cells (Karnakis 2005). In the aircraft industry, Yb:YAG fiber laser systems are used
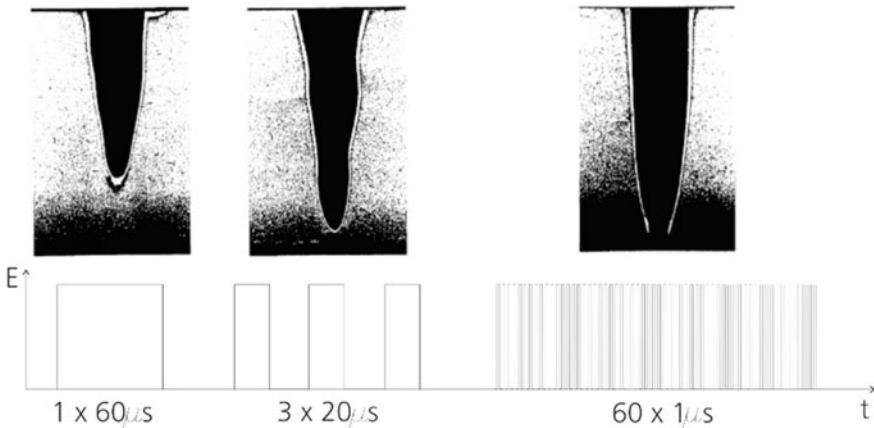
Fig. 31.8 Drill-hole geometries produced with differently modulated laser radiation (Treusch 1985)

for such applications as drilling holes in combustion-chamber plates or the blades of aircraft turbines. During the manufacture of drawing dies, tiny holes with diameters between 10 and 50 µm are drilled in diamond (Meijer et al. 2002; Niederhauser 1986). Laser drilling has also become the established method of producing micro-vias in printed circuit boards (Meijer et al. 2002; Lei and Davignon 2000). Micro-vias are feed-through connections, i.e., drilled and subsequently plated holes that connect different signaling layers.

Lubricating-oil holes in engine components have so far been drilled mechanically or by EDM / ECM due to the required drilling depths of between 8 and 20 mm and the target diameters of 800 µm. It takes several minutes to drill each hole the conventional way, whereas percussion drilling reduces this time to 9 s (Lehner et al. 2003). Holes with high aspect ratios (1:40) are percussion drilled in spinning nozzles (Fig. 31.9).

Molds for slush molding of, e.g., car dash boards require venting holes to let out the air during the forming process. The hole diameters in the functional surface of the mold have to be between 150 µm and 200 µm. Smaller holes are prone to clogging whereas larger hole diameters can be seen on the final part after the slushing process. The venting hole outlet has to be larger so that loose particles can easily exit the mold without clogging (Fig. 31.10). The percussion process starts on the outer surface (larger hole diameter) and is shut off shortly after the drill through on the inner side of the mold. The drilling time for a 45° inclined hole is approx. 24 s with a power-ramped QCW fiber laser (Uchtmann and Kelbassa 2013).
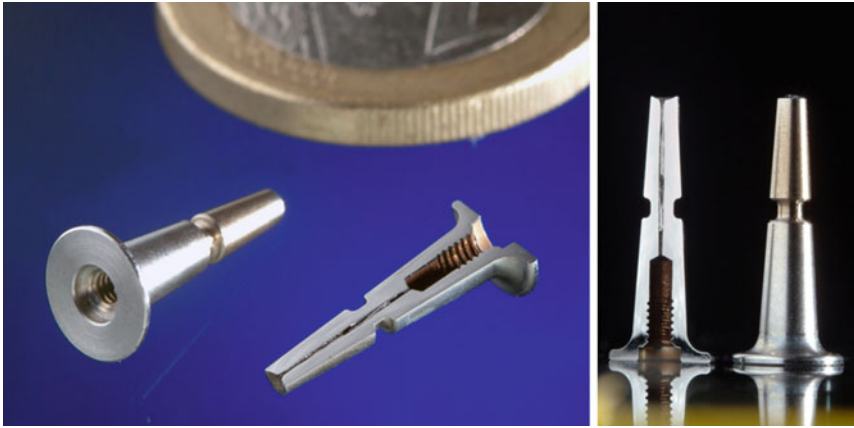
Fig. 31.9 Laser-drilled spinning nozzles. Hole diameter: 200 μm ± 20 μm, Hole length: 8 mm. *Source* ILT

Fig. 31.10 Longitudinal section of venting holes in a tool mold for car dash boards. *Source* ILT
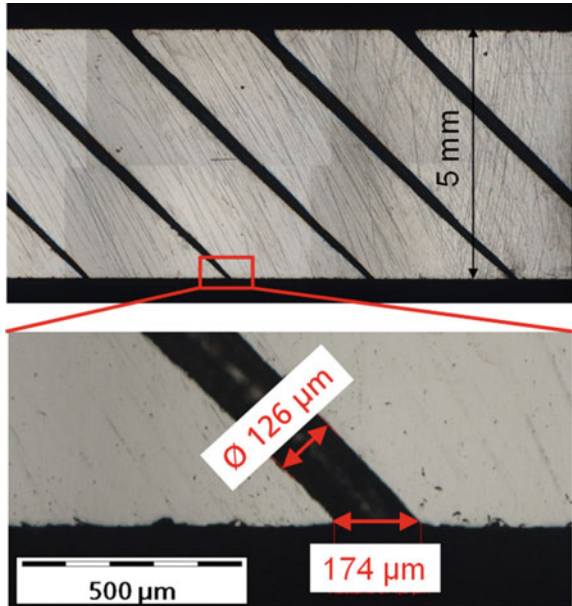
31.4 Trepanning

31.4.1 Process Description

Trepanning is a combined drilling and cutting process with a laser beam diameter that is significantly smaller than the to-be drilled hole. Firstly, a through-hole is pierced by percussion drilling. Subsequently, the final hole shape is created by cutting out the contour of the hole by a relative movement between laser beam and workpiece (Fig. 31.11) by a pulsed cutting process. This movement can be achieved using a positioning table, scanning optics, or special-purpose trepanning optics. This process allows not only drill circular holes but any other shape such as rectangular or triangular holes. The size of the laser beam defines the precision of the drilled hole. The minimum diameter of a trepanned hole and the maximum workpiece thickness are predefined by the initial percussion drilling operation. Typical drill hole diameters are 0.1–1 mm. During percussion drilling, the melt is expelled through the entry of the hole. After breakthrough and during the cutting process, the melt is expelled through the exit of the kerf or drill hole. The melt expulsion is significantly increased if a co-axial process gas is utilized which increases cutting speed and hole quality (Willach 2005; Chien and Hou 2006; Horn et al. 2000; Willach et al. 2004).

For a continuous cut in the trepanning path the laser pulses have to overlap (linear pulse overlap (PO) $\geq 0\%$) (DIN 32540 2012). The bigger the PO (with sufficient pulse energy), the thicker the materials that can be drilled through and the smoother the trepanning kerf. However, high PO values mean that the feeding rate or scanning speed is low which increases process times. Another factor to be considered is that in a melt-dominated drilling process, the heat affected zone (HAZ) can increase due to heat accumulation in the local drilling area if the pulse overlap is too high. For high productivity and materialographical quality, mostly depending on material type, thickness of the workpiece, and the geometry of the to-be drilled hole(s), a suitable process parameter window has to be identified. A general approach for process development is to count the required number of pulses for drill through of
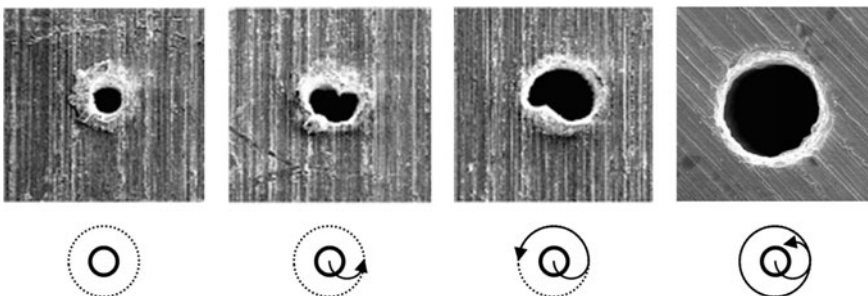
Fig. 31.11 Schematic diagram of the trepanning process (Willach et al. 2002)

the starting hole (percussion hole) and use this number as the number of pulses per spot $N_{p/s}$ on the trepanning path. Then solve for the trepanning velocity v_s:

$$N_{p/s} = \frac{1}{1 - PO} = \frac{f_{rep} \cdot (d_{foc} + v_s \cdot t_p)}{v_s}$$

with the laser repetition rate f_{rep}, the focal diameter d_{foc}, and the pulse duration t_p. For (ultra-)short pulse durations, the term $(v_s \cdot t_p)$ can often be neglected.

The taper, roundness, and roughness of the drill hole can be improved by increasing the pulse overlap or by performing repeated cycles of the trepanning path. The productivity is improved by lowering the pulse overlap and thus the number of pulses per spot. The lower the number of pulses per spot, the higher the risk of not creating a continuous trepanning kerf.

31.4.2 *Process Gas and Gas Pressure*

During trepanning, the thickness of the melt not only depends on the laser pulse properties but also on the type of process gas, gas mass flow through the hole or kerf, and the thickness of the workpiece. The melt formed during trepanning can close the holes again due to rapid deceleration at the hole wall if the mass flow through the hole or kerf is too low. This happens more likely if the static process gas pressure is below 10 bar. In order to efficiently blow out the melt, the process gas pressure or nozzle distance has to be changed in such a way that impingement of the gas jet does not hinder the melt from being expelled out of the hole (Horn et al. 2000; Failed et al. 2002; Khan et al. 2006). A multiphase CFD simulation model calculating the effective shearing force along the melt surface due to the flow of process gas was able to show that compression points of the process gas out of the co-axial gas nozzle right above the hole entry of the workpiece surface led to a reduced mass flow through the hole. Due to smaller acceleration forces induced by the process gas on the melt inside the hole, the recast layer increases. A countermeasure is to either slightly increase or sometimes even decrease the process gas pressure or to slightly change the distance of the gas nozzle to move compression shock points away from the workpiece surface. The deeper the trepanning kerf, the higher the required mass flow in order to remove the melt from the hole.

The recast thickness during trepanning of Inconel 718 has been investigated and a process gas pressure window has been identified for a given material thickness (p ~ 15 bar) where the recast layer thickness is reduced by the proper removal of molten material (Chien and Hou 2006). At larger pressure values (~25 bar) the recast layer thickness is increased and cracking can be detected in the recast layer and the base material. This can be ascribed to the forced convection cooling and thus thermal shock of the melt from hot to cold caused by the process gas (Chien and Hou 2006; Tam et al. 1993).
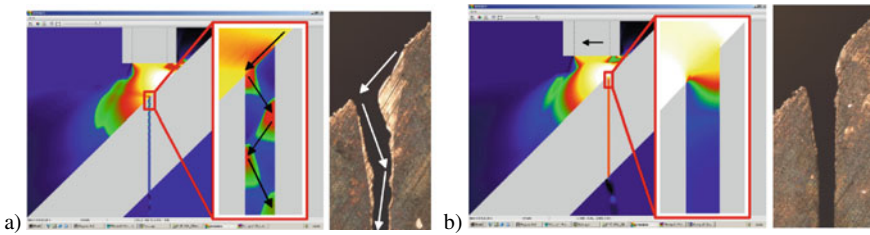
Fig. 31.12 Longitudinal sections of 45° inclined holes (trepanning, process gas argon) in CMSX-4 and simulation of static pressure with **a** centered nozzle, **b** displaced nozzle (Willach et al. 2003)

When drilling inclined holes additional effects such as local accumulations of solidified melt can occur. For that reason a simulation tool is adopted to analyze the gas jet of the conical nozzle (diameter 1 mm) placed above a 45° inclined sheet surface (Willach et al. 2003). The arrangement of a centered nozzle (Fig. 31.12a) is compared to a nozzle laterally displaced (Fig. 31.12b) in order to position the stagnation point directly above the hole.

For a centered nozzle, the stagnation point is located next to the hole, leading to a gas flow crossing the hole entry and hence not fully penetrating the hole (Fig. 31.12a). The gas flow is partly reflected into the hole entry, resulting in local maxima of the static gas pressure distribution at the hole entry in which the gas flow is redirected into the hole. The local static pressure maxima show the deflection points of the main gas flow inside the hole channel. Next to those maxima no directed flow is present but vortices are created. Those favor the accumulation of melt which can be detected in longitudinal sections at the locations of the calculated minima in the static pressure distribution within the hole (Fig. 31.12a). For the laterally displaced nozzle, the simulation predicts an increase of the pressure and a more homogeneous distribution at the hole entry and avoidance of oscillations in the pressure distribution inside the hole. As seen in the longitudinal section in Fig. 31.14b, the thickness of the solidified melt at the hole entrance can be reduced by using the laterally displaced nozzle. A more uniform flow through the hole is achieved this way and therefore no accumulations of melt are present anymore (Willach 2005; Willach et al. 2003; Lugscheider et al. 2005).

31.4.3   Type of Process Gas

Trepanning of 2 mm thick CMSX-4 samples by microsecond-pulsed laser radiation is investigated by adopting different process gases (Fig. 31.13). The mean thickness of the resolidified melt in the holes trepanned with Nitrogen is 30 µm. Chemical composition measurements of the resolidified melt show a nitration of the superalloy forming a melt with high viscosity that cannot be removed properly by the process gas flow. When using Oxygen, the resolidified melt has a thickness of 20 µm and
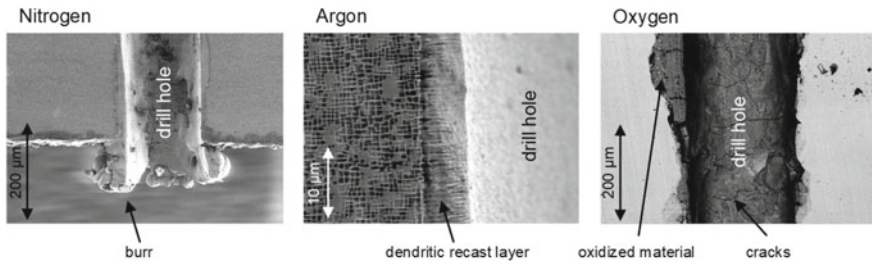
Fig. 31.13 Process gas influence during trepanning in CMSX-4 with a thickness of 2 mm (Lugscheider et al. 2005)

exhibits bubbles and cracks. Compared to nitration, oxidation forms a melt with a lower viscosity. On the other hand, melt is not removed completely by the process gas flow. Argon is found to be the most effective process gas in reducing the thickness of the recast layer (10 μm) for CMSX-4. The resolidified melt at the hole walls reveals an orientated microstructure (Lugscheider et al. 2005).

Depending on the Rayleigh length of the focused laser beam employed, the laser intensity may not be sufficient to expel it from the drill hole or trepanning kerf beyond a certain drill hole depth. The melt remains in the drill hole as a closure or recast layer on the hole wall, and cannot be entirely removed even after several trepanning cycles. The use of argon as process gas helps to cool the melt and supports the solidification process (Chien and Hou 2006; Tam et al. 1993; Lugscheider et al. 2005; Poprawe et al. 2008; Kreutz et al. 2007).

The use of oxygen as process gas generates higher temperatures and pressures in the hole during drilling as a result of the additional reaction enthalpy (Patel and Brewster 1990). This permits to drill deeper holes. The melt is highly oxidized and has less tendency to adhere to the hole entrance and exit area than in holes drilled using argon as the process gas.

31.4.4 5-axis Trepanning

It is possible to represent different drilling geometries (conical, freeform) by a 3D movement of the positioning system (Fig. 31.14a). For instance, the cylindrical profile of trepanned holes by describing the contours of a negative conical shape ($d_{ENTRY} < d_{EXIT}$) can be increased (Patel and Bovatsek 2003). Simultaneous positioning on 5 axes permits almost any freeform hole shape to be produced in addition to round drill holes. The example illustrated in Fig. 31.14b and c shows the geometry of a contoured cooling-air drill hole in a gas turbine component (Kreutz et al. 2007; Kelbassa et al. 2006). In this case, with the aid of 5-axis trepanning, the contour of the entry side is different from the contour on the exit side.
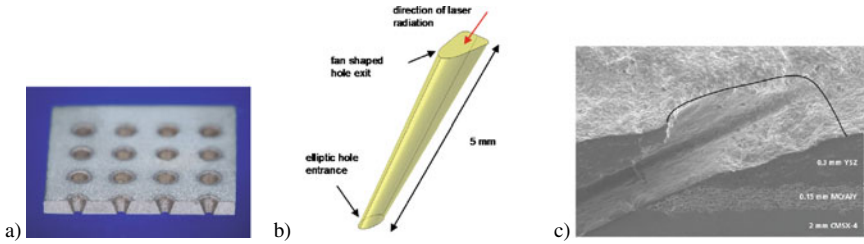
Fig. 31.14 **a** Longitudinal section through a trepanned conical drill hole in 1 mm stainless steel 1.4301, **b** Schematic diagram of the required geometry of a contoured drill hole, **c** longitudinal section of a contoured drill hole

31.4.5 *Applications*

Typical areas of application for trepanning are power-generation, turbo-machine engineering, aerospace and automotive industry, and tool making.

During the manufacture of drawing dies, tiny holes with diameters down to between 10 and 50 µm are drilled in diamond (Meijer et al. 2002). Industrial oil filters can consist of stainless steel with filtration openings in the shape of elongated holes with dimensions of 0.8 mm × 10 mm (Fig. 31.15). With a wall thickness of 2 mm the trepanning process takes 5 s per elongated hole.

5-axis trepanning is been used for drilling freeform shapes. An example is shown for the outlet of a water jet deburring nozzle (Fig. 31.16). The freeform openings are drilled under an inclination of 45° to the surface.
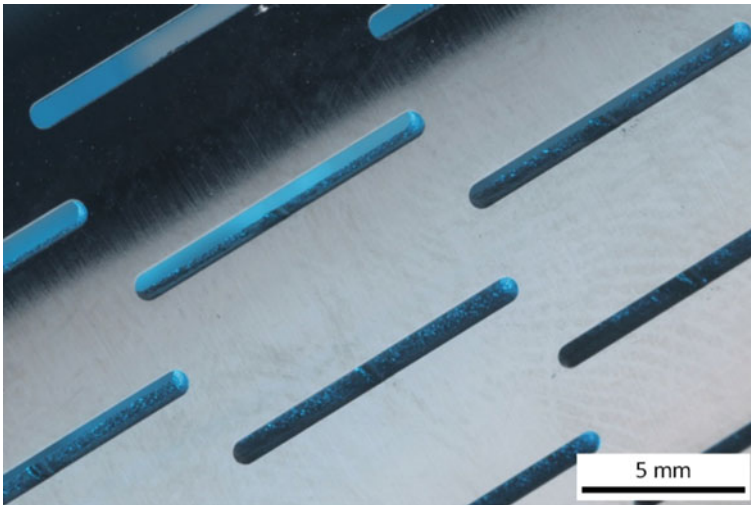
Fig. 31.15 Trepanned elongated holes in a stainless steel industrial oil filter. *Source* ILT

Fig. 31.16 Nozzle for water jet deburring. *Source* ILT

31.5 Helical Drilling

31.5.1 Process Description

Helical drilling offers the greatest precision of all currently applied laser drilling methods as it employs shorter pulse durations from the femtoseconds to the microseconds range. The material removal is therefore mostly vapor-dominated which increases the precision but also decreases the effective ablation rate significantly by an order of magnitude. The hole is created by a relative movement of the laser beam over the workpiece in multiple revolutions. Due to the small material removal rate, the ablation process takes place layer by layer. The focal plane can be moved into the material during the drilling process. This leads to the helical path of the laser beam which led to the name helical drilling (Fig. 31.17).

Helical drilling optics are also characterized by the ability of inclining the laser beam with respect to the main drilling axis in order to perform a tumbling movement. This is inevitable to create cylindrical holes, because in short and ultrashort pulse-based laser ablation, no vertical hole walls, typically above 87°, can be created. Adjusting the inclination angle of the laser beam opens up the possibility to create positive or negative conical holes, or combinations of these (Fig. 31.18).

Hole diameters between a couple of 10 μm and several 100 μm can be drilled into up to 3 mm thick materials, reaching aspect ratios up to 40. The typical achievable tolerances for the hole entry diameter and exit diameter are in the range of a few micrometer depending mainly on the focal diameter of the laser beam. Typically, geometrical deviations range between 2 and 5 μm.
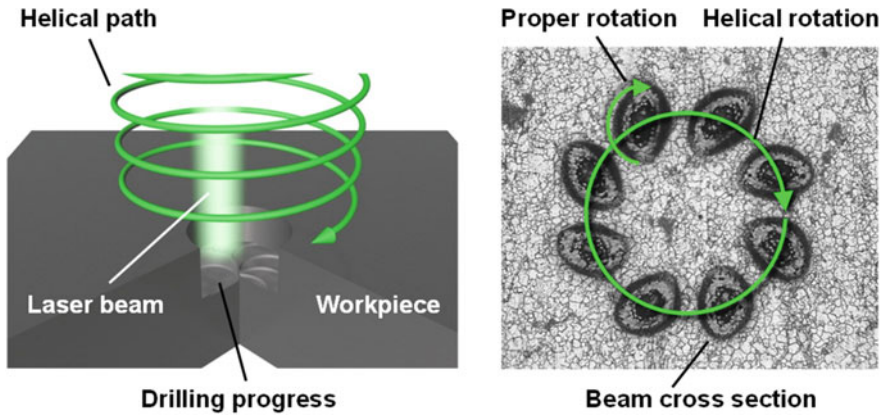
Fig. 31.17 *Left* 3D-illustration of the helical drilling process showing the penetration into the material. *Right* the superimposed rotational movements of the helical path and the proper rotation of the laser beam are shown by branding marks at low laser output power on the surface of the workpiece
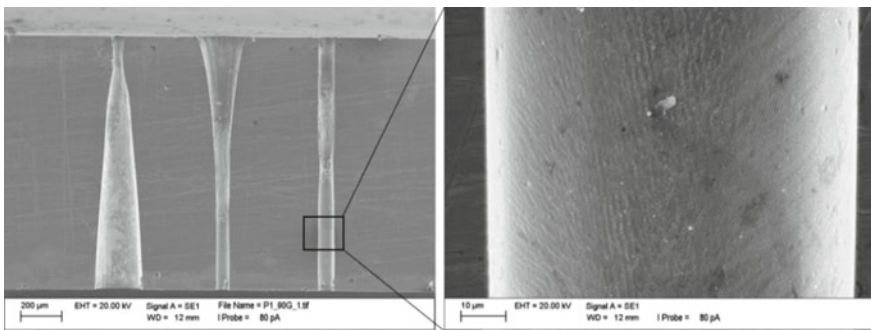
Fig. 31.18 Longitudinal section of hole created via helical drilling in 1.2 mm thick stainless steel with a negative (*left*), positive (*middle*) and quasi-zero conicity (*right*) and detail of the wall of the drilled hole

Another application that is based on helical drilling is helical (contour) cutting. In this case, similar to trepanning, a start hole is produced by helical drilling. Subsequently, the workpiece is moved on a positioning table to cut out the desired contour while the rotating laser beam creates the cutting kerf. In this process, the focal plane is set to a fixed height. This process enables the production of quasi-melt-free cut edges with an adjustable cutting flank angle.

Fig. 31.19 Principles of
laser beam rotation (Wawers
2008)
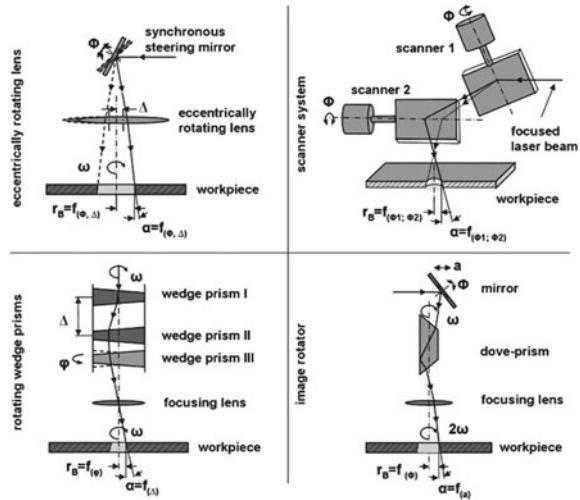
31.5.2   Types of Helical Drilling Optical Systems

Two principles can be distinguished to perform the rotation and inclination of the laser beam. One is by rotation of optically transmissive components such as prisms, cylinder lenses, or wedges. The other by using reflective components such as rotatable mirrors for the entire beam control of shifting, inclination, and deflection (Fig. 31.19).

For some systems with rotating optical components such as eccentric rotating lenses, also a synchronized rotating mirror is required. The mirror deflects the laser radiation onto the desired path (e.g., a circle) while the synchronized eccentric rotating lens imposes an inclination of the laser radiation while focusing the beam. Scanner systems with two or more independently rotatable mirrors have the advantage of guiding the laser beam over the workpiece on any programmable path with high inclination angles. This makes it possible to drill arbitrarily shaped holes as the contour and inclination can be changed freely during the drilling process. Due to this high flexibility, scanner-system-based helical drilling optical systems are more common on the market in different variants (Internet link:https 2020; Auerswald et al. 2016). Helical drilling optical systems based on rotating wedge prisms consist of three wedge prisms. By changing the distance and angular position between the wedge prisms, the hole diameter and inclination angle can be changed. As this needs to be done during the rotation of the entire unit, a complex mechanical setup is required. An image rotator can also be used to create the movement of the laser beam. In this case, a mirror that can be shifted and tilted is positioned before the rotating optical component to set up scanning diameter and inclination angle.

The tilt angle of the incident laser beam $\Delta\beta$ determines the diameter of the helical path and therefore the hole diameter. The parallel offset Δ a from the optical axis of the focusing lens determines the inclination angle of the focused laser beam and therefore
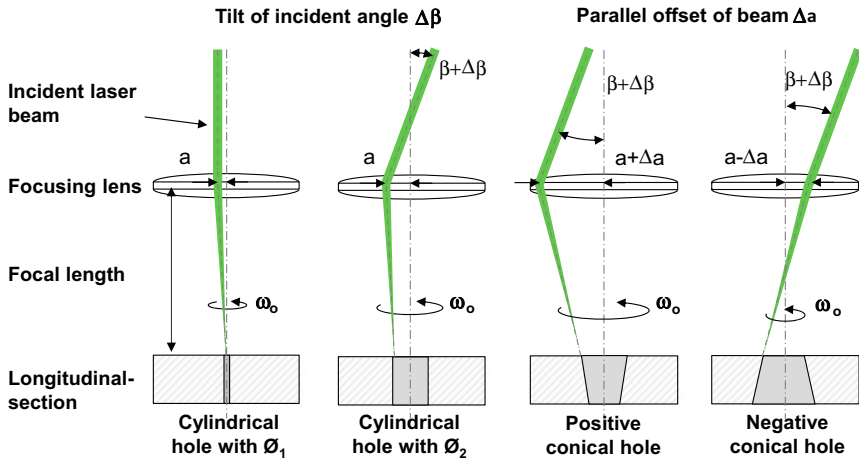
Fig. 31.20 Principle of changing diameter and taper angle of boreholes in the helical drilling process, based on (Wawers 2008)

the taper angle of the hole. By adjusting the parallel offset of the incident laser beam, holes with positive, negative, and zero conicity can be fabricated (Fig. 31.20).

When using an image rotator such as a Dove prism, two additional effects can be benefited from. Firstly, with each rotation of the optical component the laser beam itself performs two revolutions, thus increasing the rotation speed (Smith 2000). Secondly, the laser beam performs a proper rotation which prevents an influence of a non-circular focal spot on the hole geometry (Wawers 2008). The superimposed laser intensity without a proper rotation of an elliptic spot also results in an inhomogeneous intensity distribution on the helical path, showing a higher superimposed intensity on the short axis of the elliptic spot (Fig. 31.21). This causes roundness imperfections in the geometry of the hole. The proper rotation of the laser spot is therefore necessary to compensate for a non-circular beam profile. Additionally, the proper rotation evens out polarization dependent effects which could also lead to deviations in the hole shape.

31.5.3 Characterization of the Process

In a helical drilling process with a shift of the focal plane into the material, the convergent laser beam needs to be fully coupled into the hole. If a fraction of the laser radiation is shielded at the hole entry, two unwanted effects occur. Firstly, the entry diameter will be widened due to the absorption of the shielded pulse energy fraction. Secondly, this fraction of shielded pulse energy is missing at the hole base which can eventually lead to a drill stop. To ensure that the entire laser beam is coupled into the material, a few boundary conditions need to be met (Fig. 31.22):
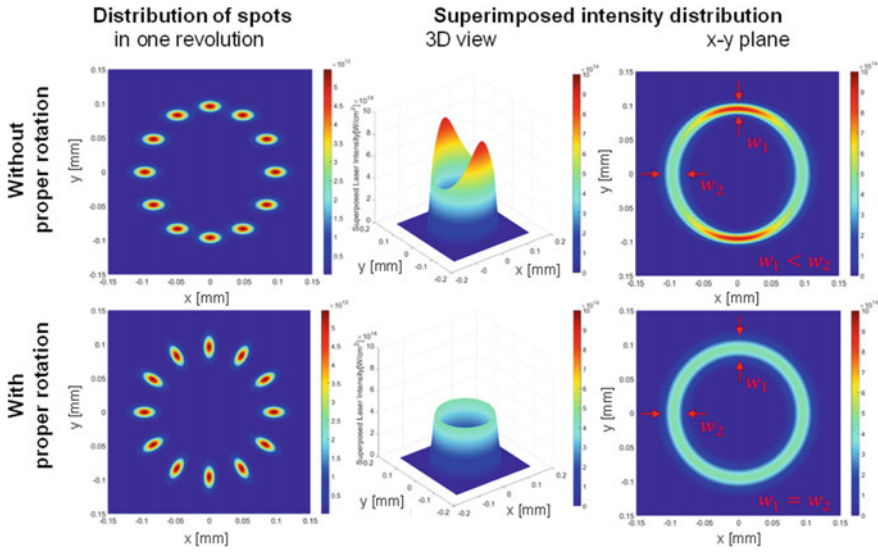
Fig. 31.21 Comparison of the laser intensity distribution on the helical path in the plane of incidence with and without proper rotation of the laser beam

Fig. 31.22 Sketch of the geometrical restrictions when coupling the convergent laser beam into a hole
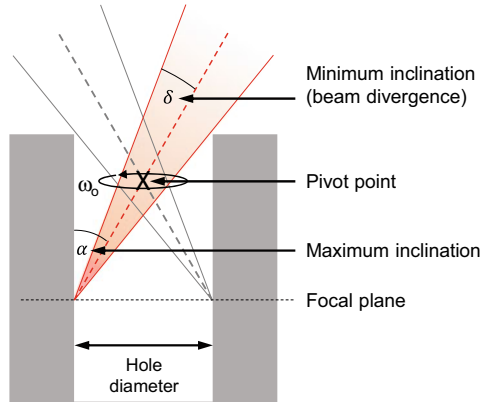
- Minimum inclination (δ): the inclination of the laser beam needs to be at least as high as the divergence of the laser beam. Otherwise, the laser radiation is shielded at the hole entry on the same side as the laser spot.
- Maximum inclination (α): the maximum inclination is reached, when the laser beam is shielded on the opposite side of the laser spot at the hole wall. This value also depends on the divergence, the hole diameter, and the position of the focal plane.

- Minimum focal diameter: the divergence of the laser beam increases for smaller focal diameters. When the beam diameter at the hole entry corresponds to the hole entry diameter, the minimum value is reached.

For the helical drilling process, three drilling phases can typically be distinguished according to the features of the hole capillary and the ablation behavior. The first phase only exists when the hole diameter is significantly larger than the focal spot diameter. In this case, due to the circular movement of the laser beam spot over the workpiece surface, a hole with an island-like pin in the middle is created (Fig. 31.23). Successive repetitions on the helical path deepen the groove and thus leading to an increase of the pin height. The ablation on the hole wall during the revolutions also creates steeper walls of the hole. As a result, the reflection of a fraction of the laser radiation is more and more directed into the center of the blind hole, ablating the pin. After removing the pin, those reflections create a funnel-like hole with a slim tip-shaped drill base which marks the beginning of the second process phase. This is quite similar to the effect that can be observed during the laser percussion drilling process. Once the tip is completely formed, its length and funnel-like profile stay quasi-constant until it reaches the backside of the workpiece. The final phase starts after breakthrough and is characterized by a widening of the exit hole diameter. Since most of the laser radiation passes through the hole without material removal, this is the most unproductive but yet a geometrical quality defining phase of the helical drilling process.

Changing the position and angle of the incident beam has the biggest influence on the shape of the hole. However, other laser process parameters can have a major impact on the achievable materialographical quality and productivity of the hole, too. Especially the combination of pulse energy, repetition rate, and rotational speed of the helical drilling path is important. Facilitating high repetition rates so that there is a very high pulse overlap or number of pulses per spot can lead to pulse-to-pulse interactions such as heat accumulation and particle (plasma) shielding. This can lead to an increase in the heat affected zone, increased melt generation and to widening of the hole diameter. Also, as the ablated material is expelled from the drill base and the hole becomes deeper, subsequent laser pulses can interact with the ablation particles which have not left the cavity of the hole yet. This leads to particle
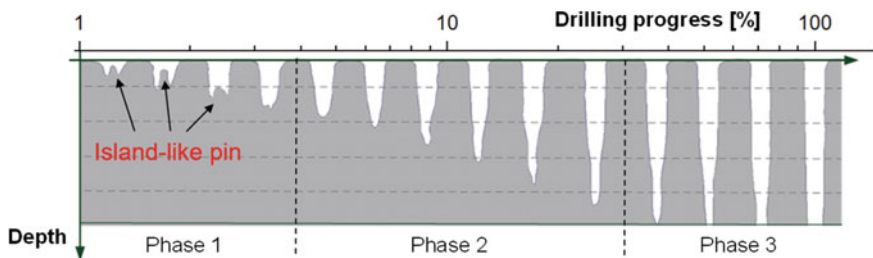

Fig. 31.23 Schematic example of temporal evolution of longitudinal sections of holes produced in a helical drilling process

shielding or deflection of subsequent laser pulses because pulses are absorbed or deflected from the ablated particles. The general approach to solve this issue is to lower the repetition rate or to increase the velocity on the helical path to achieve a higher separation between pulses. However, since the helical movement is a repeated loop, the time between two consecutive scans of the loop is decreased so that loop-to-loop, or generally called scan-to-scan, interactions can occur. The laser parameters and the helical movement must be designed in a way that both effects do not emerge.

31.5.4 Applications

Helical drilling is used in applications where high-precision micro-holes with a high surface quality and small melt deposits on the wall of the borehole, a circular borehole cross section, and the facility to produce boreholes with a positive or negative conical taper are required. Examples include injection nozzles for the automotive industry (Fig. 31.24), spinning nozzles in textile engineering, dosage nozzles for hydraulic systems, holes in air bearings, drawing dies made of diamond for wire manufacturing, and starting holes for wire cut EDM. Helical drilling can be applied to fabricate precision micro-holes with high aspect ratios in metals, semiconductors, glass, and ceramics. Helical drilled holes can be used as vent holes for injection molding and for sensor and filter technology.

By taking advantage of a dynamic helical drilling process, in which a dynamic change of the inclination angle is employed, holes with more complex profiles such as microfunnels or Laval nozzles can be fabricated as shown in Fig. 31.25 (He et al. 2019).

Helical contour cutting is being used extensively to fabricate fine mechanic components with straight or designated shaped cutting kerf, such as horological parts (Fig. 31.26).

A promising technology for upscaling the process efficiency is a multibeam technology using a diffractive optical element (DOE), which has proved to be feasible
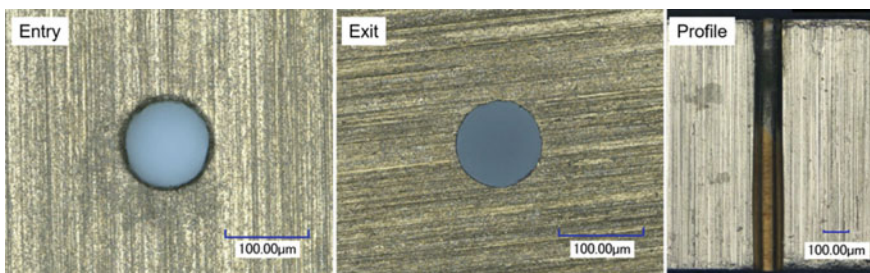
Fig. 31.24 Helical drilled hole for injection nozzle with a diameter of 100 μm, a roundness > 0.92, and a cylindrical hole profile in longitudinal cross section. Material: 1 mm thick stainless steel (1.4301)

Fig. 31.25 Different helical drilled micro-holes with complex profile in stainless steel (He et al. 2019)
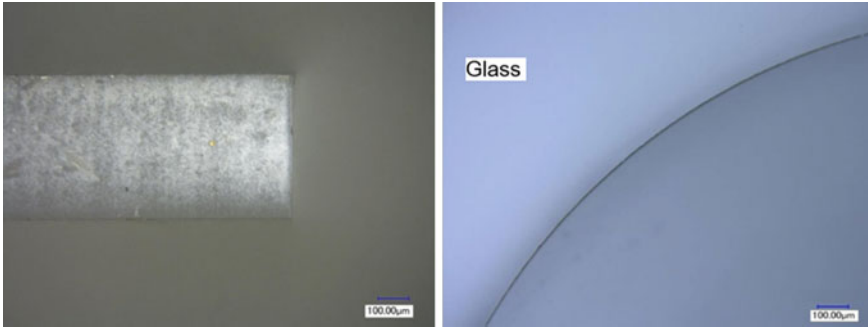

Fig. 31.26 Helical contour cutting of dielectric horologic parts with right-angled kerf and sharp edge. Material: 0.5 mm thick sapphire glass

for a helical drilling process (Gillner et al. 2019). The laser beam can be split into several identical, parallel beamlets, making it possible to use the pulse energy of the high-power lasers to full extent. Therefore, the productivity of the helical drilling process can be up-scaled correspondingly.

31.6 Multibeam Drilling

31.6.1 Introduction

The introduction of ultrashort pulse (USP) laser systems with average powers in the kilowatt range poses new challenges for material processing in terms of beam guidance and process concepts. The process technology to effectively distribute the high average power over the workpiece surface is currently the main limitation. Lasers with high repetition rates demand scanners with marking speeds up to 1,000 m/s. Lasers with high pulse energy require new beam splitting and shaping concepts. One option for making better use of high pulse energy is a multibeam concept that splits a laser beam into a multitude of beamlets. The multibeam approach for parallel processing of large areas enables an increase of productivity by maintaining high precision and surface quality of USP processes. Current state-of-the-art multibeam technologies can work with several hundred beamlets in parallel. Due to parallel

processing and the increased energy input distributed over the workpiece, attention must be taken toward heat input and heat accumulation.

31.6.2 Process Description

In order to improve the production rate of laser drilled micro-holes, the approach is to scale the single beam drilling process by parallelization. Therefore, the laser beam must be divided into multiple beamlets by means of a beam splitting element that can sustain high pulse energies and high average laser powers. For that case, diffractive optical elements (DOEs) are used. A DOE is usually designed in a manner that the distance of the partial beams corresponds to a multiple of the dimensions of the geometries to be processed. A multibeam array can consist of a specific arrangement of beamlets to meet the desired geometry of the part. For material processing, rectangular or square shaped arrays with equidistant beamlets in a square or hexagonal arrangement are commonly used. Large areas are processed by shifting the multibeam array with the scanner system and filling the spaces between the start matrix.

All material types that can be processed with USP lasers are in principle also suitable for processing with a multibeam scanner. The multibeam scanner is generally only applicable for parallel drilling of flat surfaces so that the focal position of each beamlet is in the same plane. The processible material thickness is in the range of some 10–100 µm. Furthermore, it must be taken into account that the pattern and geometries to be produced are in a periodically recurring arrangement and can be produced by offsetting the scanner.

The productivity of multibeam drilling scales with the number of beamlets used as long as the drilling productivity per beam can be maintained. Large-scale processing of many and densely packed structures with no or only relatively short scan vectors are advantageous for multibeam processing. On the other hand, large-area machining of a few, albeit densely packed, structures with long scan vectors is less suitable for multibeam processing.

The most common drilling techniques used in multibeam drilling are percussion drilling and trepanning. Percussion drilling is used to produce large areas of very small holes with diameters in the range of a few micrometers. Trepanning is used when the hole size is significantly larger than the used focus diameter of the beamlet. An example of a 10 µm thin stainless steel foil drilled by means of multibeam percussion drilling is shown in Figs. 31.27 and 31.28. The beamlet pitch for this process is 300 µm in a squared arrangement of 12 × 12 beamlets. The drilled area has been filled evenly with an equidistant spacing of the beamlets by shifting the multibeam array by an increment of 10 µm in both axis directions.

The dark violet surface areas in Fig. 31.27a are already perforated and illuminated from the backside. An X–Y stage is used to stitch the multibeam batches next to each other for the processing of large areas. One multibeam batch has a length and width of about 3.6 mm. Figure 31.27b illustrates the heat accumulation of a multibeam

process of four batches in a 2×2 batch matrix. This specific multibeam drilling process with 144 beamlets is capable of a drilling rate up to 20,000 holes per second. A density of more than 10,000 holes/mm^2 can be drilled into a 10 μm thick stainless steel foil. In Fig. 31.28, the hole entry and exit side of the perforated foil are shown. The hole entry diameter is in the range of 7 μm while the exit diameter can be adjusted by choice of the process parameters and is for this process in the range between 650 and 1,000 nm.

When processing thin foils of several 10–100 μm of thickness as raw material, the workpiece is thinned out compared to its initial volume. Over the course of the scan job, this leads to a steady reduction of available workpiece mass that is capable of dissipating the residual heat. These aspects must be taken into account in the processing strategy (Finger 2017; Buesing 2016; Barthels and Reininghaus 2018; Gretzki and Gillner 2017). To increase processing speed while avoiding thermal damages during multibeam processing, the heat load of the workpiece has to be controlled by laser parameters, scanning strategies, and cooling conditions of the workpiece to dissipate residual heat.
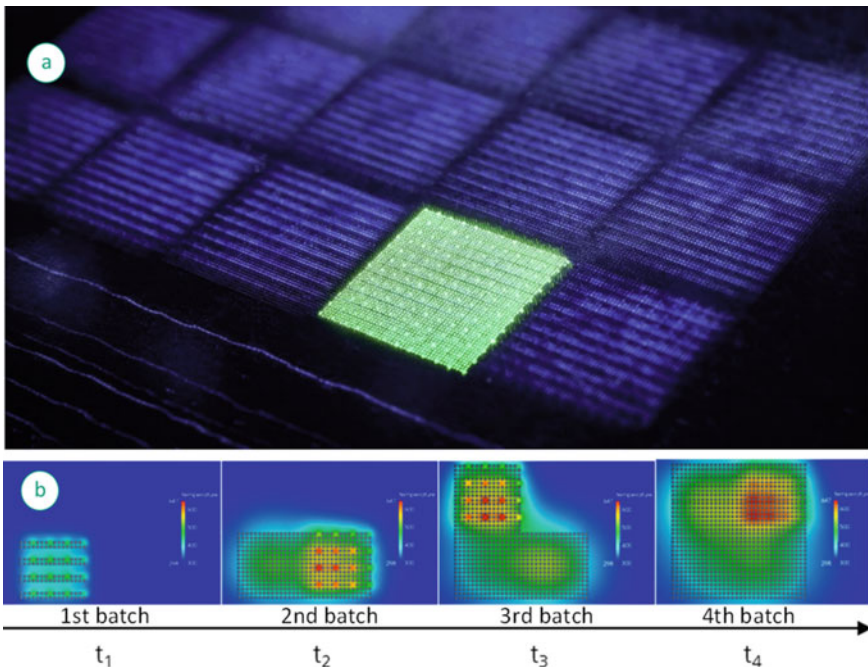
Fig. 31.27 **a** Multibeam batch processing of stainless steel with 144 beamlets in parallel, **b** rise of heat accumulation during processing of several batches
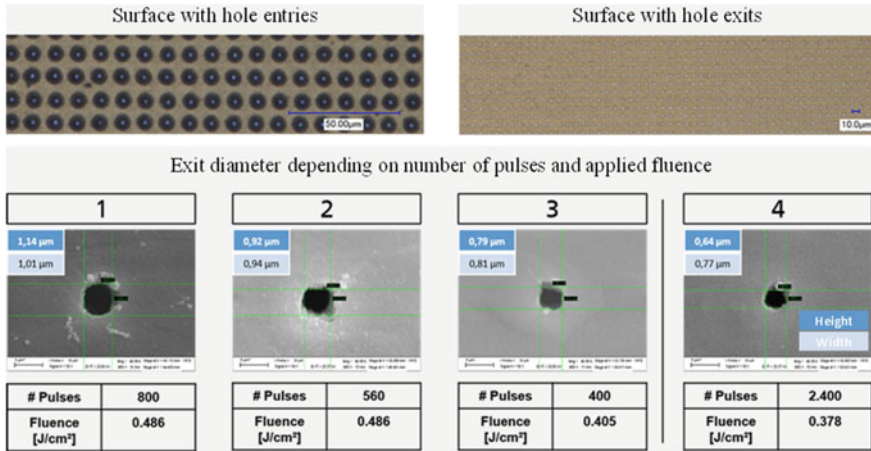
Fig. 31.28 Drilling results showing hole entry and hole exit side of 10 μm stainless steel foil and the hole exit shape using a multibeam scanner with a percussion drilling process. The hole entry diameter is about 7 μm (top left-hand picture)

31.6.3 Applications

Application examples that are particularly relevant for drilling by means of a multibeam scanner come from the field of consumer electronics and micro-filter technology. In both industries, a large number of holes with diameters that are only a few micrometers big each can be created very densely from a metal substrate that is only a few micrometer thick.

Display technology: Display masks are used to produce pixels for display panels. These masks are made from INVAR foils. By means of a multibeam scanner holes are drilled in the INVAR foil in a periodically recurring matrix. The use of a multibeam scanner is advantageous for the production of these shaped holes since the holes are only 60 μm or smaller in size, and it is more productive to generate them in a parallelized process. These masks are used in the production process for cell phone and TV displays. Current cell phone models already have 1 million or more of these pixels. In order to produce the pixels, the display mask with shaped holes is placed on a substrate and the pixels are vapor-deposited in a special process onto the substrate. With available focal diameters of a few micrometer and a heat controlled multibeam process the pixel size and pitch can be reduced to a level that pixel densities of more than 1,000 ppi are obtainable.

Filtration technology: Metal foils made of different alloys, which are approved and certified for use in medical and pharmaceutical technology as well as in food production, can efficiently be drilled with micrometer and sub-micrometer holes using a multibeam scanner. These foils can be used as micro filters for various separation tasks. Micro filters made of metallic foils have the advantage over conventional disposable filters made of plastics that they can be reprocessed by heat treatment.

Fig. 31.29 Metal foil with multibeam drilled holes. With hole diameters ranging between 10 and 30 µm and a pitch of 60 µm the foil becomes "transparent"
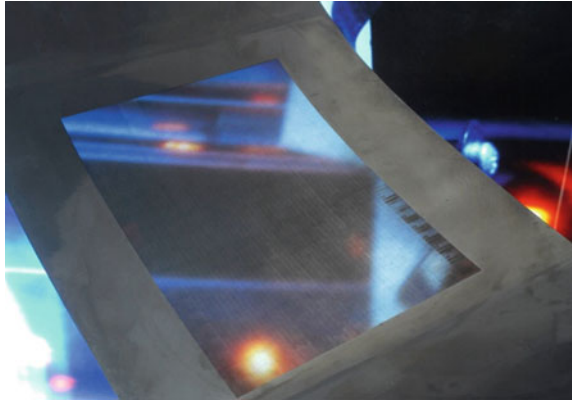
Those filters are used in food production, for example for filtering beer and wine, in order to filter out remaining but unwanted microparticles generated in the manufacturing process. Holes drilled in biomedical micro-filter membranes measure $< 20\,\mu m$ in diameter (Baumeister et al. 2007), while particularly fine filters are produced with even smaller holes measuring between $1\,\mu m$ and $15\,\mu m$ (Fig. 31.29) (Gillner 2007).

31.7 LaserMicroJet (LMJ) Drilling

LaserMicroJet (LMJ-) drilling is a special technology in the field of laser drilling. In this process, a slim laminar water jet is utilized to guide the laser radiation to the surface of the workpiece. The water jet serves as a guiding fiber as the laser radiation is contained in the jet due to total reflection at the water–air transition. The system setup with typical dimensions and parameters of the utilized parts is shown in Fig. 31.30. Typically, a green $\lambda_{Laser} = 515$ nm pulsed laser with pulse durations in the upper nanosecond regime is used with repetition rates of a few kilohertz. The water jet is created in a specially designed nozzle with purified, high pressure water in which also the laser radiation is focused into. The diameter of the water jet is typically in the range of 20–100 µm. (Internet link:https 2020).

Processing strategies are contour precision cutting for thin materials or multi-pass ablation as in helical drilling for thicker materials. The nanosecond pulsed drilling process is vapor-dominated which allows a reasonable ablation rate while maintaining a high precision.

This technology has several advantages compared to dry laser drilling but also a few drawbacks. Advantages are the independence of the position of a focal point since every point in the water jet has the same optical properties until the water jet becomes unstable and the water jet starts dripping. Therefore, in a cutting or helical-like drilling process most of the intensity is available at the drill base, because the pulse energy can be transported along the cutting kerf inside the water jet without
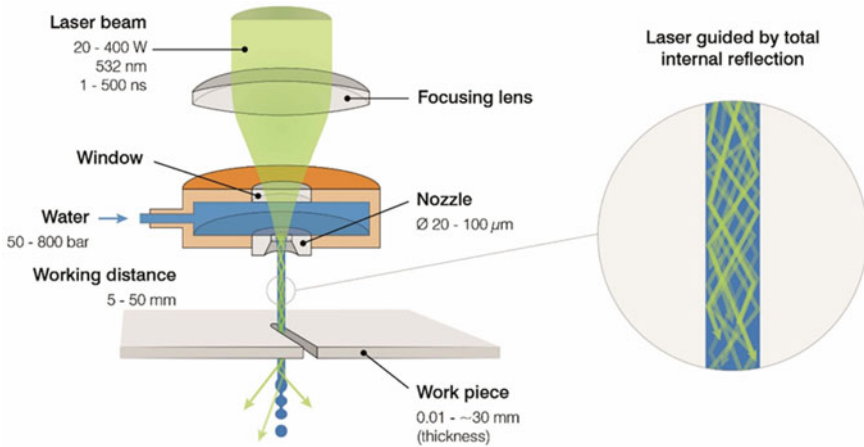
Fig. 31.30 Schematic setup of the coupling unit which combines laser beam and water jet (Internet link 2020)

significant losses. This results in steep hole wall angles close to 90° and aspect ratios up to 100. Due to the impulse and thermal conductivity of the water, ablation particles are efficiently removed from the hole and instant cooling takes place, which decreases the occurrence of heat affected zones. Since the ablation particles leave the hole in a comparably cool state, edge rounding at the entry of the hole can be minimized especially at inclined holed (Fig. 31.31).

On the other side, this technology also has drawbacks and challenges: A comparatively complex and well-designed hardware system is required to create a stable water jet. The process window with regard to a specific drilling task is rather narrow so that a carefully selected set of process parameters is required to efficiently guide the laser energy through the water jet and couple it into the material. Additionally,

Fig. 31.31 Entry of an LMJ-drilled inclined hole in stainless steel. No edge rounding or breakage is visible
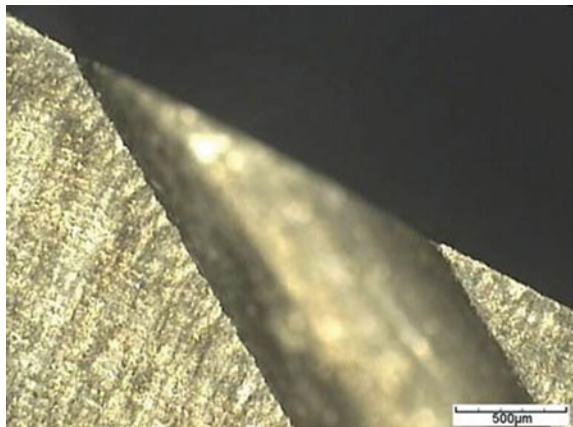
the water needs to be purified, deionized, and free of air bubbles to minimize interaction with the laser radiation. The productivity and achievable quality of the process is limited by the pulse duration, repetition rate, maximum average power, and the nozzle diameter. Also, various feedback mechanisms exist during the processing which can lead to non-reproducible results. Especially, the perturbation of the water jet due to an interaction with the cutting kerf wall, the remaining water in the drill base, and the water flowing out of the hole again significantly affect the drilling process. Most of the currently performed research and process development projects aim to understand and decrease those interactions.

Another process related drawback is the limitation to materials that must not become wet during the drilling process, e.g., technical textiles, or sensitive materials such as thin films and foils that are prone to the impulse of the water jet. A constraint for multi-axis processing is that the workpiece needs to be moved during machining because of the inertia and the strong limitation of inclining the water jet.

Areas of application for the LMJ process can be found in automotive parts, TBC high temperature alloys for stationary or flying jet engines, semiconductors, ceramics, diamond cutting, and composite materials. A large-scale laser water jet process is used for cutting rocks where the laser in the water jet is used for weakening the stone material and the drilling forces for a subsequent mechanical drilling head are reduced (Brecher et al. 2016; Schmidt et al. 2017).

31.8 Hole Characterization

The characterization of a laser drilled hole is carried out by evaluation of the geometrical and materialographical quality. The geometrical quality covers the quantitative precision of geometrical properties. The materialographical quality covers quantitative measurement and qualitative description of defects that occur during and after the laser drilling process. An exemplary overview of both the geometrical as well as materialographical quality characteristics is shown in Fig. 31.32.

The most common geometrical and materialographical quality characteristics are shown in Tab. 31.1.

The standard deviation or statistical confidence interval of each aforementioned quality characteristic depends mainly on the utilized laser source, system setup, drilling technique, process design, and the material of the workpiece. In general, the achievable quality becomes better the shorter the pulse duration. An example is shown in Fig. 31.33.

However, if the process parameters are not suitable for the drilling operation both the geometrical and the materialographical quality can suffer. For instance, if a USP-based drilling process utilizes a high average power, pulse-to-pulse interaction (heat accumulation, plasma shielding, plasma etching) is likely to take place and will increase recast layer thickness and other thermally induced defects (Haasler and Finger 2019; Finger 2017; Breitling 2010). Hence, process parameters like repetition rate, pulse energy, or pulse duration should be adapted in order to avoid the high
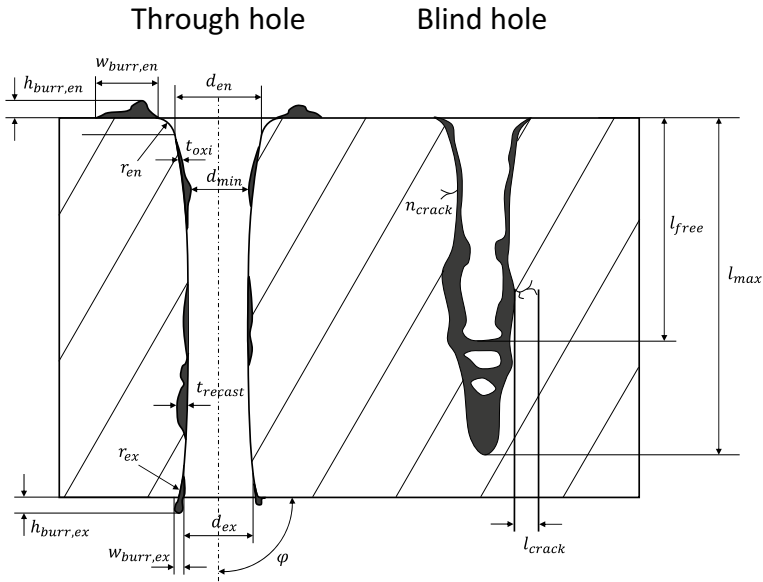
Fig. 31.32 Schematic overview of geometrical and materialographical quality characteristics, based on (Honer 2004; Dietrich 2013)

Table 31.1 Overview of geometrical and materialographical quality characteristics for laser drilled holes

Geometrical quality characteristics	Materialographical quality characteristics
Entry/Exit diameter (d_{en} resp. d_{ex})	Recast layer thickness (t_{recast})
Entry/Exit ellipticity (e_{en} resp. e_{ex})	Oxidation layer thickness (t_{oxi})
Conicity (k)	Size of surface discoloration ($t_{discolor}$)
Entry/Exit corner radius (r_{en} resp. r_{ex})	Number of cracks (n_{crack})
Smallest hole diameter (d_{min})	Crack length (l_{crack})
Hole entry/exit roundness	Entry/Exit burr width and height ($w_{burr,en}$ resp. $w_{burr,ex}$ and $h_{burr,en}$ resp. $h_{burr,ex}$)
Inclination angel of the drill axis (φ)	Maximum blind hole depth (l_{max})
Free depth of blind hole (l_{free})	Flaking
	Waviness/surface roughness
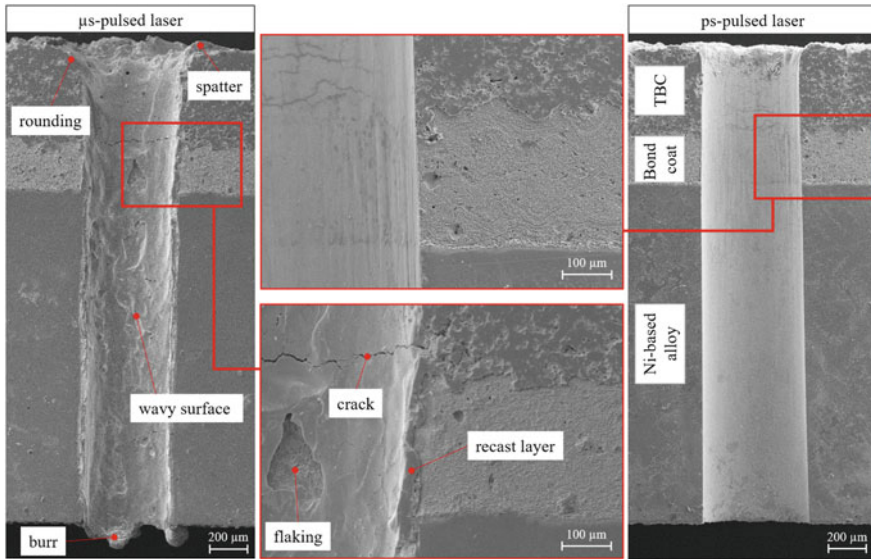
Fig. 31.33 Comparison of SEM pictures of longitudinal sections of a microsecond-pulsed and a picosecond-pulsed laser drilled hole in 2.5 mm thick thermal barrier coated (TBC-) IN 792. The drilling times are 2.6 s for the microsecond-pulsed drilling process and 40 s for the picosecond-pulsed laser drilling process

rise of temperature in the drill zone which will also lower the productivity of the drilling process. Thus, a compromise between productivity and quality has to be found depending on the application or industrial production throughput.

References

Auerswald J, Ruckli A, Gschwilm T, Weber P, Diego-Vallejo D, Schlüter H (2016) Taper angle correction in cutting of complex micro-mechanical contours with ultra-short pulse laser. J Mech Eng Autom 6:334–338

Barthels T, Reininghaus M (2018) High precision ultrashort pulsed laser drilling of thin metal foils by means of multibeam processing. Proc SPIE 10744:10

Baumeister M, Dickmann K, Hoult AP (2007) Combining high-speed laser perforation and cold roll forming for the production of biomedical microfiltration membranes. J Laser Appl 19(1):41–45

Brecher C, Janssen H, Eckert M, Schmidt F (2016) Thermal investigation of interaction between high-power cw-laser radiation and a water-jet. Phys Procedia 83:317–327

Breitling D (2010) Gasphaseneinflüsse beim Abtragen und Bohren mittels ultrakurz gepulster Laserstrahlung, Dissertation, Herbert Utz Verlag, München

Bugayev AA, Gupta MC, El-Bandrawy M (2005) Dynamics of laser hole drilling with nanosecond periodically pulsed laser. Opt Lasers Eng 44(8):797–802

Buesing (2016) Optische Systeme für die hochpräzise, scannerbasierte Multistrahlbearbeitung mit ultrakurzen Laserpulsen], Aachen (22.03.2016 /2016).

Chien W, Hou S (2006) Investigating the recast layer formed during the laser trepan drilling of Inconel 718 using the Taguchi method. Intern J Adv Manuf Techn 33(3–4):308–316

Chen X (2000) Short pulse high intensity laser machining. High Temp Mater Processes (new York) 4:151–160

DIN 32540 (2012) Laser beam removing – Thermal removing with laser beam – Terms and definitions, influence factors, procedure, Beuth, Berlin

Dietrich J (2013) Synchrone Qualitäts- und Produktivitätssteigerung beim Laserstrahlbohren, Dissertation, Aachen

Dürr U (2003) Bohren mit Nd:YAG-Lasern: Möglichkeiten und Grenzen in der Bohrqualität, Bayrische Laserseminare

French P, Naeem M, Watkins K (2003) Laser percussion drilling of aerospace material using a 10 kW peak power laser using a 400 µm optical fibre delivery system, LIA Proceedings ICALEO, CD Version

Finger J (2017) Puls-zu-Puls-Wechselwirkungen beim Ultrakurzpuls-Laserabtrag mit hohen Repetitionsraten, Dissertation, Apprimus Verlag, Aachen

Forsman A, Banks PS, Perry M, Campbell E, Dodell A, Armas M (2005) Double-pulse machining as a technique for the enhancement of material removal rates in laser machining of metals. J Appl Phys 98:033302

Gretzki P, Gillner A (2017) Programmable diffractive optic for multi-beam processing: applications and limitations. Proc SPIE 10347:31

Gillner A (2007) Micro processing with laser radiation—Trends and perspectives. Laser Tech J 4(1):21–25

Gillner A, Finger J, Gretzki P, Niessen M, Bartels T, Reininghaus M (2019) High power laser processing with ultrafast and multi-parallel beams. J Laser Micro/nanoeng 14:129–137

Haasler D, Finger J (2019) Investigation of heat accumulation of heat accumulation effects during deep hole percussion drilling by high power ultrashort pulsed laser radiation. JLA 31:022201

Hartmann C, Gillner A, Aydin Ü, Fehr T, Gehlen C, Poprawe R (2005) Increase of laser micro ablation rate of metals using ns-multi-pulses. 8th International Conference on Laser Ablation (COLA). Banff, Canada

Hermanns T (2018) Interactive Prozesssimulation für das industrielle Umfeld am Beispiel des Bohrens mit Laserstrahlung. Apprimus Verlag, Aachen

Horn A, Weichenhain R, Albrecht S, Kreutz EW, Michel J, Nießen M, Kostrykin V, Schulz W, Etzkorn A, Bobzin K, Lugscheider E, Poprawe R (2000) Microholes in zirconia coated Ni-superalloys for transpiration cooling of turbine blades. Proceedings of SPIE 4065:218–226

He C, Esch D, Gillner A (2019) Adaption of energy deposition in helical drilling of multidimensional micro holes using ultrashort laser pulses. J Laser Micro/Nanoeng 14

Honer M (2004) Prozesssicherungsmaßnahmen beim Bohren metallischer Werkstoffe mittels Laserstrahlung, Dissertation, Herbert Utz Verlag, München

Internet link (2020) https://www.synova.ch/technology/laser-microjet.html. Last accessed 04.06.2020

Internet link (2020) https://www.arges.de/industrial-products/precession. Last accessed 04.06.2020

Janssen S, Kürschner D, Hermanns T, Schulz W (2019) Asymptotic bore hole model for ultrashort pulse laser-drilled carbon fiber preforms, Proceedings of LAMP, Hiroshima, Japan

Johannes-Thomas Finger (2017) Pulse to Pulse Interactions during USP Laser Ablation Using High Repetition Rates, Aachen

Karnakis D, Rutterford G, Knowles M (2005) High power DPSS laser micromachining of silicon and stainless steel. WLT-Conf on Lasers in Manufacturing, München

Karnakis D (2005) Applications of laser microdrilling, Laser Micromachining: Developments & Applications, AILU Laser Micromachining: Developments & Applications, AILU Workshop, Bangor, UK

Kelbassa I, Walther K, Trippe L, Meiners W, Over C (2006) Potentials of manufacture and repair of nickel base turbine components used in aero engines and power plants by laser metal deposition and laser drilling. Intern Symp Jet Propulsion Power Eng Kunming 1:207–215

Khan AH, O'Neil W, Tunna L, Sutcliffe CJ (2006) Numerical analysis of gas-dynamic instabilities during the laser drilling process. Opt Lasers Eng 44:826–841

Kreutz EW, Trippe L, Walther K, Poprawe R (2007) Process development and control of laser drilled and shaped holes in turbine components. J Laser Micro/nanoeng 2(2):123–127

Kononenko T, Klimentov S, Garnov S, Konov V, Breitling D, Föhl C, Ruf A, Radtke J, Dausinger F (2002) Hole formation process in laser deep drilling with short and ultrashort pulses. SPIE 4426

Lapczyna M, Chen KP, Herman PR, Tan HW, Marjoribanks RS (1999) Ultra high repetition rate (133 MHz) laser ablation of aluminum with 1.2-ps pulses. Appl Phy Mater Sci Proc 69:883–886

Lei W, Davignon J (2000) Micro-via Drilling Applications with Solid-State Harmonic UV laser Systems. LIA Proceedings ICALEO

Lehner C, Mann K, Kaiser E (2003) Bohren von Kühl- und Schmierlöchern, Stuttgarter Lasertage (SLT), Stuttgart, pp 103–106

Low D, Li L (2002) Effects of Inter-Pulse and Intra-Pulse shaping during laser percussion drilling. Proc SPIE 4426:191–194

Low D, Li L, Byrd P (2001) The influence of temporal pulse train modulation during laser percussion drilling. Opt Lasers Eng 35(3):149–164

Niederhauser HR (1986) Laser drilling of wire drawing dies. Wire Industry 53(10):709–711

Low DKY, Li L, Corfe AG (1999) Effects of assist gas on the physical characteristics of spatter during laser percussion drilling of NIMONIC 263 alloy. Appl Surf Sci 154–155:689–695

Low D, Li L, Corfe AG (2000) The influence of assist gas on the mechanism of material ejection and removal during laser percussion drilling. Proce Inst Mech Eng Part b: J Eng Manuf 214(7):521–527

Lugscheider E, Bobzin K, Maes M, Lackner K, Poprawe R, Kreutz EW, Willach J (2005) Laser Drilled Microholes in Zirconia coated surfaces using two variants to implement the effusion cooling of first stage turbine blades. Adv Eng Mater 7(3):145–152

Meijer J, Du K, Gillner A, Hoffmann D, Kovalenko VS, Masuzawa T, Ostendorf A, Poprawe R, Schulz W (2002) Laser Machining by short and ultrashort pulses, state of the art and new opportunities in the age of the photons. CIRP Ann Manuf Technol 51(2):531–550

NASA (2002) Advanced Nacelle Acoustic Lining Concepts Development (NASA/CR-2002–211672)

Numerical study of the dynamics of the hole formation during drilling with combined ms and ns laser pulses (2019) Optics Laser Technol 112:8–19

Ostermeyer M, Kappe P, Menzel R, Sommer S, Dausinger F (2005) Laser drilling in thin materials with bursts of Ns-Pulses generated by stimulated brillouin scattering (SBS). Appl Phys A 81(5):923–927

Ocana R, Soriano C, Esmoris JI, Sánchez R (2019) Fiber laser based single pulse drilling for production of perforated titanium sheets for HLFC structures. JLMN 14(1)

Patel RS, Bovatsek JM (2003) Method for laser drilling a counter-tapered through-hole in a material, US, US000006642477B1

Patel RS, Brewster MQ (1990) Effect of oxidation and plume formation on low power Nd-Yag laser metal interaction. J Heat Transfer (transactions of the ASME, Series c) 112(1):170–177

Patel RS, Brewster MQ (1991a) Gas-assisted laser-metal drilling: experimental results. J Thermophys Heat Transfer 5(1):26–31

Patel RS, Brewster MQ (1991b) Gas-assisted laser-metal drilling: theoretical model. J Thermophys Heat Transfer 5(1):32–39

Paul S, Kudryashov SI, Lyon K, Allen SD (2007) Nanosecond-laser plasma-assisted ultradeep microdrilling of optically opaque and transparent solids. J Appl Phy 101:043106

Poprawe R, Kelbassa I, Walther K, Witty M, Bohn D, Krewinkel R (2008) Optimising and manufacturing a Laser-drilled cooling hole geometry for effusion-cooled multi-layer plates, ISROMAC-12, Honolulu, Hawaii, USA

Rapp J (2003) The laser with Bosch—a flexible tool in serial production of an automotive supplier. Proc SPIE 4831:390–396

Rodden W, Kudesia S, Hand D, Jones J (2000) Correlations between hole properties and pulse parameters in single pulse Nd:YAG laser drilling of aluminium and titanium, ICALEO.

Rohde H (1999) Qualitätsbestimmende Prozeßparameter beim Einzelpulsbohren mit einem Nd:YAG-Slablaser Universität Stuttgart

Schmidt F, Janssen H, Brecher C (2017) Realization and first time operation of a high-power laser-water-jet system, Lasers in Manufacturing Conference

Schulz W, Eppelt U (2017) Basic concepts of laser drilling. In Dowden J, Schulz W (eds), The theory of laser materials processing, pp 153–188. Springer. ISBN: 978-3-319-56711-2

Serebryakov V, Volkov M, Zhang X (2005) Optimization of laser microdrilling in heat-resisting alloys. Proc SPIE 5777:858–863

Schneider M, Fabbro R, Berthe L, Landais L, Nivard M, Laurens P (2004) Parametric study of drilling with new innovative laser source: application to percussion regime, ICALEO

Schneider M, Fabbro R, Berthe L, Muller M, Nivard M (2005) Gas investigation on laser drilling, ICALEO, Miami, Florida, USA, pp 1094–1099

Schneider M, Berthe L, Fabbro R, Muller M, Nivard M (2007) Gas investigation for laser drilling. J Laser Appl 19(3):165–169

Smith WJ (2000) Modern optical engineering 3rd Ed., Ch. 13, McGraw-Hill, Washington DC

Tam SC, Yeo CY, Lau MWS, Lim LEN, Yang LJ, Noor YM (1993) Optimization of laser deep-hole drilling of Inconel 718 using the Taguchi method. J Mater Process Technol 37(1–4):741–757

Treusch H (1985) Geometrie und Reproduzierbarkeit Einer Plasmaunterstützten Materialabtragung Durch Laserstrahlung, Physik Technische Hochschule Darmstadt

Uchtmann H, Kelbassa I (2013) Cax Process Chain for Laser Drilling of Tool Molds. Proceedings of ICALEO, pp 190–194, Miami, USA

Uchtmann H, Haasler D, Gillner A (2017) Laser micro drilling of wing surfaces for hybrid laminar flow control, LIM

Wawers W (2008) Präzisions-Wendelbohren mit Laserstrahlung, Dissertation, Shaker Verlag, Aachen

Walther K, Brajdic M, Dietrich J, Hermans M, Witty M, Horn A, Kelbassa I, Poprawe R (2008) Manufacturing of shaped holes in multi-layer plates by Laser-drilling. Proc PICALO. Beijing, China, pp 789–794

Willach J (2005) Herstellung von konturierten Bohrungen in Mehrschichtsystemen mit Nd:YAG-Laserstrahlung. Shaker Verlag, Aachen

Willach J, Michel J, Horn A, Schulz W, Kreutz EW, Poprawe R (2004) Approximate model for laser trepanning with microsecond Nd:YAG laser radiation. Appl Phys A Mater Sci Process 79(4–6):1157–1159

Willach J, Horn A, Kreutz EW (2002) Drilling of cooling holes and shaping of blow-out facilities in turbine blades by laser radiation, 7th Liège Conference on "Materials for advanced power engineering". Liège 21:743–750

Willach J, Kreutz EW, Michel J, Nießen M, Schulz W, Poprawe R (2003) Melt expulsion by a coaxial gas jet in trepanning of CMSX-4 with microsecond Nd:YAG laser radiation, 4th International Symposium on Laser Precision Microfabrication. München 5063:435–440

Yilbas BS, Sami M (1997) Liquid ejection and possible nucleate boiling mechanisms in relation to the Liquid ejection and possible nucleate boiling mechanisms in relation to the laser drilling process. J Phys D Appl Phys 30:1996–2005

Part IX
Cutting

Chapter 32
Fusion Cutting

Frank Schneider

32.1 Introduction

For laser fusion cutting, an inert gas is applied to expel material. The power to warm, melt and partially vaporize the cut kerf material is covered solely by the absorbed laser radiation.

Fusion cutting is conducted with significantly higher cutting gas pressures than is the case with laser oxygen cutting, from approx. 0.5 MPa up to over 2 MPa, dependent on the material thickness. Thus, also the term "high pressure cutting" is used for fusion cutting.

The field of application of this process is to cut material for which oxidation of the cut edges needs to be prevented, thus, above all, for the processing of stainless steels or for other steel grades e.g. if the cut flank should be welded or painted after cutting.

The most common laser sources for fusion cutting same as for Oxygen cutting are cw CO_2 or solid state lasers as fiber or disk lasers in the multi-kW power range to cover sheet metal cutting in thicknesses from some tenths of a millimeter up to 50 mm. A deployed laser power up to 8 or 10 kW is the upper level of the standard today. A still ongoing trend can be observed over the years to higher laser power, enabling higher cutting speeds and cutting of material with higher thickness, often coming along with a better cut quality in the standard thickness range. A second trend is the increasing part of solid state lasers for this application, replacing the formerly most prevalent CO_2-lasers. The list of advantages of solid state lasers as the ease of beam guidance, high efficiency of both process and machine and nearly maintenance-free use is only opposed to a better cut quality of cut flanks machined with a CO_2-laser, becoming apparent for thicknesses above app. 5 mm. Figure 32.1 shows the cut flanks of 12 mm stainless steel with a CO_2 laser.

F. Schneider (✉)
Fraunhofer ILT, Aachen, Germany
e-mail: frank.schneider@ilt.fraunhofer.de

Fig. 32.1 Cut flank of 12 mm thick stainless steel, cut with a CO_2 laser
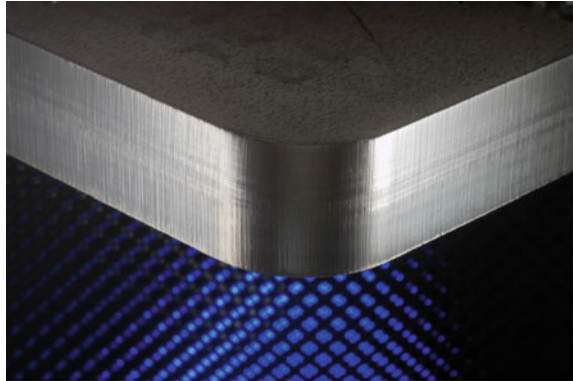
The largest field of application is 2D cutting on flat bed machines, but also 3D applications are widespread as trimming of hot stamped automotive parts as one example.

The standard cutting gas for fusion cutting is nitrogen. For a few applications, other inert gases are utilized, such as argon to cut titanium to prevent titanium nitride on the cut flank. Most for economic reasons, in the thin section range with steel or for aluminum also compressed air can be applied. With 20% Oxygen in the cutting gas the process is much more similar to pure fusion cutting than to Oxygen cutting, however the cut flank is no more oxide-free.

These oxide free cut flanks are one of the most requested advantages of fusion cutting. Others are the narrow and nearly perpendicular cut edges and the high contour accuracy, which is also sustained in complex contours, because the risk of overheating the material as in oxygen cutting by uncontrolled oxidation is excluded.

With a given laser beam power, the maximum workable sheet thicknesses for fusion cutting are smaller than for oxygen cutting, or rather with the same material thickness, higher cutting speeds can be obtained with oxygen cutting in the thick sheet range.

32.2 Process Parameters

32.2.1 Cutting Speed and Laser Power

The power balance for fusion cutting can be set up analogous to that for laser oxygen cutting, while leaving out the exothermic combustion power P_R. Corresponding to the share of the warming and fusion power of the power balance, the cutting speed attainable is reversely proportional to the material thickness. Deviations result at lower cutting speeds through a share of lateral thermal dissipation losses that cannot be ignored. Extensive description of the power balance for fusion cutting can be

found in Petring (1995) and Kaplan (2002). Apart from a limitation of the cutting speed by a power demand not covered by the absorbed laser beam power, the cutting speed can be reduced by insufficient ejection of the melt out of the kerf. However, with an appropriate choice of the cutting gas parameters the noncompliance of the power balance is the typical speed limiting sub-process.

Application-oriented cutting speeds lie in the area of 80% of the maximum speed. The power reserve serves to catch process instabilities, for example, through the variation of the nozzle distance and the focus position caused by those material flatness imperfections that cannot be compensated by the distance control of the cutting head or caused by transient thermal effects as a focus position shift, appearing at high laser power and boosted in case of contamination of the optics.

Figure 32.2 shows cutting speeds for cutting stainless steels with 5 kW laser power (Powell et al. 2017). The figure serves as an orientation, because on the one hand application adapted focusing allows in some cases higher speeds. For instance 1 mm thick material then can also be cut with more than 100 m/min, double the speed of Fig. 32.2. On the other hand, in thin sections dynamic machines are needed to make use of the possible speeds. Thus in practice the speeds are not reached in significant parts of the cut path in 2-D cutting with low dynamic machines (See also chapter "High Speed Cutting").

In thinner sheets the laser beam is absorbed on a less inclined cut front than in thick sheets. The angle dependent absorptivity for 1 and 10 μm wavelength leads to an advantage in process efficiency for 1 μm laser radiation. The thinner the sheet, the more distinct is this trend (Petring et al. 2008).

With a large excess of power for reasons of low cutting speed, a steep cutting front is formed and a large part of the laser radiation is transmitted through the kerf "unused." The temperature of the melt film surface and the melt film thickness go down with decreasing cutting speed. With a low speed of the melt and higher viscosity, the removal of the melt at the lower cut edge is impeded, so that burr formation can occur at low cutting speeds. If the speed has to be reduced, for example, to machine contours, burr-free quality can be attained by modulating the laser radiation. Simply a reduction of the cw laser power according to the power demand is not effective, but a portion-wise material ablation with a speed-dependent modulation is required.

32.2.2 Focusing

Setting up an appropriate focusing for a cutting task does not follow one general rule, but has to be adapted to the cutting regime determined e.g. by thin or thick section cutting, available laser power and beam quality, wavelength and a target oriented balance between speed, quality and process robustness. Laser caustics and focus position aim to generate narrow kerfs to minimize the power consumption of the process and thus enable high speeds. On the other hand, kerfs should be wide enough to allow an effective melt expulsion by the cutting gas flow, requiring a wider kerf with increasing sheet thickness.
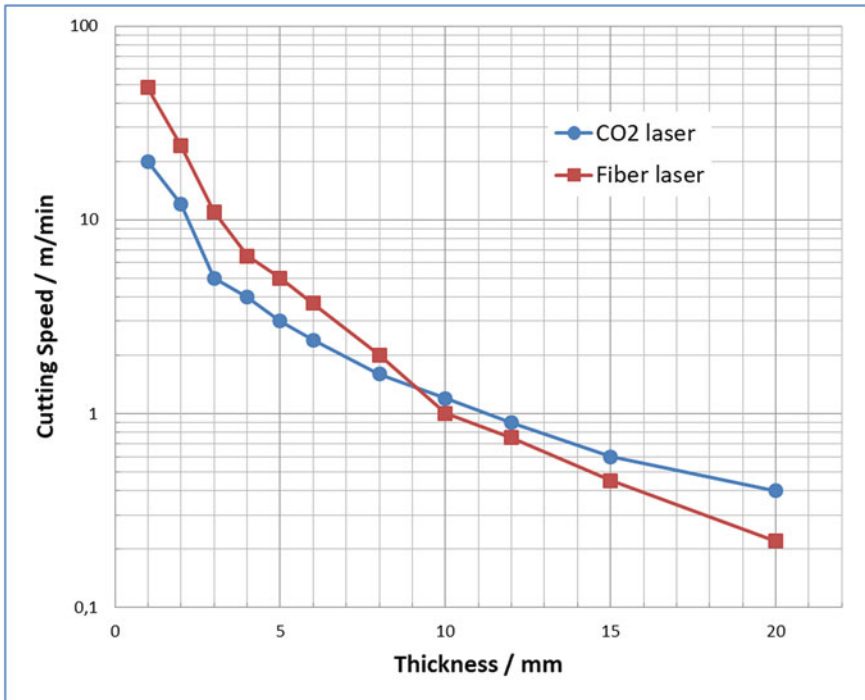
Fig. 32.2 Cutting speeds for laser fusion cutting with 5 kW laser power. Data from Powell et al. (2017)

To fulfill these demands, in laser fusion cutting lasers with high beam quality are employed. Typical multi mode fiber or disk lasers with a beam quality between 2 and 10 mm mrad are used, serving fibers with diameters between 50 and 200 µm. Not as a general rule but for good orientation, the Rayleigh length of the caustics is used to be half to double the sheet thickness. For a given beam quality, a setup with the shorter Rayleigh length and a smaller focus is more speed orientated, whereas the longer Rayleigh length and a bigger focus promotes robustness with respect to the focus position. Even when good beam quality is advantageous, single mode fiber lasers can overshoot the target, because except for very thin material long focal lengths are necessary to achieve desired spot sizes, which is unfavorable for practical reasons e.g. the usage of typical commercial cutting heads.

For fusion cutting, the focal position typically lies between the top and the bottom side of the material. A low position to the bottom side leads to an improved coupling of the cutting gas stream into the kerf, because the top of the kerf is wider than with the focus position at the surface. Thus a low focus position can be reasonable when burr formation otherwise occurs. The maximum speed—in dependence on the focal position—is reached at higher focal positions at the material surface or slightly below.

The efforts to improve the surface roughness of the cut flanks in thick section cutting with 1 μm wavelength led to numerous proprietary laser internal and external beam shaping devices. Examples are the use of multi core fibers with a central fiber and a coaxial ring fiber, superposition of partial beams to various patterns or dynamical beam shaping with scanner mirrors for small and fast movements of the beam on the cutting front.

32.2.3 Cutting Gas Flow

The primary task of the cutting gas jet is to expel the material molten by the laser on the cut front out of the kerf. Moreover, it protects the optics from process emissions and can cool the optics. Besides the interaction of laser beam with the material, the gas flow accelerating the melt in the kerf is the second important quality determining sub-process. The setting of the gas parameter, i.e. nozzle diameter, nozzle distance to the material surface and cutting gas pressure, are essential to achieve a burr free cut and affect also the roughness of the cut flank.

The optimal cutting gas pressure p_0, measured in the pressure chamber of the nozzle, increases with the sheet thickness from approx. $p_0 = 0.5$ MPa (pressure difference to the ambient pressure p_u) at material thicknesses in the area of a millimeter to over 2 MPa for sheet thicknesses above several millimeter. High pressure, same as a small nozzle distance and a large nozzle orifice, increase the melt accelerating forces, but there are undesirable negative influences that limit an appropriate pressure. Cutting gas pressure that is too low produces an insufficient expulsion of melt and leads to burr formation. Pressure that is too high hardly has a positive effect on cutting speed or cutting quality, rather it creates high gas consumption, can be destabilizing by promoting plasma formation and leads to higher roughness of the cut flank.

Typical nozzle diameters lie between 1 and 3 mm, but in thick section cutting also bigger nozzles up to 5 mm are in use.

Nozzle distances between 0.5 and 1.0 mm have proven useful. To ensure a constant nozzle distance and focus position during the processing, laser cutting heads are equipped with a capacitive distance control, in which the nozzle itself acts as an electrode. A preferably high dynamic axis orthogonal to the surface closes the control loop and prevents collisions between the material and the nozzle tip. Thus material with technically unavoidable unevenness can be cut and the start of the cut with the approximation of the cutting head to the material for piercing is much simplified.

Commonly, conic nozzles with simple cylindrical or conical outlets are utilized. Since the cutting gas pressure during fusion cutting lies over the critical pressure of 1.89 p_u, the cutting gas streams at the nozzle opening at the speed of sound in an underexpanded jet. After exiting, the jet expands at supersonic speed, and above the workpiece a vertical shock wave forms. A part of the gas jet is coupled in the cut kerf and forms periodic compression and expansion zones. Figure 32.3 shows a Schlieren optical picture of a free jet. In the free jet, a vertical shock wave forms first with a

Fig. 32.3 Schematic and Schlieren optical representation of the free jet under a cutting nozzle

strongly underexpanded jet. Bright-dark gradients are visualized in this observation method as a density gradient of the jet.

In order calculate the gas consumption of a cutting head through a nozzle, the mass flow rate is given according to Truckenbrodt (1980) for an isentropic expansion by

$$\dot{m} = \rho_0 c_0 A M a \left(1 + \frac{\kappa - 1}{2} M a^2 \right)^{-\frac{\kappa + 1}{2(\kappa - 1)}}.$$

When cutting gas pressures are above critical pressure, the Mach number at the nozzle exit for conical nozzles is limited to $Ma = 1$ and the mass flow rate depends linearly upon the exit surface A and the cutting gas pressure ρ_0. Figure 32.4 shows the gas consumption in the common specification of the volume stream under normal conditions.

The high relevance of the cutting gas flow results in numerous variants of simple conical nozzles, aiming at better cut quality, lower gas consumption or a higher distance tolerance. Examples for those nozzles are nozzles with multiple outlets, e.g. a central orifice and a concentric ring orifice to support melt ejection behind the cut front by covering a longer part of the kerf without using a very large nozzle.

Also nozzles that allow a zero distance to the sheet surface by a flexible suspension are in use, thus having an efficient incoupling of the gas into the kerf.

Another variant are double-walled nozzles (autonomous nozzles), which built up the cutting gas pressure in a ring shaped structure coaxial to the laser beam. A sealed pressure chamber, which the laser beam has to enter through a lens or a window, is not necessary. Consequently this design can be used with open focusing mirror optics and is predestinated for cutting with highest laser power, avoiding thermal stress on transmissive optics. 5 shows the principle set-up of the autonomous nozzle. The cross-section in the streaming channel has to be dimensioned in such a way that
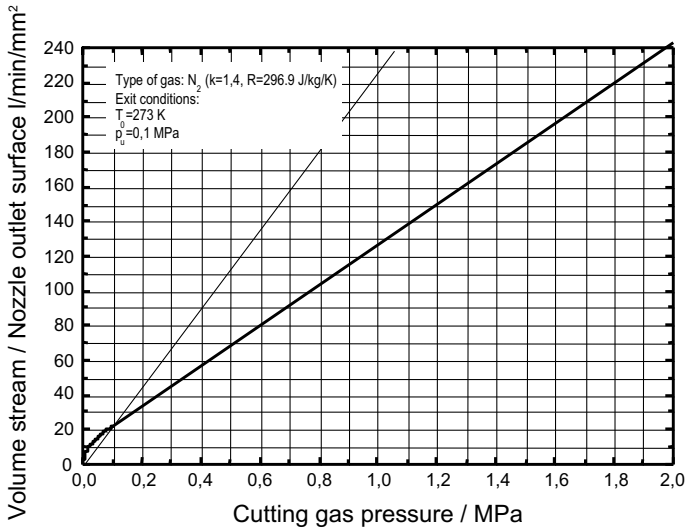
Fig. 32.4 Gas consumption dependent upon the cutting gas pressure; volume flow rate in norm liters. pn = 0.10113 MPa. Tn = 273.15 K (0 °C)

neither air is sucked in the opening through which the laser passes, thus contaminating the cutting gas, nor that a leakage stream that is too large exits through this opening.

Because the space between the nozzle and the optics is not part of the pressure chamber, this concept allows the integration of a cross-jet underneath the optics, such that the head can also be used for welding. In this case the nozzle is used to provide a coaxial protective gas flow for welding and the cross jet protects the optics against sputter and fume. With this combi-head a flexible switching between cutting and welding is possible just by switching the parameters instead of changing equipment (Fig. 32.5).

32.3 Sample Applications

In the 2D field of application, what are commonly used are flat bed machines with fiber or disk lasers and, with decreasing incidence, CO_2 lasers. This is seen, for example in "laser job shops" by service companies for sheet metal cutting. These kinds of companies take advantage of the maturity of this technology with its high flexibility and efficiency of the machines, e.g. by automated loading/unloading systems and nesting software providing optimal material utilization, for producing small to large batch sizes. The spectrum of products is very wide, including automotive parts, parts for furniture, housings, machines etc.

Applications in the 3D field lie, for example, in the processing of pipes. For this, special laser pipe cutting machines are available, with which complete lengths of
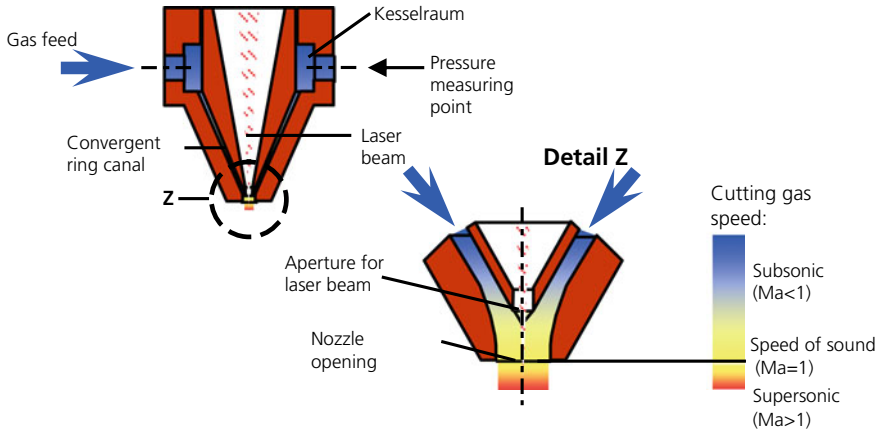
Fig. 32.5 Schematic diagram of autonomous cutting nozzle

pipe can be automatically loaded and processed. In addition to a turning axis and the axial feed of the pipe, the machines have at least two further axes to position the cutting head vertical to the pipe axis. This way, due to a extensive automation, even more complex contours can be cut, making innovative pipe connections possible.

A further example is the 3D cutting of deep-drawn parts, e.g. the trimming and cutting of holes and cut-outs in components from vehicle construction as B-pillars (see Fig. 32.6). Since high-strength steels are being used increasingly, laser processing is becoming more and more important compared to mechanical cutting, with which such materials can only be processed with great difficulty.
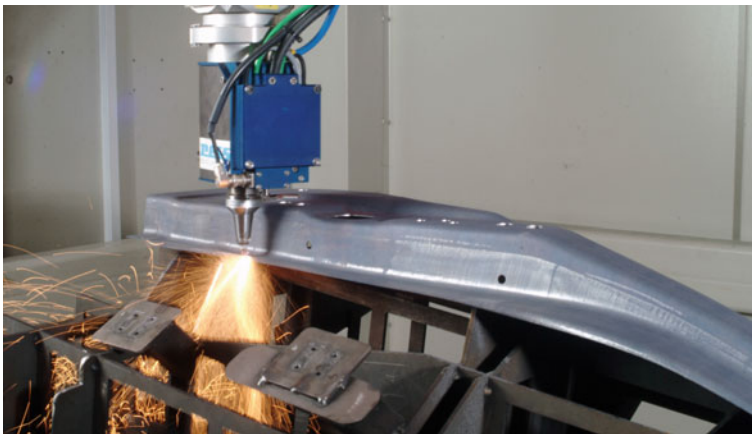
Fig. 32.6 Laser cutting of a B-pillar on a gantry robot with a fiber laser

References

Kaplan FH (2002) Theoretical analysis of laser beam cutting. Shaker-Verlag, Aachen

Petring D (1995) Anwendungsgestützte Modellierung des Laserstrahlschneidens zur rechnergestützten Prozeßoptimierung, Dissertation RWTH Aachen

Petring D, Schneider F, Wolf N, Nazery V (2008) The relevance of brightness for high power laser cutting and welding; ICALEO 2008. In: 27th international congress on applications of lasers & electro optics. Congress proceedings, Temecula, CA, USA. Orlando, Fla, LIA (LIA 611 = 101), pp 95–103

Powell J, Petring D, Pocorni J, Kaplan A (2017) LIA guide to high power laser cutting. Published by Laser Institute of America

Truckenbrodt E (1980) Fluidmechanik, Band 2. Springer, Berlin Heidelberg, New York, p 30 ff

Chapter 33
High Speed Cutting

Frank Schneider

33.1 Introduction

In standard laser oxygen and laser fusion cutting, the laser beam is absorbed on the cutting front and the molten material is ejected by the cutting gas along the front. Forced by shear stress and a pressure gradient from the cutting gas, the melt is accelerated from the top to the bottom side of the material.

The temperature of the melting layer is strongly dependent on the cutting speed. The reason is, with increasing cutting speed, the heat flow through the melt to the liquid/solid interface has to increase. Also, the mass flow of molten material and the thickness of the melting layer increase. For achieving a stationary balanced energy flow at the interphase under these conditions, the temperature on the melt surface has to increase, resulting in a higher portion of material that is heated up even beyond vaporization temperature (Petring 1995).

The evaporated material leads to azimuthal pressure gradients induced by the vapor pressure on the cutting front. These pressure gradients accelerate the melt to the edges of the emerging cutting kerf. With increasing cutting speeds the melt flows more and more around the laser beam, prior to the ejection forced by the downwards-oriented acceleration from the cutting gas. On the side of the interaction zone opposed to the cutting front, the melt is accumulated and a keyhole is formed. The ejection of the melt out of the cut kerf takes place some focal diameter behind the laser beam position and the keyhole. This cutting process with initially dominant azimuthal melt flow and a keyhole is called high speed cutting (Preißig 1995; Petring et al. 1991) in the narrow sense. However, the term high speed cutting is used also for fast standard cutting processes in the thin sheet regime, not considering the details of the laser-material interaction zone. Figure 33.1 shows sketches comparing the interaction zones in conventional and high speed cutting.

F. Schneider (✉)
Fraunhofer ILT, Aachen, Germany
e-mail: frank.schneider@ilt.fraunhofer.de
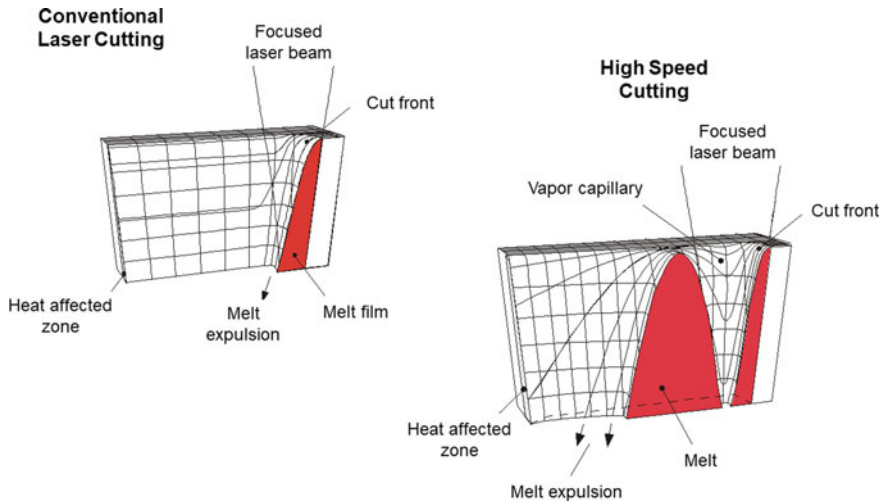
Fig. 33.1 Schematic comparison of the laser-material interaction zone for conventional cutting and high speed cutting (Preißig 1995)

The dominantly azimuthal melt flow generates a convective energy transport to the edges of the kerf, leading to an enlarging of the cut kerf. Whereas in a standard cutting process, the cut kerf width roughly equals the size of the laser beam on the sheet surface, in a high speed cutting process, the cut kerf width can be twice as wide as the laser beam diameter. Figure 33.2 shows the cut kerf width versus the maximum cutting speed. *Maximum* cutting speed implies that for each cutting speed in Fig. 33.2, just the minimal necessary laser power was applied.

Besides the melt flow, also the absorption mechanism in high speed cutting is different compared to standard cutting. The laser radiation is absorbed not only at the front in direct absorption of the laser beam and absorption of its (multiple) reflected parts, but also in absorption in the backside melt accumulation. At the backside, reflected laser radiation can be absorbed at the front and thus contribute to good process efficiency. The efficient absorption in high speed cutting is evident by the amount of transmitted laser radiation through the cut kerf: employing the minimal necessary laser power per speed, at high cutting speeds, in the example in Fig. 33.2 higher than 30 m/min, no transmitted laser power can be detected below the cut kerf. When cutting with a considerable laser power reserve, the capillary is open at the bottom side. A closed capillary can be observed at speeds higher than 80% of the maximum speed.
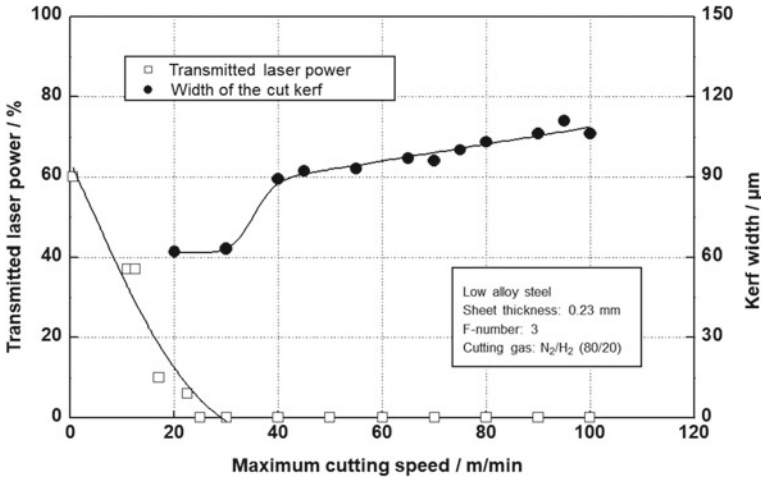
Fig. 33.2 Cut kerf width and transmitted laser power through the cut kerf at minimum laser power adapted to the cutting speed (Preißig 1995)

Fig. 33.3 Sketch of the keyhole illustrating increased absorption by multiple refections (Preißig 1995)
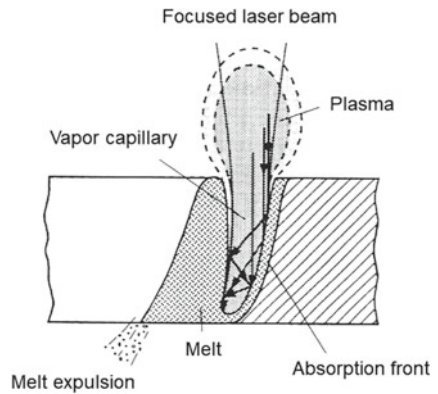
33.2 Process Description

High cutting speeds, leading to a high ratio of vaporization and thus establishing the high speed cutting process phenomena, are achieved in thin material thicknesses, with a small focal diameter and high laser power. In sheet thicknesses in the range of one millimeter, typically below one millimeter, imaging ratios down to 1:1 can be employed. This leads to small spot sizes with short, but sufficient Rayleigh lengths suitable for the thin material thickness. The process profits from excellent laser beam quality, provided by fiber and disk lasers with fibers not bigger than $100\,\mu m$ diameter (beam parameter products below 4). For the thickness of 1 mm and below, $50\,\mu m$

Maximum cutting
speeds for automotive steel
with 4 kW laser power
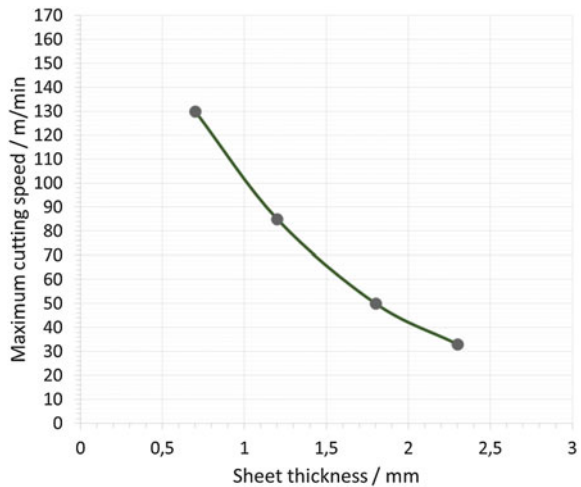
fibers down to single mode fibers with diameters smaller than 20 μm are advanta-
geous. This leads to cutting speeds over 100 m/min in 1 mm sheets of steel with 4 kW
laser power. Figure 33.4 shows the maximum cutting speeds for cutting automotive
steel with a 4 kW fiber laser and a 50 μm fiber. Also, with fundamental mode CO_2
lasers ($M^2 < 1.1$; BBP $< 3,8$) the high speed process is possible. However, especially
in thin-section cutting the process efficiency is better with 1 μm wavelength than
with 10 μm wavelength, because in thin-section cutting, the cutting front is less
inclined, and under these absorption angles the absorptivity for 1 μm radiation is
higher than for 10 μm. Together with the other advantages of 1 μm beam sources—
beam guiding by fiber, high plug efficiency, low maintenance, small sizes of laser
and chiller, etc.—the future of high speed cutting belongs to the 1 μm lasers rather
than CO_2 lasers.

   In high speed cutting, typical N_2 or air is used as cutting gas. The use of Oxygen is
not advantageous in high speed cutting. In standard cutting, the exothermal reaction
and the higher absorption increase the cutting speed in comparison with the use
of inert gas when fusion cutting at moderate laser power. With decreasing sheet
thickness and increasing laser power, the exothermal reaction is too slow to contribute
significantly to the power balance. In high speed cutting of thin sheets in the thickness
range of some tenths of a millimeter, the speed with oxygen is just about 10%
higher than with inert gas. However, the slight increase in speed is associated with
a significant loss in quality, because the melt is not only oxidized at the absorption
front, but also uncontrolled in the melt-pool behind the front.

   High speed cutting provides an excellent, burr-free cutting quality. However, at
low speeds, e.g., during the acceleration and deceleration of the machine in contours,
the melt is ejected in a standard cutting process driven by sheer stress and pressure
gradients along the cutting front. With thin sheets, the distance where the gas can
accelerate the melt is low, and in the low speed range, the melt film is thin and the

surface tension is high because of low temperatures. All this constrains the ejection and leads to a drop-shaped burr. For a burr-free quality in the low speed range, the laser power must be modulated. High intensities during beam on times generate for short times high temperatures, a temporarily thicker melt layer and vapor pressure that accelerates the melt and leads to an effective ejection.

The modulation parameters frequency and duty cycle should dynamically be adapted to the cutting speed. Important boundary conditions are a sufficient average power and sufficient overlap of laser pulses.

With increasing sheet thickness, the change of the process from high speed cutting with a keyhole formation to standard cutting is smooth. Employing high laser power, the process is also in the thickness range of one millimeter controlled by a high ratio of vaporization, but typical characteristics of the high speed process as the enlarging of the kerf width compared to the beam diameter are not found.

33.3   Application Example: Laser Blanking

The implementation of the high speed cutting process must necessarily consider the facilities of the motion system of the machine used for this application. In 1-D applications, as slitting or trimming of strip steel the maximum operating speed is constant over long periods and the productivity is directly correlated with the maximum achievable process speed.

To implement the high cutting speeds in 2-D applications, high dynamic drives are necessary to reach the maximal possible cutting speed on as much as possible cut length in contoured parts and to be as fast as possible in radii and at corners. Thanks to high dynamic direct drives and lightweight design of machine frame high acceleration up to 5 g, in exceptional cases even up to 10 g, paired with a high jerk are possible and enable also on contoured parts average cutting speeds that allow an economical substitution of punching machines.

With laser blanking, the cut out of typically automotive parts for the following pressing of body parts, a new generation of laser machines, processing the material directly from coil, competes with the commonly used punching machines. While the material is continuously decoiled and moved through the cut cabin, it is cut by one or several lasers at the same time. The advantages of using the laser are.

- No tool is needed and all correlated costs and efforts are omitted: direct tooling cost, set-up times for tool changes, required space for tool storage, tool repair, and maintenance. Using the laser, the costs are to a large extent decoupled of the lot size facilitating the trend to smaller batches and shorter time to market.
- Restrictions of tool-bound machining are overcome: new designs and change of designs even after starting a production job are easy to implement by changing the NC-controlled cut path, making it easy to carry out part optimization desired from the pressing process.

- Laser blanking allows a flexible nesting and mixing of batches for optimized material utilization and reduction of scrap.

The flexible, non-tool-bound production leads to an overall productivity of the laser process that can outrival the punching machines even if laser cutting in the primary processing time is slower. However, employing lasers with more and more power, available at economic investment and running costs, will shift this break-even point to thicker and thicker sheets.

References

Petring D (1995) Anwendungsgestützte Modellierung des Laserstrahlschneidens zur rechnergestützten Prozessoptimierung. Dissertation RWTH Aachen

Petring D, Preißig K-U, Zefferer H, Beyer E (1991) Plasma effects in laser beam cutting, 3. Internationale Konferenz Strahltechnik, Karlsruhe, 1991, DVS-Berichte Band 135, S 251 ff

Preißig K-U (1995) Verfahrens- und anlagenentwicklung zum Laserstrahlhochgeschwindigkeitsschneiden von metallischem Bandmaterial. Dissertation RWTH Aachen, 1995

Chapter 34
Sublimation Cutting

Bernd Seme and Frank Schneider

34.1 Introduction

During laser beam sublimation cutting, the workpiece is converted from the solid to the gaseous aggregate state in the area of the kerf due to the influence of laser radiation. According to the type of material to be cut, the transformation from the solid to gaseous aggregate state occurs through vaporization (e.g. Plexiglas), sublimation (e.g. graphite) or, in most cases, through chemical decomposition (e.g. polymers, wood). In the last case, complex molecules are decomposed into smaller molecules and the vaporization of volatile components occurs. Since the transition of the workpiece into the gaseous phase does not solely occur through sublimation, one also calls sublimation cutting as "laser vaporization cutting." Since the working material vaporizes within the kerf, no process gas jet is needed to expel the material when using sublimation cutting. Commonly, an inert gas is utilized, coaxial to the laser beam, in order to protect the processing optics and to prevent the workpiece from oxidizing (see Fig. 34.1). Especially appropriate for sublimation cutting are non-metals such as paper, wood, and several types of ceramics and plastics, all of which do not possess molten phases (Kaplan 2002; Herziger and Loosen 1993).

Sublimation cutting is characterized by the following advantages in comparison to laser beam fusion cutting or oxygen cutting:

- Since very little molten material arises, smooth surface kerfs result without pronounced striation structures,
- Oxide-free cut kerfs arise as in laser fusion cutting. The workpiece can be processed further without post treatment, and
- The heat-affected zone at the margins of the cut edges and the total heat load of the workpiece are minimal.

B. Seme · F. Schneider (✉)
Fraunhofer ILT, Aachen, Germany
e-mail: frank.schneider@ilt.fraunhofer.de

Fig. 34.1 Laser sublimation cutting
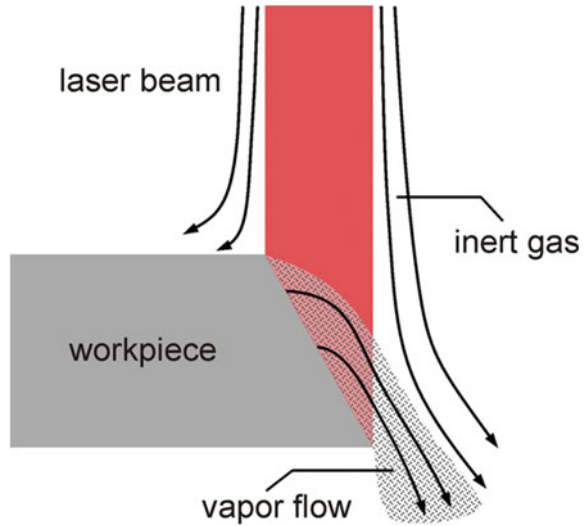
In comparison to fusion cutting, sublimation cutting requires, however, significantly higher intensities, and hence a high-performance laser of good beam quality.

34.2 Power Balance for Laser Sublimation Cutting

In the case that the entire material in the cut kerf vaporizes, the following power balance results for the cutting process:

$$AP_L = b_c d \, v_c \rho \, [c_p(T_V - T_\infty) + H_m + H_V] + P_{HL}. \tag{34.1}$$

The summands on the right side indicate the necessary output for the warming of ambient temperature to vaporization temperature, the power for the melting and vaporizing of the cut kerf volume, and the thermal dissipation losses. This power requirement has to be covered by the absorbed laser power. In the balance, A is the absorption degree of the workpiece, P_L is the laser power, b_c is the cut kerf width, d is the workpiece thickness, v_c is the cutting speed, ρ is the work material density, c_p is the specific heat conductivity of the workpiece, T_∞ is the ambient temperature, T_V is the vaporization temperature of the workpiece, H_m is the specific fusion enthalpy of the workpiece, H_V is the specific vaporization enthalpy, and P_{HL} is the thermal dissipation losses from the cutting zone.

If the entire material is sublimated in the cut kerf, the sum of the fusion enthalpy and vaporization enthalpy has to be supplied as sublimation enthalpy during the transition from the solid to the gaseous state. That is, the specific sublimation enthalpy

Table 34.1 Necessary energies (per volume) for heating and phase transformation of various materials (Kaplan 2002)

	Heating energy (melting) J/mm^3	Latent melting energy	Heating energy (evaporating)	Latent heat of vaporization	Total heat of vaporization	Melting energy (%)	Latent heat of vaporization (%)
	$e_{hm} :=$ $\rho c_p(T_m - T_\infty)$	$e_m :=$ ρH_m	$e_{hv} :=$ $\rho c_p(T_v - T_m)$	$e_v := \rho H_v$	$e_{ht} := e_{hm} + e_m + e_{hv} + e_v$	$(e_{hm} + e_m)/e_{ht}$	e_v/e_{ht}
Si	2.27	4.28	1.54	27.37	36.46	18	77
Al	1.58	1.00	4.47	30.78	37.83	7	81
Fe	5.44	2.12	4.36	52.18	64.10	12	81
Ti	3.93	4.68	3.77	102.60	114.98	7	89
Cu	3.77	6.30	5.23	147.39	162.69	7	91

H_S is given by $H_S = H_m + H_V$, and the above-indicated power balance remains valid in the case of sublimation of the material in the cut kerf.

During the chemical decomposition of the workpiece under the influence of laser radiation, $H_m + H_V$ has to be replaced by the specific decomposition enthalpy H_Z and T_V by the decomposition temperature T_Z in the balance.

In Table 34.1, the necessary energies per volume for the heating and phase transformation of various metals or semi-metals are given. Here T_m indicates the fusion temperature. The total vaporization energy in each is a degree of magnitude higher than the necessary energy for the melting. For iron, for example, this results in: $e_{ht}/(e_{hm} + e_m) = 8.5$. That is, in case different laser cutting processes can be chosen for a material, the sublimation cutting requires the highest power density. In order to reach the necessary high power densities for sublimation cutting of the materials listed in Table 34.1, pulsed laser radiation is used. The short effective duration of the intensive laser pulses limits, in addition, the heat transport into those materials with good heat conductivity. Hence, the thermal dissipation losses are small and cuts are possible which have a very small heat affected zone. Sublimation cutting of the named materials is thus advantageous when complex contours should be cut out with very high precision from thin workpieces. In all of the other cases, fusion cutting is more advantageous when processing metals due to its lower power demand.

34.3 Sample Applications for Sublimation Cutting of Non-metals

For the sublimation cutting of non-metals such as ceramics, wood, paper, plastics or leather, CO_2 lasers can be used efficiently, since the materials named exhibit a very high degree of absorption at a wavelength of 10.6 m. Furthermore, since the thermal conductivity of these materials is several orders of magnitude lower than that of metals

Table 34.2 Comparison of heat conductivity of several metals and non-metals (Ready 2001)

Material	Heat conductivity (W/mK)
Copper	$4 * 10^2$
Aluminum	$2.4 * 10^2$
Iron	$8 * 10^1$
Plexiglas	$1.9 * 10^{-1}$
Wood (oak)	$1.6 * 10^{-1}$
Cotton	$4 * 10^{-2}$
Cork	$3 * 10^{-2}$

(see Table 34.2), the heat losses are much lower than when metals are processed. The heat conductivity of the workpiece is, therefore, minimal. Figure 34.2 indicates cutting speeds for various non-metals at 500 W cw CO_2 laser power. Figure 34.3 shows a cut edge made in pine wood using CO_2 laser radiation.

With Nd:YAG lasers, many organic materials cannot be cut or only cut poorly, since they are transparent for radiation with a wavelength of 1064 nm or only have a minimal degree of absorption. For some organic materials, the absorption can be increased using additives such as carbon dust so that here also cutting with Nd:YAG lasers is possible. The ability to cut strongly depends, however, on the type and amount of additive. Many non-organic non-metals can be cut well with pulsed Nd:YAG laser radiation. The Nd:YAG laser is mainly used here when precise cuts and complex contours are required.
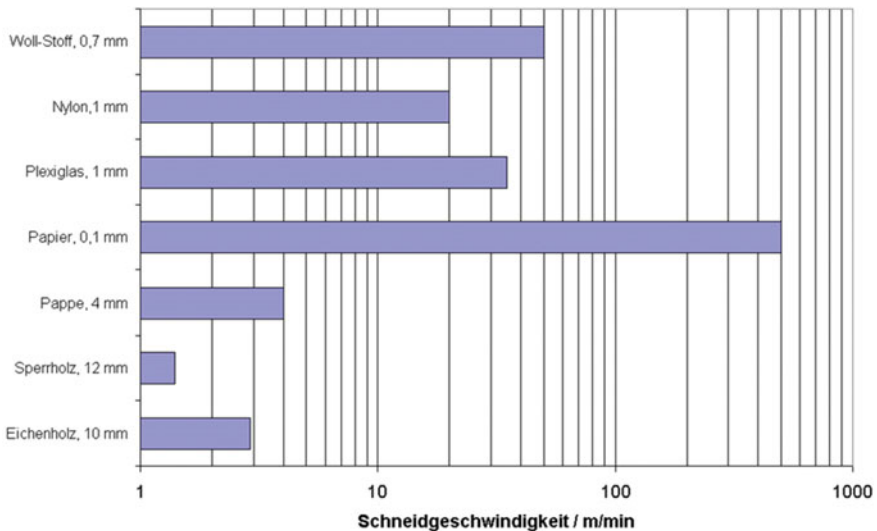
Fig. 34.2 Cutting speeds in several non-metals when using CO_2 laser radiation, power 500 W (cw) (Ready 2001)
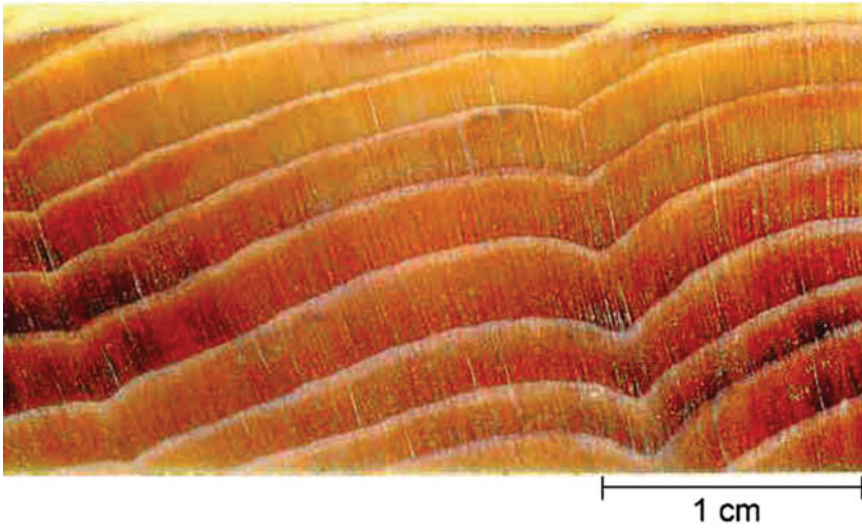
Kiefer, d = 24 mm, v = 1.5 m/min, P = 1200 W, CO_2 Laser

Fig. 34.3 Pine wood cut with laser radiation (*Source* ILT)

References

Herziger G, Loosen P (1993) Werkstoffbearbeitung mit Laserstrahlung, Grundlagen-Systeme-Verfahren. Carl Hanser Verlag, München, Wien

Kaplan AFH (2002) Theoretical analysis of laser beam cutting. Shaker Verlag, Aachen (Berichte aus der Fertigungstechnik)

Ready JF (2001) Handbook of laser materials processing. Laser Institute of America

Chapter 35
Remote Cutting

Frank Schneider

35.1 Process Description

Laser remote cutting stands for a cutting technique that dispenses with the use of a gas flow from a cutting nozzle to eject the material out of the cut kerf. In remote cutting, the laser beam is fast moved over the workpiece usually directed by a scanner, and the material removal is made by the pressure gradient arising from vaporization or sublimation in the process zone. In contrast to oxygen cutting, fusion cutting or sublimation cutting, the term remote cutting is not defined by the physical process in the interaction zone of the laser beam and processed material, but by the setup that avoids the cutting head with a nozzle close to the workpiece and works from remote.

Thus for materials that decompose or sublimate, remote cutting is one technical implementation of the sublimation cutting process described in the previous chapter. However, also thin metals up to a thickness of some tenths of a millimeter can efficiently be processed with remote cutting. The vaporization pressure of the vaporized portion of the material is used to eject also the portion in molten phase. High intensity laser beams, as available with single-mode fiber lasers in the kilowatt power range and speeds in the range of meters per minute, are required to open up a process window to provide the required ratio of vaporized material and the pressure gradients for the material removal (Petring et al. 2008).

On the other hand, the required high speeds define and limit the penetration depth that can be achieved with one beam pass over the material. Consequently, to cut material that is thicker than the ablation depth achieved in one pass, the processable thickness can be increased by repeated ablation on the same contour (multi-pass remote cutting) until full penetration is reached. However, with increasing kerf depth, the process efficiency can be reduced because the ejection of material gets constrained by the kerf walls when the aspect ratio of kerf depth and width increases.

F. Schneider (✉)
Fraunhofer ILT, Aachen, Germany
e-mail: frank.schneider@ilt.fraunhofer.de

The system setup using a galvo scanner for the beam movement provides essential requirements to enable the remote process and features the following benefits:

1. The processing dynamics are much higher than moving a cutting head over the contour even when high dynamic machine axes are used. This leads to better efficiency in applications with strongly contoured cut geometries when possible cutting speeds are not reached by cutting machines in corners and small radii. Also applications with many jump movements from one contour to the next profit from the scanner dynamics.
2. The fast processing speed per pass with short local interaction times on the material reduces the heat impact on the material and leads to small heat affected zones at the cut flanks.

Point one is predominately addressed when remote cutting is applied for metals, point two is the main reason for cutting thermally sensitive materials such as fiber reinforced plastics with scanners.

35.2 Remote Cutting of Metals

The efficient use of metal remote cutting covers the application area of thin material in the sub-millimeter thickness range as foils, bipolar plates or electrode sheets.

The effective cutting speed v_{eff}, defined by the cutting speed of the beam movement divided by the number of passes on the contour required for a complete cut, is dependent on various parameters. The laser power, the spot size of the beam, the speed of the beam movement, and the material and its thickness are the most important ones. Laser power above 1 kW, focus size below 100 μm, and scan speeds in the range of several meters per second mark parameter settings that open appropriate process windows to enable the material ejection without cutting gas support (Musiol 2015). Figure 35.1 shows cutting speeds in dependence of thickness and laser power covering the typical power range of metal remote cutting. These speeds are not as high as a gas supported high speed process could provide (see Fig. 35.4; Chap. 33 High Speed Cutting), because more material is vaporized in remote cutting, whereas with cutting gas support, material can more efficiently be ejected in the molten phase. However, the high speeds are not reached in small contours, and therefore, remote cutting with the practical inertia-free scanner can be more efficient in the thickness range up to a few tenths of a millimeter (Lütke et al. 2011).

The simplification in system setup by avoiding the movement of a cutting head has to be seen against the constraint that the cut contours are limited to a size that fits into the working field of the scanner. Accepting a higher effort in control and system setup, coupled machine and scanner axes can extend the working area with a relative movement between scanner and workpiece.
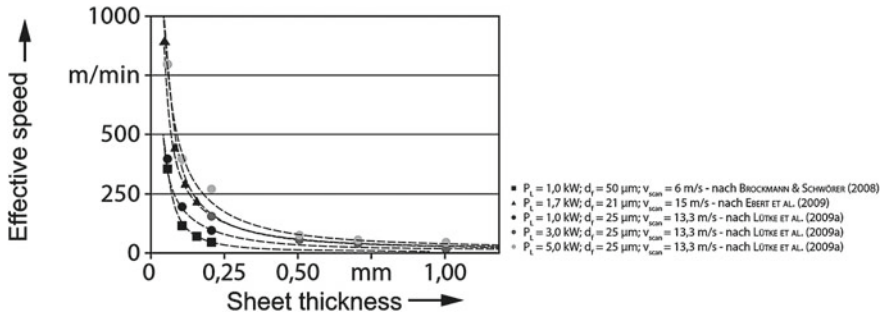
Fig. 35.1 Remote cutting speeds in stainless steel 1.4301 for various settings of laser power P_L, focus diameter d_f, and scan speed v_{scan} (Brockmann and Schwörer 2008; Ebert et al. 2009; Lütke et al. 2009, quoted in Musiol (2015)

35.3   Remote Cutting of Fiber Reinforced Plastics

When cutting fiber reinforced plastics (FRP) with glass fiber and carbon fiber reinforcement (GFRP, CFRP) to mention the most common materials in this material class, the challenge of the thermal processing is to prevent the matrix material from damage while melting (glass fibers) or sublimating (carbon fibers) the fibers to form the cut kerf. Depending on the material, the stability of the matrix is in the range of 150–300 °C, whereas carbon fibers must be heated up to more than 3600 °C for sublimation. By heat conduction, the material near the process zone heats up, and therefore, appropriate thermal process management is needed to minimize the degradation of the matrix. Thus, narrow heat-affected zones (HAZs) at profitable cutting speeds are a primary requirement for laser cutting processes of composite material.

While short and ultrashort pulsed lasers allow high edge quality with HAZs < 20 µm as shown (Freitag et al. 2015), multi-kilowatt high power cw lasers offer high cutting rates of several meters per minute at acceptable quality with a HAZ in a range of 50–100 µm in optimized processes (Schneider et al. 2015; Stock 2017; Staehr et al. 2016). To achieve this, the multi-pass scanning technique of remote cutting is used to dissipate the heat input into small portions. In addition to the scan speed, the interval time between one scan and the next is an important parameter to control the heating of the kerf bottom and walls by the laser beam.

At low scan speed, the long laser-material interaction time and a high volume of ablated material lead to a high thermal load. Accordingly, the heat impact caused by a single scan can be reduced by increasing the scan speed at the expense of the amount of removed material going along with an increase of the required number of passes for the whole cut (Fig. 35.2). Typically, the following scan is carried out before the initial temperature of the material is reached again. Consequently, the temperature level rises from scan to scan and this heat accumulation can cause thermal damage that increases with shorter scan-to-scan interval times. For sufficient long interval times that enable a nearly complete cooling from scan to scan, Fig. 35.2 shows the
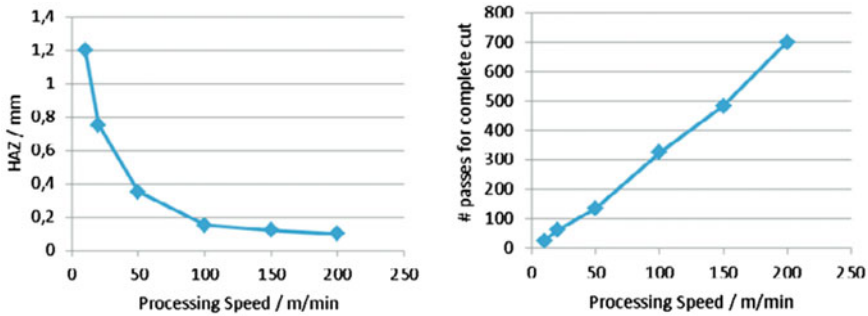
Fig. 35.2 Dependence of the heat affected zone (HAZ) on the processing speed (left) and the number of passes to reach a full separation cut versus processing speed (right) for C/PA [(0,90)]9 (2.1 mm thickness). Parameters: CO_2-laser, 1 kW average power, 500 ns pulses, crossjet gas assistance (Schneider et al. 2013)

decrease of the HAZ with increasing scan speed and the corresponding increase of the required scans.

In Fig. 35.3, streak images show the heat accumulation during processing and cross sections of the cut flanks, pointing out the importance of the cooling time between the scans. The material in this example is a stacked sandwich material with unidirectional carbon fibers reinforcement at the top and a compression mold glass fiber PA6 composite with randomly oriented fibers at the bottom. The cross sections in Fig. 35.4 show a wider HAZ for 150 ms interval time than for 550 ms interval time. In the CFRP layer with the short interval time, the HAZ is 400 μm, whereas it is reduced to 50 μm when the long interval time is applied (Schneider et al. 2019).

For pulsed processes, the scenario of heat accumulation from scan to scan has to be expanded by considering also the influence of heat input by single pulses and by pulse overlap, as it is explained in Weber et al. (2017).

The multi-pass processing is applied in particular to carbon fiber reinforced material. If glass fiber material is cut with a laser, typically a single-pass gas supported standard process is used, because in contrast to carbon, the glass is predominantly transformed into the molten phase during cutting, and thus the process profits from a gas supported ejection. In addition, glass fibers have a lower heat conductivity, and many glass composites consist of randomly oriented fibers. Both diminish the dispersion of a large HAZ. Because of the high absorption in glass, CO_2 lasers are the preferred laser source for glass composites (Schneider and Petring 2018).

For CFRP cutting, high intensities are applied, as provided by single-mode fiber lasers or multimode lasers with high brightness. The small spot sizes at high power in the kilowatt range minimize the thermal load. However, narrow kerfs limit the applicable thickness even in multi-pass cutting, because with an intrinsic inclination of the kerf flanks, the kerf width and the ablation rate decreases with higher depth. Widening of the kerf by adjacent scan paths can increase the thickness range and improve efficiency due to better absorption conditions and material ejection through the kerf being formed. The example in Fig. 35.5 shows a cut flank of 8 mm thick
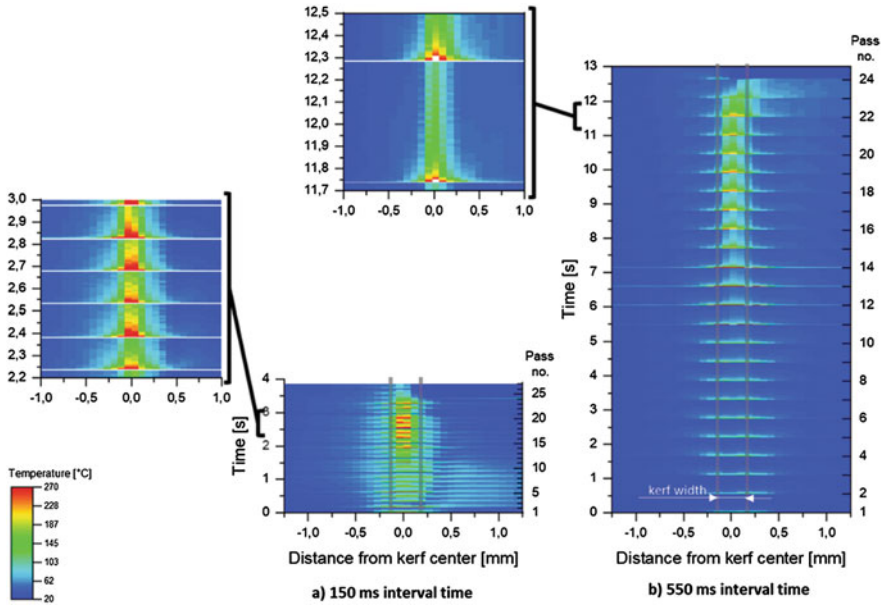
Fig. 35.3 Temperatures on a line perpendicular to the cut path (top view) vs time for two interval times. **a** 150 ms and **b** 550 ms (scan speed 10 m/s, single-mode fiber laser, 5 kW laser power, focus size 50 μm), showing the higher temperature load of the edges at short interval times. The enlargements shortly before the end of the cut show, that after each pass high temperatures in the kerf are hold for a longer time with short interval time. The white lines are video frames during the processing, which cannot be evaluated due to oversteer and image falsification by hot vapor emissions (Schneider et al. 2019)
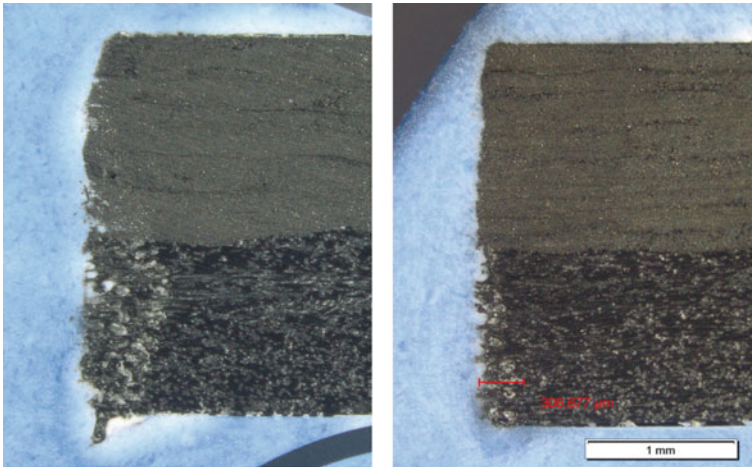
Fig. 35.4 Cross section of a CFRP/GFRP sandwich material with 150 ms interval time (left) and 550 ms interval time (right). Cuts from processing analyzed in Fig. 35.4
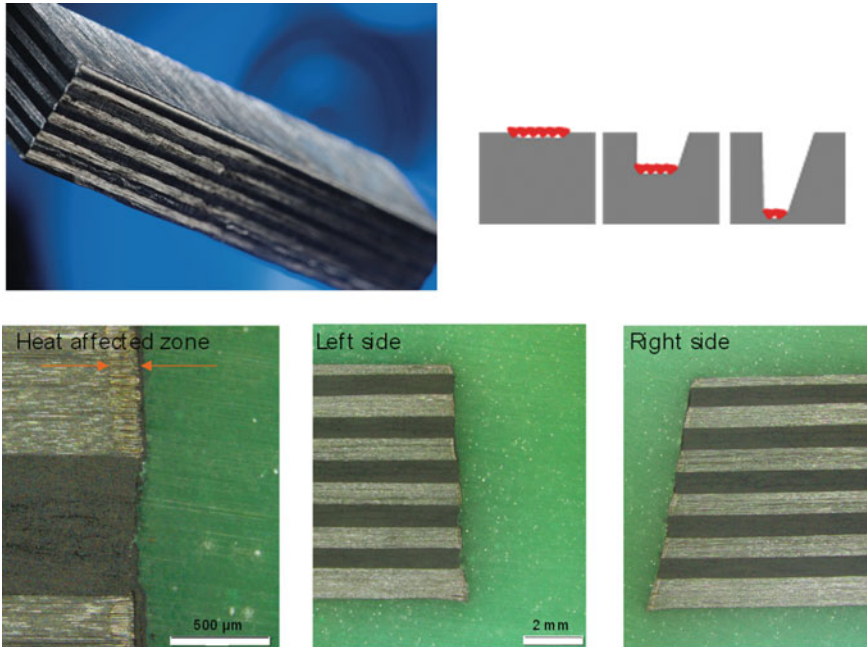
Fig. 35.5 Cut flank of CFRP, 8 mm thickness. The sketch (top right) shows the scan strategy to achieve a deep cut accessibility and the beam orientation for a one-sided perpendicular cut flank. (laser power 5 kW, scan speed 5 m/s, effective cutting speed 0.5 m/min, material carbon fiber UD plies [0/90] with epoxy matrix, fiber volume 59%)

CFRP cut with a 5 kW single-mode fiber laser with an effective cutting speed of 0.5 m/min (Schneider and Petring 2015).

References

Brockmann R, Schwörer T (2008) Anwendungen moderner Strahlquellen und Scanneroptiken fur die Remote-Bearbeitung. In: Systemtechnik für die Remote-Bearbeitung. Nürnberg, 18 Nov 2008

Ebert R, Hartwig L, Hagemann T, Peuckert F, Kloetzer S, Schille J, Wischmann S, Exner H (2009) High rate ablation with 3 kW single mode fibre laser. In: Ostendorf A, Graf T, Petring D, Otto A (Hrsg.) Proceedings of the 5th international WLT conference on lasers in manufacturing LIM. München, pp 565–570

Freitag C, Wiedenmann M, Negel J-P, Loescher A, Onuseit V, Weber R, Abdou Ahmed M, Graf T (2015) High-quality processing of CFRP with a 1.1-kW picosecond laser. Appl Phys A Mater Sci Process 119(4):1237–1243

Lütke M, Himmer T, Wetzig A, Beyer E (2009) Opportunities to enlarge the application area of remote-cutting. In: LIA (Hrsg.) Proceedings of the 28th ICALEO conference. Orlando, 2–5 Nov 2009, pp 311–318

Lütke M, Bartels F, Hauptmann J, Wetzig A, Beyer E (2011) The energetic efficiency of remote cutting in comparison to conventional fusion cutting. In: 30th international congress on applications of lasers and electro-optics, ICALEO 2011, pp 16–24

Musiol JD (2015) Remote-Laserstrahl-Abtragschneiden; Forschungsberichte IWB. München Utz. ISBN:978-3-8316-4523-7

Petring D, Schneider F, Wolf N, Nazery V (2008) The relevance of brightness for high power laser cutting and welding. In: ICALEO 2008, 27th international congress on applications of lasers & electro optics. Congress proceedings, Temecula, CA, USA. LIA, Orlando, Fla. (LIA 611=101), pp 95–103

Schneider F, Petring D (2015) Laser cutting of CFRP. Annual Report Fraunhofer ILT, Aachen, p 125. https://www.ilt.fraunhofer.de/content/dam/ilt/en/documents/annual_reports/AR2015.pdf

Schneider F, Petring D (2018) CFRP is demanding—also on laser cutting. Laser Technik J 15(2):61–65

Schneider F, Wolf N, Petring D (2013) High power laser cutting of fiber reinforced thermoplastic polymers with cw- and pulsed lasers, LiM 2013, Lasers in Manufacturing. In: 7th WLT conference on lasers in manufacturing. Proceedings: Munich, Germany, May 13–16, 2013. Elsevier, Amsterdam (Physics Procedia 41, 2013), pp 415–420

Schneider F, Wolf N, Engelmann C, Moll W, Petring D (2015) Laser cutting and joining in a novel process chain for fibre rein-forced plastics. In: LiM 2015, 8th international WLT-conference on lasers in manufacturing, proceedings, München, Germany

Schneider F, Petring D, Wolf N (2019) Cutting of composite materials: a quality and processing time optimized scan strategy for GFRP and CFRP. In: Lasers in manufacturing conference 2019. Wissenschaftliche Gesellschaft für Lasertechnik e.V. -WLT-. - Aachen: RWTH (2019)

Staehr R, Bluemel S, Jaeschke P, Suttmann O, Overmeyer L (2016) Laser cutting of composites—two approaches toward an industrial establishment. J Laser Appl 28

Stock J (2017) Remote-Laserstrahltrennen von kohlenstofffaserverstärktem Kunststoff. Diss., München, Techn. Univ., p 112

Weber R, Graf T, Freitag C, Feuer A, Kononenko T, Konov V (2017) Processing constraints resulting from heat accumulation during pulsed and repetitive laser materials processing. Opt Express 25:3966–3979

Chapter 36
Laser Fine Cutting

Check for
updates

Arnold Gillner

36.1 Introduction and Application Areas

Laser fine cutting today is used for numerous applications in fine mechanics, medical industry, and electronics. The main fields of use can be found in thin materials with thicknesses <0.5 mm and generally complex structures with feature sizes <200 µm. Laser types, which are used in this field are pulsed solid-state lasers and fiber lasers for metals but also short pulsed Nd:YAG and Nd:VO$_4$-Lasers in Q-switch and mode-locking mode. The spectrum of materials and applications is summarized in the following table.

Metals	Stents, stencils for solder paste printing, metallic prototypes, lead frame prototypes, cannulas for medical products, spinnerets, cutting tools
Ceramics	Printed circuit boards, spinnerets
Polymers	Printed circuit boards, labels
Semiconductors	Semiconductor components, solar cells, displays
Optics	Microlenses, protective lens covers

Especially for the last two applications, where thermal influence has to be minimized and surface absorption plays a crucial role concerning the achievable quality, frequency-converted lasers at 532 nm and 355 nm are used. Due to the short wavelength, the laser energy is absorbed in the surface of the material, rather than in volume, thus leading to clean ablation results and high cutting quality. Moreover, the achievable spot size is much smaller, leading to smaller cutting kerfs and less energy deposition.

A. Gillner (✉)
Fraunhofer ILT, Aachen, Germany
e-mail: Arnold.gillner@ilt.fraunhofer.de

36.2   Process Principle

Laser fine cutting of metals does not distinguish it from the general cutting process applied for macro applications. The material, which has to be ablated is heated and melted by the laser radiation. The melt is then driven out of the cutting kerf by a high pressure gas jet. In contrast to macro laser cutting, in fine cutting, the laser radiation is applied in a pulse mode with very high pulse power. With sufficient pulse power, the material is mainly vaporized during the laser pulse, and the molten material is driven out by the pressure of the vaporized material. In this way, laser fine cutting is similar to single pulse drilling with the difference, that in fine cutting the single pulses are applied with an overlap of typically 50–90% leading to a continuous cutting kerf. In Fig. 36.1, the principle of laser fine cutting is shown. With this process approach, the necessary laser energy and laser intensity can be applied for melting the material, but the overall energy deposited into the material is kept low. Otherwise, the small geometries to be cut would be overheated and destroyed. The focus of the laser beam is set to the surface of the material to achieve the highest intensity and reduce thermal impact.

By using pulsed laser radiation, the energy for cutting and ablation is applied only for short time intervals. Depending on material and material thickness, the process parameters for different materials can be summarized with the following values.
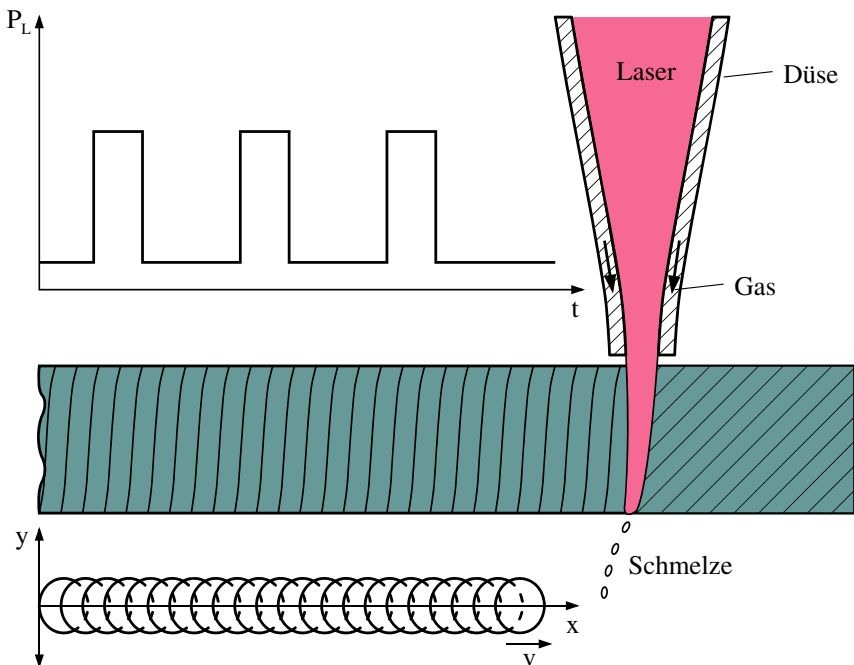
Fig. 36.1   Schematic presentation of laser fine cutting process (© Fraunhofer ILT)

Material	Thickness (mm)	Pulse power	Speed (mm/min)	Pulse frequency
Metal	0.1–0.5	500 W–1 kW	50–200	1–5 kHz
Ceramics	0.3–0.5	1 kW–5 kW	25–100	100 Hz–1 kHz
Polymers	0.05–0.2	>10 kW	100–1000	10–20 kHz

The advantage of pulsed energy deposition is the moderate overall heating of the entire workpiece, whereas in laser cutting with continuous laser radiation, over-heating at small structures will cause increased molten areas and reduced accuracy. This holds especially at complex structures at thin materials, where the restrictions in acceleration of the machining system reduces the achievable cutting speed and where the machine has to reduce the speed nearly down to zero with subsequent overheating of the material. In this case, the energy deposition has to be matched to the resulting speed by selective pulse repetition adaption.

For the heating of the material without melting within a single laser pulse, the following equation can be derived from the general heat conduction equation:

$$
\begin{aligned}
\Delta T &= 2(1-R)\frac{I_0}{K}v_{rep}\tau\sqrt{\kappa t}\cdot ierfc\left(\frac{z}{\sqrt{4\kappa t}}\right) \\
&= 2(1-R)\,\frac{I_0}{K}v_{rep}\tau\sqrt{\frac{\kappa t}{\pi}},\ z=0 \\
&= 2(1-R)\cdot\varepsilon\cdot v_{rep}\sqrt{\frac{t\cdot K}{\rho\cdot c_P\cdot\pi}}
\end{aligned}
\tag{36.1}
$$

The overall temperature at the surface of the workpiece is increasing by heat accumulation with respect to the pulsed energy input slowly and reaches a steady state value after a starting phase. The steady-state value is lower than the melting temperature of the material, so that the overheating of the workpiece is avoided. In Fig. 36.2, the temperature rise within each single laser pulse and the resulting overall temperature are shown schematically.

With this approach, even filigree structures with structure sizes <10 µm and cutting kerf widths of <20 µm can be cut with high-quality laser beams. For these applications, lasers with high beam quality $M^2 < 1.5$ and low beam parameter products are necessary to allow spot sizes of 10 µm and even smaller.

With the development of high power ultrashort pulsed lasers, this new generation of laser beam sources has become a versatile tool for high precision cutting. Ultrashort pulsed lasers provide pulse durations from a few 100 fs to 10 ps with pulse powers up to several Megawatts. At this high power, the entire material within the spot geometry is vaporized leading to an almost melt-free cutting kerf. Due to the fact that the material vapor is removed within nanoseconds up to microseconds by its own vapor pressure, there is no heat transfer from the vapor to the bulk material. Especially for materials, which are very sensitive to heat, such as nitinol for medical stents, this technology is widely used. However, the cutting speed is low, when using this technology because of the necessary energy for vaporization of the material.
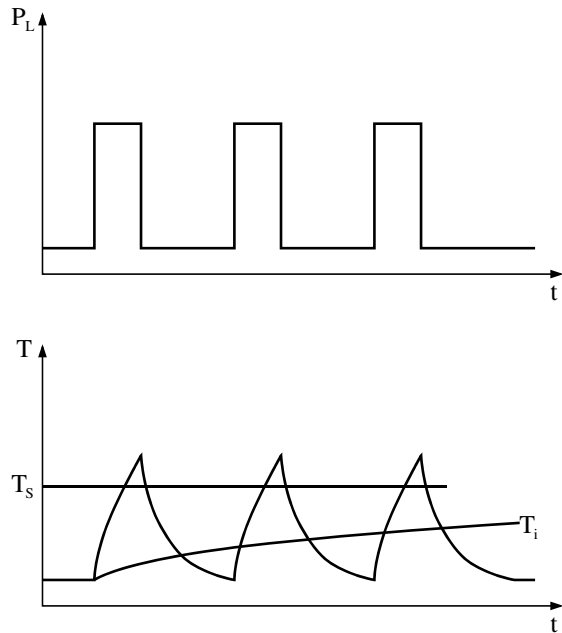
As an alternative to gas assisted though cutting, a second technology for laser
fine cutting has been established, in which the material is ablated layer by layer by
using subsequent laser ablation, in which the material is removed by vaporization.
By scanning the cutting geometry with a fast galvanometer scanner, the material is
ablated layer by layer until the entire material thickness is reached.

With the availability of high power ultrashort pulsed lasers, a new technology for
fine cutting of transparent material such as glass has been introduced. especially for
display glass cutting. Glass normally does not absorb laser radiation in the visible or
near-infrared wavelength range. However at very high intensities and photon fluxes
multi photon absorption takes place, so that free electrons are produced inside the
glass volume leading to a nonlinear absorption phenomena with high absorption
efficiencies. In Fig. 36.3, the principle of this nonlinear absorption effect is shown.
As soon as sufficient free electrons are produced by multi-photon absorption, linear
absorption of the laser radiation increases the energy input into the glass volume. With
this linear absorption, the material properties are changed and internal stresses are
produced. By generation of lines of material modifications, the material cracks, and
a cut is produced. Due to the fact that the material modification also changes the laser
beam propagation inside the material, a self-light guiding structure is produced along
the entire material thickness (see Fig. 36.4). With this technology, called filament
cutting, crack-free cutting of glass and other transparent materials can be obtained.
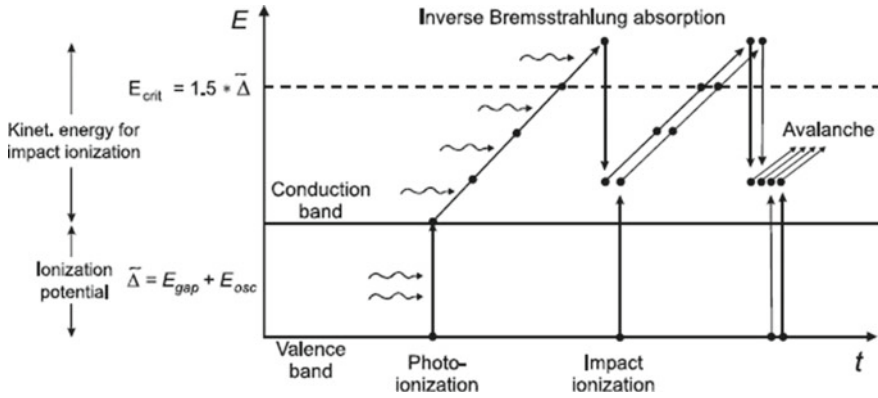
Fig. 36.3 Multiphoton absorption of ultrashort pulsed lasers followed by linear absorption for glass cutting (© Fraunhofer ILT)
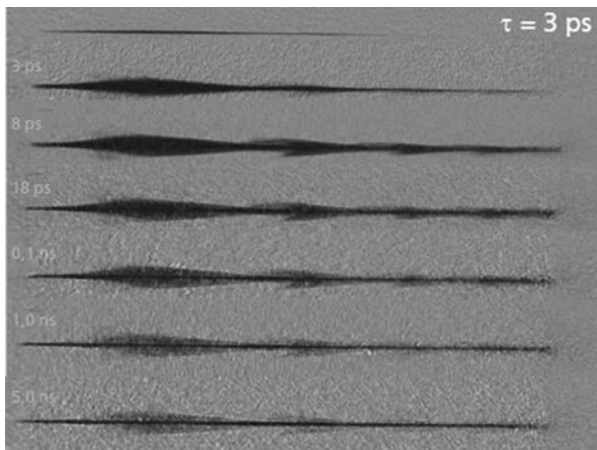
Fig. 36.4 Electron density distribution inside a glass volume with self focusing and filament generation at different times of pulse propagation through the glass volume and a pulse duration of 3 ps (© Fraunhofer ILT)

36.3 Laser Sources for Fine Cutting

Today, for laser fine cutting, typical fiber lasers and diode pumped solid-state lasers are used. These lasers provide very high beam quality near the optimum value of the beam parameter product. Fiber lasers are available at high average powers of more than a kilowatt at beam qualities of $M^2 < 1.1$, which allow spot sizes of a few μm with very high intensities. For precision cutting at low energy input, Q-switched fiber lasers with adaptable pulse durations of 10–200 ns and peak pulse powers of

up to 10 kW are available. These lasers are widely used for cutting thin foils without thermal input due to the entire vaporization of the material.

For laser fine cutting of metal parts, diode-pumped fiber lasers and solid-state lasers are currently the right choice for an economic cutting process. For thicker material and small cutting geometries with complex curves, fast laser pulsing with higher laser pulse power and higher pulse energy is necessary to achieve economic cutting speeds. As an alternative to former lamped pumped solid-state lasers with limited beam quality, quasi-cw-pulsed lasers are available today. These fiber lasers are not pumped by diode lasers in a continuous mode but with high pulsed pumping power, resulting in high peak powers of the fiber laser of up to several kW with a pulse duration of some 100 μs. With this type of laser, highly precise laser cuts with limited melt film thickness at the cutting kerf can be achieved.

For even less residual melt at the cutting kerf and for thermally sensitive materials, short-pulsed lasers, such as Q-switch-lasers with pulse durations from 10–100 ns or even modelocked ultrashort pulsed lasers with pulse durations from 100 fs to 10 ps must be used. Due to the short pulse duration, the thermal influence on the material is minimized according to the thermal penetration depth

$$d_w = \sqrt{4\kappa t} \tag{36.2}$$

where κ is the thermal diffusivity of the material and t is the pulse duration.

Since the intensities using these lasers are generally higher than the vaporization threshold, the whole cutting process is based on sequential vaporization. The laser passes several times across the cutting contour and typically ablates several micrometers of material. With this approach, heat accumulation can be minimized and laser cuts with very high quality can be produced.

Moreover, diode-pumped Q-switch-lasers provide the possibility of frequency conversion with resulting laser wavelengths in the visible light and UV range. Starting from the base wavelength of the Nd:YAG-Laser, the following laser wavelengths can be set for industrial applications.

Base wavelength	$\lambda = 1064$ nm
Frequency doubling	$\lambda = 532$ nm
Frequency tripling	$\lambda = 355$ nm

The conversion of the base wavelength to shorter wavelengths has two advantages:

1. The spot size of the focused laser beam can be reduced according to the beam parameter product, which scales linearly with the wavelength
2. The absorption of all material at shorter wavelengths increases according to Fig. 36.10; leading to less volume absorption and high cutting quality.

With this wavelength reduction, laser absorption takes place directly on the surface of the material within a few nanometers, and the material is directly vaporized. Therefore, the energy input in the material is limited, and very high cutting precision can be achieved even with very sensitive materials such as polymers.
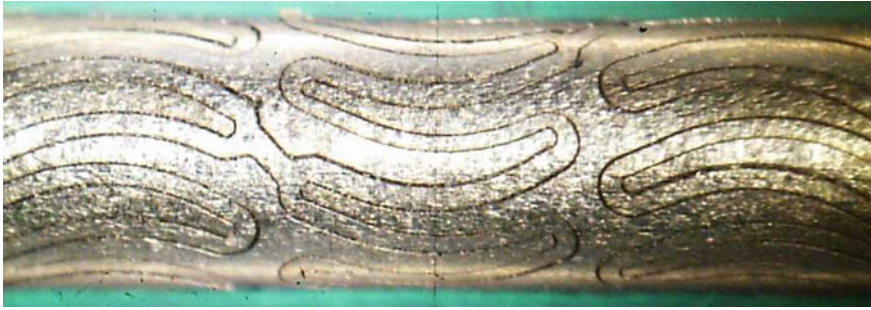
Fig. 36.5 Laser cut stent (diameter 1.6 mm) after cutting (© Fraunhofer ILT)

36.4 Applications

36.4.1 Cutting of Stents

One of the most prominent applications of laser fine cutting is the manufacturing of cardiovascular stents. Stents are small expandable stainless steel tubes with a diameter of 1.6–2 mm, which are implanted in the cardiovascular vessels, and expanded by a balloon catheter, thus expanding and stabilizing the vessel walls. Since the structure of the stent has to be designed in a way that it has to provide maximum stability and at the same time maximum expansion by the catheter, the residual structures are as small as 50–100 μm. The only technology, which can be used for the production of those small features in miniaturized tubes is laser fine cutting.

In Fig. 36.5, a laser cut tube with the stent design is presented.

Figure 36.6 shows a similar stent design after expansion on the catheter. Currently, these stents are made from stainless steel and stay in the vessel. However, to avoid restenosis due to plaque production on the inner wall of the stent, a degradation of the stent after a certain time would be favorable. Therefore, laser cut polymer stents from biodegradable polymers or stents from magnesia are investigated.

In applications where the stent has to be flexible, a special type of material, such as nitinol is used. This material has superelastic properties, which result from a careful heating and cooling process. Laser cutting with fiber laser would introduce excessive heat in the material which causes loss of the specific property of the material. Therefore, ultrashort pulsed lasers are used here for fine cutting with no thermal input.

36.4.2 Cutting of Spinnerets

For the manufacturing of polymer fibers for textiles, micro-structured spinning nozzles called spinnerets are used. The fluid polymer mass is pressed through the

Fig. 36.6 Laser cut stent (diameter 1.6 mm) after polishing (© Fraunhofer ILT)

Fig. 36.7 Laser cut spinneret (© IFSW)
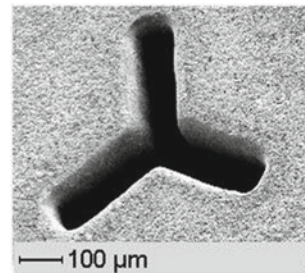
nozzles which form the geometry of the fibers and which solidifies after the nozzle tool. For textiles with special features and functionalities, spinnerets with partly very complex shapes have to be generated. Sometimes, feature geometries, like circles, stars, and triangles with feature size geometry of 100–500 μm and cutting geometries <20 μm are necessary. In Fig. 36.7, a threefold geometry is shown, which has been produced with a frequency-tripled short-pulse laser.

36.4.3 Cutting of Flex Board with UV Laser Radiation

By frequency conversion, the base wavelength of an infrared Nd:YAG Laser can be transformed in the UV range. This leads to an adaption of the absorption and reduction of the penetration depths to the surface of the material varying from several 100 nm to several microns depending on the material. With this reduction of the optical penetration, the thermal effects for the entire workpiece can be further decreased. This holds especially for polymers, which are more or less transparent in the near-infrared and visible area, but absorb very well in the UV region. In Fig. 36.8, the absorption spectra for different materials are schematically shown in dependence on
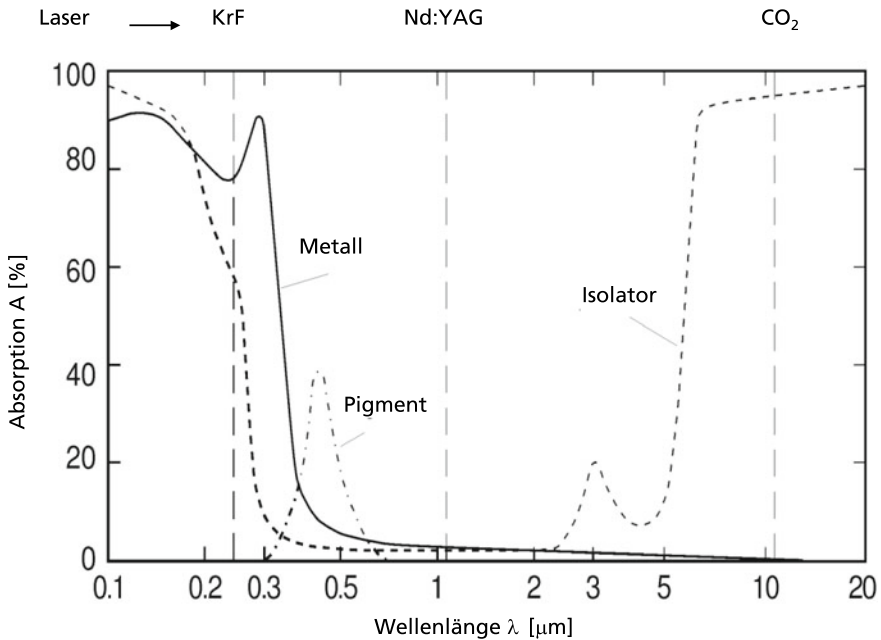
Fig. 36.8 Absorption spectra of different materials depending on the wavelength (© Fraunhofer ILT)

the wavelength. From this picture, it is clear that for polymer cutting, where surface absorption is necessary, either far-infrared laser radiation with wavelength >3 μm or UV radiation <400 nm should be used.

According to the high absorption of polymers in the UV range, for micro processing of polymers, Excimer Lasers as well as frequency tripled solid-state lasers are used. Especially for cutting flexible printed circuit boards from polyimide, high repetition rate Nd:YAG- and Nd:Vanadate Lasers at 355 nm are used. In comparison to excimer lasers with even shorter wavelengths, those lasers provide much higher repetition rates >20 kHz, which allow higher processing speeds. High cutting speeds not only reduce the costs for manufacturing, but also increase cutting quality since the interaction time for laser and materials is reduced and heat accumulation is minimized. In Fig. 36.9, as an example, a laser-cut printed circuit board from PI is shown.

Laser fine cutting of glass is an emerging application field in precision manufacturing. Precise glass parts are needed especially for displays in mobile phones and tablets with multiple openings and complex geometries. For this application, filament cutting and other ultrashort-based cutting technologies are used with internal glass modifications and subsequent breaking through internal stresses. In Fig. 36.10, an example of glass geometries is shown with clear and chipless cutting edges.
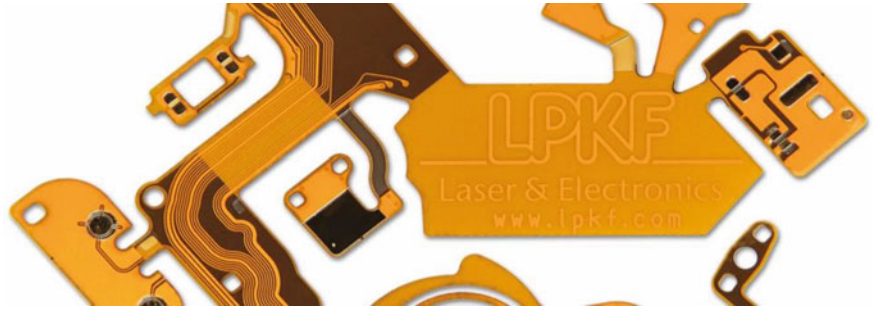
Fig. 36.9 Laser-cut printed circuit board (© LPKF)

Fig. 36.10 Laser glass cutting using internal stress modification by ultrashort pulsed lasers (© Fraunhofer ILT)

Part X
System Technology

Chapter 37
Process Monitoring and Control

Peter Abels, Christian Knaak, Kerstin Kowalick, Stefan Kaierle, Andrea Lanfermann, and Boris Regaard

37.1 Introduction

Manufacturers are forced to bring their products to market faster and cheaper but at the same time place emphasis on high quality. Advanced product design, high production accuracy, as well as flexibility for handling design changes and small lot production, are only a few matters material processing stands to benefit from laser technology. New markets are continuously opened to laser-assisted manufacturing through enhanced laser performance and system improvement. Yet new production technologies and the increasing complexity of the equipment and processes make great demand on adherence to production parameters and raise sensitivity with regard to disturbance variables. In addition, sources of error also result from heightening productivity up to physical limitations. Therefore, increasing demands on production quality as well as improved processing techniques lead to further requirements for quality assurance. It can also be observed in recent years that requirements for all-embracing quality assurance have continuously increased. This is reflected in strict customer requirements of reliability and documentation of workpiece quality (e.g. process capability index Cpk[1]), requirements by law (e.g. for safety relevant components), self-imposed quality standards of the manufacturer, and not least the implementation of industrial standards such as DIN EN ISO 9000ff. Today's manufacturers are increasingly forced to keep a record of their full production. To meet those demands, frequent post-processing quality checks have to be conducted. However, these steps are usually adherent to significant efforts and are often restricted to surface checks. Destructive testing to check for inner defects can only be applied to a few parts.

---

[1] A measurement how well a process in chain production meets the specifications.

P. Abels · C. Knaak (✉) · K. Kowalick · S. Kaierle · A. Lanfermann · B. Regaard
Fraunhofer ILT, Aachen, Germany
e-mail: christian.knaak@ilt.fraunhofer.de

The appraisal of production quality during processing also reduces the exigency of subsequent destructive techniques for quality evaluation. Particularly long and expensive production cycles, therefore, call for online monitoring strategies identifying production anomalies immediately or even avoiding them in advance in order to minimize scrap and costs.

37.2 Sensors

Modern laser systems, in addition to their basic components such as the beam source and the beam guiding and handling optics, comprise a considerable number of sensors. These are responsible for monitoring, controlling or ideally regulating the state of the system and the laser process.

The values and states recorded by the sensors are usually converted to electrical signals and subsequently processed using evaluation algorithms. There are a variety of different types of sensors for measuring physical or chemical properties. In addition to the usual sensors for measuring such parameters as traveled distance, time, angle, acceleration or velocity, laser technology also relies, in particular, on sensor systems that measure electromagnetic radiation, mainly in the visible and near-infrared range (photodiodes, cameras, and pyrometers) to monitor tool characteristics or process states during operation.

Acoustic sensor systems, on the other hand, are rarely used in industrial laser materials processing. This is because the analysis of acoustic emissions—such as those produced by changes in thermal gradients, the formation of holes and cracks, and rapid pressure fluctuations in the keyhole (Ion 2005)—barely allows reliable conclusions to be drawn about the processing result. Supporting tasks, such as measuring the distance to or between objects or monitoring machine operating limits (e.g. triggering an emergency shut-off if the threshold is mechanically exceeded), are performed by mechanical sensors, usually in the form of push-button or switch sensors, or inductive or capacitive transducers.

The laser process is influenced by a variety of factors. The following list classifies the most important parameters:

- Laser beam tool

    o Power
    o Caustic
    o Polarization

- Gases

    o Flow rate
    o Properties

- Workpiece

    o Material properties

    o Material metallurgy
    o Structure (e.g. wall thickness, seam width)
    o Shape (e.g. dimensional stability, geometrical accuracy, dimensions)

- Machine

    o Beam shaping optics
    o Beam guiding optics
    o Workpiece clamping
    o Generation of relative movement

- Method

    o Production sequence
    o Pre-treatment

- Planning accuracy

    o Path planning
    o Process planning

- Filler materials
- Human factors

However, a full top-down analysis of the entire machining process reveals many more parameters that influence the processing result either directly or indirectly in a cause-and-effect relationship (N.N.: Sonderforschungsbereich 1994; Kaierle et al. 1997). The various signals being measured need to be recorded and processed in different ways. The volume of measurement data differs from case to case, as does the frequency with which measurements are carried out and adjustments made. While some information, such as the position of the workpiece or the laser beam parameters, is calculated offline, other data such as the feed rate or process emissions are analyzed during the machining process at repetition rates up to the kilohertz range. In this way, any necessary adjustments, such as regulating the laser output as a function of the feed rate, can be made on the spot. The cause-and-effect relationships of the observed parameters must be of a nature that can be described in models or determined in tests. Pure monitoring of the process and the machine, however, is not subject to this type of limitation.

Most of the mechanical and electrical sensors employed to monitor parameters are part of the system's standard configuration and work independently of the laser tool. They are, therefore, not relevant to the following evaluation. Given that it is impossible to record all the existing parameters and sources of interference, it is very important to monitor and analyze the machining zone during the laser process by means of optoelectronic sensors to ensure the best possible quality and to keep post-processing steps to a minimum.

The following descriptions and examples mainly refer to the monitoring of laser-processed metal parts. Emphasis is also given to the welding process, since in industrial production, it has been most widely established in comparison to other laser material processing methods.

37.3 Electromagnetic Radiation Sensors

The detection of electromagnetic processes and laser radiation is normally restricted to the visible and near-infrared range. The various different detectors available are distinguished, in particular, by their spectral sensitivity, temporal resolution, and the spatial resolution that they are able to achieve in combination with the right lenses. The most important types include one-dimensional temporal resolution sensors such as photodiodes, pyrodetectors, and thermopiles, and spatial resolution measuring and imaging sensors (arrays of light-sensitive cells), such as CCD or CMOS cameras. Integrally measuring detectors only register the intensity of the monitored radiation, and not its spatial distribution. Photodiodes are mainly used to monitor highly dynamic processes due to their high temporal resolution and are easy to handle; thanks to their comparatively moderate demands on data acquisition software and hardware. Pyrodetectors differ from photodetectors primarily in terms of their spectral sensitivity and generally lower temporal resolution. Imaging sensors or cameras are made up of arrays of light-sensitive cells, or pixels, uniformly arranged in rows and columns. They monitor in spatial resolution, which means they not only deliver information on the brightness of an object or beam source, but also on its shape, size, and position. However, the data stream delivered by a camera is higher by the number of its pixels than that of a simple photodetector, and the time required to read out all the image data results in a lower overall temporal resolution than with single light-sensitive cells. Consequently, imaging systems place higher demands on hardware and cost more to buy, but are nevertheless suitable for industrial use. In principle, sensors with spatial resolution can be built up from all integrally measuring detectors by suitably combining various elements. However, the most practicable solutions for process monitoring are camera systems based on CCD or CMOS sensors. These are increasingly being used to supplement or replace photodiodes both in research and in industry, and are opening the door to a large number of new applications. Inline process monitoring, which places high demands on the frame rate (temporal resolution), is generally performed using CMOS technology where, unlike with CCD sensors, the electron charge is transformed into a measurable voltage at the chip level. Each pixel contains a light-sensitive diode and its own evaluation electronics, and can be addressed individually and read out at high frame rates. CMOS cameras are also smaller in size than CCD cameras.

37.4 Measurement Techniques Based on Optoelectronic Sensor Systems

In the measurement of characteristic variables from laser machining operations, a distinction is made according to whether direct or indirect measurement techniques are used. Whereas direct measurement methods enable the desired parameter to be measured straight from the source, indirect measurement techniques require a

Table 37.1 Quality determining values for laser beam welding

• Splatters	• Root undercut
• Penetration notches	• Penetration depth
• Scratches	• Lack of fusion
• Humping	• Seam width
• Seam swelling	• Undercut
• Seam patterning	• Surface voids
• Cracks/surface cracks	• Pores
• Annealing colors	• Distortion
• Root width	• Root inspection

detour through one or several auxiliary variables from whose measurement quantitative or qualitative conclusions can be drawn about the value sought. With reference to the example of laser beam welding, the multitude of quality-determining parameters (possible defects) can be represented in Table 37.1 (N.N.: Sonderforschungsbereich 1997). Only very few of the parameters listed can be directly measured. Characteristics such as tarnishing or humping are difficult to register by means of sensors. Variables such as cracks and lack of side wall fusion can only be determined when the welding process has been completed. Quality assurance is optimized by a balanced combination of techniques for monitoring the condition of the tool (laser), the handling system, beam guidance, the workpiece (e.g. shape, position), consumables (gases, filler materials), and for direct as well as subsequent observation of the processing zone.

37.4.1 Position and Time of Measurement

It has become established practice to break down the monitoring procedure into pre-, in-, and post-process phases (Fig. 37.1) according to the time and position of the measurement in the laser processing operation. Pre-process monitoring takes place at a time and/or position before the laser processing operation. The aim is to avoid process defects offline, and therefore, time-uncritical assurance of constant input parameters (e.g. measurement of the beam's caustic curve) and online control of parameters near the processing zone in terms of time and position (e.g. seam tracking). In-process monitoring includes the measurement of primary[2] and secondary process radiation which is emitted or reflected directly from the processing zone. It enables conclusions to be drawn about the subsequent quality of the product. These techniques allow quality-relevant findings to be made which go beyond simple surface

---

[2] The term primary radiation denotes the direct or reflected radiation of the processing and illuminating laser respectively, whereas secondary radiation refers to the radiation which is induced by the process itself.
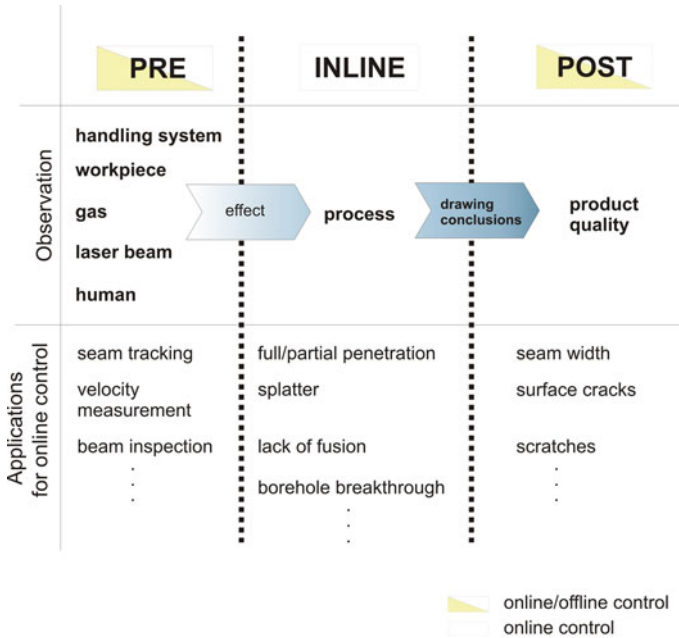
Fig. 37.1 Phases of Process Monitoring

properties. Time-consuming manual or even destructive testing methods can be minimized. Post-process monitoring includes methods for assessing the already solidified processing zone and, in the case of online control using optoelectronic sensors, permits speedy automated evaluation of surface properties and rapid feedback to manipulated variables.

In the course of this chapter, various applications featuring inline monitoring of the processing zone as well as monitoring methods before and after the process operation will be explained more closely with reference to examples. In order to provide a better understanding, however, fundamental conditions and relationships will first be described.

Detector arrangement

In practice, the preferred arrangement is to position the detectors above the workpiece because this permits a direct view into the zone of interaction between the laser and the workpiece. Measurements from below the component are not possible in many cases simply because the underside of the workpiece is not accessible.

The alignment of the detectors is stated relative to the axis of the laser beam and the direction of processing. Arrangements, where the angle of the laser beam axis is around 0°, are referred to as being coaxial and quasi-coaxial at an angle of up to approx. 10°. At greater angles, the arrangement is described as being lateral.

Regarding inline monitoring, tests of welding operations using CO_2 lasers reveal that the viewing angle of the sensors has a significant influence on the measured results from plasma monitoring with photodetectors. Depending on the viewing angle relative to the laser beam axis, the detectors cover different proportions of surface and capillary plasma. Sensors arranged quasi-coaxially to the laser beam mainly detect the plasma from the vapor capillary, whereas sensors arranged parallel to the top of the workpiece observe the surface plasma.

The coaxial arrangement is suitable in cases where the detectors can be integrated into the processing head, the beam path, or the laser itself. The advantage of such installations is that the sensors are protected against contamination and other undesirable effects of the processing operation while at the same time permitting maximum visual access to the interaction zone. A potential problem with the lateral arrangement is that, when used for inline monitoring, the detector might become contaminated during processing, but this can either be avoided by appropriate design measures (e.g. inert gas nozzles) or by means of regular maintenance. In compact systems, lateral detectors can be fitted to the processing head or can be integrated into the processing gas nozzle.

Lateral detector arrangements (e.g. light section sensor) enable a correlation to be established between the measurement signals and geometrical defects which, when, for example, welding lap and butt joints, can be used for pre- or post-process monitoring to identify sagging, edge misalignment, gaps and holes.

37.4.2 Optical Components

The majority of the high-power lasers used in laser material processing emit wavelengths in the range of 1 μm (e.g. Nd:YAG lasers, fiber lasers) or 10 μm (CO_2 lasers). This makes it necessary to realize the focusing and deflection of the laser beam with various optical devices. In coaxial process monitoring, the laser beam and observation share the same beam path and so the process monitoring system has to be adapted to the different substrate materials of the optical devices (i.e. lenses and mirrors) needed for guiding and focusing the laser beam (see Fig. 37.2 comparison of CO_2 and Nd:YAG).

As a rule, lasers with beam sources in the 1 μm wavelength range use glass or, at higher outputs, fused silica as the substrate material for mirrors and lenses. Zinc selenide is a frequently used mirror and lens material for CO_2 lasers. Glass, silica glass, and zinc selenide are transparent for electromagnetic waves in the visible and near-infrared range. The properties of the mirror are determined by a specific coating. So-called dichroitic mirrors reflect the laser light and transmit the secondary radiation to be measured, or vice versa, depending on the coating. In beam splitters, the coating causes a fixed proportion of the laser light at the same wavelength to be reflected or transmitted according to the division ratio. Focusing is realized by means of lenses. At very high outputs, such as those required to weld thick metal plates, or in applications demanding a high degree of mechanical stability, metallic substrates are
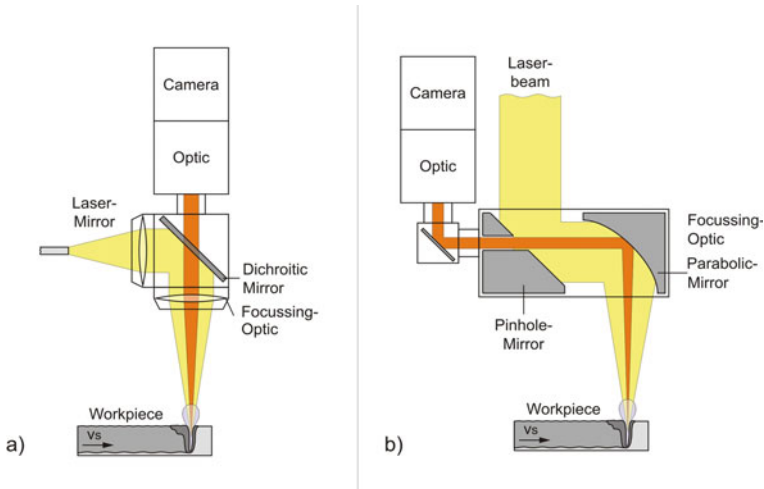
Fig. 37.2 Process monitoring setup **a** for Nd:Yag-Laser, **b** for CO_2-Laser

preferably used for CO_2 laser beam sources. At wavelengths in the 10 μm range, high thermal stress can lead to imaging defects or even cause the destruction of the optical components on transmissive optical devices. Metallic optical devices are easier to clean and less sensitive to contamination. The beam is deflected by reflection off a plane mirror. Parabolic mirrors are used to focus the beam. If metallic mirrors are used for guiding and focusing the laser beam, coaxial observation along the laser beam axis is more difficult than for lasers in the 1 μm wavelength range. Here the secondary process radiation can be observed through a pinhole (diameter typically 1–2 mm) drilled in the center of one of the last mirrors in the beam path. Mirrors with such a drilled hole are designated as pinhole mirrors. The loss of laser power caused by the drilled hole can be regarded as negligible in actual practice as only a small fraction of the output is lost, and beam quality is not affected in any way relevant to the process. The losses occasioned by these mirrors are of the same magnitude as those caused by mirrors in the beam path, i.e. approx. 1% per mirror, which has to be compensated by means of cooling. A mirror with a large hole in its center is described as a scraper mirror. The diameter of the hole is selected so as to allow the laser light to pass through the mirror unimpeded. Scraper mirrors filter out secondary radiation emitted at a narrow angle to the laser beam axis via the mirrored edge around the hole, for forwarding to the detector. Such mirrors can be used to obtain integrated measurements of light emitted by the process approaching the quality of coaxial measurements.

Another important element in process monitoring is optical filters damping signals or filtering out the spectral range of interest. The latter is of great relevance, particularly with regard to detecting primary radiation reflecting from the processing zone.
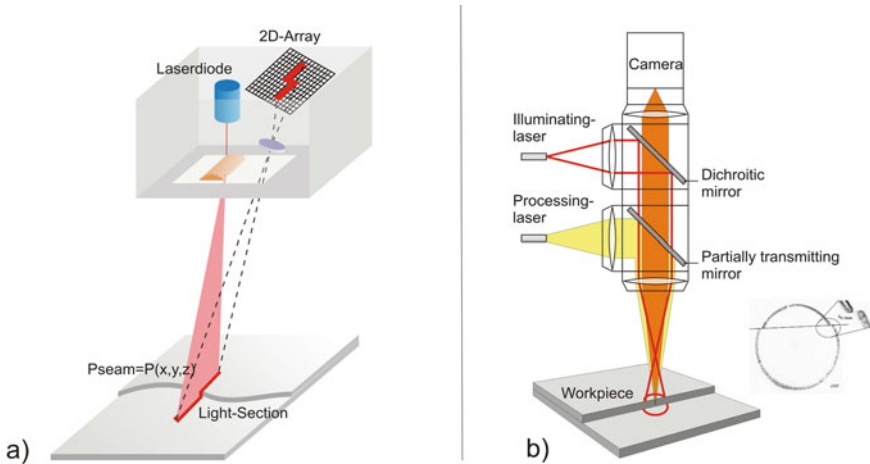
Fig. 37.3 Seam-tracking principle **a** based on a scanning triangulation sensor, **b** light section with coaxial ring projection

External secondary light sources

Certain aspects of relevance to the quality of the production process cannot be monitored by recording the primary radiation of the processing laser or secondary process radiation from the processing zone. This is true, especially for pre- and post-process monitoring. Examples include the position of the laser beam in relation to the desired working position (seam tracking) or the profile of the solidified seam in laser beam welding. To detect such features, external light sources (mostly LEDs or Diodelasers) are used to illuminate the workpiece. For some measurement applications in pre- and post-process monitoring, special light projections are formed (e.g. lines or circles) and recorded by the light section method (Fig. 37.3).

Figure 37.4 illustrates additional illumination strategies which can be used to identify various contours of objects and surface properties. At present there is no single optimum illumination strategy that is the right choice for the multiplicity of applications and criteria/failure to be observed. Furthermore, the type of illumination is in many cases restricted by the mechanical or optical conditions of the process or handling system.

One method, in which the processing zone is illuminated coaxially (brightfield) to the processing laser beam by an additional laser of lower output, has opened up new areas of application for process monitoring for all process zones. Using a partially transmissive mirror or a pinhole mirror, it is possible to couple in illumination radiation coaxially (Fig. 37.5). The reflected radiation of the illumination laser is likewise observed coaxially to the processing laser beam with a spatially resolving sensor. Among other things, this method enables the liquid/solid phase boundary of the material processed to be measured as well as the relative movement between
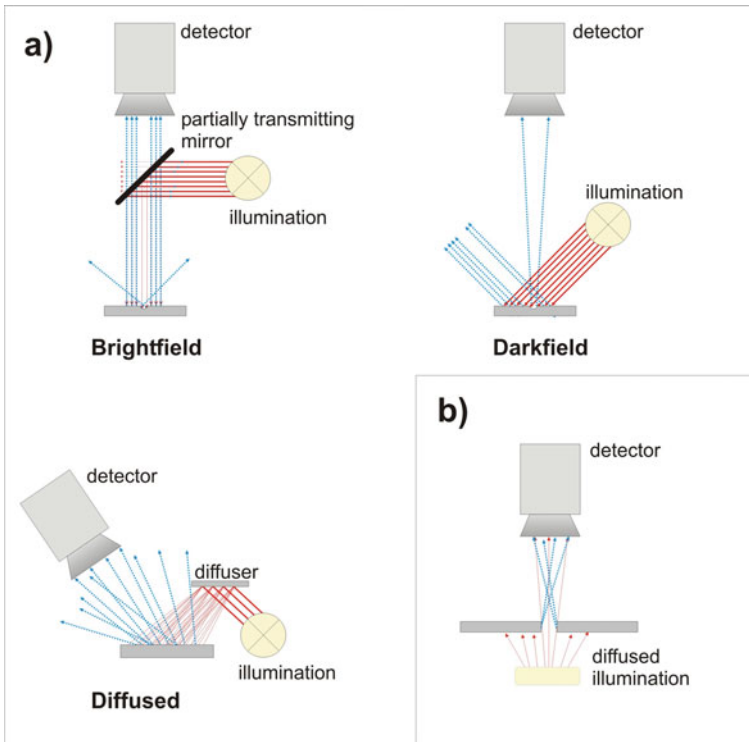
Fig. 37.4 Illumination strategies **a** incident light, **b** backlight

the processing head and workpiece. Both applications are described in more detail below.

Detected radiation

In laser material processing, the light emitted by the laser beam is the primary source of electromagnetic radiation. The most important lasers in industrial production are CO_2 lasers ($\lambda = 10,640$ nm), Nd:YAG lasers ($\lambda = 1064$ nm), diode lasers (mainly used at $\lambda \approx 808$–980 nm) and fiber lasers (also available at various wavelengths but predominantly used at $\lambda \approx 1030$–1080 nm).

Online measurement of laser output and beam distribution involves decoupling a small percentage of the laser light (primary radiation). Process-relevant information can also be derived from the detection of back-reflected primary radiation from the laser processing zone. The use of an additional light source enables specific data to be recorded not only from the processing zone, but also from the area around it. This can be useful when measuring the position of the laser beam in relation to the desired working position. The secondary sources of electromagnetic radiation are laser-induced plasma, metal vapor emission, and emissions from liquid material. These radiate from the zone of interaction between the laser beam and the workpiece, or

Fig. 37.5 Process monitoring setup with coaxial illumination
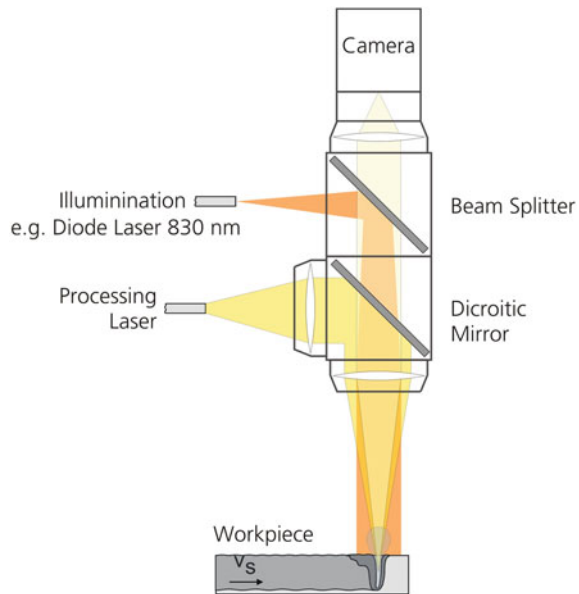
from the direct surroundings (Fig. 37.6). It is well-known that the secondary radiation contains information about the dynamics of the laser process and about the quality of the processed workpieces.

Signal evaluation

Techniques for signal evaluation are strongly related to the type of detector and the method used for process monitoring. Photodiodes, for example, just provide information about the temporal distribution of the measured signal intensity. The signal processing is therefore limited to an evaluation of the signal amplitude and frequency. A common approach used in most inline monitoring systems using spatially integrating sensors is the comparison of the signal amplitude (intensity profile) during a production process with predefined tolerance bands. Figure 37.7 shows a reference signal calculated from one or more signals recorded during reference processes (upper diagram). For the supervision of a production step, a tolerance band is generated around the reference signal (lower diagram). With this setup, a production process is rated as "good" if its detector signal lies always inside the predefined tolerance band. In addition, machine learning methods can be used to analyze pre-, inline, and post-monitoring signals in much more detail compared to tolerance bands (see Chap. 0).

Imaging sensors can also be used as "smart photo diodes" by programmatically selecting single pixel or groups of pixel as the source of a signal comparable to one of a photo diode. At present, most spatially resolving inline process monitoring systems, detecting process radiation, are using algorithms comparing process images with reference films (Fig. 37.8).
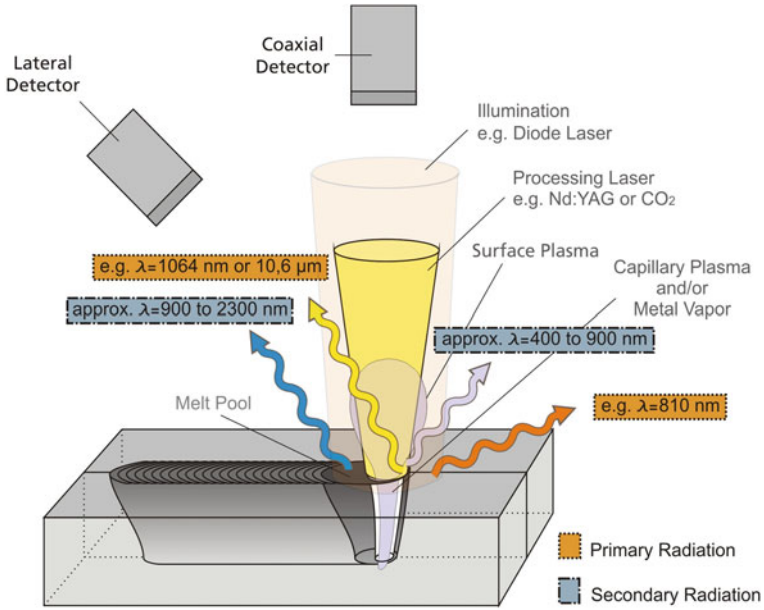
Fig. 37.6 Sources of electromagnetic radiation in laser material processing

Fig. 37.7 Quality evaluation by comparison of the signal intensity monitored during welding with reference Process top: Reference signals down: tolerance bands
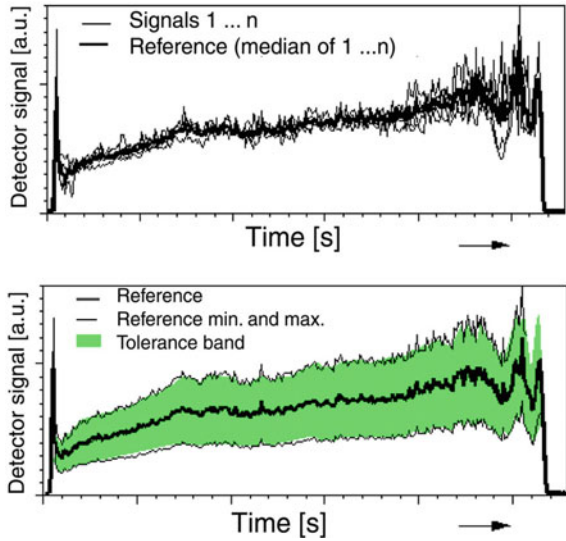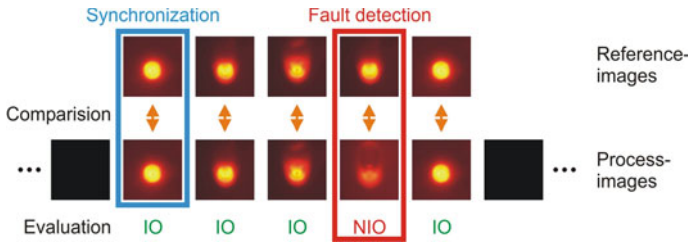
Fig. 37.8 Quality evaluation by comparison of the camera images monitored during welding with reference film

One particular area of interest in current research is the detection of specific process conditions on the basis of physical effects without having to compare image data with reference data. This will enable the development of widely applicable, robust process monitoring methods to detect defined classes of fault that can be applied without the need for special training.

With regard to pre- and post-process monitoring, especially applications using grayscale image analysis require complex imaging techniques in order to guaranty a stable recognition of the sought-after attribute. The extracting procedure depends on the surface properties. Figure 37.9 shows an example where edge detection filters were applied to a camera image of a welded seam in order to separate the seam from the unprocessed material. The extraction of the seam is useful to eliminate the influence of different surface conditions on the evaluation of the seam properties, especially when detecting surface voids (Rousselange 1998). In further steps, the appearance of the seam can be evaluated in terms of irregularities by using, e.g. the method of conjugate gradients or the threshold method. By extracting the seam in the first step, the region of interest is reduced and the evaluation of the seam is thus faster than exploring the entire picture.
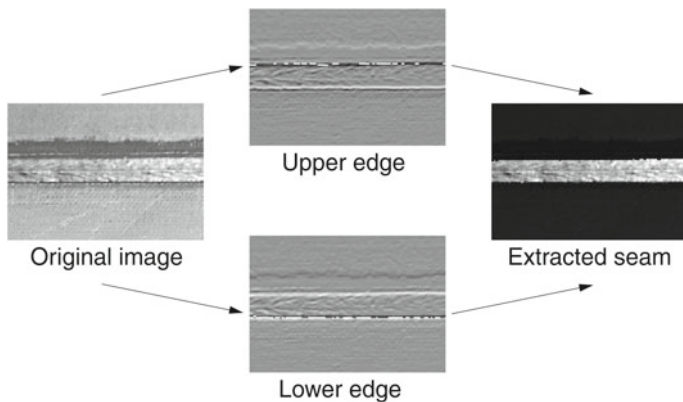
Fig. 37.9 Separation of the seam from camera images

Examples—Laser welding of Metals

The welding of metals using laser beams is one of the first processes in which process monitoring systems were used on an industrial scale. Most systems use optical sensors that, for example, determine weld seam width, joining errors, drop formation or splatter by coaxially or laterally observing primary and secondary radiation.

Inline Monitoring

The majority of the inline monitoring systems in industrial use today still operate on the principle of spatially integrated photo detectors with a high time resolution (5–20 kHz). Intensity is evaluated by means of frequency and amplitude signal analyses. If the focal position or the weld depth is altered during welding, this causes changes to the secondary process radiation. Process disorders can frequently be detected in this way, but it is difficult to discover precisely what has happened and why. Meanwhile, imaging sensors that register the emitted process radiation in spatial resolution on the basis of the plasma, metal vapor, and molten mass are becoming increasingly popular. The spatial resolution measurement enables errors to be detected with greater reliability.

For instance, on welding of tailored blanks or other sheet metal with a thickness below three millimeters, characteristic changes in the distribution of the secondary radiation can be measured when the process changes from full to partial penetration. These changes do not necessarily come along with a change in the overall amplitude of the measured radiation. Hence, changes might not be recognized by a photo detector-based system. Figure 37.10 shows a comparison of the camera images recorded during laser welding of a tailored blank and an approximation of photo detector signals (calculated from the camera images by spatial intensity integration). The camera images clearly indicate different process states, while the spatial integrated (photo detector) signal only shows minor changes in the amplitude.

Most monitoring systems distinguish good welds from insufficient welds by comparing signals acquired during production with reference images taken before. In the following sections, more advanced signal analysis methods based on different machine learning algorithms are explained in detail with two different use cases. Another method to realize inline monitoring is to identify welding failures and certain process states by detecting determined signal attributes without comparing the signal to a reference.

One concept for imaging monitoring systems is based on the usually coaxial insertion of an additional beam source via a beam splitting mirror. The processing zone is illuminated in order to make the solid–liquid phase boundaries between the basic material and the molten mass visible and thus capable of being measured during processing. The light from the illumination source is reflected differently by the molten mass and the solid material, producing distinctly different textures. The smooth convex surface of the molten mass reflects the illumination light deterministically over a wide area, increasing its divergence. On the rough solid surface of the basic material, the light from the illumination source is reflected stochastically in numerous small patches. Working on the basis of Planck's law of radiation, the
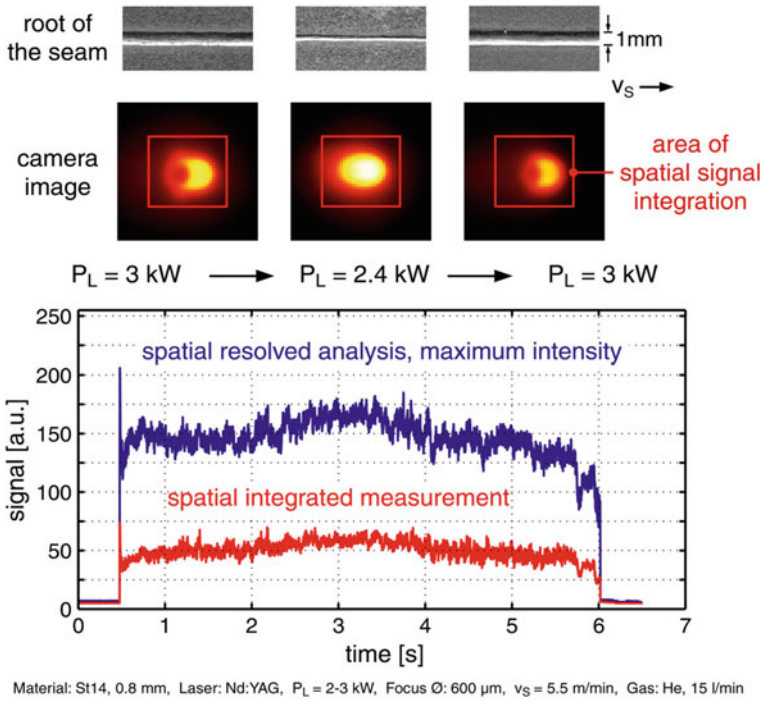
Fig. 37.10 Comparison of spatially resolved and spatially integrated measurement. **top**: backside of a laser-welded tailored blank showing a broad seam (3 kW laser power) and a narrow seam (2.4 kW laser power). **middle**: camera images of the keyhole area showing an intensity distribution with a local minimum (3 kW laser power) and an intensity distribution without a local minimum (2.4 kW laser power). **bottom**: diagram showing a spatial resolved analysis of the recorded camera images (maximum intensity) and an approximation for the signal of a single photo detector (spatial integrated measurement)

secondary process radiation reaches maximum intensities in the wavelength range below 600 nm, particularly during the processing of metals. To enable the proportion of process radiation to be reduced relative to the reflected radiation from the external light source, diode lasers with wavelengths of around 800 nm have proven to be suitable as an illumination source. The spectral sensitivity of the camera is also great enough at these wavelengths. The use of narrow-band band pass filters enables radiation-intensive portions of the secondary radiation to be filtered out or weighted in comparison to the reflected radiation of the illumination source. Illumination sources with an output between 100 and 150 mW are sufficient for most applications.

The measurement principle utilizes the fact, that technical surfaces of workpieces, e.g. used in laser welding applications possess a rough surface finish, thus causing alternating bright and dark areas on the camera image (Fig. 37.11).
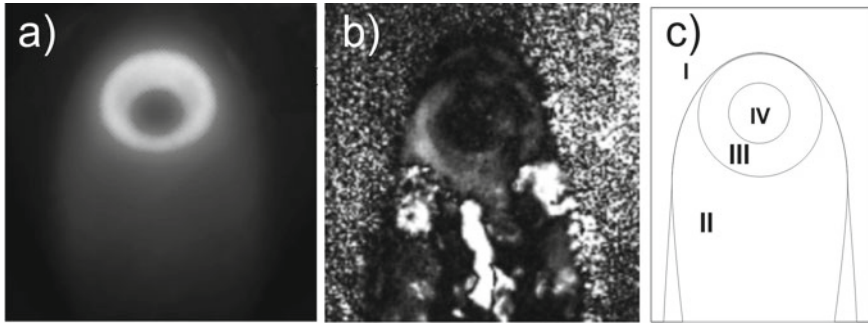
Fig. 37.11 Welding process radiation while welding **a** without external illumination, **b** illuminated with 150 mW diode laser, **c** phase boundaries I: solid surface II: melt pool geometry III: thermal radiation surrounding the capillary IV: capillary

The differentiation of solid and molten material can be done by texture analysis and is utilizable for visual inspection as well as automatic processing. However, texture analysis is sensitive to differing workpiece surfaces. A more robust approach uses the fact, that the solid material is—essentially—stationary to the workpiece, while the molten material is unsettled.

The algorithm principle can be subdivided into four steps. First, the displacement of the solid surface between two consecutive images is determined. The solid surface structure of the workpiece is unique and stationary; therefore, a relative displacement between the sensor and the workpiece can be measured by finding the maximum cross correlation of a dedicated template area of one image in the consecutive image. By calculating the pixel-to-pixel difference of the two images, features stationary to the workpiece displacement are cleared, while non-stationary areas are enlightened. To eliminate small-scaled image irregularities, median filtering is used. The separation of stationary and non-stationary features is computed by binary threshold filtering. The reflection on molten areas is unsettled and fast altering; therefore, the pixel-to-pixel difference is unpredictable. However, by superposition of consecutive analyzed images, there is a good probability that sufficient brightness difference appears on the molten area. To determine the melt pool boundary, the computed image has to be noise-free, which is done by erosion filtering and dilatation filtering. The boundary then can be found by searching the first non-zero pixel in a row respectively column. The analysis of the melt pool contour can be utilized for robust gap- and lack-of-fusion detection.

Compared to state-of-the-art reference-based process monitoring systems, this allows higher reliability and less pseudo errors, model-based error classification, and the possibility of real-time process control (Fig. 37.12).

A special challenge for the described image processing algorithm is surface contamination, e.g. by a grease film as well as coated workpieces.

Fig. 37.12 Welding overlap joint **a** Image processing for melt pool contour analysis (zero gap weld): 1. (left top): raw image; 2. (right top): Pixel-to-pixel difference of adjusted consecutive images and binary threshold; 3. (left bottom): Overlay of 8 consecutive analyzed images 4. (right bottom): Filtered image with calculated boundaries **b** Melt pool of a lap weld with 0.15 mm gap

(a)

(b)
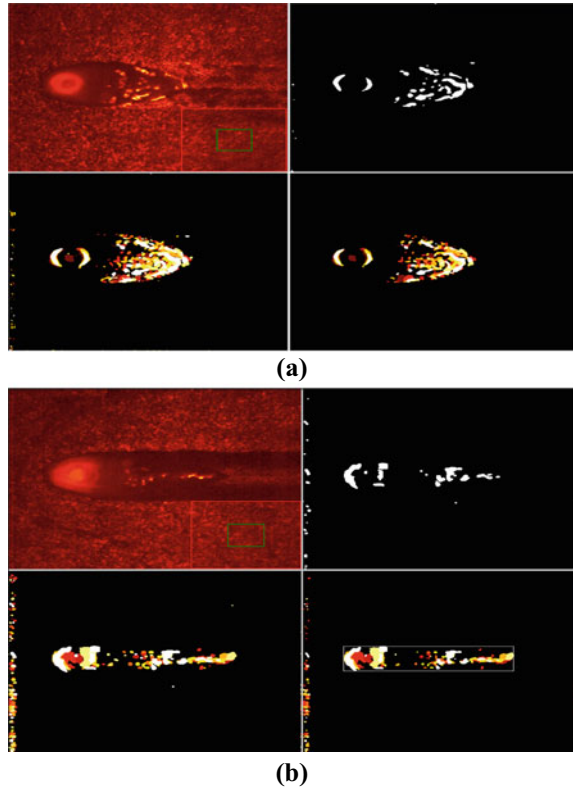
Seam Tracking—Pre-Process Monitoring

When materials are joined together, e.g. by laser beam welding, accurate positioning of the laser beam relative to the joint is of paramount importance. This is true for all joints (butt joint, overlap joint, fillet joint, etc.). Additionally, it has to be assured that no jumping in thickness of sheet metal parts that have to be joined occurs. Not least edge damages and geometrical data have to be identified in order to obtain high-quality welds at any time.

Predominant seam tracking sensor concepts are based on the triangulation principle. First setups are using a deflecting mirror to scan the workpiece surface around the joint using point-shaped laser beams and line cameras (Reek 2000). The joint position is recognized as a discontinuity in the measured distance between the sensor and the workpiece surface (Fig. 37.13). The triangulation algorithm is fast and simple. However, the robustness is not optimal due to moveable parts and the time resolution is limited.

Later, light section sensors were most commonly used. They also utilize the triangulation principle, but stretch it to a second dimension. Instead of a point-shaped triangulation laser beam, a laser line is projected onto the workpiece surface. As
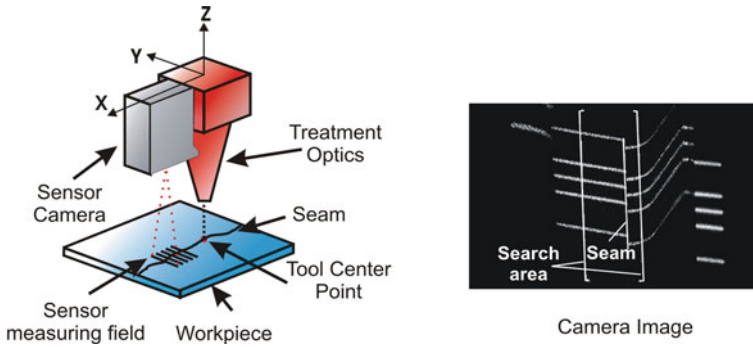
Fig. 37.13 Seam-tracking principle based on a scanning triangulation sensor

all parts are static, the setup is much more robust. The detector is two-dimensional (CMOS or CCD camera) which allows much higher temporal resolution (dependent on the camera framerate and image processing algorithm). The measurement resolution in the feed direction can be further increased by using multiple laser lines. The joint position is then measured at different positions in parallel and imaged on one camera, which is close to an increase in the camera framerate (Reek 2000).

The seam tracking sensor is usually fixed to the welding head. The sensor moves with the TCP.[3] Since the TCP matches the current joint position, the sensor is continuously readjusted, and therefore, is able to cover a great deviation between joint and robot trajectory (Lastname et al. 2002). The tracking axis also may be abandoned and replaced by direct robot trajectory adjustment.

To reduce the sensor forerun and size, the sensor can be integrated into the welding head using a coaxial projection of a circular light section and observing the workpiece coaxially to the laser beam (Regaard et al. 2005). Further advantages are the possibility to recognize joints independently from the welding travel direction. However, the smaller triangulation angle caused by the setup principle requires a higher resolution of the camera.

Yet another concept using grayscale image analysis under incident illumination is existing. This sensor type also uses a two-dimensional detector (camera) to observe the workpiece surface. The joint and workpiece are illuminated by diffuse vertical or slightly transversal light. The joint position is recognized by separating areas of different reflectivity (or brightness). Since no triangulation angle is needed small sensor designs are possible. The detection of very thin butt joints can be realized and the sensor adjustment in relation to the joint direction is not of relevance. Drawbacks are the limited observation angle which should not exceed 3° to 7° to the surface normal and a limited illumination. Seam tracking with grayscale image analysis, therefore, has limits when applied to overlap joints with strong edge misalignment. Hence, it is used in particular to measure gap width and edge damage (Fig. 37.14).

---

[3] Tool Center Point: the position where the focused laser beam hits the workpiece.
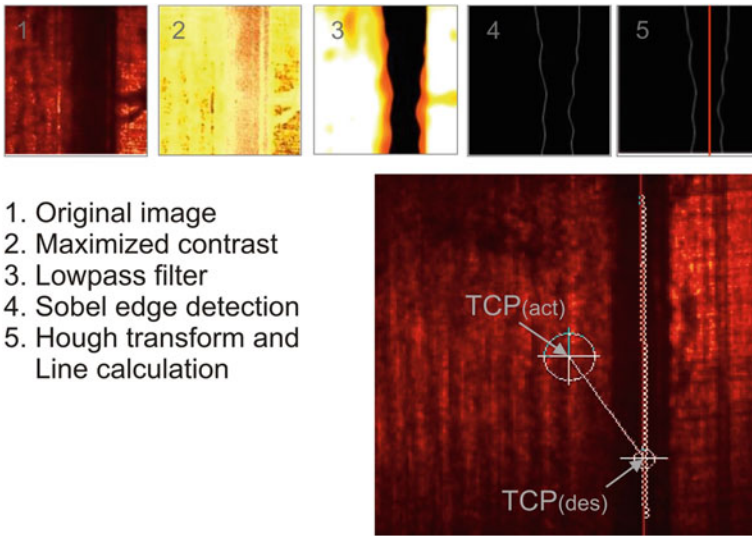
Fig. 37.14 Algorithm for seam tracking with grayscale image analysis

Especially light section sensors imply a constant linear robot movement, requiring:

- a constant feed rate
- no transversal movement of the robot's hand
- no rotation of the welding head of the robot's hand

In numerous real applications, these requirements are not given, thus leading to positioning errors (Fig. 37.15).

All error causes can be attributed to a lack of information. The seam tracking sensor only measures the gap position relative to the current TCP position. The position of the TCP relative to the workpiece is not available.

The shown problems can be solved if the relative position of the welding head relating to the workpiece robot $\vec{r}_{robot}$ or alternatively the TCP position $\vec{r}_{TCP}$ is determined. Some robot systems maintain the real-time output of the robot position with the required accuracy, but they are cost expensive and the interfacing of the sensor system to the robot control is laborious.

Therefore, a concept has been developed also measuring the relative velocity between the workpiece and the sensor. It consists of a high-speed CMOScamera and a coaxially integrated laser diode illumination. The camera observes an area of approx. $6 \times 6\,\text{mm}^2$ was carried out on the same image as the measurement of the gap position. The observed structure is unique and stationary on the workpiece. A relative displacement between the sensor and the workpiece therefore can be measured by finding the maximum cross correlation of areas in consecutive observed images (Fig. 37.16). The relative velocity corresponds to the displacement normalized to
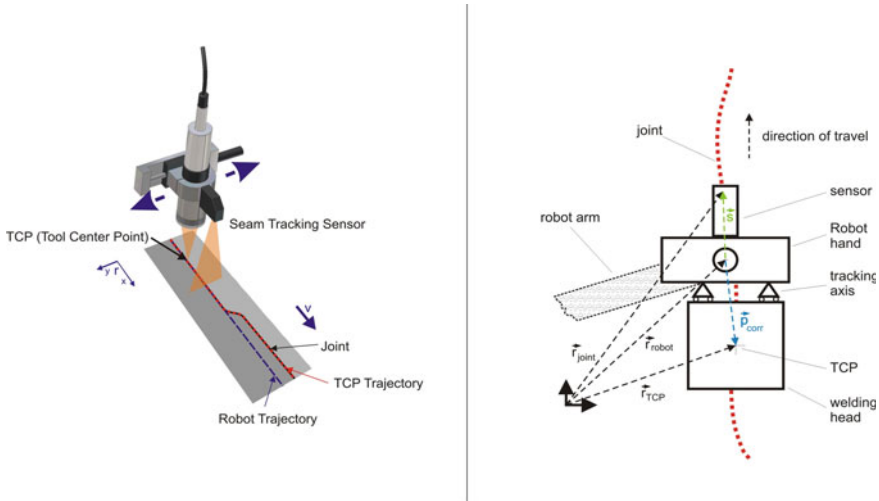
Fig. 37.15 Tracking axis

the framerate of the camera. The resolution can be enhanced by applying sub-pixel comparison.

If necessary, light section measurement can also be integrated using additional illumination. However, grayscale image analysis turned out to be very stable for different materials such as stainless steel, mild steel, copper, and alloys with punched or laser cut edges. Knowing the relative velocity $\dot{\vec{r}}_{TCP}(t)$ and a reference position $\vec{r}_{const}$, the absolute TCP position related to the workpiece can be determined through integration.

$$\vec{r}_{TCP}(t) = \vec{r}_{const} + \int_0^t \dot{\vec{r}}_{TCP}(t) \cdot dt \tag{37.1}$$

The absolute gap position now can be determined by

$$\vec{r}_{gap}(t) = \vec{r}_{TCP}(t) + \vec{s}(t) \tag{37.2}$$

For self-guided seam tracking, the relevant gap position related to the TCP position can be found by

$$\vec{r}_{target}(t) = \vec{r}_{gap}(i)\big|_{r_{gap,x}(i)=r_{TCP,x}(t)} \tag{37.3}$$

The correction vector equals the vector difference

$$\vec{p}_{corr}(t) = \vec{r}_{target}(t) + \vec{p}_{axis}(t) - \vec{r}_{TCP}(t) \tag{37.4}$$

Fig. 37.16 Measurement of relative displacement between consecutive images by finding the maximum cross correlation of areas in consecutive observed images
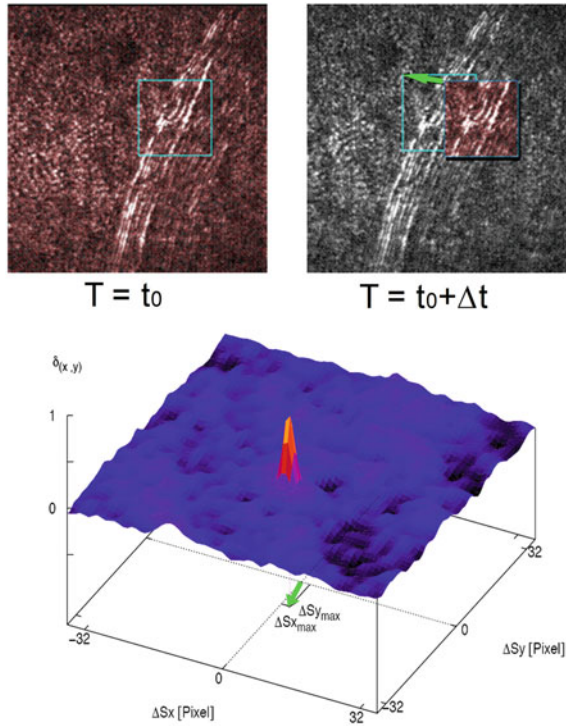
With this concept, the seam tracking is two-dimensional position-based instead of time-based. The previously described errors caused by a lack of position information are inexistent. Carrying out the laser beam correction with a robot-independent scanner system, seam tracking can actually be performed completely independently from the handling system.

In fact, this reduces costs in robot systems due to lower accuracy and output requirements. It simplifies interfacing an installation and disengages from sensor calibration necessities (Fig. 37.17).

Machine Learning for process monitoring

Laser material processing generally leads to a complex multi-phase system as a result of high local energy input into the material. In particular, the final product quality is affected by several factors, such as the thermal conditions during laser material interaction, deviations in the material properties, contaminations on the workpiece surface, and alteration to the laser beam properties, resulting in a not acceptable product.

Due to high process dynamics, an approach based on precise physical modeling of the process is not practical for real-time process monitoring and control. Additionally, the correlation of individual measurement signals with product quality in practice
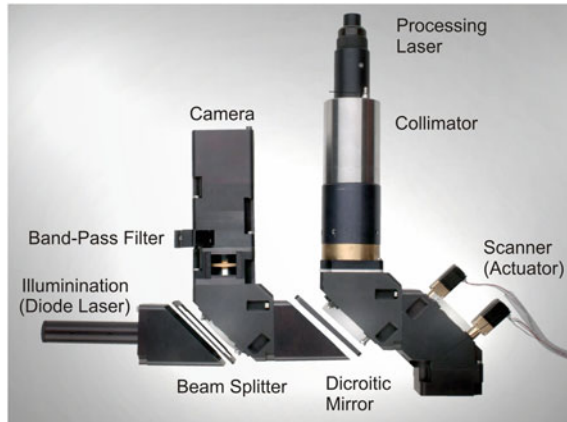
often leads to inaccurate statements of the monitoring system, which can result in unwanted non-recognition of faulty parts or high false alarms.

However, recent advances in sensing technology and an increasing number of sensors applied on laser machines and processes, enable online process monitoring with higher precision by combining multiple data sources. Similarly, complex sensors such as thermal camera systems have become reasonably priced and can be used as a data source for in-process quality monitoring. In order to process these multidimensional signals, which potentially originate from several sources such as machine condition monitoring, manufacturing resource planning, and inline sensors, advanced methods from the field of machine learning enable more robust and precise process control and prediction of critical defects as well as process deviations.

An advantage of data-driven methods such as machine learning is, that it is not necessary to explicitly model the physical behavior of the system in order to build a statistical model. However, process understanding helps considerably to design and develop the right feature set and to select relevant sensors and signal sources as input for such models. A data-driven model utilizes input variables (features) extracted from the raw measurement signals to establish a statistical model between those features and the observed phenomena, e.g. weld defects during the welding process, based on examples (supervised learning). If no example of input/output pairs is available, unsupervised machine learning can be used to find patterns and structures in data, for example using clustering algorithms. A third type of machine learning algorithm utilizes a software agent that can learn to take actions (e.g. increase/decrease laser power) in a specific environment, for example, the laser cutting experiment in order to maximize a given cumulative reward function (e.g. sufficient part quality).

Several machine learning algorithms can be used for a specific supervised classification or regression task. A list of commonly used algorithms for supervised machine learning is given as follows:

- Decision Tree (DT),
- K-nearest neighbor (kNN),

- Random Forests (RF),
- Support Vector Machines (SVM),
- Logistic Regression (LogReg),
- Artificial neural networks (ANN).

A detailed overview and discussion of these algorithms can be found in several textbooks such as (Bishop 2013; Nixon 2012; Runkler 2012). Although these algorithms can be used to create a statistical model for the given training data, the final prediction performance and processing time required for a certain task are hard to estimate in advance. In practice, it is often necessary to try out different algorithms using different hyperparameter configurations for a given problem. Especially in the field of image recognition in order to create models not only with high prediction performance and less overfitting, but also with fast execution times and a higher degree of comprehensibility, these algorithms and the resulting prediction models often require feature engineering as a preliminary stage, Engineered features that describe the significant characteristics of the signal are required and are often manually designed and depend on the signal type (e.g. image data or data from high-speed photodiodes) and the output variable.

Conventional machine learning is based on feature engineering and classification or regression algorithms. Since a loss of information can result in a performance decrease when wrong features are selected, this approach is labor-intensive and error-prone. Nevertheless, deep learning methods have evolved as a comprehensive learning approach that includes the process of feature extraction as part of the model. The following types of deep learning algorithms are often used in practice to solve problems in several domains such as image processing and video and audio signal processing (Goodfellow et al. 2016):

- Convolutional neural networks (CNN) (Krizhevsky et al. 2012)
- Recurrent Neural Networks (RNN)

  o Gated Recurrent Units (GRU) (Cho et al. 2014),
  o Long-short Term Memory (LSTM) (Hochreiter and Schmidhuber 1997)

Deep learning models with multiple layers of artificial neurons are based on the findings in neuroscience. These multi-stage deep neural networks allow humans to perform complex signal processing tasks such as object and voice recognition (Krüger et al. 2013; Mohamed et al. 2011). As a result, deep learning models can extract more abstract and invariant features. Therefore, they probably have the ability to yield higher classification accuracies than traditional approaches based on feature engineering and conventional classifiers. The use of deep learning models, especially convolutional neural networks (CNN) showed remarkable results in image recognition competitions such as ImageNet in 2012 and has become a common solution for complex computer vision tasks (Krizhevsky et al. 2017).

CNNs can not only be used for image data, but they bring certain advantages for these applications, such as translation invariance through weight sharing and local connectivity that takes the spatial structure of images into account. For some other applications, where spatial relations are important, these model assumptions of

CNNs may also be applicable. CNNs usually consist of three basic types of layers, which are stacked multiple times to create a deep neural network model:

1. Convolutional layer,
2. Pooling layer,
3. Fully connected layer.

Another important part of deep neural networks is RNNs which provide a temporal dimension. These networks belong to one of the most effective methods to approximate complex temporal dynamics in signals. RNNs are designed to recognize patterns in sequences of data, such as numerical time series data originating from sensors, audio signals or text data. Nowadays, it is possible to train large multi-layered CNN/RNN networks, typically consisting of convolutional, pooling, and fully connected layers on GPU[4]-hardware, with the help of open source deep learning frameworks such as TensorFlow,[5] PyTorch[6] or Caffe.[7]

In the following section, two example applications for machine learning are explained using laser welding as an example. Deep learning architectures are subsequently compared with classical machine learning approaches based on individual prediction performance and on their training and inference timings.

Example 1: Quality monitoring for laser beam welded tapes out of fiber-reinforced plastics

Quality monitoring during the manufacture of pressure vessels made of fiber-reinforced plastics (FRPs) is decisive for product safety. During the ongoing manufacturing process, quality statements are made about the consolidation of the layers located on top of each other. Quality monitoring is based on the combination of infrared technology and machine learning. In order to be able to utilize the process monitoring, the tapes must be embossed with testing structures using ultrasonic hot embossing before the joining (Fig. 37.18).

The laser beam welding process developed for the winding of tapes made of fiber-reinforced plastic is used, for example, for the manufacture of pressure tanks for trucks which must withstand a pressure of 15 bar and must, therefore, be produced without any defects. In order to check the quality, previously defined embossments with a height of 300 μm, a width of 500 μm, and a length of 1,600 μm are incorporated into the surfaces of the tapes using ultrasonic hot embossing. The embossments serve the monitoring process as testing structures and can be detected by means of thermography. The initial height of the microstructure is reduced during the winding process depending on the chosen process parameters and the consolidation quality so that it becomes recognizable whether the tape exhibits suitable bonding to the preceding layer. In order to develop the monitoring process, the laser beam welding process was simulated by heating up already welded tapes (Fig. 37.19).

---

[4] Graphics processing unit.

[5] https://www.tensorflow.org/.

[6] https://pytorch.org/.

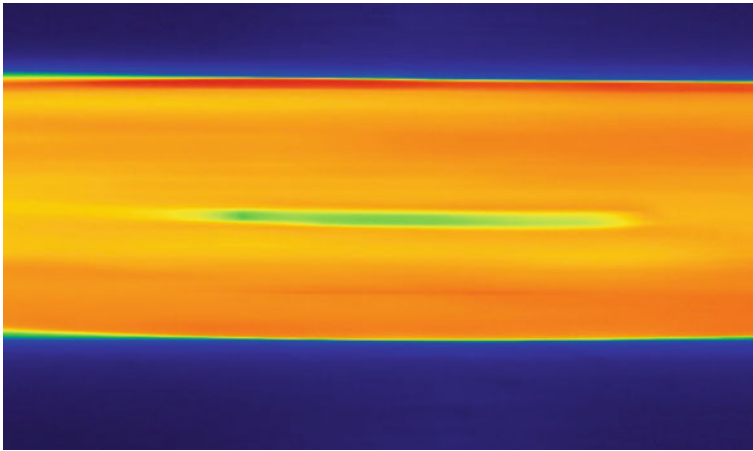[7] https://caffe.berkeleyvision.org/.

Fig. 37.18 Thermographic image of an FRP tape with incorporated embossment during the laser beam welding process
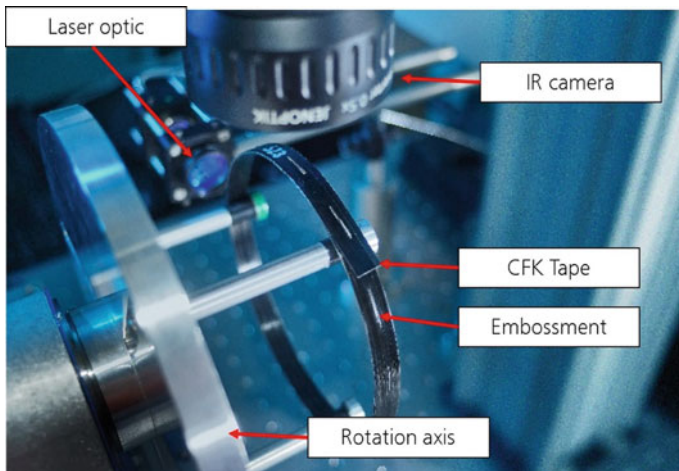

Fig. 37.19 Experimental setup for the development of the monitoring process

For this purpose, the FRP tape was clamped on a rotation axis which moves at the uniform speed as in the industrial process. The tape was heated with a diode laser (wavelength: 808 nm) and observed with an infrared camera offset by 90°. The analysis begins with the first image of the thermal camera. The heat distribution and the cooling rate of the material in the region of the embossment alter as a result of the consolidation quality. Therefore, statistical values of the measured temperature radiation which are characteristic of the state of the consolidation are calculated from every image of the thermal camera in a defined section. With the aid of this setup, it

was possible to elaborate on the recognition of the differences between the various consolidation states.

During the preliminary investigations, the data analysis uses the infrared images recorded in the laser beam welding process in order to identify the consolidation quality of two layers. The process images are analyzed individually with the aid of machine learning methods. For this purpose, a defined, stationary image area in each thermal image is investigated and six characteristics that correspond to the heat radiation in the observed area are calculated. These include the mean, maximum, and minimum values, the standard deviation as well as the skewness and kurtosis of the temperature distribution. While the statistical values are extremely dependent on the level of the measured temperature radiation, the skewness and the kurtosis describe the distribution of the values and are more difficult to influence by the absolute level of the temperature radiation. The skewness describes the extent of the asymmetry of the distribution and the kurtosis describes its steepness. In order to develop the evaluation method, parameter sets corresponding to sufficient and insufficient consolidation were stipulated for the laser beam process. The resulting welded rings were investigated destructively using cross sections and the consolidation quality was determined. From every specimen, the image sections of the infrared images were assessed manually and assigned to various states. These states are embossment, no embossment, and, in the case of embossment, sufficient and insufficient consolidation. The machine learning process is carried out with the aid of these results for known joining processes in order to recognize the states automatically in the event of any new unknown process images. The evaluation process is divided into two stages. In the first step, it is determined whether an embossment is located in the analysis region of the infrared image and it is thus decided whether the consolidation quality is differentiated in the second step. This ensures the quickest possible analysis of large data quantities. The principle of the decision forests is used for the first stage. In this respect, up to 150 different decision trees are used in order to make the correct statement. At various nodal points, every decision tree appraises what state exists in the current image. In this respect, the six characteristics specified above serve as nodal points. The sequence in which the statistical characteristics are incorporated varies between the different decision trees. The final statement is ultimately established using the majority of the results (Bishop 2013; Mathworks and Inc.: 2016). 25% of the total data from the training set is used for every training session and the remaining 75% serves to evaluate the trained model as a test data set. During the calculation of the first step of the model, a total of 150 images were used as test data. No embossment can be seen on 123 images and an embossment can be seen on 27 images. The machine learning algorithm did not assign any embossment to 120 images on which there is no embossment in reality either. The algorithm mistakenly assigned embossments to the three remaining images without any embossment. The images on which embossments exist were all assigned correctly. This corresponds to an accuracy of 98%.

In Fig. 37.20a, this result is portrayed in a confusion matrix in which it is compared to how the images are actually classified and how the algorithm classifies the images itself. For the second step, a 'support vector machine' (SVM) is used in order to

train the model since this principle exhibits a higher accuracy for this case than the decision trees. According to the 'support vector machine' principle, all the training objects are represented as vectors in the vector space. A linear separating line is drawn in order to separate the objects so that the largest possible region without any further measuring points is located around one point cloud. If the measured data varies extremely, the vector space is transferred into a higher-dimensional space in which the data is linearly separable (Bishop 2013; Mathworks and Inc: 2016). In the second step, a 100% probability of the correctness of the assessment is achieved with the aid of the available data.

This is also reflected in the confusion matrix in Fig. 37.20b. A total of 27 images with embossment were taken out as a test data set. In this respect, ten images belong to sufficient consolidation and 17 to insufficient consolidation. All the images were assigned correctly by the trained algorithm. The number of test data is small because of the available specimens. Therefore, this result only offers an initial approach for the evaluation of the measured data. If more specimen material is available, this approach can be extended and optimized even further. In the event of a larger quantity of measured data, it may be necessary to choose another training principle for the machine learning algorithm or the number of characteristics varies. Variations in the characteristics may lead to better results if, for example, the system is over classified and reacts to targeted cases only. In order to estimate the characteristics,
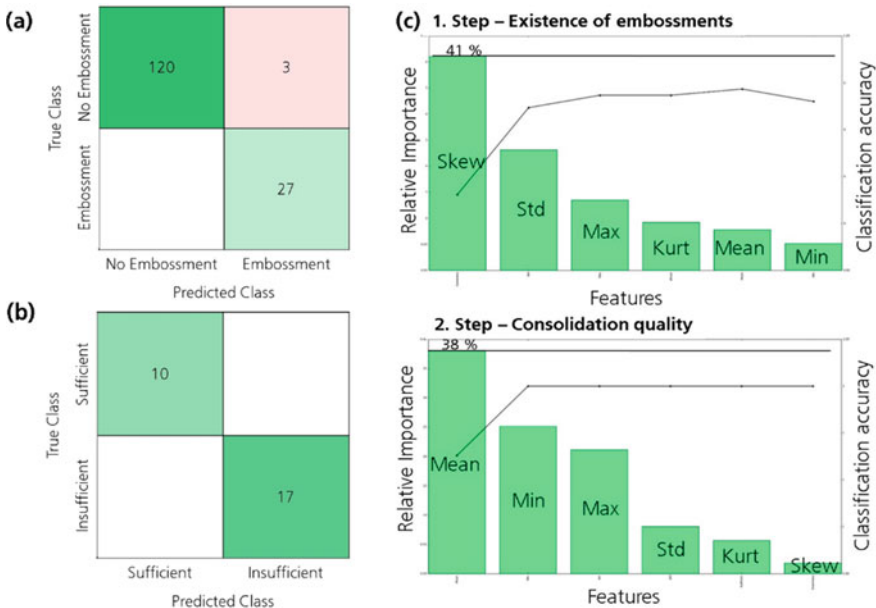
Fig. 37.20 **a** Confusion matrix of the machine-learned model in order to find embossments on the surfaces of FRP tapes. **b** Confusion matrix of the machine-learned model in order to establish the consolidation qualities of welded FRP tapes. © Accuracies and relevances of the individual features, top: recognition of embossments, bottom:recognition of the consolidation

the influences of the individual features can be calculated depending on the model's accuracy.

In Fig. 37.20c, these accuracies can be seen for the six chosen characteristics. The relevances of the individual characteristics are shown on the bar chart and the accuracy of the model as a graph. When making distinctions between the existence of embossments in the measuring region, the skewness is, with a weighting of 42%, the most important characteristic for the analysis but, on its own, is not sufficient in order to allocate the image completely. In contrast with this, the mean value is the most important characteristic in the second step. The mean value varies extremely with the absolute temperature values. Thus, a slight change in the external influences might falsify the result. However, this can be prevented by using supplementary characteristics, in this case, the minimum. Basically, the selection of the characteristics as well as the quantity of training data can be varied in order to optimize the accuracy of the algorithm. In summary, the algorithm is capable of automatically recognizing which of the three stipulated states is shown on the individual images. The condition of the bonding between two layers during the laser beam welding of the FRP tapes can be recognized in this way. The overall system is connected with a controller which transfers the result (in this case, in the form of an analog signal) so that a reaction to the bonding state can already be made before the end of the process. If the process is altered (no matter whether by using other process parameters or by welding another material), the algorithm can be adjusted easily with new training data and the model can be retrained. The basic prerequisite for the functionality of this monitoring system is that the properties to be recognized give rise to correlations that can be observed with the infrared camera.

Example 2: Machine Learning for Defect Detection in Laser welding

In order to detect changes in process conditions and quantify process imperfections such as lack of fusion, lack of penetration and sagging, online process monitoring based on thermal imaging can be used in combination with different machine learning methods.

In some cases, it may be necessary not only to determine whether the weld is sufficient or insufficient (OK and NO OK), but also to differentiate between different welding defects to be able to take targeted actions afterward (e.g. re-weld or declare as scrap). Process monitoring based on supervised machine learning can help to recognize different welding defects such as "lack of fusion", "lack of penetration" and "sagging" during to process (You et al. 2015; Ungers 2019; Knaak et al. 2018) (Fig. 37.21).

To generate annotations for this supervised classification task, the image data can be compared with the weld seam photography (top/bottom view) and the associated metallographic characterization (cross-sectional view) by matching the datasets via process start and end points (if process velocity v = const.). Alternatively, sensor fusion techniques can be used to map robot or handling system positions to sensor readings in order to synchronize the metallographic analysis and sensor data.

For traditional machine learning, individual features must first be extracted from the image data and then passed to the learning algorithm in the form of a feature
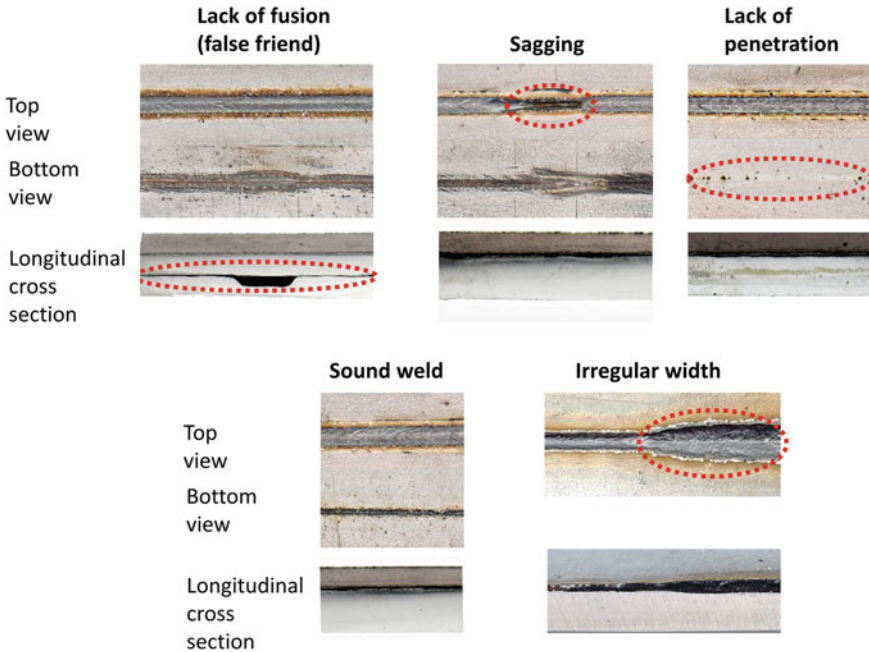
Fig. 37.21 Photographs from different perspectives of welding defects

vector together with its respective quality annotation. Therefore, initially, geometrical and statistical features are extracted from thermal image data (MWIR[8] and NIR[9] camera) recorded during the welding process to describe the keyhole- and weld pool characteristics for each time step. The features are based on higher order image moments, shape descriptors, and descriptive statistics and are used to create a high dimensional feature vector.

For process images showing heat radiation, feature extraction can be applied based on the following image processing steps which are performed for each image in the dataset:

1. Binarize the image based on a specific pixel value threshold (keyhole threshold > weld pool threshold)
2. Detect the contour (connected boundary line of an object) based on the algorithm proposed by Suzuki and Be (1985) and select the largest contour from all contours found in the image
3. Calculate contour properties such as centroids, and other image moments
4. Fit an ellipse to the found contour
5. Obtain geometrical parameters of the ellipse

---

[8] PbSn-Sensor (Sensitivity range: 1-5 μm; Framerate 500 Hz; Res.: 32×32pixel.

[9] Si-Sensor (Sensitivity range: 400-900 nm; Framerate 100 Hz; Res.: 1312×1080pixel.

6. Calculate additional features such as statistical and sequence-based features

The extracted contour can be fit as an ellipse to obtain geometrical parameters such as the length and width of the keyhole and weld pool area. An example of the ellipse fitting can be seen in Fig. 37.22a, b. The calculation of image moments based on the extracted contour object provides additional contour properties such as area, geometric center, contour orientation, and information on symmetry (Flusser et al. 2009). The calculation of moments of order p and q, of the gray value-function $I(x, y)$ for discrete images can be approximated by Nixon (2012)

$$m_{pq} = \sum_{x} \sum_{y} x^p y^q I(x, y) \Delta A \qquad (37.19)$$

where ΔA describes the area of one pixel. The zero-order moment, m_{00} represents the area of an object. For binary images, these values are proportional to the object's center coordinates. By dividing the first-order moments by the zero-order components
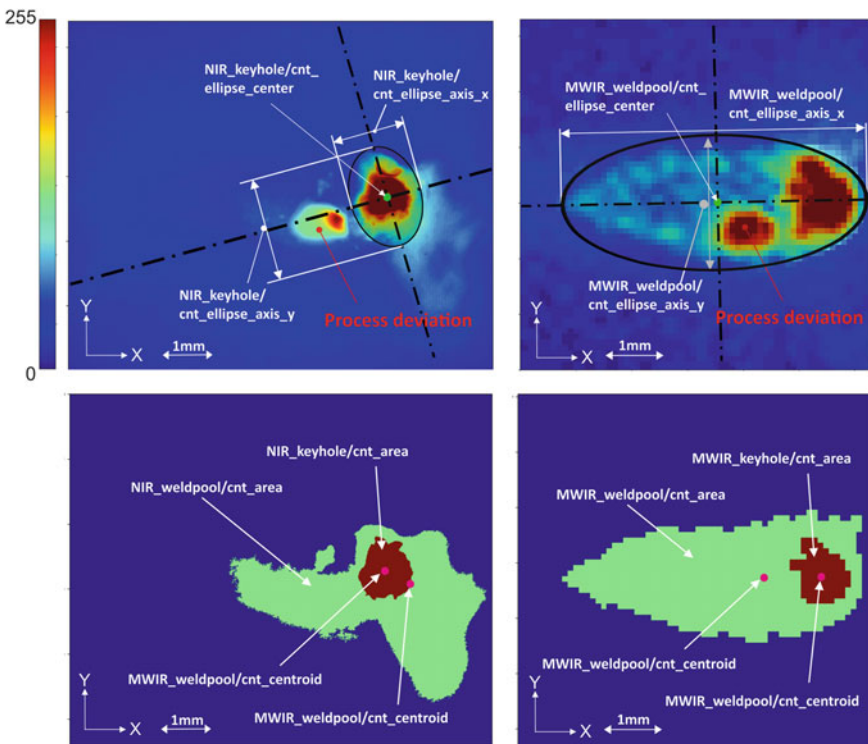
Fig. 37.22 **a** and **b** Original image and geometrical features extracted from keyhole and weld pool regions. **c** and **d** Detected keyhole and weld pool contours (filled) based on two-step binarization of the original images

as shown in Table 37.1, the result can be interpreted as the center of gravity of the contour. In addition, statistical features such as *mean, minimum, maximum, variance, median, skewness,* and *kurtosis* can be calculated based on the pixel values that represent the keyhole and weld pool contour area respectively. Taking into account two different image types (NIR and MWIR), this would result in 80 features, calculated for every *i* th image for each image type.

Feature importance

After calculating the features for each image and frame source, the importance of the features can be assessed using the random forest algorithm, which is part of supervised machine learning.

To find the most important features that are able to separate the different welding defects, a random forest classifier determines the relative importance of each feature. Random forests, introduced in Breiman (2001), can be considered as a combination of a specific number of decision trees while each tree represents a single classification model. The procedure of growing a decision tree starts with the random selection of a specific number of features at each node.

Subsequently, the feature that provides the best split according to an objective function is used to do a split on that node. Often, Gini impurity is chosen as the criterion.

For a feature X_i its importance can be determined by the computation of the sum of the weighted impurity decreases of all nodes in the forest at which a split on X_i has occurred, divided by the number of trees.

Results of such a random forest-based evaluation can be found in Fig. 37.23 (green bars). The right axis shows the prediction accuracy of weld defects of the k-nearest neighbor model trained with the accumulated feature sets, starting with the leftmost feature.

Moreover, the importance of different image sources (MWIR & NIR) can be assessed (see Fig. 37.23). The figure clearly shows that the accuracy of separating the welding defect classes reaches 99.8% by using the first five features and remains at this value. If more features are used, the accuracy decreases to 99.1%, probably related to the cause of dimensionally.[10]

In this use case, data acquired with the Si-sensor (NIR) at 840 nm wavelength first appear at position nine (orange-marked feature) in the bar plot. At this point, the accuracy of the classification model that shows the ability to detect different welding defects also decreases. The reason for this could be the fact that, according to Planck's law, the optimum wavelength for melt pool observation is about 1634 nm (1737 K), which is preferably observed with the MWIR camera. It can be concluded that information in the image data captured with the MWIR camera can be used to perform the presented classification task sufficiently (Knaak et al. 2018).

---

[10] Statistical phenomena that describes the problem of increasing data requirements in case of increasing data dimensions to obtain statistical significance.
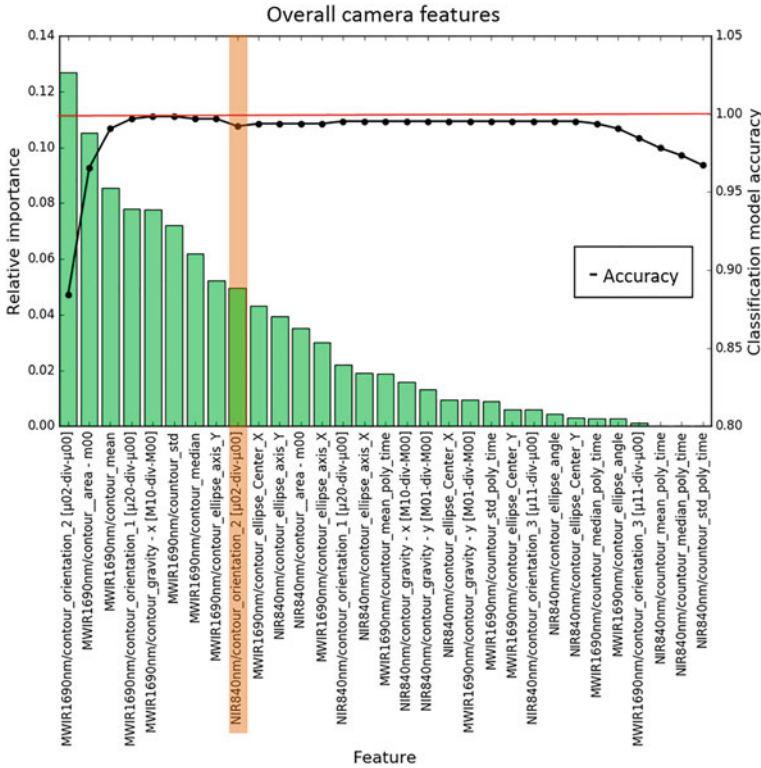
Fig. 37.23 Importance of the extracted features (left axis) and classification accuracy (right axis) of separating different welding defects based on image data from both cameras

The next step involves the most important features which can be used to train various classification models that perform grid searches for hyperparameter tuning, resulting in a fine-tuned model for predicting welding defects.

Additionally, a new deep learning-based approach for data-driven feature extraction and inline weld defect classification can be used to build a prediction model without the need for additional feature engineering (Knaak et al. 2021).

The architecture, as shown in Fig. 37.24, is based on convolutional neural networks (CNN) which are often used for image classification. Although in-process data are available in form of images, some important information may only be available in the time domain of the welding video stream. Therefore, the CNN can be combined with a recurrent neural network (RNN), specifically gated recurrent units (GRU) or Long short-term memory (LSTM). The advantage of CNNs to extract relevant spatial information and the ability of GRUs to learn meaningful temporal characteristics are combined to automatically extract a spatiotemporal feature representation of a given image sequence.
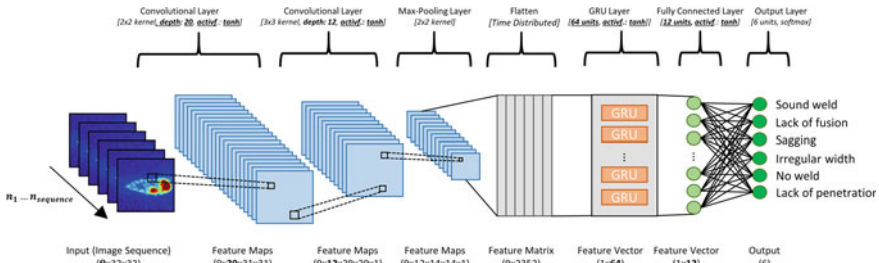
Fig. 37.24 Deep neural network architecture based on convolutional layers and gated recurrent units (GRU) for image sequence classification (Knaak et al. 2021)

Although deep learning (CNN) models are often considered a black box model, visualization of layer-wise activation maps can provide useful information for understanding how successive intermediate convolutional layers transform their input. It also offers a first idea of the meaning of the learned filter properties and which image regions might be important for distinguishing the weld defects. In Fig. 37.25, activation maps for the first convolutional layer are shown. For different input images, the activation map for each filter learned during the training is shown. The left column shows the activation maps evoked by a process of a sound weld image and the second column shows the activation maps based on several images showing different process deviations. The differences in the filter maps are depicted in the right column. The feature maps show different results depending on the camera image that was given as input. Overall, each defect shows its own fingerprint in the form of activation maps extracted from the CNN. The similarities between the activation maps for the defects "lack of fusion" and "sagging" show in the CNN's tendency to confuse these classes. In case of "lack of fusion", "sagging" or "lack of penetration" most activation maps show high activity in the keyhole area and its immediate surroundings. Additionally, when the defects "irregular width" and "sagging" occur, areas related to the weld pool show increased activity in the activation maps.

In this example application, the evaluation of different conventional algorithms and deep learning methods results in Fig. 37.26. It can be seen that for this application, both conventional and deep machine learning methods can lead to sufficient models with high prediction accuracies and comparable training and inference times. The defect detection performance of some of the evaluated models on unseen welding trials is given in Fig. 37.27. The highest average performance of 93.8% can be achieved by combining all three classifiers via a majority vote.

Overall, conventional and deep learning techniques are both well suited to predict critical weld defects such as "lack of fusion" (false friends), "sagging", "irregular seam width", and "lack of penetration" with high accuracy. However, conventional machine learning methods require extracting informative features (e.g. based algorithms from the field of computer vision and descriptive statistics). Moreover, if deep learning architecture based on CNNs and GRUs are employed to detect weld defects, their ability to learn to extract relevant spatiotemporal features from raw video data
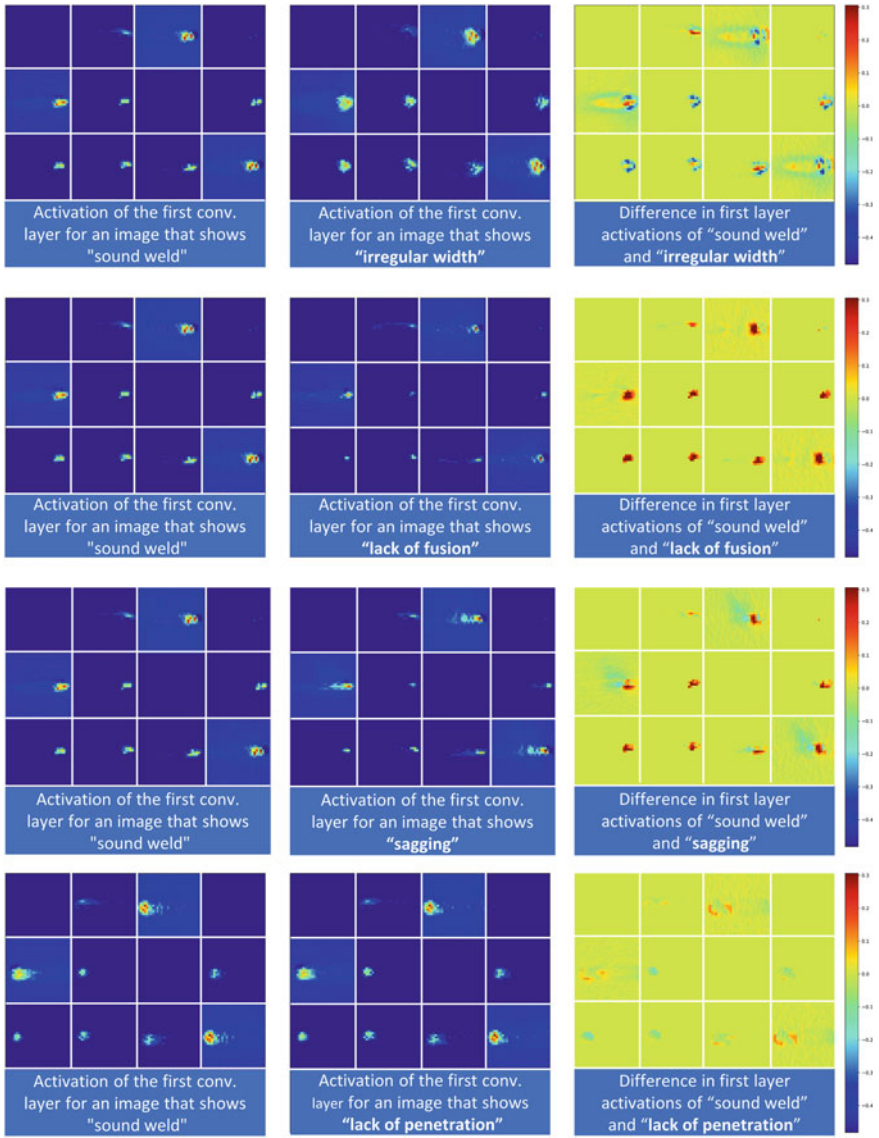
Fig. 37.25 Layer activations based on twelve different filter kernels in the first layer of a CNN that was trained to recognize welding defects based on images from the MWIR camera. Each square shows a single activation map
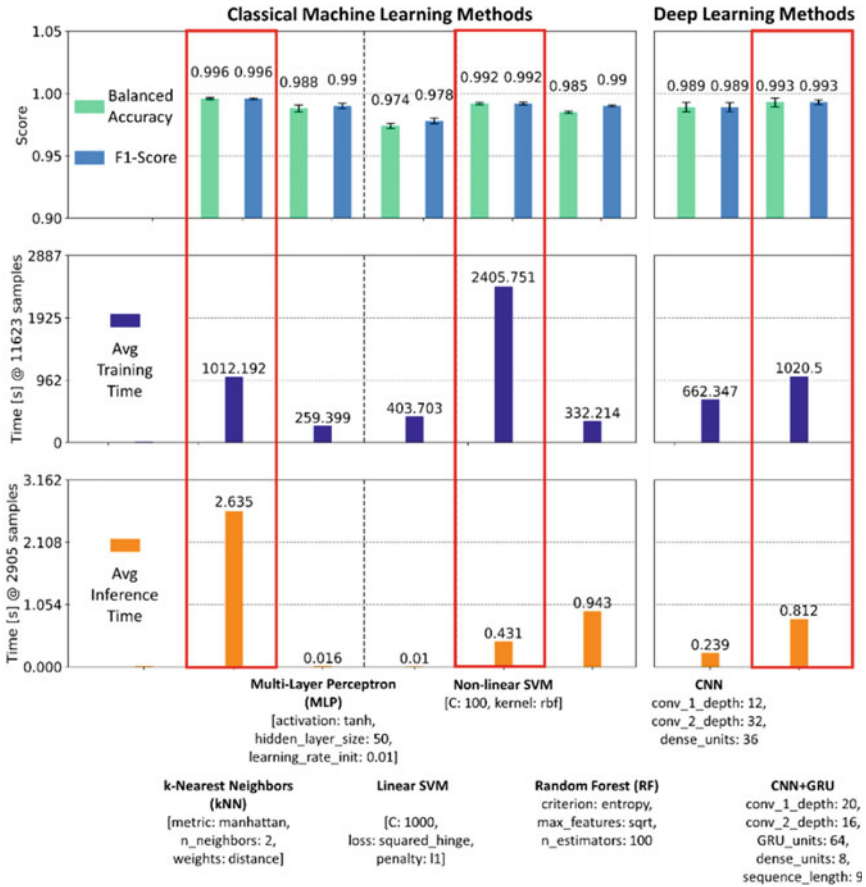
Fig. 37.26 Performance comparison of different conventional machine learning and deep learning classification methods. Optimal hyperparameters for each classifier were found via grid search and nested cross-validation

can be exploited. On the other hand, features from the time domain must be engineered by hand in such a way that they can be used accordingly for the conventional approach.

For many different sensors, especially with higher spatial, temporal or spectral dimensions, fused with additional data sources, statistical models can be employed for many use cases in the laser domain. Machine learning systems can not only be used for defect detection, but also for predictive maintenance, data-driven control of laser sources and processes or data-driven development of process parameters.

Conclusions

The majority of today's commercialized process monitoring systems is used in the macro processing of metal parts. Trends in laser material processing are set by the
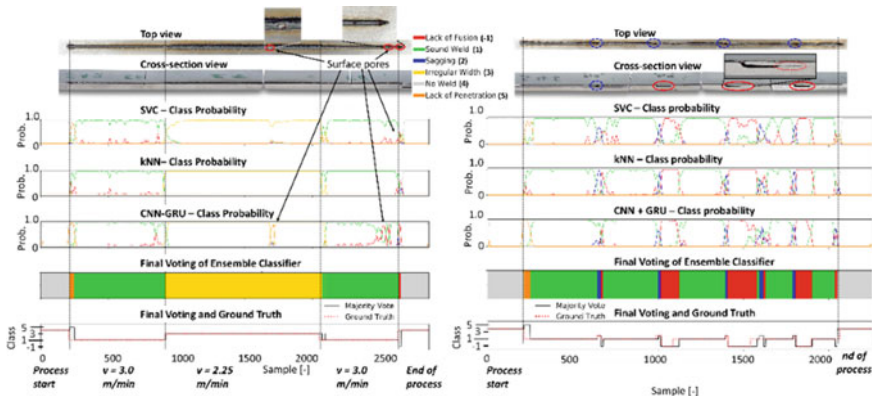
Fig. 37.27 The metallographic characterization, the resulting ground truth data, and the classification results for weld 42 (left) and weld 46 (right) based on the majority vote of SVC, kNN, and CNN-GRU classifiers

development of innovative processes, new materials, and strong miniaturization of workpieces. Currently established methods of process monitoring, therefore, have to be refined with regard to new requirements or new approaches have to be considered.

Nonetheless, also macro material processing is still faced with numerous challenges. Even with well calibrated tools and carefully selected parameters, it cannot be assumed that a process will run continuously free of perturbations. Unpredictable influences from the environment can have a significant impact on the processing results, thus leading to unacceptable errors. Partly this can be compensated by closed loop controls. For the implementation of such closed loop controls, robust process parameters, both on the input and output side, are crucial. They have to be independent of fluctuations from batch to batch, e.g. measurement of laser power, positioning at workpiece, melt pool, and seam width/length. Using such parameters will be much more reliable compared to evaluating process or heat radiation which can only be measured indirectly. Former approaches to implement process monitoring and control in laser beam welding have been mainly based on the evaluation of process radiation thus predicting the quality or specific features of the process result. It appears to be evident that such indirect measurements of quality features can lead to considerable uncertainty since the indirect measurement method in this case bears a risk of false interpretation, especially if the signal is being measured only one-dimensional. It is also apparent that the measurement of distinct variables and parameters such as real position, speed, gap, laser power, melt pool or seam geometry will certainly lead to a much improved analysis of the real state of the process and processing results. It is of great benefit to combine all the parameters (direct and indirect) in a summarized evaluation of the process and machine state. With the help of various machine learning and deep learning methods, the versatile parameters of the process and the measurement data can be combined and used in detail for analysis and process control. The mechanical and optical boundary conditions of a laser plant

or the process itself result in clear limits for the degree of possible integration of additional components. The simultaneous measurement of these parameters—most of them combined in one measurement device—will be a major step forward.

A controllable process requires a good understanding of the effects of the influencing parameters. Therefore, the successful implementation of a closed loop process control requires a good grasp of the process and its interdependencies. Practically this means, online process monitoring and closed loop control offer high potential for rationalization of workflow if anomalies can be detected and evaluated reliably. Using currently available commercial optical-based monitoring systems, a complete and automated determination of standardized quality features is not fully possible yet. In practice, it can, therefore, not totally be avoided to include post-process nondestructive testing methods like radiological examination with X-rays or ultrasonic measurement or even imply destructive checks like strength tests or metallographic inspection. Even for well established processing techniques, the knowledge about sources for instabilities is not totally resolved. Process monitoring will, therefore, be required in the near future for the enhancement of process understanding besides industrial quality assurance.

References

Bishop CM (2013) Pattern recognition and machine learning, 11th edn. Springer, New York [u.a.]

Boillot et al (2002) Robot feature tracking devices and methods. Patent No. US 6,430,472 B1

Breiman L (2001) Random forests. Mach Learn 45(1):5–32. https://doi.org/10.1023/A:101093340 4324

Cho K, van Merrienboer B, Gulcehre C, Bahdanau D, Bougares F, Schwenk H et al (2014) Learning phrase representations using RNN encoder-decoder for statistical machine translation

Flusser J, Suk T, Zitov B (2009) Moments and moment invariants in pattern recognition. Wiley, Chichester, West Sussex, U.K, Hoboken, N.J: J

Goodfellow I, Bengio Y, Courville A (2016) Deep learning. MIT Press, Cambridge, Massachusetts, London, England

Hochreiter S, Schmidhuber J (1997) Long short-term memory. Neural Comput 9(8):1735–1780. https://doi.org/10.1162/neco.1997.9.8.1735

Institute for Control Engineering of Machine Tools and Manufacturing Units (ISW) (2002) University Stuttgart: Workshop. Sensoren für die Schweissautomatisierung. Stuttgart, Deutschland, FISW GmbH

Ion JC (2005) Laser processing of engineering materials: principles, procedure and industrial application. ISBN: 0750660791, Butterworth-Heinemann, Oxford

Kaierle S, Dahmen M, Diekmann A, Kreutz EW, Poprawe R (1997) Failure analysis for laser beam welding. In: Proceedings of the ICALEO 97, San Diego, California, USA, pp 63–72

Knaak C, Thombansen U, Abels P, Kröger M (2018) Machine learning as a comparative tool to determine the relevance of signal features in laser welding. Procedia CIRP 74:623–627. https://doi.org/10.1016/j.procir.2018.08.073

Knaak C, von Eßen J, Kröger M, Schulze F, Abels P, Gillner AA (2021) Spatio-temporal ensemble deep learning architecture for real-time defect detection during laser welding on low power embedded computing boards. Sens 21:4205. https://doi.org/10.3390/s21124205

Krizhevsky A, Sutskever I, Hinton GE (2017) ImageNet classification with deep convolutional neural networks. Commun ACM 60(6):84–90. https://doi.org/10.1145/3065386

Krizhevsky A, Sutskever I, Hinton GE (2012) ImageNet classification with deep convolutional neural networks. In: Pereira F, Burges CJC, Bottou L, Weinberger KQ (eds) Advances in neural information processing systems, vol 25. Curran Associates, Inc, pp 1097–1105

Krüger N, Janssen P, Kalkan S, Lappe M, Leonardis A, Piater J et al (2013) Deep hierarchies in the primate visual cortex: what can we learn for computer vision? IEEE Trans Pattern Anal Mach Intell 35(8):1847–1871. https://doi.org/10.1109/TPAMI.2012.272

Mohamed A-R, Sainath TN, Dahl G, Ramabhadran B, Hinton GE, Picheny MA (2011) Deep belief networks using discriminative features for phone recognition. In: 2011 IEEE international conference on acoustics, speech and signal processing (ICASSP). IEEE, pp 5060–5063

N.N.: Sonderforschungsbereich 368 (1996) Autonome Produktionszellen. Arbeits- und Ergebnisbericht 1994/1995/1996. RWTH Aachen

N.N.: Sonderforschungsbereich 368 (1999) Autonome Produktionszellen. Arbeits- und Ergebnisbericht 1997/1998/1999. RWTH Aachen

Nixon M (2012) Feature extraction & image processing for computer vision. Elsevier

Reek A (2000) Strategien zur Fokuspositionierung beim Laserstrahlschweißen. Dissertation, Forschungsberichte iwb Band 138, H. Utz Verlag, München

Regaard B, Kaierle S, Schulz W, Moalem A (2005) Advantages of external illumination for monitoring and control of laser materials processing. Proceeding of ICALEO 2005, Paper #2307, Miami

Rousselange O (1998) Entwicklung eines Sensors zur Detektion von Schweißfehlern beim "Tailored-Blank"- Schweißen mit Laserstrahlung. Diplomarbeit, Lehrstuhl für Lasersetechnik, RWTH Aachen

Runkler TA (2012) Data analytics: models and algorithms for intelligent data analysis. Vieweg+Teubner Verlag, Wiesbaden

Suzuki S, Be K (1985) Topological structural analysis of digitized binary images by border following. Comput Vision, Graph Image Process 30(1):32–46. https://doi.org/10.1016/0734-189X(85)90016-7

The Mathworks Inc. (2016) Applying supervised learning

Ungers M (2019) Image based process monitoring and control for quality assurance of laser brazing applications. 1. Auflage. Aachen: Apprimus Verlag (Ergebnisse aus der Lasertechnik)

You D, Gao X, Katayama S (2015) WPD-PCA-based laser welding process monitoring and defects diagnosis by using FNN and SVM. IEEE Trans Ind Electron 62(1):628–636. https://doi.org/10.1109/TIE.2014.2319216

Chapter 38
Numerically Controlled Tooling Machines for Laser Materials Processing

Oliver Steffens

38.1 Models of Tooling Machines

A system for processing with laser radiation is divided according to a DVS guideline into the following components (Abels et al. 1998; Ion 2005):

- "Laser" including the components source of laser radiation, gas supply, and cooling system
- "Beam manipulation" including the components beam guidance and beam forming
- "Handling of workpiece" including the components loading and unloading, positioning, movement as well as working gas and inert gas
- "Control" including the components laser control, numerical control, and monitoring
- "Safety equipment" including the components safety tube, safety cabinet, and beam shutter

This classification, based on machines with CO_2 lasers, is not general-valid. Hence, a more comprehensive classification is shown in Fig. 38.1. This classification is independent of the used laser system and shows the flow of material, energy, control, and information. "Supply" means the supply of additional materials, like welding wire and working gas. The supply takes place right at the region of processing.

The disposal includes the disposal of material wastes but also dissipation of heat resp. exhausting dust and smoke. Supply, disposal, and handling—which enclose the workpiece admission up to the clamping devices, transport, and generation of the relative movements between laser beam and workpiece—build the mechanical subsystem of the tooling machine. The optical system encloses beam generation and

O. Steffens (✉)
System Technology, Lunovo GmbH, Herzogenrath, Germany
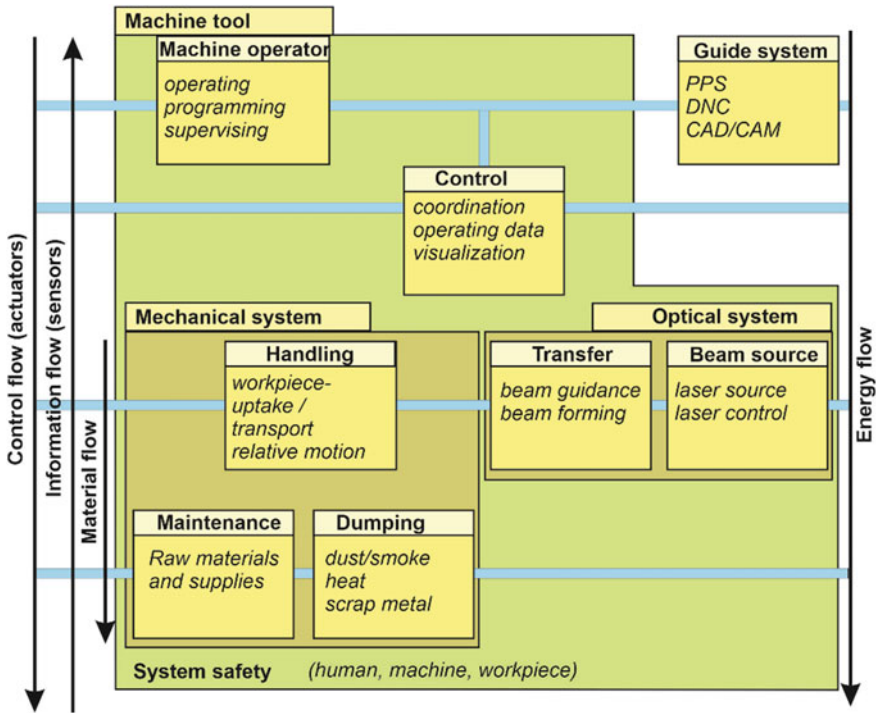e-mail: steffens69@gmx.net

Fig. 38.1 Principle of a tooling machine for laser materials processing

beam guidance from the source up to the processing area. Moreover, to consider the sociological requirements of the system, the machine operator is integrated into the tooling machine. With his experience and creative competence, he can prepare the machine for the current task and to recognize and adjust the failures of the system (NN 1999).

One possibility for specifying the production process is the transfer of NC programs by management systems that do not belong directly to the tooling machine. Management systems can coordinate production processes beyond the considered system. In practice, such systems have a data interface to the NC control and do release the machine operator from his program task. However, every single process is coordinated again by the NC control and is supervised by the machine operator.

The control is an interface between the mechanical system, optical system, and machine operator. Nowadays, its functionality goes beyond its historical task of path interpolation. Besides the geometrical data, the NC program contains instructions concerning the whole coordination of the process control. This means the control of the optical and mechanical system including supplement and disposal of waste.

The control flow moves from the control to the connected systems, which split up the data traffic to the actuators, transferring the flow of information into mechanical action. In addition to its control tasks, the control takes up information on associated

systems. This information is produced by sensors that record the actual state of a workpiece, mechanical or optical system, and send the recorded data to the control. This information can be filtered and stored (recording operating data) or can be formatted for the machine operator (visualization). A survey of operating data in this sense means that recorded data are converted directly into a control action, e.g. by switching off the energy supply of the operating system, at least when programmed sequences of motion cannot be achieved within a defined local tolerance limit.

The quantity of manufacturing processes shows the flexibility of lasers in production. Although the specifications of the different methods are different concerning their physical processes, there is a set of similarities, which in sum determine the requirements of the machine. To specify these requirements, another point of view is introduced as a basic mode (Fig. 38.2). In this, the numeric control is the main control instance. All data flow begins or ends with the control.

In the following, the functions and control-specific demands of the mended classes are being described without mentioning the machine operator. His tasks can only be described in the full sense by looking at the whole productional surroundings. The main systems represent the sort of systems that have a technical interface toward the control, but do not mean an enhancement of the functional range of application or production.
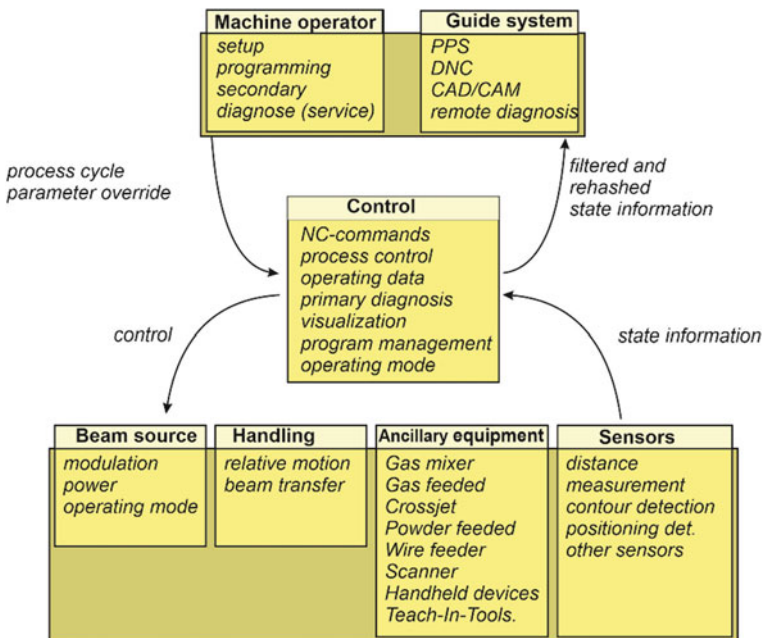
Fig. 38.2 Base model of a numerical controlled machine tool

38.2   Components of the Basic Model

38.2.1   *Source of Laser Radiation*

The source of laser radiation includes laser control, which possesses a data interface to NC. Laser control determines modulation and power depending on the operation mode. The choice of the source depends on the chosen processing method as well as on economic efficiency.

38.2.2   *Handling*

The Handling is supposed to create a relative movement between working optics and workpiece to move the focus of the laser toward a defined trajectory within the working area. Handling also includes active beam transfer that can be realized by a mirror system or a fiber. In contrast, the passive beam transfer, in which components are not integrated into the machine, cannot be regarded as isolated (see additional equipment).

For the positioning of the working optics in relation to the workpiece, surface robots are used. To cover a broad field of treatment tasks, special systems are used whose cinematics are chosen in a way the focus of the laser beam can be positioned in a three-dimensional space. Besides, it should be guaranteed that the ray axis can be oriented by any angle to the workpiece surface. A choice of suitable cinematics for the robots is shown in Fig. 38.3.

Robots are distinguished by the following features:

- Number of axes
- Kind of Movement of the main axes (cinematics)
- Working Area
- Nominal load
- Maximum speed of treatment
- Exactness of positioning, repeating accuracy, and path accuracy

Because of their high geometrical precision, cartesian robots (constructed as a portal) are used in cutting and joining (Reek 2000). The axes of portal robots are arranged in the way of three linear axes that make up a right-handed, right-angled coordinate system (DIN 66217 1975). Moreover, there can be up to two axes that enable the laser beam to tilt and turn relative to the workpiece. This happens either by moving the optics (using rotary axes) or by moving the workpiece itself (e.g. using a rotary table).

If the quality of the working results is not bounded to high geometrical precision—for example in hybrid processing or in de-focused or scanned treatment of surfaces—low-priced articulated robots are used. These are characterized by three main axes. Their working area is spherical. The advantages of articulated robots are
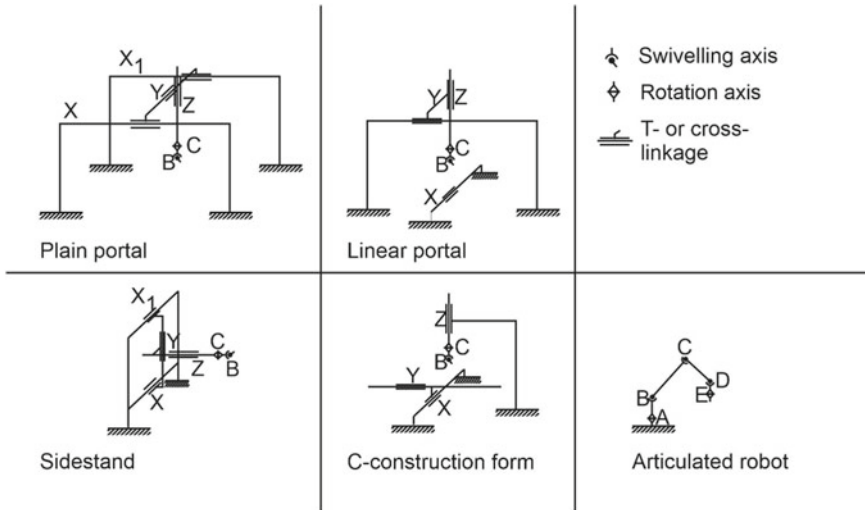
Fig. 38.3 Cinematics of robots for treatment of free-form surfaces (VDI 2861 1988)

the low price—in comparison to portal robots—as well as the higher accessibility of laser beam toward the workpiece (because of the spherically shaped working area). Their disadvantage lies in a lower exactness of positioning because the faults of the single axes cumulate. Moreover, the machine operator cannot reconstruct the robot's movement as easily because having just one linear movement within the process area means that at least two axes are involved.

The relative movement between the TCP (for Tool Center Point) and the workpiece is generated by the coordinated proceeding of the robot axes within the process area. The movement of the TCP, which means the intersection of the laser beam and the workpiece, describes a trajectory with a defined speed. Additionally, the angle of incidence is defined by the optical orientation toward the workpiece surface.

38.2.3   Additional Equipment

Additional equipment means all those tools which provide auxiliary and supplement material during the working process, and therefore, influence the result. The choice of equipment depends on the specific production process. Further equipment can be integrated, depending on the tasks of the machine operator (e.g. additional tools for preparation).

Following the functional analysis of the process, additional equipment can also be defined as tools, which control feeding, dose, and combination of gas (working gas, protection gas, cross jet) or which manipulate the beam.

While consistency, as well as supply of wire, powders, and gases, are usually set up during the phase of working preparations with the help of nozzles and other mechanical equipment, it can be meaningful to adjust the following parameters during the process (Regaard et al. 2005):

- the pressure of gases (using pressure control devices)
- the volumetric flow rate of gases and powder (using flow controller)
- the feed rate of wire (using wire feeder) or powder.

Purity and temperature of the materials, which are normally adjusted before the beginning of the treatment, have an additional impact on the process result. Very often, supply mechanisms are already integrated into the mechanical system of the machine, e.g. a cutting head often possesses guidance for gases, cooling, and powder (IFSW Institut 2003). The functions of further equipment vary depending on the specific demands and the technical development (e.g. Teach-In-panel or scanner device).

38.2.4 Sensors

Sensors and actuators are taken as a collective term for all those components which either record and convert process data (sensors) or influence the process by controlling elements directly or indirectly (actuators). They are useful to increase precision and tolerance of error as well as the flexibility of the tool machine (DVS 3203-1 2017).

Sensors and actuators work in a closed loop system, which means that actuators are controlled based on sensor data. Besides laser source, handling and equipment have not only actuators but possess their own sensors as well. These sensors serve either the internal regulation of the desired values or the system state returning them to the controlling device or to another supervising unity. Sensors represent all additional devices that measure certain variables and transfer this information to the control.

During the processing experiments in (Schunk 1992), a list was set up containing all sensors and actuators applied during the process (online). On the base of Table 38.1, those sensors can be separated out according to Fig. 38.2 Base model of a numerical controlled machine tool already belonging to handling, beam source or to additional equipment. The remaining sensor may be classified as follows:

- switches
- temperatures sensors, pyrometer
- capacitive, inductive, and tactile sensors
- camera systems (image processing)
- triangulation sensors

Sensors for monitoring beam position, laser radiation power or intensity within the processing area cannot be used according to the present state of technology during the treatment process. These data are checked off-line before starting the treatment or in recurring service intervals (off-line used sensors for quality management).

Table 38.1 Sensors and actuators

(S)ensor/ (A)ctuator	Belongs to	Comment
Switches and buttons (S, A)	Handling Additional Equipment Beam Source Sensors	Digital information flow (on/off, open/close); by use of sensors: e.g. ok/error
Way und angle sensor (S)	Handling	Integrated into the axis positioning cycle, weight balance
Force and torque sensor (S)	Handling Additional Equipment	Axis positioning cycle other devices for the process
Acceleration sensors (S)	Handling	axis positioning cycle
Temperature sensors (S)	Handling Sensors	Monitoring state of handling or measuring process relevant temperatures (surface treatment)
Current- voltage- and power consumption (S)	Handling Beam Source Control Sensors	Monitoring of current-carrying system parts; by use of sensors: capacitive, inductive, and tactile sensors (e.g. end switches, distance control)
Camera-based measurement systems (S)	Sensors	Measuring the workpiece's position, properties and contours
Photodiodes and high-speed CCD/ CMOS-cameras (S)	Sensors	Measurement of the emission of laser radiation for online quality check
Triangulation sensors (S)	Sensors	Measurement of distances
Sensors for laser power, beam guidance and intensity dispersion (S)	Beam Source (Sensors)	Monitoring of the beam guidance and -formation for quality assurance
Valves and engines (A)	Handling Additional Equipment	Cooling, gas feed

Sensors, like additional equipment, can already be integrated into the mechanical system. In commercially available cutting heads, a capacitive distance sensor is integrated already (Oebels 1992). In Table 38.2, some examples of applications of sensors are listed.

Table 38.2 Application examples for sensors

	Application example	
Sensor	Process	Description
Switches or buttons	all	Measurement of a 3D surface and data feedback to a system for the generation of geometric data (path planning) for the control (NN 2021)
Temperature sensor	Surface treatment	Measurement of the current temperature at the workpiece's surface near the treatment position and regulation of the laser power (Xianfeng X et al. 2020)
Capacitive approximation sensor	Cutting	Integration of the sensor in the cutting head; Regulation of the working distance on a defined value by the movement of the optics along the beam axis (Oebels 1992)
Tactile sensors	Hybrid-welding	Measurement of the root of a V joint in oil tanks and guidance of the laser beam focus (Wolf 1994)
Camera system (Seam Tracking)	Welding	Detection and measurement of the weld seam and automatical guidance of the laser beam focus (TCP) (Steffens 1995)
Camera system (Image Processing)	all	Detection of the workpiece's position and orientation within the working area before process treatment (Bin-Picking) (Buchholz 2015)
Triangulation sensors or OCT sensors	Material removal	Material removal from surface layers (thickness of a few micrometers), Measurement of the surface, and control of the laser power (In-Process Wafer Step Height Measurement 2019)
Triangulation sensors	Cutting and welding	Measurement of the distance between optics and workpiece while Teach-in phase, Digitalizing (Steffens 2003)

38.3 Numerical Control

Tasks of the NC control of a tooling machine with laser

Because of its universality regarding local, flexible, and intelligent workstations, the laser is an ideal tool. Not at least by this quality the laser gains importance in industrial manufacturing (Wolf 1994; Steffens 2003). The laser consists of the laser beam source, in which the laser beam is produced and emitted by means of optical components, and laser control, which is to control and supervise the beam source. Moreover, the laser is provided with a cooling system, security equipment as well as components and systems which supply the beam source and the control with energy and auxiliary materials.

The transfer of laser beam to the workpiece is achieved by beam guidance—\consisting of mirrors or optical fibers according to the construction of laser—and optical components for beam forming, e.g. focusing lenses. The task of handling the

tooling machine is the creation of a relative movement between the laser beam and the workpiece. To realise the handling, that means moving the workpiece or moving the laser optics relative to each other, articulated robots or cartesian portal robots can be used. These robots consist of several axes whose movements are steered by motors, gears, and drives. Normally, the axes are set up in a fixed mechanical relation and thereby determine the cinematic of the robot.

The handling, which means industrial robots, beam transfer, and laser beam, together with security systems and machine operator form the main and most important part of the tooling machine. Further on, other devices, sensors, and actuators are applied to the system, which is used for the material treatment with laser radiation (e.g. supply of auxiliary materials, waste management, process sensors).

The numeric control is used for control and survey of the technical system components as well as for information exchange with the machine operator or any other connected systems. In that way, the control forms the coordinating element within the system "tooling machine". According to the cinematic of the robot, controls are either generally called NC control (NC for Numerical Control) or, having an articulated robot, a RC control (RC for Robot Control). In the following, the term NC control is applied without distinction between NC and RC.

With a rising degree of automation of manufacturing processes, the task of process control also increases by the NC in complexity (NN 2000). The treatment of a workpiece on a NC is described by a program (NC program or part program) (Weck 1989; DIN 66025 1983). The data stored in the program are decoded by the control and is processed after geometrical and technological data separated.

In essence, the tasks of the NC control can be divided into the control of the robot movements and into the control of the ray source and the additional equipment (Kief 1992). Moreover, it applies itself to take of the data NC of sensors, to process and to affect the process expiration based on sensor data about the actuators. At least operating data can be visualized at the MMI (MMI for Man Machine interface). The tool owner can determine the process sequence by use of the MMI and affect and supervise with the help of the visualized operating data.

The NC controls the robot movements based on interpolation points (geometry data in part program) and generates a trajectory by connecting the programmed points. The cinematic of the robot, as well as the mechanical dimensions and limitations, are passed in the machine date of the control and are considered by the interpolation algorithm of the trajectory. The control of additional equipment and laser device takes place on the bases of the technology data given in the NC program. Besides, an essential aspect of the treatment of the technology data is the temporal or local coordination of these issues with the robot movements. The assignment of geometrical data and technology data is given by the part program.

Internal structure of a numerical control.

The internal structure of control was designed for the different functions of the control. While the hardware of the NC adapted itself constantly to the technological innovations in computer technology and information technology, the structural construction of commercially available NC controls stayed the same. The structural

elements of the control are the MMI with a program interface, the NC kernel, and the programmable logic control (PLC, Fig. 38.4). Different procedures are used for the programming of a control. In laser technology, three kinds of NC programming predominate (Heekenjann et al. 1996), computer-aided indirect programming far of the tooling machine, direct programming by use of the editor of the NC, and direct programming by means of Teach In. In every case, the NC program about the MMI is filed into the memory of the control for the processing.

The NC kernel is responsible for the processing of part programs (Nitsch 1996). Movements of the robot and the processing of technology data during the process are coordinated by the NC kernel. The program decoder takes over the task to separate geometry and technology data and to convert in an internal structure to be treated for the control. The decoder reads the data from the NC program memory. These data are applied to the interpolator to calculate the trajectory in firmly given time intervals (interpolation time). Besides, cinematic and mechanical borders of the system are considered. If a technology function is called dependent on position, the Interpolator takes over the issues to the connected devices, either directly ("fast" periphery) or about the detour of the PLC. The PLC as a part of the NC control takes over the task from inputs and issues near connected devices. The necessity of the PLC is founded

Fig. 38.4 Architecture of a numerical control
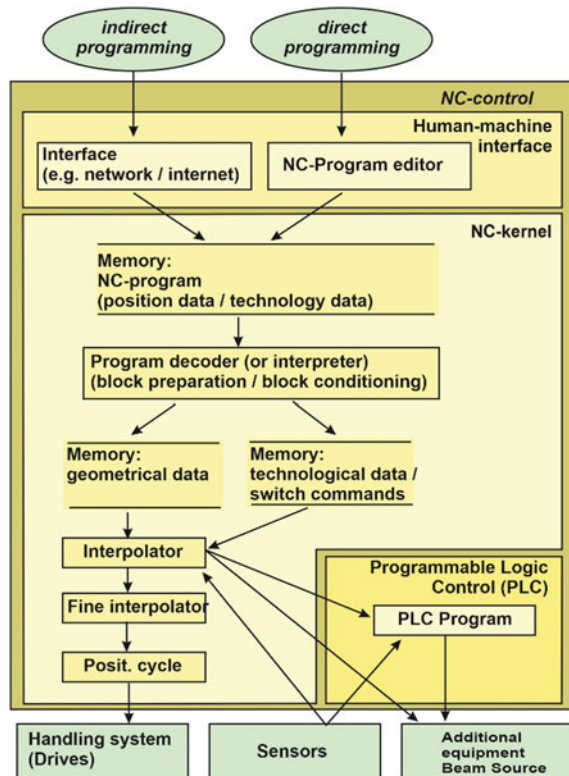
in the fact that it checks based on logical connectives in the PLC program whether the machine tool is in a safe condition. In addition, it is decoupled hardware-sided and software-sided by the NC kernel. All security equipment (e.g., protection doors, emergency stop, end switches) are to be connected to the entrances of the PLC. Issues directly about the Interpolator take place when they are connected temporally closely with the steps of the process consequence (real time). The administration of these issues within the Interpolator needs additional time which gets lost for the continuous calculation of interpolation points along the programmed trajectory. The permissible number of issues to be administered is limited on account of the capacity of the Interpolator and the given interpolation time. Certainly, a rise in the interpolation time is possible in modern controls. However, the increasing time of interpolation leads to a more inaccurate interpolation of the trajectory and to higher differences between the desired and actual path. Therefore, direct controls of the periphery from the Interpolator are limited to the necessary. However, with the rising capacity and reliability of the processor's tasks of the PLC can be shifted increasingly to the Interpolator. At present, systems are already offered based on PC technology which distinguishes logically between PLC and NC kernel, but processing takes place together on a single processor (PC-based controls). Process times are assigned with the time slice procedure.

The sensors can supply additional information regarding the process. This information is processed either by the Interpolator or by the PLC program. Based on sensor data, issues can be adapted in manipulation, beam source or additional components.

The control of the robot's movement is realized by means of a closed loop positioning cycle. Besides, the positioning cycle serves as the physical control of the drives and the monitoring of the positions of the robot axes (Fig. 38.5). The functions of a two-stage position regulator are distributed to NC kernel and robot. Besides, the system borders are not unambiguous. It differs according to the complexity of the positioning cycle, the used control, and the applied drives.
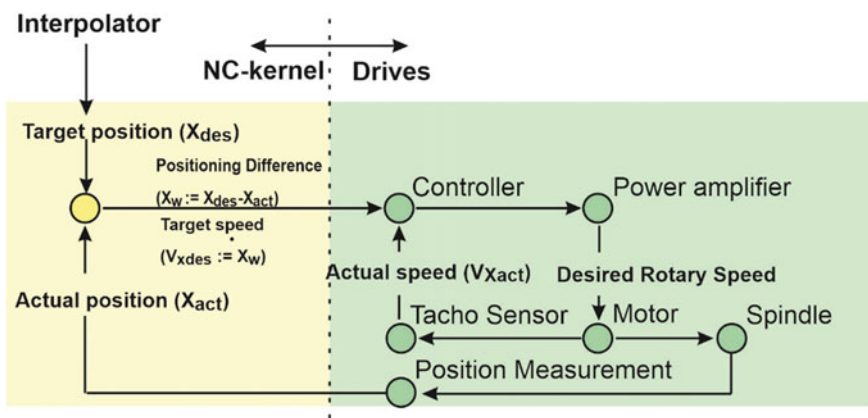
Fig. 38.5 Two-staged positioning control circuit

To acquire and visualize information from the connected devices, data flows bottom-up into the NC kernel, and from there to the MMI. Other tasks of the MMI are the filtering and putting into graphs of operating data as well as the administration of NC programs and other user's inputs and the supply of interfaces to other connected systems, like CAD/CAM systems, to shop-floor systems or DNC systems (Stupp 2000; Fembacher 2000; Leinmüller and Treicher 2000).

38.4 Extensions of Numerically Controlled Machine Tools for the Material Treatment with Laser Radiation

38.4.1 Challenges of Laser Processing

Often the purchase of laser machines is associated with a high initial investment (Hügel 2014). Customers expect fast processes, high accuracies, and a high degree of repeatable process quality. To justify the costs it is necessary to guide and monitor the laser process to reach an appropriate level of automation. Laser machines should not be idle, so also all times for work preparation, loading and unloading and maintenance are to be considered.

The use of numerical control as a central "intelligent" part of the machine as well as the property as the user interface is of great importance (Jihong et at. 2019). The control combined with the electromechanical parts realizes the needed accelerations and velocities. Process-specific sensors and actuators support process quality and reduce preparation times.

For example, nowadays, the cutting speed of a laser tool can be more than a hundred meters per minute (Petring 2011). New laser sources have the capability to generate pulses in the GHz range. For that, controls must work in cycle times far less than a millisecond (typical cycle times are 125 or 64 μs). Within one cycle, a steadily growing amount of sensor and actor data must be acquired and evaluated, and even faster devices must be controlled.

On the other hand, the control provides interfaces to common IT infrastructure such as network or internet. The interaction between network/internet is growing fast. Modern business models are based on creating inquiries and tasks for machines directly via the internet by use of a wide range of different machines distributed all over the world.

In the following, a few applications for numerical control machines are described which are all based on the need for adaption for laser processing.

38.4.2 Preparation and Path Planning by Use of a Scanner

There is a general tendency from serial production to individual products with a batch size of one. For mass production, the time for preparing the machine is of minor priority. But for small batches, work preparation is a significant indicator of production costs. Usually, preparation is done by using CAD/CAM system and simulation to reduce the idle times of the machine. Programming on-site or Teach In is only used in the rarest of cases. But in a rising number of applications, there is no or inaccurate CAD data available, especially in additive manufacturing. In this case, it is useful to generate these data by digitizing them (NN 2021). If digitizing is integrated in the machine tool and is combined with the used robotics, it can be used to prepare the process at the machine, directly. This is a powerful tool to reduce work preparation and makes a CAD/CAM system obsolete.

A possible process chain assumes an integrated line scanner (Fig. 38.6). The line scanner is lead above the workpiece surface. A point cloud representing the workpiece's surface is calculated by the use of the scanner data and the robot's actual positions. The point cloud can be converted into a data format that is readable by CAD/CAM tools. Using fast software tools implemented on the control makes the operator capable to plan processes without programming any line. For that, the operator has to mark the area to be processed and the software calculates the path (path planning). Process parameters such as laser power or feed may be added by use of a database.
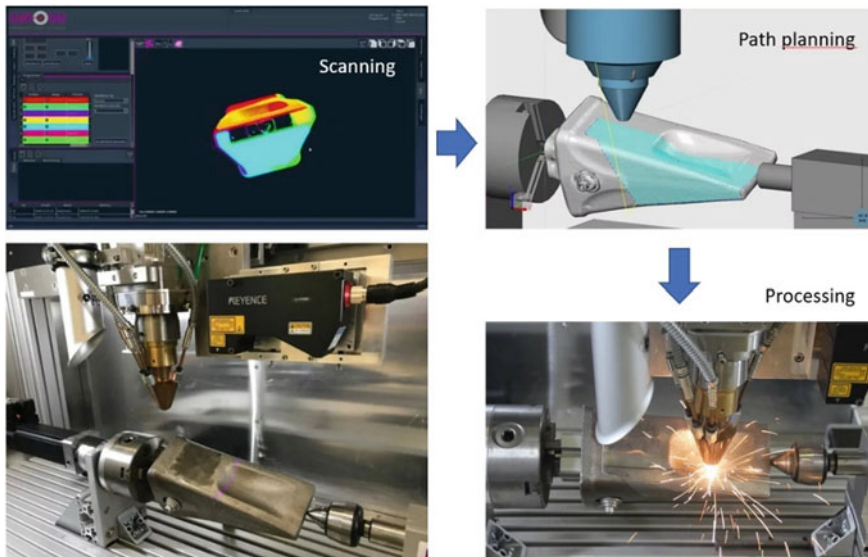
Fig. 38.6 Process Chain Scanning, Path planning, and Processing by LUNOVU pLMD; *Source of image* LUNOVU GmbH, Herzogenrath, Germany

38.4.3   1D/3D-Distance Control

The correct focus position of the laser beam relative to the workpiece surface is an essential factor of influence for a qualitatively good process result. A correction of the focus position can be supported by the use of sensors to measure the distance between optics and the workpiece surface. Distance control belongs to the area of "Path Control" and "Sensor Integration". Moreover, the quality of the process result can be supervised by monitoring the working distance during the process. Monitoring of the operating area of the sensors or the evaluation of a digital signal with a touch of the workpiece raises the operational safety of the machine tool.

The distance control differs in a 1D distance regulation with which a separate axis is driven by sensor data, and a 3D distance regulation with which the distance is corrected between optics and workpiece surface along the beam axis (Fig. 38.7). Measuring the distances is realized by distance measuring sensor systems fixed appropriately to the optics.

Usually, the 1D distance regulation applies sensors that are not integrated into the optics. The form and the measuring procedure make it not possible to measure directly at the point of treatment (TCP) during the process. The measuring point lies around a defined distance to the TCP forerunning in the working direction.

The 3D distance regulation can be realised by us of a sensor which is integrated into a cutting head. In addition, nozzles are available which lead the working gas or protection gas to the working point and dispose of a capacitive sensor at the nozzle top also.

Inductive, capacitive, optical or tactile sensors are used. The sensor system generates an analogous value in dependence on the distance between the sensor head and
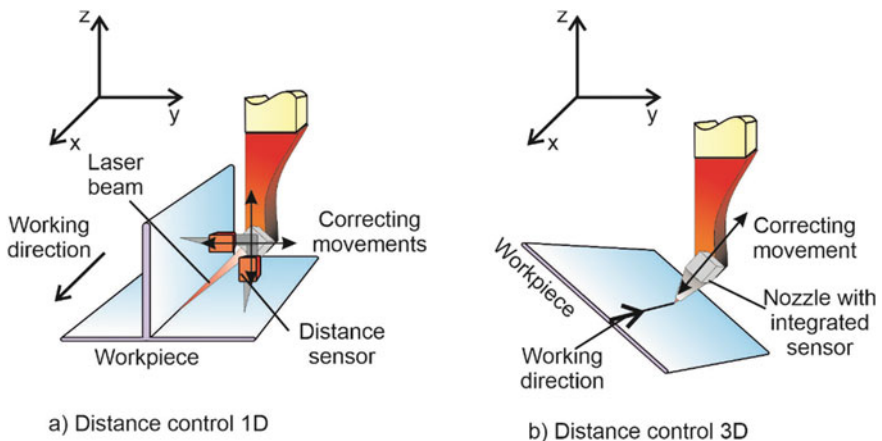
Fig. 38.7 Principles of distance controls (1D and 3D). **a** Distance control 1D with two axes simultaneously **b** Distance control 3D along the beam axis

the workpiece surface. To parameterize and control the distance control, a set of new NC commands is implemented (Fohn 1997).

To realize the distance control, the NC calculated desired values for the axes movements are overwritten by desired values calculated by the use of the sensor measurements in each interpolation cycle. The 1D distance control requires the feed along one of the cartesian axis (leading axis without loss of generality X). The sensor measures along an orthogonal axis (following axis Y). The calculation of new desired values takes place in every interpolation cycle (Fig. 38.8). For that, in the first step, the actual sensor measured distance value is used to calculate a new desired value for the TCP taking the forward run into account. These coordinates are stored in a ring buffer as the second step.

Within the same interpolation cycle, the ring buffer is used to read two values which coordinate X enclose the actual value X of the leading axis. By use of these values, a new desired value is interpolated for the following axis Y. Taking the maximum velocities and acceleration into account, the corrected desired value Y is written into the internal NC memory (as a new interpolated position).

In contrast to the 1D distance control, used sensors for 3D distance control measure directly at the treatment area (TCP). So the algorithm requires the last entry of the ring buffer, only. The integration of the sensor values within the NC internal interpolation is based upon the transformation of the measured values along the cinematic chain
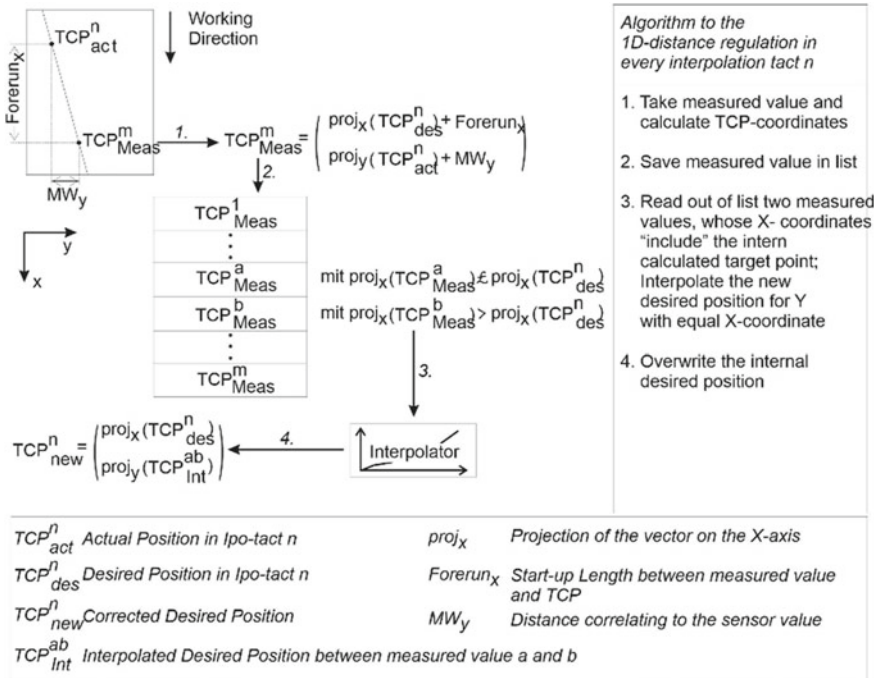
Fig. 38.8 Algorithm of 1D distance control
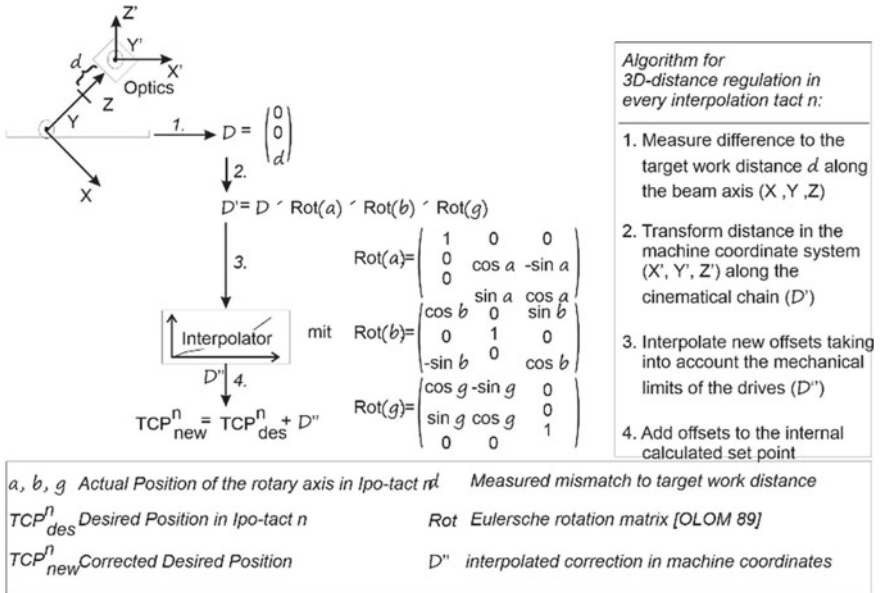
Fig. 38.9 Algorithm of 3D distance control

of the robot (Fig. 38.9). Therefore, the actual position of the rotary axes is recorded (step 1). The transformed sensor values (step 2) are used to calculate an offset to the machine axes (step 3). Similar to the 1D distance correction, the maximum velocity and acceleration are taken into account. The last step is used to add the calculated offset to the NC internal calculated desired TCP position.

For example, the usage of the 3D distance control is illustrated in Fig. 38.10 which shows the operation of the "Rotocut". Within the cutting head, a distance measuring capacitive sensor is integrated, which generates a signal when touching the workpiece by the nozzle. This signal is evaluated by the PLC program and interrupts the treatment immediately when this signal rises.

38.4.4   Seam Tracking

Seam tracking is of high importance for flexibility and automation. Seam tracking means the automatic control of robot axes in that way that the TCP is guided along a geometrical contour upon the workpiece's surface detected by the used sensor system (Steffens 1995). For that, optical sensor systems are used. These systems contain a laser diode whose emitted light is projected upon the workpiece surface like a line by means of optics. This line is recorded by a CCD camera and is to be evaluated (light section method, Fig. 38.11).

Fig. 38.10. 3D laser cutting by use of solidcutter; *Source of image* Precitec GmbH and Co. KG, Gaggenau-Bad Rotenfels, Germany
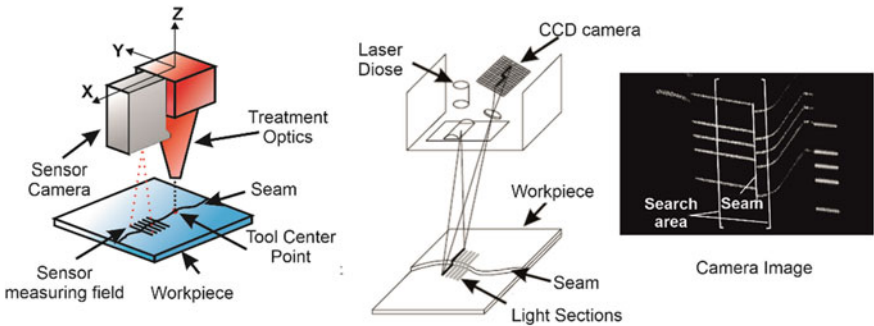
Fig. 38.11 Measurement principle of a seam tracking sensor and the light section method

Within the camera image, the detected contour is identifiable by the point of discontinuity. The width of the gap between the line segments can be used to calculate the gap width of the workpiece's seam. The measuring values are transferred to the control by a fieldbus protocol.

For seam tracking, the sensor head is assembled at the optics in a forward direction concerning the treatment feed to protect the sensor from process heat and the emitted light by the process plasma. On the other hand, the sensor should not influence the process itself. Further on, it takes some time to record and evaluate a camera image
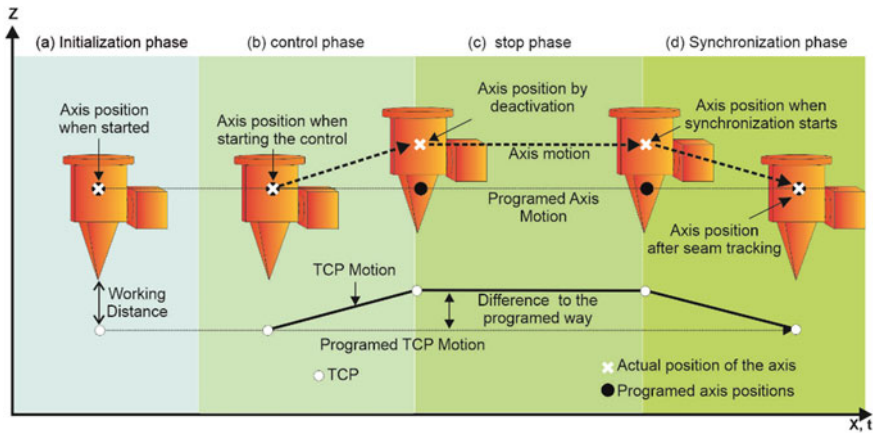
Fig. 38.12 Seam tracking phases

as well as to transfer the data to the NC (dead time) which demands a certain forerun of the sensor.

If a safe recognition of the contour is possible and the geometric boundaries for using the seam tracking are fulfilled, the seam tracking can be subdivided into a phase model to structure the sequences by their time order (Fig. 38.12). The parameters of the single phases are set by NC instructions while the phase of initialization. This enables the seam tracking to be used without interruption of the robot's movement while processing (Steffens 2003; Fohn 1999).

The tasks during the separated phases are:

- Phase of Initialization: Parameterization, Move to Start Position, Switch On Sensor, Regulate the Forerun
- Phase of Control: Control axes by use of sensor values (if necessary control of the wire feeder or the laser power)
- Phase of Stopping: Switch Off the Sensor, and freeze the distance between the programmed and current path, leading the treatment optics in an area safe against collision
- Phase of Synchronization: Stop Movements, Synchronize the actual and desired axis positions, Finish the Seam Tracking

The separate phases can be affected by a set of new NC commands and can be started or stopped. The advantage of this kind of realization is that existing programs can be adapted without great effort by adding the appropriate commands at the beginning and end of the processing cycle.

By use of the seam tracking tolerances of the workpiece, the workpiece's clamped position or tolerances caused by the process treatment can be compensated. Furthermore, the efforted time to program the control is reduced. In practice, the fields of application are limited because of the optical method to measure. In particular, complex 3D applications are very intricate because all robot axes have to be used

to position the focus point of the laser beam upon the workpiece's surface and the rotary axes are used to adjust the appropriate angle of incidence. The guidance of the measuring field of the sensor to detect the desired contour is difficult. In addition to that, the orientation of the sensor head toward the workpiece is changing continuously. This results in a shift and tilt of the projected laser line within the CCD camera image and leads to geometrical errors when evaluating the 2D camera image. To compensate for these errors, complex algorithms are needed.

An example of usage is the simultaneous operation of two sensor systems to weld T-joints in shipbuilding can be found in (Steffens et al. 2000).

38.4.5   IoT, Machine Learning, and Artificial Intelligence

With the start of the fourth industrial revolution, machines are supposed to be connected not only with the production environment, but also worldwide. The growing possibilities for data processing are of great importance to improve laser processes. Often the result of a laser process depends on more than a hundred parameters. Tolerances of process parameters are small, so the development of a stable and robust process is difficult. Using sensors and intelligent algorithms may supervise and control some of these parameters, but controlling all of the process parameters seems to be very complex.

Artificial Intelligence and Machine Learning are a chance to open up new fields of applications or to improve the existing ones. Numerical controls as center of data acquisition with its connected sensors and actuators as well as the various interfaces already used today will have an important role in development. To enable new possibilities with industrial proven components, controls are extended by enhanced hardware to collect the amount of data that is needed for AI algorithms and to handle these data lakes without stressing the control of the machine ("Edge Computing"). These devices are equipped with fast interfaces to the machine as well as appropriate interfaces to the ethernet and internet. That facilitates all modern forms of communication and protocols and accelerates the usage of the Internet of Things, 5G, Big Data, and Artificial Intelligence.

References

Abels P, Kaierle S, Kreutz EW, Poprawe R (1998) Failure recognition in tailored blank welding by image processing. ICALEO 98, USA

Buchholz D (2015) Bin-Picking – New Approaches for a Classical Problem, Dissertation TU Braunschweig, Springer Verlag, Heidelberg

DIN 66217 (1975) 1975-12: Axis and motion nomenclature for numerically controlled machines; 1975-12; Beuth Verlag, Berlin

DVS 3203-1 (2017) Laserstrahlschweißen von metallischen Werkstoffen - Verfahren und Laserstrahlschweißanlagen; Ausgabe 2017-06, Beuth Verlag, Berlin

DIN 66025 (1983) Numerical control of machines, format; general requirements, Beuth Verlag, Berlin

Fembacher W (2000) Produktivitätssteigerung durch Steuerungsvernetzung; in: Werkstatt und Betrieb 3/2000, Seite 24–31, Carl Hanser Verlag, München

Fohn M (1997) Abstandsregelung V2.01, Bedienungsanleitung, Fraunhofer Institut für Lasertechnik, Aachen

Fohn M (1999) Spezifizierung und Implementierung eines Profibus-Protokolls zwischen Sensorsystem "SCOUT" und der CNC "Sinumerik 840D" zur Nahtfolge, Diplomarbeit, RWTH Aachen

Heekenjann P, Köhler A, van der Laan CK (1996) Robotergestützte 3D-Lasermaterialbearbeitung; n: Laser, Ausgabe 2-1996, b-quadrat, Kaufering

Hügel H (2014) Laser in der Fertigung: Grundlagen der Strahlquellen, Systeme, Fertigungsverfahren; Springer, Heidelberg, Berlin

IFSW Institut f'ur Strahlungswerkzeuge Stuttgart "Integration optischer Messmethoden zurProzesskontrolle beim Laserstrahlschweißen", Laser Magazin (2003)

In-Process Wafer Step Height Measurement (2019) White Paper Spring 2019, Precitec, Gaggenau

John C Ion (2005) Laser processing of engineering materials: principles, procedure and industrial application. ISBN: 0750660791, Butterworth-Heinemann, Oxford

Jihong C et al. (2019) Toward intelligent machine tool. Engineering 5(4):679-690. Elsevier BV. Nethrlands

Kief B (1992) NC/CNC Handbuch '92, Carl Hanser Verlag, München, Wien

Leinmüller M, Treicher N (2000) Entscheidungsunterstützung durch ein Produktionsinformationssystem; in: ZWF, 10/1999, Seite 597–600, Carl Hanser Verlag, München

NN (1999) Sonderforschungsbereich 368 "Autonome Produktionszellen". Arbeits- und Ergebnisbericht 1997/1998/1999. RWTH Aachen

NN (2000) Offene Prozessschnittstellen für integrierte Steuerungsapplikationen, Resümee zum Forschungsbedarf im Rahmen der BMBF-Dringlichkeitsuntersuchung "Forschung für die Produktion von Morgen", Stuttgart

NN (2021) https://lunovu.com/en/scan-toolpath-generation; Intelligence brought into the LMD process; LUNOVU GmbH, Herzogenrath (2021)

Nitsch H (1996) Planung und Durchf'uhrung der Materialbearbeitung mit Laserstrahlung aus steuerungstechnischer Sicht, Dissertation RWTH Aachen, 1995, Aachen: Shaker

Oebels H (1992) Verfahrensentwicklung als integrierter Bestandteil moderner Qualitätssicherung am Beispiel des Laserstrahlschneidens, Dissertation, RWTH Aachen

Petring, D (2011) Schneller schneiden auf Maschinen mit fasergekoppelten Lasern; MM Maschinenmarkt Nr. 13, pp 32-34, Vogel Communications Group, Würzburg

Reek A (2000) Strategien zur Fokuspositionierung beim Laserstrahlschweißen. Dissertation, Forschungsberichte iwb Band 138, H. Utz Verlag, M¨unchen

Regaard B, Kaierle S, Schulz W, Moalem A (2005) Advantages of External Illumination for Monitoring and Control of Laser Materials Processing" Proceeding of ICALEO 2005, Paper #2307, Miami

Stupp L (2000) Der Griff zur richtigen Tastatur; in: Werkstatt und Betrieb, Ausgabe 3/2000, Seite [24–31] Carl Hanser Verlag, München

Steffens O (2003) Adaption von numerischen Werkzeugmaschinensteuerungen an das Fertigungsumfeld bei der Materialbearbeitung mit Laserstrahlung, Dissertation RWTH Aachen, Shaker Verlag, Aachen

Steffens O, Kaierle S, Poprawe R (2000) Simultaneous Laser BeamWelding of T-Joints by Use of Seam Tracking Systems. Proceedings of the ICALEO 2000, Detroit, USA

Schunk HR (1992) Laser für die Oberflächenbehandlung: Konzeption geeigneter Systeme; VDIVerlag, Düsseldorf

Steffens O (1995) Anforderungsdefinition, Spezifikation und Implementierung eines Systems zur Bahnkorrektur bei der Werkstückbearbeitung mit numerischen Steuerungen in Echtzeit, Diplomarbeit, RWTH Aachen

VDI 2861 (1988) Assembling and handling; characteristics of industrial robots; designation of coordinates; 1988-06; Beuth Verlag, Berlin

Wolf U (1994) Integration der Laserbearbeitung in ein Produktionssystem: Zur Vorgehensweise bei der Einführung innovativer Produktionstechnik Fügen mit CO2-Laserstrahlung, Dissertation RWTH Aachen, Shaker Verlag, Aachen

Weck M (1989) Werkzeugmaschinen, Bd. 3 Automatisierung und Steuerungstechnik – 3. Neubearbeitete und erweiterte Auflage, VDI Verlag, Düsseldorf

Xianfeng X et al. (2020) Towards monitoring laser welding process via a coaxial pyrometer. J Mater Proc Technol 277:2020-03. Elsevier B.V., Nethrlands

Part XI
Laser Measurement Technology

Chapter 39
Optical Coherence Tomography

Stefan Hölters, Fabian Wendt, and Reinhard Noll

39.1 Introduction

Various methods are available to measure geometric features inside condensed matter using electromagnetic radiation, e.g. X-ray radiography (XRT) and magnetic resonance imaging (MRI). For X-ray radiography, a beam of X-rays is directed to an object where this radiation is absorbed depending on the density and composition of the object. A detector positioned behind the object registers the transmitted radiation and yields a projection of the object in terms of an absorption pattern. Extending this scheme to multiple X-ray measurements taken from different projection directions enables so-called tomographic images, i.e. cross-sectional images of the object. Such computed tomography (CT) scans are mainly deployed for medical and technical applications. Photon energies applied are in the range of 15 keV to 110 keV for medical and beyond 100 keV for technical applications depending on the size and structure of the object to be measured. The disadvantage of XRT is the radiation dose and the linked potential radiation damage caused by ionizing radiation.

In contrast to XRT, optical coherence tomography (OCT) not only makes use of much smaller photon energies but also enables a look inside an object if the object is translucent (Drexler and Fujimoto 2008; Bouma and Tearney 2002). Translucent objects are, e.g. organic materials (tissue, polymers, varnish) and ceramics. However, due to the much lower photon energy—in the range of 0.9 to 1.5 eV—the radiation undergoes multiple scattering processes. Especially at visible and near-infrared wavelengths, scattering is strong in turbid media. The penetration depths from which spatial information can be gained are reduced accordingly to the order of tens of microns up to a few millimeters.

S. Hölters · F. Wendt · R. Noll (✉)
Fraunhofer ILT, Aachen, Germany
e-mail: noll.reinhard@arcor.de

Most applications are found in biophotonics and clinical biomedical imaging and here especially in ophthalmology. Technical applications range from the measurement of the thickness of coatings and sheets, the structure of translucent layers and the detection of subsurface defects to the monitoring of welding processes and additive/subtractive manufacturing processes.

Beyond its tomographic feature, OCT can be considered as an absolute measuring interferometric method which allows to measure distances to an opaque object, i.e. without any penetration of the measuring radiation into this object. Measuring absolute distances to an object, such as a metal sheet or a metallic workpiece, is of paramount importance for inline measuring tasks in a production line since any interruption of the measuring beam during a measurement—e.g. by a blocking of the beam propagation path—does not require any subsequent reset action. The measurement immediately continues to yield the absolute distance to the object after the beam path is open again.

39.2   Principle of OCT

The basic setup for OCT is shown in Fig. 39.1 (Donges and Noll 2015). A light source, which emits light with a low coherence length, is coupled into a Michelson interferometer. The beam is split into reference and measuring beams. The mirror in the reference path can be shifted. The beam in the measuring path irradiates the measuring object and penetrates partially into the object. Inside the object, the light is attenuated and scattered depending on the chosen wavelength and the properties of the object material. At interfaces between regions of different refractive indices, the light is reflected. A part of this radiation propagates in the backward direction and another part—depending on the thickness of the object—is leaving the object as transmitted radiation on the backside.

Radiation from the reference and measuring path is recombined at the beam splitter and the detector registers the interference signal, if the optical path difference (OPD) between both signals is smaller than the coherence length of the applied light. Since
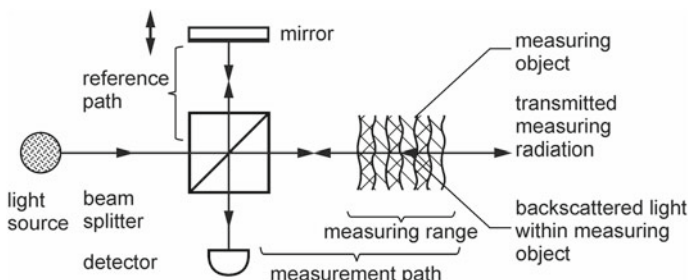
Fig. 39.1   Basic setup for optical coherence tomography
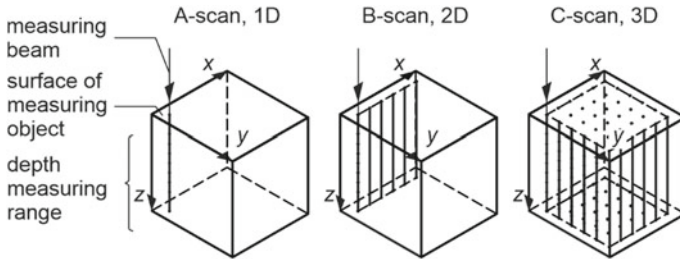
Fig. 39.2 Scan modes for optical coherence tomography, 1D/2D/3D—one/two/three dimensional

the coherence length was chosen to be small, for most scattering centers of the object this path difference will be greater than the coherence length. As a result, only an incoherent superposition occurs. The reference mirror is now translated to match the reference path length to a defined measuring path length thus yielding a coherent superposition of both beams for a defined depth inside the measuring object. A high modulation degree of the superimposed beams in the sense of a high interference fringe visibility is detected. With a step-by-step translation of the reference mirror and its known position, depth scans are generated.

Such depth scans are called A-scans—a terminology taken over from ultrasonic methods (Cobbold 2007). They correspond to a one-dimensional measurement. By a lateral relative motion between the measuring beam and the object, two- and three-dimensional images of translucent objects can be obtained. Figure 39.2 illustrates these A-, B- and C-scans.

The absolute measuring capability of the setup shown in Fig. 39.1 results from the fact that in contrast to conventional interferometry not only one wavelength (or small bandwidths of wavelengths) contributes to the interference but a superposition of many wavelengths. For a single wavelength, the interference signal is a periodic function, and a distance measurement is restricted to the measurement of differences in distances by counting passing interference fringes (or fractions of passing interference fringes). If the beam is interrupted, this counting information is lost. If a multitude of wavelengths is interfering, the unambiguous measuring range is extended considerably. For a light source with an increasingly broad continuous spectrum, the coherence length approximates the value zero. Then only one interference fringe remains, and this is for those distances to the measuring object which exactly correspond to the reference path length (in other words, the optical path difference becomes zero).

The axial resolution of OCT is given by the coherence length of the light source:

$$L_c \approx \frac{\pi}{\Delta k} \tag{39.1}$$

where

$$k = \frac{2\pi}{\lambda} \tag{39.2}$$

is the angular wavenumber, λ the wavelength and Δk the wavenumber width of the spectrum of the light source. For a sufficiently small wavelength width $\Delta\lambda$ and a central wavelength λ_0, the coherence length and axial resolution are given by:

$$L_c = \frac{1}{2}\frac{\lambda_0^2}{\Delta\lambda}. \tag{39.3}$$

(In some references the prefactor is stated as $2\ln(2)/\pi$ (instead of ½), which is just a consequence of the used definition of the interference fringe contrast for an optical path difference of L_c. Relation (39.3) holds for an interference contrast of ~0.4 at an OPD equal to the coherence length L_c.)

In the following, we consider Spectral-domain OCT (SD-OCT). Assuming multiple reflections or scattering processes among various structures inside the sample can be neglected, the complex spectral field strengths of the reference and measuring beam are described as follows:

$$E_{\mathrm{r},k} = E_{0,k}e^{i(\omega t - 2kz_{\mathrm{r}})}, \tag{39.4}$$

$$E_{\mathrm{m},k} = E_{0,k}\sum_{j=1}^{N} r_{\mathrm{m},j}e^{i(\omega t - 2kz_{\mathrm{m},j})}, \tag{39.5}$$

where $E_{0,k}$ denotes the spectral amplitude at wavenumber k, ω the angular frequency, z_{r} the position of the reference mirror, $z_{\mathrm{m},j}$ the position of a structure j of the measuring object with a reflection coefficient $r_{\mathrm{m},j}$ yielding a backscattered signal and N denotes the number of structures within the object. The positions z_{r} and $z_{\mathrm{m},j}$ are given as optical path lengths, i.e. they are affected by the refractive index of the materials of, e.g. optical elements or the measurement object in the beam path. For simplicity, we assume that $r_{\mathrm{m},j} = r_{\mathrm{m},j}^* = \sqrt{R_{\mathrm{m},j}}$ holds where $R_{\mathrm{m},j}$ is the reflectivity. The superposition of the electric fields given by (39.4) and (39.5) yields

$$E_k = E_{0,k}e^{i(\omega t - 2kz_{\mathrm{r}})} + \sum_{j=1}^{N} r_{\mathrm{m},j}E_{0,k}e^{i(\omega t - 2kz_{\mathrm{m},j})}. \tag{39.6}$$

The time-averaged intensity is proportional to the square of the absolute value of the electric field:

$$I_k \propto E_k E_k^* = E_{0,k}E_{0,k}^*\left(e^{-i2kz_r} + \sum_{j=1}^{N}\sqrt{R_{\mathrm{m},j}}e^{-i2kz_{\mathrm{m},j}}\right)\ldots \\ \ldots \times \left(e^{i2kz_{\mathrm{r}}} + \sum_{n=1}^{N}\sqrt{R_{\mathrm{m},n}}e^{i2kz_{\mathrm{m},n}}\right) \tag{39.7}$$

After some rearrangements, we obtain:

$$I_k(k) = I_{0,k} \left(\begin{array}{l} \left[1 + \sum_{j=1}^{N} R_{m,j}\right] + 2\sum_{j=1}^{N} \sqrt{R_{m,j}} \; cos\left(2k(z_{m,j} - z_r)\right)... \\ ... + 2\sum_{v=1}^{N} \sum_{w=1, v\neq w}^{N} \sqrt{R_{m,v}} \sqrt{R_{m,w}} \; cos\left(2k(z_{m,v} - z_{m,w})\right) \end{array} \right).$$

$$(39.8)$$

Expression (39.8) has three terms. The first term (see squared brackets in (39.8)) describes the background of the detected signal, which does not depend on the OPD. The second term is the interference term having as an argument of the cosine-function the expression $\left(2k(z_{m,j} - z_r)\right)$ depending on the OPD between the measuring arm and the reference arm. Term three is an autocorrelation term which depends on optical path differences within the measuring object.

For Spectral-domain OCT, the position of the reference mirror is kept constant, i.e. $z_r =$ const., while the signal is detected spectrally resolved. Thus, we have for the detector signal:

$$S_k(k) = \eta I_k(k, z_r = const.),$$

$$(39.9)$$

where η is the detector constant assuming a linear detector response and I_k is the spectral intensity of the interference, see relation (39.8).

Figure 39.3 shows the simplified setup with a fixed reference mirror and a spectrometer with a detector array. In the first step, we transform the measured spectrum $S_\lambda(\lambda)$ to the equivalent representation $S_k(k)$ by use of relation (39.2). The spectrum $S_k(k)$ is a function of the angular wavenumber k.

Fig. 39.3 Principle of Spectral-domain OCT. The reference mirror is fixed. The superimposed signals from reference and measurement beams are detected by a spectrometer as a function of the wavelength λ
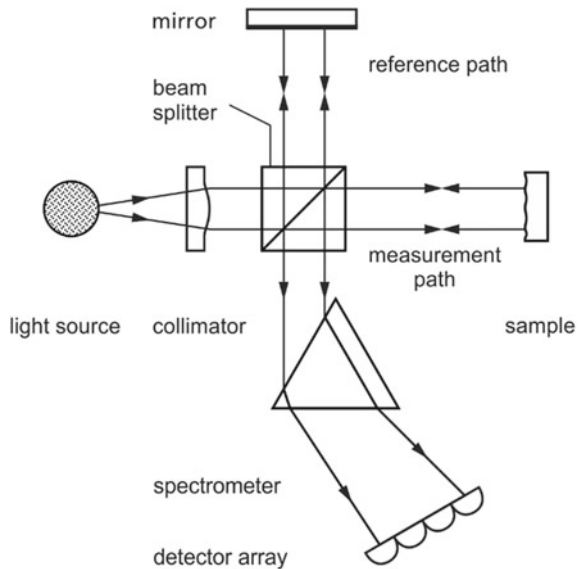
Fig. 39.4 Schematic
detector signal versus
angular wavenumber gained
with a Spectral-domain OCT.
The spectrum, e.g. has a
bell-shaped envelope with a
width corresponding to the
bandwidth of the light source
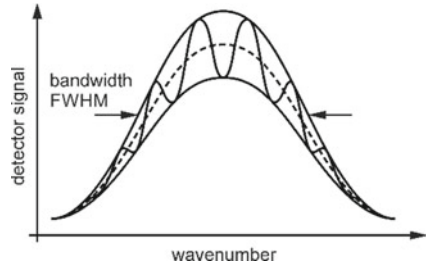
The principal characteristics of the detected spectrum are shown in Fig. 39.4. The spectrum has an envelope with bandwidth and shape equal to the bandwidth and shape of the light emitted by the source. This envelope is modulated. For a given single scattering surface of the measurement object, a simple modulation occurs as shown schematically in Fig. 39.4. The modulation contains the information about the distance to the scattering structure of the object, see Eq. (39.8).

To extract this information, the signal $S_k(k)$ is processed by an inverse Fourier transform to go from the k-space to the spatial z-space:

$$\tilde{S}(z) = \frac{1}{2\pi} \int\limits_{-\infty}^{\infty} S_k e^{ikz} \mathrm{d}k. \tag{39.10}$$

Assuming a spectrum of the light source with a Gaussian shape, Fig. 39.5 illustrates exemplarily the result of this inverse Fourier transform for a measuring object with backscattered light from two distances z_{m1} and z_{m2}. The inverse Fourier transform of the measured spectrum shows seven peaks; see Fig. 39.5, right.

The central peak is the inverse Fourier transform of the spectrum of the light source. The relation between the FWHM width of the Gaussian-shaped spectrum of the light source and the FWHM width of the inverse Fourier transform—i.e. the FWHM width of the central peak in Fig. 39.5, right—is given by
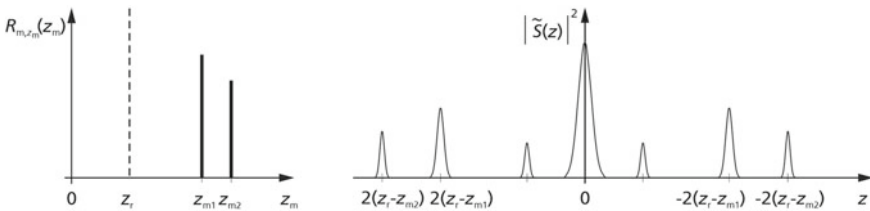
Fig. 39.5 Left: reflectivity per unit length as a function of the distance z_m. The dashed vertical line indicates the position of the reference mirror. The height of the bold bars at z_{m1} and z_{m2} illustrate different reflectivities (higher at position 1 than at position 2). Right: schematic presentation of the square of the absolute value of the inverse Fourier transform $\left|\tilde{S}(z)\right|^2$ according to (39.10)

Fig. 39.6 Spectrum of the interfering signals for a Spectral-domain OCT as a function of the angular wavenumber
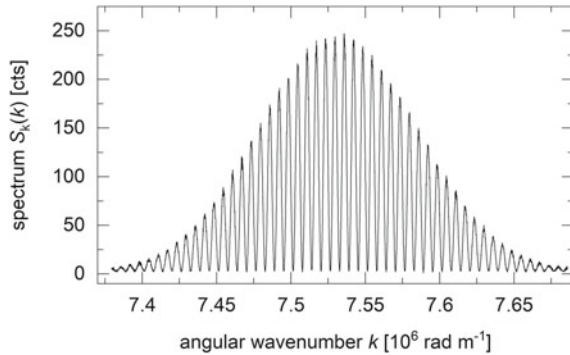
$$\Delta z_{\text{FWHM}} = 8 \ln 2 / \Delta k_{\text{FWHM}}. \tag{39.11}$$

According to relation (39.11), a broader spectrum of the light source corresponds to a narrower width of the inverse Fourier transform in the z-space. As a numerical example, let's assume a light source with a central wavelength of 860 nm and a wavelength width of 65 nm, corresponding to a wavenumber width of $\Delta k_{\text{FWHM}} = 5.52 \cdot 10^5 \text{ rad m}^{-1}$. Inserted in (39.11), we obtain $\Delta z_{\text{FWHM}} \approx 10 \, \mu\text{m}$.

The two peaks on the positive z-axis correspond to the locations where backscattering occurs, leading to OPDs of $2(z_{m1} - z_r)$ and $2(z_{m2} - z_r)$, respectively. From these two peak positions, the distances z_{m1} and z_{m2} to be measured are deduced for a given position of the reference arm z_r. The small peaks in the direct neighborhood of the central maximum are due to the autocorrelation term, see relation (39.8), last summand in the brackets (positions: $\pm 2(z_{m2}-z_{m1})$).

Figures 39.6 and 39.7 show the spectrum of the interfering signals for a single back-scattering surface in the measuring path and the corresponding inverse Fourier transform. The latter shows a distinct peak at an optical path difference of ~0.4 mm which is by orders of magnitude higher than the noise level. In the case of an open path propagation with a refractive index of 1, this value corresponds to the distance of the single backscattering surface related to the position of the reference mirror. The determination of the position of this peak yields sought-after measuring information.

39.3 OCT Sensors

Fraunhofer ILT has developed Spectral-domain OCT sensors with a fiber-optic beam guiding suited for inline measuring tasks. Instead of free beam paths in the Michelson interferometer as shown in Fig. 39.3, fiber optics are used to guide the light from the light source, to split the light into reference and measurement paths, to combine the backpropagating signals and finally to transmit the superimposed light beams to the detector. Typically, as a light source a superluminescent diode is applied. Figure 39.8 shows a schematic of such a sensor. The control unit comprises a light

Fig. 39.7 Square of the absolute value of the inverse Fourier-transformed (FT^{-1}) spectrum of Fig. 39.6 as a function of the optical path difference z related to the position of the reference mirror. For a propagation medium with refractive index equal to 1, the peak at ~0.4 mm indicates the distance to the measuring object
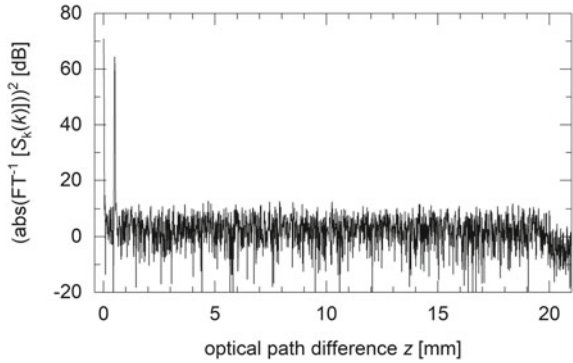
source, reference arm, spectrometer, electronics for signal processing and input/output interfaces.

The objectives of these developments are (a) large measuring ranges (8–25 mm), (b) small linearity error (< 0.003%), (c) measurements can be triggered externally, (d) easy integration of sensor(s) in different application environments with respect to spatial and temporal requirements and (e) multi-point measurement, i.e. determination of several distances at different locations. The sensor product line is called » bd-x «, where "bd" stands for bidirectional, indicating that the measuring beam propagates forth and back along the same line. Due to this feature, the measuring head is compact and the size of the optical window is reduced to a minimum. The "x" refers to the number of measuring spots, e.g. 1, 2 and 4, depending on the expansion stage of the control unit. Table 39.1 gives an overview of typical technical data achieved with these sensors.

The response time—in terms of a change of the delivered measuring value after a change of a position of the measuring object—amounts to 20 ms if the signals are processed by a personal computer or 110 µs in case of signal processing by a FPGA (field programmable gate array) integrated into the control unit. These short response times make it possible to set up real-time feedback loops for processes monitored by » bd-x « sensors.

In order to allocate geometric data gained with » bd-x « sensors to other signals of a machine or a production environment, e.g. the position of translation stages or rotational axes, the measurements can be triggered by external events (e.g. a rotary
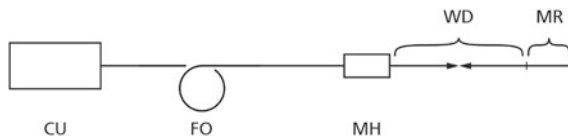
Fig. 39.8 Schematics of the Spectral-domain OCT sensor developed by Fraunhofer ILT. CU is control unit, FO fiber optics, MH measuring head, WD working distance, and MR measuring range

Table 39.1 Typical data of variants of » bd-1 « sensors from Fraunhofer ILT. MR is measuring range

Features	Data				
Central wavelength [nm]	860	835	835	1550	1064
Spectral width [nm]	65	60	60	60	20
Measuring range [mm]	4.4	13.3	20.0	23.0	18.2
Temporal repeatability at end of MR [nm]	170	50	120	120	60
Linearity error [nm]	90	200	150	300	300
Relative linearity error [%]	0.002	0.0015	0.0008	0.0013	0.0016
Measuring frequency [kHz]	70	80	80	80	80
Time constant of exposure control [ms]	10	10	< 0.1	10	10
Length of fiber optics to measuring head [m]	1 to 50				
Size of measuring head [mm]	55 x Ø18				

Table 39.2 Typical data of variants of » bd-1 « sensors from Fraunhofer ILT. PC is personal computer, FPGA field programmable gate array PC personal computer, TTL transistor-transistor logic and LVDS low voltage differential signaling

Signals	Processing unit	
	PC	FPGA
Trigger input	TTL/LVDS	TTL/LVDS
Output interfaces	analog ± 10 V	analog ± 10 V
Response time	20 ms	110 μs

encoder or a position encoder). Measuring results are provided at analog or digital interfaces. Table 39.2 shows variants of input and output signals.

Figure 39.9 shows a photo of the control unit, the fiber optics and a measuring head of a » bd-2 « system (with in total two measuring heads) to measure distances. Depending on the configuration of the sensor, working distances (distance between the last optical surface of the measuring head and the beginning of the measuring range; see Fig. 39.8) ranging typically from 30 to 300 mm are realized.

Figure 39.10 shows an opened 19-inch rack with a spectrometer to implement the SD-OCT method for » bd-x «.

The » bd-x « sensors are calibrated using ultra-precision linear stages whose positions are measured by a conventional interferometer (DIN 32877-2 2019). Figure 39.11 shows the deployed calibration setup. The precision stages are mounted on a damped optical table. The whole setup is enclosed by an acrylic glass cover to reduce the effects of refractive index variations caused by changing atmospheric conditions in the optical beam paths.

Figure 39.12 shows exemplarily the linearity error of a » bd-1 « sensor with a measuring range of 20 mm. The linearity error describes the maximum measurement

Fig. 39.9 Control unit (19-inch rack), fiber optics (yellow cables) and measuring head (black cylindric housing) of a » bd-2 « sensor. *Photo* Fraunhofer ILT

Fig. 39.10 Spectrometer of a » bd-1 « sensor

Fig. 39.11 Calibration setup for » bd-x « sensors with ultra-precision linear stages

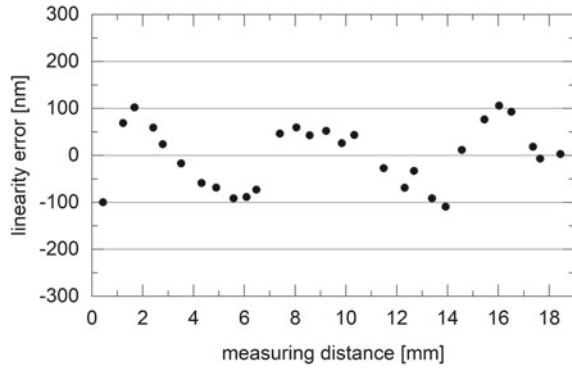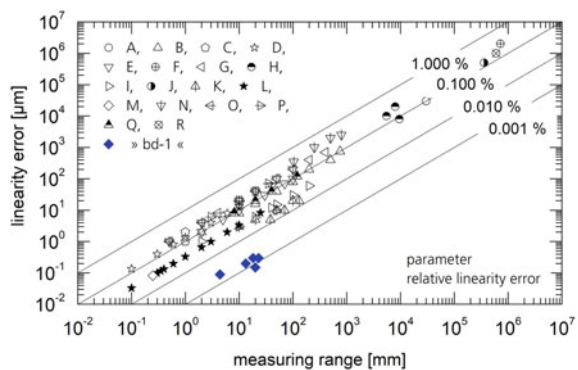**Fig. 39.12** Linearity error of a » bd-1 « sensor as a function of the measuring distance

Fig. 39.13 Linearity error as a function of the measuring range for various optical distance measuring units based on conventional triangulation sensors (A to R, Hölters 2012) and » bd-1 « sensors (blue diamond symbols)

deviation in the measuring range, whereby the influences of measurement value fluctuations are reduced by averaging (DIN 32877-2 2019). The linearity error deduced from Fig. 39.12 amounts to ~100 nm.

Figure 39.13 shows an overview of the linearity error of conventional triangulation sensors compared to those achieved for » bd-1 « sensors. For measuring ranges from 8 to 20 mm, the linearity error for distance measurements can be reduced by about an order of magnitude in relation to triangulation sensors (Hölters 2012).

39.4 Examples of Applications

An overview of the principal application fields of » bd-x « sensors is given in Fig. 39.14. Stand-off feature and fast measuring frequency enable inline measurements of geometric quantities in process and production lines. Integration in a production environment is facilitated due to the fiber-optic coupling of the measuring head and its small size.
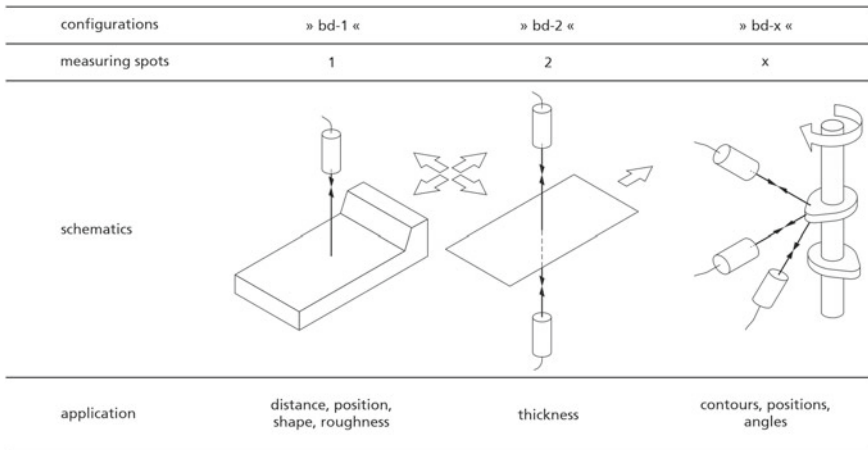
Fig. 39.14 Overview of application fields of » bd-x « sensors. x number of sensor heads

With one measuring head (column » bd-1 «), the distance to an object is measured if the object is, e.g. a metallic workpiece. In this case, the measuring radiation does not penetrate into the measuring object but is backscattered at the surface. If the object is translucent as, e.g. an organic material, then the irradiated light propagates into the substance and is backscattered by internal structures of the object linked with variations of its refractive index (see Fig. 39.1). In this case, a series of distance information is gained originating from the surface as well as from the internal structures (A-scan; see Fig. 39.2). By a relative movement between measuring head and object, raster scans can be performed to measure surface contours or micro-topographies of objects (shape, roughness) or to gain B- and C-scans in case of translucent objects.

Two measuring heads (column » bd-2 «) can be arranged at opposite sides of a sheet passing through to measure the thickness of this object. The control unit synchronizes the measuring cycle and time in order to assure that the determined distances are allocated precisely to the respective positions of the moving sheet. Up to sixteen measuring heads can be controlled to register simultaneously 16 distances at various parts of a measuring object. In the last column of Fig. 39.14, an example of three measuring heads is shown to acquire various geometric features of a rotating cam shaft.

Scanning a measuring head of » bd-1 « across a surface yields the microtopography of that surface which can be correlated to its roughness. Figure 39.15 shows a set of reference samples with different surface roughness values *Ra* describing the arithmetical mean deviation of the assessed profile.

Figure 39.16 gives the results of comparative measurements of the surface roughness value *Ra* using two different conventional contact profilometers and results gained with » bd-1 «. Within the roughness range from 0.1 to 10 μm, deviations to the reference value are of the same order as for the conventional contact profilometers. However, the advantage of » bd-1 « is the contactless measurement, which does

Fig. 39.15 Set of roughness standards with various levels of the arithmetical mean deviation *Ra*
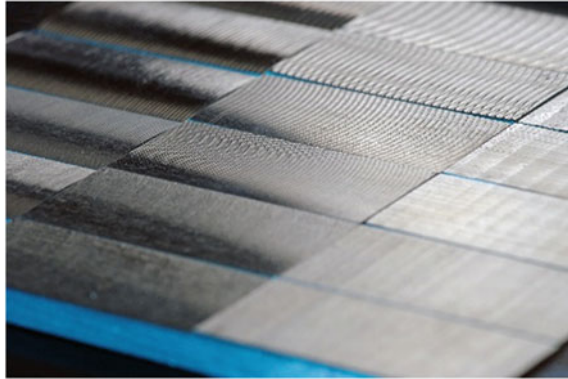
not damage the surface of the measuring object and due to the stand-off measurement can be easily integrated into a production line to monitor the surface roughness of processed goods.

With a fixed position of the measuring head directed to the outer rim of a rotating spindle, very precise roundness measurements can be conducted. Figure 39.17 shows the setup with the measuring head of » bd-1 « targeting onto a spindle of an ultra-precision CNC (computerized numerical control) lathe (Nanoform 250 Ultra, Precitech Inc.; spindle diameter Ø 200 mm) rotating with 5000 rpm resulting in a surface speed of the spindle of 3000 m/min.

Figure 39.18 shows the results of the roundness measurements averaging over 250 revolutions, deploying a measuring frequency of 50 kHz. The polar diagram shows deviations from an ideal circular shape in the range of $\pm$ 30 nm.

The capability of » bd-1 « for inline process monitoring is validated with the setup shown in Fig. 39.19. A lance is deployed to conduct laser material deposition (LMD) inside of tubes. The lance has a length of 800 mm in which a processing laser beam with a radiant flux of ~1 kW is guided to the tip (on the left in Fig. 39.19). At the tip, the laser beam is deflected by 90°, exits the lance in the radial direction and is focused onto a workpiece. Parallel to the processing laser beam, the measuring

Fig. 39.16 Comparative measurements of the surface roughness *Ra*—arithmetical mean deviation—with conventional contact profilometers and » bd-1 «
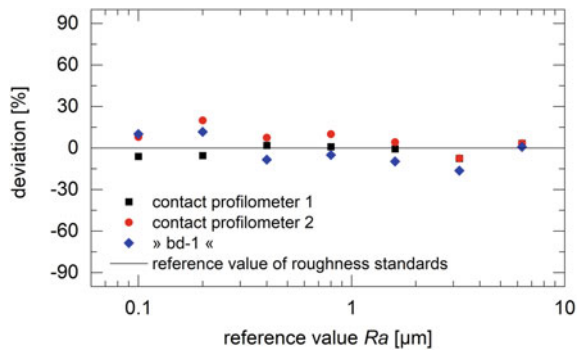
Fig. 39.17 Measuring head of » bd-1 « directing the measuring beam onto the outer rim of a rotating spindle of an ultra-precision lathe
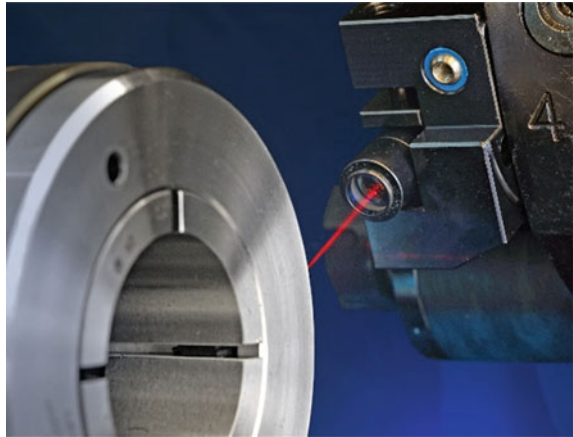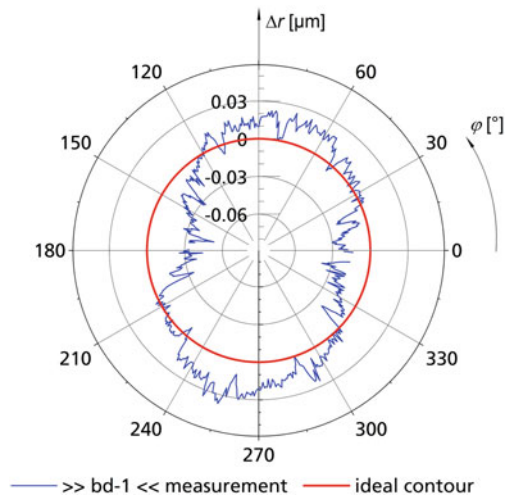

Fig. 39.18 Polar diagram of the roundness deviation Δr in μm (blue) as a function of the rotation angle φ; the red curve shows an idealized circular contour

beam of » bd-1 « is guided toward the processing spot. A test workpiece is placed in the processing area onto which several tracks have been applied by LMD (powder Nistelle C-276).

Figure 39.20 shows an end-on view of the lance during the LMD process on a test workpiece (screenshot of a process video).

A set of tracks with increasing heights were generated. Figure 39.21 shows the measuring results gained with » bd-1 « while moving the measuring beam perpendicularly across the generated LMD tracks. The baseline shows a small inclination of the substrate plate. Peak heights given in the figure refer to their respective height above the local surface position.
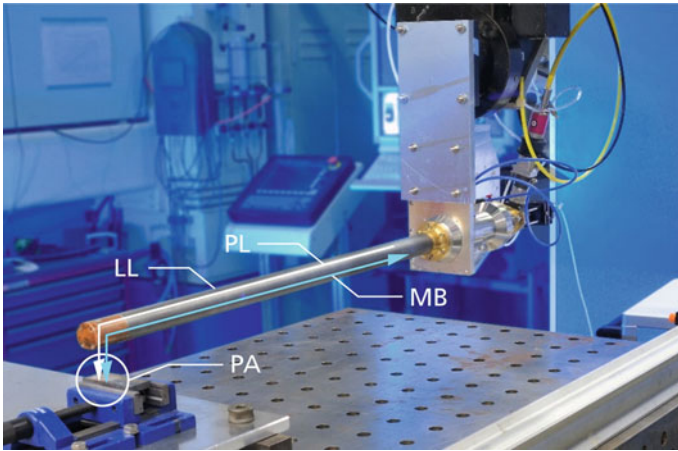
Fig. 39.19 Setup for inline monitoring of LMD processing with » bd-1 «. LL is lance for LMD inside tubes, PL processing laser beam, MB measuring beam, and PA process area

Fig. 39.20 End-on view on the lance (see LL in Fig. 39.19) during LMD process on a test workpiece
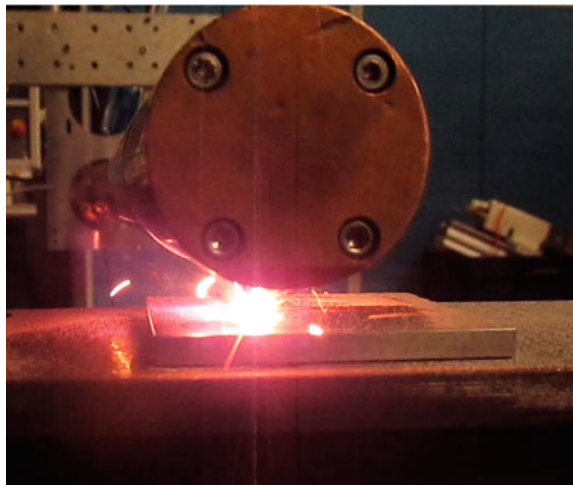
A cross-section polish of the generated workpiece with conventionally measured track heights is shown in Fig. 39.22. The results confirm the values obtained during the measurement with maximum deviations in the order of 70 μm.

Multilayer polymer films are deployed as packaging materials offering mechanical stability, protection against UV irradiation and diffusion barriers for water, oxygen, carbon dioxide and nitrogen. Figure 39.23 illustrates exemplarily such a packaging foil with an internal structure consisting of three layers. If the material is sufficiently translucent, then these three thicknesses can be monitored by SD-OCT. A blown film line equipped with an inline monitoring system based on SD-OCT (MS) is shown in
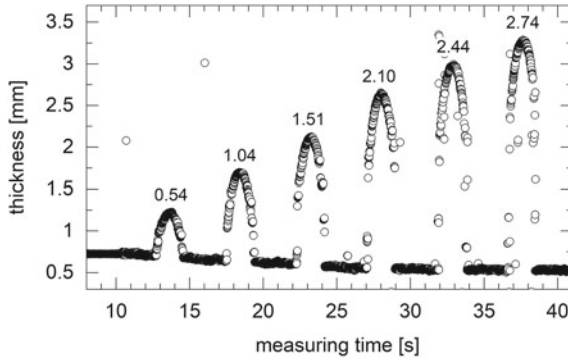
Fig. 39.21 Inline measured thicknesses of LMD-generated tracks on a workpiece. Numbers given at the peaks show the height of the respective peak in mm above the surface of substrate plate
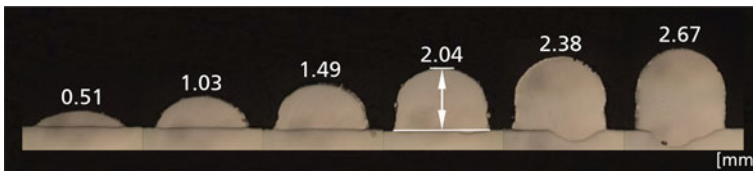

Fig. 39.22 Cross-section polish of generated workpiece; cf. Fig. 39.21 and see text

Fig. 39.24. The arrow indicates the direction of movement of the monitoring system mounted at a carousel rotating around the blown film tube. By this, the thicknesses of multilayer films are measured as a function of the azimuth angle, see Fig. 39.25.

The main application field of » bd-2 « are inline thickness measurements of metal sheets (Noll et al. 2013). The thickness measurement system » bd-2 « consists of two interferometric sensors and a C-frame; see Fig. 39.26. The sensors measure the metal sheet passing through to determine the exact thickness.

In contrast to radiometric methods, the real geometric thickness of the product is measured and not an indirect value, which has to be converted on the basis of the material composition. The contactless measuring process is suited especially for fast inline measurements of moving objects. The measuring heads are fixed in a stable manner at the C-frame and equipped with minimal-sized optical windows. Data

Fig. 39.23 Multilayer polymer film consisting of three layers with the thicknesses L_1, L_2 and L_3
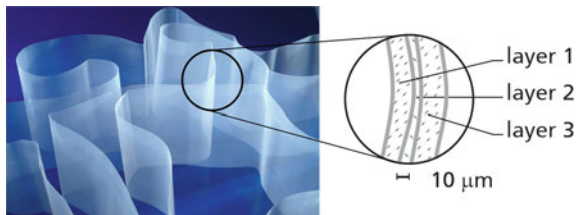
Fig. 39.24 Blown film line with an extruded multilayer film being transported upwards in vertical direction. MS inline monitoring system based on SD-OCT to measure the multilayer thicknesses
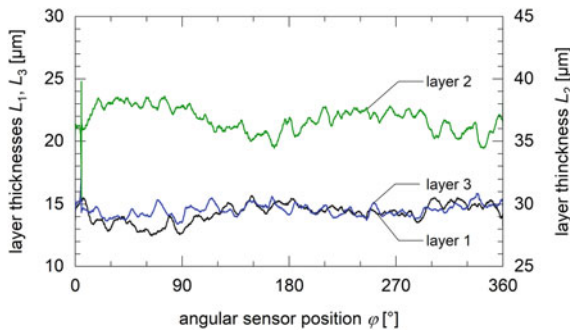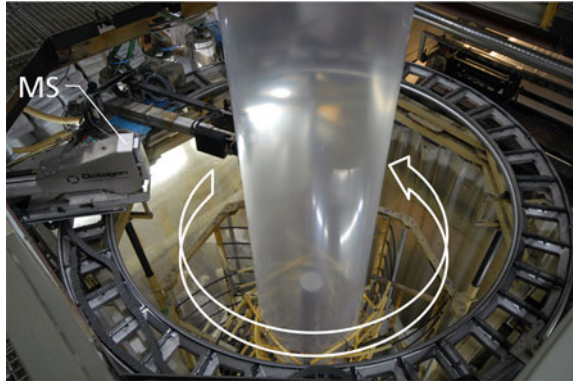

Fig. 39.25 Inline measured single-layer thicknesses (L_1, L_2, L_3) at a blown film line producing a three-layer film as a function of the angular sensor position
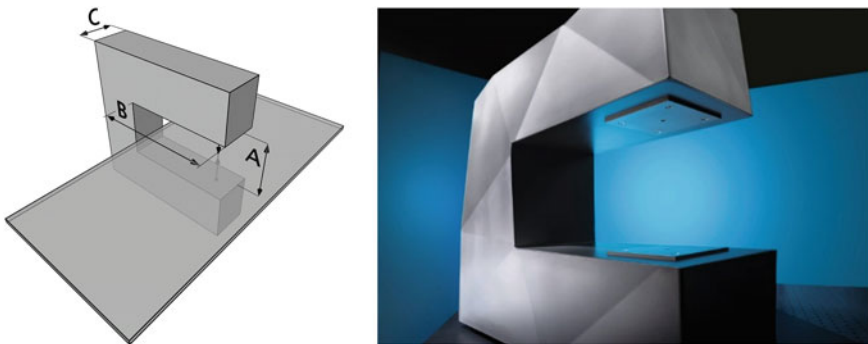

Fig. 39.26 Thickness measurement with two measuring heads mounted in a C-frame (» bd-2 «). Left: Geometry of C-frame with A: free gap; B: depth of C-frame; C: extension of C-frame and an exemplary sheet to be measured passing through the C-frame. Right: C-frame with stainless steel housing. Photo: Fraunhofer ILT, Aachen

transfer is accomplished in a purely optical way via fiber optics from the C-frame to a separate control unit. The optical access withstands even the strongest loads. The application range covers thickness measurements of, e.g. rolled sheets, cold rolled strip, metal foils and dark to polished surfaces made from different materials (steel, aluminum, copper, …). Table 39.3 summarizes typical data of the thickness measuring system.

Figure 39.27 shows the correctness of thickness measurements based on » bd-2 «. As reference values, a set of thirteen certified gauge blocks were used and these were positioned at extreme positions inside the thickness measuring range. Each data point and the respective error bars refer to the average thickness deviation for three identically constructed thickness measuring systems and the standard deviation. The maximum deviation for a 12 mm range of thicknesses is ≤ 500 nm.

Figure 39.28 shows exemplarily results of thickness measurements at a steel sheet in a roller stand moving with a speed of 30 m/min to test the repeatability. Deviations among repetitive measurements are $< 1\,\mu$m.

Multiple measuring heads—as illustrated in the last column in Fig. 39.14—are suited to inspect the geometrical properties of shafts, i.e. camshafts, drive shafts and crankshafts, with sub-micrometer precision (Noll and Kämmerling 2015). Due to the compact and lightweight design of » bd-1 «, these sensors are especially suited for operation in high-precision cylindrical coordinate measuring gauges (CCMM) for cam shafts. This sensor measures all types of surfaces such as bright, ground and rough surfaces. In contrast to laser triangulation sensors, » bd-1 « is suited to measure shape and position tolerances of rotating shafts and additionally the surface roughness (cf. Figure 39.16). Moreover, boreholes and notches with high aspect ratios can be measured. Further inspection tasks are roundness and distance measurements in CNC machine tools, with the option of simultaneous roughness measurements.

Table 39.3 Typical data of a thickness measurement system based on » bd-2 « sensors

Features	Data
Thickness measurement range	13 mm
Thickness uncertainty (thickness gauge)	$< 0.8\,\mu$m
Temporal repeatability	< 25 nm
Exposure time	down to $1.2\,\mu$s
Measuring frequency	80 kHz
Dynamics	~60 dB
Length of optical fiber connection from control unit to measuring head	up to 50 m
Size of control unit	$600 \times 520 \times 420$ mm^3
C-frame A	180 mm
B	280 mm
C	200 mm
Size	$540 \times 680 \times 200$ mm^3

Fig. 39.27 Thickness
deviation for » bd-2 « as a
function of the reference
thickness of gauge blocks
positioned at different
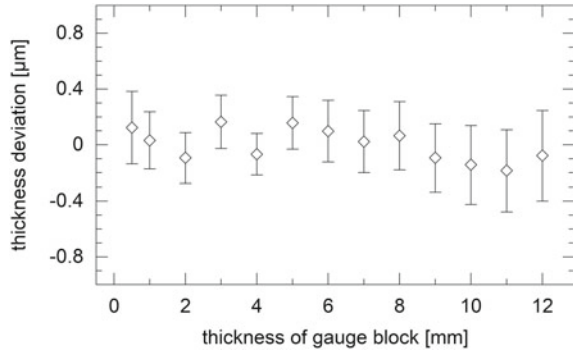locations inside the thickness
measuring range

Fig. 39.28 Three repetitive
measurements of the
thickness of a moving steel
sheet versus the sheet
position measured with
» bd-2 «. For clarity of
presentation, +2 µm were
added to the results of the
second measurement (2.),
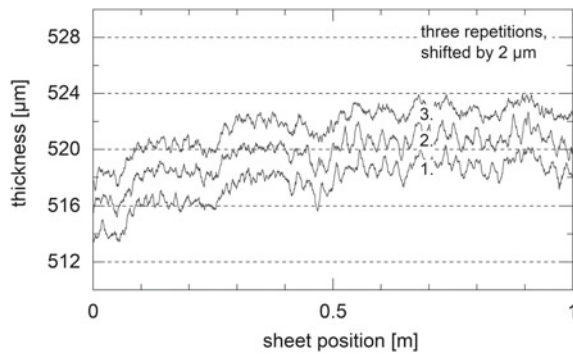and +4 µm to the results of
the third measurement (3.)

Figure 39.29 shows an inspection machine where the shaft to be measured is fixed axially and rotated during the measuring sequence.

Figure 39.30 shows the measured contour of a cam in a polar diagram. Two repetitive measurements were executed. In the scale used for that diagram, the contours of these two measurements are completely overlapping (differences are smaller than 95 nm). Figure 39.31 shows the results of a comparative contour measurement of a cam section made with » bd-1 « and a conventional tactile inspection machine with a higher spatial resolution.

The standard deviation of the difference between the shown two contour curves (each measured for one-time only) amounts to $s = 260$ nm. Measuring results are consistent and show the high precision achieved with » bd-1 «.

For bone surgery with lasers, an essential monitoring information is to detect inline the residual thickness of the hard tissue in order to stop the laser ablation in time prior to cutting through (Tulea et al. 2015). Figure 39.32, top, shows a prepared bone sample (substantia compacta from an animal thigh; preparation by milling) with stepwise increasing thicknesses. The first four steps have the following thicknesses (from left to right in Fig. 39.32, top): 0.18 mm, 0.27 mm, 0.44 mm and 0.8 mm. Figure 39.32, bottom, shows a B-scan taken with an OCT sensor operating at 905 nm. The measuring beam running parallel to the z-axis scans in the x-direction
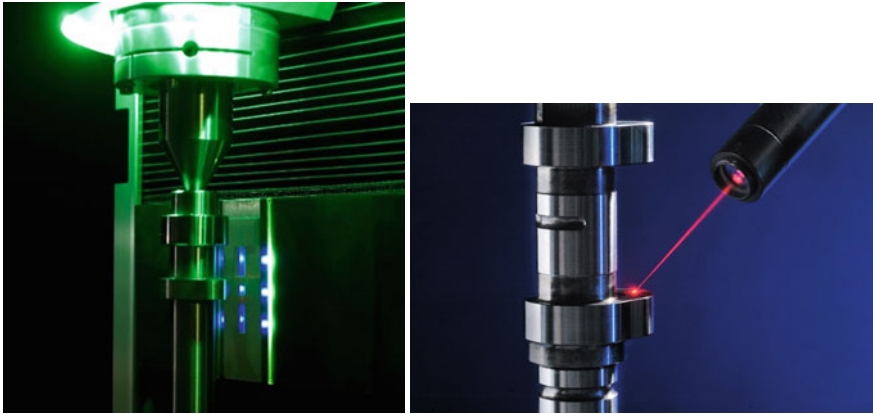
Fig. 39.29 Left: Inspection machine for shafts. Right: Detailed view with a » bd-1 « sensor directed to a cam mounted at the shaft

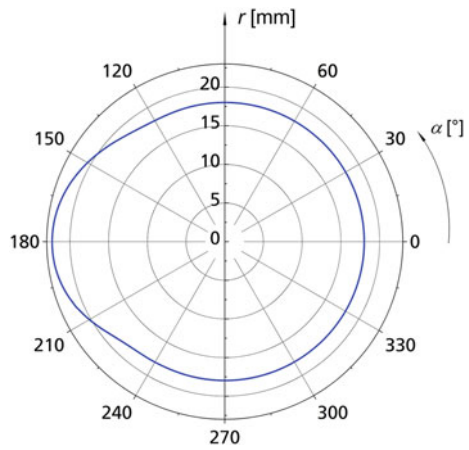**Fig. 39.30** Polar diagram of the measured contour $r = r(\alpha)$ of a cam

Fig. 39.31 Comparative measurement of the contour of a cam with » bd-1 « and a conventional tactile inspection machine for shafts
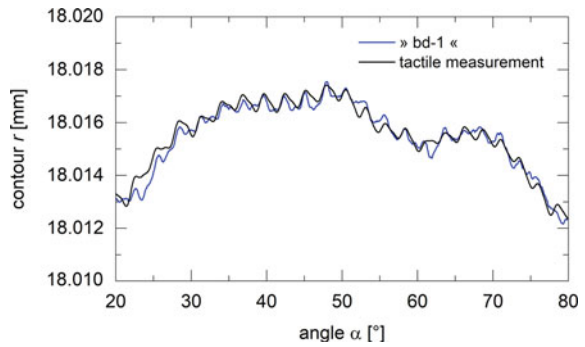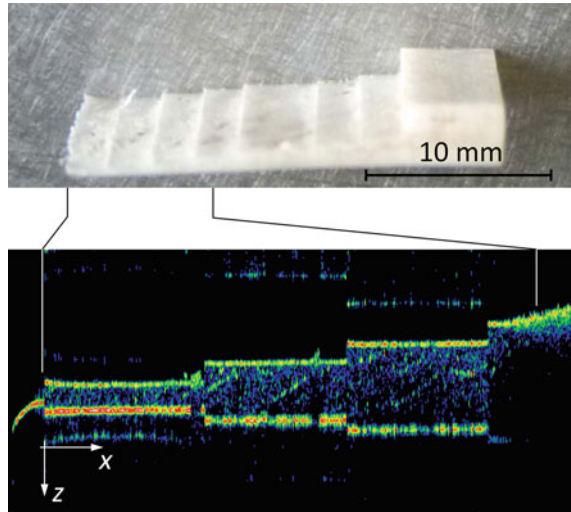
Fig. 39.32 Top: Prepared bone sample with stepwise increasing thicknesses. Bottom: B-scan with OCT sensor. *x* scan direction of OCT measuring beam, *z* propagation direction of OCT measuring beam

across the sample. The B-scan demonstrates the capability to measure both sides of a hard tissue artifact up to a thickness of 0.44 mm. For the thickness step of 0.8 mm, only the upper surface of the bone is detected whereas the signal from the backside is very low and barely visible (Fig. 39.32, bottom right).

The thickness measured with the OCT sensor is always greater than the actual geometric thickness due to the refractive index of the translucent material. For the bone sample shown in Fig. 39.32, the refractive index amounts to $n \approx 1.5$.

Another tomographic OCT application is the inline monitoring of the welding depth during laser drilling, laser welding or laser powder bed fusion (Webster et al. 2011, Kanko et al. 2016). Figure 39.33 shows a setup with a coaxial superposition of the measuring beam of » bd-1 « and the high-power laser beam of a fiber laser (1030 nm). Both beams are focused by a lens with a focal length of 200 mm. Figure 39.34 shows the results of the OCT measurements superimposed with a cross-section polish of the workpiece. The following experimental parameters were used: speed of laser processing head in relation to the stationary workpiece is 14 m/min; variation of radiant flux of fiber laser: 0.5–6 kW; inert gas flow: argon; workpiece material: high-alloy steel 1.4301; measuring frequency 70 kHz.

Figure 39.34 shows an overlay of the inline measured welding depths (blue data points) with a cross-section polish of the sample. For this experiment, the laser radiant flux was increased monotonously from 0.5 kW (start at $s \approx 39$ mm in Fig. 39.34; first a remelting can be seen; at $s \approx 36$ mm keyhole formation sets in) up to 6 kW (at $s \approx 3.5$ mm). On average, 30 to 60 depth values are measured per millimeter. The measured depths are consistent with the depth contour of the welding seam visible from the texture difference in the microscopic image of the cross-section polish.

Future developments of OCT sensors strive for further enhancements of measuring uncertainties, measuring frequencies and signal-to-noise ratios to cope with the demands of inline measuring applications. New wavelength regions will be accessed

Fig. 39.33 Setup for inline monitoring of welding depth during laser welding. The measuring beam of » bd-1 « is guided coaxially to the processing laser beam from a fiber laser. MH is measuring head, FO fiber optics, L lens, BS beam splitter, FL fiber laser, WP workpiece and *s* translation coordinate
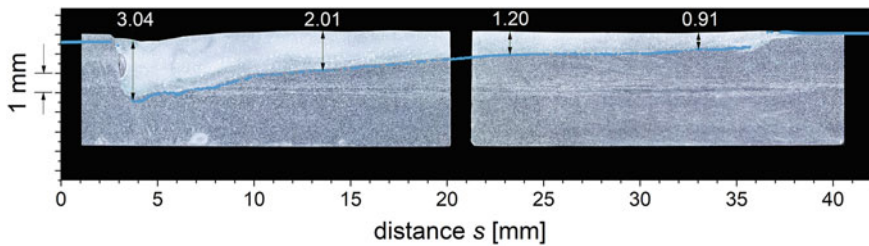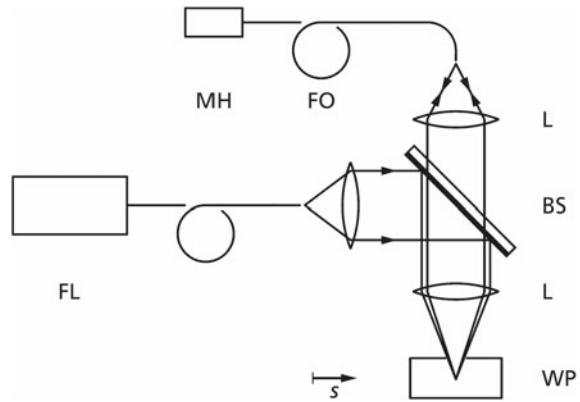

Fig. 39.34 Inline measured welding depth (blue data points) overlayed with a cross-section polish of the sample. Numbers given at the top refer to local welding depth values in mm

via entangled photon sources which will offer interaction with measuring objects in the mid-infrared region with a wavelength of 2 to 10 μm (Okano et al. 2015; Vanselow et al. 2020). The capability of OCT to monitor laser material processing inline by coaxial guidance of measuring and processing beams constitutes a key advantage. Promising future application fields are, e.g. the inline monitoring of laser powder bed fusion (LPBF) to detect local irregularities and thus enable fast feedback loops for optimized process control and corrective actions (Noll and Kämmerling 2020).

References

Bouma B, Tearney G (eds) (2002) Handbook of Optical Coherence Tomography. M. Dekker Inc.

Cobbold R (2007) Foundations of biomedical ultrasound. Oxford University Press Inc., New York

Donges A, Noll R (2015) Laser Measurement Technology—Fundamentals and Applications. Springer-Verlag, Heidelberg, ISBN 978–3–662–43633–2, Chapt. 9

DIN 32877-2, Geometrical product specification (GPS)—Optoelectronic measurement of length—Part 2: Design characteristics and metrological characteristics for backward scattering measuring principles, Deutsche Norm, December 2019

Drexler W, Fujimoto J (eds) (2008) Optical Coherence Tomography. Springer

Hölters S (2012) Optische Kohärenztomographie zur Einzelschichtdickenmessung von Kunststoff-folien, Dissertation, RWTH Aachen University

Kanko J, Sibley A, Fraser J (2016) In situ morphology-based defect detection of selective laser melting through inline coherent imaging. J Materials Proc Techn. 231:488–500

Noll R, Hölters S, Kämmerling J, Lenenbach A (2013) Laserabstandssensoren messen die Dicke von Walzbändern. Qualität und Zuverlässigkeit 58(2013)10, 44–47

Noll R, Kämmerling J (2015) Verfahren und Vorrichtung zur hochgenauen optischen Messung an Objekten mit anhaftenden fluidischen Schichten, Patent DE 10 2015 202 470, 1.8.2018

Noll R, Kämmerling J (2020) Method and device for the additive manufacture of components, Patent EP 3 463 811 B1, 12.8.2020

Okano M, Lim H, Okamoto R, Nishizawa N, Kurimura S, Takeuchi S (2015) 0.54 μm resolution two-photon interference with dispersion cancellation for quantum optical coherence tomography, Scientic Rep., 5:18042, https://doi.org/10.1038/srep18042

Tulea C, Caron J, Gehlich N, Lenenbach A, Noll R, Loosen P (2015) Laser cutting of bone tissue under bulk water with a pulsed ps-laser at 532 nm, J of Bioanal Optics 20(2015)105007–1, -9

Vanselow A, Kaufmann P, Zorin I, Heise B, Chrzanowski H, Ramelow S (2020) Frequency domain optical coherence tomography with undetected mid-infrared photons. Optica 7:1729–1736

Webster P, Wright L, Mortimer K, Leung B, Yu J, Fraser J (2011) Automatic real-time guidance of laser machining with inline coherent imaging, J of Laser Appl. 23(2011)022001–1, -6

Chapter 40
Laser-Induced Breakdown Spectroscopy

Cord Fricke-Begemann, Volker Sturm, and Reinhard Noll

40.1 Introduction

The chemical composition of a substance is an essential property for many tasks in process control and quality assurance in industrial production and environmental engineering. Conventional methods for chemical analysis normally comprise the following steps:

1. taking samples of the substance or removal of a workpiece from the production line,
2. transportation to analyzing system or laboratory,
3. preparation for chemical analysis,
4. separation of species (optional), and
5. determination of the composition.

The first two steps are necessary for conventional analysis because the analyzing systems are normally not installed directly in or at a production site. The third step turns the sample into a physical–chemical state required for the respective method. Step 4 is a separation process like dissolving in an acid to obtain the insolvable fraction. Laser-based methods—such as Laser-Induced Breakdown Spectroscopy (LIBS) (Noll 2012)—are predestined for chemical inline analysis and allow simplifying or superseding Steps 1 to 4. The terminus *inline analysis* refers to the application scenario where the laser measuring unit is installed *in* a production line or *in* a processing environment and analyzes the measuring objects in their present physical state (solid, liquid, gaseous, temperature, and state of movement) without taking them away from their route.

Figure 40.1 shows schematically a LIBS system for inline process monitoring embedded in an exemplary production chain. Fast direct chemical analysis of an

C. Fricke-Begemann · V. Sturm · R. Noll (✉)
Fraunhofer ILT, Aachen, Germany
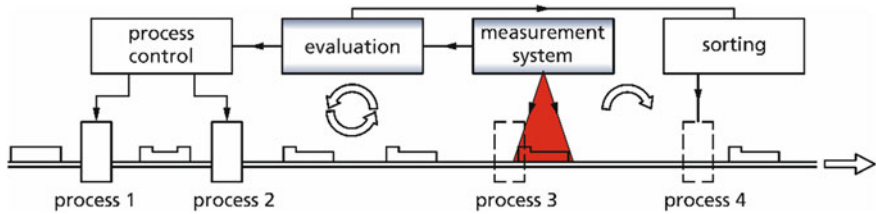e-mail: noll.reinhard@arcor.de

Fig. 40.1 LIBS system for inline chemical analyses embedded in a schematic production chain

object in or close to a processing line allows for efficient feedback actions for preceding process steps or a real-time decision taken for subsequent classification or sorting actions of the product.

Automated spectral analyses allow the determination of several tenths of elements in a fraction of a second. Limits of detection down to μg/g (parts per million) can be reached while measuring a few micrograms of the tested material. The measurements can be conducted at various measuring distances from centimeters to meters, under different atmospheric conditions, or even in closed containers where access to the measuring object is provided via optical windows. Both, the laser beam and the radiation to be measured can be guided through the same optical window or via fiber optics. Over the last decades, various areas of applications for LIBS were studied and industrial applications were realized (Noll et al. 2014a, 2018):

- material analysis and mix-up examination (Mönch et al. 2000; Noll et al. 2001; Vrenegor et al. 2006; Sturm et al. 2017; Gaft et al. 2014),
- slag analysis (Kraushaar et al. 2003; Sturm et al. 2008; Sturm et al. 2014),
- molten metal analysis (Peter et al. 2003; Hudson et al. 2016; Sun et al. 2015; Sun et al. 2018; https://tecnar.com/galvalibs-2-0/),
- high-speed identification of polymers and metals for material-specific recycling (Sattmann et al. 1998; Stepputat and Noll 2003; Liu et al. 2019; Werheit et al. 2011),
- classification of technical glasses (Rodriguez-Celis et al. 2008; Teklemariam and Gotera 2019),
- analysis of nuclear materials (Martin et al. 2012),
- analysis of aerosols (Hahn and Lunden 2000; Caranza et al. 2001; Panne et al. 2001),
- microanalysis of inclusions in metallic matrices (Bette and Noll 2004; Bette et al. 2005; Boué-Bigne 2007; Boué-Bigne 2008),
- thickness measurement of coatings and monitoring of depth profiles (Balzer et al. 2005; Balzer et al. 2006), and
- stand-off detection of materials (Sallé et al. 2007).

Optical emission spectroscopy (OES) allows in principle the identification and quantitative analysis of all elements of the periodic table. Conventional excitation sources for OES, like spark discharge (SD), show disadvantages with respect to the analysis of non-conducting materials, materials covered by oxide layers, or their

capability for automated inline inspection tasks. Generally, SD-OES requires a preparation or a finishing treatment of the workpiece. With LIBS on the other hand, the laser beam itself can carry out a local preparation of the measuring object. For example, pulsed laser radiation is able to ablate oxide or scale layers before the underlying material is analyzed. Another advantage is the variable measurement distance between the laser source and the measuring object, which can reach from a few centimeters up to several meters. LIBS allows analysis of conductive as well as insulating materials in any state of aggregation.

40.2 Principle of Laser-Induced Breakdown Spectroscopy

40.2.1 Evaporation and Plasma Ignition

For Laser-Induced Breakdown Spectroscopy material is vaporized and excited to emit radiation. To get effective emission, the measuring object is locally heated up to its boiling or decomposition temperature by a focused pulsed laser beam. A part of the irradiated pulse energy is absorbed by the target material. Thereby, the heat conduction of the sample influences the level of heating. It dissipates the absorbed energy out of the radiated zone (Donges and Noll 2015).

Important parameters influencing the interaction between a laser beam and a solid target material (for simplicity, we assume a plane semi-infinite body where the incident laser beam direction is aligned parallel to the surface normal) are.

- beam diameter on the surface of sample $2w$,
- optical penetration depth δ_{opt}, and
- heat penetration depth δ_h.

The optical penetration depth equals the distance inside the measuring object, within which the irradiance of the laser beam drops down to approximately 37% of its value at the surface. This depth depends on the absorption characteristics of the material. For metals and laser wavelengths in the visible and near-infrared, δ_{opt} typically amounts to 10^{-6} cm–10^{-5} cm. The heat penetration depth describes how far the heat propagates into the material after the start of the irradiation. The heat penetration depth as a function of time can be estimated by Carslaw and Jaeger (1959):

$$\delta_h = 2\sqrt{\kappa t}, \tag{40.1}$$

where κ is the thermal diffusivity.

The heat equation describes the heating of the irradiated material. Analytical solutions can be given for specific cases. In the following, we consider surface and volume absorption:

(a) surface absorption ($\delta_{opt} << \delta_h$).

The optical penetration depth is significantly smaller than the heat penetration depth. This applies, e.g., for steel at radiation times $t > 10^{-9}$ s ($\kappa_{steel} = 0.04$ cm^2/s). In the heat equation, the source term is described as the surface source. In this case, the temperature as a function of time assuming a Gaussian intensity profile on the sample surface at the center of the beam is:

$$T(t) = \frac{A I_0 w}{\sqrt{2\pi\kappa\rho c}} \arctan \frac{\sqrt{8\kappa t}}{w}, \tag{40.2}$$

with A being absorption coefficient, I_0 irradiance of the laser beam at its center at $r = 0$, T temperature on the sample surface at the center of the laser beam, κ thermal diffusivity, ρ density, c specific heat capacity, t time, and w beam radius.

As an example, it is possible with the help of Eq. (40.2) to determine the time, after which the temperature on the surface of the measuring object reaches the boiling point, and therefore enhanced vaporization takes place for a given absorbed laser irradiance. The absorbed irradiance required for vaporization decreases with the increasing time of irradiation. The laser irradiance on the target surface has to be chosen higher according to the absorption coefficient to reach the vaporization threshold. Typical absorption coefficients for steel and aluminum are 0.03 to 0.1. For Q-switched lasers with pulse durations between 10 and 100 ns irradiances greater than 10^7 W/cm^2 are necessary.

(b) volume absorption ($\delta_{opt} >> \delta_h$).

The optical penetration depth is significantly greater than the heat penetration depth. This case holds, e.g., for polymer materials. The optical penetration depth is approximately 3.5 mm for polymers like polyamide at the wavelength of Nd:YAG lasers. With a thermal diffusivity of $\kappa_{polyamide} = 1.3 \cdot 10^{-3}$ cm^2/s, the optical penetration depth is greater than the heat penetration depth calculated with Eq. (40.1) for times $t < 20$ s. If heat conduction can be ignored, the increase in temperature can be calculated directly from the locally absorbed laser irradiance. The decrease of the laser irradiance inside the absorbing medium is given by:

$$I(z) = (1 - R) I_0 \exp(-z/\delta_{opt}), \tag{40.3}$$

with R being reflectivity, I_0 laser irradiance at the object surface, z coordinate in propagation direction of the laser beam, and $z = 0$ mm is the sample surface.

The factor $(1-R)$ in Eq. (40.3) describes the part of the incident irradiance that enters the measuring object. Contrary to case (a), the surface absorption cannot be taken as absorption A because the absorption is not limited to the sample surface. The absorbed energy per unit volume after the time t is

$$-(\mathrm{d}I/\mathrm{d}z)t = (1 - R)I_0/\delta_{\mathrm{opt}} \exp(-z/\delta_{\mathrm{opt}})t. \tag{40.4}$$

The absorbed energy causes the temperature of the unit volume to rise by the temperature difference ΔT, described by

$$\Delta q = \rho c \Delta T, \tag{40.5}$$

with Δq being heat energy per unit volume, ρ density, c specific heat capacity, and ΔT temperature rise. Based on $-(\mathrm{d}I/\mathrm{d}z)t = \Delta q$, the following equation results from (40.4), (40.5) for the surface ($z = 0$ mm):

$$(1 - R)I_0 = \rho c \Delta T \delta_{\mathrm{opt}}/t. \tag{40.6}$$

If ΔT equals the temperature difference from the initial evaporation or decomposition temperature of the polymer material, the necessary irradiance can be calculated as a function of time of irradiation using Eq. (40.6).

40.2.2   Evaporated Mass of Material

To estimate the amount of material vaporized by a laser pulse, we use a simplified energy balance. We assume that the absorbed laser energy is transferred completely into the evaporation process:

$$A W_{\mathrm{L}} = \rho V (\varepsilon_V + c \Delta T), \tag{40.7}$$

with A being absorption coefficient, W_{L} incident energy of a laser pulse, ρ density, V ablated volume, ε_V evaporization enthalpy, c specific heat capacity, and ΔT temperature difference between room and boiling temperatures.

Equation (40.7) does not consider losses caused by heat conduction and radiation, melt expulsion, and re-condensation of vaporized material. Additionally, for further simplification, we have ignored that the parameters A, ρ, and c are not constant during heating and vaporization. The parameters are taken as constant at their initial values. For example, the approximated amount of material removed from a steel sample by a laser pulse with $A W_{Laser} = 10$ mJ estimated with (40.7) is $\rho V = 1.6 \cdot 10^{-6}$ g ($\varepsilon_V = 6 \cdot 10^3$ J/g, $c = 0.51$ J/(gK), $\Delta T = 2{,}600$ K).

The density of the resulting vapor can be rated with the help of the Clausius-Clapeyron relation. For orientation only, typical vapor densities are between 10^{18} and 10^{20} cm^{-3}, and for absorbed irradiances between 10^6 and 10^7 W/cm^2. Because of the high temperature of the vapor, free electrons exist, which can take energy out of the radiation field and transfer it to the vapor's atoms by collision processes. Collisions between electrons and atoms are the reason why electrons take energy out of the oscillating electric field of the laser beam. Without the collisions, electrons would absorb and emit energy periodically and therefore would not gain energy on

average. The electrons reach high average energy levels, which are sufficient to ionize a fraction of the vapor's atoms. This generates a plasma—a physical state determined by the collective effect of ions and electrons. Inside the plasma, atoms and ions are excited and emit radiation.

With the help of balance equations for particle densities, momentums, and energies, the state of the plasma can be described. Model calculations show that within a few nanoseconds after the beginning of the laser irradiation, the electrons reach energies between 0.25 and 1 eV. The electron density rises to values between 10^{16} and 10^{18} cm^{-3} because of impact ionization processes. The plasma temperature typically is between 5,000 and 20,000 K.

40.2.3 Method Description

Laser-Induced Breakdown Spectroscopy is a method for elemental analysis, which is based on the detection of spectral lines emitted by transitions of atoms and ions between outer electron orbits. For this, a high-energy laser beam is focused on a solid, liquid, or gaseous object. In doing so, a fast local energy transfer is realized. In the focal area, material is atomized and the atoms are excited. The relaxation of the excited atoms causes characteristic emissions of these elements. Spectrally resolved detection of the emitted line radiation allows determining the quantitative composition of the sample. The spectral signal intensities are a measure of the concentrations of the analytes.

Figure 40.2 illustrates schematically this method in eight phases. The laser beam is focused on the sample (phase (1)). The material heats up locally, because of its natural absorption, and with sufficiently high laser irradiance, a fraction of the sample is vaporized (phases (2), (3)). The vaporized material partly absorbs the laser beam. The vapor reaches higher temperatures, and a part of the atoms are excited to higher energy states. Partly, the energy is even high enough to ionize some atoms. The system of neutral particles, ions, and electrons is called a plasma (phase (4)).

The excited atoms or ions inside the laser-induced plasma transfer their excitation energy—among others—by the process of spontaneous emission. The frequency spectrum of this emission is characteristic of the composition of the analyzed material (phases (5)–(7)). The radiation is detected and evaluated.

Later on, the plasma decays and—because of the vaporized material—a crater is formed in a solid sample (phase (8)). The diameter of the crater typically measures between 10 and 300 μm.

The diagram at the top of Fig. 40.3 shows schematically an emission spectrum of a laser-induced plasma. In the spectrum, there are several emission lines. These lines are characteristic of the different elements comprised in the analyzed sample. Each line can be associated with a specific element. The line's height is a measure of the quantity (and indirectly of the concentration) of the element inside the sample. The line intensity however is also affected by a set of other factors. Normally, the intensity of the line of the element j to be determined (the so-called analyte line)

Fig. 40.2 Principle of laser material analysis based on laser-induced breakdown spectroscopy (LIBS) shown in phases 1 to 8. LB is incident laser beam, S sample or measuring object, H region of energy deposition, V material vapor, P plasma, E element specific emission, CR crater (in case of a solid sample), and PT particulates. The times given depict the temporal evolution after start of irradiation of the laser pulse
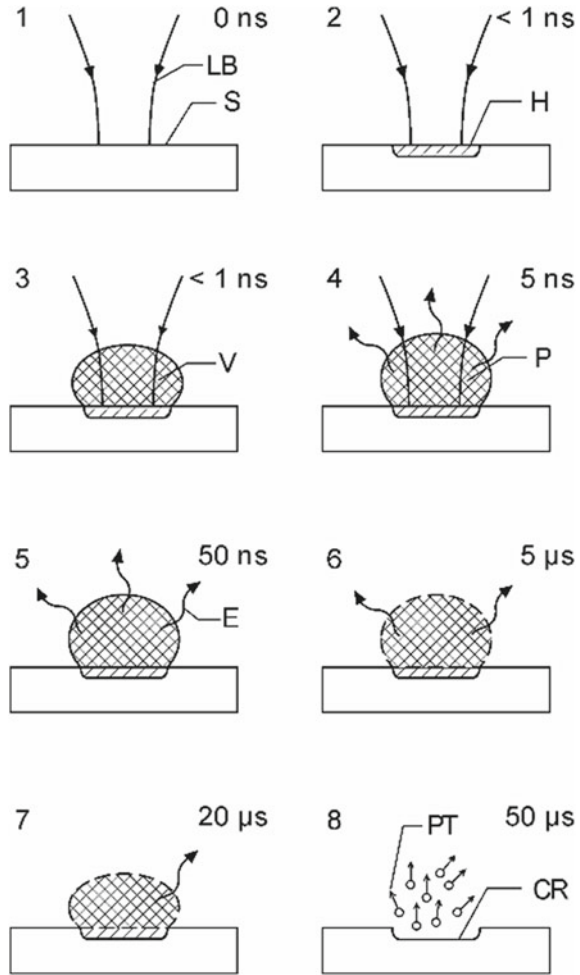

is set in a ratio to a reference line *r*. For example, a dominating element inside the analyzed material (normally an element of the matrix) is taken as the reference line.

To gain quantitative results, a calibration of the method is necessary using samples with known composition. Figure 40.3 (bottom) shows a schematic of a calibration curve where the ratio of the intensities of an element and a reference line is plotted as a function of the known elemental concentration of the calibration samples. Usually, the curves are non-linear. For an unknown sample, the concentration of an element is determined from the inverse function of the calibration curve, which is called the analysis curve.

A typical setup for LIBS is shown in Fig. 40.4. A Q-switched solid-state laser can be used as a light source. Pulses generated by those lasers have a duration between 5 and 100 ns with an energy between 100 μJ and 2 J. With this pulse energy, it

Fig. 40.3 Schematic of an
emission spectrum (top) of a
laser-induced plasma and a
calibration curve (bottom)
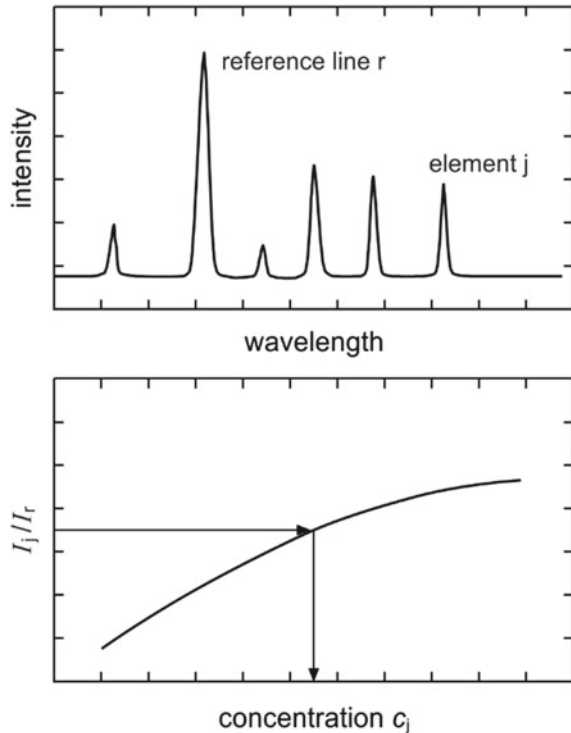
is possible to reach an irradiance of more than 10^6 W/cm^2 in the focus of lens L, which typically is necessary for the vaporization of a material. The plasma radiation is measured with a spectrometer via fiber optics. For the recording of the spectrum, basically two different methods are used. One alternative is to place detectors in specific positions inside the spectrometer, where the emission lines of the relevant elements are. For this, e.g. photomultipliers are used. The advantage of this method is that only information necessary for the analysis is recorded and processed.

The second alternative images the whole spectral range on solid-state image detectors (as e.g. photodiode arrays or CCD image sensors). A spectrum similar to the one shown in Fig. 40.3 (top) can be recorded in that way. For both methods, the registered signals are digitized and evaluated with a computer.

40.2.4 Time-Resolved Spectroscopy

The laser-induced plasma exists only for a short time. Hence, the excited atoms and ions are emitting transiently. To estimate the order of magnitude of the plasma lifetime, the geometry of the plasma is assumed to be spherical. Inside the sphere
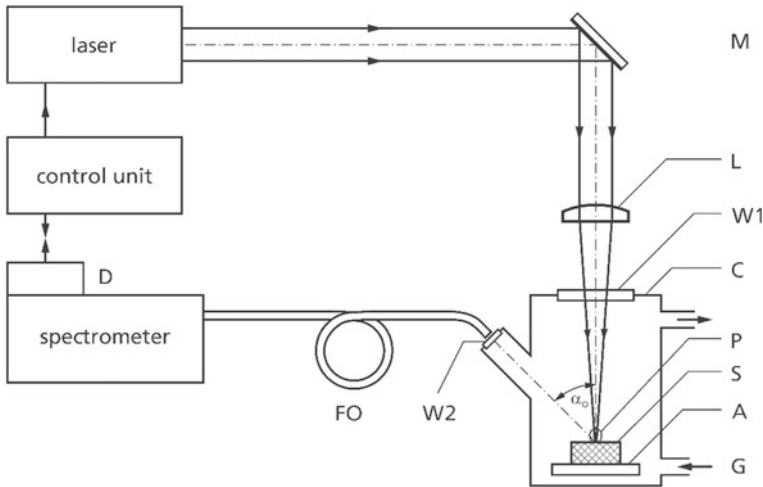
Fig. 40.4 Typical setup for LIBS. M is mirror, L focusing lens, W1 entrance window, W2 exit window, C measurement chamber, P plasma, S sample, A positioning system, G gas stream, α_o observation angle, FO fiber optic cable, and D detector

is a hot gas, whose particles move with an average thermal velocity v_{th}. Because of this nondirectional movement, the sphere begins to disintegrate. A measure for that time is calculated with:

$$\tau = \frac{d_p}{v_{th}}, \tag{40.8}$$

where τ is lifetime of the plasma, d_p diameter of the plasma, v_{th} average thermal velocity of atoms and ions inside the plasma.

For a plasma of iron atoms and ions at a temperature of 9,000 K and a diameter of $d_p = 2$ mm, the lifetime estimated by (40.8) is $\tau = 1.1$ μs. In practice, one can observe line emission of the plasma in a time interval from approximately 200 ns to 10 μs after irradiation of the laser pulse onto a measuring object.

Figure 40.5 schematically shows emission spectra at three different times after the irradiance of the laser pulse. At time t_1, the plasma shows a mostly continuous spectrum caused by free-free transitions of electrons (so-called Bremsstrahlung). Only a small number of atoms and ions are excited for emission. Accordingly, line intensities are low. At time t_2, the plasma has cooled down and the line emissions of atoms and ions gain intensity. At time t_3, the plasma temperature is even lower and the line emission intensities are decreasing.

Time-resolved spectroscopy observes the emission of radiation within a certain time interval. At time t_2 in Fig. 40.5, there are, e.g., beneficial conditions to record emission lines with high intensities relative to the background. In the setup of

Fig. 40.5 Schematic
illustration of the emission
spectra of a laser-induced
plasma at different times
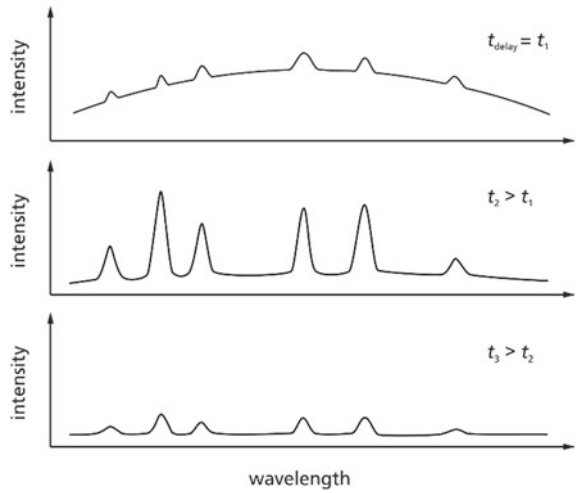after irradiation of the laser
pulse onto the sample

Fig. 40.4, a signal electronic (part of the control unit) enables the detectors (photo-multipliers, photodiode arrays, ...) to only record the line emissions in a specific time interval after plasma ignition (integration time gate).

40.2.5 Data Evaluation

Line intensities of elements of interest are determined from the measured spectra, which normally are gained in a digital form. The observed intensity at a given emission wavelength is in general a superposition of different parts; see Fig. 40.6. In the following, we will assume that the spectral intensity $S_\lambda(\lambda)$ at the wavelength λ is a combination of only two parts—namely the line radiation I_λ and the background radiation u_λ:

$$S_\lambda(\lambda) = I_\lambda(\lambda) + u_\lambda(\lambda), \tag{40.9}$$

with $S_\lambda(\lambda)$ being spectral intensity, radiant flux per surface unit and wavelength interval, $[S_\lambda] = \mathrm{W/m^3}$, $u_\lambda(\lambda)$ spectral intensity of the background radiation, $[u_\lambda(\lambda)] = \mathrm{W/m^3}$, $I_\lambda(\lambda)$ spectral intensity of the line radiation, $[I_\lambda] = \mathrm{W/m^3}$, and λ wavelength of the emitted radiation.

For evaluation, the so-called net line intensity is calculated:

$$J = \int_{\lambda_1}^{\lambda_2} (S_\lambda(\lambda) - u_\lambda(\lambda))\mathrm{d}\lambda = \int_{\lambda_1}^{\lambda_2} I_\lambda(\lambda)\mathrm{d}\lambda, \tag{40.10}$$

Fig. 40.6 Superposition of background (top) and line (middle) emission of the laser-induced plasma
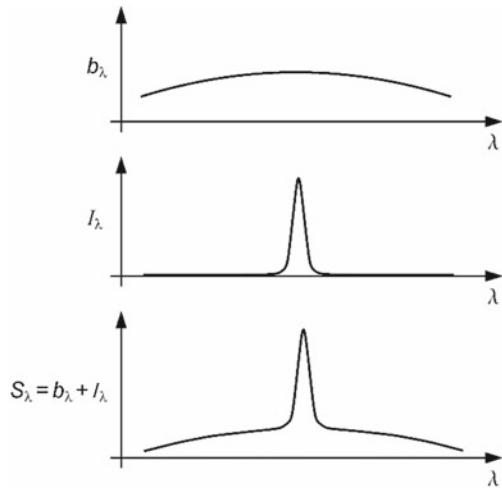
with J being net line intensity, $[J] = \text{W/m}^2$; λ_1, λ_2 integration limits, within the wavelength interval (λ_1, λ_2) the spectral intensity I_λ has non-zero values, and $[\lambda] =$ m. The values of the function u_λ in the region of the emission line are interpolated from u_λ in the line-free neighborhood of that line.

The observed emission lines are assigned to the different atomic and ionic lines i = 1, ..., m with the help of tables or databases of spectral lines (Zaidel' et al. 1970; https://lweb.cfa.harvard.edu/amp/ampdata/kurucz23/sekur.html; http://physics.nist.gov/cgi-bin/AtData/main_asd). For a chosen number of lines λ_i, Eq. (40.10) is used to calculate the net line intensity J_i. The intensities J_i are each a measure of the number of particles N_i of the respective element i in the laser-induced plasma.

Furthermore, for simplicity we assume that the plasma is optically thin. In this case, the emitted radiation is not significantly absorbed inside the plasma. The line emission intensity of the whole plasma volume is therefore directly proportional to the number of emitting particles N_i inside the plasma. Generalized, the factors influencing J_i can be described as

$$J_i = N_i \cdot F_i(I_0, E_\text{L}, w, t_\text{delay}, t_\text{int}, p_\text{a}; c_1, \ldots, c_\text{m}|_{\text{m} \neq i}). \qquad (40.11)$$

The function F_i describes the dependence of the line intensity J_i on the laser irradiance I_0, the laser pulse energy E_L, the beam radius w in the interaction region, the recording time t_delay, the integration time t_int, the ambient gas pressure p_a as well as the concentrations c_m of all elements in the measuring object except the analyte i. The latter dependence results from the absorption and vaporization process, which is not independent of the composition of the sample. Also, the emission of the plasma depends on the collisions, which involve all species. In analytics, these effects are called matrix-effects. In general, the function F_i is not known and has to be found

empirically with calibration measurements. Practically, line ratios, like $J_1/J_2 = N_1/N_2$, often are used to compensate at least partly the influence of the factors mentioned.

40.2.6 Measurement Range

Typical characteristic quantities and measuring ranges of LIBS analysis are summarized in Table 40.1.

Since the material of the measuring object is vaporized purely optically, it is irrelevant to consider whether the sample under investigation is an insulator or a conductor of electricity. The free distance between the optic and the workpiece is determined mainly through the focal length of the focusing lens, L, in Fig. 40.4. An enlargement of the focal length using the same illuminated lens aperture leads to a larger focus diameter. In this case, higher laser pulse energies are necessary in order that the vaporization irradiances are reached.

The lateral resolution is limited by the diameter of the laser beam at the surface of the workpiece and material properties. The beam waist diameter is again influenced by the focal length and aperture of the focusing lens, as well as the quality of the laser beam (beam propagation ratio, cf. European Standard 2005). The given values correspond to commercial Nd:YAG lasers. The detection sensitivities are element and matrix dependent. In Table 40.1, typical values are listed and determined using calibration curves gained with certified reference samples (CRM).

The measuring frequency is determined by the repetition frequency of the Q-switched laser. For better measurement accuracy, several plasmas are ignited and their spectra are evaluated, in order to gain average net line intensity values.

The reproducibility of LIBS describes to which extent the results of a series of measurements at a homogeneous workpiece deviate from one another. It depends on the stability of system parameters such as the laser pulse energy, focusing, and gas

Table 40.1 Characteristics and measurement ranges of laser-induced breakdown spectroscopy

Characteristics	Data	Remarks
Material	Metallic, nonmetallic	All states of aggregation
Free distance between optics and workpiece	< 300 cm	No principal limit, depends on laser pulse energy
Lateral resolution	1 μm–300 μm	A consequence of the finite beam waist diameter and material properties
Detection sensitivity	1 μg/g–1000 μg/g	Element dependent
Measuring frequency	0.1 Hz–1000 Hz*	Refers to evaluation of the spectral emission of each induced plasma

* Higher frequencies up to 30 kHz are possible, if the spectral emission of a series of plasmas is summed up within the exposure time of the detector

exchange rate in the interaction regions, as well as on the properties of the induced plasma over several measurements. By averaging a measurement over a series of spectra, the reproducibility is considerably increased. For example, with a pulse frequency of 20 Hz, 100 spectra can be recorded in 5 s. The net line intensities obtained deviate from those of another measurement at the same workpiece by only a few percent.

40.3 Examples of Applications

40.3.1 Fast, Spatially Resolved Material Analysis

For the production of high-quality steel products, like thin wires for energy-saving steel belt tires or thin foil for lightweight packaging, high-quality steel is needed. Inclusions lower the quality of the respective steel grade, so that, e.g., the diameter of wires in steel belt tires or the thickness of sheets for beverage cans cannot go below a certain limit.

Therefore, for the development of high-quality steel, a method of analysis is required that can detect inclusions, like Al_2O_3, AlN, TiC, SiC, CaO, ZrO_2, etc., in steel in a fast, reliable, and cost-effective way.

The steel cleanness analysis by LIBS is a method to solve that problem (Bette and Noll 2004). To do so, samples are scanned with a precisely focused, pulsed laser beam, and the induced plasmas are evaluated spectrally. Each location is measured only with a single laser pulse. The frequency of measurement amounts to up to 1,000 Hz.

The use of a laser offers the following advantages: in contrast to spark-OES, contamination with electrode material is not possible. The zone of interaction between laser radiation and sample material can be determined in a very accurate way, in contrast to spark-OES, which is influenced by the local electric field distribution (e.g. at the edges of the insulating inclusions). Concerning wet-chemical processes and the SEM–EDX method (scanning electron microscope with energy dispersive X-ray fluorescence detection), complex sample preparation and long measuring times can be avoided.

For the task mentioned above, Fraunhofer ILT has developed an analysis system to inspect steel cleanness. Figure 40.7 shows the schematic setup of the SML system (**S**canning **M**icroanalysis with **L**aser spectrometry) (Bette and Noll 2004). A diode-pumped solid-state laser (DPSSL) was used for the excitation of the plasma. The laser is operated in Q-switch mode at a wavelength of 1064 nm. The other laser parameters are repetition rate up to 1000 Hz, pulse energy 2 mJ, pulse width (FWHM) 5 – 6 ns, and time-diffraction-factor $M^2 < 1.3$ (European Standard 2005). The laser beam is coupled to a gas-tight measuring chamber; see C in Fig. 40.7. Inside the measuring chamber, an argon gas atmosphere is maintained. The use of inert gas allows to
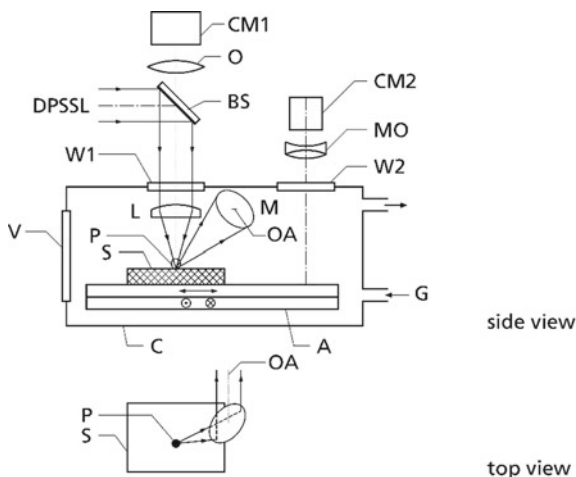
Fig. 40.7 Schematic setup for high-speed scanning microanalysis with LIBS. DPSSL is beam of the diode-pumped solid-state laser, BS beam splitter, W1 window for the laser beam, L focusing lens, S sample, A *x*-, *y*-translation stages, P laser-induced plasma, M spherical mirror to collect the plasma emission, OA optical axis of the spectrometer (perpendicular to plane of projection), W2 window to observe the sample surface, MO microscope zoom objective (10 x); CM1, CM2 CCD-cameras to observe the interaction region and the generated craters; G gas flushing of the measurement chamber, C measuring chamber, and V transfer port

transmit the ultraviolet (UV) emission of the laser-induced plasma to a Paschen–Runge spectrometer. The sample to be analyzed is brought into the chamber through a transfer port (V). The sample is clamped in a sample cassette which is fixed to the *x*-, *y*-translation stages (A) installed inside the chamber (C). These translation stages allow shifting the sample with respect to the position of the laser focus in two perpendicular directions. The positioning accuracy of the axes is 1 μm, and the minimum step size amounts to 5 μm.

The laser beam is focused by an objective to a spot size of ~4 μm. The waist of the beam focus is positioned on the surface of the sample. The maximum irradiance is in the order of 10^{12} W/cm^2. The emission of the laser-induced plasma is collimated by a spherical mirror to the entrance slit of a Paschen-Runge vacuum spectrometer having a Rowland circle diameter of 1 m and covering a spectral range of 130 nm to 777 nm (Noll 2012). Along the Rowland circle exit slits, photomultipliers are positioned at pre-defined spectral positions to detect the radiation of up to 48 emission lines simultaneously. The signals of the photomultiplier tubes detecting the transient radiation are transmitted to multi-channel-integrator electronics.

The sample surface can be observed by an optical system consisting of a microscope zoom objective (MO) and a CCD-camera (CM2). The optical axis of this microscope is oriented parallel to the optical axis of the analyzing laser beam. For an inspection of the generated craters, the sample can be moved by the translation stages toward the field of view of the microscope and the CCD-camera; see MO and CM2 in Fig. 40.7.

Fig. 40.8 High-speed scanning LIBS microanalysis system SML to measure steel samples for the analysis of segregations, inclusions, and decarburization zones

DPSSL, translation stages, and multi-channel-integrator electronics are synchronized to allow for single-shot data evaluation and a defined allocation of the spectral signals to the respective measuring position, i.e., the *x*-, *y*-positions. At 1 kHz measuring frequency and a scanned area of 1×1 cm^2 with a step size of 20 μm, a data volume of about 48 MByte is collected which is then processed to generate element mappings. Figure 40.8 shows the constructed scanning LIBS system SML developed by Fraunhofer ILT.

In the middle of Fig. 40.9, the raw signals of the photomultiplier for the Mn-263.82 nm emission line are shown in a 2D mapping for a scan area of 10×10 mm^2. Only those signals, which exceed the sum of the average plus five times the standard deviation of the overall intensity distribution, are shown color coded. Local inclusions of manganese are clearly visible; see enlarged section of this map with dimensions 1×1 mm^2 shown at the bottom of Fig. 40.9. A simultaneously measured elemental mapping of sulfur (emission line 180.73 nm) shows the existence of local correlations between sulfur intensity peaks and manganese intensity peaks. This is illustrated exemplarily by the vertical arrow linking such corresponding intensity peaks. These spatial correlations of Mn- and S-peaks indicate inclusions consisting of manganese sulfide (MnS).

With high-speed LIBS, the steel cleanness analysis can be accelerated significantly. The high-speed identification of other inclusions, like oxides or nitrides, is also possible with this method (Bette et al. 2005; Boué-Bigne 2007). The sensibility is even high enough to analyze segregation zones. Numerous disadvantages can be avoided in comparison to conventional methods. Advantageous in particular are the high savings of time and costs for measurement and sample preparation. Table 40.2 shows the technical details of the measuring system SML.

Fig. 40.9 Signals of sulfur (top) and manganese (middle and bottom) exceeding a threshold shown in a raster field of 10×10 mm^2 with 500×500 measuring points (middle and top), at the bottom an enlarged section of the manganese map is shown
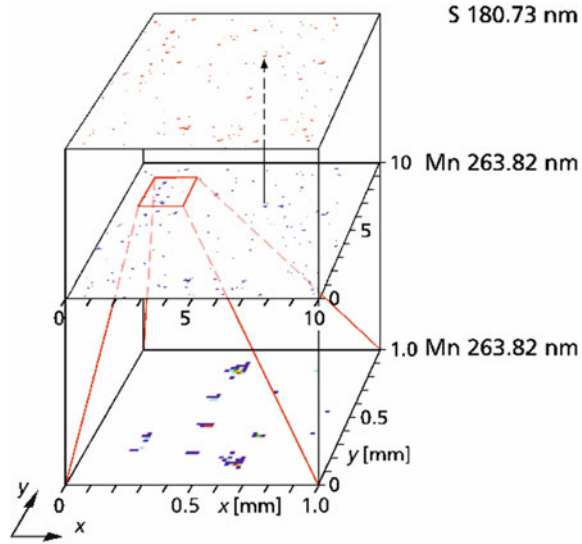

Table 40.2 Technical data of SML

Parameter	Data
Sample positioning accuracy	<1 μm
Minimal point-to-point distance	5 μm
Diameter of laser focus	~4 μm
Spatial resolution[a]	<20 μm
Measuring frequency	1 kHz
Number of photomultipliers[b]	41
Number of different detected elements	24, including O, N, C, P, and S
Wavelength range	130–777 nm
Maximum size of scan field	110×45 mm^2
Measuring atmosphere	Argon

[a] refers to the spectroscopic analysis of metallic samples,
[b] for some elements more than one emission line is detected to extend the dynamic range while detecting large ranges of analyte concentrations

40.3.2 Mix-up Examination in a Rolling Mill

An inline LIBS measurement at metallic piece goods in a rolling mill is shown in Fig. 40.10. The fed steel blooms of about 2–3 tons have scale layers with non-representative surface composition (Meinhardt et al. 2016; Sturm et al. 2017b). The
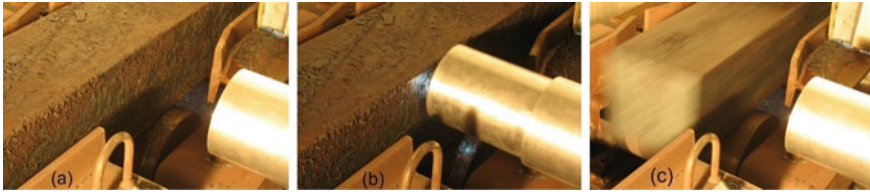
Fig. 40.10 Inline measurement of steel blooms: **a** the bloom is transported on a roller table and stopped in front of the measuring lance, **b** the front part of the lance has approached the side face of the bloom, laser irradiation is activated to locally ablate the scale layer and to analyze the bulk composition, **c** the measuring lance is pulled back to the stand-by position and the bloom moves on to the right. Diameter of measuring lance: 170 mm (Sturm et al. 2017b)

task is a mix-up detection in order to assure that always the correct steel grade is transported to the subsequent furnace and first roll stand.

In Fig. 10a, the bloom is just arriving on the roller table from the left; at the right side, the front part of the laser measuring lance is visible. The optical working distance is 300 mm. The bloom is stopped for about 1 min, while the measuring lance approaches the side face of the bloom and the laser ablation and LIBS analysis is activated; cf. Figure 10b. The automatic approaching of the lance is executed to improve the gas flow conditions in the interaction zone. The stop period of 1 min lies within the regular feeding rate of the subsequent continuous furnace and thus does not imply a retarding in the production flow.

A process was developed consisting of two phases as follows: (a) local removal of scale layer with cleaning pulses, (b) LIBS analysis using double pulses (Meinhardt et al. 2016; Sturm et al. 2017b); see Fig. 40.11. In the first phase, a scale layer of thickness 200–600 μm has to be penetrated. Within 20 s, an effective crater depth of >2 mm in scale material is achieved.

The deployed Nd:YAG laser is a Q-switched diode-pumped oscillator followed by a flash lamp-pumped amplifier emitting pulses of 20–40 ns at a wavelength of 1064 nm. The beam is focused by a lens with a 300 mm focal length. Figure 40.11a shows the standard situation with a fixed lateral focal position. The contact of the LIBS plasma with the crater side wall adds impurities of scale into the plasma, and these interfere with the analysis of the bulk steel. Therefore, the focal spot is slightly moved by a motorized mirror during the scale ablation step in order to enlarge the "cleaned" spot; see Fig. 40.11b. This reduces side effects from the scale at the crater wall (Noll et al. 2005; Meinhardt and Noll 2021).

Figure 40.12 shows the results of laboratory tests at ground (i.e., non-scaled) and primary-scaled surfaces for steel grades with chromium contents ranging from 0.1 wt.-% to 17 wt.-%. The analysis curve (straight line in Fig. 40.12) was set up on the basis of 64 ground samples. To characterize the prediction error of Cr concentrations of scaled blooms, 53 different scaled steel samples were measured. The root mean square error (RMSE) amounts to 0.32 wt.-% for this set of scaled samples. The developed two-phase measuring process yields about the same results for ground

Fig. 40.11 a Schematic cross section of laser-generated crater in a scaled steel workpiece for standard LIBS with fixed lateral focal position; **b** cross section of crater generated with a moving laser spot during the ablation step prior to analysis (Sturm et al. 2017b)
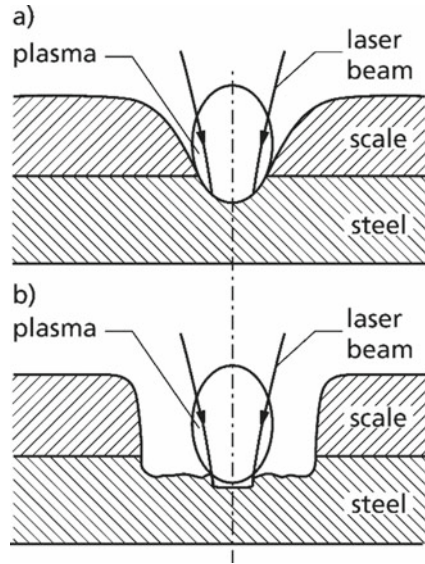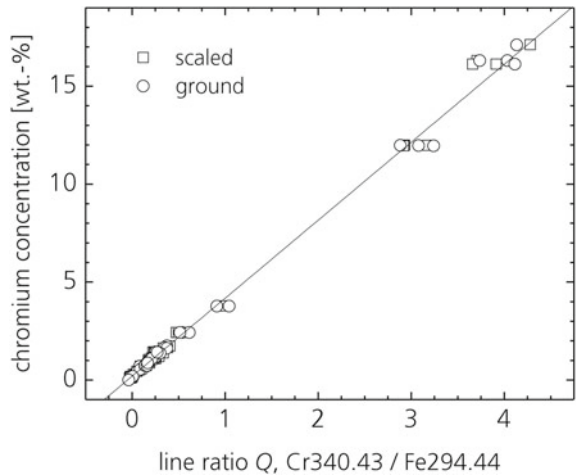

Fig. 40.12 Analysis curve of chromium for scaled and ground surfaces of steel grades deploying a two-phase measuring sequence of laser ablation and LIBS analysis (Meinhardt et al. 2016)

(circular data points) and scaled samples (square data points) and is thus capable to provide bulk analysis of blooms in their "natural" state with primary-scaled surfaces.

LIBS measurements were taken for 481 steel blooms during routine production on several days. According to the rolling sequence, the steel blooms on the roller table are coming in different batch quantities from a few up to roughly one hundred blooms which have the same nominal material and reference analysis. The measured mass fractions of each bloom in m.-% are plotted exemplarily for Ni in Fig. 40.13 together with the nominal reference mass fractions. Each bloom has an individual

Fig. 40.13 Direct tracking
of the rolling sequence and
comparison of the LIBS
measurements (black) of the
mass fractions of Ni with the
nominal reference values
according to a batch analysis
(blue) of the steel bloom
material (Sturm et al. 2017b)
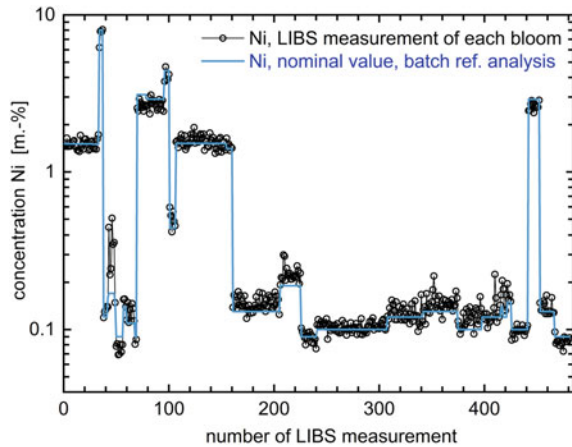
LIBS value, but there is only one single reference value for the blooms of the same
batch, i.e., for these sections the (blue) reference values are horizontal straight lines
in Fig. 40.13.

40.3.3 Sorting of Alloyed Metal Scrap

The economics of recycling scrap alloys depends on the one hand on the alloy,
the element concentrations involved, and their value, and on the other hand on the
recycling methods used and their costs. Scraps are traded on the market like products.
They are differentiated into different qualities. For a stainless CrNi-steel, the content
of chromium and nickel is crucial. To be able to set and bill the corresponding
prices for the purchased alloys, the alloy composition must be known. Hence, the
core of the inspection of incoming goods in the trade with alloyed scrap is the
identification of the delivered alloy, the determination of the concentrations of the
contained elements, and, if necessary, the sorting. Common tools in the identification
of alloys are portable spectrometers, which are, e.g., based on X-ray fluorescence
(XRF). In the mass markets of scrap processing, not a complete but a representative
review of the incoming goods takes place.

For certain material flows, the smelters require a sorted preparation. This may
include a complete inspection of all scrap pieces. Examples of such niche markets
are nickel base superalloys, titanium alloys, high-speed steels (HSS), and hard metals
(HM). The state of the art in terms of sorting is hand picking and visual inspection
supported by spectrometric methods (XRF, SD-OES). For metal scrap with low
individual weights per piece and low-grade alloys, this sorting process is often not
economical. This creates material flows in which not all elements are specifically
recycled and recovered leading to down-cycling. In order to prevent this, a pilot
plant was developed that identifies individual scrap pieces of the material classes
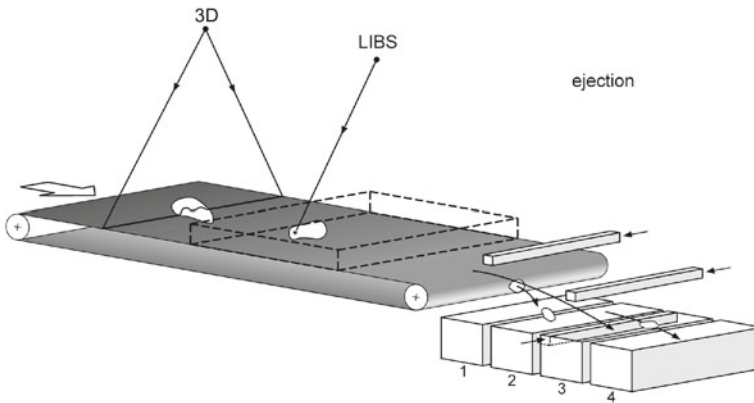
Fig. 40.14 Schematic for high-speed sorting of piece goods. The process flow runs from left to right with the following sequence: inline 3D measurement of single objects transported on a belt conveyor, LIBS analysis, and sorting to different fractions 1 to 4 by pneumatic ejection

high-speed steel, hard metal, and titanium and discharges them into several target fractions (Geisler et al. 2019).

The methodical approach for object recognition and LIBS measurement follows the setup shown in Fig. 40.14 (Werheit et al. 2011). Singularized objects are, e.g., scrap pieces, bricks, and printed circuit boards which shall be sorted piece by piece in different fractions depending on their chemical composition. In that case, the object moving on a belt conveyor is tracked with a galvanometer scanner guiding the laser beam to the right position on the object. The 3D geometry of the singularized object is measured upstream of the LIBS measuring volume and evaluated in real time in order to control the tracking procedure via the scanner. Figure 40.14 illustrates this approach for scrap pieces. The dashed box indicates the measuring volume in which a measuring location for LIBS can be positioned.

Figure 40.15, left, shows exemplary photos of the processed pieces, in this case thread cutters. The 3D data gained by the laser light section are processed to recognize the object contour, to define circumscribing rectangles and last but not the least potential measuring locations for the subsequent LIBS measurements; see Fig. 40.15, right.

A tailored laser pulse train is irradiated to penetrate non-representative surface layers prior to the LIBS measurement. The laser beam tracks the moving piece so that cleaning and measuring pulses are focused on the same spot. The speed of the conveyor belt can be varied between 0.15 and 5 m/s. Depending on the requirements of the analyses, either up to 60 measurements can be carried out on one sample or a high sample throughput can be generated with one measurement per piece. Figure 40.16 shows photos of LIBS measurements at a twist drill moving with 0.3 m/s.

The classification logic follows the conditions of recycling alloyed metal scrap. The three main classes of high-speed steel, hard metal, and titanium are basically
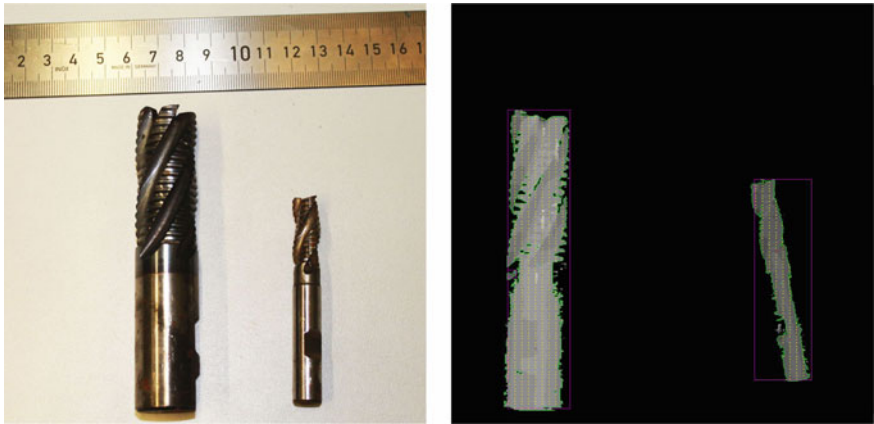
Fig. 40.15 Left: Photo of two different thread cutters. Right: Evaluated 3D data of these objects: contour (green), circumscribing rectangles (purple), height information (gray scale), and indication of potential measuring spots for subsequent LIBS measurements (yellow)
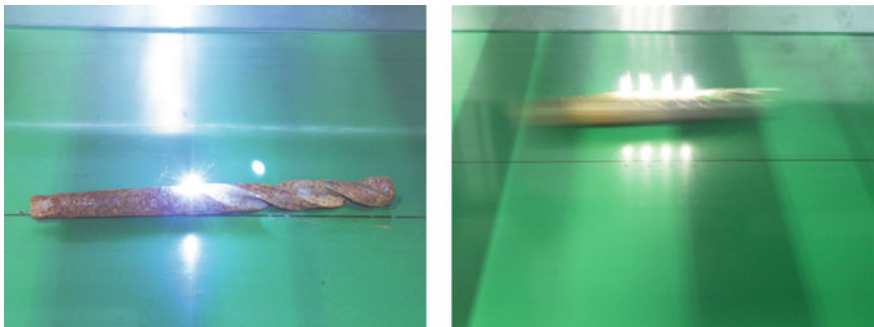

Fig. 40.16 Left: Photo of a single LIBS measurement at a twist drill transported on a belt conveyor. Right: Photo with an extended exposure time to visualize a sequence of LIBS measurements at a single measuring object

separated when recycling the scrap, but may have low impurities. The aim of the classification is the distinction of subclasses, which are related to the alloying elements. The specified limit values result from the composition of the alloys. Identifiers for main and subclasses are introduced. They are composed of the main class (1xx, 2xx, or 3xx) and the respective subclass (xx = 01–11). The matrix element for the main class "100/HSS" is iron, for "200/titanium" it is titanium, and for "300/HM" it is tungsten. To differentiate the individual alloy classes, the contents of the elements Fe, Ti, W, Co, Al, Nb, and Ni are measured with LIBS. Furthermore, the elements Mo, V, Cr, Mn, Sn, Zr, C, Cu, and Pd are examined.

For the LIBS measurements, signals from more than 60 spectral lines were selected and averaged over five measurements each. The obtained measurement vectors are

standardized and evaluated by a linear discriminant analysis (LDA) according to their class membership. Figure 40.17 shows scatter diagrams for the various subclasses belonging to the main class "100/HSS". With a set of four vectors (see axes Vec2, Vec3 and Vec1, Vec2 in Fig. 40.17), all 8 subclasses can be discriminated clearly.

After the metal scrap has been identified by the LIBS module of the pilot plant, the material on the conveyor belt reaches the automated discharge station. A delta robot hanging above the conveyor belt grabs the piece and discharges it to the allocated target fraction. The delta robot offers high handling capacity, flexibility, process reliability, and economic efficiency.

One challenge is the variability of object geometries occurring. The first test gripper designed is shown in Fig. 40.18. It is a pneumatic gripper which is particularly suited for rod- or pin-shaped objects. After grabbing the scrap parts from the belt,

Fig. 40.17 Top: Scatterplot of high-speed steel subclasses 104 to 111. In the shown vector space (Vec2, Vec3), five sub-classes are well separated whereas the subclasses 105, 106, and 108 are partially overlapping. Bottom: Using further vectors (Vec1, Vec2), the classes 105, 106, and 108 can be discriminated as well
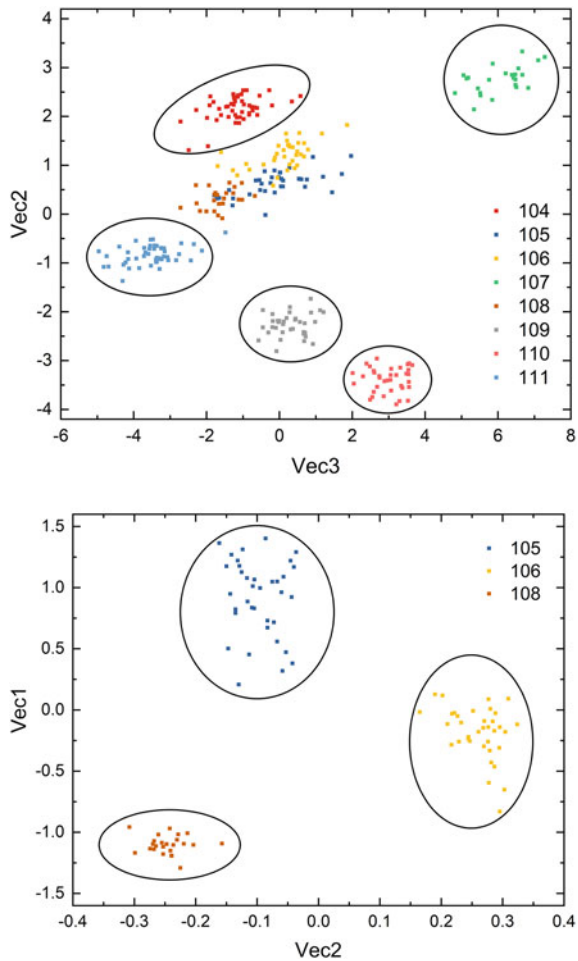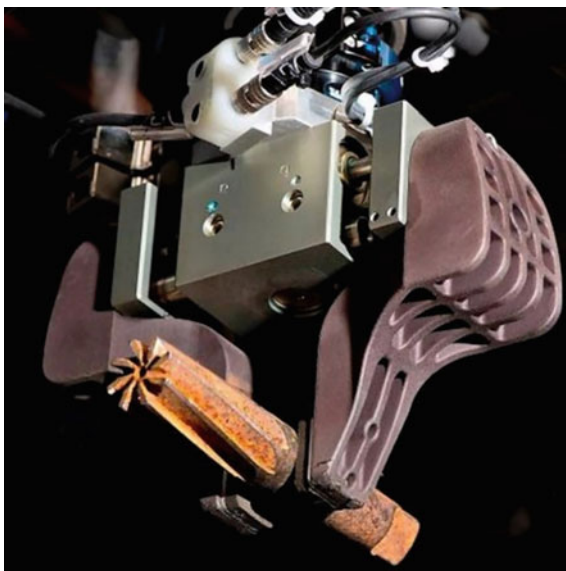
Fig. 40.18 Gripper of the delta robot with a piece of HSS scrap

these are dropped on up to six different discard slides guiding the pieces to the specified sorting fractions.

40.3.4 LIBS as Key Methodology for Inverse Production of End-of-Life Electronics

Inverse production strives for a selective dismantling of industrial mass products at their end-of-life (EOL) with the goal to generate highly enriched fractions of valuable materials for subsequent tailored recovery procedures. This is an essential step to establishing efficient circular economy concepts. While for conventional industrial production input materials and components are—as a rule—known, the situation of a process line for selective treatment of EOL electronics is much more challenging.

The variety of features of the material to be processed is very broad and often limited or no information is available about the chemical composition. Hence, there is a need for a fast analyzing methodology to set up the data space for inverse production as a key element of an inverse production line to automatically dismantle and sort valuable components from EOL electronics. Within a European project, a consortium of R&D institutes and companies has developed processes and machines to demonstrate the feasibility of a novel approach for automated selective disassembly of consumer and professional EOL electronics (EU project, www.ADIR.eu, 2018–2020). The target of the ADIR project was to use selective physical separation methods to gain highly enriched sorting fractions of valuable materials for tailored recycling and recovery of these substances.

LIBS was studied to identify inline—i.e., within a process line of inverse production—valuable materials in electronic components and to allocate this analytical information to the location of the measuring object within the structure of the EOL electronics, i.e., the printed circuit boards (PCBs). Geometry data gained by optical 2D- and 3D measurements are fused with LIBS data and deployed for a subsequent selective disassembly and sorting of electronic components with high contents of valuable materials such as tantalum. The developed scanning LIBS method, the gained results and the integration of the LIBS measurements in the worldwide first inverse production line to process EOL printed circuit boards and cell phones are described in the following.

Two classes of input material were studied: printed circuit boards from cell phones and PCBs from servers and computers. These boards span a wide range of geometries with dimensions from 50×100 mm^2 to 500×500 mm^2.

The target components are mainly capacitors and surface acoustic wave (SAW) filters owing to tantalum, integrated circuits for gold, and unbalance masses of vibration alerts for tungsten. The considered size range of the capacitors in their packaging format as surface mounted devices (SMD) goes down to the dimensions $1 \times 0.5 \times 0.5$ mm^3. In general, from the external appearance of, e.g., capacitors (labeling, color of housing), it cannot be seen whether a tantalum capacitor is present. Moreover, data from the manufacturers of the PCBs or the electronic components with respect to the chemical composition are not available. To illustrate the heterogeneous structure of such components, Fig. 40.19 shows a microscope image of the typical cross section of a SMD capacitor, in this case a tantalum capacitor. An investigation of the cross section by SEM–EDX reveals different materials as epoxy resin molding for the housing (yellow), electrodes made of copper, silver contact layers, and as dominant part of the volume the dielectric consisting of tantalum oxide (Ta$_2$O$_5$). In order to identify the composition of the dielectric of such capacitors with LIBS, an adequate measuring location has to be found and the dielectric inside the component housing and partially underneath metallic electrodes and contact layers has to be accessed.

A scanning LIBS system combined with 2D-, 3D-geometry measurements was developed at Fraunhofer ILT. Figure 40.20 shows the setup and illustrates a measuring sequence in a time series t_0, t_1, and t_2.

The beam of a Nd:YAG laser is guided via a focus shifter to a galvanometer scanner optics (SO) directing the focused laser beam to any point within a measuring volume

Fig. 40.19 Cross section of a SMD tantalum capacitor. On the right, a blind boring (see arrow) generated by laser ablation is seen penetrating a contacting electrode and ending within the dielectric (dark brown) of the capacitor
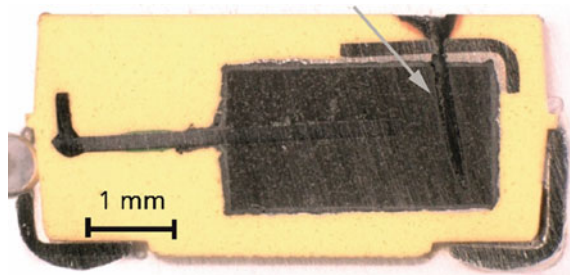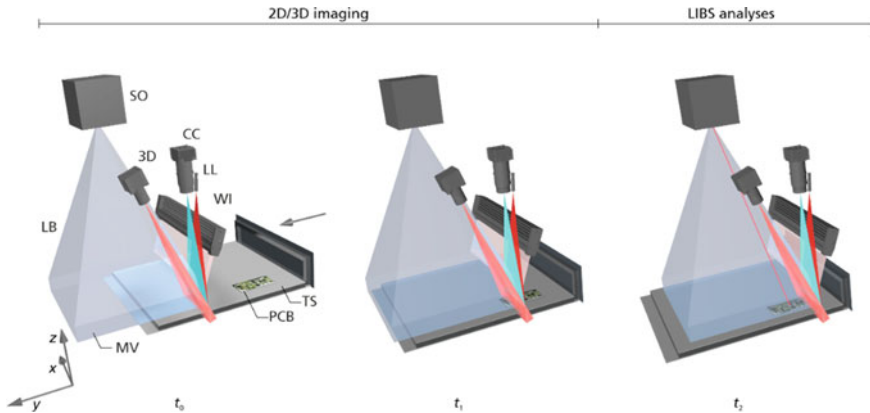
Fig. 40.20 Scanning LIBS setup combined with 2D-, 3D-geometry measurements. SO is scanner optics with orthogonal galvanometer-driven mirrors, LB region of the scanned laser beam for LIBS, MV measuring volume for LIBS, CC color camera, LL laser line for 3D measurements, WI white light illumination, 3D camera for laser light section measurement, PCB printed circuit board as measuring object, TS translation stage moving in *y*-direction

(MV) with the dimensions $500 \times 500 \times 60 \text{ mm}^3$. The laser source runs at a repetition rate of 100 Hz and can be operated in two modes: (i) ablation pulses, so-called free-running laser generating pulse bursts within a time interval of $\approx 100 \,\mu\text{s}$; (ii) Q-switch mode generating pulses with a duration of 15 ns used for LIBS measurements.

The PCB to be measured is placed and clamped at time t_0 on a translation stage (implemented as a drawer) in the *xy*-plane. Then the drawer moves in positive *y*-direction (t_1) and the geometry of the measuring object is measured in 2D with a strip-shaped white light illumination (WI) and a color line camera (CC). Simultaneously, the 3D shape is measured by the projection of a laser line (LL) and observation of this line under an angle with a further camera (3D) using the triangulation principle (laser light section method or 2D laser triangulation). With this information, the LIBS measurements are started (t_2), and the LIBS laser beam can be directed by the scanner sequentially to any point of the measuring object inside the measuring volume. Local LIBS measurements are conducted at selected components or small line scans on single objects or raster scans of the whole PCB. Table 40.3 summarizes the data of the setup.

A prerequisite for LIBS measurements on the 3D surface profile of a PCB are highly resolved geometry measurements to locate the position, orientation, and height of electronic components on the PCB. Very tiny objects with characteristic dimensions down to 1 mm and less are clearly resolved within the setup shown in Fig. 40.20. The estimated spatial resolution in the *xy*-plane amounts to $\leq 60 \,\mu\text{m}$ within an overall image with extensions of $500 \times 420 \text{ mm}^2$.

The coordinates (*x, y*) of a component are not sufficient to assure that the LIBS laser beam is directed and focused to a defined location at the upper surface of an electronic component due to the required deflection angles of the scanned LIBS laser

Table 40.3 Data of scanning LIBS setup with 2D-, 3D-geometry measurements. MCS is multi-channel signal electronics, MV measuring volume, and δλ spectral resolution

Item	Data
Translation stage	x-, y-axes; max. speed 1000 mm/s
2D camera	line array, 4096 pixels, 3 colors
3D camera	laser line section, 1280×1024 pixels
2D/3D measuring time	<30 s for a 500×500 mm^2 PCB
Scanner for LIBS laser	dual-axis mirror galvanometer, axial focus shifter, vertical distance to bottom of MV: 650 mm
MV, scan field including focusing	$500 \times 500 \times 60$ mm^3
LIBS laser	1064 nm, ~100 mJ, 100 Hz; ablation pulses ≈ 100 μs, Q-switch pulses 15 ns
Spectrometer	Paschen-Runge system with 8 CCD line arrays along the Rowland circle, 234–545 nm, $\delta\lambda \approx 15$ pm@234 nm, MCS

beam and the different heights of the respective electronic components. Figure 40.21 shows a 3D color-encoded image of a PCB from a cell phone taken with the setup of Fig. 40.20. The estimated height resolution is ≤500 μm. The gained 2D *and* 3D data are fused to obtain a comprehensive digital representation of the PCB.

In the first step, a series of raster scans of a complete PCB from a cell phone was performed with Q-switched laser pulses at a fixed step size in *x*- and *y*-directions of
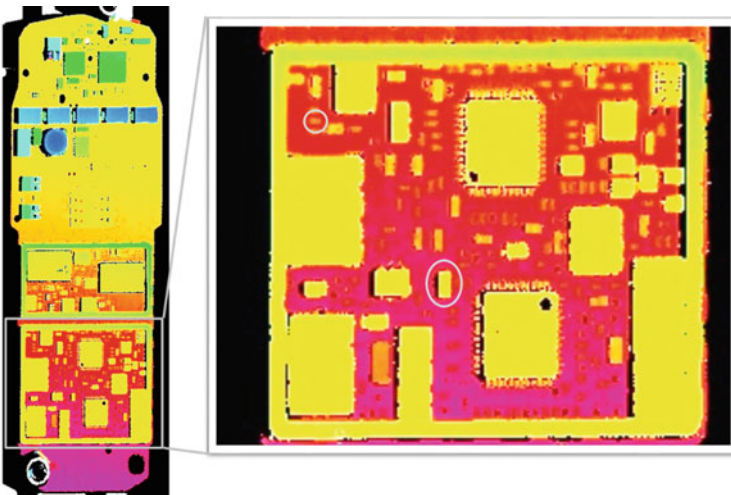

Fig. 40.21 3D image of the PCB of a cell phone; heights are color-coded. Left: overall view of the PCB; right: enlarged section of the rectangle marked on the left image. Markings (white circle and ellipse) show SMD components with the dimensions $1 \times 0.5 \times 0.5$ mm^3, $2 \times 1.5 \times 1.2$ mm^3, respectively

2 mm in order to get an overview of where to find electronic components containing, e.g., tantalum. Figure 40.22 shows a series of such scans with false color presentations of the elemental signals of tantalum and copper (arbitrary units). The first raster scan—here denoted as "depth = 1"—already reveals some positions where significant tantalum emission signals occur. Copper signals are visible at much more locations; they are simply a consequence of the copper layers of the PCB. By repetition of the raster scans, the laser ablation proceeds and reaches deeper regions. At the fifth and tenth raster scan (depth = 5 and 10), even more locations become visible with a clear tantalum signal. Finally, the chemical images are overlayed with the color photograph of the PCB taken prior to the LIBS measurements—see bottom, right of Fig. 40.22—which allows to allocate the dimensions of the respective electronic components comprising the valuable target element.
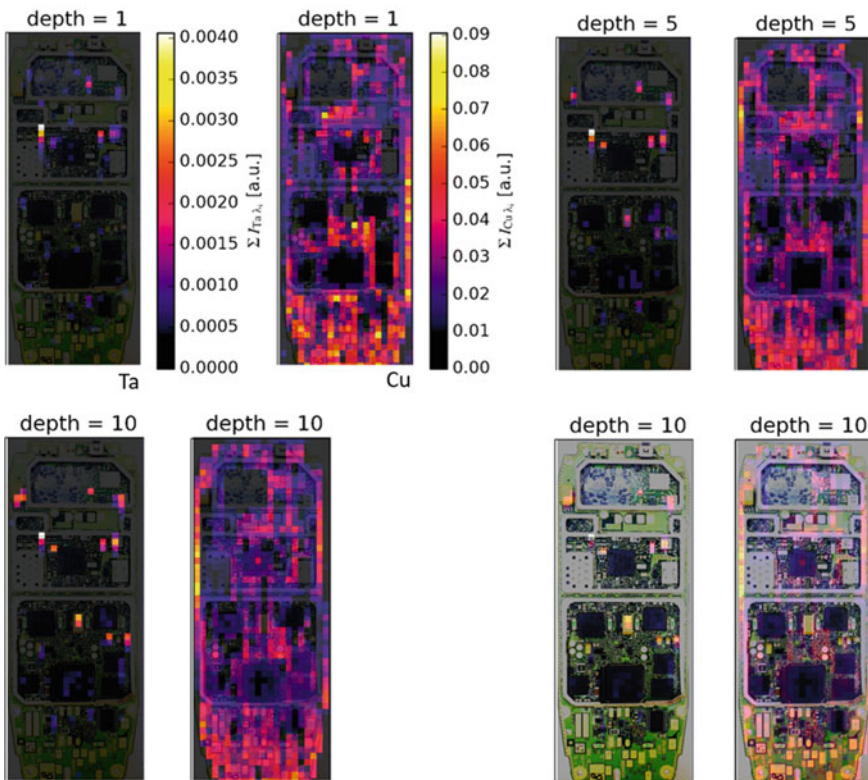

Fig. 40.22 LIBS raster scans with a step size of 2 mm of a complete PCB from a cell phone. Top, left: tantalum and copper mappings gained with a single laser pulse at each measuring position (here called "depth 1"). Top, right: tantalum and copper mappings for the fifth scan with the same raster. Bottom, left: tantalum and copper map for the 10th scan. Bottom, right: overlay presentation of the 10th raster scans with a color photo of the original PCB
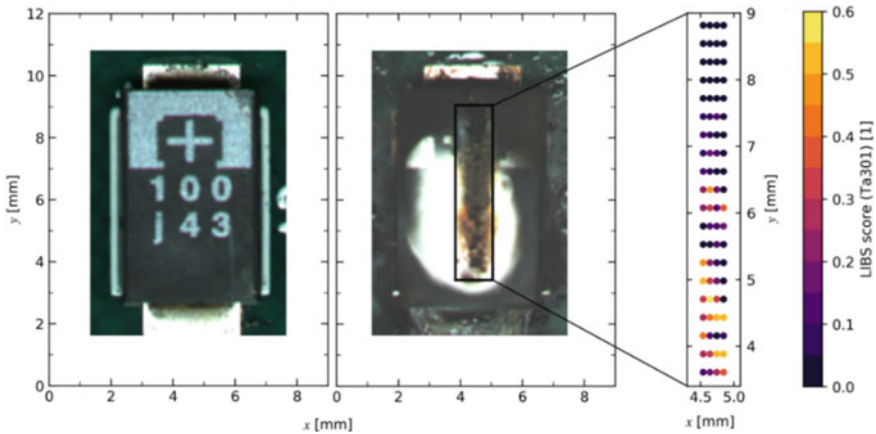
Fig. 40.23 Left: Picture of a SMD tantalum capacitor. The plus sign shows the position of the anode. Center: Picture of the same component after local penetration of the housing with laser ablation pulses; the result is a trench parallel to the longitudinal axis of the component (*y*-axis). Right: LIBS scores for tantalum in a raster scan of 20 × 4 measurement points within the trench. The rightmost color scale shows the respective values of the LIBS score in the range from 0 to 0.6

Besides global raster scans, local scans within an electronic component were studied. Figure 40.23 illustrates the individual phases of such a measurement. The left picture shows a SMD component (package size $7.3 \times 4.3 \times 2.0$ mm^3)—a tantalum capacitor—as a selected electronic component. The picture in the middle shows this component after penetrating the housing by a linear raster scan of laser ablation pulses. Finally, within the trench created, laser measuring pulses are irradiated to analyze the exposed inner material.

The figure on the right shows the determined LIBS scores for the element tantalum for a measuring grid with 20 × 4 measuring points (step size $\Delta y = 270$ µm, $\Delta x = 100$ µm; measuring time per measuring point: 0.5 s, number of spectra per spot: 50). The LIBS score is a semi-quantitative dimensionless measure of the content of a target analyte in an inhomogeneous measuring object based on reference measurements of sets of homogeneous high-content and zero-content samples. In the lower part of the graph, i.e., for coordinates 3.6 mm < *y* < 6.3 mm, the LIBS scores reach values of up to 0.6. The observed asymmetric distribution of the tantalum pentoxide dielectric within the SMD capacitor is consistent with the results of measurements on longitudinal sections of such capacitors, which were carried out with SEM–EDX (cf. Figure 40.19). These show that the dielectric only partially fills the volume of the component and that its center of gravity is shifted toward the cathode (which is located at the bottom edge of the component in Fig. 40.23, left). The volume fraction filled by the dielectric varies strongly depending on the electronic properties of the component. Together with the measured volume of the electronic component (based on the 2D and 3D images), the LIBS scores provide an assessment basis to

classify the composition of the component and to decide whether a dismantling of that component is meaningful.

Figure 40.24 shows the LIBS system in its configuration for integration in an inverse production line (Noll and Fricke-Begemann 2015). All components of the setup shown in Fig. 40.20 are built into a closed housing to enable operation as a laser class 1 system.

The lid shown in Fig. 40.24 (LD) is used only for manual loading or taking out of measuring objects. For the LIBS system integrated into the inverse production line, the loading and unloading are executed automatically by a manipulator system (LD is removed for this operation mode).

The scanning LIBS system was integrated into an inverse production pilot line (www.ADIR.eu; Noll et al. 2020). In field test campaigns, 1080 items of cell phones and 816 PCBs from servers were automatically processed yielding, e.g., total masses of extracted tantalum capacitors of 6675 g and integrated circuits of 1286 g. In the case of Ta, 97.7% were recovered from the fraction of capacitors. The gold recovery rate achieved was over 98%.

Fig. 40.24 Scanning LIBS setup with 2D-, 3D-geometry measurements. EC is electric cabinet with supply for scanner, axes, and control electronics; CP control panel; CC control computer, laser cooler, laser power supply; SP multi-CCD spectrometer; LD lid to be opened to load the drawer (translation stage); DW drawer to charge the measuring objects; MC measuring cabinet with 2D, 3D cameras, scanner, laser source; SL signal light; HMI touch screen; WN observation window according to laser safety requirements
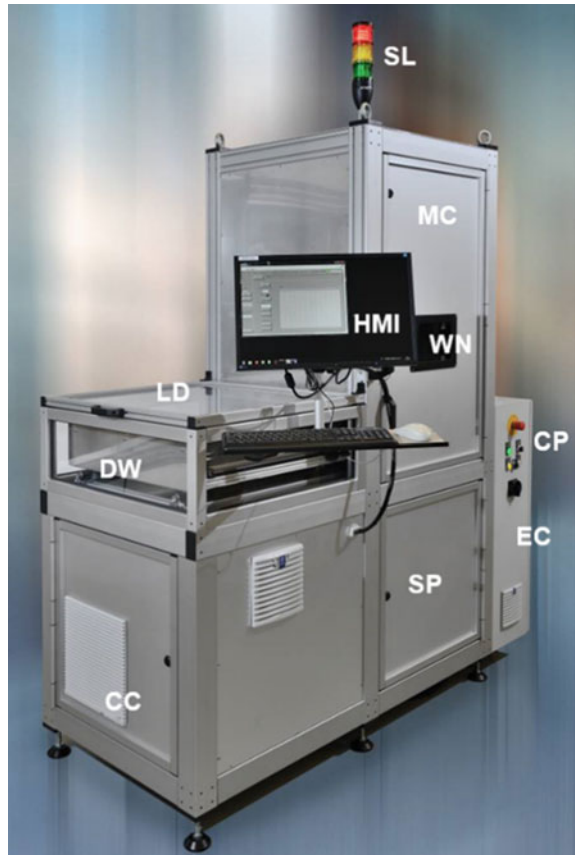
40.3.5   Compact LIBS Analyzers

A reduction of the working distance to a few centimeters allows reducing significantly the laser pulse energy to generate a LIBS plasma (Noll et al. 2018). Instead of hundreds of millijoules as in most cases applied for LIBS, pulse energies in the range of a few millijoule or even less are sufficient. From a scientific point of view, the question is to which extent the pulse energy can be further reduced while still allowing to gain reliable analytic information. The small laser pulse energies imply that only small total ablated masses are transferred to the plasma state. At the same time, the short focusing distance enlarges the susceptibility to variations of the working distance or the microtopology of the surface of the measuring object studied.

Reduced laser pulse energies and average laser radiant fluxes allow for a strongly reduced size of a LIBS apparatus and thus open the possibility of mobile or handheld LIBS analyzers. These were studied already more than fifteen years ago for environmental and industrial applications (Yamamoto et al. 1996; Hilbk-Kortenbruck et al. 2002). Reviews from 2014 and 2021 give an overview of the situation covering person-transportable LIBS devices (Rakovský et al. 2014; Senesi et al. 2021). Studies showed that with multivariate spectral data evaluation, an analytical performance of mobile LIBS can be achieved being even better than that of mobile X-ray fluorescence (XRF) instruments as demonstrated for analytes in a steel and aluminum matrix (Scharun et al. 2013).

Figure 40.25 shows a schematic setup of a handheld LIBS system. The beam of a diode-pumped solid-state laser is focused onto a measuring object which is brought into close contact with the tip of the instrument. The front opening is closed by the measuring object to enable a defined gas atmosphere in the measuring cavity and to assure laser safety. The emission of the laser-induced plasma is guided to one or several spectrometers covering different spectral ranges with spectral resolving power adapted to the respective analytical task. A display unit shows the measuring results for the user and an electronics controls all sub-systems. The electrical power supply is provided by a rechargeable battery.

For the analysis of light metals in a steel matrix, the analytical performance of handheld LIBS systems does so far not achieve that of stationary laboratory instruments but it is approaching useful features for onsite measurements. In 2019, a limit of detection (LOD, 3-sigma criterion) of 34 µg/g was shown for the first time for carbon with a compact setup suited for handheld LIBS units (Sturm et al. 2019). Figure 40.26 shows a similar setup comprising the laser source, a miniaturized VUV spectrometer (vacuum ultraviolet), and a beam guiding optics.

The miniature spectrometer and the Nd:YAG laser were designed and assembled at Fraunhofer ILT with the target to be useful for handheld LIBS. Emphasis was placed on compact size and enabling low-level detection of carbon (C) in steel. The 808-nm single-emitter pump diode is triggered with a repetition rate of 1 kHz and the pump pulses are fiber-coupled to the rear mirror of the laser with a Cr:YAG crystal-based passive Q-switch. The energy and duration of the laser pulses are $Q \approx$ 0.6 mJ, and $\tau_\mathrm{p} \approx 5$ ns (FWHM), respectively. The measurement is repeated at 5 or

Fig. 40.25 Schematic setup of a handheld LIBS device for chemical analysis. GS is gas supply with inert gas, VCSEL vertical cavity surface emitting laser, SSL VCSEL-pumped solid-state laser; SP1, SP2 spectrometer optics; OP optics module for beam guidance, deflection of the laser beam and transmission of the received radiation, MC measuring cavity with gas flow, MO measuring object, EC electronics, RB rechargeable battery, DS display
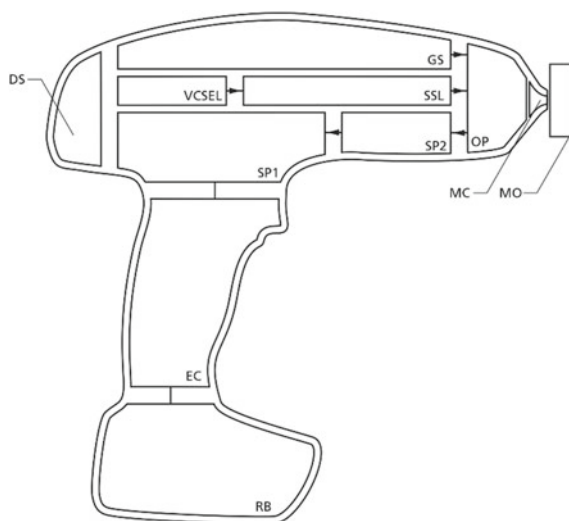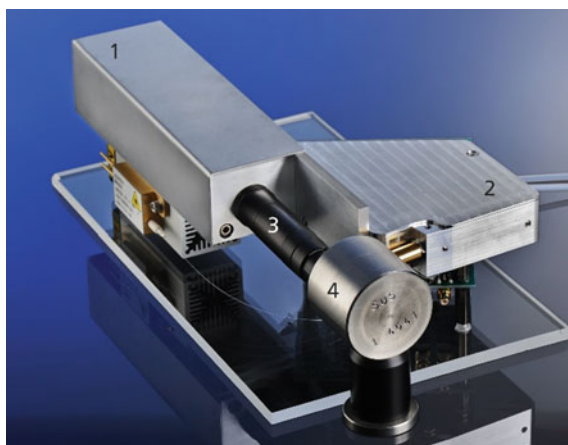

Fig. 40.26 Compact LIBS setup for a handheld system. 1 laser source, 2 VUV spectrometer, 3 beam guiding optics, and 4 sample. The dimensions of the spectrometer are $110 \times 80 \times 21$ mm^3

10 spots after shifting the sample laterally at the mechanical stop. The net duration of the laser bursts is therefore 5×0.14 s $= 0.7$ s, or 10×0.14 s $= 1.4$ s, respectively.

For low C measurements and LOD determination, 15 certified reference materials (CRM) were used (Sturm et al. 2019). Figures 40.27 and 40.28 show carbon calibration curves in different mass fraction ranges (Sturm et al. 2019). Coefficients of determination higher than 0.96 are achieved.

Figure 40.29 shows a calibration curve for chromium. On the ordinate, the ratio of the integrated line intensity of Cr II at 206.16 nm to the intensity of the matrix line of Fe II at 193.18 nm is shown. The coefficient of determination is greater than 0.99.

Fig. 40.27 Calibration curve for carbon in the range up to 830 μg/g. Intensity ratio of carbon line (193.0 nm) to iron reference line (193.2 nm) as a function of the mass fraction of carbon. R^2 coefficient of determination, CRM certified reference material, SUS setting-up samples (Sturm et al. 2019)
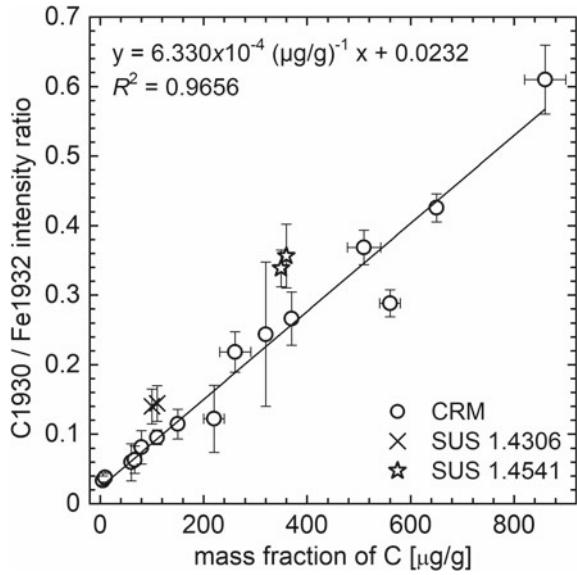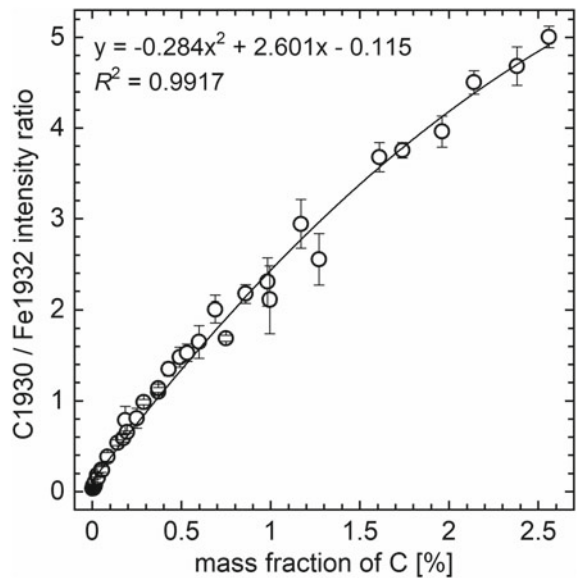
$$y = 6.330 \times 10^{-4} \, (\mu g/g)^{-1} \, x + 0.0232$$
$$R^2 = 0.9656$$

C1930 / Fe1932 intensity ratio

mass fraction of C [μg/g]

○ CRM
× SUS 1.4306
☆ SUS 1.4541

Fig. 40.28 Calibration curve for carbon in the range up to 2.5% (Sturm et al. 2019)

$$y = -0.284x^2 + 2.601x - 0.115$$
$$R^2 = 0.9917$$

C1930 / Fe1932 intensity ratio

mass fraction of C [%]

One important steel application for handheld LIBS is the separation of the widely used stainless steel grades 304 and 304L, also known as 1.4301 and 1.4307. Their compositions differ only by carbon with a standard specification of < 0.08% for 304, and < 0.03% for the low-carbon version 304L, but their properties change significantly and they have to be clearly identified. In Fig. 40.27, the measured values

Fig. 40.29 Calibration
curve for chromium in the
range up to 7.5% (Sturm
et al. 2019)
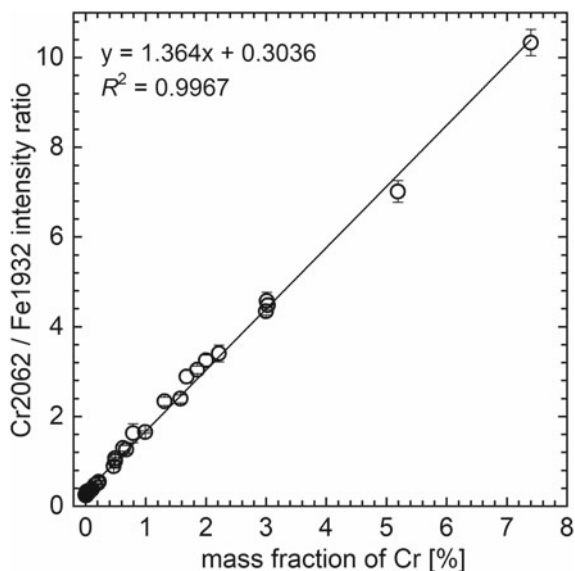
of two SUS samples of stainless steel with 0.01% C and 0.035% C are added. The
mass fractions are the guiding values by the SUS supplier. The standard specifications
for the steel types 1.4306 and 1.4541 are < 0.03% C, and <0.08% C, and therefore
identical to 304L and 304. The samples are measured twice and the data show the
clear separation capability for these stainless steel grades based on their low-level
carbon content (Sturm et al. 2019).

References

Balzer H, Höhne M, Sturm V, Noll R (2005) Online thickness measurement and depth profiling
of zinc coated sheet steel by laser-induced breakdown spectroscopy. Spectrochim Acta Part B
60:1172–1178

Balzer H, Höhne M, Noll R, Sturm V (2006) New approach to online monitoring of the Al depth
profile of the hot-dip galvanised sheet steel using LIBS. Anal Bioanal Chem 385:225–233

Bette H, Noll R, Müller G, Jansen H-W, Nazikkol Ç, Mittelstädt H (2005) High-speed scanning
laser-induced breakdown spectroscopy at 1000 Hz with single pulse evaluation for the detection
of inclusions in steel. J Laser Appl 17:183–190

Bette H, Noll R (2004) High-speed laser-induced breakdown spectrometry for scanning microanal-
ysis. J Phys D: Appl Phys 37:1281–1288

Boué-Bigne F (2007) Analysis of oxide inclusions in steel by fast laser-induced breakdown
spectroscopy scanning: an approach to quantification. Appl Spectrosc 61:333–337

Boué-Bigne F (2008) Laser-induced breakdown spectroscopy applications in the steel industry:
rapid analysis of segregation and decarburization. Spectrochimica Acta Part B 63:1122–1129

Caranza J, Fisher BB, Yoder G, Hahn D (2001) On-line analysis of ambient air aerosols using
laser-induced breakdown spectroscopy. Spectrochim Acta Part B 56:851–864

Carslaw H, Jaeger J (1959) Conduction of heat in solids, 2nd edn. Oxford University Press, Oxford

Donges A, Noll R (2015) Laser measurement technology—fundamentals and applications. Springer, Heidelberg, p 422. ISBN 978-3-662-43633-2

European Standard DIN EN ISO 11146-1 (2005) Lasers and laser-related equipment—test methods for laser beam widths, divergence angles and beam propagation ratios—part 1: stigmatic and simple astigmatic beams

EU project (2018–2020) Next generation urban mining—automated disassembly, separation and recovery of valuable materials from electronic equipment, 2018–2020. Grant Agreement no. 680449, www.ADIR.eu

Gaft M, Nagli L, Groisman Y (2014) Industrial online raw materials analyzer based on laser-induced breakdown spectroscopy. Appl Spectrosc 68:1004–1015

Geisler M, Connemann S, Fricke-Begemann C (2019) Sensorgestützte Sortierung von legierten Metallschrotten. In: Thiel S, Holm O, Thomé-Kozmiensky E, Goldmann D, Friedrich B (eds) Recycling und Rohstoffe. Thomé-Kozmiensky Verlag GmbH, Neuruppin, Germany, pp 567–579. ISBN 978-3-944310-46-6

Hahn D, Lunden M (2000) Detection and analysis of aerosol particles by laser-induced breakdown spectroscopy. Aerosol Sci Techn 33:30–48

Hilbk-Kortenbruck F, Höhne M, Noll R, Freit M, Joosten J, Falk H (2002) Compact measuring system for laser emission spectrometry of coated and uncoated metals. Anwendertreffen Röntgenfluoreszenz- und Funkenemissionsspektrometrie. Proc 9: 59–69

Hudson S, Craparo J, De Saro R, Apelian D (2016) Laser-induced breakdown spectroscopy: a new tool for real time melt cognition. La Metallurgia Italiana 6:5–8

https://lweb.cfa.harvard.edu/amp/ampdata/kurucz23/sekur.html

http://physics.nist.gov/cgi-bin/AtData/main_asd

Kraushaar M, Noll R, Schmitz H-U (2003) Slag analysis with laser-induced breakdown spectrometry. Appl Spectrosc 57:1282–1287

Liu K, Tian D, Li C, Li Y, Yang G, Ding Y (2019) A review of laser-induced breakdown spectroscopy for plastic analysis. Trends Anal Chem 110:327–334

Martin M, Allman S, Brice D, Martin R, Andre N (2012) Exploring laser-induced breakdown spectroscopy for nuclear materials analysis and in-situ applications. Spectrochim Acta Part B 74–75:177–183

Meinhardt C, Sturm V, Fleige R, Fricke-Begemann C, Noll R (2016) Laser-induced breakdown spectroscopy of scaled steel samples taken from continuous casting blooms. Spectrochim Acta, Part B 123:171–178

Meinhardt C, Noll R, Fricke-Begemann C (2021) Crosstalk effects of surface layers of metallic samples on laser-induced breakdown spectroscopy measurements. J Anal Spectrom. https://doi.org/10.1039/D0JA00445F

Mönch I, Noll R, Buchholz R, Worringer J (2000) Laser identifies steel grades. Stainless Steel World 12(4):25–29

Noll R (2012) Laser-induced breakdown spectroscopy—fundamentals and applications. Springer, Heidelberg, p 543. ISBN 978-3-642-20667-2

Noll R, Fricke-Begemann C, Brunk M, Connemann S, Meinhardt C, Scharun M, Sturm V, Makowe J, Gehlen C (2014) Laser-induced breakdown spectroscopy expands into industrial applications. Spectrochim Acta Part B 93:41–51

Noll R, Fricke-Begemann C, Connemann S, Meinhardt C, Sturm V (2018) LIBS analyses for industrial applications—an overview of developments from 2014 to 2018. J Anal Spectrom 33:945–956

Noll R, Bette H, Brysch A, Kraushaar M, Mönch I, Peter L, Sturm V (2001) Laser-induced breakdown spectrometry—applications for production control and quality assurance in the steel industry. Spectrochim Acta, Part B 56:637–649

Noll R, Sturm V, Vrenegor J (2005) Verfahren und Vorrichtung zur Analyse fester Materialien mit der Laser-Emissionsspektrometrie. Patent DE 103 61 727

Noll R, Bergmann K, Fricke-Begemann C, Schreckenberg F (2020) Inverse Produktion für nachhaltige Wertstoffkreisläufe—aktuelle Entwicklungen zur automatisierten Demontage und Entstückung von Elektronikplatinen. Chem Ing Techn 92:360–367

Noll R, Fricke-Begemann C (2015) Verfahren und Vorrichtung zur automatisierten Identifikation, Demontage, Vereinzelung und Sortierung von Komponenten elektronischer Baugruppen und Geräte für das werkstoffliche Recycling mit Laserstrahlung. Patent DE 10 2011 012 592

Panne U, Neuhauser R, Theisen M, Fink H, Niessner R (2001) Analysis of heavy metal aerosols on filters by laser-induced plasma spectroscopy. Spectrochim Acta Part B 56:839–850

Peter L, Sturm V, Noll R (2003) Liquid steel analysis with laser-induced breakdown spectrometry in the vacuum ultraviolet. Appl Optics 42:6199–6204

Project funded by BMBF, r+Impuls, Innovative Technologien für Ressourceneffizienz, PLUS—Pilotanlage zur lasergestützten Sortierung von Sonderlegierungen, 033R181, 1.1.2017–31.12.2019

Rakovský J, Čermák P, Musset O, Veis P (2014) A review of the developments of portable laser-induced breakdown spectroscopy and its applications. Spectrochim Acta, Part B 101:269–287

Real-time bath chemistry monitoring of galvanizing lines, product: galvalibs 2.0. https://tecnar.com/galvalibs-2-0/

Rodriguez-Celis E, Gornushkin I, Heitmann U, Almirall J, Smith B, Winefordner J, Omenetto N (2008) Laser-induced breakdown spectroscopy as a tool for discrimination of glass for forensic appications. Anal Bioanal Chem 391:1961–1968

Sattmann R, Mönch I, Krause H, Noll R, Couris S, Hatziapostolou A, Mavromanolakis A, Fotakis C, Larrauri E, Miguel R (1998) Laser-induced breakdown spectroscopy for polymer identification. Appl Spectrosc 52:456–461

Sallé B, Mauchien P, Maurice S (2007) Laser-induced breakdown spectroscopy in open-path configuration for the analysis of distant objects. Spectrochim Acta Part B 62:739–768

Scharun M, Fricke-Begemann C, Noll R (2013) Laser-induced breakdown spectroscopy with multi-kHz fibre laser for mobile metal analysis tasks—a comparison of different analysis methods and with a mobile spark-discharge optical emission spectroscopy apparatus. Spectrochim Acta, Part B 87:198–207

Senesi G, Harmon R, Hark R (2021) Field-portable and handheld laser-induced breakdown spectroscopy: historical review, current status and future prospects. Spectrochim Acta, Part B 175:106013

Sturm V, Erben B, Fleige R, Wirz W (2019) Carbon analysis of steel using compact spectrometer and passively Q-switched laser for laser-induced breakdown spectroscopy. Opt Express 27:36855–36863

Sturm V, Meinhardt C, Fleige R, Fricke-Begemann C, Eisbach J (2017) Fast identification of steel bloom composition at a rolling mill by laser-induced breakdown spectrocopy. Spectrochim Acta, Part B 136:66–72

Sturm V, Schmitz H-U, Reuter T, Fleige R, Noll R (2008) Fast vacuum slag analysis in a steel works by laser-induced breakdown spectroscopy. Spectrochimica Acta Part B 63:1167–1170

Sturm V, Fleige R, de Kanter M, Leitner R, Pilz K, Fischer D, Hubmer G, Noll R (2014) Laser-induced breakdown spectroscopy for 24/7 automatic liquid slag analysis at a steel works. Anal Chem 86:9687–9692

Stepputat M, Noll R (2003) On-line detection of heavy metals and brominated flame retardants in technical polymers with laser-induced breakdown spectrometry. Appl Optics 42:6210–6220

Sun L, Yua H, Cong Z, Xina Y, Li Y, Qi L (2015) In situ analysis of steel melt by double-pulse laser-induced breakdown spectroscopy with a Cassegrain telescope. Spectrochim Acta Part B 112:40–48

Sun L, Yu H, Cong Z, Lu H, Cao B, Zeng P, Dong W, Li Y (2018) Applications of laser-induced breakdown spectroscopy in the aluminum electrolysis industry. Spectrochim Acta Part B 142:29–36

Teklemariam T, Gotera J (2019) Application of laser-induced breakdown spectroscopy in food container glass discrimination. Spectrochim Acta Part B 155:34–43

Vrenegor J, Sturm V, Noll R, Hemmerlin M, Thurmann U, Flock J (2006) Preparation and analysis of production control samples by a two-step laser method. In: Angeli J (ed) 7th international workshop progress in analytical chemistry in the steel and metal industries, Glückauf GmbH, Essen, pp 81–86

Werheit P, Fricke-Begemann C, Gesing M, Noll R (2011) Fast single piece identification with a 3D scanning LIBS for aluminium cast and wrought alloys recycling. J Anal Spectrom 26:2166–2174

Yamamoto K, Cremers D, Ferris M, Foster L (1996) Detection of metals in the environment using a portable laser-induced breakdown spectroscopy instrument. Appl Spectrosc 50:222–233

Zaidel' AN, Prokov'ev VK, Raiskii SM, Slavnyi VA, Shreider EY (1970) Tables of spectral lines. Ifi/Plenum, New York

Chapter 41
Light Scattering for In-Line Process Monitoring

Check for
updates

Christoph Janzen and Reinhard Noll

41.1 Introduction

In general, light scattering comprises any kind of interaction of light with matter, in which the light is not absorbed permanently. This definition includes the effects of reflection and refraction. In a narrower sense, the term light scattering deals only with interaction processes with microscopic particles, e.g. atoms or dust particles.

The scattering of light appears in a great variety. Therefore, we distinguish different types of scattering: elastic scattering, inelastic scattering, coherent scattering, and incoherent scattering. In the case of elastic scattering, the wavelength and frequency of the scattered light remain—unlike inelastic scattering—conserved. Coherent or induced scattering is an elastic scattering, in which between the incident and scattered wave a defined phase relationship exists. If not, the scattering is incoherent or spontaneous.

The field of light scattering is very extensive. We therefore restrict our considerations to the case of scattering at small particles. Rayleigh scattering occurs when the particle diameter $2a$ is small compared to the wavelength λ of the irradiated light. When a particle interacts with the electric field of a linearly polarized light wave, it will see an approximately homogeneous alternating electric field because of $2a << \lambda$. The scattering particle is polarized dynamically by the alternating electric field of the light wave. It becomes a Hertzian dipole, which oscillates at the frequency of the incident light. The dipole axis is determined by the direction of polarization of the incident wave. The particle emits, as each oscillating dipole, electromagnetic waves. The frequency of the emitted waves coincides with the frequency of the oscillating dipole and therefore with the frequency of the incident light. Hence, Rayleigh scattering is an elastic scattering. The intensity of the scattered light increases with the fourth power of the reciprocal wavelength. Blue light is, therefore, scattered more

C. Janzen · R. Noll (✉)
Fraunhofer ILT, Aachen, Germany
e-mail: noll.reinhard@arcor.de

© Springer-Verlag GmbH Germany, part of Springer Nature 2024 869
R. Poprawe et al. (eds.), *Tailored Light 2*, RWTHedition,
https://doi.org/10.1007/978-3-030-98323-9_41

intensely than red. This is the reason why the sky looks blue on a clear day. The dipole radiation is predominantly emitted perpendicularly to the dipole axis. No radiation is emitted in the direction of the dipole axis. The emission characteristic is independent of the geometry of the scattering particle. The scattered intensity emitted by the dipole is described by (see e.g. Donges and Noll 2015)

$$I_{\text{sc}} \propto \frac{\alpha^2}{\lambda_{\text{in}}^4} \frac{\sin^2 \phi}{R^2} I_{\text{in}} \tag{41.1}$$

where ϕ is the angle between the viewing direction and the dipole axis, λ_{in} the incident wavelength, α the polarizability of the scattering particle, I_{in} the intensity of the incident wave, and R the distance from the dipole. For a small particle, all individual waves scattered by the atoms/molecules inside the particle are superimposed approximately in-phase, hence the scattered intensity scales with the particle diameter as follows: $I_{\text{sc}} \propto (2a)^6$.

In this chapter, we present laser light scattering methods to determine the size distributions of small particles suspended in fluids. Measuring particle sizes and size distributions in colloidal suspensions is of great importance in many technical processes. These processes are necessary for the production of polymers, pharmaceutical active ingredients, and additives for the food, cosmetic, and paint industries (Black et al. 1996). For better process monitoring of these technical processes, online measurements of the particle size without time-consuming sampling are needed.

Dynamic light scattering (DLS) is one of the standard methods for measuring particle sizes in fluids and has been established for many years (Pecora 2000). This method is based on the examination of random particle movement due to constant Brownian motion. The collision of particles with surrounding liquid molecules results in a diffusional process with small particles moving faster than large particles. To monitor this diffusion, the sample is illuminated with a monochromatic laser beam. Depending on the position of the particles relative to each other, light scattered by the particles undergoes constructive or destructive interference. The resulting intensity fluctuations are detected time-resolved by a photomultiplier positioned at a certain angle to the incident light. The decay of the autocorrelation of the measured intensity is correlated to the translational diffusion coefficient, which in turn is used to calculate the hydrodynamic radius of the particles using the Stokes–Einstein equation.

For accurate determination of the diffusion coefficient, multiple light scattering has to be avoided. In concentrated suspensions, which are typical in industrial polymer production, the incident light is scattered multiple times before it is detected, which directly influences the intensity autocorrelation. To circumvent this issue, there are different enhancements of DLS, such as two color-cross correlation (Segrè et al. 1995; Pusey 1999) and 3D cross correlation (Sinn et al. 1999).

An essential demand for industrially applicable particle sizing is the possibility of direct in-line measurements. While able to measure in concentrated suspensions, both cross-correlation DLS methods involve complex optical setups and are not suitable for in-line measurements. In contrast, fiber-optic quasi-elastic light scattering

(FOQELS) (Stieber and Richtering 1995) or fiber-optic dynamic light scattering
(FODLS) (Thomas and Dimonie 1990) methods use an immersion probe with a
simple and robust optical setup and are therefore ideally suited for in-line applica-
tions. With small penetration depths, concentrated dispersions with high solid content
up to 40 wt.-% (Stieber and Richtering 1995) can be measured (Horn et al. 2000).

In the next section, the theoretical background of dynamic light scattering is
presented leaned on a fundamental paper by Clark et al. (1970).

41.2   Principle of Dynamic Light Scattering

Brownian motion can be described by a conditional probability density given by

$$P(\vec{r}, t|0, 0) = \frac{1}{(4\pi Dt)^{3/2}} e^{-r^2/(4Dt)} \tag{41.2}$$

where $\vec{r}$ denotes the position of a particle after an elapsed time t starting at $\vec{r} = 0$
for $t = 0$, and D is the diffusion coefficient of the particle in a fluid (unit m²/
s). The exponent of the denominator contains a "3"; this is a consequence of the
three-dimensional character of the random walk. The unit of $P(\vec{r}, t|0, 0)$ is $1/m^3$,
describing a probability per volume element.

The Stokes–Einstein relation for a spherical particle of diameter $2a$ yields the
diffusion coefficient (Einstein 1956):

$$D = \frac{k_B T}{6\pi \eta a}, \tag{41.3}$$

with k_B being Boltzmann´s constant, T temperature, and η viscosity. As a numerical
example, we consider spheres with a diameter of $2a = 100$ nm, $T = 293$ K, and
viscosity of water $\eta = 0.001$ Ns/m²; with (41.3) we have $D = 4.3 \cdot 10^{-12}$ m²/s.

Figure 41.1 shows the principle setup of laser light scattering at particles dispersed
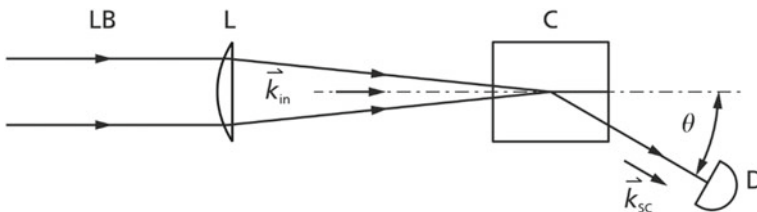in a fluid inside a cuvette.

Fig. 41.1 Principle setup for laser light scattering at particles dispersed in a fluid inside a cuvette.
LB is incident laser beam, L lens, C cuvette, D detector; $\vec{k}_{in}, \vec{k}_{sc}$ wave vectors of incident and
scattered light, and θ scattering angle

The incoming wave is described as a plane wave:

$$\vec{E}_{\text{in}} = \vec{E}_0 \exp\left(\text{i}\left(\vec{k}_{\text{in}}\vec{r} - \omega_{\text{in}}t\right)\right). \tag{41.4}$$

At the position $\vec{R}$, the detector receives the sum of the scattered fields of each particle j:

$$\vec{E}_{\text{det}}(t) = \sum_{j=1}^{N} \vec{E}_j(t) = \sum_{j=1}^{N} \vec{E}_0' \exp\left(\text{i}\left(\varphi_j(t) - \omega_{\text{in}}t\right)\right), \tag{41.5}$$

where $\vec{E}_0'$ is the electric field scattered by one of the N particles and φ_j is the time-dependent phase of the scattered light relative to a chosen origin. For Rayleigh scattering, i.e. particles being significantly smaller than the wavelength of the incident laser light ($2a \ll \lambda$), the scattered field at a distance R where the detector is placed, is described by

$$\vec{E}_0' = \frac{1}{4\pi\varepsilon_0} \vec{E}_0 \frac{\exp\left(\text{i}\vec{k}_{\text{sc}}\vec{R}\right)}{R} \left(\frac{\omega_{\text{in}}}{c}\right)^2 (\alpha - \alpha_{\text{fl}}) \sin\phi, \tag{41.6}$$

where $\vec{k}_{\text{sc}}$ is the angular wave vector of the scattered radiation, $(\alpha - \alpha_{\text{fl}})$ the difference of the polarizability of the particle and the fluid (unit: $(\text{As}\,\text{m}^2)/\text{V}$), ϕ the angle between the detection direction and the polarization direction of the incident light, and ε_0 the vacuum permittivity. Squaring the absolute value of relation (41.6) shows the known frequency and angular dependence for Rayleigh scattering (cf. relation (41.1)):

$$I_{sc} \propto \left|\vec{E}_0'\right|^2 \propto \frac{(\omega_{\text{in}})^4}{R^2} \sin^2\phi. \tag{41.7}$$

The phase $\varphi_j(t)$ of a particle j depends on its position; see Fig. 41.2. For the phase caused by the path difference of the line segments $\overline{\text{AP}}$ and $\overline{\text{OB}}$, we obtain

$$\varphi_j(t) = \frac{2\pi}{\lambda}\left(\overline{\text{AP}} - \overline{\text{OB}}\right) = \left(\vec{k}_{\text{in}} - \vec{k}_{\text{sc}}\right) \cdot \vec{r}_j \tag{41.8}$$

The difference between the wave vectors is called the scattering vector:

$$\vec{K} = \left(\vec{k}_{\text{in}} - \vec{k}_{\text{sc}}\right). \tag{41.9}$$

Figure 41.3 illustrates the calculation of the absolute value of the scattering vector:

$$K = 2k_{\text{in}}\sin(\theta/2) = \frac{4\pi}{(\lambda_{\text{in}}/n)}\sin(\theta/2) \tag{41.9a}$$
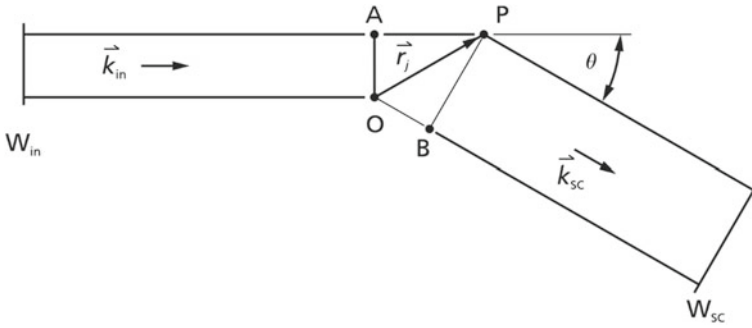
Fig. 41.2 Derivation of the optical path difference for an incident plane wave scattered at a particle at point P in relation to the origin O. W_{in} is wavefront of incident beam, W_{sc} wavefront of scattered beam, and $\vec{r}_j$ position of scattering particle with respect to the origin

Fig. 41.3 Wave vectors of incident and scattered waves and resulting scattering vector $\vec{K}$. θ scattering angle
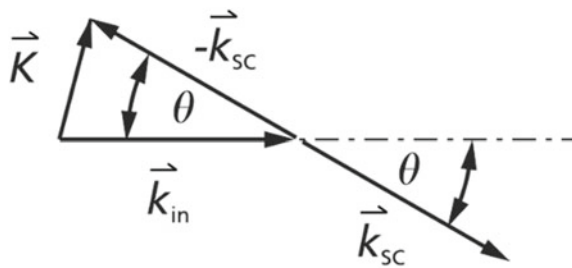
with λ_{in} being wavelength of incident radiation, and n refractive index of the fluid.

Due to the scalar product in (41.8), the phase of the wave scattered at $\vec{r}_j$ changes only if the particle moves in the $\vec{K}$-direction:

$$\varphi_j(t) = \vec{K} \cdot \vec{r}_j. \tag{41.10}$$

The correlation functions of the electric field, see Eq. (41.5), and the intensity are described by the following expressions:

$$R_{E_{det}}(\tau) = \left\langle E_{det}^*(t) \, E_{det}(t + \tau) \right\rangle, \tag{41.11}$$

$$R_{I_{det}}(\tau) = \left\langle I_{det}(t) \, I_{det}(t + \tau) \right\rangle. \tag{41.12}$$

By use of the Wiener–Khintchine theorem, the spectrum can then be calculated as follows (Hecht and Zajac 1997):

$$S_{\omega, E_{det}}(\omega) = \int_{-\infty}^{+\infty} e^{i\omega\tau} R_{E_{det}}(\tau) \, d\tau, \tag{41.13}$$

$$S_{\omega,\, I_{\text{det}}}(\omega) = \int\limits_{-\infty}^{+\infty} e^{i\omega\tau}\, R_{I_{\text{det}}}(\tau)\, \mathrm{d}\tau. \tag{41.14}$$

Inserting (41.5) in (41.11) yields

$$R_{E_{\text{det}}}(\tau) = N\left|E_0'\right|^2 e^{-i\omega_{\text{in}}\tau - DK^2|\tau|}. \tag{41.15}$$

The decay of the autocorrelation is described by the decorrelation time:

$$\tau_{\text{c}} = \frac{1}{DK^2}. \tag{41.16}$$

Let's estimate this time with a concrete approach. The mean square distance a particle j moves is

$$\langle r_j^2 \rangle = 6Dt. \tag{41.17}$$

If the phase of each scattered wave changes by about π, then we can expect that the superposition of all scattered waves changes significantly, i.e. the correlation to the previous state is lost. According to (41.10), a phase change of π corresponds to a distance in the order of

$$\left|\vec{r}_j\right| \approx \frac{\pi}{K}. \tag{41.18}$$

If we equate the square of (41.18) with (41.17), we can estimate the decorrelation time as follows:

$$\tau_{\text{c}} \approx \frac{\pi^6}{6}\frac{1}{DK^2}, \tag{41.19}$$

which reveals the same dependence with respect to D and K as we have found with relation (41.16). With (41.15) and (41.13), we obtain the spectrum of the scattered light:

$$S_{\omega,\, E_{\text{det}}}(\omega) = 2N\left|E_0'\right|^2 \frac{DK^2}{(\omega - \omega_{\text{in}})^2 + \left(DK^2\right)^2}. \tag{41.20}$$

The spectrum described by (41.20) has a Lorentzian shape centered at the incoming angular frequency ω_{in}. The half frequency width at half maximum (HWHM) is

$$\Delta f_{\text{HWHM}} = \frac{DK^2}{2\pi}. \tag{41.21}$$

To illustrate the order of magnitude of the resulting frequency width, we take the example given for (41.3) and calculate K with (41.9a), choosing $\theta = 180°$ (backscattering), $\lambda_{\text{in}} = 780$ nm, and the refractive index of water $n = 1.33$: $\Delta f_{\text{HWHM}} = 157$ Hz which corresponds to a wavelength widths of $2 \cdot 10^{-6}$ pm. Such a small value cannot be measured directly by usual optical spectrometers.

Instead of looking at correlations and spectra of electric field fluctuations, we now turn to intensities. With the electric field given by (41.5), an intensity is described by (averaging over the high optical frequencies, which cannot be directly resolved by a detector)

$$I_{\text{det}}(t) = \frac{\langle |E_{\text{det}}(t)|^2 \rangle}{Z}, \qquad (41.22)$$

with Z being wave impedance of the vacuum ($120\pi \, \Omega$). After some calculation steps, we obtain the intensity correlation function:

$$R_{I_{\text{det}}}(\tau) = \frac{N^2 |E_0'|^4}{Z^2} \left(1 + e^{-2DK^2|\tau|} \right). \qquad (41.23)$$

Inserting (41.23) in (41.14) yields the spectrum of the intensity fluctuations:

$$S_{\omega, \, I_{\text{det}}}(\omega) = \frac{N^2 |E_0'|^4}{Z^2} \left(2\pi \delta(\omega) + \frac{2(2DK^2)}{\omega^2 + (2DK^2)^2} \right). \qquad (41.24)$$

The first term in the brackets refers to the scattered light in case no particle movements exist (DC-part). The second term is again a Lorentz-shaped function, but in contrast to relation (41.20) this function is centered around $\omega = 0$. The half frequency width at half maximum is for (41.24)

$$\Delta f_{\text{HWHM}} = \frac{DK^2}{\pi}. \qquad (41.25)$$

Relation (41.25) describes a width which is proportional to $\Delta f_{\text{HWHM}} \propto D / \lambda_{\text{in}}^2$. That is a dependence which we would expect from a Doppler shift of light scattered at a particle moving with a velocity v:

$$\Delta f_{\text{Doppler}} \propto \frac{v}{\lambda_{\text{in}}}. \qquad (41.26)$$

We estimate the velocity by (41.17) and the decorrelation time (41.16) as follows:

$$v \approx \frac{\sqrt{6D\tau_{\text{c}}}}{\tau_{\text{c}}} = \sqrt{\frac{6D}{\tau_{\text{c}}}} = \sqrt{6}DK. \qquad (41.27)$$

With (41.9a), we have

$$v \propto \frac{D}{\lambda_{\text{in}}}. \tag{41.28}$$

Inserting (41.28) in (41.26) then yields finally

$$\Delta f_{\text{Doppler}} \propto \frac{D}{\lambda_{\text{in}}^2}. \tag{41.29}$$

This dependence is exactly that which we have found in (41.25). So the frequency broadening deduced via calculations of the autocorrelation of intensities and the Wiener-Khintchine theorem lead to a result which basically can be interpreted as a Doppler broadening of the incident laser beam scattered by particles executing Brownian motions.

The quantity DK^2 is called characteristic frequency ω_0 (Berne and Pecora 1976). With (41.3) and (41.9a), we have

$$\omega_0 = DK^2 = \frac{8\pi}{3} \frac{k_{\text{B}}T}{\eta a} \frac{n^2}{\lambda_{\text{in}}^2} \sin^2(\theta/2). \tag{41.30}$$

Introducing the average scattered optical intensity $\langle I_{\text{sc}} \rangle$, we rewrite (41.24) without the DC-part as follows:

$$S_{\omega, I_{\text{det}}}^{\text{ho}}(\omega) = \langle I_{\text{sc}} \rangle^2 \frac{2\omega_0}{\omega^2 + (2\omega_0)^2}. \tag{41.31}$$

So far, we have only considered the detection of the interferences of the light waves scattered at the particles; see (41.5). This approach is called homodyne detection (see index "ho" in (41.31)). Figure 41.4a illustrates this concept. For heterodyne detection, a part of the incident laser beam is guided to the detector and superimposed with the light waves scattered by the particles; see Fig. 41.4b (DIN ISO 22412 2018). This reference laser beam has an unshifted frequency. If we call its intensity I_r and follow a corresponding derivation as for (41.32), we obtain the spectrum in the heterodyne mode:

$$S_{\omega, I_{\text{det}}}^{\text{ht}}(\omega) = I_r \langle I_{\text{sc}} \rangle \frac{2\omega_0}{\omega^2 + (\omega_0)^2}. \tag{41.32}$$

Comparing relations (41.32) and (41.31), we see that the frequency width for the heterodyne mode is just half of that of the homodyne mode. This is immediately clear if we consider that the reference laser beam with its unshifted frequency has on average just half the beat frequency with the scattered Doppler-shifted waves emanating from the scattering particles as these waves have among themselves.
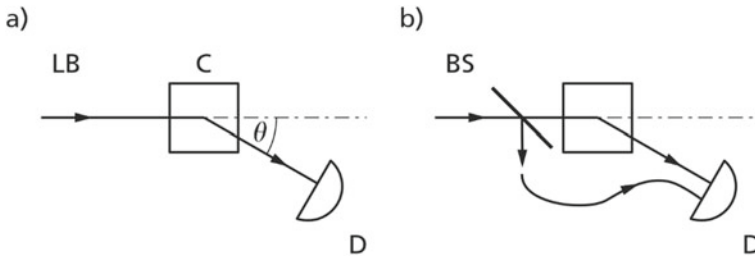
Fig. 41.4 Optical setups for dynamic light scattering. **a** homodyne detection; **b** heterodyne detection. LB is laser beam, C cell with fluid and suspended particles, and BS beam splitter

Since the radiant flux of the reference laser beam can be increased to a large extent, high signal levels of the interfering signals to be detected can be achieved which allow the use of silicon photodiode detectors (instead of photomultiplier tubes). Moreover, the measuring range with respect to particle diameters can be extended to smaller particles which have low optical scattering cross sections.

Figure 41.5 shows exemplarily normalized spectra $S_{\omega, I_{det}}^{ht}(\omega)$ according to (41.32). The following data is taken: $T = 293$ K, $\eta = 10^{-3}$ Ns/m^2 (water at 293 K), $n = 1.33$, $\lambda_{in} = 780$ nm, $\theta = 180°$ (backscattering; cf. Figure 41.1), and $a = 5$, 50, or 500 nm.

For a logarithmic transform of (41.32), we introduce dimensionless variables as follows:

$$\tilde{\omega} = \omega/\text{rad s}^{-1}, \ \tilde{\omega}_0 = \omega_0/\text{rad s}^{-1}. \tag{41.33}$$

Fig. 41.5 Normalized spectra of detected signals for heterodyne mode according to relation (41.32). Parameter is the radius of particles suspended in water. The scattering angle amounts to 180° corresponding to a backscattering setup
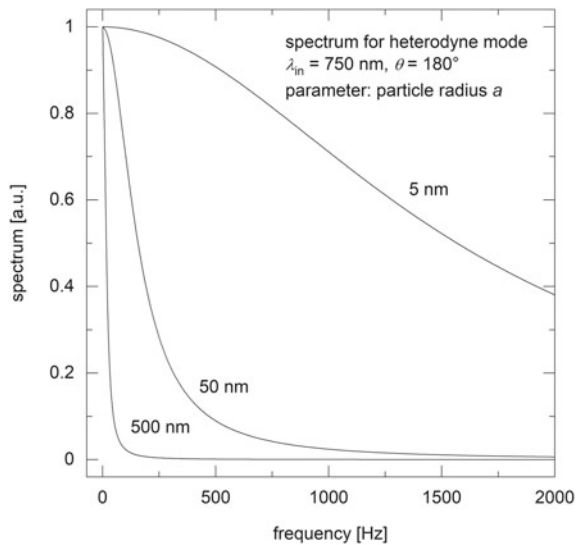
We can rewrite (41.32) as a numerical value equation with respect to the angular frequencies:

$$S^{\text{ht}}_{\tilde{\omega}, I_{\text{det}}} (\omega) = I_r \langle I_{\text{sc}} \rangle \frac{2\tilde{\omega}_0}{\tilde{\omega}^2 + (\tilde{\omega}_0)^2} \text{rad}^{-1}\text{s}. \tag{41.32a}$$

We introduce as new variables:

$$x = \ln \tilde{\omega}, \ x_0 = \ln \tilde{\omega}_0. \tag{41.34}$$

The differential of x holds

$$\text{d}x = \frac{\text{d}\tilde{\omega}}{\tilde{\omega}}. \tag{41.35}$$
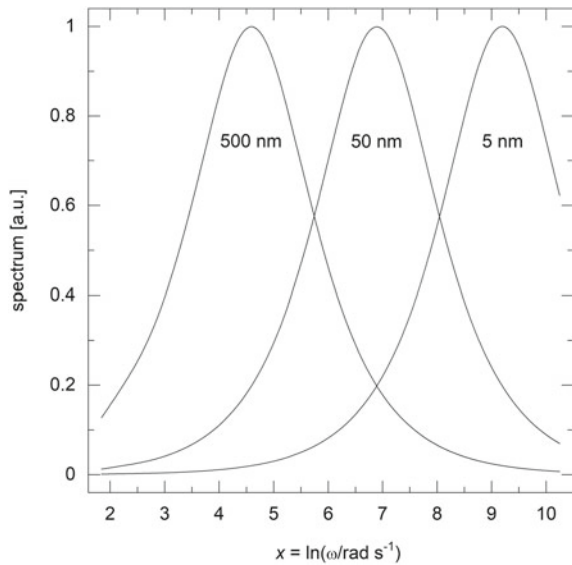
With the relation:

$$S^{\text{ht}}_{\tilde{\omega}, I_{\text{det}}} \text{d}\tilde{\omega} = S^{\text{ht}}_{x, I_{\text{det}}} \text{d}x,$$

and (41.32a), (41.33), and (41.34), we obtain

$$S^{\text{ht}}_{x, I_{\text{det}}} (x) = I_r \langle I_{\text{sc}} \rangle \frac{2}{e^{x-x_0} + e^{-(x-x_0)}} \text{rad}^{-1}\text{s}. \tag{41.36}$$

Figure 41.6 shows normalized spectra as a function of x for the examples shown in Fig. 41.5.

Fig. 41.6 Logarithmic transformed normalized spectra of Fig. 41.5 using Eq. (41.36)

For a size distribution of particles, such functions are weighted and superimposed. The resulting spectrum has to be deconvoluted to gain the size distribution and to determine, e.g. the D50 parameter giving the value of the particle diameter at 50% in the cumulative distribution.

41.3   In-Line DLS-Sensor

From the various DLS setups, the fiber-optic DLS probe (FODLS) (Auweter and Horn 1985; Wiese and Horn 1991) which can be immersed in a fluid with dispersed particles is principally best suited for in-line measuring tasks. Figure 41.7 shows the basic setup (Wiese and Horn 1991). The incident laser beam is guided via fiber optics to the tip of the probe. The light exiting the fiber is focused, e.g. by a GRIN-lens (gradient-index) to a spot directly behind the attached window. Hence, the incident laser light is scattered by the dispersed particles in the adjacent fluid region. Backscattered light is coupled into the fiber and propagates via a coupler (e.g. a 2×2 single-mode coupler) to the detector.

In-line DLS measurements are challenging since laboratory as well as industrial reactors typically are stirred. Accurate particle sizing using DLS necessitates a resting fluid in the measured sample. In actively mixed fluids, the diffusion is overlaid by turbulent convection, which prohibits diffusion measurements. Hence, it is not possible to apply DLS in fluids that exhibit forced convection either due to stirring or even due to sufficiently large pressure or temperature gradients.

Apart from DLS, there are several other methods to determine the particle size in fluids (Barth and Flippen 1995), such as angular resolved static light scattering (SLS) of particles. This method is capable of sizing particles with diameters of at least a size several tens of nanometers. To avoid multiple scattering, SLS measurements

Fig. 41.7 Principle setup of a fiber-optic DLS probe (FODLS). LS is laser source, FO fiber optic, FC fiber coupler, D detector, SV sleeve, GL GRIN-lens, W window, and PT particles suspended in a fluid
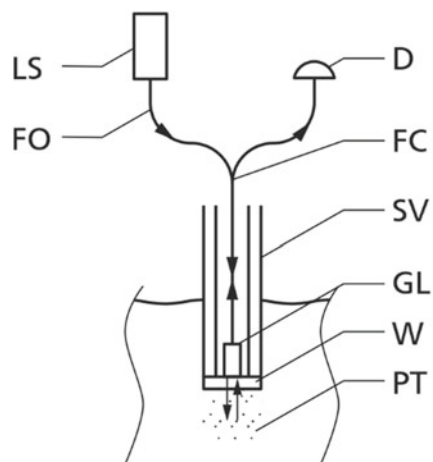
are usually performed in highly diluted samples. Therefore, SLS is not applicable for in-line monitoring of samples with high solid content. Also commonly used for size determination of industrial polymers or macromolecules is size exclusion chromatography (SEC), a method that involves sample drawing and uses small flow rates (Wu 2003) and hence is not suitable for in-line monitoring.

In practice, the aforementioned methods are used either off-line by taking samples from the production line to the laboratory or by installing fully automated online trains in bypasses or loops (Alb and Reed 2010). Sampling and further sample preparation by dilution or separation are time-consuming and induce a delay of up to several minutes between sampling and size information. In contrast, in-line measurements can provide real-time data or only have a delay of a few seconds, depending on the applied method, facilitating possible improvements in process and quality control. Hence, a particle sizing method capable of measuring in-line in undiluted and stirred suspensions and enabling a close to real-time monitoring of technical processes is strived for.

By measuring the bulk turbidity of a sample, one can calculate the particle size for monodisperse particles with known optical constants (Crawley et al. 1997). Since these optical constants can vary during polymerization processes, turbidity measurements are not sufficient for reliable particle size measurements. Optical imaging methods have also been applied in combination with in-line probes in stirred vessels (Wei et al. 2007). These methods are based on capturing images using a CCD camera, and are as such restricted by the optical diffraction limit and cannot detect nanometer-sized particles. A promising approach for in-line particle sizing of stirred turbid colloidal suspensions is Photon Density Wave (PDW) spectroscopy (Hass and Reich 2011). Using a special in-line probe, intensity-modulated light is detected at multiple distances between excitation and collection fiber. Since the method relies on strong multiple scattering, it can only be applied for dispersions exhibiting at least a certain level of turbidity (Hass et al. 2015) and hence cannot be used to monitor the initial stage of particle growth in processes that still exhibit single scattering.

At the Chair of Laser Technology (LLT), RWTH Aachen University and the Fraunhofer Institute for Laser Technology (ILT), Aachen, a novel probe head was developed to enable in-line FODLS measurements in stirred colloidal suspensions (Janzen et al. 2014; Kanter et al. 2016). Figure 41.8 shows schematically the setup (not to scale). A DLS probe (cf. Fig. 41.7) is put into a probe head having at least one opening for an exchange of a fluid sample from a fluid with dispersed particles in a reactor.

A rotating axis with an attached rotor is arranged within the probe head, by means of which at least a partial volume of the sample volume can be mechanically closed off to form a closed measuring chamber. An optical measuring window at this closed measuring chamber allows to pass incident and scattered laser radiation into and out of the measuring chamber. The probe head can be inserted directly into the liquid to be measured, whereby a measuring chamber isolated from the environment can be formed by stepwise rotation of the rotor and liquid can also be exchanged. This approach enables in-line measurement of, for example, particle sizes in moving liquids.

Fig. 41.8 Concept of probe
head for in-line DLS
measurements (Janzen et al.
2014). LS is laser source, FC
fiber optic coupler, D
detector, FO fiber optics, DP
DLS probe, PH probe head,
RC reactor, FL fluid, RA
rotating axis, RT rotor, and
OP opening
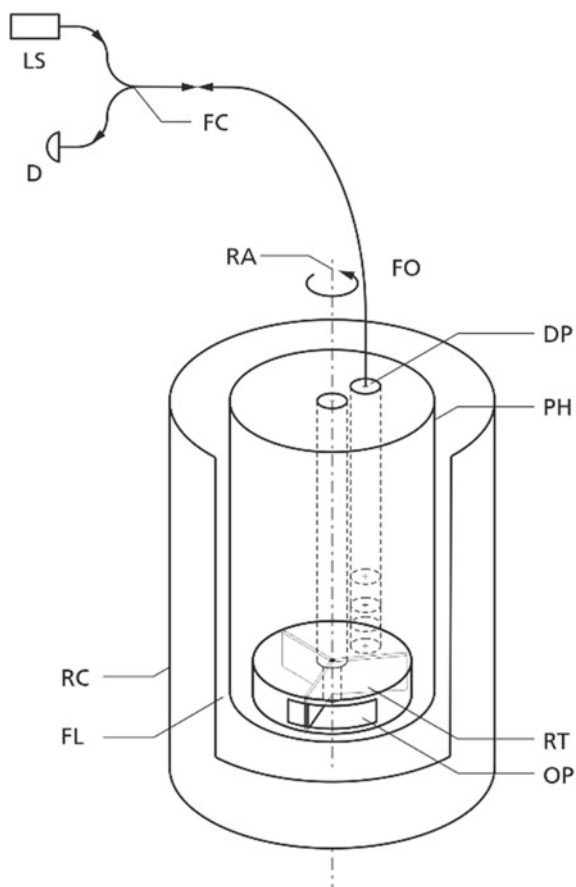
    A possible application of such an in-line particle sizing method is the monitoring
of microgel particle growth in the precipitation polymerization process. Microgels are
soft colloidal particles formed by cross-linked polymer chains (Pich et al. 2006). The
particle growth during precipitation polymerization depends on the reaction condi-
tions like concentration of main reagents (monomer(s), crosslinker, surfactant, and
initiator) as well as reaction temperature. Higher polymerization temperatures and
initiator concentrations result in faster particle growth. A typical microgel synthesis
takes 5–20 min from initiation to final conversion (Meyer-Kirschner et al. 2016).
For highly diluted syntheses at low temperatures, the growth of microgel particles
inside a cuvette was successfully monitored using static light scattering (Virtanen
and Richtering 2014). Kara et al. conducted microgel syntheses inside quartz cells at
room temperature (Kara and Pekcan 2000, 2001) and for temperatures up to 50 °C
(Kara et al. 2002). Placing the cell inside a UV–VIS spectrometer, they observed
a decrease in transmitted intensity during the gelation process. This decrease was

attributed to an increase in light scattered by the particles. The scattered light intensity was correlated to the particle volume using Rayleigh's equation, which is only valid for particles smaller than 0.1 of the laser wavelength (Virtanen and Richtering 2014). To monitor microgel particle growth at lab production scale in undiluted and stirred systems without being restricted to particles smaller than 40–70 nm (Virtanen and Richtering 2014), this method is not suitable.

The probe head according to Fig. 41.8 is combined with a commercial DLS probe. The working principle of that DLS probe is shown in Fig. 41.7. This device is factory-equipped with an immersion probe, which allows easy access to the sample due to the probe's small form factor. The light emitted by a laser (780 nm) is guided to the optical probe by a fiber and is focused into the sample close to the protective sapphire window, allowing measurements in highly concentrated suspensions of up to ~10 wt.-% solids depending on the nature of the sample. The 180° backscattered light is collected and guided through a fiber to a detector. The laser light reflected by the protective window is also guided to the detector. The scattered light of the particles and the reflected light from the protective window are overlaid on the detector and cause interferences. The time-resolved intensity fluctuations correlate with the motion of the particles from which the particle size distribution is calculated by suitable mathematical models. This device covers a particle size range of 0.8 nm–6.5 μm. The heterodyne method—see Sect. 41.2—improves the signal-to-noise ratio especially for small particles (<100 nm) and low particle concentrations and enables accurate particle sizing over a large concentration area (Freud 2007; Trainer et al. 1992).

To perform measurements in stirred fluids, a custom-designed probe head shown in Fig. 41.9 was developed. The probe head was tailored to be attached directly to the commercial probe, which is then immersed together with the probe head into the reaction fluid. The task of this probe head is to separate a small amount of volume from the bulk fluid—a compartmentalization—which can then be measured using DLS. Additionally, the probe head has to actively exchange the sample volume between two measurements. The requirement for this probe head was compactness, so it can be applied in common laboratory reactors and it had to be robust enough to be used in industrial stirred reaction vessels. The separated sample volume should be as small as possible, it should be exchanged sufficiently fast between each measurement, and most importantly it has to be protected from external motion and stray light.

The probe head's outer diameter is 35 mm and its length is 82 mm. The probe head consists of three parts for the enclosure (A, B, C) made from stainless steel. A miniature stepper motor with a diameter of 6 mm is secured by a stainless steel holder (D). The rotor made from polytetrafluorethylen (PTFE) (F) is attached to the stepper motor. There are several sealings in the probe head to keep moisture away from the stepper motor.

The custom probe head (A, B, C) surrounds the optical DLS probe (G) of the DLS device and provides a small enclosed sample chamber (~0.65 ml) for the DLS measurements. The exchange of the sample fluid is carried out by the miniature stepper motor. The miniature stepper motor stops the rotor in a defined position after exchanging the sample so the optical path for the DLS probe is free and the
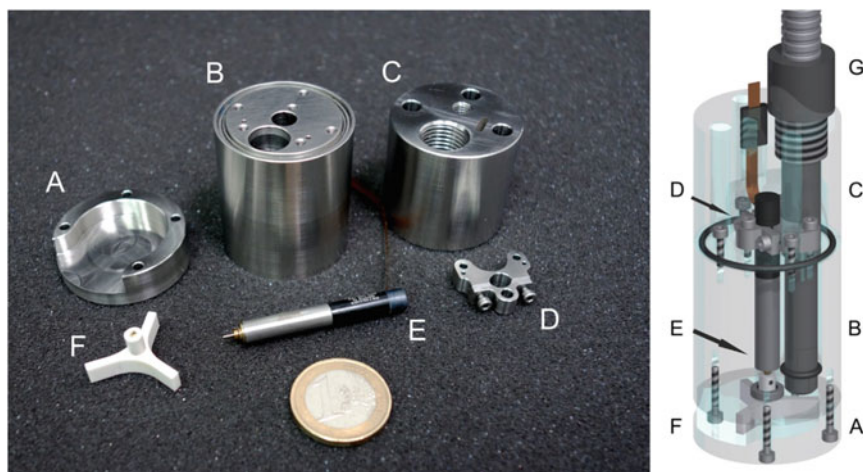
Fig. 41.9 Left: Components of disassembled probe head for DLS measurements in stirred solutions. 1€-coin is shown for size reference. Right: CAD image of assembled probe head with DLS measurement probe. Photo, CAD drawing: Fraunhofer ILT

measurement chamber is properly capsulated. Because of the small sample chamber size, the fluid stalls very fast and does not disturb the measurement due to any overlaid motion. The stepper motor is controlled by a motion controller and software to program the motion profile.

Before the probe head is applied for in-line measurements during microgel synthesis, the suitability of the compartmentalization is tested on previously synthesized microgel particles (PVCL, poly-N-vinylcaprolactam). Therefore, the probe head was immersed into a beaker filled with the colloidal microgel suspension, and a magnetic stir bar was added. The beaker was placed on top of a magnetic stirrer. Measurements were conducted with and without stirring. For comparison, the same measurements were repeated without the probe head. The integration time of the scattered light for each DLS measurement was 30 s with six repeated measurements per setup.

Four different conditions were examined. First, the bare optical probe of the DLS device was used in stirred and unstirred microgel suspension. The magnetic stirrer was set to 1000 rpm for the stirred measurements. Afterwards, the optical probe of the DLS device was equipped with the new probe head, and the measurements in stirred and unstirred microgel were repeated.

Figure 41.10 shows the results of these measurements. Sector 1 shows the particle size determined from repeated measurements with the bare probe in the unstirred suspension for a size reference. Sector 2 displays the sizes resulting from measurements taken during active stirring. Due to the convection, the particle sizes are erroneously identified to be remarkably smaller. The calculated sizes differ between 70 and 350 nm, and a reliable value cannot be evaluated. Sector 3 contains particle sizes from measurements using the custom probe head, albeit without stirring. The
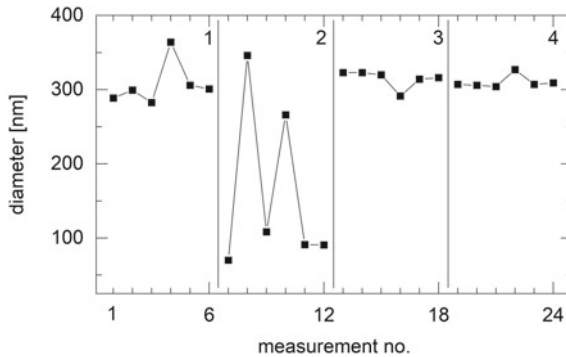
Fig. 41.10 Measured D50 diameters by DLS for 24 performance tests of the new probe head with PVCL microgel. Comparison of the measurements with bare and custom probes (cf. Figure 41.9) in stirred and unstirred samples. Sector 1: unstirred liquid, bare optical DLS probe; 2: stirred liquid, bare optical DLS probe; 3: unstirred liquid, custom probe head; 4: stirred liquid, custom probe head

deviation between the detected sizes is slightly smaller than the deviation without the custom probe head (sector 1). This smaller distribution of measured particle sizes could be caused by the compartmentalization of the sample, which effectively keeps away ambient light from the detector and restricts even small liquid movements. The particle sizes of measurements with the new probe head under stirred conditions are depicted in sector 4. The particle sizes determined under agitated condition match the values determined in unstirred condition, which ultimately proves the operational capability of the developed probe head.

Table 41.1 shows the calculated values of the average and standard deviation of the determined D50 particle diameter for each sector. The standard deviation for the measurements with the attached custom probe head is improved by a factor of 2.4–3.2 over the measurements with the bare probe of the DLS device. The deviations of the averages from sector 3 and sector 4 are within the deviation of sector 1.

The results of the measurements of the colloidal microgel suspension show that the design of the custom probe head is suitable to isolate and measure a small volume from the system, thereby preventing any interference of the encapsulated sample with the stirred bulk fluid. The accuracy of the custom probe under stirred conditions is at least as good as the bare probe in unstirred conditions. This renders reliable DLS measurements even in vigorously stirred environments possible.

Table 41.1 Average size of D50 and its deviation of the comparison measurements from Fig. 41.10

⇒ Sector	Average size (nm)	Standard deviation (nm)
1	307	29
2	N/A	115
3	330	12
4	316	9

Following the test of compartmentalization in the open beaker, the probe head was applied to monitor microgel synthesis in the temperature-controlled one-liter reactor under a nitrogen atmosphere (experiments were carried out at the Aachener Verfahrenstechnik AVT, RWTH Aachen university in the context of the SFB project (http://www.microgels.rwth-aachen.de/)). Figure 41.11 displays the particle size monitoring during the polymerization of PVCL at a reaction temperature of 60 °C. This temperature was chosen since it is the lowest temperature that reliably starts the polymerization of PVCL using AMPA (2,2'-Azobis(2-methylpropionamidine)dihydrochloride) as initiator and hence permits most measurements during the particle growth phase. Each dot in the figure represents one particle size measurement, of which the red triangles were visually identified as outliers and excluded for computation of the floating mean, which is determined piecewise over three successive values. The two outliers might be caused by small air bubbles that reached the measurement chamber.

The first measurements after the addition of the initiator at time zero show a particle size of 2–3 nm due to background scattering. From minute five onwards, the growth of the particles can be seen very well. Approximately twelve minutes after initiation, the particle sizes reach a plateau at ~81 nm $\pm$ 3 nm SD diameter. The time between the first noticeable change in particle size and the onset of the plateau is about 8 min.

The second system monitored using the probe head was a polymerization of PNIPAM (poly-N-isopropylacrylamide) at a reaction temperature of 65 °C. The corresponding in-line recorded particle sizes are displayed in Fig. 41.12.

To assess the validity of the particle sizes determined using the novel probe head, samples were taken during a microgel synthesis, directly quenched to stop further reaction, and subsequently analyzed off-line. In Fig. 41.12, the particle sizes measured using the in-line probe head are depicted using black squares and the particle sizes measured off-line using blue dots. Again, red triangles represent visually selected outliers. The slopes of both measurements are in good agreement with each other. While the in-line measured sizes remain at their initial level until minute ten, the off-line measurements are able to depict small particle growth from minute

Fig. 41.11 Monitoring of particle size during polymerization of PVCL at 60 °C in a 1 L laboratory reactor. Triangles show visually identified outliers
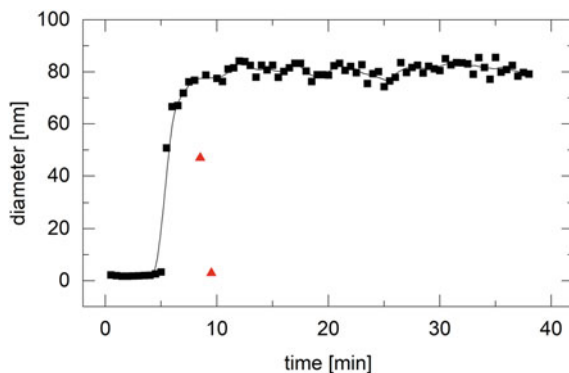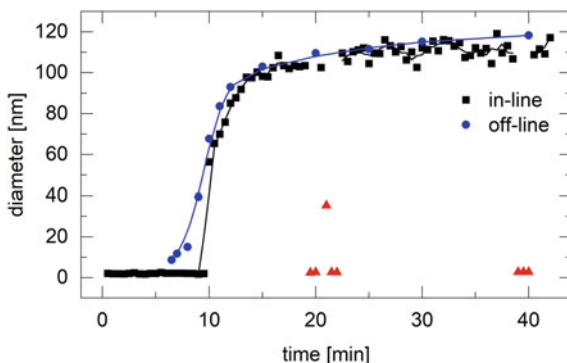
Fig. 41.12 Monitoring of
particle size taken in-line
(squares) during
polymerization of PNIPAM
at 65 °C in a 1 L laboratory
reactor together with off-line
DLS reference
measurements (circles).
Triangles show visually
identified outliers

six. Starting with the significant jump to 55 nm at minute 10, the in-line measurements display a constant particle growth, which is in accordance with the off-line measurements. The differences between both measurement techniques present at early reaction times decrease as the reaction progresses. The particle sizes from both techniques reach a plateau of 111 ± 4 nm SD for the in-line and 114 nm for the off-line measurements, respectively. A reason for the decreasing differences between in-line and off-line data could be the integration time of the DLS probe (Kara et al. 2002). Since the particles continue to grow during the acquisition time, the scattering pattern changes as well. The DLS evaluation method then determines a particle size that best approximates the measured signal, which might be distorted due to the shifting scattering pattern. The slower the reaction becomes, the smaller are the differences between both methods. The handling time from taking the sample and stopping the reaction with fluid nitrogen also takes a certain amount of time in which the particles keep growing.

After the synthesis, minor contamination from chemical residue is visible on the surface of the probe head and on the protective window of the optical DLS probe. Examination of the DLS measurements shows no remarkable influence of these contaminations on the detected particle sizes. The residue rather causes a static reduction of the mean scattering intensity and thus might increase the measurement time necessary to retain the targeted measurement uncertainty. Nevertheless, the accuracy reached using the custom probe head in stirred surroundings is in a region that is at least as good as measurements performed with a bare DLS probe in unstirred fluids.

A novel probe design has been introduced to enable in-line monitoring of particle sizes inside a stirred fluid based on dynamic light scattering without the need for sampling and dilution. It was shown that the fluid compartmentalization in the probe head is sufficient to exclude any influences of the stirred bulk liquid. The growth of microgel particles could be suitably followed during stirred polymerization. A comparison between the direct in-line measurements and off-line determined particle sizes using a state-of-the-art device showed that both measurement techniques are in good agreement with each other. The application of the probe design in industrial

environments that currently rely on tedious off-line analysis of drawn samples could vastly facilitate product quality control. In batch productions, it could lead to faster reaction times, since the end of particle growth can automatically be detected. It renders possible the discovery of unexpected product conditions and the triggering of counteractive measures that might be untraced for considerably longer times with conventional monitoring techniques.

References

Auweter H, Horn D (1985) Fiber-optical quasi-elastic light scattering of concentrated dispersions. J Colloid Interface Sci 105:399–409

Alb A, Reed W (2010) Funamental measurements in online polymerization reaction monitoring and control with a focus on ACOMP. Macromol React Eng 4:470–485

Barth H, Flippen R (1995) Particle size analysis. Anal Chem 67:257R-272R

Berne B, Pecora R (1976) Dynamic light scattering with applications to chemistry, biology, and physics. Wiley, New York

Black D, McQuay M, Bonin M (1996) Laser-based techniques for particle-size measurement: a review of sizing methods and their industrial applications. Prog Energy Combustion Sci 22:267–306

Clark N, Lunacek J, Benedek G (1970) A study of Brownian motion using light scattering. Am J Phys 38:575–585

Crawley G, Cournil M, Di Benedetto D (1997) Size analysis of fine particle suspensions by spectral turbidimetry: potential and lmits. Powder Techn 91:197–208

de Kanter M, Meyer-Kirschner J, Viell J, Mitsos A, Kather M, Pich A, Janzen C (2016) Enabling the measurement of particle sizes in stirred colloidal suspensions by embedding dynamic light scattering into an automated probe head. Measurements 80:92–98

DIN ISO 22412 (2018) Partikelgrößenanalyse—Dynamische Lichtstreuung (DLS), Deutsche Norm, September 2018, 42 p

Donges A, Noll R (2015) Laser measurement technology—fundamentals and applications. Springer, Heidelberg, 422 p. ISBN 978-3-662-43633-2

Einstein A (1956) Investigations on the theory of Brownian movement, R Furth, Ed. Dover Publishing, New York

Freud P (2007) Nanoparticle sizing: dynamic light scattering analysis in the frequency spectrum mode. Microtrac Inc.

Hass R, Reich O (2011) Photon density wave spectroscopy for dilution-free sizing of highly concentrated nanoparticles during starved-feed polymerization. ChemPhysChem 12:2572–2575

Hass R, Munzke D, Ruiz S, Tippmann J, Reich O (2015) Optical monitoring of chemical processes in turbid biogenic liquid dispersions by photon density wave spectroscopy. Anal Bioanal Chem 12:2791–2802

Hecht E, Zajac A (1997) *Optics*, Pearson, 1997

Horn F, Richtering W, Bergenholtz J, Willenbacher N, Wagner N (2000) Hydrodynamic and colloidal interactions in concentrated charge-stabilized polymer dispersions. J Colloid Interface Sci 225:166–178

Janzen C, Noll R, de Kanter M (2014) Vorrichtung und Verfahren zur Durchführung faseroptischer Messungen in Flüssigkeiten. Patentschrift 10 2014 016 993.6, 18.11.2014

Kara S, Pekcan Ö (2000) Photon transmission technique for monitoring free radical crosslinking-copolymerization in various crosslinker contents. Polymer 41:3093–3097

Kara S, Pekcan Ö (2001) In situ real-time photon transmission technique for monitoring formation of polyacrylamide gels at various crosslinker contents. J Appl Polymer Sci 80:823–830

Kara S, Okay O, Pekcan O (2002) Real-time temperature and photon transmission measurements for monitoring phase separation during the formation of poly(N-isopropylacrylamide) gels. J Appl Polymer Sci 86:3589–3595

Meyer-Kirschner J, Kather M, Pich A, Engel D, Marquardt W, Viell J, Mitsos A (2016) In-line monitoring of monomer and polymer content during microgel synthesis using precipitation polymerization via Raman spectroscopy and indirect hard modeling. Appl Spectrosc 70:416–426

Nanotrac 250 from Particle Metrix/Microtrac Europe GmbH, Germany

Particle-Metrix GmbH, Am Latumer See 13, 40668 Meerbauch, Germany, www.particle-metrix.de

Pecora R (2000) Dynamic light scattering measurement of nanometer particles in liquids. J Nanoparticle Res 2:123–131

Pich A, Tessier A, Boyko V, Lu Y, Adler H-JP (2006) Synthesis and characterization of poly(vinylcaprolactam)-based microgels exhibiting temperature and pH-sensitive properties. Macromolecules 39:7701–7707

Pusey P (1999) Suppression of multiple scattering by photon cross-correlation techniques. Curr Opinion Colloid Interface Sci 4:177–185

Segrè P, van Megen W, Pusey P, Schätzel K, Peters W (1995) Two-colour dynamic light scattering. J Modern Opt 42:1929–1952

Sinn C, Niehüser R, Overbeck E, Palberg T (1999) Particle characterization using multiple scattering decorrelation methods. Part 1: standard latex particles, Part. Part Syst Charact 16:95–101

Sonderforschungsbereich SFB 985, Funktionale Mikrogele und Mikrogelsysteme, http://www.microgels.rwth-aachen.de/

Stieber F, Richtering W (1995) Fiber-optic-dynamic-light-scattering and two-color-cross-correlation studies of turbid, concentrated, sterically stabilized polystyrene latex. Langmuir 11:4724–4727

Thomas J, Dimonie V (1990) Fiber optic dynamic light scattering from concentrated dispersions. 3: particle sizing in concentrates. Appl Opt 29:5332–5335

Trainer M, Freud P, Leonardo E (1992) High-concentration submicron particle size distribution by dynamic light scattering. Am Laboratory, Fairfield, Connecticut, pp 34–38

Virtanen O, Richtering W (2014) Kinetics and particle size control in non-stirred precipitation polymerization of N-isopropylacrylamide. Colloid Polym Sci 292:1743–1756

Wei N, You J, Friehs K, Flaschel E, Nattkemper T (2007) An in situ probe for on-line monitoring of cell density and viability on the basis of dark field microscopy in conjunction with image processing and supervised machine learning. Biotechnol Bioeng 97:1489–1500

Wiese H, Horn D (1991) Single-mode fibers in fiber-optic quasielastic light scattering: a study of the dynamics of concentrated latex dispersions. J Chem Phys 94:6429–6443

Wu C-S (ed) (2003) Handbook of size exclusion chromatography and related techniques: revised and expanded, vol 91. CRC Press

Part XII
EUV Sources and Applications

Chapter 42
Pulsed Plasma EUV Sources

Klaus Bergmann and Reinhard Noll

42.1 Extreme Ultraviolet Radiation

The application of extreme ultraviolet (EUV or XUV) is an emerging field which is currently mainly driven by the development of EUV lithography for future chip manufacturing. The considered wavelength interval ranges from 1 to 50 nm or in terms of photon energies from 20 eV to 1 keV. This part of the electromagnetic spectrum has some special features, which makes it attractive for new applications for analysis and structuring on the nanometer scale. These features are:

– significantly shorter wavelengths compared to visible and UV radiation lead to spatial resolutions on the nanometer scale,
– strong interaction with matter, mostly due to the photoelectric effect, and high elemental selectivity due to inner shell interaction for a variety of analyses,
– ionizing radiation to be used for chemical processes like resisting exposure and
– increase of available optical components for beam shaping or imaging systems.

42.2 Plasma Radiation Sources

This chapter focuses on thermal emitters of short-wavelength radiation. Matter is heated up to high temperatures, which will convert this matter into a plasma state consisting of ionized atoms and freely moving electrons. The generated plasma radiates mainly via electronic transitions of the ions, which are excited by collisions with hot electrons. With this type of radiator, high conversion of the input energy into radiation can be achieved, since the deposited energy mainly can be released

K. Bergmann (✉) · R. Noll
Fraunhofer ILT, Aachen, Germany
e-mail: klaus.bergmann@ilt.fraunhofer.de

Fig. 42.1 Radiation source (RS) with input and output flows
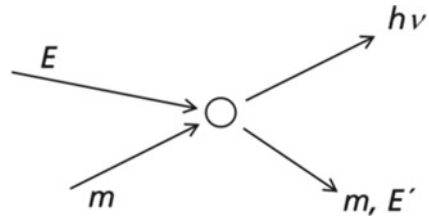
via radiative channels. In addition, these radiative channels are in the desired short-wavelength range. A counterexample is the X-ray tube, where most of the energy is lost by heat conduction via the anode (radiation yield is typically in the order of 1% for the emitted superimposed line and Bremsstrahlung spectra with respect to the electric input energy).

Figure 42.1 illustrates a simplified radiation source with its input and output flows. Energy (E) and mass (m) are fed to a small spatial region—ideally a point—where a high energy density is achieved to stimulate electronic transitions in the partially ionized matter and to generate electromagnetic radiation ($h\nu$). The radiating mass has finally residual energy (E'). All approaches to realizing a EUV source have to deal with the way of feeding the energy to a small mass to be converted into an emitter within a short time interval in order to reach high energy densities.

After the radiation act, the mass remaining or flowing out of the excitation zone carries a residual energy content (E'). Input and output flows have to be handled in a controlled way to achieve a reliable radiation source.

However, a real light source is not a mathematical point. A more realistic approximation is a small sphere or a cylinder, which in the simplest case can be described by one or two geometric parameters.

There are two methodological approaches to creating such plasmas. These are laser-induced plasmas (LPP) or discharge-produced plasmas (DPP), which will be discussed in more detail below. Figure 42.2 shows a photograph of a discharge-generated plasma. Due to the high energy density of the transient plasma the lifetime is limited, which is described as a decay time. As a consequence, laboratory-scale plasmas are always pulsed, with lifetimes being typically in the range below 1 ns for LPP to maximum 1 μs for DPPs. To get access to the radiation, these plasmas are usually generated in a vacuum vessel or a low-pressure environment due to the strong absorption of EUV radiation in atmospheric gases.

An estimation of the required plasma temperature for efficiently radiating at short wavelengths can be achieved with the help of Planck's formula. The spectral radiance (unit W/(m^2 sr m)) of a blackbody radiator gives an upper limit for emitted radiation:

$$B(\lambda) = \frac{2hc^2}{\lambda^5} \frac{1}{e^{\frac{hc}{k_B T \lambda}} - 1}, \tag{42.1}$$

Fig. 42.2 Photography of a EUV emitting plasma generated by a pulsed gas discharge in a low-pressure Xenon atmosphere (10 mm diameter of the borehole)
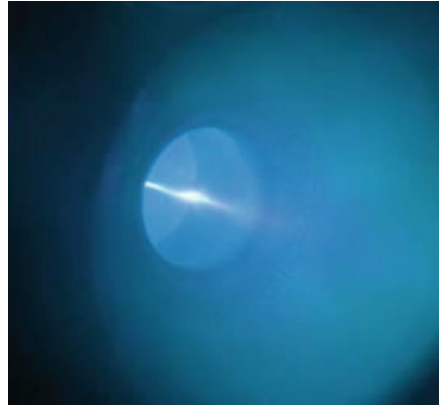
with h being Planck's constant, c speed of light, λ wavelength and k_B Boltzmann constant.

According to Wien's law, the spectral radiance attains a maximum for

$$\lambda_\text{max} \times k_B T = 249.7\,\text{nm}\,\text{eV}.$$

A temperature of 18.5 eV is required for a maximum emission at 13.5 nm. Usually, the plasma has not enough radiative channels and is not dense enough to emit in the whole spectral range as a blackbody radiator.

However, for some line transitions with sufficiently large Einstein coefficients of spontaneous emission, this theoretical limit for a thermal radiator can be reached. Relation (42.1) for the blackbody radiator can be regarded as an envelope for the factual emission of the plasma. Note that the blackbody envelope has a spectral bandwidth which is in the same order as the wavelength of the maximum.

At temperatures in the range from 10 eV to several 100 eV, the plasma is fully ionized, i.e., there are no neutral atoms, and the ions are in a highly ionized stage. For noble gases, e.g., Xenon (nuclear charge $Z = 54$), the species are typically ionized up to 10- to 20-fold. These highly ionized ions usually feature mainly radiative transitions with wavelengths, which obey Wien's law, when taking for T the electron temperature.

In the following, laser-induced plasmas and gas discharge plasmas are discussed in more detail. Other overviews on EUV sources can be found in Refs. (Sources and for Lithography, Vivek Bakshi (editor), 2006; Juschkin et al. 2008).

42.3 Laser-Induced Plasmas

A hot plasma can be produced by focusing a pulsed laser beam onto a target. The laser radiation is absorbed by the mechanism of inverse Bremsstrahlung (Griem 1964). The density above the surface varies from the target density decreasing to lower densities. The plasma heating takes place in a region where the critical electron density occurs, which is determined by the frequency of the laser light (Chen 1977):

$$n_c = \frac{\varepsilon_0 m_e \omega_L^2}{e^2} = 1.12 * 10^{21} \text{cm}^{-3} \left(\frac{\lambda_L}{\mu\text{m}}\right)^{-2} \tag{42.2}$$

with ε_0 being dielectric constant, m_e electron mass, e elementary charge and ω_L angular frequency of the incident laser light. For densities larger than the one given by (42.2), an electromagnetic wave of wavelength λ_L cannot propagate inside the plasma. Hence this density describes a cutoff condition.

In a simplified image, most of the EUV emission can be assumed to occur from the plasma region close to the critical density. In order to achieve sufficiently high temperatures for efficient emission of EUV radiation, the laser irradiance should be typically in the range above 10^{11}–10^{12} W/cm^2.

Typical electron densities are ranging from 10^{19} cm^{-3} for a CO_2 laser with $\lambda = 10.6$ μm to 10^{21} cm^{-3} for a frequency-doubled Nd:YAG laser with $\lambda = 532$ nm, according to (42.2). Usually, lower densities are preferred, where the self-absorption of the short-wavelength radiation is reduced.

The main technological challenge with laser-induced plasmas is to provide a regenerative, long-lifetime target. Examples of technical solutions are rotating cylinders consisting of the target material, gas jets, liquid gases or droplets, and liquid jets or droplets from molten solids.

The most prominent example of a LPP source is Cymer's source used in EUV lithography scanners (van de Kerkhof et al. 2017). In this case, a pulsed CO_2 laser irradiates a small tin droplet, which is injected into a vacuum chamber. A typical parameter is taken from Ref. (Fomenkov et al. 2010). In this case, the pulse energy of the laser beam is 440 mJ at a repetition rate of 40 kHz, which leads to an average laser radiant flux of 17.5 kW. The conversion of this power into characteristic light from the tin at a wavelength of 13.5 nm, into a spectral bandwidth of 2%, leads to an average EUV photon flux of 525 W/2πsr from the tin plasma.

42.4 Discharge Produced Plasmas

Another method to heat up matter to the required temperatures for the efficient generation of EUV radiation makes use of high pulsed currents. Usually, these currents flow between two electrodes, which are in a gaseous environment at pressures around

several 10 to several 100 Pa. The current heats up the gas or plasma and compresses the plasma channel by the self-magnetic field to electron densities of typically $n_e \sim 10^{19}$ cm^{-3}. The required peak current, I_0, can be estimated by applying the Bennet relation for a plasma column, where the magnetic and the plasma pressures are in equilibrium (Krall and Trivelpiece 1986):

$$\frac{\mu_0}{8\pi} \frac{I_0^2}{r_p^2} = (n_i + n_e)k_B T_e, \tag{42.3}$$

with μ_0 being magnetic field constant, r_p, radius of plasma cylinder, n_e and n_i, electron and ion density, respectively, k_B Boltzmann constant and T_e electron temperature (for simplicity, we assumed here that the electron temperature is equal to the ion temperature, $T_e = T_i$). Looking, for example, at a Xenon plasma with tenfold ionized ions, i.e., $n_e = 10n_i$, and $n_i r_p^2 = n_0 a^2$ being estimated from the product of neutral gas density, n_0, and the starting radius, a, of typically a few millimeters will lead to a current in the range of several 10 kA. The pulse duration is usually in the range of several 100 ns. The pulsed current is created by a fast discharge of a charged storage capacity with typical pulse energies in the range from 1 J to several 100 J. There are a variety of technical concepts for the current generator and the special design of the electrode system. In comparison to Laser-induced plasma, the electron density is at least 2 orders of magnitudes lower. As a consequence, the emission spectra show qualitative differences, where LPPs show a more broadband emission due to the excitation of more and overlapping of spectral lines. The lower density of DPP will also lead to excitation rates which are in the same order of magnitude compared to the plasma lifetime of ~100 ns. Thus, this plasma can be highly transient, meaning that the ionization will not achieve the level at a given plasma temperature as would be possible in a steady-state case, which can be a limiting factor in some cases. This chapter will focus exemplarily on the hollow cathode-triggered gas discharge concept (HCT), which is under investigation at Fraunhofer ILT.

A scheme of the electrode system is shown in Fig. 42.3. The electrode systems consist of an anode connected to ground potential, a cathode and an intermediate electrode. The electrodes have cylindrical symmetry. They are connected with a storage capacity of around 1 μF which is charged to voltages of 1–5 kV. The electrode interspace is filled with a gas, which is fed from the inlet at the cathode and pumped down on the anode side. The pressure is between 10 and 100 Pa. The EUV emitting plasma is generated in the center between the anode and intermediate electrode on the axis of symmetry as indicated in the cross section shown in Fig. 42.3, right, by a small dark spot. The whole system is integrated with a Faraday cage as shown in Fig. 42.3, left. Usually, the anode has a conical opening to have better optical access at larger angles with respect to the axis of symmetry. In practice, a total angle of up to 90° is usable and can be collected by an optical system, which is attached to the electrode system.

In this special concept, the plasma is ignited inside the hollow cathode, when the breakdown voltage is exceeded. This hollow cathode plasma expands into the region
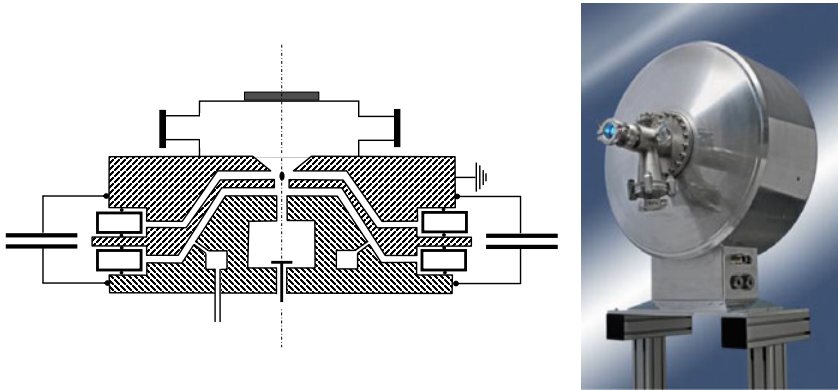
Fig. 42.3 Example for the HCT plasma concept with cross section of the electrode scheme (left) and photo of the source head (right)

toward the anode and forms a low resistive plasma channel, which allows for a fast discharge of the storage capacity. The ignition of the hollow cathode can be triggered by switching a positive blocking potential, which is applied to the center electrode. This electrode protrudes into the hollow cathode at the bottom of the scheme. More details about this concept can be found in Refs. (Bergmann et al. 1999; Vieker and Bergmann 2017).

Figure 42.4 shows a typical axial emission profile of a Xenon pinch plasma at a wavelength of 13.5 nm. This profile has been recorded using a camera sensitive to that wavelength, which has been attached under an observation angle of 32° with respect to the optical axis. The diameter of the EUV emitting region amounts to typically 200–500 μm (FWHM). The axial emission profile along the optical axis, which is calculated from the camera image, is also shown. In this case, the maximum of the emission is located in the center between the anode and the intermediate electrode.

42.5 Emission Spectra

Emission spectra for different gases for the HCT discharge are shown in Fig. 42.5. These spectra are normalized to the respective maximum for better comparability. Usually, gases with low atomic numbers show few emission lines, like nitrogen or oxygen. With higher atomic numbers more transitions are available, which leads to distinct broadband emissions and overlapping of emission lines. The latter is called unresolved transition arrays (UTA, Bauche and Bauche-Arnoult 1988). The spectra cover a range from the water window region (2.3–4.4 nm), which is of interest for soft X-ray microscopy, to 20 nm.

The highest photon flux around 13.5 nm is achieved with xenon. With the system operated at Fraunhofer ILT, photon fluxes at 13.5 nm into a bandwidth of 2% of
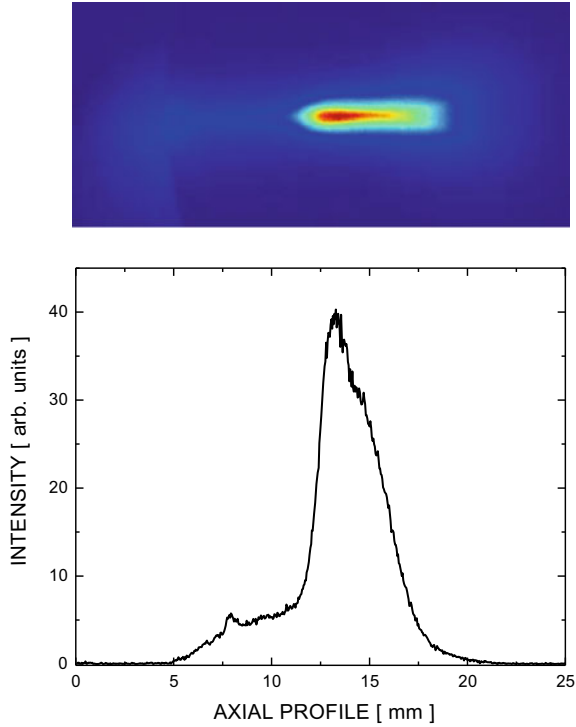
Fig. 42.4 Emission profile of a Xenon pinch plasma at 13.5 nm with CCD image (top) and center intensity line-scan (bottom)
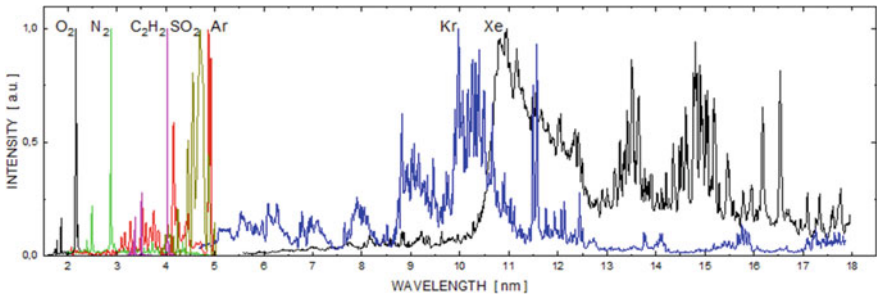

Fig. 42.5 Emission spectra of different operation gases from HCT pinch plasmas normalized to the respective maximum

up to 40 W/2πsr or brightness of up to 12 W/mm^{2}sr for the end-on observation direction are achieved. With nitrogen, intense emissions into a small bandwidth are concentrated around 2.9 nm. Typical emission power into this single line is up to 4 W/2πsr or in terms of brightness up to 4.0 * 10^9 Photons/sr μm^{2}s.
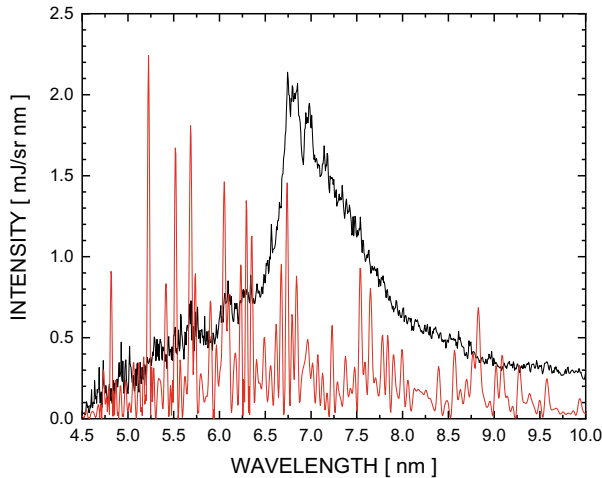
Fig. 42.6 Emission spectra of Gadolinium and Aluminum for a laser-induced plasma. Laser parameters: frequency-doubled Nd:YAG at 532 nm, pulse energy of 140 mJ, pulse duration 2.4 ns and intensity on target of $5 * 10^{12}$ W/cm^2 (Wezyk et al. 2019)

There are numerous studies on the EUV emission of laser-induced plasmas, covering different target materials, target concepts and laser parameters. As an example, Fig. 42.6 shows the emission of gadolinium and aluminum, which have been investigated in this special case as efficient target materials for emissions around 6–7 nm. Gadolinium with a higher atomic number shows a more broadband and smooth emission spectrum, whereas for aluminum—with a low atomic number—single, resolved emission lines can be observed. The Al emission arises from transitions in fivefold to tenfold ionized ions. For Gd, we see the emission of 4d-4f and 4p-4d transitions of 18- to 27-fold ionized ions.

42.6 Debris

For both concepts, LPP and DPP, the emission of debris in the form of highly ionized ions and material detached from the electrodes or target is an important topic to be considered for the development of such sources for future commercial use. After the emission of the soft X-rays, the hot plasmas decay and ions are accelerated up to typically several 10–100 keV. Due to operation in vacuum or a low-pressure environment, the ions can move without losing energy and hit and sputter the surface of optical elements. It may also happen that the optical elements are covered by the target material, which will also lead to a loss of reflectivity. The activities and efforts on mitigation of such debris are comparable to or even higher than the mere light generation itself. There are a variety of technical concepts to protect or enhance
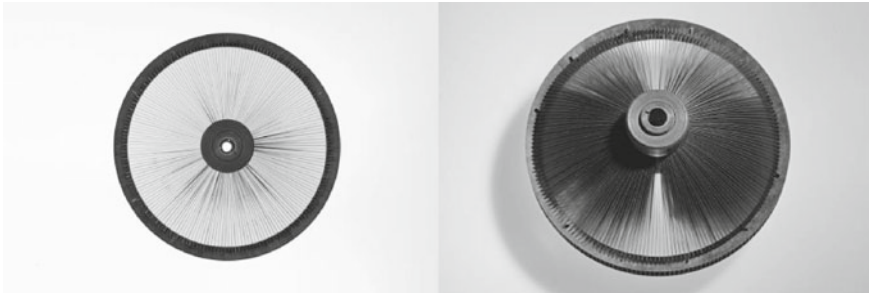
Fig. 42.7 Foil trap viewed from different directions. Left: for a position close to the source on the axis of symmetry, the system shows a high optical transmission. Right: low optical transmission appears looking at an angle with respect to that axis

the lifetime of the attached optical systems. Such concepts may also be applied in combination:

- A buffer gas atmosphere with high transmission in the EUV and reasonable stopping power for the fast ions or low energy debris. For 13.5 nm radiation, argon is often used as such a buffer gas.
- Foil traps, usually in combination with a buffer gas, consisting of thin lamellas. Such systems have a high optical transmission of up to 80%, where the debris has to pass the lamellas with a width of several centimetres. The debris is deflected by collisions with a buffer gas and trapped at the surface of the lamellas. Such foil traps may also be rotating to deflect large and slow droplets from liquid targets or electrodes.
- External magnetic fields to deflect the ions.
- Sacrificial layers or coatings to maintain the optical properties in spite of being sputtered.
- In situ cleaning of the optical elements, e.g., using atomic hydrogen for the conversion of tin-coated surfaces into volatile tin hydride.
- Liquid, regenerative coatings on grazing incidence collector mirrors, e.g., using liquid tin.

An overview of some debris mitigation strategies can be found in Ref. (Ruzic 2006). Figure 42.7 shows an example of a foil trap.

42.7   XUV Laser

In general, the required pumping power for achieving population inversion scales with the wavelength according to λ^{-4} (Elton 1990). Thus, the effort to access short wavelengths increases significantly. Nevertheless, population inversions for EUV wavelengths have been achieved in the past, mainly for laser-induced plasmas (Elton
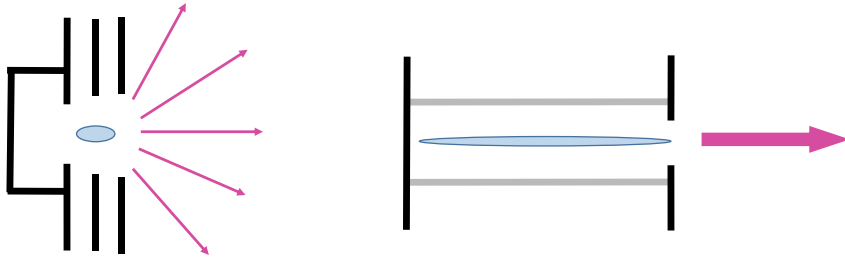
Fig. 42.8 Principal emission characteristics of discharge-generated plasmas with different aspect ratios of length to diameter. Left: aspect ratio at about 1–3; right: aspect ratio >>1. Arrows indicate dominant emission directions

1990; Bleiner 2012). Due to the short plasma lifetime, and the lack of mirrors, which could be used as resonators, such plasmas only emit partly coherent ASE radiation (Amplified Spontaneous Emission). Different pumping schemes have been realized and plasmas emitting down to a wavelength of 4,318 nm have been achieved, e.g., a laser-induced nickel-like tungsten plasma (Wang et al. 2005). Usually, such plasmas require a relatively advanced and expensive drive laser. Thus, from a technological point of view making use of a gas discharge plasma is of interest. In most of the gas discharge concepts, a plasma column of a few millimeter in length and diameters of a few 100 μm is produced. An example, like the one presented above is shown in Fig. 42.8, left. Such plasma is nearly an isotropic emitter of radiation. If the aspect ratio is increased, i.e., the plasma length is increased—cf. Figure 42.8, right—and the plasma parameters and dynamics allow for a population inversion; ASE can occur.

Such a system has been demonstrated with an argon-filled capillary discharge, where a cylindrical plasma of up to 21 cm in length is generated with an electrical discharge with ~100 J, 22 kA peak current and 200 ns electrical pulse duration (MacGowan et al. 1987).

As an example, the plasma conditions to achieve population inversion are discussed in more detail. The energy level scheme of the involved Argon transitions of the eightfold ionized neon-like argon ions is shown in Fig. 42.9, left. The population inversion occurs between levels 2 and 1, where the transition has a wavelength of 46.9 nm. The population inversion is achieved by electron collisional pumping. Note that the radiative decay from level 2 to 0 is forbidden. The rates C_{ij} denote electron collisional excitation and de-excitation. Furthermore, spontaneous emission from levels 2 and 1 and 1 to 0 are taken into account. The rate equations for this system can be solved, where electron density and temperature are taken as input parameters assuming steady-state conditions, $dn_i/dt = 0$ for all levels. In the first step, the photon density of the lasing transition, which may influence the population density by induced emission and absorption, is neglected.

With this simplified system, the gain coefficient G_0, which expresses the exponential growth of initial photon flux, I_0, along the plasma column according to $I(d) = I_0 \exp(G_0 * d)$ can be expressed by
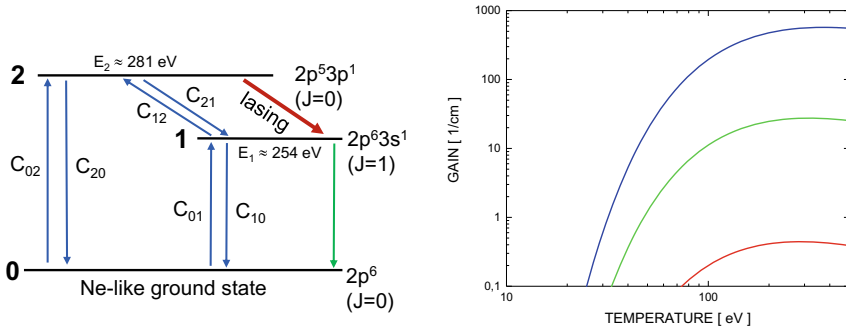
Fig. 42.9 Energy level scheme of neon-like argon as example for a collisional pumped laser system and estimated gain coefficient for different electron densities (red: 10^{17} cm^{-3}, green: 10^{18} cm^{-3}, blue: 10^{19} cm^{-3})

$$G_0 = \frac{h\lambda_0}{c} B_{21} n_2 f(\lambda_0)\left(1 - \frac{g_2}{g_1}\frac{n_1}{n_2}\right)$$

where B_{21} is the Einstein coefficient for induced emission, n_2, the population density of level 2 and $f(\lambda_0)$, the spectral line shape at the central wavelength. The resulting gain coefficient for the neon-like argon system as a function of the temperature is shown in Fig. 42.9, right, for three typical electron densities, which can be achieved in gas discharge plasmas. For real systems, a gain of ~10 1/cm should be achieved. Thus, an electron density of $>10^{18}$ cm^{-3} at a temperature of around 100 eV is required. To determine the final intensity from a plasma medium of a certain length, limiting effects like diffraction of the laser light or saturation due to reduction of the population inversion by the light have to be taken into account.

References

Bauche J, Bauche-Arnoult C (1988) Phys Scr 37:659–663

Bergmann K, Schriever G, Rosier O, Müller M, Neff W, Lebert R (1999) Appl Opt 38(25):5413–5417

Bleiner D (2012) Comparison of laboratory-scale XUV laser with xFELs. In: Proceedings of SPIE 8678, Short-Wavelength Imaging and Spectroscopy Sources, p 867806

Chen F (1977) Introduction to plasma physics. Plenum Press

Elton RC (1990) X-ray lasers. Academic Press, New York

EUV Sources for Lithography, Vivek Bakshi (ed). SPIE Press (2006)

Fomenkov IV et al (2010) Laser-produced plasma light source for EUVL. In: Proceedings of SPIE 7636, Extreme Ultraviolet (EUV) lithography, p 763639

Griem H (1964) Plasma spectroscopy. McGraw-Hill, New York

Heinbuch S, Grisham M, Martz D, Rocca JJ (2005) Opt Express 13:4050–4055

Juschkin L, Derra G, Bergmann K (2008) EUV light sources. In Hippler R (ed) Low temperature plasmas. Wiley-VCH

van de Kerkhof M et al (2017) Enabling sub-10nm node lithography: presenting the NXE:3400B EUV scanner. In: Proceedings of SPIE 10143, Extreme Ultraviolet (EUV) lithography, p 101430D

Krall N, Trivelpiece A (1986) Principles of plasma physics. San Francisco Press Inc

MacGowan B et al (1987) Phys Rev Lett 59:2157–2160

Ruzic DN (2006) Origin of debris in EUV sources and its mitigation, p 957

Vieker J, Bergmann K (2017) J Phys D: Appl Phys 50:345601

von Wezyk A, Adrianov K, Wilhein Th, Bergmann K (2019) J Phys D: Appl Phys 52:505202

Wang et al (2005) Phys Rev A 72:053807

Chapter 43
EUV Optics

Klaus Bergmann and Jochen Vieker

43.1 Basic Considerations

Future applications based on extreme ultraviolet radiation in nano-patterning and surface analysis benefit from the recent progress in the development of suitable optical elements for beam shaping and imaging. The main aspect is the achievement of accuracy on the nanometer and sub-nanometer scale concerning the figure error as well as the roughness of optical surfaces and multilayer coatings. The determining parameter for any optical element is the index of refraction for the related material:

$$n = 1 - \delta + i\beta$$

For extreme ultraviolet radiation, the real part of the refractive index is usually close to below 1. Thus, the optical elements are not based on refraction in most cases. Furthermore, the imaginary part is so large that the penetration depth into a solid material is typically less than 1 μm, which also prohibits refractive-based elements apart from only a few exceptions.

In order to achieve a diffraction-limited resolution, the figure error of the optical elements has to be on the nanometer scale. In addition, the roughness of any involved surfaces or layers has to be on the nanometer scale or below in order to achieve sufficient high reflectivity close to the theoretical limit, which is determined by the chosen material. For reflective optics, the imaging properties are determined by the shape of the substrate and the degree of reflectivity by the coating. Latter has to be matched to the respective wavelength. Examples will be given in the proceeding chapters. An overview of X-ray optics is given in Spiller (1994).

K. Bergmann · J. Vieker (✉)
Fraunhofer ILT, Aachen, Germany
e-mail: jochen.vieker@ilt.fraunhofer.de

One simple element, which is widely used for imaging of sources, is the pinhole camera with pinhole diameters in the range of several tens of micrometer. An overview of further existing optical elements is listed below.

- Gracing incidence optics
- Multilayer-based Bragg mirrors
- Fresnel zone plates
- Bragg crystals
- Reflective gratings
- Refraction optics.

43.2 Grazing Incidence Optics

For many elements, the real part of the refractive index is slightly below 1 in the given spectral range. Thus, in gracing incidence total reflection occurs with a high degree of reflectivity. Especially for the EUV spectral region, the critical angle for total reflection is relatively large, which is attractive for a design of optical elements with a high collection angle. The reflectivity for a certain complex refractive index can be calculated by the Fresnel formula. For small angles, i.e. for gracing incidence conditions, the reflectivity can be expressed by

$$R(\theta) = \frac{\left| \theta - \sqrt{\left(\theta^2 - \theta_c^2\right) - 2i\beta} \right|^2}{\left| \theta + \sqrt{\left(\theta^2 - \theta_c^2\right) - 2i\beta} \right|^2}$$

With the critical angle given by the real part of the refractive index:

$$\theta_c \approx \sqrt{2\delta}$$

Figure 43.1 shows the reflectivity according to the above formula for different ratios of β/δ for the refractive index. For low absorption, β, the reflectivity is close to 1 below the critical angle and drops quickly for values above. With an increasing ratio of β/δ, the decay in reflectivity is less steep.

Figure 43.2 shows an example of the situation with $\beta/\delta \sim 0.1$ for Ruthenium, which is often used in gracing incidence optics for radiation with a wavelength around 13.5 nm. The Fresnel formula allows determining the reflectivity of an ideally smooth surface. Real surfaces show a decrease in reflectivity with increasing roughness σ. This influence can be expressed by an exponential factor, which is dependent on roughness and the wavelength. An example is the Debye–Waller factor.

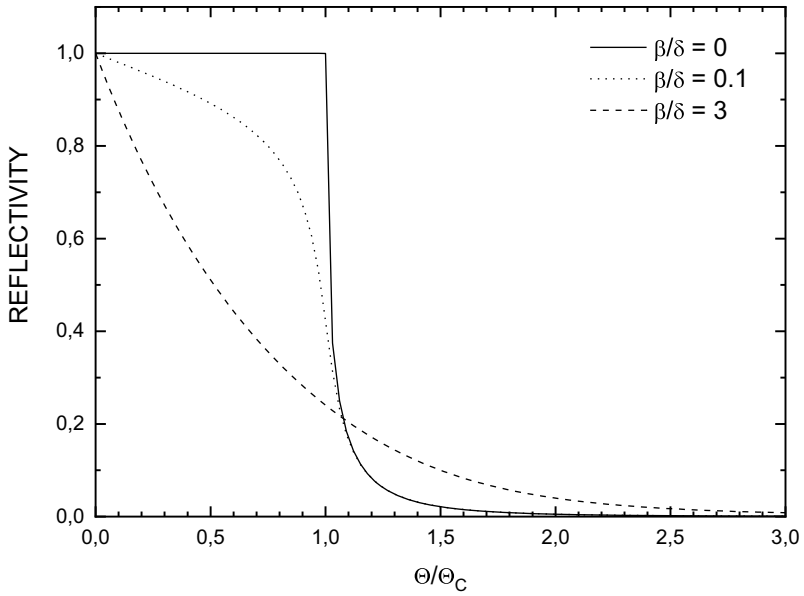$$\mathrm{Exp}\left(-8\pi^2\sigma^2/\lambda^2\right).$$

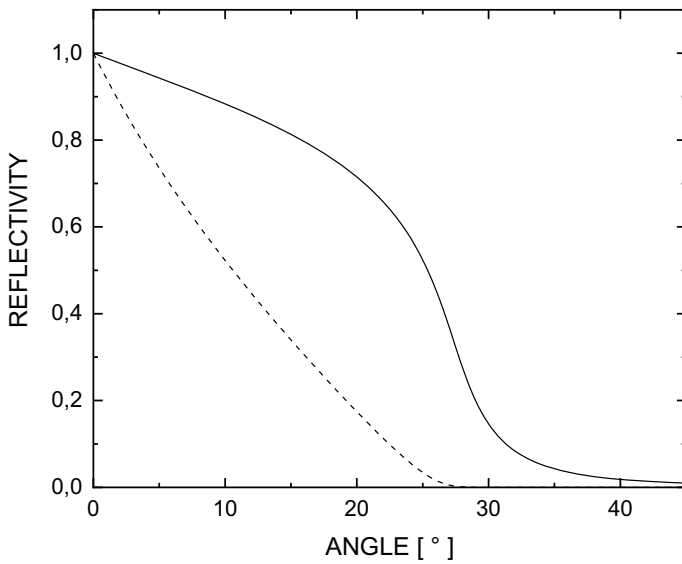**Fig. 43.1** Gracing incidence reflectivity for different ratios of δ/β for the refractive index

Fig. 43.2 Calculated reflectivity for Ruthenium for a surface with roughness of σ = 0 nm (full) and σ = 10 nm (dotted) according to atomic data from CXRO for a wavelength of 13.5 nm (92 eV) (Henke et al. 1993)

Fig. 43.3 Gracing incidence ellipsoidal collector for water window radiation at λ = 2.9 nm (inner diameter ~3 cm, material Aluminum)
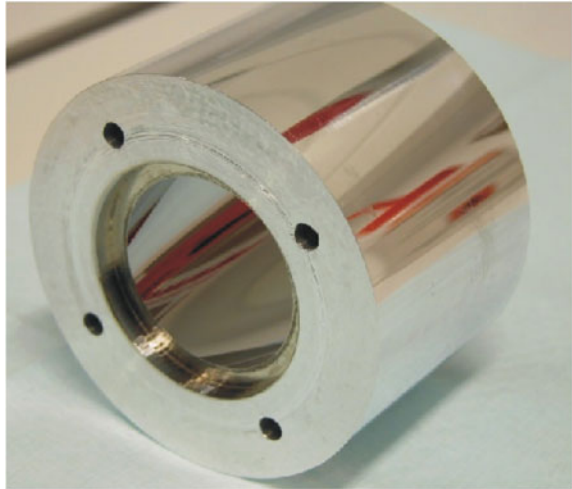
To achieve a reflectivity close to the theoretical limit, the roughness should be much smaller than the wavelength. For EUV optics, the roughness is usually in the range 0.1–1.0 nm. To illustrate the need for low roughness, the theoretical reflectivity with a roughness of 10 nm is shown for Ruthenium, where the drop in reflectivity for large angles between 10° and 20° is not tolerable anymore; see Fig. 43.3.

A typical application of gracing incidence-based optics is to collect the light from isotropic emitting light sources and focus it onto a sample or into an optical system. An example is a nested Wolter-type collector consisting of several shells with hyperbolical and ellipsoidal-shaped surfaces. With two reflections, high collection angles of up to 100° can be achieved with reasonably high transmission for 13.5 nm using Ru-coated shells (Bianucci et al. 2009; Marcuk and Egle 2005). Another example of a collector, as used in a soft X-ray microscope operating at a wavelength of 2.9 nm, is shown in Fig. 43.3.

43.3 Multilayer Bragg Mirrors

A high reflectivity for soft X-ray and extreme ultraviolet radiation can be achieved when using a multilayer coated surface as shown schematically in Fig. 43.4. Small fractions of the incident light, which is reflected at each boundary of the multilayer structure, are superimposed to an integrated reflected beam. Dependent on the wavelength, an appropriate material system for the multilayer structure has to be chosen. In order to achieve a high overall reflectivity, the surface roughness of the substrate and the layer boundaries have to be small, typically in the range of 0.1 nm.

With the number of multilayers, the peak reflectivity increases while the bandwidth decreases. Typically, up to 200 double layers are chosen in order to achieve
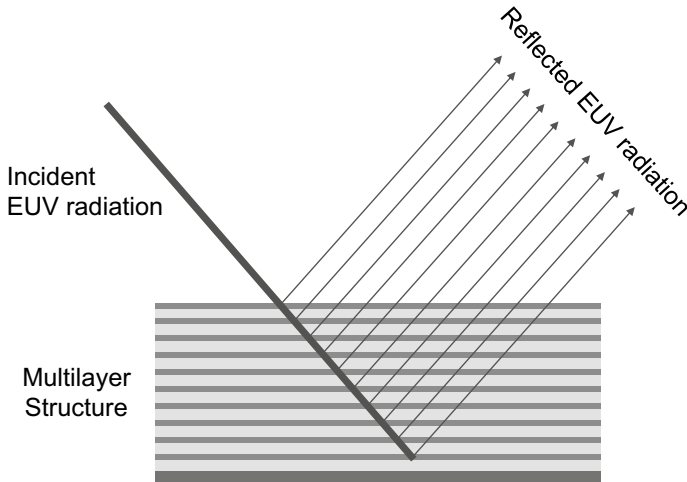
Fig. 43.4 Cross-section schematic of the reflection from a multilayer-coated surface

the theoretical limit of the reflectivity. The wavelength for the peak reflectivity can be expressed by the Bragg equation (with d being thickness of the double layer, m diffraction order, θ angle of incidence and δ' the bilayer weighted average of the real part of the refractive index):

$$m\lambda = 2dsin\theta\sqrt{1 - 2\delta'/sin^2\theta}$$

As an example of such multilayer coatings, Fig. 43.5 shows the theoretically achievable reflectivity for two material systems with peak reflectivity at 6.7 and 13.5 nm in the first diffraction order. The Mo/Si system is used for the optical system in a EUV lithography scanner (Marcuk and Egle 2005; Fu et al. 2019). Today, the achieved degree of reflectivity is close to this theoretical limit for the Mo/Si systems. The lower the wavelength, the more challenging it is to achieve this limit due to the reduced layer thickness down to a few nanometres and the increasing influence of roughness and diffusion at the boundaries (Wu and Kumar 2007).

The above-cited Bragg equation is valid for angles close to normal incidence. In general, the reflectivity is dependent on the polarization of the incident light. Especially, for 45° the p-polarization can be suppressed almost completely, and thus polarized EUV radiation can be obtained.

Current research on multilayer mirrors focuses on the increase of reflectivity by:

- further reduction of roughness and diffusion, e.g. by introducing further interlayers,
- development of broadband mirrors obtained by a variation of the layer thicknesses,
- capping layers to protect the multilayer systems from external influences like ion bombardment or contamination, or
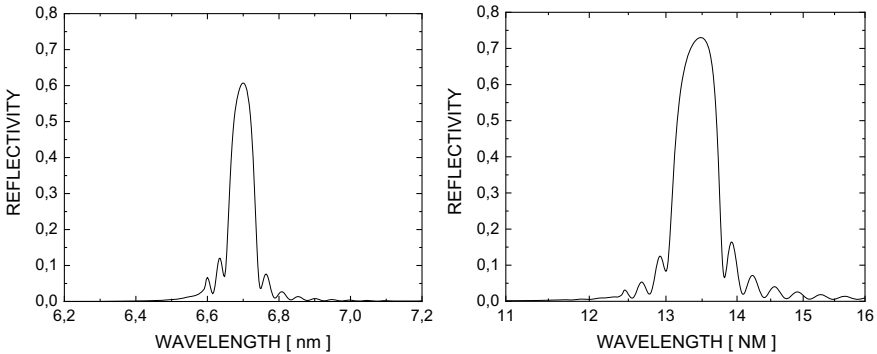
Fig. 43.5 Calculated multilayer reflectivity with center wavelength at 6.7 nm (La/B$_4$C with d = 3.44 nm, 140 layers) and 13.5 nm (Mo/Si with d = 6.9 nm, 40 layers) at normal incidence θ = 90° (Henke et al. 1993)

- cleaning techniques for contaminated mirror systems, especially caused by hydrocarbons.
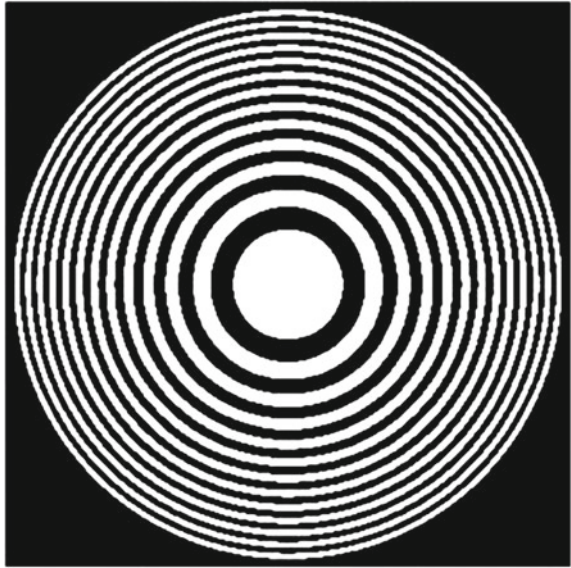
43.4 Zone Plates

One concept for an optical element with imaging properties is the Fresnel zone plate. Such zone plates are operating either in transmission or reflection. The principle should be illustrated with the transmission zone plate, which is shown schematically in Fig. 43.6. The area of either the transmitting or absorbing sections is the same. Thus, from an incident plane wave, only half of the light is transmitted and focused into the focal plane due to constructive interference at this point of the transmitted sectors at the zone plate. The focal length f, the wavelength λ and the radius r_n of the nth zone are related by

$$r_n^2 = n\lambda f + \frac{n^2\lambda^2}{4}$$

The focal intensity corresponds to an Airy disk where the radius, i.e. the spatial resolution, is limited by the thickness of the outermost shell Δr. In the case of this ideal configuration of completely absorbing and transmitting zones, the theoretical diffraction efficiency is $\eta = 1/\pi^2$. Higher diffraction efficiencies can be achieved using phase-shifting zone plates, where—instead of complete absorption—the phase is shifted in order to achieve constructive interference in the focal plane (Xu and Evans 1994).

The most prominent example of the applications of transmission zone plates is soft X-ray microscopy in the spectral range of the water window, i.e. from 2.3–4.4 nm (Kirz 1974). An absorbing structure, e.g. Gold or Nickel, is attached to a thin silicon

Fig. 43.6 Scheme of a
transmission Zone plate with
alternating transmission
(white) and absorption areas
(black)

nitride membrane with a thickness of about 100 nm thickness, which has a high
transmission for soft X-ray radiation. More information about zone plate fabrication
can be found in Refs. (Schneider 2003; Fujisaki et al. 1988).

References

Bianucci G et al (2009) Design and fabrication considerations of EUVL collectors for HVM. Proc
    SPIE 7271:72710C
Fu N, Liu Y, Ma X, Chen Z (2019) EUV lithography: state-of-the-art review. J Microelectron Manuf
    2(2):19020202
Fujisaki H (1988) Materials for phase zone plate fabrication for use with soft x-rays. Jpn J Appl
    Phys 27(7):1335–1337
Henke BL, Gullikson EM, Davis JC (1993) X-ray interactions: photoabsorption, scattering, trans-
    mission, and reflection at E=50-30000 eV, Z = 1–92. At Data Nucl Data Tables 54(2):181–342.
    www.henke.lbl.gov/optical_constants
Kirz J (1974) Phase zone plates for x rays and the extreme uv. J Opt Soc Am 64(3):301–309
Marcuk P, Egle W (2005) Grazing-incidence EUV collectors. In: Bakshi V (ed) EUV sources for
    lithography. SPIE Press, pp 873–892
Reinspach J, Lindblom M, Hofsten OV, Bertilson M, Hertz HM, Holmberg A (2010) Process
    development for improved soft X-ray zone plates. Microelectron Eng 87:1583–1586
Spiller E (1994) Soft x-ray optics. SPIE. ISBN: 9780819416544

Schneider G (2003) X-ray microscopy: methods and perspectives. Anal Bioanal Chem 376:558–561
Wu B, Kumar A (2007) Extreme ultraviolet lithography: a review. J Vac Sci Technol B 25(6):1743
Xu S, Evans BL (1994) The performance simulation of multilayer reflectors in soft x-ray and EUV regions. Model Simul Mater Sci Eng. 2:1079–1092

Chapter 44
EUV Measurement Technologies

Serhiy Danylyuk and Klaus Bergmann

44.1 Introduction

The main property of the EUV wavelength region is its strong absorption in all materials. It does not propagate through air gaps larger than a millimeter, and its solid-state penetration depth is below a micrometer. This labels this spectral region as being rather surface-sensitive, which makes it attractive for a large part of modern science, where the structure and composition of surfaces on the scale of several hundred nanometers is of interest. Being combined with the presence of many characteristic atomic resonances with energies in the EUV range makes these wavelengths inherently suitable for analytic techniques with high depth resolution and elemental sensitivity. Short wavelength in itself additionally provides high spatial resolution for imaging, further increasing the application potential of EUV radiation.

The technological base for the realization of EUV-based measurement methods and tools has become available only in the last decade, when EUV has been introduced as a new working wavelength for high-volume manufacturing (HVM) of semiconductor devices (Peeters et al. 2013). There, a specific wavelength (13.5 nm) out of the EUV range is used due to the availability of highly reflecting multilayer Bragg mirrors, which allows for the creation of efficient imaging optics. The technological and scientific advancement, required for the HVM introduction, led to the development of efficient and compact EUV sources (Bergmann et al. 1999), extremely smooth mirrors with large surfaces (Lowisch et al. 2010), large-area ultra-thin membranes (pellicles) with high EUV transmission (Turkot et al. 2016) and high-speed in-vacuum positioning systems with single nanometer precision (Jong et al. 2009). The need for actinic (at-wavelength) metrology also led to the development of the first laboratory-based EUV metrology systems, such as mask blank inspection tools (Tchikoulaeva et al. 2013; Juschkin et al. 2011), aerial image metrology

S. Danylyuk (✉) · K. Bergmann
Fraunhofer ILT, Aachen, Germany
e-mail: serhiy.danylyuk@ilt.fraunhofer.de

system (AIMS) (Hellweg et al. 2011) or tools for measurements of pellicle transmission uniformity and EUV resist tester (Lebert et al. 2019). As a result, significant scientific and technological know-how has been accumulated regarding the production, utilization and measurement of EUV radiation. This has opened the way for the practical realization of optical metrology in the EUV wavelength range.

The following two exemplary applications will be described in detail—EUV detection of nanoscale multilayer defects by EUV dark-field microscopy and broadband EUV reflectometry for thin film characterization.

44.2 EUV Dark-Field Microscopy

One of the consequences of short wavelengths is an efficient scattering and diffraction of EUV radiation on nanoscale-sized structures, especially when compared with longer UV and visible wavelengths. This can be utilized for the detection and inspection of nanoparticles and nanodefects even when the size of structures drops to the single nanometer range.

This difference in scattering efficiency and character can be conveniently illustrated by employing the Mie scattering theory, which provides a precise analytical solution for the scattering of light on spherical particles (Bohren and Huffmann 1983; Herbert 2018).

As can be seen from Fig. 44.1, the scattering of 13.5 nm radiation on a spherical particle with a diameter of 25 nm has strong directionality and feature-rich angular scattering profile in contrast to the often utilized 193 nm DUV wavelength. Despite the backscattering (at 180° angle) intensity being higher for 193 nm irradiation (see Fig. 44.1a), for such small particles the absolute integrated diffraction efficiency is higher for EUV irradiation, as DUV interacts with deeply subwavelength-sized particle weakly (see Fig. 44.1b). Even more importantly, most of the energy is contained in the vicinity of the propagating beam, which allows for practical utilization of the effect.

This enhanced scattering of EUV radiation is being employed for an important task of defect inspection of EUV masks and mask blanks in semiconductor manufacturing. The size of the EUV mask is $6'' \times 6''$ and for advanced lithographic nodes, the defects of 10 nm in size or above become critical. Inspecting such large areas with high-resolution techniques, such as scanning electron microscopy (SEM) or atomic force microscopy, would take weeks if not months, making direct resolving techniques impractical. The solution is to use the strong scattering of EUV on nanodefects without resolving them by dark-field microscopy.

The typical scheme of such a system is shown in Fig. 44.2. The radiation from the compact EUV source is collected by the grazing incidence collector and then guided through the deflection mirror to the inspected multilayer-coated mask blank. The directly reflected light is then blocked by the mirror, and only light scattered to higher angles is collected by a Schwarzschild-type objective and imaged onto the CCD detector with ~1 μm resolution. In this case of a clean mask surface, no bright
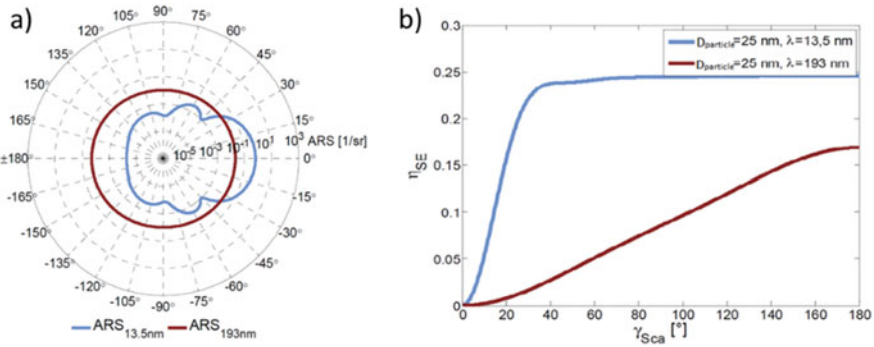
Fig. 44.1 a Angular resolved scattering (ARS) profiles of light with wavelengths 193 nm (red) and 13.5 nm (blue) on spherical Cr particle with diameter of 25 nm. **b** Integrated scattering efficiency in dependence of half-angle of angular range of integration

spot is observed on the camera, but in case of a defect the collected signal increases strongly and the defect gets detected (see inset in Fig. 44.2).

In this way, the defect position is registered with ~1 µm precision. The second magnification step is required to resolve the defect with a higher resolution. But in this way, large mask area can be fully inspected within 4–6 h (Herbert 2018), enabling quality and degradation control and subsequent defect mitigation strategies, such as selective defect removal or covering of the defect with an absorber layer. Additionally, an analysis of scattering signal behavior in dependence on incidence angle, θ (see
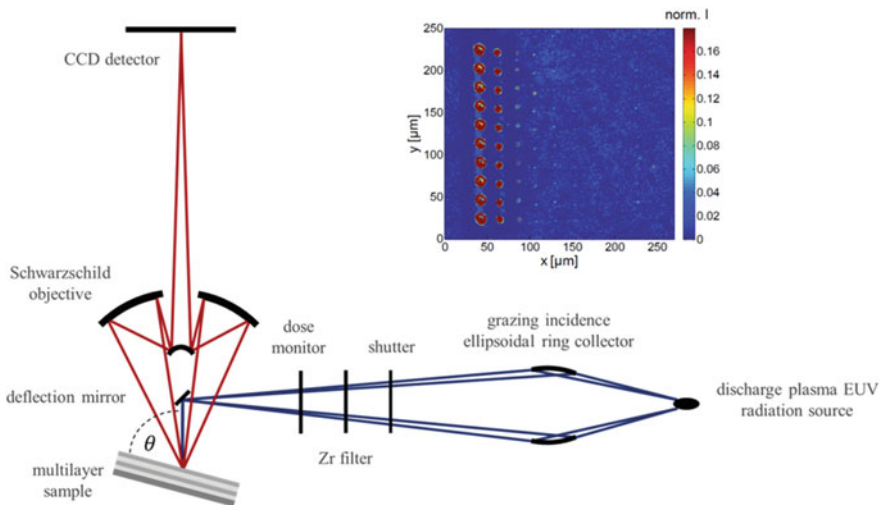

Fig. 44.2 Scheme of EUV dark-field microscopy for defect inspection. Inset: Exemplary image of array of programmed defects with lateral sizes down to 40 nm

Fig. 44.2) can be performed to obtain additional information about the in-depth location of a defect and its composition (Bahrenberg et al. 2013).

44.3   Broadband EUV Reflectometry

Modern nanotechnology trend is not only to decrease the lateral feature size of employed nanostructures but also to utilize films and film stacks with sub-10 nm layer thicknesses (Clark 2014). As the variety of employed materials moves away from basic silicon/silicon oxide stacks, the chemical composition of layers and inter-layers becomes more complex, which requires novel high-precision non-destructive characterization methods. The ideal method should, on the one hand, be fast enough for industrial use, and, on the other hand, provide information about the chemical composition of thin films and interlayers, their thicknesses with sub-nm precision and be non-destructive. One of the most promising methods is spectroscopic reflectom-etry in the extreme ultraviolet (EUV) wavelength range (Banyay et al. 2012). Devel-oped previously with synchrotrons as radiation sources (Scholze et al. 2005), the method is currently under development with laboratory plasma-based EUV sources (Bakshi et al. 2007; Bergmann et al. 2009) which should enable its widespread application. Especially practical is the utilization of grazing incidence angles under or near the critical angle (see Chap. 42) that provide high reflectivity and, conse-quently, high throughput of the measurement tools. For Si-based applications, the wavelength region near the $L_{2,3}$ absorption edges near the 12.4 nm wavelength is of special interest. Here, one can expect enhanced sensitivity to the stoichiometry of Si-based compounds and materials, such as SiOx, SiNx, poly-Si and SiGe.

EUV radiation sources, based on high Z-element plasmas, are inherently broad-band (see Chap. 41). It is efficient to utilize broadband approaches that can use most of the photons produced by the source. Recently, the first experimental realiza-tion of a multi-angle spectroscopic reflectometer operating in the wavelength region between 9 and 17 nm and with grazing illumination angles between 2° and 13° was reported (Danylyuk et al. 2013). The combination of spectrally and angularly broad-band measurements enables a significant increase in the precision and decrease in the ambiguity of the analysis.

The principal scheme and a photo of the setup are shown in Fig. 44.3.

Depending on the used gas or gas mixture, the EUV source can produce light in the whole EUV wavelength region between 5 and 40 nm. For spectroscopic reflectometry, quasi-continuous spectra from heavy gases, such as xenon, are preferable, enabling single pulse measurements of reflectivity in the wavelength range from 10.5 to 16 nm (Banyay et al. 2012; Banyay and Juschkin 2009). To extend this range, an optimized krypton/xenon mixture was utilized to produce quasi-continuous spectra in the region between 9.5 and 17 nm that in the future can be extended down to ~7 nm or even further utilized by more complex gas mixtures (see exemplary spectra in Chap. 41).

The emitted light propagates through a slit of 50 μm width. After the beam passes the first grating, the resulting first diffraction order is measured by the first
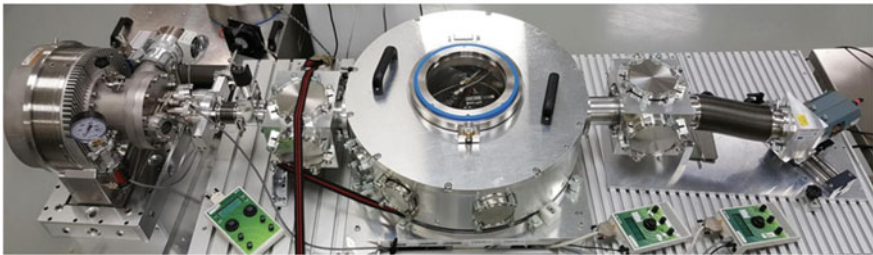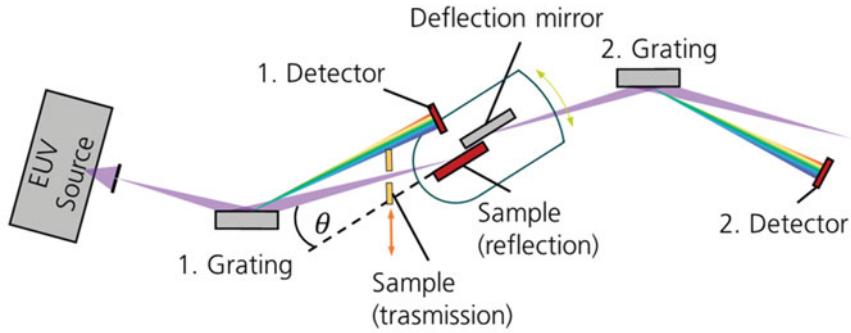
Fig. 44.3 Principal scheme (top) and photo (bottom) of a laboratory-based broadband EUV reflectometer

CCD detector and the zeroth order is focused onto the sample. The normal incidence beam size on the sample is 55 μm $\times$ 3.5 mm. The beam, reflected from the sample, propagates to a deflection mirror, which is parallel to the sample and mounted on a linear stage that moves parallel to the sample. Both, the sample and the mirror are mounted on a rotational stage, so that the incidence angle to the sample can be varied while keeping the sample and the mirror parallel. By that, the beam, reflected from the mirror, has a constant position for different incidence angles to the sample and propagates to the second grating. The first diffraction order of the second grating is detected by the second CCD detector. The exposure times of both detectors are synchronized, so that they detect the same light pulse from the source at a time.

To extract the thickness and roughness parameters of an unknown layer system, the measured reflectivity spectrum can be used as a target spectrum for modeling the layers. The modeling procedure contains layer thicknesses and roughnesses as variables, so the best match of the modeled and experimental reflectivity spectra will reveal the parameters of the sample. The modeling can be performed using both absolute reflectivity data and also on relative reflectivity curves, where reflectivity at all angles is normalized to reflectivity on a single, typically lowest used angle. Such self-calibration increases the quality and consistency of measurements of the laboratory reflectometer tool.

The sensitivity of the method was demonstrated by measuring a set of HfO_2 thin layers of different thicknesses that were grown using atomic layer deposition on p-Si (001) substrates (Danylyuk et al. 2013). The spectra measured at 12° incidence were
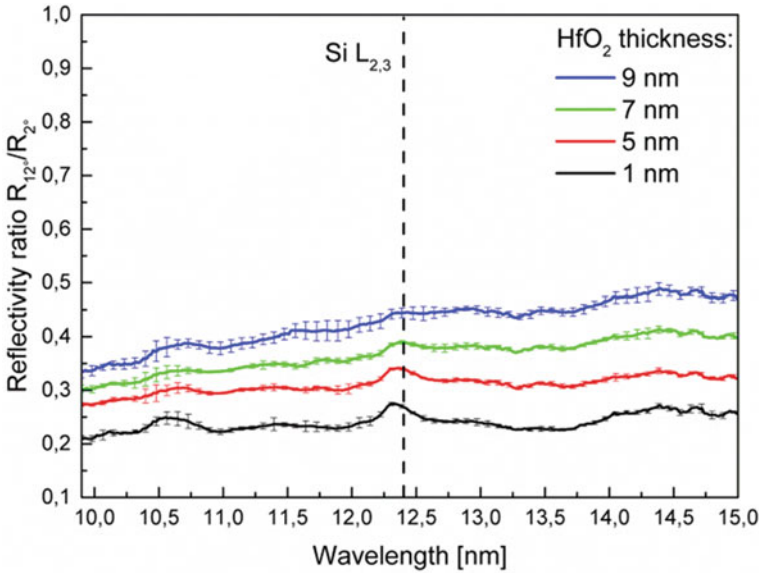
Fig. 44.4 Measured EUV reflectivity ratios $R_{12°}/R_{2°}$ of the HfO_2 thin layers (Danylyuk et al. 2013)

normalized to measurements done at $2°$. The resulting relative reflectivity curves are shown in Fig. 44.4. The high sensitivity of the method is apparent, since a few-nanometer difference in the layer thicknesses results in a considerable difference between the measured curves.

Subsequent modeling of the obtained reflectivity together with multiple incidence angle data allows for the extraction of detailed layer parameters. For example, the reflectivity data at several incidence angles of the HfO_2 test sample with 9 nm target thickness (Fig. 44.5) can be used as a fit basis to obtain the following structural model: thickness of intermediate SiO_2 layer—0.26 nm, and HfO_2 layer thickness 10.0 nm with a slight excess of oxygen ($HfO_{2.075}$) leading to the reduced density of the film (8.43 g/cm³). Here, atomic scattering factors from Henke et al. (1993) were used as a basis for modeling. At the surface, there is a 0.68 nm thick amorphous carbon contamination layer. This model agrees well with the experimental results at all measured angles. The result is also in good agreement with an expectation from the growth parameters.

The developed reflectometry tool allows fast, precise and non-destructive measurements of the properties of thin films and film stacks. The multi-angle reflectometry measurements enable not only thin film modelings but also the unambiguous determination of the complex refractive indices, which is a non-trivial task in the EUV wavelength region. It is also envisioned to extend this method to the analysis of not only flat films and film stacks but also to structural and compositional analysis of nano- and microstructured surfaces and interfaces (Bahrenberg et al. 2019).
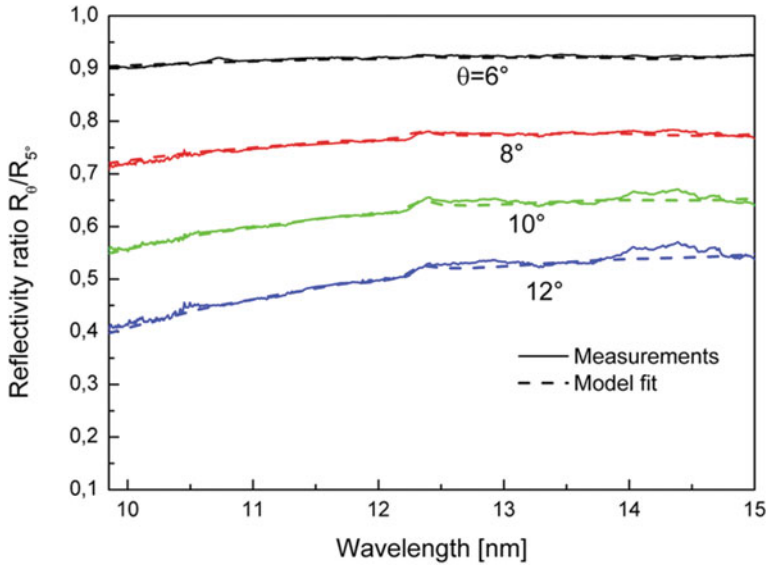
Fig. 44.5 Measured reflectivity ratios $R_\theta/R_{5°}$ of the samples with HfO_2 target thickness of 9 nm with $\theta = 6°$, $8°$, $10°$ and $12°$. Solid line—laboratory tool measurements; dashed lines—fitted model curves (Danylyuk et al. 2013)

References

Bahrenberg L, Herbert S, Tempeler J, Maryasov A, Hofmann O, Danylyuk S, Lebert R, Loosen P, Juschkin L (2013) Analysis of distinct scattering of extreme ultraviolet phase and amplitude multilayer defects with an actinic dark-field microscope. In: Proceedings of SPIE, extreme ultraviolet (EUV) lithography VI, vol 9422, p 942229

Bahrenberg L, Danylyuk S, Michels R, Glabisch S, Ghafoori M, Brose S, Stollenwerk J, Loosen P (2019) Spectroscopic reflectometry in the extreme ultraviolet for critical dimension metrology. In: Proceedings of SPIE—the international society for optical engineering, vol 10959, p 109591X

Bakshi V, Lebert R, Jägle B, Wies Ch, Stamm U, Kleinschmidt J, Schriever G, Ziener Ch, Corthout M, Pankert J, Bergmann K, Neff W, Egbert A, Gustafson D (2007) Status report on EUV source development and EUV source applications in EUVL. In: Proceedings of SPIE, vol 6533, p 653313-1

Banyay M, Juschkin L (2009) Table-top reflectometer in the extreme ultraviolet for surface sensitive analysis. Appl Phys Lett 94:063507–063511

Banyay M, Juschkin L, Bersch E, Franca D, Liehr M, Diebold A (2012) Cross characterization of ultrathin interlayers in HfO2 high-k stacks by angle resolved x-ray photoelectron spectroscopy, medium energy ion scattering, and grazing incidence extreme ultraviolet reflectometry. J Vac Sci Technol A 30:041306–041311

Bergmann K, Schriever G, Rosier O, Müller M, Neff W, Lebert R (1999) Highly repetitive, extreme-ultraviolet radiation source based on a gas-discharge plasma. Appl Optics 38(25):5413–5417

Bergmann K, Danylyuk SV, Juschkin L (2009) Optimization of a gas discharge plasma source for extreme ultraviolet interference lithography at a wavelength of 11 nm. J Appl Phys 106:073309–073311

Bohren C, Huffmann D (1983) Absorption and scattering of light by small particles. Wiley

Clark RD (2014) Emerging applications for high K materials in VLSI technology. Materials 7:2913

Danylyuk S, Herbert S, Loosen P, Lebert R, Schäfer A, Schubert J, Tryus M, Juschkin L (2013) Multi-angle spectroscopic extreme ultraviolet reflectometry for analysis of thin films and interfaces. Phys Status Solidi C 12(3):318–322

Hellweg D, Ruoff J, Herkommer A, Stühler J, Ihl Th, Feldmann H, Ringel M, Strößner U, Perlitz S, Harnisch W (2011) AIMS EUV: the actinic aerial image review platform for EUV masks. In: Proceedings of SPIE, extreme ultraviolet (EUV) lithography II, vol 7969, p 79690H

Henke BL, Gullikson EM, Davis JC (1993) Atomic data and nuclear data tables. 54(2):181

Herbert S (2018) Bildgebung im kurzwelligen Spektralbereich zur Inspektion von Nanodefekten. Dissertation, Rheinisch-Westfälische Technische Hochschule Aachen

de Jong F, van der Pasch B, Castenmiller T, Vleeming B, Droste R, van de Mast F (2009) Enabling the lithography roadmap: an immersion tool based on a novel stage positioning system. In: Proceedings of SPIE, optical microlithography XXII, vol 7274, p 72741S

Juschkin L, Maryasov A, Herbert S, Aretz A, Bergmann K, Lebert R (2011) EUV dark-field microscopy for defect inspection. In: AIP conference proceedings, vol 1365, no 1, pp 265–268

Lebert R, Biermanns-Föth A, Arps J, Missalla Th, Phiesel Ch, Piel Ch (2019) EUV metrology tools diversified from common building blocks and experience. In: Proceedings of SPIE, International conference on extreme ultraviolet lithography 2019, vol 11147, p 111471E

Lowisch M, Kuerz P, Mann H-J, Natt O, Thuering B (2010) Optics for EUV production. In: Proceedings of SPIE, extreme ultraviolet (EUV) lithography, vol 7636, p 763603

Peeters R, Lok S, van Alphen E, Harned N, Kuerz P, Lowisch M, Meijer F, Ockwell D, van Setten E, Schiffelers G, van der Horst J-W, Stoeldraijer J, Kazinczi R, Droste R, Meiling H, Kool R (2013) ASML's NXE platform performance and volume introduction. In: Proceedings of SPIE, extreme ultraviolet (EUV) lithography IV, vol 8679, p 86791F

Scholze F, Laubis Ch, Buchholz Ch, Fischer A, Plöger S, Wagner H, Ulm G (2005) Status of EUV reflectometry at PTB. In: Proceedings of SPIE, vol 5751

Tchikoulaeva A, Miyai H, Suzuki T, Takehisa K, Kusunose H, Yamane T, Terasawa T, Watanabe H, Inoue S, Mori I (2013) EUV actinic blank inspection: from prototype to production. In: Proceedings of SPIE, extreme ultraviolet (EUV) lithography IV, vol 8679, p 86790I

Turkot B, Carson SL, Lio A, Liang T, Phillips M, McCool B, Stenehjem E, Crimmins T, Zhang G, Sivakumar S (2016) EUV progress toward HVM readiness. In: Proceedings of SPIE, extreme ultraviolet (EUV) lithography VII, vol 9776, p 977602